



MAM SCHOOL OF ENGINEERING

Accredited By NAAC

Approved by AICTE, New Delhi || Affiliated to Anna University, Chennai
Siruganur, Trichy-621105

Faculty publications details 2020-2021

S.No	NAME OF THE FACULTY	TITLE	PUBLISHED IN
1	K.SATHISH KUMAR	Fast Detection of Transformed Data Leaks in Wireless Sensor Network	International Journal of Scientific Research in Engineering and Management (IJSREM)

K. Sathish Kumar
HOD 25/4/21

Head of the Department
Department of Computer Science & Engineering
M.A.M. School of Engineering
Siruganur, Tiruchirappalli - 621 105.


PRINCIPAL

PRINCIPAL
M.A.M. SCHOOL OF ENGINEERING
SIRIGANUR, TIRUCHIRAPPALLI-621 105



ISSN: 2582-3930

International Journal of Scientific Research in Engineering and Management

is hereby awarding this certificate to

SATHISH KUMAR K

in recognition the publication of manuscript entitled

Fast Detection of Transformed Data Leaks in Wireless Sensor Network

published in Ijsrem. Journal Volume 05 Issue 04 April, 2021

www.ijrem.com


Editor in Chief
E-mail: editor@ijrem.com

Fast Detection of Transformed Data Leaks in Wireless Sensor Network

SATHISH KUMAR K¹, THANGAM M², SOWMIYA M³

¹Computer Science and Engineering & M.A.M. School of Engineering, Trichy

²Computer Science and Engineering & M.A.M. School of Engineering, Trichy

³Computer Science and Engineering & M.A.M. School of Engineering, Trichy

Abstract -Wireless Sensor Networks (WSNs) are emerging as a promising technology because of their wide range of applications in industrial, environmental monitoring, etc. Because of their inherent resource-constrained characteristics, they are prone to various security attacks that seriously affect data collection. The current trust-based route strategies face some challenging issues: (1) the core of a trust route lies in obtaining trust. (2) Energy efficiency. Because it is difficult to locate malicious nodes, the security route is still a challenging issue. Thus, there are still issues worthy of further study. Security and trust routing through an active detection route protocol is proposed in this project. The Active Trust scheme fully uses residue energy to construct multiple detection routes.

Key Words: resource-constrained, trust-based, Energy efficiency

1. INTRODUCTION

A WSN can generally be described as a network of nodes that cooperatively sense and control the environment, enabling interaction between persons or computers and the surrounding environment.

WSNs nowadays usually include sensor nodes, actuator nodes, gateways, and clients. A large number of sensor nodes deployed randomly inside or near the monitoring area (sensor field), form networks through self-organization. Sensor nodes monitor the collected data to transmit along to other sensor nodes by hopping. It is the user who configures and manages the WSN with the management node: publishes monitoring missions and collection of the monitored data.

2. OBJECTIVE

The Active Trust scheme has better security performance. Compared with previous research, nodal trust can be obtained in Active Trust. The route is created by the following principle. First, choose nodes with high trust to avoid the potential attack, and then route along a successful detection route. Through the above approach, network security can be improved.

3. EXISTING SYSTEM

The main feature is to create a route by selecting nodes with high trust because such nodes have a higher probability of routing successfully; thus, routes created in this manner can forward data to the sink with a higher success probability. However, the current trust-based route strategies face some challenging issues.

4. DISADVANTAGES

Attacks in mobile wireless networks are very challenging because the network topology can be highly dynamic due to node movements. Therefore, techniques that are designed for static networks are not applicable.

The network may not always be connected. Therefore, approaches that rely on network connectivity have limited applicability.

The limited resources (computation, communication, and battery life) demand that node attacks must be performed in a resource-conserving manner.

5. LITERATURE SURVEY

AD HOC ON-DEMAND DISTANCE VECTOR ROUTING:

The Ad hoc On-Demand Distance Vector (AODV) algorithm enables dynamic, self-starting, multihop routing between participating mobile nodes wishing to establish and maintain an ad hoc network. AODV allows mobile nodes to obtain routes quickly for new destinations and does not require nodes to maintain routes to destinations that are not in active communication. AODV allows mobile nodes to respond to link breakages and changes in network topology timely manner. The operation of AODV is loop-free, and avoiding the Bellman-Ford "counting to infinity" problem offers quick convergence when the ad hoc network topology changes (typically, when a node moves in the network). When links break, AODV causes the affected set of nodes to be notified so that they can invalidate the routes using the lost link.

GRADIENT-BASED ROUTING:

The key idea in GBR is to memorize the number of hops when the interest is diffused through the whole network. As such, each node can calculate a parameter called the height of the node, which is the minimum

number of hops to reach the BS. The difference between a node's height and that of its neighbor is considered the gradient on that link. A packet is forwarded on a link with the largest gradient. GBR uses some auxiliary techniques such as data aggregation and traffic spreading to uniformly divide the traffic over the network. When multiple paths pass through a node, which acts as a relay node, that relay node may combine data 12 according to a certain function.

6. ROUTING PROTOCOLS WITH RANDOM WALKS

The objective of the random walks-based routing technique is to achieve load balancing in a statistical sense and by making use of multi-path routing in WSNs. This technique considers only large-scale networks where nodes have very limited mobility. In this protocol, it is assumed that sensor nodes can be turned on or off at random times. Further, each node has a unique identifier but no location information is needed. Nodes were arranged such that each node falls exactly on one crossing point of a regular grid on a plane, but the topology can be irregular.

7. PROPOSED SYSTEM

Active Detection Routing Protocol: A detection route refers to a route without data packets whose goal is to convince the adversary to launch an attack so the system can identify the attack behavior and then mark the attack location.

Thus, the system can lower the trust of suspicious nodes and increment the trust of nodes in successful routing routes.

Through active detection routing, nodal trust can be quickly obtained, and it can effectively guide the data route in choosing nodes with high trust to avoid attacks.

8. ADVANTAGES

Our approach has the advantage that it is applicable to both connected and disconnected networks. Our schemes achieve high failure detection rates, low false-positive rates, and low communication overhead.

Table -1: Software & Hardware Requirements

Software Specification	
Server Side Programming	PHP
Middleware Programming	JAVASCRIPT
Operating System	Windows 8
Web Server	Internet Information Server
Client Script	HTML, CSS and Java Script
Database	MYSQL

Hardware Specification	
Processor	Intel Core i3-2330M CPU 2.20 GHz
Hard Disk	160 GB
Monitor	LG 17" Color Monitor
RAM	4 GB
Keyboard	104 Keys Multimedia Keyboard
Mouse	wireless Optical Mouse
CD - ROM	52X CD-ROM

9. SYSTEM ARCHITECTURE

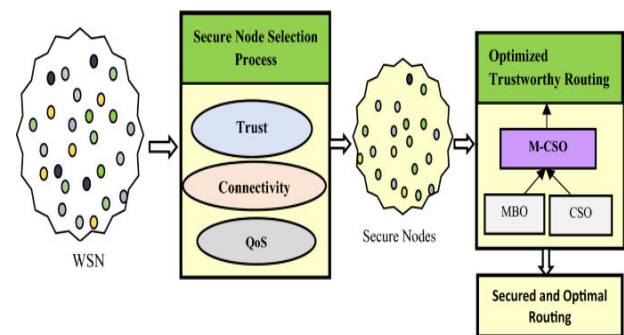


Fig -1: Figure

3. CONCLUSIONS

The proposed a novel security and trust routing scheme based on active detection and it has the following excellent properties: (1) High successful routing probability, security, and scalability. The ActiveTrust scheme can quickly detect the nodal trust and then avoid suspicious nodes to quickly achieve a nearly 100% successful routing probability. (2) High energy efficiency. The ActiveTrust scheme fully uses residue energy to construct multiple detection routes. The theoretical analysis and experimental results have shown that our scheme improves the successful routing probability by more than 3 times, up to 10 times in some cases. Further, our scheme improves both energy efficiency and network security performance. It has important significance for wireless sensor network security.

REFERENCES

1. Y. Hu, M. Dong, K. Ota, et al. "Mobile Target Detection in Wireless Sensor Networks with Adjustable Sensing Frequency," IEEE System Journal, Doi: 10.1109/JSYST.2014.2308391, 2014.
2. M. Dong, K. Ota, A. Liu, et al. "Joint Optimization of Lifetime and Transport Delay under Reliability Constraint Wireless Sensor Networks," IEEE transactions on Parallel and Distributed Systems, vol. 27, no. 1, pp. 225-236, 2016.

3. S. He, J. Chen, F. Jiang, et al. "Energy provisioning in wireless rechargeable sensor networks," IEEE transactions on mobile computing, vol. 12, no. 10, pp. 1931-1942, 2013.
4. X.Liu, M. Dong, K. Ota, P. Hung, A. Liu. "Service Pricing Decision in Cyber-Physical Systems: Insights from Game Theory," IEEE Transactions on Services Computing, vol. 9, no. 2, pp. 186-198, 2016.
5. C. Zhu, H. Nicanfar, V. C. M. Leung, et al. "An Authenticated Trust and Reputation Calculation and Management System for Cloud and Sensor Networks Integration," IEEE Transactions on Information Forensics and Security, vol. 10, no. 1, pp. 118-131, 2015.

Automatic Lake Cleaning Robot Using IOT

P.Kavitha Head of the department/ECE

M.A.M.SCHOOL OF ENGINEERINGS

SiruganurTrichy

T.Ashok,Head of the Department/BME

Kongunadu College of Engineering,Tholurpatti

S.Subha, K.Malavika, A.Mohanapriya

M.A.M.SCHOOL OF ENGINEERING

SiruganurTrichy

Abstract:

The world is covered by $\frac{3}{4}$ th of water and in our country there were lots of water saving techniques such as dams, water tanks, lakes, pools, etc... but the important problem of the water is that it has easily get polluted by solid waste and makes bad odour causes due to the industries, humans who disposed the solid waste in the stagnant water such as ponds, lake and in the sea. Due to these water pollution the aquatic animals that living in water may dead and land animals drink the water gets infected not only for animals ,polluted water causes skin disease to human being . We have proposed a technique to control the water pollution by using robot. A new generation of river cleaning robot have been presented in this research. The enhancement accomplished by the new design & features that makes river cleaning robot with iot technology more competitive.

Key Words: microcontroller, IOT receiver, DC motor, motor driver etc.

I. Introduction

The solid waste in water can removed by using this water cleaning robot . This machine is consists of cleaner mechanism which collect & remove the wastage, garbage& from water bodies.Machine will if the waste

surface debris from the water bodies, this will ultimately result in reduction of water pollution and lastly the aquatic animal's death others problems can reduce. It consists of Belt drive mechanism which lifts the debris from the water. The use of this project will made in rivers, ponds, lakes and other water bodies for to clean the surface water debris from bodies. Similarly they are lots of problems of water pollution under Godavari, Gangai River which affect the acoustic, human life & beauty of River. The biggest impact of cleaning the chemical wastes can cause respiratory diseases and it plays a challenging issue for municipality officers. Water damage is classified as three types of contaminated water. They are clean water, gray water and black water. Clean water is from a broken water supply line or leaking faucet. If not treated quickly, this water can turn into black water or gray water, depending on length of time, temperature, and contact with surrounding contaminants. Drainage pipes used for the disposal of sewage and unfortunately sometimes there will be loss of human life while cleaning the blockages in the drainage pipes. The municipality workers are only responsible to ensure that the sewage is clean or not though they clean the ditch the sat the

side of buildings, they can't clean very wide sewage. The municipality workers need to get down into the sewage sludge to clean the wide sewage. It affects the health badly and causes skin allergies.

II. Existing Method

- Man Power
- Vacuum Cleaner
- Road Runner

Disadvantage of this system is Low efficiency

- Takes more time
- Costly

III. Proposed Method

To overcome those issues, we have designed and simulated a rubbish collecting system that is expected to further develop experimentally for the application in the real world. Hence, it will be able to get a wide assortment of debris, including gliding litter, trash, logs, disposed tires and others. Thus, it is expected to enhance the demand and need for a design of a river cleaning machine that is able for tidying up waste from rivers, channels and lakes and overcome the current issues. The integrated system incorporates the usage of IoT technology that has the ability to monitor and control the entire process.

IV. Hardware requirements

- Arduino UNO.
- L293D Motor Driver or H-Bridge.
- DCMotor.
- IOT MODULE.

V. Software requirements

- Arduino IDE.
- PROTEUS SOFTWARE : The proteus design suite is a proprietary software tool suite used primarily for electronic design automation. To create schematics and electronics prints for manufacturing printed

circuited boards ,Size 248 Mb

Literature Survey :

A. Metallic Scrap Collection Robot with Efficient Trajectory

We have developed an electromagnetic robot that can recognize and collect various metal scraps spread across an area. The process of recognition is carried out with the help of the image processing techniques on the images obtained through the camera installed in the area. The robot collects the scrap using the electromagnetic arm by visiting it. Our aim in this work is to control the robot's trajectory so that all the scraps identified can be collected within a minimum time by minimizing the distance travelled by the robot.

Disadvantage

Cannot be used in different locations

B. Development of an autonomous beach cleaning robot

The paper discusses two aspects of the robot: the refuse collection mechanism and the autonomous navigation system. In order to enable effective collection of refuse from a sandy surface, we developed a mechanism that mimics cleaning of a floor using a broom and dustpan. To identify its own position, the robot was equipped with a scanning range finder, which measured the position of two poles placed at the corners of the designated work area

Disadvantages

works only on water surface cannot be multiuse .

C. Mechanism that collected items as if humans clean a floor with a broom and dustpan

We have been developing a compact beach cleaning robot "Hirottaro 3". In order to collect small refuse effectively on a sandy surface, the robot was equipped with a. Furthermore, the robot was capable of traveling autonomously on the sandy beach that had insufficient natural landmarks by self-localization using poles and a scanning range finder. This paper reports the performance evaluation of refuse collection and autonomous navigation on the sandy beach

Disadvantage

Unable to collect at sand

D. Review on the Development of Road Cleaning and Scrap Collecting Robotic Vehicle

This paper shows continuous examination done on the advancement of Road Cleaning and Scrap Collecting Robotic Vehicle and its uses on different surfaces. As neatness of our condition has its own ideal conditions which makes it a basic topic of research nowadays as it goes under Swacchh Bharat Abhiyan, an activity taken by the legislature of India additionally it favors green collecting structures and we pointed conveying cleaner streets by utilizing least endeavors.

Disadvantage

Needs 2 different mechanism to operate complex structure too.

E. Garbage Collection Robot on the Beach using Wireless Communications

This article presents the garbage collection robot on the beach

using wireless communications.

The user can control a robot via a program developed from Visual Basic 2005 application based on Window XP. The commands from user are sent via IOT to the processor for processing The results of robot performances were found that the robot can move with an average speed of 0.5 meters per second on the sand via wireless communication and collect the big garbage with side 12.5 x 49 cm, for example, glass bottles, and plastic, etc.

Disadvantage

Size constraint and controlling range is small .

VII. Block Diagram

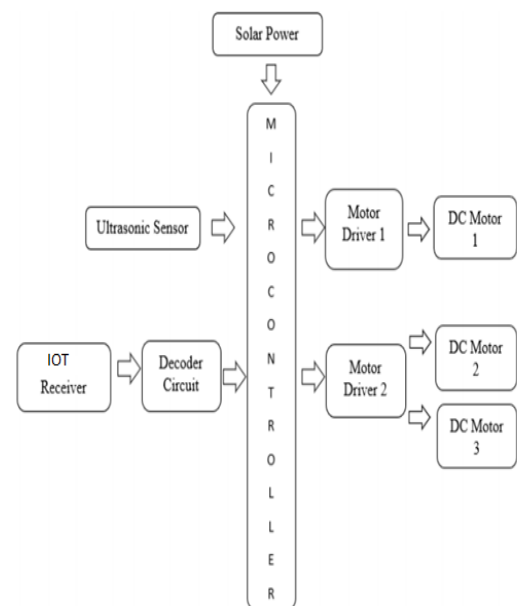


Fig -1: Block Diagram

The river cleaning robot is integrated into three segments shown in Figure 1. The first segment of the system involves the input source of the mechanism that consists of the magnetic switch mobile phone application and solar panel. The processor development was the second segment of system development. In this segment, the microcontroller processor is integrated using the Arduino IDE software is to

perform coding of the source code. The software enables compilation of the necessary commands and source code into the NODEMCU V2 processor. Meanwhile, the third segment of the system focused on the output source for the mechanism. The output source consists of the integration of mechanical segments such as DC motor. The circuit diagram for this system designed using Proteus software, software developed by England Labcenter Electronics Ltd for schematic capture, simulation, and printed circuit board layout design [9-10]. This circuit diagram consists of an Arduino, motor driver, switches and motors as shown in Figure. The controller acts accordingly on the DC motor of the robot. The robot in the project can be made to move in all the four directions using the android phone. The direction of the robot is indicators using LED indicators of the Robot system. In achieving the task the controller is loaded with program written using Embedded 'C' Languages.

VIII. Mechanism:

F. Waste that will be able collected by this robot is floating on the surface of waterways, such as bottles, plastic cans, covers, and etc... It is collected through a belt conveyor then placed in the designed place. This conveyor designed rotating continuously. Cleaning work by naturally provide great maneuverability and collect trash easily.

IX. Experimental setup

X. Mechanical Requirements

Axle Shaft:

It as the place for the propeller to rotate, thus the robot could move correctly.

Power Cell:

The power of the system has to be consumed by the solar power, the harvested energy has made the battery at least $\frac{1}{4}$ times longer than only using battery. It is perhaps is a small value, but could be designed for larger capacity if only the space could be created in future study for the solar cell.

Ultrasonic Sensor: the electronic device measures target of the distance object by emitting ultrasonic waves & converts reflected sound wave into electrical signal. The waves travel faster compared to speed of audible sound (i.e. the sound that humans can hear) Obstacles will be detected and send as an alert message to Iot server. Principle of the ultrasonic sensors emits short, high –frequency sound pulses at regular intervals. Range: 40 to 70 kHz, the frequency determines the range and resolution.

Dc Motor: It consists of a stator, an armature, a rotor and a commutated with brushes. DC motors are attached to wheels of the robot for paddling. DC motors is any type of rotators electrical machines that converts direct current electrical energy into mechanical energy. The most common types rely on the forces produced by magnetic fields. Nearly all the types of DC motors have some internal mechanism, either electromechanical or electronic; to

periodically change the directions of current flow in the part of the motor.

Motor Driver: It is a integrated circuit chip used as a motor controlling device is autonomous robots & embedded circuit L293D & UL93D are most commonly used motor drive IC, the direction of motor based on the command or instruction receives from the controller. It receives the signal from the microprocessor, it transmits the converted signal to motor .This signal can receive from microcontroller but it cannot change the input value of signal (i.e.: high voltage to low voltage),it will pass the same signal that receive from the microcontroller .

Arduino MicrocontrollerIt consists of both physical programmable circuit board and, software piece that runs on your computer code to the physical board.

Front Slab:It is used for directing the waste on the water surface and introducing it to the conveyor so that the trash could be transferred to trashcans.

Trashcans:These are used for the place of waste after erected by front slab and conveyor.

Propellers: This will be connected to two DC motors therefore; it could be controlled including turning move and upward & backward. A tube-like boat body is used as the main body of the robot. This design is chosen to enable robot floating on the water.

Microcontroller:It is a small computer on a single metal oxide semiconductor integrated circuit chip microcontroller contains one or more CPUs along with memory and programmable input output peripheral .They run one specific program and are dedicated to a single task. Microcontroller can take input from

the device them controlling and retain control by sending the device signal to different parts of device.

Conveyor:which is used for the delivery system of the waste from the water to the designated trashcans? A conveyor belt is the carrying medium of a belt conveyor system. Typically, conveyor systems consist of a belt stretched across two or more pulleys. The belt forms a closed loop around the pulleys so it can continually rotate. One pulley, known as the drive pulley, drives or tows the belt, moving items from one location to another The conveyor belt carries the garbage to the dustbin an drop it over there.

Decoder:It is a circuit used to change the code into a set of signals, it has reversed of encoding A digital decoder converts a set of digital signal into corresponding decimal code.

Relays: These are switches that open and close circuits electromechanically or electronically. Relays control one electrical circuit by opening and closing contacts in another circuit. As relay diagrams show, when a relay contact is normally open (NO), there is an open contact when the relay is not energized. Relays activate the wheel motors and to control the speed of the paddle.

XI. Results

G. The result to the complete system is given below with step by step process

- allows IoT features, such as Amazon Web Services (AWS).
- d) The waterproof ultrasonic sensor will be applied in the system, since the robot will work with the watery environment. However, the ultrasonic sensor will still be protected physically by some sort of shield.
 - e) PH sensor will be located thus introducing a monitoring system of a pH level of surrounding water in the river through a robot.
- H.** Turn ON the power supply. After that all the components get activated. However, to meet the functional design necessary for some particular application, this model, perhaps, will be changed. In order to maintain the main function of this robot, here is several of the main function that should be accommodated by a river cleaning robot designed in this study as depicted in Figure 5. These features could be breakdown into more tangible components, they are: The system will be fully controlled by microcontroller that is now very much used in IoT application.
- a) GPS module will be connected to Arduino and thus introducing the possibility to locate the robot when its working with a large area of water, minimizing the possibility of the robot miss-controlled or lost during the operation.
 - b) For solar cell, the harvested energy has made the battery at least $\frac{1}{4}$ times longer than only using battery. It is perhaps is a small value, but could be designed for larger capacity if only the space could be created in future study for the solar cell.
 - c) IoT system will be managed by some sort of cloud system that

10. Advantages

- Man power is reduced due to automated self-service.
- The robot gives non conventional and makes eco friendly.
- Its maintenance cost is low.
- The human interaction is low this is the main advantage.
- The cleaning of garbage in the water makes the pollution free & keeps the environment healthy.
- Harvesting of garbage in the water makes flow of water in the pipelines.

11. Conclusion

The problem of water logging due to plastic paper, sand, metal leads to pest growth and it favors diseases like malaria, typhoid etc. This is unsafe for human life. The proposed system cleans the garbage present in small land big lake and minimizes the use of fuel operated garbage collector. The aquatic animals can save & reduced the time, efforts, and diseases for human by cleaning the lake by this robot.

References

- [1] M. Mohamed Idhris, M. Elamparthi, C. Manoj Kumar, Dr. N. Nithyavathy, Mr. K. Suganeswaran

- [2] Mr. S. Arunkumar, "Design and fabrication of remote controlled sewage cleaning Machine", IJETT – Volume-45 Number2 -March 2017
- [3] .Abhijeet.M. Ballade, Mr. Vishal.S. Garde, Mr.Akash.S.LahaneandMr.Pranav.V.Boob, "Design&fabricationofrivercleaning system", IJMTER Volume 04, Issue 2, [February– 2017] ISSN(Online):2349–9745.
- [4] Mr. P. M. Sirsat, Dr. I. A. Khan, Mr. P. V. Jadhav, Mr. P. T. Date, "Design and fabrication of River Waste Cleaning Machine", IJCMES 2017 Special Issue-1 ISSN:2455-5304
- [5] Pankaj Singh Sirohi, Rahul Dev, ShubhamGautam,Vinay Kumar Singh, SarojKumar,"Review on Advance River Cleaner", IJIR Vol-3, Issue-4, 2017 ISSN:2454-1362.
- [6] Prof.N.G.Jogi, AkashDambhare,KundanGolekar, AkshayGiri,"Efficientlakegarbagecollectorbyusingpedaloperatedboat",IJRTE RVol02,Issue04;April-2016[ISSN:2455-1457].
- [7] Swachhhasth – A water cleaning robot ,publisher name – IJERT ISSN(Online) : 2278-0181
- [8] Siddhanajanani,H N Supreetha, Boomika , yogithasree RP, pallavi M .Maharaja institute of Mysore.
- [9] A.jevtic, p.Gazi, D.Andina&M.jamshidi,"building a swarm of robotics bees"world automation congress 2010.



ISSN-1671-4512

CERTIFICATE

OF PUBLICATION

This is to certify that

P.Kavitha

Head of the department/ECE, M.A.M.SCHOOL OF ENGINEERINGS,
SiruganurTrichy

Published a paper entitled

"Automatic Lake Cleaning Robot Using IOT"

in

Journal of Huazhong University of Science and Technology

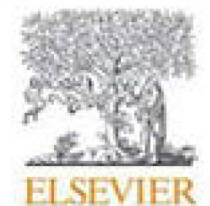
VOLUME 50 ISSUE 04 - 2021

PAPER ID: HST-0421-350

<http://hustjournal.com/>



Chief Editor



DOAJ DIRECTORY OF
OPEN ACCESS
JOURNALS

Scopus®

A NOVELTY APPROACH FOR ATM SECURITY USING SMART VISION

P. Kavitha*¹, S. Abinaya*², P. Ammudevi*³, R. Kaviya*⁴

*¹Associate Professor/HOD, ECE, MAM School Of Engineering, Trichy, Tamilnadu, India

*^{2,3,4}Final Year student, ECE, MAM School Of Engineering, Trichy, Tamilnadu, India

ABSTRACT

Automated teller machines (ATMs) are widely recognized gadgets normally utilized by people to perform a whole lot of character and enterprise monetary transactions and/or banking functions. ATMs have come to be very famous with the overall public for their availability and fashionable consumer friendliness. ATMs at the moment are observed in many places for example, restaurants, super markets, malls, banking centers, airports and myriad of different places. The paper studies presents, if any man or woman attempts to interrupt the ATM it'll detected the use of vibration sensor and the door can be locked immediately. On the premise of the characteristic extraction, the Support Vector Machine (SVM) classifies the hobby of the captured pictures as ordinary or abnormal.

Keywords : ATM, Histogram of Oriented Gradient, Support Vector Machine

I. INTRODUCTION

It is very important to automatically read the human activities from videos, because from the fast few years a wondered success of social networks and multimedia technologies, moving forward to the generation of vast amount of videos are getting uploaded, so as to provide value added service to the end user, number of research studies have focused on this particular challenging topic. Even though massive progresses in human action recognition have been achieved by recent studies, there are still two problems which need to be considered for its future enhancements. Cameras play a very vital role in now days life. One has to look at the recorded images and videos whenever any incident happens.

The main objective for movement recognizes the events and aims of one or more people from the progression of observations on the people's action. Supervised learning and understanding of unusual human being deeds is more complex, difficult and wide task. Surveillance is used to observe the behavior, changing information, or activities, commonly of publics for the cause of Influencing, organization, and directing or to defend them. It is used for diverse works such as, authorities for intelligence gathering, the prohibition of crime, the safety of a process, person, institution or object, or for the Inspection of crime scenes.

Human behavioral pattern and face recognition plays very important part in person recognition. Visual records are a key supply for such identifications. Surveillance videos provide such visual information which can be viewed as live videos, or it can be played back for future references. Now days 'automation' has its impact even in the field of video analytics. Analyzing Video may be used for extensive range of packages like human pastime prediction, individual identification, motion detection, abnormality prediction, humans counting at crowded places, vehicle counting etc. The actions of human may be overlapped by background changes or camera motion. Especially, camera motion may interfere with detecting the true human activity. Secondly, it is still challenging to recognize human activities in realistic unconstrained videos because of a large amount of intra-class action variations.

There are two stages in this architecture, training and testing. In training stage we consider normal and abnormal images as input sample images, sample images which we are using as input sample are taken from the camera and later those images are preprocessed from color images to gray scale images. To foreshorten human activity accurately and efficiently, the HOG features are employed for feature reduction. Result, feature reductions are trained to SVM classifier and will dump to knowledge base as a result database.

Modeling human behaviors and interest styles for reputation or detection of unique occasion has attracted sizable studies hobby in latest years. Diverse methods that are abound for building intelligent vision systems aimed at scene understanding and making correct semantic inference from the observed dynamics of moving targets. Most applications are in surveillance, video content retrieval, and human-computer interfaces. This paper presents an extending preceding associated surveys, however additionally a focal point on contextual peculiar human conduct detection specially in video surveillance applications. The main purpose of this survey is to extensively identify existing methods and characterize the literature in a manner that brings key challenges to attention. Nowadays research is going on in the field of crime detection and avoidance in the

ATM. But until now there may be no superior technology got here with inside the subject of ATM. So the concept of designing and implementation of safety for ATM task are born from the commentary of our actual life incidents occurring round us. Over the beyond three a long time customers have come to rely on and believe the ATM to effectively meet their banking needs. In current years there was a proliferation of ATM frauds throughout the globe. for ATM safety in cooperation ATM software. The proposed approach will makes use of a couple of object detection approach and occasion reputation strategies of pc vision

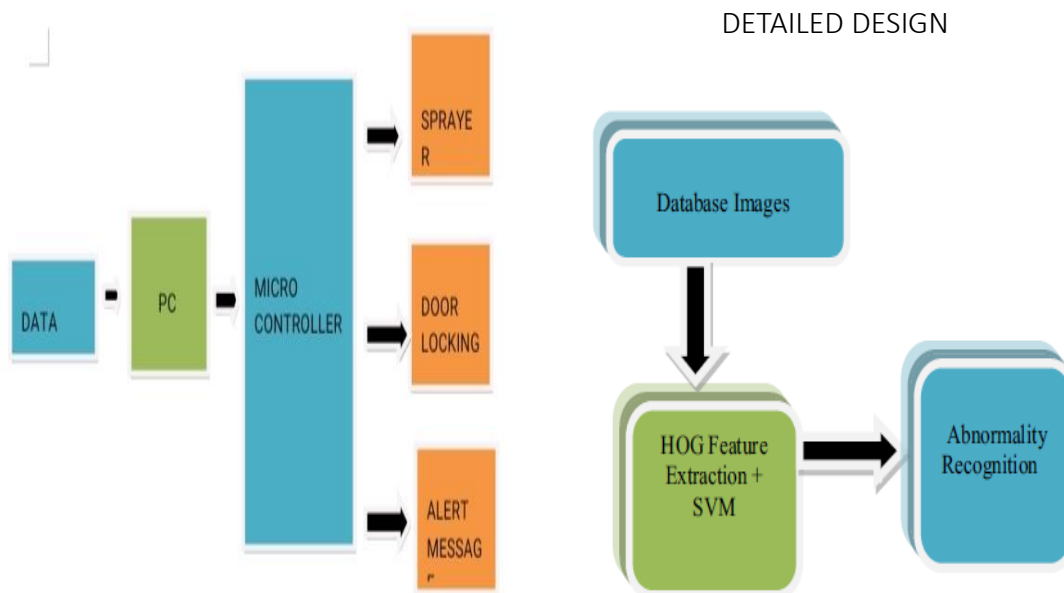
II. METHODOLOGY AND ANALYSIS

EXISTING SYSTEM

- In a few ATM Machines Hooks are connected to the probes stopping the cardboard from being lower back to the client at the end of the transaction.
- Skimming Devices: Skimming approach is the most regularly used approach of illegally acquiring card tune records. Skimmers are gadgets utilized by criminals to seize the records saved with inside the magnetic strip of the card.
- Shoulder Surfing: Shoulder Surfing technique is the act of direct observation, watching what percentage that man or woman faucets onto the keypad. 4] Utilizing a Fake PIN Pad Overlay: In this case, a faux Pin pad is located over the authentic keypad. This overlay of PIN pad captures the PIN statistics and shops the facts into its memory. The Duplicate PIN pad is then removed, and recorded PINs are downloaded

PROPOSED SYSTEM

Preparation of the database images. HOG feature extractions and SVM classifier. Abnormality recognition, if the abnormal activity is detected then an alarm is raised to security or either nearby police station. The software is used for the development of project is Matlab. Firstly, captured an image that is taken as input and trained our system and then to check its working accurately and efficiently or not, we have testing image to test the system. The (HOG) Histogram of Oriented Gradient is used to extract the significant features from the images. On the basis of result from the feature extraction the Support Vector Machine (SVM) classifies the activity of capture image is normal or abnormal.



HOG FEATURES

HOG is a characteristic descriptor. It is used to make the classification easier under divergent conditions and characteristic is to establish the thing in such a mode that the same object produces as close as possible to the same feature descriptor. The developers of this approach trained a SVM to identify the HOG descriptors of natives Abnormal activity detection is very interesting field and it has got interesting future works, we have seen different kind algorithms like HOG, SURF, Harris corner detection, fast method, Graph cut method and

many more which are implemented in different ways to overcome the possible problems occurring in detecting abnormality in ATM surveillance.

Input image

It is a real time input obtained from camera the instant image captured by camera is given as input to the system Normal surveillance camera can be used.

Computer/Processor

A processor is required to process the input image and runs the algorithm to detect the object. We use windows 10 laptop with MATlab software to design and run the algorithm

Microcontroller

Microcontrollers are the part of project which controls the external hardware components connected to it. We use Node MCU wifi model controller to activate output devices and also to send alert msg

Chloroform Sprayer

A Dc motor will be activated to spray chloroform once the object is detected and confirmed. This mechanism will spray the liquid and it can be controlled using the output value

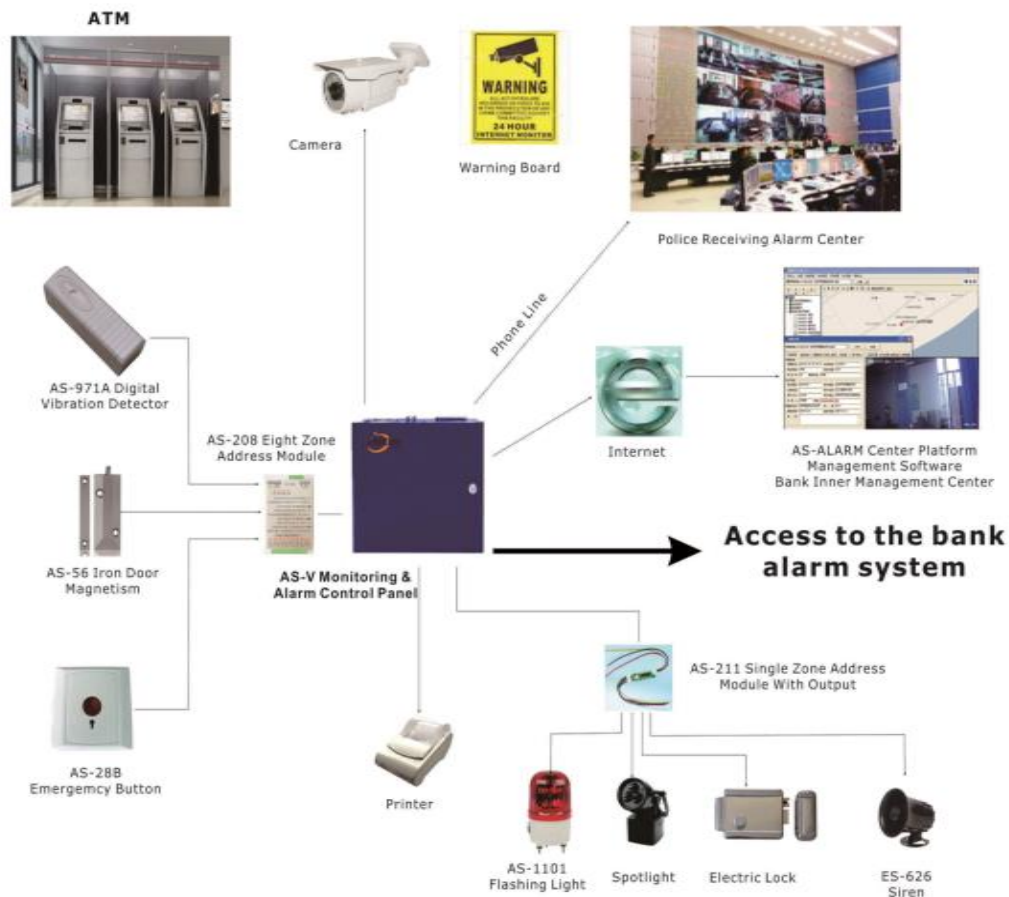
Door lock mechanism

Door locking mechanism can be activated using solenoid .The three step verification will be done before activating this mechanism.

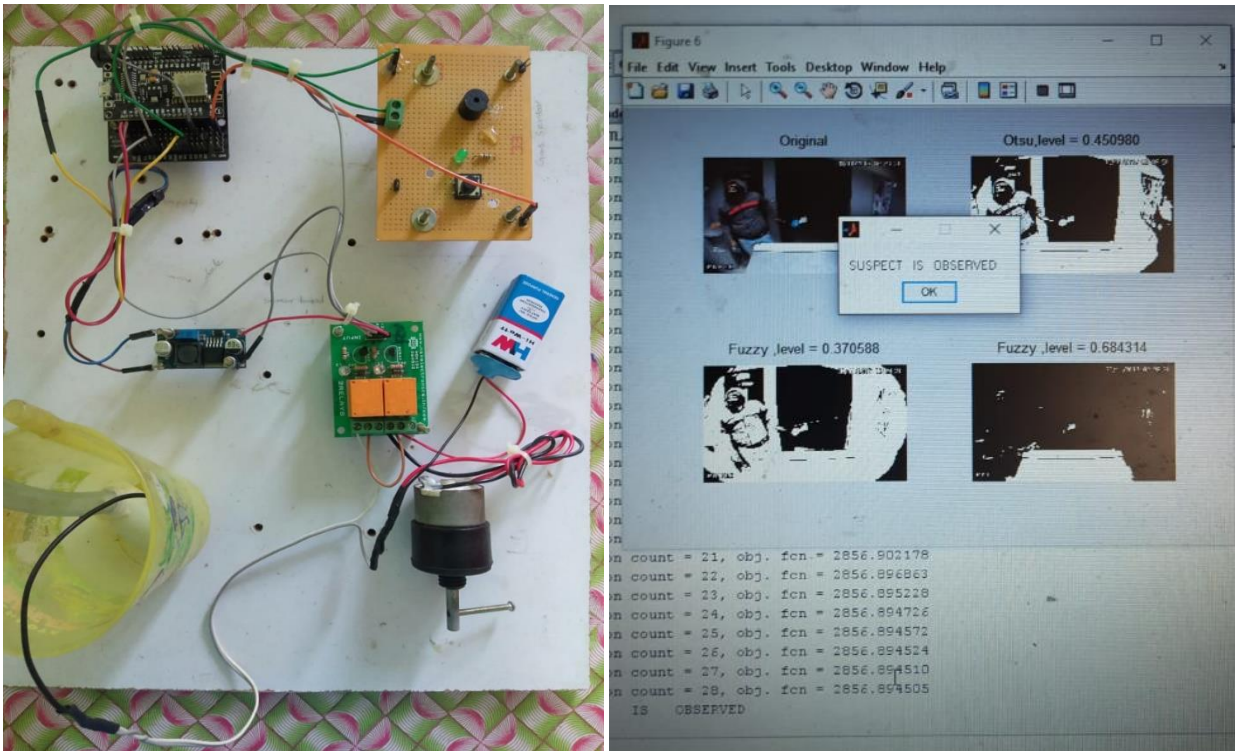
IOT MODULE

The server will be alerted with a message as the result obtained from algorithm

The IOT module connects the server with the digital devices and the external components. The server will get an alert message at once within a second when the object is detected



PHOTOGRAPHS



III. CONCLUSION

Extensive experimental outcomes affirm the performance of the proposed extraordinary activity detection, through the imply of security bases, the usage of HOG function and SVM classifier. It is concluded that this approach is greater rapid then different approach (neural network). Elapsed time for neural network is approximately 28 seconds however for this approach is approx. 12 seconds. At this time static photos are used for the experimental work. But for future, video might be used rather than static images. We work paintings on real time photos (videos).

IV. REFERENCES

- [1] Popoola, Oluwatoyin P., and Kejun Wang. "Video-based abnormal human behaviour recognition—a review." *IEEE Transactions on Systems, Man, and Cybernetics, Part C (Applications and Reviews)* 42, no. 6 (2012): 865-878.
- [2] Gowsikhaa D, Manjunath, Abirami S."Suspicious Human Activity Detection.
- [3] Aron F.Bobick and James W.Davis,"The Recognition Of Human Movement Using Temporal Templates, *IEEE Transactions on Pattern Analysis and Machine Intelligence*, vol.23, March2001.
- [4] C. Stauffer and W.E.L.Grimson, "Learning Patterns Of Activity Using Real-Time Tracking," in *PAMI*,2000.
- [5] P Bouthemy and F Meyer, "Region Based Tracking Using Affine Motion Models in Long Image Sequences,"
- [6] C. Harris and M.Stephens, "A Combined Corner and Edge Detector," in *AVC*,Manchester,1988,pp.147-151.
- [7] N.Dalal and B.Triggs, "Histograms of Oriented Gradients for Human Detection," in *CVPR*,San Diego,2005,pp.886-893.
- [8] N.Dalal , B.Triggs and C.Schmid, "Human Detection using Oriented Histograms of Flow and Apperance,"in *ECCV*,Graz,2006,pp.428-441.
- [9] B.Lucas and T.Kanade, " An Iterative Image Registration Technique," in *IJCAI*, Vancouver,1981,p.674-679. [10] B.Horn and B.G.Schunck, " Determining Optical Flow," *Artificial Ineteligence*, vol.17,pp.185-203,1981.



e-ISSN: 2582-5208

International Research Journal Of Modernization In Engineering Technology And Science

Ref: IRJMETS/Certificate/Volume 3/Issue 4/308740

Issue Date: 26/04/2021

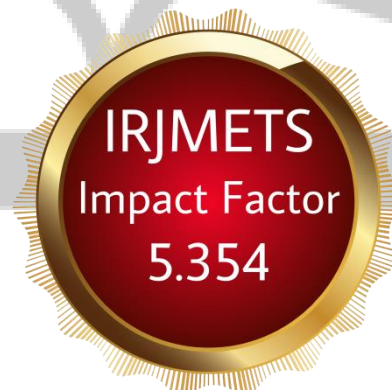
Certificate of Publication

This is to certify that author "**P. Kavitha**" with paper ID "**IRJMETS308740**" has published a paper entitled "**A NOVELTY APPROACH FOR ATM SECURITY USING SMART VISION**" in *International Research Journal Of Modernization In Engineering Technology And Science (IRJMETS)*, Volume 3, Issue 4, April 2021.

A. Devi

Editor in Chief

IRJMETS



We Wish For Your Better Future
www.irjmets.com

IOT BASED FUEL STATION MONITORING

K.KARTHIKEYAN Assistant professor/ ECE

J.Menaka, M.Sandhiya, L.Swetha

M.A.M.SCHOOL OF ENGINEERING

Siruganur, Trichy

karthikcacet121@gmail.com, menakajothivel308@gmail.com

sandhiyaece8@gmail.com, swethalawrence28@gmail.com

ABSTRACT

We deal with the implementation of new technologies we can automated the fuel stations with efficient working devices and also monitoring. A novel idea everyday life is filled with technology from the start up till to bed. In present life most seeming 50% of products all came with automation and making the consumers/users to access those products from anywhere by using their mobile or gadgets. In this project, it deals with automation of fuel station retail outlet; this method will give the sales and stock report back to the owner for each hour. The main problem is customer complaints about less quantity of fuel is issued or filled for money and proper time tank refilling and given and customers get diverted their attentiveness by operators and refill the fuel without they resetting the nozzle. Nowadays to beat these problems they replaced some electronic and computerized fuel dispensers but there are no thanks to identify inside the rotary valve adjustments by fitter.

Keywords: Cloud Computing, Global Positioning System (GPS), General Packet Ratio Services (GPRS), Global System for Mobile Communications (GSM), Internet of Things (IoT), Open-Source Hardware (OSH).

INTRODUCTION

The underlying principle of Internet-of-Things is to make real-time transfer and

synchronization of data possible among many dissimilar types of devices. For example, rooms equipped with IoT sensors can automatically report back to central systems if they are occupied or if there has been any change in temperature at any point of time. IoT makes it possible for inter-communication between any equipment or vehicle embedded with controllers and sensors in real-time and over any network path or digital services [1, 2]. Cognizant of rising costs per liter of fuel and combined with thirst for fuel across cities and semi-urban landscapes, fuel-filling station owners are keenly aware that theft of fuel can be lucrative for many who are out to make quick illegal profits. Today, many fuel-filling stations are equipped with sensors that communicate with controllers that have micro-processors to process real-time data on fuel entering or exiting fuel tanks at any given point of time.

While IoT has made the idea of electronics-enabled devices and equipment to communicate with each other and to central controllers possible, evolution in Cloud Computing technology has taken it further to a point where real-time information streamed back from IoT-enabled devices are stored in servers that may be hundreds or even thousands of miles away. Information processed by those remote servers can either be downloaded or consumed for taking decisions either immediately or strategically or transmitted to the same or different IoT enabled devices to respond to changing stimuli or under dynamic environmental conditions [3, 4]. From the point of view of construction firms, there is no single system that can help

monitor and report fuel consumption, distance travelled, and actual engine running hours of a transit mixer, and view all these information at a central location in a proper format [5]. Our research has revealed that there is a need for a system that can not only report a close approximation on fuel consumption of a transit mixer – either in operation, at standby / idling mode, or in parked condition, but also keep a daily track of all the metrics involved related to engine operational hours, distance travelled, fuel consumed, etc. Our research objective has, therefore, focused on the need to develop an IoT-based real-time fuel monitoring solution for construction companies.

II. ARCHITECTURE OF INTERNET OF THINGS

The architecture of IoT is a composite of various technologies layered in a manner such that each are able to communicate with one another. Thus, IoT-based systems can adapt to changing scenarios involving modularity, scalability and configuration [6]. The image shown below depicts functionality of each layer in an IoT-based system:

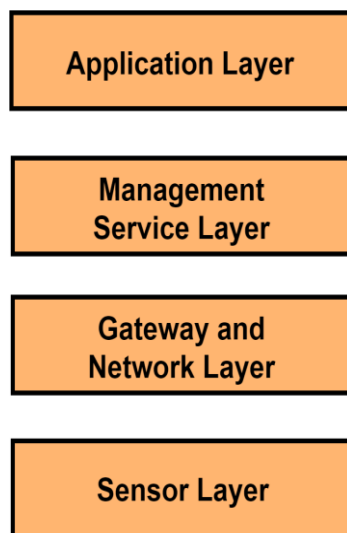


Fig: layer in an IoT-based system

A. Sensor Layer

The fundamental unit of an IoT-based system is the sensor layer. At this layer, capacitive sensors are embedded in equipment to stream back data. In the case of transit mixer, which is a heavy construction vehicle that requires large amounts of diesel fuel to stay in operations, sensor devices collect and stream back information either statically or dynamically across the Internet.

B. Gateway and Network Layer

Positioned on top of sensor layer is the Gateway and Network Layer. This is required to handle huge volumes of unstructured data that would pour in from sensors. Networks with robust protocols are deployed at this layer to aid in seamless machine-to-machine (M2M) network communication [7].

C. Management Service Layer

The purpose of this layer is to place security and access controls to data generated by the sensors. It is also at this layer that process modeling and management of devices takes place. An important feature of this layer is also establishment of business and process rule engines. With this layer in place, information and analytical insights on data generated and stored can be viewed, aggregated and monitored.

D. Application Layer

The application layer is positioned at the very top for facilitating in delivery of associated software applications to users requiring access to data streamed from IoT-enabled equipment and vehicles. Using IP based networks to provide a stable communication interface and robust end-user services, this layer accords process-to-process communications [9].

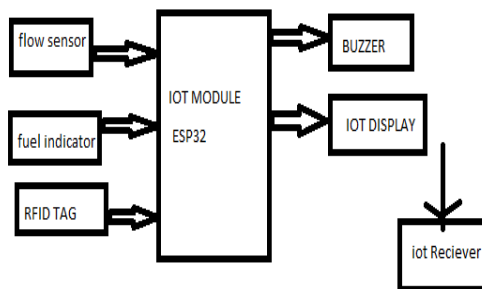
III.EXISTING SYSTEMS

- Handy control for fuel dispense
- Manual monitoring using digital displays
- Manual billing and accounting
- Regular checkups for tank refilling

IV.PROPOSED SYSTEM

- To measure the flow of the fuel using fuel flow sensor
- To measure the fuel availability fuel indication sensor
- To have the billing data at server for further analytics.

V.BLOCK DIAGRAM



The digital sensor units are interconnected with IOT module. The fuel flow sensor detects the liquid flow and check the constant value of flow if any deviation occurs it will alert user with buzzer sound. The fuel indicator sensor senses the fuel level in tank and it alerts the user for refilling at the prompt time. An alert mgs is sent to the user via IOT module and refilling can be done without fail The RFID tag is used to show purchase details The total sale in the station can be monitored easily as soon as the billing is done the value is added to the server and the total value is stored in cloud. We can use inverter power supply available at station Wifi module available for security systems.

VI.COMPONENTS AND TECHNOLOGIES

1. Fuel flow sensor

A flow meter (or flow sensor) is an instrument used to measure linear, nonlinear, mass or volumetric flow **rate** of a liquid or a gas 1/2 inch Water Flow Sensor - YF-S201 **Flow sensors** are able to detect leaks, blockages, pipe bursts, and changes in liquid concentration due to contamination or pollution



2. Fuel indication sensor

These **sensors** are mechanically connected to a float which moves up or down depending on the **fuel level** As the float moves, the resistance of the **sensor** changes. This **sensor** is part of a current balance circuit of the **fuel gauge** display circuit which typically consists of coils for actuation of the display needle.



Fuel level sensors, also known as **fuel gauges**, allow drivers to monitor **fuel** consumption and help them to determine when to refill the tank. They consist of two main components: the sensing system itself (also known as the sender) The indicator and we are going to indicate it in an IOT page.

3. RFID TAG

RFID tags are a type of tracking system that uses smart barcodes in order to identify items. RFID is short for “radio frequency identification,” and as such, **RFID tags** utilize radio frequency technology An **RFID tag** may also be called an **RFID chip**.



RFID belongs to a group of technologies referred to as Automatic Identification and Data Capture (AIDC). **RFID tags** contain an integrated circuit and an antenna, which is used to transmit data to the **RFID** reader (also called an interrogator). The reader then converts the radio waves to a more usable form of data.

4. BUZZER

A **buzzer** or beeper is an audio signaling device, which may be mechanical, electromechanical, or piezoelectric (piezo for short). Typical uses of **buzzers** and beepers include alarm devices, timers, and confirmation of user input such as a mouse click or keystroke.



5. IOT

The Internet of things describes the network of physical objects—“things”—that are embedded with sensors, software, and other technologies for the purpose of connecting and exchanging data with other devices and systems over the Internet. They are able to collect and exchange data in real time using embedded sensors. Thermostats, cars, lights, refrigerators, and more appliances can all be connected to the **IoT**.

- 1) Resolution of 1 mm enables sensor to obtain accurate readings.
- 2) Enabling data from three memory registers simultaneously allows it for fast sensor reading.
- 3) Algorithms ensure that even in conditions of changing temperatures and resultant volumetric changes, the sensor is able to compensate and obtain readings accurately.
- 4) On-board temperature compensation mechanism enables sensor to counter temperature-related drifts in circuit of the sensor.
- 5) Since, transit mixers or any vehicle as such may halt in any incline, the sensor is equipped with circuits and hardware to accommodate gravitational angles and still provide accurate readings.
- 6) The sensor does not require strap chart for calibration. A fuel tank can have any shape or even uneven surfaces, and yet the sensor can be calibrated by marking high- and low-level of fuel inside the tank.
- 7) The sensor is equipped with 42 registers to store readings such as diameter of the tank, height of tank, high- and low-level calibration marks, etc.
- 8) Since, many vehicles may share fuel tank dimensions that are the same, a common profile can be saved in central software application. This profile can be re-used to speed up process of calibration to save time and maintain consistently accurate readings.

VII. GPS-GPRS FUEL MONITORING CONTROLLER

1) The controller has been built to withstand sudden electrical changes from equipment batteries, ignition systems, etc. It has twin level of protection circuits at the supply end making it capable to function even in case of frequent voltage fluctuations.

2) It also has a device hardening feature such as a signature-based circuit. This enables seamless recovery even in case of device becoming non-responsive.

3) The controller is equipped with an external serial flash device capable of storing 8 MB of data. Considering that GPRS networks are intermittent or even non-existent in many regions in India, the device is able to store sensor data offline.

It is then able to transmit data to Cloud as soon as a stable Internet connection is detected making it suitable for operational conditions in the countryside and the most remote surroundings.

4) On-board sensors and electronics such as accelerometer enable detection of linear motion. It also provides inputs for gathering accurate geospatial coordinates along with date and time, to support calculations involving speed and distance covered.

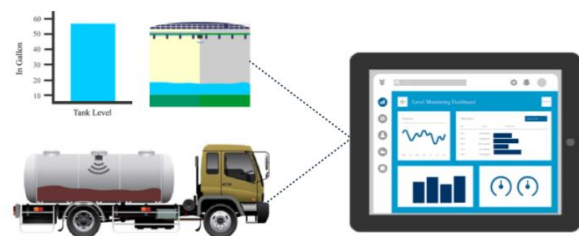
5) Firmware and configuration upgrades can be sent over-the-air. Algorithms built-in ensure that in case transmissions are lost while in the process of bulk data firmware upgrades, data integrity checks are conducted so as to ensure that only remaining portion of upgrades need only be transmitted either offline or over-the-air. This is a significant factor as it can help lower network connection costs and increase operational efficiency.

6).Since, the controller supports cellular, Bluetooth and Wi-Fi networks, it is possible to collect data from the controller using a

smartphone even in areas where vehicle may be out of mobile network coverage areas.

7) The controller uploads and downloads data to the Cloud. Algorithms used in the controller ensure that data is compressed and secured in small data packets. This feature enables speeding in data transfer. In regions where mobile network is poor, this can be an invaluable facet to transmit as much data as possible.

8) To improve signal reception, a 3-meter external antenna is coupled to the controller.



VIII. CONCLUSION

Our proposed IoT based design for a real-time fuel monitoring system involving transit mixer trucks in operational use at construction projects and at remote sites can be of significant use for construction companies in India. Our primary goal was to extend a solution that would allow managers and supervisors to monitor any number of transit mixer vehicles in operation, from a central location using a Cloud computing infrastructure. Through our research, we have been able to show average running hours, fuel consumed, fuel removed and other related parameters. However, the crucial factor of removal of fuel (whether authorized or unauthorized) is of significant concern for most construction companies as it is one of those parameters that have direct financial consequences. The benefits of our research can be extended to similar other industries where fuel monitoring is of critical concern. Through use of our novel IoT-based fuel monitoring

system, we have demonstrated that it is possible to have a detailed operational view of vehicles and engines requiring fuel to operate, across cloud computing systems using cheap yet reliable capacitive sensors.

REFERENCES

1. M. Lohstroh, E. A. Lee, "An Interface for the Internet of Things," SEFM 2015, LNCS, vol. 9276, 2015, pp. 20 – 34.
2. R. Lanotte, M. Merro, "A semantic theory of the Internet of Things," Information and Computation. vol. 259, April 2018, pp. 72 – 101.
3. S. Roy, R. Bose, D. Sarddar, "A Fog-Based DSS Model for Driving Rule Violation Monitoring Framework on Internet of Things," IJAST. vol. 82, 2015, pp. 23 – 32.
4. S. Roy, R. Bose, D. Sarddar, "Impaired Driving and Explosion Detection on Vehicle for Ubiquitous City,". IJCIR, vol. 13, 2017, pp. 1167 – 189.
5. TATA MOTORS.: LPK 2518 RMC BS IV-Technical Specifications, 2018.
6. P. Sethi, S. R. Sarangi, "Internet of Things: Architectures, Protocols, and Applications," J. Elect. and Comp. Engg. vol. 2017, Article ID 9324035, January 2017, pp. 1 – 25.
7. M. Shanmugasundaram, "M2M/ IoT Protocols: An Introduction," happiest minds blogs, 2016.
8. A. – E., M., M. Hayajneh, N.A. Ali, "Data Management for the Internet of Things: Design Primitives and Solution," Sensors (Basel), vol. 13, November 2013, pp. 15582 – 15612.
9. D. Bandyopadhyay, J. Sen, "Internet of Things: Applications and Challenges in Technology and Standardization," Wireless Personal Communications, vol. 58, 2011.

INFOKARA RESEARCH

An UGC-CARE Approved Group 2 Journal



INFOKARA

An ISO : 7021 - 2008 Certified Journal

ISSN NO: 1021-9056 / web : <http://infokara.com/>

e-mail : editor.infokara@gmail.com

Certificate of Publication

Certificate ID - IK-4335

This is to certify that the paper entitled

IOT BASED FUEL STATION MONITORING

Authored by

K.KARTHIKEYAN

From

M.A.M.SCHOOL OF ENGINEERING, Siruganur, Trichy

Has been published in

INFOKARA RESEARCH, VOLUME 10, ISSUE 4, APRIL - 2021



H. Mathew

Mathew Hull, Editor-In-Chief, INFOKARA RESEARCH



Intelligent Remainder Medicine Pill Box using IOT

Abdur Rahman.N [1], Sumathi.K [2], Gunavathi.A [3], Kasthuri.S [4]

Department of Electronics and Communication Engineering,

MAM School of Engineering, Tamil Nadu, India- 621 105

[1]ab3rahman@gmail.com, [2] sumathiece26@gmail.com, [3] ak.guna2299@gmail.com, [4] kasthuriias54@gmail.com

ABSTRACT

There are lots of challenges for blind people and elderly people who need constant help – may it be our family members, the ones who have special needs. These people apparently need the kind of care which most busy family members cannot provide. Some people may forget to take the medicines at the correct time and can forget the medicines which they have to take. So in order to help them with this liability we have developed this project. The people are provided a smart med box on which there will be a alarm with voice output which notifies the people about the medicine. Along with this we can alert them with an alarm and light indications. So that even if the person is sleeping or busy with some work the alarm helps in alerting him. To confirm that the person has taken that medicine or not we can put a sensor at the opening end of the pill box. so when the person tries to open the box the signal is sensed and the alarm will be off only if the sensor is pressed. By this data we can tell that the person has taken the medicine.. We can notify the doctor and the other one is used to notify family members about the medicine taken using IOT

Key words: Node MCU, Pill box, Buzzer, Reset Button, Mobile App

INTRODUCTION

Currently, worldwide aging and regularity of persistent diseases are flattering a broad concern. Numerous countries are undergoing hospital restructuring by reducing number of hospital beds and escalating home healthcare, which is envisioned to perk up health care quality, has fascinated wide-ranging attention.

In order to track the physical status of the elderly and, in the meanwhile, to keep them healthy, the proposed idea will be helpful. IOT expands the Internet into our everyday lives by wirelessly connecting various smart objects, and will bring significant changes in the way we live and interact with smart devices. The new wave in the era of computing will be outside the sphere of the conventional desktop.

Internet of Things (IOT) is a network where many of the objects that surrounds us will be networked in one form or another. By using this technology the health statistics of medication are observed. In this process of encryption the schedule data or doctor's prescription are sent to pill box through mobile app. The LEDs are placed for indication and buzzer for alarm alerts and reset button is used to count for medicine in cloud platform. The existing techniques to the market for the reminder include a pill box. But this does not help in checking the medicine. This proposed idea is valuable solution to the medical non-compliance problem. The innovation scheme to help patient keep trail of their medicine consumption through a series LED alarm indicator signal and audio alarm indicator signals.

The main objectives of the project are:

- Dispense of medicines from pill box at scheduled time.
- Medical alerts to care taker and retailer
- Online report generation of medicine
- Real-time health statistics monitoring of medicines
- Configuration data is send through iot website

BLOCK DIAGRAM

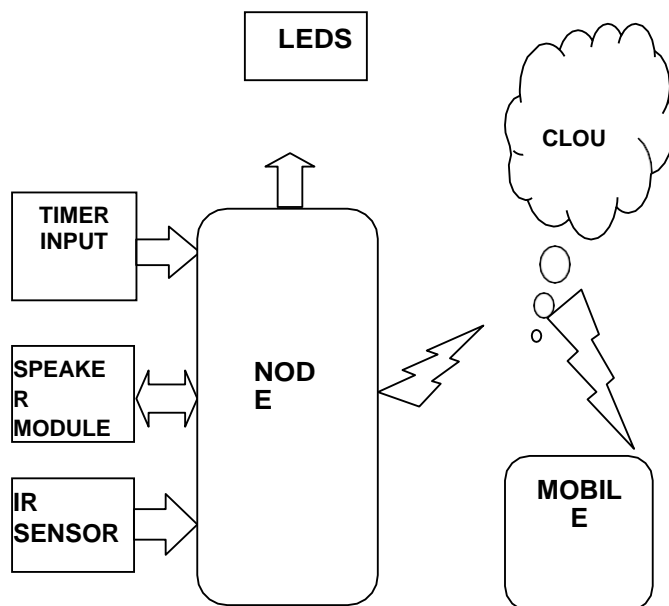


Fig 1: Working Principle of Smart pill box

INTERNET OF THINGS

The Internet of Things (IOT) is an important topic in technology industry, policy, and engineering circles and has become headline news in both the specialty press and the popular media. This technology is embodied in a wide spectrum of networked products, systems, and sensors, which take advantage of advancements in computing power, electronics miniaturization, and network interconnections to offer new capabilities not previously possible. An abundance of conferences, reports, and news articles discuss and debate the prospective impact of the “IOT revolution”—from new market opportunities and business models to concerns about security, privacy, and technical interoperability.

IOT systems like networked vehicles, intelligent traffic systems, and sensors embedded in roads and bridges move us closer to the idea of “smart cities”, which help minimize congestion and energy consumption. IOT technology offers the possibility to transform agriculture, industry, and energy production and distribution by increasing the availability of information along the value chain of production using networked sensors. However, IOT raises many issues and challenges that need to be considered and addressed in order for potential benefits to be realized.

PROPOSED METHOD

To ensure the people consume medicines as per schedule time table, here we developed a Intelligent pill box. The schedule data/configuration data is send to the pill box through Mobile app. The smart pill box contains Node MCU, SPEAKER MODULE, LEDs, IR SENSOR, buttons.

The timer input is to set propotional time to take pills. When the time is arrived the led will blink indicatind the box opened to take medicine. Moreover the voice module will give out the pill name which helps the user not to use vision to identify the pill. The corresponding box will be opened to take out the pill. Node MCU is inbuilt with Wi-Fi module. The Wi-Fi module is configured as PILL BOXAP, such that the IP address is generated in local network. by pairing the IP address generated by PILLBOXAP to the Mobile website. The configuration data is send to the smart pillbox when the configuration is in ON mode. The concerned LED glow with buzzer at schedule time and to ensure the pill is taken The ir sensor mechanism is done once the pill is taken out it will send a notify msg to doctor or other person. And the door can be closed automatically after it.



HARDWARE MODULES

- Pill box
- Node MCU
- IC2134 SPEAKER MODULE
 - buttons
 - LEDs
 - IR SENSOR

Node MCU (ESP8266-12E)

ESP8266 is an impressive, low cost WiFi module suitable for adding Wi-Fi functionality to an existing microcontroller project via a UART serial connection. The

module can even be reprogrammed to act as a standalone Wi-Fi connected device—just add power! The feature list is impressive and includes: 802.11 b/g/n protocol Wi-Fi Direct (P2P), soft-AP Integrated TCP/IP protocol stack.



ESP8266-12E board Description

RTC MODULE

A real-time clock (RTC) is an electronic device (most often in the form of an integrated circuit) that measures the passage of time. Although the term often refers to the devices in personal computers, servers and embedded systems, RTCs are present in almost any electronic device which needs to keep accurate time. This is the SparkFun Real Time Clock (RTC) Module, this little breakout that uses the DS1307 to keep track of the current year, month, day as well as the current time. SOFTWARE MODULES

SPEAKER IC2134

This module enables to record voice and send out the recorded voice in case of signal enabled. The double frequency conversion technique and audio amplifier is attached to process the audio signal

IR SENSOR

An infrared (IR) sensor is an electronic device that measures and detects infrared radiation in its surrounding environment. ... When an object comes close to the sensor, the infrared light from the LED reflects off of the object and is detected by the receiver. The emitter is an IR LED and the detector is IR photodiode. The IR photodiode is sensitive to the IR light emitted by an IR LED. The photo-diode's resistance and output voltage change in proportion to the IR light received. This is the underlying working principle of the IR sensor.

SERVER MOTOR

This brings the effective closing and opening of door mechanism. The perfect control of relay signal gives the timely effect. A servo motor is a type of motor that can rotate with great precision. Normally this type of motor consists of a control

circuit that provides feedback on the current position of the motor shaft, this feedback allows the servo motors to rotate with great precision.

SOFTWARE

- ARDUINO IDE
- Android Studio (Mobile App)

ARDUINO IDE

ARDUINO is an open-source prototyping platform based on easy-to-use hardware and software.

(IDE) - contains a text editor for writing code, a message area, a text console, a toolbar with buttons for common functions and a series of menus. It connects to the ARDUINO and GENUINO hardware to upload programs and communicate with them.

Android Studio

Android is a software platform and operating system for mobile devices, based on the Linux kernel, and developed by Google and later the Open Handset Alliance. It allows developers to write managed code in the Java language, controlling the device via Google-developed Java libraries. The unveiling of the Android platform on 5 November 2007 was announced with the founding of the Open Handset Alliance, an association of 48 hardware, software, and telecom companies devoted to advancing open standards for mobile devices. RESULTS

ADVANTAGES

- Monitoring of health statistics Medicine, alarms and medication non-compliance control.
- Emergency and medical management services.
- Wireless identifiable Embedded healthcare systems.

CONCLUSION

Integrating of Hardware modules Node MCU, speaker, Buzzer, push Button and Mobile application to PILL Box and every module has been placed carefully to give reasonable output, thus contributing to the best working of the unit. This system assures the safety of the people and also prevents the wrong dosages. It reduces the effort in remembering medicine and people will get the schedule of the medicine containing medicine name timing.

REFERENCES

[1] AlokKulkarni, SampadaSathe “Healthcare applications of the Internet of Things:A Review” ,Department of Electronics and Telecommunication, Computer Engineering Pune University, Maharashtra, India, AlokKulkar et al, / (IJCSIT) International Journal of Computer Science and Information Technologies,Vol.5, 2014, 6229-6232

[2] Ronald Sekura, Gwen Gampel Paulson, “Using A Patient-Based Information Technology Approach For Solving Prescription Medication Non-Compliance”, Presentation at Information Technology Association of America

[3] David Niewolny,”How the Internet of Things Is Revolutionizing Healthcare”,Healthcare Segment Manager, Freescale Semiconductor.

[4] Z. Pang, “Technologies and architectures of the Internet-of- Things (IoT) for health and well-being,” Ph.D. dissertation, Dept. Electron.Syst., School Inf. Commun.Technol., Royal Inst. Technology (KTH), Stockholm, Sweden, 2013.

INFOKARA RESEARCH

An UGC-CARE Approved Group 2 Journal



INFOKARA

An ISO : 7021 - 2008 Certified Journal

ISSN NO: 1021-9056 / web : <http://infokara.com/>

e-mail : editor.infokara@gmail.com

Certificate of Publication

Certificate ID - IK-4339

This is to certify that the paper entitled
Intelligent Remainder Medicine Pill Box using IOT

Authored by
ABDUR RAHMAN.N

From
MAM School of Engineering, Tamil Nadu, India

Has been published in
INFOKARA RESEARCH, VOLUME 10, ISSUE 5, MAY - 2021



H. Mathew
Mathew Hull, Editor-In-Chief, INFOKARA RESEARCH



BLUETOOTH AND GSM BASED INTELLIGENT VEHICLE SYSTEMS FOR WOMEN SAFETY USING EMBEDDED TECHNOLOGY

P.Kavitha, Associate Professor,ECE,
T.Ashok, Associate Professor,ECE
N. Gayathri, A.Karthik

M.A.M.School of Engineering,
Siruganur, Trichy
kaviakshya@gmail.com, ashoksubaash@gmail.com
gayathri12061999@gmail.com,karthikips267@gmail.com

Abstract-

In our society the safety is the prime issue for women and children. The every day the count of victim to be increased . Recent statistics show that vehicle's passengers or taxi's passengers are gone missing frequently and sometimes their death has been increasing due to improper and unnoticed security issues. In this paper the safety of women and children to be ensure for our proposing model. We implement the intelligent security system for passengers using Bluetooth technology.

Keywords – Passengers, safety and security, Detection,display, password generate ,automatic door open.

1.INTRODUCTION

In recent years, acts of a violence and assault against women are rising. With the escalation of female employees in industries and other sectors of the commercial market, it is now-coming to a necessity for females to travel at late

hours and visit distant and isolated locations as a part of their work. However, the exponential increase in assault and violence against women in the past few years is posing a threat to the growth and development of women. Protection isn't the only measure that can suffice against this increasing abuse. A security solution that creates a sense of safety among women needs to be developed. In instances of attack, it is largely reported that women's are immobilized. Therefore there is a need of a simpler safety solution that can be activated as simply as by pressing a switch and can instantly send alerts to the near ones of the victim. This project focuses on a security system that is designed uniquely to serve the purpose of providing security and safety to women. The objective of research work is to create a portable safety device for women, which provides following facilities 1. Alerts family and friends by sending emergency message 2. Captures the images/video of the attacker to maintain a proof for legal actions.

EXISTING SYSTEM

In existing system GPS based passengers tracking system has been implemented. This system tracks the passengers on the basis of vehicle history and ticket number. It provides the history of passenger movement and displays location.

The receiver will receive a link to your location every 2 minutes giving them your updated location. Also, you will get updates on the Crime Scene in India and a “Tips Feed” option exclusively giving you safety tips in an emergency situation.

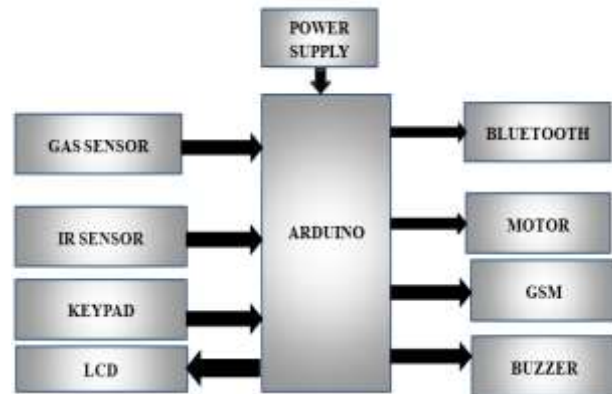
On the other hand, Internet of Things (IoT) localization technologies including RFID tags/readers or Bluetooth Low Energy (BLE) iBeacon devices can be adopted for accurate indoor positioning and efficient people guiding. In particular, iBeacon devices with BLE broadcasting and surrounding smart phones with BLE scanning can be operated in coordination to periodically collect the current locations of mobile users and cooperatively track the trajectories of moving targets. Innovative crowd sourced sensing applications and systems have been developed for Automatic Queue Time Estimation, Unobtrusive Privacy Permission Recommendation, Fine-Grained Air Quality Monitoring, and Peer-to-Peer Navigation.

DISADVANTAGE

Less security due to network issue

Door lock breaking is not implemented

II.BLOCK DIAGRAM



OPERATION

Here arduino based smart cab security system is designed. Various sensors are used to detect immoral activities in cab; the gas sensor will detect chloroform, mostly the kidnaper’s used for kidnapping. This will make the passengers to drowsiness condition. Here LCD is used to display it.

Next, the IR sensor is used here to generate password for each and every closing of door. The motor drives the car. The password is to driver and the passenger mobiles. When they enter the password, the car will be automatically stopped as the passengers mobile and the motor are paired via Bluetooth. The message will be sent to the respective persons such as their relatives or police stations through GSM, also buzzer is used here for intimating the emergency conditions. The motor drives the car which is paired to our mobile device

via Bluetooth. Finally the passenger can travel their journey without any fear.

I.ARDUINOIDE-The **Arduino** integrated development environment (**IDE**) is a cross-platform application (for Windows, macOS, Linux) that is written in the programming language **Java**. It is used to write and upload programs to Arduino board.

The source code for the IDE is released under the **GNU General Public License**, version 2. The Arduino IDE supports the languages **C** and **C++** using special rules of code structuring.^[4] The Arduino IDE supplies a **software library** from the **Wiring** project, which provides many common input and output procedures. User-written code only requires two basic functions, for starting the sketch and the main program loop, that are compiled and linked with a program stub main() into an executable **cyclic executive** program with the **GNU tool chain**, also included with the IDE distribution.^[5] The Arduino IDE employs the program avrdude to convert the executable code into a text file in hexadecimal encoding that is loaded into the Arduino board by a loader program in the board's firmware.

Arduino is an open-source electronics platform based on easy-to-use hardware and software. Arduino boards are able to read inputs - light on a sensor, a finger on a button, or a Twitter message - and turn it into an output - activating a motor, turning on an LED,

publishing something online. You can tell your board what to do by sending a set of instructions to the microcontroller on the board



II.PROTEUS

The **Proteus Design Suite** is a proprietary software tool suite used primarily for **electronic design automation**. The software is used mainly by electronic design engineers and technicians to create schematics and electronic prints for manufacturing printed circuit boards.

Proteus is a design software developed by Labcenter Electronics for electronic circuit simulation, schematic capture and PCB design. Its simplicity and user friendly design made it popular among electronics hobbyists. Proteus is commonly used for digital simulations such as

microcontrollers and microprocessors. It can simulate LED, LDR, USB Communication.

Proteus- is a simulation and design software tool developed by **Lab center Electronics for Electrical and Electronic circuit design**. It also possess **2D CAD drawing feature**.

III. ARDUINO UNO

Arduino is an open-source prototyping platform based on easy-to-use hardware and software.

Arduino boards are able to read inputs - light on a sensor, a finger on a button, or a Twitter message - and turn it into an output - activating a motor, turning on an LED, publishing something online.

You can tell your board what to do by sending a set of instructions to the microcontroller on the board.

To do so you use the Arduino programming language (based on Wiring), and the Arduino Software (IDE), based on Processing.



IV. GAS SENSOR (MQ6):

A gas detector is a device that detects the presence of gases in an area, often as part of a safety system. This type of equipment is used to detect a gas leak and interface with a control system so a process can be automatically shut down. A gas detector can sound an alarm to operators in the area where the leak is occurring, giving them the opportunity to leave. This type of device is important because there are many gases that can be harmful to organic life, such as humans or animals. Gas detectors can be used to detect combustible, flammable and toxic gases, and oxygen depletion. This type of device is used widely in industry and can be found in locations, such as on oil rigs, to monitor manufacture processes and emerging technologies such as photovoltaic. They may be used in firefighting. Gas leak detection is the process of identifying potentially hazardous gas leaks by sensors. These sensors usually employ an audible alarm to alert people when a dangerous gas has been detected. Common sensors include infrared point sensors, ultrasonic sensors, electrochemical gas sensors, and semiconductor sensors. More recently, infrared imaging sensors have come into use. All of these sensors are used for a wide range of applications and can be found in industrial plants, refineries, waste-water treatment facilities, vehicles, and homes



V. IR SENSOR

An infrared sensor circuit is one of the basic and popular sensor modules in an electronic device.

This sensor is analogous to human's visionary senses, which can be used to detect obstacles and it is one of the common applications in real time.

This circuit comprises of the following components

- ❖ LM358 IC 2 IR transmitter and receiver pair
- ❖ Resistors of the range of kilo ohms.
- ❖ Variable resistors.
- ❖ LED (Light Emitting Diode).



VI. Matrix Keypad:

A keypad is a set of buttons arranged in a block or "pad" which bear digits, symbols or alphabetical letters.

Pads mostly containing numbers are called a numeric keypad.

Numeric keypads are found on alphanumeric keyboards and on other devices which require mainly numeric input such as calculators, push-button telephones, vending machines, ATMs, Point of Sale devices



VII. LIQUID CRYSTAL DISPLAY

A liquid crystal display (LCD) is a flat panel display, electronic visual display, or video display that uses the light modulating properties of liquid crystals. Liquid crystals do not emit light directly. LCDs are available to display arbitrary images (as in a general-purpose computer display) or fixed images which can be displayed or hidden, such as preset words, digits, and 7-segment displays as in a digital clock. They use the same basic technology, except that arbitrary images are made up of a large number of small pixels, while other displays have larger elements. An LCD is a

small low cost display. It is easy to interface with a micro-controller because of an embedded controller (the black blob on the back of the board). This controller is standard across many displays (HD 44780) which means many micro-controllers (including the Arduino) have libraries that make displaying mes



sages as easy as a single line of code.

VIII. BLUETOOTH

Bluetooth is a wireless technology standard for exchanging data over short distances from fixed and mobile devices, and building personal area networks (PANs). It was originally conceived as a wireless alternative to RS-232 data cables. It can connect several devices, overcoming problems of synchronization.

IEEE 802.15.1 BLUETOOTH MODULE



Baud rate speeds: 1200bps up to 921Kbps, non-standard baud rates can be programmed.

Class 2 radio, 60 feet (20meters) distance, 4dBm output transmitter, -80dBm typical receive sensitivity

Frequency 2402 ~ 2480MHz,

FHSS/GFSK modulation, 79 channels at 1MHz intervals

Secure communications, 128 bit encryption

Error correction for guaranteed packet delivery

UART local and over-the-air RF configuration

Auto-discovery/pairing requires no software configuration

Auto-connect master, IO pin (DTR) and character based trigger modes

IX.DC MOTOR

A DC motor is a mechanically commutated electric motor powered from direct current (DC).The stator is stationary in space by definition and therefore the current in the rotor is switched by the commutator to also be stationary in space. This is how the relative angle between the stator and rotor magnetic flux is maintained near 90 degrees, which generates the maximum torque.DC motors have a rotating armature winding (winding in which a voltage is induced) but non-rotating armature magnetic

field and a static field winding (winding that produce the main magnetic flux) or permanent magnet. Different connections of the field and armature winding provide different inherent speed/torque regulation characteristics. The speed of a DC motor can be controlled by changing the voltage applied to the armature or by changing the field current. The introduction of variable resistance in the armature circuit or field circuit allowed speed control. Modern DC motors are often controlled by power electronics systems called DC drives.

X.GLOBAL SYSTEM FOR MOBILE COMMUNICATION (GSM):

- GSM stands for **G**lobal **S**ystem for **M**obile **C**ommunication. It is a digital cellular technology used for transmitting mobile voice and data services.
- The concept of GSM emerged from a cell-based mobile radio system at Bell Laboratories in the early 1970s.
- GSM is the name of a standardization group established in 1982 to create a common European mobile telephone standard.
- GSM is the most widely accepted standard in telecommunications and it is implemented globally.
- GSM is a circuit-switched system that divides each 200 kHz channel into eight 25 kHz time-slots. GSM operates on the mobile

communication bands 900 MHz and 1800 MHz in most parts of the world. In the US, GSM operates in the bands 850 MHz and 1900 MHz.

XI.BUZZER

A buzzer or beeper is a signalling device, usually electronic, typically used in automobiles, household appliances such as a microwave oven, or game shows. It most commonly consists of a number of switches or sensors connected to a control unit that determines if and which button was pushed or a preset time has lapsed, and usually illuminates a light on the appropriate button or control panel, and sounds a warning in the form of a continuous or intermittent buzzing or beeping sound. Initially this device was based on an electromechanical system which was identical to an electric bell without the metal gong (which makes the ringing noise). Often these units were anchored to a wall or ceiling and used the ceiling or wall as a sounding board.

XII.ACKNOWLEDGMENT

I wish to acknowledge Mrs.P.Kavitha, HEAD OF THE DEPARTMENT, M.A.M SHOOOL OF ENGINEERING for her advice on carrying out the performance.

XIII.CONCLUSIONS

Here we design an efficient cab for security purpose. In our day to day life, we are facing lots of troubles due to insufficient security. To avoid this we design a smart security cab by using recent

technologies. Two sensors are used here, a gas sensor which detects whether the chloroform inside the cab and if it is present, it will be notified by the LCD display and an IR sensor to detect the status of cab door and generates passwords for each closing of door. This password will be sent to the passenger through GSM. If the passenger wants to stop the car, then password can be entered either in the mobile device or in the keypad which is inside the cab connected in the seat. Then, the car will be automatically stopped. The message is also sent to the relatives or police stations. Also buzzer is placed inside the cab to intimate the emergency condition. The mobile device is configured for the motor cab via Bluetooth. Finally, the smart security system for cab has been implemented successfully.

XI. REFERENCES

- [1] J. Wang, Y. Wang, D. Zhang, and S. Helal. Energy Saving Techniques in Mobile Crowd Sensing: Current State and Future Opportunities. *IEEE Communications Magazine*, 56(5):164-169, May 2018.
- [2] S. L. Ting, S. K. Kwok, A. H. Tsang, and G. T. Ho. The Study on Using Passive RFID Tags for Indoor Positioning. *International Journal of Engineering Business Management*, 3(1):9-15, Feb. 2011.
- [3] F. Xiao, Z. Wang, N. Ye, R. Wang, and X. Li. One More Tag Enables Fine-Grained RFID Localization and Tracking. *IEEE/ACM Transactions on Networking*, 26(1):161-174, Feb. 2018.
- [4] C. Yao and W. Hsia. An Indoor Positioning System Based on the Dual-Channel Passive RFID Technology. *IEEE Sensors Journal*, 18(11):4654-4663, June 2018.
- [5] R. Faragher and R. Harle. Location Fingerprinting With Bluetooth Low Energy Beacons. *IEEE Journal on Selected Areas in Communications*, 33(11):2418-2428, Nov. 2015.
- [6] L. Yu, Y. Liu, T. Chi, and L. Peng. An iBeacon-Based Indoor and Outdoor Positioning System for the Fire Emergency Command. *Forum on Cooperative Positioning and Service (CPGPS)*, pages 326-329, May 2017.
- [7] Z. Chen, Q. Zhu, and Y. C. Soh. Smartphone Inertial Sensor-Based Indoor Localization and Tracking with iBeacon Corrections. *IEEE Transactions on Industrial Informatics*, 12(4):1540-1548, Aug. 2016.
- [8] X. Wu, R. Shen, L. Fu, X. Tian, P. Liu, and X. Wang. iBILL: Using iBeacon and Inertial Sensors for Accurate Indoor Localization in Large Open Areas. *IEEE Access*, 5:14589-14599, July 2017.
- [9] H. Zou, Z. Chen, H. Jiang, L. Xie, and C. Spanos. Accurate Indoor Localization and Tracking Using Mobile Phone Inertial Sensors, WiFi, and iBeacon. *IEEE International Symposium on Inertial Sensors and Systems*, pages 1-4, Mar. 2017.
- [10] L.-W. Chen and J.-J. Chung. Mobility-Aware and Congestion Relieved Dedicated Path Planning for Group-Based Emergency Guiding Based on Internet of Things Technologies. *IEEE Transactions on Intelligent Transportation Systems*, 18(9):2453-2466, Sep. 2017.



International Journal of Information And Computing Science

An ISO : 7021 - 2008 Certified Journal

ISSN NO: 0972-1347 / web : www.ijics.com / e-mail : submitijics@gmail.com

Address : # B11 - 157, Katraj - Dehu Road, Pune, Maharashtra - 412101.

CERTIFICATE OF PUBLICATION

Certificate ID : IJICS/S1562

This is to certify that the paper entitled

**BLUETOOTH AND GSM BASED INTELLIGENT
VEHICLE SYSTEMS FOR WOMEN SAFETY USING EMBEDDED TECHNOLOGY**

Authored by

P.Kavitha


From

M.A.M. School of Engineering, Siruganur, Trichy

Has been published in

IJICS JOURNAL, VOLUME 7, ISSUE 6, JUNE - 2020.




Dr. K. M. Pandey
Editor-In-Chief
IJICS
www.ijics.com





International Journal of Information And Computing Science

An ISO : 7021 - 2008 Certified Journal

ISSN NO: 0972-1347 / web : www.ijics.com / e-mail : submitijics@gmail.com

Address : # B11 - 157, Katraj - Dehu Road, Pune, Maharashtra - 412101.

CERTIFICATE OF PUBLICATION

Certificate ID : IJICS/S1562

This is to certify that the paper entitled

**BLUETOOTH AND GSM BASED INTELLIGENT
VEHICLE SYSTEMS FOR WOMEN SAFETY USING EMBEDDED TECHNOLOGY**

Authored by

T.Ashok


From

M.A.M. School of Engineering, Siruganur, Trichy

Has been published in

IJICS JOURNAL, VOLUME 7, ISSUE 6, JUNE - 2020.




Dr. K. M. Pandey
Editor-In-Chief
IJICS
www.ijics.com



INTERNET OF THINGS (IOT) BASED SMART ELECTRONIC DIGITAL NOTICE BOARD

A.Karthick kumar,
Assistant professor,
Dept of ECE,
M.A.M.School of Engg,
Trichy.

Mr.K.Karthickeyan,
Assistant professor,
Dept of ECE,
M.A.M School of Engg,
Trichy

Mr.P.Kavitha,
Associate professor,
Dept of ECE,
M.A.M School of Engg,
Trichy

Mr.T.Ashok
Associate professor,
Dept of ECE,
M.A.M.School of Engg,
Trichy.

Abstract—Notice boards are playing very important role in our day to day life. By replacing conventional Analog type notice board with digital notice board we can make information dissemination much easier in a paperless community. Here the admin can control notice board through internet. So information can be send anywhere in the world and can be displayed within seconds. Information may be in the form of text, image, pdf etc. mobile phone is used for sending information and node MCU is connected to internet at the receiving side. In addition to this an application which is installed on the admin's mobile phone can serve the same purpose. This application also contains a speech to text converter .So the admin can send text messages through his/her own voice.

Index terms – Internet of things, Node MCU.

I. INTRODUCTION

Notice board is an essential information gathering system in our life. In our day-to-day life we can see notice

boards in various places like, educational institutions, railway stations, shopping malls, Bus stations, offices etc. So we can say that Notice boards are the places to leave public information such as advertise events, announce events or provide attention to the public, etc. Now days a Separate person is needed to stick those information on the notice board. It will lead to lose of time as well as usage of manpower. In conventional analog type notice boards paper is the main medium for information exchange. We know that information counts are endless. So there is a usage of huge amount of paper for displaying those endless counts of information. The problems faced by the wooden or conventional type notice boards are resolved by the implementation of our digital notice board. It will bring an advanced means of passing notices around in the world in a much easier and efficient way. Due to the popularity of internet, we choose internet as a medium for transferring information. The Internet of things (IoT) is the network of physical devices, vehicles, home appliances and

other items embedded with electronics. Software, which enables these objects to connect and exchange data.

Each device is uniquely identifiable through its Embedded computing system but is able to inter operate within the existing Internet infrastructure For provide security, we add username and password type authentication system. So only respective authority can send informations. Node MCU which is the Heart of our system. A monitor is interfaced with node mcu. So information in the form of text, image and pdf can display on the large screens. Our primary aim is to get more people's attention on the display. By the usage of high definition display devices people can get more attention on the notice board rather than conventional notice boards. In conventional wireless notice board can display only texted messages. But in our newly implemented system can display images and pdf documents in addition to text messages. Because in Educational institutions majority of informations given from the higher authorities in the form of images or pdf format. So displaying these types of information make our system more user friendly. Due to the utilization of internet the sender can send message anywhere in the world. There is no range limitation for the successful exchange of information.

Internet of things



FIG1:IoT applications

The Internet of Things(IoT) is the network of devices, vehicles, and home appliances. It allows these things to connect, interact and exchange data.

IoT involves extending Internet connectivity beyond standard devices. Devices can communicate and interact over the Internet, and they can be remotely monitored and controlled. To accommodate the new demand on cities, municipalities around the globe are turning to the Internet of Things. To enhance their services, reduce costs, and improve communication.

II.OBJECTIVE

The main objective is to design an automatic, self enabled highly reliable electronic notice board. A display connected to a server system should continuously listen for the incoming messages from user, process it and display it on LCD screen. Message displayed should be updated everytime the user

sends new information. Only authenticated people should update the data to be displayed on the monitor.

III. DESIGN RATIONALE

Achieving the following criteria is the main designing goal for the architecture of the proposed system.

➤ Reduction of man power: Reduction in the effort of a separate person, who has stick notices manually on the conventional notice board.

➤ Reduction in time: The facilities in the high speed internet, the peoples can view transmitted informations on the display board within seconds. There is less waiting time for accessing the informations.

➤ Ease in accessibility: Here notice informations are accessed through internet, so there will be widespread of the information over a wide region. Also internet will give access to its respective nodes connected to its server and hence accessibility becomes easy.

➤ Improvement over technology: The sender and receiver are connected with each other with the help of internet. Thus it will enable the communication over a wide range without any physical connections between them.

➤ Reduction in the size of system: Only Node mcu is used for achieving overall

performance of the system. This single hardware makes the reduction in the system

IV. BLOCK DIAGRAM

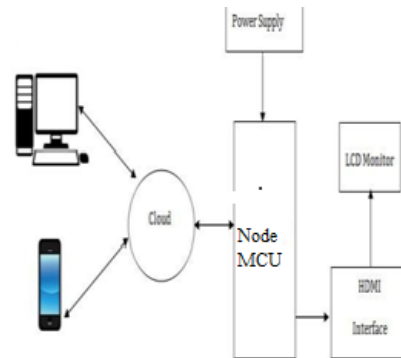


FIG :2 NODE MCU

The main objective of the system is to develop a wireless notice board that displays notices in the form of image, text, pdf.. It uses a NODE MCU as a processor. Node mcu is equipped with a Portable Projector/LCD display. We can display messages and can be easily set or changed from anywhere in the world. In addition mobile application is used to convert voice into text.. Here the voice is pass through the voice reorganization system and converted into text. The system will sent this message to cloud. Then it passes to the notice board which is connected to internet by Wi-Fi. The processor, process it and displayed on the screen. We can send the message to all the screens or desired screen.

V.COMPONENTS

1.LCD Display

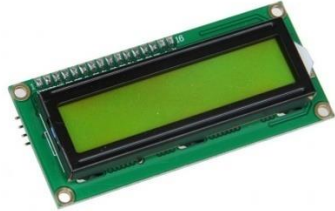


FIG:3: LIQUID CRYSTAL DISPLAY

Liquid crystal displays (LCDs) have supplies which combine the properties of both liquids and crystals. With the liquid crystal material sandwiched in between them, an LCD consists of two glass panels. The inner surface of the glass plates are covered with transparent electrodes that identify the character, symbols or patterns to be displayed and the polymeric layers are present in between the electrodes and the liquid crystal, which makes the liquid crystal molecules for maintaining a defined direction angle. The LCD does not generate light, so that the light is required for reading the display. By using backlighting, reading is feasible in the dark. The recent advances in technology have resulted in better legibility with more information displaying capability and a wider temperature range. These have resulted in the LCDs being extensively

used in telecommunications and in entertainment electronics.

2. HDMI INTERFERENCE

The Node MCU has a HDMI port which you can connect straightforwardly to a screen or TV with a HDMI link. This is the most effortless arrangement; some modern monitors and TVs have HDMI ports, and some don't, yet there are different choices.

3. NODE MCU



FIG :4: ESP 8266

NodeMCU is a low-cost open source IoT platform. It initially included firmware which runs on the ESP8266 Wi-Fi SoC from Espressif Systems, and hardware which was based on the ESP-12 module.

V. RELATED WORKS

In early days GSM technology is used for displaying informations.¹ Here GSM module which is located at digital notice board is used to receive information from the authorized user and displayed. In this work only text message is transferred .It become inefficient when we need to transfer other than text messages. By

introducing the concept of Bluetooth technology² communications become faster and efficient. Here an android application is used for enabling Bluetooth for sending message. This work mainly focused on cable replacement and data can send up to the rate of 1 Mb per sec. Bluetooth has limited range (approximately 70m to 100 m). In order to increase the range of communication Zig-bee based notice boards are introduced.³ But here data rate is only about 250 Kb per sec. Wi-Fi based digital notice boards are currently used in many places like schools, colleges, railway stations, Airports etc. Here Raspberry pi which act as a receiver and it connected with local Wi-Fi networks. When a person wants to send information to raspberry pi, the person first connected to corresponding Wi-Fi. So sender and receiver must be within the Wi-Fi range. Maximum possible range of Wi-Fi is about 100 meter. Due to this range information exchange must done within the boundaries.

VI. METHODOLOGY

The objective of the project is to display the message on the notice board from anywhere and anytime, that even provides broadcast alerts to the target users. The system was designed and developed using the Internet of Things. Arduino board integrates the display unit, Mobile App and SMS Agent through

Internet. The message to be displayed on the notice board is sent through a mobile app to the board with Arduino. The user needs to go through authentication via the Smart board android application to get access and then connect to the smart board using the WiFi. After the connection is established, the authorized user can send a notice in the form of message h to the smart board which will be displayed on the Smart board in the display. Once the user sends the notice to the smart board, the same notice will be saved on the server side of the website, which can be accessed for checking and maintaining the records of the notices being displayed.

VII.ALGORITHM

Following step by step procedure will explain the actual working of the system

1. Start
2. Login for access notice board.
3. If the user is valid then go to step 4 otherwise go to step 2.
4. Select Informations in the form of image, pdf and text files
5. Upload files.
6. Store the message.
7. Set the duration of displayed messages.
8. Set maximum limit for the size of image to be displayed.
9. If the received image is less than the limit it will directly displayed. Otherwise

image will be resized. 10. When pdf is received it will be converted to image.

11. Received image and text files

12. Display stored messages in First in first out order (FIFO)

13. Check for new notice. If it occurs go to step 8, else go to step 9

14. Repeat above steps when power supply is maintained.

15. Stop

VIII. PROPOSED PLAN OF WORK

This will be a moving message display, which might be utilized as the digital notice board, and moreover a Wi-Fi transceiver, that will be that the most recent innovation utilized for communication between the mobile and also the embedded devices. System can work like once the user desires to display or update the notice board, that is unimaginably useful to show the circulars, day by day occasions, plans are to be shown. At that point the Wi-Fi will receive the message in notice board system, the Node MCU chip has been inside the system is programmed in such a way that when the coding is written in embedded system Language receives any message it will browse the message form serial port through Wi-Fi transceiver, if the message is writing in any mobile phone then it will begin displaying the

information within the display system. The messages are displayed on the liquid crystal display. This system is to cut back the time wastage and update with any time is to be terribly simply. The serial Wi-Fi has been utilized it can be used to transmit an information from serial port communication. It implies that to display the information from to a tiny bit at a time to get the notice load up then stores it, messages are then shown in the LCD module.

IX. RESULT



FIG :5: IOT NOTICE BOARD

X. ADVANTAGES

- It can reduce use of papers and hence deforestation can be turned into afforestation.
- It can reduce physical effort of printing and distributing paper based notices.
- It can spread among more people in lesser time since large screen display is used.

XI.ACKNOWLEDGMENT

I wish to acknowledge Mr.A.KARTHICK KUMAR, AP/ECE M.A.M SHOOL OF ENGINEERING for her advice on carrying out the performance.

XII.CONCLUSIONS

Wireless technology provides fast transmission over long range data transmission. It saves time, cost of cables, and size of the system. Data can be sent from anywhere in the world. Username and password type authentication system is provided for adding securities.. Previously the notice board using Wi-Fi was used. In that there was the limit of coverage area, but in our system internet is used as communication medium. So there is no problem with coverage area. Multimedia data can be stored on chip.

REFERENCES

[1] Mr. Ramchandra K. Gurav, Mr. Rohit Jagtap, “Wireless Digital Notice Board Using GSM Technology”, International Research Journal of Engineering and Technology (IRJET), Volume: 02 Issue: 09 ,Dec-2015, e-ISSN: 2395 -0056

[2] Prof. Sudhir Kadam , Abhishek Saxena , Tushar Gaurav, “Android Based Wireless Notice Board and Printer”, International Journal of Innovative Research in

Computer and Communication Engineering, Vol. 3, Issue 12, December 2015, ISSN(Online): 2320-9801 ISSN (Print): 2320-9798.

[3] C.N.Bhoyar , ShwetaKhobragade , Samiksha Neware, “Zigbee Based Electronic Notice Board”, International Journal of Engineering Science and Computing, March 2017

[4] V.P.Pati, Onkar Hajare, Shekhar Palkhe,Burhanuddin Rangwala, “Wi-Fi Based Notification System”, The International Journal Of Engineering And Science (IJES), Volume 3 ,Issue 5 ,2014.

[5] S.ArulmuruganP P,S.AnithaP P,A.PriyangaP P,S.Sangeethapriya,” Smart Electronic Notice Board Using WI-FI”, - International Journal of Innovative Science, Engineering & Technology, Vol. 3 Issue 3, March 2016, ISSN 2348 – 7968

[6] Liladhar P. Bhamre , Abhinay P.Bhavsar , Dushyant V. Bhole , Dhanshree S. Gade, “Zigbee Based Notice Board”, IJARIE, Vol-3 Issue-1 2017,ISSN(O)-2395-4396.

[7] Jaiswal Rohit , Kalawade Sanket , Kore Amod , Lagad Sanket, “Digital - Notice Board”, International Journal of Advanced Research in Computer Engineering &

Technology (IJARCET) Volume 4 Issue 11, November 2015

[8] Bhumi Merai, Rohit Jain , Ruby Mishra, “Smart Notice Board”, International Journal of Advanced Research in Computer and Communication Engineering Vol. 4, Issue 4, April 2015, ISSN (Online) 2278-1021

[9] Modi Tejal Prakash, Kureshi Noshin Ayaz, Ostwal Pratiksha Sumtilal “Digital Notice Board”, International Journal of Engineering Development and Research, Volume 5, Issue 2,2017, ISSN: 2321-9939

[10] Suma M N, Amogh H Kashyap, Kajal D, Sunain A Paleka, “Voice over WiFi based smart wireless notice board”, SSRG International Journal of Electronics and Communication Engineering (SSRG-IJECE) – Volume 4 Issue 6 – June 2017 6

[11] P.Pavankumar , Sonita, S.Shruti, “Wireless scrolling LED display Notice board using WI-FI”, International Journal of Multidisciplinary – Innovation and Research Analysis (IJMIRA), Volume – 1; Issue 4; July- Sept 2017

[12] Prachee U. Ketkar, Kunal P. Tayade, Akash P. Kulkarni, Rajkishor M. Tugnayat: GSM Mobile Phone Based LED Scrolling Message Display System,

International Journal of Scientific Engineering and Technology Volume 2 Issue 3; PP ; 149-155

[13] Ms.Shraddha J Tupe, Ms A. R. Salunke, “Multi Functional Smart Display Using Raspberry-PI” Volume 2, Special Issue (NCRTIT 2015), January 2015. ISSN 2348 – 4853

[14] Vinod B. Jadhav, Tejas S. Nagwanshi, Yogesh P. Patil , Deepak R. Patil, “Digital Notice Board Using Raspberry PI”, International Research Journal of Engineering and Technology (IRJET), Volume 3, Issue5,May 2016W.- K.Chen,LinearNetworksandSystems.Belmont, CA:Wadsworth, 1993, pp. 123–135

[15] Ms. Sejal V. Gawande, Dr. PrashantR.Deshmukh “Raspberry Pi Technology” International Journal of Advanced Research in Computer Science and Software Engineering(IJARCSSE), Volume 5, Issue 4, April 2015

[16] RajeebLochan Dash, Mrs. A. RuhanBevi “Real-time Transmission of Voice over 802.11 Wireless Networks Using Raspberry Pi” International Journal of Engineering Development and Research (IJEDR) 2014 Volume 2, Issue 1

[17] GuoYinan, Zhang Shuguo, Xiao Dawei "Overview of Wi-Fi Technology" The 2nd International Conference on Computer Application and System Modeling 2012, Published by Atlantis Press, Paris, France.

[18] J. S. Lee, Y. W. Su, and C. C. Shen, proposed a "A Comparative Study of Wireless Protocols: Bluetooth, UWB, Zigbee, and Wi-Fi", Proceedings of the 33rd Annual Conference of the IEEE Industrial Electronics Society (IECON), pp. 46-51, November 2007



International Journal of Information And Computing Science

An ISO : 7021 - 2008 Certified Journal

ISSN NO: 0972-1347 / web : www.ijics.com / e-mail : submitijics@gmail.com

Address : # B11 - 157, Katraj - Dehu Road, Pune, Maharashtra - 412101.

CERTIFICATE OF PUBLICATION

Certificate ID : IJICS/S1601

This is to certify that the paper entitled

**“INTERNET OF THINGS (IOT) BASED SMART
ELECTRONIC DIGITAL NOTICE BOARD”**

Authored by

K.Karthickeyan


From

M.A.M.School of Engg, Trichy

Has been published in

IJICS JOURNAL, VOLUME 8, ISSUE 1, JANUARY - 2021.




Dr. K. M. Pandey
Editor-In-Chief
IJICS
www.ijics.com





International Journal of Information And Computing Science

An ISO : 7021 - 2008 Certified Journal

ISSN NO: 0972-1347 / web : www.ijics.com / e-mail : submitijics@gmail.com

Address : # B11 - 157, Katraj - Dehu Road, Pune, Maharashtra - 412101.

CERTIFICATE OF PUBLICATION

Certificate ID : IJICS/S1601

This is to certify that the paper entitled

**“INTERNET OF THINGS (IOT) BASED SMART
ELECTRONIC DIGITAL NOTICE BOARD”**

Authored by

A.Karthick kumar

From

M.A.M.School of Engg, Trichy

Has been published in

IJICS JOURNAL, VOLUME 8, ISSUE 1, JANUARY - 2021.



K.M. Pandey
Dr. K. M. Pandey
Editor-In-Chief
IJICS
www.ijics.com





International Journal of Information And Computing Science

An ISO : 7021 - 2008 Certified Journal

ISSN NO: 0972-1347 / web : www.ijics.com / e-mail : submitijics@gmail.com

Address : # B11 - 157, Katraj - Dehu Road, Pune, Maharashtra - 412101.

CERTIFICATE OF PUBLICATION

Certificate ID : IJICS/S1601

This is to certify that the paper entitled

**“INTERNET OF THINGS (IOT) BASED SMART
ELECTRONIC DIGITAL NOTICE BOARD”**

Authored by

P.Kavitha

From

M.A.M.School of Engg, Trichy

Has been published in

IJICS JOURNAL, VOLUME 8, ISSUE 1, JANUARY - 2021.



K.M. Pandey
Dr. K. M. Pandey
Editor-In-Chief
IJICS
www.ijics.com



MEDICAL HANDWRITTEN PRESCRIPTION RECOGNITION USING CRNN

1. K.Karthikeyan/Assistant professor/Department of ECE/M.A.M School of Engineering,
2. P.Kavitha/Assistant professor/Department of ECE/M.A.M School of Engineering,
3. A.Karthickkumar/Assistant professor/Department of ECE/M.A.M School of Engineering,

karthikcacet121@gmail.com, kaviakshya@gmail.com, kumar.akarthick783@gmail.com

Abstract- Reading a doctor's handwritten prescription is a challenge that most patients and some pharmacists face; an issue that, in some cases, lead to negative consequences due to wrong deciphering of the prescription. Part of the reason why doctor's prescriptions are so difficult to decipher is that doctors make use of Latin abbreviations and medical terminology that most people don't understand. This paper demonstrates how Artificial Neural Networks (ANN) is used to develop a system that can recognize handwritten English medical prescriptions. Using the Deep Convolution Recurrent Neural Network to train this supervised system, input images are segmented and processed to detect characters and classify them into the 64 different predefined characters. The results show that the proposed system yields good recognition rates and an accuracy of %98. Keywords: CRNN, RNN, ANN, prescriptions, handwritten text, OCR..

I. INTRODUCTION

Most Optical Character Recognition systems work at the link level by transforming the text-line image into a sequence of feature vectors using Recurrent Neural Networks (RNN) in order to recognize handwritten text

[1]. There are some promising results of experiments where detection was executed at a paragraph level [2]. However, the best recognition is achieved at the line level [3]; hence, a solution to decipher a handwritten medical prescription correctly is still lacking. Medical errors due to wrong interpretation of prescription are common and can result in harm to patients and sometimes lead to death, especially when the wrong dosage or medicine is taken [4] 'To Err is Human' report by the Institute of Medicine (IoM) states that medical errors cause at least an estimated 44,000 preventable deaths annually in the United States of America alone, of which 7,000 deaths are attributed to illegible handwriting [5]. In many cases it is ideal to have prescriptions deciphered or translated into digital forms rather than be paper based, in order to make pharmacists' lives easier and minimize the risk of wrongly interpreted dosages and medication. In addition, illegible handwriting can lead to adverse medico-legal implications since sloppy handwriting can be interpreted by the jury as sloppy care [6]. Handwriting recognition is the ability of a program to receive input images and transform them into digital characters by

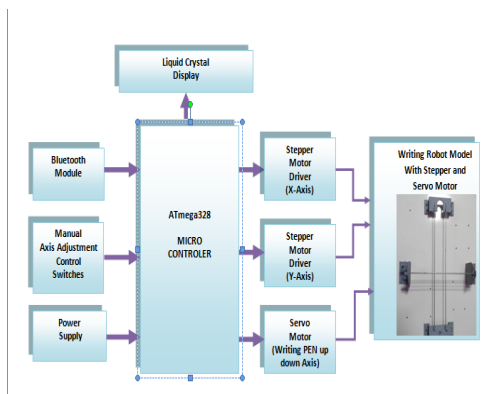
detecting handwritten letters and map them into predefined characters list. Lexicon-Driven Handwritten Text Recognition is another form of recognition. It focuses on splitting words in case of spotting a spacing between them. This proved to be effective with 74.37% according to the paper “Handwritten character strings on medical prescription reading by using lexicon- driven” [7]. This paper describes how neural network or CRNN technology is used specifically to detect medical prescriptions and translate the handwritten text.

II. BLOCK DIAGRAM
TRANSMITTER SECTION



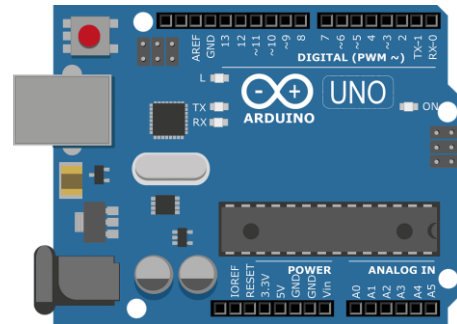
RECEIVER SECTION - WRITING ROBOT

RECEIVER SECTION



III. OPERATION

1. MICROCONTROLLER



A microcontroller is a compact integrated circuit designed to govern a specific operation in an embedded .A typical microcontroller includes a processor, memory and input/output (I/O) peripherals on a single chip. Microcontrollers are used in automatically controlled products and devices, such as automobile engine control systems, implantable medical devices, remote controls, office machines, appliances, power tools, toys and other embedded systems. Microcontrollers are embedded inside devices to control the actions and features of a product. Microcontrollers can take inputs from the device they controlling and retain control by sending the device signals to different parts of the device. A good example is a TV's microcontroller. A microcontroller is a small computer on a single IC that integrates all the features that are found in the microprocessor. In order to serve different applications, it has a high concentration of on chip facilities such as RAM, ROM, I/O ports, timers, serial port, clock circuit and interrupts.

2. BLUETOOTH MODULE

A Bluetooth module is usually a hardware component that provides a wireless product to work with the computer; or in some cases, the bluetooth may be an accessory or peripheral, or a wireless headphone. or other product (such as cellphones can use. HC-05 Bluetooth Module is an easy to use Bluetooth SPP (Serial Port Protocol) module, designed for transparent wireless serial connection setup. Its communication is via serial communication which makes an easy way to interface with controller or PC.

Class 1 transmitting at 100 mW with a range of 100 meters or 328 feet.

Class 2 transmitting at 2.5 mW with a range of 10 meters or 33 feet (most Bluetooth headsets and headphones are common Class 2 devices).

3. LCD Display



There are different materials used. But, a common material is a type of poly-silicon. An LCD is an electronically-modulated optical device made up of any number of pixels filled with liquid crystals and arrayed in front of a light source (backlight) or

reflector to produce images in color or monochrome. Liquid crystal display technology works by blocking light. ... At the same time, electrical currents cause the liquid crystal molecules to align to allow varying levels of light to pass through to the second substrate and create the colors and images that you see. Liquid crystals are basically carboxylate molecules.

4. STEPPER MOTOR



A stepper drive is the driver circuit that control how the stepper motor operates. Stepper drives work by sending current through various phases in pulses to the stepper motor. ... Two-phase-on driving has its name because two phases are on at a time. The speed of the motor is controlled by the frequency of the pulses. The stepper motor is used for precise positioning with a motor, such as hard disk drives, robotics, antennas, telescopes, and some toys. Stepper motors cannot run at high speeds, but have a high holding torque. Stepper motors are DC motors that move in discrete steps. They have multiple coils that are organized in groups called "phases". By energizing each phase in

sequence, the motor will rotate, one step at a time. With a computer controlled stepping you can achieve very precise positioning and/or speed control.

5. SERVO MOTOR



A servo motor is an electrical device which can push or rotate an object with great precision. If you want to rotate an object at some specific angles or distance, then you use servo motor. It is just made up of simple motor which run through servo mechanism. Servos are used in radio-controlled airplanes to position control surfaces like elevators, rudders, walking a robot, or operating grippers. Servo motors are small, have built-in control circuitry and have good power for their size. There is no single “type” of servo motor. ... The fundamental difference in operation between an AC and a DC motor is that the speed of an AC motor is controlled by the frequency of the applied voltage and the number of magnetic poles in the motor.

IV. METHODOLOGY

The objective of the project is to display the message on the notice board from anywhere and anytime, that even provides broadcast alerts to the target users. The system was designed and developed using the Internet of Things. Arduino board integrates the display unit, Mobile App and SMS Agent through Internet. The message to be displayed on the notice board is sent through a mobile app to the board with Arduino. The user needs to go through authentication via the Smartboard android application to get access and then connect to the smartboard using the WiFi. After the connection is established, the authorized user can send a notice in the form of message to the smartboard which will be displayed on the Smartboard in the display. Once the user sends the notice to the smartboard, the same notice will be saved on the server side of the website, which can be accessed for checking and maintaining the records of the notices being displayed.

V. APPLICATION

- Accuracy
- Less delay
- Low cost

VI. ACKNOWLEDGMENT

I wish to acknowledge Mrs.P.Kavitha, Head of the department, M.A.M School of

engineering for her advice on carrying out the performance.

VII. CONCLUSION

In this paper, a state-of-the-art CRNN system for text- words recognition of doctors' prescriptions is presented. It shows how to train such system with few labeled input data. Precisely, 10% labeled examples were provided for training. Finally, a normalized-scale for the samples is proposed in order to get better and more accurate results. This combination of normal handwriting and that of doctors' prescriptions generated accurate results. This program achieved a score of 95% accuracy, which is really great, taking into account training time and amount of data input. In order to improve these results, more work is needed on input handling. The algorithm needs to learn how to read hard paragraphs and automatically segment them into small texts. Although the network is complex, a small change in the initial parameters leads to great differences in the results. There is also a great difference between using clear texts and handwritten doctors' prescriptions in adjusting the weights. Having clear text in the training phase doesn't yield correct results while testing prescriptions, and vice-versa. Some might insist that this work is mainly focused on character recognition; however, it focuses on doctors' character recognition and not any

simple handwritten text. For the future work, this project could be implemented in a form of mobile application that can be accessible to various users, including patients, pharmacists and people responsible for double-checking doctors' prescriptions.

VIII. REFERENCE

- [1] B. Moysset, C. Kermorvant, and C. Wolf, "Full-page text recognition: Learning where to start and when to stop," arXiv preprints arXiv: 1704.08628, 2017.
- [2] T. Bluche, "Joint line Segmentation and transcription for end-to- end handwritten paragraph recognition," in *Advances in Neural Information Processing Systems*, 2016, pp. 838-846.
- [3] P. Voigtlaender, P. Doetsch, and H. Ney. "Handwriting recognition with large multidimensional long short-term memory recurrent neural networks," in *Frontiers in Handwriting Recognition (ICFHR)*, 2016 15th international Conference on. IEEE, 2016, pp. 228-233
- [4] Daniel K Sokol and Samantha Hettige. Poor handwriting remains a significant problem in medicine. *J R SOC Med.* Dec 2006; 99(12): 645-646. PMID: PMC1676338.
- [5] Dr. Nomal Chandra Borah, Chairman & Managing Director, Guwahati Neurological Research Centre. Doctor's illegible handwriting creating confusion, causing

death. April 20, 2015 [6] Stephens E. Medical-legal liability in emergency medicine. 2005.

[7] K. Simonyan and A. Zisserman, “Very deep convolutional networks for large-scale image recognition,” arXiv preprint arXiv:1409.1559, 2014.

[8] Colah. Understanding LSTM Networks. Posted on github on August 27, 2015.

[9] Roger Achkar, Mustafa El-Halabi, Elie Bassil, Rayan Fakhro, and Marny Khalil. Voice identity finder using the back propagation algorithm of an artificial neural network. *Procedia Computer Science*, 95:245–252, 2016.

[10] Youssef Harkouss, Souhad Mcheik, and Roger Achkar. Accurate wavelet neural network for efficient controlling of an active magnetic bearing system. 2010.

[11] Chafic Saide, Régis Lengelle, Paul Honeine, Cedric Richard, and Roger Achkar. Nonlinear adaptive filtering using kernel-based algorithms with dictionary adaptation. *International Journal of Adaptive Control and Signal Processing*, 29(11):1391–1410, 2015.

[12] George Abou Kassm and Roger Achkar. Lpr cnn cascade and adaptive deskewing. *Procedia Computer Science*, 114:296–303, 2017



International Journal of Information And Computing Science

An ISO : 7021 - 2008 Certified Journal

ISSN NO: 0972-1347 / web : www.ijics.com / e-mail : submitijics@gmail.com

Address : # B11 - 157, Katraj - Dehu Road, Pune, Maharashtra - 412101.

CERTIFICATE OF PUBLICATION

Certificate ID : IJICS/S1602

This is to certify that the paper entitled

“MEDICAL HANDWRITTEN PRESCRIPTION RECOGNITION USING CRNN ”

Authored by

K.Karthikeyan


From

M.A.M School of Engineering

Has been published in

IJICS JOURNAL, VOLUME 8, ISSUE 1, JANUARY - 2021.




Dr. K. M. Pandey
Editor-In-Chief
IJICS
www.ijics.com





International Journal of Information And Computing Science

An ISO : 7021 - 2008 Certified Journal

ISSN NO: 0972-1347 / web : www.ijics.com / e-mail : submitijics@gmail.com

Address : # B11 - 157, Katraj - Dehu Road, Pune, Maharashtra - 412101.

CERTIFICATE OF PUBLICATION

Certificate ID : IJICS/S1602

This is to certify that the paper entitled

“MEDICAL HANDWRITTEN PRESCRIPTION RECOGNITION USING CRNN ”

Authored by

P.Kavitha

From

M.A.M School of Engineering

Has been published in

IJICS JOURNAL, VOLUME 8, ISSUE 1, JANUARY - 2021.



K.M. Pandey
Dr. K. M. Pandey
Editor-In-Chief
IJICS
www.ijics.com





International Journal of Information And Computing Science

An ISO : 7021 - 2008 Certified Journal

ISSN NO: 0972-1347 / web : www.ijics.com / e-mail : submitijics@gmail.com

Address : # B11 - 157, Katraj - Dehu Road, Pune, Maharashtra - 412101.

CERTIFICATE OF PUBLICATION

Certificate ID : IJICS/S1602

This is to certify that the paper entitled

“MEDICAL HANDWRITTEN PRESCRIPTION RECOGNITION USING CRNN ”

Authored by

A.Karthickkumar

From

M.A.M School of Engineering

Has been published in

IJICS JOURNAL, VOLUME 8, ISSUE 1, JANUARY - 2021.



K.M. Pandey
Dr. K. M. Pandey
Editor-In-Chief
IJICS
www.ijics.com



SECURED COMMUNICATION IN AIRCRAFT SYSTEM USING LI-FI FOR MILITARY APPLICATION

1. P.Kavitha, Head of the Department/ECE, M.A.M.School of Engineering, Trichy
2. T.Ashok, Head of the Department/BME
Kongunadu College of Engineering and Technology, Tholurpatti
3. K.Karthikeyan, Assistant Professor/ECE,
4. A.Karthick Kumar, Assistant Professor/ECE, M.A.M.School of Engineering, Trichy
5. K. Umarani, Associate professor /ECE, MAM SCHOOL OF ENGINEERING, Trichy
kaviakshya@gmail.com, ashoksubaash@gmail.com, karthikacet121@gmail.com,
kumar.akarthick783@gmail.com, umaranikece@gmail.com

Abstract-Nowadays security is more important in our life. Most of the security system braked by hackers and most of the communication crashed by hackers. So we are develop most secure communication in warplane using LI-FI (Light-fidelity).In this project we are establish LI-FI based communication between two Warplane. In Li-Fi , the data is transmitted in several bit-streams through high-speed flickering of the LED bulb and decoded on the receiver side which consists of a photo detector. This happens in the form of a binary transmission of data, where ‘0’ is the LED in its ‘off state’ and ‘1’ is the LED in its ‘on-state’. This concept is based on transmit data to demonstrate the use-cases and the possible impact it can have in the ever growing field of communication.

Keywords – LI-FI, Communication, Security, High-speed.

I.INTRODUCTION

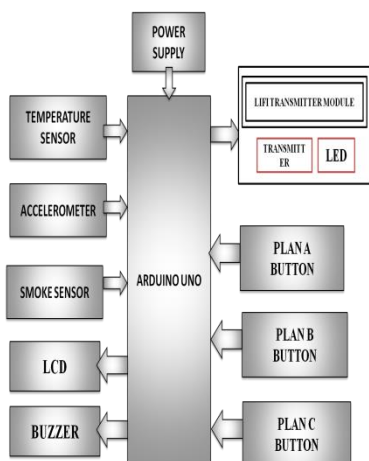
Li-Fi is an important and popular technology in the communication system. Li- Fi is nothing but the Light -fidelity communication systems. It is the very fast and inexpensive wireless communication systems and is the optical version of the Wi-Fi. The technology works by adapting light emitting diode (LED's) to send digital type of information, invisible to the

naked eye. In this, we present initial designs and results of a small-scale prototype of a vehicle to vehicle communication system using light fidelity (Li-Fi) technology.

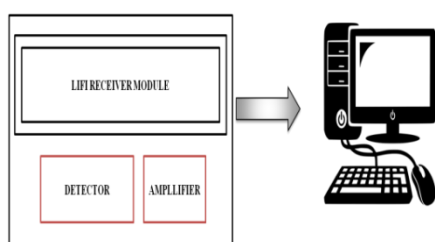
II.BLOCK DIAGRAM

Our proposed system attempts to implement LI-FI communication in war planes at war field. Li-fi is a most secured communication. It will communicate between device to device and also monitoring sensor data's.All the sensors are connected to Arduino . Temperature sensor is monitoring warplane engine heat. Accelerometer sensor detect warplane angle. Smoke sensor detect smokes from fire damaged things. LCD display will showing all the readings. switches will interfacing with arduino. Every switches will execute different plane.All the data's are transmit through LI-FI. Receiver will receives all the data and it will show on personel computer.

TRANSMITTER BLOCK



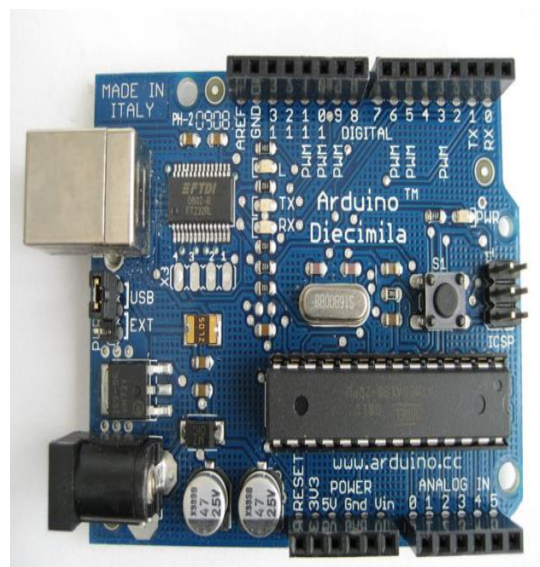
RECEIVER BLOCK



III. OPERATION

ARDUINO UNO __Arduino is an open-source prototyping platform based on easy-to-use hardware and software. Arduino boards are able to read inputs - light on a sensor, a finger on a button, or a Twitter message - and turn it into an output - activating a motor, turning on an LED, publishing something online. A set of instructions can be sent to the microcontroller on the board. To do so the Arduino programming language (based on wiring)is used ,and the Arduino software (IDE),based on processing. A circuit is designed such that the LED and a

phototransistor are interfaced with an Arduino.



To do so , the Arduino programming language (based on Wiring) is used, and the Arduino Software (IDE), based on Processing.

LCD DISPLAY



A liquid-crystal display (LCD) is a flat-panel display or other electronic visual display that uses the light-modulating properties of liquid crystals. Liquid crystals do not emit light directly.

TEMPERATURE SENSOR_LM35 is a precision IC temperature sensor with its output proportional to the temperature (in oC). The sensor circuitry is sealed and therefore it is not subjected to oxidation and other processes. With LM35, temperature can be measured more accurately than with a thermistor.It also possess low self heating and does not cause more than 0.1oC temperature rise in still air.

- In this proposed system we will implement LI-FI communication in war planes at war field
- Li-fi is a most secured communication. It will communicate between device to device and also monitoring sensor data's

All the sensors are connected to Arduino . Temperature sensor is monitoring warplane engine heat. Accelerometer sensor detect warplane angle. Smoke sensor detect smokes from fire damaged things.

LCD display will showing all the readings. Buttons will interfacing with arduino. Every buttons will execute different plans.

All the data's are transmit through LI-FI. Receiver will receives all the data and it will show on pc.

Li-Fi:

Li-Fi stands for Light-Fidelity which provides transmission of data through illumination by sending data through an LED light bulb. Li-Fi uses Light Emitting Diodes (LED) which have high modulation bandwidth and energy efficient illumination.

These LED's have high switching speeds that enable them to modulate according to the stream of bits that are sent. This transmission takes place in a parallel stream such that more data is being transmitted simultaneously.

The switching speed is too fast to be visible to the naked eye and thus this transmission is not noticeable. This technology was proposed by German physicist Harald Haas in University of Edinburgh. Li-Fi, at its core is light-based Wi-Fi with the main difference is that it uses light instead of radio waves to transmit data. The Li-Fi system

would consist of regular,off-the-shelf, LED bulbs that provide internet or data transmission as well as illumination. It utilizes the visible light portion of the electromagnetic spectrum (380 nm to 780 nm). Thus, it has 10,000 times more space available Thus more available bandwidth is present. Theoretically, it can reach the speeds up to 224 Gbps. [4]

Related Works

This section discusses the various advantages of VLC and elucidates on the differences between Li-Fi and Wi-Fi. By the year 2020, 10 billion devices will be subscribed in the LTE, which would result in an exponential growth of wireless traffic demand and result in a congested, scarce, and expensive RF-spectrum. The last few generations like 2G, 3G, etc., there have been many conventional methods employed to improve the capacity of the spectrum like spatial re-use and inter-cell interference coordination. Li-Fi can play a major role in relieving the heavy loads which the current wireless systems face since it adds a new and unutilized bandwidth of visible light to the currently available radio waves for data transfer. [7]

Visible Light Communication may also be used to complement current RF systems as Li-Fi will guarantee safer networks and higher speeds. In offices and schools the maximum data is exchange happens within the same building. Usage of Li-Fi system along with the 5G Wi-Fi, would help solve this issue. Due to Li-Fi, the transmission of video etc., will become faster, since it is viewed or downloaded, indoors and 5G can be used only when data exchange is needed outside the premises. [4] [7]

Wi-Fi is very susceptible to man-in-the-middle attacks etc. Li-Fi works only in LOS condition which thus, increases the security of the transmission. The technology is highly directional and localized as communication only takes place where the light can be seen, therefore the light can be

directed towards certain areas within the office.

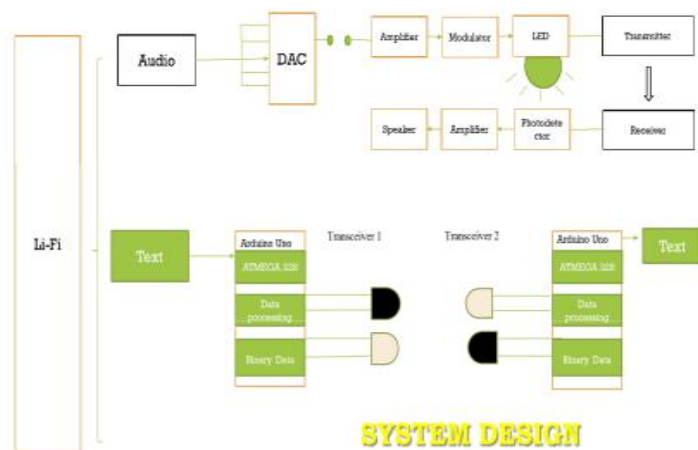
Visible light cannot penetrate opaque objects, which means that the wireless signal is constrained to within a strictly defined area of illumination. Secure can be created by closing blinds and shutting doors. [7]

Design Methodology

Li-Fi can be used for transmission of audio signals, text, images, and videos. It can also be used for providing internet.

This paper mainly deals with the transmission of two types of data; audio waves and text. We have transmitted audio signals from one source to one output (SISO), more than one source to a single output (MISO), more than one source to multiple outputs (MIMO) and studied topologies and different characteristics and variations observed in the data being transmitted at different setups. [2] We have achieved the transmission of text between two users using a setup of Arduino boards, L.E.D. and Silicon photo-diode.

Li-Fi can also be used to transmit images and eventually even provide internet by using modulation techniques like OFDM. [2] Li-Fi when combined with Wi-Fi, provides an ideal set up where the disadvantages of Li-Fi are covered up by the handoffs of the devices to Wi-Fi. [7]



AUDIO SEGMENT:

The transmission of audio signal was done through a phone at the transmitter end, providing the audio signal through the 3.5 mm jack that would convert the digital signal to an analog signal. This analog signal is amplified and sent to the array of LEDs that were connected on the breadboard. A power supply is also given to the LED array. This power supply is provided by a 9V battery that is connected to the 3.5 mm jack and the LED array.

This variation in the intensity of light, however, is captured on a solar panel that acts as a photodetector. It captures all the variations and sends the received signal to the pre-amplified speaker.

Using the same concept, instead of providing an analog signal from a phone, a text to speech software was used. A text was typed into the software and the software reads out the text.

This audio signal, generated while reading out the text, was transmitted through the fluctuation of LED arrays as mentioned above, and captured on a solar panel. This was then heard through a pre-amplified speaker. [8]

TEXT SEGMENT:

The text transmission segment was done in three parts. Firstly, text transmission from Arduino to itself. Secondly, text transmission between two Arduinos using IR. Thirdly, text transmission between two Arduinos using VLC.

Data Transmission

The transmission was done in various parts: Audio and Video.

A. Audio Transmission using Li-Fi

The transmission of audio signal was done through a Smartphone at the transmitter

end, providing the audio signal through the 3.5 mm jack. The 3.5mm audio jack and the input audio from the phone is converted from digital to analog. A typical 3.5mm audio jack has three output lines namely, right, left and the ground. The left and right have the audio output signal, which is connected to the negative of the 9V battery. The ground of the 3.5mm jack is given to the negative of the LED array connected on a breadboard and the positive of the 9V array is given to the resistors in series with the LED array.

This circuit effectively modulates the intensity of the LED's light, which acts as carrier wave, according to the effective voltage difference. The fluctuations occur at a high speed, invisible to the naked human eye. Thus, the variation in intensity of light from the LED array is not realized by the human eye.

This variation in the intensity of light, however, is captured on a solar panel that acts as a photo detector. It captures all the variations and sends the received signal to the pre-amplified speaker. The analog signal that was transmitted through the fluctuating LED array to the solar panel gets amplified in the pre-amplified speaker and emits the sound waves to be heard from the speaker. The sound intensity received from the speaker varies based on the distance of the solar panel from the LED arrays. This shows that the information can be received from the line of sight of the LED array.

As the distance between LED array and the solar panel increases, the intensity of light reduces and the light becomes more scattered thus, making it difficult for the solar panel to detect all the light rays being emitted.

IX.CONCLUSIONS

In this paper, a real-time audio broadcast prototype off the shelf LED's are used, it is envisaged that using commercial LED lamps would result in higher distances of transmission. It is shown that transmission of high quality audio with the distance of 1

m can be achieved and improvements can be made by adding focusing lens between the transmitter and the receiver.

In the data transmission prototype, the encoding and decoding can be used in the transmitter part and receiver part to reduce the error in transmission. In addition, the data transmission rate could be enhanced by using fast switching multiple LED's. The tests were carried out indoors under ambient light conditions. Larger coverage of area for transmission can be obtained by using LED arrays.

VLC is still in a very early stage; however, it is a promising technology with a wide range of prospective applications. The interest in VLC is increasing throughout the world and we can soon expect many real-world applications.

Li-Fi is a fast and cheap wireless-communication system. The increasing demand for higher bandwidths, faster and more secure data transmission as well as environmental and undoubtedly human friendly technology heralds the start of a major shift in wireless technology, a shift from RF to optical wireless technologies. The possibilities are numerous and research can provide us with many solutions. This technology can be used to make every LED bulb into a Li-Fi hotspot to transmit data wirelessly and will proceed to give us a safer, faster and a greener network.

XI.REFERENCES

- [1] Gurpinder Singh, "Li-Fi (Light Fidelity) – An Overview to future Wireless technology in Field of Data Communication", November (2015)
- [2] Xu Bao ,Guanding Yu , Jisheng Dai , Xiaorong Zhu, "Li-Fi: Light fidelity-a survey", 18 January 2015
- [3] Rahul R.Sharma, Akshay Sanganal, Sandhya Pati, "Implementation of A Simple Li-Fi Based System", October 2014

- [4] Dobroslav Tsonev, Stefan Videv and Harald Haas, "Light Fidelity (Li-Fi): Towards All-Optical Networking"
- [5] Akanksha R. Shrivastava, "Li-Fi: The Future Bright Technology"
- [6] Harald Haas, "Wireless data from every light bulb", TED Global, Edinburgh, July 2011
- [7] Ashmita Shetty, "A Comparative Study Analysis on Li-Fi and Wi-Fi", September 2016.
- [8] Yingjie He, Liwei Ding, Yuxian Gong, Yongjin Wang, "Real-time Audio & Video Transmission System Based on Visible Light Communication", June 2013.
- [9] M. Mutthamma, "A survey on Transmission of data through illumination - Li-Fi", December 2013
- [10] T. Padmapriya, V. Saminadan, "Performance Improvement in long term Evolution-advanced network using multiple input multiple output technique", Journal of Advanced Research in Dynamical and Control Systems, Vol. 9, Sp-6, pp: 990-1010, 2017.
- [11] S.V. Manikanthan and K. Baskaran "Low Cost VLSI Design Implementation of Sorting Network for ACSFD in Wireless Sensor Network", CiiT International Journal of Programmable Device Circuits and Systems, Print: ISSN 0974 – 973X & Online: ISSN 0974 – 9624, Issue : November 2011, PDCS112011008.
- [12] S.V. Manikanthan and T. Padmapriya "Recent Trends In M2m Communications In 4g Networks And Evolution Towards 5g", International Journal of Pure and Applied Mathematics, ISSN NO:1314-3395, Vol-115, Issue-8, Sep 2017.
- [13] Rajesh, M., and J. M. Gnanasekar. "CONGESTION CONTROL USING AODV PROTOCOL SCHEME FOR WIRELESS AD-HOC NETWORK." Advances in Computer Science and Engineering 16.1/2 (2016): 19.
- [14] R. Jeevidha, V. Sowmiya, K. Kiruthiga & R. Priya, "Collaboration Complexity Reducing Strategy In Cloud Computing" 124-128.



International Journal of Information And Computing Science

An ISO : 7021 - 2008 Certified Journal

ISSN NO: 0972-1347 / web : www.ijics.com / e-mail : submitijics@gmail.com

Address : # B11 - 157, Katraj - Dehu Road, Pune, Maharashtra - 412101.

CERTIFICATE OF PUBLICATION

Certificate ID : IJICS/S1597

This is to certify that the paper entitled

**“SECURED COMMUNICATION IN AIRCRAFT SYSTEM USING LI-FI FOR
MILITARY APPLICATION”**

Authored by

P.Kavitha

From

M.A.M.School of Engineering, Trichy

Has been published in

IJICS JOURNAL, VOLUME 7, ISSUE 11, NOVEMBER - 2020.



K.M. Pandey
Dr. K. M. Pandey
Editor-In-Chief
IJICS
www.ijics.com



XI.ACKNOWLEDGMENT

I wish to acknowledge Mr.A.KARTHICK KUMAR, AP/ECE M.A.M SHOOL OF ENGINEERING for her advice on carrying out the performance.

XII.CONCLUSIONS

Wireless technology provides fast transmission over long range data transmission. It saves time, cost of cables, and size of the system. Data can be sent from anywhere in the world. Username and password type authentication system is provided for adding securities.. Previously the notice board using Wi-Fi was used. In that there was the limit of coverage area, but in our system internet is used as communication medium. So there is no problem with coverage area. Multimedia data can be stored on chip.

REFERENCES

[1] Mr. Ramchandra K. Gurav, Mr. Rohit Jagtap, "Wireless Digital Notice Board Using GSM Technology", International Research Journal of Engineering and Technology (IRJET), Volume: 02 Issue: 09 ,Dec-2015, e-ISSN: 2395 -0056

[2] Prof. Sudhir Kadam , Abhishek Saxena , Tushar Gaurav, "Android Based Wireless Notice Board and Printer", International Journal of Innovative Research in

Computer and Communication Engineering, Vol. 3, Issue 12, December 2015, ISSN(Online): 2320-9801 ISSN (Print): 2320-9798.

[3] C.N.Bhoyar , ShwetaKhobragade , Samiksha Neware, "Zigbee Based Electronic Notice Board", International Journal of Engineering Science and Computing, March 2017

[4] V.P.Pati, Onkar Hajare, Shekhar Palkhe,Burhanuddin Rangwala, "Wi-Fi Based Notification System", The International Journal Of Engineering And Science (IJES), Volume 3 ,Issue 5 ,2014.

[5] S.ArulmuruganP P,S.AnithaP P,A.PriyangaP P,S.Sangeethapriya," Smart Electronic Notice Board Using WI-FI", - International Journal of Innovative Science, Engineering & Technology, Vol. 3 Issue 3, March 2016, ISSN 2348 – 7968

[6] Liladhar P. Bhamre , Abhinay P.Bhavsar , Dushyant V. Bhole , Dhanshree S. Gade, "Zigbee Based Notice Board", IJARIE, Vol-3 Issue-1 2017,ISSN(O)-2395-4396.

[7] Jaiswal Rohit , Kalawade Sanket , Kore Amod , Lagad Sanket, "Digital - Notice Board", International Journal of Advanced Research in Computer Engineering &



International Journal of Information And Computing Science

An ISO : 7021 - 2008 Certified Journal

ISSN NO: 0972-1347 / web : www.ijics.com / e-mail : submitijics@gmail.com

Address : # B11 - 157, Katraj - Dehu Road, Pune, Maharashtra - 412101.

CERTIFICATE OF PUBLICATION

Certificate ID : IJICS/S1597

This is to certify that the paper entitled

**“SECURED COMMUNICATION IN AIRCRAFT SYSTEM USING LI-FI FOR
MILITARY APPLICATION”**

Authored by

A.Karthick Kumar

From

M.A.M.School of Engineering, Trichy

Has been published in

IJICS JOURNAL, VOLUME 7, ISSUE 11, NOVEMBER - 2020.



K.M. Pandey
Dr. K. M. Pandey
Editor-In-Chief
IJICS
www.ijics.com





International Journal of Information And Computing Science

An ISO : 7021 - 2008 Certified Journal

ISSN NO: 0972-1347 / web : www.ijics.com / e-mail : submitijics@gmail.com

Address : # B11 - 157, Katraj - Dehu Road, Pune, Maharashtra - 412101.

CERTIFICATE OF PUBLICATION

Certificate ID : IJICS/S1597

This is to certify that the paper entitled

**“SECURED COMMUNICATION IN AIRCRAFT SYSTEM USING LI-FI FOR
MILITARY APPLICATION”**

Authored by

K.Karthikeyan

From

M.A.M.School of Engineering, Trichy

Has been published in

IJICS JOURNAL, VOLUME 7, ISSUE 11, NOVEMBER - 2020.



K.M. Pandey
Dr. K. M. Pandey
Editor-In-Chief
IJICS
www.ijics.com





International Journal of Information And Computing Science

An ISO : 7021 - 2008 Certified Journal

ISSN NO: 0972-1347 / web : www.ijics.com / e-mail : submitijics@gmail.com

Address : # B11 - 157, Katraj - Dehu Road, Pune, Maharashtra - 412101.

CERTIFICATE OF PUBLICATION

Certificate ID : IJICS/S1597

This is to certify that the paper entitled

**“SECURED COMMUNICATION IN AIRCRAFT SYSTEM USING LI-FI FOR
MILITARY APPLICATION”**

Authored by

K. Umarani

From

M.A.M.School of Engineering, Trichy

Has been published in

IJICS JOURNAL, VOLUME 7, ISSUE 11, NOVEMBER - 2020.



K.M. Pandey
Dr. K. M. Pandey
Editor-In-Chief
IJICS
www.ijics.com



IoT ENABLED ECONOMIC HUMAN SAFETY FOR CO EMISSION CONSTRAINTS WITH SELF-ALERT SYSTEM

T.Ashok Department of ECE,
P.Kavitha, Department of ECE
M.Chandrasekar, Department of ECE
P.M.Santhiya, N.Sathya
M.A.M. School of Engineering,
Siruganur, Trichy

ashoksubaash@gmail.com, kaviakshya@gmail.com, mchandrasekar1983@gmail.com
Sandypugal999@gmail.com, sathyananthini1234@gmai.com

ABSTRACT

Vehicles have become an integral part of every one's life. Situations and circumstances demand the usage of vehicles in this fast paced urban life. Every vehicle will have emission but the problem occurs when it is beyond the standardized values. The primary reason for this breach of emission level being the incomplete combustion of fuel supplied to engine, which is due to the improper maintenance of vehicles. This emission from vehicles cannot be completely avoided but, it definitely can be controlled. The involvement of semi-conductor sensors for detecting the various gases. The aim of the project is to monitor and control the pollutants in the vehicle by using the pollution control circuit. This pollution control circuit consists of various sensors like smoke sensor, temperature sensor and IoT, GPS kind of devices, and all of them are integrated and connected to a

Controller. This paper demonstrates an effective utilization of technology by which we save our environment by controlling the pollution of vehicles. FC date is monitored with help of a memory. If in case of FC period exit the IoT module will update the current vehicle location to the RTO office. It is also very useful for women safety. If women's are attacked by anyone, this system sends the GPS location by using switch. This paper, when augmented as a real time project, will benefit the society and help in reducing the air pollution.

I. INTRODUCTION

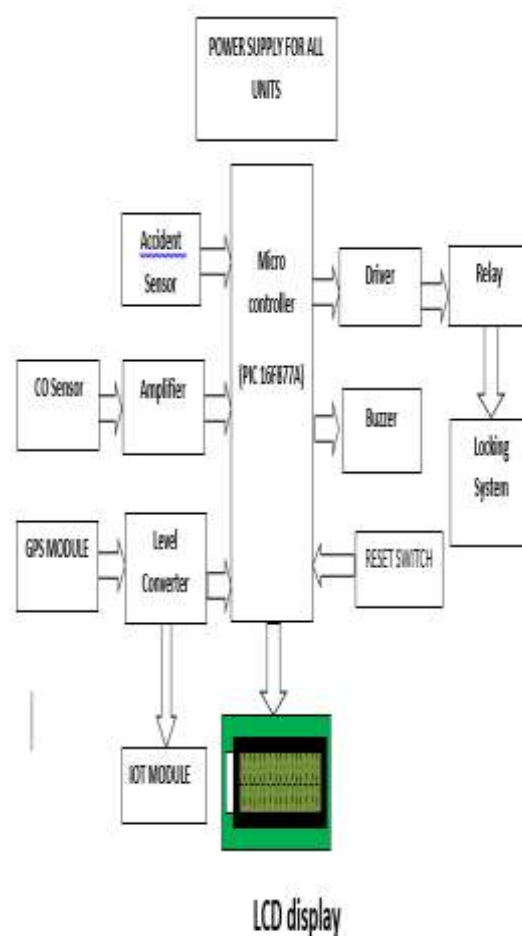
Transportation has great importance in our daily life and its development has made many of our chores much easy. But it can cause disaster to us and even can kill us through accidents. During 2008, Road Traffic Injuries ranked fourth among the leading

causes of death in the world. Nearly 1.3 million people die every year on the world's roads and 20 to 50 million people suffer non-fatal injuries, with many sustaining a disability as a result of their injury. Road traffic injuries are the leading cause of death among young people aged 15-29 years and cost countries 1-3% of the gross domestic product (GDP). If no action is taken, road traffic crashes are predicted to result in the deaths of around 1.9 million People annually by 2020. The purpose of project is to find the vehicle where it is and locate the vehicle by means of sending location using a system which is placed inside of vehicle system. Most of the times we may not be able to find accident location because we don't know where accident will happen. In order to give treatment for injured people, first we need to know where the accident happened through location tracking and sending a message to your related one or to the emergency services. So in this work the Arduino controller is used for cost effective and also for easy understanding. Here assembly programming is used for better accuracy and GPS and GPRS modules which helps to trace the vehicle anywhere on the globe. The exact location of the vehicle is sent to our remote devices (mobile phones).

The high demand of automobiles has also increased the traffic hazards and the road accidents. Life of the people is under high risk. This is because of the lack of best emergency facilities available in our country. An automatic alarm device for vehicle accidents is introduced in here. The proposed design is a system which can detect accidents

in significantly less time and sends the basic information to first aid centre within a few seconds covering geographical coordinates, the time and angle in which a vehicle accident had occurred. This alert message is sent to the rescue team in a short time, which will help in saving the valuable lives. Switch is also provided in order to terminate the sending of a message in rare case where there is no casualty, this can save the precious time of the medical rescue team.

II. BLOCK DIAGRAM



coil. The direction of the electric current in the coil is fixed, because of the split ring on the end of the coil.

4. IOT MODULE(ESP 8266 – 12E NODE MCU)

NodeMCU is an open source IoT platform. It includes firmware which runs on the ESP8266 Wi-Fi SoC from Espressif Systems, and hardware which is based on the ESP-12 module. The term "Node MCU" by default refers to the firmware rather than the dev kits. The firmware uses the Lua scripting language. It is based on the eLua project, and built on the Espressif Non-OS SDK for ESP8266.

5. RELAY DRIVER

The transistor is a compound structure consist of transistor connected in such a way that the current amplified by the transistor. This configuration gives a much higher current gain (written β , h_{fe} , or h_{FE}) than each transistor taken separately and, in the case of integrated devices, can take less space than two individual transistors because they can use a shared collector.

6. BUZZER

A buzzer or beeper is a signaling device, usually electronic, typically used in automobiles, household appliances such as a microwave oven, or game shows. It most commonly consists of a number of switches or sensors connected to a control unit that determines if and which button

was pushed or a preset time has lapsed, and usually illuminates a light on the appropriate button or control panel, and sounds a warning in the form of a continuous or intermittent buzzing or beeping sound. Initially this device was based on an electromechanical system which was identical to an electric bell without the metal gong (which makes the ringing noise). Often these units were anchored to a wall or ceiling and used the ceiling or wall as a sounding board. Another implementation with some AC-connected devices was to implement a circuit to make the AC current into a noise loud enough to drive a loudspeaker and hook this circuit up to a cheap 8-ohm speaker. Nowadays, it is more popular to use a ceramic-based piezoelectric sounder like a Sonalert which makes a high-pitched tone. Usually these were hooked up to "driver" circuits which varied the pitch of the sound or pulsed the sound on and off.

7. Accident Sensor

This sensor buffers a piezoelectric transducer. As the transducer is displaced from the mechanical neutral axis, bending creates strain within the piezoelectric element and generates voltages.

8. Battery

A 12V dc supply of battery is fed to the 7805 regulators which converts it into regulated 5V DC supply. It is then, distributed to all the driver and relay circuits. The 5V is supplied to the microcontroller and to all the components used in the system.

METHODOLOGY

Our paper aims at using those semi-conductor sensors at the emission outlets of vehicles which detects the level of pollutants and also indicates this level with a meter. When the pollution/emission level shoots beyond the already set threshold level, there will be a buzzer in the vehicle to indicate that the limit has been reached and the vehicle will stop after a certain period of time, a cushion time given for the driver to park his/her vehicle. During this time period, the GPS starts locating the nearest service stations.

After the timer runs out, the fuel supplied to the engine will be cut-off and the vehicle has to be towed to the mechanic or to the nearest service station. The synchronization and execution of the entire process is monitored and controlled by a micro controller. FC date is monitored with help of a memory. If incase of FC period exit the IoT send it to the RTO office with vehicle location. The vehicle lock mechanism can be controlled by user SMS to our system through IoT module.

APPLICATION

- Mostly used in vehicular system
- It is also used in Industry for pollution monitor and alert system

CONCLUSION

FUTURE SCOPE: This paper is extended by adding GPS with the GSM module and sending a message to the user about the details of the nearest service station. A server and database can be maintained to keep track of the pollution level of the system

and control action on the owner can be taken if the pollution level alert is ignored.

REFERENCE

- [1]. Chi-Man Vong —Application of RFID Technology and the Maximum Spanning Tree Algorithm for Solving Vehicle Emissions in Cities on Internet of Things| 2014 IEEE World Forum on Internet of Things (WF-iot)
- [2]. Chunxiao LI and Shigeru shimamoto “Etc assisted traffic light control scheme for reducing vehicles” International Journal of Managing Information Technology (IJMIT) Vol.4, No.2, May 2012. [3]. NishigandhaAthare, Prof.P.R.Badadapure
- [3] “Human safety and air pollution detection in vehicles”
- [4]. Anita kulkarni1, T. Ravi Teja ”Automated System for Air Pollution Detection and Control in Vehicles ” /ijareeie.2014.0309061
- [5]. Poonam M Baikar , “Design of PID Controller Based Information Collecting Robot in Agricultural Field”-IJAR,EEIE volume8-2014
- [6]. Poonam M Baikar, Neelam Punjabi1, ChandrakantKadu “Real Time DC Motor Speed Control using PID Controller in LabVIEW”
- [7]. J.N.Mohite, S.S.BaroteAsst professor, Department of electronics “vehicle pollution control and traffic management”
- [8]. S. Arun2 , Dr. J.L MazherIqbal, “Embedded System Based Air Pollution Detection in Vehicles V. Siva Krishna1” ,
- [9]. George F. Fine, Leon M. Cavanaugh, Ayo Afonja and Russell Binions " Metal Oxide Semi-Conductor Gas Sensors in

Environmental Monitoring", Sensors 2010, 10, 5469-5502; doi:10.3390/s100605469

[10]. J.N.Mohite, S.S.Barote Professor, "Low Cost Vehicle Pollution Monitoring System".

[11]. Areas SrinivasDevarakonda, ParveenSevusu, Hongzhang Liu, Ruilin Liu, Liviulfode, BadriNath "Real-time Air Quality Monitoring Through Mobile Sensing in Metropolitan" [12]. Darshana N. Tambe and Ms. Nikita Chavan "Detection of air pollutant using ZIGBEE" International Journal of Ad hoc, Sensor & Ubiquitous Computing (IJASUC) Vol.4, No.4, August 2013



International Journal of Information And Computing Science

An ISO : 7021 - 2008 Certified Journal

ISSN NO: 0972-1347 / web : www.ijics.com / e-mail : submitijics@gmail.com

Address : # B11 - 157, Katraj - Dehu Road, Pune, Maharashtra - 412101.

CERTIFICATE OF PUBLICATION

Certificate ID : IJICS/S1566

This is to certify that the paper entitled

**“IoT ENABLED ECONOMIC HUMAN SAFETY FOR CO EMISSION
CONSTRAINTS WITH SELF-ALERT SYSTEM”**

Authored by

T.Ashok


From

M.A.M. School of Engineering, Siruganur, Trichy

Has been published in

IJICS JOURNAL, VOLUME 7, ISSUE 6, JUNE - 2020.




Dr. K. M. Pandey
Editor-In-Chief
IJICS
www.ijics.com





International Journal of Information And Computing Science

An ISO : 7021 - 2008 Certified Journal

ISSN NO: 0972-1347 / web : www.ijics.com / e-mail : submitijics@gmail.com

Address : # B11 - 157, Katraj - Dehu Road, Pune, Maharashtra - 412101.

CERTIFICATE OF PUBLICATION

Certificate ID : IJICS/S1566

This is to certify that the paper entitled

**“IoT ENABLED ECONOMIC HUMAN SAFETY FOR CO EMISSION
CONSTRAINTS WITH SELF-ALERT SYSTEM”**

Authored by

P.Kavitha


From

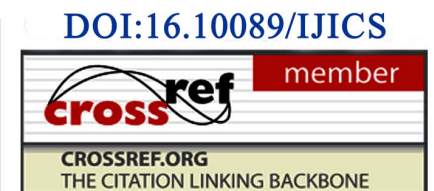
M.A.M. School of Engineering, Siruganur, Trichy

Has been published in

IJICS JOURNAL, VOLUME 7, ISSUE 6, JUNE - 2020.




Dr. K. M. Pandey
Editor-In-Chief
IJICS
www.ijics.com





International Journal of Information And Computing Science

An ISO : 7021 - 2008 Certified Journal

ISSN NO: 0972-1347 / web : www.ijics.com / e-mail : submitijics@gmail.com

Address : # B11 - 157, Katraj - Dehu Road, Pune, Maharashtra - 412101.

CERTIFICATE OF PUBLICATION

Certificate ID : IJICS/S1566

This is to certify that the paper entitled

**“IoT ENABLED ECONOMIC HUMAN SAFETY FOR CO EMISSION
CONSTRAINTS WITH SELF-ALERT SYSTEM”**

Authored by

M.Chandrasekar


From

M.A.M. School of Engineering, Siruganur, Trichy

Has been published in

IJICS JOURNAL, VOLUME 7, ISSUE 6, JUNE - 2020.




Dr. K. M. Pandey
Editor-In-Chief
IJICS
www.ijics.com





Eradication of hydraulic anomalies using smart sewer inspection robot

P.Kavitha

kaviakshya@gmail.com

MAM School of Engineering, Siruganur, Tamil Nadu

ABSTRACT

This paper presents a robotic mechanism for detecting and eliminating blockages in sewage pipes. It is a robot that will be used to clean the interior of the pipes using a brushing mechanism. One of the critical areas of the oil and gas industry is the transport of oil and other fluids through a network of pipes. Over time these pipes have accumulated the amount of slug and other deposits; this leads to a decrease in a pipeline carrying capacity, reduced reliability, loss of power due to higher pumping pressure required and irregular flow. This will not only clean the interior of the pipe but also be able to send live video feedback to the personnel on the ground depicting the kind of residues found in the pipes. The robot can also be added with additional sensors to relay any other critical information.

Keywords— Sewage, Cleaning, Blockages, Robot, Detection, Rotating. Pipelines

1. INTRODUCTION

Drainage is the natural or artificial removal of surface and sub-surface water from an area. As long as the draining system is considered the function of the main drainage system is to collect, transport and dispose of the water through an outfall or outlet. There is a need for the development of cleaning the drainage wastes by using robots. Since drainage cleaning involves manual scavenging which leads to several health hazards to the person entering the manholes of the drainage.

Many deaths occur due to drowning, trench collapses, falls, and exposure to chlorine or Hydrogen- sulphide gas. Peoples are also affected by cardiovascular degeneration, musculoskeletal disorders like osteoarthritic changes and intervertebral disc herniation, infections like hepatitis, leptospirosis and helicobacter, skin problems, respiratory system problems. Those who die during the duty are replaced by others, waiting to put their lives in danger just to earn a living for themselves and their families. The impurities present in drainage water can cause blockage in the drainage system. Hence, there is a need to replace manual work with high tech robots. Robots can be used safely at these dangerous conditions. The human safety is

guaranteed by these robots and enormous human workforce are replaced.

2. BLOCK DIAGRAM

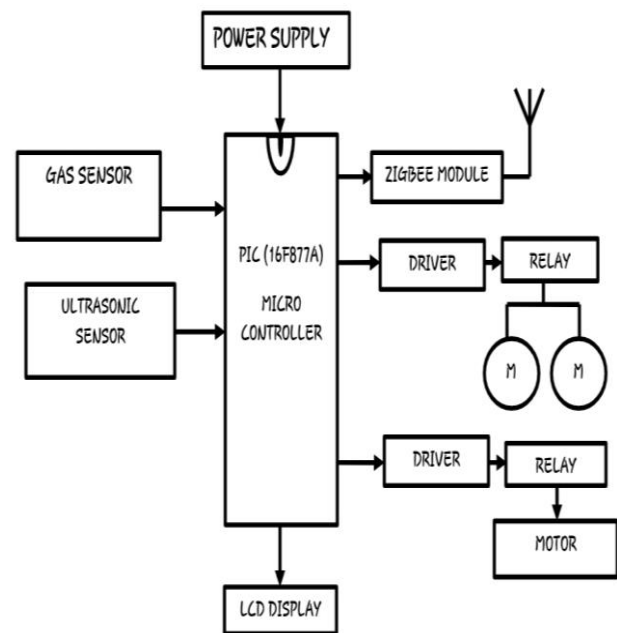


Fig. 1: Block diagram of unit I

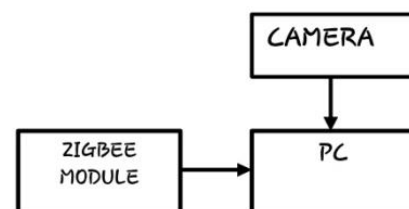


Fig. 2: Block diagram of unit II

Our proposed system attempts to detect and completely eliminate the blockages using a sewer robot. The block diagram comprises a PIC microcontroller. This controller is interfaced with the wheel motors, camera, ultrasonic sensor, gas sensor, a driver circuit, and Zigbee modules.

3. OPERATION

PIC microcontroller PIC16F877A is used to control the operation of mechanical parts. PIC microcontroller can perform different tasks and it can be controlled by software.

All the activities of the robot are controlled by this centralized microcontroller attached to this robot. The driver circuit is enabled by the Microcontroller when the Robot is turned the driver circuit enables the motion of robot inside the pipeline by turning on the motors.

This project is designed to keep clean the drainage system and helps for the smooth working of the system. It is an easy way of cleaning the drainage system and preventing blockage.

In our system following functions are performed:

- Activities are controlled by PIC microcontroller
- Enabling the motion of robot using a driver circuit.
- The camera transmits information to the controller.
- An ultrasonic sensor detects the blockages inside the drain.
- “Turn on rotating mechanism” to clear blocks.
- The gas sensor is used to detect the presence of poisonous gases
- The Motor can be operated on a battery.

Once a block is identified and its distance is measured using the ultrasonic sensor, the next step is to clear the block using a rotating mechanism which comprises of fan-like structured sharp blades. It has been developed with the aim of removing stubborn dirt under tough working conditions. Water gets things so clean because its molecules have a slight electrical polarity (one end is positively charged and the other is negatively charged). Detergents (soap chemicals) help water to do its job even better by breaking down gunges and grease and making it easier for water to flush away. If the block is cleared using the blades, it is indicated to the robot by using the ultrasonic sensor distance measurement and the robot proceeds to clear the next blockage along the length of the pipe

4. ULTRASONIC SENSOR

The ultrasonic sensor is used to detect an object. It is generally used to measure the distance of an object using sound waves.



Fig. 3: Ultrasonic sensor

The robot moves through the pipe by balancing on its wheels. Ultrasonic sensor HCSR04 is assembled in the robot.

5. GAS SENSOR

It is a type of chemical sensor which detects and measures the concentration of gas in its vicinity. They are used in various industries ranging from medicine to aerospace.



Fig. 4: Gas sensor

The gas sensor is turned on only in a rare case if both the pumping mechanism and rotating mechanism are unable to remove the block. In such a case, the output of the gas sensor is used to determine whether poisonous gases such as chlorine or carbon monoxide are present inside the pipeline. This provides precautionary measures for the sewage workers before getting into the drain.

6. ZIGBEE MODULE

This technology formed on IEEE 802.15.4 which describes the operation of low rate Wireless Personal Area Networks.



Fig. 4: ZigBee module

This system provides continuous visual monitoring through the small camera attached to the mobile robot, continuously sending data to the control unit when necessary.

7. CAMERA

The wireless camera continuously transmits the information to the controller which shows it in the user's display device.

8. DC MOTOR

DC motors transform electrical energy into mechanical energy. The basic principle of DC motors is the same as electric motors in general, the magnetic interaction between the rotor and the stator that will generate spin.

9. MECHANISM FOR BLOCKAGE CLEARANCE

Once a block is identified and its distance is measured using the ultrasonic sensor, the next step is to clear the block using a pumping mechanism which comprises of a high-pressure washer. High-pressure washers remove stubborn dirt under tough working conditions.

Efficient flow rates are achieved using a high flow rate and high pressure. Water gets things so clean because its molecules have a slight electrical polarity (one end is positively charged and the other is negatively charged).

Detergents (soap chemicals) help water to do its job even better by breaking down gunges and grease and making it easier for water to flush away. But some kinds of ground-on dirt just won't budge, no matter how hard we try. That's when a pressure washer is used. It uses a narrow, high-pressure jet of hot or cold water to blast dirt free. Because the water is travelling fast, it hits the dirty surface with high kinetic energy, knocking dirt and dust away like a constant rain of tiny hammer blows. It's only water, though, so it doesn't damage most hard surfaces.

If the block is cleared using the high-pressure pump, it is indicated to the robot by using the ultrasonic sensor distance measurement and the robot proceeds to clear the next blockage along the length of the pipe.

Microcontroller does the following function.

When the operator turns on the robot, the microcontroller enables the driver circuit. The movements of the robot can be controlled by the preprogrammed instructions. The motion of the robot inside the pipeline is enabled by the driver circuit. The wireless camera continuously transmits the information to the controller which shows it in the user's display device.

The output values of the ultrasonic sensor are sent to the controller periodically. The abrupt deviation in these values are sensed by the controller and the presence of a blockage is confirmed. The driver circuit is interrupted by the controller and the pumping mechanism is turned ON. The pumping mechanism is operated till the output values of the ultrasonic sensor return to normal.

The control is now returned back by the controller to the driver circuit and the robot is moved in the forward direction.

Stubborn blockages such as wood pieces, thick sheets etc which cannot be removed by pumping mechanism are removed by a rotating mechanism.

It consists of a rotating fan-like structure with very sharp blades. This is capable of cutting the wood pieces, covers, boxes etc. The hard pieces are cut by the robot with the help of these blades. Later, the pumping mechanism can be used to clear the remains of the block.

The display device is interfaced with the controller and continuous monitoring can be done by the user.

The gas sensor is turned on only in a rare case if both the pumping mechanism and rotating mechanism are unable to remove the block.

In such a case, the output of the gas sensor is used to determine whether poisonous gases such as chlorine or carbon monoxide are present inside the pipeline. This provides precautionary measures for the sewage workers before getting into the drain.

10. DISADVANTAGES

This robot is not fully automated. It needs humans to control the operation.

11. CONCLUSIONS

In this paper, the proposed robot is designed with the motive of helping the sewage cleaners to prevent them from getting affected by serious diseases because of entering the drainage. The death rate of sewage cleaners is alarming. It is high time that this robot should be implemented to clean the sewage pipes all over the world. Moreover, this robot will help to find the poisonous gases inside the drain which will help the authorities to curb the dumping of untreated raw waste from the industries into the drains. This will not lead to unemployment of sewage workers but will just make the job easier and healthier for them. When this robot would be implemented in real time, it will save thousands of poor people's lives who come forward to clean the drainage just to earn a few bucks a day. In this modern society, a human cleaning the sewage waste shows that very less

attention has been given to those people's lives due to their poverty. Hence, this robot helps to have clean and hygienic drain systems everywhere.

12. PHOTOGRAPHY

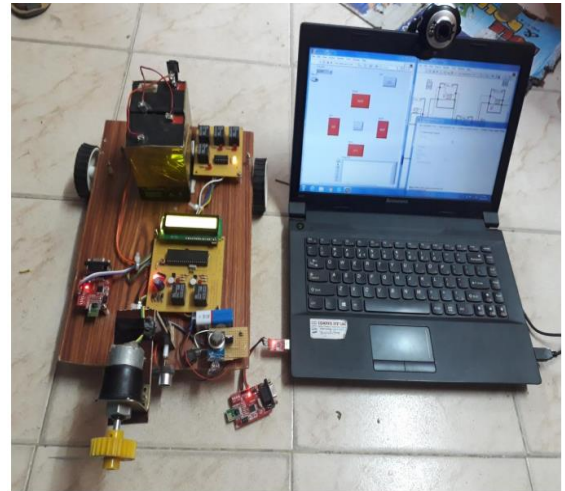


Fig. 5: Final Outcome

13. REFERENCES

- [1] Atu.A.Gargade, Dr.Shantipal.S.Ohol, "Development of In-Pipe Inspection Robot" in IOSR Journal of Mechanical and Civil Engineering on 18th July 2017.
- [2] M. Saida, Y. Hirata and K. Kosuge, "Motion control of a passive mobile robot with multiple casters based on feasible braking force and moment," in Proc. of the 2010 IEEE/RSJ International Conference on Intelligent Robots and Systems, Taipei, Taiwan, 2010, pp. 3130-3137.
- [3] Y. Hirata, A. Muraki and K. Kosuge, "Motion control of intelligent walker based on renewing of estimation parameters for user state," in Proc. of the 2006 IEEE/RSJ International Conference on Intelligent Robots and Systems, Beijing, China, 2006, pp. 1050-1055.
- [4] Y. H. Hsieh, K. Y. Young and C. H. Ko, "Effective maneuver for a passive robot walking helper based on user intention," IEEE Transactions on Industrial Electronics, vol. 62, no. 10, pp. 6404-6416, 2015.
- [5] B. Graf, "An adaptive guidance system for robotic walking aids," Journal of Computing and Information Technology, vol. 17, no. 1, pp. 109-120 2009.
- [6] J. Manuel, H. Wandosell and B. Graf, "Non-holonomic navigation system of a walking-aid robot," in Proc. of IEEE International Workshop on Robot and Human Interactive Communication, Berlin, Germany, 2002, pp. 518-523.
- [7] M. Spenko, H. Yu and S. Dubowsky, "Robotic personal aids for mobility and monitoring for the elderly," IEEE Transactions on Neural Systems and Rehabilitation Engineering, vol. 14, no. 3, pp. 344-351, 2006.
- [8] O. Y. Chuy Jr., Y. Hirata, Z. Wang and K. Kosuge, "A control approach based on passive behavior to enhance user interaction," IEEE Transactions on Robotics vol. 23, no. 5, pp. 899-908, 2007.

INTERNATIONAL JOURNAL OF ADVANCE RESEARCH, IDEAS AND INNOVATIONS IN TECHNOLOGY

CERTIFICATE OF PUBLICATION

This is to certify that

P. Kavitha

published a paper entitled

Eradication of hydraulic anomalies using smart sewer inspection robot

Volume-5, Issue-2 - March-April, 2019

ISSN:2454-132X
IMPACT FACTOR 4.295



Ref No...OAP/IJ/192/859...

editor@ijariit.com, ijariit@gmail.com

Editor-in-Chief





SMART ENERGY MONITORING SYSTEM USING IOT

K. Umarani

Associate Professor, MAM School of Engineering,
Srirangam, Tiruchirappalli, Tamilnadu.

Cite This Article: K. Umarani, "Smart Energy Monitoring System Using IOT", International Journal of Computational Research and Development, Volume 4, Issue 1, Page Number 10-15, 2019.

Abstract

Smart application has become more and more popular in recent years. It aims at helping people manage the various devices freely and build an ecofriendly environment. This project introduces a wireless solution based on Internet protocol to manage the industrial units easily. Smart application system can connect the various units together and provide a unified interface for users to interact with the monitoring block. Some main features are load cycle or motor control, load control, temperature control of motor, security and safety. Based this control the energy loss consumed which can be monitored using IOT. As with the development of the Internet, Internet based remote monitoring and control solutions for industry has been proposed.

Key Words: Energy Consumption, Industrial Monitoring, Load Control, Motor Control, Fan Sensor, Airline L240, IOT & Temperature Sensor

1. Introduction:

Electricity plays an important role in our life. Every moment of our life depends upon electricity. Electricity has several components and equipment helping human to transfer and regulate the distribution according to usage. The most crucial equipment of transmission and distribution of electric power is transformer. In power systems, an electrical equipment distribution transformer directly distributes power to the low-voltage users and its operation condition is an important criterion of the entire network operation. The majority of these devices have been in service for many years in different (electrical, mechanical and environmental) conditions.

Automation has much more importance in industry because due to automation overall productivity is increases. Quality of the product is also increases due to automation. It also reduces manufacturing cost. There are another several reasons such as lack of availability of skilled person, lack of industrial training centers so that automation got importance. Most of the developed countries suffer from lack of human resources. Those persons who work for their industry some many years they are leaving the industry. If they want to hire new candidate to replace old candidate then first problem is that new candidate is non-organized. So we have to arrange training session. Candidate may leave the industry if workload is more. In case of developing country skill become important factor. They have more manpower but these people are not technically strong. Hence automation is become need.

Technologies which are invented for the industrial automation deals with the monitoring and controlling of the various activities and different manufacturing process running in the industry. Machinery used in the industry has its own specification. In industry boilers are used for heating purposes. These boilers have own their operating temperature range. If the temperature of the boiler exceed beyond the threshold level then there is possibility of explosion of the boiler which become more dangerous. Hence controlling of temperature is important. All other parameters such as speed of the motor, torque of the motor, pressure, available light etc. must be monitor and control. In day today life people want to leave world in their fingerprints. That means use of internet is increased in great extent. Internet of things is a new emerging technology which connects all the living or nonliving things of the world using internet. Internet of things allows the communication between the people and thing anytime, anywhere using large internet networks. To monitor and control such automation processes we can use concept of internet of things. We can also control this parameter by providing appropriate feedback command. For this communication between devices and web page we are controlling device through IOT.

2. Block Diagram

This is our proposed system block diagram. Our smart energy monitoring system consists Airline fan, temperature and fan sensors, power supply, led, load, motor, IOT, server and relay.



M.A.M. SCHOOL OF ENGINEERING
DEPARTMENT OF ELECTRICAL AND ELECTRONICS ENGINEERING
VACCINATION DETAILS
IV EEE (2018-2022)

Sl No	Name of the author/s	Title of paper	Name of journal	Year of publication	ISSN number	Link to the recognition in UGC enlistment of the Journal
1	G. Purushothaman	Neural Network Controller Based U HVDC For Enhancement Of Transient Compensation In Integrating Offshore Wind Power Plant	IJRAR	2020	ISSN: 2349-5138	http://www.ijrar.org/IJRAR19W1220.pdf
2	G. Purushothaman	Photovoltaic Charge Controller For Electric Vehicle Using Back Stepping Algorithm.	IJMER	2021	ISSN:2277-7881, VOLUME:10, ISSUE:2(4)	http://s3-ap-southeast-1.amazonaws.com/ijmer/pdf/volume10/volume10-issue2(4)/26.pdf
3	G. Purushothaman	Solar Powered Water Management System Using Smart Card.	Turkish journal of computer & mathematics education	2021	ISSN: 2879-2883	https://www.turcomat.org/index.php/turkbilmat/article/view/4375
4	A.SenthamaraiKannan	Neural Network Controller Based U HVDC For Enhancement Of Transient Compensation In Integrating Offshore Wind Power Plant	IJRAR	2020	ISSN: 2349-5138	http://www.ijrar.org/IJRAR19W1220.pdf
5	Dr.M.Sangeetha	Neural Network Controller Based U HVDC For Enhancement Of Transient Compensation In Integrating Offshore Wind Power Plant	IJRAR	2020	ISSN: 2349-5138	http://www.ijrar.org/IJRAR19W1220.pdf
6	Dr.M.Sangeetha	Photovoltaic Charge Controller For Electric Vehicle Using Back Stepping Algorithm.	IJMER	2021	ISSN:2277-7881, VOLUME:10, ISSUE:2(4)	http://s3-ap-southeast-1.amazonaws.com/ijmer/pdf/volume10/volume10-issue2(4)/26.pdf
7	Dr.M.Sangeetha	Solar Powered Water Management System Using Smart Card.	Turkish journal of computer & mathematics education	2021	ISSN: 2879-2883	https://www.turcomat.org/index.php/turkbilmat/article/view/4375
8	Dr.M.Sangeetha	Design and Implementation of Row or Column wise Banana Tree Cutter using IoT	Grenze International Journal of Engineering & Technology	2021	ISSN (Online): 2395-5295 ISSN (Print): 2395-5287	http://www.thegrenze.com/doigrenze/Grenze ID: 01.GIJET.7.1.613

G. Purushothaman
23/8/2022
HOD
HEAD OF THE DEPARTMENT
ELECTRICAL and ELECTRONICS ENGINEERING
MAM SCHOOL OF ENGINEERING
SIRIGANUR, TRICHY - 621 105.

[Signature]
PRINCIPAL
M.A.M. SCHOOL OF ENGINEERING
SIRIGANUR, TIRUCHIRAPPALLI-621 105.

Design and Implementation of Row or Column wise Banana Tree Cutter using IoT

J.Karthikeyan¹, Dr.M.Sangeetha², and L.GlaridaAmala³

¹Assistant Professor in EEE Department, Kongunadu College of Engineering and Technology, Thottiyam, Trichy, Tamilnadu, India

Karthikeyan249@gmail.com

²Associate Professor in EEE Department, M.A.M School of Engineering, Trichy, Tamilnadu, India
sangee2maya@gmail.com

³Assistant Professor in EEE Department, Dhanalakshmi Srinivasan Institute of Technology, Trichy, Tamilnadu, India
glrdamala@gmail.com

Abstract—This paper intends to design a Row or Column wise Banana Tree Cutter for formers who cultivate banana. The Formers cultivate the banana in large area of field. After a cultivation, the banana tree need to cut. Nowadays, the banana trees cut by two ways, in first way by the people by manually using weapons. In second way, it is done by truck which totally convert the whole tree into mixture. There is no use of mixture. In this module, which has mechanical system and electrical system. Fire base system is adopted for cultivation process control and IoT integration. Two motors are connected and one for cutting and another for transfer. Node MCU control the over all operations of the system. The programming is developed and executed as per the farmer premises.

Index Terms— DC motors, Internet of Things(IoT),Frictional Wires, Cloud computing , Firebase,etc.

I. INTRODUCTION

This system can cut the Banana tree with help of frictional wire using IoT buttons through the imaginary buttons in IoT. Now a days, the communication and technology, the dramatic growth of electronics, smart phones and internet. Through those things, the communication can be done communicated physically or wirelessly and become the fundamental tool of human life. The future generation of connected world is Internet of Things (IoT). It consists of devices, sensors, appliances, vehicles in the world. The devices or objects may include the tablets, smart phones, sensors, etc.

By using IoT, The system can connect anything, access from all the places at any time, with high performance access any service and information about all the objects. The IoT objective is to improve the benefits of Internet with remote control skills, data spreading, constant connectivity and so on. Using an embedded sensors, those are always on condition and collect the data, the entire equipment's will be integrated to local and global networks. The word 'IoT' always called Internet of all things, which was introduced by Kevin Ashton in 1999.

The IoT technology controls the big amount of data about living things, non-living things, time and area. When combining the Internet concepts and IoT, which deliver a large amount of space and innovative things based on minimal cost of sensors and wireless technology. Cloud computing and IPv6 accelerate the improved and

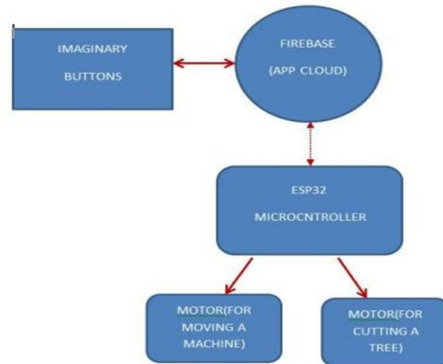


integrated Internet and IoT. Which provides more possibilities of collecting of data, processing of data, port management system and all other new activities. All the objects are connected to IoT needs a defined address or identification with IPv6. There are so many people in the world whose health may suffer because they have not proper access to hospitals and health monitoring.

The IoT(Advanced Internet of Things or AIoT) is the inter connection of physical devices, vehicles, buildings and other things-embedded with electronic devices, software, sensors, actuators, and network connectivity that enable these objects to extract and transferring the data. The Global Standards Initiative on Internet of Things (IoT-GSI) described the IoT as "the infrastructure of the collective information world." The IoT permits the objects that sensed or controlled remotely across existing network infrastructure, opportunity creation and better integration of the physical world into microcontroller-based systems, and resulting in improved efficiency, accuracy and economic aspects.

II. PROPOSED MODULE

The system architecture and flowchart has implemented and given below



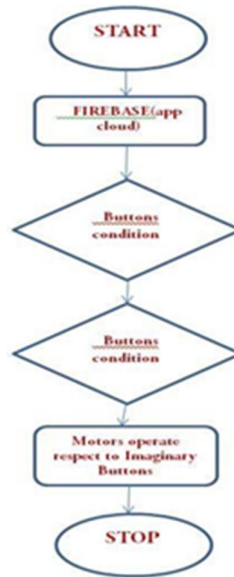
Block Diagram of Proposed System

III. WORKING METHODOLOGY

In this three methods are proposed

1. Electrical system
2. Mechanical System
3. Network System

The system in Electrical provides all needs of supply and logical condition in controllers. The IoT imaginary or Touch Buttons send signal to Fire base the app cloud. The touch buttons which created in API using AndriodStudio ,MITappInventeretc..The button when pressed in mobile sends a character to HTTP which is protocols that send to Firebase. The Fire Base send signal to the Controller we have used (ESP32).If the moving



Flow chart of Proposed System

buttons pressed it sends signal Moving motor relay where it is Forward or Backward. When the cutting button is pressed then it send signal to the cutting motor's relay. The Movement of module developed by using faraday's law in motors. The cutting method is based on the frictional motion of Newton's Law and Energy conversion of Thermodynamics law. The frictional force creates the Heat energy which helpful in cutting the tree and frictional wire the makes the tear in banana tree sheath. Hence the tree to be cut.

IV. COMPONENTS REQUIRED

A. ESP32(Controllor)



Node MCU is a series of minimal cost, low-power consuming on a microcontroller with integrated wire less technology and dual-mode Bluetooth. The ESP32 series require a TensilicaXtensaLX6 microprocessor in both dual-core and single-core variations. It can be incorporated with built-in switches of antenna, RF balun, and power amplifier, high quality receiving amplifier, filters, and power-management modules. ESP32 is created and developed by a Shanghai-based Chinese company, and is manufactured by Cussing their 40 nm process.

B. Relay



A relay is an electronic switch. It consists of input terminals set for a single, and operating contact terminal set. The switch has two number of contacts in multiple contact formation such as make contacts, break contacts, or combinations.

C. Motors



The electrical motor is used to convert electric energy into kinetic energy. Generally, electric motors operate by means of the relation between the stator magnetic field and current flow in the rotor. To generate force by means of rotation of a rotor shaft. Electric motors can be operated by direct current(DC) sources, such as from DC sources, motor vehicles or rectifiers, or by alternating current(AC) sources, such as a power grid, inverters electrical generators. An electric generator is physically coupled to an electric motor, but which operates in the reverse direction, converting mechanical energy into electrical energy.

D. Frictional Wires



The frictional that can able to cut the banana tree of sheath. It is made iron steel. These are inner cable is very important for the bicycle brake or gear shifting control systems. The primary aim of providing best quality products lies upon the capability to incorporate and master each manufacture processes. The structure and properties of steel is the very important factor for tensile, and surface treatment is the most critical factor to reduce the friction. As a result, a straighten-processed and seal processed inner cable provide the longest service life.

V. PROGRAMMING

In this system ESP IDF programming is used to control measurement and display the outputs. Codes are installed in ESP32 controller to control and monitoring the devices used and battery system. This same system can also be designed for Arduino nano for compactness. Embedded C or C++ language based programming is used in this system with loops and conditions for repeated operations. The embedded system based devices has miniature controller based in which device ESP32 controller and it is programmed by embedded C language to control the all components used in this device.

A. Firebase

Firebase is a platform for development of mobile and web application. Which had developed by Firebase, Inc. in 2011, then acquired by Google in 2014. In 2018, the Firebase platform had 18 products, which were accessed by 1500000 apps.

B. Firebase Cloud Messaging

At initially, It was known as Google Cloud Messaging(GCM), Firebase Cloud Messaging(FCM) was a cross-platform solution for messages and notifications for Android,iOS and web applications, which as of 2016 can accessed at free of cost.

C. Firebase Realtime Database

Firebase deliver a real-time database and back-end as a service routine. This platform provides application developers an API that permit application data need to synchronized across clients and stored on Firebase's cloud. The company provides client libraries that enable integration with Android,iOS, JavaScript, Java,

Objective-C Swift and Java applications. The database has accessible through a REST API and bindings for several JavaScript frame works such as Angular JS, React and Backbone.js. The REST API uses the Server-Sent Events protocol, which is an API for creating HTTP connections for receiving push notifications from a server. Developers using the real time database can secure their data by using the company's server-side-enforced security rules.

D. Cloud Firestore

In 2019, Cloud Fire store was officially brought out of beta, making it an official product of the Firebase line up. It is the successor to the actual data of firebase is basing system, Real-time system, and allows for nested documents and fields rather than the tree-view provided in the Real-time systems.

E. Firebase Hosting

Hosting of Firebase system is a static and dynamic web hosting service which launched in 2014. That supports hosting static files such as CSS,HTML, JavaScript and other files, as well as support through Functions of cloud. The system delivers the contents over a content delivery network(CDN) through HTTP Secure(HTTPS) and Safety Sockets Layer encryption (SSL). Partners of firebase with quickly response, a CDN, to provide the CDN backing Firebase Hosting.

VI. ADVANTAGES

Due to the Integration of Sensors, The system become a Portable system .The process of cutting trees will quickly done because row wise cutter. Reduction of analog components make the system is affordable system. With the help of Implementation of Row or Column wise Banana Tree Cutter using IoT, the tree can be converted into useful bio-product.

VII. CONCLUSION

The Row wise banana cutter is designed to reduce the farmers work after cultivation. Because farmers are the backbone of every country. This system helpful in cutting a banana tree.In many areas Banana cultivation is most thing done in acres range. This device will helpful and reducetheir time and work. And also after cutting it can be used in making of Bio-products.

REFERENCES

- [1] S. M. B. P. Samarakoon, M. A. V. J. Muthugala, A. Vu Le and M. R. Elara, "hTetro-Infri: A Reconfigurable Floor Cleaning Robot With Infinite Morphologies," in *IEEE Access*, vol. 8, pp. 69816-69828, 2020, doi: 10.1109/ACCESS.2020.2986838.
- [2] P. Veerajagadheswar, M. R. Elara, T. Pathmakumar and V. Ayyalusami, "A Tiling-Theoretic Approach to Efficient Area Coverage in a Tetris-Inspired Floor Cleaning Robot," in *IEEE Access*, vol. 6, pp. 35260-35271, 2018, doi: 10.1109/ACCESS.2018.2848662.
- [3] R. Parween, L. T. L. Clarissa, M. Y. Naing, N. A. F. B. M. Fuad and M. R. Elara, "Modeling and Analysis of the Cleaning System of a Reconfigurable Tiling Robot," in *IEEE Access*, vol. 8, pp. 137770-137782, 2020, doi: 10.1109/ACCESS.2020.3009120.
- [4] M. A. V. J. Muthugala, S. M. B. P. Samarakoon and M. R. Elara, "Tradeoff Between Area Coverage and Energy Usage of a Self-Reconfigurable Floor Cleaning Robot Based on User Preference," in *IEEE Access*, vol. 8, pp. 76267-76275, 2020, doi: 10.1109/ACCESS.2020.2988977.
- [5] R. Parween, M. Vega Heredia, M. M. Rayguru, R. Enjikalayil Abdulkader and M. R. Elara, "Autonomous Self-Reconfigurable Floor Cleaning Robot," in *IEEE Access*, vol. 8, pp. 114433-114442, 2020, doi: 10.1109/ACCESS.2020.2999202.
- [6] Imran, S. Ahmad and D. H. Kim, "Quantum GIS Based Descriptive and Predictive Data Analysis for Effective Planning of Waste Management," in *IEEE Access*, vol. 8, pp. 46193-46205, 2020, doi: 10.1109/ACCESS.2020.2979015.
- [7] T. J. Sheng et al., "An Internet of Things Based Smart Waste Management System Using LoRa and Tensorflow Deep Learning Model," in *IEEE Access*, vol. 8, pp. 148793-148811, 2020, doi: 10.1109/ACCESS.2020.3016255.
- [8] L. Catarinucci, R. Colella, S. I. Consalvo, L. Patrono, C. Rollo and I. Sergi, "IoT-Aware Waste Management System Based on Cloud Services and Ultra-Low-Power RFID Sensor-Tags," in *IEEE Sensors Journal*, vol. 20, no. 24, pp. 14873-14881, 15 Dec. 15, 2020, doi: 10.1109/JSEN.2020.3010675.
- [9] S. Ahmad, Imran, F. Jamil, N. Iqbal and D. Kim, "Optimal Route Recommendation for Waste Carrier Vehicles for Efficient Waste Collection: A Step Forward Towards Sustainable Cities," in *IEEE Access*, vol. 8, pp. 77875-77887, 2020, doi: 10.1109/ACCESS.2020.2988173.
- [10] "Relay"-news-newspapers-books-scholar-. JSTOR(November 2009)

PHOTOVOLTIC CHARGE CONTROLLER FOR ELECTRIC VEHICLE USING BACK STEPPING ALGORITHM

Dr. M .Sangeetha ¹, G .Purusothaman ², R . Senthamarai kannan ³

Abstract – The electric vehicles are widely used in transport system in present day. It is pollution less and cost effective transport method. The ultimate aim of the project is to design and development of solar charge controller for electric vehicle. The battery is the primary source of electric vehicle since the proposed method is to charge the battery properly by using back stepping algorithm. The pic16f877a microcontroller used to measure photo voltaic (PV) panel output and boost converter output and generate pulse width modulation (PWM) signal to control boost converter for proper charging of battery.

Keywords- solar, boost converter, Pic16f877a and PWM.

I. INTRODUCTION

The performance of smart charge controller system is used to extend the life time of battery for electric vehicle. When the battery energy is deficient then the energy is importing from solar PV panel. When the battery energy is excess then energy is exporting to the electric vehicle.

II. PROPOSED METHOD

The proposed system is uses pic16f877a microcontroller because it has built in analog to digital converter (ADC) and pulse width modulator (PWM). Generally the boost converter placed at the load side but in our proposed system uses boos converter in

between solar PV array and battery. Because of the battery should charge properly for increases battery life.

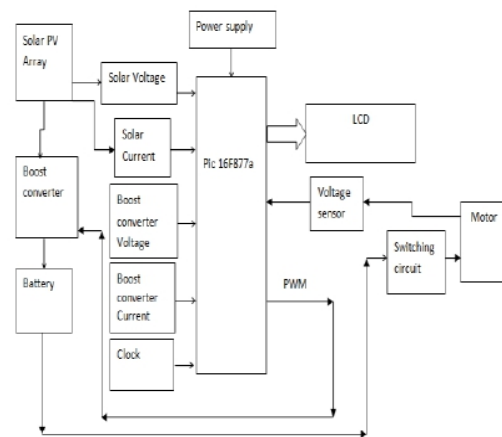


Fig.1. Block diagram of charge controller

The voltage and current sensor connected with ADC channel of Pic16f877a micro controller. The 16 character and 2 line alphanumeric display is used for monitoring the solar voltage, solar current, boost converter output voltage , boost converter output current. The Fig.1 shows the block diagram of proposed charge controller system.

The Fig. 2 shows the circuit diagram of project. It has reset circuit, oscillator circuit, boost converter circuit, and LCD circuit.

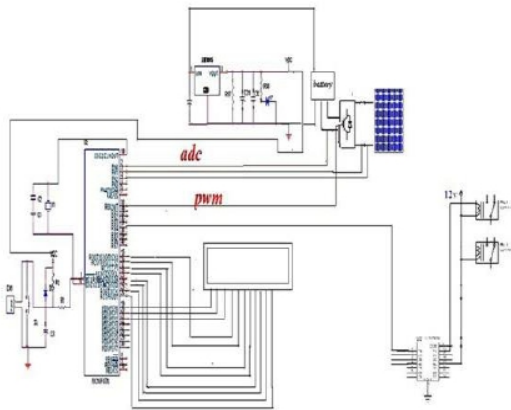


Fig.2. Circuit diagram of charge controller

The algorithm measures the error between output power and required power. The PWM adjust the boost converter output due to required power.

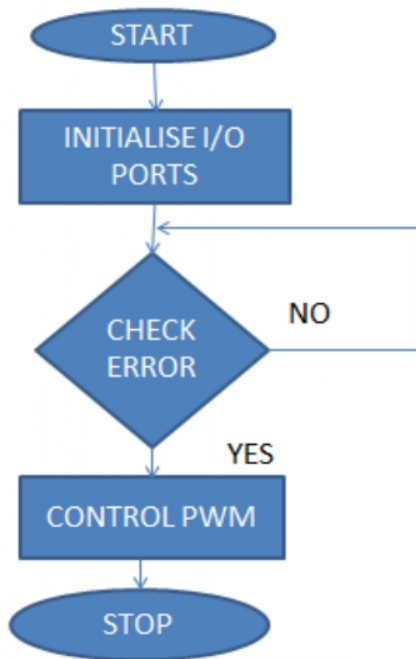


Fig.3. Flow of charge controller

The Fig. 3 shows the flow diagram of proposed system.

III. ADVANTAGES

- It uses renewable energy source
- Less cost
- Emission less
- It completely reduces pollution.

IV. SIMULATION AND RESULT

The simulation result of this concept is verified by proteus 8 professional software.

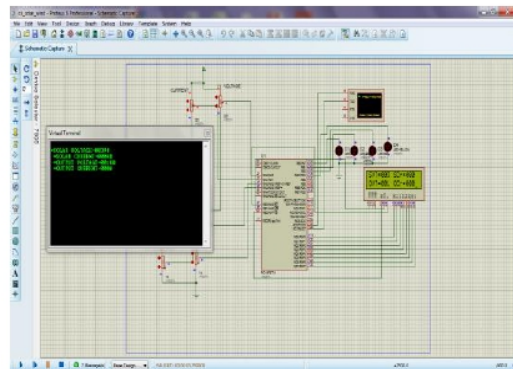


Fig.4. simulation of proteus software

The software has built in library for pic16f877a, LCD, serial terminal, analog and digital inputs/ outputs. The micro controller embedded c code is converted into .hex file format. The pot connected to the ADC channel for voltage and current analog input simulation.



Fig.5. experimental charge controller

The experimental hardware has same .hex file loaded into the pic16f877a. It has relay driver ic (ULN2003) for driving electromagnetic relay. The electromagnetic relay used for driving dc motor. The experimental hardware has 12V/2.5A battery with 6W solar panel.

V. CONCLUSION

The EV charging controller is proposed and its performance is analyzed by experimental output. The proposed controller examined the output power requirement of boost converter for proper charging. The back stepping algorithm is better to adjust the PWM for required output. The PWM is controls the boost converter for required output power.

VI. REFERENCES

1. Mauri G, Bertini D, Fasciolo E, Fratti S. The impact of EV's fast charging stations on the MV distribution grids of the Milan metropolitan area. In: 22nd International conference and exhibition on electricity distribution (CIRED 2013); 10–13 June 2013, pp. 1–3.
2. Marra F, Traholt C, Larsen E, Qiuwei W. Average behavior of battery-electric vehicles for distributed energy studies. In: Innovative smart grid technologies conference Europe (ISGT Europe); 2010 IEEE PES, pp. 1–7.
3. Cicconi P, Germani M, Landi D. Analytical thermal model for characterizing a Li-ion battery cell. In: 27th International electric vehicle symposium & exhibition. Barcelona, Spain; November 17–20, 2013.
4. Erdinc O, Vural B, Uzunoglu M. A dynamic lithium-ion battery model considering the effects of temperature and capacity fading. In: International conference on clean electrical power; 2009, pp. 383–86.
5. Masoum A, Deilami S, Moses P, Abu-Siada A. Impacts of battery charging rates of Plug-in Electric Vehicle on smart grid distribution systems. In: Innovative smart grid technologies conference Europe (ISGT Europe). IEEE PES; 2010, pp.1–6.
6. Putrus G, Suwanapingkarl P, Johnston D, Bentley E, Narayana M. Impact of electric vehicles on power distribution networks. In: IEEE vehicle power and propulsion conference VPPC2009, pp. 827–31.
7. Chitra L , Prabhu Raj M , Keerthivaishnavi B , Madhusowmiya G, Rathna Praveen P , Design of Charge Controller for Electric Vehicle . IN : International Journal of Recent Technology and Engineering (IJRTE) , ISSN: 2277-3878, Volume-8 Issue-6, March 2020.

Neural Network Controller based UHVDC for Enhancement of Transient Compensation in Integrating Offshore Wind Power Plant

M.Sangeetha
Associate Professor
Department of Electrical and
Electronics Engineering
M.A.M.S.E
Trichy – 621 105

A. Senthamarai kannan
Associate Professor
Department of Electrical and
Electronics Engineering
M.A.M.S.E
Trichy - 621 105

G.Purushothaman
Assistant Professor
Department of Electrical and
Electronics Engineering
M.A.M.S.E
Trichy – 621 105

Abstract

This paper presents a novel neural network based control technique for improving compensation of transients and fast power transfer between a large scale offshore wind power plant (WPP) and onshore grid through high voltage direct current (HVDC) transmission. The onshore end of the HVDC is reconfigured with series compensator and shunt compensator which named as ultra-HVDC (UHVDC). To achieve optimum power transfer, transient management scheme is done using DQ control technique. In proposed control technique, the compensation component is determined in such a way to minimize power oscillation and DC link voltage overshoots. The proposed control technique is analyzed using proportional integral (PI) controller and neural network controller. The test system is designed and evaluated in MATLAB simulink environment. A comprehensive simulation studies validate the capability of the proposed control scheme for achieving smooth power transfer and management of transients in the electrical grid.

Keywords: Transient Compensation, Neural Network Controller, PI controller, HVDC, wind power plant, and DC link voltage.

1. Introduction

Wind energy conversion systems have potential to fulfill the world's increasing energy demand. Generally the turbines of wind power plant (WPP) is based on either permanent magnet synchronous generator (PMSG) or doubly fed induction generator (DFIG) [1]. The more attention is given to PMSG based WPP because of its benefits of higher efficiency and it doesn't requires gearbox [2]. The interconnection of wind power plant with grid system is done using back to back voltage source converter (VSC). This ensures increased system reliability and cost efficient. The interconnection of such large scale offshore wind plant is carried out through high voltage direct current (HVDC) transmission system [3].

HVDC is a high power electronic technology which has been widely used in electric power system to transmit large amount of power for long distance, asynchronous interconnection, power flow control [4]. Thus the VSC-HVDC system provides independent control of active and reactive power flow in a transmission system.

The important consideration during the bulk power transmission of HVDC system is grid fault disturbances which lead to stability problem. In [5] discussed about the performance of HVDC system and the significance of maintaining the system to be energetic during different fault conditions. The different configuration of VSC-HVDC system and its performance can be analyzed in [5] – [7]. From the discussion, it is concluded that the VSC- HVDC system configuration must provide fast fault detection and the large scale WPP should contains fault ride through capability. This is achieved by implement proper control strategy of converter stations and many authors proposes different control methodologies. The ultimate aim of the control technique is to enhance the FRT capability of the system without affecting the wind power transfer and hence protect the entire system from severe fault disturbances. A new multilevel VSC – HVDC configuration is proposed in [8], but the system does not compensate the external grid fault. This paper proposes series and shunt compensator named as UHVDC with enhanced fault ride through (FRT) capability. The proposed system has the series and shunt compensation devices to provide symmetrical and asymmetrical fault condition, smooth power transfer, regulated dc link voltage, transient management and hence improved reliability. This can be possible by adopting DQ control technique. To reduce transient during fault period the proposed configuration utilizes neural network (NN) based control technique. This system proposes a comparison for proportional integral controller (PI) and NN based control. The proposed system assures to reduce the transients,

dc link regulation. This proposed large scale WPP with UHVDC system is designed and the results of different case studies are analyzed with MATLAB/ SIMULINK environment.

2. System Configuration

The offshore WPP contains the PMSG based number of wind turbines connected either in series and shunt configuration [9]. Conventionally, the traditional/classic HVDC system is based on thyristor valve for interconnection of two AC network. Generally classic HVDC link employed current source converter (CSC) for interconnection. However the traditional HVDC transmission system has its own limitations such as larger in size hence requires large AC network [1].

Many researches are going on to overcome the conventional HVDC system by a voltage source current converter VSC-HVDC system. It employs modern semiconductor switches such as IGBT/GTO which is compact in size compared to classic thyristor valve based converters. It is based on self-commutated pulse width modulation (PWM) technology. Also IGBT has the ability to turn ON and OFF with much higher frequency. Unlike conventional CSC based HVDC system the VSC-HVDC link does not requires any reactive power support [4]. This VSC-HVDC system is suitable for changing the direction of power flow when the voltage is maintained in dc network. The different configurations of VSC-HVDC system is monopole, bipole, back-to-back or asymmetric, multi terminal [3] and [10]. The Fig 1 shows the system configuration of proposed multi-terminal VSC-HVDC system for wind power plant is connected with standard IEEE 9 bus system. The proposed configuration is called as UHVDC system which provides both series and shunt compensation. The WPP of proposed system has offshore and onshore VSC station. The Offshore station accommodate one converter and the onshore station contains two independent converters namely series and shunt converters. The onshore VSC station is connected with the electrical grid system through two shunt connected transformers (T_{r3} and T_m).

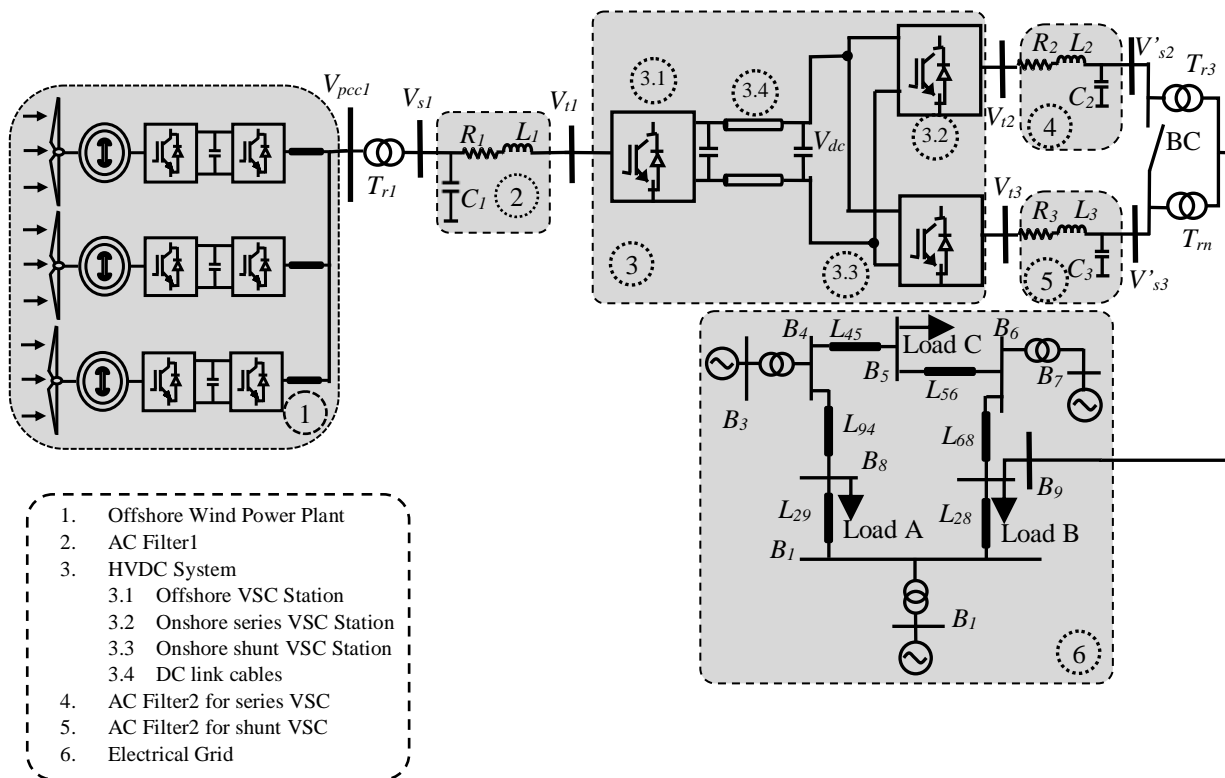


Fig.1. Configuration of VSC-HVDC connected to an IEEE-9 bus system

The power produced by the WPP is transferred to the electrical grid system through this step-up transformer. The converters of both onshore and offshore station should be capable to handle the power generated by the wind farms and the power is delivered to the electrical grid through HVDC system. In the diagram, BC is the bus coupler used to deliver the power and B9 is the point of common coupling (PCC) where the HVDC and the electrical grid system is interconnected [8] and [11]. The advantage of proposed configuration is to give series and shunt compensation to the system during any grid fault without requiring any additional compensation device. This helps to reduce the additional converter costs and hence the proposed system is a cost effective one.

If the fault is occurred in any one of the voltage source, the series transformer delivers the series voltage to prevent the entire system from the severe grid fault. If any fault occurs in V_{s2} , the transformer injects V_{ser} voltage at V_{s3} side so that the UHVDC system does not affected by any of the grid disturbances. Simultaneously, the proposed system provides voltage and current compensation by series and shunt VSC of onshore station. Similarly if the fault is created at V_{s3} side, the series voltage is injected at V_{s2} side. The changeover from one operation into another during both steady state and transient condition is achieved by the proper handling of converter switches in UHVDC system [12]. The operating principle of the proposed system is discussed in next chapter.

3. Mathematical modeling of proposed system

Fig2shows the equivalent circuit for proposed system, consists of two voltage sources V_{g1} and V_{g2} . The two voltage sources are connected with the system through a series transformer $T_{r\ ser}$. The flexibility of active and reactive power flow into the system is achieved with the help of this series transformer. The proposed system is similar to that of a simplified AC network. The two voltage source consists of transmission impedances Z_{g1} and Z_{g2} .

The series converter of proposed U-HVDC system is considered as a generalized voltage source represented as V_{ser} . The controllable voltage magnitude of this voltage source is rated as $0 \leq V_{ser} \leq V_{ser,max}$ and angle ρ rated as $0 \leq \rho \leq 2\pi$. From the Fig. 2(a), let us consider both the transmission impedances Z_{g1} and Z_{g2} contains pure reactance of same value X_g .

When the fault is created in any one of the ac transmission system either V_{g1} or V_{g2} , the series converter of UHVDC system provides compensation by injecting the required series voltage into the system. This causes the transmission line current flows though the series voltage source. Thus the exchange of real and reactive power flow (P_{ser} and Q_{ser}) takes place between series transformer and ac transmission system. Where P_{ser} is the real power generated by the offshore wind power plant and the reactive power Q_{ser} is generated from the converter station. The total active power generated from the WPP is represented as P_w . It can be delivered by the series and shunt converter P_{3n} and P_{ser} .

Let us assume the fault is created at V_{s2} side, there will be a voltage injection at V_{s3} side which causes the real and reactive power P_{3n} and Q_{3n} supplied at V_{s2} .

This ensures the proper power transfer in the HVDC system during the grid fault condition [1] and [13]. The phasor diagram of proposed UHVDC system is shown in Fig 2(b). From the diagram, the voltage dip is occurred at V_{s2} , the

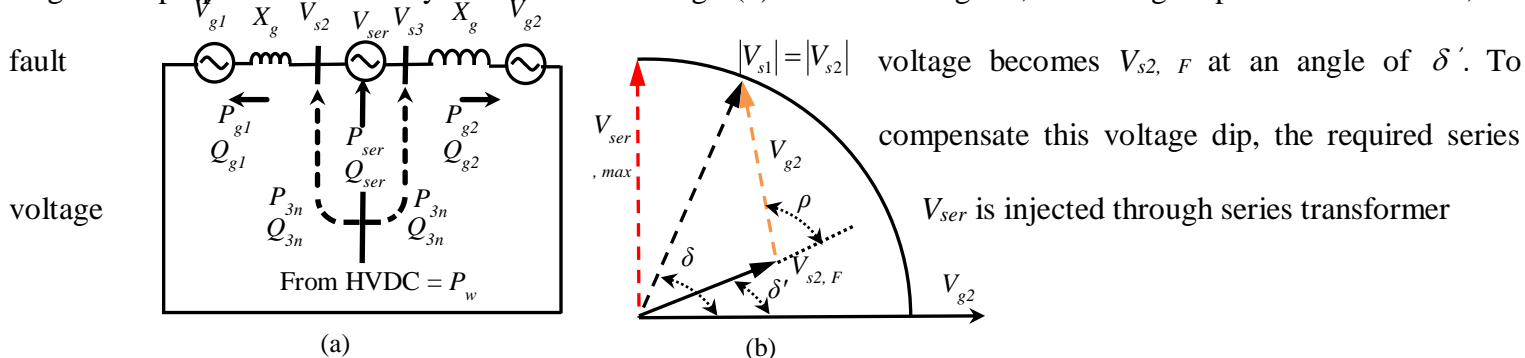


Fig. 2(a) Equivalent circuit and, 2(b) Vector diagram for proposed U-HVDC system

at V_{s3} . Thus the real and reactive power flow at the voltage source V_{g2} can be formulated by the following equations,

$$P_{g_2} = \frac{V_{g_2}}{X_g} \left[V_{s2,F} \sin \delta' + V_{ser} \sin(\delta' + \rho) \right] + P_{3n}$$

$$Q_{g_2} = \frac{V_{g_2}}{X_g} \left[V_{g_2} - V_{s2,F} \cos \delta' + \frac{V_{ser}}{X_g} \cos(\delta' + \rho) \right] + Q_{3n}$$
(1)

From the equation (1), the active and reactive power at V_{g2} is divided into three parts, that is, power due to fault voltage $V_{s2,F}$, power due to series voltage V_{ser} and the power flows takes place to the shunt converter of system.

$$P_{ser} - jQ_{ser} = \frac{V_{g_2}}{X_g} \left[V_{ser} \sin(\delta' + \rho) - jV_{ser} \cos(\delta' + \rho) \right]$$
(2)

The equation (2) describes the separation of series active and reactive power. The rating of series converter is given by,

$$S_{ser,max} = \sqrt{P_{ser}^2 + Q_{ser}^2} = \frac{V_{g_2} V_{ser,max}}{X_g}$$
(3)

For a fixed transmission line, the voltage source V_{g2} is maintained constant at 1 p.u. and the reactance X_g is also considered as constant. The maximum voltage injected by the series converter during fault condition is $V_{ser,max}$. Thus the overloading capability of the proposed system is utilized more during FRT condition. This is accomplished by IGBT's of converters. Hence the FRT capability of proposed UHVDC system is enhanced. From the above analysis, many researchers concluded that the overloading capability of VSC is mostly preferable for a healthy transmission system [4] and [14].

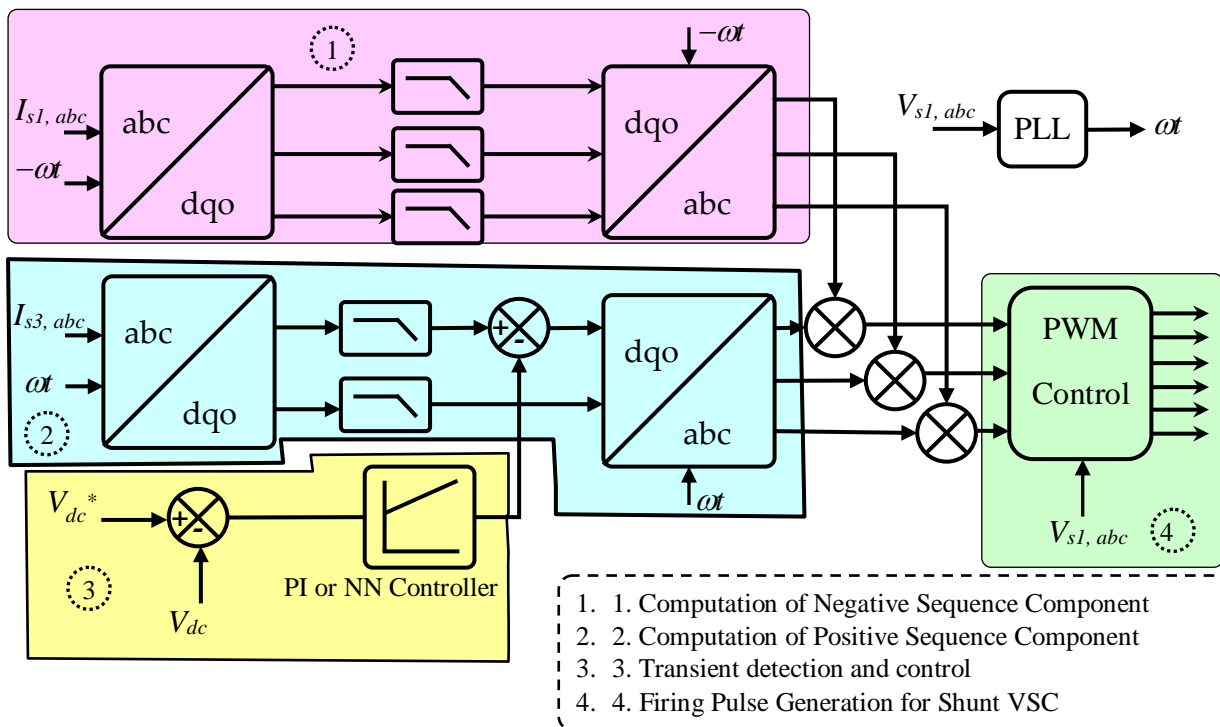


Fig.3. Control Scheme for onshore and offshore shunt VSC- HVDC

4. Control scheme of onshore and offshore system

Here the control scheme of onshore and offshore VSC-HVDC system is discussed under steady state and faulted conditions. The onshore VSC is used to regulate dc link voltage at PCC. The offshore VSC is used to deliver the power generated from WPP and control the grid voltage. Conventional control structure of the system has fast inner current control loop and slower outer control loop [15].

4.1. Control structure of shunt Compensator

The control scheme of onshore and offshore shunt UHVDC system is shown in Fig 3. From the figure, it is observed that there will be four parts of the control scheme of shunt converter of UHVDC station. The first part is used to extract the negative sequence component and the second part performs computation of positive sequence component. The third part deals with transient detection and management scheme by either analytical or neural network (NN) method. The final part is the pulse generation part for shunt VSC. The positive and negative sequence ($dq0$) component of the shunt station is computed using positive and negative PLL angle ωt . The transformation is done from three phase (abc to $dq0$) to find out the positive and negative sequence ($dq0$)

components. The $dq0$ components are extracted directly from the voltage and current of the offshore station. The shunt VSC performs the current compensation and hence it deals with transformation of distorted three phase current to $dq0$ quantities. Finally the transformed reference current is given to pulse generation block to produce the required firing pulse of converter station [16].

The general equation for three phase current in stationary axis (abc) is transformed into two phase rotating coordinates ($dq0$) is given below,

$$\begin{bmatrix} i_{Ld} \\ i_{Lq} \\ i_{L0} \end{bmatrix} = \begin{pmatrix} \cos \theta & \cos(\theta - \frac{2\pi}{3}) & \cos(\theta + \frac{2\pi}{3}) \\ \sin \theta & \sin(\theta - \frac{2\pi}{3}) & \sin(\theta + \frac{2\pi}{3}) \\ \frac{1}{2} & \frac{1}{2} & \frac{1}{2} \end{pmatrix} \begin{bmatrix} i_{sa}^* \\ i_{sb}^* \\ i_{sc}^* \end{bmatrix} \quad (4)$$

Finally, the desired reference current is calculated by taking inverse transformation of ($dq0$) axis into three phase (abc) rotating frame axis and is derived by the following equation (5).

$$\begin{bmatrix} i_{sa}^* \\ i_{sb}^* \\ i_{sc}^* \end{bmatrix} = \begin{pmatrix} \sin \theta & \cos \theta & \frac{1}{2} \\ \sin(\theta - \frac{2\pi}{3}) & \cos(\theta - \frac{2\pi}{3}) & \frac{1}{2} \\ \sin(\theta + \frac{2\pi}{3}) & \cos(\theta + \frac{2\pi}{3}) & \frac{1}{2} \end{pmatrix} \begin{bmatrix} i_{Ld} \\ i_{Lq} \\ i_{L0} \end{bmatrix} \quad (5)$$

4.2. Control structure of series Compensator

Here the control strategy for series onshore UHVDC system is discussed and the diagram for the same is shown in Fig 4. The series converter provides the voltage and transient compensation. When the fault is created at any one of the voltage source (V_{g1} or V_{g2}) the power transfer within the system is gets affected. To protect the WPP turbines based HVDC system from fault disturbances and severe transient, a series converter provides series voltage V_{ser} . This voltage is injected into the system at PCC through series transformer [17] and [18]. The equation for series voltage with phase angle is given below,

$$V_{ser} \angle \rho = V_{s3} \angle \delta - V_{s2,F} \angle \delta' \quad (6)$$

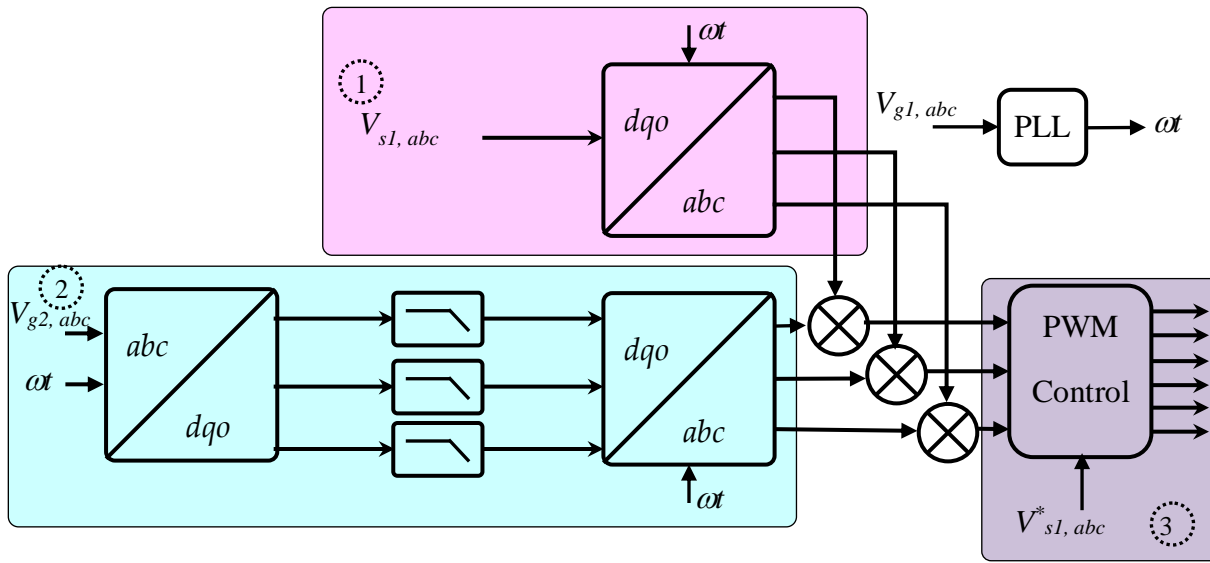


Fig.4. Control Scheme for series VSC of onshore WPP based UHVDC system

From the above equation, the positive sequence component of voltage magnitude and phase angle can be separated as,

$$|V_{ser}| = \sqrt{(V_{s3} \cos \delta - V_{s2,F} \cos \delta')^2 + (V_{s3} \sin \delta - V_{s2,F} \sin \delta')^2} \tag{7}$$

$$\rho = \tan^{-1} \left(\frac{V_{s3} \sin \delta - V_{s2,F} \sin \delta'}{V_{s3} \cos \delta - V_{s2,F} \cos \delta'} \right) \tag{8}$$

From the above expressions, the reference positive sequence voltage is determined by the pre fault grid voltage and measured grid voltage and is named as $V_{ser,dq,ref}^+$. When a fault is created at V_{s2} side, the compensation is done at shunt side V_{s3} . The total power delivered at series UHVDC system is given by the equation (9).

$$P_{tot,ser} = P_{ser} + P_{cos} \cos(2\omega t) + P_{sin} \sin(2\omega t) \tag{9}$$

The total active power $P_{tot, ser}$ is divided into three parts, series average power, cosine power and sine power and this power can be derived in equation (10) as given below,

$$\begin{bmatrix} P_{ser} \\ P_{cos} \\ P_{sin} \end{bmatrix} = \begin{pmatrix} I_{ser,d}^+ & I_{ser,q}^+ & I_{ser,q}^- \\ I_{ser,d}^- & I_{ser,q}^- & I_{ser,q}^+ \\ I_{ser,q}^- & -I_{ser,d}^- & I_{ser,d}^+ \end{pmatrix} \begin{bmatrix} V_{ser,d}^+ \\ V_{ser,q}^+ \\ V_{ser,d}^- \\ V_{ser,q}^- \end{bmatrix} \tag{10}$$

From the above expression, $V_{ser,dq}$ and $I_{ser,dq}$ is the series voltage and current dq component. The sine and cosine terms of power is cancelled and equated to zero by the generation of reference negative sequence component of series voltage $V_{ser-dq,ref}$.

The negative sequence voltage component is obtained by solving the above equation and is written as below in equation (11).

$$\begin{bmatrix} V_{ser.d,ref}^- \\ V_{ser.q,ref}^- \end{bmatrix} = - \begin{pmatrix} I_{ser.d}^+ & I_{ser.q}^+ \\ -I_{ser.q}^+ & I_{ser.d}^+ \end{pmatrix}^{-1} * \begin{pmatrix} I_{ser.d}^- & I_{ser.q}^- \\ I_{ser.q}^- & -I_{ser.d}^- \end{pmatrix} \begin{bmatrix} V_{ser.d}^+ \\ V_{ser.q}^+ \end{bmatrix} \quad (11)$$

Finally, the three phase voltages are given to pulse generation block to generate firing pulses for series VSC system.

5. Design of neural network controller

The neural network is an artificial intelligence tool used to formulate mapping between target data and input data. The procedure for training the neural network is shown in Fig5. Initial process is to collect the training data, i.e., input data and target data. This is the most important process, because it determines efficiency of neural network controller on compensation of transient and DC link voltage control [19]. The input data are error and integral error of DC link voltage and target data is compensation component of the current. DC link voltage error is the difference of reference and actual DC link voltage. Next process is the network creation, for this case two input and one output two-layer feedforward network is used. After neural network created, it must be configured for best network performance. The network configuration step consists of examining the input and target data, setting input and output sizes of the network to match the data and choosing an appropriate transfer function. After configuration, the weights of the two layers are initialized [20]. After trained and validation, the network is implemented in the simulation.

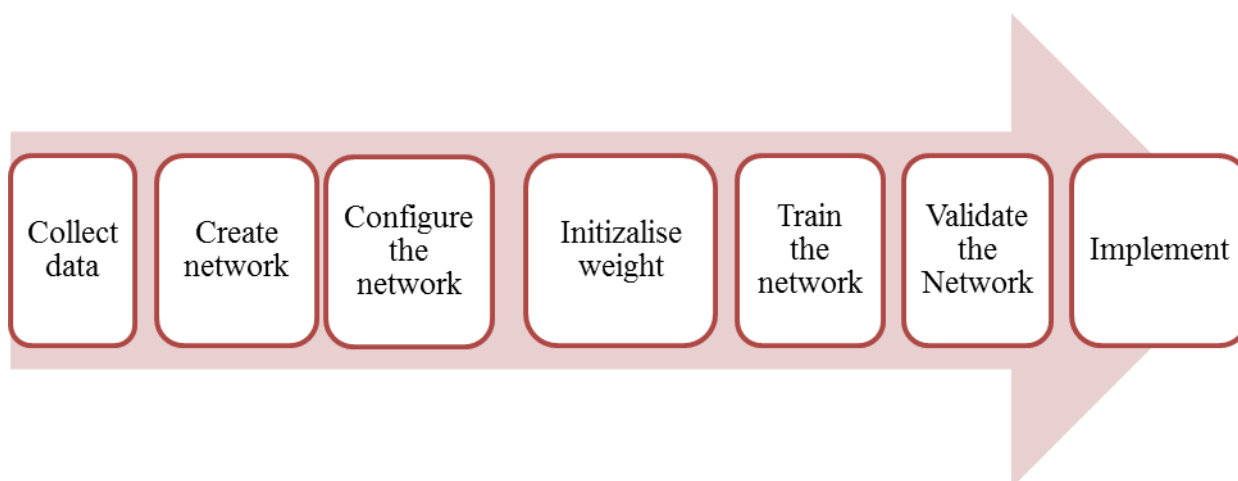


Fig.5. Procedure for training the neural network

Let $E = V_{dc Ref} - V_{dc}$ be DC link voltage and EI be Integral of error and a_1 to a_5 be constants used to train the neural network. $Y(K)$ be the output of artificial neural network, $W(K)$ and $CW(K)$ be the weight and change in weight of the update algorithm. The output and update equation of the artificial neural network is represented in the following equations

$$Y(k) = a_1 * W(k-1) + \alpha * CW(k-1) + a_2 * CW(k) + a_3 \quad (12)$$

$$CW(k) = \gamma * (a_4 * E(K) + a_5 * EI(K)) \quad (13)$$

The simulation responses for neural network training are shown in Fig 6. The total epoch is set to 1000 and best performance is reached at 608th epoch. From the obtained results it is observed that the output and target data are tracking well. Hence it is found the network is ready to implement in the simulation environment.

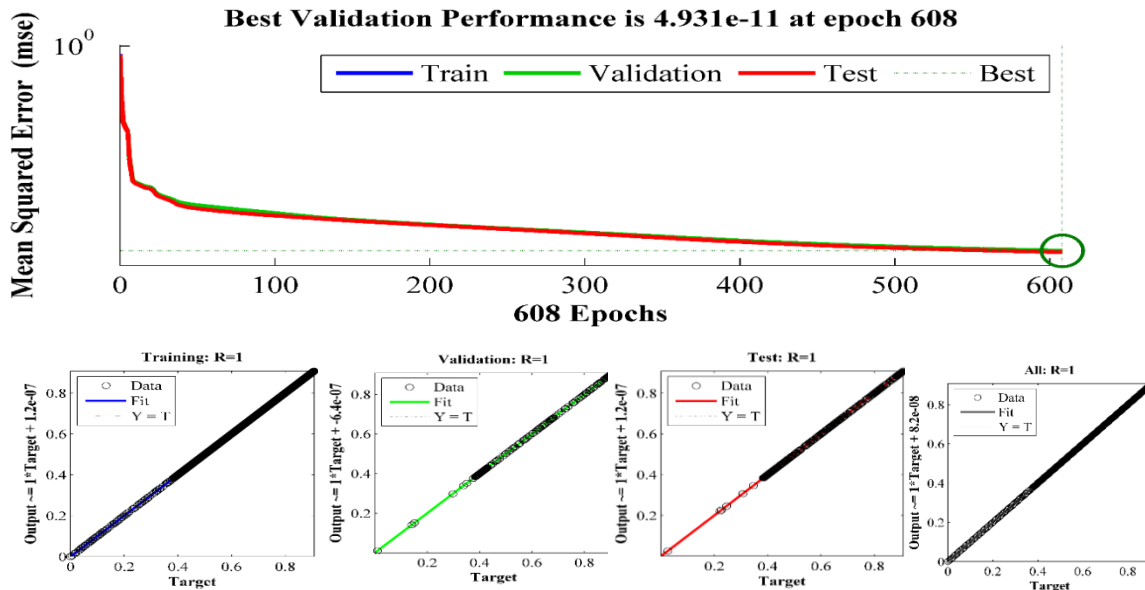


Fig 6. Simulation responses of performance of the neural network training

6. Simulation Results and discussion

Simulation analysis on a power system network connected to the offshore WPP connected through UHVDC utilizing PI and proposed NN controllers based DQ theory is carried out in this section. This section demonstrates the effectiveness of the proposed control technique for enhancing the compensation of transients and to provide fast power transfer under normal and faulted operating conditions. The voltage rating of the network is 230KV and the rating of HVDC is 250KVA which is equivalent to the offshore WPP. Parameter taken for simulation is given in table 2.

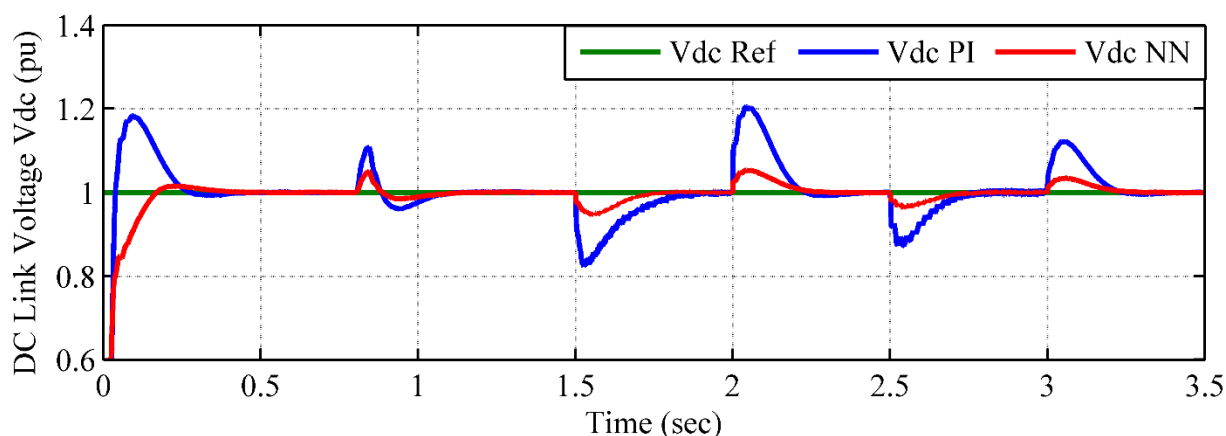


Fig.7. DC link Voltage control using PI and NN controllers

6.1. Analyze on control of DC link voltage

The optimum compensation of transients and fast transfer of power between offshore WPP and power system network are determined by the finest control of DC link voltage of UHVDC at rated value. In this case study, the DC link voltage is controlled at 400KV using PI controller and proposed NN controller. The pu simulation result of DC link voltage control using PI and proposed NN controllers under WPP and grid sides disturbances are shown in Fig. 7. The operating condition for this case study is fault injected in WPP at 0.8 sec, grid side faults are under voltage fault is injected between 1.5 sec to 2 sec and over voltage fault is injected at 2.5 to 3 sec. for initial condition, the peak overshoot of DC link voltage using PI controller is found to be 18.3% whereas 1.415% while using NN controller. Under WPP side fault condition, the peak overshoot of DC link voltage using PI controller is found to be 11% whereas 5% while using NN controller. Under grid side fault condition, the peak overshoot of DC link voltage using PI controller is found to be 20.5% whereas 4% while using NN controller. The performance of PI and NN controllers are analyzed and compared in table 1. This demonstration confirms that the better minimization transients and better control of DC link voltage is achieved by the proposed NN controller.

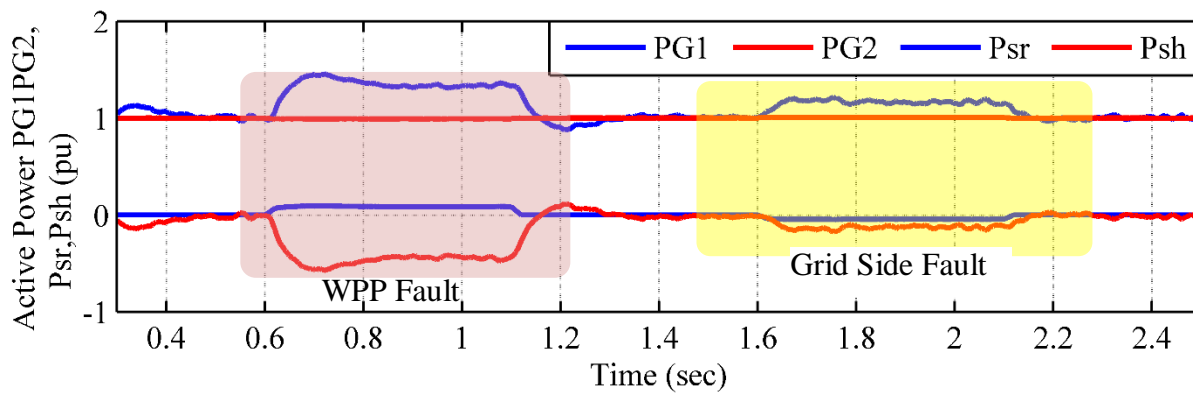


Fig. 8.a. Real power transfer using PI controllers

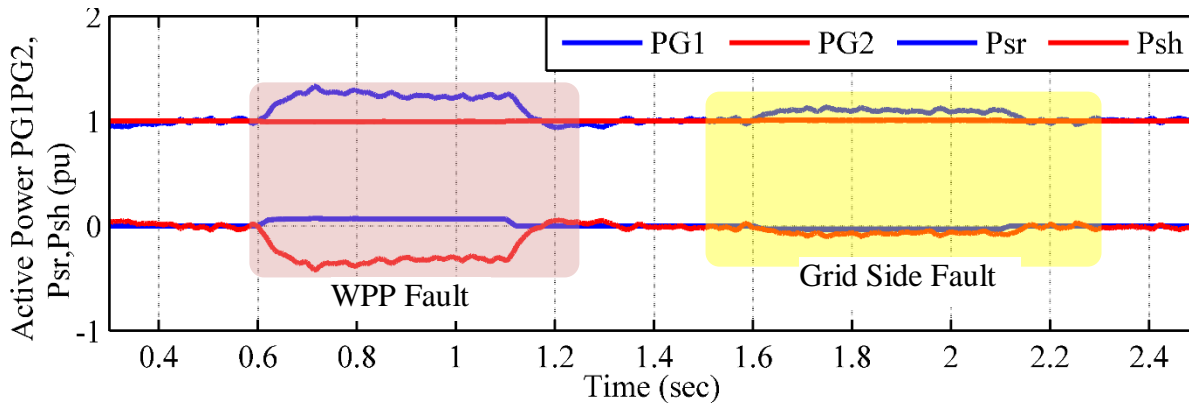


Fig. 8.b. Real power transfer using NN controllers

6.2. Analyze on real power transfer using PI and NN controllers

Simulation analysis on real power transfer between offshore WPP and power system networks through UHVDC using PI controller and proposed NN controller is carried out in this section. The simulation results for control of real power transfer using PI controller and proposed NN controller under WPP and grid side faults are shown in Fig. 8.a and Fig. 8.b respectively. The operating condition for this case study is 10% voltage drop is injected in WPP from 0.6 sec to 1.2 sec and 10% voltage drop is introduced in power system network between 1.6 sec to 2.6 sec. The main objective of this investigation is to maintain real power at the second grid (PG2) at 250 MW. The voltage drops in WPP created 0% power drop at first grid (PG1) for without compensation. For maintaining PG2, the series VSI injects series power (P_{sr}) 20% at point of common coupling there by PG2 is successfully maintained. While using PI controller, PG1 and P_{sr} have more peak overshoot and high oscillation. Whereas, NN controller PG1 and P_{sr} are successfully controlled with minimum oscillation and optimally regulated PG2.

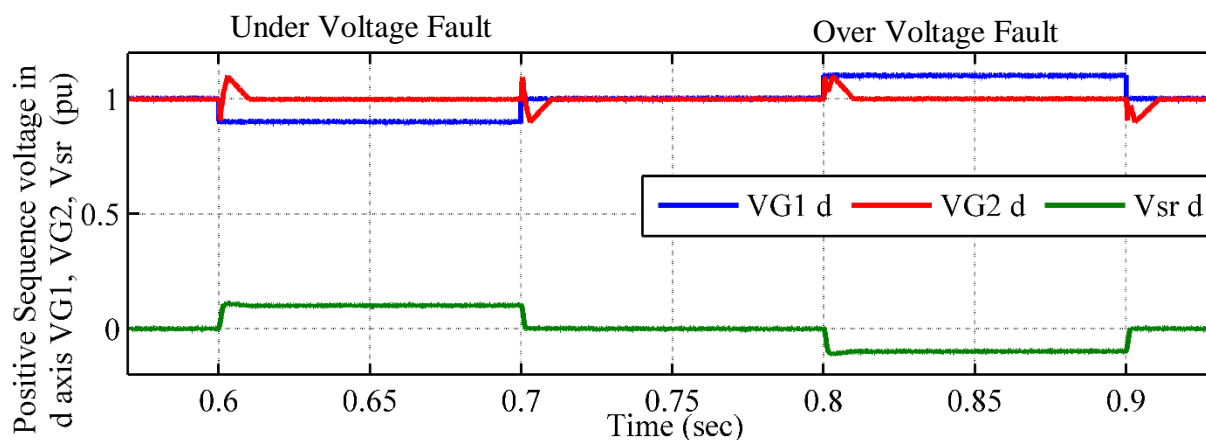


Fig. 9.a. Compensation of positive sequence voltage in d axis using PI controller

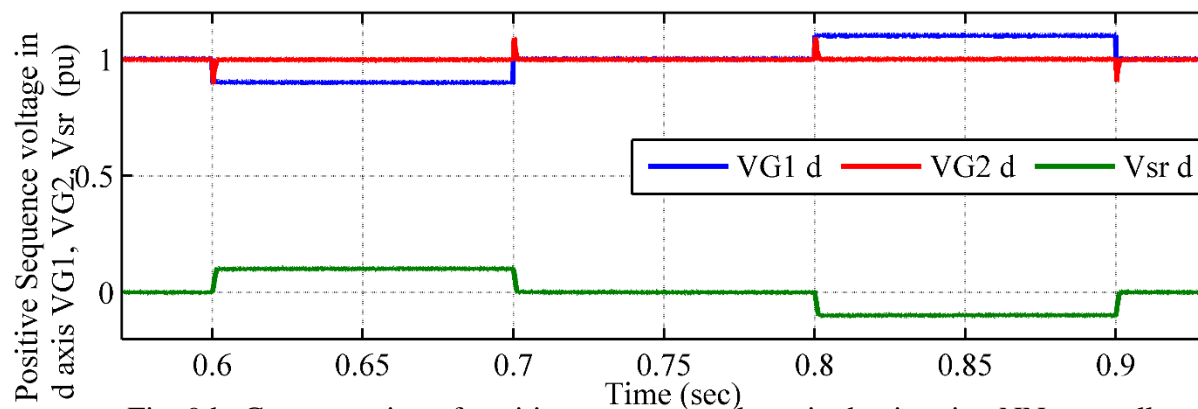


Fig. 9.b. Compensation of positive sequence voltage in d axis using NN controller

6.3. Analysis on compensation on voltage at point of common coupling

This section demonstrates regulation of rated voltage of 230 KV at point of common coupling using PI controller and NN controller. The simulation results of regulation of positive sequence voltage V_{G1} , V_{G2} and V_{sr} in d axis using PI controller and NN controller are shown in Fig. 9.a and Fig. 9.b respectively. 10% under voltage is introduced between 0.6 sec to 0.7 sec and 10% of over voltage is injected at VG1 between 0.8 sec to 0.9 sec. The main objective of the proposed configuration is to maintain rated voltage 230KV at point of common coupling.

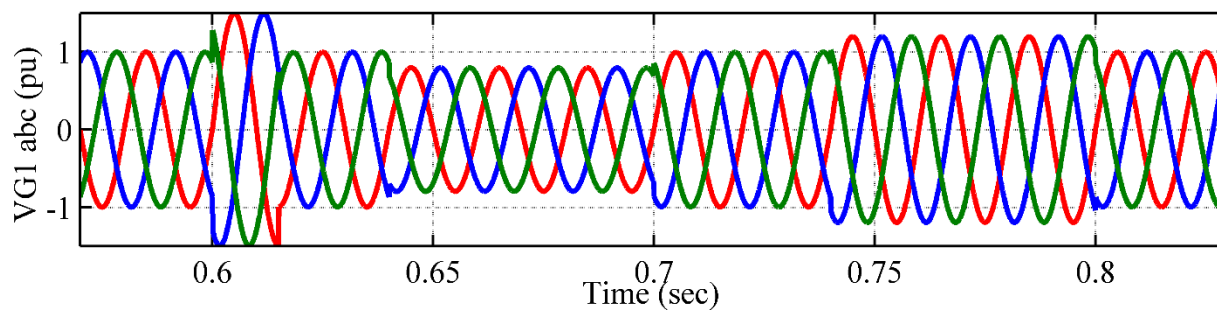


Fig. 9.c. Simulation result for three phase grid 1 voltage

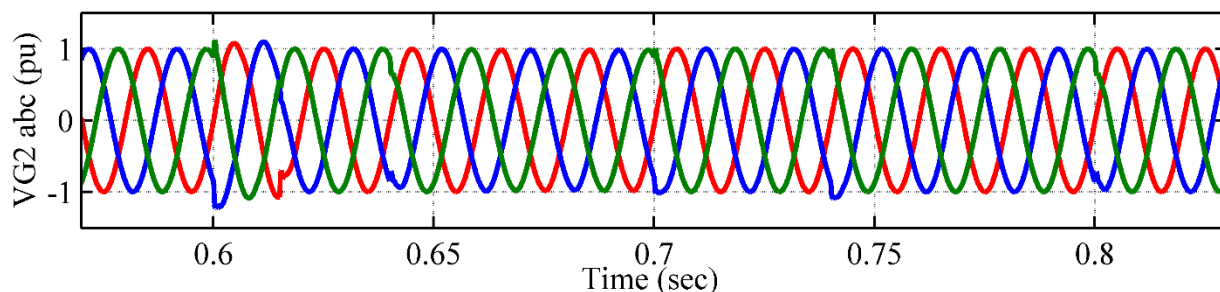


Fig. 9.d. Simulation result for three phase grid 2 voltage

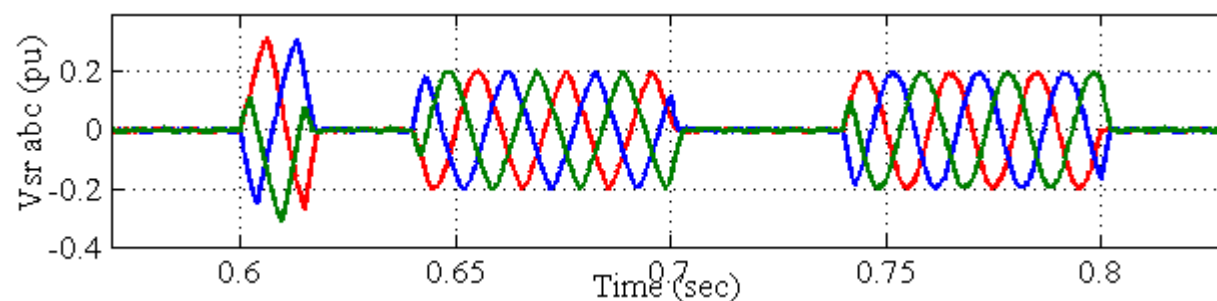


Fig. 9.e. Simulation result for three phase series voltage

Under normal operating conditions, $VG1$ and $VG2$ are in equal and Vsr is found to be zero. For under voltage condition, required voltage is injected by series VSI and thereby rated voltage is maintained at point of common coupling. For over voltage condition, required voltage is absorbed by series VSI and thereby rated voltage is maintained. While using PI controller, transient detection is found to be poor and it requires more time to compensate whereas using NN controller, transient detection is found to be optimum and it has fast compensation time. This analyzes are clearly projected in Fig. 9.a and Fig. 9.b. respective. The simulation results for three phase voltage of grid 1, grid 2 and series voltage or compensation voltage are shown in Fig. 9.c, Fig. 9.d and Fig. 9.e respectively. Under normal condition, rated voltage is maintained whereas under faulted condition the require voltage is injected by the series VSI such that it maintains rated voltage at grid 2.

7. Conclusion

A neural network DQ control technique based UHVDC is proposed for the management of transient and fast power transfer between offshore WPP and onshore electric grid. The performance of the proposed neural network control scheme is investigated under disturbances in both WPP and electric grids and compared with PI controller. From the test results, it is found that neural network based control technique has better capability to compensate transients and superior power transfer between WPP and electric grid.

References

- [1]. Ahmed Moawwad, Mohamad Shawky El Moursi and Weidong Xiao, "A Novel control strategy for VSC-HVDC connecting offshore wind power plant," *IEEE Trans. Sustain. Ener.*, vol. 5, no.3 pp. 1204–1212, 2014.
- [2]. P. Bresesti, W. L. Kling, R. L. Hendriks, and R. Vailati, "HVDC connection of offshore wind farms to the transmission system," *IEEE Trans. Energy Convers.*, vol. 22, no. 1, pp. 37–43, Mar. 2007.
- [3]. N. Flourentzou, V. Agelidis, and G. Demetriades, "VSC-based HVDC power transmission systems: An overview," *IEEE Trans. Power Electron.*, vol. 24, no. 3, pp. 592–602, Mar. 2009.
- [4]. A. Egea-Alvarez, F. Bianchi, A. Junyent-Ferre, G. Gross, and O. Gomis-Bellmunt, "Voltage control of multiterminal VSC-HVDC transmission systems for offshore wind power plants: Design and implementation in a scaled platform," *IEEE Trans. Ind. Electron.*, vol. 60, no. 6, pp. 2381–2391, Jun. 2013.
- [5]. Q. Guo, J. Zhao, and L. Niu, "Faults predictions and analysis on reliability of the 660 kV Nngdong HVDC power transmission system," in *Proc. 4th Int. Conf. Electric Utility Deregulation and Restructuring and Power Technol.*, 2011, pp. 99–103.
- [6]. X. Chen, C. Zhao, and C. Cao, "Research on the fault characteristics of HVDC based on modular multilevel converter," in *Proc. IEEE Trans. Electr. Power Energy Conf.*, Oct. 3–5, 2011, pp. 91–96.
- [7]. S. Alepuz et al., "Control strategies based on symmetrical components for grid-connected converters under voltage dips," *IEEE Trans. Ind. Electron.*, vol. 56, no. 6, pp. 2162–2173, Jun. 2009.
- [8]. G. P. Adam, K. H. Ahmed, S. J. Finney, K. Bell, and B. W. Williams, "New breed of network fault-tolerant voltage-source-converter HVDC transmission system," *IEEE Trans. Power Syst.*, vol. 28, no. 4, pp. 335–346, Feb. 2013.
- [9]. P. H. Huang, M. El Moursi, W. Xiao, and J. Kirtley, "Novel fault ride through configuration and transient management scheme for doubly fed induction generator," *IEEE Trans. Energy Conv.*, vol. 28, no. 1, pp. 86–94, Mar. 2013.
- [10]. R. T. Pinto et al., "A novel distributed direct-voltage control strategy for grid integration of offshore wind energy systems through MTDC network," *IEEE Trans. Ind. Electron.*, vol. 60, no. 6, pp. 2429–2441, Jun. 2013.
- [11]. S. K. Chaudhary, R. Teodorescu, P. Rodriguez, P. C. Kjaer, and A. M. Gole, "Negative sequence current control in wind power plants with VSC-HVDC Connection," *IEEE Trans. Sustain. Energy*, vol. 3, no. 3, pp. 535–544, Jul. 2012.
- [12]. N. G. Hingorani, L. Gyugyi, and M. El-Hawary, *Understanding FACTS: Concepts and Technology of Flexible AC Transmission Systems*. New York, NY, USA: IEEE, 2000.
- [13]. N. Flourentzou, V. G. Agelidis, and G. D. Demetriades, "VSC-based HVDC power transmission systems: An overview," *IEEE Trans. Power Electron.*, vol. 24, no. 3, pp. 592–602, Mar. 2009.
- [14]. Z. Chen, J. Guerrero, and F. Blaabjerg, "A review of the state of the art of power electronics for wind turbines," *IEEE Trans. Power Electron.*, vol. 24, no. 8, pp. 1859–1875, Aug. 2009.
- [15]. M. Baradar and M. Ghandhari, "A multi-option unified power flow approach for hybrid AC/DC grids incorporating multi-terminal VSC-HVDC," *IEEE Trans. Power Syst.*, vol. PP, no. 99, pp. 1–8.
- [16]. D. Roiu, R. I. Bojoi, L. R. Limongi, and A. Tenconi, "New stationary frame control scheme for three-phase PWM rectifiers under unbalanced voltage dips conditions," *IEEE Trans. Ind. Appl.*, vol. 46, no. 1, pp. 268–277, Jan./Feb. 2010.
- [17]. S. K. Chaudhary, R. Teodorescu, P. Rodriguez, P. C. Kjaer, and A. M. Gole, "Negative sequence current control in wind power plants with VSC-HVDC connection," *IEEE Trans. Sustain. Energy*, vol. 3, no. 3, pp. 535–544, Jul. 2012.
- [18]. Ahmed Moawwad, Mohamad Shawky El Moursi and Weidong Xiao, "Novel configuration and transient management strategy for VSC-HVDC," *IEEE Trans. Power Syst.*, vol. 29, no.5 pp. 2478–2488, 2014.
- [19]. B. Singh and S. R. Arya, "Back-propagation control algorithm for power quality improvement using DSTATCOM," *IEEE Trans. Indus. Elec.* 61(3) (2014) 1204–1212.

[20]. B. Singh, V. Verma, and J. Solanki, "Neural network-based selective compensation of current quality problems in distribution system," IEEE Trans. Indus. Elect., vol. 54, no. 1, pp.53–60, 2007.

Nomenclature	
BC	bus coupler
DQ	direct and quadrature axis
E, EI	error and integral of error
FRT	fault ride through
HVDC	high voltage direct current
$I_{ser, dq}$	Series current of dq component
NN	neural network
PCC	point of common coupling
PMSG	permanent magnet synchronous generator
PI	proportional and integral controller
P_{3n}, Q_{3n}	Real and reactive power at shunt compensator
P_{g2}, Q_{g2}	Real and reactive power at source 2
P_{ser}, Q_{ser}	Series real and reactive power
P_w	Total real power generated by WPP
$S_{ser, max}$	Rating of series converter
UHVDC	unified high voltage direct current
V_{dc}	dc link capacitor voltage
V_{dc}^*	reference dc link capacitor voltage
VSC	field programmable gate array
V_{s1}	Voltage at offshore VSC
V_{s2}, V_{s3}	Voltage at onshore series and shunt converter
$V_{s2, F<\delta}$	Voltage during fault
V_{ser}	series voltage
$V_{ser, dq}$	Series voltage of dq component
$V_{ser, dq}^-$	Negative sequence dq frame series voltage
$V_{ser, dq}^+$	positive sequence dq frame series voltage
$V_{ser, dq, ref}^-$	reference negative sequence dq series
WPP	wind power plant
Z_{g1}, Z_{g2}	Transmission line impedances

Solar Powered Water Management System Using Smart Card

Dr.M.Sangeetha^a, Dr. R. Arulmozhiyal^b, Mr.G.Purushothaman^c

^a

Associate Professor, Department of EEE, M.A.M. School of Engineering,
Trichy – 621105, Tamilnadu, India

^bProfessor, Department of EEE, Sona College of Technology, Salem – 636 005, Tamilnadu, India.

^cAssociate Professor, Department of EEE,

M.A.M. School of Engineering, Trichy – 621105, Tamilnadu, India.

Article History Received: 10 January 2021; Revised: 12 February 2021; Accepted: 27 March 2021; Published online: 20 April 2021

Abstract: With rapid development of economy and urban growth, water shortage and resource pollution is now a serious problem for urban water supply in many cities. At same time, with enlargement of urban areas and increase of sealing areas results in reduction of green spaces, new road and building construction etc., runoffs of rainwater increase greatly. Networked, smart systems will help make enhanced use of energy, avoid superfluous and water losses and lessen the consumption of resources. In addition to automation and drive technology, this paper introduce solar powered drinking water supply management using RFID technology. In this paper RFID technology is used to manage the supply of water to the people, if the RFID card is placed near to the RFID reader, LCD displays the details regarding that card holder. According to the details, the DC Motor will pump the water and the message will be sent to the card holder regarding the water consumed

Keywords: LDR, MPPT, Arduino Nano board, Smart card.

1. Introduction

Energy plays a major role in the evolution of the country. Present day scenario, immense quantity of power is produced using non-renewable power sources. 85% of power production is dependent on fossil fuels [1]. The resources of the combustible are finite and its usage is resulting to global warming due to emission of conservatory gases. To provide a sustainable power production and safe world to the future generation, there is a rapid increase in need of vitality from renewable resources like solar, wind, geothermal and ocean tidal wave [2]. Solar radiations are converted into electrical energy by solar panels. Solar panel constitutes of solid state conductor substance. Major component used in the making of solar panel is Silicon, which is 24.5% efficient.[3].

To have the maximum utilization of the amount of intensity captured it is essential to use the tracking system and hence to maintain accuracy and precession. The control circuit for solar tracker is done by Arduino Uno board. This is programmed to detect sunlight using LDR and actuate the stepper motor to position the solar panel where it can receive maximum sunlight. Stepper motor is controllable, energy efficient, steady and have high tracking accuracy and suffers little environmental affect. The water pump is attached to the battery. Since the pump works on DC power supply, it is directly attached to the battery. The water pumping system also consists of water level sensors used to detect water levels for automatic turn on and off of the water pump. This helps in the automation of water pumping systems in hospitals, factories, schools, public places etc. hence reducing manpower also maintaining the adequate usage of the resources[4] [5].

Solar based power is a rule progressively used worldwide as an inexhaustible wellspring of vitality. India has tremendous undiscovered sun powered off-frame work openings. This paper gives data about advancement methodology of an installed framework for off grid water system frame work [7]. Resource of water is indispensable for satisfying daily human needs varying, from agriculture to energy production. The demand of water for irrigation purpose is still an issue to be solved in developing countries, mainly rural areas with energy crisis and environmental pollution created mostly by the use of fossil fuel, this problem has unfolded a solution using solar photovoltaic water pumping system. Solar photovoltaic water pumping system has become so popular not only in the agriculture sector but also for drinking water and micro irrigation applications [8].

Abundant water supply in remote locations is required to ensure the grazing evenly. Water pumping is most accepted and admired application of solar energy in developing countries such as India. The proposed system is reliable, simple and requires less maintenance [9]. Many villages in India use fossil fuel based water pumping system for irrigation due to a shortage of electricity. Fossil fuel causes great damage to the environment as they release harmful greenhouse gases. In this research work, we propose a solar energy based automated water pumping system is implemented to these villagers in terms of cost and profit. In addition, this can save a lot of water and is environment- friendly [10]. Increase in cell efficiency, maximizing the power output and employing a tracking system with solar panel are the three major ways to increase the overall efficiency.

To develop single axis solar tracking system which captures maximum intensity from the sun rays efficiently store the generated energy in the battery for the future application to develop automated water pumping system

which helps to save water and minimize man power. Overall objective is to build a power conserving, less use of manpower, resource conserving project for the sustainable development and to help the mankind save time.

2. Solar Tracking System

The proposed system mainly consists of two parts, solar tracking and water pumping system. The first part of the system, the solar tracking system consists of LDR, stepper motor and solar panel. These LDR's are connected to the two ends of the solar panel. Based on the intensity of light falling on the LDR the arduino will decide the direction of rotation of stepper motor. Stepper motor is in turn connected to the panel. Thus arduino controls the rotation of both stepper motor and solar panel The second part of the project namely the water pumping system consists of water level sensors, DC motor and battery. The water level sensor is used to control and detect water level in the tank. The solar energy is stored and it is collected in battery. The absorbed power is then sent to the motor which runs the pump.

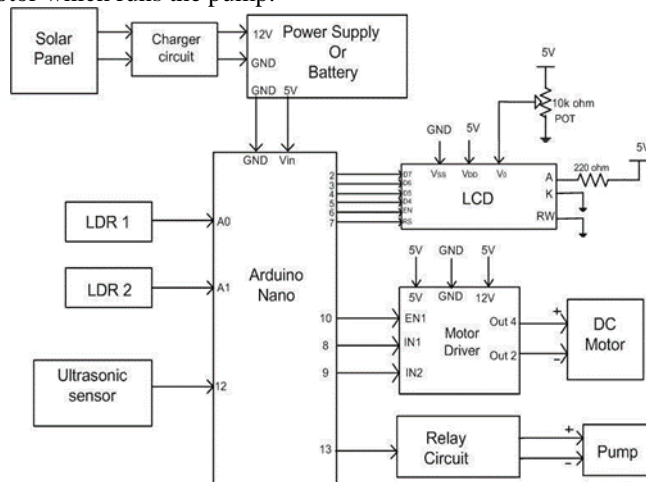


Figure 1: Configuration of Solar Tracking and Water Pumping System

Solar Panel

Solar panel mainly consists of numerous photovoltaic (PV) cells which is combined to form a module. These PV cells are made up of semiconductor material namely silicon that is usually connected in series or parallel to get additive voltage or current. The solar panel is basically a P-N junction, when sunlight falls on the PV cell; the electrons gain energy and jumps out of the atom hence leading to the flow of electricity.

Table 1: Solar panel specification

Parameter	Value
Maximum Power	10 W
Vmax	18Volts
Imax	0.56Amps
Voc	21.6Volts
Vsc	0.64Amps
Rechargeable Battery	12Volts
Dimension	280*54*22
Weight	1.5kg

Solar Charging Circuit

This circuit is mainly used to maintain constant DC voltage obtaining from solar panel. This provides protection from over charging and over discharging of the battery life cycle of the battery eventually decreases. To maintain the battery life and to have better performance, battery should never be overcharged or over discharged.

Solar Charging Circuit

This circuit is mainly used to maintain constant DC voltage obtaining from solar panel. This provides protection from over charging and over discharging of the battery.

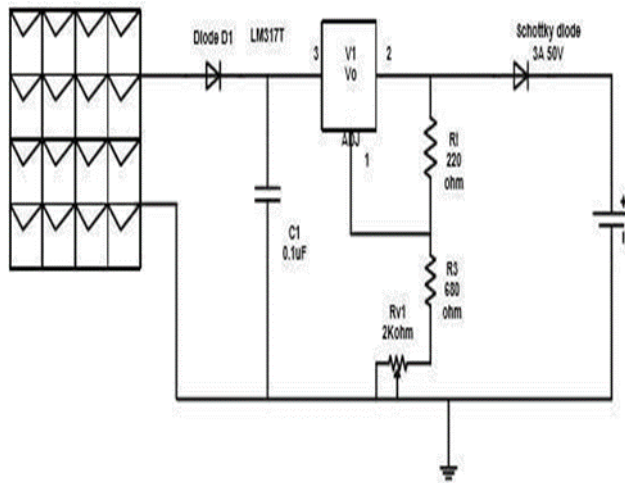


Figure 2: Circuit diagram of Solar Charger circuits

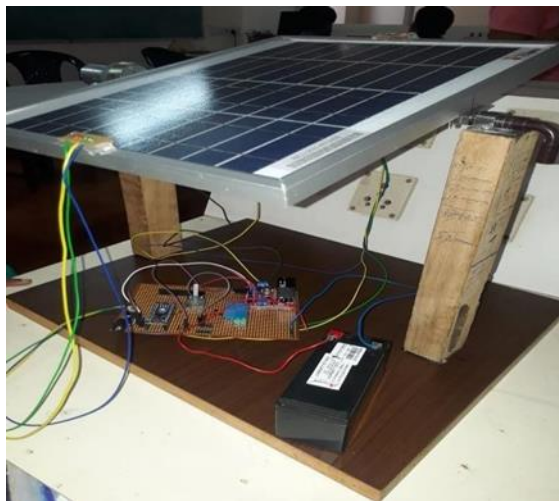


Figure 3: Solar Tracking Unit

Solar panel Characteristic

The current voltage characteristic of the solar module provides useful information. The parameters obtained from the I-V curve include short circuit current 'Isc', open circuit voltage Voc, maximum current Imax, and maximum voltage Vmax at the maximum power point Pmax.

Solar panel characterization is done by connecting the solar panel in series with the ammeter followed by a rheostat and voltmeter connected across the rheostat. The resistance is varied and corresponding solar panel voltage and current are recorded, the I-V curve plotted for a 10W solar panel is shown in the below figure 4.

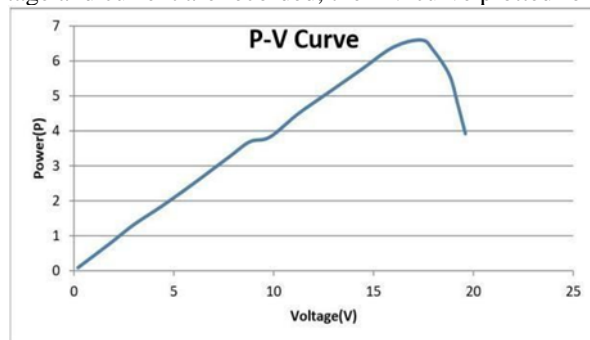


Figure 4: I-V Characteristics of solar panel

The IV curve for the solar panel is plotted during the peak time of the day say approx 2pm. The graph is plotted by taking voltage along x-axis and current along y-axis. The graph having the maximum current of 0.4A obtained at voltage of 10V.

Figure5. IV curve

This graph is obtained by taking solar panel voltage along x- axis and power (obtained by multiplying voltage and current at each point) along y-axis .It can be seen that the maximum power of 6.61W is obtained at voltage

17.4V and current 0.38A. From the above graph it can be inferred that the solar isolation is not constant throughout the day and the power generated varies accordingly, therefore, there is a need to store the electrical energy generated by the solar panel during maximum productivity. To achieve this battery is used as, renewable energy along with batteries allows stand- alone operations and therefore the batteries are now a standard component of solar power system.



Figure 6:Solar Tracking and water pumping unit
RFID-Technology:

RFID identification (RFID) is term is used to explain a method that transmits the identity the object wirelessly using radio waves. RFID technology is assembled with the most general Automatic Identification (Auto ID) technologies.

An RFID system consists of two separate components: a tag and a reader.

The tag contains an antenna linked to a small microchip that contains as much as two kilobytes of information. The readers or scanner functions much like a bar code scanner. However, while a bar code scanner utilizes a laser light to scan the bar code, an RFID scanner uses electromagnetic waves. To deliver these waves, the scanner uses an antenna that transmits a signal contacting the tags antenna

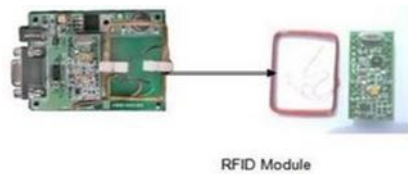
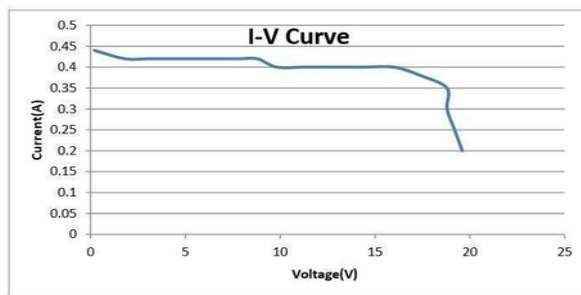


Figure 7 : RFID module



3. Design of Proposed Systems

When the solar panel is exposed to sunlight, the LDR sensors are activated through arduino code and then the LDR senses the intensity of the sunlight and then decide whether the LDR1 or LDR2 is receiving maximum sunlight. And followed by the rotation of the solar panel through the DC motor driven by motor driver L298N in the direction of the maximum intensity.

Once the solar energy is obtained it is made to store in the lead acid battery for the future scope and for the protection of the battery the power trapped by the panel is made to pass

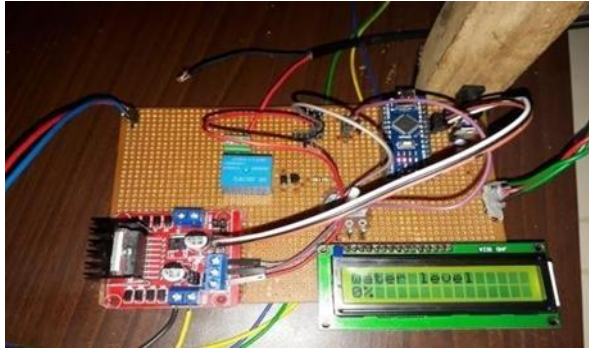


Figure 8: LCD display showing the water level

4. Result And Conclusion

In this paper the single axis solar tracking system is successfully implemented. The constant DC voltage of 12V is obtained with help of solar charger circuit. The energy obtained from the panel is stored into the rechargeable battery of 4.5Ah. The charge controller circuit prevents over charging and over discharging of the battery. Later implemented automation of water pumping system which senses the water level in the tank and automatically turns on and off the pump, based on the water sensed in the tank which is programmed using Arduino Uno. This paper aims at reducing wastage of drinking water and providing purified water to the village people. An RFID Reader can access the data of the card holder from a family . The RFID Reader is capable of reading 40 tags per second. This results in reduction of waste of drinking water ,cost of electricity by utilize the renewable energy source and provide a purified drinking water to the village people

References

1. J.Rizik and Y.Chaiko , "Solar tracking system : More efficient Use of solar panels"-2008
2. M.Reyasudin basir khan, "Solar Tracking System Utilizing Pyranometer For optimal Photovoltaic Module Positioning"- 2012
3. Jeng -Nan Jung and R.Radharamanan, 'Design of a solar tracking system for Renewable energy'-2014
4. M. Ouada, M.S. Meridjet and N. Talbi, 'Optimization Photovoltaic Pumping System Based BLDC Using Fuzzy Logic MPPT Control', International Renewable and Sustainable Energy Conference (IRSEC), pp.27- 31, 7-9 March 2013.
5. Neha Yadav, Manju Gupta, K. Sudhakar. "Energy assessment of floating photovoltaic system", International Conference on Electrical Power and Energy Systems (ICEPES) 2016, pp.264 – 269.
6. Yashar Ghiassi-Farrokhfal, Fiodar Kazhamiaka, Catherine Rosenberg, Srinivasan Keshav. "Optimal Design of Solar PV Farms With Storage", IEEE of Solar PV Farms With Storage", IEEE With Storage", IEEE
7. Y.J.Zuo "survivable RFID system : Issues ,challenges,and techniques" IEEE Trans .Syst ., Man, Cybern. C, Appl.Rev.,vol. 40, no. 4, pp.406-418 2010
8. H.H.Bi and D.K.Lin "RFID –enabled discovery of supply networks",IEEE
9. Trans.Eng.Manag.,vol.56,no.1,pp.129-141 2009
10. J.D. porter and D.S.Kim "An RFID- enabled road pricing system for transportation",IEEE Syst. J.,vol .2,no. 2,pp 248-257 2008
11. K.Finkenzeller RFID Handbook : Fundamentals and application in contactless smart card and identification,2003 : Wiley.

Neural Network Controller based UHVDC for Enhancement of Transient Compensation in Integrating Offshore Wind Power Plant

M.Sangeetha
Associate Professor
Department of Electrical and
Electronics Engineering
M.A.M.S.E
Trichy – 621 105

A. Senthamarai kannan
Associate Professor
Department of Electrical and
Electronics Engineering
M.A.M.S.E
Trichy - 621 105

G.Purushothaman
Assistant Professor
Department of Electrical and
Electronics Engineering
M.A.M.S.E
Trichy – 621 105

Abstract

This paper presents a novel neural network based control technique for improving compensation of transients and fast power transfer between a large scale offshore wind power plant (WPP) and onshore grid through high voltage direct current (HVDC) transmission. The onshore end of the HVDC is reconfigured with series compensator and shunt compensator which named as ultra-HVDC (UHVDC). To achieve optimum power transfer, transient management scheme is done using DQ control technique. In proposed control technique, the compensation component is determined in such a way to minimize power oscillation and DC link voltage overshoots. The proposed control technique is analyzed using proportional integral (PI) controller and neural network controller. The test system is designed and evaluated in MATLAB simulink environment. A comprehensive simulation studies validate the capability of the proposed control scheme for achieving smooth power transfer and management of transients in the electrical grid.

Keywords: Transient Compensation, Neural Network Controller, PI controller, HVDC, wind power plant, and DC link voltage.

1. Introduction

Wind energy conversion systems have potential to fulfill the world's increasing energy demand. Generally the turbines of wind power plant (WPP) is based on either permanent magnet synchronous generator (PMSG) or doubly fed induction generator (DFIG) [1]. The more attention is given to PMSG based WPP because of its benefits of higher efficiency and it doesn't requires gearbox [2]. The interconnection of wind power plant with grid system is done using back to back voltage source converter (VSC). This ensures increased system reliability and cost efficient. The interconnection of such large scale offshore wind plant is carried out through high voltage direct current (HVDC) transmission system [3].

HVDC is a high power electronic technology which has been widely used in electric power system to transmit large amount of power for long distance, asynchronous interconnection, power flow control [4]. Thus the VSC-HVDC system provides independent control of active and reactive power flow in a transmission system.

The important consideration during the bulk power transmission of HVDC system is grid fault disturbances which lead to stability problem. In [5] discussed about the performance of HVDC system and the significance of maintaining the system to be energetic during different fault conditions. The different configuration of VSC-HVDC system and its performance can be analyzed in [5] – [7]. From the discussion, it is concluded that the VSC- HVDC system configuration must provide fast fault detection and the large scale WPP should contains fault ride through capability. This is achieved by implement proper control strategy of converter stations and many authors proposes different control methodologies. The ultimate aim of the control technique is to enhance the FRT capability of the system without affecting the wind power transfer and hence protect the entire system from severe fault disturbances. A new multilevel VSC – HVDC configuration is proposed in [8], but the system does not compensate the external grid fault. This paper proposes series and shunt compensator named as UHVDC with enhanced fault ride through (FRT) capability. The proposed system has the series and shunt compensation devices to provide symmetrical and asymmetrical fault condition, smooth power transfer, regulated dc link voltage, transient management and hence improved reliability. This can be possible by adopting DQ control technique. To reduce transient during fault period the proposed configuration utilizes neural network (NN) based control technique. This system proposes a comparison for proportional integral controller (PI) and NN based control. The proposed system assures to reduce the transients,

dc link regulation. This proposed large scale WPP with UHVDC system is designed and the results of different case studies are analyzed with MATLAB/ SIMULINK environment.

2. System Configuration

The offshore WPP contains the PMSG based number of wind turbines connected either in series and shunt configuration [9]. Conventionally, the traditional/classic HVDC system is based on thyristor valve for interconnection of two AC network. Generally classic HVDC link employed current source converter (CSC) for interconnection. However the traditional HVDC transmission system has its own limitations such as larger in size hence requires large AC network [1].

Many researches are going on to overcome the conventional HVDC system by a voltage source current converter VSC-HVDC system. It employs modern semiconductor switches such as IGBT/GTO which is compact in size compared to classic thyristor valve based converters. It is based on self-commutated pulse width modulation (PWM) technology. Also IGBT has the ability to turn ON and OFF with much higher frequency. Unlike conventional CSC based HVDC system the VSC-HVDC link does not requires any reactive power support [4]. This VSC-HVDC system is suitable for changing the direction of power flow when the voltage is maintained in dc network. The different configurations of VSC-HVDC system is monopole, bipole, back-to-back or asymmetric, multi terminal [3] and [10]. The Fig 1 shows the system configuration of proposed multi-terminal VSC-HVDC system for wind power plant is connected with standard IEEE 9 bus system. The proposed configuration is called as UHVDC system which provides both series and shunt compensation. The WPP of proposed system has offshore and onshore VSC station. The Offshore station accommodate one converter and the onshore station contains two independent converters namely series and shunt converters. The onshore VSC station is connected with the electrical grid system through two shunt connected transformers (T_{r3} and T_m).

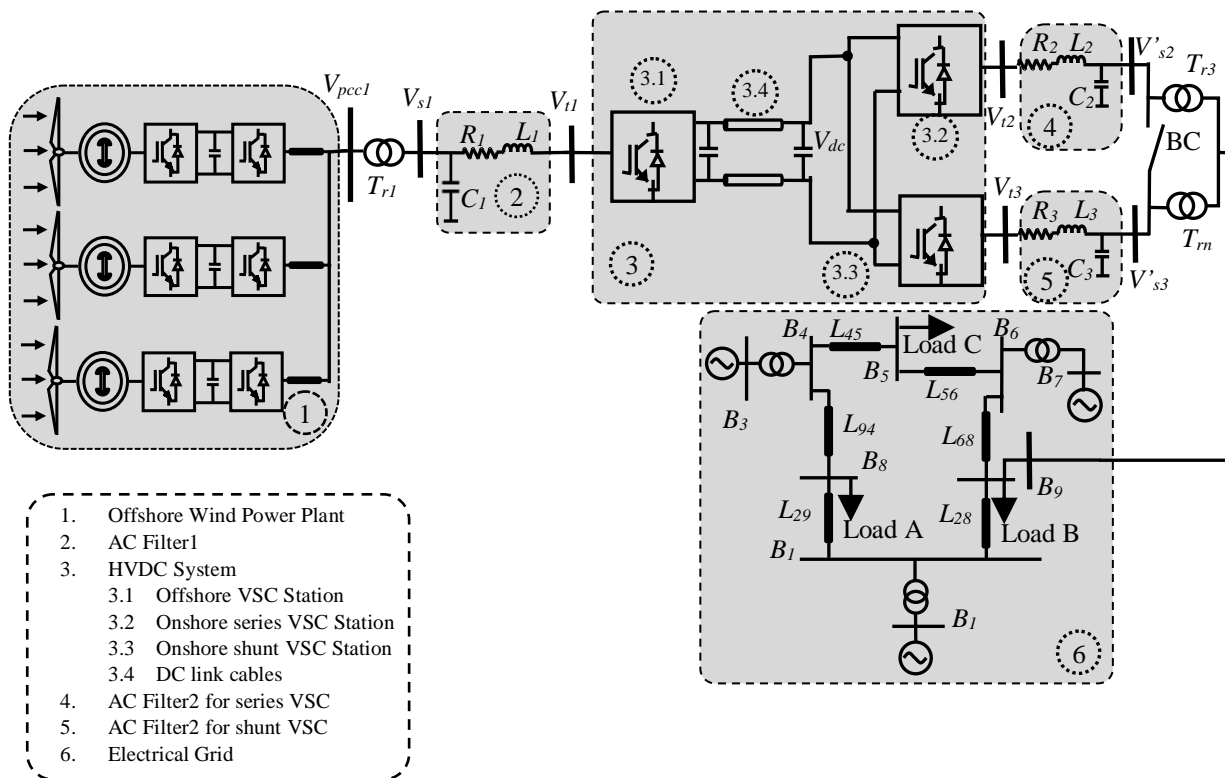


Fig.1. Configuration of VSC-HVDC connected to an IEEE-9 bus system

The power produced by the WPP is transferred to the electrical grid system through this step-up transformer. The converters of both onshore and offshore station should be capable to handle the power generated by the wind farms and the power is delivered to the electrical grid through HVDC system. In the diagram, BC is the bus coupler used to deliver the power and B9 is the point of common coupling (PCC) where the HVDC and the electrical grid system is interconnected [8] and [11]. The advantage of proposed configuration is to give series and shunt compensation to the system during any grid fault without requiring any additional compensation device. This helps to reduce the additional converter costs and hence the proposed system is a cost effective one.

If the fault is occurred in any one of the voltage source, the series transformer delivers the series voltage to prevent the entire system from the severe grid fault. If any fault occurs in V_{s2} , the transformer injects V_{ser} voltage at V_{s3} side so that the UHVDC system does not affected by any of the grid disturbances. Simultaneously, the proposed system provides voltage and current compensation by series and shunt VSC of onshore station. Similarly if the fault is created at V_{s3} side, the series voltage is injected at V_{s2} side. The changeover from one operation into another during both steady state and transient condition is achieved by the proper handling of converter switches in UHVDC system [12]. The operating principle of the proposed system is discussed in next chapter.

3. Mathematical modeling of proposed system

Fig2shows the equivalent circuit for proposed system, consists of two voltage sources V_{g1} and V_{g2} . The two voltage sources are connected with the system through a series transformer $T_{r\ ser}$. The flexibility of active and reactive power flow into the system is achieved with the help of this series transformer. The proposed system is similar to that of a simplified AC network. The two voltage source consists of transmission impedances Z_{g1} and Z_{g2} .

The series converter of proposed U-HVDC system is considered as a generalized voltage source represented as V_{ser} . The controllable voltage magnitude of this voltage source is rated as $0 \leq V_{ser} \leq V_{ser,max}$ and angle ρ rated as $0 \leq \rho \leq 2\pi$. From the Fig. 2(a), let us consider both the transmission impedances Z_{g1} and Z_{g2} contains pure reactance of same value X_g .

When the fault is created in any one of the ac transmission system either V_{g1} or V_{g2} , the series converter of UHVDC system provides compensation by injecting the required series voltage into the system. This causes the transmission line current flows though the series voltage source. Thus the exchange of real and reactive power flow (P_{ser} and Q_{ser}) takes place between series transformer and ac transmission system. Where P_{ser} is the real power generated by the offshore wind power plant and the reactive power Q_{ser} is generated from the converter station. The total active power generated from the WPP is represented as P_w . It can be delivered by the series and shunt converter P_{3n} and P_{ser} .

Let us assume the fault is created at V_{s2} side, there will be a voltage injection at V_{s3} side which causes the real and reactive power P_{3n} and Q_{3n} supplied at V_{s2} .

This ensures the proper power transfer in the HVDC system during the grid fault condition [1] and [13]. The phasor diagram of proposed UHVDC system is shown in Fig 2(b). From the diagram, the voltage dip is occurred at V_{s2} , the

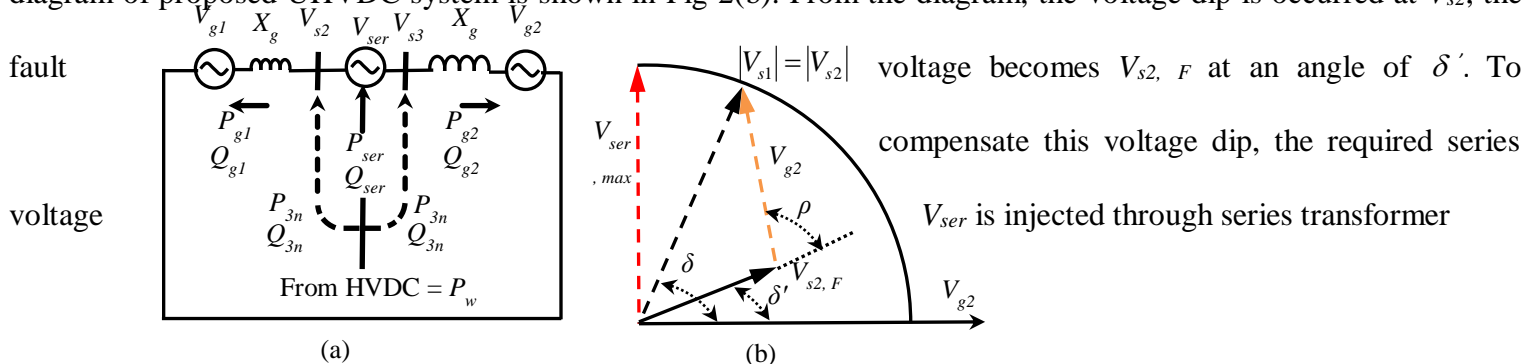


Fig. 2(a) Equivalent circuit and, 2(b) Vector diagram for proposed U-HVDC system

at V_{s3} . Thus the real and reactive power flow at the voltage source V_{g2} can be formulated by the following equations,

$$P_{g_2} = \frac{V_{g_2}}{X_g} \left[V_{s2,F} \sin \delta' + V_{ser} \sin(\delta' + \rho) \right] + P_{3n}$$

$$Q_{g_2} = \frac{V_{g_2}}{X_g} \left[V_{g_2} - V_{s2,F} \cos \delta' + \frac{V_{ser}}{X_g} \cos(\delta' + \rho) \right] + Q_{3n}$$
(1)

From the equation (1), the active and reactive power at V_{g2} is divided into three parts, that is, power due to fault voltage $V_{s2,F}$, power due to series voltage V_{ser} and the power flows takes place to the shunt converter of system.

$$P_{ser} - jQ_{ser} = \frac{V_{g_2}}{X_g} \left[V_{ser} \sin(\delta' + \rho) - jV_{ser} \cos(\delta' + \rho) \right]$$
(2)

The equation (2) describes the separation of series active and reactive power. The rating of series converter is given by,

$$S_{ser,max} = \sqrt{P_{ser}^2 + Q_{ser}^2} = \frac{V_{g_2} V_{ser,max}}{X_g}$$
(3)

For a fixed transmission line, the voltage source V_{g2} is maintained constant at 1 p.u. and the reactance X_g is also considered as constant. The maximum voltage injected by the series converter during fault condition is $V_{ser,max}$. Thus the overloading capability of the proposed system is utilized more during FRT condition. This is accomplished by IGBT's of converters. Hence the FRT capability of proposed UHVDC system is enhanced. From the above analysis, many researchers concluded that the overloading capability of VSC is mostly preferable for a healthy transmission system [4] and [14].

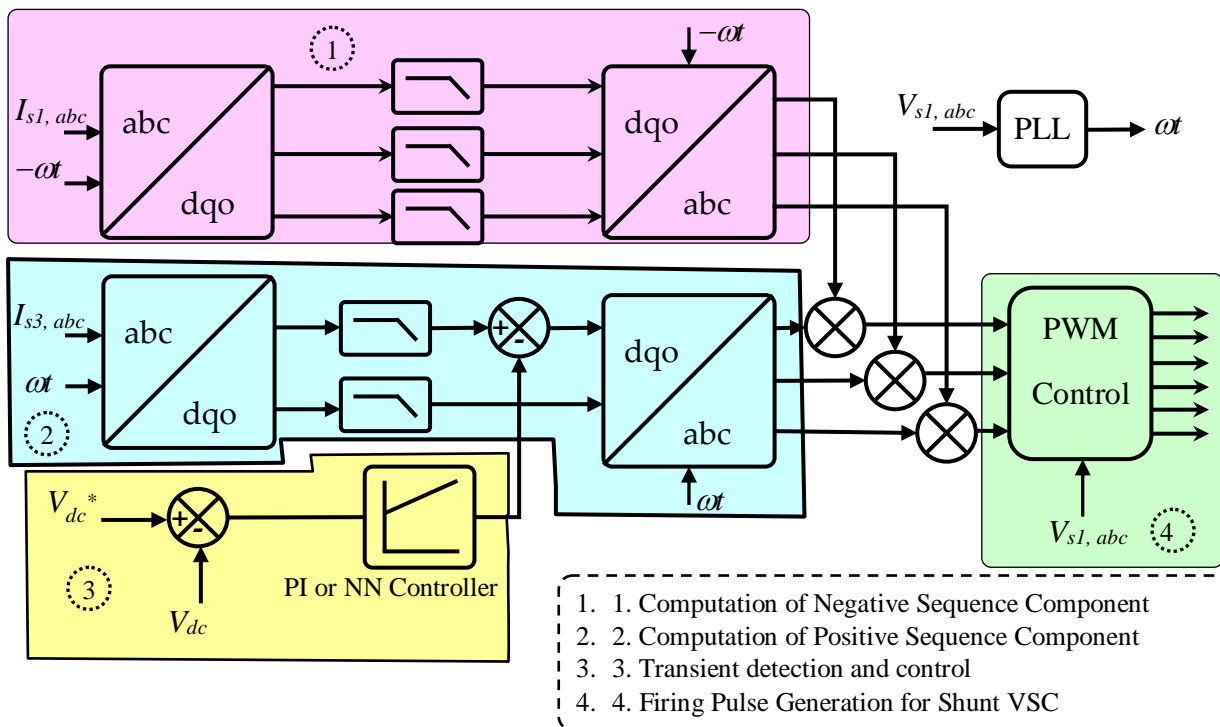


Fig.3. Control Scheme for onshore and offshore shunt VSC- HVDC

4. Control scheme of onshore and offshore system

Here the control scheme of onshore and offshore VSC-HVDC system is discussed under steady state and faulted conditions. The onshore VSC is used to regulate dc link voltage at PCC. The offshore VSC is used to deliver the power generated from WPP and control the grid voltage. Conventional control structure of the system has fast inner current control loop and slower outer control loop [15].

4.1. Control structure of shunt Compensator

The control scheme of onshore and offshore shunt UHVDC system is shown in Fig 3. From the figure, it is observed that there will be four parts of the control scheme of shunt converter of UHVDC station. The first part is used to extract the negative sequence component and the second part performs computation of positive sequence component. The third part deals with transient detection and management scheme by either analytical or neural network (NN) method. The final part is the pulse generation part for shunt VSC. The positive and negative sequence ($dq0$) component of the shunt station is computed using positive and negative PLL angle ωt . The transformation is done from three phase (abc to $dq0$) to find out the positive and negative sequence ($dq0$)

components. The $dq0$ components are extracted directly from the voltage and current of the offshore station. The shunt VSC performs the current compensation and hence it deals with transformation of distorted three phase current to $dq0$ quantities. Finally the transformed reference current is given to pulse generation block to produce the required firing pulse of converter station [16].

The general equation for three phase current in stationary axis (abc) is transformed into two phase rotating coordinates ($dq0$) is given below,

$$\begin{bmatrix} i_{Ld} \\ i_{Lq} \\ i_{L0} \end{bmatrix} = \begin{pmatrix} \cos \theta & \cos(\theta - \frac{2\pi}{3}) & \cos(\theta + \frac{2\pi}{3}) \\ \sin \theta & \sin(\theta - \frac{2\pi}{3}) & \sin(\theta + \frac{2\pi}{3}) \\ \frac{1}{2} & \frac{1}{2} & \frac{1}{2} \end{pmatrix} \begin{bmatrix} i_{sa}^* \\ i_{sb}^* \\ i_{sc}^* \end{bmatrix} \quad (4)$$

Finally, the desired reference current is calculated by taking inverse transformation of ($dq0$) axis into three phase (abc) rotating frame axis and is derived by the following equation (5).

$$\begin{bmatrix} i_{sa}^* \\ i_{sb}^* \\ i_{sc}^* \end{bmatrix} = \begin{pmatrix} \sin \theta & \cos \theta & \frac{1}{2} \\ \sin(\theta - \frac{2\pi}{3}) & \cos(\theta - \frac{2\pi}{3}) & \frac{1}{2} \\ \sin(\theta + \frac{2\pi}{3}) & \cos(\theta + \frac{2\pi}{3}) & \frac{1}{2} \end{pmatrix} \begin{bmatrix} i_{Ld} \\ i_{Lq} \\ i_{L0} \end{bmatrix} \quad (5)$$

4.2. Control structure of series Compensator

Here the control strategy for series onshore UHVDC system is discussed and the diagram for the same is shown in Fig 4. The series converter provides the voltage and transient compensation. When the fault is created at any one of the voltage source (V_{g1} or V_{g2}) the power transfer within the system is gets affected. To protect the WPP turbines based HVDC system from fault disturbances and severe transient, a series converter provides series voltage V_{ser} . This voltage is injected into the system at PCC through series transformer [17] and [18]. The equation for series voltage with phase angle is given below,

$$V_{ser} \angle \rho = V_{s3} \angle \delta - V_{s2,F} \angle \delta' \quad (6)$$

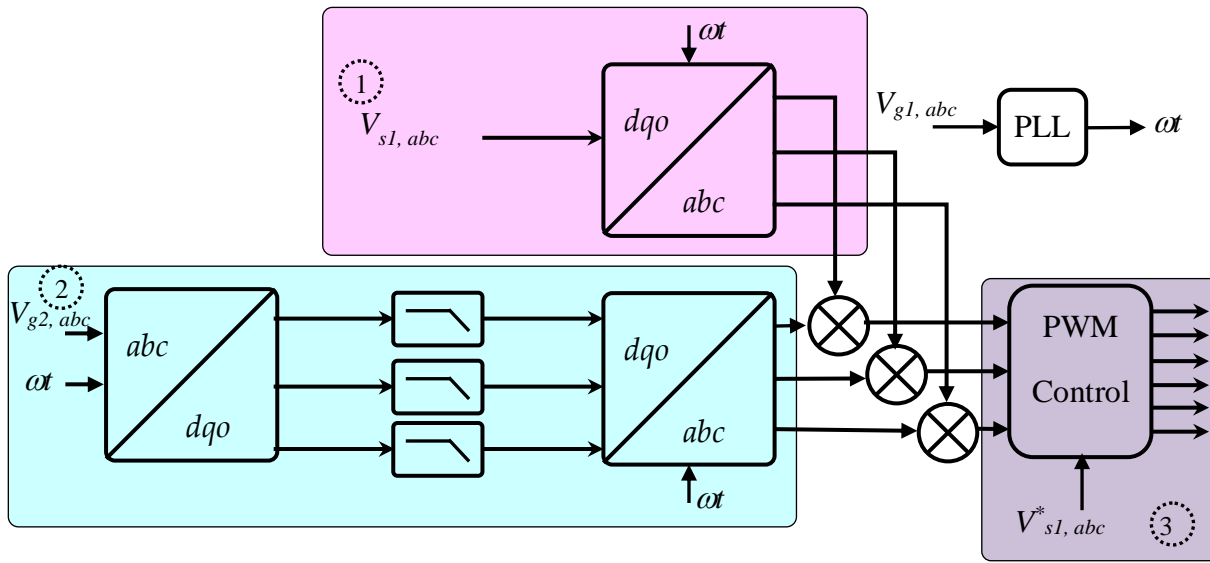


Fig.4. Control Scheme for series VSC of onshore WPP based UHVDC system

From the above equation, the positive sequence component of voltage magnitude and phase angle can be separated as,

$$|V_{ser}| = \sqrt{(V_{s3} \cos \delta - V_{s2,F} \cos \delta')^2 + (V_{s3} \sin \delta - V_{s2,F} \sin \delta')^2} \tag{7}$$

$$\rho = \tan^{-1} \left(\frac{V_{s3} \sin \delta - V_{s2,F} \sin \delta'}{V_{s3} \cos \delta - V_{s2,F} \cos \delta'} \right) \tag{8}$$

From the above expressions, the reference positive sequence voltage is determined by the pre fault grid voltage and measured grid voltage and is named as $V_{ser,dq,ref}^+$. When a fault is created at V_{s2} side, the compensation is done at shunt side V_{s3} . The total power delivered at series UHVDC system is given by the equation (9).

$$P_{tot,ser} = P_{ser} + P_{cos} \cos(2\omega t) + P_{sin} \sin(2\omega t) \tag{9}$$

The total active power $P_{tot, ser}$ is divided into three parts, series average power, cosine power and sine power and this power can be derived in equation (10) as given below,

$$\begin{bmatrix} P_{ser} \\ P_{cos} \\ P_{sin} \end{bmatrix} = \begin{pmatrix} I_{ser,d}^+ & I_{ser,q}^+ & I_{ser,q}^- \\ I_{ser,d}^- & I_{ser,q}^- & I_{ser,q}^+ \\ I_{ser,q}^- & -I_{ser,d}^- & I_{ser,d}^+ \end{pmatrix} \begin{bmatrix} V_{ser,d}^+ \\ V_{ser,q}^+ \\ V_{ser,d}^- \\ V_{ser,q}^- \end{bmatrix} \tag{10}$$

From the above expression, $V_{ser,dq}$ and $I_{ser,dq}$ is the series voltage and current dq component. The sine and cosine terms of power is cancelled and equated to zero by the generation of reference negative sequence component of series voltage $V_{ser-dq,ref}$.

The negative sequence voltage component is obtained by solving the above equation and is written as below in equation (11).

$$\begin{bmatrix} V_{ser.d,ref}^- \\ V_{ser.q,ref}^- \end{bmatrix} = - \begin{pmatrix} I_{ser.d}^+ & I_{ser.q}^+ \\ -I_{ser.q}^+ & I_{ser.d}^+ \end{pmatrix}^{-1} * \begin{pmatrix} I_{ser.d}^- & I_{ser.q}^- \\ I_{ser.q}^- & -I_{ser.d}^- \end{pmatrix} \begin{bmatrix} V_{ser.d}^+ \\ V_{ser.q}^+ \end{bmatrix} \quad (11)$$

Finally, the three phase voltages are given to pulse generation block to generate firing pulses for series VSC system.

5. Design of neural network controller

The neural network is an artificial intelligence tool used to formulate mapping between target data and input data. The procedure for training the neural network is shown in Fig5. Initial process is to collect the training data, i.e., input data and target data. This is the most important process, because it determines efficiency of neural network controller on compensation of transient and DC link voltage control [19]. The input data are error and integral error of DC link voltage and target data is compensation component of the current. DC link voltage error is the difference of reference and actual DC link voltage. Next process is the network creation, for this case two input and one output two-layer feedforward network is used. After neural network created, it must be configured for best network performance. The network configuration step consists of examining the input and target data, setting input and output sizes of the network to match the data and choosing an appropriate transfer function. After configuration, the weights of the two layers are initialized [20]. After trained and validation, the network is implemented in the simulation.

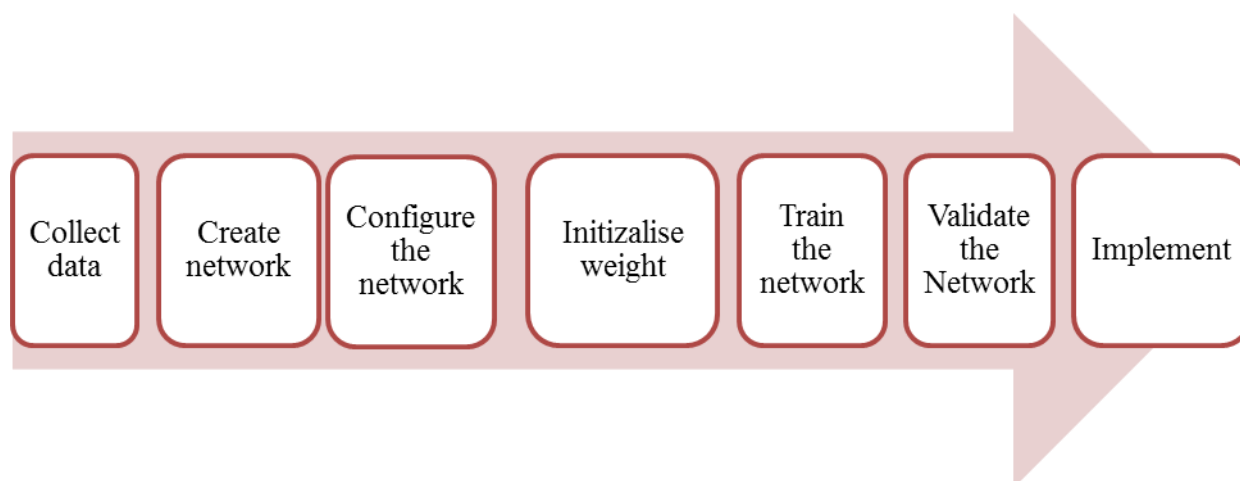


Fig.5. Procedure for training the neural network

Let $E = V_{dc Ref} - V_{dc}$ be DC link voltage and EI be Integral of error and a_1 to a_5 be constants used to train the neural network. $Y(K)$ be the output of artificial neural network, $W(K)$ and $CW(K)$ be the weight and change in weight of the update algorithm. The output and update equation of the artificial neural network is represented in the following equations

$$Y(k) = a_1 * W(k-1) + \alpha * CW(k-1) + a_2 * CW(k) + a_3 \quad (12)$$

$$CW(k) = \gamma * (a_4 * E(K) + a_5 * EI(K)) \quad (13)$$

The simulation responses for neural network training are shown in Fig 6. The total epoch is set to 1000 and best performance is reached at 608th epoch. From the obtained results it is observed that the output and target data are tracking well. Hence it is found the network is ready to implement in the simulation environment.

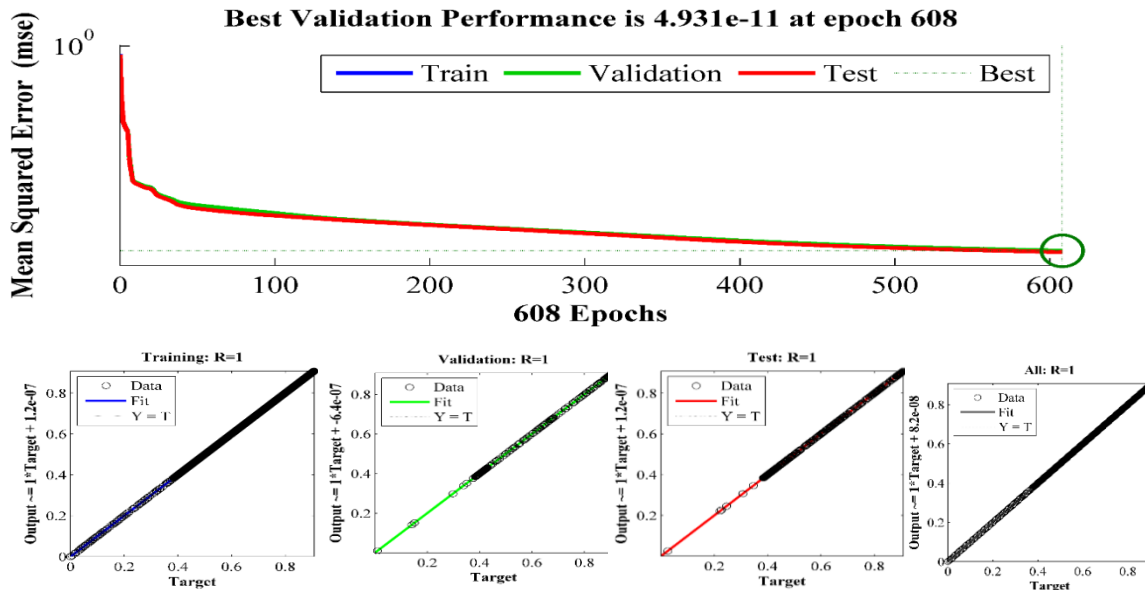


Fig 6. Simulation responses of performance of the neural network training

6. Simulation Results and discussion

Simulation analysis on a power system network connected to the offshore WPP connected through UHVDC utilizing PI and proposed NN controllers based DQ theory is carried out in this section. This section demonstrates the effectiveness of the proposed control technique for enhancing the compensation of transients and to provide fast power transfer under normal and faulted operating conditions. The voltage rating of the network is 230KV and the rating of HVDC is 250KVA which is equivalent to the offshore WPP. Parameter taken for simulation is given in table 2.

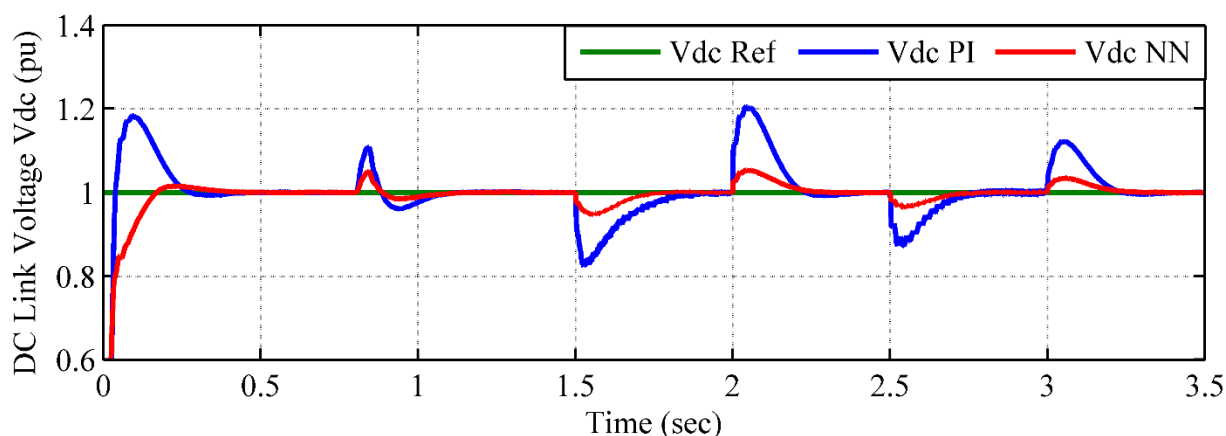


Fig.7. DC link Voltage control using PI and NN controllers

6.1. Analyze on control of DC link voltage

The optimum compensation of transients and fast transfer of power between offshore WPP and power system network are determined by the finest control of DC link voltage of UHVDC at rated value. In this case study, the DC link voltage is controlled at 400KV using PI controller and proposed NN controller. The pu simulation result of DC link voltage control using PI and proposed NN controllers under WPP and grid sides disturbances are shown in Fig. 7. The operating condition for this case study is fault injected in WPP at 0.8 sec, grid side faults are under voltage fault is injected between 1.5 sec to 2 sec and over voltage fault is injected at 2.5 to 3 sec. for initial condition, the peak overshoot of DC link voltage using PI controller is found to be 18.3% whereas 1.415% while using NN controller. Under WPP side fault condition, the peak overshoot of DC link voltage using PI controller is found to be 11% whereas 5% while using NN controller. Under grid side fault condition, the peak overshoot of DC link voltage using PI controller is found to be 20.5% whereas 4% while using NN controller. The performance of PI and NN controllers are analyzed and compared in table 1. This demonstration confirms that the better minimization transients and better control of DC link voltage is achieved by the proposed NN controller.

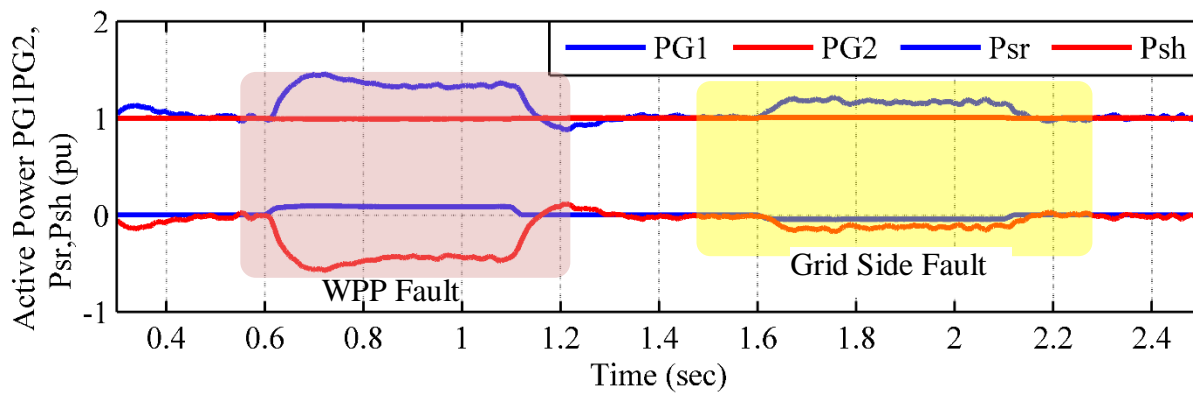


Fig. 8.a. Real power transfer using PI controllers

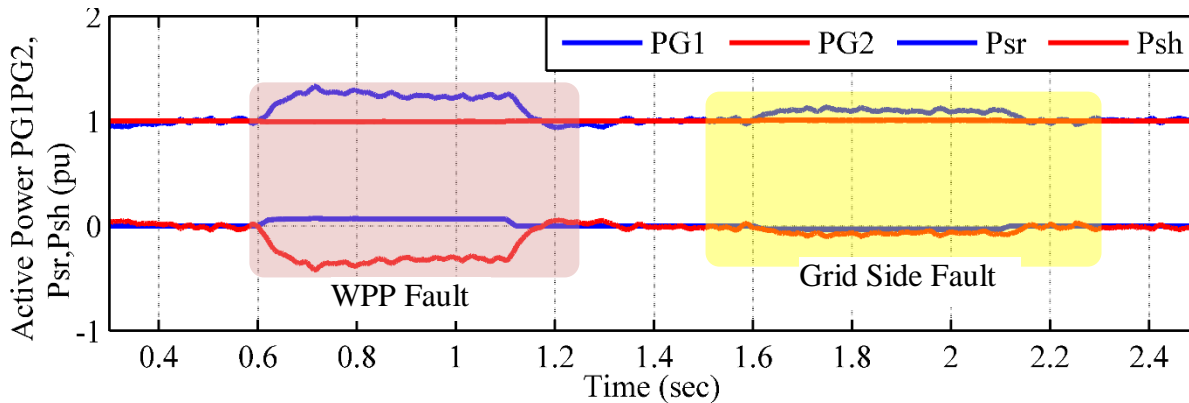


Fig. 8.b. Real power transfer using NN controllers

6.2. Analyze on real power transfer using PI and NN controllers

Simulation analysis on real power transfer between offshore WPP and power system networks through UHVDC using PI controller and proposed NN controller is carried out in this section. The simulation results for control of real power transfer using PI controller and proposed NN controller under WPP and grid side faults are shown in Fig. 8.a and Fig. 8.b respectively. The operating condition for this case study is 10% voltage drop is injected in WPP from 0.6 sec to 1.2 sec and 10% voltage drop is introduced in power system network between 1.6 sec to 2.6 sec. The main objective of this investigation is to maintain real power at the second grid (PG2) at 250 MW. The voltage drops in WPP created 0% power drop at first grid (PG1) for without compensation. For maintaining PG2, the series VSI injects series power (P_{sr}) 20% at point of common coupling there by PG2 is successfully maintained. While using PI controller, PG1 and P_{sr} have more peak overshoot and high oscillation. Whereas, NN controller PG1 and P_{sr} are successfully controlled with minimum oscillation and optimally regulated PG2.

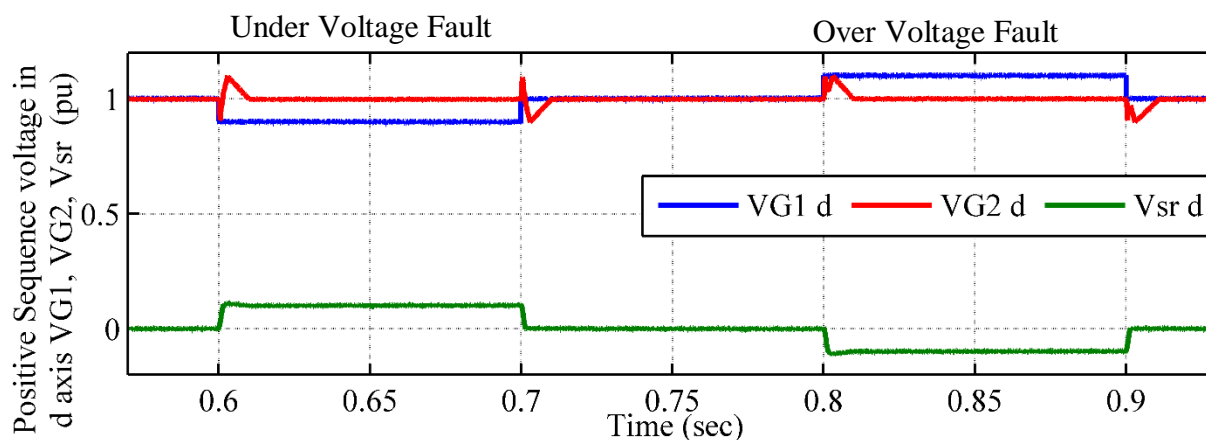


Fig. 9.a. Compensation of positive sequence voltage in d axis using PI controller

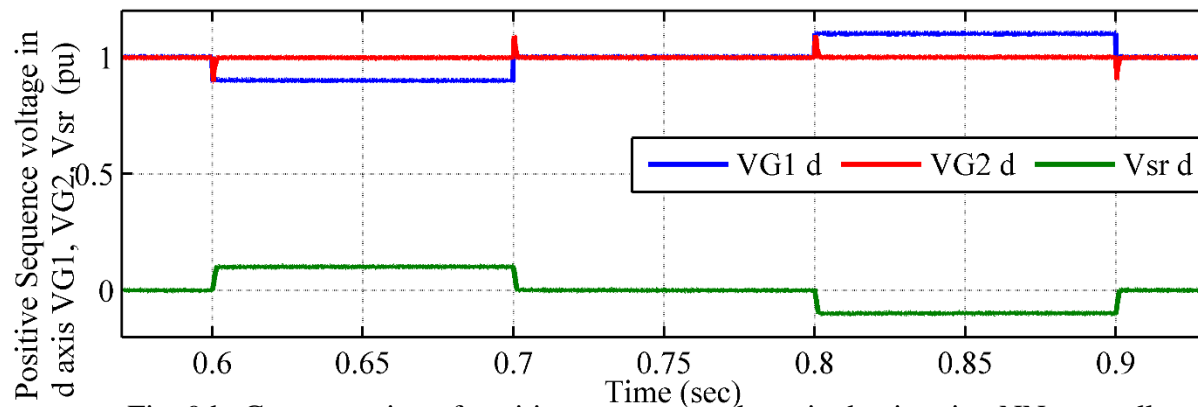


Fig. 9.b. Compensation of positive sequence voltage in d axis using NN controller

6.3. Analysis on compensation on voltage at point of common coupling

This section demonstrates regulation of rated voltage of 230 KV at point of common coupling using PI controller and NN controller. The simulation results of regulation of positive sequence voltage V_{G1} , V_{G2} and V_{sr} in d axis using PI controller and NN controller are shown in Fig. 9.a and Fig. 9.b respectively. 10% under voltage is introduced between 0.6 sec to 0.7 sec and 10% of over voltage is injected at VG1 between 0.8 sec to 0.9 sec. The main objective of the proposed configuration is to maintain rated voltage 230KV at point of common coupling.

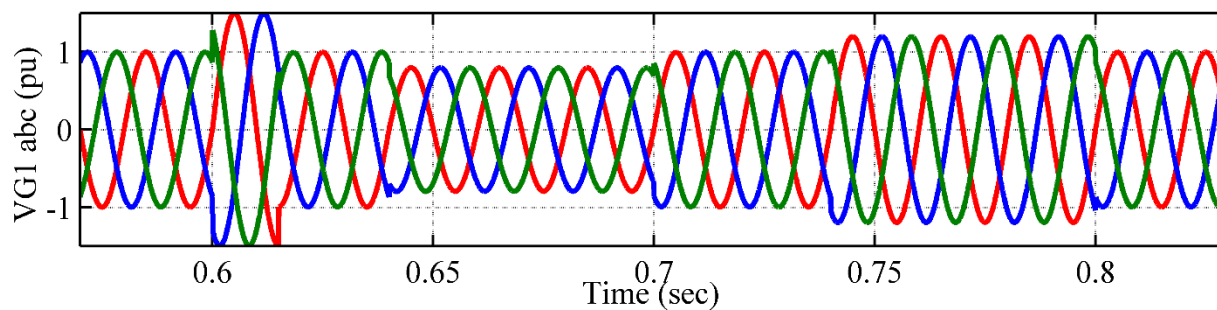


Fig. 9.c. Simulation result for three phase grid 1 voltage

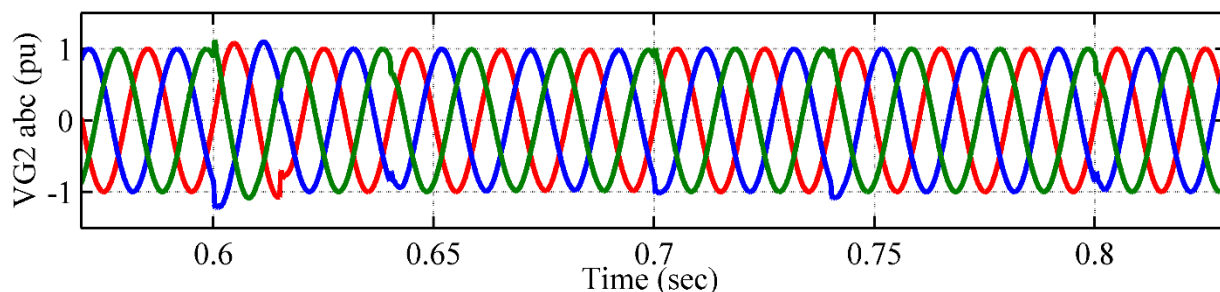


Fig. 9.d. Simulation result for three phase grid 2 voltage

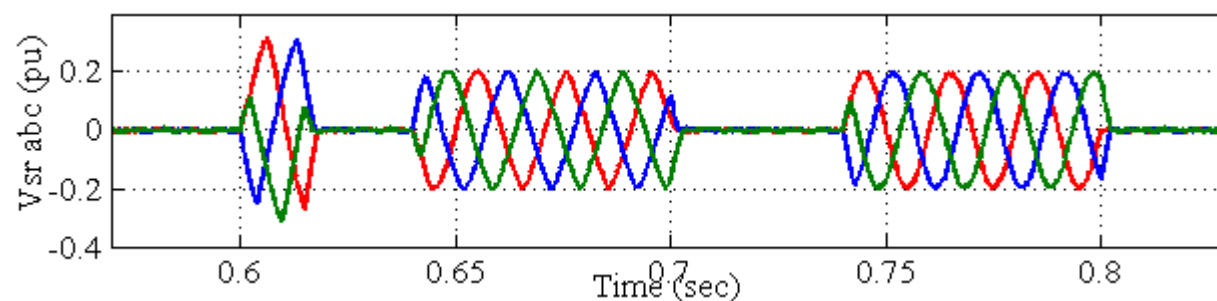


Fig. 9.e. Simulation result for three phase series voltage

Under normal operating conditions, $VG1$ and $VG2$ are in equal and Vsr is found to be zero. For under voltage condition, required voltage is injected by series VSI and thereby rated voltage is maintained at point of common coupling. For over voltage condition, required voltage is absorbed by series VSI and thereby rated voltage is maintained. While using PI controller, transient detection is found to be poor and it requires more time to compensate whereas using NN controller, transient detection is found to be optimum and it has fast compensation time. This analyzes are clearly projected in Fig. 9.a and Fig. 9.b. respective. The simulation results for three phase voltage of grid 1, grid 2 and series voltage or compensation voltage are shown in Fig. 9.c, Fig. 9.d and Fig. 9.e respectively. Under normal condition, rated voltage is maintained whereas under faulted condition the require voltage is injected by the series VSI such that it maintains rated voltage at grid 2.

7. Conclusion

A neural network DQ control technique based UHVDC is proposed for the management of transient and fast power transfer between offshore WPP and onshore electric grid. The performance of the proposed neural network control scheme is investigated under disturbances in both WPP and electric grids and compared with PI controller. From the test results, it is found that neural network based control technique has better capability to compensate transients and superior power transfer between WPP and electric grid.

References

- [1]. Ahmed Moawwad, Mohamad Shawky El Moursi and Weidong Xiao, "A Novel control strategy for VSC-HVDC connecting offshore wind power plant," *IEEE Trans. Sustain. Ener.*, vol. 5, no.3 pp. 1204–1212, 2014.
- [2]. P. Bresesti, W. L. Kling, R. L. Hendriks, and R. Vailati, "HVDC connection of offshore wind farms to the transmission system," *IEEE Trans. Energy Convers.*, vol. 22, no. 1, pp. 37–43, Mar. 2007.
- [3]. N. Flourentzou, V. Agelidis, and G. Demetriades, "VSC-based HVDC power transmission systems: An overview," *IEEE Trans. Power Electron.*, vol. 24, no. 3, pp. 592–602, Mar. 2009.
- [4]. A. Egea-Alvarez, F. Bianchi, A. Junyent-Ferre, G. Gross, and O. Gomis-Bellmunt, "Voltage control of multiterminal VSC-HVDC transmission systems for offshore wind power plants: Design and implementation in a scaled platform," *IEEE Trans. Ind. Electron.*, vol. 60, no. 6, pp. 2381–2391, Jun. 2013.
- [5]. Q. Guo, J. Zhao, and L. Niu, "Faults predictions and analysis on reliability of the 660 kV Nngdong HVDC power transmission system," in *Proc. 4th Int. Conf. Electric Utility Deregulation and Restructuring and Power Technol.*, 2011, pp. 99–103.
- [6]. X. Chen, C. Zhao, and C. Cao, "Research on the fault characteristics of HVDC based on modular multilevel converter," in *Proc. IEEE Trans. Electr. Power Energy Conf.*, Oct. 3–5, 2011, pp. 91–96.
- [7]. S. Alepuz et al., "Control strategies based on symmetrical components for grid-connected converters under voltage dips," *IEEE Trans. Ind. Electron.*, vol. 56, no. 6, pp. 2162–2173, Jun. 2009.
- [8]. G. P. Adam, K. H. Ahmed, S. J. Finney, K. Bell, and B. W. Williams, "New breed of network fault-tolerant voltage-source-converter HVDC transmission system," *IEEE Trans. Power Syst.*, vol. 28, no. 4, pp. 335–346, Feb. 2013.
- [9]. P. H. Huang, M. El Moursi, W. Xiao, and J. Kirtley, "Novel fault ride through configuration and transient management scheme for doubly fed induction generator," *IEEE Trans. Energy Conv.*, vol. 28, no. 1, pp. 86–94, Mar. 2013.
- [10]. R. T. Pinto et al., "A novel distributed direct-voltage control strategy for grid integration of offshore wind energy systems through MTDC network," *IEEE Trans. Ind. Electron.*, vol. 60, no. 6, pp. 2429–2441, Jun. 2013.
- [11]. S. K. Chaudhary, R. Teodorescu, P. Rodriguez, P. C. Kjaer, and A. M. Gole, "Negative sequence current control in wind power plants with VSC-HVDC Connection," *IEEE Trans. Sustain. Energy*, vol. 3, no. 3, pp. 535–544, Jul. 2012.
- [12]. N. G. Hingorani, L. Gyugyi, and M. El-Hawary, *Understanding FACTS: Concepts and Technology of Flexible AC Transmission Systems*. New York, NY, USA: IEEE, 2000.
- [13]. N. Flourentzou, V. G. Agelidis, and G. D. Demetriades, "VSC-based HVDC power transmission systems: An overview," *IEEE Trans. Power Electron.*, vol. 24, no. 3, pp. 592–602, Mar. 2009.
- [14]. Z. Chen, J. Guerrero, and F. Blaabjerg, "A review of the state of the art of power electronics for wind turbines," *IEEE Trans. Power Electron.*, vol. 24, no. 8, pp. 1859–1875, Aug. 2009.
- [15]. M. Baradar and M. Ghandhari, "A multi-option unified power flow approach for hybrid AC/DC grids incorporating multi-terminal VSC-HVDC," *IEEE Trans. Power Syst.*, vol. PP, no. 99, pp. 1–8.
- [16]. D. Roiu, R. I. Bojoi, L. R. Limongi, and A. Tenconi, "New stationary frame control scheme for three-phase PWM rectifiers under unbalanced voltage dips conditions," *IEEE Trans. Ind. Appl.*, vol. 46, no. 1, pp. 268–277, Jan./Feb. 2010.
- [17]. S. K. Chaudhary, R. Teodorescu, P. Rodriguez, P. C. Kjaer, and A. M. Gole, "Negative sequence current control in wind power plants with VSC-HVDC connection," *IEEE Trans. Sustain. Energy*, vol. 3, no. 3, pp. 535–544, Jul. 2012.
- [18]. Ahmed Moawwad, Mohamad Shawky El Moursi and Weidong Xiao, "Novel configuration and transient management strategy for VSC-HVDC," *IEEE Trans. Power Syst.*, vol. 29, no.5 pp. 2478–2488, 2014.
- [19]. B. Singh and S. R. Arya, "Back-propagation control algorithm for power quality improvement using DSTATCOM," *IEEE Trans. Indus. Elec.* 61(3) (2014) 1204–1212.

[20]. B. Singh, V. Verma, and J. Solanki, "Neural network-based selective compensation of current quality problems in distribution system," IEEE Trans. Indus. Elect., vol. 54, no. 1, pp.53–60, 2007.

Nomenclature	
BC	bus coupler
DQ	direct and quadrature axis
E, EI	error and integral of error
FRT	fault ride through
HVDC	high voltage direct current
$I_{ser, dq}$	Series current of dq component
NN	neural network
PCC	point of common coupling
PMSG	permanent magnet synchronous generator
PI	proportional and integral controller
P_{3n}, Q_{3n}	Real and reactive power at shunt compensator
P_{g2}, Q_{g2}	Real and reactive power at source 2
P_{ser}, Q_{ser}	Series real and reactive power
P_w	Total real power generated by WPP
$S_{ser, max}$	Rating of series converter
UHVDC	unified high voltage direct current
V_{dc}	dc link capacitor voltage
V_{dc}^*	reference dc link capacitor voltage
VSC	field programmable gate array
V_{s1}	Voltage at offshore VSC
V_{s2}, V_{s3}	Voltage at onshore series and shunt converter
$V_{s2, F<\delta}$	Voltage during fault
V_{ser}	series voltage
$V_{ser, dq}$	Series voltage of dq component
$V_{ser, dq}^-$	Negative sequence dq frame series voltage
$V_{ser, dq}^+$	positive sequence dq frame series voltage
$V_{ser, dq, ref}^-$	reference negative sequence dq series
WPP	wind power plant
Z_{g1}, Z_{g2}	Transmission line impedances

PHOTOVOLTIC CHARGE CONTROLLER FOR ELECTRIC VEHICLE USING BACK STEPPING ALGORITHM

Dr. M .Sangeetha ¹, G .Purusothaman ², R . Senthamarai kannan ³

Abstract – The electric vehicles are widely used in transport system in present day. It is pollution less and cost effective transport method. The ultimate aim of the project is to design and development of solar charge controller for electric vehicle. The battery is the primary source of electric vehicle since the proposed method is to charge the battery properly by using back stepping algorithm. The pic16f877a microcontroller used to measure photo voltaic (PV) panel output and boost converter output and generate pulse width modulation (PWM) signal to control boost converter for proper charging of battery.

Keywords- solar, boost converter, Pic16f877a and PWM.

I. INTRODUCTION

The performance of smart charge controller system is used to extend the life time of battery for electric vehicle. When the battery energy is deficient then the energy is importing from solar PV panel. When the battery energy is excess then energy is exporting to the electric vehicle.

II. PROPOSED METHOD

The proposed system is uses pic16f877a microcontroller because it has built in analog to digital converter (ADC) and pulse width modulator (PWM). Generally the boost converter placed at the load side but in our proposed system uses boos converter in

between solar PV array and battery. Because of the battery should charge properly for increases battery life.

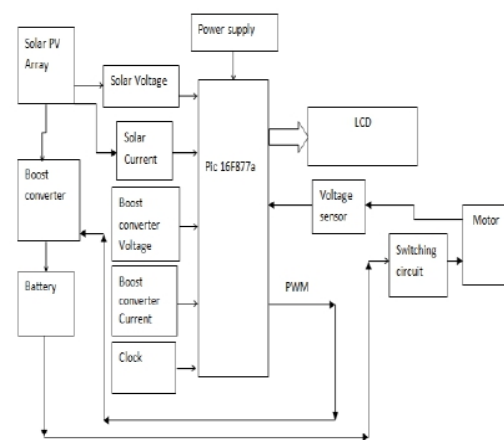


Fig.1. Block diagram of charge controller

The voltage and current sensor connected with ADC channel of Pic16f877a micro controller. The 16 character and 2 line alphanumeric display is used for monitoring the solar voltage, solar current, boost converter output voltage , boost converter output current. The Fig.1 shows the block diagram of proposed charge controller system.

The Fig. 2 shows the circuit diagram of project. It has reset circuit, oscillator circuit, boost converter circuit, and LCD circuit.

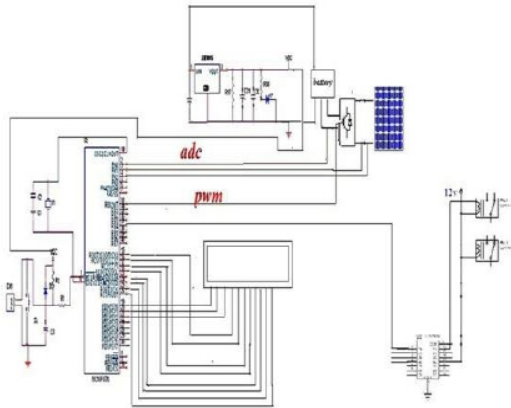


Fig.2. Circuit diagram of charge controller

The algorithm measures the error between output power and required power. The PWM adjust the boost converter output due to required power.

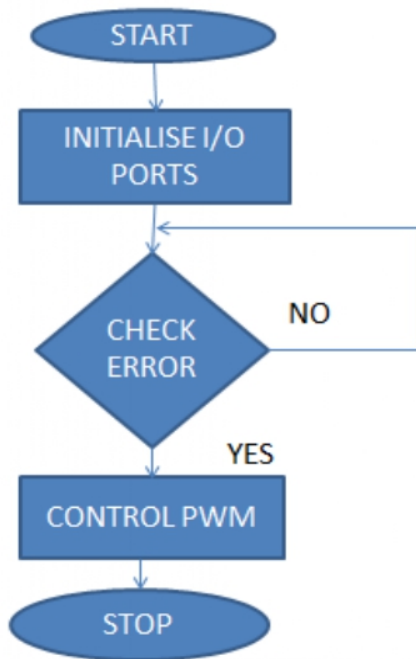


Fig.3. Flow of charge controller

The Fig. 3 shows the flow diagram of proposed system.

III. ADVANTAGES

- It uses renewable energy source
- Less cost
- Emission less
- It completely reduces pollution.

IV. SIMULATION AND RESULT

The simulation result of this concept is verified by proteus 8 professional software.

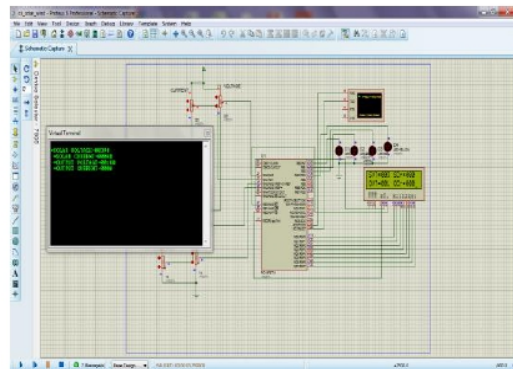


Fig.4. simulation of proteus software

The software has built in library for pic16f877a, LCD, serial terminal, analog and digital inputs/ outputs. The micro controller embedded c code is converted into .hex file format. The pot connected to the ADC channel for voltage and current analog input simulation.



Fig.5. experimental charge controller

The experimental hardware has same .hex file loaded into the pic16f877a. It has relay driver ic (ULN2003) for driving electromagnetic relay. The electromagnetic relay used for driving dc motor. The experimental hardware has 12V/2.5A battery with 6W solar panel.

V. CONCLUSION

The EV charging controller is proposed and its performance is analyzed by experimental output. The proposed controller examined the output power requirement of boost converter for proper charging. The back stepping algorithm is better to adjust the PWM for required output. The PWM is controls the boost converter for required output power.

VI. REFERENCES

1. Mauri G, Bertini D, Fasciolo E, Fratti S. The impact of EV's fast charging stations on the MV distribution grids of the Milan metropolitan area. In: 22nd International conference and exhibition on electricity distribution (CIRED 2013); 10–13 June 2013, pp. 1–3.
2. Marra F, Traholt C, Larsen E, Qiuwei W. Average behavior of battery-electric vehicles for distributed energy studies. In: Innovative smart grid technologies conference Europe (ISGT Europe); 2010 IEEE PES, pp. 1–7.
3. Cicconi P, Germani M, Landi D. Analytical thermal model for characterizing a Li-ion battery cell. In: 27th International electric vehicle symposium & exhibition. Barcelona, Spain; November 17–20, 2013.
4. Erdinc O, Vural B, Uzunoglu M. A dynamic lithium-ion battery model considering the

effects of temperature and capacity fading. In: International conference on clean electrical power; 2009, pp. 383–86.

5. Masoum A, Deilami S, Moses P, Abu-Siada A. Impacts of battery charging rates of Plug-in Electric Vehicle on smart grid distribution systems. In: Innovative smart grid technologies conference Europe (ISGT Europe). IEEE PES; 2010, pp.1–6.
6. Putrus G, Suwanapingkarl P, Johnston D, Bentley E, Narayana M. Impact of electric vehicles on power distribution networks. In: IEEE vehicle power and propulsion conference VPPC2009, pp. 827–31.
7. Chitra L , Prabhu Raj M , Keerthivaishnavi B , Madhusowmiya G, Rathna Praveen P , Design of Charge Controller for Electric Vehicle . IN : International Journal of Recent Technology and Engineering (IJRTE) , ISSN: 2277-3878, Volume-8 Issue-6, March 2020.

Solar Powered Water Management System Using Smart Card

Dr.M.Sangeetha^a, Dr. R. Arulmozhiyal^b, Mr.G.Purushothaman^c

^a

Associate Professor, Department of EEE, M.A.M. School of Engineering,
Trichy – 621105, Tamilnadu, India

^bProfessor, Department of EEE, Sona College of Technology, Salem – 636 005, Tamilnadu, India.

^cAssociate Professor, Department of EEE,

M.A.M. School of Engineering, Trichy – 621105, Tamilnadu, India.

Article History Received: 10 January 2021; Revised: 12 February 2021; Accepted: 27 March 2021; Published online: 20 April 2021

Abstract: With rapid development of economy and urban growth, water shortage and resource pollution is now a serious problem for urban water supply in many cities. At same time, with enlargement of urban areas and increase of sealing areas results in reduction of green spaces, new road and building construction etc., runoffs of rainwater increase greatly. Networked, smart systems will help make enhanced use of energy, avoid superfluous and water losses and lessen the consumption of resources. In addition to automation and drive technology, this paper introduce solar powered drinking water supply management using RFID technology. In this paper RFID technology is used to manage the supply of water to the people, if the RFID card is placed near to the RFID reader, LCD displays the details regarding that card holder. According to the details, the DC Motor will pump the water and the message will be sent to the card holder regarding the water consumed

Keywords: LDR, MPPT, Arduino Nano board, Smart card.

1. Introduction

Energy plays a major role in the evolution of the country. Present day scenario, immense quantity of power is produced using non-renewable power sources. 85% of power production is dependent on fossil fuels [1]. The resources of the combustible are finite and its usage is resulting to global warming due to emission of conservatory gases. To provide a sustainable power production and safe world to the future generation, there is a rapid increase in need of vitality from renewable resources like solar, wind, geothermal and ocean tidal wave [2]. Solar radiations are converted into electrical energy by solar panels. Solar panel constitutes of solid state conductor substance. Major component used in the making of solar panel is Silicon, which is 24.5% efficient.[3].

To have the maximum utilization of the amount of intensity captured it is essential to use the tracking system and hence to maintain accuracy and precession. The control circuit for solar tracker is done by Arduino Uno board. This is programmed to detect sunlight using LDR and actuate the stepper motor to position the solar panel where it can receive maximum sunlight. Stepper motor is controllable, energy efficient, steady and have high tracking accuracy and suffers little environmental affect. The water pump is attached to the battery. Since the pump works on DC power supply, it is directly attached to the battery. The water pumping system also consists of water level sensors used to detect water levels for automatic turn on and off of the water pump. This helps in the automation of water pumping systems in hospitals, factories, schools, public places etc. hence reducing manpower also maintaining the adequate usage of the resources[4] [5].

Solar based power is a rule progressively used worldwide as an inexhaustible wellspring of vitality. India has tremendous undiscovered sun powered off-frame work openings. This paper gives data about advancement methodology of an installed framework for off grid water system frame work [7]. Resource of water is indispensable for satisfying daily human needs varying, from agriculture to energy production. The demand of water for irrigation purpose is still an issue to be solved in developing countries, mainly rural areas with energy crisis and environmental pollution created mostly by the use of fossil fuel, this problem has unfolded a solution using solar photovoltaic water pumping system. Solar photovoltaic water pumping system has become so popular not only in the agriculture sector but also for drinking water and micro irrigation applications [8].

Abundant water supply in remote locations is required to ensure the grazing evenly. Water pumping is most accepted and admired application of solar energy in developing countries such as India. The proposed system is reliable, simple and requires less maintenance [9]. Many villages in India use fossil fuel based water pumping system for irrigation due to a shortage of electricity. Fossil fuel causes great damage to the environment as they release harmful greenhouse gases. In this research work, we propose a solar energy based automated water pumping system is implemented to these villagers in terms of cost and profit. In addition, this can save a lot of water and is environment- friendly [10]. Increase in cell efficiency, maximizing the power output and employing a tracking system with solar panel are the three major ways to increase the overall efficiency.

To develop single axis solar tracking system which captures maximum intensity from the sun rays efficiently store the generated energy in the battery for the future application to develop automated water pumping system

which helps to save water and minimize man power. Overall objective is to build a power conserving, less use of manpower, resource conserving project for the sustainable development and to help the mankind save time.

2. Solar Tracking System

The proposed system mainly consists of two parts, solar tracking and water pumping system. The first part of the system, the solar tracking system consists of LDR, stepper motor and solar panel. These LDR's are connected to the two ends of the solar panel. Based on the intensity of light falling on the LDR the arduino will decide the direction of rotation of stepper motor. Stepper motor is in turn connected to the panel. Thus arduino controls the rotation of both stepper motor and solar panel The second part of the project namely the water pumping system consists of water level sensors, DC motor and battery. The water level sensor is used to control and detect water level in the tank. The solar energy is stored and it is collected in battery. The absorbed power is then sent to the motor which runs the pump.

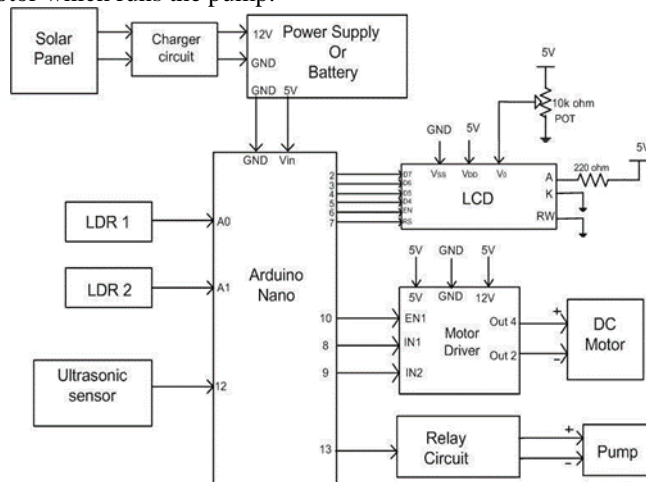


Figure 1: Configuration of Solar Tracking and Water Pumping System

Solar Panel

Solar panel mainly consists of numerous photovoltaic (PV) cells which is combined to form a module. These PV cells are made up of semiconductor material namely silicon that is usually connected in series or parallel to get additive voltage or current. The solar panel is basically a P-N junction, when sunlight falls on the PV cell; the electrons gain energy and jumps out of the atom hence leading to the flow of electricity.

Table 1: Solar panel specification

Parameter	Value
Maximum Power	10 W
Vmax	18Volts
Imax	0.56Amps
Voc	21.6Volts
Vsc	0.64Amps
Rechargeable Battery	12Volts
Dimension	280*54*22
Weight	1.5kg

Solar Charging Circuit

This circuit is mainly used to maintain constant DC voltage obtaining from solar panel. This provides protection from over charging and over discharging of the battery life cycle of the battery eventually decreases. To maintain the battery life and to have better performance, battery should never be overcharged or over discharged.

Solar Charging Circuit

This circuit is mainly used to maintain constant DC voltage obtaining from solar panel. This provides protection from over charging and over discharging of the battery.

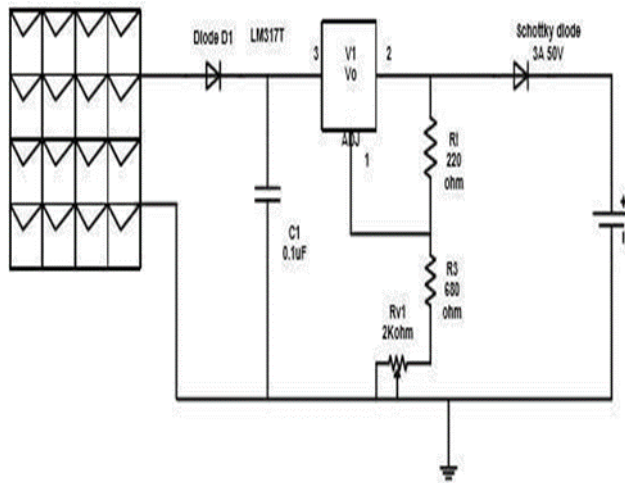


Figure 2: Circuit diagram of Solar Charger circuits

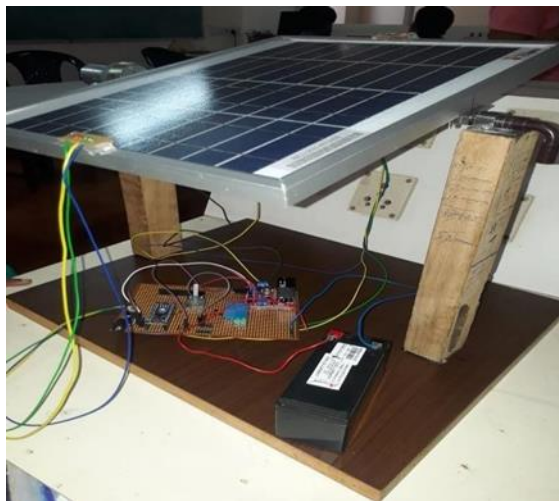


Figure 3: Solar Tracking Unit

Solar panel Characteristic

The current voltage characteristic of the solar module provides useful information. The parameters obtained from the I-V curve include short circuit current 'Isc', open circuit voltage Voc, maximum current Imax, and maximum voltage Vmax at the maximum power point Pmax.

Solar panel characterization is done by connecting the solar panel in series with the ammeter followed by a rheostat and voltmeter connected across the rheostat. The resistance is varied and corresponding solar panel voltage and current are recorded, the I-V curve plotted for a 10W solar panel is shown in the below figure 4.

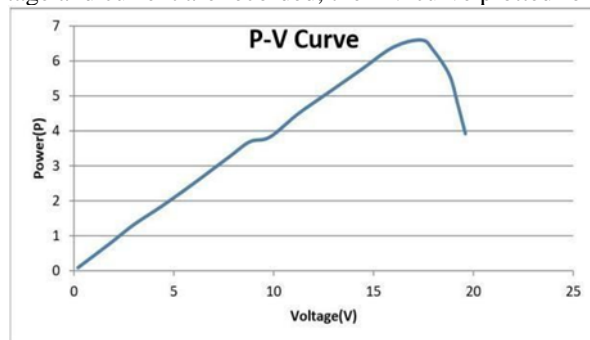


Figure 4: I-V Characteristics of solar panel

The IV curve for the solar panel is plotted during the peak time of the day say approx 2pm. The graph is plotted by taking voltage along x-axis and current along y-axis. The graph having the maximum current of 0.4A obtained at voltage of 10V.

Figure5. IV curve

This graph is obtained by taking solar panel voltage along x- axis and power (obtained by multiplying voltage and current at each point) along y-axis .It can be seen that the maximum power of 6.61W is obtained at voltage

17.4V and current 0.38A. From the above graph it can be inferred that the solar isolation is not constant throughout the day and the power generated varies accordingly, therefore, there is a need to store the electrical energy generated by the solar panel during maximum productivity. To achieve this battery is used as, renewable energy along with batteries allows stand- alone operations and therefore the batteries are now a standard component of solar power system.



Figure 6:Solar Tracking and water pumping unit
RFID-Technology:

RFID identification (RFID) is term is used to explain a method that transmits the identity the object wirelessly using radio waves. RFID technology is assembled with the most general Automatic Identification (Auto ID) technologies.

An RFID system consists of two separate components: a tag and a reader.

The tag contains an antenna linked to a small microchip that contains as much as two kilobytes of information. The readers or scanner functions much like a bar code scanner. However, while a bar code scanner utilizes a laser light to scan the bar code, an RFID scanner uses electromagnetic waves. To deliver these waves, the scanner uses an antenna that transmits a signal contacting the tags antenna

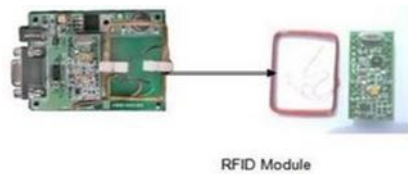
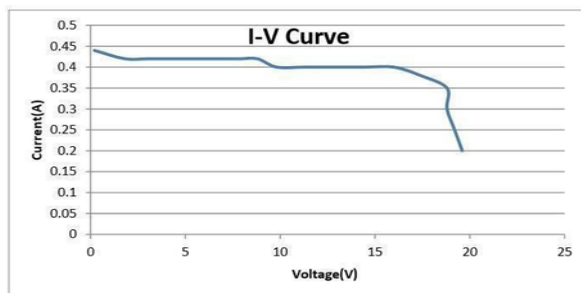


Figure 7 : RFID module



3. Design of Proposed Systems

When the solar panel is exposed to sunlight, the LDR sensors are activated through arduino code and then the LDR senses the intensity of the sunlight and then decide whether the LDR1 or LDR2 is receiving maximum sunlight. And followed by the rotation of the solar panel through the DC motor driven by motor driver L298N in the direction of the maximum intensity.

Once the solar energy is obtained it is made to store in the lead acid battery for the future scope and for the protection of the battery the power trapped by the panel is made to pass

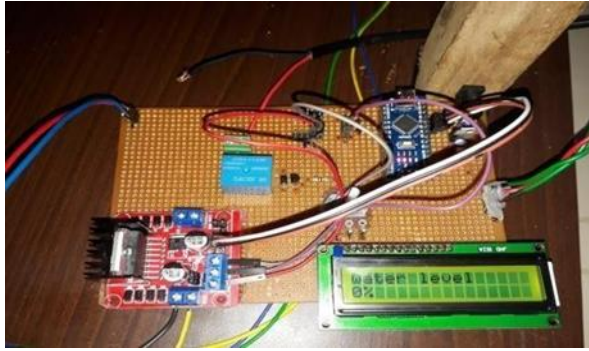


Figure 8: LCD display showing the water level

4. Result And Conclusion

In this paper the single axis solar tracking system is successfully implemented. The constant DC voltage of 12V is obtained with help of solar charger circuit. The energy obtained from the panel is stored into the rechargeable battery of 4.5Ah. The charge controller circuit prevents over charging and over discharging of the battery. Later implemented automation of water pumping system which senses the water level in the tank and automatically turns on and off the pump, based on the water sensed in the tank which is programmed using Arduino Uno. This paper aims at reducing wastage of drinking water and providing purified water to the village people. An RFID Reader can access the data of the card holder from a family . The RFID Reader is capable of reading 40 tags per second. This results in reduction of waste of drinking water ,cost of electricity by utilize the renewable energy source and provide a purified drinking water to the village people

References

1. J.Rizik and Y.Chaiko , "Solar tracking system : More efficient Use of solar panels"-2008
2. M.Reyasudin basir khan, "Solar Tracking System Utilizing Pyranometer For optimal Photovoltaic Module Positioning"- 2012
3. Jeng -Nan Jung and R.Radharamanan, 'Design of a solar tracking system for Renewable energy'-2014
4. M. Ouada, M.S. Meridjet and N. Talbi, 'Optimization Photovoltaic Pumping System Based BLDC Using Fuzzy Logic MPPT Control', International Renewable and Sustainable Energy Conference (IRSEC), pp.27- 31, 7-9 March 2013.
5. Neha Yadav, Manju Gupta, K. Sudhakar. "Energy assessment of floating photovoltaic system", International Conference on Electrical Power and Energy Systems (ICEPES) 2016, pp.264 – 269.
6. Yashar Ghiassi-Farrokhfal, Fiodar Kazhamiaka, Catherine Rosenberg, Srinivasan Keshav. "Optimal Design of Solar PV Farms With Storage", IEEE of Solar PV Farms With Storage", IEEE With Storage", IEEE
7. Y.J.Zuo "survivable RFID system : Issues ,challenges,and techniques" IEEE Trans .Syst ., Man, Cybern. C, Appl.Rev.,vol. 40, no. 4, pp.406-418 2010
8. H.H.Bi and D.K.Lin "RFID –enabled discovery of supply networks",IEEE
9. Trans.Eng.Manag.,vol.56,no.1,pp.129-141 2009
10. J.D. porter and D.S.Kim "An RFID- enabled road pricing system for transportation",IEEE Syst. J.,vol .2,no. 2,pp 248-257 2008
11. K.Finkenzeller RFID Handbook : Fundamentals and application in contactless smart card and identification,2003 : Wiley.

Design and Implementation of Row or Column wise Banana Tree Cutter using IoT

J.Karthikeyan¹, Dr.M.Sangeetha², and L.GlaridaAmala³

¹Assistant Professor in EEE Department, Kongunadu College of Engineering and Technology, Thottiyam, Trichy, Tamilnadu, India

Karthikeyan249@gmail.com

²Associate Professor in EEE Department, M.A.M School of Engineering, Trichy, Tamilnadu, India
sangee2maya@gmail.com

³Assistant Professor in EEE Department, Dhanalakshmi Srinivasan Institute of Technology, Trichy, Tamilnadu, India
glrdamala@gmail.com

Abstract—This paper intends to design a Row or Column wise Banana Tree Cutter for formers who cultivate banana. The Formers cultivate the banana in large area of field. After a cultivation, the banana tree need to cut. Nowadays, the banana trees cut by two ways, in first way by the people by manually using weapons. In second way, it is done by truck which totally convert the whole tree into mixture. There is no use of mixture. In this module, which has mechanical system and electrical system. Fire base system is adopted for cultivation process control and IoT integration. Two motors are connected and one for cutting and another for transfer. Node MCU control the over all operations of the system. The programming is developed and executed as per the farmer premises.

Index Terms— DC motors, Internet of Things(IoT),Frictional Wires, Cloud computing , Firebase,etc.

I. INTRODUCTION

This system can cut the Banana tree with help of frictional wire using IoT buttons through the imaginary buttons in IoT. Now a days, the communication and technology, the dramatic growth of electronics, smart phones and internet. Through those things, the communication can be done communicated physically or wirelessly and become the fundamental tool of human life. The future generation of connected world is Internet of Things (IoT). It consists of devices, sensors, appliances, vehicles in the world. The devices or objects may include the tablets, smart phones, sensors, etc.

By using IoT, The system can connect anything, access from all the places at any time, with high performance access any service and information about all the objects. The IoT objective is to improve the benefits of Internet with remote control skills, data spreading, constant connectivity and so on. Using an embedded sensors, those are always on condition and collect the data, the entire equipment's will be integrated to local and global networks. The word 'IoT' always called Internet of all things, which was introduced by Kevin Ashton in 1999.

The IoT technology controls the big amount of data about living things, non-living things, time and area. When combining the Internet concepts and IoT, which deliver a large amount of space and innovative things based on minimal cost of sensors and wireless technology. Cloud computing and IPv6 accelerate the improved and

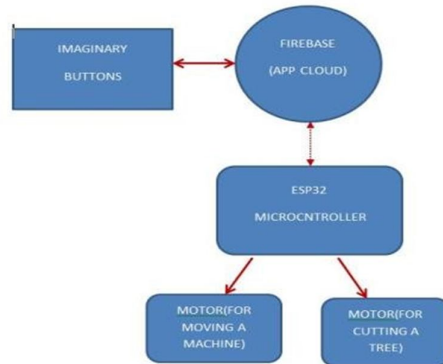


integrated Internet and IoT. Which provides more possibilities of collecting of data, processing of data, port management system and all other new activities. All the objects are connected to IoT needs a defined address or identification with IPv6. There are so many people in the world whose health may suffer because they have not proper access to hospitals and health monitoring.

The IoT(Advanced Internet of Things or AIoT) is the inter connection of physical devices, vehicles, buildings and other things-embedded with electronic devices, software, sensors, actuators, and network connectivity that enable these objects to extract and transferring the data. The Global Standards Initiative on Internet of Things (IoT-GSI) described the IoT as "the infrastructure of the collective information world." The IoT permits the objects that sensed or controlled remotely across existing network infrastructure, opportunity creation and better integration of the physical world into microcontroller-based systems, and resulting in improved efficiency, accuracy and economic aspects.

II. PROPOSED MODULE

The system architecture and flowchart has implemented and given below



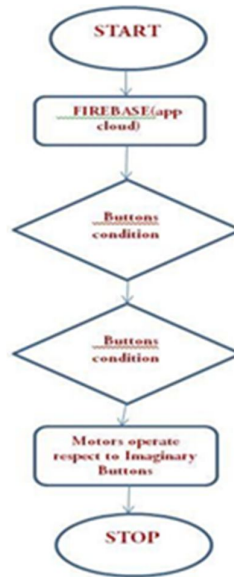
Block Diagram of Proposed System

III. WORKING METHODOLOGY

In this three methods are proposed

1. Electrical system
2. Mechanical System
3. Network System

The system in Electrical provides all needs of supply and logical condition in controllers. The IoT imaginary or Touch Buttons send signal to Fire base the app cloud. The touch buttons which created in API using AndriodStudio ,MITappInventeretc..The button when pressed in mobile sends a character to HTTP which is protocols that send to Firebase. The Fire Base send signal to the Controller we have used (ESP32).If the moving



Flow chart of Proposed System

buttons pressed it sends signal Moving motor relay where it is Forward or Backward. When the cutting button is pressed then it send signal to the cutting motor's relay. The Movement of module developed by using faraday's law in motors. The cutting method is based on the frictional motion of Newton's Law and Energy conversion of Thermodynamics law. The frictional force creates the Heat energy which helpful in cutting the tree and frictional wire the makes the tear in banana tree sheath. Hence the tree to be cut.

IV. COMPONENTS REQUIRED

A. ESP32(Controllor)



Node MCU is a series of minimal cost, low-power consuming on a microcontroller with integrated wire less technology and dual-mode Bluetooth. The ESP32 series require a TensilicaXtensaLX6 microprocessor in both dual-core and single-core variations. It can be incorporated with built-in switches of antenna, RF balun, and power amplifier, high quality receiving amplifier, filters, and power-management modules. ESP32 is created and developed by a Shanghai-based Chinese company, and is manufactured by Cussing their 40 nm process.

B. Relay



A relay is an electronic switch. It consists of input terminals set for a single, and operating contact terminal set. The switch has two number of contacts in multiple contact formation such as make contacts, break contacts, or combinations.

C. Motors



The electrical motor is used to convert electric energy into kinetic energy. Generally, electric motors operate by means of the relation between the stator magnetic field and current flow in the rotor. To generate force by means of rotation of a rotor shaft. Electric motors can be operated by direct current(DC) sources, such as from DC sources, motor vehicles or rectifiers, or by alternating current(AC) sources, such as a power grid, inverters electrical generators. An electric generator is physically coupled to an electric motor, but which operates in the reverse direction, converting mechanical energy into electrical energy.

D. Frictional Wires



The frictional that can able to cut the banana tree of sheath. It is made iron steel. These are inner cable is very important for the bicycle brake or gear shifting control systems. The primary aim of providing best quality products lies upon the capability to incorporate and master each manufacture processes. The structure and properties of steel is the very important factor for tensile, and surface treatment is the most critical factor to reduce the friction. As a result, a straighten-processed and seal processed inner cable provide the longest service life.

V. PROGRAMMING

In this system ESP IDF programming is used to control measurement and display the outputs. Codes are installed in ESP32 controller to control and monitoring the devices used and battery system. This same system can also be designed for Arduino nano for compactness. Embedded C or C++ language based programming is used in this system with loops and conditions for repeated operations. The embedded system based devices has miniature controller based in which device ESP32 controller and it is programmed by embedded C language to control the all components used in this device.

A. Firebase

Firebase is a platform for development of mobile and web application. Which had developed by Firebase, Inc. in 2011, then acquired by Google in 2014. In 2018, the Firebase platform had 18 products, which were accessed by 1500000 apps.

B. Firebase Cloud Messaging

At initially, It was known as Google Cloud Messaging(GCM), Firebase Cloud Messaging(FCM) was a cross-platform solution for messages and notifications for Android,iOS and web applications, which as of 2016 can accessed at free of cost.

C. Firebase Realtime Database

Firebase deliver a real-time database and back-end as a service routine. This platform provides application developers an API that permit application data need to synchronized across clients and stored on Firebase's cloud. The company provides client libraries that enable integration with Android,iOS, JavaScript, Java,

Objective-C Swift and Java applications. The database has accessible through a REST API and bindings for several JavaScript frame works such as Angular JS, React and Backbone.js. The REST API uses the Server-Sent Events protocol, which is an API for creating HTTP connections for receiving push notifications from a server. Developers using the real time database can secure their data by using the company's server-side-enforced security rules.

D. Cloud Firestore

In 2019, Cloud Fire store was officially brought out of beta, making it an official product of the Firebase line up. It is the successor to the actual data of firebase is basing system, Real-time system, and allows for nested documents and fields rather than the tree-view provided in the Real-time systems.

E. Firebase Hosting

Hosting of Firebase system is a static and dynamic web hosting service which launched in 2014. That supports hosting static files such as CSS,HTML, JavaScript and other files, as well as support through Functions of cloud. The system delivers the contents over a content delivery network(CDN) through HTTP Secure(HTTPS) and Safety Sockets Layer encryption (SSL). Partners of firebase with quickly response, a CDN, to provide the CDN backing Firebase Hosting.

VI. ADVANTAGES

Due to the Integration of Sensors, The system become a Portable system .The process of cutting trees will quickly done because row wise cutter. Reduction of analog components make the system is affordable system. With the help of Implementation of Row or Column wise Banana Tree Cutter using IoT, the tree can be converted into useful bio-product.

VII. CONCLUSION

The Row wise banana cutter is designed to reduce the farmers work after cultivation. Because farmers are the backbone of every country. This system helpful in cutting a banana tree.In many areas Banana cultivation is most thing done in acres range. This device will helpful and reducetheir time and work. And also after cutting it can be used in making of Bio-products.

REFERENCES

- [1] S. M. B. P. Samarakoon, M. A. V. J. Muthugala, A. Vu Le and M. R. Elara, "hTetro-Infri: A Reconfigurable Floor Cleaning Robot With Infinite Morphologies," in *IEEE Access*, vol. 8, pp. 69816-69828, 2020, doi: 10.1109/ACCESS.2020.2986838.
- [2] P. Veerajagadheswar, M. R. Elara, T. Pathmakumar and V. Ayyalusami, "A Tiling-Theoretic Approach to Efficient Area Coverage in a Tetris-Inspired Floor Cleaning Robot," in *IEEE Access*, vol. 6, pp. 35260-35271, 2018, doi: 10.1109/ACCESS.2018.2848662.
- [3] R. Parween, L. T. L. Clarissa, M. Y. Naing, N. A. F. B. M. Fuad and M. R. Elara, "Modeling and Analysis of the Cleaning System of a Reconfigurable Tiling Robot," in *IEEE Access*, vol. 8, pp. 137770-137782, 2020, doi: 10.1109/ACCESS.2020.3009120.
- [4] M. A. V. J. Muthugala, S. M. B. P. Samarakoon and M. R. Elara, "Tradeoff Between Area Coverage and Energy Usage of a Self-Reconfigurable Floor Cleaning Robot Based on User Preference," in *IEEE Access*, vol. 8, pp. 76267-76275, 2020, doi: 10.1109/ACCESS.2020.2988977.
- [5] R. Parween, M. Vega Heredia, M. M. Rayguru, R. Enjikalayil Abdulkader and M. R. Elara, "Autonomous Self-Reconfigurable Floor Cleaning Robot," in *IEEE Access*, vol. 8, pp. 114433-114442, 2020, doi: 10.1109/ACCESS.2020.2999202.
- [6] Imran, S. Ahmad and D. H. Kim, "Quantum GIS Based Descriptive and Predictive Data Analysis for Effective Planning of Waste Management," in *IEEE Access*, vol. 8, pp. 46193-46205, 2020, doi: 10.1109/ACCESS.2020.2979015.
- [7] T. J. Sheng et al., "An Internet of Things Based Smart Waste Management System Using LoRa and Tensorflow Deep Learning Model," in *IEEE Access*, vol. 8, pp. 148793-148811, 2020, doi: 10.1109/ACCESS.2020.3016255.
- [8] L. Catarinucci, R. Colella, S. I. Consalvo, L. Patrono, C. Rollo and I. Sergi, "IoT-Aware Waste Management System Based on Cloud Services and Ultra-Low-Power RFID Sensor-Tags," in *IEEE Sensors Journal*, vol. 20, no. 24, pp. 14873-14881, 15 Dec. 15, 2020, doi: 10.1109/JSEN.2020.3010675.
- [9] S. Ahmad, Imran, F. Jamil, N. Iqbal and D. Kim, "Optimal Route Recommendation for Waste Carrier Vehicles for Efficient Waste Collection: A Step Forward Towards Sustainable Cities," in *IEEE Access*, vol. 8, pp. 77875-77887, 2020, doi: 10.1109/ACCESS.2020.2988173.
- [10] "Relay"-news-newspapers-books-scholar-. JSTOR(November 2009)

Wear Characterization Of aluminium (Lm25) Metal Matrix Composite Reinforced with Sic and Mos2 on Various Heat Treatments

S. Venkatraman¹, R. Ramanathan², A. Mohankumar³, M. Vimalkumar⁴

^{1,3,4}Assistant Professor, Department of Mechanical Engineering, M.A.M School Of Engineering, Trichy, Tamil Nadu, India

²Associate Professor, Department of Mechanical Engineering, M.A.M School Of Engineering, Trichy, Tamil Nadu, India

ABSTRACT

In this study, investigates abrasive wear characteristic of the aluminium (LM 25) hybrid metal matrix composite reinforced with SiC and MoS₂ by sand casting technique and the test is carried in a micro-abrasion test with the help of various loads. From the study on physical properties and tribological response of Al-SiC composite, the following conclusions are drawn: Addition of SiC(Silicon carbide) to the aluminium metal matrix increases 25% strength. Increases SiC content (from 10% - 15%) enhances the strength only by above 10%. Beyond 15% SiC content, the MMC reduces wear due to its lubricating property. With increasing content of SiC and MoS₂, the MMC exhibits enhancement in hardness. The addition of the Molybdenum disulfide increases the wear resistance. Composites Al-SiC(10% - 15%) with 5% MoS₂ exhibits a close variables of coefficient of friction with change in normal load. Among the composites Al-15% SiCp-5% MoS₂ composite exhibits least sliding wear. The mixture aluminum matrix composites are heated with different temperatures (350^oC, 400^oC, 450^oC) by aging technique in furnace to examine the wear properties respectively. Presence of partial glazed texture and discrete material pull-out indicating dominant adhesion mode of wear. Surface roughness of different temperature aged specimens before and after wear characteristic are also seen.

Keywords: Combination of Metal Matrix Composite (CMMC), Sand Casting, Micro Wear Abrasion Tester, Wear Rates, Coefficient of Friction, Surface Roughness (Ra).

INTRODUCTION

Composite materials are fabricated of the two or more component materials with naturally different physical or chemical properties, that when incorporate to produce a material with characteristics different from the piece of components. The piece of components remain separate for the combined material and specifically within the finished structure.

A combination of metal matrix composite (CMMC) is composite material with atleast two components parts, one being a metal necessarily, the other materials may be a different metal matrix or another material, such a ceramic material or organic material. When at least two or more materials are present, it is called a hybrid composite. The CMMC is the monolithic material into which the reinforcement is submerged and is completely continuous. In structural and automobile applications, the matrix is usually a lighter and stonger metal such as aluminium, magnesium or titanium and provided a submissive support for the reinforcement. The reinforcement material is embedded into a matrix. The matrix reinforcement does not always serve an essentially structural task (reinforcing the matrix compound), but is also used to alter solution for physical properties such as wear resistance, friction coefficient, or thermal conductivity.

Combination Metal Matrix Composites are mostly to increasingly used in aerospace and automobile industries owing to their strengthen the properties such as elastic modulus, hardness, tensile strength at room and raised temperatures, wear resistance combined with significant weight for reinforcement alloys. They commonly used metallic matrices include Al, Mg, Cu and their alloys. These alloys are preferred matrix materials for the production of CMMCs. To find applications as cylinder blocks, crankshaft, pistons, piston insert rings, brake disks and other automobile parts. The strength of these metal matrices composites is proportional to the percentage volume and fineness of the reinforced particles. The structure and the properties of these composites material are submerged by the size of the reinforcement and also the nature of strengthen the material. From the contributions of many researchers, some of the most techniques are development of these composites are stir casting, sand casting powder metallurgy, co-deposition, plasma spraying

and squeeze-casting.

The scope of micro-abrasion test is an interesting and more relatively and the recent environment to choose this tribo-testing method to be used, where small particles of less than 10 mm are employed between contact surfaces. It is popular for a number of reasons; its sincere relation to the mechanisms of the wear testing process in tribological method, ease in conducting reports and the better repeatability of the test results.

It has global applications in conditions used in the space and onshore industries to bio-engineering for artificial joints and implants. In research for micro-abrasion characteristics of materials is mostly used, ranging from work basic metal matrix to nano-structural coatings. Anyway, there is no significant work is noted on the micro-abrasion resistance of composite materials. Hence, this paper looks at the performance of composite materials with composition of 80% Al, 15% SiCp, 5% MoS2 in different load condition (2,2.5,3,3.5kgs) and treated in different temperatures (350°C,400°C,450°C) their wear behavior is studied and concluded from the best. G. G. Sozhamannan Conventional stir casting and sand casting process has been employed for producing disordered particle reinforced metal matrix composites for decagon.

The major problem of this proceeding is to obtain sufficient wettish of particle by liquid metal and to get a homogenous dispersion of the ceramic particles. In the recent study, aluminium metal matrix composites were compose by different processing temperatures with different holding time to understand the influence of process parameters on the distribution of Micro particle in the matrix and the precipitate mechanical properties. The distribution is assess by microstructure analysis, hardness distribution and density distribution. J. Hashim Combining high specific strength with better corrosion resistance, metal matrix composites (CMMCs) are materials that are bewitching for a large range of engineering applications. Given the factors of reinforcement type, form, and quantity, which can be varied in differently obtained, in addition to matrix characteristics, the composites have a large potential for being tailored for particular applications and enhance it. One factor that, to noted, has restricted the widespread use of CMMCs has been their comparatively high cost.

This is mostly related to the excessive processing techniques used currently to produce more quality composites to produce. In this researcher, the relatively low cost sand casting technique is evaluated for use in the production and manufacturing of silicon carbide/aluminium alloy CMMCs. The technical difficulties associated with a uniform distribution of reinforcement, good weld ability between substances, and a low porosity material are presented and more useful to increase their strengthen. Mingwu Bai, The friction and wear behavior of LM25 aluminum alloy reinforced with 15 vol.% Sic whiskers against 52100 steel was consider in an oscillating sliding wear tester at ambient temperature condition. The Al-Sic composites exhibited good wear resistance than the 2024-Al alloy under the same conditions to be applied. With increasing load, the Al-Sic composites enclose high friction coefficient. The steel/Al alloy pair was mainly consider as aluminum oxide, while the refuse of steel/Al-Sic composite pair was mainly ferrite oxide is used.

MATERIAL USED

As a basis of all experiments a commercial alloy Al LM 25 was obtained in bar form, silicon carbide particulates and graphite are obtained in the powder form. Table 1 shows the chemical composition of the aluminium metal matrix alloy and table 2 shows the details of reinforcement materials.

Table 1: Chemical composition of the aluminium metal matrix (LM25)

Element	Mg	Ni	Si	Fe	Mn	Sn	Zn	Pb	Cu	Ti	Al
Content %	0.60	0.1	7.5	0.5	0.3	0.05	0.1	0.1	0.1	0.2	remainder

Table 2 Details of reinforcements

Reinforcement	Average grain size [µm]	Density [g/cm ³]
SiC	45	3.21
MoS2	42	5.06

Aerospace industries are more important to compare other areas of transportation and structural materials. The highly useful compounds of aluminium, at least on a weight consideration, are the oxides and sulfates. Aluminium is a comparatively lightweight and also more less density with appearance, depending on the surface roughness is well change. It is nonmagnetic and does not easily ignite. The yield strength of pure aluminium is 8–12 MPa, while aluminium alloys have been yield strengths ranging from 210 MPa to 650 MPa. Aluminium has about one-third of the density properties & stiffness of steel is better.

It is easily machined, casting, drawn and extruded. Corrosion resistance can be more effectively due to a thin surface layer of aluminium oxide that forms and the metal is exposed to ambient, effectively deterring the further oxidation. The strongest aluminium alloys are less corrosion resistant due to galvanic reactions with alloyed copper. It is a mixture of silicon and carbon with chemical formula SiC. It occurs naturally as the extremely unique mineral moissanite. Silicon carbide powder has been mass-produced since 18's for use as an abrasive. Grains of silicon carbide can be grip together by sintering to form very strong ceramics which are widely used in automobiles parts applications requiring high endurance, such as car brakes, car clutches and ceramic plates. Electric and electronic applications of silicon carbide material as light emitting diodes (LEDs) and the detectors in being of the radio, today SiC is widely used in high temperature/high-voltage of the semiconductor as a electronics device.

This researcher discusses about the chemical properties and applications of molybdenum disulfide nanoparticles. Molybdenum does not occur easily as a free metal on global. Generally, molybdenum disulfide has good chemical stability and good thermal stability. They can form a highly capable dry lubricating film. Molybdenum disulfide nanoparticles possess a low friction coefficient and form better catalytic activity, and good physical properties. They also have a large active surface area, high reactivity, and effectively increased adsorption capacity compared to the extent material. Molybdenum disulfide nanoparticles appear in a black solid colour.

Fabrication

The term "sand molded casting" can also refer to an object produced to the sand casting process and specialized factories say as foundries. In augmentation to the sand, a suitable molded bonding agent is mixed or occurs with the sand and the agent is clay. The compound is moistened, constantly with water, but sometimes with other substances to be added, to develop strength of the material and plasticity of the clay is good bonding agent and to make the aggregate suitable for mold the ceramics. The sand is constantly contained in a system of frames called as a flask. The mold cavities are developed by close packed the sand casting around models. Al/SiC–MoS₂ composites, 15% of SiC and 5% MoS₂ by weight were prepared by sand casting technique. A measured amount of silicon carbide particles and graphite was preheated at around 800⁰C for 2 hrs to make their surfaces oxidized to achieve better weldability and also to prevent decarburization of SiC and MoS₂ at high temperature. A measured amount of Aluminium alloy (ingots) was melted in the furnace. Pre-heated silicon carbide particles and MoS₂ were added to the aluminium melt. After sometimes to the melt was stirred for 20 min at an average coalesce speed of 300-400 rpm to make a swirl in order to disperse the particles uniform in the melt because of good mixing. The SiC particles and MoS₂ are uniformly distributed in the matrix when the processing temperature is around 700⁰C to 800⁰C as a hold of 10 minutes. After thorough stirring, the melt was poured into sand moulds and allowed to cool to obtain cast rods and then machined to 23 mm diameter 12 mm thickness respectively. The cast specimen of 23mm diameter and 12mm thickness (12 Nos) was used for micro-abrasion wear evaluation.

450⁰C respectively. Initially all the specimens are heated to 300⁰C and maintained it for 2 hours. Then each set of specimens are heated to three different temperatures (350⁰C, 400⁰C, 450⁰C) and maintained it for 1/2 hour each. These specimens are then cooled with oil quenched process.



Fig:1 Fabrication work

Experimental Work

Micro-abrasion checking were performed with a trade a available apparatus, the TE-66, micro-abrasion checker (Phoenix tribology Ltd., UK). A rotating 25mm diameter ball was in contact with a stationary specimen, which was held between two-coaxial shafts, each carried by a support bearing. A variable speed DC motor was used to drive single shaft to run the machine. By selecting a constant number of revolutions, a test could be run for a fixed sliding

distance. The test specimen was vice onto a platform, which is fitted to the pivoted L-shaped arm was rotated around its pivot usually the specimen became in contact with the specimen ball. The beam was in balance when the specimens were in contact and the load was applied by adding dead weights to a cantilever arm. The specimen surfaces were ground and polished by conventional metallographic methods before testing (final grinding and polishing operations were carried out with 4000 grit size abrasive paper). The arm, which holds the specimen, could be moved horizontally in order that several tests on a single specimen could be carried out. The specimen was then pull out from the apparatus and the diameters of the evolve abrasion wound were measured with a metrological equipment. Following the test, the worn specimens were examined by optical microscopy and scanning electron microscopy.



Fig:2 Micro-abrasion tester

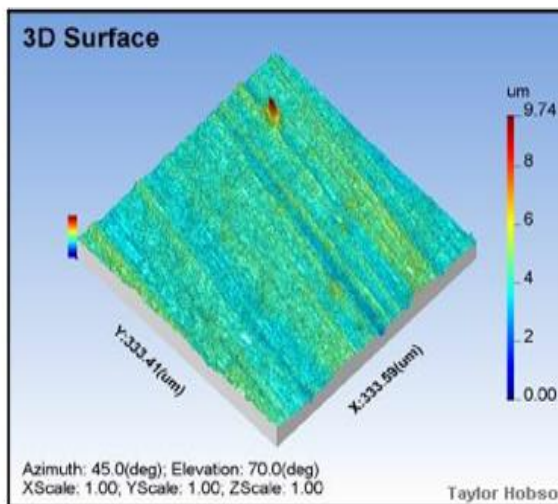
The experiments are further carried out to different aged specimens. By keeping the speed (450 RPM) constant, the different loads (2N, 2.5N, 3N, 3.5N) are

Observation

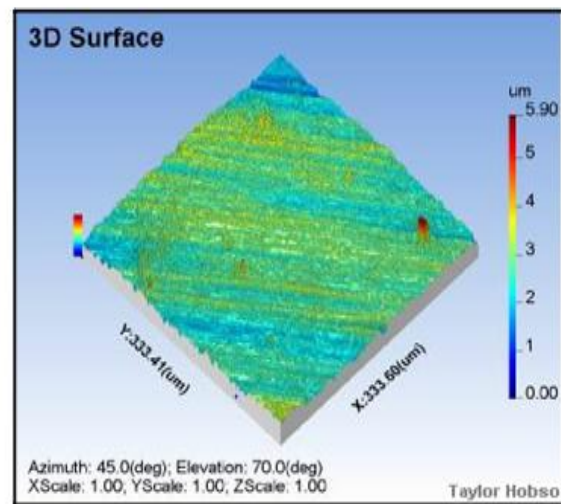
Observation on surface roughness (Ra) values:

The following shown 3D surface image shows the surface of different temperature aged specimens before and after wear test.

At 350 °C before wear test

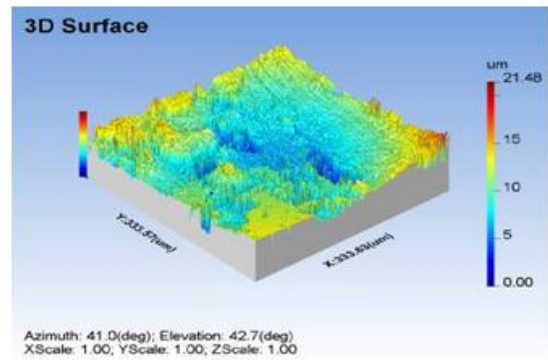
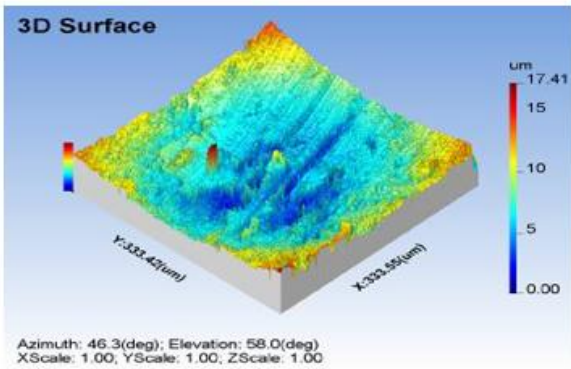


Specimen 1 (2N)



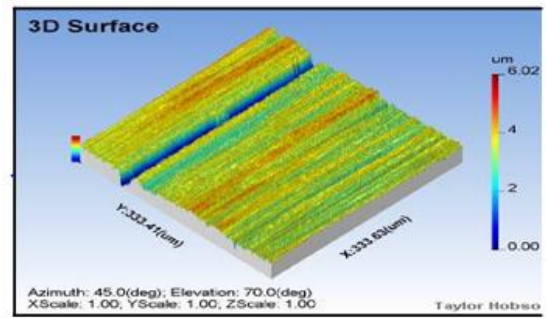
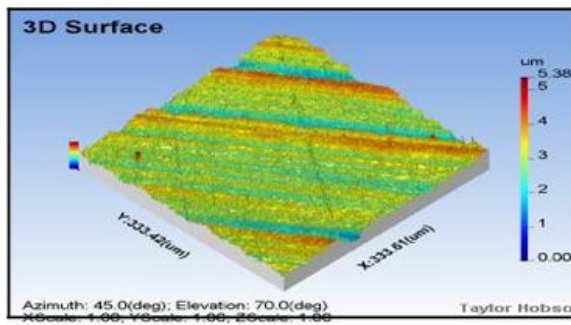
Specimen 2 (3.5N)

At 350°C after wear test



Specimen 1 (2N)

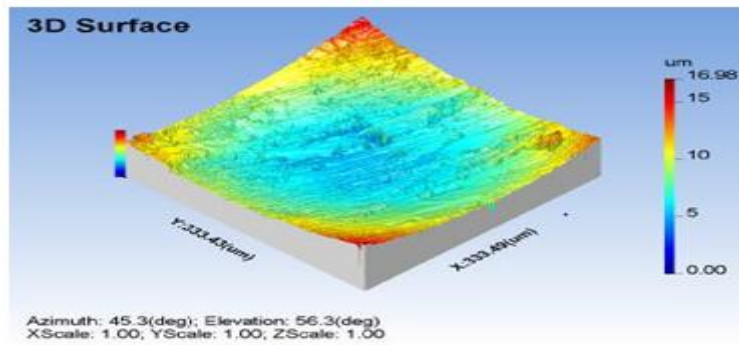
Specimen 2 (3.5N)



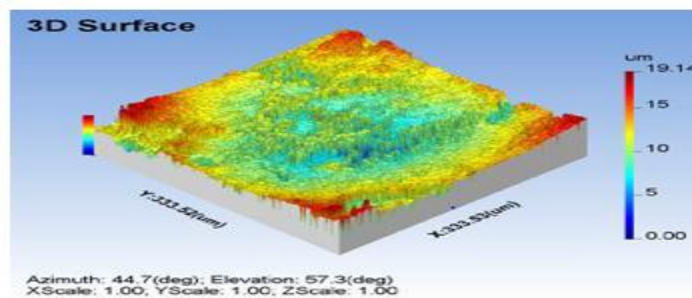
Specimen 1 (2N)

Specimen 2 (3.5N)

At 400°C before wear test

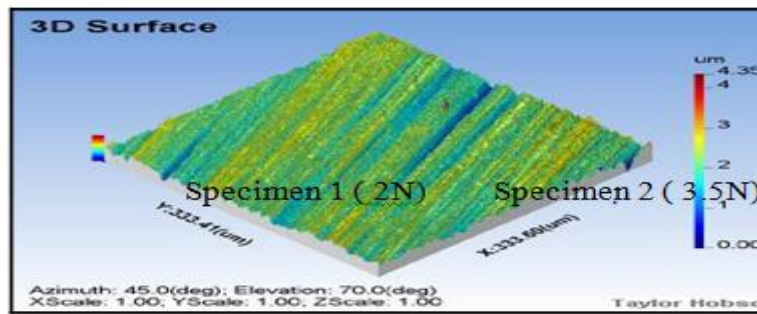


Specimen 1 (2N)

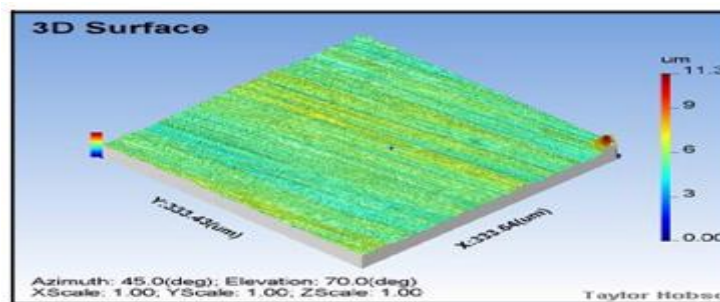


Specimen 2 (3.5N)

At 400°C after wear test



Specimen 1 (2N)



Specimen 2 (3.5N)

The following table 3 show the surface roughness Ra values with varying load characteristics and temperatures such as 2kg, 2.5kg, 3kg, 3.5kg

S.no	Temp	Load	Ra values	
			without load	with load
1	350	2	0.252	1.622
2	350	3.5	0.439	0.623
3	400	2	0.187	0.582
4	400	3.5	0.135	1.02
5	450	2	0.201	0.155
6	450	3.5	0.223	0.232
		MEAN	0.2395	0.705

Observation on wear rates on various loads (2,2.5,3,3.5 kgs) at different temperatures (350,400,450 C).

The following table 4 shows the wear rate values of different temperature aged specimens at different applied loads.

Load (kg)	Wear rates at		
	350° C	400° C	450° C
2	0.0288	0.0222	0.0152
2.5	0.0290	0.0299	0.0188
3	0.0302	0.0324	0.0287
3.5	0.0352	0.0370	0.0310

Observation of various loads (2,2.5,3,3.5 kgs) and coefficient of frictionAt 350 °C

The following table 5 shows the coefficient of friction values of 350°C aged specimens with respect to different applied loads.

Load (kg)	CoF1	CoF 2	CoF 3	CoF4
2	0.72	0.38	0.82	0.68
2.5	0.43	0.18	0.76	0.70
3	0.78	0.36	0.52	0.95
3.5	0.41	0.99	0.20	0.78

At 400°C

The following table 6 shows the coefficient of friction values of 400°C aged specimens with respect to different applied loads.

Load (kg)	CoF1	CoF 2	CoF 3	CoF 4
2	0.92	0.37	0.60	0.19
2.5	0.36	0.74	0.52	0.88
3	0.31	0.48	0.81	0.67
3.5	0.80	0.59	0.35	0.99

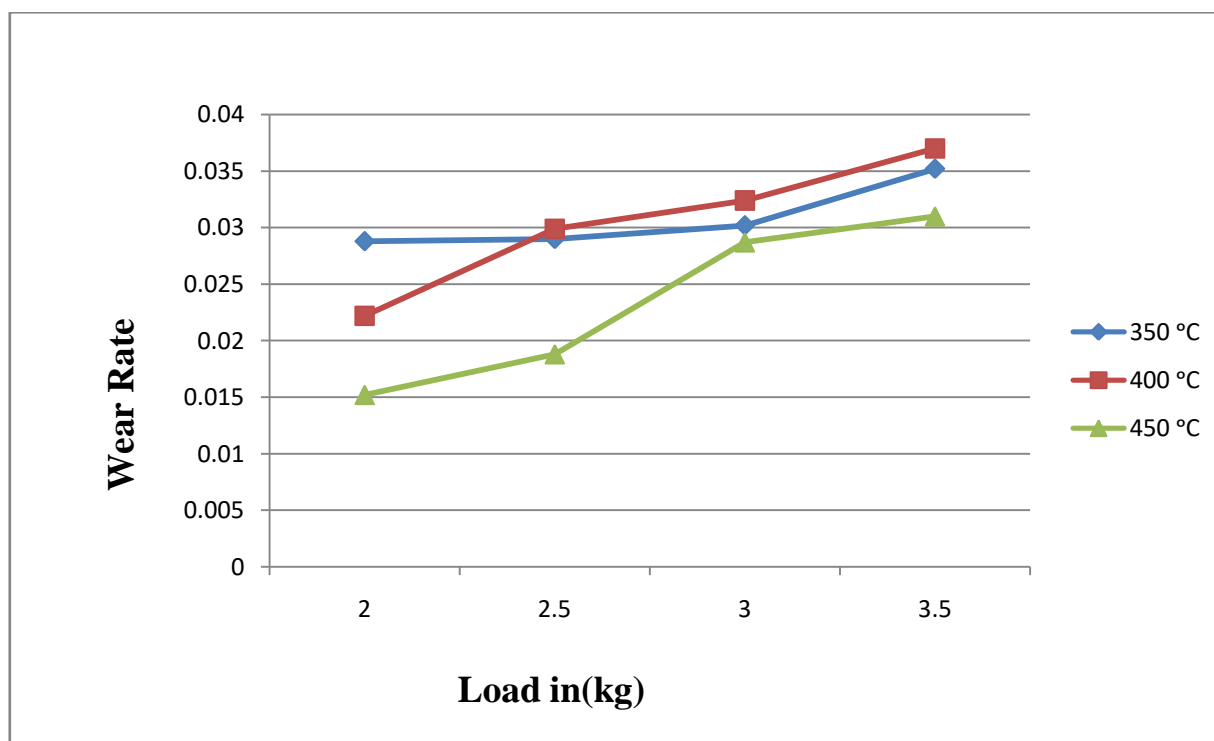
At 450°C

Load (kg)	Wear rates at 350° C	Wear rates at 400° C	Wear rates at 450° C
2	0.0288	0.0222	0.0152
2.5	0.0290	0.0299	0.0188
3	0.0302	0.0324	0.0287
3.5	0.0352	0.0370	0.0310

RESULTS

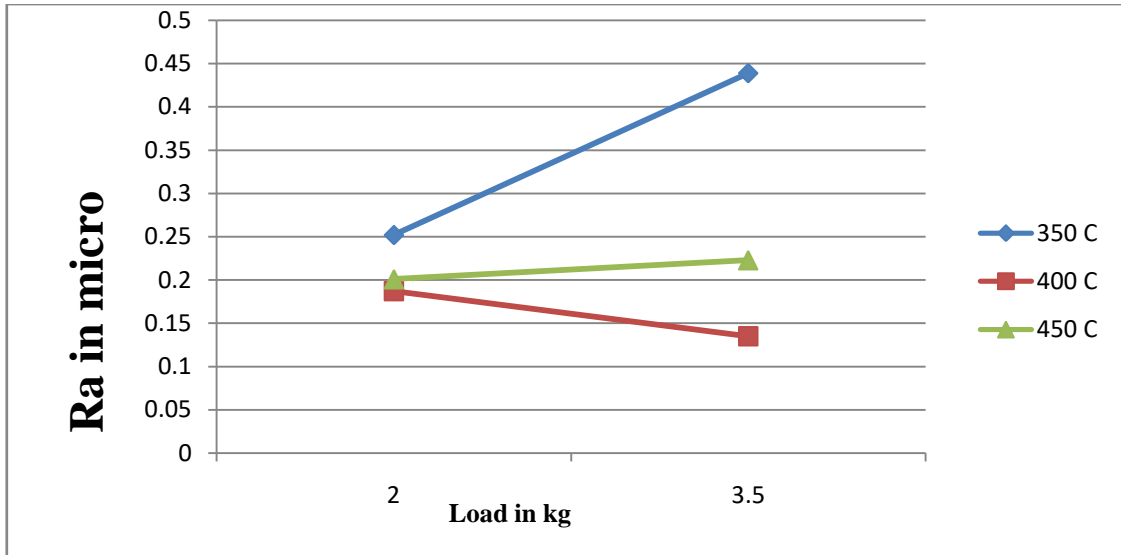
wear rates on various loads (2,2.5,3,3.5 kgs) at different temperatures(350,400,450°C)

From the graph it seen that the wear rate is very less at 450c when compared to 350c and 400c.



The surface roughness Ra values with varying load characteristics and temperatures such as 2kgs, 2.5kgs, 3kgs, 3.5kgs and 350c, 400c, 450c.

LOAD IN kg	350 C	400 C	450 C
2	0.252	0.187	0.201
3.5	0.439	0.135	0.223



CONCLUSION

From the experimental results obtained the following conclusion can be drawn:

1. The surface roughness of the balls importantly affects the wear rates and wear characteristic of the specimens.
2. The wear rates decrease with increasing SiC and MoS₂ of the reinforcement, the reason for that is Al (Im25) is having a nature of smooth surface undergoes more wear rate but when it is prepared composite hard SiC and MoS₂ particles resist the applied load and form lesser wear rate.
3. As the load increases the wear rate increases and as the % of reinforcement increases wear rate decreases because SiC and MoS₂ particles are crushed and form work harden layer between pin and the counter face.
4. The result also provides that lubricating nature of reinforcement material enhances the wear resistance and this property can be considered as a factor in design of new materials for different application.
5. For the obtained wear property the various wear rates after undergoing aging are (At 350°C the wear rate is 0.0288gm/s, at 400°C the wear rate is 0.0222gm/s, at 450°C the wear rate is 0.0152gm/s).

The above wear rate shows it is better as compared to other composites.

Materials	Wear Rates Gm/S
Aluminium-SiC Composite	0.0421
Sintered iron	0.0587

The surface roughness Ra values are less at the aging temperature increases. So, at 450°C the surface roughness value is less both before and after wear.

Load In kg	350 C	400 C	450 C
2	0.252	0.187	0.201
3.5	0.439	0.135	0.223

REFERENCES

- [1]. Siddesh Kumar N G, Ravindranath V M, G S Shiva Shankar, wear behavior of Aluminium Hybrid Metal Matrix Composites.
- [2]. Rabinowicz E. Friction and wear of materials. New York: Wiley
- [3]. Eyre TS. Wear characteristics of metals.
- [4]. Shipway PH, Hodge CJB. Micro-abrasion of glasses critical role of ridge formation.
- [5]. Stack MM, Mathew MT, Jawan H Construction of micro-abrasion maps for a steels/polymer couple in corrosive environment.
- [6]. Gun Y. Lee a,c, C.K.H. Dharan a,*, R.O. Ritchie b,c. A physically-Based abrasive wear model for composite materials.
- [7]. T.N Tiegs, K.B Alexander, K.P Plunkett ceramic composites with a ductile Ni₃Al binder phase
- [8]. P.Shanmugaselvam, S.Sivaraj, P.Subash, Investigating the wear and hardness of aluminium LM25 alloy reinforced with nano Al₂O₃ and nano TiB₂.

PAPER • OPEN ACCESS

Optimization of Parameters for Nitronic-60 on Wire-Cut Electrical Discharge Machining using Zinc-Coated Wire

To cite this article: V. Srinivasa Reddy *et al* 2021 *IOP Conf. Ser.: Mater. Sci. Eng.* **1126** 012043

View the [article online](#) for updates and enhancements.



240th ECS Meeting ORLANDO, FL

Orange County Convention Center **Oct 10-14, 2021**

Abstract submission deadline extended: April 23rd

SUBMIT NOW

Optimization of Parameters for Nitronic-60 on Wire-Cut Electrical Discharge Machining using Zinc-Coated Wire

V. Srinivasa Reddy^{1*}, V. Gopinath^{1*}, M. Haritha^{1*}, P Marimuthu^{12*},
K.Chandrasekaran³, and N S Kalyan Chakravarthy^{4*}

¹Department of Mechanical Engineering,

³Department of Mechanical Engineering, MAM School of Engineering,
Tiruchirappalli, India

⁴Department of Data Science and Business Systems

*QIS College of Engineering and Technology, Vengamukkapalem, Ongole,
Prakasam

District, Andhrapradesh-523 272, India

²Email: pmarimuthu69@gmail.com (Corresponding author)

Abstract. The objectives of this work are to research the effective parameters of pulse ON time; pulse OFF time; voltage & wire feed whereas machined on Nitronic-60 exploitation wire-cut discharge machining exploitation zinc-coated wire. During this work, metal removal rate, surface roughness, and kerfwidth are taken as output parameters. The experimental results planned an optimum combination of parameters that provide the utmost material removal rate, minimum surface roughness, and kerf dimension. Finally, confirmation experiments were disbursed to spot the effectiveness of the planned technique. Multivariate analysis and ANOVA are performed exploitation Response Surface Linear Model.

1. Introduction

Machining eliminates certain components of work piece items to alter them to finished components. Machining are classified into ancient machining and Non-traditional machining. Ancient Machining, conjointly referred to as typical machining needs the tougher tool than the work piece. This tool ought to be pierced within the workpiece to a definite depth. Besides, a motion between tool and workpiece is to blame for creating or producing the desired form. The nonappearance of any of those parts in machining method like the absence of tool and workpiece contact or relative motion makes the method a non-traditional one.



2. Literature survey

Vinod Kumar et al (2015) have planned a mathematical model and experimented by taking six WEDM method parameters. They have used D2 alloy steel employing Zn coated Copper wire conductor. Output such as MRR, Surface Roughness, and Kerf were used for further analysis. Soundrarajan et al (2015) have mentioned and investigated the analysis of various parameters using RSM. ANOVA is employed to search out the share contribution of serious method parameters. WEDM was used for machining A413 alloy which are making tools.

Pujari Srinivasa et al (2016) experimented the work on Ti6AL4V alloy for analysing the result of voltage, material pressure, and pulse on time and pulse off-time. It is concluded that pulse on-time and pulse off time are important parameters that affect the spark gap of WEDM. Antar et al (2011) studied the various factors that affect the WEDM of Inconel-600 using RSM method. They have used four input method parameters of WEDM to review the method performance. Brajaesh lodhi and Sanjay Agarwal (2014) investigated the results of the responses by varying WEDM method parameters on the machining AISI 304 chrome steel and got the optimized results from the analysis.

Panchal Yogesh Ratilal et al (2018) used L_{18} OA for conduction of experiments for solving single response problem. H-21 die alloy steel was taken as work piece material and Zn coated brass wire was taken as tool material. Herbert et al (2012) have conducted experiments on Nickel based super alloy for the evaluation of surface integrity in hole making process.

A detailed review was given by Chennakeseva Reddy Alavala and Naresh Baki (2016) in the area of application of CNC EDT for Aerospace application. RSM is the powerful tool that can be used for optimization of WEDM process (Gopalakannan et al 2012) and (Balasubramanian and Senthilvelan 2014). Sharanya Nair and Nehal Joshi (2014) reviewed the various works carried out on composite materials using WEDM. Kamal Jangara (2012) conducted the experiments in WEDM for studying unmachined area in intricate machining after roughcut.

Several machining parameters optimization were carried out by the previous researchers on different materials using WEDM and RSM was used for the development of mathematical models. But there is a lacking in WEDM study of Nitronic 60 material which is used for making stack liners, ducts, dampers, scrubbers etc. So in this work experiments were conducted on Nitronic 60 material in WEDM and RSM method is used for developing mathematical model for the important responses such as machining time and surface roughness and kerfwidth.

3. Experimental details

Experiments were conducted on corrosion materials of Nitronic 60 using a wire electrical discharge machine (WEDM). Zinc wires is used as tool.

Table 1 shows the composition of Nitronic 60 and Table 2 shows its properties.

Table 1 Composition of Nitronic 60

MATERIALS	COMPOSITION (%)
Ni	8-9
Cr	16-18
N	0.08-0.18
Mn	7-9 Max.
C	0.1 Max.
Si	3.5-4.5 Max.

Table 2 Properties of Nitronic 60

Density @ 72° F	7700-7700 lb/in. ³
Melting Temperature	1450° F to 1510° F
Specific heat	460-460 Btu/lb. ° F
Electrical Resistivity @ 75° F	0.55-0.55 $\mu\Omega$.m

Zinc anodes are sensibly protected and can be concentrated also. They yield unexpected voltages in comparison to the copper cells. In a specific, magnesium or copper cells can create voltage as extensive as 1.6v in lemon cells. This voltage is bigger than zinc or copper cells. It is similar to that of standard family unit 1.5v which helps control gadgets. Zinc is a somewhat blue-white, radiant metal. It is weak at normal temperatures yet pliable at 373-545k. It is a reasonable transmitter of power and consumes noticeable all around at high red warmth with an assessment of white billows of oxides. The metal is utilized in various amalgams with different metals. Metal, nickel, silver, business bronze, and aluminium are probably the most significant amalgams. Enormous amounts of zinc are utilized to deliver bite the dust projecting, which are utilized widely via auto, electrical, and equipment businesses. So Zinc terminals are utilized for wire electrical release machining of Nitronic 60. The test results have appeared in Table 3. Reaction Surface Methodology is utilized for additional examination.

4. Result and discussions

The primary objectives of this work is to analyze various input parameters in WEDM for machining Nitronic 60. Ton, Toff, Voltage and Wire feed were taken as input parameters and Machining time, Surface roughness and Kerfwidth were taken as responses. RSM was used for further analysis. Table 4 and Figure 1 shows the regression analysis for machining time.

Table 3 Experimental Results

T on	T off	Volta ge	Wire feed	Machining time	Surface roughness	Kerfwidth
4	2	40	2	477.38	2.18	0.247
4	4	45	4	557.07	2.03	0.291
4	6	50	6	671.96	1.8	0.289
4	8	55	8	796.43	1.64	0.294
6	2	50	4	465.75	1.69	0.297
6	4	55	6	562.08	1.85	0.32
6	6	40	8	500.24	2.03	0.289
6	8	45	2	556.47	1.99	0.29
8	2	55	6	463.32	1.86	0.292
8	4	50	8	472.12	1.83	0.293
8	6	45	2	488.27	1.84	0.355
8	8	40	4	208.37	2.17	0.344
10	2	45	8	445.53	2	0.332
10	4	40	6	459.38	2.26	0.357
10	6	55	4	568.47	1.69	0.368
10	8	50	2	559.75	1.79	0.367

Table 4 Regression analysis for machining time

Response	1	Machining tim			
ANOVA					
	Sum of		Mean	F	p-va
Source	Squares	Df	Square	Value	Pr
Model	31950	10			0.000
A-T on	31950	1			0.001
B-T off		1			-
C-		1			0.005
D-		1			
AB		1			
AC		1			
AD		1			
BC		1			
BD		1			
CD		1			
		5			
		15			
			R-		
			-		
			-		

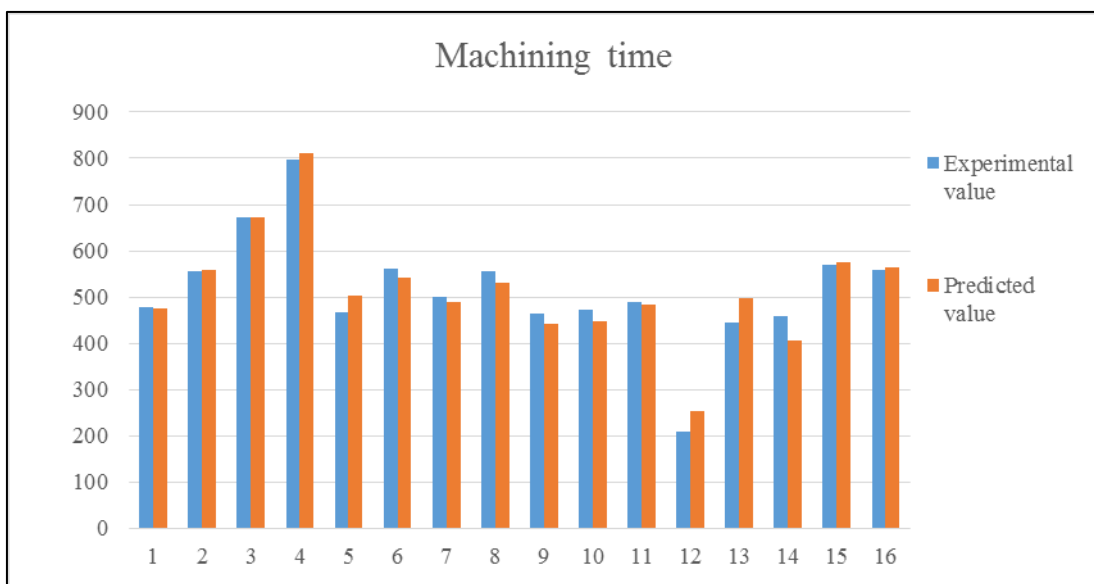


Figure 1 Machining time

From Table 4 and figure 1, the Pred R-Squared" is 0.2164 and Adj R-Squared is 0.8508 "Adeq Precision" measures the signal-to-noise ratio. A ratio greater than 4 is desirable. A ratio of

14.180 indicates satisfactory signal. The model developed for machining time from this study is given below

$$\text{Machining time} = +685.03319 + 22.19034 * T_{\text{on}} - 192.37313 * T_{\text{off}} - 13.26234 * \text{Voltage} + 196.16216 * \text{Wirefeed} - 9.66693 * T_{\text{on}} * T_{\text{off}} + 0.76868 * T_{\text{on}} * \text{Voltage} - 8.40988 * T_{\text{on}} * \text{Wirefeed} + 5.90026 * T_{\text{off}} * \text{Voltage} - 4.90879 * T_{\text{off}} * \text{Wirefeed} - 2.58316 * \text{Voltage} * \text{Wirefeed}$$

From Table 5 and Figure 2, it is observed that Model F-value is 9.30 that implies the model is significant. There is only a 0.15% chance that a "Model F-value" this large could occur due to noise.

The "Pred R-Squared" of 0.5652 is reasonable with the "Adj R-Squared" of 0.6889. A ratio of 8.519 indicates satisfactory signal. The model for surface roughness is shown below

$$\text{Surface roughness} = +3.25645 + 5.12500E-003 * T_{\text{on}} - 0.012348 * T_{\text{off}} - 0.027961 * \text{Voltage} + 2.63587E-003 * \text{Wire feed}$$

Table 5 Regression analysis for surface roughness

Response	2		Surface roughness		
ANOVA					
	Sum of		Mean	F	p-value
Source	Squares	Df	Square	Value	Prob> F
Model	0.400905109	4	0.100226277	9.304597	0.0015
A-T on	0.00210125	1	0.00210125	0.195071	0.6673
B-T off	0.011689275	1	0.011689275	1.085184	0.3199
C-Voltage	0.3746174	1	0.3746174	34.77794	0.0001
D-Wirefeed	0.000511359	1	0.000511359	0.047472	0.8315
Residual	0.118488641	11	0.010771695		
Cor Total	0.51939375	15			
Std. Dev.	0.103786775		R-Squared	0.771871	
Mean	1.915625		Adj R-Squared	0.688915	
C.V. %	5.417906688		Pred R-Squared	0.565183	
PRESS	0.225841212		Adeq Precision	8.519386	

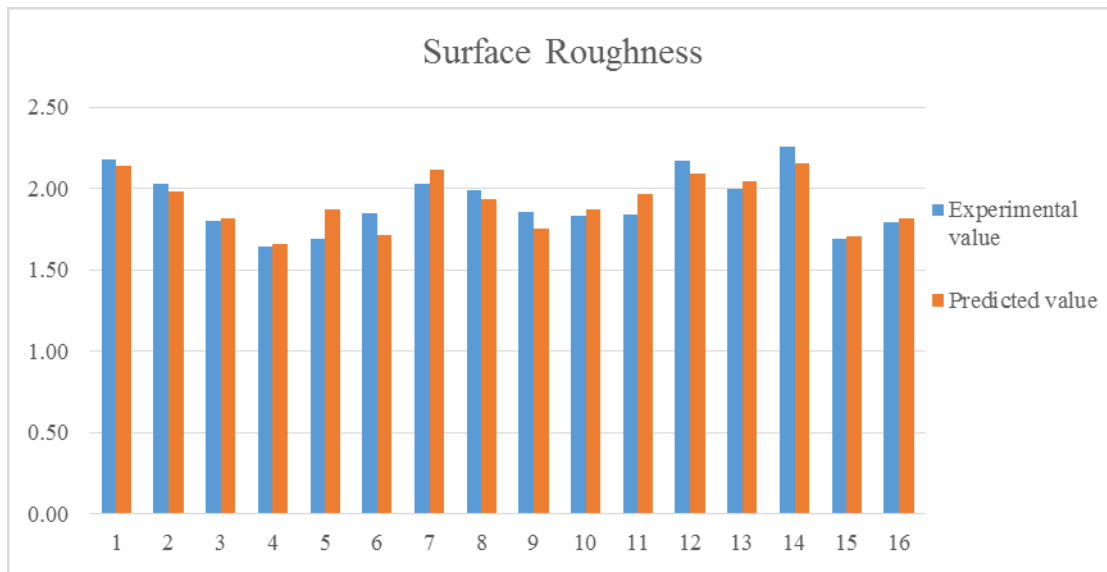


Figure 2 Surface roughness

Table 6 Regression analysis for Kerfwidth

Response	3	Kerfwidth			
ANOVA					
	Sum of		Mean	F	p-value
Source	Squares	Df	Square	Value	Prob> F
Model	0.014964	4	0.003741	10.26591	0.001
A-T on	0.012425	1	0.012425	34.09576	0.0001
B-T off	0.001851	1	0.001851	5.078177	0.0456
C-Voltage	0.000164	1	0.000164	0.449651	0.5163
D-Wirefeed	0.000225	1	0.000225	0.616601	0.4489
Residual	0.004009	11	0.000364		
Cor Total	0.018973	15			
Std. Dev.	0.01909		R-Squared	0.78872	
Mean	0.314063		Adj R-Squared	0.711891	
C.V. %	6.078325		Pred R-Squared	0.586968	
PRESS	0.007836		Adeq Precision	10.31731	

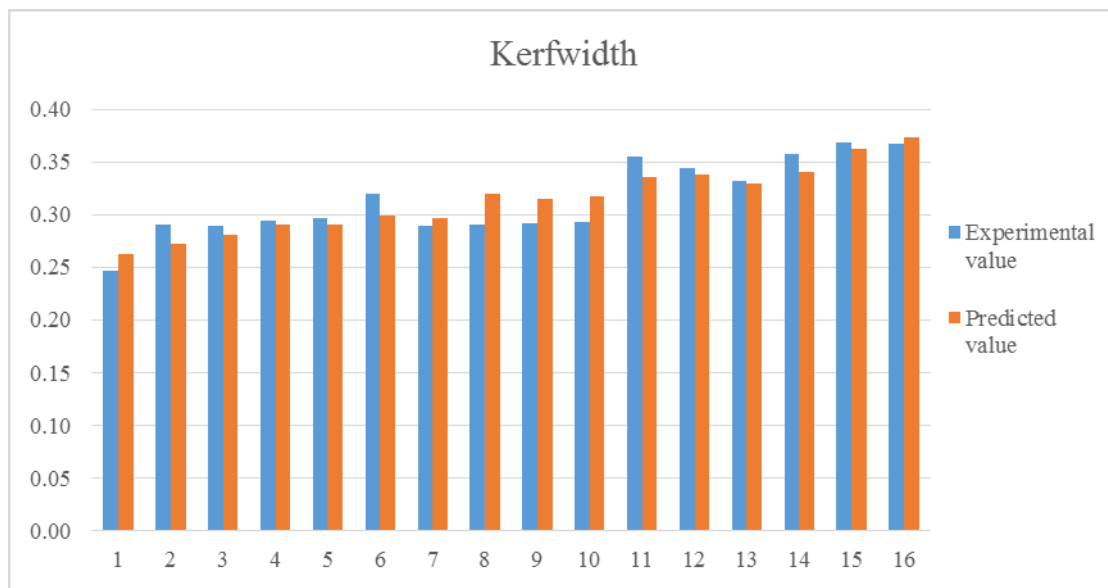


Figure 3 kerfwidth

Table 6 and Figure 3 shows the Regression analysis for Kerfwidth. From Table 6 and Figure 3, it is observed that The Model F-value is 10.27 that implies the model is significant. are many insignificant model terms (not counting those required to support hierarchy), model reduction may improve your model.

The Pred R-Squared" of 0.5870 is in reasonable with the Adj R-Squared" of 0.7119.

A ratio of 10.317 indicates an adequate signal. The developed model for Kerfwidth is shown below.

$$\text{Kerfwidth} = +0.18322 + 0.012463 * T_{on} + 4.91304E-003 * T_{off} + 5.84783E-004 * \text{Voltage} - 1.74728E-003 * \text{Wire feed}$$

5. Conclusion

This experimental work uncovers the accompanying ends on the WEDM procedure on Nitronic 60 workpiece material. The main principle objective was to build up the experimental model utilizing RSM. The reaction surface philosophy is probably the best method to recognize the impacts of machining boundaries on the WEDM cycle. The voltage and heartbeat off time significantly affect machining time. The more elevated level of current produces lower machining time. The reaction surface models were created dependent on the plan of the analysis with current, voltage, and beat on schedule, and heartbeat off time as info, and machining time and surface harshness were the reactions. The reaction surface model has a more modest deviation from test information and affirms that the created model can be utilized to foresee the machining time and surface unpleasantness esteem adequately.

References

- [1] Vinod Kumar, Vikas Kumar, and Kamal Kumar Jangra (2015), "An Experimental Analysis and Optimization Of Machining Rate And Surface Characteristics In Wedm Of Monel-400 Using RSM And Desirability Approach", Journal of Industrial Engineering International, Vol. 11, pp. 297-307.

- [2] R. Soundrarajan, A. Ramesh, N. Mohanraj and N. Parthasarathi (2016), "An investigation of material removal rate and surface roughness of squeeze cast a413 alloy a WEDM by multi-response optimization using RSM", *Journal Of Alloy And Compounds*, Vol. 685, pp. 533-545.
- [3] Pujari Srinivasa Rao, Koonam Ramji, and Beela Satyanarayan (2016), "Effect Of Wire EDM Conditions On Generation Of Residual Stresses In Machining Of Aluminium 2014 T6 Alloy" *Alexandria Engineering Journal*, Vol. 55 issues 2, pp. 1077-1084.
- [4] M. T. Antar, S. L. Soo, D. K. Aspinwall, D. Jones and R. Perez (2011), "Productivity And Workpiece Surface Integrity When WEDM Aerospace Alloys Using Coated Wires", *Procedia Engineering*, Vol. 19, pp. 3-8.
- [5] Brajaesh Iodhi and Sanjay Agarwal (2014), "Modeling Of Wire Electrical Discharge Machining Of AISI D3 Steel Using Response Surface Methodology" 5th International & 26th All India Manufacturing Technology, Design, and Research Conference (AIMTDR 2014), IIT Guwahati, Assam, India
- [6] Panchal Yogesh Ratilal, Nilesh K. Patel and Kapil S. Banker (2018), "Review Of Research Work In Wire Cut Electrical Discharge Machining On Metal Matrix Composite Materials" *Procedia Manufacturing*, Vol. 20, pp. 253-258.
- [7] C. R. J. Herbert, J. Kwong, D. A. Axinte, M. C. Hardy and P. J. Witters (2012), "Evaluation Of The Evaluation Of Work Piece Surface Integrity In Hole Making Operations For A Nickel-Based Superalloy" *Journal Of Materials Processing Technology*, Vol. 212, Issue 8, pp. 1723-1730.
- [8] Chennakesava Reddy Alavala and Naresh Baki (2016), "Application of CNC Electrical Discharge Turning for Aerospace Materials – A Review", *International Journal of science and research*, Vol. 5, issue 11, pp. 1647-1653
- [9] T. Gopalakannan, S. Senthilvelan and S. Ranganathan (2012), "Modeling and Optimization of EDM Process Parameters on Machining of Al 7075-B4C MMC Using RSM", *Procedia Engineering*, Vol. 38, pp. 685-690.
- [10] P. Balasubramanian and T. Senthilvelan (2014), "Optimization of Machining Parameters in EDM Process Using Cast and Sintered Copper Electrodes", *Procedia Materials Science*, Vol. 6, pp. 1292-1302.
- [11] Sharanya Nair and Nehal Joshi (2014), "A review on wire electrical discharge machining (WEDM) of composite materials", *International Journal of Engineering Trends and Technology* Vol. 17, Number 9, Pp. 415-420.
- [12] Kamal Jangra (2012), "Study of the unmachined area in intricate machining after rough cut in WEDM", *International Journal of Industrial Engineering Computations*, 3 Issue 5 pp. 887-892.



Contents lists available at ScienceDirect

Materials Today: Proceedings

journal homepage: www.elsevier.com/locate/matpr

Characteristic analysis of dissimilar metal weld for AISI304 with SA213T22 in super heater coils

K. Chandrasekaran^{a,*}, P. Ranjith Kumar^a, R. Ramanathan^a, J. Chandradass^b, T.T.M. Kannan^c, A. John Rajan^d

^a Department of Mechanical Engineering, MAM School of Engineering, Trichy 621105, India

^b Centre for Automotive Materials, Department of Automobile Engineering, SRM Institute of Science and Technology, Kattankulathur, Chennai 603203, India

^c Department of Mechanical Engineering, PRIST Deemed University, Thanjavur 613403, India

^d Department of Manufacturing Engineering, School of Mechanical Engineering, Vellore Institute of Technology, Vellore 632 014, India

ARTICLE INFO

Article history:

Received 11 November 2020

Accepted 14 December 2020

Available online xxx

Keywords:

AISI304

SA213T22

TIG Welding

Taguchi method

Grey Analysis

ABSTRACT

Super heater is an inevitable component of any boiler system and failure of super heater leads to breakdown of whole plant. The integration of efficient quality welding technologies for dissimilar metals will be a key component in the successful weld quality for power plant components. In this investigation, an attempt has been made to study the dissimilar material AISI304 and SA213T22 tungsten inert gas welding is performed under different welding conditions current (100, 115, 130 Amps), gas flow rate (6, 8, 10 ltr/min), speed (2, 2.5, 3 mm/sec) and micro structure analysis performed to find influence of fusion heat. The Taguchi analysis is implemented to obtain single response optimization and grey relational analysis used to attain multi response for best yield strength, the ultimate strength, Vickers hardness and the elongation of the metals.

© 2021 Elsevier Ltd. All rights reserved.

Selection and peer-review under responsibility of the scientific committee of the International Conference on Mechanical, Electronics and Computer Engineering 2020: Materials Science. This is an open access article under the CC BY-NC-ND license (<http://creativecommons.org/licenses/by-nc-nd/4.0/>).

1. Introduction

Super heater is basically a heat exchanger in which heat is transferred from furnace gas to the steam. Improper heat transfer between steam and furnace gas leads to problems of localized heating and damage the welding spots. These coils are made up of alloy steel SA213T22 which has corrosion resistance and it cannot withstand continuous high temperature. The super-heater coils are made up of SA213T22 which can withstand up to 540 °C metal temperatures and final stage super-heater stream temperature of more than 565 °C with the increase in steam pressure with their required dissimilar materials. AISI304 has superior properties such as resistance to fire side corrosion and a stream temperature of 650 °C for final super-heater. Hence, the dissimilar materials are introduced to reduce the damage and an interchange material AISI304 is attempted to replace this super-heated coil. The dissimilar material welding is not possible to make a fusion weld and welding parameters are affecting the welding quality. The dissim-

ilar materials welding have been continuously explored and the related valuable studies presented by the past researchers are given below. Guo Ming et al. [2] studied the dynamic temperature field of laser welding on stainless steel. It was dynamically simulated by the FEA software ANSYS using transient heat conduction equation. Kain et al. [3] studied the failure of a few super heater tubes at localized regions in an atmospheric fluidized bed combustor. Uger esme and Mehim bayramoglu et al. [4] have used AISI 304 Stainless steel plate. TIG welding machine is used. The input parameters are travel speed, current, nozzle plate distance. The output parameters are bead penetration and tensile load. The optimal weld pool geometry has four smaller-the-better quality characteristics, i.e. the front height, front width, back height and back width of the weld pool. The modified Taguchi method is adopted to solve the optimal weld pool geometry with four smaller-the-better quality characteristics. Experimental results have shown that the front height, front width, back height and back width of the weld pool in the TIG welding of stainless steel are greatly improved by using this approach. Ahmad et al. [1] investigated excessive hoop stresses are the cause of failure in on a super alloy Inconel-800 super heater tube. Vibhav gupta et al. [6] found primary reason

* Corresponding author.

E-mail address: kchandrasekaran1984@gmail.com (K. Chandrasekaran).

<https://doi.org/10.1016/j.matpr.2020.12.671>

2214-7853/© 2021 Elsevier Ltd. All rights reserved.

Selection and peer-review under responsibility of the scientific committee of the International Conference on Mechanical, Electronics and Computer Engineering 2020: Materials Science.

This is an open access article under the CC BY-NC-ND license (<http://creativecommons.org/licenses/by-nc-nd/4.0/>).

Table 1
Chemical composition of the AISI304 and SA213T22.

AISI304								
C	Cr	Fe	Mn	Ni	P	S	Si	Mo
0.08	19	70	2	10	0.045	0.03	1	-
SA213T22								
0.15	2.60	-	0.60	-	0.025	0.025	0.50	1.13

Table 2
Factors and levels for similar and dissimilar welding.

Factor/ Levels	Level 1	Level 2	Level 3
Current (Amps)	100	115	130
Gas Flow Rate (ltr/min)	6	8	10
Speed (mm/sec)	2	2.5	3

Table 3
Experimental result for AISI304 to SA213T22 dissimilar metal weld.

AISI304 TO AISI304 similar metal weld								
Trials	A	B	C	YS (MPa)	US (MPa)	EL (%)	H (Hv)	
1	1	1	1	573.20	625.80	17.50	198.9	
2	1	2	2	447.50	635.32	27	197.3	
3	1	3	3	365	569.45	14.50	196.3	
4	2	1	2	429.90	660.60	20	183.5	
5	2	2	3	314	511.62	29.50	177.1	
6	2	3	1	370.20	594.65	13.50	185.3	
7	3	1	3	433	655.81	30	190.1	
8	3	2	1	396.80	571.96	17	206.1	
9	3	3	2	400.10	599.47	18	230.1	

for premature failure of super heater tubes led severe oxidation and creep. Gokula Krishnan et al. [5] presented occurrences of phase transformation and formation of aluminide phase such as Ni₃Al. Faith Dokme et al. [7] explained that weld zone micro structural analysis exhibited the existence of multi directional grain growth in all specimens on AISI 316L side. Yu Sun et al. [8] found that Iron alloy is exposed to a high temperature oxidation environment, outer layer of super heater will gradually oxidize into stable

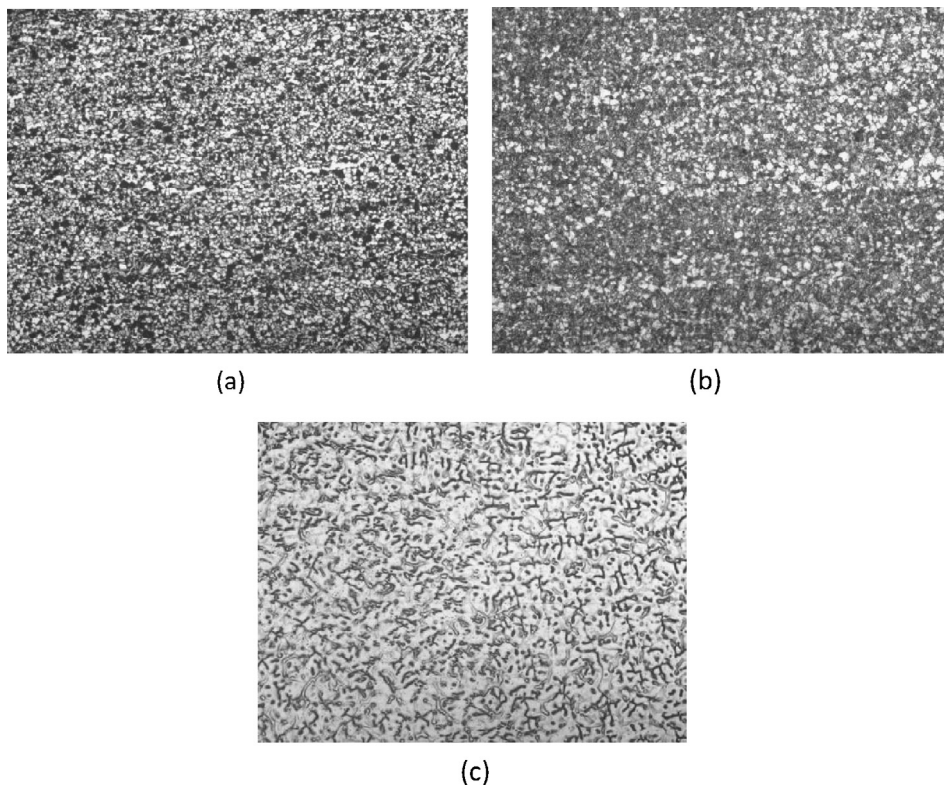


Fig. 1. Micro graph (Mag: 200x) for fusion (a) Parent material of SA213T22; (b) Dissimilar material HAZ of SA213T22; (c) Dissimilar material weld spot.

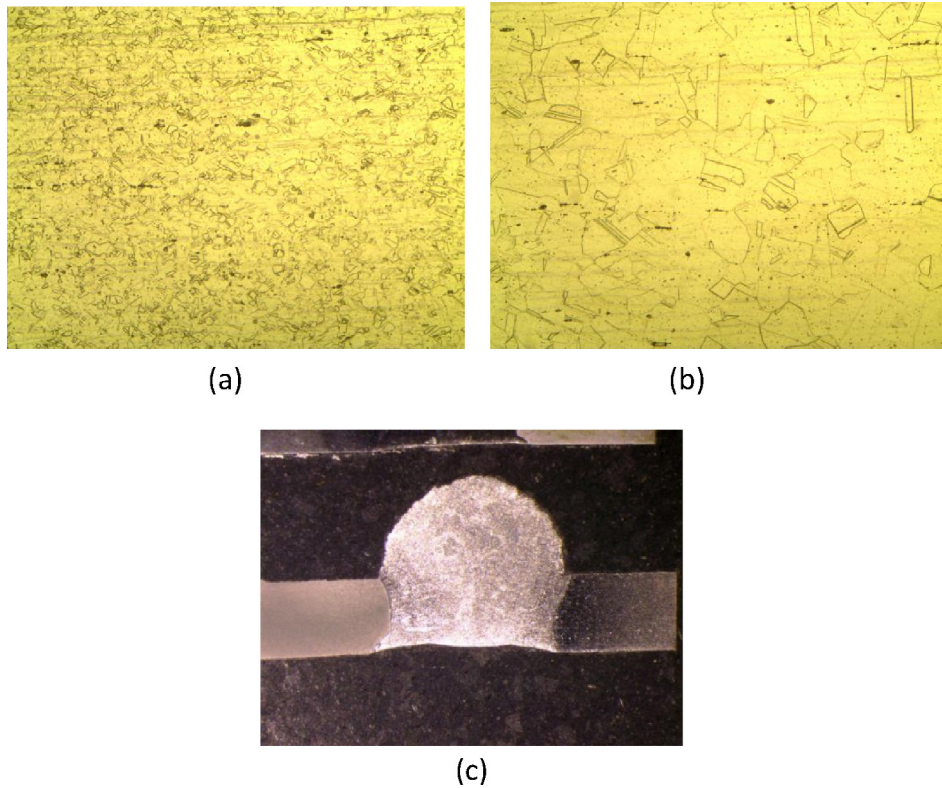


Fig. 2. Micrograph (Mag: 200x) for fusion (a) Parent material of AISI304; (b) Dissimilar material HAZ of AISI304; (c) Macro graph (Mag: 5x) dissimilar material weld spot.

Table 4

Signal to noise ratio for AISI304 to SA213T22 dissimilar metal weld.

AISI304 TO AISI304 similar metal weld								
Trials	A	B	C	YS (MPa)	US (MPa)	EL (%)	H (Hv)	
1	1	1	1	55.1661	55.9287	24.8608	45.9727	
2	1	2	2	53.0159	56.0599	28.6273	45.9025	
3	1	3	3	51.2459	55.1091	23.2274	45.8584	
4	2	1	2	52.6673	56.3988	26.0206	45.2727	
5	2	2	3	49.9386	54.1790	29.3964	44.9644	
6	2	3	1	51.3687	55.4852	22.6067	45.3575	
7	3	1	3	52.7298	56.3356	29.5424	45.5796	
8	3	2	1	51.9714	55.1473	24.6090	46.2816	
9	3	3	2	52.0434	55.5553	25.1055	47.2383	

Table 5

Taguchi Analysis: YS & US versus A, B, C.

Level	YS			US		
	A	B	C	A	B	C
1	53.14	53.52	52.84	55.70	56.22	55.52
2	51.32	51.64	52.58	55.35	55.13	56.00
3	52.25	51.55	51.30	55.68	55.38	55.21
Delta	1.82	1.97	1.53	0.34	1.09	0.80
Rank	2	1	3	3	1	2

and dense oxide film. From the study it was observed that flux used as the most significant effect on depth of penetration followed by welding current. Most of the researchers concentrate on the different directions but AISI304 over SA213T22 dissimilar materials weld was not performed yet and hence it is an important to study for the power plant components. Considering all the points into account in this present work. AISI304 to SA213T22 dissimilar

TIG welding process is performed under different welding conditions.

2. Experimental details

The paper aims to investigate and identify key improvements in weld mechanical properties and the microstructural compounds of

Table 6
Taguchi Analysis: YS and US versus A, B, C.

Level	EL			H		
	A	B	C	A	B	C
1	25.57	26.81	24.03	45.91	45.61	45.87
2	26.01	27.54	26.58	45.20	45.72	46.14
3	26.42	23.65	27.39	46.37	46.15	45.47
Delta	0.85	3.90	3.36	1.17	0.54	0.67
Rank	3	1	2	1	3	2

Table 7
Normalized- Grey Relational Coefficient and Grey Relational grade.

Trial No.	Normalized values of Z_{ij}				Grey Relational Co-efficient				Grey Relational grade
	YS	US	EL	H	YS	US	EL	H	
1	1.000	0.788	0.325	0.443	0.333	0.388	0.606	0.530	0.464
2	0.589	0.847	0.868	0.413	0.459	0.371	0.365	0.548	0.436
3	0.250	0.419	0.089	0.393	0.667	0.544	0.848	0.560	0.655
4	0.522	1.000	0.492	0.136	0.489	0.333	0.504	0.787	0.528
5	0.000	0.000	0.979	0.000	1.000	1.000	0.338	1.000	0.835
6	0.274	0.588	0.000	0.173	0.646	0.459	1.000	0.743	0.712
7	0.534	0.972	1.000	0.271	0.484	0.340	0.333	0.649	0.451
8	0.389	0.436	0.289	0.579	0.563	0.534	0.634	0.463	0.548
9	0.403	0.620	0.360	1.000	0.554	0.446	0.581	0.333	0.479

Table 8
Main effects on Grey grades.

Levels	1	2	3
Current (Amps)	0.518	0.692	0.493
Gas Flow Rate (ltr/min)	0.481	0.606	0.615
Speed (mm/sec)	0.575	0.481	0.647

dissimilar metals. This information helps lay a baseline for TIG welding process specifications and also demonstrates the significant factors affecting the TIG welding processes on dissimilar metals. The materials selected for dissimilar welding are AISI304 and SA213T22 and the chemical composition is given in Table 1. The diameter of the tube is taken as 60.3 mm, thickness is 4.5 mm and length is 250 mm. The electrode selected for similar welding is E309L whose dimension is 2.4 m in length. The argon is used as gas and its pressure is 3.5 kg/cm² during welding. The affecting factors and level selected for dissimilar welding AISI304 and SA213T22 is given in Table 2 and the experimental results of yield strength, the ultimate strength, Vickers hardness and the elongation of the metals is given in Table 3.

The physical properties of two metals are being very different from each other which lead to complexities in the weld pool shape, solidification microstructure and segregation patterns. Fig. 1 shows the micro-structure of the parent, heat affected zone and the SA213T22 weld spot at magnification 200x. Fig. 2 shows the macro-structure of the dissimilar materials welding spot at magnification of 5x and the micro-structure of the AISI304 weld spot at

Table 9
General Linear Model: Analysis of Variance for YS.

Source	DF	Seq SS	Adj SS	Adj MS	F	P
A	2	12383.3	12383.3	6191.7	7.98	0.111
B	2	18686.9	18686.9	9343.5	12.05	0.077
C	2	9266.3	9266.3	4633.2	5.97	0.143
Error	2	1551.1	1551.1	775.6		
Total	8	41887.7				

S = 27.8487 R-Sq = 96.30% R-Sq(adj) = 85.19%.

magnification 200x. It shows the macro-structure shows the dissimilar materials weld geometry such as reinforcement, width, penetration and weld bead.

3. Taguchi methodology

The main goal of the parameter design is to selecting the best process parameter to improve quality characteristics and to identify the product parameter values under the optimal process parameter values using Taguchi methodology. Moreover implementing that the optimal process parameter values obtained from the parameter design are insensitive to the variation of environmental conditions and other noise factors. Since the quality characteristic is to be maximization, the larger the better category is used to calculate the S/N ratio for responses Equation 1 shows the larger the better characteristic.

$$S/N \text{ ratio } (\eta) = -10 \log_{10}(1)$$

Taguchi technique is used to find the optimum setting of dissimilar materials weld and experiments are conducted based on the L₉ orthogonal array. The aim function is maximization of the yield strength, ultimate strength, Elongation and Vickers hardness, so experimental results are converted to signal to noise ratio for reduction of variance using Eq. (1). The signal to noise ratio yield strength, ultimate strength, and elongation and Vickers hardness is presented in Table 4. The Taguchi analysis for yield strength and ultimate strength is given Table 5, it clearly shows that the optimal welding parameters for maximization of yield strength is

Table 10

General Linear Model: Analysis of Variance for US.

Source	DF	Seq SS	Adj SS	Adj MS	F	P
A	2	857	857	429	0.23	0.813
B	2	9308	9308	4654	2.51	0.285
C	2	4313	4313	2156	1.16	0.463
Error	2	3714	3714	1857		
Total	8	18,192				

S = 43.0931 R-Sq = 79.58% R-Sq(adj) = 18.34%

Table 11

General Linear Model: Analysis of Variance for EL.

Source	DF	Seq SS	Adj SS	Adj MS	F	P
A	2	6.22	6.22	3.11	0.10	0.911
B	2	139.39	139.39	69.69	2.19	0.314
C	2	116.22	116.22	58.11	1.82	0.354
Error	2	63.72	63.72	31.86		
Total	8	325.56				

S = 5.64456 R-Sq = 80.43% R-Sq(adj) = 21.71%.

Table 12

General Linear Model: Analysis of Variance for H.

Source	DF	Seq SS	Adj SS	Adj MS	F	P
A	2	1086.46	1086.46	543.23	5.76	0.148
B	2	286.01	286.01	143.00	1.52	0.397
C	2	376.60	376.60	188.30	2.00	0.334
Error	2	188.65	188.65	94.32		
Total	8	1937.72				

S = 9.71208 R-Sq = 90.26% R-Sq(adj) = 61.06%.

current set as 100 amps, gas flow rate 6 lit/min and welding speed set as 2 mm/sec. Optimal welding parameters for maximization of ultimate strength is current set as 100 amps, gas flow rate 6 lit/min and welding speed set as 2.5 mm/sec. The Taguchi analysis for Elongation and Vickers hardness is given Table 6, it shows that the optimal welding parameters for maximization of Elongation is current set as 130 amps, gas flow rate 8 lit/min and welding speed set as 3 mm/sec. Optimal welding parameters for maximization of Vickers hardness is current set as 130 amps, gas flow rate 10 lit/min and welding speed set as 2.5 mm/sec.

4. Grey relational analysis methodology

In this work, a grey relational approach has been applied to solve multi response optimization of yield strength, ultimate strength, elongation and Vickers hardness using grey relational analysis. The proposed steps can determine effectively the optimal factor level combination for multi response problems. It quantifies all influences of various factors and their relation, which is called the whitening of factor relation. As a result, optimization of the multi responses can be converted into optimization of a single relational grade. In short, there is an ample scope of applying the proposed methodology of grey relational analysis with the multiple responses for the optimization of yield strength, ultimate strength, elongation and vickers hardness.

The objective of the dissimilar material weld AISI304 to SA213T22 is maximization of yield strength, ultimate strength, elongation and Vickers hardness. This was termed as the larger the better type problem where maximization of the characteristic was intended. S/N Ratio was calculated for the responses using the larger the better formula Equations 1. The experimental result

and computed S/N ratios for yield strength, ultimate strength, Elongation and Vickers hardness are shown in Table 6. The S/N ratio values were normalized by Eq. (2) and grey relational co-efficient was calculated for the normalized S/N ratio values by using Eq. (3). The grey relational grade was computed from grey relational co-efficient for by Eq. (4). The normalized signal to noise ratio, grey relational co-efficient and grey relational grades are given in Table 7. The main effects were tabulated in Table 8 and considering maximization of grade values in Table 8 the optimal parameter conditions obtained were A₁B₃C₃. Multi response optimization of dissimilar material weld AISI304 to SA213T22 for maximization of yield strength, ultimate strength, Elongation and Vickers hardness, current set as 110 amps, gas flow rate 10 lit/min and welding speed set as 3 mm/sec.

In this study, the analysis of variance is used to find the statistically significant welding parameters. The analysis of variance for yield strength is given in Table 9. It clearly shows that the gas flow rate most significantly affects the yield strength with F:P value of 12.05:0.077. The analysis of variance for ultimate strength is given in Table 10. It mention that the gas flow rate most significantly affects the ultimate strength with F:P value of 2.51:0.285. The analysis of variance for elongation is given in Table 11. It represents the gas flow rate most significantly affects the elongation with F: P value of 2.19:0.314. The analysis of variance for Vickers hardness is given in Table 12. It denotes the current most significantly affects the Vickers hardness with F: P value of 5.76:0.148.

5. Conclusion

The function of the super heater coil is transfer heat energy, during transfer of high transfer damage happen in weld spot. So

aim of the investigation is to study the performance of the dissimilar material AISI304 to SA213 T22 TIG welding the following are the outcomes

- Optimal TIG welding parameters for dissimilar material maximization of yield strength is current set as 100 amps, gas flow rate 6 lit/min and welding speed set as 2 mm/sec.
- Optimal TIG welding parameters for dissimilar material maximization of ultimate strength is current set as 100 amps, gas flow rate 6 lit/min and welding speed set as 2.5 mm/sec.
- Optimal TIG welding parameters for dissimilar material maximization of Elongation is current set as 130 amps, gas flow rate 8 lit/min and welding speed set as 3 mm/sec.
- Optimal TIG welding parameters for dissimilar material maximization of Vickers hardness is current set as 130 amps, gas flow rate 10 lit/min and welding speed set as 2.5 mm/sec.
- Multi response optimization of dissimilar material weld AISI304 to SA213T22 for maximization of yield strength, ultimate strength, Elongation and Vickers hardness, current set as 110 amps, gas flow rate 10 lit/min and welding speed set as 3 mm/sec.

Declaration of Competing Interest

The authors declare that they have no known competing financial interests or personal relationships that could have appeared to influence the work reported in this paper.

References

- [1] J. Ahmad, J. Purbolaksono, L.C. Beng, Failure analysis on high temperature superheater Inconel 800 tube, *Eng. Fail. Anal.* 17 (2010) 328–333.
- [2] G. Ming, Q.H. XiaoyanZeng, Effects of gas shielding parameters on weld penetration of CO₂ laser-TIG hybrid welding, *J. Mater. Process. Technol.* 184 (2007) 177–183.
- [3] V. Kain, K. Chandra, B.P. Sharma, Failure of carbon steel tubes in a fluidized bed combustor, *Eng. Fail. Anal.* 15 (2008) 182–187.
- [4] Uger Esme, Mehim Bayramoglu, Optimization of weld bead geometry in TIG welding process using gray relation analysis and Taguchi method, *material technology* 43 (2009) 143149.
- [5] A. Gokulakrishnan, K. Karuppasamy, Experimental investigation of Nickel Aluminide (Ni3Al) nano structured coated economiser tube boiler, *Int. J. Eng. Sci. Manage. Res.*, 2016, pp. 1–7.
- [6] Vibhav gupta, Harsh vardhan, S.K. Yadaw, CORCON-2017, (2017). pp. 1-9.
- [7] Fatih Dokme Mustafa Kuleci Ugur Esme Micro structural and mechanical characterization of dissimilar metal welding of Inconel 625 and AISI 316L Metals. 8 10 (2018),797. 797 10.3390/met8100797
- [8] Yu Sun, Maozhen Yue, Yungang Li, Reaction Kinetics of chlorine corrosion to heating surfaces during coal and Biomass cofiring, *J. Chem.* 2020 (2020) 1–10.



A Study of Added SiC Powder in Kerosene for the Blind Square Hole Machining of CFRP Using Electrical Discharge Machining

PV Arul Kumar¹ · J. Vivek² · N. Senniangiri³ · S. Nagarajan⁴ · K. Chandrasekaran⁵

Received: 26 March 2021 / Accepted: 28 June 2021
© Springer Nature B.V. 2021

Abstract

Carbon Fiber Reinforced Polymers (CFRPs) have been applied potentially for various application components owing to their lightweight and better mechanical properties. However, the machining of CFRP has been observed to be poor machinability due to the properties of the CFRP composites. Micro-feature fabricating on CFRP macro-component is a challenging task due to the selection of inadequate process parameters and machines. However, micron-level blind square holes are required in CFRPs for proposing the applications of micro-robotics, micro-vibration measurements, and micro-detection of cracking. These square holes produced on CFRP have the difficult task of being machined using the Electrical Discharge Machining (EDM) process. In this research, the effects of concentration of silicon carbide, pulse duration, duty cycle, and current on squareness, hole depth, and surface roughness of CFRPs are analyzed using Electrical Discharge Machining (EDM) with the square copper electrode. The input parameters, the various percentage of concentration of silicon carbide, pulse duration, duty cycle, and current for EDM are selected. The responses, squareness, hole depth, and surface roughness are considered. Also, an electrode wear length and surface defects have been analyzed. The modeling has been performed for selected responses. Additive Ratio Assessment (ARAS) is used for obtaining optimum parameters. The overall analysis found that the silicon carbide concentration and pulse duration are greatly affected all the responses. Also, the square electrodes produced unstable spark phenomena in the EDM process.

Keywords CFRP · EDM · Silicon carbide · Squareness · Depth

1 Introduction

Carbon Fiber Reinforced Polymers (CFRPs) are used in aerospace, satellite, electronic field, and commercial parts. The reasons for using these CFRPs are low density, high strength, low friction coefficient, high toughness, and good wear resistance. Square holes are required in CFRPs for proposing the applications of micro-robotics, micro-vibration measurements, micro-detection of cracks, micron-level

relative humidity measurements, micron-level - thermal strain measurements, micro - level -temperature measurements, detection of micro - delamination, and micro-fiber optics. Thereby, the square holes were fabricated on CFRP by using EDM [1–3], laser machining [4], mechanical drilling [5, 6], and micro-EDM [7]. Also, the square hole is mostly used in the precision manufacturing sector for manufacturing the micron-level square in the 3D micro-components for microfluid transportation purposes and

✉ PV Arul Kumar
arulumarveera@gmail.com

J. Vivek
vivekdynamech18@gmail.com

N. Senniangiri
senniagirinarajan1987@gmail.com

S. Nagarajan
arsnagarajan@gmail.com

K. Chandrasekaran
kchandrasekaran1984@gmail.com

¹ Department of Mechanical Engineering, Bharath Niketan Engineering College, Aundipatty, Tamil Nadu 625536, India

² Department of Mechanical Engineering, Solamalai College of Engineering, Madurai, Tamil Nadu 625020, India

³ Department of Mechanical Engineering, Nandha Engineering College, Erode, Tamil Nadu 628052, India

⁴ Department of Mechanical Engineering, College of Engineering and Technology, Mettu University, Post Box. No 318, Mettu, Ethiopia

⁵ Department of Mechanical Engineering, MAM School of Engineering, Trichy, Tamil Nadu 621105, India

increasing the heat transfer rate with acceptable dimensional accuracy. Among the various machining processes, the non-contact and stress-free machining process for EDM is selected to perform machining on CFRP. The performance measures of CFRPs are highly associated with many factors such as electrode materials (copper, graphite, tungsten carbide, etc.), electrode dimensions (micron and micron size), polarity, types of dielectric mediums (kerosene, EDM oil, distilled water, etc.) and additives in dielectric mediums (SiC, Si, Cu, etc.) and selection of process parameters (pulse duration, pulse interval, etc.). The selection of electrode materials is an important task for obtaining better performance measures. Hence, tungsten carbide electrodes were fabricated by using a wire electric discharge grinding. The 0.110 mm diameter-fabricated electrodes were used for providing the holes on CFRP by using EDM and a 1.2 mm depth of cut was achieved [8]. In another work, 0.5 mm diameter copper electrodes were fabricated for providing blind holes on CFRP by using EDM and 0.25 mm depth of cut was achieved [9]. To evaluate the different electrode material performance over the CFRP machining, copper and graphite electrodes were used on CFRP by using EDM. The results found that copper electrodes gave better performance than graphite electrodes based on the electrode wear and surface finish [10]. Using copper electrodes for making blind holes on CFRP was performed using 1.5 amp current and 200 μ s pulse duration and 5.14 μ m surface roughness was achieved [11]. The copper electrode wear rate was analyzed for drilling on CFRP by using 1 amp current and 150 μ s pulse duration and 0.0056 mg/min electrode wear rate was observed [12]. To reduce the burr formation of CFRP drilled holes, the copper, brass, and aluminum electrodes were selected for drilling on CFRP by using EDM. The results found that the copper electrode gave better results than other electrodes [13]. In another work, burr formation was also reduced using EDM with different electrodes such as aluminum, brass, steel, and copper were selected for processing on CFRP. The results found that the copper electrode produced better results than other electrodes [14]. Besides, the selection of EDM parameters is also important to improve performance measures. The current was directly proportional to the tool wear rate by EDM drilling on CFRP [15]. Hence, the low electrode wear was observed by lowering the current. The 5 amp current and 100 μ s pulse duration were used to obtain the 4.8 μ m surface roughness of CFRP. The results found that the current was increased with an increase in the surface roughness. Hence, the low current is recommended for obtaining low surface roughness and less thermal damages [16]. The approximately 4 μ m surface roughness was obtained using a pulse duration of 70 μ s and a current of 2 amp in EDM drilling [17]. The Powder-Mixed Electric Discharge Machining (PMEDM) is also used for improving the performance measures. The dielectric medium has also played an

important role in improving machining characteristics by alternating ionization, heat dissipation, and dielectric flushing. Besides, dielectric medium physical parameters such as breakdown strength, flash point, thermal conductivity, pressure, flushing velocity, density, and viscosity influence the performance of EDM. Hence, these properties are directly associated with the selection of hydrocarbon dielectric fluid, water-based dielectric fluid, and gas-based dielectric fluid. The special technological behaviors of hydrocarbon dielectric fluids are small tool wear, high metal removal, and no corrosion of sample, low flash point, and no deionization necessary. Therefore, the hydrocarbon dielectric fluid of kerosene has been selected as a dielectric medium for obtaining more stable and effective machining performance than another dielectric medium [18]. Also, the dielectric medium performances are improved by adding different types of additives such as carbon, aluminum, copper, nickel, silicon, graphite, tungsten, and titanium powder [19]. Among the various additives, SiC powder is selected as an additive because of its superior properties. Hence, the effects of PMEDM process parameters on squareness, hole depth, and surface roughness of CFRPs are focused on it. The reasons for selecting the PMEDM are enlargement of the discharge gap, widening of discharge passage, multiple discharges, and influences of powder properties on machining characteristics. The surface roughness was reduced by increasing the concentration of SiC powder added to EDM oil [20]. Similarly, the material removal depth was decreased by increasing the concentration of SiC powder added to pure water [21]. SiC powder ranging from 5 g/l to 20 g/l was added to deionized water for improving the surface roughness. The result found that the 25 μ s pulse duration produced the 6.77 μ m surface roughness and it was a higher surface roughness value compared to 50 μ s pulse duration due to the uneven distribution of discharges [22]. The material removal depth and surface roughness were analyzed by adding Al to kerosene and SiC to kerosene and kerosene. The result identified the addition of Al/SiC to kerosene-improved performance measures compared to kerosene [23]. Kerosene is one of the main dielectric fluid mediums for machining micro-hole on steel and produces effective machining on steel using EDM. The results found that the entrance diameter was greater than the exit diameter and the tungsten carbide electrode wear was 273 μ m obtained [24]. The hybrid machining processes were also used to fabricate the micro-holes of diameter 250 μ m on steel using micro-EDM with 100 V voltage and 1500 pF capacitance [25]. The electrode diameter greatly affected the MRR, TWR, and taper angle. Increasing in the MRR, TWR, and taper angle were observed by increasing the electrode diameter [26]. Micro-hole comparative studies were made between the laser and micro-EDM on nickel-based superalloy by using selected optimum process parameters. The results found that micro-EDM has

produced better hole geometry than laser processes [27]. In another strategy, the $0.32\ \mu\text{m}$ surface roughness of AA-10%SiCp MMC was achieved by using powder concentration $4\ \text{g/L}$, pulse duration $100\ \text{ms}$, current $3\ \text{A}$, and voltage $50\ \text{V}$ [28]. Comparative surface roughness was studied between the aluminum powder and silicon powder in the machining of EDM by using selected working conditions. The results found that $2\ \text{mm}$ surface roughness was obtained and an aluminum powder gave a greater influence on surface roughness than silicon powder [29]. The performance of PMEDM and Rotary-EDM were studied based on the material removal rate (MRR) and tool wear rate (TWR). The results identified that the PMEDM process gave better performance than die-sinking EDM [30]. The EDM process can also be used for removing the burr from the machined CFRP due to the spark energy. The results found that oxygen showed higher MRR than negative polarity. Moreover, EDM oil gave a more effective performance for unwanted burrs removal from the EDM [31]. The coated carbide drill was used for machining of CFRP based on the tool life and hole quality CFRP/titanium stack. The output of the result found that the CFRP/titanium stack produced poorer quality than the individual machining of material [32]. The performance nano-powder of Fe_2O_3 over the Co-Cr-Mo sample was studied by using micro-EDM. The results identified that material depth was significantly improved by adding $2\ \text{g/l}$ of nanopowder in the dielectric medium [33]. To reduce the machining time, the morphology of the machined surface, and deviation in channel width, the assisting-electrode method was used for creating micro-channels (depth: $400\ \mu\text{m}$ and length: $3000\ \mu\text{m}$) on CFRP using brass and copper of $960\ \mu\text{m}$ in diameter. The SEM results found that peripheral surface damage, spalling, fiber breakage, and debris accumulation were observed [34]. Influencing in the cut direction and process parameters on depth of cut and surface roughness were studied and found that a 16% increasing in the material removal rate was observed when machining parallel to fiber direction compared to cutting perpendicular to the fibers, which was attributed to the higher electrical conductivity of the workpiece along the fiber length leading to greater discharge energies [35]. The low-frequency vibration-assisted EDM on CFRP was also used for improving machining efficiency and stability [36]. The shape of electrode and assisting-electrode were used for improving the micro-electrical-discharge drilling performance of CFRP resulting in the voltage was a significant factor that affecting the performance measures [37]. The influence of a short circuit on machined surface quality CFRP was investigated using EDM and found that the machining was stopped when the EDM in an unstable state due to the short circuit [38]. To increasing the material removal rate of CFRP and reducing in tool wear, carbon black and graphite (fillers) were added to the matrix for increasing the electrical and thermal

conductivity and the result found that high machinability, low thermal damage, and good surface quality were observed [39]. The μEDM integrated with a rotary tool and assisting-electrode was used for efficient spark generation in EDM. The result found that the material removal mechanism was a complex phenomenon where sparking happened both at the side surface and end face of the tool [40]. The effect of EDM process parameters such as feed rate and voltage on the hole quality was studied by micro-EDM and found that the microhole of $2500\ \mu\text{m}$ deep was achieved in CFRP [41]. The sandwich assisting-electrode method was used for cutting off thin CFRP and found that matrix cracking, breakage of carbon fibers, and fiber-matrix debonding were observed [42]. The preheating method was used for machining CFRP and found that very small, thin, and deep microfeature creating on CFRP was observed for enhancing their micro-features performance and function [43]. The previous studies found that the addition of powder particles in the dielectric medium effects on MMCs have also been used for improving the process performance of different work materials [44–49]. The optimization tools such as Taguchi's method, support vector machine, artificial neural network, and response surface methodology have also been used for improving the performance measures of polymer-based composites [50–52].

Few works have been found that effects of micron-level square shape electrodes with EDM process parameters and various percentages of SiC powder-mixed in the kerosene medium effects on squareness, hole depth, and surface roughness of CFRPs have been studied. More works have focused on macron-level circular hole profile processing on CFRP using EDM. Hence, the blind square holes in CFRPs have been focused on using the EDM parameters with a concentration of SiC powder. The CFRP application component requires blind-square holes during their usage. But, the blind square holes produced on CFRP have a difficult task by using electrical discharge machining process parameters with micron-level copper electrodes due to the variations in the material properties of carbon fiber and epoxy resin. Moreover, blind holes produced on CFRP are a challenging task due to the low melting point of copper electrodes produced by high electrode wear in the micro-scale machining of CFRP. Therefore, the machinability of CFRP has been analyzed on the basis that the squareness, hole depth, and surface roughness are focused on it. The micron-level square blind holes fabricating on CFRPs are the primary task. Hence, squareness and hole depth are important geometrical features for affecting the functionality of the relative motion between the machined parts. Therefore, these responses are mainly focused on it. The most contributing factor is identified by analysis of variance. Additive Ratio Assessment (ARAS) is used for obtaining optimum parameters. The electrode wear and surface defects are also analyzed. Finally, a comparative

analysis is carried out between a present study and previous results.

2 Material and Methods

2.1 Fabrication of CFRP

The autoclave process is normally used for producing CFRP laminates and this process is carried out under a pressurized vessel for applying pressure and heat to both parts that have been sealed in a vacuum bag. A prepreg carbon fiber-epoxy material is laid out on a work table to ensure that fiber orientation meets the design requirement, where the prepreg material consists of unidirectional long-carbon fibers in a partially cured epoxy matrix. The pieces of the prepreg material are cut out and placed on top of each other on a shaped tool to form a laminate. The layers could be placed in different directions to produce the desired strength pattern since the highest strength of each layer is in the direction parallel to the fibers. After the required number of layers has been properly placed, the tooling and the attached laminate are vacuum bagged, for removing the entrapped air from the laminated part. Finally, the vacuum bag and the tooling are put into an autoclave for the final curing of the epoxy resin. After removal from the autoclave method, the composite material is ready for further finishing operations.

2.2 Micro-Drilling

The micro-holes in the form of square shapes were performed on CFRP, a problematic task owing to their properties of composites. Table 1 shows the properties of SiC, kerosene, copper electrode, carbon fiber, and epoxy resin. Specification of EDM drill is shown in Table 2. Table 3 shows the selection of EDM process parameters and difficulties faced by selecting the EDM process parameters. Therefore, the blind square hole was performed on CFRP using EDM. These square holes produced on CFRP were a difficult task of being machined using the Electrical Discharge Machining (EDM) process due to the need for

Table 2 Technical specification of EDM drill

Machine tool	value
Work table	400 × 400
Max electrode length	400 mm
Size of electrode diameter	0.3 to 3.0 mm
Maximum drill depth	250 mm
Maximum coolant pressure	60 kg/cm ²
Maximum weight of work piece	300 kg
Work tank	690 × 470 × 83 mm
Net weight	750 kg
Connected load	2 KVA
Input power supply	3 phase, AC 415 V, 50 Hz
Maximum machining current	20 amp

selection of proper parameters, its associated performance measures, and variations in the CFRP material properties. Electrical Discharge Machining (EDM) has been used to machine difficult to cut material and the process is not related to the hardness of the material. The EDM and Abrasive Jet Machining (AJM) processes have also been used for machining CFRP. Moreover, the strength of CFRP is reduced after AJM processing due to the more water-absorbing properties of CFRP [53]. The usage of abrasive water jets for machining CFRP is not considered due to the delamination, burr, fiber pull-out, poor geometrical shape, dimension accuracy, and kerf width reduction [43], the more striation formation on the machined surface [54], abrasive grain size greatly affected the surface roughness [55], approximately the surface roughness varying from 3 to 4 μm [56, 57], low penetration depth [58]. Hence, compared to previous works [54–58], the abrasive water jet machine is producing lower performance measures compared to the EDM process [7, 10, 11, 16, 22]. Therefore, EDM is selected for processing on CFRP. The kerosene dielectric pressure was 0.7 kg/cm² fixed as constant. According to the design of the experiment, the blind square holes were performed on CFRP for studying the effects of the parameters on squareness (Sq. ness), hole depth (HD), and Surface Roughness (SR). The schematic line diagram and photocopy of EDM are shown in Fig. 1.

Table 1 Properties of SiC, kerosene, copper electrode, carbon fiber and epoxy resin

Material	Specific heat (J/kg K)	Breakdown Strength (kV/mm)	Density (g/cm ³)	Electrical Resistivity (μΩ cm)	Flash point (°C)	Melting Point (°C)	Thermal Conductivity (W/mK)
Silicon carbide (SiC)	510–650	–	3.22	1013	–	2730	300
Kerosene	2100	24	0.81	–	37–65	–	0.14
Copper	0.39	–	8.93	0.009–0.07 μΩ × 10 ⁻⁴	–	1083	401
Carbon fiber	2020 at 1230 °C	–	2.267	–	–	3652–3697	0.17–0.79
Epoxy resin	1110 J/kg °C	–	1.1–1.4	–	–	140	0.2

Table 3 Selection of process parameters

Parameters	Units/ Symbol	Levels				Machine limits/ From the literature papers/ Problems observed
		1	2	3	4	
Concentration of SiC	g/l / Cp	4	8	12	16	[59, 60]
Pulse duration	μs / Ton	15	30	45	60	Machine limit
Duty cycle	% / DC	1	3	5	7	Slow material removal rate
Current	amp/ I	2	4	6	8	Higher electrode wear observed by rising above 8 amp

Figure 2 shows the EDAX for CFRP composites and found that the chemical compositions of CFRPs identified by EDX are 84.12% C, 0.20% Si, 14.92% O, 0.28% Cl, 0.20% Na, 0.21% Ca and 0.10% K. The responses such as Concentration of SiC (g/l), Pulse duration (μs), Duty cycle (%), and Current (amp) were taken as EDM inputs. To achieve the blind square holes on CFRPs, the square copper electrodes were prepared using a vertical machining center and the sample copper electrode is shown in Fig. 3. The fresh copper electrode dimensions were measured using a coordinate measuring machine. The mean widths and standard deviations for 0.8 mm square electrodes were in the dimension of 0.8018 ± 0.017 mm. The hole depth, major axis, and minor axis of the blind hole parameter are shown in Figs. 4 (a-b). The scanning electron microscope (ZEISS: Coordinate Measuring Machines), video-measuring system (VMS-2010 F) were used for measuring the squareness, hole depth, and surface roughness. The top surface of blind square hole squareness is calculated using Eq. 1. The squareness value ranges from zero to one. Squareness value is one denoted as a perfect square. The electrode wear length can be measured along with the height of the electrode by taking the difference between the fresh electrode lengths to worn out electrode length and surface roughness were measured using SURFCOM TOUCH 50 tester.

$$\text{Squareness (sq.ness)} = \frac{\text{Major axis}}{\text{Minor axis}} \quad (1)$$

2.3 Additive Ratio Assessment (ARAS)

The additive ratio assessment is a multi-criteria decision-making method [61]. The method is presented in the tabular form and not in matrix form for a better understanding of the mechanism. ARAS selects the best alternative based on many attributes and the final ranking of alternatives is made by determining the utility degree of each alternative. ARAS has one of the compensatory methods, and qualitative attributes are converted into quantitative attributes and attributes are independent. The steps are given below.

Step 1: Forming of Decision-making matrix (DMM).

The under-mentioned DMM of preferences (X_{ij}) for 'm' alternatives (rows) rated on 'n' criteria (columns):

$$X = \begin{bmatrix} x_{01} & x_{01} & \cdots & x_{0n} \\ x_{11} & x_{12} & \cdots & x_{1n} \\ \vdots & \vdots & \ddots & \vdots \\ \vdots & \vdots & \vdots & \vdots \\ x_{m1} & x_{m2} & \cdots & x_{mn} \end{bmatrix} \quad (2)$$

Where $i = 0, 1, \dots, m$; $j = 1, 2, \dots, n$.

X_{ij} is the value corresponding to the performance value of the alternative named i , under the j criterion while x_{0j} is the optimal value for the j criterion. When the optimal value of the j criterion is absent, then

$$X_{0j} = \begin{cases} \max x_{ij} \text{ if } J \in B \\ \min x_{ij} \text{ if } J \in C \end{cases} \quad (3)$$

Here, B and C are denoted the benefit criteria to be maximized and non-benefit criteria to be minimized, respectively.

Step 2: Normalization of decision-making matrix.

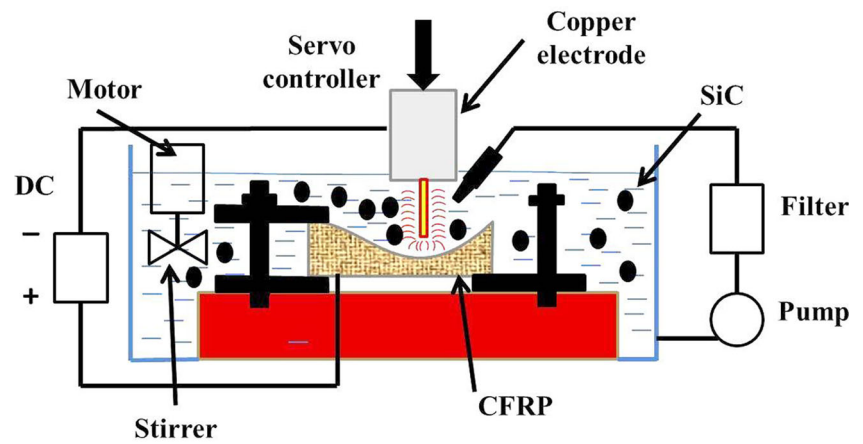
Linear normalization methodology is used to different criteria.

$$\bar{x}_{ij} = \frac{x_{ij}}{\sum_{i=0}^m x_{ij}} \quad (4)$$

The minimum criteria are normalized through a two-stage process.

$$x_{ij} = \frac{1}{x_{ij}^*}; \bar{x}_{ij} = \frac{x_{ij}}{\sum_{i=0}^m x_{ij}} \quad (5)$$

Fig. 1 EDM: (a) Schematic diagram, (b) photocopy of EDM



(a)



(b)

Step 3: Weighted normalized decision matrix

$$\hat{X}_{ij} = \bar{x}_{ij} * w_j; \quad i = 0, \dots, m,$$

(6)

$$\hat{X} = \begin{bmatrix} \hat{x}_{01} & \hat{x}_{02} & \dots & \hat{x}_{0n} \\ \hat{x}_{11} & \hat{x}_{12} & \dots & \hat{x}_{1n} \\ \vdots & \vdots & \ddots & \vdots \\ \hat{x}_{m1} & \hat{x}_{m2} & \dots & \hat{x}_{mn} \end{bmatrix}$$

(7)

Where, $i = 0, 1, \dots, m$; $j = 1, 2, \dots, n$.

\hat{X}_{ij} is the weighted normalized performance rating of the i alternative through the j criterion.

Step 4: Determine the optimality function (S_i) for the alternative

$$S_i = \sum_{j=1}^n \hat{x}_{ij} \quad (8)$$

Where, $i = 0, 1, \dots, m$; $j = 1, 2, \dots, n$. and High S_i value is better alternative.

Step 5: Determine the degree of utility (K_i) for each alternative.

$$K_i = \frac{S_i}{S_o}; \quad i = 0, 1, \dots, m \quad (9)$$

Step 6: Rank the alternatives based on K_i values.

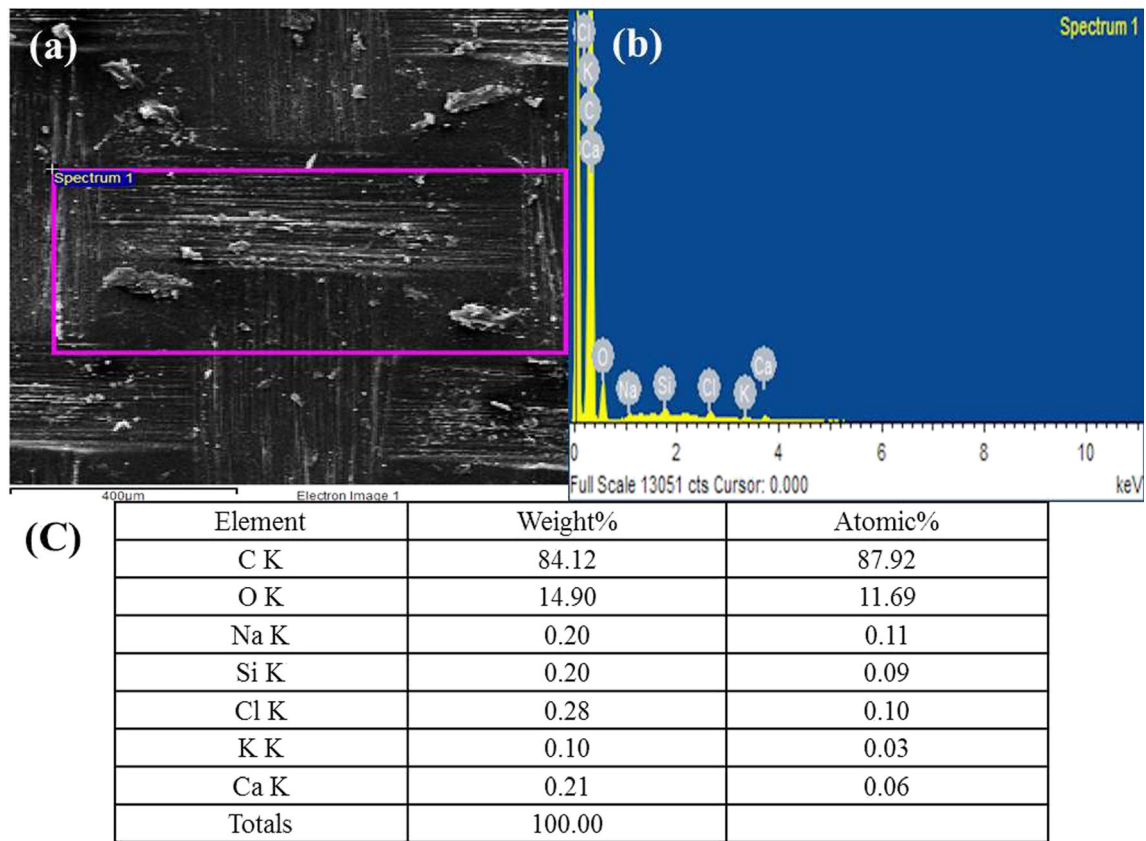


Fig. 2 EDAX for CFRP

3 Results and Discussions

The primary purpose of the work is to fabricate a blind square hole on CFRP using EDM process parameters. Also, the effects of the addition of SiC particles in the kerosene fluid on squareness, hole depth, and surface roughness of CFRPs are studied. The analysis of blind square hole feature studies is an important task. This is because the selected responses greatly affected productivity and production. The responses such as

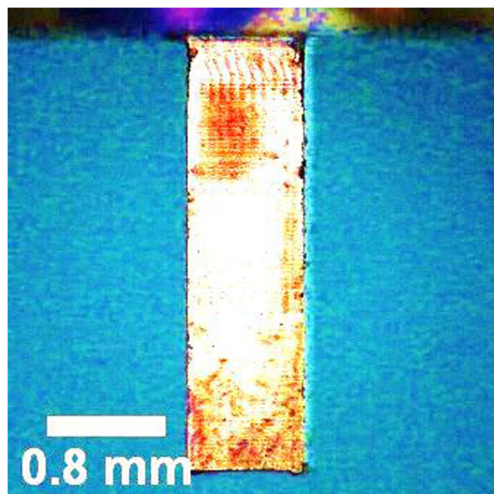


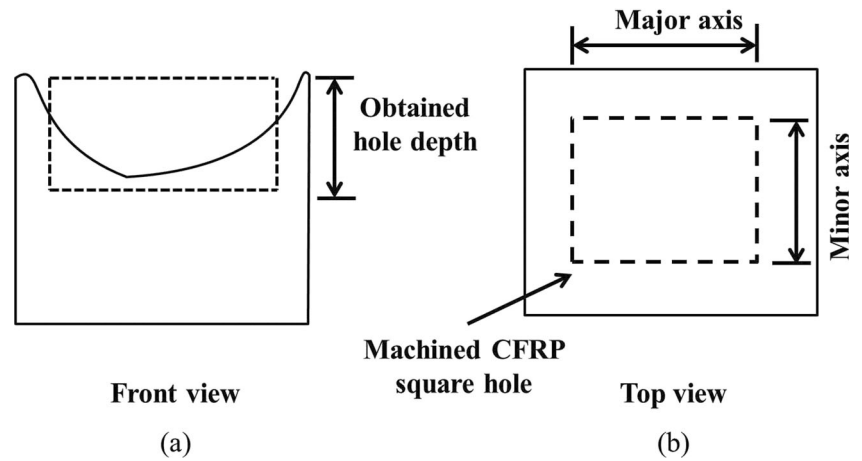
Fig. 3 Optical microscope image of copper electrode

squareness, hole depth, and surface roughness are considered. The blind square hole tests are carried out on CFRP as per the design of the experiment. The responses are measured and recorded. Table 4 shows the design layout and result of squareness, hole depth, and surface roughness of CFRP. Table 5 shows the calculation of the mean response.

3.1 Squareness

Experimental results found that the squareness value was greater than one in the entire square hole. This was due to the major axis being higher than the minor axis. Variations in the thermal properties of carbon fiber, epoxy resin, and SiC particles were also reasoned for obtaining a squareness value greater than one. The direction of the dielectric kerosene flushing, pressure, and concentration of SiC was also a reason for varying the square hole size in the experimental results. The unstable spark generated from the non-circular electrodes and corner radiuses of micro-feature formed on the work materials were observed. The previous works found that the non-circular electrode shapes were produced the unstable spark to Inconel 718 and Inconel 625 [62, 63]. In another way, to enhance the thermal properties of the dielectric medium strength, the addition of SiC concentration to kerosene was carried out and it was proved that the addition of SiC

Fig. 4 Schematic diagram for blind square hole: (a) hole depth, (b) major axis and minor axis



concentration to kerosene was greatly affected dielectric medium-strength [44]. Hence, the addition of SiC concentration to kerosene was carried out. After drilling, the graphs were drawn between the process parameters and responses. On increasing the concentration of SiC and pulse duration, the squareness increased and it is shown in Fig. 5. The squareness variations of micro-holes were due to the differences in the melting point of carbon fiber and epoxy resin. Also, epoxy resin has a lesser melting point compared to carbon fiber. Variations in the thermal conductivity and melting points were observed between the carbon fiber and epoxy resins that also reasoned for variation in the squareness of micro-holes. Moreover, the square shape copper electrode was generated non-uniform high-density sparks to CFRPs, resulting in

increasing squareness. More electrothermal energy was used for melting and vaporizing the CFRP. In addition, the direction of kerosene-flushing pressure was also intended for increasing the squareness. Therefore, squareness increased. With an increase in the duty cycle, the squareness decreased. The eroded materials were difficult to remove away from the machined zone by increasing the viscosity of the dielectric medium. Also, decreasing in the squareness was due to the effect of SiC powder particles on CFRP, surface properties, particle size, and electrostatic forces. Therefore, the squareness decreased. On increasing the current, the squareness decreased up to the level of 4 amp current and then rose above 4 amp current. This was due to the unstable spark generated from the square electrode to CFRP. The debris accumulation

Table 4 Design and experimental results

Exp. No.	Input process parameters				Quality performances		
	Concentration of SiC (g/l)	Pulse duration (μ s)	Duty cycle (%)	Current (amp)	Squareness –	Hole depth (mm)	Surface roughness (μ m)
1	4	15	1	2	1.044	0.177	1.941
2	4	30	3	4	1.067	0.180	2.565
3	4	45	5	6	1.120	0.181	3.623
4	4	60	7	8	1.132	0.197	3.652
5	8	15	3	6	1.026	0.222	3.691
6	8	30	1	8	1.076	0.255	4.254
7	8	45	7	2	1.121	0.297	4.656
8	8	60	5	4	1.135	0.322	4.752
9	12	15	5	8	1.049	0.342	4.796
10	12	30	7	6	1.089	0.370	5.044
11	12	45	1	4	1.145	0.394	5.374
12	12	60	3	2	1.158	0.405	5.836
13	16	15	7	4	1.031	0.409	5.846
14	16	30	5	2	1.099	0.446	6.005
15	16	45	3	8	1.147	0.466	6.094
16	16	60	1	6	1.161	0.505	6.527

Table 5 Mean responses calculation

Levels	Cp	Ton	DC	I
Squareness				
1	1.091	1.038	1.107	1.105
2	1.090	1.083	1.099	1.095
3	1.110	1.133	1.101	1.099
4	1.109	1.147	1.093	1.101
Maximum	1.110	1.147	1.107	1.105
Minimum	1.090	1.038	1.093	1.095
Delta	0.020	0.109	0.013	0.011
Rank	2	1	3	4
Improvement percentage (IP)	1.84	9.51	1.18	0.99
Hole depth				
1	0.184	0.287	0.333	0.331
2	0.274	0.313	0.318	0.326
3	0.378	0.335	0.323	0.320
4	0.457	0.357	0.318	0.315
Maximum	0.457	0.357	0.333	0.331
Minimum	0.184	0.287	0.318	0.315
Delta	0.273	0.070	0.014	0.016
Rank	1	2	4	3
IP	59.79	19.51	4.33	4.95
Surface roughness				
1	2.945	4.068	4.524	4.609
2	4.338	4.467	4.546	4.634
3	5.263	4.936	4.794	4.721
4	6.118	5.192	4.799	4.699
Maximum	6.118	5.192	4.799	4.721
Minimum	2.945	4.068	4.524	4.609
Delta	3.173	1.123	0.276	0.112
Rank	1	2	3	4
IP	51.86	21.64	5.74	2.36

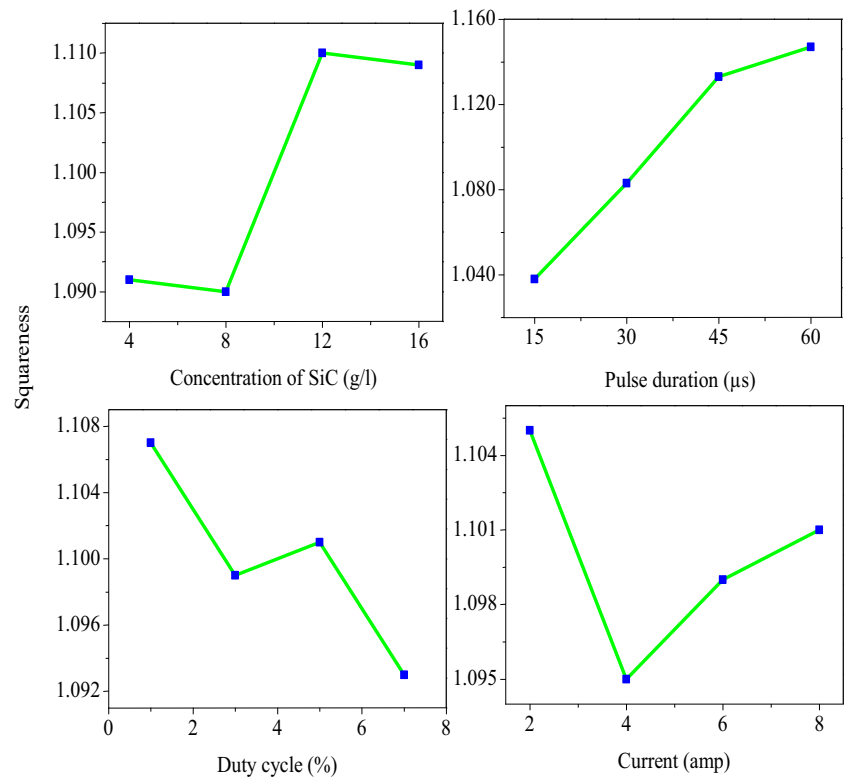
in the machined zone was also reasoned for variations in the squareness. Hence, the applied current showed that the steep V-shaped change in the behavior of squareness. In Table 5, it was found that the pulse duration was the most significant factor that affects the squareness of blind square holes. Improvement in the squareness percentages was calculated based on the parameters to rate the different machining performances. The pulse duration was used for obtaining a maximum improvement in the 9.51% squareness. Thereby, the minimum squareness was obtained using the 8 g/l concentration of SiC, 15 μ s pulse duration, 7% duty cycle, and 4 amp current. Also, the duty cycle and current were used for improving the squareness at a low level. Previous results identified that the metal removal rate of CFRP was increased using 500 μ s pulse duration [11]. Here, metal removal rate and squareness behavior were similar owing to both responses related to geometric features. Hence, lowering the pulse

duration was used for obtaining minimum squareness. In another study, the thermal conductivity of the dielectric medium was increased by increasing the concentration of graphite to dielectric fluid for improving the material removal rate [24]. Similar results were also obtained in this work. The unstable sparks generated from EDM electrodes were affecting the process performances. The direction of dielectric fluid flushing was also greatly affecting the machined surface [64].

3.2 Hole Depth

The hole depth (machined depth) varied by increasing the process parameters and it is shown in Fig. 6. It was found that the concentration of SiC and pulse duration were the most influenced factors on hole depth. The 16 g/l concentration of SiC and 60 μ s pulse duration were used for obtaining the maximum hole depth on CFRP. This was due to the higher thermal energy generated from the SiC mixed dielectric fluid to the machining region. SiC powder mixed with kerosene has provided stable machining by increasing the thermal conductivity of the dielectric fluid. Hence, hole depth increased. Besides, by raising the pulse duration, the hole depth increased owing to the unstable spark with higher thermal energy produced in the square electrode to CFRP. The effects of SiC powders mixed to dielectric fluid; the powder energized and performs in a zigzag movement between the copper electrode and CFRP. Effects of zigzag movement of particles formed the chain structure in the machining zone and reduce the dielectric fluid strength and develop a series discharge. The result found that the electrode sparking area produced effective discharge transmissivity owing to the raises in thermal conductivity. Therefore, the hole depth increased. Raising in the duty cycle and current, and the hole depth decreased. The hole depth variations in the micro-holes due to the differences in the melting point of carbon fiber and epoxy resin. Also, epoxy resin has a lesser melting point compared to carbon fiber. Variations in the thermal conductivity were also observed between the carbon fiber and epoxy resins that also reasoned for variation in the hole depth of micro-holes. Hence, hole depth varied. Normally, the current was directly related to metal removal. Nonetheless, the decrement in the metal removal was due to the eroded materials' difficulty to move away from the machined zone by increasing the viscosity and conductivity of the dielectric medium. More debris and thicken heat-affected zone were formed on the machined zone. The selection of dielectric fluid pressure also greatly affects the electrical properties of dielectric fluid due to the contamination of electrolytes resulting in reducing the efficiency of material removal. In this work, the 0.7 kg/cm² kerosene dielectric pressure was selected for processing. It was found that the pressure value was inadequate for removing the debris from the machining zone resulting in debris clogs in the

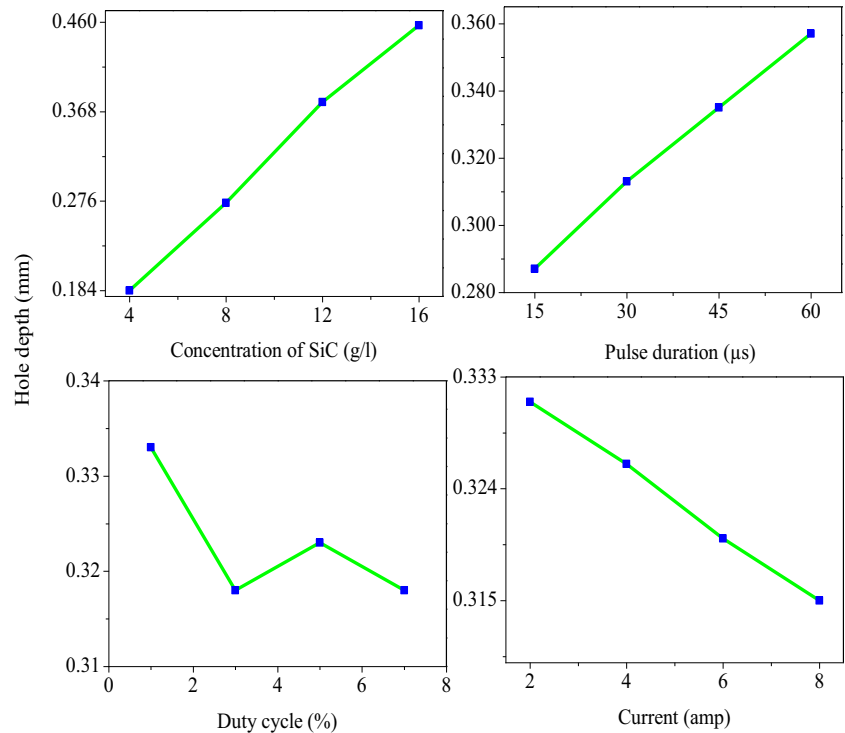
Fig. 5 Effect of parameters on squareness



machining zone. Simultaneously, the spark was supplied continuously without removing work material resulting in a thickened heat affected zone formed. Hence, the hole depth decreased. The 59.79% hole depth was achieved using the 16 g/l SiC concentration. Therefore, the maximum hole

depth was obtained using 16 g/l SiC concentration, 60 μs pulse duration, 1% duty cycle, and 2 amp current. The copper electrode wears also affected the width and depth of the hole [25]. Another result found that a higher depth of cut on copper was obtained using a 2.3 amp current and 0.2 μs

Fig. 6 Effect of parameters on hole depth



pulse duration. The present hole depth agreed well with the previous result [26]. The duty cycle equally affecting the squareness and hole depth due to the nature of CFRP material properties. Hence, the duty cycle produced similar trends over the squareness and hole depth. But, slight variances were also observed between the squareness and hole depth due to the geometrical differences.

3.3 Surface Roughness

Variation in the surface roughness was observed by varying the process parameters and it is shown in Fig. 7. It was found that the concentrations of SiC and pulse duration were the most influencing factors that affecting the surface roughness. The 4 g/l concentration of SiC and 15 μ s pulse duration were used for obtaining low surface roughness. The SiC powder mixed dielectric medium destroyed the insulation easily for reducing the electrical resistivity of the medium and leaving the discharge gap resulting in reduce the impulse force of the discharge channel. This influence on the machining gap generated a high plasma channel from a sample to an electrode for increasing the material removal rate. The higher thermal conductivity of copper electrodes was also supported by increasing the material removal rate. Also, carbon fiber and epoxy resin were easily melted, and smoothly surface formed due to the electrothermal effect. Hence, the machined surface showed an uneven small size crater and small debris, resulting in produced low surface roughness. Increasing the surface roughness was observed by raising the SiC concentration, pulse duration, duty cycle, and current. This was due to the increased thermal conductivity and impulsive force in the plasma region. The melting point difference between the carbon fiber and copper electrode was three times higher, resulting in the large and deep crater produced on the machined surface. Hence, higher surface roughness is produced. In short, the low concentration of SiC with low thermal energy sparks produced a lower surface roughness. Thereby, low thermal energy produced small crater sizes in the machined zone. SiC concentration and pulse duration were increased, and surface roughness was increased. The unstable sparks produced deep and wide surface irregularities in the machined zone. Hence, surface roughness increased. Similar behavior was observed in the current and duty cycle. The 51.86% surface roughness was achieved by lowering the SiC concentration. Hence, the minimum surface roughness was obtained using 4 g/l SiC concentration, 15 μ s pulse duration, 1% duty cycle, and 2 amp current. The erosion process produced a 10 amp current, which was used to obtain the 1.95 μ m surface roughness on titanium [24]. Compared to another study, higher surface roughness was observed in a previous study [27]. This result agreed well with this surface roughness result.

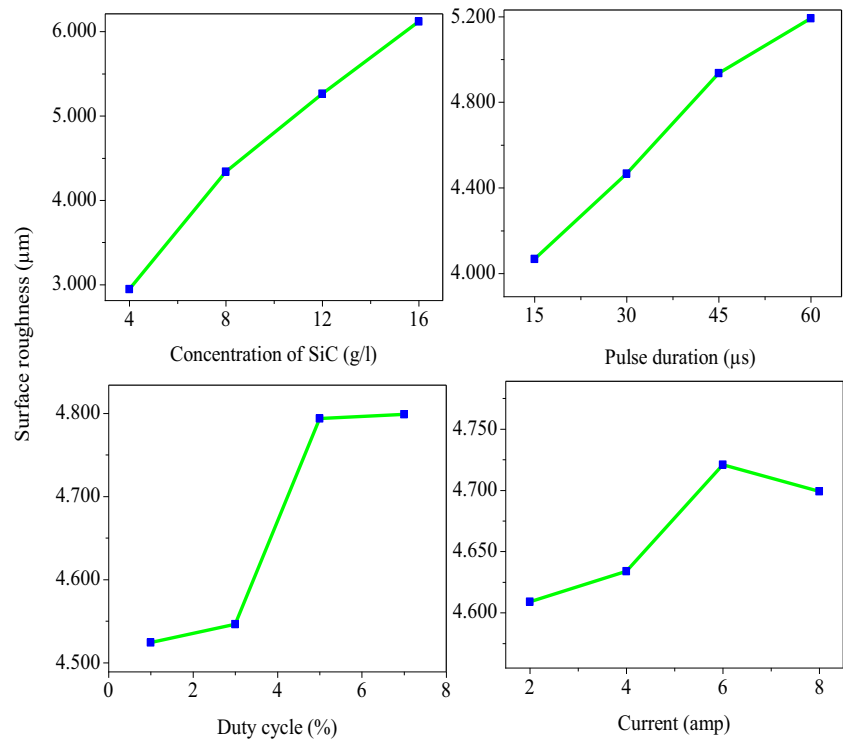
3.4 Electrode Wear Length

Figure 8 shows the copper electrode worn-out surface and worn-out length. After machining, the square form of the copper electrode was transformed into a semi-spherical shape electrode with worn-out length and surface. The main reason for the higher worn-out surface and length was unstable discharge energy produced in the square electrode. Initially, the sharp edge of the copper electrode was worn out and the surface of the electrode was secondly worn out due to the difference in the stress concentration. The copper electrode was a low melting point compared to carbon fiber, epoxy resin, and SiC particles. Hence, the copper electrode was worn out in a short time compared to other materials. Nonetheless, powder mixed dielectric fluid motivated to reduce the worn-out length due to the uniform discharge to sample and increasing the thermal conductivity of the dielectric fluid. Similar behavior was observed in the cylindrical shape electrode due to the skin effect [28]. Hence, electrode wear was an unavoidable problem in spark machining. The work was also focused on reducing the worn-out length of copper electrodes. The electrode worn-out length is reduced by increasing the SiC concentration in the dielectric fluid because SiC powder added to kerosene disturbs the adherence of atoms attached to the electrode surface and reduces the electrode-worn length. Also, SiC powder concentration was equally spread over the dielectric medium and it was nominal electrode-worn length obtained due to better conduction of discharge. The worn-out length of the electrode was varied from 0.31 mm to 1.168 mm by increasing the SiC concentration. The worn-out length was greatly associated with powder properties (concentration, density, thermal conductivity, and electrical resistivity) and it was affecting the machining performance, worn-out surface, and worn-out length. Similar results were observed in previous studies [13, 29]. The heat-affected zone formation and worn-out surface on the copper electrode were also reduced by increasing the SiC powder concentration due to the uniform mixing of powder in the dielectric fluid produces consistent discharge. The small cracks and pores were formed on the copper electrode due to the high impulsive forces developing on the machining zone. The reason for developing high impulsive force was high discharge energy produces more melting and evaporation.

3.5 Surface Defects

In Fig. 9, the corner radius was formed in the machined square hole. The reason for forming a corner radius was the square copper electrode wear. The different melting points of SiC, copper electrode, carbon fiber, matrix resin, and a high degree of short-circuit development were also reasoned. Sharp edges of square copper electrodes were first worn out for generating the round-shaped edges in the machining.

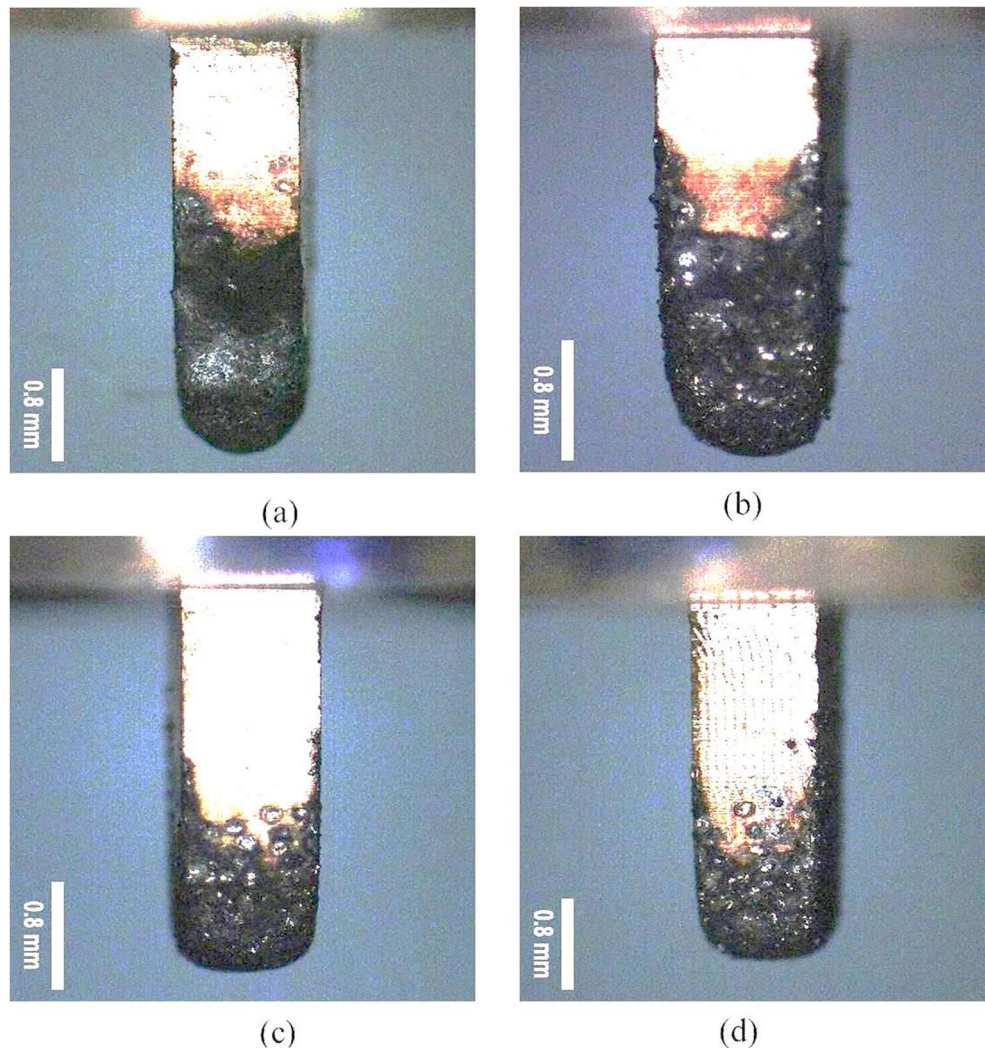
Fig. 7 Effect of parameters on surface roughness



This was due to the difference in the stress concentration factor between the copper electrode and machined hole of the CFRP composite. Simultaneously, the copper electrode wear reflected the sample through sparking. Hence, a corner radius was formed due to the non-uniform spark generated. The burrs were formed on the machined surface due to the long duration of time for developing plasma spark. The copper electrode produced a burr in the machined CFRP using 150 µs pulse duration and it is shown in a previous study [30]. The delamination was also observed due to the longer pulse duration. More heat energy generation at high pulse duration was the reason for generating delamination in the machined CFRP. Moreover, the fibers pulled in/out were observed. A different melting point of carbon fiber and matrix resin was reasoned. A similar result was observed in a previous study [31]. Another study stated that the direction of heat transformed was related to the direction of the carbon fiber orientation and not to the direction of current flow [12]. But, the argument result was observed in this study due to the electrothermal energy developed from the higher pulse duration and current. The heat-affected zone formed around the micro square hole was due to the different thermal conductivity of carbon fiber and epoxy resin. The heat transfer rate of carbon fiber was greater than the epoxy resin due to the higher thermal conductivity of carbon fiber. Due to the poor thermal conductivity of epoxy resin, the problem in heat-transferred rate was observed, affecting the heat-affected zone formation. Similar results were also observed in the previous work [32]. The corner radius was also formed in

the machined monel 400 alloy using EDM [65]. This was good supportive work for forming the corner radius formed in the machined surface. More debris and black products were formed in the machined surface of CFRP and the amount of debris formation was highly related to material removal mechanism, selection of the shape of electrode and material, dielectric fluid pressure, EDM process parameters (pulse duration, duty cycle, current) and physical and thermal properties of a powder particle. There were various reasons for forming debris and black portion (thickened heat affected zone formation), which were described below as. By using the low discharge energy in the deep hole machining, debris removal was a challenging issue due to the narrow sparking gap between the electrode and workpiece. The narrow gap was the main problem for blocking the material removal from the machining zone and more debris concentration in the bottom of the electrode resulting in thickened heat affected zone formation. This narrow sparking gap affected the material removal mechanism of CFRP and it was a complex phenomenon in the macro-EDM and micro-EDM where sparking happened both at the end face and side surface of the square electrode resulting in more debris formed. The stage of the burning of the matrix and resin was varied due to variation in thermal properties resulting in unbalancing to removing material from the machining zone. This phenomenon was related to the amount of pulse duration, current, and duty cycle. An unbalancing effect of material removal of CFRP greatly affects the properties of the electrolyte. This was also the reason for forming debris in the

Fig. 8 Worn out electrode at bottom view: (a) 4st experiment, (b) 8th experiment, (c) 12th experiment, (d) 16th experiment



machining zone. The selection of dielectric fluid pressure also greatly affects the electrical properties of dielectric fluid due to the contamination of electrolytes resulting in reducing the efficiency of material removal. In this work, the 0.7 kg/cm^2 kerosene dielectric pressure was selected for processing. It was found that the pressure value was inadequate for removing the debris from the machining zone resulting in debris clogs in the machining zone. Simultaneously, the spark was supplied without removing work material resulting in a thickened heat affected zone formed. On the other hand, SiC particles play an important role in the EDM process. The effects of the addition of SiC to dielectric fluid were reducing the insulating strength and increasing the sparking gap distance, resulting in a high material removal rate. Inversely, debris formation greatly affected the material removal rate. Hence, low dielectric fluid pressure was the main reason for the formation of debris and black products in the machined zone. The remaining process parameters were not much affecting the material removal rate and debris formation.

3.6 Modeling

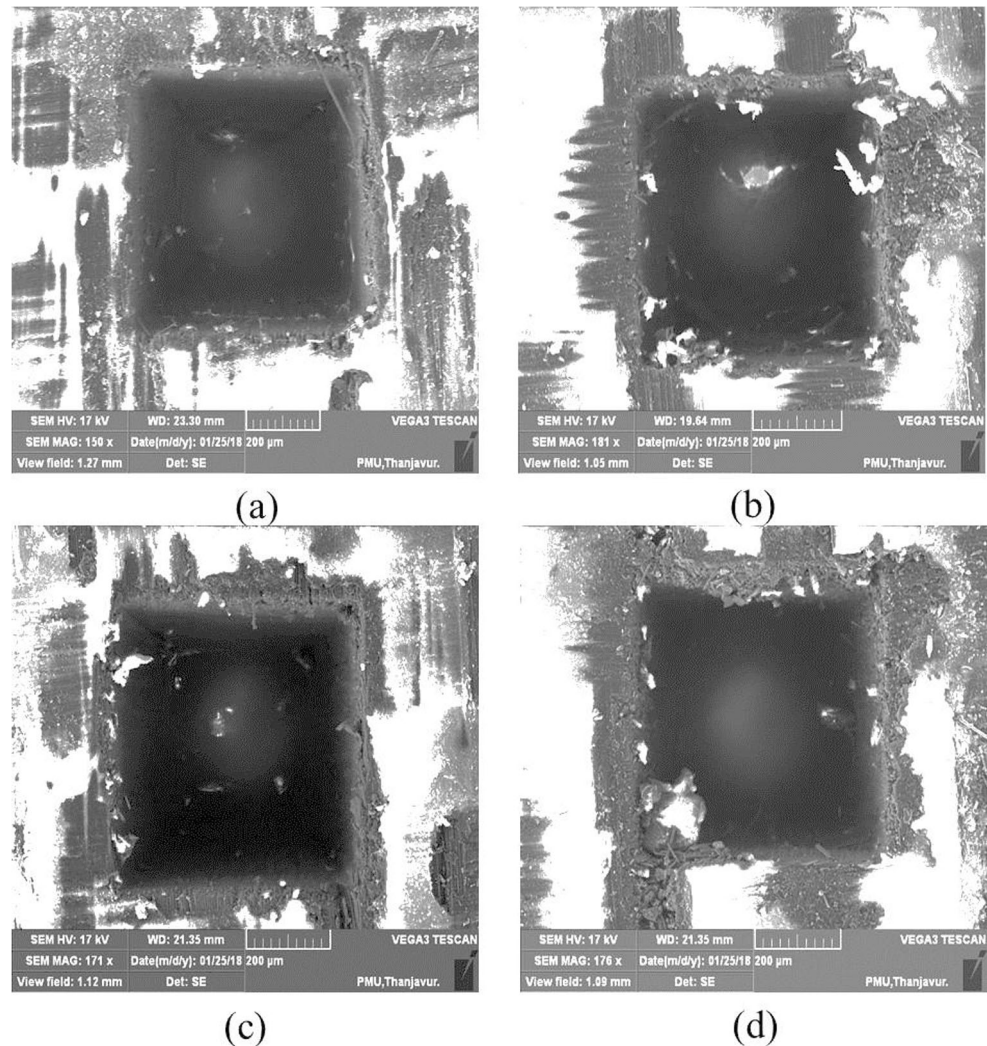
The modeling was used to find the relation between the process parameters and responses. The regression equations were developed in the squareness, hole depth, and surface roughness using statistical software. The regression equations found that the sum of square value, R-square value, and R-square adjusted values were obtained in good-fit for further prediction.

$$\begin{aligned} \text{Squareness} &= 0.996 + 0.0019 \times C_p + 0.0025 \times T_{on} - 0.00192 \times DC - 0.00045 \times I \\ S &= 0.014, R\text{-Sq} = 93.3\%, R\text{-Sq}(\text{adj}) = 90.8\% \end{aligned} \quad (10)$$

$$\begin{aligned} \text{Hole depth} &= 0.0564 + 0.023 \times C_p + 0.00154 \times T_{on} - 0.00195 \times DC - 0.00277 \times I \\ S &= 0.013, R\text{-Sq} = 98.8\%, R\text{-Sq}(\text{adj}) = 98.4\% \end{aligned} \quad (11)$$

$$\begin{aligned} \text{Surface roughness} &= 0.792 + 0.261 \times C_p + 0.0256 \times T_{on} + 0.0537 \times DC + 0.0178 \times I \\ S &= 0.267, R\text{-Sq} = 96.9\%, R\text{-Sq}(\text{adj}) = 95.8\% \end{aligned} \quad (12)$$

Fig. 9 Details of machined surface defects: (a) 4st experiment, (b) 8th experiment, (c) 12th experiment, (d) 16th experiment



The unit of different responses and input parameters are given below.

Squareness (Sq. ness) = no unit.

Hole depth (HD) = mm.

Surface roughness (SR) = μm .

Concentration of SiC (Cp) = g/l.

Pulse duration (Ton) = μs .

Current (I) = amp.

Duty cycle (DC) = %.

The contribution percentages for squareness, hole depth, and surface roughness also formed, which is shown in Fig. 10. The variance analysis found that the pulse duration has a highly contributing percentage for improving the squareness of the hole. Similarly, the concentration of SiC has a highly contributing percentage for improving the surface roughness and hole depth. Table 6 shows the experimental data related to numerical results of squareness, hole depth, and surface roughness and found that percentage deviations are an acceptable limit.

3.7 Determination of Optimum Process Parameters

To determine the optimum parameters of multiple objectives, and the ARAS method was used. The ARAS calculating procedure is presented in Table 7. The surface roughness and squareness were considered lower, whereas the hole depth was considered as higher the better. In the ARAS method, the hole depth was considered beneficial criteria, whereas the surface roughness and squareness were considered non-beneficial criteria. The non-beneficial criteria were converted into beneficial criteria by inverting the non-beneficial criteria. The responses were formed as a decision matrix. The normalization of responses was calculated based on the response objectives. The hole depth was considered 0.4 weightage whereas surface roughness and squareness were considered 0.3 weightage. The weightage of responses was selected based on the industrial expert. The weighted normalization of responses for beneficial criteria was calculated. The optimality function and degree of utility were calculated for each alternative. The rank was calculated according to the degree of

Table 6 Experimental data related with numerical results of squareness, hole depth and surface roughness

S.No.	Actual experimental data			Predicted by linear regression			Deviation in % between Actual vs linear regression		
	Sq. ness	HD	SR	Sq. ness	HD	SR	Sq. ness	HD	SR
1	1.044	0.177	1.941	1.038	0.164	2.309	0.548	7.339	-18.975
2	1.067	0.18	2.565	1.071	0.178	2.836	-0.379	1.294	-10.577
3	1.12	0.181	3.623	1.104	0.191	3.363	1.446	-5.707	7.168
4	1.132	0.197	3.652	1.137	0.205	3.890	-0.403	-4.056	-6.525
5	1.026	0.222	3.691	1.040	0.241	3.532	-1.388	-8.572	4.310
6	1.076	0.255	4.254	1.081	0.262	3.844	-0.435	-2.937	9.636
7	1.121	0.297	4.656	1.109	0.291	4.444	1.038	2.185	4.564
8	1.135	0.322	4.752	1.150	0.312	4.756	-1.304	3.115	-0.078
9	1.049	0.342	4.796	1.043	0.324	4.719	0.562	5.383	1.608
10	1.089	0.37	5.044	1.078	0.348	5.175	1.041	5.857	-2.591
11	1.145	0.394	5.374	1.128	0.389	5.201	1.521	1.353	3.221
12	1.158	0.405	5.836	1.162	0.413	5.657	-0.358	-2.077	3.072
13	1.031	0.409	5.846	1.049	0.423	5.799	-1.713	-3.367	0.802
14	1.099	0.446	6.005	1.091	0.455	6.040	0.737	-2.087	-0.585
15	1.147	0.466	6.094	1.130	0.466	6.424	1.522	0.067	-5.407
16	1.161	0.505	6.527	1.172	0.498	6.665	-0.929	1.341	-2.107

utility. The first experiment has been found as the best alternative process parameters based on the high optimality function and the first rank of the degree of utility. The best alternative process parameters for machining CFRPs were the concentration of SiC: 4 g/l, pulse duration: 15 μ s, duty cycle: 1%, and current: 2 amp. The rank-based comparisons were carried out between the GRA, DFA, and proposed algorithm and it is shown in Table 8. The best alternative process parameters were verified through a confirmation test and it is shown in Table 9. The ARAS method has improved CFRP performance. In addition, the non-contact roughness measurement was used for measuring the cross-section of surface roughness

of 0.8-mm blind micro square hole and roughness of 1.28 μ m was achieved, which was better than the confirmation test roughness value.

3.8 Comparison with Previous Studies

Comparative studies were conducted between the current study and published works, which are shown in Table 10. More works were focused to study the surface roughness and removal of burrs in the machined CFRP. No works were found that the effect of SiC concentration on squareness, hole depth, and surface roughness of CFRP was studied using EDM with the square copper electrode. The trail tests found that the through-hole was not obtained by increasing the above 16 g/l SiC due to the higher electrode wear observed. The squareness of the blind square hole of CFRP has not been studied using more researchers. More works were focusing on circular holes forming on CFRPs using EDM [7–11]. The hole depth was directly proportional to the current and pulse duration due to the heat energy. SiC powder mixed kerosene has improved the hole depth due to the increased thermal conductivity of the dielectric medium. The hole depth variation was observed between the previous study [8] and the current result due to the electrode thermal conductivity. Compared to the surface roughness of CFRP between the SiC powder mixed dielectric fluid [20, 22] and non-power mixed dielectric fluid performance [10, 11, 44], the SiC power mixed dielectric fluid produces better performance. The surface roughness of the current study was better than other studies [10, 11, 16, 17,

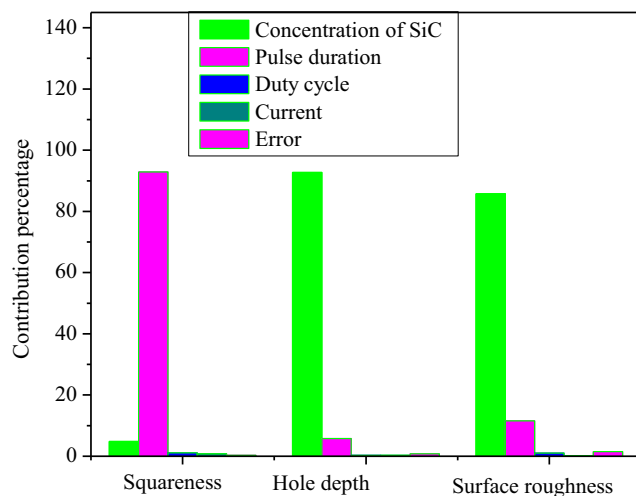
**Fig. 10** Contribution percentage for responses

Table 7 Additive ratio assessment calculations

Max or Min	Experimental results			Decision-making matrix			Normalized data			Weight normalized data			Si	Ki	Rank
	Sq. ness	HD	SR	Sq. ness	HD	SR	Sq. ness	HD	SR	Sq. ness	HD	SR			
No.	1.026	0.505	1.941	0.975	0.505	0.515	0.063	0.089	0.119	0.019	0.036	0.036	0.090	1.000	
1	1.044	0.177	1.941	0.958	0.177	0.515	0.062	0.031	0.119	0.018	0.012	0.036	0.067	0.740	1
2	1.067	0.18	2.565	0.937	0.180	0.390	0.060	0.032	0.090	0.018	0.013	0.027	0.058	0.641	6
3	1.12	0.181	3.623	0.893	0.181	0.276	0.057	0.032	0.064	0.017	0.013	0.019	0.049	0.545	16
4	1.132	0.197	3.652	0.883	0.197	0.274	0.057	0.035	0.063	0.017	0.014	0.019	0.050	0.554	15
5	1.026	0.222	3.691	0.975	0.222	0.271	0.063	0.039	0.063	0.019	0.016	0.019	0.053	0.591	12
6	1.076	0.255	4.254	0.929	0.255	0.235	0.060	0.045	0.054	0.018	0.018	0.016	0.052	0.579	14
7	1.121	0.297	4.656	0.892	0.297	0.215	0.057	0.052	0.050	0.017	0.021	0.015	0.053	0.588	13
8	1.135	0.322	4.752	0.881	0.322	0.210	0.057	0.057	0.049	0.017	0.023	0.015	0.054	0.602	11
9	1.049	0.342	4.796	0.953	0.342	0.209	0.061	0.060	0.048	0.018	0.024	0.014	0.057	0.632	10
10	1.089	0.37	5.044	0.918	0.370	0.198	0.059	0.065	0.046	0.018	0.026	0.014	0.058	0.638	7
11	1.145	0.394	5.374	0.873	0.394	0.186	0.056	0.069	0.043	0.017	0.028	0.013	0.058	0.638	8
12	1.158	0.405	5.836	0.864	0.405	0.171	0.056	0.071	0.040	0.017	0.029	0.012	0.057	0.633	9
13	1.031	0.409	5.846	0.970	0.409	0.171	0.062	0.072	0.040	0.019	0.029	0.012	0.059	0.659	5
14	1.099	0.446	6.005	0.910	0.446	0.167	0.059	0.079	0.039	0.018	0.031	0.012	0.061	0.672	4
15	1.147	0.466	6.094	0.872	0.466	0.164	0.056	0.082	0.038	0.017	0.033	0.011	0.061	0.677	3
16	1.161	0.505	6.527	0.861	0.505	0.153	0.055	0.089	0.035	0.017	0.036	0.011	0.063	0.697	2

20, 22, 44] due to the addition of SiC to kerosene to provide better results. The better copper electrode wear was observed compared to previous results [7, 44] due to the electrode thermal conductivity.

Table 8 Rank comparison based on the GRA, DFA and proposed algorithm

S. No.	GRA [49]	DFA [50]	Proposed algorithm
1	1	1	1
2	2	2	6
3	4	5	16
4	5	7	15
5	3	3	12
6	7	4	14
7	9	8	13
8	11	11	11
9	8	6	10
10	10	9	7
11	13	12	8
12	14	15	9
13	6	10	5
14	12	13	4
15	15	14	3
16	16	16	2

4 Conclusions

A great effort is made to study the concentration of SiC powder and EDM parameters on squareness, hole depth, and surface roughness on square blind hole CFRP using EDM with the square copper electrode. The conclusions have the following as.

- The percentage of concentration of SiC and pulse duration greatly affect the squareness, hole depth, surface roughness, and electrode wear length.
- A corner radius has formed on the machined square holes due to the area effect and the skin effect.
- Low thermal heat energy has been used for producing the minimum surface roughness and minimum thermal damage.
- Deformed electrode wears were formed in all the CFRP machined corners due to unstable sparking produced.
- Cutting edge irregularity has formed in the machined edges.
- Regression models for EDMs are a good fit for prediction.
- ARAS method provides consistent results with other standard methods and improved the performance measures.

Acknowledgments The authors thank the COVAI EDM at Coimbatore for providing a machining facility. The authors are also thankful to Periyar Maniammai Institute of Science & Technology at Vallam for providing a scanning electron microscopy facility.

Table 9 Confirmation experiment

	Raw Data	Experiment
Conditions	Cp=4 g/l/ Ton=15 μ s/ DC=1%/ I=1 amp	Cp=4 g/l/ Ton=15 μ s/ DC=1%/ I=1 amp
Squareness (–)	1.044	1.015
Hole depth (mm)	0.177	0.234
Surface roughness (μ m)	1.941	1.231
Ki	0.740	0.818
Improvement in Ki=0.078		

Contributions PV Arul Kumar: Conceptualization, Methodology, Writing Reviewing discussion and Editing. J. Vivek: computation, Methodology, Software, Writing discussion and N. Senniangiri: Conceptualization and analysis, Writing-review, writing the manuscript, Methodology, Software, and writing – discussion, S. Nagarajan: review manuscript language, B. Alshahrani: review manuscript language, K. Chandrasekaran: review manuscript language.

Funding The authors did not receive support from any organization for the submitted work.

Data Availability The available data and material had been used and discussed in the manuscript.

Declaration

Consent to Participate All persons named as authors in this manuscript have participated in the planning, design, and performance of the research and the interpretation of the results.

Consent for Publication All authors have endorsed the publication of this research.

Ethics Declarations The manuscript has not been published elsewhere and it has not been submitted simultaneously for publication elsewhere.

Declaration of Competing Interest The authors declare that they have no known competing financial interests or personal relationships that could have appeared to influence the work reported in this paper.

References

- Samal P, Babu DM, Kiran SV, Surekha B, Vundavilli PR, Mandal A (2020). Study of microstructural and machining characteristics of hypereutectic Al-Si alloys using wire-EDM for photovoltaic application. *Silicon*, pp.1–13
- Phan NH, Muthuramalingam T (2020) Multi criteria decision making of vibration assisted EDM process parameters on machining silicon steel using Taguchi-DEAR methodology. *Silicon*, pp.1-7
- Muthuramalingam T, Saravanakumar D, Babu LG, Phan NH, Pi VN (2019) Experimental investigation of white layer thickness on EDM processed silicon steel using ANFIS approach. *Silicon*, pp.1-7

Table 10 Comparison of present results with published literatures

R.No.	Materials/ Additives	Dielectric medium	Electrode Material/size	Cp (g/l)	Ton (μ s)	DC (%)	I (amp)	Sq. ness	Hole depth (mm)	SR (μ m)	Tool Wear (mm)
[7]	CFRP/–	Oil	WC / 0.3 mm	–	50	–	–	–	0.2	8	0.025
[8]	CFRP/–	EDM oil	WC/0.110 mm	–	–	–	–	–	1.2	–	–
[9]	CFRP/–	–	Cu/0.5	–	–	–	–	–	0.25	–	–
[10]	CFRP/–	Esso mentor	Cu/10 mm	–	25–160	–	1–4	–	–	15–45	–
[11]	CFRC/–	Castrol	Cu/4.42 mm	–	200	–	1.5	–	–	5.14	–
[16]	CFRP/–	kerosene	Gr/ 1 mm	–	100	–	5	–	–	4.8	–
[17]	CFRP/–	EDM oil	Cu/2 mm	–	70	–	2	–	–	4	–
[20]	Die steel/SiC	EDM oil	Cu/square	6	150	90	3	–	–	3	–
[21]	Titanium/SiC	EDM oil	Cu/42 mm	25	2–20	80	0.1, 1	–	2.6	–	–
[22]	Titanium/SiC	–	–	5–20	25	–	–	–	–	6.77	–
[34]	CFRP/–	Kerosene	Cu/8 mm	–	50	–	–	–	–	7	1.2 g/min
Current experimental results											
Present work	CFRP/SiC	kerosene	Cu/0.8 mm square electrode	4	15	1	2	1.015	0.234	1.231	0.31–1.168

4. Ramanujam N, Dhanabalan S, Raj Kumar D, Jeyaprakash N (2021) "Investigation of micro-hole quality in drilled CFRP laminates through CO2 laser." *Arab J Sci Eng* 1–19
5. Raj Kumar D, Jeyaprakash N, Yang C, Sivasankaran S (2020) "Optimization of drilling process on carbon-fiber reinforced plastics using genetic algorithm." *Surface Review and Letters* 2050056
6. Raj Kumar D, Jeyaprakash N, Yang C-H, Ramkumar KR (2020) Investigation on drilling behavior of CFRP composites using optimization technique. *Arab J Sci Eng* 45:8999–9014
7. Teicher U, Müller S, Münzner J, Nestler A (2013) Micro-EDM of carbon fibre-reinforced plastics. *Procedia Cirp* 6:320–325
8. Kumar R, Agrawal PK, Singh I (2018) Fabrication of micro holes in CFRP laminates using EDM. *J Manuf Process* 31:859–866
9. Park SH, Kim G, Lee W, Min BK, Lee SW and Kim TG (2015). Microhole machining on precision CFRP components using electrical discharging machining. In 20th international conference on composite materials, Copenhagen, Denmark
10. Lau WS, Wang M, Lee WB (1990) Electrical discharge machining of carbon fibre composite materials. *Int J Mach Tools Manuf* 30(2): 297–308
11. Gourgouletis K, Vaxevanidis NM, Galanis NI, Manolakos DE (2011) Electrical discharge drilling of carbon fibre reinforced composite materials. *Int J Mach Mach Mater* 10(3):187–201
12. George PM, Raghunath BK, Manocha LM, Warriar AM (2004) EDM machining of carbon-carbon composite—a Taguchi approach. *J Mater Process Technol* 145(1):66–71
13. Kurniawan R, Kumaran ST, Prabu VA, Zhen Y, Park KM, Kwak YI, Islam MM, Ko TJ (2017) Measurement of burr removal rate and analysis of machining parameters in ultrasonic assisted dry EDM (US-EDM) for deburring drilled holes in CFRP composite. *Measurement* 110:98–115
14. Islam MM, Li CP, Won SJ, Ko TJ (2017) A deburring strategy in drilled hole of CFRP composites using EDM process. *J Alloys Compd* 703:477–485
15. Mazarbhuiya RM, Dutta H, Debnath K, Rahang M (2020) Surface modification of CFRP composite using reverse-EDM method. *Surfaces and Interfaces* 18:100457
16. Guu YH, Hocheng H, Tai NH, Liu SY (2001) Effect of electrical discharge machining on the characteristics of carbon fiber reinforced carbon composites. *J Mater Sci* 36(8):2037–2043
17. Lodhi BK, Verma D, Shukla R (2014) Optimization of machining parameters in EDM of CFRP composite using Taguchi technique. *Int J Mech Eng Technol* 5(10):70–77
18. Niamat M, Sarfraz S, Aziz H, Jahanzaib M, Shehab E, Ahmad W, Hussain S (2017) Effect of different dielectrics on material removal rate, electrode wear rate and microstructures in EDM. *Procedia Cirp* 60:2–7
19. Das S, Paul S, Doloi B (2020) Feasibility assessment of some alternative dielectric mediums for sustainable electrical discharge machining: a review work. *J Braz Soc Mech Sci Eng* 42(4):1–21
20. Tripathy S, Tripathy DK (2017) Surface characterization and multi-response optimization of EDM process parameters using powder mixed dielectric. *Materials Today: Proceedings* 4(2):2058–2067
21. Chow HM, Yang LD, Lin CT, Chen YF (2008) The use of SiC powder in water as dielectric for micro-slit EDM machining. *J Mater Process Technol* 195(1–3):160–170
22. Öpöz TT, Yaşar H, Ekmekci N, Ekmekci B (2018) Particle migration and surface modification on Ti6Al4V in SiC powder mixed electrical discharge machining. *J Manuf Process* 31:744–758
23. Chow HM, Yan BH, Huang FY, Hung JC (2000) Study of added powder in kerosene for the micro-slit machining of titanium alloy using electro-discharge machining. *J Mater Process Technol* 101(1–3):95–103
24. Jung JH, Kwon WT (2010) Optimization of EDM process for multiple performance characteristics using Taguchi method and Grey relational analysis. *J Mech Sci Technol* 24(5):1083–1090
25. Chen ST, Yeh MC (2016) Development of an in-situ high-precision micro-hole finishing technique. *J Mater Process Technol* 229:253–264
26. Liu Q, Zhang Q, Zhu G, Wang K, Zhang J, Liu Q et al (2016) Effect of electrode size on the performances of micro-EDM. *Mater Manuf Process* 31:391–396
27. Al-Ahmari AMA, Rasheed MS, Mohammed MK, Saleh T (2016) A hybrid machining process combining micro-EDM and laser beam machining of nickel – titanium-based shape memory alloy. *Mater Manuf Process* 31:447–455
28. Kumar H, Davim JP (2011) Role of powder in the machining of Al-10% SiCp metal matrix composites by powder mixed electric discharge machining. *J Compos Mater* 45(2):133–151
29. Mohri N, Saito N, Higashi M (1991) A new process of finish machining on free surface by EDM methods. *Annals of CIRP* 40(1): 207210
30. Vishwakarma UK, Dvivedi A, Kumar P (2014) Comparative study of powder mixed EDM and rotary tool EDM performance during machining of Al-SiC metal matrix composites. *Int J Mach Mach Mater* 16(2):113–128
31. Islam MM, Li CP, Ko TJ (2017) Dry electrical discharge machining for deburring drilled holes in CFRP composite. *International Journal of Precision Engineering and Manufacturing-Green Technology* 4(2):149–154. <https://doi.org/10.1007/s40684-017-0018-x>
32. Isbilir O, Ghassemieh E (2013) Comparative study of tool life and hole quality in drilling of CFRP/titanium stack using coated carbide drill. *Mach Sci Technol* 17:380–409
33. Elsit, N.M. and Noordin, M.Y., 2017. Experimental investigations into the effect of process parameters and Nano-powder (Fe2O3) on material removal rate during micro-EDM of co-Cr-Mo. In *Key engineering materials* (Vol. 740, pp. 125-132). Trans tech publications ltd.
34. Debnath K, Dutta H, Sarma DK (2021). Influence of different tool materials on the machining performance in μ ED-milling of CFRP composites. In *machining and machinability of Fiber reinforced polymer composites* (pp. 207-224). Springer, Singapore
35. Abdallah R, Soo SL, Hood R (2021) The influence of cut direction and process parameters in wire electrical discharge machining of carbon fibre-reinforced plastic composites. *Int J Adv Manuf Technol* 113(5):1699–1716
36. Devi, L., Paswan, K., Chattopadhyaya, S. and Pramanik, A., 2021. Influence of low-frequency vibration in die sinking EDM: a review. In *IOP conference series: materials science and engineering* (Vol. 1104, no. 1, p. 012010). IOP publishing
37. Dutta H, Debnath K, Sarma DK (2021) Improving the micro-electrical-discharge drilling performance of carbon fibre-reinforced polymer: role of assisting-electrode and shaped tool. *Int J Mach Mach Mater* 23(2):191–207
38. Hashizu M, Hayakawa S, Itoigawa F (2020) Influence of short-circuiting on machined surface quality in electrical discharge machining of carbon fiber reinforced plastics. *Procedia CIRP* 95: 403–407
39. Kumaran VU, Kliuev M, Billeter R, Wegener K (2020) Influence of carbon based fillers on EDM machinability of CFRP. *Procedia CIRP* 95:437–442
40. Dutta H, Debnath K, Sarma DK (2020) Multi-objective optimization of hole dilation at inlet and outlet during machining of CFRP by μ EDM using assisting-electrode and rotating tool. *Int J Adv Manuf Technol* 110(9):2305–2322
41. Makudapathy C, Sundaram M (2020) High aspect ratio machining of carbon Fiber reinforced plastics by electrical discharge machining process. *Journal of Micro and Nano-Manufacturing*
42. Dutta H, Debnath K, Sarma DK (2021). Investigation on cutting of thin carbon fiber-reinforced polymer composite plate using sandwich electrode-assisted wire electrical-discharge machining.

- Proceedings of the institution of mechanical engineers, part E: journal of process mechanical engineering, p.09544089211013318
43. Wu C, Cao S, Zhao YJ, Qi H, Liu X, Liu G, Guo J, Li HN (2021) Preheating assisted wire EDM of semi-conductive CFRPs: principle and anisotropy. *J Mater Process Technol* 288:116915
 44. Selvakumar G, Sarkar S, Mitra S (2012) Experimental investigation on die corner accuracy for wire electrical discharge machining of Monel 400 alloy. *Proceedings of the Institution of Mechanical Engineers, Part B: Journal of Engineering Manufacture* 226(10):1694–1704
 45. Balamurugan K, Uthayakumar M, Ramakrishna M, Pillai UTS (2020) Air jet Erosion studies on mg/SiC composite. *Silicon* 12(2):413–423
 46. Chinnamahammad Bhasha A, Balamurugan K (2020) Studies on Al6061 nanohybrid composites reinforced with SiO₂/3x% of TiC-a agro-waste. *Silicon*, pp.1-14
 47. Garikapati P, Balamurugan K, Latchoumi TP and Malkapuram R (2020). A cluster-profile comparative study on machining AlSi 7/63% of SiC hybrid composite using agglomerative hierarchical clustering and K-means. *Silicon*, pp1–12
 48. Balamurugan K, Uthayakumar M, Sankar S, Hareesh US, Warriar KGK (2020) Process optimisation and exhibiting correlation in the exploitable variable of AWJM. *Int J Mater Prod Technol* 61(1):16–33
 49. Balamurugan K, Uthayakumar M, Sankar S, Hareesh US, Warriar KGK (2017) Mathematical modelling on multiple variables in machining LaPO₄/Y₂O₃ composite by abrasive water jet. *Int J Mach Mach Mater* 19(5):426–439
 50. Antil P, Kumar Antil S, Prakash C, Królczyk G, Pruncu C (2020). Multi-objective optimization of drilling parameters for orthopaedic implants. *Measurement and Control*, p.0020294020947126
 51. Kharb SS, Antil P, Singh S, Antil SK, Sihag P, Kumar A (2020) Machine learning-based Erosion behavior of silicon carbide reinforced polymer composites. *Silicon*. 13:1113–1119. <https://doi.org/10.1007/s12633-020-00497-z>
 52. Antil SK, Antil P, Singh S, Kumar A, Pruncu CI (2020) Artificial neural network and response surface methodology based analysis on solid particle Erosion behavior of polymer matrix composites. *Materials* 13(6):1381
 53. Bachchan AA, Das PP, Chaudhary V (2021) Effect of moisture absorption on the properties of natural fiber reinforced polymer composites: a review. *Materials Today: Proceedings*
 54. Bañon F, Sambruno A, González-Rovira L, Vazquez-Martinez JM, Salguero J (2021) A review on the abrasive water-jet machining of metal–carbon fiber hybrid materials. *Metals* 11(1):164
 55. Prasad KS, Chaitanya G (2021). Optimization of process parameters on surface roughness during drilling of GFRP composites using taguchi technique. *Materials today: proceedings*, 39, pp.1553-1558
 56. Kumaran ST, Ko TJ, Uthayakumar M, Islam MM (2017) Prediction of surface roughness in sabrative water jet machining of CFRP composites using regression analysis. *J Alloys Compd* 724:1037–1045
 57. Kumaran ST, Ko TJ, Kurniawan R, Li C, Uthayakumar M (2017) ANFIS modeling of surface roughness in abrasive waterjet machining of carbon fiber reinforced plastics. *J Mech Sci Technol* 31(8):3949–3954
 58. Thakur RK, Singh KK, Ramkumar J (2021) Impact of nanoclay filler reinforcement on CFRP composite performance during abrasive water jet machining. *Materials and Manufacturing Processes*, pp:1–10
 59. Dahooie JH, Zavadskas EK, Abolhasani M, Vanaki A, Turskis Z (2018) A novel approach for evaluation of projects using an interval-valued fuzzy additive ratio assessment (ARAS) method: a case study of oil and gas well drilling projects. *Symmetry* 10(2):45
 60. Dhanabalan S, Sivakumar K, Narayanan CS (2013) Optimization of machining parameters of EDM while machining Inconel 718 for form tolerance and orientation tolerance
 61. Dhanabalan S, Sivakumar K, Sathiyaraj Narayanan C (2014) Analysis of form tolerances in electrical discharge machining process for Inconel 718 and 625. *Mater Manuf Process* 29(3):253–259
 62. Yadav RN (2019) Electro-chemical spark machining–based hybrid machining processes: research trends and opportunities. *Proc Inst Mech Eng B J Eng Manuf* 233(4):1037–1061
 63. Jafferson JM, Hariharan P, Ram Kumar J (2014) Effects of ultrasonic vibration and magnetic field in micro-EDM milling of non-magnetic material. *Mater Manuf Process* 29(3):357–363
 64. Jeyaprakash N, Yang CH, Raj Kumar D (2020) Machinability study on CFRP composite using Taguchi based grey relational analysis. *Materials Today: Proceedings* 21(3):1425–1431
 65. Rajkumar D, Ranjithkumar P and Narayanan CS (2017) Optimization of machining parameters on microdrilling of CFRP composites by Taguchi based desirability function analysis

Publisher's Note Springer Nature remains neutral with regard to jurisdictional claims in published maps and institutional affiliations.



A Study of Added SiC Powder in Kerosene for the Blind Square Hole Machining of CFRP Using Electrical Discharge Machining

PV Arul Kumar¹ · J. Vivek² · N. Senniangiri³ · S. Nagarajan⁴ · K. Chandrasekaran⁵

Received: 26 March 2021 / Accepted: 28 June 2021
© Springer Nature B.V. 2021

Abstract

Carbon Fiber Reinforced Polymers (CFRPs) have been applied potentially for various application components owing to their lightweight and better mechanical properties. However, the machining of CFRP has been observed to be poor machinability due to the properties of the CFRP composites. Micro-feature fabricating on CFRP macro-component is a challenging task due to the selection of inadequate process parameters and machines. However, micron-level blind square holes are required in CFRPs for proposing the applications of micro-robotics, micro-vibration measurements, and micro-detection of cracking. These square holes produced on CFRP have the difficult task of being machined using the Electrical Discharge Machining (EDM) process. In this research, the effects of concentration of silicon carbide, pulse duration, duty cycle, and current on squareness, hole depth, and surface roughness of CFRPs are analyzed using Electrical Discharge Machining (EDM) with the square copper electrode. The input parameters, the various percentage of concentration of silicon carbide, pulse duration, duty cycle, and current for EDM are selected. The responses, squareness, hole depth, and surface roughness are considered. Also, an electrode wear length and surface defects have been analyzed. The modeling has been performed for selected responses. Additive Ratio Assessment (ARAS) is used for obtaining optimum parameters. The overall analysis found that the silicon carbide concentration and pulse duration are greatly affected all the responses. Also, the square electrodes produced unstable spark phenomena in the EDM process.

Keywords CFRP · EDM · Silicon carbide · Squareness · Depth

1 Introduction

Carbon Fiber Reinforced Polymers (CFRPs) are used in aerospace, satellite, electronic field, and commercial parts. The reasons for using these CFRPs are low density, high strength, low friction coefficient, high toughness, and good wear resistance. Square holes are required in CFRPs for proposing the applications of micro-robotics, micro-vibration measurements, micro-detection of cracks, micron-level

relative humidity measurements, micron-level - thermal strain measurements, micro - level -temperature measurements, detection of micro - delamination, and micro-fiber optics. Thereby, the square holes were fabricated on CFRP by using EDM [1–3], laser machining [4], mechanical drilling [5, 6], and micro-EDM [7]. Also, the square hole is mostly used in the precision manufacturing sector for manufacturing the micron-level square in the 3D micro-components for microfluid transportation purposes and

✉ PV Arul Kumar
arulumarveera@gmail.com

J. Vivek
vivekdynamech18@gmail.com

N. Senniangiri
senniagirinarajan1987@gmail.com

S. Nagarajan
arsnagarajan@gmail.com

K. Chandrasekaran
kchandrasekaran1984@gmail.com

¹ Department of Mechanical Engineering, Bharath Niketan Engineering College, Aundipatty, Tamil Nadu 625536, India

² Department of Mechanical Engineering, Solamalai College of Engineering, Madurai, Tamil Nadu 625020, India

³ Department of Mechanical Engineering, Nandha Engineering College, Erode, Tamil Nadu 628052, India

⁴ Department of Mechanical Engineering, College of Engineering and Technology, Mettu University, Post Box. No 318, Mettu, Ethiopia

⁵ Department of Mechanical Engineering, MAM School of Engineering, Trichy, Tamil Nadu 621105, India

increasing the heat transfer rate with acceptable dimensional accuracy. Among the various machining processes, the non-contact and stress-free machining process for EDM is selected to perform machining on CFRP. The performance measures of CFRPs are highly associated with many factors such as electrode materials (copper, graphite, tungsten carbide, etc.), electrode dimensions (micron and micron size), polarity, types of dielectric mediums (kerosene, EDM oil, distilled water, etc.) and additives in dielectric mediums (SiC, Si, Cu, etc.) and selection of process parameters (pulse duration, pulse interval, etc.). The selection of electrode materials is an important task for obtaining better performance measures. Hence, tungsten carbide electrodes were fabricated by using a wire electric discharge grinding. The 0.110 mm diameter-fabricated electrodes were used for providing the holes on CFRP by using EDM and a 1.2 mm depth of cut was achieved [8]. In another work, 0.5 mm diameter copper electrodes were fabricated for providing blind holes on CFRP by using EDM and 0.25 mm depth of cut was achieved [9]. To evaluate the different electrode material performance over the CFRP machining, copper and graphite electrodes were used on CFRP by using EDM. The results found that copper electrodes gave better performance than graphite electrodes based on the electrode wear and surface finish [10]. Using copper electrodes for making blind holes on CFRP was performed using 1.5 amp current and 200 μ s pulse duration and 5.14 μ m surface roughness was achieved [11]. The copper electrode wear rate was analyzed for drilling on CFRP by using 1 amp current and 150 μ s pulse duration and 0.0056 mg/min electrode wear rate was observed [12]. To reduce the burr formation of CFRP drilled holes, the copper, brass, and aluminum electrodes were selected for drilling on CFRP by using EDM. The results found that the copper electrode gave better results than other electrodes [13]. In another work, burr formation was also reduced using EDM with different electrodes such as aluminum, brass, steel, and copper were selected for processing on CFRP. The results found that the copper electrode produced better results than other electrodes [14]. Besides, the selection of EDM parameters is also important to improve performance measures. The current was directly proportional to the tool wear rate by EDM drilling on CFRP [15]. Hence, the low electrode wear was observed by lowering the current. The 5 amp current and 100 μ s pulse duration were used to obtain the 4.8 μ m surface roughness of CFRP. The results found that the current was increased with an increase in the surface roughness. Hence, the low current is recommended for obtaining low surface roughness and less thermal damages [16]. The approximately 4 μ m surface roughness was obtained using a pulse duration of 70 μ s and a current of 2 amp in EDM drilling [17]. The Powder-Mixed Electric Discharge Machining (PMEDM) is also used for improving the performance measures. The dielectric medium has also played an

important role in improving machining characteristics by alternating ionization, heat dissipation, and dielectric flushing. Besides, dielectric medium physical parameters such as breakdown strength, flash point, thermal conductivity, pressure, flushing velocity, density, and viscosity influence the performance of EDM. Hence, these properties are directly associated with the selection of hydrocarbon dielectric fluid, water-based dielectric fluid, and gas-based dielectric fluid. The special technological behaviors of hydrocarbon dielectric fluids are small tool wear, high metal removal, and no corrosion of sample, low flash point, and no deionization necessary. Therefore, the hydrocarbon dielectric fluid of kerosene has been selected as a dielectric medium for obtaining more stable and effective machining performance than another dielectric medium [18]. Also, the dielectric medium performances are improved by adding different types of additives such as carbon, aluminum, copper, nickel, silicon, graphite, tungsten, and titanium powder [19]. Among the various additives, SiC powder is selected as an additive because of its superior properties. Hence, the effects of PMEDM process parameters on squareness, hole depth, and surface roughness of CFRPs are focused on it. The reasons for selecting the PMEDM are enlargement of the discharge gap, widening of discharge passage, multiple discharges, and influences of powder properties on machining characteristics. The surface roughness was reduced by increasing the concentration of SiC powder added to EDM oil [20]. Similarly, the material removal depth was decreased by increasing the concentration of SiC powder added to pure water [21]. SiC powder ranging from 5 g/l to 20 g/l was added to deionized water for improving the surface roughness. The result found that the 25 μ s pulse duration produced the 6.77 μ m surface roughness and it was a higher surface roughness value compared to 50 μ s pulse duration due to the uneven distribution of discharges [22]. The material removal depth and surface roughness were analyzed by adding Al to kerosene and SiC to kerosene and kerosene. The result identified the addition of Al/SiC to kerosene-improved performance measures compared to kerosene [23]. Kerosene is one of the main dielectric fluid mediums for machining micro-hole on steel and produces effective machining on steel using EDM. The results found that the entrance diameter was greater than the exit diameter and the tungsten carbide electrode wear was 273 μ m obtained [24]. The hybrid machining processes were also used to fabricate the micro-holes of diameter 250 μ m on steel using micro-EDM with 100 V voltage and 1500 pF capacitance [25]. The electrode diameter greatly affected the MRR, TWR, and taper angle. Increasing in the MRR, TWR, and taper angle were observed by increasing the electrode diameter [26]. Micro-hole comparative studies were made between the laser and micro-EDM on nickel-based superalloy by using selected optimum process parameters. The results found that micro-EDM has

produced better hole geometry than laser processes [27]. In another strategy, the $0.32\ \mu\text{m}$ surface roughness of AA-10%SiCp MMC was achieved by using powder concentration $4\ \text{g/L}$, pulse duration $100\ \text{ms}$, current $3\ \text{A}$, and voltage $50\ \text{V}$ [28]. Comparative surface roughness was studied between the aluminum powder and silicon powder in the machining of EDM by using selected working conditions. The results found that $2\ \text{mm}$ surface roughness was obtained and an aluminum powder gave a greater influence on surface roughness than silicon powder [29]. The performance of PMEDM and Rotary-EDM were studied based on the material removal rate (MRR) and tool wear rate (TWR). The results identified that the PMEDM process gave better performance than die-sinking EDM [30]. The EDM process can also be used for removing the burr from the machined CFRP due to the spark energy. The results found that oxygen showed higher MRR than negative polarity. Moreover, EDM oil gave a more effective performance for unwanted burrs removal from the EDM [31]. The coated carbide drill was used for machining of CFRP based on the tool life and hole quality CFRP/titanium stack. The output of the result found that the CFRP/titanium stack produced poorer quality than the individual machining of material [32]. The performance nano-powder of Fe_2O_3 over the Co-Cr-Mo sample was studied by using micro-EDM. The results identified that material depth was significantly improved by adding $2\ \text{g/l}$ of nanopowder in the dielectric medium [33]. To reduce the machining time, the morphology of the machined surface, and deviation in channel width, the assisting-electrode method was used for creating micro-channels (depth: $400\ \mu\text{m}$ and length: $3000\ \mu\text{m}$) on CFRP using brass and copper of $960\ \mu\text{m}$ in diameter. The SEM results found that peripheral surface damage, spalling, fiber breakage, and debris accumulation were observed [34]. Influencing in the cut direction and process parameters on depth of cut and surface roughness were studied and found that a 16% increasing in the material removal rate was observed when machining parallel to fiber direction compared to cutting perpendicular to the fibers, which was attributed to the higher electrical conductivity of the workpiece along the fiber length leading to greater discharge energies [35]. The low-frequency vibration-assisted EDM on CFRP was also used for improving machining efficiency and stability [36]. The shape of electrode and assisting-electrode were used for improving the micro-electrical-discharge drilling performance of CFRP resulting in the voltage was a significant factor that affecting the performance measures [37]. The influence of a short circuit on machined surface quality CFRP was investigated using EDM and found that the machining was stopped when the EDM in an unstable state due to the short circuit [38]. To increasing the material removal rate of CFRP and reducing in tool wear, carbon black and graphite (fillers) were added to the matrix for increasing the electrical and thermal

conductivity and the result found that high machinability, low thermal damage, and good surface quality were observed [39]. The μEDM integrated with a rotary tool and assisting-electrode was used for efficient spark generation in EDM. The result found that the material removal mechanism was a complex phenomenon where sparking happened both at the side surface and end face of the tool [40]. The effect of EDM process parameters such as feed rate and voltage on the hole quality was studied by micro-EDM and found that the microhole of $2500\ \mu\text{m}$ deep was achieved in CFRP [41]. The sandwich assisting-electrode method was used for cutting off thin CFRP and found that matrix cracking, breakage of carbon fibers, and fiber-matrix debonding were observed [42]. The preheating method was used for machining CFRP and found that very small, thin, and deep microfeature creating on CFRP was observed for enhancing their micro-features performance and function [43]. The previous studies found that the addition of powder particles in the dielectric medium effects on MMCs have also been used for improving the process performance of different work materials [44–49]. The optimization tools such as Taguchi's method, support vector machine, artificial neural network, and response surface methodology have also been used for improving the performance measures of polymer-based composites [50–52].

Few works have been found that effects of micron-level square shape electrodes with EDM process parameters and various percentages of SiC powder-mixed in the kerosene medium effects on squareness, hole depth, and surface roughness of CFRPs have been studied. More works have focused on macron-level circular hole profile processing on CFRP using EDM. Hence, the blind square holes in CFRPs have been focused on using the EDM parameters with a concentration of SiC powder. The CFRP application component requires blind-square holes during their usage. But, the blind square holes produced on CFRP have a difficult task by using electrical discharge machining process parameters with micron-level copper electrodes due to the variations in the material properties of carbon fiber and epoxy resin. Moreover, blind holes produced on CFRP are a challenging task due to the low melting point of copper electrodes produced by high electrode wear in the micro-scale machining of CFRP. Therefore, the machinability of CFRP has been analyzed on the basis that the squareness, hole depth, and surface roughness are focused on it. The micron-level square blind holes fabricating on CFRPs are the primary task. Hence, squareness and hole depth are important geometrical features for affecting the functionality of the relative motion between the machined parts. Therefore, these responses are mainly focused on it. The most contributing factor is identified by analysis of variance. Additive Ratio Assessment (ARAS) is used for obtaining optimum parameters. The electrode wear and surface defects are also analyzed. Finally, a comparative

analysis is carried out between a present study and previous results.

2 Material and Methods

2.1 Fabrication of CFRP

The autoclave process is normally used for producing CFRP laminates and this process is carried out under a pressurized vessel for applying pressure and heat to both parts that have been sealed in a vacuum bag. A prepreg carbon fiber-epoxy material is laid out on a work table to ensure that fiber orientation meets the design requirement, where the prepreg material consists of unidirectional long-carbon fibers in a partially cured epoxy matrix. The pieces of the prepreg material are cut out and placed on top of each other on a shaped tool to form a laminate. The layers could be placed in different directions to produce the desired strength pattern since the highest strength of each layer is in the direction parallel to the fibers. After the required number of layers has been properly placed, the tooling and the attached laminate are vacuum bagged, for removing the entrapped air from the laminated part. Finally, the vacuum bag and the tooling are put into an autoclave for the final curing of the epoxy resin. After removal from the autoclave method, the composite material is ready for further finishing operations.

2.2 Micro-Drilling

The micro-holes in the form of square shapes were performed on CFRP, a problematic task owing to their properties of composites. Table 1 shows the properties of SiC, kerosene, copper electrode, carbon fiber, and epoxy resin. Specification of EDM drill is shown in Table 2. Table 3 shows the selection of EDM process parameters and difficulties faced by selecting the EDM process parameters. Therefore, the blind square hole was performed on CFRP using EDM. These square holes produced on CFRP were a difficult task of being machined using the Electrical Discharge Machining (EDM) process due to the need for

Table 2 Technical specification of EDM drill

Machine tool	value
Work table	400 × 400
Max electrode length	400 mm
Size of electrode diameter	0.3 to 3.0 mm
Maximum drill depth	250 mm
Maximum coolant pressure	60 kg/cm ²
Maximum weight of work piece	300 kg
Work tank	690 × 470 × 83 mm
Net weight	750 kg
Connected load	2 KVA
Input power supply	3 phase, AC 415 V, 50 Hz
Maximum machining current	20 amp

selection of proper parameters, its associated performance measures, and variations in the CFRP material properties. Electrical Discharge Machining (EDM) has been used to machine difficult to cut material and the process is not related to the hardness of the material. The EDM and Abrasive Jet Machining (AJM) processes have also been used for machining CFRP. Moreover, the strength of CFRP is reduced after AJM processing due to the more water-absorbing properties of CFRP [53]. The usage of abrasive water jets for machining CFRP is not considered due to the delamination, burr, fiber pull-out, poor geometrical shape, dimension accuracy, and kerf width reduction [43], the more striation formation on the machined surface [54], abrasive grain size greatly affected the surface roughness [55], approximately the surface roughness varying from 3 to 4 μm [56, 57], low penetration depth [58]. Hence, compared to previous works [54–58], the abrasive water jet machine is producing lower performance measures compared to the EDM process [7, 10, 11, 16, 22]. Therefore, EDM is selected for processing on CFRP. The kerosene dielectric pressure was 0.7 kg/cm² fixed as constant. According to the design of the experiment, the blind square holes were performed on CFRP for studying the effects of the parameters on squareness (Sq. ness), hole depth (HD), and Surface Roughness (SR). The schematic line diagram and photocopy of EDM are shown in Fig. 1.

Table 1 Properties of SiC, kerosene, copper electrode, carbon fiber and epoxy resin

Material	Specific heat (J/kg K)	Breakdown Strength (kV/mm)	Density (g/cm ³)	Electrical Resistivity (μΩ cm)	Flash point (°C)	Melting Point (°C)	Thermal Conductivity (W/mK)
Silicon carbide (SiC)	510–650	–	3.22	1013	–	2730	300
Kerosene	2100	24	0.81	–	37–65	–	0.14
Copper	0.39	–	8.93	0.009–0.07 μΩ × 10 ⁻⁴	–	1083	401
Carbon fiber	2020 at 1230 °C	–	2.267	–	–	3652–3697	0.17–0.79
Epoxy resin	1110 J/kg °C	–	1.1–1.4	–	–	140	0.2

Table 3 Selection of process parameters

Parameters	Units/ Symbol	Levels				Machine limits/ From the literature papers/ Problems observed
		1	2	3	4	
Concentration of SiC	g/l / Cp	4	8	12	16	[59, 60]
Pulse duration	μs / Ton	15	30	45	60	Machine limit
Duty cycle	% / DC	1	3	5	7	Slow material removal rate
Current	amp/ I	2	4	6	8	Higher electrode wear observed by rising above 8 amp

Figure 2 shows the EDAX for CFRP composites and found that the chemical compositions of CFRPs identified by EDX are 84.12% C, 0.20% Si, 14.92% O, 0.28% Cl, 0.20% Na, 0.21% Ca and 0.10% K. The responses such as Concentration of SiC (g/l), Pulse duration (μs), Duty cycle (%), and Current (amp) were taken as EDM inputs. To achieve the blind square holes on CFRPs, the square copper electrodes were prepared using a vertical machining center and the sample copper electrode is shown in Fig. 3. The fresh copper electrode dimensions were measured using a coordinate measuring machine. The mean widths and standard deviations for 0.8 mm square electrodes were in the dimension of 0.8018 ± 0.017 mm. The hole depth, major axis, and minor axis of the blind hole parameter are shown in Figs. 4 (a-b). The scanning electron microscope (ZEISS: Coordinate Measuring Machines), video-measuring system (VMS-2010 F) were used for measuring the squareness, hole depth, and surface roughness. The top surface of blind square hole squareness is calculated using Eq. 1. The squareness value ranges from zero to one. Squareness value is one denoted as a perfect square. The electrode wear length can be measured along with the height of the electrode by taking the difference between the fresh electrode lengths to worn out electrode length and surface roughness were measured using SURFCOM TOUCH 50 tester.

$$\text{Squareness (sq.ness)} = \frac{\text{Major axis}}{\text{Minor axis}} \tag{1}$$

2.3 Additive Ratio Assessment (ARAS)

The additive ratio assessment is a multi-criteria decision-making method [61]. The method is presented in the tabular form and not in matrix form for a better understanding of the mechanism. ARAS selects the best alternative based on many attributes and the final ranking of alternatives is made by determining the utility degree of each alternative. ARAS has one of the compensatory methods, and qualitative attributes are converted into quantitative attributes and attributes are independent. The steps are given below.

Step 1: Forming of Decision-making matrix (DMM).

The under-mentioned DMM of preferences (X_{ij}) for ‘m’ alternatives (rows) rated on ‘n’ criteria (columns):

$$X = \begin{bmatrix} x_{01} & x_{01} & \dots & x_{0n} \\ x_{11} & x_{12} & \dots & x_{1n} \\ \vdots & \vdots & \ddots & \vdots \\ \vdots & \vdots & \vdots & \vdots \\ x_{m1} & x_{n2} & \dots & x_{mn} \end{bmatrix} \tag{2}$$

Where $i = 0, 1, \dots, m; j = 1, 2, \dots, n$.

X_{ij} is the value corresponding to the performance value of the alternative named i, under the j criterion while x_{oj} is the optimal value for the j criterion. When the optimal value of the j criterion is absent, then

$$X_{oj} = \begin{cases} \max x_{ij} \text{ if } J \in B \\ \min x_{ij} \text{ if } J \in C \end{cases} \tag{3}$$

Here, B and C are denoted the benefit criteria to be maximized and non-benefit criteria to be minimized, respectively.

Step 2: Normalization of decision-making matrix.

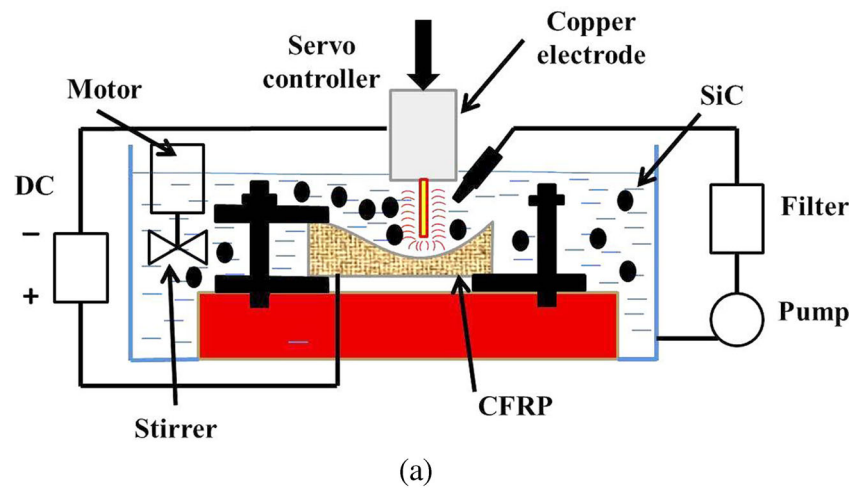
Linear normalization methodology is used to different criteria.

$$\bar{x}_{ij} = \frac{x_{ij}}{\sum_{i=0}^m x_{ij}} \tag{4}$$

The minimum criteria are normalized through a two-stage process.

$$x_{ij} = \frac{1}{x_{ij}^*}; \bar{x}_{ij} = \frac{x_{ij}}{\sum_{i=0}^m x_{ij}} \tag{5}$$

Fig. 1 EDM: (a) Schematic diagram, (b) photocopy of EDM



Step 3: Weighted normalized decision matrix

$$\hat{X}_{ij} = \bar{x}_{ij} * w_j; \quad i = 0, \dots, m,$$

$$\hat{X} = \begin{bmatrix} \hat{x}_{01} & \hat{x}_{02} & \dots & \hat{x}_{0n} \\ \hat{x}_{11} & \hat{x}_{12} & \dots & \hat{x}_{1n} \\ \vdots & \vdots & \ddots & \vdots \\ \hat{x}_{m1} & \hat{x}_{m2} & \dots & \hat{x}_{mn} \end{bmatrix} \quad (7)$$

Where, $i = 0, 1, \dots, m$; $j = 1, 2, \dots, n$.

\hat{X}_{ij} is the weighted normalized performance rating of the i alternative through the j criterion.

Step 4: Determine the optimality function (S_i) for the alternative

$$S_i = \sum_{j=1}^n \hat{x}_{ij} \quad (8)$$

Where, $i = 0, 1, \dots, m$; $j = 1, 2, \dots, n$. and High S_i value is better alternative.

Step 5: Determine the degree of utility (K_i) for each alternative.

$$K_i = \frac{S_i}{S_o}; \quad i = 0, 1, \dots, m \quad (9)$$

Step 6: Rank the alternatives based on K_i values.

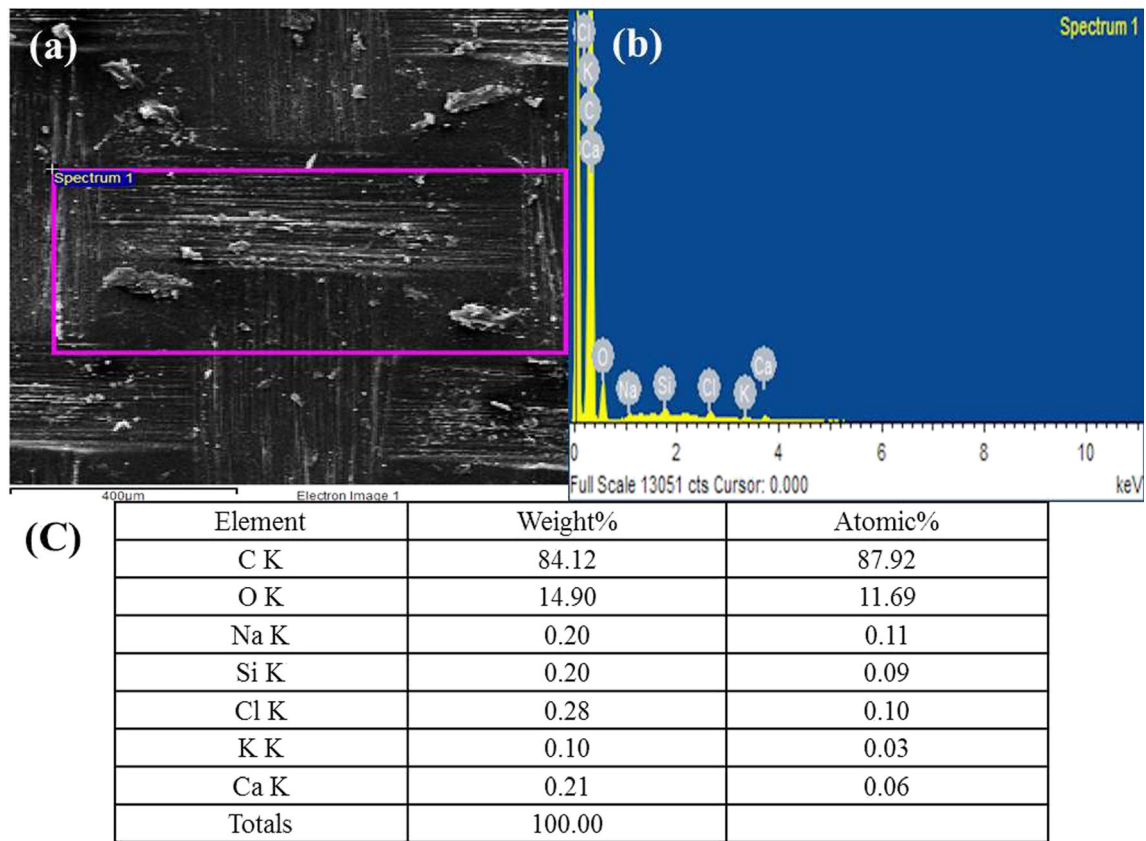


Fig. 2 EDAX for CFRP

3 Results and Discussions

The primary purpose of the work is to fabricate a blind square hole on CFRP using EDM process parameters. Also, the effects of the addition of SiC particles in the kerosene fluid on squareness, hole depth, and surface roughness of CFRPs are studied. The analysis of blind square hole feature studies is an important task. This is because the selected responses greatly affected productivity and production. The responses such as

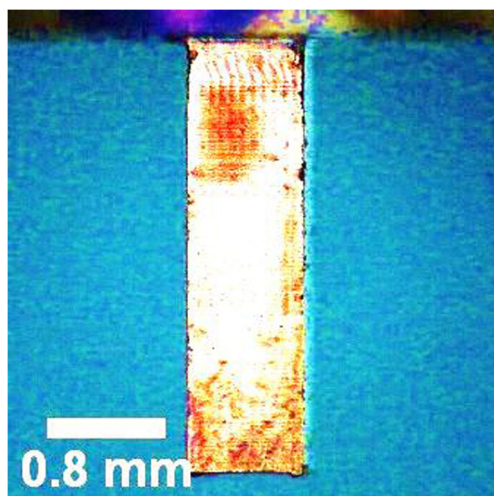


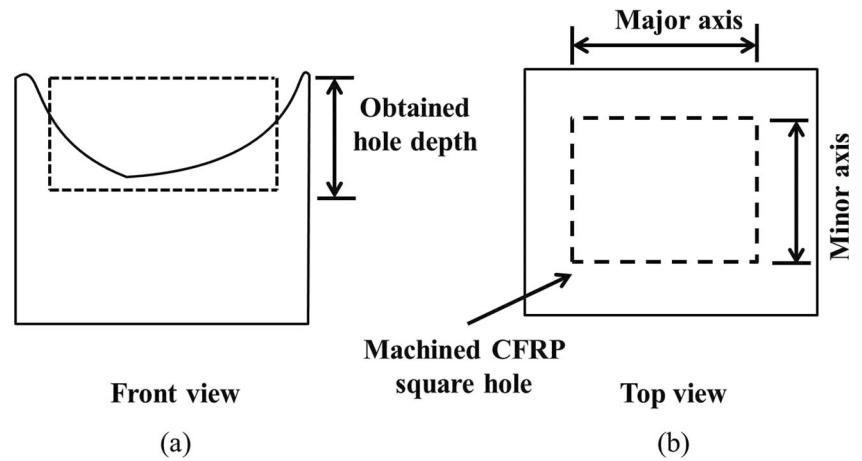
Fig. 3 Optical microscope image of copper electrode

squareness, hole depth, and surface roughness are considered. The blind square hole tests are carried out on CFRP as per the design of the experiment. The responses are measured and recorded. Table 4 shows the design layout and result of squareness, hole depth, and surface roughness of CFRP. Table 5 shows the calculation of the mean response.

3.1 Squareness

Experimental results found that the squareness value was greater than one in the entire square hole. This was due to the major axis being higher than the minor axis. Variations in the thermal properties of carbon fiber, epoxy resin, and SiC particles were also reasoned for obtaining a squareness value greater than one. The direction of the dielectric kerosene flushing, pressure, and concentration of SiC was also a reason for varying the square hole size in the experimental results. The unstable spark generated from the non-circular electrodes and corner radiuses of micro-feature formed on the work materials were observed. The previous works found that the non-circular electrode shapes were produced the unstable spark to Inconel 718 and Inconel 625 [62, 63]. In another way, to enhance the thermal properties of the dielectric medium strength, the addition of SiC concentration to kerosene was carried out and it was proved that the addition of SiC

Fig. 4 Schematic diagram for blind square hole: (a) hole depth, (b) major axis and minor axis



concentration to kerosene was greatly affected dielectric medium-strength [44]. Hence, the addition of SiC concentration to kerosene was carried out. After drilling, the graphs were drawn between the process parameters and responses. On increasing the concentration of SiC and pulse duration, the squareness increased and it is shown in Fig. 5. The squareness variations of micro-holes were due to the differences in the melting point of carbon fiber and epoxy resin. Also, epoxy resin has a lesser melting point compared to carbon fiber. Variations in the thermal conductivity and melting points were observed between the carbon fiber and epoxy resins that also reasoned for variation in the squareness of micro-holes. Moreover, the square shape copper electrode was generated non-uniform high-density sparks to CFRPs, resulting in

increasing squareness. More electrothermal energy was used for melting and vaporizing the CFRP. In addition, the direction of kerosene-flushing pressure was also intended for increasing the squareness. Therefore, squareness increased. With an increase in the duty cycle, the squareness decreased. The eroded materials were difficult to remove away from the machined zone by increasing the viscosity of the dielectric medium. Also, decreasing in the squareness was due to the effect of SiC powder particles on CFRP, surface properties, particle size, and electrostatic forces. Therefore, the squareness decreased. On increasing the current, the squareness decreased up to the level of 4 amp current and then rose above 4 amp current. This was due to the unstable spark generated from the square electrode to CFRP. The debris accumulation

Table 4 Design and experimental results

Exp. No.	Input process parameters				Quality performances		
	Concentration of SiC (g/l)	Pulse duration (μ s)	Duty cycle (%)	Current (amp)	Squareness –	Hole depth (mm)	Surface roughness (μ m)
1	4	15	1	2	1.044	0.177	1.941
2	4	30	3	4	1.067	0.180	2.565
3	4	45	5	6	1.120	0.181	3.623
4	4	60	7	8	1.132	0.197	3.652
5	8	15	3	6	1.026	0.222	3.691
6	8	30	1	8	1.076	0.255	4.254
7	8	45	7	2	1.121	0.297	4.656
8	8	60	5	4	1.135	0.322	4.752
9	12	15	5	8	1.049	0.342	4.796
10	12	30	7	6	1.089	0.370	5.044
11	12	45	1	4	1.145	0.394	5.374
12	12	60	3	2	1.158	0.405	5.836
13	16	15	7	4	1.031	0.409	5.846
14	16	30	5	2	1.099	0.446	6.005
15	16	45	3	8	1.147	0.466	6.094
16	16	60	1	6	1.161	0.505	6.527

Table 5 Mean responses calculation

Levels	Cp	Ton	DC	I
Squareness				
1	1.091	1.038	1.107	1.105
2	1.090	1.083	1.099	1.095
3	1.110	1.133	1.101	1.099
4	1.109	1.147	1.093	1.101
Maximum	1.110	1.147	1.107	1.105
Minimum	1.090	1.038	1.093	1.095
Delta	0.020	0.109	0.013	0.011
Rank	2	1	3	4
Improvement percentage (IP)	1.84	9.51	1.18	0.99
Hole depth				
1	0.184	0.287	0.333	0.331
2	0.274	0.313	0.318	0.326
3	0.378	0.335	0.323	0.320
4	0.457	0.357	0.318	0.315
Maximum	0.457	0.357	0.333	0.331
Minimum	0.184	0.287	0.318	0.315
Delta	0.273	0.070	0.014	0.016
Rank	1	2	4	3
IP	59.79	19.51	4.33	4.95
Surface roughness				
1	2.945	4.068	4.524	4.609
2	4.338	4.467	4.546	4.634
3	5.263	4.936	4.794	4.721
4	6.118	5.192	4.799	4.699
Maximum	6.118	5.192	4.799	4.721
Minimum	2.945	4.068	4.524	4.609
Delta	3.173	1.123	0.276	0.112
Rank	1	2	3	4
IP	51.86	21.64	5.74	2.36

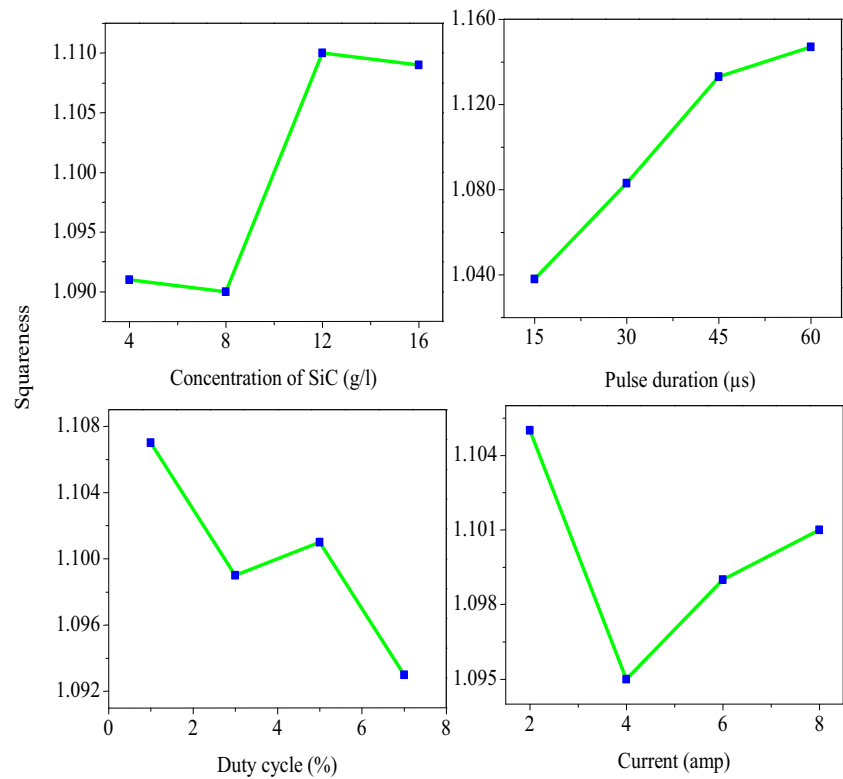
in the machined zone was also reasoned for variations in the squareness. Hence, the applied current showed that the steep V-shaped change in the behavior of squareness. In Table 5, it was found that the pulse duration was the most significant factor that affects the squareness of blind square holes. Improvement in the squareness percentages was calculated based on the parameters to rate the different machining performances. The pulse duration was used for obtaining a maximum improvement in the 9.51% squareness. Thereby, the minimum squareness was obtained using the 8 g/l concentration of SiC, 15 μ s pulse duration, 7% duty cycle, and 4 amp current. Also, the duty cycle and current were used for improving the squareness at a low level. Previous results identified that the metal removal rate of CFRP was increased using 500 μ s pulse duration [11]. Here, metal removal rate and squareness behavior were similar owing to both responses related to geometric features. Hence, lowering the pulse

duration was used for obtaining minimum squareness. In another study, the thermal conductivity of the dielectric medium was increased by increasing the concentration of graphite to dielectric fluid for improving the material removal rate [24]. Similar results were also obtained in this work. The unstable sparks generated from EDM electrodes were affecting the process performances. The direction of dielectric fluid flushing was also greatly affecting the machined surface [64].

3.2 Hole Depth

The hole depth (machined depth) varied by increasing the process parameters and it is shown in Fig. 6. It was found that the concentration of SiC and pulse duration were the most influenced factors on hole depth. The 16 g/l concentration of SiC and 60 μ s pulse duration were used for obtaining the maximum hole depth on CFRP. This was due to the higher thermal energy generated from the SiC mixed dielectric fluid to the machining region. SiC powder mixed with kerosene has provided stable machining by increasing the thermal conductivity of the dielectric fluid. Hence, hole depth increased. Besides, by raising the pulse duration, the hole depth increased owing to the unstable spark with higher thermal energy produced in the square electrode to CFRP. The effects of SiC powders mixed to dielectric fluid; the powder energized and performs in a zigzag movement between the copper electrode and CFRP. Effects of zigzag movement of particles formed the chain structure in the machining zone and reduce the dielectric fluid strength and develop a series discharge. The result found that the electrode sparking area produced effective discharge transmissivity owing to the raises in thermal conductivity. Therefore, the hole depth increased. Raising in the duty cycle and current, and the hole depth decreased. The hole depth variations in the micro-holes due to the differences in the melting point of carbon fiber and epoxy resin. Also, epoxy resin has a lesser melting point compared to carbon fiber. Variations in the thermal conductivity were also observed between the carbon fiber and epoxy resins that also reasoned for variation in the hole depth of micro-holes. Hence, hole depth varied. Normally, the current was directly related to metal removal. Nonetheless, the decrement in the metal removal was due to the eroded materials' difficulty to move away from the machined zone by increasing the viscosity and conductivity of the dielectric medium. More debris and thicken heat-affected zone were formed on the machined zone. The selection of dielectric fluid pressure also greatly affects the electrical properties of dielectric fluid due to the contamination of electrolytes resulting in reducing the efficiency of material removal. In this work, the 0.7 kg/cm² kerosene dielectric pressure was selected for processing. It was found that the pressure value was inadequate for removing the debris from the machining zone resulting in debris clogs in the

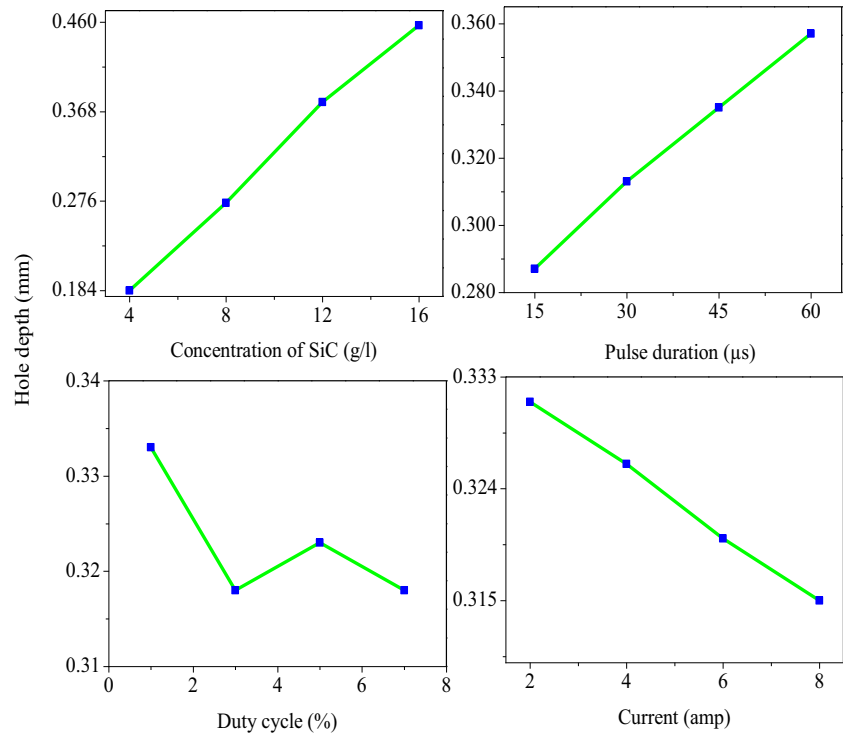
Fig. 5 Effect of parameters on squareness



machining zone. Simultaneously, the spark was supplied continuously without removing work material resulting in a thickened heat affected zone formed. Hence, the hole depth decreased. The 59.79% hole depth was achieved using the 16 g/l SiC concentration. Therefore, the maximum hole

depth was obtained using 16 g/l SiC concentration, 60 μs pulse duration, 1% duty cycle, and 2 amp current. The copper electrode wears also affected the width and depth of the hole [25]. Another result found that a higher depth of cut on copper was obtained using a 2.3 amp current and 0.2 μs

Fig. 6 Effect of parameters on hole depth



pulse duration. The present hole depth agreed well with the previous result [26]. The duty cycle equally affecting the squareness and hole depth due to the nature of CFRP material properties. Hence, the duty cycle produced similar trends over the squareness and hole depth. But, slight variances were also observed between the squareness and hole depth due to the geometrical differences.

3.3 Surface Roughness

Variation in the surface roughness was observed by varying the process parameters and it is shown in Fig. 7. It was found that the concentrations of SiC and pulse duration were the most influencing factors that affecting the surface roughness. The 4 g/l concentration of SiC and 15 μ s pulse duration were used for obtaining low surface roughness. The SiC powder mixed dielectric medium destroyed the insulation easily for reducing the electrical resistivity of the medium and leaving the discharge gap resulting in reduce the impulse force of the discharge channel. This influence on the machining gap generated a high plasma channel from a sample to an electrode for increasing the material removal rate. The higher thermal conductivity of copper electrodes was also supported by increasing the material removal rate. Also, carbon fiber and epoxy resin were easily melted, and smoothly surface formed due to the electrothermal effect. Hence, the machined surface showed an uneven small size crater and small debris, resulting in produced low surface roughness. Increasing the surface roughness was observed by raising the SiC concentration, pulse duration, duty cycle, and current. This was due to the increased thermal conductivity and impulsive force in the plasma region. The melting point difference between the carbon fiber and copper electrode was three times higher, resulting in the large and deep crater produced on the machined surface. Hence, higher surface roughness is produced. In short, the low concentration of SiC with low thermal energy sparks produced a lower surface roughness. Thereby, low thermal energy produced small crater sizes in the machined zone. SiC concentration and pulse duration were increased, and surface roughness was increased. The unstable sparks produced deep and wide surface irregularities in the machined zone. Hence, surface roughness increased. Similar behavior was observed in the current and duty cycle. The 51.86% surface roughness was achieved by lowering the SiC concentration. Hence, the minimum surface roughness was obtained using 4 g/l SiC concentration, 15 μ s pulse duration, 1% duty cycle, and 2 amp current. The erosion process produced a 10 amp current, which was used to obtain the 1.95 μ m surface roughness on titanium [24]. Compared to another study, higher surface roughness was observed in a previous study [27]. This result agreed well with this surface roughness result.

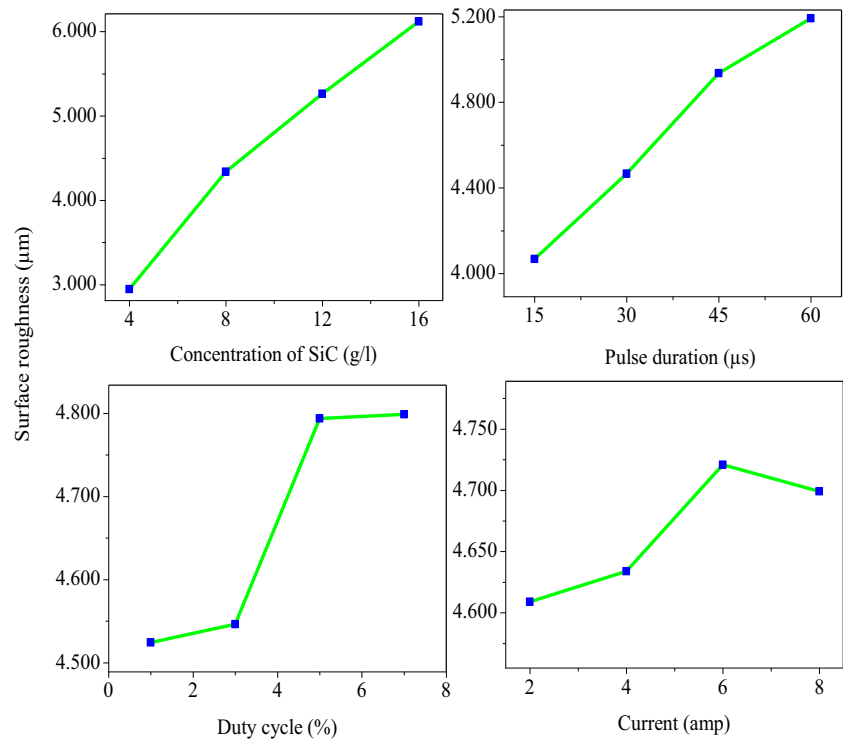
3.4 Electrode Wear Length

Figure 8 shows the copper electrode worn-out surface and worn-out length. After machining, the square form of the copper electrode was transformed into a semi-spherical shape electrode with worn-out length and surface. The main reason for the higher worn-out surface and length was unstable discharge energy produced in the square electrode. Initially, the sharp edge of the copper electrode was worn out and the surface of the electrode was secondly worn out due to the difference in the stress concentration. The copper electrode was a low melting point compared to carbon fiber, epoxy resin, and SiC particles. Hence, the copper electrode was worn out in a short time compared to other materials. Nonetheless, powder mixed dielectric fluid motivated to reduce the worn-out length due to the uniform discharge to sample and increasing the thermal conductivity of the dielectric fluid. Similar behavior was observed in the cylindrical shape electrode due to the skin effect [28]. Hence, electrode wear was an unavoidable problem in spark machining. The work was also focused on reducing the worn-out length of copper electrodes. The electrode worn-out length is reduced by increasing the SiC concentration in the dielectric fluid because SiC powder added to kerosene disturbs the adherence of atoms attached to the electrode surface and reduces the electrode-worn length. Also, SiC powder concentration was equally spread over the dielectric medium and it was nominal electrode-worn length obtained due to better conduction of discharge. The worn-out length of the electrode was varied from 0.31 mm to 1.168 mm by increasing the SiC concentration. The worn-out length was greatly associated with powder properties (concentration, density, thermal conductivity, and electrical resistivity) and it was affecting the machining performance, worn-out surface, and worn-out length. Similar results were observed in previous studies [13, 29]. The heat-affected zone formation and worn-out surface on the copper electrode were also reduced by increasing the SiC powder concentration due to the uniform mixing of powder in the dielectric fluid produces consistent discharge. The small cracks and pores were formed on the copper electrode due to the high impulsive forces developing on the machining zone. The reason for developing high impulsive force was high discharge energy produces more melting and evaporation.

3.5 Surface Defects

In Fig. 9, the corner radius was formed in the machined square hole. The reason for forming a corner radius was the square copper electrode wear. The different melting points of SiC, copper electrode, carbon fiber, matrix resin, and a high degree of short-circuit development were also reasoned. Sharp edges of square copper electrodes were first worn out for generating the round-shaped edges in the machining.

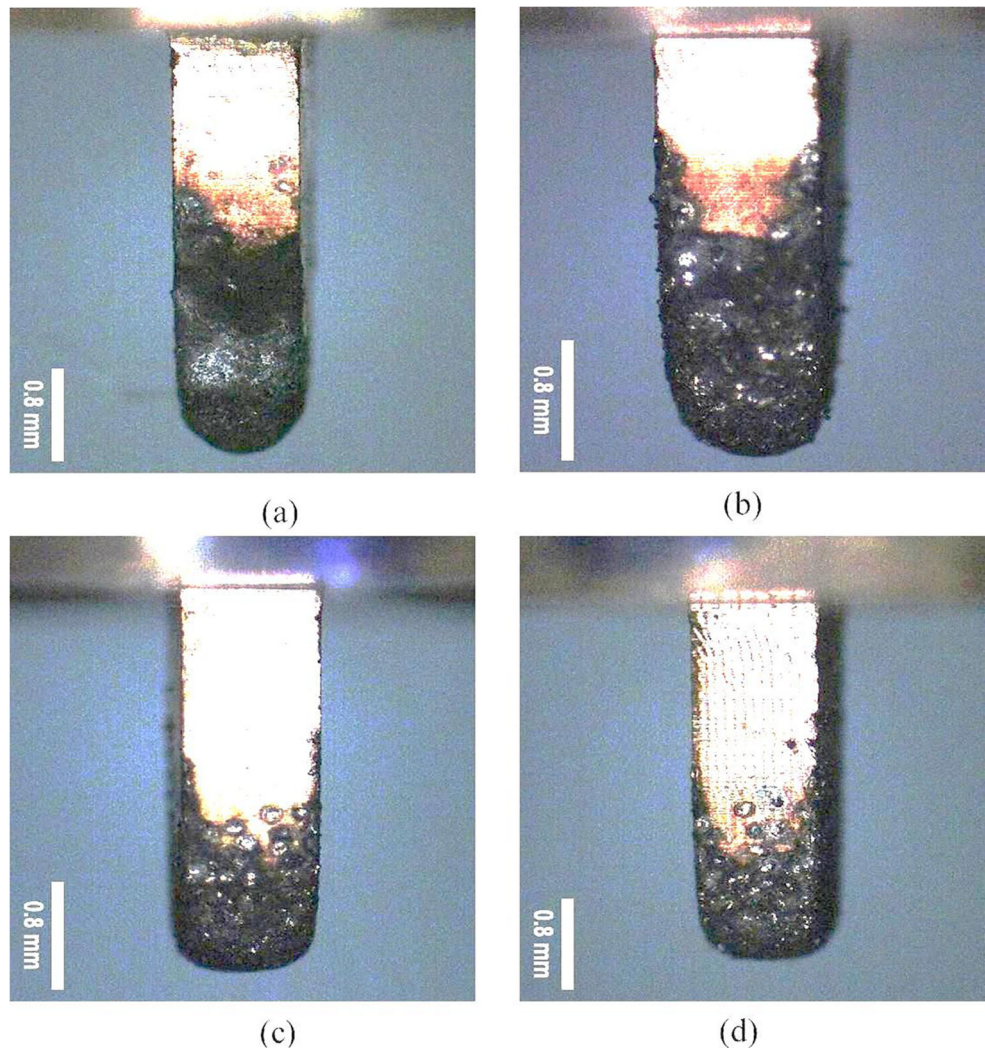
Fig. 7 Effect of parameters on surface roughness



This was due to the difference in the stress concentration factor between the copper electrode and machined hole of the CFRP composite. Simultaneously, the copper electrode wear reflected the sample through sparking. Hence, a corner radius was formed due to the non-uniform spark generated. The burrs were formed on the machined surface due to the long duration of time for developing plasma spark. The copper electrode produced a burr in the machined CFRP using 150 µs pulse duration and it is shown in a previous study [30]. The delamination was also observed due to the longer pulse duration. More heat energy generation at high pulse duration was the reason for generating delamination in the machined CFRP. Moreover, the fibers pulled in/out were observed. A different melting point of carbon fiber and matrix resin was reasoned. A similar result was observed in a previous study [31]. Another study stated that the direction of heat transformed was related to the direction of the carbon fiber orientation and not to the direction of current flow [12]. But, the argument result was observed in this study due to the electrothermal energy developed from the higher pulse duration and current. The heat-affected zone formed around the micro square hole was due to the different thermal conductivity of carbon fiber and epoxy resin. The heat transfer rate of carbon fiber was greater than the epoxy resin due to the higher thermal conductivity of carbon fiber. Due to the poor thermal conductivity of epoxy resin, the problem in heat-transferred rate was observed, affecting the heat-affected zone formation. Similar results were also observed in the previous work [32]. The corner radius was also formed in

the machined monel 400 alloy using EDM [65]. This was good supportive work for forming the corner radius formed in the machined surface. More debris and black products were formed in the machined surface of CFRP and the amount of debris formation was highly related to material removal mechanism, selection of the shape of electrode and material, dielectric fluid pressure, EDM process parameters (pulse duration, duty cycle, current) and physical and thermal properties of a powder particle. There were various reasons for forming debris and black portion (thickened heat affected zone formation), which were described below as. By using the low discharge energy in the deep hole machining, debris removal was a challenging issue due to the narrow sparking gap between the electrode and workpiece. The narrow gap was the main problem for blocking the material removal from the machining zone and more debris concentration in the bottom of the electrode resulting in thickened heat affected zone formation. This narrow sparking gap affected the material removal mechanism of CFRP and it was a complex phenomenon in the macro-EDM and micro-EDM where sparking happened both at the end face and side surface of the square electrode resulting in more debris formed. The stage of the burning of the matrix and resin was varied due to variation in thermal properties resulting in unbalancing to removing material from the machining zone. This phenomenon was related to the amount of pulse duration, current, and duty cycle. An unbalancing effect of material removal of CFRP greatly affects the properties of the electrolyte. This was also the reason for forming debris in the

Fig. 8 Worn out electrode at bottom view: (a) 4st experiment, (b) 8th experiment, (c) 12th experiment, (d) 16th experiment



machining zone. The selection of dielectric fluid pressure also greatly affects the electrical properties of dielectric fluid due to the contamination of electrolytes resulting in reducing the efficiency of material removal. In this work, the 0.7 kg/cm^2 kerosene dielectric pressure was selected for processing. It was found that the pressure value was inadequate for removing the debris from the machining zone resulting in debris clogs in the machining zone. Simultaneously, the spark was supplied without removing work material resulting in a thickened heat affected zone formed. On the other hand, SiC particles play an important role in the EDM process. The effects of the addition of SiC to dielectric fluid were reducing the insulating strength and increasing the sparking gap distance, resulting in a high material removal rate. Inversely, debris formation greatly affected the material removal rate. Hence, low dielectric fluid pressure was the main reason for the formation of debris and black products in the machined zone. The remaining process parameters were not much affecting the material removal rate and debris formation.

3.6 Modeling

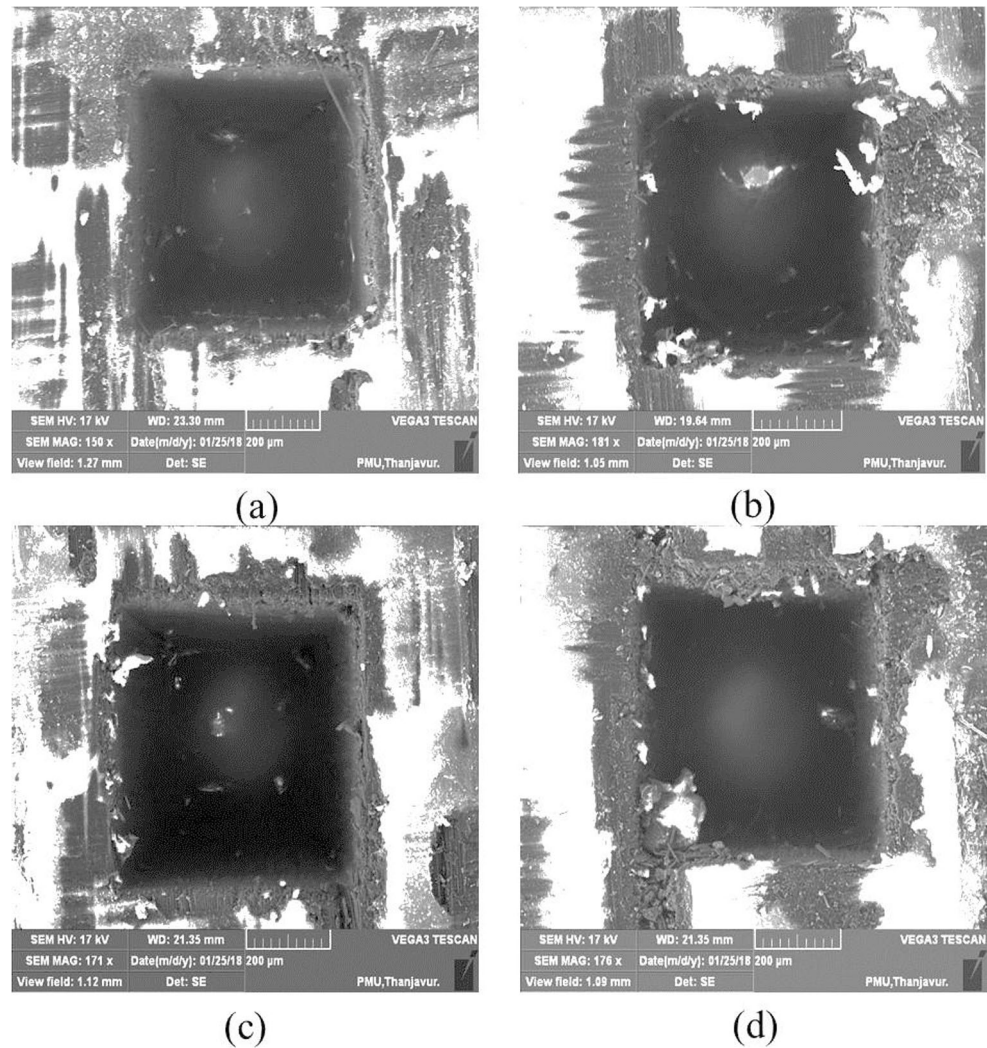
The modeling was used to find the relation between the process parameters and responses. The regression equations were developed in the squareness, hole depth, and surface roughness using statistical software. The regression equations found that the sum of square value, R-square value, and R-square adjusted values were obtained in good-fit for further prediction.

$$\begin{aligned} \text{Squareness} &= 0.996 + 0.0019 \times C_p + 0.0025 \times T_{on} - 0.00192 \times DC - 0.00045 \times I \\ S &= 0.014, R\text{-Sq} = 93.3\%, R\text{-Sq (adj)} = 90.8\% \end{aligned} \quad (10)$$

$$\begin{aligned} \text{Hole depth} &= 0.0564 + 0.023 \times C_p + 0.00154 \times T_{on} - 0.00195 \times DC - 0.00277 \times I \\ S &= 0.013, R\text{-Sq} = 98.8\%, R\text{-Sq (adj)} = 98.4\% \end{aligned} \quad (11)$$

$$\begin{aligned} \text{Surface roughness} &= 0.792 + 0.261 \times C_p + 0.0256 \times T_{on} + 0.0537 \times DC + 0.0178 \times I \\ S &= 0.267, R\text{-Sq} = 96.9\%, R\text{-Sq (adj)} = 95.8\% \end{aligned} \quad (12)$$

Fig. 9 Details of machined surface defects: (a) 4st experiment, (b) 8th experiment, (c) 12th experiment, (d) 16th experiment



The unit of different responses and input parameters are given below.

Squareness (Sq. ness) = no unit.

Hole depth (HD) = mm.

Surface roughness (SR) = μm .

Concentration of SiC (Cp) = g/l.

Pulse duration (Ton) = μs .

Current (I) = amp.

Duty cycle (DC) = %.

The contribution percentages for squareness, hole depth, and surface roughness also formed, which is shown in Fig. 10. The variance analysis found that the pulse duration has a highly contributing percentage for improving the squareness of the hole. Similarly, the concentration of SiC has a highly contributing percentage for improving the surface roughness and hole depth. Table 6 shows the experimental data related to numerical results of squareness, hole depth, and surface roughness and found that percentage deviations are an acceptable limit.

3.7 Determination of Optimum Process Parameters

To determine the optimum parameters of multiple objectives, and the ARAS method was used. The ARAS calculating procedure is presented in Table 7. The surface roughness and squareness were considered lower, whereas the hole depth was considered as higher the better. In the ARAS method, the hole depth was considered beneficial criteria, whereas the surface roughness and squareness were considered non-beneficial criteria. The non-beneficial criteria were converted into beneficial criteria by inverting the non-beneficial criteria. The responses were formed as a decision matrix. The normalization of responses was calculated based on the response objectives. The hole depth was considered 0.4 weightage whereas surface roughness and squareness were considered 0.3 weightage. The weightage of responses was selected based on the industrial expert. The weighted normalization of responses for beneficial criteria was calculated. The optimality function and degree of utility were calculated for each alternative. The rank was calculated according to the degree of

Table 6 Experimental data related with numerical results of squareness, hole depth and surface roughness

S.No.	Actual experimental data			Predicted by linear regression			Deviation in % between Actual vs linear regression		
	Sq. ness	HD	SR	Sq. ness	HD	SR	Sq. ness	HD	SR
1	1.044	0.177	1.941	1.038	0.164	2.309	0.548	7.339	-18.975
2	1.067	0.18	2.565	1.071	0.178	2.836	-0.379	1.294	-10.577
3	1.12	0.181	3.623	1.104	0.191	3.363	1.446	-5.707	7.168
4	1.132	0.197	3.652	1.137	0.205	3.890	-0.403	-4.056	-6.525
5	1.026	0.222	3.691	1.040	0.241	3.532	-1.388	-8.572	4.310
6	1.076	0.255	4.254	1.081	0.262	3.844	-0.435	-2.937	9.636
7	1.121	0.297	4.656	1.109	0.291	4.444	1.038	2.185	4.564
8	1.135	0.322	4.752	1.150	0.312	4.756	-1.304	3.115	-0.078
9	1.049	0.342	4.796	1.043	0.324	4.719	0.562	5.383	1.608
10	1.089	0.37	5.044	1.078	0.348	5.175	1.041	5.857	-2.591
11	1.145	0.394	5.374	1.128	0.389	5.201	1.521	1.353	3.221
12	1.158	0.405	5.836	1.162	0.413	5.657	-0.358	-2.077	3.072
13	1.031	0.409	5.846	1.049	0.423	5.799	-1.713	-3.367	0.802
14	1.099	0.446	6.005	1.091	0.455	6.040	0.737	-2.087	-0.585
15	1.147	0.466	6.094	1.130	0.466	6.424	1.522	0.067	-5.407
16	1.161	0.505	6.527	1.172	0.498	6.665	-0.929	1.341	-2.107

utility. The first experiment has been found as the best alternative process parameters based on the high optimality function and the first rank of the degree of utility. The best alternative process parameters for machining CFRPs were the concentration of SiC: 4 g/l, pulse duration: 15 μ s, duty cycle: 1%, and current: 2 amp. The rank-based comparisons were carried out between the GRA, DFA, and proposed algorithm and it is shown in Table 8. The best alternative process parameters were verified through a confirmation test and it is shown in Table 9. The ARAS method has improved CFRP performance. In addition, the non-contact roughness measurement was used for measuring the cross-section of surface roughness

of 0.8-mm blind micro square hole and roughness of 1.28 μ m was achieved, which was better than the confirmation test roughness value.

3.8 Comparison with Previous Studies

Comparative studies were conducted between the current study and published works, which are shown in Table 10. More works were focused to study the surface roughness and removal of burrs in the machined CFRP. No works were found that the effect of SiC concentration on squareness, hole depth, and surface roughness of CFRP was studied using EDM with the square copper electrode. The trail tests found that the through-hole was not obtained by increasing the above 16 g/l SiC due to the higher electrode wear observed. The squareness of the blind square hole of CFRP has not been studied using more researchers. More works were focusing on circular holes forming on CFRPs using EDM [7–11]. The hole depth was directly proportional to the current and pulse duration due to the heat energy. SiC powder mixed kerosene has improved the hole depth due to the increased thermal conductivity of the dielectric medium. The hole depth variation was observed between the previous study [8] and the current result due to the electrode thermal conductivity. Compared to the surface roughness of CFRP between the SiC powder mixed dielectric fluid [20, 22] and non-power mixed dielectric fluid performance [10, 11, 44], the SiC power mixed dielectric fluid produces better performance. The surface roughness of the current study was better than other studies [10, 11, 16, 17,

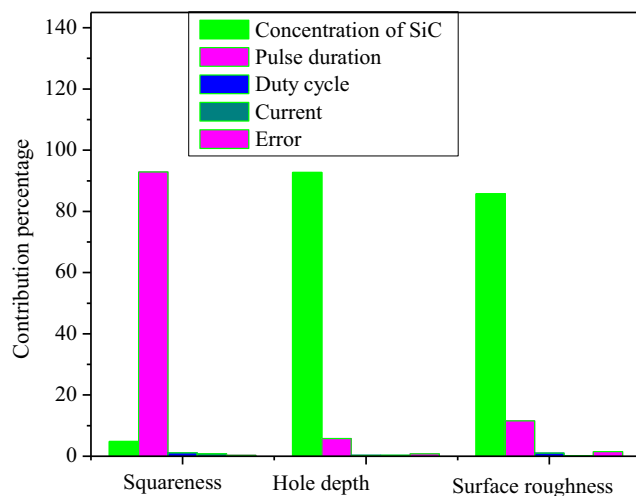
**Fig. 10** Contribution percentage for responses

Table 7 Additive ratio assessment calculations

Max or Min	Experimental results			Decision-making matrix			Normalized data			Weight normalized data			Si	Ki	Rank
	Sq. ness	HD	SR	Sq. ness	HD	SR	Sq. ness	HD	SR	Sq. ness	HD	SR			
No.	1.026	0.505	1.941	0.975	0.505	0.515	0.063	0.089	0.119	0.019	0.036	0.036	0.090	1.000	
1	1.044	0.177	1.941	0.958	0.177	0.515	0.062	0.031	0.119	0.018	0.012	0.036	0.067	0.740	1
2	1.067	0.18	2.565	0.937	0.180	0.390	0.060	0.032	0.090	0.018	0.013	0.027	0.058	0.641	6
3	1.12	0.181	3.623	0.893	0.181	0.276	0.057	0.032	0.064	0.017	0.013	0.019	0.049	0.545	16
4	1.132	0.197	3.652	0.883	0.197	0.274	0.057	0.035	0.063	0.017	0.014	0.019	0.050	0.554	15
5	1.026	0.222	3.691	0.975	0.222	0.271	0.063	0.039	0.063	0.019	0.016	0.019	0.053	0.591	12
6	1.076	0.255	4.254	0.929	0.255	0.235	0.060	0.045	0.054	0.018	0.018	0.016	0.052	0.579	14
7	1.121	0.297	4.656	0.892	0.297	0.215	0.057	0.052	0.050	0.017	0.021	0.015	0.053	0.588	13
8	1.135	0.322	4.752	0.881	0.322	0.210	0.057	0.057	0.049	0.017	0.023	0.015	0.054	0.602	11
9	1.049	0.342	4.796	0.953	0.342	0.209	0.061	0.060	0.048	0.018	0.024	0.014	0.057	0.632	10
10	1.089	0.37	5.044	0.918	0.370	0.198	0.059	0.065	0.046	0.018	0.026	0.014	0.058	0.638	7
11	1.145	0.394	5.374	0.873	0.394	0.186	0.056	0.069	0.043	0.017	0.028	0.013	0.058	0.638	8
12	1.158	0.405	5.836	0.864	0.405	0.171	0.056	0.071	0.040	0.017	0.029	0.012	0.057	0.633	9
13	1.031	0.409	5.846	0.970	0.409	0.171	0.062	0.072	0.040	0.019	0.029	0.012	0.059	0.659	5
14	1.099	0.446	6.005	0.910	0.446	0.167	0.059	0.079	0.039	0.018	0.031	0.012	0.061	0.672	4
15	1.147	0.466	6.094	0.872	0.466	0.164	0.056	0.082	0.038	0.017	0.033	0.011	0.061	0.677	3
16	1.161	0.505	6.527	0.861	0.505	0.153	0.055	0.089	0.035	0.017	0.036	0.011	0.063	0.697	2

20, 22, 44] due to the addition of SiC to kerosene to provide better results. The better copper electrode wear was observed compared to previous results [7, 44] due to the electrode thermal conductivity.

Table 8 Rank comparison based on the GRA, DFA and proposed algorithm

S. No.	GRA [49]	DFA [50]	Proposed algorithm
1	1	1	1
2	2	2	6
3	4	5	16
4	5	7	15
5	3	3	12
6	7	4	14
7	9	8	13
8	11	11	11
9	8	6	10
10	10	9	7
11	13	12	8
12	14	15	9
13	6	10	5
14	12	13	4
15	15	14	3
16	16	16	2

4 Conclusions

A great effort is made to study the concentration of SiC powder and EDM parameters on squareness, hole depth, and surface roughness on square blind hole CFRP using EDM with the square copper electrode. The conclusions have the following as.

- The percentage of concentration of SiC and pulse duration greatly affect the squareness, hole depth, surface roughness, and electrode wear length.
- A corner radius has formed on the machined square holes due to the area effect and the skin effect.
- Low thermal heat energy has been used for producing the minimum surface roughness and minimum thermal damage.
- Deformed electrode wears were formed in all the CFRP machined corners due to unstable sparking produced.
- Cutting edge irregularity has formed in the machined edges.
- Regression models for EDMs are a good fit for prediction.
- ARAS method provides consistent results with other standard methods and improved the performance measures.

Acknowledgments The authors thank the COVAI EDM at Coimbatore for providing a machining facility. The authors are also thankful to Periyar Maniammai Institute of Science & Technology at Vallam for providing a scanning electron microscopy facility.

Table 9 Confirmation experiment

	Raw Data	Experiment
Conditions	Cp=4 g/l/ Ton=15 μ s/ DC=1%/ I=1 amp	Cp=4 g/l/ Ton=15 μ s/ DC=1%/ I=1 amp
Squareness (–)	1.044	1.015
Hole depth (mm)	0.177	0.234
Surface roughness (μ m)	1.941	1.231
Ki	0.740	0.818
Improvement in Ki=0.078		

Contributions PV Arul Kumar: Conceptualization, Methodology, Writing Reviewing discussion and Editing. J. Vivek: computation, Methodology, Software, Writing discussion and N. Senniangiri: Conceptualization and analysis, Writing-review, writing the manuscript, Methodology, Software, and writing – discussion, S. Nagarajan: review manuscript language, B. Alshahrani: review manuscript language, K. Chandrasekaran: review manuscript language.

Funding The authors did not receive support from any organization for the submitted work.

Data Availability The available data and material had been used and discussed in the manuscript.

Declaration

Consent to Participate All persons named as authors in this manuscript have participated in the planning, design, and performance of the research and the interpretation of the results.

Consent for Publication All authors have endorsed the publication of this research.

Ethics Declarations The manuscript has not been published elsewhere and it has not been submitted simultaneously for publication elsewhere.

Declaration of Competing Interest The authors declare that they have no known competing financial interests or personal relationships that could have appeared to influence the work reported in this paper.

References

- Samal P, Babu DM, Kiran SV, Surekha B, Vundavilli PR, Mandal A (2020). Study of microstructural and machining characteristics of hypereutectic Al-Si alloys using wire-EDM for photovoltaic application. *Silicon*, pp.1–13
- Phan NH, Muthuramalingam T (2020) Multi criteria decision making of vibration assisted EDM process parameters on machining silicon steel using Taguchi-DEAR methodology. *Silicon*, pp.1-7
- Muthuramalingam T, Saravanakumar D, Babu LG, Phan NH, Pi VN (2019) Experimental investigation of white layer thickness on EDM processed silicon steel using ANFIS approach. *Silicon*, pp.1-7

Table 10 Comparison of present results with published literatures

R.No.	Materials/ Additives	Dielectric medium	Electrode Material/size	Cp (g/l)	Ton (μ s)	DC (%)	I (amp)	Sq. ness	Hole depth (mm)	SR (μ m)	Tool Wear (mm)
[7]	CFRP/–	Oil	WC / 0.3 mm	–	50	–	–	–	0.2	8	0.025
[8]	CFRP/–	EDM oil	WC/0.110 mm	–	–	–	–	–	1.2	–	–
[9]	CFRP/–	–	Cu/0.5	–	–	–	–	–	0.25	–	–
[10]	CFRP/–	Esso mentor	Cu/10 mm	–	25–160	–	1–4	–	–	15–45	–
[11]	CFRC/–	Castrol	Cu/4.42 mm	–	200	–	1.5	–	–	5.14	–
[16]	CFRP/–	kerosene	Gr/ 1 mm	–	100	–	5	–	–	4.8	–
[17]	CFRP/–	EDM oil	Cu/2 mm	–	70	–	2	–	–	4	–
[20]	Die steel/SiC	EDM oil	Cu/square	6	150	90	3	–	–	3	–
[21]	Titanium/SiC	EDM oil	Cu/42 mm	25	2–20	80	0.1, 1	–	2.6	–	–
[22]	Titanium/SiC	–	–	5–20	25	–	–	–	–	6.77	–
[34]	CFRP/–	Kerosene	Cu/8 mm	–	50	–	–	–	–	7	1.2 g/min
Current experimental results											
Present work	CFRP/SiC	kerosene	Cu/0.8 mm square electrode	4	15	1	2	1.015	0.234	1.231	0.31–1.168

4. Ramanujam N, Dhanabalan S, Raj Kumar D, Jeyaprakash N (2021) "Investigation of micro-hole quality in drilled CFRP laminates through CO2 laser." *Arab J Sci Eng* 1–19
5. Raj Kumar D, Jeyaprakash N, Yang C, Sivasankaran S (2020) "Optimization of drilling process on carbon-fiber reinforced plastics using genetic algorithm." *Surface Review and Letters* 2050056
6. Raj Kumar D, Jeyaprakash N, Yang C-H, Ramkumar KR (2020) Investigation on drilling behavior of CFRP composites using optimization technique. *Arab J Sci Eng* 45:8999–9014
7. Teicher U, Müller S, Münzner J, Nestler A (2013) Micro-EDM of carbon fibre-reinforced plastics. *Procedia Cirp* 6:320–325
8. Kumar R, Agrawal PK, Singh I (2018) Fabrication of micro holes in CFRP laminates using EDM. *J Manuf Process* 31:859–866
9. Park SH, Kim G, Lee W, Min BK, Lee SW and Kim TG (2015). Microhole machining on precision CFRP components using electrical discharging machining. In 20th international conference on composite materials, Copenhagen, Denmark
10. Lau WS, Wang M, Lee WB (1990) Electrical discharge machining of carbon fibre composite materials. *Int J Mach Tools Manuf* 30(2): 297–308
11. Gourgouletis K, Vaxevanidis NM, Galanis NI, Manolakos DE (2011) Electrical discharge drilling of carbon fibre reinforced composite materials. *Int J Mach Mach Mater* 10(3):187–201
12. George PM, Raghunath BK, Manocha LM, Warriar AM (2004) EDM machining of carbon-carbon composite—a Taguchi approach. *J Mater Process Technol* 145(1):66–71
13. Kurniawan R, Kumaran ST, Prabu VA, Zhen Y, Park KM, Kwak YI, Islam MM, Ko TJ (2017) Measurement of burr removal rate and analysis of machining parameters in ultrasonic assisted dry EDM (US-EDM) for deburring drilled holes in CFRP composite. *Measurement* 110:98–115
14. Islam MM, Li CP, Won SJ, Ko TJ (2017) A deburring strategy in drilled hole of CFRP composites using EDM process. *J Alloys Compd* 703:477–485
15. Mazarbhuiya RM, Dutta H, Debnath K, Rahang M (2020) Surface modification of CFRP composite using reverse-EDM method. *Surfaces and Interfaces* 18:100457
16. Guu YH, Hocheng H, Tai NH, Liu SY (2001) Effect of electrical discharge machining on the characteristics of carbon fiber reinforced carbon composites. *J Mater Sci* 36(8):2037–2043
17. Lodhi BK, Verma D, Shukla R (2014) Optimization of machining parameters in EDM of CFRP composite using Taguchi technique. *Int J Mech Eng Technol* 5(10):70–77
18. Niamat M, Sarfraz S, Aziz H, Jahanzaib M, Shehab E, Ahmad W, Hussain S (2017) Effect of different dielectrics on material removal rate, electrode wear rate and microstructures in EDM. *Procedia Cirp* 60:2–7
19. Das S, Paul S, Doloi B (2020) Feasibility assessment of some alternative dielectric mediums for sustainable electrical discharge machining: a review work. *J Braz Soc Mech Sci Eng* 42(4):1–21
20. Tripathy S, Tripathy DK (2017) Surface characterization and multi-response optimization of EDM process parameters using powder mixed dielectric. *Materials Today: Proceedings* 4(2):2058–2067
21. Chow HM, Yang LD, Lin CT, Chen YF (2008) The use of SiC powder in water as dielectric for micro-slit EDM machining. *J Mater Process Technol* 195(1–3):160–170
22. Öpöz TT, Yaşar H, Ekmekci N, Ekmekci B (2018) Particle migration and surface modification on Ti6Al4V in SiC powder mixed electrical discharge machining. *J Manuf Process* 31:744–758
23. Chow HM, Yan BH, Huang FY, Hung JC (2000) Study of added powder in kerosene for the micro-slit machining of titanium alloy using electro-discharge machining. *J Mater Process Technol* 101(1–3):95–103
24. Jung JH, Kwon WT (2010) Optimization of EDM process for multiple performance characteristics using Taguchi method and Grey relational analysis. *J Mech Sci Technol* 24(5):1083–1090
25. Chen ST, Yeh MC (2016) Development of an in-situ high-precision micro-hole finishing technique. *J Mater Process Technol* 229:253–264
26. Liu Q, Zhang Q, Zhu G, Wang K, Zhang J, Liu Q et al (2016) Effect of electrode size on the performances of micro-EDM. *Mater Manuf Process* 31:391–396
27. Al-Ahmari AMA, Rasheed MS, Mohammed MK, Saleh T (2016) A hybrid machining process combining micro-EDM and laser beam machining of nickel – titanium-based shape memory alloy. *Mater Manuf Process* 31:447–455
28. Kumar H, Davim JP (2011) Role of powder in the machining of Al-10% SiCp metal matrix composites by powder mixed electric discharge machining. *J Compos Mater* 45(2):133–151
29. Mohri N, Saito N, Higashi M (1991) A new process of finish machining on free surface by EDM methods. *Annals of CIRP* 40(1): 207210
30. Vishwakarma UK, Dvivedi A, Kumar P (2014) Comparative study of powder mixed EDM and rotary tool EDM performance during machining of Al-SiC metal matrix composites. *Int J Mach Mach Mater* 16(2):113–128
31. Islam MM, Li CP, Ko TJ (2017) Dry electrical discharge machining for deburring drilled holes in CFRP composite. *International Journal of Precision Engineering and Manufacturing-Green Technology* 4(2):149–154. <https://doi.org/10.1007/s40684-017-0018-x>
32. Isbilir O, Ghassemieh E (2013) Comparative study of tool life and hole quality in drilling of CFRP/titanium stack using coated carbide drill. *Mach Sci Technol* 17:380–409
33. Elsit, N.M. and Noordin, M.Y., 2017. Experimental investigations into the effect of process parameters and Nano-powder (Fe2O3) on material removal rate during micro-EDM of co-Cr-Mo. In *Key engineering materials* (Vol. 740, pp. 125-132). Trans tech publications ltd.
34. Debnath K, Dutta H, Sarma DK (2021). Influence of different tool materials on the machining performance in μ ED-milling of CFRP composites. In *machining and machinability of Fiber reinforced polymer composites* (pp. 207-224). Springer, Singapore
35. Abdallah R, Soo SL, Hood R (2021) The influence of cut direction and process parameters in wire electrical discharge machining of carbon fibre-reinforced plastic composites. *Int J Adv Manuf Technol* 113(5):1699–1716
36. Devi, L., Paswan, K., Chattopadhyaya, S. and Pramanik, A., 2021. Influence of low-frequency vibration in die sinking EDM: a review. In *IOP conference series: materials science and engineering* (Vol. 1104, no. 1, p. 012010). IOP publishing
37. Dutta H, Debnath K, Sarma DK (2021) Improving the micro-electrical-discharge drilling performance of carbon fibre-reinforced polymer: role of assisting-electrode and shaped tool. *Int J Mach Mach Mater* 23(2):191–207
38. Hashizu M, Hayakawa S, Itoigawa F (2020) Influence of short-circuiting on machined surface quality in electrical discharge machining of carbon fiber reinforced plastics. *Procedia CIRP* 95: 403–407
39. Kumaran VU, Kliuev M, Billeter R, Wegener K (2020) Influence of carbon based fillers on EDM machinability of CFRP. *Procedia CIRP* 95:437–442
40. Dutta H, Debnath K, Sarma DK (2020) Multi-objective optimization of hole dilation at inlet and outlet during machining of CFRP by μ EDM using assisting-electrode and rotating tool. *Int J Adv Manuf Technol* 110(9):2305–2322
41. Makudapathy C, Sundaram M (2020) High aspect ratio machining of carbon Fiber reinforced plastics by electrical discharge machining process. *Journal of Micro and Nano-Manufacturing*
42. Dutta H, Debnath K, Sarma DK (2021). Investigation on cutting of thin carbon fiber-reinforced polymer composite plate using sandwich electrode-assisted wire electrical-discharge machining.

- Proceedings of the institution of mechanical engineers, part E: journal of process mechanical engineering, p.09544089211013318
43. Wu C, Cao S, Zhao YJ, Qi H, Liu X, Liu G, Guo J, Li HN (2021) Preheating assisted wire EDM of semi-conductive CFRPs: principle and anisotropy. *J Mater Process Technol* 288:116915
 44. Selvakumar G, Sarkar S, Mitra S (2012) Experimental investigation on die corner accuracy for wire electrical discharge machining of Monel 400 alloy. *Proceedings of the Institution of Mechanical Engineers, Part B: Journal of Engineering Manufacture* 226(10):1694–1704
 45. Balamurugan K, Uthayakumar M, Ramakrishna M, Pillai UTS (2020) Air jet Erosion studies on mg/SiC composite. *Silicon* 12(2):413–423
 46. Chinnamahammad Bhasha A, Balamurugan K (2020) Studies on Al6061 nanohybrid composites reinforced with SiO₂/3x% of TiC-a agro-waste. *Silicon*, pp.1-14
 47. Garikapati P, Balamurugan K, Latchoumi TP and Malkapuram R (2020). A cluster-profile comparative study on machining AlSi 7/63% of SiC hybrid composite using agglomerative hierarchical clustering and K-means. *Silicon*, pp1–12
 48. Balamurugan K, Uthayakumar M, Sankar S, Hareesh US, Warriar KGK (2020) Process optimisation and exhibiting correlation in the exploitable variable of AWJM. *Int J Mater Prod Technol* 61(1):16–33
 49. Balamurugan K, Uthayakumar M, Sankar S, Hareesh US, Warriar KGK (2017) Mathematical modelling on multiple variables in machining LaPO₄/Y₂O₃ composite by abrasive water jet. *Int J Mach Mach Mater* 19(5):426–439
 50. Antil P, Kumar Antil S, Prakash C, Królczyk G, Pruncu C (2020). Multi-objective optimization of drilling parameters for orthopaedic implants. *Measurement and Control*, p.0020294020947126
 51. Kharb SS, Antil P, Singh S, Antil SK, Sihag P, Kumar A (2020) Machine learning-based Erosion behavior of silicon carbide reinforced polymer composites. *Silicon*. 13:1113–1119. <https://doi.org/10.1007/s12633-020-00497-z>
 52. Antil SK, Antil P, Singh S, Kumar A, Pruncu CI (2020) Artificial neural network and response surface methodology based analysis on solid particle Erosion behavior of polymer matrix composites. *Materials* 13(6):1381
 53. Bachchan AA, Das PP, Chaudhary V (2021) Effect of moisture absorption on the properties of natural fiber reinforced polymer composites: a review. *Materials Today: Proceedings*
 54. Bañon F, Sambruno A, González-Rovira L, Vazquez-Martinez JM, Salguero J (2021) A review on the abrasive water-jet machining of metal–carbon fiber hybrid materials. *Metals* 11(1):164
 55. Prasad KS, Chaitanya G (2021). Optimization of process parameters on surface roughness during drilling of GFRP composites using taguchi technique. *Materials today: proceedings*, 39, pp.1553-1558
 56. Kumaran ST, Ko TJ, Uthayakumar M, Islam MM (2017) Prediction of surface roughness in sabrative water jet machining of CFRP composites using regression analysis. *J Alloys Compd* 724:1037–1045
 57. Kumaran ST, Ko TJ, Kurniawan R, Li C, Uthayakumar M (2017) ANFIS modeling of surface roughness in abrasive waterjet machining of carbon fiber reinforced plastics. *J Mech Sci Technol* 31(8):3949–3954
 58. Thakur RK, Singh KK, Ramkumar J (2021) Impact of nanoclay filler reinforcement on CFRP composite performance during abrasive water jet machining. *Materials and Manufacturing Processes*, pp:1–10
 59. Dahooie JH, Zavadskas EK, Abolhasani M, Vanaki A, Turskis Z (2018) A novel approach for evaluation of projects using an interval-valued fuzzy additive ratio assessment (ARAS) method: a case study of oil and gas well drilling projects. *Symmetry* 10(2):45
 60. Dhanabalan S, Sivakumar K, Narayanan CS (2013) Optimization of machining parameters of EDM while machining Inconel 718 for form tolerance and orientation tolerance
 61. Dhanabalan S, Sivakumar K, Sathiyaraj Narayanan C (2014) Analysis of form tolerances in electrical discharge machining process for Inconel 718 and 625. *Mater Manuf Process* 29(3):253–259
 62. Yadav RN (2019) Electro-chemical spark machining–based hybrid machining processes: research trends and opportunities. *Proc Inst Mech Eng B J Eng Manuf* 233(4):1037–1061
 63. Jafferson JM, Hariharan P, Ram Kumar J (2014) Effects of ultrasonic vibration and magnetic field in micro-EDM milling of non-magnetic material. *Mater Manuf Process* 29(3):357–363
 64. Jeyaprakash N, Yang CH, Raj Kumar D (2020) Machinability study on CFRP composite using Taguchi based grey relational analysis. *Materials Today: Proceedings* 21(3):1425–1431
 65. Rajkumar D, Ranjithkumar P and Narayanan CS (2017) Optimization of machining parameters on microdrilling of CFRP composites by Taguchi based desirability function analysis

Publisher's Note Springer Nature remains neutral with regard to jurisdictional claims in published maps and institutional affiliations.



Contents lists available at ScienceDirect

Journal of Bioresources and Bioproducts

journal homepage: www.elsevier.com/locate/jobab

Rain tree (*Samanea saman*) seed oil: Solvent extraction, optimization and characterization

S. Chandra Sekhar^{a,*}, K. Karuppasamy^b, M. Vimal Kumar^c, D. Bijulal^d, N Vedaraman^e, Ravishankar Sathyamurthy^{f,*}^a Department of Mechanical Engineering, N.B.K.R Institute of Technology(Autonomous), Vidyanagar-524 413, Andhra Pradesh, India^b Department of Mechanical Engineering, Anna University Regional Campus, Tirunelveli, Tamil Nadu, 627007, India^c Department of Mechanical Engineering, M.A.M School of Engineering, Tiruchirappalli, 621 105, Tamil Nadu, India^d Department of Mechanical Engineering, Govt. Engineering College, Barton Hill, Thiruvananthapuram, 695035, Kerala, India^e Department of Chemical Engineering, Central Leather Research Institute (CSIR-CLRI), Chennai, Tamil Nadu, 600020, India^f Department of Mechanical Engineering, KPR Institute of Engineering and Technology, Arasur, Coimbatore, Tamil Nadu, 641407, India

ARTICLE INFO

Keywords:

Soxhlet apparatus
Response Surface Methodology
Box-Behnken design (BBD)
Analysis of variance
mg per KOH g of oil

ABSTRACT

The present investigation reports the soxhlet assisted solvent extraction technique to derive the oil from seeds of the rain tree. The optimization of the factors affecting the extraction process has been carried out by Response Surface Methodology (RSM) technique, and a Box-Behnken Design (BBD) consisting of three process variables has been developed to optimize the yield of oil. Using the RSM technique, the predicted optimum oil yield of 11.15% at an optimized condition of powder weight of 20 g, volume of solvent of 380 mL, and extraction time of 6 h. The physiochemical properties of the oil showed liquid greenish-yellow with 0.88, 1.473 of specific gravity and refractive index, respectively. Similarly, the moisture content, free fatty acid, acid value, saponification value, iodine value, and peroxide value were found to be 0.16%, 13.615, 27.23, 187.1 mg KOH per g oil, 65.8 g I₂ per 100 g, and 4.02 meq O₂ per kg, respectively. From the obtained results, it was found that the extracted oil could be used for various applications.

1. Introduction

Demand of energy is increasing day to day and the need of alternative is increasing exponentially (Bharathwaaj et al., 2018; Sekhar et al., 2018; Balaji et al., 2019; Sekhar et al., 2019; Velmurugan et al., 2019; Kaimal et al., 2020; Karuppan et al., 2020; Subramaniam et al., 2020; Sundar et al., 2020). Solvent extraction is a means of separation of the oil from oil-bearing materials with the aid of solvents. There are various organic and inorganic solvents used to extract oils from seeds. The most commonly utilized solvents for the extraction process are methanol, ethanol, hexane, chloroform, petroleum ether, and isopropyl alcohol. The food-grade hexane or n-hexane, a petroleum-derived product, is normally used to separate oil from seeds due to its lower corrosiveness, lower greasy residual effect, lower vaporization temperature and higher stability (Yahaya et al., 2016). The solvent extraction approach was used to convert the pine seed biomass solid waste into bio-oil (Islama et al., 2015). In their conversion process, hexane was used as the solvent in the form of miscella known as a mixture of solvent and oil. After the extraction of oil, the distillation process was used to retrieve the solvent. The bio-oil obtained was analyzed for their properties and compared with petroleum-based diesel since they wanted to use the oil as an alternate fuel. The soxhlet assisted extraction of oil from Date palm seed (*Phoenix dactylifera*) using n-hexane as a

* Corresponding authors.

E-mail addresses: chandruthermal@gmail.com (S.C. Sekhar), raviannauniv23@gmail.com (R. Sathyamurthy).<https://doi.org/10.1016/j.jobab.2021.04.005>

Received 15 May 2020; Received in revised form 11 August 2020; Accepted 8 September 2020

Available online xxx

2369-9698/© 2021 The Author(s). Published by Nanjing Forestry University. This is an open access article under the CC BY-NC-ND license (<http://creativecommons.org/licenses/by-nc-nd/4.0/>)Please cite this article as: S.C. Sekhar, K. Karuppasamy, M.V. Kumar et al., Rain tree (*Samanea saman*) seed oil: Solvent extraction, optimization and characterization, Journal of Bioresources and Bioproducts, <https://doi.org/10.1016/j.jobab.2021.04.005>

solvent has been carried out by [Ali et al. \(2015\)](#). The oil produced from *P. dactylifera* seeds using n-hexane solvent was very similar to other bio-oils in basic fuel properties and chemical composition. [Abdulrasheed et al. \(2015\)](#) extracted oil from castor bean seeds by employing hexane as the solvent. In their scrutiny, the soxhlet extractor was utilized for the removal of oil from the castor beans. From the characterization results, they concluded that the castor seed oil extract has the potential ability to be utilized in medicated soap production. In another experiment, oil was separated from a pre-pressed jojoba meal using the solvent extraction mechanism by [Zaher et al. \(2004\)](#). In their investigation, the hexane and petroleum ether were used as the solvents for the extraction process. In addition, many experiments were performed by varying the temperature and solvent to meal ratio. They observed that the hexane solvent gives a better percentage of oil recovery than that of petroleum ether. [Kahla and SafeKordi \(2012\)](#) evaluated the effect of type of solvent and temperature on the peach kernel oil extraction using three different methods. The normal soxhlet, digital soxhlet, and maceration methods of oil extractions were compared with each other. From the oil yields, they found that the soxhlet method with n-hexane solvent gives good yield than that of the ethanol and aqueous ethanol solvents. Oleic acid is available in rich quantity from the extracted oil, and it is commercially used in cosmetic and food industries. The oil is extracted using chemical support from natural and olive cake employing solvents like ethanol, carbon tetrachloride, isopropyl alcohol, petroleum ether, and hexane was performed in soxhlet extractor by [Banat et al. \(2013\)](#). From the results, it was found that the oil yield obtained using natural and dried olive cake were 7.5% and 12.7% respectively using hexane as solvent. Furthermore, they concluded that the process parameters such as size of particle and solvent to seed ratio are influential parameters on yield of oil produced. [Capellini et al. \(2017\)](#) extracted the rice bran oil using the alcohol solvent and characterized the physicochemical properties of oil. It was concluded that the yield of oil was greatly influenced by the solvent hydration, temperature and type of solvent. Results showed that the yield reduced with increased solvent hydration. [Agu et al. \(2020\)](#) optimized the process parameters such as particle size, temperature and time of kernel oil using Response Surface Methodology (RSM) and Artificial Neural Network (ANN) techniques. Results showed that using optimum process parameters, the predicted yield of kernel oil is almost close to the experimental values by using ANN technique compared with RSM technique. The optimal production of Jatropha Methyl Ester (JOME) using RSM technique was carried out by [Sasikumar et al. \(2020\)](#). The results showed that the production of JOME is greatly influenced by the quantity of methanol used, amount of catalyst and speed of stirrer. [Reshad et al. \(2015\)](#) extracted the oil derived from rubber seeds using process optimization technique for higher oil yield. [Jisieike and Betiku \(2020\)](#) used n-hexane and isopropanol as solvent to extract oil from rubber seeds. It was concluded that n-hexane produced higher yield compared with isopropanol. Also, unsaturated fatty acid content of nearly 78% was present in the extracted oil. [Kemerli-Kalbaran and Ozdemir \(2019\)](#) optimized the process parameters such as solvent ratio, temperature and time of reaction in extracting oil from pine nut. [Somnuk et al. \(2017\)](#) used the spent coffee grounds for extracting the oil and used four different solvent for maximum yield.

The oil yield from the solvent extraction process using the soxhlet apparatus was influenced by numerous factors such as seed powder weight, particle size, the volume of solvent, time for extraction, and operating temperature. Hence, it is important to determine the effect of these variables on oil yields from different seeds to reduce the amount of energy use, loss of oil, and, finally, the extraction cost. Therefore, the proper selection of the values of the factors affecting the oil recovery process is crucial to get a high oil yield, which can be accomplished by optimization technique ([Umamaheshwari and Dinesh Sanker Reddy, 2016](#)).

At present, the utilization of statistical techniques such as RSM attained more significance when determining the optimum conditions for the oil extraction from a solvent extraction process. The RSM, originally portrayed by Box and Wilson, is defined as a combination of mathematical and statistical methods helpful for modeling and analysis of problems in which a response of concern is affected by different variables, and the aim is to optimize this response ([Box and Wilson, 1951](#); [Montgomery, 2012](#)). Recently, The RSM has been successfully applied to optimize the soxhlet assisted solvent extraction of oils from *Moringa* seed kernel ([Mani et al., 2007](#)), beniseed ([Betiku et al., 2012](#)), chia ([Martínez et al., 2012](#)), neem seed ([Awolu, 2013](#)) and kapok seed ([Bokhari et al., 2015](#)).

Rain tree (*Samanea saman*), a member of the Fabaceae family, is a tall tree, usually reaching a height of 15–25 m, native to tropical America. It is a large Indian tree and is known by various names in different parts of India. The mature tree yields an average of 200–250 kg of pods per tree per season. Seeds are plumply ellipsoidal, 8–11.5 mm long, 5–7.5 mm wide, marginally flattened from side to side, dark glossy brown with a narrowly U-shaped yellowish terming on the smoothed sides. There are 15–20 seeds per each pod, and one kilogram of seeds averages 4000–6000 seeds. The seeds were used in making seed necklaces and other craft items in Hawaii ([Degado et al., 2014](#); [Staples and Elevitch, 2006](#)). These seeds contain approximately 5.2% of oil when extracted with hexane in a soxhlet extractor for 24 h ([Knothe et al., 2015](#)). However, detailed parameter values and quality assessment of oil are not available. This study is focused on oil extraction from rain tree seeds using the solvent extraction technique. The optimization of process parameters such as powder weight, solvent volume, and extraction time in extraction of oil from rain tree seed is performed by using RSM technique. To determine the possible application of the oil, the quality is determined by assessing the physicochemical characterization.

2. Materials and methods

2.1. Chemicals and reagents

All chemicals and reagents (n-hexane, ethanol, diethyl ether, potassium hydroxide, sodium hydroxide, iodine monochloride potassium iodide, sodium thiosulphate, and hydrochloric acid) used for synthesis is analytical reagent grade and purchased from Chennai, Tamil Nadu, India and used as received without further purification.



Fig. 1. Rain tree pods.



Fig. 2. Rain tree seeds.



Fig. 3. Dehulled seeds.

2.2. Seed preparation

The rain tree seeds were collected from nearby villages of Nellore district, Andhra Pradesh, India. Seeds which were collected was processed into powder form by the following steps: 1) Screening of seeds: the selected seeds screened manually to remove bad seeds, stones, foreign materials, etc.; 2) Cleaning: for removing the dust or mud on the seeds, they were washed with distilled water; 3) Drying: for a period of seven days, the seeds which were washed are dried; 4) Dehulling: the seeds which were dried must be dehulled. This was done with the help of an electric mixer; and 5) Grinding: dehulled seeds were ground into coarse powder form.

Prior to the oil extraction, the powder was stored in polythene bags. The processing of seed powder is shown in [Figs. 1–4](#).

2.3. Oil extraction procedure

A 500 mL soxhlet apparatus consisting of a round bottom flask, extraction chamber, and reflux condenser was used in this work. The n-hexane was selected as a solvent medium for the extraction. The working of the apparatus is described as follows. Initially, a



Fig. 4. Seed powder.

Table 1
Range of Process variables for Box- Behnken design.

Factor	Name	Low	Medium	High
A [Numeric]	Sample powder weight (g)	20	30	40
B [Numeric]	Solvent volume (mL)	300	350	400
C [Numeric]	Extraction time (h)	2	4	6

small quantity of cotton wool was placed in the bottom of the thimble, and the known amount of seed powder was placed above the cotton wool. At the top of round bottom flask, an extraction chamber was attached while the n-hexane solvent in known quantity was kept in the round bottom flask. At the tail end of Soxhlet extraction unit, a reflux condenser was attached tightly. Water is circulated through the condenser containing inlet at the bottom and outlet at the top. The whole assembly was placed on the heating mantle. The solvent was heated at a constant temperature of 70°C, after which the solvent got vaporized. The solvent vapor travelled up through the condenser and got condensed. The liquid solvent trickled down into the extraction chamber, comprised the seed powder, and gradually filled with the solvent. The oil extracted from the powder was dissolved into the solvent.

The Soxhlet extraction chamber is designed in such a way that, when the solvent reaches a certain level, it is automatically emptied by the siphon side arm, moving back down to the cylindrical flask. The cycle is allowed to repeat for the given time. During every cycle of operation, a fraction of oil diffuses in the solvent. After various cycles of operations within the given time, the desired oil compound is settled down in the flask. After extraction, the n-hexane solvent is recovered, consistently by means of a rotary evaporator distillation process. Fig. 5 shows the photographic view of the soxhlet equipment.

The yield of oil in terms of percentage is calculated by using Eq. (1):

$$\text{Oil yield(\%)} = \frac{w_o}{w_p} \times 100\% \quad (1)$$

where w_p is weight of the seed powder (g), w_o is weight of the oil extract (g).

2.4. Experimental design procedure

From the experimental procedure and literature related to similar extraction processes, the most influencing factors of the current process are identified as weight of powder, volume of solvent, and time of extraction. The Box-Behnken Design (BBD) with RSM was used to optimize these parameter values. A three-level design consisting of three factors; weight of powder (g), volume of solvent (mL), and oil time of extraction (h) was developed. The actual values of the independent variables for different levels is listed in Table 1.

Table 2 presents the seventeen runs with 6 axial points, 5 central points, and 6 factorial points of the BBD. All the 17 experiments have been conducted at the design levels of variables according to Table 2. The results obtained from 17 runs were analyzed and input parameter optimization was conducted using RSM. From Table 2, it is seen that from experiment 1 and 5 the minimum and maximum yield of 5.16% and 11.10% were obtained, respectively. A best fit second-order equation was developed by the Design-Expert software 10.0.3 trail version (Stat-Ease Inc., Minneapolis, USA). The prediction by the best-fit equation and the experimental values are shown in Table 2.

$$y_o = \beta_0 \pm \sum_{i=1}^n \beta_i X_i \pm \sum_{i=1}^n \beta_{ii} X_i^2 \pm \sum_{i=1}^{n-1} \sum_{j=i+1}^n \beta_{ij} X_i X_j \quad (2)$$

where y_o is oil yield (%), β_0 is constant, β_i is regression coefficient (linear terms), β_{ii} is regression coefficient (quadratic terms), β_{ij} is regression coefficient (interaction terms), $X_i X_j$ is coded variables, and n is number of independent variables.



Fig. 5. Soxhlet apparatus.

Table 2

Box-Behnken Design (BBD) matrix layout.

Run	Powder weight (g)	Solvent volume (mL)	Extraction time (h)	Response (R, percentage of oil yield) (%)	
				Experimental value	Predicted value
1	30	400	2	5.16	5.26
2	20	350	2	7.00	7.02
3	30	350	4	9.33	9.59
4	30	350	4	9.50	9.59
5	20	350	6	11.10	11.20
6	30	350	4	9.73	9.59
7	30	300	2	8.60	8.57
8	40	400	4	8.21	8.20
9	30	350	4	9.50	9.60
10	30	400	6	9.88	9.90
11	40	300	4	9.50	9.63
12	20	400	4	8.26	8.14
13	30	300	6	8.50	8.40
14	40	350	2	9.65	9.55
15	40	350	6	9.87	9.84
16	20	300	4	8.50	9.50
17	30	350	4	9.90	9.59

The Eq. (2) shows the fitted polynomial equation:

Table 3
Statistical summary of BBD.

Source	Sequential model sum of squares	df	Mean square	F value	P-value Prob > F	Note
Mean vs. total	1362.46	1	1362.46			
Linear vs. mean	12.30	3	4.10	3.17	0.0603	
2FI vs. linear	9.85	3	3.28	4.72	0.0266	
<u>Quadratic vs. 2FI</u>	<u>6.68</u>	<u>3</u>	<u>2.23</u>	<u>57.00</u>	<u>≤ 0.0001</u>	<u>Suggested</u>
Cubic vs. quadratic	0.074	3	0.025	0.49	0.7053	<u>Aliased</u>
Residual	0.20	4	0.050			
Total	1391.56	17	81.86			
Lack of fit tests						
Linear	16.60	9	1.84	36.99	0.0017	
2FI	6.75	6	1.13	22.57	0.0048	
<u>Quadratic</u>	<u>0.074</u>	<u>3</u>	<u>0.025</u>	<u>0.49</u>	<u>0.7053</u>	<u>Suggested</u>
Cubic	0.000	0				<u>Aliased</u>
Pure Error	0.20	4	0.050			
Model summary statistics						
	SD	R-squared	Adjusted R-squared	Predicted R-squared	PRESS	
Linear	1.14	0.4227	0.2895	0.1340	33.0	
2FI	0.83	0.7661	0.6177	0.0818	26.72	
<u>Quadratic</u>	<u>0.20</u>	<u>0.9906</u>	<u>0.9785</u>	<u>0.9486</u>	<u>1.50</u>	<u>Suggested</u>
Cubic	0.22	0.9931	0.9726		+	<u>Aliased</u>

Notes: df, degree of freedom; SD, standard deviation; PRESS, predicted sum of squares.

Table 4
Analysis of variance (ANOVA) for response surface quadratic model.

Source	Sum of squares	df	Mean square	F value	P-value Prob > F	Significance
Model	28.83	9	3.20	82.00	< 0.0001	Significant
A-Powder Weight	0.70	1	0.70	17.97	0.0038	
B-Solvent Volume	1.61	1	1.61	41.24	0.0004	
C-Extraction Time	9.99	1	9.99	255.74	< 0.0001	
AB	0.28	1	0.28	7.06	0.0326	
AC	3.76	1	3.76	96.34	< 0.0001	
BC	5.81	1	5.81	148.68	< 0.0001	
A ²	0.16	1	0.16	4.21	0.0792	
B ²	5.79	1	5.79	148.11	< 0.0001	
C ²	0.62	1	0.62	15.96	0.0052	
Residual	0.27	7	0.039			
Lack of fit	0.074	3	0.025	0.49	0.7053	Not significant
Pure error	0.20	4	0.050			
Correlation total	29.10	16				

2.5. Physicochemical characterization of extracted oil

The refractive index at 30 °C was measured by Abbe's refractometer (Vinay et al., 2014). Measurement of specific gravity at 30 °C referred the procedure in AOAC (1997). Moisture content (%) was determined by the oven-dry method. Physicochemical properties are determined namely, peroxide value (meq O₂ per kg oil), free fatty acid value (mg KOH per g oil), acid value (mg KOH per g oil), saponification value (mg KOH per g oil) and iodine value (g I₂ per 100 g oil). The AOAC (1997) test methods were followed.

3. Results and discussion

3.1. Model fitting and summary of design

The statistical summary and model summary statistics of optimization of rain tree seed oil extraction process by BBD is shown in Table 3.

From the sequential sum of squares of the model, the second-order polynomial is selected, where the extra terms are important, and the model is not aliased. Based on the lack of fit tests, it was found that the model has insignificant lack-of-fit. From the model summary statistics, the model maximized the values of adjusted R-squared and predicted R-squared. The quadratic model is proposed for the optimization of rain tree seed oil extraction process.

The resulted quadratic model equation is given by Eq. (3).

$$R = +9.59 + 0.30A - 0.45B + 1.12C - 0.26AB - 0.97AC + 1.21BC + 0.20A^2 - 1.17B^2 - 0.38C^2 \quad (3)$$

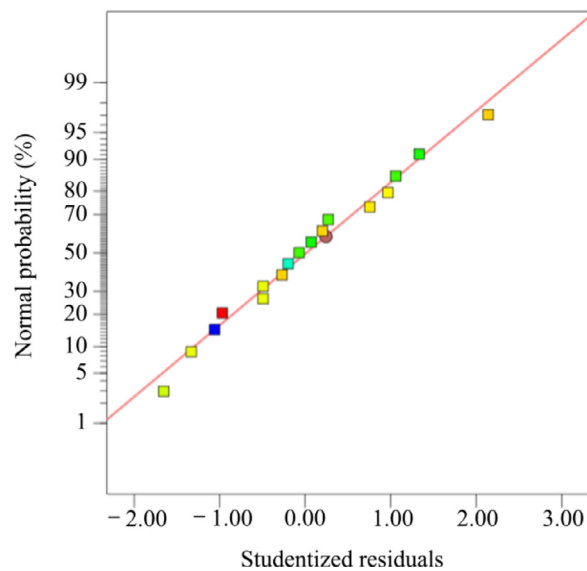


Fig. 6. Normal plot of residuals.

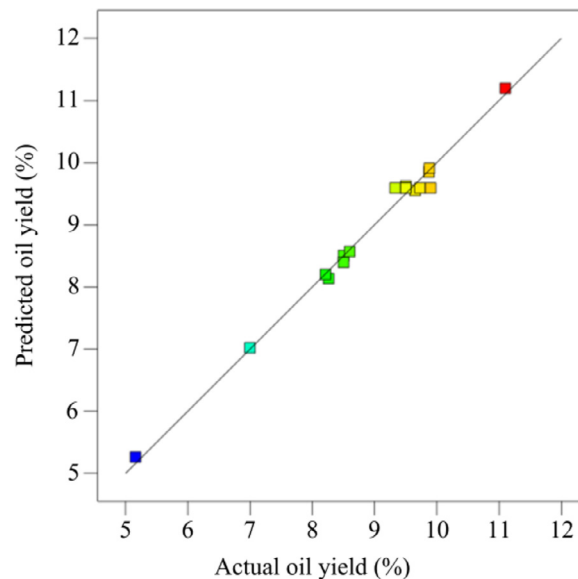


Fig. 7. Actual and predicted values of response.

To make the predictions for responses, coded variables are used and levels are given for each factor as shown in Eq. (3). The low level factors and high level factors are given in terms of code as -1 and +1. To identify the impact of process parameters, Eq. (3) is used for comparing the factor coefficients. In terms of variables, the final model equation is given by Eq. (4).

$$y_o = -42.052050 + 0.28872 \times w_p + 0.28680 \times v_s - 1.43425 \times t_e - 5.250E - 0.4 \times w_p \times v_s - 0.04850 \times w_p \times t_e + 0.012050 \times v_s \times t_e + 1.97750E - 0.3 \times w_p^2 - 4.6890E - 0.4 \times v_s^2 - 0.096188 \times t_e^2 \quad (4)$$

where w_p is powder weight, v_s is solvent volume (mL), t_e is extraction time (h), and E is exponential power.

3.2. Analysis of variance (ANOVA)

From the results of ANOVA, it is found that the present model is more significant as the P -value is lower than 0.05. The three cross products (AB , AC , BC), the three linear terms (A , B , C) and the two quadratic terms (B^2 , C^2) have a confidence level of 95% and it is found to be significant. From the large Fisher F -Test (i.e., F -value) and low corresponding probability values (P -values), it was observed that all the linear terms, the cross products (AC , BC), and the quadratic terms (B^2 , C^2), have strong effects on the percentage

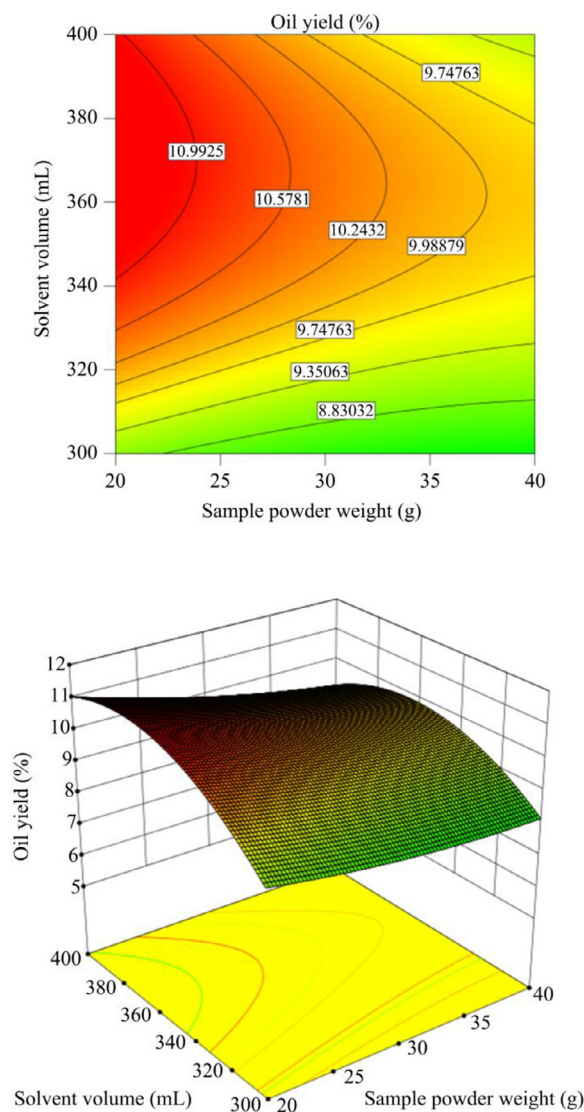


Fig. 8. (a) Contour plot; (b) 3D plot of response with respect to powder weight and solvent volume.

of oil yield. Furthermore, the lack-of-fit F -value 0.49 indicates the lack-of-fit is insignificant relative to the error. In this design, a non-significant lack of fit is favorable. The predicted R -squared of 0.9486 is in reasonable agreement with the adjusted R -squared of 0.9785. The goodness of fit of the regression model is further confirmed by the coefficient of determination (R^2). The R^2 value of 0.9906 indicates that the proposed model is capable of explaining 99.06% of the sample variance of the oil extraction process. Table 4 summarizes the results of ANOVA using the quadratic model, and the model fits are examined.

3.3. Model diagnostic plots

The two diagnostic plots of the model, namely residual plots and predicted vs. actual plots are shown in Figs. 6 and 7. The normal probability graph shown in Fig. 6 indicates the residuals follow a normal distribution. It is evident since the residuals are concentrated towards the straight line. Hence the error in the proposed quadratic model is distributed normally and identically, i.e., approx $N(0, 1)$.

The response values actually obtained from experimental runs, were plotted against the predicted response values (Fig. 7). This plot helps to find a value, or group of values, that are not easily predicted by the model. It can be clearly seen that the proposed model in predicting the yield with the actual has a linear relationship.

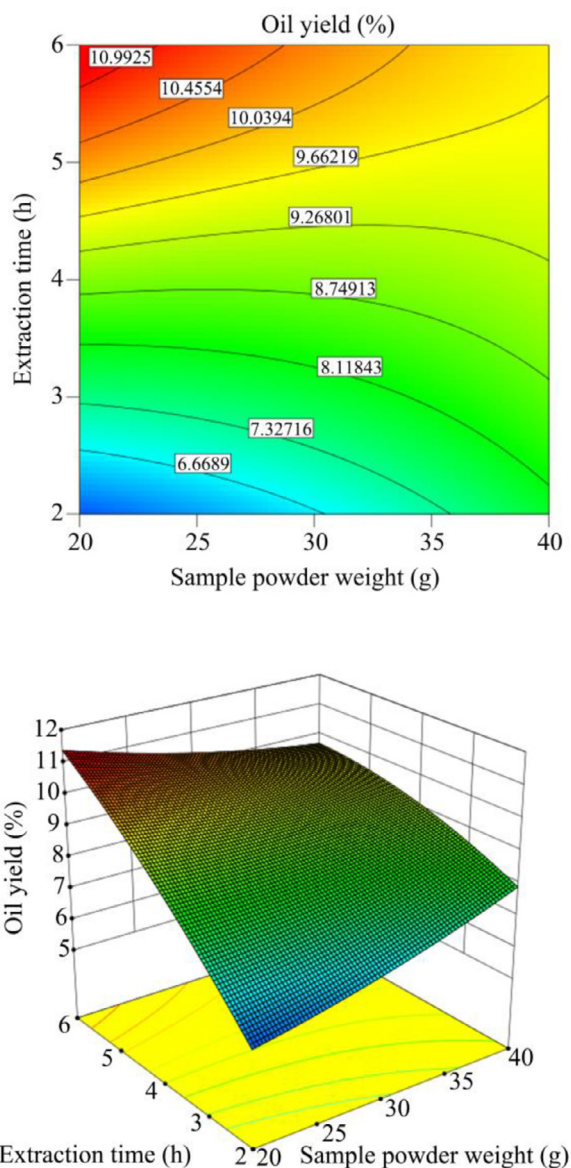


Fig. 9. (a) Contour plot; (b) 3D plot of response with respect to extraction time and powder weight.

3.4. Response surface plots

The graphical illustration of the impact of variables to response has been presented in Figs. 8–10. The contour plots in Fig. 8a and 3D surface plot of response in Fig. 8b indicate the effect of the interaction of solvent volume and powder weight on percentage yield of rain tree seed oil while keeping the extraction time as constant at its optimum value of 6 h. From the response plot, it can be detected that higher solvent volume and low powder weight favor an increase in oil yield. The powder weight seems to have more influence on the oil yield than the solvent volume.

The 3D response surface plot and contour plot in Fig. 9a and b shows the mutual interaction between extraction time and powder weight on the percentage recovery of oil from rain tree seeds, by keeping the solvent volume at its optimum value of 380 mL. From the figures, it can be observed that the higher oil yield was recorded at lower powder weight and higher extraction time.

The effect of solvent volume and extraction time and their interaction on the percentage of oil yield, while powder weight maintained at a constant level, and it is graphically represented in Fig. 10a and b. The combination of higher solvent volume and higher extraction time provides higher oil yield. However, the solvent volume has a greater significance on the oil yield than that of extraction time.

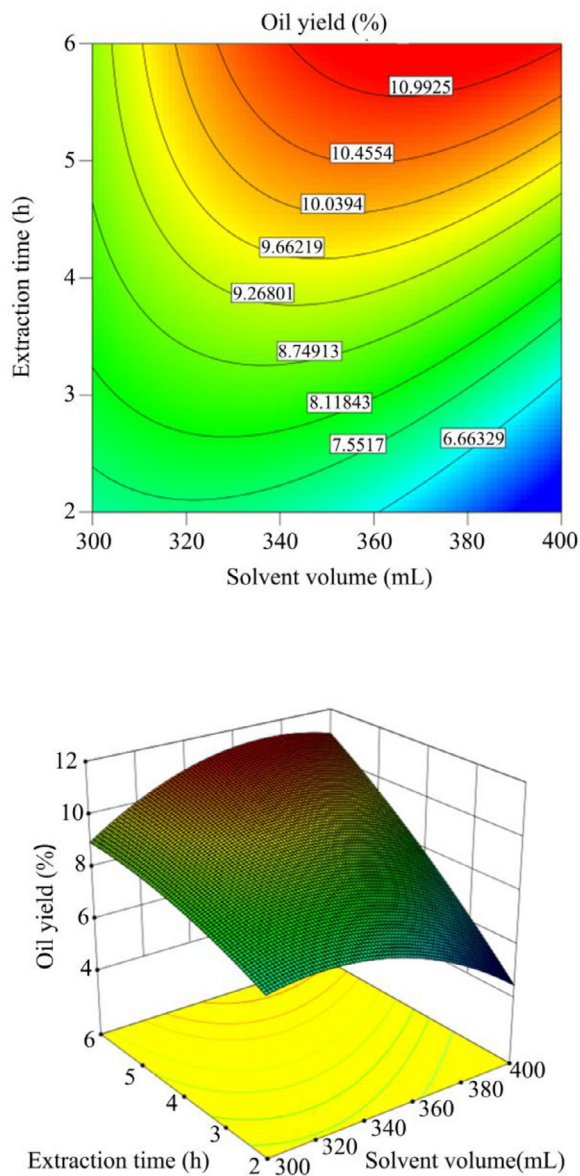


Fig. 10. (a) Contour plot; (b) 3D plot of response with respect to solvent volume and extraction time.

The parameter optimization of the oil extraction process has been conducted by RSM on the developed regression equation. The optimal conditions for this extraction process were obtained as $w_p^* = 20$ g, $v_s^* = 380$ mL, and extraction time $t_e^* = 6$ h (where w_p^* is value of optimized powder weight (g), v_s^* is value of optimized solvent volume (mL), and t_e^* is value of optimized extraction time (h)). The yield of rain tree seed oil extraction at this optimal condition was obtained as $y_o^* = 11.15\%$ (y_o^* , value of optimized oil yield (%)). By using these optimized values for three factors, the experimentation was replicated three times. Mean yield of 11.05% was obtained for rain tree seed oil extraction at this optimum parameter setting. This value is within the range predicted by the model. It is found that the oil yield obtained in this work is higher than that previously reported (Knothe et al., 2015).

3.5. Physicochemical analysis of extracted rain tree seed oil

The physicochemical properties of the extracted oil were analyzed and are shown in Table 5. The oil was a greenish-yellow color with a refractive index and moisture content of 1.473 and 0.16%, respectively. The specific gravity of the oil obtained in this work was 0.88. The acid value and free fatty acid content of the extracted oil were determined to be 27.23 mg KOH per g oil and 13.615 mg KOH per g oil, respectively. These values are found to be similar to that of moringa oil (Bhutada et al., 2016). The iodine value indicates unsaturation levels of the oil, was found to be 65.8 g I₂ per 100 g for rain tree seed oil. Low iodine value (below 100 g I₂

Table 5
Physical properties of rain tree seed oil.

Parameter	Analyzed results
Physical appearance at 30 °C	Greenish yellow
Specific gravity at 30 °C	0.880
Refractive index at 30 °C	1.473
Moisture content (%)	0.16
Acid value (mg KOH per g oil)	27.23
Free fatty acid (mg KOH per g oil)	13.615
Iodine value (g I ₂ per 100g oil)	65.8
Saponification value (mg KOH per g oil)	187.1
Peroxide value (meqO ₂ per kg)	4.02

per 100 g) classifies the oil as non-drying (Adelola, 2012). The iodine value of rain tree seed oil shows a high level of unsaturation, and it is a good feedstock for biodiesel production (Akintunde et al., 2015). The value obtained is close to that of moringa oil with an iodine value of 75.06 g I₂ per 100 g (Bhutada et al., 2016). The saponification value of oil is 187.1 mg KOH per g oil shows a high content of triacylglycerols demonstrating their potential to be used in the cosmetics and soap producing industries. The peroxide value is an index of deterioration of oils was evaluated to be 4.02 meq O₂ per kg indicating that the oil is of good quality (Malacrida and Jorge, 2012).

4. Conclusions

The extraction of oil from rain tree seeds was carried out using the soxhlet apparatus assisted solvent extraction technique. The traditional food grade n-hexane solvent was utilized for the oil extraction method. Three extraction parameters, such as powder weight, solvent volume, and extraction time, were optimized using RSM based on BBD. For process optimization, a quadratic model was generated and validated. The ANOVA for the predicted quadratic model was performed, which indicated that all the parameters of oil extraction and their interactions have a significant influence on the yield of the process. Furthermore, from the optimized results, it was found that the maximum oil yield of rain tree seed, i.e., 11.15%, at the powder weight of 20 g, a solvent volume of 380 mL and extraction time of 6 h. This optimized extraction process is suitable for laboratory scale applications. For commercial extraction processes, suitable optimization of the process need to be conducted. This optimized solvent extraction process provides better oil yields than that of the previous experimental research. From the physicochemical characterization, it can be concluded that the rain tree seed oil can be used as a feedstock in several industries, including food, soap, cosmetics, and biodiesel.

Declaration of Competing Interest

There are no conflicts to declare.

References

- Abdulrasheed, A., Arok, e U.O., Muazu, M.T., 2015. Characterization and utilization of castor been seed oil extract for production of medicated soap. *Am. J. Eng. Res.* 4, 67–72.
- Adelola, O.B., 2012. Extraction and characterization of cottonseed (*Gossypium*) oil. *Int. J. Basic Appl. Sci.* 1, 384–388.
- Agu, C.M., Menkiti, M.C., Ekwe, E.B., Agulanna, A.C., 2020. Modeling and optimization of *Terminalia catappa* L. kernel oil extraction using response surface methodology and artificial neural network. *Artif. Intell. Agric.* 4, 1–11.
- Akintunde, A.M., Ajala, S.O., Betiku, E., 2015. Optimization of *Bauhinia monandra* seed oil extraction via artificial neural network and response surface methodology: a potential biofuel candidate. *Ind. Crop. Prod.* 67, 387–394.
- Ali, M.A., Al-Hattab, T.A., Al-Hydary, I.A., 2015. Extraction of date palm seed oil (phoenix dactylifera) by soxhlet apparatus. *Int. J. Adv. Eng. Technol.* 8, 261–271.
- AOAC (Official Methods of Analysis), 1997. The Association of Official Analytical Chemists, 17th ed. AOAC, Washington D.C., USA.
- Awolu, O., 2013. Optimization of solvent extraction of oil from neem (*Azadirachta indica*) and its characterizations. *J. Sci. Res. Rep.* 2, 304–314.
- Balaji, D., Mathevan Pillai, T., Gnanasekaran, K., Balachandrar, M., Ravikumar, T.S., Sathish, S., Sathyamurthy, R., 2019. Dataset for compression ignition engine fuelled with corn oil methyl ester biodiesel. *Data Brief* 27, 104683.
- Banat, F., Pal, P., Jwaied, N., Al-Rabadi, A., 2013. Extraction of olive oil from olive cake using soxhlet apparatus. *Am. J. Oil Chem. Technol.* 1, 1–8.
- Betiku, E., Adepoju, T.F., Omole, A.K., Aluko, S.E., 2012. Statistical approach to the optimization of oil extraction from beniseed (*Sesamum indicum*) oilseeds. *J. Food Sci. Eng.* 2, 351–357.
- Bharathwaaj, R., Nagarajan, P.K., Kabeel, A.E., Madhu, B., Mageshbabu, D., Sathyamurthy, R., 2018. Formation, characterization and theoretical evaluation of combustion of biodiesel obtained from wax esters of *A. Mellifera*. *Alex. Eng. J.* 57, 1205–1215.
- Bhutada, P.R., Jadhav, A.J., Pinjari, D.V., Nemade, P.R., Jain, R.D., 2016. Solvent assisted extraction of oil from *Moringa oleifera* Lam. seeds. *Ind. Crop. Prod.* 82, 74–80.
- Bokhari, A., Chuah, L.F., Yusup, S., Ahmad, J., Aziz, H., 2015. Kapok seed oil extraction using soxhlet extraction method: optimization and parametric study. *Aust. J. Basic Appl. Sci.* 9, 429–443.
- Box, G.E.P., Wilson, K.B., 1951. On the experimental attainment of optimum conditions. *J. R. Stat. Soc.: Ser. B Methodol.* 13, 1–38.
- Capellini, M.C., Giacomini, V., Cuevas, M.S., Rodrigues, C.E.C., 2017. Rice bran oil extraction using alcoholic solvents: physicochemical characterization of oil and protein fraction functionality. *Ind. Crop. Prod.* 104, 133–143.
- Delgado, D.C., Hera, R., Cairo, J., Orta, Y., 2014. *Samanea saman*, a multi-purpose tree with potentialities as alternative feed for animals of productive interest. *Cuba. J. Agric. Sci.* 48, 205–212.
- Islam, M.N., Sabur, A., Ahmed, R., Hoque, M.E., 2015. Oil extraction from pine seed (*Polylathia longifolia*) by solvent extraction method and its property analysis. *Procedia Eng.* 105, 613–618.

- Jisieike, C.F., Betiku, E., 2020. Rubber seed oil extraction: effects of solvent polarity, extraction time and solid-solvent ratio on its yield and quality. *Biocatal. Agric. Biotechnol.* 24, 101522.
- Kahla, N.E., SafeKordi, A.A., 2012. Evaluation of temperature & solvent effect on peach kernel oil extraction & determination & quantification of its fatty. *J. Natl. Sci. Res.* 2, 1–7.
- Kaimal, V.K., Vijayabalan, P., Balachandar, M., Padmanaba Sundar, S., Sathyamurthy, R., 2020. Effect of using plastic nanofuel as a fuel in a light-duty diesel engine. *Heat Transf.* 49, 726–742.
- Karuppan, D., Muthu Manokar, A., Vijayabalan, P., Sathyamurthy, R., Madhu, B., Mageshbabu, D., Bharathwaaj, R., Jenoris Muthiya, S., 2020. Experimental investigation on pressure and heat release HCCI engine operated with chicken fat oil/diesel-gasoline blends. *Mater. Today: Proc.* 32, 437–444.
- Kemerli-Kalbaran, T., Ozdemir, M., 2019. Multi-response optimization of oil extraction from pine nut (*Pinus pinea* L.) by response surface methodology: extraction efficiency, physicochemical properties and antioxidant activity. *LWT* 103, 34–43.
- Knothe, G., Phoo, Z.W.M.M., de Castro, M.E.G., Razon, L.F., 2015. Fatty acid profile of *Albizia lebeckand Albizia saman* seed oils: presence of coronaric acid. *Eur. J. Lipid Sci. Technol.* 117, 567–574.
- Malacrida, C.R., Jorge, N., 2012. Yellow passion fruit seed oil (*Passiflora edulis* f. *flavicarpa*): physical and chemical characteristics. *Braz. Arch. Biol. Technol.* 55, 127–134.
- Mani, S., Jaya, S., Vadivambal, R., 2007. Optimization of solvent extraction of *Moringa (Moringa oleifera)* seed kernel oil using response surface methodology. *Food Bioprod. Process.* 85, 328–335.
- Martinez, M.L., Marín, M.A., Salgado Faller, C.M., Revol, J., Penci, M.C., Ribotta, P.D., 2012. Chia (*Salvia hispanica* L.) oil extraction: study of processing parameters. *LWT-Food Sci. Technol.* 47, 78–82.
- Montgomery, D.C., 2012. *Design and Analysis of Experiments*. John Wiley & Sons, New Jersey.
- Reshad, A.S., Tiwari, P., Goud, V.V., 2015. Extraction of oil from rubber seeds for biodiesel application: optimization of parameters. *Fuel* 150, 636–644.
- Sasikumar, C., Balamurugan, K., Jegadheeswaran, S., Sathyamurthy, R., 2020. Optimization of process parameter in the production of *Jatropha* Methyl Ester using response surface methodology. *Biocatal. Agric. Biotechnol.* 27, 101693.
- Sekhar, S., Karuppasamy, K., Vedaraman, N., Kabeel, A.E., Sathyamurthy, R., Elkelay, M., Alm Eldin Bastawissi, H., 2018. Biodiesel production process optimization from *Pithecellobium dulce* seed oil: performance, combustion, and emission analysis on compression ignition engine fuelled with diesel/biodiesel blends. *Energy Convers. Manag.* 161, 141–154.
- Sekhar, S.C., Karuppasamy, K., Sathyamurthy, R., Elkelay, M., Bastawissi, H.A.E.D., Paramasivan, P., Sathiyamoorthy, K., Edison, P., 2019. Emission analysis on compression ignition engine fuelled with lower concentrations of *Pithecellobium dulce* biodiesel-diesel blends. *Heat Transf.—Asian Res.* 48, 254–269.
- Somnuk, K., Eawlex, P., Prateepchaikul, G., 2017. Optimization of coffee oil extraction from spent coffee grounds using four solvents and prototype-scale extraction using circulation process. *Agric. Nat. Resour.* 51, 181–189.
- Staples, G.W., Elevitch, C.R., 2006. *Samanea saman* (rain tree), ver. 2.1. In: Elevitch, C.R. (Ed.), *Species Profiles for Pacific Island Agroforestry*. Permanent Agriculture Resources (PAR) Available at www.traditionaltree.org.
- Subramaniam, M., Solomon, J.M., Nadanakumar, V., Anaimuthu, S., Sathyamurthy, R., 2020. Experimental investigation on performance, combustion and emission characteristics of DI diesel engine using algae as a biodiesel. *Energy Rep.* 6, 1382–1392.
- Sundar, P.S., Sathyamurthy, R., Chamkha, A.J., 2020. Influence of oxygen enrichment on performance, combustion, and emission characteristics of a stationary diesel engine fuelled with *Calophyllum Inophyllum* biodiesel blend. *Asia-Pac. J. Chem. Eng.* 15, e2472.
- Umamaheshwari, P., Dinesh Sankar Reddy, P., 2016. Effect of operating parameters on extraction of oil from bitter gourd seeds: a kinetic and thermodynamic study. *Int. J. Sci. Res. IJSR* 5, 1243–1246.
- Velmurugan, R., Mayakrishnan, J., Induja, S., Raja, S., Nandagopal, S., Sathyamurthy, R., 2019. Comprehensive study on the effect of CuO nano fluids prepared using one-step chemical synthesis method on the behavior of waste cooking oil biodiesel in compression ignition engine. *J. Therm. Sci. Eng. Appl.* 11, 041003.
- Vinay, S., Gajra, G., Afroz, A., 2014. Extraction and characterization of industrially valuable oil from *Eruca sativa* (L.) Mill. through FT-IR and GC-MS analysis. *Am. J. Biol. Chem.* 2, 23–28.
- Yahaya, S., Giwa, S.O., Ibrahim, M., Giwa, A., 2016. Extraction of oil from *Jatropha* seed kernels: optimization and characterization. *Int. J. Chemtech. Res.* 9, 758–770.
- Zaher, F.A., El Kinawy, O.S., El Haron, D.E., 2004. Solvent extraction of jojoba oil from pre-pressed jojoba meal. *Grasas Aceites* 55, 129–134.

Investigation on mechanical and tribological properties of AA5083/Gr/BN and AA5083/Gr/Al₂O₃ hybrid composites for marine applications

J.Vivek^{a*}, J. Bensam Raj^b, K. Chandrasekaran^c, R. Karuppasamy^d

^aDepartment of Mechanical Engineering, Solamalai College of Engineering, Madurai, Tamilnadu, India

^bDepartment of Mechanical Engineering, Muthayammal Engineering College, Rasipuram, Tamilnadu, India

^cDepartment of Mechanical Engineering, MAM School of Engineering, Trichy, Tamilnadu, India

^dDepartment of Mechanical Engineering, Sethu Institute of Technology, Kariapatti, Tamilnadu, India

*Corresponding author: jviveksolamalai@gmail.com

Abstract:

Aluminum alloy AA5083 is attracted in naval architecture field to fabricate ship and boat due to its high corrosive resistance behavior with sea water. In this investigation, AA5083 was reinforced with graphine (Gr), boron nitride (BN) and aluminum oxide (Al₂O₃) partilces using stir casting method and the mechanical and tribological behavior were analyzed for naval architect applications. Mechanical study showed that the AA5083/Gr/Al₂O₃ composite exhibited a maximum tensile strength and hardness of 317 MPa and 153 HB at 16wt% Al₂O₃ respectively. Tribological study displayed that the wear rate of AA5083/Gr/Al₂O₃ and AA5083/Gr/BN composites depended on applied load and sliding velocity. AA5083/Gr/BN composite showed more wear rate compared to that of AA5083/Gr/Al₂O₃ composite due to the reinforcement of the composite with lower hardness BN particle. Hence, as the AA5083/Gr/Al₂O₃ composite showed improved tensile and hardness properties and displayed less wear, this could be a suitable material to be applicable in naval architecture field.

Keywords: AA5083 aluminum alloy, Graphite, Boron nitride, Aluminum oxide, Hybrid composite

1. INTRODUCTION

Aluminium Alloys are majorly used in various applications like marine, aerospace and petro-chemical industries due to its lightweight, superior mechanical strength and high corrosion resistance. AA5083 aluminium alloy is one of the alloy materials attracted by researchers and industrialists because of its superior corrosive resistance to chemicals and seawater due to the presence of major alloying elements such as Magnesium, Manganese, and Chromium. Hence, AA5083 aluminium alloy material is mostly used in ship building constructions [1]. Many researchers have focused their study on AA5083 aluminium alloy and improved the physical properties by adding metal reinforcement [2-3] and ceramic reinforcement [4-5] with AA5083. Alexis et al. [6] improved the mechanical properties of AA5083 alloy material with MWCNT for automobile applications and the report showed that the mechanical property of AA5083/MWCNT was improved by 36% compared to AA5083. Further, the Brinell hardness value of the composite was enhanced from 74 BHN to 84 BHN. Idrisi et al. [7] studied the wear behavior of AA5083/SiC composite and found that the experiment time and SiC wt% had the significant effect on wear performance followed by applied load.

Aluminium oxide (Al_2O_3) is a high melting point abrasive material used as forming tools, refractive materials and substrates. Several investigators concentrated on Al_2O_3 particle to use as reinforcement in metal matrix composites [8-9]. For example, Hariprasad et al. [10] carried out wear study on AA5083/ Al_2O_3 / B_4C composites and found that the wear resistance increased due to the addition of Al_2O_3 and B_4C to base metal. Sonawane et al. [11] performed tensile strength

test on Al6061/Al₂O₃/SiC-Gr composites and reported that the tensile strength was enhanced due to the addition of Al₂O₃.

Boron nitride (BN) is a refractive particle, has high resistance to chemical and thermal, mostly used to make high temperature equipments. Palanivel et al. [12] used BN as a reinforcement particle with AA6082 and studied the sliding wear behavior of AA6082/TiB₂/BN hybrid composite. The report showed that the BN particles addition enhanced the sliding wear resistance of the Aluminium matrix composites. Chi et al. [13] performed the tribological test on Al2024/TiB₂/BN composites and the results revealed that the addition of BN improved the tribological performance at low load and low sliding speed.

Based on the literature review, it is concluded that the Al₂O₃ and BN particles have the potential to use as reinforcements in aluminium alloys. Hence, in this investigation, an attempt has been made to prepare AA5083 based composites reinforced with Al₂O₃ and BN particles. Further, graphite (Gr) is a solid lubricant material used in aluminium composite materials. Early researchers have found that the presence of small amount (5 wt %) of graphite in the composite improved the wear behavior of the composite compared to base material [14]. Hence, it is worthy to include 5wt% graphite as self lubricating element in AA5083 aluminium alloy. Hence, the present investigation deals with the fabrication of two types of composites namely AA5083/Gr/Al₂O₃ and AA5083/Gr/BN and additionally, the mechanical and tribological properties of the prepared composite materials are to be analyzed to understand the suitability of the material for naval architects applications.

2. EXPERIMENTAL DETAILS

2.1 Materials and Preparation

Commercial grade AA5083 aluminium alloy was used as base material and Gr, Al₂O₃ and BN particles were used as reinforcements. The chemical composition of base material and reinforcements are given in Table 1 - 4. The average particle size of AA5083, Gr, Al₂O₃ and BN used in this investigation were 20, 65, 75 and 400 microns respectively. Two types of hybrid composites were prepared by stir casting method (figure 1) namely AA5083/Gr/BN and AA5083/Gr/Al₂O₃. Each hybrid composites contained a constant value of 5 wt% Gr and various wt% of BN and Al₂O₃ particles ranging from 4 – 16 wt% in the corresponding composite. The AA5083 was melted in a furnace and cooled slowly to reach a semi solid state. The reinforcements Gr and BN were preheated at 500 °C to eliminate thermal mismatch [15] and added with the semi solid state AA5083. Again, the furnace temperature was raised to 1000 °C to completely melt the reinforced particles along with AA5083. In order to achieve uniform distribution of matrix with reinforced particles, the mechanical stirring was carried out for 15 min at 600 rpm. The molten AA5083/Gr/BN hybrid composite was poured into the preheated mild steel mould and allowed to cool at room temperature. Similar preparation method was employed for making of AA5083/Gr/Al₂O₃ hybrid composites and the samples were cut according to ASTM standards for testing.

Table 1 Chemical composition of AA5083

Element	Al	Mn	Cu	SiC	Zn	Ti	Cr	Mg	Fe
Weight %	92.7	4.0-4.9	0.4-1.0	0.4	0.25	0.05-0.25	0.05-0.25	0.15	0.1

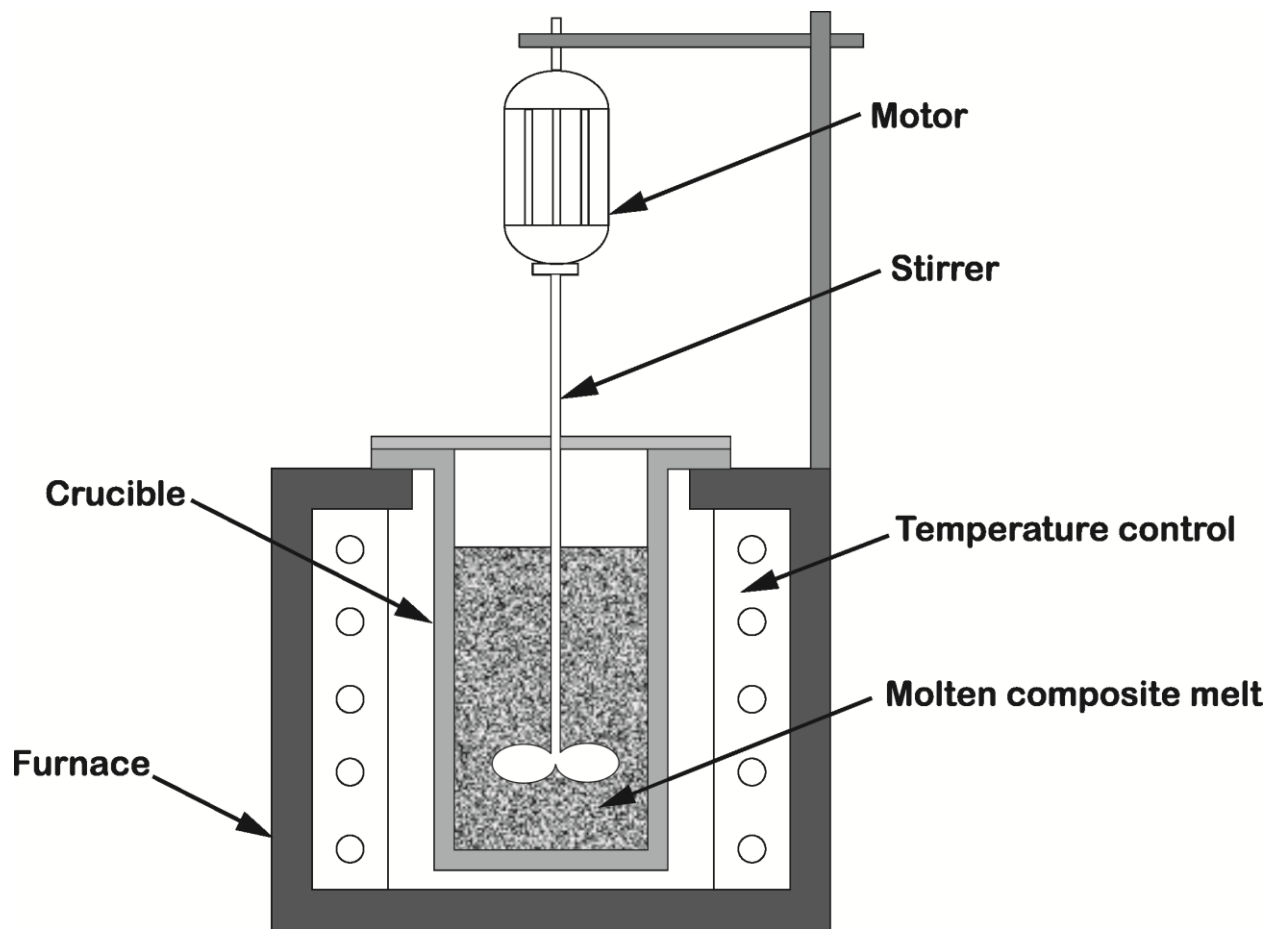


Figure 1 Stir casting setup

Table 2 Chemical composition of Gr

Element	C	S	Fe
Weight %	95	0.1	0.5

Table 3 Chemical composition of Al₂O₃

Element	γ -Al ₂ O ₃	Ca	Fe	Si	Co
Weight %	99.97	0.00016	0.00002	0.00035	0.00008

Table 4 Chemical composition of BN

Element	B	N	C
Weight %	55.31	40.21	4.48

2.2 Mechanical test

Mechanical properties were assessed using tensile and hardness test. Tensile test was performed on universal testing machine according to the standard ASTM E08-8. During the test 10 kN load was applied on the specimen and five specimens were tested for each run. Hardness test was performed in Brinell hardness testing machine according to the standard ASTM E10-07 and a load of 250 N was applied using steel ball indenter of 5 mm diameter. Hardness test was conducted at room temperature, the readings were taken at three different places and average value was considered for the analysis.

2.3 Tribological test

Dry sliding wear tests were carried out on pin-on-disc machine according to the standard ASTM G99-05(2010). Cylindrical pins of 10 mm diameter and 30 mm height were machined

from AA5083/Gr/BN and AA5083/Gr/Al₂O₃ composites for tribology test. The load was varied from 20 – 80 N and the sliding velocity was varied from 1 – 3 m/s.

3. Results and discussion

3.1 Density

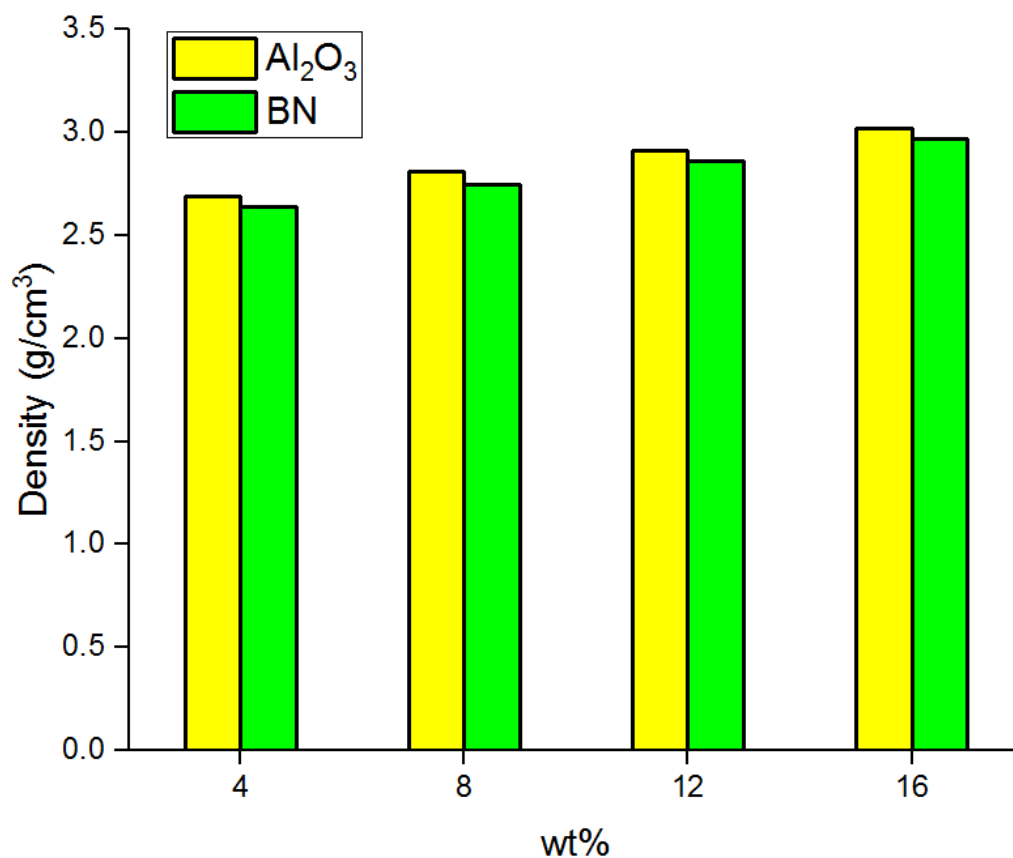


Figure 2 Density of composites

Experimental density was calculated by Archimedes principles [16] according to ASTM standard B962-13. Figure 2 shows the experimental density of the fabricated composites. Density of the composites enhanced with the increase of wt% of reinforcement. The composites reinforced with

Al_2O_3 particles showed increase in density compared to the density of composite reinforced with BN particles. As the density of Al_2O_3 particles were superior to the density of BN particles (Table 5), the AA5083/Gr/ Al_2O_3 composite showed improved density compared to AA5083/Gr/BN composite [17].

Table 5 Properties of reinforcements

Property	Al_2O_3	BN
Density (g/cm^3)	3.98	2.3
Hardness (MPa)	22050	3000
Tensile strength (MPa)	665	83.3
Young's modulus (GPa)	413	100
Shear modulus (GPa)	165	41.3

3.2 Tensile study

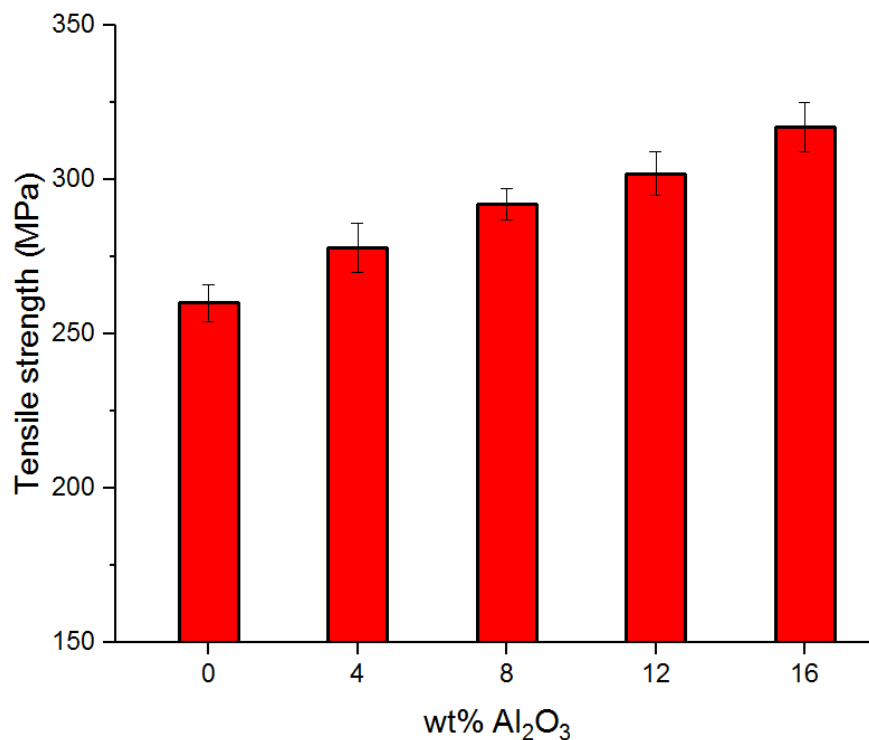


Figure 3 Tensile strength of AA5083/Gr/ Al_2O_3 composite

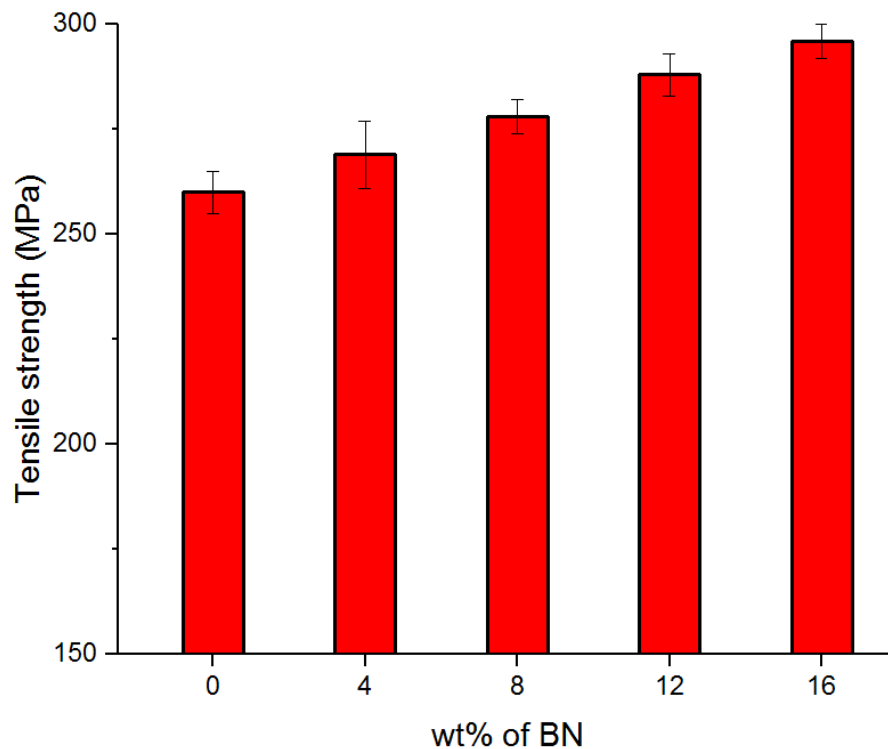


Figure 4 Tensile strength of AA5083/Gr/BN composite

Figure 3 shows the variation of tensile strength of AA5083/Gr composite for various wt% of Al_2O_3 particles. As can be seen from figure 3, the tensile strength increased with the increase of Al_2O_3 wt%. Tensile strength reached a maximum value of 317 MPa while including 16wt% Al_2O_3 particle that is 22% greater than the tensile strength of AA5083 alloy. Tensile strength improved steadily in the range of 4 – 16wt% of Al_2O_3 and followed the linear correlation with the wt% of Al_2O_3 . Hence, the addition of 16wt% Al_2O_3 with AA5083 alloy showed a better reinforcement effect. The enhancement in tensile strength could be attributed by two reasons (1) the inclusion of more reinforcements improved the stress transfer between AA5083 and Al_2O_3 and enhanced the tensile strength; (2) enhancement due to Orowan bowing mechanism [18-19]. According to Orowan bowing mechanism, the precipitates formed during composite preparation

act as pinning point for dislocation. Dislocation bends continuously around the precipitate, encloses completely and leaving a dislocation loop around the precipitate. The looped precipitate withstands the dislocation further and improved the stress transfer.

Figure 4 shows the tensile strength of AA5083/Gr composite for various wt% of BN particles. The variation of tensile strength followed the same trend similar to the variation of tensile strength of AA5083/Gr/Al₂O₃ composite. Tensile strength of the composite increased while increasing the wt% of the BN particles and showed the superior value of 296 Mpa for the inclusion of 16wt% BN particle that is 14% greater than the tensile strength of AA5083. Similar type of experimental results was reported by previous investigators [20-21]. They claimed that the BN strengthened the bonding strength and hinder the dislocation of grain movement. Further, the addition of hard ceramic particles decreased the grain size of the alloy and enhanced the strength [22]. Additionally, the ceramic particle inclusion increased the dislocation density and improved the strength [23].

Figure 5 shows the comparison of tensile strengths of AA5083/Gr/Al₂O₃ and AA5083/Gr/BN composites. As can be seen from figure 3, the addition of Al₂O₃ particle in AA5083/Gr composite exhibited the superior tensile strength compared to the tensile strength of AA5083/Gr reinforced with BN particle. For example, the tensile strength of AA5083/Gr/Al₂O₃ showed the value of 317 Mpa at 16wt% Al₂O₃ particle that is 7% greater than the tensile strength of AA5083/Gr/BN for the same quantity of BN particle. This could be due to the intrinsic property of the reinforcement particles and further, the tensile strength of Al₂O₃ particle is superior than that of BN particle that could be another reason for the enhancement of tensile

strength of AA5083/Gr/Al₂O₃ composite compared to the tensile strength of AA5083/Gr/BN composite.

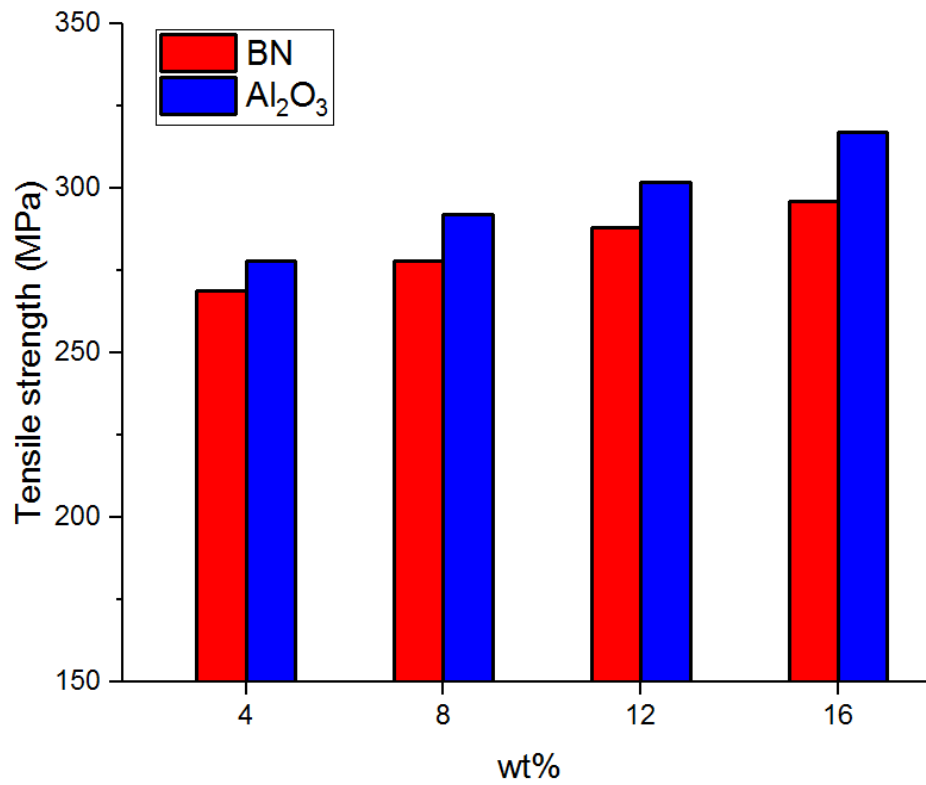


Figure 5 Comparison of tensile strengths of AA5083/Gr/BN and AA5083/Gr/Al₂O₃ composites

3.3 Hardness study

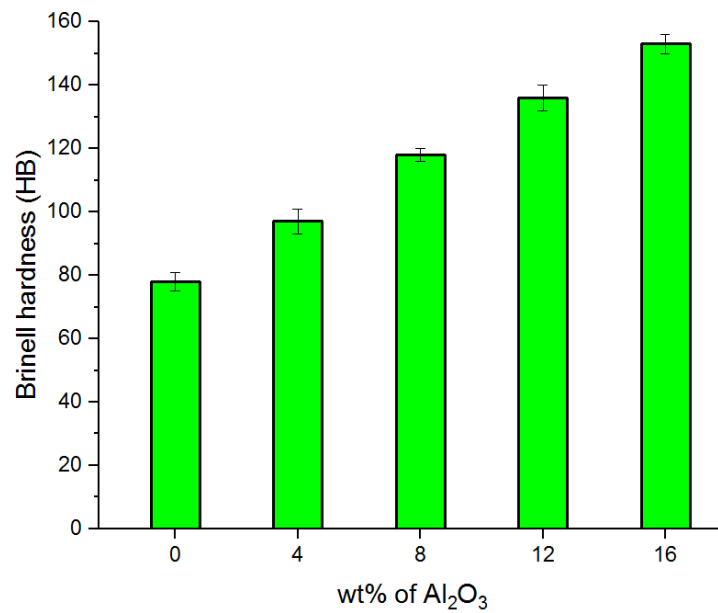


Figure 6 Hardness of AA5083/Gr/Al₂O₃ composite

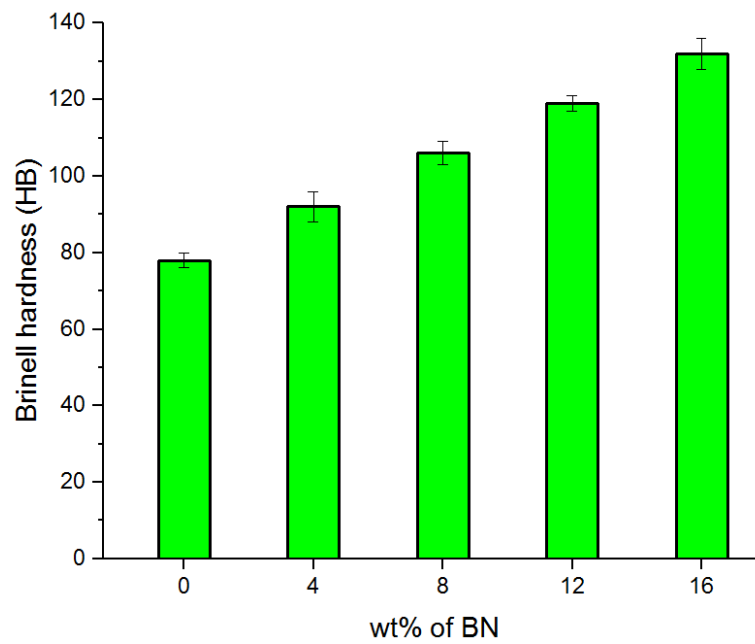


Figure 7 Hardness of AA5083/Gr/BN composite

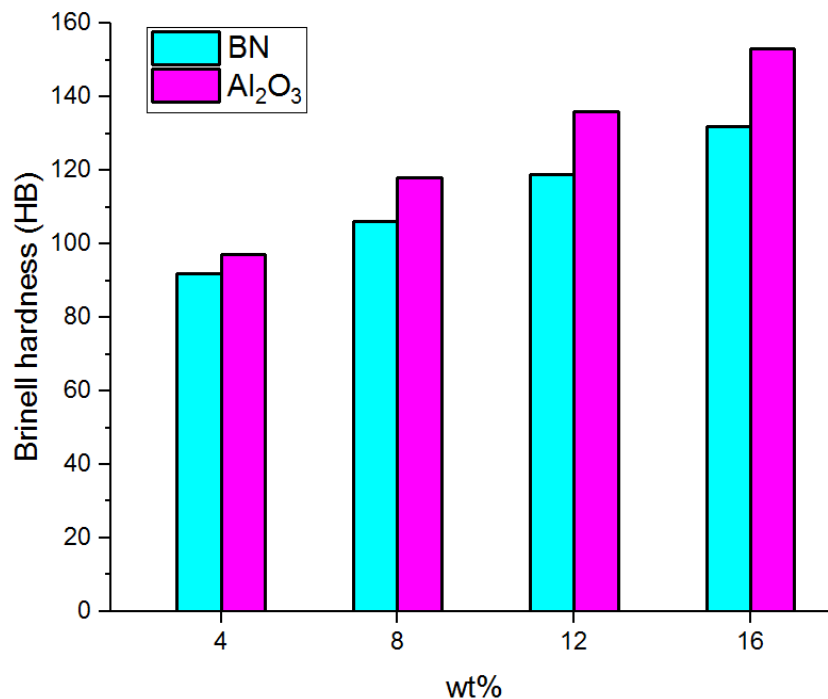


Figure 8 Comparison of hardness of AA5083/Gr/BN and AA5083/Gr/Al₂O₃ composites

Figure 6 & 7 shows the effect of Al₂O₃ and BN particles on the hardness of AA5083/Gr composite. It is obviously seen that the hardness of both the composite increased as the wt% percentage of reinforcement increased due to the increase of the density of the composite. AA5083/Gr composite showed the maximum hardness value of 153 HB and 132 HB while adding 16wt% of Al₂O₃ and BN particles respectively. The hard reinforcement particles i.e Al₂O₃ and BN prevented the deformation and dislocation of the grain and hinder the penetration that improved the hardness of the composites [24]. Figure 8 shows the comparison of hardness values of AA5083/Gr/Al₂O₃ and AA5083/Gr/BN composites with respect to wt% of reinforcement. As the figure 6 obviously shows, the AA5083/Gr/Al₂O₃ composite displayed the superior hardness value compared to that of the AA5083/Gr/BN composite. For example, AA5083/Gr/Al₂O₃ composite exhibited 16% higher hardness value compared to AA5083/Gr/BN composite while

adding 16wt% of reinforcement owing to the greater density of Al_2O_3 particles compared to the density of BN particles.

3.4 Wear study

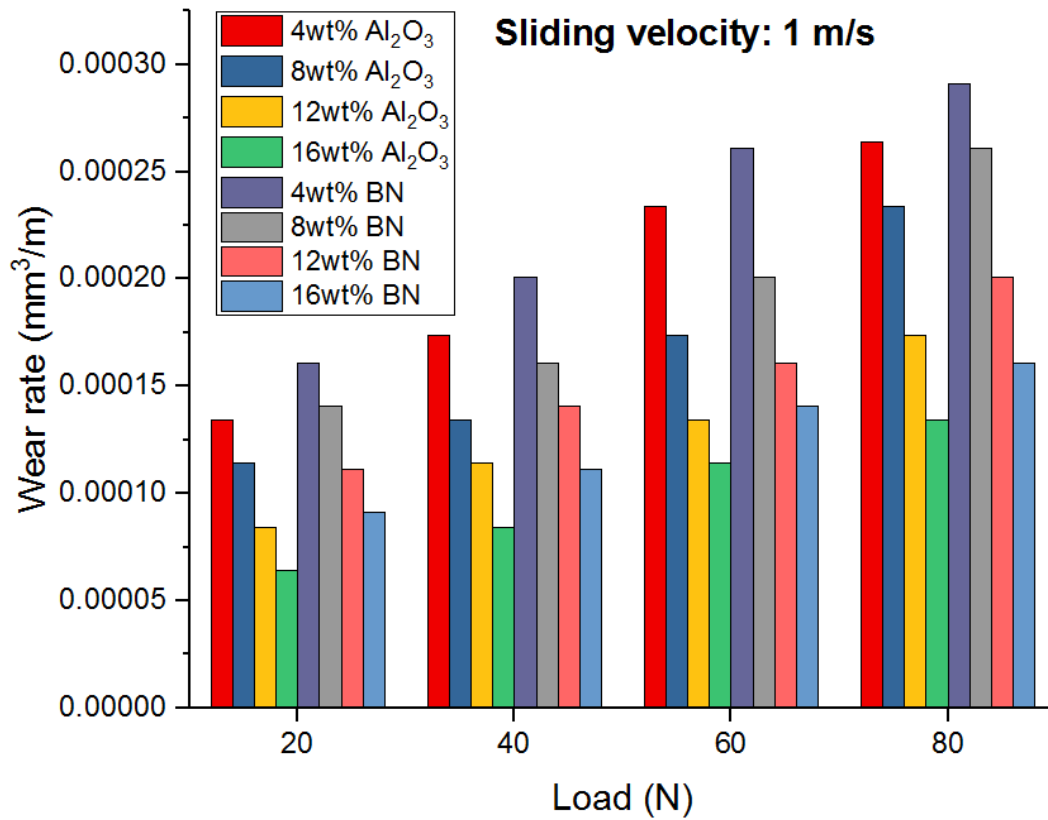


Figure 9 (a) wear behavior of composites for sliding velocity 1 m/s

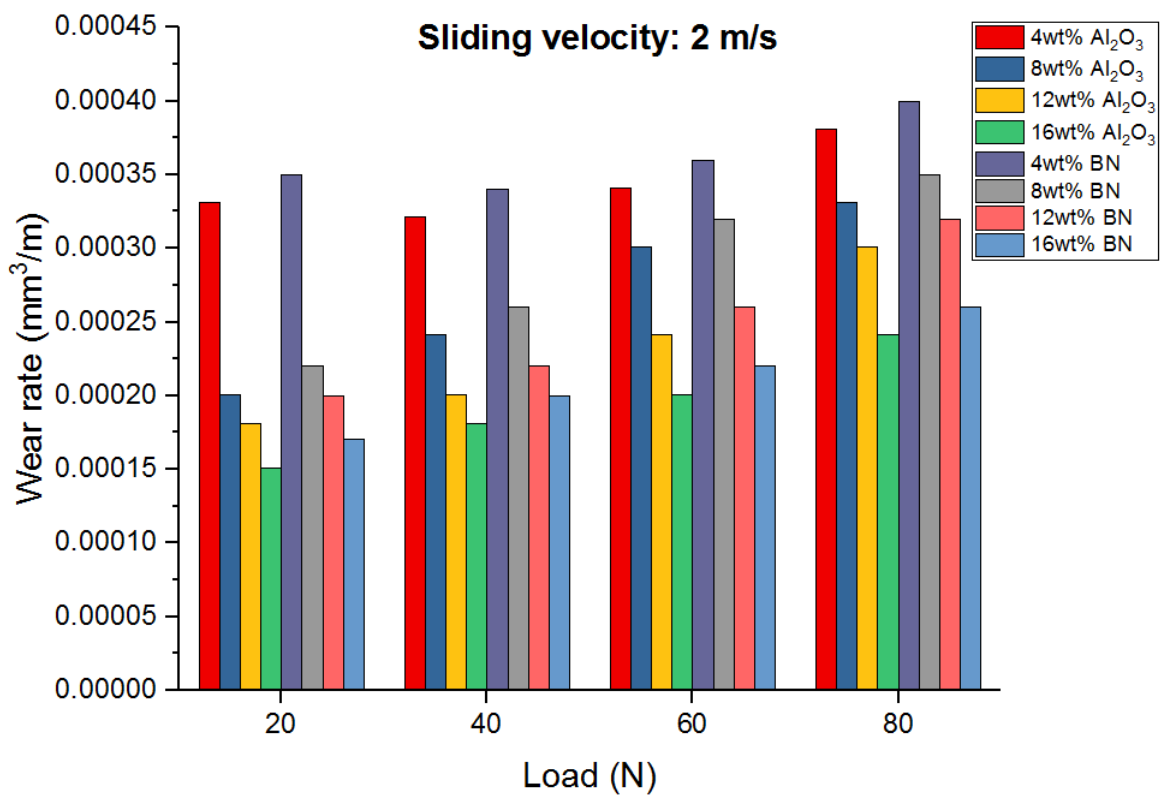


Figure 9 (b) wear behavior of composites for sliding velocity 2 m/s

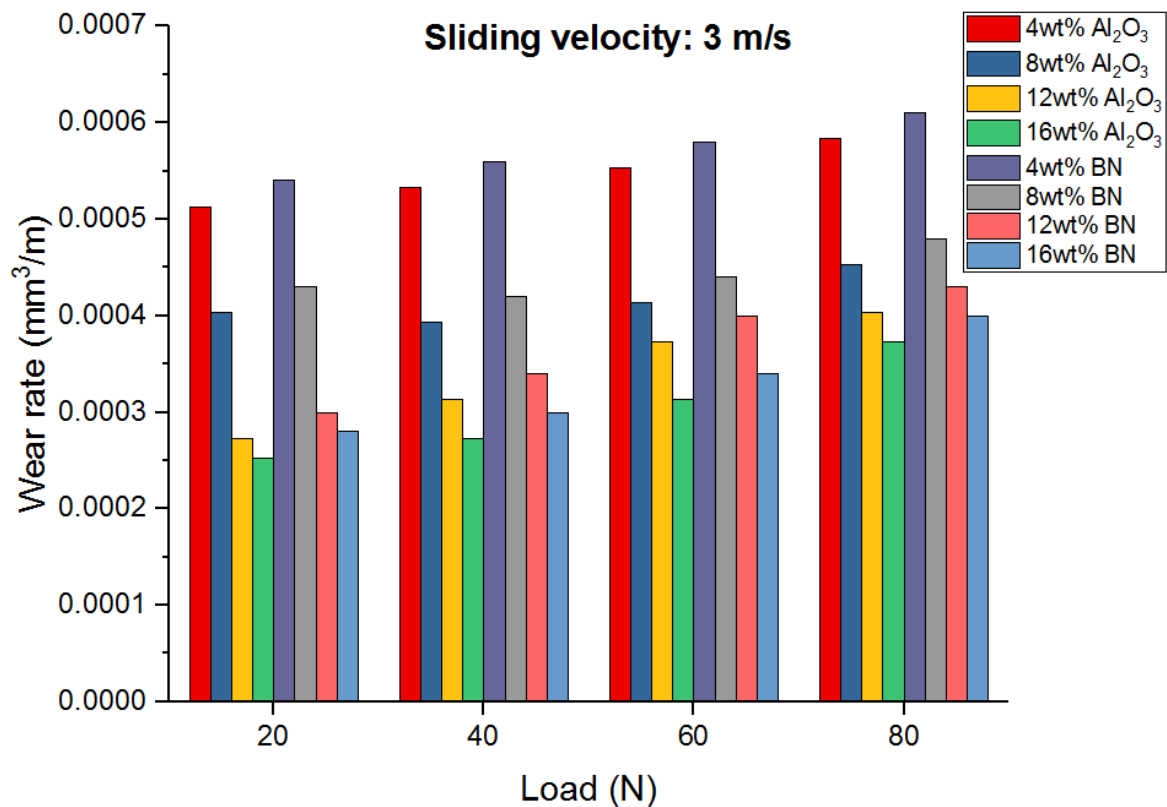


Figure 9 (c) wear behavior of composites for sliding velocity 3 m/s

Figure 9 shows the variation of wear rate of composites with respect to load for various sliding velocities. As can be seen from figure 9, all the composites showed increased wear rate with increase of load and decreased wear rate with increase of reinforcement wt%. While increasing the load, the interface between the disc and pin experienced the increase of temperature that led to the de-bonding of the atoms and finally the erosion of the material happened [25]. Wear rate of the composite decreased while increasing the wt% of reinforcement due to the increase of hardness that prevented the erosion of material. Figure 10 shows the wear rate of composite material with respect to reinforcement wt% measured at the sliding velocity of 1 m/s and the load of 20 N. As the figure 10 obviously shown, the wear rate of AA5083/Gr/Al₂O₃ and

AA5083/Gr/BN composites displayed the decreasing tendency with the increase of wt% of Al_2O_3 and BN particles. Further, the AA5083/Gr/ Al_2O_3 composite exhibited the lower wear rate compared to the wear rate of AA5083/Gr/BN composite because of the superior hardness of the AA5083/Gr/ Al_2O_3 composite as previously discussed. Figure 11 shows the wear rate of AA5083/Gr/ Al_2O_3 and AA5083/Gr/BN composite with respect to sliding velocity measured at the reinforcement of 16wt% the and load of 20 N. The wear rate of AA5083/Gr/BN composite increased with the increase of sliding velocity compared to that of AA5083/Gr/ Al_2O_3 composite because of the lower hardness of BN particles compared to the hardness of Al_2O_3 particles.

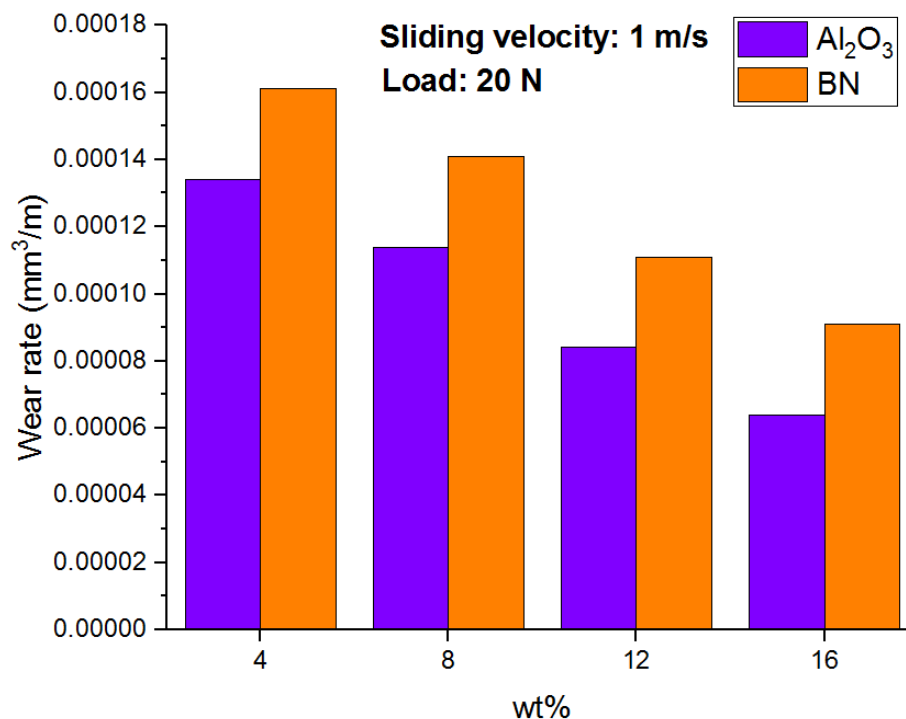


Figure 10 Comparison of wear behavior of composite with varying wt% of reinforcement

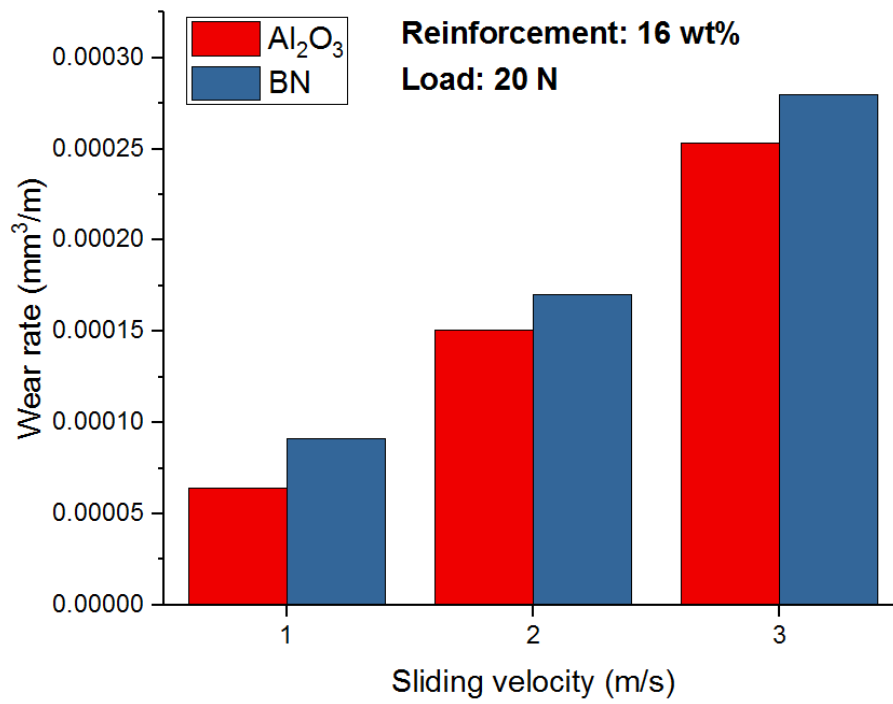
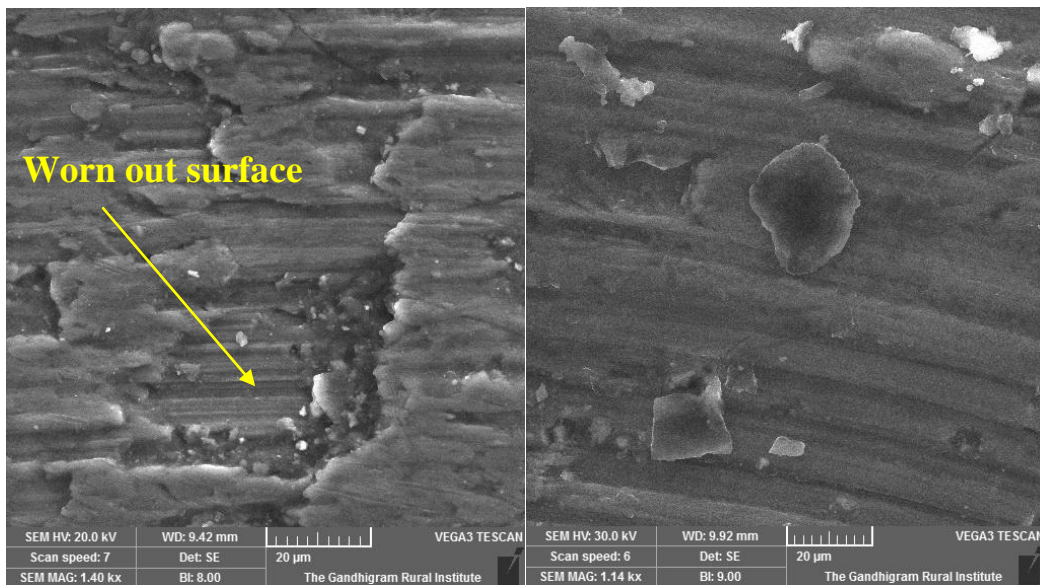


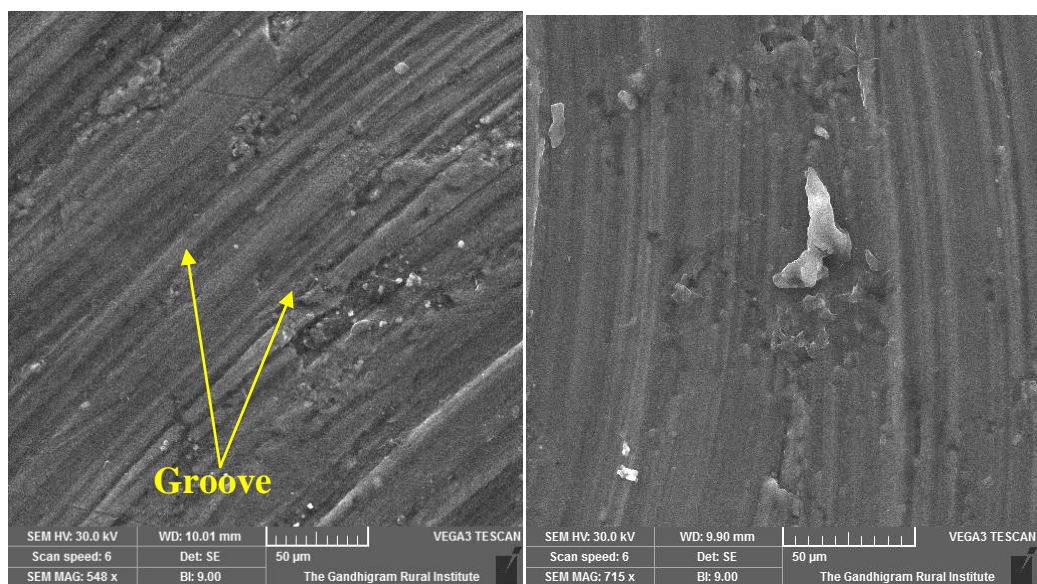
Figure 11 Comparison of wear behavior of composite with varying sliding velocity

3.5 Morphological study



(a)

(b)



(c)

(d)

Figure 12 SEM image of AA5083/Gr/BN (a & b) and AA5083/Gr/Al₂O₃ (c & d)

Morphological study was performed on the worn surfaces of composites reinforced with 16wt% reinforcement particles and experienced a sliding velocity of 1 m/s under 20 N load. Figure 12 (a & b) shows the SEM image of the worn-out surface of AA5083/Gr/BN composite and figure 12 (c & d) shows the SEM image of the worn-out surface of AA5083/Gr/Al₂O₃ composite. Figure 12 clearly depicts that the composite AA5083/Gr/BN displayed more worn-out surfaces and deep grooves compared to AA5083/Gr/Al₂O₃ composite. This confirms that the AA5083/Gr/Al₂O₃ composite experienced less wear compared to AA5083/Gr/BN.

4. Conclusions

Aluminum alloy based hybrid composites were fabricated using stir casting method. AA5083 aluminum alloy was used as base material and graphite, boron nitride, aluminum oxide were used as reinforcements. Mechanical and tribological tests were carried out on the prepared composites and the following conclusions were made from the experimental study.

- Tensile test revealed that the addition of BN and Al₂O₃ particles improved the tensile strength of the AA5083/Gr/BN and AA5083/Gr/Al₂O₃ composites respectively. Tensile strength improved as wt% of reinforcement improved. AA5083/Gr/Al₂O₃ composite showed the superior tensile strength of 317 MPa at 16wt% reinforcement that is 7% greater than the tensile strength of AA5083/Gr/BN due to the Orowan bowing mechanism.
- Hardness study showed that the AA5083/Gr/Al₂O₃ composite exhibited a superior hardness of 153 HB compared to AA5083/Gr/BN composite owing to the addition of hard Al₂O₃ particle

- Tribological study displayed that the sliding velocity and applied load influenced the wear rate of the composite. Further, the wear rate decreased as wt% of reinforcement increased in both AA5083/Gr/BN and AA5083/Gr/Al₂O₃ composites. Additionally, AA5083/Gr/Al₂O₃ composite showed less wear rate compared to AA5083/Gr/BN composite owing to the reinforcement of AA5083/Gr composite with hard Al₂O₃ particles
- Morphological study exhibited that the AA5083/Gr/BN composite depicted more grooves and worn-out surfaces compared to that of AA5083/Gr/Al₂O₃ composite

References

- [1] Prasad, V.J., Rao, N.M., Kamaluddin, S. and Surya, K.V.P., *Materials Today: Proceedings*, 5(2018), 8232-8240.
- [2] Mirjavadi, S.S., Alipour, M., Emamian, S., Kord, S., Hamouda, A.M.S., Koppad, P.G. and Keshavamurthy, R., *Journal of Alloys and Compounds*, 712 (2017), 795-803.
- [3] Zayed, E.M., El-Tayeb, N.S.M., Ahmed, M.M.Z. and Rashad, R.M., In *Engineering Design Applications* (2019), 11-26.
- [4] Kumar, S.H., Suman, K.N.S., Sekhar, S.R. and Bommana, D., *Materials Today: Proceedings*, 5(2018), 23743-23751.
- [5] Jain, V.K.S. and Muthukumaran, S., *Metallurgical and Materials Transactions A*, 50(2019), 2933-2944.
- [6] Alexis, S.J., Kumar, P.S.R., Vinoth, K.R., Ragul, V.V. and Kumar, N.S., *International Journal of Vehicle Structures & Systems*, 10(2018), 278-281.
- [7] Idrisi, A.H., Mourad, A.H.I., Thekkuden, D.T. and Christy, J.V., In *IOP Conference Series: Materials Science and Engineering* (Vol. 324, No. 1(2018), 012087).
- [8] Quader, S.M., Murthy, B.S. and Reddy, P.R., *Journal of Minerals and Materials Characterization and Engineering*, 4(2016), 135.
- [9] Kandpal, B.C. and Singh, H., *Materials Today: Proceedings*, 4(2017), 2783-2792.
- [10] Hariprasad, T., Varatharajan, K. and Ravi, S., *Procedia Engineering*, 97 (2014), 925-929.

- [11] Sonawane, P.M. and Karnik, M.G., *Materials Today: Proceedings*, 4(2017), 3290-3299.
- [12] Palanivel, R., Dinaharan, I., Laubscher, R.F. and Davim, J.P., *Materials & Design*, 106 (2016), 195-204.
- [13] Chi, H., Jiang, L., Chen, G., Kang, P., Lin, X. and Wu, G., *Materials & Design*, 87 (2015), 960-968.
- [14] Baradeswaran, A. and Perumal, A.E., *Composites Part B: Engineering*, 56 (2014), 464-471.
- [15] Jurwall, V., Pandey, A. and Sharma, A.K., In *IOP Conference Series: Materials Science and Engineering* (Vol. 377, No. 1 (2018), 012142).
- [16] Vinod, B., Ramanathan, S., Ananthi, V. and Selvakumar, N., *Silicon*, 11(2019), 817-829.
- [17] Rakshath, S., Suresha, B., Kumar, R.S. and Saravanan, I., (2019), *Materials Today: Proceedings*.
- [18] Kannan, C. and Ramanujam, R., *Journal of advanced research*, 8(2017), 309-319.
- [19] Reddy, A.C. and Zitoun, E., *International Journal of Materials Sciences*, 6(2011), 147-157.
- [20] Yamaguchi, M., Pakdel, A., Zhi, C., Bando, Y., Tang, D.M., Faerstein, K., Shtansky, D. and Golberg, D., *Nanoscale research letters*, 8(2013), 3.
- [21] Xue, Y., Jiang, B., Bourgeois, L., Dai, P., Mitome, M., Zhang, C., Yamaguchi, M., Matveev, A., Tang, C., Bando, Y. and Tsuchiya, K., *Materials & Design*, 88(2015), 451-460.
- [22] Rajesh, G.L., Auradi, V. and Kori, S.A., *Procedia Materials Science*, 5(2014), 289-294.

[23] Prasad, D.S., Shoba, C. and Ramanaiah, N., *Journal of Materials Research and Technology*, 3(2014), 79-85.

[24] Kök, M. and Özdin, K., *Journal of Materials Processing Technology*, 183(2007), 301-309.

[25] Surappa, M.K., *Wear*, 265(2008), 349-360.

Investigation of Nitronic-60 using Zinc Coated Wire

P.Ranjith kumar¹, K.Chandrasekaran^{2*}, R.Ramanathan³, M.Panneer selvam⁴

^{1,2,3,4}Professor, Department of Mechanical Engineering, MAM School of Engineering, Tamilandu, India,
*Email:kchandrasekaran1984@gmail.com

ABSTRACT

The objectives of this work is to investigate the effective parameters for pulse ON time; pulse OFF time; voltage & wire feed while machined on Wire-Cut Electrical Discharge Machining composite super alloy material. The experimental results proposed optimal combination of parameters which give the maximum material removal rate, surface roughness and kerf width. Finally, confirmation experiments were carried out to identify the effectiveness of the proposed method. In this experiment carried alloy material of NITRONIC 60 through optimization of metal removal rate; surface roughness and kerf width are output parameters these are all performed in methodology Regression analysis and ANOVA for Response Surface Linear Model.

Key words: WEDM, Nitronic-60, Response Surface Linear Model, ANOVA, SR, MRR

Introduction

Machining removes certain parts of the work pieces to change them to final parts. Machining nowadays has been classified in two types: Traditional Machining; Non-traditional Machining [1]. Traditional machining is also known conventional machining requires the presence of a tool that is harder than the work piece to be machined. WEDM is considered as a unique adoption of the conventional EDM process which comprises of a main worktable, wire drive mechanism, a CNC controller, working fluid tank and attachments [2]. Vinothkumar have proposed a quadratic mathematical model and conducted experiments by taking six WEDM process parameters are discharge current, pulse duration, pulse frequency, wire speed, wire tension and dielectric flow rate [3]. Soundrarajan have discuss and investigate the significant process parameters along with the percentage contribution of each parameter. ANOVA is used to find the percentage contribution of significant process parameters [4]. Pujari evaluates the effect of voltage, dielectric pressure, pulse on time and pulse off-time on spark gap of Ti6AL4V alloy. It is found that the pulse on time, pulse off time, the interaction of dielectric pressure and pulse off time, and interaction of pulse on time and pulse off time are significant parameters which affect the spark gap of WEDM [5]. Antar study has been made to optimize the process parameters during machining of Inconel-600 by wire electrical discharge machining (WEDM) using response surface methodology (RSM). Four input process parameters of WEDM (Peak Current (IP), Pulse on time (TON), Pulse off time (TOFF) and Wire Feed rate (WF) were chosen as variables to study the process performance in terms of Material Removal Rate(MRR) [6]. Brajaeshlodhi have investigated the effects of the various WEDM process parameters on the machining quality of AISI 304 stainless steel and to obtain the optimal sets of process parameters so that the quality of machined parts can be optimized. The working ranges and levels of the WEDM process parameters are found using one factor at a time approach [7]. The objectives are as follows:-

- To achieve the shortest machining time whilst at the same time satisfying the requirements of accuracy and surface roughness.
- To discuss the cause – effect relationship of machining parameters & machine performance in WEDM.
- To determine significant parameters affecting the machining performance.
- To establish the mathematical models relating the machining performance & machining parameters by regression & correlation analysis.
- Finally the optimal machining parameters are obtained under the constraints & requirements.

EXPERIMENTATION DETAILS

NITRONIC 60

Corrosion materials Nitronic 60 is a solid solution strengthened, nickel-molybdenum-chromium alloy with a small amount of tungsten which exhibits excellent corrosion resistant in an assortment of harsh environments.

Applications include are not limited to, stack liners, ducts, dampers, scrubbers, stack-gas re-heaters, heat exchangers reaction vessels and evaporators.

Industries were C-276 can be utilized are petrochemical and chemical processing, power generations, pharmaceutical, pulp and paper production and waste treatment to name a few.

Table 1 Chemical Composition

MATERIALS	COMPOSITION (%)
Ni	8-9
Cr	16-18
N	0.08-0.18
Mn	7-9 Max.
C	0.1 Max.
Si	3.5-4.5 Max.

Table 3.1 Composition of Nitronic 60

Selection of electrode

Zinc electrodes are reasonably safe and easy to obtain other metals such as lead, iron, magnesium, etc., can be studied as well; they yield different voltages than the copper cells. In a particular, magnesium or copper cells can generate voltage as large as 1.6v in lemon cells.

DESIGN OF EXPERIMENT

Process Parameters

Throughout this dissertation work input parameters considered for Wire cut EDM are machining parameters like as pulse on time, pulse off time, flushing pressure, servo voltage, wire feed rate, wire tension and output parameters are surface roughness and material removal rate.

Pulse on time (Ton)

During WEDM all the work is done during pulse duration (On time). The erosion rates are affected mainly by pulse parameter. The spark gap is bridged, current is generated and the work is accomplished. The longer the spark is sustained, the higher is the material removal

Pulse off time (Toff)

While most of the machining takes place during on time of the pulse, the off time during which the pulse rests and the re-ionization of the die-electric takes place, can affect the speed of the operation in a large way. Longer is the off time greater will be the machining time.

Servo voltage (Sv)

Servo voltage is also another important primary input of WEDM process. The voltage determines the width of spark gap between the leading edge of the electrode and the work piece. High voltage setting increases the gap of machining.

Flushing pressure (Fp)

Flushing pressure is important to achieve a stable machining condition. Its play important role as far as cutting speed is concerned .both the nozzles (upper and lower) should be just about 0.1-0.2 mm away from the work piece, otherwise cutting performance drops considerably. Also the both nozzle should be checked periodically for damages.

Wire feed rate (Wf)

The rate at which the wire electrode travels and continuously fed along the wire guide path for continuous sparking is called wire feed. The wire feed range available on the present WEDM machine is available in two levels, i.e. low (4 m/sec) and high speed (11m/sec). Maximum wire feed is required in order to avoid wire breakage, to have better machining and better material removal rates.

Wire tension (Wt)

The amount of stretch in the wire between the upper and lower wire guides is called the wire tension and it is measured as gram equivalent load. In order to keep wire straight between two guides wire is kept continuously kept under tension. Wire tension is directly proportional to the thickness of the work piece, i.e. more the thickness of work piece more the tension required. Improper setting of tension may result in the in accuracies as well as wire breakage.

Response Variables

WEDM performance is mainly measured by the material removal rate (MRR), gap current and surface roughness of the work piece that has been machined. These three machining characteristics have been identified by the research as the most significant machining criteria that can influence the WEDM performance. The process parameters should be chosen properly so as to have maximum MRR, minimum roughness value.

Material removal rate (MRR)

The material removal rate (MRR) of the work piece is the amount of the material removed per minute. MRR and Cutting speed capabilities of WEDM have increased-enormously over the years. They are influenced by the age and type of machine along with the properties and characteristics of the work piece being cut. The machine setting set by the operator and programmer also affect the MRR and cutting speed.

Surface roughness (SR) or surface finish

The smoothness of the part surface machined by a given process is referred to as surface finish. No standard has been universally adopted for measuring the surface finish of parts. Different methods for calculating the numerical representation of t

Results and Discussions

RSM explores the relationship between several explanatory variables and one or more response variables. This method was introduced by G.E.P.BOX and K.B.Wilson in 1951.The main idea of RSM is to use a sequence of designed experiments to obtain an optimal response. They acknowledge that this model is only an approximation,

but use it because such a model is easy to estimate and apply, even when little is known about the process. An easy way to estimate a first degree polynomial model is to use a factorial experiment or a fractional factorial design. This is sufficient to determine which explanatory variables are left then a more complicated design, such as a central composite design can be implemented to estimate a second degree polynomial model, which is still only an approximate at best.

Table 2 Working conditions

Work condition	Description
Electrode	Zinc coated wire
Work piece	Nitronic 60 C276 (100x100x10mm)
Voltage	120 to 200 V
Peak current	8 to 64 A
Pulse duration	1.6 to 50 μ s
Interval time	3.2 to 800
Dielectric fluid	Water

Table 3 Experimental Readings

T on	T off	Voltage	Wire feed	Machining time	Surface roughness	Kerfwidth
4	2	40	2	477.38	2.18	0.247
4	4	45	4	557.07	2.03	0.291
4	6	50	6	671.96	1.8	0.289
4	8	55	8	796.43	1.64	0.294
6	2	50	4	465.75	1.69	0.297
6	4	55	6	562.08	1.85	0.32
6	6	40	8	500.24	2.03	0.289
6	8	45	2	556.47	1.99	0.29
8	2	55	6	463.32	1.86	0.292
8	4	50	8	472.12	1.83	0.293
8	6	45	2	488.27	1.84	0.355
8	8	40	4	208.37	2.17	0.344
10	2	45	8	445.53	2	0.332
10	4	40	6	459.38	2.26	0.357
10	6	55	4	568.47	1.69	0.368
10	8	50	2	559.75	1.79	0.367

Table 4 Regression analysis

Source	Squares	Df	Square	Value	Prob> F
Model	214396.9	10	21439.6889	9.550327755	0.0112
A-T on	31950	1	31949.99962	14.23215465	0.013
B-T off	1717.577	1	1717.576805	0.765096057	0.4218
C-Voltage	13780.75	1	13780.74551	6.138644874	0.056
D-Wirefeed	5278.945	1	5278.944858	2.351510502	0.1857

AB	8746.831	1	8746.830521	3.896283136	0.1054
AC	526.5104	1	526.5103892	0.234534503	0.6486
AD	2803.898	1	2803.898386	1.248998934	0.3145
BC	62741.26	1	62741.26249	27.94814904	0.0032
BD	2241.242	1	2241.24209	0.998363206	0.3636
CD	4562.817	1	4562.816535	2.032510528	0.2133
Residual	11224.58	5	2244.916557		
Cor Total	225621.5	15			
Std. Dev.	47.38055		R-Squared		0.950250379
Mean	515.7869		Adj R-Squared		0.850751136
C.V. %	9.186071		Pred R-Squared		0.21641521
PRESS	176793.6		Adeq Precision		14.18041228

The "Pred R-Squared" of 0.2164 is not as close to the "Adj R-Squared" of 0.8508 as one might normally expect. This may indicate a large block effect or a possible problem with your model and/or data. Things to consider are model reduction, response, transformation, outliers, etc.

"Adeq Precision" measures the signal to noise ratio. A ratio greater than 4 is desirable. Your ratio of 14.180 indicates an adequate signal. This model can be used to navigate the design space.

$$\text{Machining time} = +685.03319 + 22.19034 * T \text{ on} - 192.37313 * T \text{ off} - 13.26234 * \text{Voltage} + 196.16216 * \text{Wirefeed} - 9.66693 * T \text{ on} * T \text{ off} + 0.76868 * T \text{ on} * \text{Voltage} - 8.40988 * T \text{ on} * \text{Wirefeed} + 5.90026 * T \text{ off} * \text{Voltage} - 4.90879 * T \text{ off} * \text{Wirefeed} - 2.58316 * \text{Voltage} * \text{Wirefeed}$$

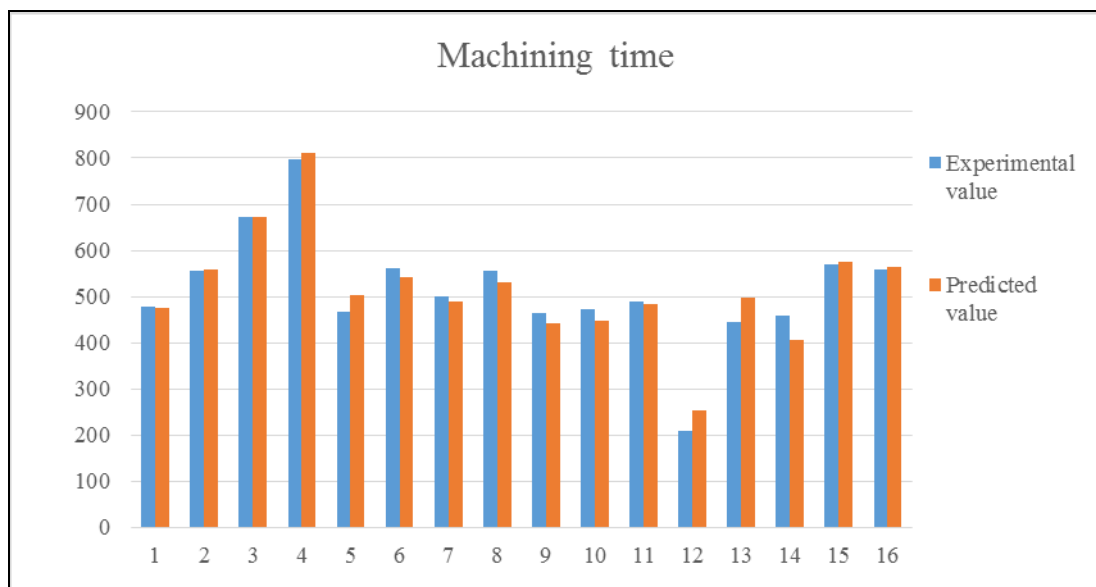


Figure 1 Graph for machining time

Table 5 Regression analysis

Source	Squares	Df	Square	Value	Prob> F
Model	0.400905109	4	0.100226277	9.304597	0.0015
A-T on	0.00210125	1	0.00210125	0.195071	0.6673
B-T off	0.011689275	1	0.011689275	1.085184	0.3199

C-Voltage	0.3746174	1	0.3746174	34.77794	0.0001
D-Wirefeed	0.000511359	1	0.000511359	0.047472	0.8315
Residual	0.118488641	11	0.010771695		
Cor Total	0.51939375	15			
Std. Dev.	0.103786775		R-Squared	0.771871	
Mean	1.915625		Adj R-Squared	0.688915	
C.V. %	5.417906688		Pred R-Squared	0.565183	
PRESS	0.225841212		Adeq Precision	8.519386	

The Model F-value of 9.30 implies the model is significant. There is only a 0.15% chance that a "Model F-Value" this large could occur due to noise.

Values of "Prob> F" less than 0.0500 indicate model terms are significant. In this case C are significant model terms. Values greater than 0.1000 indicate the model terms are not significant. If there are many insignificant model terms (not counting those required to support hierarchy), model reduction may improve your model.

The "Pred R-Squared" of 0.5652 is in reasonable agreement with the "Adj R-Squared" of 0.6889. "Adeq Precision" measures the signal to noise ratio. A ratio greater than 4 is desirable. Your ratio of 8.519 indicates an adequate signal. This model can be used to navigate the design space.

$$\text{Surface roughness} = +3.25645 + 5.12500\text{E-}003 * \text{T on} - 0.012348 * \text{T off} - 0.027961 * \text{Voltage} + 2.63587\text{E-}003 * \text{Wire feed}$$

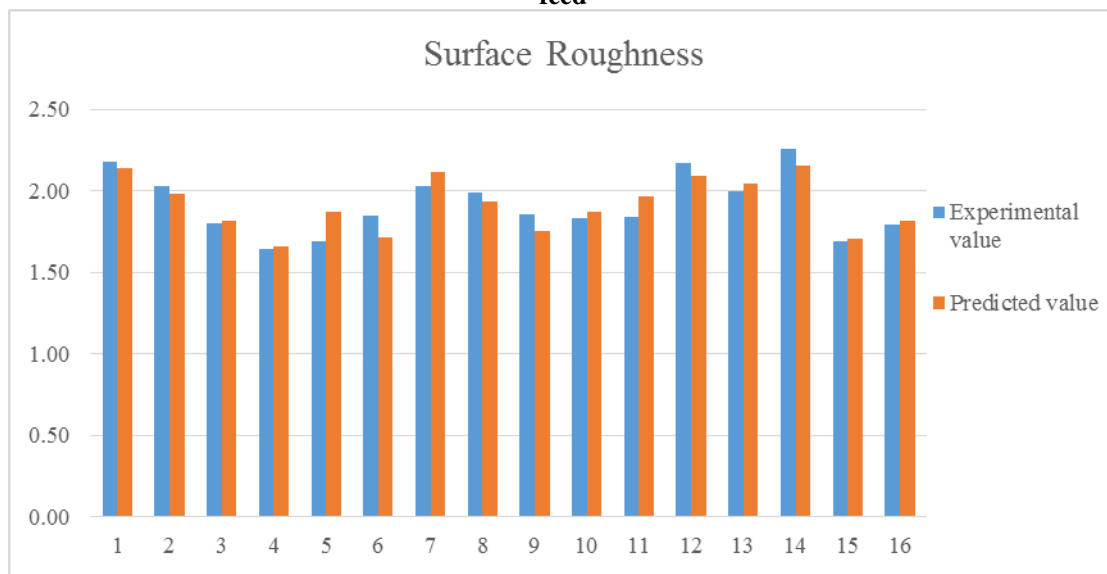


Figure 2 Graph for surface roughness

Table 6 Regression analysis

Source	Squares	Df	Square	Value	Prob> F
Model	0.014964	4	0.003741	10.26591	0.001
A-T on	0.012425	1	0.012425	34.09576	0.0001
B-T off	0.001851	1	0.001851	5.078177	0.0456
C-Voltage	0.000164	1	0.000164	0.449651	0.5163

D-Wirefeed	0.000225	1	0.000225	0.616601	0.4489
Residual	0.004009	11	0.000364		
Cor Total	0.018973	15			
Std. Dev.	0.01909		R-Squared	0.78872	
Mean	0.314063		Adj R-Squared	0.711891	
C.V. %	6.078325		Pred R-Squared	0.586968	
PRESS	0.007836		Adeq Precision	10.31731	

The Model F-value of 10.27 implies the model is significant. There is only a 0.10% chance that a "Model F-Value" this large could occur due to noise. Values of "Prob> F" less than 0.0500 indicate model terms are significant. In this case A, B are significant model terms. Values greater than 0.1000 indicate the model terms are not significant. If there are many insignificant model terms (not counting those required to support hierarchy), model reduction may improve your model.

The "Pred R-Squared" of 0.5870 is in reasonable agreement with the "Adj R-Squared" of 0.7119. "Adeq Precision" measures the signal to noise ratio. A ratio greater than 4 is desirable. Your ratio of 10.317 indicates an adequate signal. This model can be used to navigate the design space.

$$\text{Kerfwidth} = +0.18322 + 0.012463 * T_{on} + 4.91304E-003 * T_{off} + 5.84783E-004 * \text{Voltage} - 1.74728E-003 * \text{Wire feed}$$

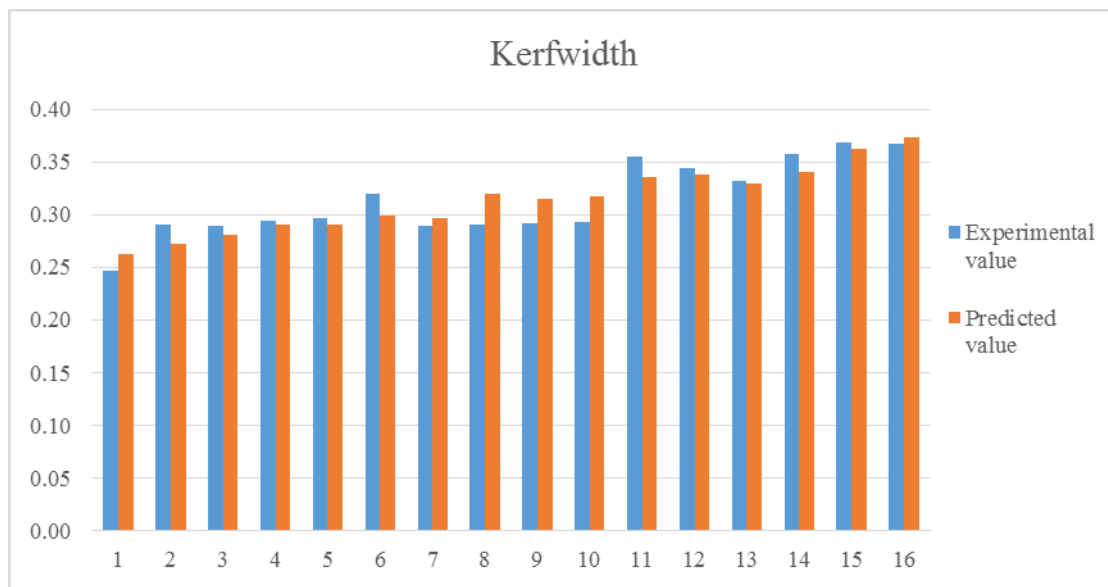


Figure 3 Graph for kerfwidth

Conclusions

This experimental work reveals the following conclusions on WEDM operation on Nitronic 60 work piece material. Main objective of this work is to develop the empirical model using RSM. The response surface methodology is one of the best techniques to identify the effects of machining parameter on WEDM process. The voltage and pulse-off time have the significant effect on machining time. The higher level of current produce lower machining time. The voltage, current, pulse-on time and pulse-off time have significant effect on surface roughness. The higher level of current, voltage, pulse-on time and pulse-off time have the poor surface finish. The response surface models were

developed based on design of experiment with current, voltage, pulse-on time and pulse-off time as an input and machining time and surface roughness were response. The response surface model has smaller deviation from experimental data and confirms that the developed model can be used to predict the machining time and surface roughness value in effective manner.

References

- [1] Gowri, S., Ranjith Kumar, P., Vijayaraj, R., and Balan, A.S.S., 2007, 'Micromachining: Technology for the Future', International Journal of Materials Materials and Structural Integrity, Vol.1/2/3, pp.161-179
- [2] Mathalai Sundaram, C., Sivasubramanian, R., and Chandrasekaran, K., 2016, Experimental investigations of new powder metallurgy electrode in electrical discharge machining of OHNS using Taguchi method', International Journal of Advanced Engineering Technology, vol.08, no.01, pp.559-564.
- [3] Vinodkumar, Vikaskumar, Kamalkumarjangra, 2015, 'An Experimental Analysis and Optimization Of Machining Rate And Surface Characteristics In WEDM Of Monel-400 Using RSM And Desirability Approach', Organisational Research , 17 March (2015).
- [4] Soundrarajan, R., Ramesh, A., Mohanraj, N., and Parthasarathi, N., 2016, 'An investigation of material removal rate and surface roughness of squeeze casted AISI413 alloy an WEDM by multi response optimization using RSM', Journal Of Alloy And Compounds ,25 May (2016)
- [5] Pujarisrinivasarao, Koonaramji, Beelasatyanarayan, 2016, 'Effect Of Wire EDM Conditions On Generation Of Residual Stresses In Machining Of Aluminium 2014 T6 Alloy', Alexandria Engineering Journal,13 March (2016).
- [6] Antar, M.T., Soo, S.L., Aspinwall, DK., Jones, D., and Perez, R., 2015, 'Productivity And Workpiece Surface Integrity When WEDM Aerospace Alloys Using Coated Wires' University Of Birmingham 14, pp-44-50.
- [7] Rajaeshlodhi, B., and Sanjay, A., 2014, 'Modeling Of Wire Electrical Discharge Machining Of AISI D3 Steel Using Response Surface Methodology', Design And Research Conference, 4, pp 23-30.
- [8] Melkote, S.N., and Endres, W.J.,1998, 'The importance of including size effect when modeling slot millin', Journal of Manufacturing science and Engineering, Vol. 120(1), pp.68–75
- [9] Sinan Filiz., Caroline M Conley., Matthew B Wasserman., and Burak Ozdoganlar, N., 2007, 'An experimental investigation of micromachinability of copper 101 using tungsten carbide micro-endmills' International Journals of Machine Tools and Manufacture, Vol. 47, pp.1088–1100

OPTIMIZATION OF DRILLING PROCESS PARAMETERS OF ELECTRICAL DISCHARGE MACHINING IN INCONEL 718 MATERIAL

P.Ranjith kumar¹, K.Chandrasekaran^{2*} M.Panneer selvam³, R.Ramanathan⁴

^{1,2,3,4}Professor, Department of Mechanical Engineering, MAM School of Engineering,
Tamilandu, India,

*Email:kchandrusekaran1984@gmail.com

Abstract-

Electrical Discharge Machining is becoming an important machining process in the fields of manufacturing 3D complex shapes and using a simple shaped electrode tools. The present work deals with the experimental investigation of Electrical Discharge Spark machining on Inconel 718 material. The holes of 1.5mm deep were machined using EMS3050 Manual EDM with various combinations of input parameters such as pulse current and pulse on time (Ton). The Material removal rate and Surface roughness are taken as the output parameters as more focus is given to the dimensional accuracy of the machined components. The Taguchi method of optimization is used. The result shows the effect of input parameters on material removal rate and surface roughness. Also the optimum values are estimated.

Key words: EDM, electrode, material removal rate, surface roughness, Taguchi method

1. INTRODUCTION

Nickel based super alloy, Inconel 718 is one of the most difficult-to-machine material which attributed to its ability to maintain hardness at elevated temperature and consequently it's very useful for hot working environment. Formation of complex shapes by this material along with reasonable speed and surface finish is not possible in traditional machining. This alloy is characteristically difficult to machine due to its poor thermal properties, high toughness, high hardness, and high work hardening rate. Usually, a nonconventional machining method like electrical discharge machining (EDM) is chosen for machining Inconel 718 in order to overcome such limitations. However, due to the great physical properties of Inconel 718, the cutting process for this material is become an issue in order to improve the speed of machining process. This alloy has attracted many researchers because of its increasing applicability and the machining ability of aerospace alloys will continually decline as service demands increase in order to satisfy the demand for higher temperature capability for structural engine alloys. The Fig. 1 shows the working principle of Spark EDM. Spark erosion EDM, also called cavity type EDM or volume EDM consists of an electrode and work piece submerged in an insulating liquid such as, more typically, oil or, less frequently, other dielectric fluids. The electrode and work piece are connected to a suitable power supply. The power supply generates an electrical potential between the two parts.

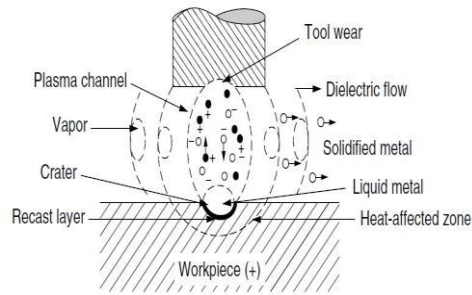


Figure 1 Working of spark EDM

2. LITERATURE REVIEW

Carbon or Silicon carbide is mixed into the dielectric fluid in the same tank or in a separate tank. The powder particles filling the spark gap get energized and are accelerated by the electric field and act like conductors forming chains which bridge the gap between the tool electrode and the workpiece leading to an early explosion [1]. The wire electrical discharge machining (WEDM) is a widely accepted non-traditional thermo-electrical material removal process used to manufacture components with intricate shapes and profiles. WEDM utilizes a continuously travelling wire electrode made of thin copper, brass, molybdenum or tungsten of diameter 0.05–0.3 mm, which is capable of achieving very small corner radii. The machining principle is based on erosion of the work-piece material using a successive discrete discharges occurring between the electrode (wire) and work piece [2]. The Material Removal Rate (MRR) is the rate at which material is removed from the workpiece. MRR depends not only on the workpiece material and electrode qualities, but also on the parameters applied in EDM and the characteristics of dielectric fluid [3]. The influence of machining parameters on electrical discharge machining of managing steels concluded that MRR increases with increase in current and decreases with increase with pulse-on time [4]. An almost positive linear relationship between material removal rate and pulse-on time [5]. An experimental investigation to determine the main EDM parameters which contribute to recast layer formation in Inconel 718 and found that average recast layer thickness increased primarily with energy per spark, peak discharge current, and current pulse duration [6]. The MRR increases proportionally with increase in current, voltage and pulse-on time. They reported an almost linear relationship for peak currents of 3 and 12A with MRR ranging from 3 to 40 mm³/min [7]. The EDM process uses thermal energy to erode the tool and the workpiece immersed in a dielectric fluid through a series of current discharges subject to an electric voltage. When a voltage of 35 – 320V is applied between the tool electrode and the workpiece placed close to each other, an electric field in the range of 10⁵- 10⁷ V/m is generated [8]. The performance of Copper electrode when EDM of Nickel Based Super Alloy, Inconel 718 is at higher peak current and pulse duration. The results shows that the highest material removal rate (MRR) with value 34.94 mm³/min, whereas machining at a peak current of 20A and pulse duration of 400μs yields the lowest electrode wear rate (EWR) with value -0.0101 mm³/min. The lowest surface roughness (Ra) is 8.53 μm achieved at a lowest peak current used of 20A and pulse duration of 200μs [9]. Wire EDM is a specialized thermal machining process capable of accurately machining parts of hard materials with

complex shapes. Parts having sharp edges that pose difficulties to be machined by the main stream machining processes can be easily machined by WEDM process [10]. An experimental investigation of Wire-EDM of titanium alloy to investigate the effect of seven process parameters including pulse width, servo reference voltage, pulse current, and wire tension on process performance parameters (such as cutting speed, wire rupture and surface integrity) and found that the cutting speed increases with peak current and pulse interval. Surface roughness was found to increase with pulse width and decrease with pulse interval [11]. The material removal characteristics of the EDM process. The results were supposed to be helpful for material removal mechanism of EDM [12].

3. MATERIAL AND METHODS

During the drilling operation in electrical discharge machining there may be a chance of getting surface disintegration and less material removal rate and the time factor which mainly affects the structure of the machined area. To minimize this objective machining was carried out using the input parameter such as input current, time on (Ton) and the output values are calculated to these input parameters. The main objective of the project is to minimize and maximize the various output parameters for the given input by keeping inconel 718 material as the work piece and copper as the electrode. Tab.1 shows the composition of inconel 718 material. Tab. 2 shows the properties of the inconel 718.

Table 1 Composition of inconel 718

Element	Content
Ni + Co	50-55%
Cr	17-21%
Fe	Bal
Nb + Ta	4,75-5,5%
Mo	2,8-3,3%
Ti	0,65-1,15%
Al	0,2-0,8%

Table 2 Properties of inconel 718

S. No.	Properties	Value
1	Density	8,19 g/cm ³
2	Melting point	1336°C
3	Co-Efficient of Expansion	13 μm/m°C (20 - 100° C)
4	Modulus of rigidity	77,2 kN/mm ²
5	Modulus of elasticity	204,9 kN/mm ²

In the presence of EDM oil as the electrolyte by minimizing the output such as surface roughness leads of making of perfect die. The constraints are the MRR- maximum, SR –

minimize and T - minimize. The experiment is carried in Spark EDM for drilling operation with various input parameters such as pulse on time and pulse current. Taguchi Optimization technique is used to optimize the value of various input parameters like pulse on time and pulse current.

4. EXPERIMENTAL WORK

The experiment is conducted as per design matrix using EDM machine (Make EMS5030). Fig. 2 shows the spark EDM experimental setup with the following specification. Mechanism of process Controlled erosion (evaporation and melting) through a series of electric sparks; Maximum work piece height 175 mm; Main table traverse (X, Y) 280, 200 mm; Electrode diameter range 0,25 mm to 15 mm; Generator EMS 5030; Interpolation Linear and circular.

The plate to be machined is cleaned thoroughly and then the plates are fitted to the fixture. The tool and workpiece are shown in Fig. 3. The fixture is used to provide support for the plates and to restrict the deformation of plate during welding due to axial pressure. It also exerts some back pressure on the plate when pressure is applied during welding. The work piece plate is placed in the fixture and firmly clamped on the machine table of Electric discharge machine. One of the important factors in a successful EDM operation is the removal of debris (chips) from the working gap. Flushing these particles out of the working gap is very important, to prevent them from forming bridges that cause short circuits. EDMs have a built-in power adaptive control system that increases the pulse spacing as soon as this happens and reduces or shuts off the power supply. Flushing – process of introducing clean filtered dielectric fluid into spark gap. The Fig. 4 shows the flushing of dielectric during machining. The electric spark is concentrated between the electrode and work piece for maximum metal removal, and minimum scattering and energy loss that may lead to overheating and premature oxidation. The Fig. 5 shows the Spark erosion during drilling process. EDM oil as a result, provides extended service life with minimum power consumption.



Figure 2 Spark EDM experimental setup



Figure 3 Tool and workpiece fixed



Figure 4 Flushing of dielectric during machining

4.1 Input parameters

The various input parameters like pulse on time and pulse current are considered for this study.

Pulse on time (s):

Metal removing process that takes place when current is allowed to flow is called Pulse on Time. Material Removal is directly proportional to the amount of energy applied during this time. This energy is really controlled by Pulse Current and the length of Pulse on time

Pulse Current (A):

Pulse Current is the amount of power used in discharge machining, measured in units of amperage. The maximum amount of amperage is governed by the surface area of the cut. The greater the amount of surface area, the more amperage is applied. Higher amperage is used in roughing operations and in cavities with large surface areas.

4.2 Calculation of Output parameters

The output parameters like Time (T), Material Removal Rate (MRR) and Surface Roughness (SR).

Time (T)

Time is one of the most important criteria during the machining of material. The machining time is calculated using stopwatch. Material removal rate may varies depending on the machining time.

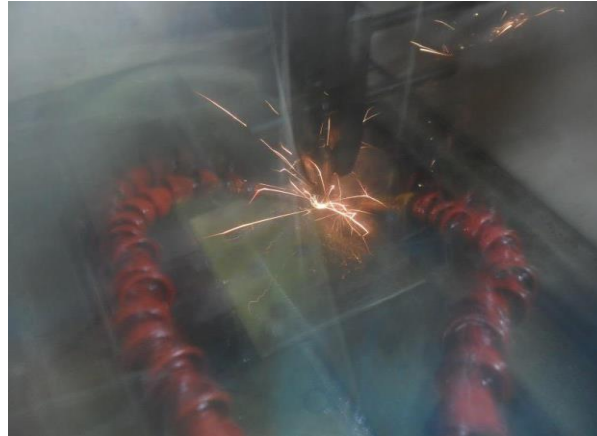


Figure 5 Spark erosion during process

Material Removal Rate (MRR)

MRR is used to evaluate machining Performance. MRR has increased when electrodes have been used with Positive polarity in all cases of semi-sintered electrodes. In case of the copper Electrode, EDM cannot be used when positive polarity has been selected. The material Removal Rate is expressed as the work piece removal rate. Under a period of machining time in minute (t), after machining, the Material Removal Rate has been estimated by using the following equation.

$$\text{MRR} = \frac{W_i - W_f}{\rho \times t}$$

Where, W_f is the final machining weights of work piece material and W_i is the Initial machining weight of the work piece material respectively and 't' is the machining time and ' ρ ' is the density of the material. The weight of the work piece materials are calculated in electronic weighing machine.

Surface Roughness (SR)

Surface Roughness has an increasing trend with the increase of pulse on time and at the same time it decreases with the increase of pulse off time. The surface roughness is most affected by the amount of discharge energy, which increases with the increase in pulse on time. Surface Roughness depends on the size of spark crater.



Figure 6 Work piece after drilling

Fig. 6 shows the work piece of nine holes with 1.5 mm deep is drilled in the spark EDM. The material removal rate are estimated for three different pulse time such as 29, 38, 47. The estimated MRR is tabulated in Tab. 3. Fig. 7 shows the work piece of nine holes with 1.5 mm deep is drilled in the spark EDM. The surface roughness are estimated for two trials and the average of the two trials is taken for study. The estimated surface roughness is tabulated in Tab. 4.



Figure 7 Testing surface roughness

Table 4 Calculated Surface Roughness (SR)

S. No.	Pulse Time	Peak Current	Trial - 1	Trial - 2	Average SR (μm)
1	29	0,05	2,567	2,970	2,768
2	29	0,15	3,507	3,826	3,666
3	29	0,25	4,301	4,672	4,486
4	38	0,05	3,065	3,191	3,128
5	38	0,15	3,876	4,012	3,944
6	38	0,25	4,427	4,621	4,524
7	47	0,05	3,125	2,976	3,251
8	47	0,15	4,568	4,829	4,698
9	47	0,25	5,012	5,365	5,180

5. OPTIMIZATION OF PROCESS PARAMETERS

Taguchi method is an efficient problem solving tool, which can improve the performance of the product, process, design and system with a significant slash in experimental time and cost. Taguchi method employs a special design of orthogonal arrays to study the entire process parameters space with small number of experiments. The optimal result could be generated out of Taguchi method by means of systematic analysis of data and the dominant factor involved in optimization. The two fundamental terms are used in Taguchi methods (i) orthogonal arrays (ii) Signal to noise ratio (S/N) and Mean Squared Deviation (MSD). Taguchi method utilizes orthogonal arrays from design of experiments theory to study a large number of variables with a small number of experiments. Taguchi recommends the use of signal to noise ratio (S/N) as opposed to simple process optimizing process parameters. S/N ratio selection is based on Mean Squared Deviation (MSD) for analysis of repeated results. For selection of orthogonal arrays, the actual combinations of input process parameters are shown in Tab. 3 and 4. The two factors and their levels are shown in the Tab. 5.

Table 5 Factors and Levels

Factors	Levels		
	1	2	3
A (Pulse on time)	29	37	48
B (Pulse Current)	0,05	0,15	0,25

Samples are prepared with same dimension according to the L₉ orthogonal array which is given in the Tab. 6. The pulse on time and input current values are given in the machine and the hole diameters and hole depth are fixed in the tool. The MINITAB is used for analyzing the parameters in the Taguchi design. The figure 8 shows the various parameters considered for optimization process and entered in the MINITAB worksheet. The Taguchi orthogonal array design has been done. The optimum value of MRR and Surface Roughness are evaluated based on the Pulse ON current and Pulse on time.

Table 6 Experimental Layout of L₉ Orthogonal array

Experimental Run	Input Parameters	
	A	B
1	1	1
2	1	2
3	1	3
4	2	1
5	2	2
6	2	3
7	3	1
8	3	2
9	3	3

The result of the above designed experiment is listed in the table 7. The Signal to Noise ratio

for the outputs is also provided in it. The approach of Smaller the better is applied for Surface Roughness and the approach of Larger the better is used for Material Removal Rate.

6. RESULTS AND DISCUSSION

The experimental investigation of spark EDM drilling process in inconel 718 material has been carried out in a plate of nine holes of deep 1.5 mm. And also the Taguchi method is used for optimization of process parameters in this study. The results obtained are discuss as bellow: Fig. 9 shows the relationship between Pulse on time and Peak current on Material Removal Rate (MRR) in the drilling process of spark EDM in Inconel 718 material. From the graph it is understood that the MRR will be maximum at Level 1 of Pulse on time and level 3 of peak current. Fig. 10 shows the relationship between Pulse ON time and Peak current with Surface Roughness (SR) in the drilling process of spark EDM in Inconel 718 material. It shows that, the Pulse ON time decreases with increase in the Surface Roughness. The peak current also exhibits the same effect. The Surface Roughness will be minimum whenever the Level 1 of Pulse on time and Level 1 of Peak current is used. Fig. 12 shows the relationship between Peak current and Surface Roughness (SR) in the drilling process of spark EDM in inconel 718 material. It shows that, the peak current increases With increases in the Surface Roughness. It reveal that the peak current is also directly proportional to the Surface Roughness of the machined part. From the experimental study it is observed that the pulse time and peak current are increases with increase in the surface roughness. An increase in the pulse time with decrease in MRR and increase in peak current with increase in MRR in the spark EDM drilling process in inconel 718 material.

Table 7 Experimental results and SN ratio

Pulse ON	Peak current	SR	SNRA1	MRR	SNRA2
29	0.05	2.7685	-8.844890557	9.82E-08	-8.844890557
29	0.15	3.6665	-11.28503379	1.1508E-06	-11.28503379
29	0.25	4.4865	-13.03815344	1.3889E-06	-13.03815344
38	0.05	3.128	-9.905334888	8.35E-08	-9.905334888
38	0.15	3.944	-11.91873813	9.097E-07	-11.91873813
38	0.25	4.524	-13.11045193	1.2628E-06	-13.11045193
47	0.05	3.0505	-9.687420587	6.84E-08	-9.687420587
47	0.15	4.6985	-13.43918462	9.764E-07	-13.43918462
47	0.25	5.1885	-14.30083642	1.1326E-06	-14.30083642

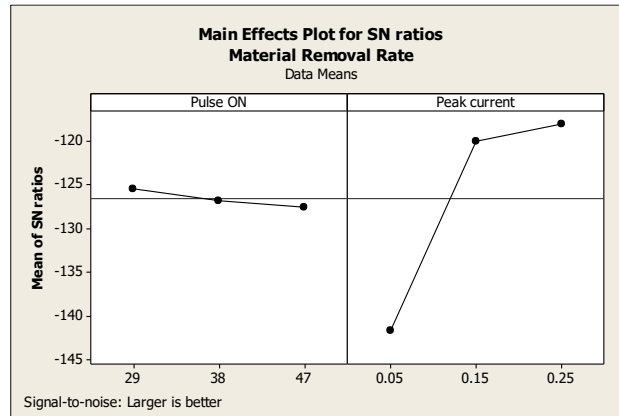


Figure 9 SN ratio plot for MRR

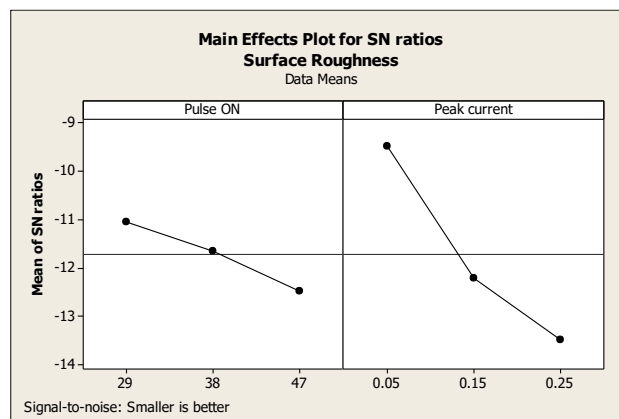


Figure 10 SN ratio for Surface Roughness

7. CONCLUSION

The following conclusions are arrived from the experimental work and optimization process is carried out in the Spark EDM drilling in Inconel 718 material.

- When pulse on time is increases, the MRR is decreased. The higher the pulse on time, intensity of spark is decrease due to expansion of plasma channel and results in less metal removal will takes place.
- When the current is increased, surface roughness is also increased. Because due to increase in current, the spark intensity is also increases. So the MRR per minute increases. Finally the surface roughness is increased.
- When the Pulse on time is increased, surface roughness is decreased, because due to increase in pulse on time, the spark intensity is also decreases. So the MRR per minute decreases. Finally the surface roughness is decrease.
- When current increases, the MRR also increases. The higher the current, intensity of spark is increased and results in high metal removal will takes place. The material removal rate (MRR) mainly affected by peak current (I_p). Pulse on time (T_{on}) has least effect on it.
- The surface roughness (SR) is mainly dependent on pulse current (I_p). Optimum parameters of input factors are as follows; Pulse Time: 38 μ s, Pulse current : 0,05 Amp

REFERENCES

1. Amorim, F. L.; Weingaertner, W. L. Influence of duty factor on the die sinking electrical discharge machining of high-strength aluminium alloy under rough machining. *Journal of Brazilian Society of Mechanical Sciences*. 24 (2002), pp. 194-199.
2. Ho, K. H, Newman, S. T, Rahimifard, S and Allen, R. D (2004) "State of the art in wire electrical discharge machining (WEDM)", *International Journal of Machine Tools & Manufacture*, vol. 44, pp. 1247-1259.
3. S.A. Celik, (2007) "Surface roughness investigation in the electrical discharge machining of power metal material", *Journal of Applied Sciences*, 7(12), pp. 1608-1613.
4. G.K.M. Rao, S. Satyanarayana and M. Praveen, (2008) "Influence of machining parameters on electric discharge machining of maraging steels – An experimental investigation", *Lecture Notes in Engineering and Computer Science*, 2171(1), pp. 1536-1541.
5. H. Singh and R. Garg, Effects of process parameters on material removal rate in WEDM. *Journal of Achievements in Materials and Manufacturing Engineering*, 32(1) (2009), 70-74.
6. Thomas R., (2009) "Investigation of the effect of process parameters on the formation and characteristics of recast layer in wire-EDM of Inconel 718", *Materials Science and Engineering*, vol. A 513, pp. 208–215.
7. P.S. Bharti, S. Maheshwari and C. Sharma, Experimental investigation of Inconel 718 during die-sinking electric discharge machining, *International Journal of Engineering Science and Technology*, 2(11) (2010), 6464-6473.
8. P. Singh, A. Kumar, N. Beri and V. Kumar, (2010), "Some experimental investigation on the aluminum powder mixed EDM on machining performance of hastelloy steel", *International Journal of Advanced Engineering Technology, Part A*, 1(2) (2010), 28-45.
9. Ahmad S and Lajis M A., (2013) "Electrical discharge machining (EDM) of Inconel 718 by using copper electrode at higher peak current and pulse duration", 2nd International Conference on Mechanical Engineering Research (ICMER 2013), pp. 1-7, doi:10.1088/1757-899X/50/1/012062.
10. Li, Guo, Wei, (2013) "Surface integrity characteristics in wire-EDM of Inconel-718 at different discharge" - *CIRP* 6, pp. 220 – 225.
11. Rajurkarb and Malshe (2013) "Wire electro-discharge machining of titanium alloy" - *CIRP* 5, pp. 13 – 18.
12. Zhang, Liu, (2014) "Investigation on the influence of the dielectrics on the material removal characteristics of EDM" *Journal of Materials Processing Technology*, pp. 1052–1061.



Contents lists available at ScienceDirect

Materials Today: Proceedings

journal homepage: www.elsevier.com/locate/matpr

Characteristic analysis of dissimilar metal weld for AISI304 with SA213T22 in super heater coils

K. Chandrasekaran^{a,*}, P. Ranjith Kumar^a, R. Ramanathan^a, J. Chandradass^b, T.T.M. Kannan^c, A. John Rajan^d

^a Department of Mechanical Engineering, MAM School of Engineering, Trichy 621105, India

^b Centre for Automotive Materials, Department of Automobile Engineering, SRM Institute of Science and Technology, Kattankulathur, Chennai 603203, India

^c Department of Mechanical Engineering, PRIST Deemed University, Thanjavur 613403, India

^d Department of Manufacturing Engineering, School of Mechanical Engineering, Vellore Institute of Technology, Vellore 632 014, India

ARTICLE INFO

Article history:

Received 11 November 2020

Accepted 14 December 2020

Available online xxx

Keywords:

AISI304

SA213T22

TIG Welding

Taguchi method

Grey Analysis

ABSTRACT

Super heater is an inevitable component of any boiler system and failure of super heater leads to breakdown of whole plant. The integration of efficient quality welding technologies for dissimilar metals will be a key component in the successful weld quality for power plant components. In this investigation, an attempt has been made to study the dissimilar material AISI304 and SA213T22 tungsten inert gas welding is performed under different welding conditions current (100, 115, 130 Amps), gas flow rate (6, 8, 10 ltr/min), speed (2, 2.5, 3 mm/sec) and micro structure analysis performed to find influence of fusion heat. The Taguchi analysis is implemented to obtain single response optimization and grey relational analysis used to attain multi response for best yield strength, the ultimate strength, Vickers hardness and the elongation of the metals.

© 2021 Elsevier Ltd. All rights reserved.

Selection and peer-review under responsibility of the scientific committee of the International Conference on Mechanical, Electronics and Computer Engineering 2020: Materials Science. This is an open access article under the CC BY-NC-ND license (<http://creativecommons.org/licenses/by-nc-nd/4.0/>).

1. Introduction

Super heater is basically a heat exchanger in which heat is transferred from furnace gas to the steam. Improper heat transfer between steam and furnace gas leads to problems of localized heating and damage the welding spots. These coils are made up of alloy steel SA213T22 which has corrosion resistance and it cannot withstand continuous high temperature. The super-heater coils are made up of SA213T22 which can withstand up to 540 °C metal temperatures and final stage super-heater stream temperature of more than 565 °C with the increase in steam pressure with their required dissimilar materials. AISI304 has superior properties such as resistance to fire side corrosion and a stream temperature of 650 °C for final super-heater. Hence, the dissimilar materials are introduced to reduce the damage and an interchange material AISI304 is attempted to replace this super-heated coil. The dissimilar material welding is not possible to make a fusion weld and welding parameters are affecting the welding quality. The dissim-

ilar materials welding have been continuously explored and the related valuable studies presented by the past researchers are given below. Guo Ming et al. [2] studied the dynamic temperature field of laser welding on stainless steel. It was dynamically simulated by the FEA software ANSYS using transient heat conduction equation. Kain et al. [3] studied the failure of a few super heater tubes at localized regions in an atmospheric fluidized bed combustor. Uger esme and Mehim bayramoglu et al. [4] have used AISI 304 Stainless steel plate. TIG welding machine is used. The input parameters are travel speed, current, nozzle plate distance. The output parameters are bead penetration and tensile load. The optimal weld pool geometry has four smaller-the-better quality characteristics, i.e. the front height, front width, back height and back width of the weld pool. The modified Taguchi method is adopted to solve the optimal weld pool geometry with four smaller-the-better quality characteristics. Experimental results have shown that the front height, front width, back height and back width of the weld pool in the TIG welding of stainless steel are greatly improved by using this approach. Ahmad et al. [1] investigated excessive hoop stresses are the cause of failure in on a super alloy Inconel-800 super heater tube. Vibhav gupta et al. [6] found primary reason

* Corresponding author.

E-mail address: kchandrasekaran1984@gmail.com (K. Chandrasekaran).

<https://doi.org/10.1016/j.matpr.2020.12.671>

2214-7853/© 2021 Elsevier Ltd. All rights reserved.

Selection and peer-review under responsibility of the scientific committee of the International Conference on Mechanical, Electronics and Computer Engineering 2020: Materials Science.

This is an open access article under the CC BY-NC-ND license (<http://creativecommons.org/licenses/by-nc-nd/4.0/>).

Table 1
Chemical composition of the AISI304 and SA213T22.

AISI304								
C	Cr	Fe	Mn	Ni	P	S	Si	Mo
0.08	19	70	2	10	0.045	0.03	1	-
SA213T22								
0.15	2.60	-	0.60	-	0.025	0.025	0.50	1.13

Table 2
Factors and levels for similar and dissimilar welding.

Factor/ Levels	Level 1	Level 2	Level 3
Current (Amps)	100	115	130
Gas Flow Rate (ltr/min)	6	8	10
Speed (mm/sec)	2	2.5	3

Table 3
Experimental result for AISI304 to SA213T22 dissimilar metal weld.

AISI304 TO AISI304 similar metal weld								
Trials	A	B	C	YS (MPa)	US (MPa)	EL (%)	H (Hv)	
1	1	1	1	573.20	625.80	17.50	198.9	
2	1	2	2	447.50	635.32	27	197.3	
3	1	3	3	365	569.45	14.50	196.3	
4	2	1	2	429.90	660.60	20	183.5	
5	2	2	3	314	511.62	29.50	177.1	
6	2	3	1	370.20	594.65	13.50	185.3	
7	3	1	3	433	655.81	30	190.1	
8	3	2	1	396.80	571.96	17	206.1	
9	3	3	2	400.10	599.47	18	230.1	

for premature failure of super heater tubes led severe oxidation and creep. Gokula Krishnan et al. [5] presented occurrences of phase transformation and formation of aluminide phase such as Ni₃Al. Faith Dokme et al. [7] explained that weld zone micro structural analysis exhibited the existence of multi directional grain growth in all specimens on AISI 316L side. Yu Sun et al. [8] found that Iron alloy is exposed to a high temperature oxidation environment, outer layer of super heater will gradually oxidize into stable

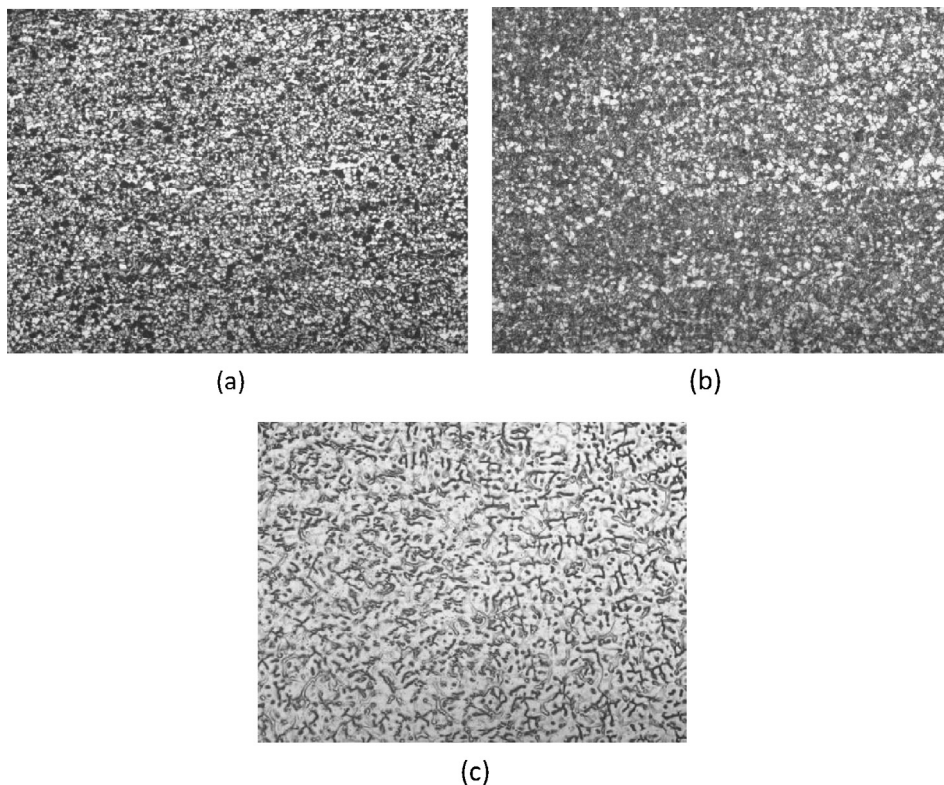


Fig. 1. Micro graph (Mag: 200x) for fusion (a) Parent material of SA213T22; (b) Dissimilar material HAZ of SA213T22; (c) Dissimilar material weld spot.

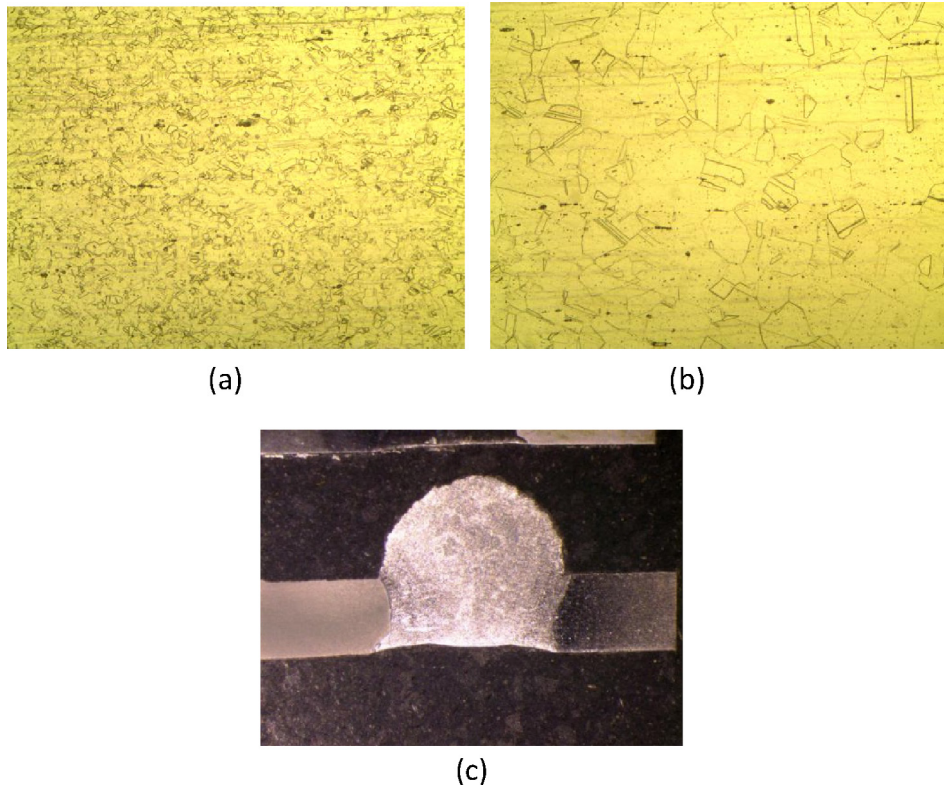


Fig. 2. Micrograph (Mag: 200x) for fusion (a) Parent material of AISI304; (b) Dissimilar material HAZ of AISI304; (c) Macro graph (Mag: 5x) dissimilar material weld spot.

Table 4

Signal to noise ratio for AISI304 to SA213T22 dissimilar metal weld.

AISI304 TO AISI304 similar metal weld								
Trials	A	B	C	YS (MPa)	US (MPa)	EL (%)	H (Hv)	
1	1	1	1	55.1661	55.9287	24.8608	45.9727	
2	1	2	2	53.0159	56.0599	28.6273	45.9025	
3	1	3	3	51.2459	55.1091	23.2274	45.8584	
4	2	1	2	52.6673	56.3988	26.0206	45.2727	
5	2	2	3	49.9386	54.1790	29.3964	44.9644	
6	2	3	1	51.3687	55.4852	22.6067	45.3575	
7	3	1	3	52.7298	56.3356	29.5424	45.5796	
8	3	2	1	51.9714	55.1473	24.6090	46.2816	
9	3	3	2	52.0434	55.5553	25.1055	47.2383	

Table 5

Taguchi Analysis: YS & US versus A, B, C.

Level	YS			US		
	A	B	C	A	B	C
1	53.14	53.52	52.84	55.70	56.22	55.52
2	51.32	51.64	52.58	55.35	55.13	56.00
3	52.25	51.55	51.30	55.68	55.38	55.21
Delta	1.82	1.97	1.53	0.34	1.09	0.80
Rank	2	1	3	3	1	2

and dense oxide film. From the study it was observed that flux used as the most significant effect on depth of penetration followed by welding current. Most of the researchers concentrate on the different directions but AISI304 over SA213T22 dissimilar materials weld was not performed yet and hence it is an important to study for the power plant components. Considering all the points into account in this present work. AISI304 to SA213T22 dissimilar

TIG welding process is performed under different welding conditions.

2. Experimental details

The paper aims to investigate and identify key improvements in weld mechanical properties and the microstructural compounds of

Table 6
Taguchi Analysis: YS and US versus A, B, C.

Level	EL			H		
	A	B	C	A	B	C
1	25.57	26.81	24.03	45.91	45.61	45.87
2	26.01	27.54	26.58	45.20	45.72	46.14
3	26.42	23.65	27.39	46.37	46.15	45.47
Delta	0.85	3.90	3.36	1.17	0.54	0.67
Rank	3	1	2	1	3	2

Table 7
Normalized- Grey Relational Coefficient and Grey Relational grade.

Trial No.	Normalized values of Z_{ij}				Grey Relational Co-efficient				Grey Relational grade
	YS	US	EL	H	YS	US	EL	H	
1	1.000	0.788	0.325	0.443	0.333	0.388	0.606	0.530	0.464
2	0.589	0.847	0.868	0.413	0.459	0.371	0.365	0.548	0.436
3	0.250	0.419	0.089	0.393	0.667	0.544	0.848	0.560	0.655
4	0.522	1.000	0.492	0.136	0.489	0.333	0.504	0.787	0.528
5	0.000	0.000	0.979	0.000	1.000	1.000	0.338	1.000	0.835
6	0.274	0.588	0.000	0.173	0.646	0.459	1.000	0.743	0.712
7	0.534	0.972	1.000	0.271	0.484	0.340	0.333	0.649	0.451
8	0.389	0.436	0.289	0.579	0.563	0.534	0.634	0.463	0.548
9	0.403	0.620	0.360	1.000	0.554	0.446	0.581	0.333	0.479

Table 8
Main effects on Grey grades.

Levels	1	2	3
Current (Amps)	0.518	0.692	0.493
Gas Flow Rate (ltr/min)	0.481	0.606	0.615
Speed (mm/sec)	0.575	0.481	0.647

dissimilar metals. This information helps lay a baseline for TIG welding process specifications and also demonstrates the significant factors affecting the TIG welding processes on dissimilar metals. The materials selected for dissimilar welding are AISI304 and SA213T22 and the chemical composition is given in Table 1. The diameter of the tube is taken as 60.3 mm, thickness is 4.5 mm and length is 250 mm. The electrode selected for similar welding is E309L whose dimension is 2.4 m in length. The argon is used as gas and its pressure is 3.5 kg/cm² during welding. The affecting factors and level selected for dissimilar welding AISI304 and SA213T22 is given in Table 2 and the experimental results of yield strength, the ultimate strength, Vickers hardness and the elongation of the metals is given in Table 3.

The physical properties of two metals are being very different from each other which lead to complexities in the weld pool shape, solidification microstructure and segregation patterns. Fig. 1 shows the micro-structure of the parent, heat affected zone and the SA213T22 weld spot at magnification 200x. Fig. 2 shows the macro-structure of the dissimilar materials welding spot at magnification of 5x and the micro-structure of the AISI304 weld spot at

Table 9
General Linear Model: Analysis of Variance for YS.

Source	DF	Seq SS	Adj SS	Adj MS	F	P
A	2	12383.3	12383.3	6191.7	7.98	0.111
B	2	18686.9	18686.9	9343.5	12.05	0.077
C	2	9266.3	9266.3	4633.2	5.97	0.143
Error	2	1551.1	1551.1	775.6		
Total	8	41887.7				

S = 27.8487 R-Sq = 96.30% R-Sq(adj) = 85.19%.

magnification 200x. It shows the macro-structure shows the dissimilar materials weld geometry such as reinforcement, width, penetration and weld bead.

3. Taguchi methodology

The main goal of the parameter design is to selecting the best process parameter to improve quality characteristics and to identify the product parameter values under the optimal process parameter values using Taguchi methodology. Moreover implementing that the optimal process parameter values obtained from the parameter design are insensitive to the variation of environmental conditions and other noise factors. Since the quality characteristic is to be maximization, the larger the better category is used to calculate the S/N ratio for responses Equation 1 shows the larger the better characteristic.

$$S/N \text{ ratio } (\eta) = -10 \log_{10}(1)$$

Taguchi technique is used to find the optimum setting of dissimilar materials weld and experiments are conducted based on the L₉ orthogonal array. The aim function is maximization of the yield strength, ultimate strength, Elongation and Vickers hardness, so experimental results are converted to signal to noise ratio for reduction of variance using Eq. (1). The signal to noise ratio yield strength, ultimate strength, and elongation and Vickers hardness is presented in Table 4. The Taguchi analysis for yield strength and ultimate strength is given Table 5, it clearly shows that the optimal welding parameters for maximization of yield strength is

Table 10

General Linear Model: Analysis of Variance for US.

Source	DF	Seq SS	Adj SS	Adj MS	F	P
A	2	857	857	429	0.23	0.813
B	2	9308	9308	4654	2.51	0.285
C	2	4313	4313	2156	1.16	0.463
Error	2	3714	3714	1857		
Total	8	18,192				

S = 43.0931 R-Sq = 79.58% R-Sq(adj) = 18.34%

Table 11

General Linear Model: Analysis of Variance for EL.

Source	DF	Seq SS	Adj SS	Adj MS	F	P
A	2	6.22	6.22	3.11	0.10	0.911
B	2	139.39	139.39	69.69	2.19	0.314
C	2	116.22	116.22	58.11	1.82	0.354
Error	2	63.72	63.72	31.86		
Total	8	325.56				

S = 5.64456 R-Sq = 80.43% R-Sq(adj) = 21.71%

Table 12

General Linear Model: Analysis of Variance for H.

Source	DF	Seq SS	Adj SS	Adj MS	F	P
A	2	1086.46	1086.46	543.23	5.76	0.148
B	2	286.01	286.01	143.00	1.52	0.397
C	2	376.60	376.60	188.30	2.00	0.334
Error	2	188.65	188.65	94.32		
Total	8	1937.72				

S = 9.71208 R-Sq = 90.26% R-Sq(adj) = 61.06%

current set as 100 amps, gas flow rate 6 lit/min and welding speed set as 2 mm/sec. Optimal welding parameters for maximization of ultimate strength is current set as 100 amps, gas flow rate 6 lit/min and welding speed set as 2.5 mm/sec. The Taguchi analysis for Elongation and Vickers hardness is given [Table 6](#), it shows that the optimal welding parameters for maximization of Elongation is current set as 130 amps, gas flow rate 8 lit/min and welding speed set as 3 mm/sec. Optimal welding parameters for maximization of Vickers hardness is current set as 130 amps, gas flow rate 10 lit/min and welding speed set as 2.5 mm/sec.

4. Grey relational analysis methodology

In this work, a grey relational approach has been applied to solve multi response optimization of yield strength, ultimate strength, elongation and Vickers hardness using grey relational analysis. The proposed steps can determine effectively the optimal factor level combination for multi response problems. It quantifies all influences of various factors and their relation, which is called the whitening of factor relation. As a result, optimization of the multi responses can be converted into optimization of a single relational grade. In short, there is an ample scope of applying the proposed methodology of grey relational analysis with the multiple responses for the optimization of yield strength, ultimate strength, elongation and vickers hardness.

The objective of the dissimilar material weld AISI304 to SA213T22 is maximization of yield strength, ultimate strength, elongation and Vickers hardness. This was termed as the larger the better type problem where maximization of the characteristic was intended. S/N Ratio was calculated for the responses using the larger the better formula Equations 1. The experimental result

and computed S/N ratios for yield strength, ultimate strength, Elongation and Vickers hardness are shown in [Table 6](#). The S/N ratio values were normalized by Eq. (2) and grey relational co-efficient was calculated for the normalized S/N ratio values by using Eq. (3). The grey relational grade was computed from grey relational co-efficient for by Eq. (4). The normalized signal to noise ratio, grey relational co-efficient and grey relational grades are given in [Table 7](#). The main effects were tabulated in [Table 8](#) and considering maximization of grade values in [Table 8](#) the optimal parameter conditions obtained were $A_1B_3C_3$. Multi response optimization of dissimilar material weld AISI304 to SA213T22 for maximization of yield strength, ultimate strength, Elongation and Vickers hardness, current set as 110 amps, gas flow rate 10 lit/min and welding speed set as 3 mm/sec.

In this study, the analysis of variance is used to find the statistically significant welding parameters. The analysis of variance for yield strength is given in [Table 9](#). It clearly shows that the gas flow rate most significantly affects the yield strength with F:P value of 12.05:0.077. The analysis of variance for ultimate strength is given in [Table 10](#). It mention that the gas flow rate most significantly affects the ultimate strength with F:P value of 2.51:0.285. The analysis of variance for elongation is given in [Table 11](#). It represents the gas flow rate most significantly affects the elongation with F: P value of 2.19:0.314. The analysis of variance for Vickers hardness is given in [Table 12](#). It denotes the current most significantly affects the Vickers hardness with F: P value of 5.76:0.148.

5. Conclusion

The function of the super heater coil is transfer heat energy, during transfer of high transfer damage happen in weld spot. So

aim of the investigation is to study the performance of the dissimilar material AISI304 to SA213 T22 TIG welding the following are the outcomes

- Optimal TIG welding parameters for dissimilar material maximization of yield strength is current set as 100 amps, gas flow rate 6 lit/min and welding speed set as 2 mm/sec.
- Optimal TIG welding parameters for dissimilar material maximization of ultimate strength is current set as 100 amps, gas flow rate 6 lit/min and welding speed set as 2.5 mm/sec.
- Optimal TIG welding parameters for dissimilar material maximization of Elongation is current set as 130 amps, gas flow rate 8 lit/min and welding speed set as 3 mm/sec.
- Optimal TIG welding parameters for dissimilar material maximization of Vickers hardness is current set as 130 amps, gas flow rate 10 lit/min and welding speed set as 2.5 mm/sec.
- Multi response optimization of dissimilar material weld AISI304 to SA213T22 for maximization of yield strength, ultimate strength, Elongation and Vickers hardness, current set as 110 amps, gas flow rate 10 lit/min and welding speed set as 3 mm/sec.

Declaration of Competing Interest

The authors declare that they have no known competing financial interests or personal relationships that could have appeared to influence the work reported in this paper.

References

- [1] J. Ahmad, J. Purbolaksono, L.C. Beng, Failure analysis on high temperature superheater Inconel 800 tube, *Eng. Fail. Anal.* 17 (2010) 328–333.
- [2] G. Ming, Q.H. XiaoyanZeng, Effects of gas shielding parameters on weld penetration of CO₂ laser-TIG hybrid welding, *J. Mater. Process. Technol.* 184 (2007) 177–183.
- [3] V. Kain, K. Chandra, B.P. Sharma, Failure of carbon steel tubes in a fluidized bed combustor, *Eng. Fail. Anal.* 15 (2008) 182–187.
- [4] Uger Esme, Mehim Bayramoglu, Optimization of weld bead geometry in TIG welding process using gray relation analysis and Taguchi method, *material technology* 43 (2009) 143149.
- [5] A. Gokulakrishnan, K. Karuppasamy, Experimental investigation of Nickel Aluminide (Ni₃Al) nano structured coated economiser tube boiler, *Int. J. Eng. Sci. Manage. Res.*, 2016, pp. 1–7.
- [6] Vibhav gupta, Harsh vardhan, S.K. Yadaw, CORCON-2017, (2017). pp. 1-9.
- [7] Fatih Dokme Mustafa Kuleci Ugur Esme Micro structural and mechanical characterization of dissimilar metal welding of Inconel 625 and AISI 316L Metals. 8 10 (2018),797. 797 10.3390/met8100797
- [8] Yu Sun, Maozhen Yue, Yungang Li, Reaction Kinetics of chlorine corrosion to heating surfaces during coal and Biomass cofiring, *J. Chem.* 2020 (2020) 1–10.

Investigation of Nitronic-60 using Zinc Coated Wire

P.Ranjith kumar¹, K.Chandrasekaran^{2*}, R.Ramanathan³, M.Panneer selvam⁴

^{1,2,3,4}Professor, Department of Mechanical Engineering, MAM School of Engineering, Tamilandu, India,
*Email:kchandrusekaran1984@gmail.com

ABSTRACT

The objectives of this work is to investigate the effective parameters for pulse ON time; pulse OFF time; voltage & wire feed while machined on Wire-Cut Electrical Discharge Machining composite super alloy material. The experimental results proposed optimal combination of parameters which give the maximum material removal rate, surface roughness and kerf width. Finally, confirmation experiments were carried out to identify the effectiveness of the proposed method. In this experiment carried alloy material of NITRONIC 60 through optimization of metal removal rate; surface roughness and kerf width are output parameters these are all performed in methodology Regression analysis and ANOVA for Response Surface Linear Model.

Key words: WEDM, Nitronic-60, Response Surface Linear Model, ANOVA, SR, MRR

Introduction

Machining removes certain parts of the work pieces to change them to final parts. Machining nowadays has been classified in two types: Traditional Machining; Non-traditional Machining [1]. Traditional machining is also known conventional machining requires the presence of a tool that is harder than the work piece to be machined. WEDM is considered as a unique adoption of the conventional EDM process which comprises of a main worktable, wire drive mechanism, a CNC controller, working fluid tank and attachments [2]. Vinothkumar have proposed a quadratic mathematical model and conducted experiments by taking six WEDM process parameters are discharge current, pulse duration, pulse frequency, wire speed, wire tension and dielectric flow rate [3]. Soundrarajan have discuss and investigate the significant process parameters along with the percentage contribution of each parameter. ANOVA is used to find the percentage contribution of significant process parameters [4]. Pujari evaluates the effect of voltage, dielectric pressure, pulse on time and pulse off-time on spark gap of Ti6AL4V alloy. It is found that the pulse on time, pulse off time, the interaction of dielectric pressure and pulse off time, and interaction of pulse on time and pulse off time are significant parameters which affect the spark gap of WEDM [5]. Antar study has been made to optimize the process parameters during machining of Inconel-600 by wire electrical discharge machining (WEDM) using response surface methodology (RSM). Four input process parameters of WEDM (Peak Current (IP), Pulse on time (TON), Pulse off time (TOFF) and Wire Feed rate (WF) were chosen as variables to study the process performance in terms of Material Removal Rate (MRR) [6]. Brajaeshlodhi have investigated the effects of the various WEDM process parameters on the machining quality of AISI 304 stainless steel and to obtain the optimal sets of process parameters so that the quality of machined parts can be optimized. The working ranges and levels of the WEDM process parameters are found using one factor at a time approach [7]. The objectives are as follows:-

- To achieve the shortest machining time whilst at the same time satisfying the requirements of accuracy and surface roughness.
- To discuss the cause – effect relationship of machining parameters & machine performance in WEDM.
- To determine significant parameters affecting the machining performance.
- To establish the mathematical models relating the machining performance & machining parameters by regression & correlation analysis.
- Finally the optimal machining parameters are obtained under the constraints & requirements.

EXPERIMENTATION DETAILS

NITRONIC 60

Corrosion materials Nitronic 60 is a solid solution strengthened, nickel-molybdenum-chromium alloy with a small amount of tungsten which exhibits excellent corrosion resistant in an assortment of harsh environments.

OPTIMIZATION OF DRILLING PROCESS PARAMETERS OF ELECTRICAL DISCHARGE MACHINING IN INCONEL 718 MATERIAL

P.Ranjith kumar¹, K.Chandrasekaran^{2*} M.Panneer selvam³, R.Ramanathan⁴

^{1,2,3,4}Professor, Department of Mechanical Engineering, MAM School of Engineering, Tamilandu, India,

*Email:kchandrasekaran1984@gmail.com

Abstract-

Electrical Discharge Machining is becoming an important machining process in the fields of manufacturing 3D complex shapes and using a simple shaped electrode tools. The present work deals with the experimental investigation of Electrical Discharge Spark machining on Inconel 718 material. The holes of 1.5mm deep were machined using EMS3050 Manual EDM with various combinations of input parameters such as pulse current and pulse on time (Ton). The Material removal rate and Surface roughness are taken as the output parameters as more focus is given to the dimensional accuracy of the machined components. The Taguchi method of optimization is used. The result shows the effect of input parameters on material removal rate and surface roughness. Also the optimum values are estimated.

Key words: EDM, electrode, material removal rate, surface roughness, Taguchi method

1. INTRODUCTION

Nickel based super alloy, Inconel 718 is one of the most difficult-to-machine material which attributed to its ability to maintain hardness at elevated temperature and consequently it's very useful for hot working environment. Formation of complex shapes by this material along with reasonable speed and surface finish is not possible in traditional machining. This alloy is characteristically difficult to machine due to its poor thermal properties, high toughness, high hardness, and high work hardening rate. Usually, a nonconventional machining method like electrical discharge machining (EDM) is chosen for machining Inconel 718 in order to overcome such limitations. However, due to the great physical properties of Inconel 718, the cutting process for this material is become an issue in order to improve the speed of machining process. This alloy has attracted many researchers because of its increasing applicability and the machining ability of aerospace alloys will continually decline as service demands increase in order to satisfy the demand for higher temperature capability for structural engine alloys. The Fig. 1 shows the working principle of Spark EDM. Spark erosion EDM, also called cavity type EDM or volume EDM consists of an electrode and work piece submerged in an insulating liquid such as, more typically, oil or, less frequently, other dielectric fluids. The electrode and work piece are connected to a suitable power supply. The power supply generates an electrical potential between the two parts.



Investigation of Micro-Hole Quality in Drilled CFRP Laminates Through CO₂ Laser

N. Ramanujam¹ · S. Dhanabalan² · D. Raj Kumar³ · N. Jeyaprasakash^{4,5}

Received: 28 August 2020 / Accepted: 25 February 2021
© King Fahd University of Petroleum & Minerals 2021

Abstract

Carbon fiber-reinforced polymer (CFRP) composites are increasingly replacing the metals and other composites in automotive and aerospace industries due to their excellent properties. These application components have required micro-holes on CFRP for joining different components. In the present work, micro-holes are fabricated on CFRP using CO₂ laser for achieving the high-quality-dimensional precision and accurate hole. The input parameters such as laser power, cutting velocity and argon pressure were varied. The responses such as heat-affected zone, kerf width, kerf angle and aspect ratio were measured using video measurement system. Besides, analyses of variances, regression modeling and microstructural analysis were presented. Results showed that the cutting velocity is most influential factor that affecting the heat-affected zone and kerf width and followed by power.

Keywords CFRP · Laser drilling · Heat-affected zone · Kerf width · Kerf angle · Aspect ratio

1 Introduction

Carbon fiber-reinforced polymer (CFRP) is one of the polymer-based composite and tailorable material design characteristics, in which carbon fiber provides the higher stiffness

and strength when compared to steel. In addition to that, epoxy resin provides toughness by developing cohesive force between carbon fiber and epoxy resin to protect and hold the carbon fiber together. The desired properties of CFRP can be achieved by varying the quantity, length, direction, size of fiber and selection of polymer matrix. The mechanical properties of CFRP have varied from conventional metals due to directionality of carbon fiber [1]. Hence, the CFRPs are applied to various fields such as mechanical, construction, electronic and aerospace [2]. These application components are required micro-holes on CFRP for joining different components. In the conventional machining, there are some problems such as excessive dust generation, high tool wear, high delamination, spalling, fuzzing, fiber pullouts and matrix cracking which was observed because of their inherent heterogeneity and anisotropy [3, 4]. These problems are mainly affecting the mechanical properties of CFRP. During the conventional drilling on CFPR, the abrasive nature of carbon fiber produced the high delamination of 2.6 [5]. In order to reduce delamination in the conventional drilling, the abrasive water jet machining is used to machine the CFRP, the results are maximum delamination length of 5.51 mm, kerf angle ratio of 1.738 and top kerf width of 1.509 mm is observed [6]. In the kerf width analysis, the abrasive water jet machining on CFRP produced the top kerf width of 1.38 mm, bottom kerf width of 1.13 mm and taper ratio of

✉ N. Jeyaprasakash
prakash@ntut.edu.tw; prakash84gct@gmail.com

N. Ramanujam
ramanujam@egspec.org

S. Dhanabalan
dhanabalan69@gmail.com

D. Raj Kumar
profdraj कुमार@gmail.com

¹ Department of Mechanical Engineering, E.G.S. Pillay Engineering College, Nagapattinam, Tamilnadu 611002, India

² Department of Mechanical Engineering, M. Kumarasamy College of Engineering, Karur, Tamilnadu 639113, India

³ Department of Mechanical Engineering, MAM School of Engineering, Tiruchirappalli, Tamilnadu 621105, India

⁴ Additive Manufacturing Center for Mass Customization Production, National Taipei University of Technology, Taipei 10608, Taiwan, ROC

⁵ Graduate Institute of Manufacturing Technology, National Taipei University of Technology, Taipei 10608, Taiwan, ROC



0.015 is achieved [7]. In another way to reduce kerf width of CFRP, wire cut electrical discharge machining produced the top kerf width of 263.67 μm and bottom kerf width of 262.97 μm is obtained [8]. Additionally, during the electrical discharge machining on CFRP, the hole taper of 0.05 mm and heat-affected zone width of 0.9 mm are obtained [9]. The hole defects analysis of CFRP found that the conventional drilling, wire cut electrical discharge machining, electrical discharge machining and abrasive water jet machining have produced high hole defects. Therefore, laser beam machining has selected to minimize the hole defect of CFRP. In the laser beam machining, Kumar and gururaja [10] studied the quality of drill on Ti/CFRP/Ti laminates and reported that heat-affected zone (HAZ) of entry and exit is 0.3 mm and 1.1 mm, and 1.7 degrees taper angle was measured. Gautam and Mishra [11] investigated the kerf width on basalt fiber-reinforced polymer and result showed that 0.221 mm of kerf width and 0.44 degrees taper angle were observed through Nd: YAG laser machining. Leone and Genna [12] examined the HAZ on CFRP material through Nd: YAG laser machining and reported that HAZ at entry and exit is 0.14 mm and 0.07 mm, respectively. Oh et al. [13] studied the cut quality of CFRP material using fiber laser.

Based on the previous literature and also shown in Table 1, it is found that a limited number of conventional [14, 15] and non-conventional machines [16–18] were used for performing micro-hole on CFRP and studied the quality characteristics of micro-holes. In addition to that, most of the lasers machining characteristics are decided by inadequate selection of process parameters [19, 20]. Hence, the research is focused on studying the effects of process parameters on heat-affected zone at entry and exit, kerf width at entry and exit, kerf angle and aspect ratio of micro-drilled CFRP. Therefore, in the present study, a CO_2 laser was used to drill 0.5-mm holes on CFRP material by varying the input parameters such as power, cutting velocity and argon pressure. The prime novelty of this work, the 0.5-mm hole making on CFRP using CO_2 laser and the responses such as heat-affected zone and kerf width were measured through twelve points selection. Further, analysis of variance and regression equations were formed for all the responses and hole quality was discussed in terms of structural aspects.

2 Experimental Details

The CFRP composite has 55% carbon fiber reinforced with epoxy resin and having 12 layers with alternative arrangement in the fiber orientation, namely 0° and 90° with a thickness of 3 mm. The CFRP laminates fabricated through M/s GALARK Industry using autoclave method. Figure 1a, b shows the SEM picture of CFRP with their orientation and energy-dispersive X-ray spectroscopy

(EDAX) graph. Table 2 shows the chemical composition of CFRP. The EDAX method is used to identify the chemical characterization of a CFRP through X-ray excitation. The micro-holes of 0.5 mm are produced on CFRP using a computer numerical controlled (CNC) continuous wave CO_2 laser drilling machine with design of experiment. The L16 orthogonal array is selected based on the three factors with four levels. There are a number of factors affecting the quality of machined CFRP such as type of laser, laser mode setting, laser power, cutting velocity, type of assist gas, gas pressure, nozzle diameter, stand-off distance, focal plane position, focal length, focal lens diameter and beam spot diameter. There are various factors that have to be taken into account when using lasers as drilling tools, the main considerations including the absorption of the energy and how this varies with the temperature of the material, the thermal diffusivity of the material and reaction temperature. There are other considerations, such as the dimensions of the heat-affected zone, which is the zone where the capability of stress transfer from the matrix to the fibers is reduced or absent. Further concerns include the formation of burrs and dross, thermal expansion of the material and consideration of the tolerances required for reaction products, the assist gas and finally safety. All of these elements must be considered. Another problem with the laser drilling of composites occurs because the constituents of the material are completely different. Because of the properties of various fibers and resins, there is a vast range of temperatures at which the materials melt (soften or decompose). The laser beam has a certain power and thus has a defined heat input into the material. However, because of the different properties of the fiber and matrix, the two components can react very differently to the thermal input. Hence, power, cutting velocity and argon pressure are selected. These factors are highly affecting the quality of cutting compared to other factors. In order to increase the productivity of the process, the Minitab 18 statistical trail software is used. The number of levels is normally varied from 2 to 5 for 3 factors. The L9 and L27 design layouts are suggested for three factors with three levels. Similarly, the L25 design layout is presented for three factors with four levels. Hence, optimum design layout of L16 is selected for this study. Based on the industrial experience and selected lens, the focal length of 127 mm on the surface of the workpiece is selected. The schematic of the CO_2 laser drilling process is shown in Fig. 2. The laser spiral trepanning drilling process parameters are selected based on the machine specifications and trail tests/literature review which is shown in Table 3. The CO_2 laser machine specification is shown in Table 4. The responses, HAZ at entry (HAZent) and exit (HAZext) and kerf width at entry (KWent) and exit (KWext), are measured by using a video measurement system (VMS-2010 F). The kerf angle (KA) and aspect ratio (AR) are measured through the kerf width.



Table 1 Literature review on pulsed, continuous wave and ultra-short lasers effects on CFRP

Ref. no	Type of laser sources	Conditions used	HAZ (mm)	KW (mm)	KA (°)
[19]	Pulsed Nd: YAG	P (W)= 300 v (mm/s)=0.6–1 E (J)=0.2–2.2 tp (ms)=0.2–1 fp (Hz)= 30–50 p (kg/cm ²)=4–8	0.753–1.750	0.211–0.356 (T) 0.085–0.197 (B)	–
[22]	CW fiber laser	P (W)= 100–400 v (mm/min)=500–2000 fp (Hz)= 1000–10,000	–	0.4–0.3 (T) 1.4–1.3 (B)	–
[32]	CW CO ₂ laser	P (W)= 200–400 v (mm/min)=0.2 – 0.4 p (bar)=2.5–3.5	0.23 – 0.39	–	–
[38]	Ultra short	P (W)= 400 v (mm/s)= 300–1500 fp (MHz)= 2–20	<0.025	–	–
[39]	CW CO ₂ laser	P (W)= 200–500 v (m/min)=0.6–1 p (bar)= 2–3	0.23 – 0.39	–	1.8–1.1
[35]	CW CO ₂ laser	P (W)= 600 v (mm/s)= 10–60	–	0.55–0.5	89
[31]	CW CO ₂ laser	P (W)= 280–750 v (mm/min)= 250–3000 p (bar)=0.5 – 4	0.06 – 0.13	–	–
[33]	Pulsed CO ₂ laser	P (W)= 1500 v (m/min)=4 – 5	0.3–0.35	0.140 – 0.190	–
[24]	Pulsed and CW CO ₂ laser	P (W)= 300–3000 v (mm/min)= 200–4000 p (bar)= 2–6 fp (MHz)= 1000–4000	CW 0.7–1 Pulsed 1.2	0.2 0.15	0.016 – 0.12 0.01 – 0.02
[40]	Pulsed Nd: YAG	P (W)= 120 v (mm/min)= 20–100 E (J)= 0.8–2.0 tp (ms)= 1–2 fp (Hz)= 15 –45 p (Mpa)=0.3	1.4 – 0.8	–	–
[41]	CW CO ₂ laser	P (W)= 230–550 v (mm/min)= 450–550 p (Mpa)=0.25–45	0.258 – 0.431	–	0.763–1.405
[36]	CW CO ₂ laser	P (W)= 800–2000 v (m/min)= 7.5–30 p (bar)= 3–16	–	0.103	2.06
[12]	Pulsed Nd:YAG	P (W)= 95 v (mm/s)= 10	0.170	–	–
[42]	Pulsed Nd: YAG	tp (ms)= 1.22 v (mm/s)= 1.86 p (Mpa)= 0.1	0.125	0.081	2.71
[43]	Nd:YVO ₄ Picosecond Pulsed	P (W)= 20–28 v (mm/s)= 1000–1800 m	–	0.400 (T) 0.080 (B)	4.2
[44]	Picosecond pulsed Nd: YAG	P (W)= 200 Wave length (nm)= 515 Repetition rate (kHz)= 800 Pulse length (ps)= 1	–	–	3.5

P (W) is power; v (mm/s) is cutting speed; E (J) is pulse energy; tp (ms) is pulse duration; fp (Hz) is pulse repetition rate; p (kg/cm²) is gas pressure; T is noted as top surface; B is noted as bottom surface

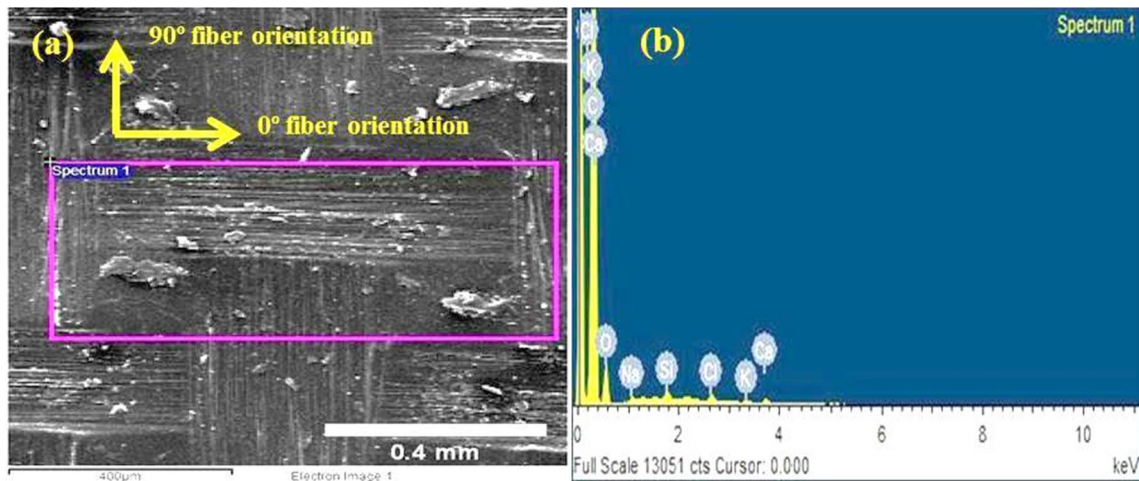


Fig. 1 a SEM picture of CFRP composite with orientation, and their corresponding EDAX graph (b)

Table 2 Chemical composition of CFRP

Elements	C	O	Na	Si	Cl	K	Ca
% wt	84.12	14.92	0.20	0.20	0.28	0.10	0.21

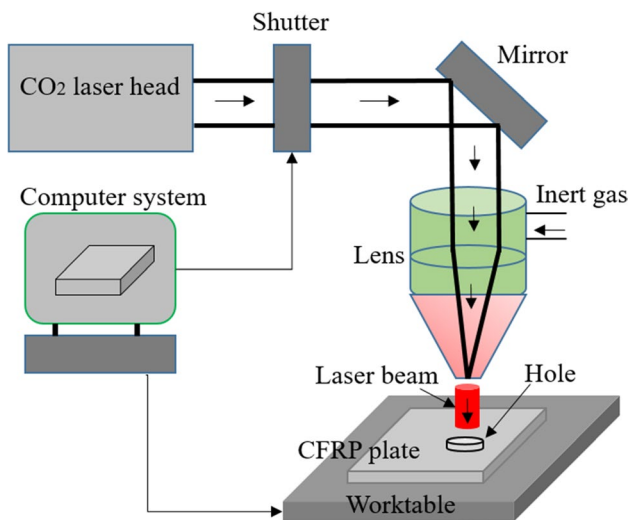


Fig. 2 Schematic diagram for CO₂ laser experimental setup

In order to get accurate results, each experimental condition is carried out three times. The mean values of responses are considered for further analysis. The machined work material with marked portion on CFRP is shown in Fig. 3. The schematic diagram of heat-affected zone (HAZ), kerf width and kerf angle is shown in Fig. 4.

3 Results and Discussion

The micro-holes of 48 (16 × 3 = 48 holes, the 16 represents number of experimental conditions used in this study and 3 represents each experimental conditions are carried out in three time) were made on CFRP using CO₂ laser under the design of experiment. The outputs such as HAZ at entry and exit, kerf width at entry and exit, kerf angle and aspect ratio were measured using video measurement system and the mean responses, which is given in Table 5. The drilled holes

Table 3 Laser drilling parameters and their levels [45]

Control parameters	Symbol	Levels				Problems raised/reference	
		1	2	3	4	By selecting below limit	By selecting Above limit
Power, W	<i>P</i>	15	30	45	60	Through hole not achieved	Low taper angle observed
Cutting velocity, mm/rev	<i>v</i>	20	40	60	80	High taper angle	High HAZ formation
Argon pressure, KPa	<i>p</i>	200	300	400	500	[31, 32]	

Table 4 Specifications of the CO₂ laser [45]

Parameters	Specification
Operating mode	CW
Wavelength	10.6 μm
Peak laser output power	1640 W
Pulse width/frequency	2-400 μs/0-130KHz
Spot size at focus	0.5 mm
Beam quality M ²	1.7
Assist gas	Argon
Stand-off	1.5 mm
Focus position	Surface
Maximum power	650 W
Focal length	127 mm
Nozzle diameter	2 mm

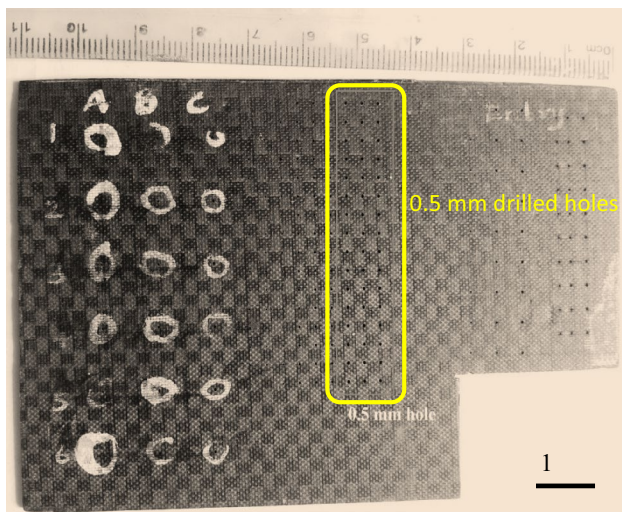


Fig. 3 Macrograph of drilled CFRP laminates

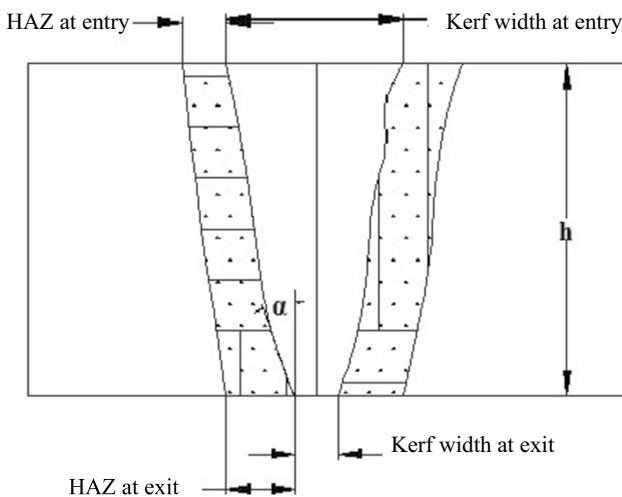


Fig. 4 Schematic of responses which is indicating entry and exit of heat-affected zone and Kerf width [33]

of 0.5 mm at entry and exit images are shown in Figs. 5a–p and 6a–p, respectively. Indeed, the errors of roundness of drilled holes were significantly affecting the HAZ measurement. The irregular boundary regions of HAZ were formed around the micro-holes due to the variation in the rate of heat transfer of different fiber orientations varied based on the thermal conductivity of fiber and matrix. The laser located position on fiber orientation also affected HAZ values. The areas of HAZ of micro-holes were also important one for evaluating performance measures. There were two methods used to measure the HAZ of the micro-hole through a video measuring system. The boundary line was manually formed around the HAZ of the micro-hole for measuring area of HAZ. The numbers of lines were manually drawn from the edge of the micro-hole to the boundary line of HAZ for measuring the thickness of HAZ. Increasing the number of lines with equal interval angle was formed around the micro-hole for improving the accuracy of measurement. Therefore, the thickness of HAZ was selected over the area of HAZ. The heat-affected zones around the micro-holes were measured by twelve marked letters such as a, b, c, d, e, f, g, h, i, j, k and l. In Figs. 5a–p and 6a–p, the result found that the heat-affected zones at the entry side of the micro-holes have greater than the heat-affected zones at the exit side of the micro-holes. This is because of the more interacting time of thermal energy to CFRP work material on the entry side of micro-holes than the exit side of micro-holes. Generally, the formation of heat-affected zone has purely related to thermal conductivity and melting point of carbon fiber and resin. Thereby, the variations of HAZ around micro-holes were obtained by different in thermal conductivity and melting point of carbon fiber and resin. Normally, the thermal conductivity of carbon fiber ($k = 50 \text{ W/mK}$) has greater than the resin ($k = 0.1 \text{ W/mK}$). Therefore, the heat transfer rate of the carbon fiber has faster than resin. In addition, the formation of HAZ by laser processing has also related to the carbon fiber orientation and selection of process parameters. This is also due to the thermal conductivity of CFRP and anisotropy properties of CFRP laminates. This was also a reason for higher HAZ at entry side and the formed elliptical micro-holes on CFRP [21]. In addition, the HAZ is actually a thermally affected area around the micro-hole and combination of the melted portion and the non-melted portion of (damaged by heat) carbon fiber with resin. However, the thermal effects have also altered microstructural and obtain the smaller micro-hole at exit. The non-diffusion of heat across the thickness of the work material is the reason for obtaining smaller micro-hole at the exit side [22]. The schematic representation of HAZ measurement (a), micrograph of actual HAZ measurement (b) is shown in Fig. 7a, b respectively. Similarly, the HAZ measurement procedure was applied to kerf width measurement. The actual diagram for measurement of kerf width

Table 5 Performance measures for micro-holes [45]

Exp. no	Process parameters			Responses					
	Power (W)	Cutting velocity (mm/rev)	Argon pressure (KPa)	HAZ _{ent} (mm)	HAZ _{ext} (mm)	KW _{ent} (mm)	KW _{ext} (mm)	KA deg	AR
1	15	20	200	1.251	0.497	0.558	0.352	1.967	6.593
2	15	40	300	1.190	0.439	0.471	0.274	1.881	8.054
3	15	60	400	1.151	0.402	0.415	0.219	1.872	9.464
4	15	80	500	1.071	0.363	0.385	0.205	1.719	10.169
5	30	20	300	1.259	0.504	0.582	0.407	1.671	6.067
6	30	40	200	1.213	0.455	0.483	0.306	1.690	7.605
7	30	60	500	1.152	0.411	0.432	0.258	1.662	8.696
8	30	80	400	1.118	0.372	0.383	0.218	1.576	9.983
9	45	20	400	1.282	0.512	0.586	0.447	1.327	5.808
10	45	40	500	1.216	0.438	0.492	0.349	1.366	7.134
11	45	60	200	1.191	0.412	0.471	0.312	1.518	7.663
12	45	80	300	1.142	0.379	0.402	0.253	1.423	9.160
13	60	20	500	1.333	0.526	0.663	0.521	1.356	5.068
14	60	40	400	1.261	0.452	0.589	0.461	1.222	5.714
15	60	60	300	1.239	0.435	0.523	0.407	1.108	6.452
16	60	80	200	1.181	0.411	0.482	0.372	1.050	7.026

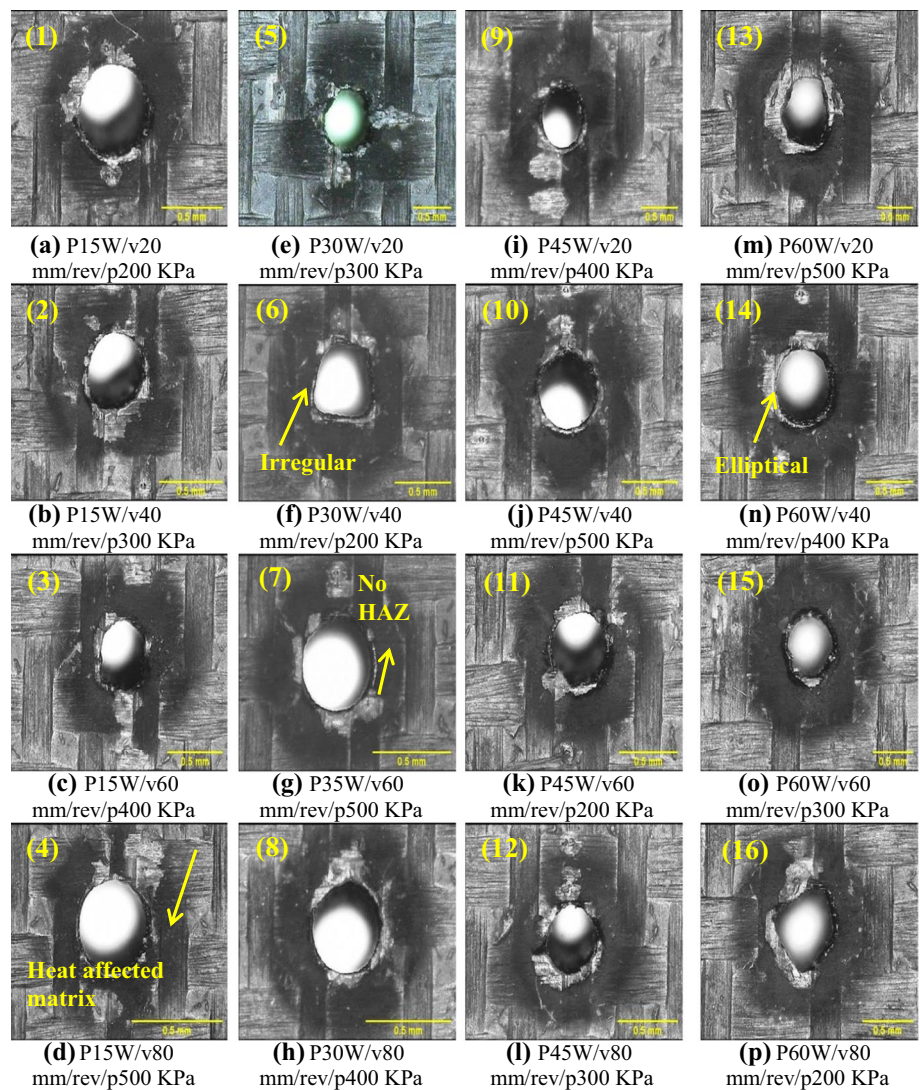
is shown in Fig. 7c. Generally, geometrical micro-features of micro-holes were described in different aspects such as the kerf width, kerf angle and aspect ratio. The kerf widths at entry side of micro-holes have greater than exit side of micro-holes. The shrinkage of material is reason for decreasing the diameter of micro-hole [23]. As per the mathematical formula, the kerf angle has purely based on the geometrical features of kerf width at entry and exit. The variations of kerf width were affecting the kerf angle of micro-hole. The aspect ratio of micro-hole is defined as the ratio of length of cut to mean of kerf width at entry and exit. The variations of kerf width were also affecting the aspect ratio of micro-hole. The mean for each response is calculated based on the design of experiment, which is presented in Table 6. In Table 6, the delta value is calculated by taking difference between the maximum values to minimum value of response for each parameter. The rank has formed based on the delta value. The higher delta value has denoted as highest rank. The rank is also used to find the most influential parameter. The cutting velocity has most influential factor based on the HAZ at entry, HAZ at exit, kerf width at entry and aspect ratio. The power has most influential factor based on the kerf width at exit and kerf angle. The responses over process parameters graphs are drawn based on the mean value.

3.1 Heat-affected zone

The HAZ at entry and exit formation over process parameters is drawn, and these are shown in Figs. 8 and 9, respectively. The minimum HAZ of micro-holes at entry

and exit was obtained through 15 W power, 80 mm/rev cutting velocity and 500 kPa argon pressure. The HAZ at entry and exit can be minimized by decreasing the power and increasing the cutting velocity and argon pressure. The laser power has used to control the amount of heat energy supplied into the work material. By increasing the laser power, the HAZ was also increased. The continuous output power of square wave laser produces heat energy. The increment of power parameter promotes a greater HAZ owing to the high value of energy releasing into sample during the processing [24, 25]. While applying the power of 15 W, the minimum HAZ of micro-holes at entry and exit was obtained as 1.166 mm and 0.425 mm, respectively. In overall, the HAZ results were varied from 1 to 2 mm and other researchers also were found the same [26–29]. The higher HAZ was observed, when compared to 0.5-mm micro-hole. This is due to the spiral trepanning parameters and thermal conductivity of matrix and resin. The higher amount of wavelength is to melt the fiber and matrix because of the higher absorbing property of CO₂ laser wavelength. Therefore, the high HAZ was formed in the drilled CFRP hole by laser. Generally, the cutting velocity controls the interaction time of the laser beam to the work material. The formations of HAZ were decreased due to the higher vaporization of carbon fiber and resin by shorter interaction time by increasing the cutting velocity. Therefore, minimum HAZ at entry and exit was obtained when the cutting velocity and argon pressure increased. This mechanism has inversely produced when the cutting velocity and argon pressure decreased. The

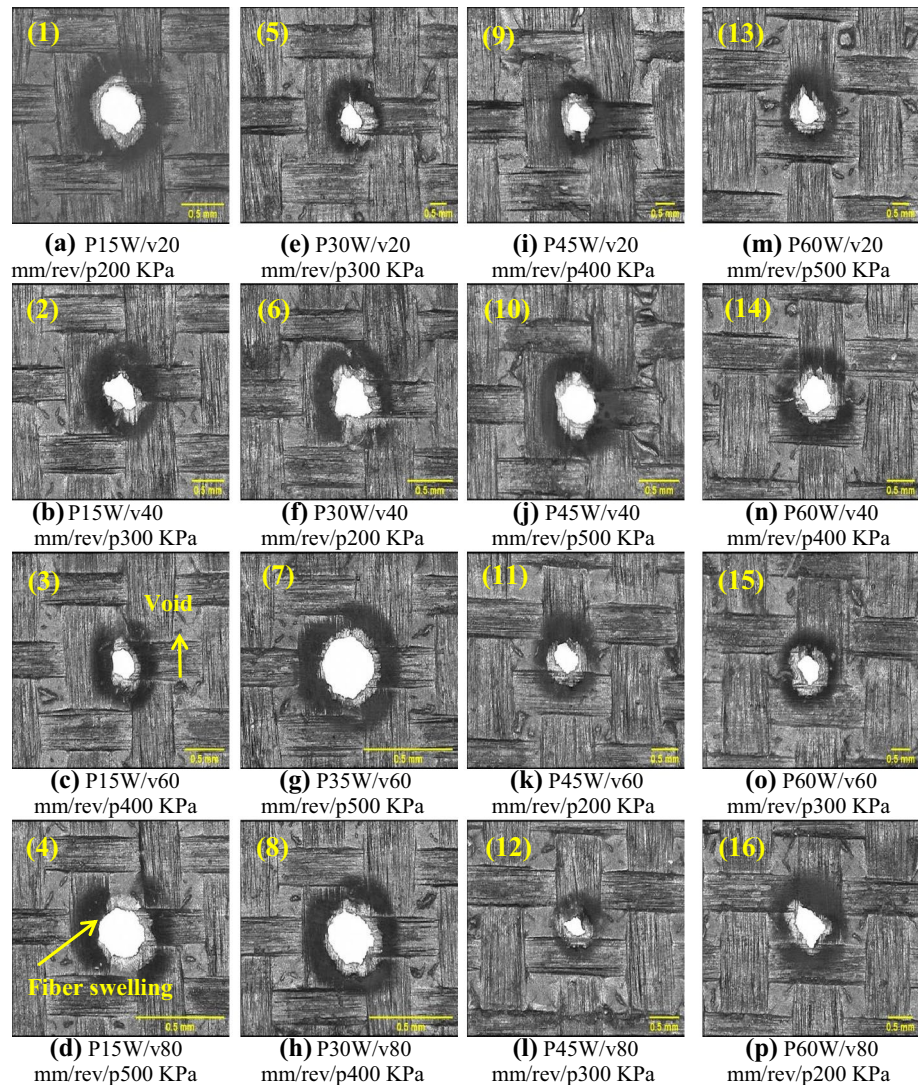
Fig. 5 Micrograph of 0.5-mm drilled holes at entry side [33]



present outcomes of this result well agreed with previous researchers [30–32]. From this analysis, it was found that the argon pressure was a negative linear relationship to HAZ. By raising the argon pressure, the formation of HAZ was reduced due to combined effect of thermal conductivity of argon, carbon fiber and resin [33]. Additionally, the carbon fiber presented in this CFRP was 0° and 90° fiber orientation angle with an alternative form of 12 layers. The laser beam contact point on CFRP, spiral trepanning drilling mechanism and fiber orientation angle was majorly affecting the HAZ formation. The laser beam contact point was strike on CFRP sample in various points, namely the laser beam contact point placed on 0° carbon fiber bundle (or) 90° carbon fiber bundle orientation angle, the laser beam contact point placed on intersection edges of carbon fiber between 0° and 90° (or) intersection between 90° and 0° and the laser beam contact point placed on

second layer of sample. Therefore, the laser beam contact point on sample was deciding the amount of HAZ presented in the sample. The higher HAZ was observed in this experimental data when the laser beam contact point impacted on 0° carbon fiber bundle (or) 90° carbon fiber bundle orientation angle because the horizontal fiber bundle width was varying from 0.277 mm to 0.381 mm (mean = 0.333 mm and standard deviation = 0.50) and the vertical fiber bundle width was varying from 0.149 mm to 0.166 mm (mean = 0.157 mm and standard deviation = 0.007). The micro-hole drilling parameters with spiral trepanning mechanism were highly affected by the HAZ formation due to the micro-hole size being greater than the horizontal and vertical fiber bundle. Also, the standard deviation of HAZ formation was also highly observed in the drilled sample due to the anisotropic properties of CFRP. **Fig. 8** HAZ at entry against process parameters

Fig. 6 Micrograph of 0.5-mm drilled holes at exit side [33]



3.2 Kerf Width

The kerf width is defined as the micro-hole profile formed on the work material through the axis of micro-hole. The kerf width at entry and exit over process parameter graphs is drawn based on the mean kerf width at entry and mean kerf width at the exit which is presented in Figs. 10 and 11, respectively. The similar performance trends were observed between the impact of process parameters over the kerf width at entry and exit. The minimum kerf width at entry and exit was obtained using 15 W power, 80 mm/rev cutting velocity and 500 kPa argon pressure. The kerf width at entry and exit was minimized by decreasing the power and increasing cutting velocity and argon pressure. The kerf width at entry was higher than the kerf width at the exit. The reason for decreasing the laser beam density is through the axis of the micro-hole of work material [34]. By increasing the cutting velocity, the minimum kerf width at entry and

exit was obtained using 80 mm/rev cutting velocity. The high cutting velocity was reduced to the kerf width both entry and exit level. The low cutting velocity was produced higher kerf width both entry and exit side. The high thermal energy processed on the work materials reasoned [35, 36]. While increasing the argon pressure, the kerf width at entry and exit was decreased. The high pressure purges the dross from the kerf site, and it minimizes the kerf enlargement [36]. The obtained minimum kerf width at entry was 0.413 mm when using the cutting velocity of 80 mm/rev. The obtained minimum kerf width at exit was 0.263 mm when using power 15 W. From the HAZ and kerf width analysis, it was found that HAZ formation was decided on the basis of kerf width formation. Therefore, kerf width formation is directly proportional to HAZ formation. The micro-hole drilling parameters with spiral trepanning mechanism also highly affect the kerf width variation. The mechanism for kerf width variation is due to the incident radiation reacted

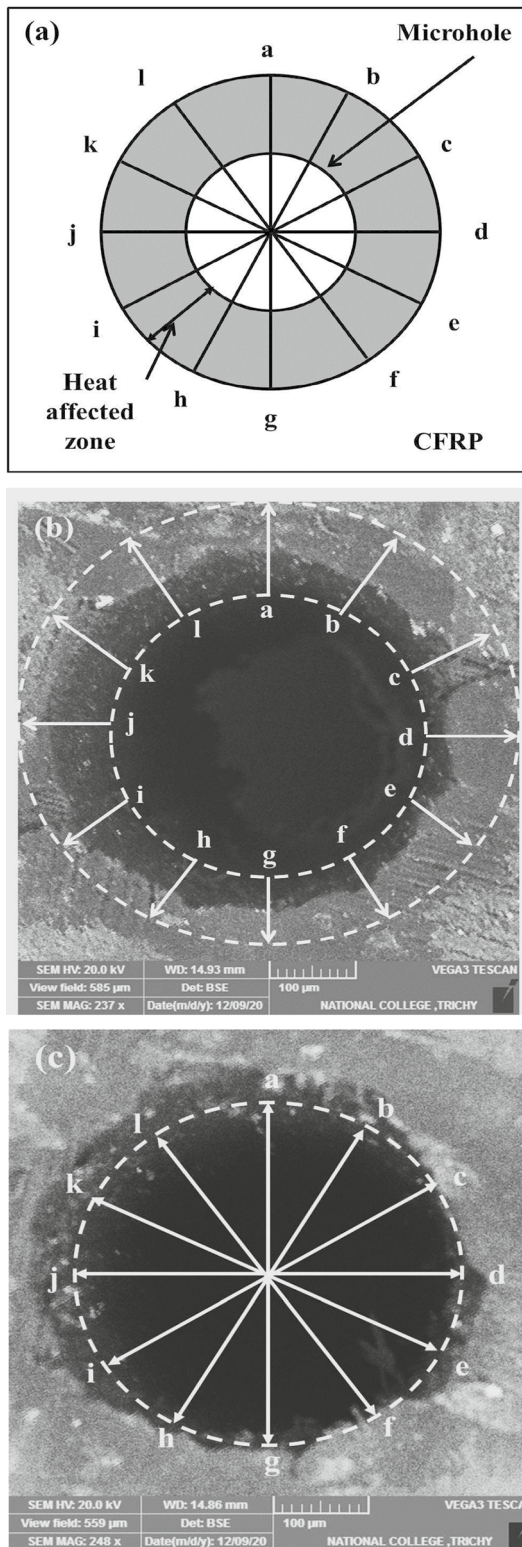


Fig. 7 Schematic representation of HAZ measurement (a), micrograph of actual HAZ measurement (b), and kerf width measurement (c)

with plasma columns, the power losses observed through the absorption and reflection. Therefore, energy absorption capability of material is reduced in the direction of spiral trepanning drilling depth. Another reason for variation in the kerf width is due to the divergence of laser beam beyond the focal plane which leads to decreasing power density in the direction of spiral trepanning drilling depth. Also, the standard deviation of kerf width was also highly observed in the drilled sample due to the anisotropic properties of CFRP. The supplied power was used partially for reflection and remaining for absorption. Hence, the machined micro-hole behaves as a laser blackbody. Therefore, these properties were also affecting the kerf width variation. In addition, beam deviations may be also observed, when the power density decreases along the micro-hole. This was also the reason for formation of higher HAZ and Kerf width in the CFRP. The selection of focal length and spot diameter was also reasoned for observing higher variation in the HAZ and kerf width formation in the CFRP sample.

3.3 Kerf Angle

The kerf angle is also highly related to the geometry of the machined profile. The reason for forming kerf angle in the drilling on CFRP is the poor heat conduction along the depth of cut (thickness). This is owing to the higher quantity materials removed in the top surface of CFRP. Thereby, taper kerf is formed. Hence, the graphs are drawn between the process parameters and mean of kerf angle which is shown in Fig. 12. The minimum kerf angle was obtained using 60 W power, 80 mm/rev cutting velocity and 400 kPa argon pressure. The kerf angle was minimized by increasing the power and cutting velocity. While increasing the power, the kerf angle was decreased. This is owing to the penetration effect on the kerf width [31]. A large amount of thermal energy is used to transmit to the machining zone, which is resulted in a straight cut hole. This is due to the high thermal diffusivity of carbon fibers rapidly along the depth and length of micro-hole. Another way, a larger taper angle was observed using lower power. This is due to the less amount of heat transmitted to the machining zone. While increasing the cutting velocity, the kerf angle was decreased. The reason for small kerf angle formation is due to the combined effect of high power with short cutting velocity of laser beam generated. Generally, thermal diffusivity describes the rate of temperature spread through a material. Thermal diffusivity is the thermal conductivity divided by density and specific heat capacity at constant pressure. It measures the ability of a material to conduct thermal energy relative to its ability to store thermal energy. High diffusivity means heat transfers rapidly. From this kerf angle analysis, it was found that the thermal diffusivity of carbon fiber and resin was decreased with an increasing temperature. The present result

Table 6 Mean responses calculated based on the design of experimental level

Levels	Power (P)	Cutting velocity (v)	Argon pressure (p)	Levels	Power (P)	Cutting velocity (v)	Argon pressure (p)
a. HAZ at entry				b. HAZ at exit			
1	1.166	1.281	1.209	1	0.425	0.510	0.444
2	1.186	1.22	1.208	2	0.436	0.446	0.439
3	1.208	1.183	1.203	3	0.435	0.415	0.435
4	1.254	1.128	1.193	4	0.456	0.381	0.435
Delta	0.088	0.153	0.016	Delta	0.031	0.129	0.009
Rank	2	1	3	Rank	2	1	3
c. Kerf width at entry				d. Kerf width at exit			
1	0.457	0.597	0.499	1	0.263	0.432	0.336
2	0.470	0.509	0.495	2	0.297	0.348	0.335
3	0.488	0.460	0.493	3	0.340	0.299	0.336
4	0.564	0.413	0.493	4	0.440	0.262	0.333
Delta	0.107	0.184	0.006	Delta	0.178	0.170	0.003
Rank	2	1	3	Rank	1	2	3
e. Kerf angle				f. Aspect ratio			
1	1.860	1.580	1.556	1	8.570	5.884	7.222
2	1.650	1.540	1.521	2	8.088	7.127	7.433
3	1.409	1.540	1.499	3	7.441	8.069	7.742
4	1.184	1.442	1.526	4	6.065	9.085	7.767
Delta	0.676	0.138	0.057	Delta	2.505	3.201	0.545
Rank	1	2	3	Rank	2	1	3

Fig. 8 HAZ at entry against process parameters

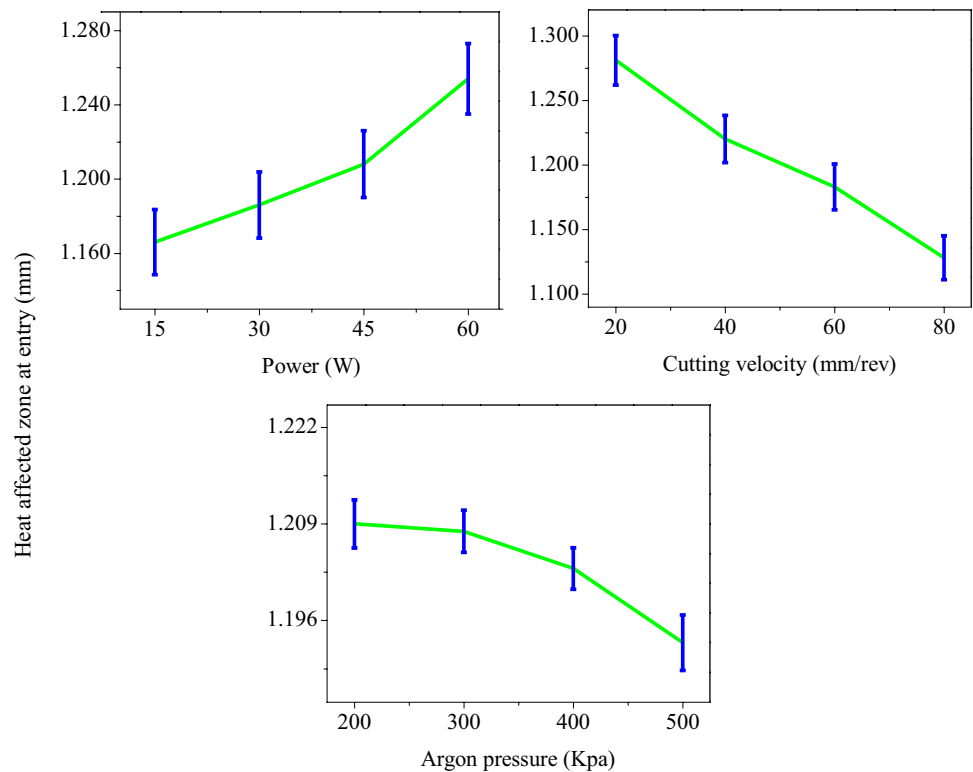


Fig. 9 HAZ at exit against process parameters

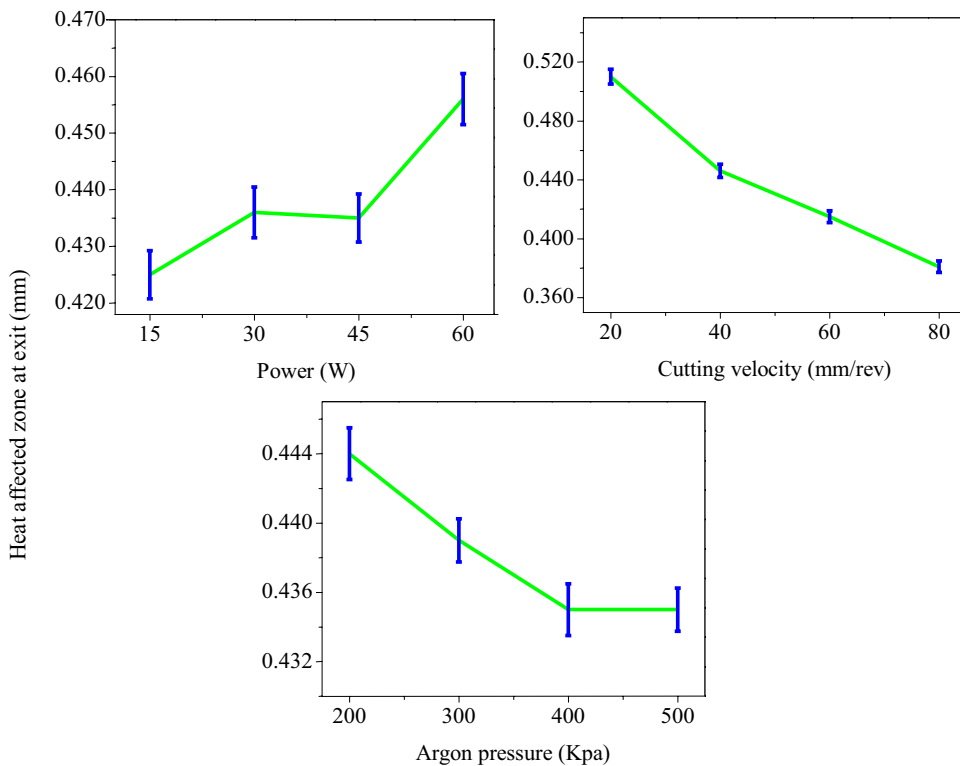
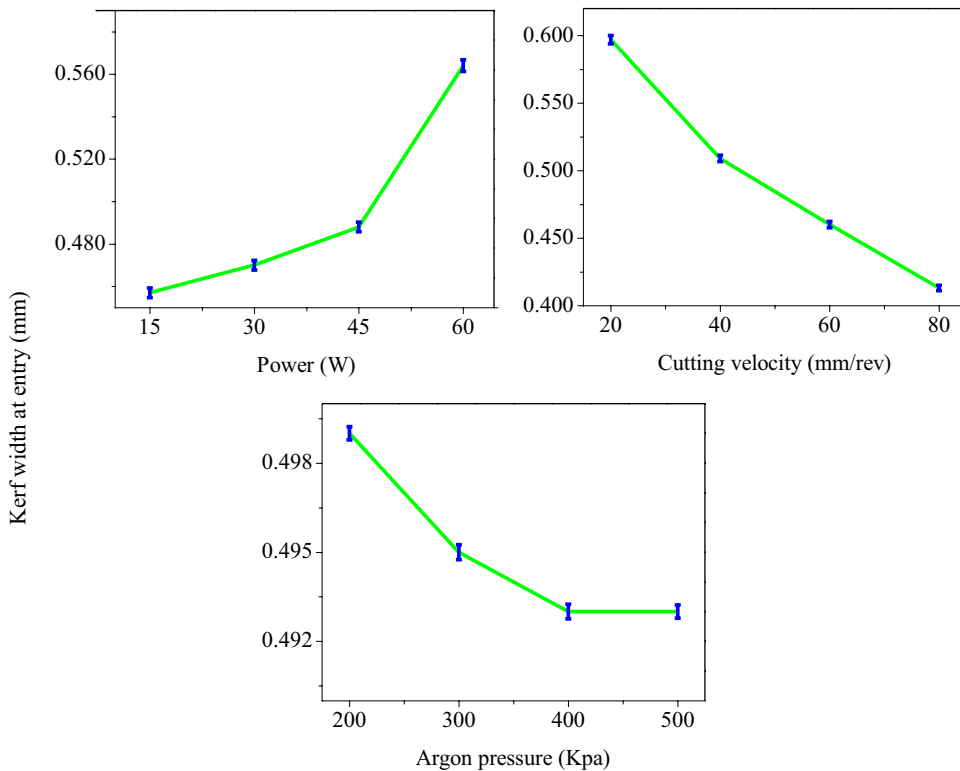


Fig. 10 Kerf widths at entry against process parameters



is consistent with earlier observations [30]. When increasing the pressure up to 400 kPa, the kerf angle was decreased. This is because of the sufficient pressure involved in the

removal of molten material from the machined zone. The obtained minimum kerf angle was 1.184 degree when using the power 60 W.

Fig. 11 Kerf widths at exit against process parameters

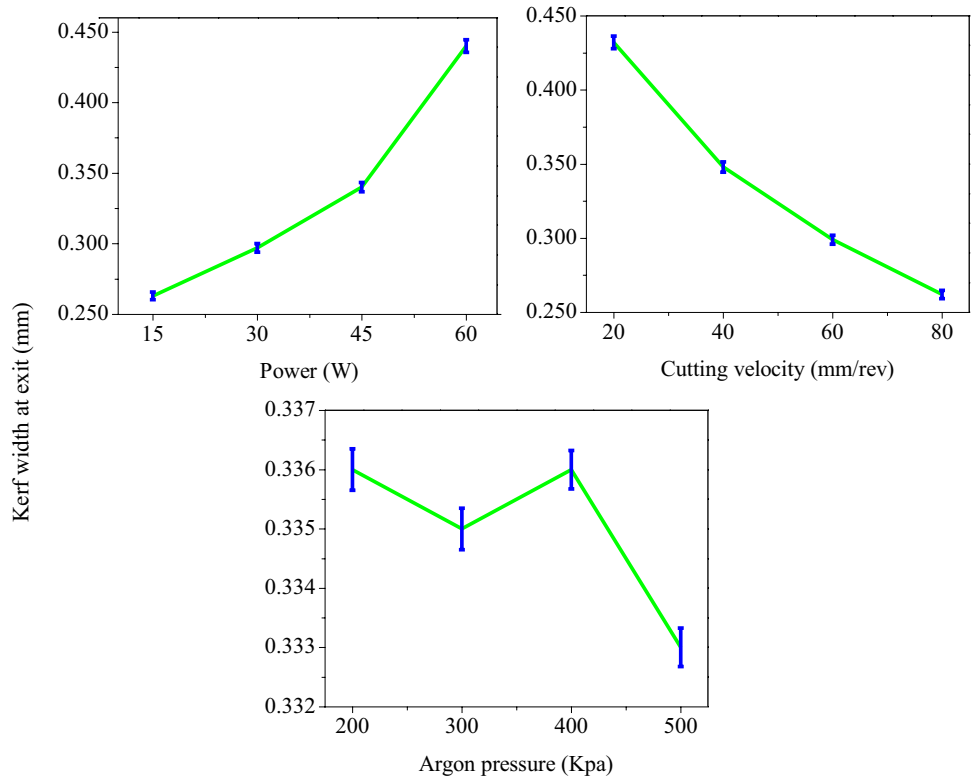
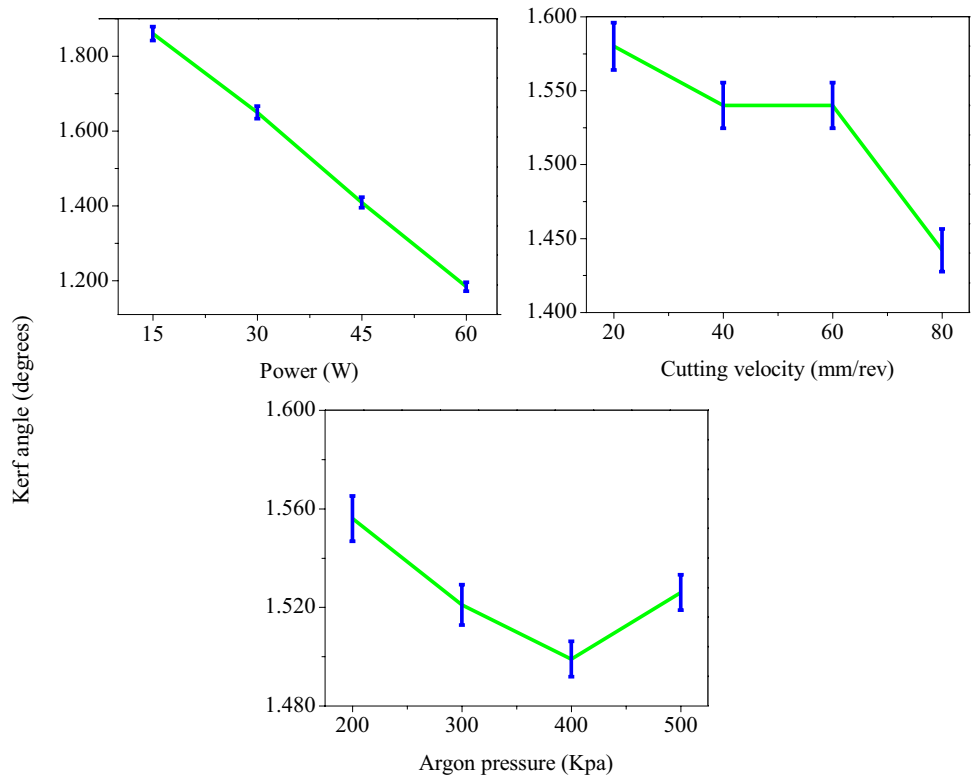


Fig. 12 Kerf angle against process parameters



3.4 Aspect Ratio

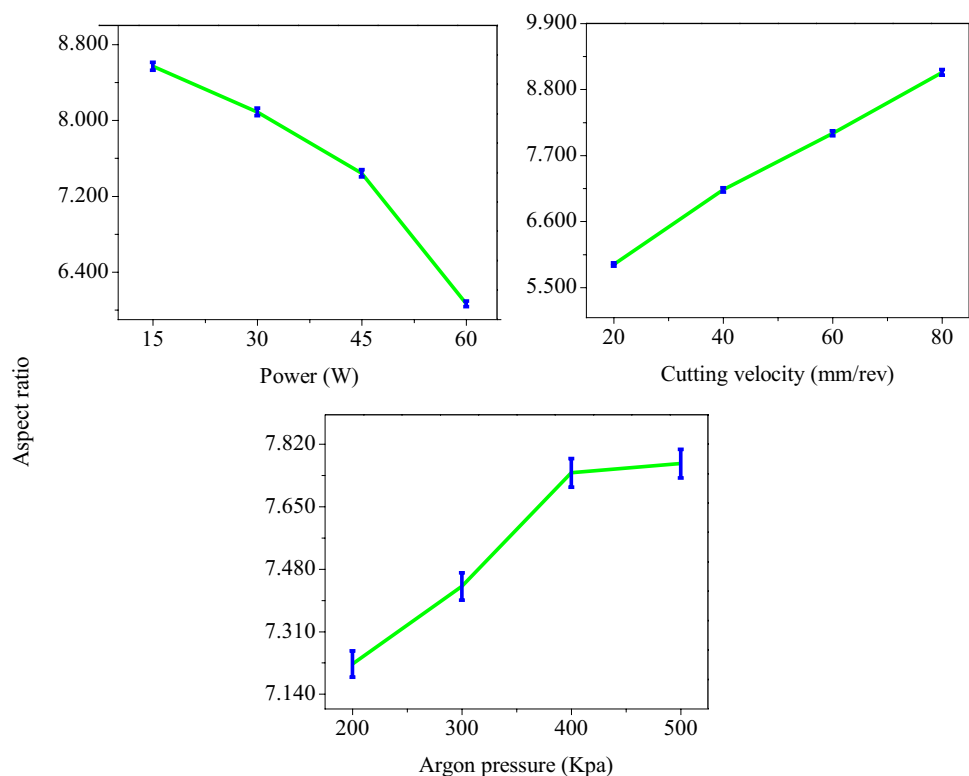
The aspect ratio is defined as the ratio of the length of cut to mean kerf width at entry and exit. The aspect ratio has also highly related to the mean kerf width at entry and exit. The graphs are drawn between the process parameters and mean of aspect ratio which is shown in Fig. 13. The maximum aspect ratio was obtained using 15 W power, 80 mm/rev cutting velocity and 500 kPa argon pressure based on the higher aspect ratio. The aspect ratio was maximized by decreasing the power and increasing the cutting velocity and argon pressure. The aspect ratio trend is behaving inverse of heat-affected zone and kerf width trend in the laser drilling process. Generally, heat-affected zone and kerf width trends are directly proportional to power and indirectly proportional to cutting velocity and gas pressure [19, 20]. The obtained maximum aspect ratio was 9.085 when using the cutting velocity of 80 mm/rev.

3.5 Correlation Analysis

Machining characteristics correlation analysis is used to find the relationship between the different responses such as HAZ at entry, HAZ at exit, kerf width at entry, kerf width at exit, kerf angle and aspect ratio. The effect of laser micro-machining process parameters on machining characteristics of CFRP is described in Table 6. From Table 6, it was identified that the cutting velocity and power were

a most eminent parameter which is affecting the different responses. Among the various process parameters, the cutting velocity was most influential parameter. Therefore, the machining characteristics trends were analyzed based on the cutting velocity. The different combination of machining characteristics was drawn which is shown in Fig. 14. The graphs identified that the HAZ at entry was directly proportional to HAZ at exit. The kerf width at entry was directly proportional to kerf width at exit. Normally, the HAZ and kerf width were increased when increasing the power due to increased thermal energy. The HAZ at entry and exit was directly proportional to kerf width at entry and exit. The effect of heat transfer rate on work material was increased; the melting and vaporization of carbon fiber and resin were also increased (kerf width increased). The mean kerf width (average of kerf width at entry and kerf width at exit) was directly proportional to kerf angle. The correlation was good in mathematical and experimental because the kerf angle was formed based on the kerf width at entry and exit. The processed aspect ratio of CFRP was indirectly proportional to mean kerf width, kerf angle and mean HAZ. This is because of constant depth of cut. The mean HAZ (average of HAZ at entry and HAZ at exit) is directly proportional to kerf angle. The effect of heat transfer rate on work material was increased; the melting and vaporization of carbon fiber and resin were also increased (kerf angle increased). The R-squared values were also good fit to experimental value. The result

Fig. 13 Aspect ratio over process parameters



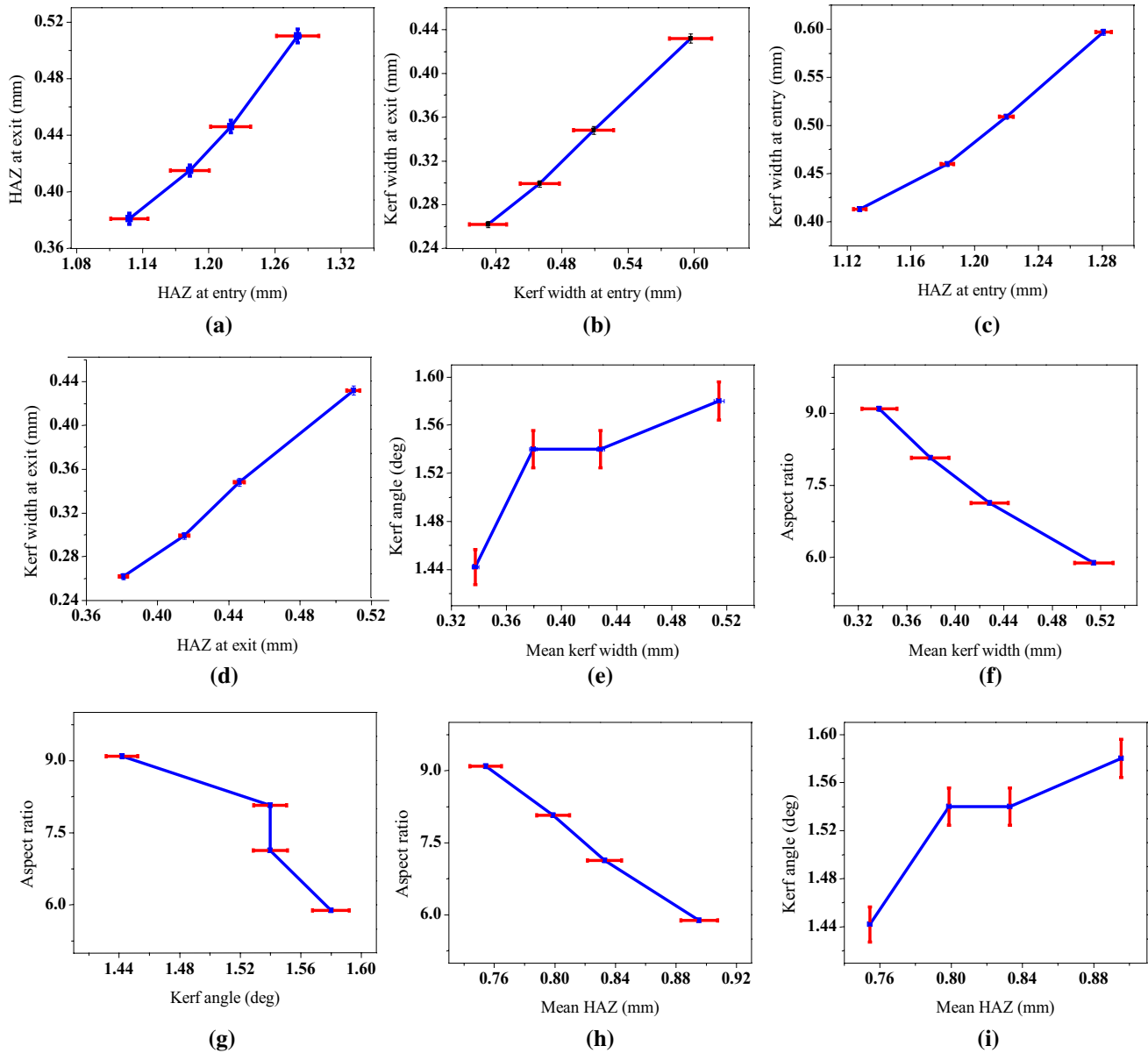


Fig. 14 Different trend curves; **a** HAZ at entry over HAZ at exit, **b** kerf width at entry over kerf width at exit, **c** HAZ at entry over kerf width at entry, **d** HAZ at exit over kerf width at exit, **e** mean kerf

width over Kerf angle, **f** mean kerf width over aspect ratio, **g** kerf angle over aspect ratio, **h** mean HAZ over aspect ratio and **i** mean HAZ over kerf angle

identified that the kerf width was directly proportional to slope of cut (kerf angle) [31].

3.6 Analysis of Variance

ANOVA is formed by the Minitab 18 software which is used to identify the significant parameters that mostly contributing to each response which is shown in Table 7. The number of experiments conducted must be greater than the degree of freedom of the experiment conducted, which is calculated based on the number of parameters and their corresponding levels. The two conditions which must be satisfied for the

selection of orthogonal array are: 1) Degree of freedom of an orthogonal array is greater and equal to degree of freedom of experiment. 2) Level of orthogonal array is equal to level of experiment. The degree of freedom is defined as the number of independent aspects associated with an experimental design or a factor. In the ANOVA table, S is denoted as the standard deviation of the distance between the response values and the fitted values. The S is used to assess how well the model describes the response. Hence, the lower the value of S, the better the model describes the response. The R-squared is the percentage of variation in the response that is explained by the model. It is calculated

Table 7 Analysis of variance for different responses

Source	DF	Seq SS	Adj SS	Adj MS	F	P	CP
a. HAZ at entry							
Power (P)	3	0.017066	0.017066	0.005689	58.6	0.00	25.10
Cutting velocity (v)	3	0.049708	0.049708	0.016569	170.67	0.00	73.12
Argon pressure (p)	3	0.000625	0.000625	0.000208	2.15	0.20	0.92
Error	6	0.000583	0.000583	9.71E-05			0.86
Total	15	0.067982					100
S=0.00985309 R-Sq=99.14% R-Sq(adj)=97.86%							
b. HAZ at exit							
P	3	0.002002	0.002002	0.000667	11.13	0.01	5.21
v	3	0.035847	0.035847	0.011949	199.42	0.00	93.24
p	3	0.000237	0.000237	7.88E-05	1.32	0.35	0.62
Error	6	0.00036	0.00036	5.99E-05			0.94
Total	15	0.038444					100
S=0.00774059 R-Sq=99.06% R-Sq(adj)=97.66%							
c. Kerf width at entry							
P	3	0.027592	0.027592	0.009197	66.78	0.00	26.84
v	3	0.074302	0.074302	0.024767	179.83	0.00	72.28
p	3	0.000078	0.000078	0.000026	0.19	0.90	0.08
Error	6	0.000826	0.000826	0.000138			0.80
Total	15	0.102798					100
S=0.0117358 R-Sq=99.20% R-Sq(adj)=97.99%							
d. Kerf width at exit							
P	3	0.071146	0.071146	0.023715	109.93	0.00	51.92
v	3	0.064567	0.064567	0.021522	99.77	0.00	47.12
p	3	0.00002	0.00002	0.000007	0.03	0.99	0.01
Error	6	0.001294	0.001294	0.000216			0.94
Total	15	0.137027					100
S=0.0146877 R-Sq=99.06% R-Sq(adj)=97.64%							
e. Kerf angle							
P	3	1.02989	1.02989	0.3433	30.82	0.00	89.96
v	3	0.04153	0.04153	0.01384	1.24	0.37	3.63
p	3	0.00663	0.00663	0.00221	0.2	0.89	0.58
Error	6	0.06682	0.06682	0.01114			5.84
Total	15	1.14487					100
S=0.105533 R-Sq=94.16% R-Sq(adj)=85.41%							
f. Aspect ratio							
P	3	14.1852	14.1852	4.7284	44.87	0.00	37.38
v	3	22.3127	22.3127	7.4376	70.58	0.00	58.79
p	3	0.82	0.82	0.2733	2.59	0.15	2.16
Error	6	0.6323	0.6323	0.1054			1.67
Total	15	37.9501					100
S=0.324624 R-Sq=98.33% R-Sq(adj)=95.83%							

as 1 minus the ratio of the error sum of squares (which is the variation that is not explained by model) to the total sum of squares (which is the total variation in the model). Use R-squared to determine how well the model fits observed data. The higher R-squared value, the better the model fits your data. R-squared is always between 0 and 100%. Adjusted R-squared is the percentage of the variation in the

response that is explained by the model, adjusted for the number of predictors in the model relative to the number of observations. Adjusted R-squared is calculated as 1 minus the ratio of the mean square error (MSE) to the mean square total (MS Total). The adjusted R-squared is used to compare models that have different numbers of predictors. Predicted R-squared is calculated with a formula that is equivalent to

systematically removing each observation from the dataset, estimating the regression equation, and determining how well the model predicts the removed observation. The predicted R-squared is used to determine how well the model predicts the response for new observations. Models have larger predicted R-squared values and have better predictive ability. The better model is identified based on the lower S, higher R-squared, adjusted R-squared and predicted R-squared. The F-value is the test statistic used to determine whether the term is associated with the response. Use the p-value in the ANOVA output to determine whether the differences between some of the means are statistically significant. To determine whether any of the differences between the means are statistically significant, compare the p-value to your significance level to assess the null hypothesis. The null hypothesis states that the population means are all equal. Usually, a significance level (denoted as α or alpha) of 0.05 works well. A significance level of 0.05 indicates a 5% risk of concluding that a difference exists when there is no actual difference. The contribution percentage is also used to evaluate the most influential parameters affecting the response. It is calculated by ratio sequential sum of square value of each parameter to total sequential sum of square value and multiplying by 100. The cutting velocity was the most significant parameter which identified based on the sequential sum of the square test. Also, the cutting velocity has a higher percentage of contribution for the heat-affected zone at entry and exit, kerf width at entry and aspect ratio compared to other parameters. In addition, the power has a higher percentage of contribution for kerf width at the exit and kerf angle. The experimental errors for all responses were lesser than 5%, and it was acceptable value. The R-squared and adjusted R-squared for responses were above 90%, and the experimental data were a good fit for prediction. It is also found that the low S, high R-squared, adjusted R-squared and predicted R-squared were identified and produce a better model summary for all the responses.

3.7 Modeling

Modeling is expressed as the relation between the outputs to input process parameters. The modeling was used for further prediction of experimental data. The multiple linear regression equations were formed using Minitab 18 software. The R-squared and adjusted R-squared for responses were above 90% obtained which also denoted as the experimental data were a good fit for prediction. The equations found that the HAZ at entry and exit, kerf width at entry and exit were directly proportional to power and inversely proportional to cutting velocity and argon pressure. The kerf angle was inversely proportional to power, cutting velocity and argon pressure. The aspect ratio was directly proportional to cutting velocity and argon pressure and indirectly proportional

to power. These trends were identified based on the coefficient value (positive and negative). The positive coefficient value of power was used to increasing the HAZ at entry and exit and KW at entry and exit. The negative coefficient value of power was used to decreasing the HAZ at entry and exit and KW at entry and exit. The different coefficient values were observed in the kerf angle and aspect ratio. Among the different responses, HAZ and KW were significant responses. This is due to the other responses related to HAZ and KW formation. The formed regression equations are expressed as below (1–6).

$$\begin{aligned} \text{HAZ at entry} &= 1.27 + 0.00190 \times \text{Power} - 0.00248 \\ &\quad \times \text{Cutting velocity} - 0.000052 \times \text{Argon pressure} \\ S &= 0.0123356 \quad R - Sq = 97.3\% \\ R - Sq \text{ (adj)} &= 96.6\% \end{aligned} \quad (1)$$

$$\begin{aligned} \text{HAZ at exit} &= 0.531 + 0.000613 \times \text{Power} - 0.00208 \\ &\quad \times \text{Cutting velocity} - 0.000032 \times \text{Argon pressure} \\ S &= 0.0124013 \quad R - Sq = 95.2\% \\ R - Sq \text{ (adj)} &= 94.0\% \end{aligned} \quad (2)$$

$$\begin{aligned} \text{Kerf width at entry} &= 0.567 + 0.00226 \times \text{Power} - 0.00301 \\ &\quad \times \text{Cutting velocity} - 0.000018 \times \text{Argon pressure} \\ S &= 0.0249747 \quad R - Sq = 92.7\% \quad R - Sq \text{ (adj)} = 90.9\% \end{aligned} \quad (3)$$

$$\begin{aligned} \text{Kerf width at exit} &= 0.332 + 0.00384 \times \text{Power} - 0.00279 \\ &\quad \times \text{Cutting velocity} - 0.000006 \times \text{Argon pressure} \\ S &= 0.0264425 \quad R - Sq = 93.9\% \\ R - Sq \text{ (adj)} &= 92.3\% \end{aligned} \quad (4)$$

$$\begin{aligned} \text{Kerf angle} &= 2.24 - 0.0151 \times \text{Power} - 0.00207 \\ &\quad \times \text{Cutting velocity} - 0.000113 \times \text{Argon pressure} \\ S &= 0.0810040 \quad R - Sq = 93.1\% \\ R - Sq \text{ (adj)} &= 91.4\% \end{aligned} \quad (5)$$

$$\begin{aligned} \text{Aspect ratio} &= 6.27 - 0.0544 \times \text{Power} + 0.0527 \\ &\quad \times \text{Cutting velocity} + 0.00194 \times \text{Argon pressure} \\ S &= 0.369596 \quad R - Sq = 95.7\% \\ R - Sq \text{ (adj)} &= 94.6\% \end{aligned} \quad (6)$$

Table 8 shows the comparison between numerical and experimental results of CO₂ laser cutting. Overall, it shows that the numerical results agree well with the experiment concerning HAZ, kerf width, kerf angle and aspect ratio. Therefore, the regression model proves to be suitable for simulating of CO₂ laser cutting on CFRP.



Table 8 Experimental and numerical results of kerf width and HAZ

Exp. no	Predicted						Deviation					
	HAZ _{ent}	HAZ _{ext}	KW _{ent}	KW _{ext}	KA	AR	HAZ _{ent}	HAZ _{ext}	KW _{ent}	KW _{ext}	KA	AR
	(mm)	(mm)	(mm)	(mm)	deg		(%)					
1	1.239	0.492	0.537	0.333	1.950	6.896	1.00	0.97	3.75	5.51	0.89	-4.60
2	1.184	0.447	0.475	0.276	1.897	8.144	0.53	-1.91	-0.87	-0.80	-0.84	-1.12
3	1.129	0.403	0.413	0.220	1.844	9.392	1.92	-0.15	0.46	-0.37	1.49	0.76
4	1.074	0.358	0.351	0.163	1.791	10.640	-0.29	1.43	8.81	20.29	-4.21	-4.63
5	1.262	0.498	0.569	0.390	1.712	6.274	-0.22	1.15	2.20	4.28	-2.44	-3.41
6	1.217	0.460	0.511	0.334	1.682	7.134	-0.36	-1.05	-5.76	-9.28	0.50	6.19
7	1.152	0.409	0.445	0.277	1.606	8.770	-0.02	0.59	-3.06	-7.29	3.35	-0.85
8	1.108	0.370	0.387	0.222	1.576	9.630	0.91	0.49	-0.99	-1.65	-0.01	3.54
9	1.285	0.504	0.601	0.447	1.474	5.652	-0.24	1.53	-2.61	0.09	-11.07	2.69
10	1.230	0.459	0.539	0.390	1.421	6.900	-1.18	-4.88	-9.61	-11.81	-4.04	3.28
11	1.196	0.427	0.485	0.336	1.414	7.372	-0.45	-3.73	-2.87	-7.76	6.87	3.80
12	1.142	0.383	0.423	0.280	1.361	8.620	0.04	-0.95	-5.10	-10.59	4.36	5.90
13	1.308	0.510	0.633	0.504	1.236	5.030	1.85	3.01	4.46	3.34	8.84	0.75
14	1.264	0.472	0.575	0.448	1.206	5.890	-0.24	-4.38	2.38	2.73	1.31	-3.08
15	1.220	0.433	0.517	0.393	1.176	6.750	1.57	0.37	1.22	3.39	-6.13	-4.62
16	1.175	0.395	0.458	0.338	1.146	7.610	0.49	3.90	4.94	9.14	-9.12	-8.31

3.8 Microstructural Analysis

The microstructural changes are shown in Figs. 5a–p and 6a–p. The irregular micro-hole profiles were observed in all the conditions of work material at entry and exit. The reasons are variation of heat conduction through fiber direction, fiber swelling, matrix melting and high process temperature. Therefore, the slight elliptical hole formation was observed in all the work material. The microstructural changes were affecting the tensile strength and compressive strength of work material. In addition, the microstructural variations in laser drilling of CFRP are due to the absorption of the energy, thermal diffusivity of the material and reaction temperature. The fiber swelling was observed in

the experimental number 4 at exit. The fiber swelling was formed based on the heat treatment and volatilization of impurities present in the fiber [37]. The heat-affected zone was also considered as microstructural variation of CFRP. The reason for variation of HAZ is due to the difference in melting temperature of fiber and resin. In general, the selection of laser process parameters on machining of CFRP was difficult due to the properties of fiber and resin. The heat energy required for vaporization of carbon fiber was higher than resin. The reason is carbon fiber that has higher heat conduction than resin.

Table 9 Comparison of present results with published literatures

S. no	Referencess	Materials/method	P (W)	CV (mm/min)	P (bar)	HAZ at entry (mm)	HAZ at exit (mm)	KW at entry (mm)	KW at exit (mm)	Kerf angle (°)
1	[24]	CFRP/CO ₂	1000	2000	5	0.7	–	0.16	0.09	0.01
2	[30]	CFRP/CO ₂	300	270–280	10	0.88	1.22	–	–	0.09
3	[46]	CFRP/Nd: YAG	6000	2 m/s	–	–	–	0.2	–	–
4	[47]	CFRP/Fiber laser	340	20 mm/s	2	–	–	0.112	0.015	–
5	[12]	CFRP/Nd: YAG	95	10 mm/s	10	0.17	–	0.17	0.05	1.7
6	[33]	CFRP/CO ₂	1500	–	–	0.45	–	0.15	–	–
Current experimental results										
		CFRP	60	80 mm/rev	–	1.128	0.381	0.413	0.262	1.18

3.9 Comparison with Previous Studies

Comparative studies were made between the current study and published works which is shown in Table 9. The power is a major factor affecting the kerf angle. The trail experiments found that the through hole is not achieved by lowering below the power of 15 W and higher taper angle is observed by increasing above the power of 60 W. Similarly, the higher taper angle is observed by lowering below the cutting velocity of 20 mm/rev and the higher heat-affected zone is observed by increasing above the cutting velocity of 80 mm/rev. The power of 60 W and cutting velocity of 80 mm/rev for current results are producing the kerf angle of 1.18° in the CFRP. The kerf angle achieved in the current study is lower than the previous study [12]. This is because of the wavelength difference between the Nd:YAG laser and CO₂ laser and power. The HAZ at exit for current study is better than the previous study [30]. This is due to the optimum power and cutting velocity. The HAZ and KW obtained in the current study are also higher than the previous study due to the thermal conductivity different between carbon fiber and resin. The amount of resin presented in the matrix, direction of fiber, number of layer formed and manufacturing method are reason for variation in the HAZ and KW. The power used in the current study is lower than other previous study. The micro-hole with aspect ratio of 9.085 is obtained by using the 80 mm/rev cutting velocity and used for producing miniaturization.

4 Conclusion

The laser micro-machining has conducted on CFRP composites using CO₂ laser. In order to evaluate the laser micro-drilled hole, twelve points have marked around the micro-holes accurately to estimate the micro-hole quality characteristics. Based on the obtained results, the following conclusions have drawn.

Based on the single objective optimization, the minimum HAZ, kerf width and maximum aspect ratio of micro-holes have obtained through power: 15 W, cutting velocity: 80 mm/rev, argon pressure: 500 Kpa.

Similarly, minimum kerf angle has obtained using 60 W power, 80 mm/rev cutting velocity and 400 kpa argon pressure.

The cutting velocity has a higher percentage of contribution for the heat-affected zone and kerf width at entry and exit compared to other parameters and followed by power.

The experimental error for all responses has lesser than 5%. The R-squared and adjacent R-squared for responses have above 90%, and the experimental data have a good fit for prediction.

Further, irregular micro-hole profiles have observed in all the conditions of work material at entry and exit due to the variation of heat conduction through fiber direction, fiber swelling, matrix melting and high process temperature. CO₂ laser for the selected parameters can be used in future to CFRP drill to obtain an accurate hole.

Acknowledgements All authors wish to thank M/s Nano Markers, Tiruchirappalli, India, and M/s Sri Angalamman Industries, Thuvakudi, Tiruchirappalli, India, for all support required to carried out this research.

References

- Nattapat, M.; Marimuthu, S.; Kamara, A.M.; Esfahani, M.R.N.: Laser surface modification of carbon fiber reinforced composites. *Mater. Manuf. Processes* **30**(12), 1450–1456 (2015). <https://doi.org/10.1080/10426914.2015.1019097>
- Nelyub, V.; Tarasov, V.: Ion-beam processing of metallized carbon fiber-reinforced plastics. *Mater. Manuf. Processes* (2020). <https://doi.org/10.1080/10426914.2020.1711926>
- El-Hofy, M.H.; El-Hofy, H.: Laser beam machining of carbon fiber reinforced composites: a review. *Int J Adv Manuf Technol* **101**, 2965–2975 (2019). <https://doi.org/10.1007/s00170-018-2978-6>
- Solati, A.; Hamed, M.; Safarabadi, M.: Comprehensive investigation of surface quality and mechanical properties in CO₂ laser drilling of GFRP composites. *Int J Adv Manuf Technol* **102**, 791–808 (2019). <https://doi.org/10.1007/s00170-018-3164-6>
- Kumar, D.; Gururaja, S.: Investigation of hole quality in drilled Ti/CFRP/Ti laminates using CO₂ laser. *Opt. Laser Technol.* **126**, 106130 (2020). <https://doi.org/10.1016/j.optlastec.2020.106130>
- Haeger, A.; Schoen, G.; Lissek, F.; Meinhard, D.; Kaufeld, M.; Schneider, G.; Schuhmacher, S.; Knoblauch, V.: Non-destructive detection of drilling-induced delamination in CFRP and its effect on mechanical properties. *Procedia Eng* **149**, 130–142 (2016)
- Dhanawade, A.; Kumar, S.: Experimental study of delamination and kerf geometry of carbon epoxy composite machined by abrasive water jet. *J. Compos. Mater.* **51**(24), 3373–3390 (2017)
- El-Hofy, M.; Helmy, M.O.; Escobar-Palafox, G.; Kerrigan, K.; Scaife, R.; El-Hofy, H.: Abrasive water jet machining of multi-directional CFRP laminates. *Procedia Cirp* **68**, 535–540 (2018)
- Abdallah, R.; Soo, S.L.; Hood, R.: A feasibility study on wire electrical discharge machining of carbon fibre reinforced plastic composites. *Procedia Cirp* **77**, 195–198 (2018)
- Sheikh-Ahmad, J.Y.: Hole quality and damage in drilling carbon/epoxy composites by electrical discharge machining. *Mater. Manuf. Processes* **31**(7), 941–950 (2016)
- Gautam, G.D.; Mishra, D.R.: Firefly algorithm based optimization of kerf quality characteristics in pulsed Nd: YAG laser cutting of basalt fiber reinforced composite. *Compos. B Eng.* **176**, 107340 (2019). <https://doi.org/10.1016/j.compositesb.2019.107340>
- Leone, C.; Genna, S.: Heat affected zone extension in pulsed Nd: YAG laser cutting of CFRP. *Compos. B Eng.* **140**, 174–182 (2018). <https://doi.org/10.1016/j.compositesb.2017.12.028>
- Oh, S.; Lee, I.; Park, Y.-B.; Ki, H.: Investigation of cut quality in fiber laser cutting of CFRP. *Opt. Laser Technol.* **113**, 129–140 (2019). <https://doi.org/10.1016/j.optlastec.2018.12.018>
- Raj Kumar, D.; Jeyaprakash, N.; Yang, C.-H.; Ramkumar, K.R.: Investigation on drilling behavior of CFRP composites using optimization technique. *Arab. J. Sci. Eng.* (2020). <https://doi.org/10.1007/s13369-020-04649-6>



15. Jeyaprakash, N.; Yang, C.H.; Raj Kumar, D.: Machinability study on CFRP composite using Taguchi based grey relational analysis. *Mater Today: Proc* **21**(3), 1425–1431 (2020)
16. Krishnamoorthy, A.; Rajendra Boopathy, S.; Palanikumar, K.: Delamination prediction in drilling of CFRP composites using artificial neural network. *J Eng Sci Technol* **6**(2), 191–203 (2011)
17. Sahoo, S.; Thakur, A.; Gangopadhyay, S.: Application of analytical simulation on various characteristics of hole quality during micro-drilling of printed circuit board. *Mater. Manuf. Processes* **31**(14), 1927–1934 (2016)
18. Hinds, B.K.; Treanor, M.: Drilling of printed circuit boards: factors limiting the use of smaller drill sizes. *Proc Inst Mech Eng Part B: J Eng Manuf* **214**(1), 35–45 (2000)
19. Mathew, J.; Goswami, G.L.; Ramakrishnan, N.; Naik, N.K.: Parametric studies on pulsed Nd: YAG laser cutting of carbon fibre reinforced plastic composites. *J Mater Process Technol* **89**, 198–203 (1999)
20. Salama, A.; Yan, Y.; Li, L.; Mativenga, P.; Whitehead, D.; Sabli, A.: Understanding the self-limiting effect in picosecond laser single and multiple parallel pass drilling/machining of CFRP composite and mild steel. *Mater. Des.* **107**(5), 461–469 (2016)
21. Li, M.; Li, S.; Gan, G.; Zhang, Y.; Liang, Z.; Yang, X.: Experimental study on hole quality and tensile progressive failure following fiber laser cutting of multidirectional carbon fiber reinforced plastic laminates. *J. Laser Appl.* **31**(1), 012004 (2019). <https://doi.org/10.2351/1.5046549>
22. Hejjaji, A.; Singh, D.; Kubher, S.; Kalyanasundaram, D.; Gururaja, S.: Machining damage in FRPs: Laser versus conventional drilling. *Compos.: Part A* **82**, 42–52 (2016)
23. Nawab, Y.; Tardif, X.; Boyard, N.; Sobotka, V.; Casari, P.; Jacquemin, F.: Determination and modelling of the cure shrinkage of epoxy vinyl ester resin and associated composites by considering thermal gradients. *Compos. Sci. Technol.* **73**, 81–87 (2012). <https://doi.org/10.1016/j.compscitech.2012.09.018>
24. Riveiro, A.; Quintero, F.; Lusquiños, F.; del Val, J.; Comesaña, R.; Boutinguiza, M.; Pou, J.: Experimental study on the CO₂ laser cutting of carbon fiber reinforced plastic composite. *Compos. A Appl. Sci. Manuf.* **43**(8), 1400–1409 (2012). <https://doi.org/10.1016/j.compositesa.2012.02.012>
25. Pan, C.T.; Hocheng, H.: Prediction of extent of heat affected zone in laser grooving of unidirectional fiber-reinforced plastics. *J Eng Mater Technol* **120**(4), 321–327 (1998)
26. Emmelmann, C.; Goeke, A.: Influence of laser cutting parameters on CFRP part quality. *Phys Procedia* **5**, 253–258 (2010)
27. Pan, C.; Hocheng, H.: The anisotropic heat affected zone in the laser grooving of fiber-reinforced composite material. *J Mater Process Technol* **62**, 54–60 (1996)
28. Pan, C.; Hocheng, H.: Prediction of laser-induced damage of fiber mat and fiber mat-ud reinforced polymers. *J Mater Eng Perform* **7**, 751–756 (1998)
29. Tagliaferri, V.; Caprino, G.: Maximum cutting speed in laser cutting of fiber reinforced plastics. *J Mach Tools Manuf* **28**, 389–398 (1987)
30. Kumar, D.; Singh, K.K.: Effect of nanofiller on fibre laser drilling quality of carbon fibre reinforced polymer composite laminates. *Proc Inst Mech Eng Part E: J Process Mech Eng* **233**(4), 857–870 (2019)
31. Davim, J.P.; Barricas, N.; Conceição, M.; Oliveira, C.: Some experimental studies on CO₂ laser cutting quality of polymeric materials. *J. Mater. Process. Technol.* **198**(1–3), 99–104 (2008). <https://doi.org/10.1016/j.jmatprotec.2007.06.056>
32. Choudhury, I.A.; Shirley, S.: Laser cutting of polymeric materials: an experimental investigation. *Opt. Laser Technol.* **42**(3), 503–508 (2010). <https://doi.org/10.1016/j.optlastec.2009.09.006>
33. Goeke, A.; Emmelmann, C.: Influence of laser cutting parameters on CFRP part quality. *Phys Procedia* **5**, 253–258 (2010). <https://doi.org/10.1016/j.phpro.2010.08.051>
34. Mathew, J.; Goswami, G.L.; Ramakrishnan, N.; Naik, N.K.: Parametric studies on pulsed Nd:YAG laser cutting of carbon fibre reinforced plastic composites. *J. Mater. Process. Technol.* **89–90**, 198–203 (1999). [https://doi.org/10.1016/S0924-0136\(99\)00011-4](https://doi.org/10.1016/S0924-0136(99)00011-4)
35. Cenna, A.A.; Mathew, P.: Analysis and prediction of laser cutting parameters of fibre reinforced plastics (FRP) composite materials. *Int. J. Mach. Tools Manuf* **42**(1), 105–113 (2002). [https://doi.org/10.1016/S0890-6955\(01\)00090-6](https://doi.org/10.1016/S0890-6955(01)00090-6)
36. El-Taweel, T.A.; Abdel-Maaboud, A.M.; Azzam, B.S.; Mohammad, A.E.: Parametric studies on the CO₂ laser cutting of Kevlar-49 composite. *Int J Adv Manuf Technol* **40**(9–10), 907–917 (2008). <https://doi.org/10.1007/s00170-008-1412-x>
37. Voisey, K.T.; Fouquet, S.; Roy, D.; Clyne, T.W.: Fibre swelling during laser drilling of carbon fibre composites. *Opt. Lasers Eng.* **44**(11), 1185–1197 (2006). <https://doi.org/10.1016/j.optlaseng.2005.10.008>
38. Salama, A.; Li, L.; Mativenga, P.; Sabli, A.: High-power picosecond laser drilling/machining of carbon fibre-reinforced polymer (CFRP) composites. *Appl. Phys. A* **73**, 122 (2016)
39. Choudhury, I.A.; Chong, W.C.; Vahid, G.: Hole qualities in laser trepanning of polymeric materials. *Opt. Lasers Eng.* **50**(9), 1297–1305 (2010)
40. Lau, W.S.; Lee, W.B.; Pang, S.Q.: Pulsed Nd: YAG laser cutting of carbon fibre composite materials. *CIRP Ann.* **39**(1), 179–182 (1990)
41. Nagesh, S.; Murthy, H.N.N.; Pal, R.; Krishna, M.; Satyanarayana, B.S.: Influence of nanofillers on the quality of CO₂ laser drilling in vinyl ester/glass using orthogonal array experiments and grey relational analysis. *Opt. Laser Technol.* **69**, 23–33 (2015)
42. Yang, L.J.; Cheng, X.L.; Wang, G.W.; Xue, Q.M.; Ding, Y.; Wang, Y.: Experimental evaluation of cutting quality of carbon fibre reinforced polymer with pulsed laser. In: *Applied Mechanics and Materials*, vol. 868, pp. 172–177. Trans Tech Publications Ltd, 2017
43. Hu, J.; Zhu, D.: Experimental study on the picosecond pulsed laser cutting of carbon fiber-reinforced plastics. *J. Reinf. Plast. Compos.* **37**(15), 993–1003 (2018)
44. Choi, I.; Lee, S.-J.; Shin, D.; Suh, J.: Green picosecond laser machining of thermoset and thermoplastic carbon fiber reinforced polymers. *Micromachines.* **12**(2), 205 (2021). <https://doi.org/10.3390/mi12020205>
45. Balasubramaniam, V.; Raj kumar, D.; Ranjithkumar, P.; Sathiyarayanan, C.: Comparative study of mechanical technologies over laser technology for drilling carbon fiber reinforced polymer materials. *Indian J Eng Mater Sci* **27**, 19–32 (2020)
46. Herzog, D.; Schmidt-Lehr, M.; Oberlander, M.; Canisius, M.; Radek, M.; Emmelmann, C.: Laser cutting of carbon fibre reinforced plastics of high thickness. *Mater. Des.* **92**, 742–749 (2016)
47. Negarestani, R.; Li, L.: Fibre laser cutting of carbon fibre-reinforced polymeric composites. *Proc Inst Mech Eng Part B: J Eng Manuf* **227**(12), 1755–1766 (2013)



See discussions, stats, and author profiles for this publication at: <https://www.researchgate.net/publication/346684057>

Optimization of Drilling Process on Carbon-Fiber Reinforced Plastics Using Genetic-Algorithm

Article in *Surface Review and Letters* · November 2020

DOI: 10.1142/S0218625X20500560

CITATION

1

READS

50

4 authors, including:



N. Jeyaprakash

National Taipei University of Technology

49 PUBLICATIONS 175 CITATIONS

[SEE PROFILE](#)



Che-Hua Yang

National Taipei University of Technology

96 PUBLICATIONS 393 CITATIONS

[SEE PROFILE](#)



Sivasankaran S.

Qassim University

114 PUBLICATIONS 1,219 CITATIONS

[SEE PROFILE](#)

Some of the authors of this publication are also working on these related projects:



Implementation of Mathematical linear and non-linear modeling techniques in mechanically alloyed/milled consolidated nanocomposites for predicting both mechanical and physical properties [View project](#)



Laser claddd hard micron layers for sliding wear application [View project](#)

OPTIMIZATION OF DRILLING PROCESS ON CARBON-FIBER REINFORCED PLASTICS USING GENETIC ALGORITHM

D. RAJ KUMAR^{*§}, N. JEYAPRAKASH^{†‡}, CHE-HUA YANG^{†‡**}
and S. SIVASANKARAN^{§††}

^{*}*Department of Mechanical Engineering,
MAM School of Engineering,
Tiruchirappalli-621105, India*

[†]*Additive Manufacturing Center for
Mass Customization Production,
National Taipei University of Technology,
Taipei-10608, Taiwan*

[‡]*Institute of Manufacturing Technology,
National Taipei University of Technology,
Taipei-10608, Taiwan*

[§]*Department of Mechanical Engineering,
College of Engineering, Qassim University,
Qassim 51452, Saudi Arabia*
^{*}*profdraykumar@gmail.com*
[†]*prakash@ntut.edu.tw*
^{**}*chyang@ntut.edu.tw*
^{††}*sivasankaran@qec.edu.sa*

Received 10 April 2020
Revised 27 September 2020
Accepted 3 November 2020
Published 16 December 2020

The usages of carbon-fiber reinforced polymer (CFRP) in aerospace, defense, and structural fields are increasing due to their excellent properties. However, the materials design, forming of material, machine tool and processing conditions are major tasks in manufacturing industries. Particularly, the micro feature making on macro-components using vertical machining center is a challenge nowadays. In this work, two different drill bits, such as high-speed steel (HSS) and solid carbide (SC) micro-drill, were used to make drilling on CFRP material. The performance of drills was evaluated by obtaining minimum delamination and stress in drilling by varying cutting velocity (CV), feed rate (FR), and air pressure (AP). Regression equations were formed according to the measured quality performance characteristics. The linear weighted method-based combined objective function algorithm and Genetic Algorithm was followed to multi-objective optimization. Besides, the most influencing factors were also identified and discussed using analysis of variance. The results explained that the SC micro-drill performance was better than HSS micro-drill. Also, the CV has the most eminent parameters followed by FR.

Keywords: CFRP; drilling; delamination; stress; cutting velocity; feed rate; air pressure; genetic algorithms.

[†]Corresponding author.

1. Introduction

Carbon-fiber reinforced polymers (CFRPs)-based composites progressively replace the conventional metals. This is due to less weight, more specific strength, and stiffness. Among the different types of polymer fibers, CFRP is the most needed material because of its properties. Recently, the CFRP material has been highly utilized in various applications in the field of defense industry and aerospace sector.¹ The foremost aim of this work is to fabricate fault-free micro-hole on CFRP. The need of providing micro-features on CFRP sample is required for its applications in the components such as electronic boards, doors, satellite antenna, pipes, panels and body panels. These components have required the micro-drilling process on sample with perfect dimensions. Therefore, experimental process has been tried in micro-drilling of CFRP sample. Among the various hole making processes, one of the mechanical holes making process using vertical machining process is widely used in CFRP sample to join different materials. Normally, machining the nature of CFRP samples creates issues such as the delamination, overcut, chipping of edge, circularity error, hole shrinkage, fiber pull-out/pull-in, and fuzzing. These problems are raised due to the inhomogeneous characteristic of CFRP.²

Therefore, in order to obtain the faultless holes, the adequate selection of process parameter in drilling the CFRP composites needs to be considered. Some of the authors suggested³⁻⁵ that the drilling of CFRP plates using macro-drills and the quality of hole edge profile is associated with drilling factors, geometry of tool and material of tool. Prior to machining, the effects of unsuitable selections of drilling factors, geometry and materials lead to unsatisfactory results quality of hole such as fiber pull-in, fiber pull-out, delamination, thermal damage, matrix cratering, circularity error, and overcut. Among those defects, delamination is a major issue and rejection ratio is higher in aerospace industries. The different drill materials such as helical flute straight-shank drill, spur drill, and brad drill performance on delamination of processed samples were analyzed to improve quality characteristics. The brad and spur drill produced minimum delamination on the processed sample than straight shank drill and feed rate (FR), which were the most influential parameters.⁶ Further,

the influence of drill flute direction on the delamination was investigated and it was found that drill with left hand helix was the most serious delamination at the exit side.⁷ Machinability of CNT-Epoxy/CF and Epoxy/CF was investigated and minimize delamination was obtained using low FR with high cutting speed.⁸ Drilling behavior of aramid and carbon fiber-reinforced composite was studied and it was found that the critical threshold FR was used to avoid damage.⁹ Investigation of peel up and push out delamination for CFRP/Ti stacks was studied and found that low FR and high FR were used to get the deep fiber peel up and pullout.¹⁰ Comparative delamination length was studied between the CFRP-Ti stacks and CFRP using drilling and found that the CFRP-Ti stacks produced larger delamination length than CFRP.¹¹

The performance of twist drill, Zhukov-point drill, and multi-face drill with high speed on FRP was studied. The multi-face drill found better performance than the other drills based on the delamination value.¹² The influence of drill parameters on delamination of CFRP was studied. The result found that the elliptical shape hole at exit was observed. The process parameters were mainly affecting the delamination at exit. The spalling and fiber-overhangs were observed in the hole exit.¹³ The effect of process parameters on carbide tool temperature was studied and found that the speed and feed were directly proportional to tool temperature.¹⁴ The effect of cryogenic treated CFRP on delamination was studied and found that low speed and high feed produced high delamination.¹⁵ Comprehensive analysis of multi-facet drill and candle stick drill performance on delamination CFRP was investigated. The result found that multi-facet drill performance was better than candle stick drill.¹⁶ The influence of process parameters on FRP composites with SiC fillers was studied. The output found that the thrust force decreases with increase in speed and FR.¹⁷ The analysis of process parameters on delamination CFRP/Ti stacks was made and found that the low speed and feed was used to find the minimum delamination at entry and exit.¹⁸ Another result found that the delamination increased with increase of speed and FR in the CFRP drilling.¹⁹ The effect of control variables on thrust force and delamination in drilling of CFRP was studied and found that the maximum delamination of 1.8 was observed by using

the 125 N thrust force developed from the drill.²⁰ Comparative performances were conducted between the CVD coated dagger drill and CVD coated twist drill over the CFRP. The result found that the dagger drill gave better drilling performance than the twist drill.²¹ A study was made between the thrust forces over the delamination of CFRP and found that the chisel edge length and point angle were the important factors to affect the delamination.²² The negligible defects for CFRP drilling were observed by using the high speed, low feed, and low point angle of drill.²³ A good relationship was observed between the drill diameter, FR, and spindle speed over the delamination by using the design of experiment.²⁴ A TiAlN coated on solid carbide (SC) drill performance on CFRP was studied and found that a genetic algorithm was used to optimize the process parameters and found better results.²⁵

Based on the previous literature papers, no works were found that the hole size of 0.3 mm diameters has not been made on CFRP by using conventional machining center with SC drill and high-speed steel (HSS) drill. Therefore, the effects of SC drill and HSS drill performance with process parameters on delamination and stress of CFRPs have improved by using optimization. Design of experiment was employed to perform the experimental trails. The regression equations for SC drill and HSS drill were formed by Minitab 18. The genetic algorithm was used to find

the optimum process parameters. Further, the most influencing parameters were identified using analysis of variances.

2. Materials and Methods

The CFRP composite samples are fabricated by autoclave process with alternative arrangement such as fiber orientation: 0/90°, a total number of layers: 12, thickness of sample: 3 mm. Figure 1(a) shows the optical micrograph of CFRP material. The chemical composition and properties of CFRP sample are shown in Tables 1 and 2. The drill tools are made up of HSS and SC with 0.3 mm circular shape cross section, 130° point angle, 30° helix angle, and 38 mm total length drill bit. Figures 1(b) and 1(c) show macrograph of HSS and SC drill bits, respectively. The machining conditions are selected based on earlier literature studies and trial test parameters. Table 3 shows the set levels in each process parameter. CV, FR, and air pressure (AP) have been selected as the process parameters. The external compressed air was supplied between the tool and workpiece for cooling the drill and removing CFRP chip in machining. In order to achieve the green machining and to improve the quality characteristic, dry machining is chosen for this work. The quality characteristic is enhanced when the AP is considered as one of the input parameters for small hole fabrication.

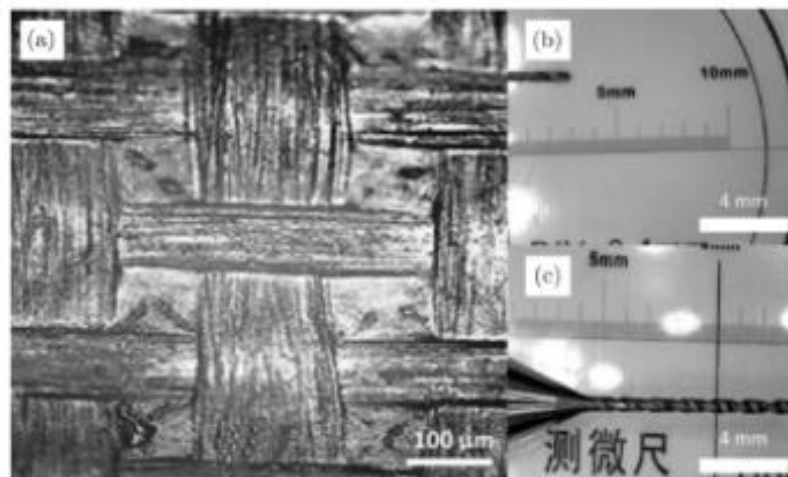


Fig. 1. (a) Optical micrograph of CFRP, (b) Macrograph of HSS drill bit, and (c) carbide drill bit.

Table 1. Chemical composition of CFRP sample.

Elements	C	O	Na	Si	Cl	K	Ca
Weight (%)	84.12	14.92	0.20	0.20	0.28	0.10	0.21

Table 2. Mechanical properties of CFRP sample.

Fiber type	T300
Carbon fiber Content W_f (%)	56
Tensile strength kgf/mm ²	360
Modulus of elongation 10 ³ kgf/mm ²	23.5
Density g/cm ³	1.76

Table 3. Machining conditions used in drilling process.

Process parameters	Symbols	Levels		
		Low	Medium	High
Cutting velocity (m/min)	v	1.88	2.36	2.83
Feed rate (mm/min)	f	0.01	0.03	0.05
Air pressure (kpa)	p	100	300	500

Therefore, external compressed AP is proposed on machining CFRP composites. The processes were carried out by dry condition. The vertical machining center (VMC) was controlled by CV, FR, and AP. Figures 2(a) and 2(b) show the schematic diagram of VMC and experimental setup. During the drilling process, the thrust forces (Brand: RMS controls and Model: Drill tool) are measured using a dynamometer. After drilling process, assessment of hole features has been measured using computerized video measuring system (VMS). The delamination factor (F_d) has been calculated by using ratio of maximum area (A_{max}) of damaged hole surface area to area of drill (A). The optical microscopic image of drilled hole is taken from VMS. Figures 2(c) and 2(d) show the schematic diagram of VMS and experimental setup. The hole image was imported to image analyzing software (ImageJ) and drawn the damaged area and found the damaged area. The delamination factor (F_d) value is expressed in the following equation:

$$F_d = \frac{A_{max}}{A}. \quad (1)$$

The entry radius (R1) and exit radius (R2) of machined holes were measured using VMS. The area

of hole was expressed in Eq. (2). The stress (σ) was expressed in Eq. (3).

$$\text{Area of hole} = \pi(R1 + R2) \sqrt{(R1 - R2)^2 + h^2}, \quad (2)$$

$$\text{Stress}(\sigma) = \frac{\text{Thrust force}}{\text{Area of hole}}. \quad (3)$$

Here, h is noted as the machined depth (3 mm). The experimental plan and its results are shown in Table 4. In order to get accurate result of delamination value, three replicas were performed; the delamination value, stress were calculated, and mean responses have taken to analysis the different set of drilling parameters. The mathematical model for delamination factor and stress was developed for HSS drill bit and SC drill bit through Minitab 18 software. The higher coefficients of correlation indicate the strength of predicted model. The model for multi-linear regression expression is illustrated in the following equation:

$$Y = \beta_0 + \beta_1 X_1 + \beta_2 X_2 + \dots + \beta_k X_k \quad (4)$$

where Y is the response variable to which it is related to (k) regression variables. The parameters (β and j are varying from 0 to k) are regression coefficients. In this case, the respective mathematical model for HSS drill and SC drill is computed as follows:

HSS drill:

$$E_d = 0.391 + 0.330 \times CV + 6.22 \times FR - 0.000082 \times AP (R\text{-Sq.} = 90.8\% \text{ } R\text{-Sq.}(\text{adj}) = 85.3\%), \quad (5)$$

$$\sigma = 0.462 - 0.0612 \times CV + 0.0495 \times FR + 0.00500 \times AP (R\text{-Sq} = 97.1\% \text{ } R\text{-Sq}(\text{adj}) = 95.4\%). \quad (6)$$

SC drill:

$$E_d = -0.074 + 0.542 \times CV + 5.75 \times FR + 0.000047 \times AP (R\text{-Sq.} = 91.3\% \text{ } R\text{-Sq.}(\text{adj}) = 86.1\%), \quad (7)$$

$$\sigma = 0.438 - 0.0660 \times CV + 0.0517 \times FR + 0.00300 \times AP (R\text{-Sq} = 97.5\% \text{ } R\text{-Sq}(\text{adj}) = 96.0\%). \quad (8)$$

Cutting velocity (CV) which is denoted as v and unit is m/min, FR which is denoted as the f and unit is mm/min and pressure which is denoted as the AP and unit is kpa. The R^2 value obtained was greater

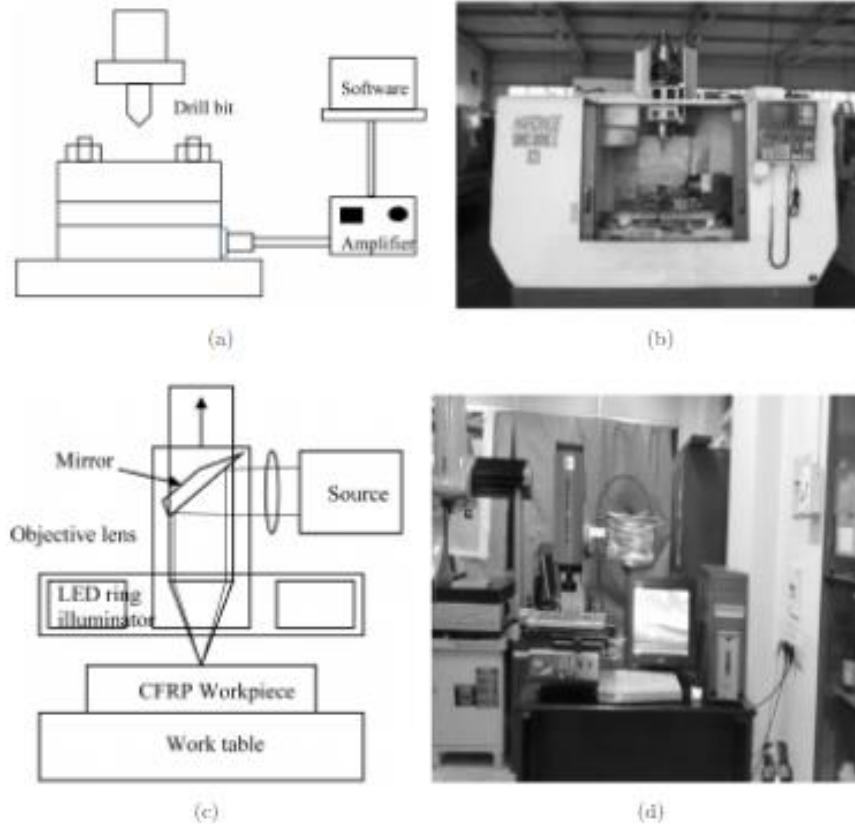


Fig. 2. (a) Schematic of VMC, (b) macro picture of experimental setup, (c) schematic of VMS, and (d) macro picture of experimental setup.

Table 4. Design layout and delamination factor and stress for HSS and solid carbide.

Runs	v (m/min)	f (mm/min)	p (kpa)	Delamination factor (F_d)		Stress (σ) N/mm ²	
				HSS	Solid carbide	HSS	Solid carbide
1	1.88	0.01	100	1.099	1.141	0.458	0.425
2	1.88	0.03	300	1.127	1.169	0.488	0.464
3	1.88	0.05	500	1.268	1.268	0.570	0.539
4	2.36	0.01	300	1.225	1.155	0.419	0.386
5	2.36	0.03	500	1.394	1.338	0.458	0.425
6	2.36	0.05	100	1.366	1.394	0.500	0.466
7	2.83	0.01	500	1.507	1.324	0.335	0.287
8	2.83	0.03	100	1.648	1.493	0.375	0.342
9	2.83	0.05	300	1.887	1.704	0.439	0.403

than 0.8. Therefore, the delamination and stress data obtained are fit and satisfactory.

The objective function was defined for each objective according to the relative function of quality

characteristics. The simple objective function was expressed mathematically as $m_i e_i(y)$ for i th objective, where M_i is a scalar and denotes the weight assigned to the corresponding objective. Besides, the

combined objective function method is defined as weighted sum of objective functions as mentioned below. The following equation was used to accumulate the weighted objective values from the combined objective function:

$$\begin{aligned} & \text{MIN}\{m_1 e_1(y) + m_2 e_2(y), \dots, m_k e_k(y)\} \\ & \times \sum_{i=1}^k m_i = 1, \quad m_i \geq 0, \end{aligned} \quad (9)$$

where M_i denotes the equivalent objective function for the decision variables. The different objective functions represented as $e_1(y), e_2(y), \dots, e_k(y)$. The multiple functions were defined as a sum of individual functions by changing weight coefficients for the individual performance. Further, the optimized multi-objective parameters such as delamination and stress can be determined. In addition, Linear weighted method was applied to solve the multi-objective functions by converting from multi-regression model to single combined regression model. Here, there are two minimization functions and machining variables, were adopted. The minimization functions, such as delamination and stress, were combined together as a single objective function. Then, half of the weightage was given to both the objectives such as delamination and stress and assigned 0.50 weightage factor. The regression equations were formed for selected objective function and combined objective function, as mentioned in the following equations:

$$\begin{aligned} \text{HSS} = & 0.4265 + 0.1344 \times \text{CV} + 3.13475 \\ & \times \text{FR} - 0.002459 \times \text{AP}, \end{aligned} \quad (10)$$

$$\begin{aligned} \text{SC} = & 0.182 + 0.238 \times \text{CV} + 2.90085 \\ & \times \text{FR} + 0.001524 \times \text{AP}. \end{aligned} \quad (11)$$

3. Genetic Algorithm (GA)

GA is the most famous optimization technique to identify the optimum factors. It has been solved by using manual method or computerized method. The major steps involved in the GA are 1: representation; 2: fitness evaluation; 3: selection; and 4: genetic operations.²⁶ The developed regressions models have given to GA. The GA procedure has written using C++ code and execution of program has performed in

Table 5. Genetic algorithms parameters.

Variables	Values
Number of variables	3
Chromosome length	10
Selection operator	Rank order
Population size	100
Cross-over probability	0.7
Mutation probability	0.1
Cross-over operator	Single point crossover
Fitness parameter	cutting velocity, feed rate, and air pressure

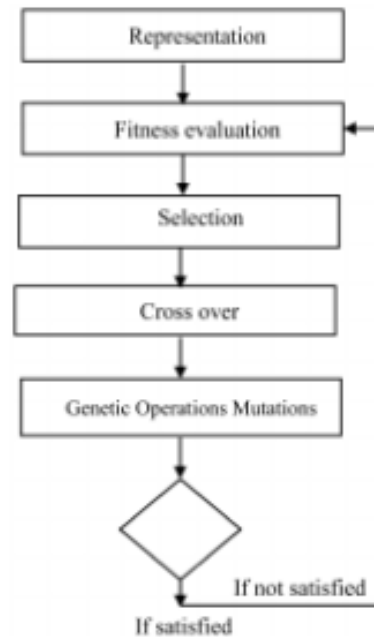


Fig. 3. Schematic representation explains the working of genetic algorithm.

visual basic 6.0. The initial setting was carried out in GA. The mostly used tuning parameters for GA are illustrated in Table 5. The adequate GA report for HSS drill bit were explained that the optimal factor was cutting speed 1.91343 m/min, FR 0.01004 mm/min, and AP 500 kpa. The best GA results produced for SC drill in which the optimal parameters were cutting speed 2.02673 m/min, FR 0.02881 mm/min, and AP 104.69209 kpa. Therefore, the both drill materials were having the varied optimum parameters. Figure 3 shows the schematic representation of GA.

4. Results and Discussion

4.1. Effect of cutting velocity

The relationship between CV and F_d is shown in Fig. 4(a) for HSS drill and SC drill. The F_d for HSS drill increases from 1.164 to a maximum of 1.681 when the CV was increased from 1.88 m/min to 2.83 m/min. For carbide drill, F_d increases also from 1.192 to a maximum of 1.507 for the same interval of CV. The micro-level carbon fiber and matrix are strongly stick on the drill bit flute surface may be the reason for increasing the delamination. Also, the top surface of uncut fiber has increased the delamination. Self-induced vibration of drill bit material has also increased the delamination. The drilling trends are same for both HSS drill and SC drill with increased CV. Normally, the CV is increased by increasing the heat generation in the machining zone resulting to soften and shear the matrix in which the thrust force is reduced.²⁷ In another way, delamination discussed that the carbon fiber presented in this sample is 0° and 90° fiber orientation angle in the alternative form of 12 layers of laminated sheet with 3 mm thickness, as shown in Fig. 5(a). The drill bit contact point and fiber orientation angle are majorly affecting the delamination.²⁸ The drill bit contact point has strike on CFRP sample in various points namely the drill bit contact point placed on 0° carbon fiber bundle (or) 90° carbon fiber bundle orientation angle (point 1;

Fig. 5(b)), the drill bit contact point placed on intersection edges of carbon fiber between 0° and 90° (or) intersection between 90° and 0° (point 2; Fig. 5(c)) and the drill bit contact point placed on second layer of sample (point 3; Fig. 5(d)). Therefore, the drill bit contact point on the sample decides the amount of delamination presented in the sample. The higher delamination was observed in this experimental data when the drill bit contact point impact was on 0° carbon fiber bundle (or) 90° carbon fiber bundle orientation angle (denoted as 1). The horizontal fiber bundle width was varying from 0.277 mm to 0.381 mm (mean = 0.333 mm and standard deviation = 0.50) and the vertical fiber bundle width was varying from 0.149 mm to 0.166 mm (mean = 0.157 mm and standard deviation = 0.007).

The drill diameter was less than the horizontal fiber bundle width and greater than the vertical fiber bundle width. The higher thrust force has generated in this drill bit during cutting the fiber bundle at high CV. The minimum delamination was observed in the sample when the drill bit contact point made an impact on the second layer of sample. This is because of the area of drill diameter that is greater than the area of the rectangular portion of second layer (mean = 0.0323 mm^2 and standard deviation = 0.05). The medium level delamination was observed in the sample when the drill bit contact point had an impact on the intersection edges of carbon fiber between 0°

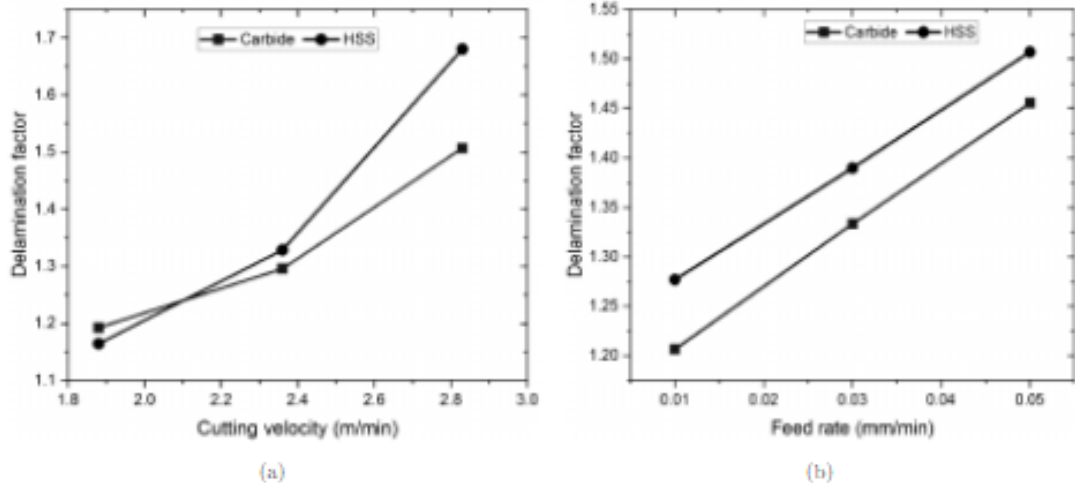


Fig. 4. (a) Relations between delamination factor and cutting velocity (m/min); (b) Relations between delamination factor and feed rate (mm/min).

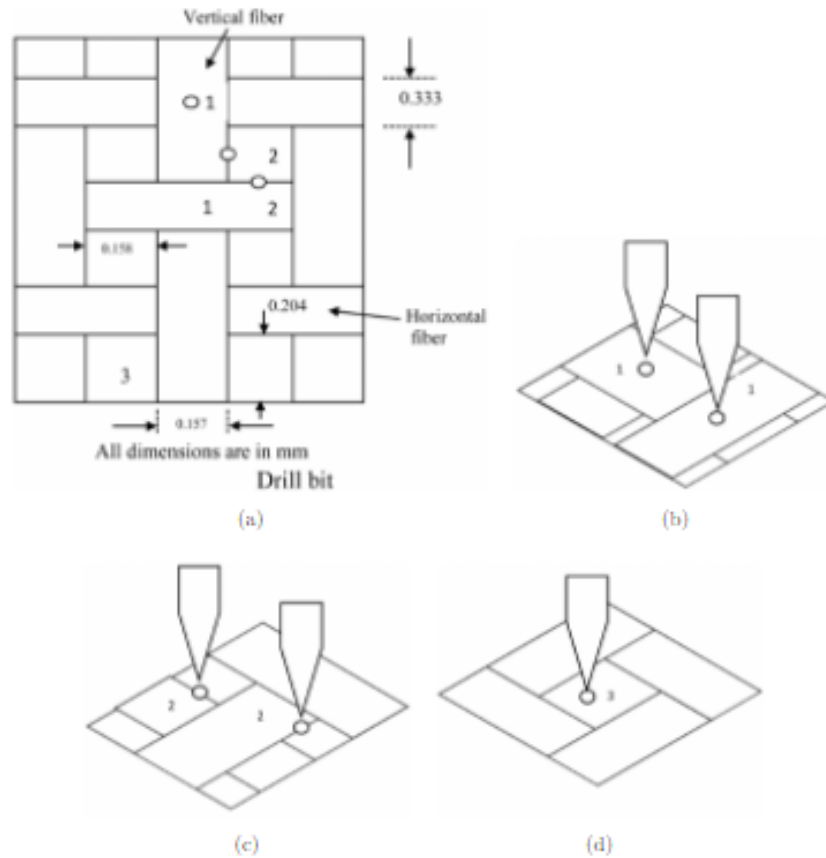


Fig. 5. Schematic representation of fiber orientation with 0° and 90° (a), drill bit contact point placed on 0° carbon fiber bundle (or) 90° carbon fiber bundle orientation angle (b), drill bit contact point placed on intersection edges of carbon fiber between 0° and 90° (or) intersection between 90° and 0° (c), drill bit contact point placed on second layer of sample (d).

and 90° (or) intersection between 90° and 0° . This is because of the area of drill diameter that is greater than the area of rectangular portion of second layer and width of vertical carbon fiber bundle. In addition to this, the induced thrust force in drill bit was directly proportional to delamination.²⁰ Therefore, the induced thrust force has varied by drill bit contact point and CV. The HSS drill bit gave higher delamination than SC drill bit. The properties of SC have high hardness, high wear resistance, low thermal conductivity, and high heat dissipation rate. Also, compared to HSS drill, the SC drill has less heat generation and less stick-slip frictions generated. The physical and mechanical properties of this drill bit material might have produced the differences in delamination.

4.2. Effect of feed rate

The relationship between FR and F_d is shown in Fig. 4(b) for HSS drill and SC drill. The F_d for HSS drill increases from 1.277 to a maximum of 1.507 when the FR (the rate of movement of drill bit) was increased from 0.01 mm/min to 0.05 mm/min. For SC drill, F_d increases also from 1.207 to a maximum of 1.455 for the same interval of FR. The low FR has sufficient machining time resulted to get the minimum F_d . Similarly, the high FR has very short machining time resulted to get the maximum F_d . The uncut carbon fiber and micron level carbon burr were placed between the drill bit flute and hole wall. This increases the thrust force to cut sample. Therefore, the delamination is increased by increasing the FR. The

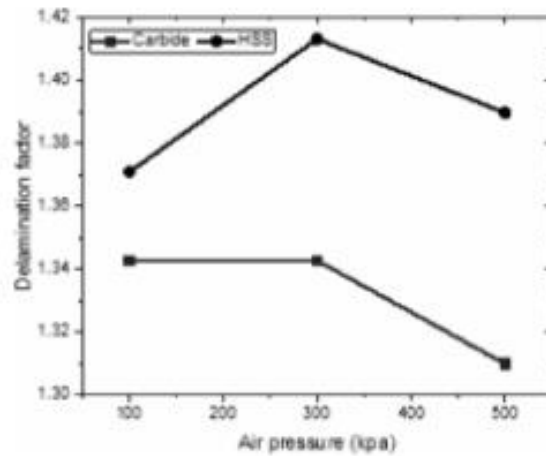
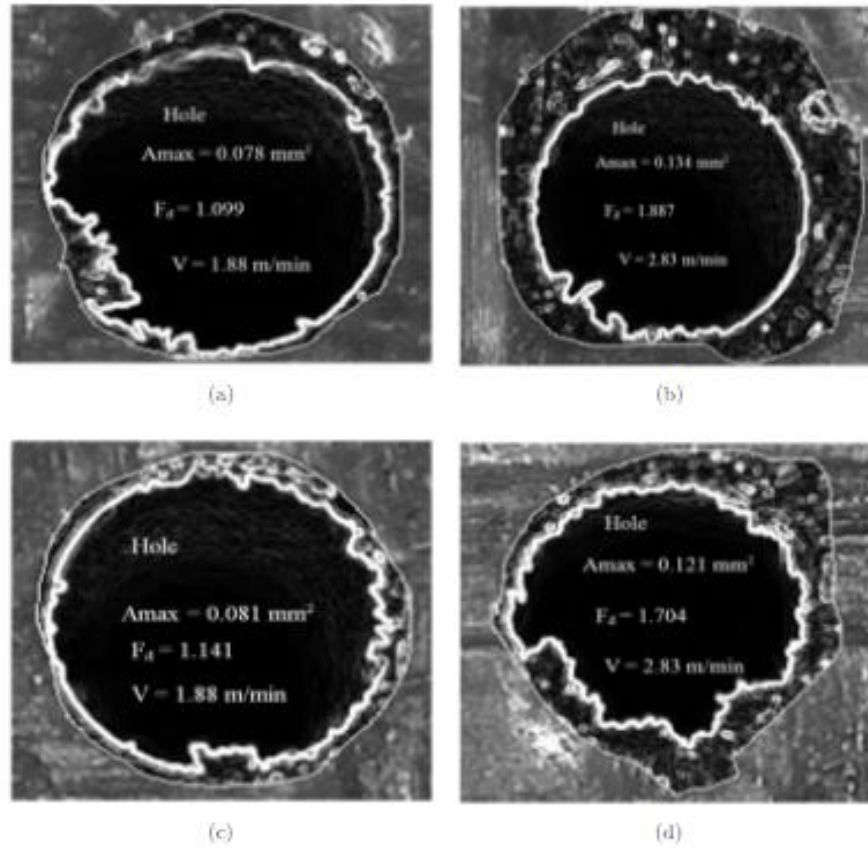


Fig. 6. Delamination factor (F_d) in function of cutting velocity (HSS): (a) $v = 1.88 \text{ m/min}$, (b) $v = 2.83 \text{ m/min}$, Delamination factor (F_d) in function of cutting velocity (solid carbide): (c) $v = 1.88 \text{ m/min}$, (d) $v = 2.83 \text{ m/min}$, and (e) Relation between delamination factor and air pressure (kpa).

FR was found to correlate with the thrust force and delamination damaged area.³⁰ The drilling trends were same for both HSS drill and SC drill with increases FR. Additionally, it was proved that the F_d increases while CV increases. The obtained hole image from VMS was imported to Image software in order to finding damaged area of hole and edge of hole. Figures 4(b) and 6 show the impact of the tuning drill parameters on the delamination factor. In Fig. 6, HSS drill showed the evidence of effect of increase in the CV with F_d increases by maximum damaged area (A_{max}) which increases from 0.078 mm² to 0.134 mm² at constant

FR. Similarly, in Figs. 6(c) and 6(d), SC drill showed the evidence of effect of increases in the CV with F_d increases by maximum damaged area (A_{max}) that increases from 0.081 mm² to 0.121 mm² at constant FR. The yellow line represents the damaged area and white line represents the hole edge.

4.3. Effect of air pressure

The relationship between AP and F_d can be seen in Fig. 6(e) for HSS drill and SC drill. The F_d for HSS drill increases from 1.371 to a maximum of 1.413

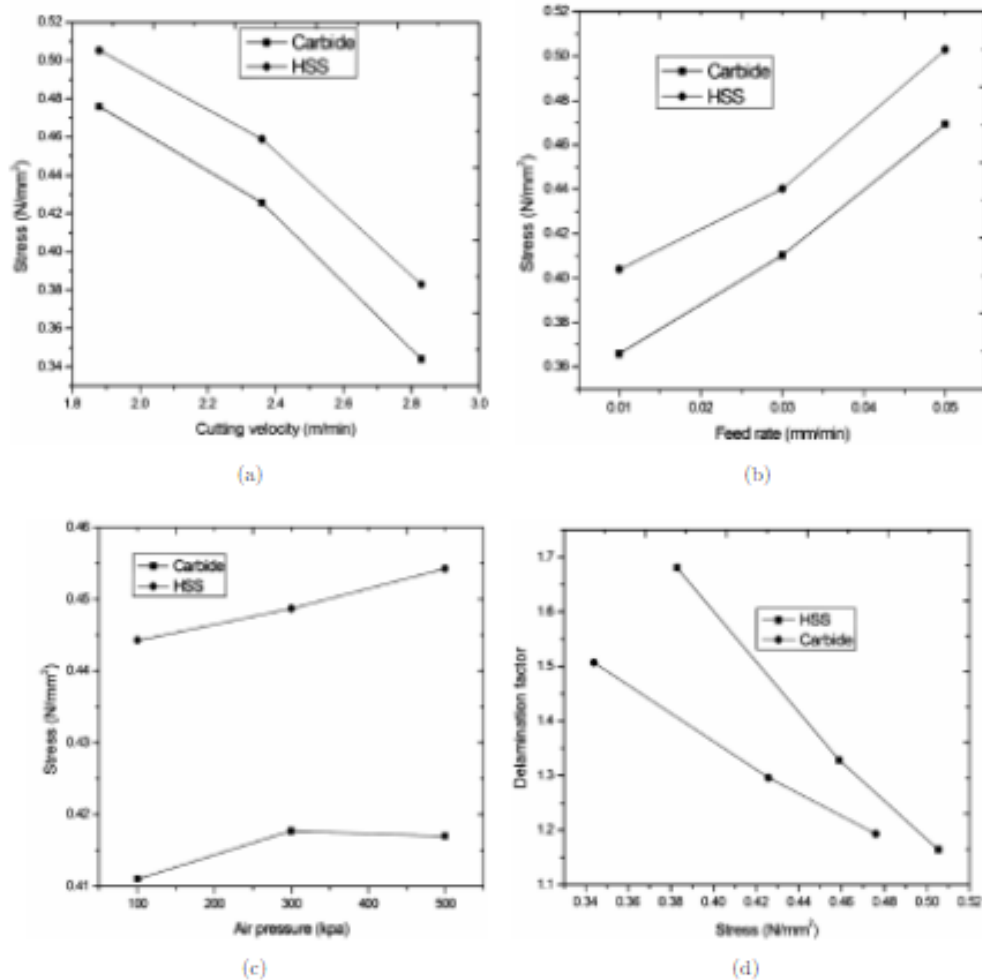


Fig. 7. Various relation graphs for HSS and SC drill (a) Cutting velocity over stress, (b) Feed rate over stress, (c) Air pressure over stress and (d) stress over delamination.

when the AP was increased from 100 kpa to 300 kpa. After that, the F_d decreases from 1.413 to a minimum of 1.390 when the AP was increased from 300 kpa to 500 kpa. For SC drill, F_d was constant 1.343 when the AP was increased from 100 kpa to 300 kpa. After that, the F_d decreased from 1.343 to a minimum of 1.310 when the AP was increased from 300 kpa to 500 kpa. The AP influence on delamination factor which was found to be fluctuating with an elevating in AP because of the characteristic of the hole that was the main reason for chip clogging in the small hole. In addition, the SC drill produced hole having less damage around the hole than HSS drill material using same drilling conditions. It was due to differences in drill geometry.

4.4. Cutting velocity against stress

The relation between the CV and induced stress for HSS and carbide drill is drawn and presented in Fig. 7(a). The minimum stress is induced in the work material under the high CV for both HSS and carbide drill because of frictional heating. In addition, the thermal conductivity of carbide ($k = 110 \text{ W/mk}$) is higher than HSS ($k = 41 \text{ W/mk}$). Hence, HSS drill induced higher stress on the work material due to low rate of frictional heating is developed between the HSS drill and work material. Also, the density of HSS ($\rho = 0.008138 \text{ g/mm}^3$) is lower than SC ($\rho = 0.01563 \text{ g/mm}^3$). Hence, the higher density HSS drill produced higher stress on the work material

Table 6. Analysis of variance (ANOVA).

Delamination for HSS drill						
Source of variance	Degree of freedom	Sum of squares	Mean sum of squares	F-value	P-value	% CP
$v(\text{m/min})$	2	0.41718	0.20859	16.96	0.056	79.64
$f(\text{mm/min})$	2	0.07936	0.03968	3.23	0.237	15.15
$p(\text{kpa})$	2	0.00266	0.00133	0.11	0.903	0.51
Error	2	0.0246	0.0123			4.70
Total	8	0.5238				100.00
$R\text{-Sq} = 95.30\%$ $R\text{-Sq}(\text{adj}) = 81.21\%$						
Delamination for Solid carbide drill						
$v(\text{m/min})$	2	0.154076	0.077038	8.68	0.103	57.77
$f(\text{mm/min})$	2	0.092764	0.046382	5.23	0.161	34.78
$p(\text{kpa})$	2	0.002134	0.001067	0.12	0.893	0.80
Error	2	0.01775	0.008875			6.65
Total	8	0.266724				100.00
$R\text{-Sq} = 93.35\%$ $R\text{-Sq}(\text{adj}) = 73.38\%$						
Stress for HSS drill						
$v(\text{m/min})$	2	0.022888	0.011444	73.94	0.013	59.61
$f(\text{mm/min})$	2	0.015048	0.007524	48.61	0.02	39.19
$p(\text{kpa})$	2	0.000151	7.54E-05	0.49	0.672	0.39
Error	2	0.00031	0.000155			0.81
Total	8	0.038397				100
$R\text{-Sq} = 99.19\%$ $R\text{-Sq}(\text{adj}) = 96.78\%$						
Stress for Solid carbide drill						
$v(\text{m/min})$	2	0.026627	0.013313	60.03	0.016	61.53
$f(\text{mm/min})$	2	0.016124	0.008062	36.35	0.027	37.26
$p(\text{kpa})$	2	8.09E-05	4.04E-05	0.18	0.846	0.19
Error	2	0.000444	0.000222			1.03
Total	8	0.043276				100
$R\text{-Sq} = 98.98\%$ $R\text{-Sq}(\text{adj}) = 95.90\%$						

Table 7. Confirmation test.

	First experimental data		Confirmation test		Improvement in %	
	HSS	SC	HSS	SC	HSS	SC
Conditions	CV1FR1AP1		CV (1.91 m/min), FR (0.01 mm/min), and AP (500 kpa)	CV (2.02 m/min), FR (0.02 mm/min), and AP (104.69 kpa)	CV (1.91 m/min), FR (0.01 mm/min), and AP (500 kpa)	CV (2.02 m/min), FR (0.02 mm/min), and AP (104.69 kpa)
Delamination factor	1.099	1.141	1.032	1.012	6.10	11.31
Stress	0.458	0.425	0.414	0.356	9.61	16.24

during machining. The relation between the FR and induced stress for HSS and carbide drill is presented in Fig. 7(b). The minimum stress is induced on the work material under the low FR for both HSS and carbide drill. The stresses were increased due to high impact of the drill bit edges on fiber. Besides, while increasing the FRs, there is a possibility to increase the feed angle which can minimize the effective clearance angle. Therefore, the rubbing with work material results higher thrust force due to directionally proportional to induced stress. The relation between the AP and induced stress for HSS and carbide drill is shown in Fig. 7(c). The minimum stress is induced in the work material under the low AP for both HSS and carbide drill. From Fig. 7(c), it can be identified that the AP is directly proportional to thrust force and not supported to smooth metal removal from the machined zone. Because of micron level carbon fiber and resin locked inside the drill flute, the sticking of carbon fiber and resin on the both HSS and SC drill was the reason for chip locking. The higher sticking and low thermal conductivity of HSS is the reason for producing higher stress on the work material. The new relation graph is drawn based on the stress and delamination factor for HSS and SC drill, as shown in Fig. 7(d). The induced stress is increased with decrease in delamination factor for both HSS and SC drill. The lower stress is induced for SC drill than HSS drill because of thermal conductivity and density.

4.5. Analysis of variance

ANOVA results for HSS and SC drill are illustrated in Table 6. The CV (percentage contribution, PC – 79.64%), FR factor (PC – 15.15%) and AP factor (PC – 0.51%) were observed for HSS drill material. The CV factor has the most statistical and physical

significance while HSS drill is used. Therefore, the dominated factor was CV. The experimental error related to table of ANOVA (for HSS) for the F_d was less than 5%. The CV (PC – 57.77%), FR factor (PC – 34.78%) and AP factor (PC – 0.80%) were observed for SC drill material. Here also, the CV factor has the most statistical and physical significance while SC drill was used. Therefore, the dominated factor was CV. The experimental error related to table of ANOVA (for carbide) for the F_d was 7%. Therefore, the CV was found to be the most dominating factor for both HSS and SC drills.³¹ Similarly, the CV factor has the most statistical and physical significance while SC drill was used for induced stress. Confirmation tests were also performed in HSS drill and SC drill with corresponding optimum setting (GA result) on CFRP. The confirmations results are shown in Table 7. The optimized factors are significantly improved in performance.

5. Conclusions

Micro-drilling of CFRP samples is carried out using HSS and SC drill. The qualities were analyzed in terms of delamination and stress.

- Optimizing the process parameters was performed by GA in which it was found that $v_c f_t$ was nearer to optimum level for both HSS and SC drill and except in AP.
- In addition, the variation of drilling parameters trends on the responses with increasing of CV and FR has explained same for both HSS drill and SC drill (micron-level drill).
- In ANOVA, it was found that CV has most eminent parameters followed by FR.
- The confirmation tests have proved the error related to the delamination factor and stress was acceptable level.

- Overall, the SC drill can be considered as alternative for the HSS drill to perform drilling of CFRP.
- The delamination factor was decreased by increasing the drill bit stress on the work material and by increasing the thrust force developed in the drill and reducing the area of hole.

Acknowledgments

The authors wish to thank National Taipei University of Technology, Taiwan and MAM School of Engineering, Tiruchirappalli, India for their support to carry out this research.

References

1. V. Nelyub and V. Tarasov, *Mater. Manuf. Process.* **35** (2020), 172, <https://doi.org/10.1080/10426914.2020.1711926>.
2. R. Sathiyamurthy and M. Duraiselvam, *Mater. Manuf. Process.* **34** (2019), 1296, <https://doi.org/10.1080/10426914.2019.1644453>.
3. K. Shummugesh and P. Kavan, *Pigment Resin Technol.* **46** (2017) 21, <https://doi.org/10.1108/PRT-03-2016-0029>.
4. M. P. Jenarathanan and R. Jeyapaul, *Pigment Resin Technol.* **43** (2014), 35, <https://doi.org/10.1108/prt-12-2012-0088>.
5. M. P. Jenarathanan and R. Jeyapaul, *Pigment Resin Technol.* **44** (2015), 48, <https://doi.org/10.1108/prt-11-2013-0107>.
6. J. P. Davim and P. Reis, *Mater. Des.* **24** (2003), 315, [https://doi.org/10.1016/S0261-3069\(03\)00062-1](https://doi.org/10.1016/S0261-3069(03)00062-1).
7. Z. Jia, Y. Bai, F. Wang, J. Ma, D. Cheng and Z. Zhang, *Polym. Compos.* **40** (2019), E1434, <https://doi.org/10.1002/pc.25040>.
8. H. B. Kaybal, A. Ünüvar, M. Koyunbakan and A. Avci, *Int. J. Adv. Manuf. Technol.* **100** (2019), 2995, <https://doi.org/10.1007/s00170-018-2873-1>.
9. M. S. Won and C. K. H. Dharan, *J. Manuf. Sci. Eng.* **124** (2002), 778, <https://doi.org/10.1115/1.1505854>.
10. V. Krishnaraj, A. Prabhakarathi, M. Santhosh, M. Senthilkumar and R. Zitoune, *ASME 2012 Int. Manuf. Sci. Eng. Conf.* (American Society of Mechanical Engineers Digital Collection, 2012), pp. 269–275, <https://doi.org/10.1115/msec2012-7216>.
11. K.-H. Park, A. Beal, P. Kwon and J. Lantrip, *J. Manuf. Sci. Eng.* **136** (2014), 014501-1, <https://doi.org/10.1115/msec.2011-50114>.
12. V. Krishnaraj, S. Vijayarangan and A. Kaldos, *J. Manuf. Sci. Prod.* **7** (2006), 187, <https://doi.org/10.1515/ijmsp.2006.7.3-4.187>.
13. A. Faraz and D. Biermann, *Adv. Eng. Mater.* **15** (2013) 449, <https://doi.org/10.1002/adem.201200342>.
14. K. Weinert and C. Kempmann, *Adv. Eng. Mater.* **6** (2004), 684, <https://doi.org/10.1002/adem.200400025>.
15. U. Koklu and S. Morkavuk, *Surf. Rev. Lett.* **26** (2019) 1950060, <https://doi.org/10.1142/s0218625x19500604>.
16. C.-D. Wang, K.-X. Qiu, M. Chen and X.-J. Cai, *Int. J. Mod. Phys. B* **29** (2015) 1540031, <https://doi.org/10.1080/10426914.2020.1711926>.
17. M. S. Kumar, *J. Adv. Manuf. Syst.* **9** (2010), 63, <https://doi.org/10.1142/s0219686710001818>.
18. M. Senthilkumar, A. Prabhakarathi and V. Krishnaraj, *Int. J. Mater. Eng. Innov.* **8** (2017) 222, <https://doi.org/10.1504/ijmatei.2017.090235>.
19. E. Ghassemieh, *Int. J. Mater. Prod. Technol.* **43** (2012) 165, <https://doi.org/10.1504/ijmpt.2012.047682>.
20. I. Shyha, S. L. Soo, D. Aspinwall and S. Bradley, *J. Mater. Process. Technol.* **210** (2010) 1023, <https://doi.org/10.1016/j.jmatprotec.2010.02.011>.
21. J. Xu, Q. An, X. Cai and M. Chen, *Int. J. Precis. Eng. Man.* **14** (2013) 1687, <https://doi.org/10.1007/s12541-013-0252-2>.
22. A. Celik, I. Lazoglu, A. Kara and F. Kara, *J. Mater. Process. Technol.* **223** (2015) 39, <https://doi.org/10.1016/j.jmatprotec.2015.03.040>.
23. A. Krishnamoorthy, S. Rajendra Boopathy, K. Palanikumar and J. Paulo Davim, *Measurement*, **45** (2012) 1286, <https://doi.org/10.1016/j.measurement.2012.01.008>.
24. A. Krishnamoorthy, S. Rajendra Boopathy and K. Palanikumar, *J. Compos. Mater.* **43** (2009) 2885, <https://doi.org/10.1177/0021998309345309>.
25. K. Abhishek, S. Datta and S. S. Mahapatra, *Measurement*, **77** (2016) 222, <https://doi.org/10.1016/j.measurement.2015.09.015>.
26. K. Palanikumar, B. Latha, V. Senthilkumar and P. Davim, *Mater. Manuf. Process.* **27** (2012) 297, <https://doi.org/10.1080/10426914.2011.577865>.
27. K. Dhiraj Kumar, K. Singh and R. Zitoune, *Adv. Manuf. Polym. Compos. Sci.* **2** (2016) 47, doi: 10.1080/20550340.2016.1187434.
28. V. Sathiyamoorthy and T. Sekar, *Int. J. Enterp. Netw. Manag.* **7** (2016) 133, <https://doi.org/10.1504/IJENM.2016.077528>.
29. J. P. Davim and P. Reis, *Compos. Struct.* **59** (2003) 481, [https://doi.org/10.1016/S0263-8223\(02\)00257-X](https://doi.org/10.1016/S0263-8223(02)00257-X).
30. V. Krishnaraj, R. Zitoune and J. P. Davim, *Drilling of Polymer-Matrix Composites* (Springer, 2013), <https://doi.org/10.1007/978-3-642-38345-8>.
31. A. Velayudham and R. Krishnamurthy, *J. Mater. Process. Technol.* **185** (2007) 204, <https://doi.org/10.1016/j.jmatprotec.2006.03.146>.



Original Article

Machinability evaluation and comparison of Incoloy 825, Inconel 603 XL, Monel K400 and Inconel 600 super alloys in wire electrical discharge machining



K. Manikandan^{a,*}, P. Ranjith kumar^b, D. Raj kumar^b, K. Palanikumar^{c,*}

^a Department of Mechanical Engineering, MAMCE, Tiruchirappalli, Tamilnadu 621105, India

^b Department of Mechanical Engineering, MAMSE, Tiruchirappalli, Tamilnadu 621 105, India

^c Department of Mechanical Engineering, Sri Sai Ram Institute of Technology, Chennai 600 044, India

ARTICLE INFO

Article history:

Received 11 May 2020

Accepted 12 August 2020

Keywords:

Wire cut electrical discharge machining

Superalloys

Straightness

Perpendicularity

Surface roughness

ABSTRACT

Machinability comparisons have been made between superalloys such as Incoloy 825, Inconel 603 XL, Monel K400, and Inconel 600 using wire cut electrical discharge machining based on straightness, surface roughness and perpendicularity. The squared holes have been cut out on different superalloys as per the orthogonal array. Pulse duration, voltage, pulse interval, wire feed and mean current consisting of five levels have been selected as inputs tuning factors for wire cut electrical discharge machining. The scanning electron microscope analysis have been employed to study the machined surface defects of superalloys and unique optimum process parameters respectively. Monel K400 produced better results than other superalloys.

© 2020 The Authors. Published by Elsevier B.V. This is an open access article under the CC BY-NC-ND license (<http://creativecommons.org/licenses/by-nc-nd/4.0/>).

1. Introduction

Superalloys have a group of nickel-iron-chromium (Incoloy 825), nickel-chromium (Inconel 603 XL and Inconel 600), nickel-copper (Monel K400) and are used in various components such as thrust reversers, high-pressure turbine blades, and combustion chamber. The superalloys are generally difficult to cut material through conventional machining processes. This is because of high strength, high stiffness and

high toughness and excellent heat resistant. The superalloys are machined through conventional machining processes resulting in higher surface roughness, higher dimensional deviation and poor surface integrity [1]. Similarly, the higher taper angle and higher dimensional deviation are observed when the electrical discharge machining process on superalloys [2]. Higher heat-affected zone, higher taper angle and higher power consumption are produced using laser beam machining on superalloys [3]. Striation formation, wear track

Abbreviations: WEDM, Wirecut electrical discharge machining; St.ness, Straightness; Per.Ty, Perpendicularity; SR, Surface roughness; CMM, Co-ordinate measuring machine; SEM, Scanning electron microscope.

* Corresponding authors.

E-mails: kmanidps@gmail.com (K. Manikandan), palanikumar@sairamit.edu.in (K. Palanikumar).

<https://doi.org/10.1016/j.jmrt.2020.08.049>

2238-7854/© 2020 The Authors. Published by Elsevier B.V. This is an open access article under the CC BY-NC-ND license (<http://creativecommons.org/licenses/by-nc-nd/4.0/>).

and pits formation are observed through abrasive water jet machining on superalloys [4]. Poor dimensional accuracy and environmental pollutions are obtained through electrochemical machining on superalloys [5]. Among the unconventional machining processes on superalloys, Wire cut Electrical Discharge Machining (WEDM) has the ability to machine complex profile on difficult-to-cut material. The selection of WEDM process parameters for machine Incoloy 825, Inconel 603 XL, Monel K400, and Inconel 600 are difficult task. This is because of different mechanical and thermal properties of superalloys. Hence, the previous papers are studied for improving the straightness, perpendicularity and surface roughness of Incoloy 825, Inconel 603 XL, Monel K400, and Inconel 600. Dhanabalan et al. [6] studied straightness and perpendicularity of square holes during machining of Inconel 718. The result found that straightness of 0.03 mm and perpendicularity of 89.67° achieved in Inconel 718 using process parameters such as 12 A peak current, 600 μs pulse on time and 10 μs pulse off time. Dhanabalan et al. [7] studied perpendicularity of square holes during machining of Inconel 718 and Inconel 625. The result found that perpendicularity index decreased with an increase in pulse on time up to 350 μs and increase with a further increase in the pulse on time. Dhanabalan et al. [8] studied the form tolerances of Inconel 718 and Inconel 625 using EDM with multiple hole electrodes and found the values of form tolerances decreased with an increase in pulse on time up to 350 μs and form tolerances increases with increase in the pulse on time. Ramakrishnan and Karunamoorthy [9] found that a material removal rate of 71 mm^3/min and surface roughness of 3.198 μm for Inconel 718 obtained by using optimum parameters of 1.2 μs pulse on time, 8 m/min wire feed and 12 A ignition current. Muthukumar et al. [10] investigated the material removal rate and kerf width of Incoloy 800 by WEDM. A material removal rate of 0.0576 g/min, a minimum surface roughness of 3.10 μm , and kerf width of 0.296 mm are obtained by using optimum parameters of 50 V gas voltage, 10 μs pulse on time, 6 μs pulse off time and 8 mm/min wire feed. Gurusamy Selvakumar et al. [11] identified that a material removal rate of 3.17 mm^3/min and a surface roughness of 0.902 μm for Monel 400 obtained by using pulse on time of 0.35 μs , pulse frequency of 41.068 KHz, and current of 60 A. Rajyalakshmi [12] found that a material removal rate of 4.8595 mm^3/min and surface quality of 11.1028 μm for Monel 400 obtained by using 70 μs pulse on time, 4 μs pulse off time, 4 A peak current and 70 mm/min wire feed. Selvakumar et al. [13] studied that a surface roughness of 1.4 μm for Monel-400 achieved by using a flushing nozzle of 5 mm height, 4.91 N wire tension, 30-degree corner angle, 15 V voltage, 4 μs pulse duration, 50 μs pulse interval, and 0 mm travel speed. Tejas Ajay et al. [14] compared the material removal rate of Inconel 825, Incoloy 800, and Monel 400 by WEDM. The results showed that a material removal rate of 21.84 mm^3/min achieved in Incoloy 800 when compared to Inconel 825 and Monel 400. The surface roughness of 7.624 μm achieved in Inconel 825 when compared to Incoloy 800 and Monel 400.

The previous superalloys investigation found that selections of process parameters are difficult task in the different thermal conductivity superalloys using WEDM. Many authors are focused to improve the MRR [15–20], width of kerf [21–26], and roughness profile [27,28] of superalloys through WEDM.

The research gap is identified that no works have performed to improve the straightness and perpendicularity of machined Incoloy 825, Inconel 603 XL, Monel K400, and Inconel 600 superalloys using WEDM. The research gap is filled by optimizing WEDM process parameters on straightness and perpendicularity of the squared holes in the superalloys. In addition, the most significant parameters are identified through the mean effect data for each superalloy. The most significant process parameters' effects on straightness, perpendicularity, and surface roughness are analyzed for each superalloy. The best superalloy is identified based on the straightness, perpendicularity, and surface roughness and/or mean responses graph. The machined surface defects are analyzed for all the selected superalloys.

2. Materials and method

2.1. Machine setup

The machining experiments were carried out in SODICK ALN600 G WED machine. The brass wire diameter of $\phi 0.25$ mm was used. The 5 N wire tension was used for all experiments. The wire tension was varying from 3 N to 23 N. The maximum wire feed rate was 420 mm/s for all experiments.

2.2. Selection of superalloys

Superalloys: Incoloy 825, Inconel 603 XL, Monel K400, and Inconel 600 were used in this investigation in the form sheet. The chemical composition obtained for the superalloys is illustrated in Table 1. The mechanical properties of the superalloys are illustrated in Table 2. The straightness, perpendicularity and surface roughness of machined superalloys were selected to evaluate the machinability of different thermal conductivity superalloys through wire cut electrical discharge machining.

2.3. Selection of process parameters

The limits of machining factors were selected from a previous studies [9,10,13] and trial tests. There were some problems raised in the selection of process parameters during the machining of Incoloy 825, Inconel 603 XL, Monel K400, and Inconel 600 by trial and error methods. The WEDM process parameters used in the investigations are given in Table 3. The input parameters such as Pulse duration (Ton), Pulse interval (Toff), Mean current (I), Voltage (V), and Wire feed (WF) were selected.

2.4. Taguchi orthogonal array design

Taguchi orthogonal array design is one of the types of general fractional factorial design. Taguchi orthogonal array has ability to balance the multiple factors at multiple levels equally. For this reason, the factors are evaluated independently of each other despite the fractionality of the design. In the design expert software, five factors and four levels were decided to use the L16 orthogonal array for this work. In this study, the five parameters namely Pulse dura-

Table 1 – Chemical composition of superalloys [29–32].

Materials/Elements (%)	Incoloy 825		Monel k 400		Inconel 600		Inconel 603 XL	
	Nominal values % by wt	Actual values % by wt	Nominal values % by wt	Actual values % by wt	Nominal values % by wt	Actual values % by wt	Nominal values % by wt	Actual values % by wt
Ni	38–46	40.99	63.0 min	65.3	72 min	72.70	Remaining	73.23
Cu	1.5–3.0	1.648	28.0 -34.0	31	0.50 max	0.25	–	–
Cr	19.5 – 23.5	23.09	–	–	14.0–17.0	16.50	15–23	21.36
Fe	22 min	28.49	2.5 max	2.1	6.0–10.0	9.46	–	–
Si	0.5 max	0.123	0.50 max	0.13	0.5 max	0.292	2	1.004
C	0.05 max	0.017	0.3 max	0.0950	0.15 max	0.072	0.3 max	0.21
S	0.03 max	0.037	0.024 max	0.0030	0.015 max	0.001	–	–
Mn	1.0 max	0.372	2 max	0.96	1 max	0.233	0.3 max	0.21
Mo	2.5–3.5	3.107	–	–	–	–	4	2.83
Al	0.2 max	0.095	–	–	–	–	0.5 max	0.194
Ti	0.6–1.2	0.874	–	–	–	–	0.5 max	0.323
B	–	–	–	–	–	–	–	–
Co	–	–	–	–	–	–	–	–
Rare earths	–	–	–	–	–	–	0.1 max	0.037

Table 2 – Mechanical properties of super alloys [29–32].

Superalloys	Incoloy 825 (Nickel-iron-chromium)	Monel k 400 (Nickel – copper alloy)	Inconel-600 (Nickel – chromium alloy)	Inconel 603 XL (Nickel – chromium alloy)
Density (g/cm ³)	8.14	8.8	8.47	8.54
Tensile strength (MPa)	690	550	655	795
Yield Strength (MPa)	310	240	310	420
Elastic modulus (GPa)	196	179	200	218
Elongation to break (%)	65	40	40	30
Vickers Hardness	199	110–265	140–320	150–350
Thermal conductivity (W m ⁻¹ c ⁻¹)	7.9	21.8	14.9	11
Poisson's ratio	0.29	0.32	0.31	0.33
Specific heat (J kg ⁻¹ k ⁻¹)	440	427	444	439
Melting temperature (°C)	1370–1400	1300- 1350	1354–1413	1380–1400

Table 3 – Process parameters used in WEDM.

Parameters	Units	Levels				Below lower limit	Above upper limit
		1	2	3	4		
Pulse duration, (A/Ton)	μs	110	120	130	140	Low MRR	High SR, Wire breakage
Pulse interval, (B/Toff)	μs	40	50	60	70	Wire breakage	Low MRR
Mean current, (C/I)	A	100	110	120	130	Low MRR	High SR
Voltage, (D/V)	V	10	20	30	40	Low range	Low gap
Wire feed, (E/WF)	mm/s	2	4	6	8	Low SR	Wire breakage

tion (Ton), Pulse interval (Toff), Mean current (I), Voltage (V), and Wire feed (WF) were selected as input and each parameter designed to have four levels denoted by 1, 2, 3 and 4.

2.5. Straightness

Straightness (St. ness) is defined as the machined work surfaces that have peaks and valleys at a low level between the selected lines. The unit of straightness is millimeter which is measured by co-ordinate measuring machine based on the computational geometric techniques. Fifteen measurement points on each machined surfaces are considered to measure straightness. There are four straightness measurements

on the surface of the machined superalloys and mean value considered for further study.

2.6. Perpendicularity

Perpendicularity (Per. Ty) is a tolerance that controls perpendicularity between two 90° surfaces, or features. The unit of perpendicularity is degree which is measured by co-ordinate measuring machine based on the computational geometric techniques. Fifteen measurement points on each machined surfaces are considered to measure perpendicularity. There are four perpendicularity measurements on the surface of the machined superalloys and mean value considered for further study.

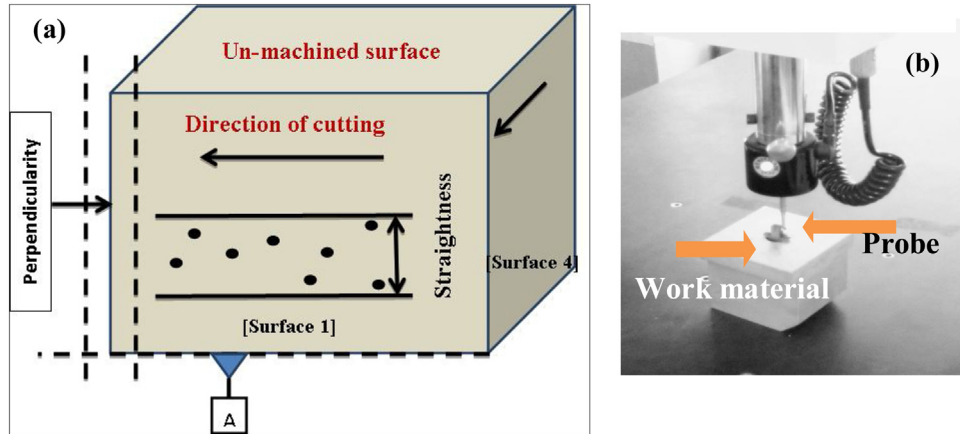


Fig. 1 – Schematic of square shape machined superalloys (a); Co-ordinate measuring machine with work material used for experimentation.

2.7. Surface roughness

The surface roughness (SR) of the machined surface was measured through a portable surface roughness tester. Ra was measured around four machined surfaces of superalloys and mean value considered for further study.

2.8. Inspecting square hole quality

The square shaped superalloys have 4 machined surfaces and 2 un-machined surfaces. The schematic diagram of the square shaped superalloys with the direction of cutting and representation of straightness and perpendicularity is shown in Fig. 1. The work material mounted on a Co-ordinate Measuring Machine (CMM) is also illustrated in Fig. 1.

3. Results and discussion

The results were summarized in Table 4 based on the experimental value of straightness, perpendicularity and surface roughness of Incoloy 825, Inconel 603 XL, Monel K400 and Inconel 600. The mean straightness, perpendicularity and surface roughness were calculated based on the design of experiment and presented in Tables 5–7. The rank was formed based on the delta value. The delta value was calculated by difference between the maximum value to minimum value. Among the five input process parameters, the pulse duration, pulse interval and wire feed have a significant effect on straightness, perpendicularity, and surface roughness based on the rank. The effect of pulse duration, pulse interval and wire feed on straightness, perpendicularity, and surface roughness of superalloys were studied in the following sections.

3.1. Straightness analysis

The machined surface straightness comparisons were drawn by increasing the pulse duration and it is shown in the Fig. 2. The minimum surface straightness was observed in

the Monel K400 using 110 μs pulse duration. It was also observed that the less surface straightness when machining of Monel K400 compared to Incoloy 825, Inconel 603 XL, and Inconel 600. The less surface straightness for Monel K400 observed. By lowering pulse duration, the surface was produced at the small peak, valley, and waviness in size on the machined surface because sufficient heat energy passed to work material for melting and evaporation. For all the selected superalloys, the machined surface straightness was increased up to 130 μs pulse duration and after decreased. Therefore, similar trends were observed for all the selected superalloys based on the pulse duration. While increasing pulse duration above 110 μs, there is a huge thermal energy developed on the work materials. Consequently, the longer and wider peaks and valleys were formed in the machined surface. Therefore, surface straightness increased due to a large amount of molten material irregularly deposited on the work material [29]. In addition, in order to evaluate the different superalloys performance, the percentage of reduction is calculated by using Eq. (1).

$$\text{Percentage of reduction} = \frac{(\text{High straightness} - \text{Small straightness})}{\text{High straightness}} \times 100 \quad (1)$$

The surface straightness was reduced of 47.973% (the range is 0.037 mm to 0.019 mm) for Monel K400, 37.419% (the range is 0.046 mm to 0.029 mm) for Inconel 600, 33.43% (the range is 0.052 mm to 0.034 mm) for Inconel 603 XL and 31.885% (the range is 0.054 mm to 0.037 mm) for Incoloy 825 by increasing the pulse duration.

The straightness comparisons were made based on the mean pulse interval and it is shown the Fig. 3. The minimum straightness was observed in the Monel K 400 using 40 μs and 70 μs mean pulse interval. It was also observed that less surface straightness during machining of Monel K 400 compared to Incoloy 825, Inconel 603 XL, and Inconel 600. By increasing pulse interval at above 60 μs or decreasing pulse interval at below 60 μs, the surface straightness was reduced. Also, the

Table 4 – Straightness, Perpendicularity and surface roughness of superalloys.

Exp. no.	Std Pulse duration μs	Pulse interval μs	Mean current A	Voltage volt	Wire feed mm/s	Incoloy 825	Inconel 603 XL	Monel K400	Inconel 600	Incoloy 825	Inconel			Incoloy 825	Inconel			Monel K400	Inconel 600
											603 XL	K400	600		603 XL	K400	600		
							Straightness (mm)				Perpendicularity (degrees)				Surface roughness (μm)				
1	14	140	40	130	20	6	0.046	0.043	0.028	0.037	90.01	89.98	89.76	89.85	3.641	3.455	2.924	3.177	
2	8	140	50	120	10	8	0.047	0.044	0.029	0.038	90.00	89.97	89.75	89.84	4.153	3.501	2.972	3.245	
3	13	120	70	120	20	2	0.049	0.046	0.031	0.040	89.99	89.96	89.74	89.83	2.748	2.329	1.656	2.052	
4	6	140	70	100	30	4	0.041	0.038	0.023	0.032	90.02	89.99	89.77	89.86	2.539	2.221	1.116	2.145	
5	9	110	60	120	30	6	0.051	0.048	0.032	0.042	89.98	89.95	89.73	89.82	2.934	2.598	1.876	2.676	
6	2	130	40	120	40	4	0.045	0.042	0.026	0.036	89.96	89.93	89.71	89.80	4.101	3.595	2.105	2.578	
7	5	110	50	110	20	4	0.027	0.024	0.008	0.018	90.70	90.68	90.45	90.54	2.652	2.634	2.095	2.993	
8	12	110	70	130	40	8	0.028	0.025	0.009	0.019	90.40	90.38	90.15	90.24	2.741	2.784	1.827	2.156	
9	7	120	40	110	30	8	0.037	0.034	0.019	0.028	90.24	90.21	89.99	90.08	3.526	3.255	2.324	3.320	
10	16	130	60	100	20	8	0.045	0.042	0.027	0.036	90.13	90.10	89.88	89.97	2.504	2.456	2.424	2.157	
11	4	130	50	130	30	2	0.067	0.064	0.049	0.058	89.92	89.89	89.67	89.76	3.893	3.167	2.526	3.170	
12	1	140	60	110	40	2	0.060	0.057	0.042	0.051	89.70	89.67	89.45	89.54	3.571	3.321	2.371	2.387	
13	15	120	60	130	10	4	0.067	0.066	0.052	0.060	90.02	89.99	89.77	89.86	3.842	3.938	2.650	2.775	
14	3	110	40	100	10	2	0.041	0.040	0.028	0.036	90.67	90.65	90.42	90.51	2.363	2.613	1.506	1.570	
15	10	130	70	110	10	6	0.059	0.058	0.046	0.054	89.81	89.78	89.56	89.65	3.641	3.455	2.924	3.177	
16	11	120	50	100	40	6	0.042	0.041	0.029	0.037	89.99	89.96	89.74	89.83	4.153	3.501	2.972	3.245	

Table 5 – Mean straightness for superalloys.

Parameter level	Pulse duration (μs)	Pulse interval (μs)	Current (amp)	Voltage (volt)	Wire feed (mm/s)
(a) Incoloy 825					
1	0.037	0.042	0.042	0.054	0.054
2	0.049	0.046	0.046	0.042	0.045
3	0.054	0.056	0.048	0.049	0.050
4	0.049	0.044	0.052	0.044	0.039
Delta	0.017	0.014	0.010	0.012	0.015
Rank	1	3	5	4	2
(b) Inconel 603 XL					
1	0.034	0.040	0.040	0.052	0.052
2	0.047	0.043	0.043	0.039	0.043
3	0.052	0.053	0.045	0.046	0.048
4	0.046	0.042	0.050	0.041	0.036
Delta	0.017	0.014	0.009	0.013	0.016
Rank	1	3	5	4	2
(c) Monel K 400					
1	0.019	0.025	0.027	0.039	0.038
2	0.033	0.029	0.029	0.024	0.027
3	0.037	0.038	0.030	0.031	0.034
4	0.031	0.027	0.035	0.027	0.021
Delta	0.018	0.013	0.008	0.015	0.017
Rank	1	4	5	3	2
(d) Inconel 600					
1	0.029	0.034	0.035	0.047	0.046
2	0.041	0.038	0.038	0.033	0.037
3	0.046	0.047	0.039	0.040	0.043
4	0.040	0.036	0.044	0.036	0.030
Delta	0.017	0.013	0.008	0.014	0.016
Rank	1	4	5	3	2

Table 6 – Mean perpendicularity for superalloys.

Parameter level	Pulse duration (μs)	Pulse interval (μs)	Current (amp)	Voltage (volt)	Wire feed (mm/s)
(a) Incoloy 825					
1	90.43	90.22	90.20	90.12	90.07
2	90.06	90.15	90.11	90.20	90.17
3	89.95	89.95	89.98	90.04	89.94
4	89.93	90.05	90.08	90.01	90.19
Delta	0.50	0.26	0.22	0.19	0.24
Rank	1	2	4	5	3
(b) Inconel 603 XL					
1	90.42	90.19	90.18	90.10	90.04
2	90.03	90.13	90.09	90.18	90.15
3	89.93	89.93	89.95	90.01	89.92
4	89.90	90.03	90.06	89.99	90.17
Delta	0.512	0.265	0.222	0.195	0.247
Rank	1	2	4	5	3
(c) Monel K 400					
1	90.19	89.97	89.95	89.88	89.82
2	89.81	89.90	89.86	89.96	89.93
3	89.71	89.71	89.73	89.79	89.70
4	89.68	89.81	89.84	89.76	89.94
Delta	0.505	0.263	0.220	0.195	0.245
Rank	1	2	4	5	3
(d) Inconel 600					
1	90.28	90.06	90.04	89.97	89.91
2	89.90	89.99	89.95	90.05	90.02
3	89.80	89.80	89.82	89.88	89.79
4	89.77	89.90	89.93	89.85	90.03
Delta	0.505	0.262	0.220	0.195	0.245
Rank	1	2	4	5	3

Table 7 – Mean surface roughness for superalloys.

Parameter level	Pulse duration (μ s)	Pulse interval (μ s)	Current (amp)	Voltage (volt)	Wire feed (mm/s)
(a) Incoloy 825					
1	2.67	3.41	2.89	3.50	3.14
2	3.57	3.71	3.35	2.89	3.28
3	3.53	3.21	3.48	3.22	3.59
4	3.48	2.92	3.53	3.64	3.23
Delta	0.895	0.796	0.640	0.755	0.449
Rank	1	2	4	3	5
(a) Inconel 603 XL					
1	2.66	3.23	2.70	3.38	2.86
2	3.26	3.20	3.17	2.72	3.10
3	3.17	3.08	3.01	2.81	3.25
4	3.12	2.70	3.34	3.30	3.00
Delta	0.599	0.532	0.638	0.658	0.395
Rank	3	4	2	1	5
(c) Monel K 400					
1	1.83	2.21	2.00	2.51	2.01
2	2.40	2.64	2.43	2.27	1.99
3	2.49	2.33	2.15	1.96	2.67
4	2.35	1.88	2.48	2.32	2.39
Delta	0.669	0.761	0.477	0.553	0.683
Rank	3	1	5	4	2
(d) Inconel 600					
1	2.35	2.66	2.28	2.69	2.29
2	2.85	3.16	2.97	2.59	2.62
3	2.77	2.50	2.64	2.83	3.07
4	2.74	2.38	2.82	2.59	2.72
Delta	0.499	0.781	0.690	0.236	0.774
Rank	4	1	3	5	2

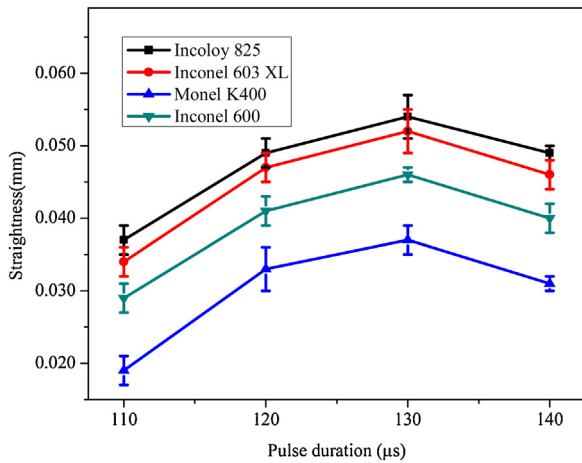


Fig. 2 – Pulse duration over straightness.

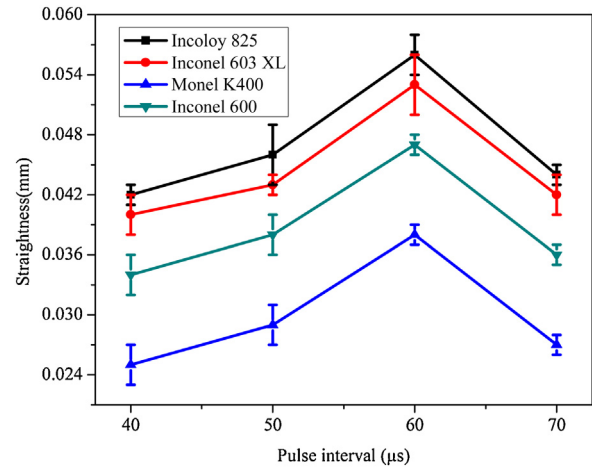


Fig. 3 – Mean pulse interval over straightness.

maximum surface straightness was achieved using 60 μ s pulse interval. The increase of surface straightness for Incoloy 825, Inconel 603 XL, Monel K400, and Inconel 600 was observed due to the high rate of electrons striking on the work material [23]. The impact of a higher rate of electrons striking on work materials produced the maximum peaks and valleys on the surface. Therefore, surface straightness increased. In addition, the perfect axial force was imposed on the wire to ensure straightness during cutting at a low pulse interval. Hence, the size of peaks and valleys varied based on the thermal conductivity of superalloys [30]. The straightness was reduction of 33.987%, for Monel K400, 27.513% for Inconel 600, 25.352%

for Inconel 603 XL and 24.215% for Incoloy 825 by increasing the mean pulse interval. Therefore, the highest reduction percentage was observed in Monel K 400 compared to other superalloys.

The straightness comparisons were made based on the wire feed and it is shown the Fig. 4. The minimum straightness was observed in the Monel K400 at 8mm/s wire feed. It was also inferred that minimum surface straightness when machining of Monel K400 compared to Incoloy 825, Inconel 603 XL and Monel K400. The straightness was decreased of 40% for monel K400, 34.59% for Inconel 600, 29.95% for Inconel 603 XL and 27.65% for Incoloy 825 by increasing the wire feed.

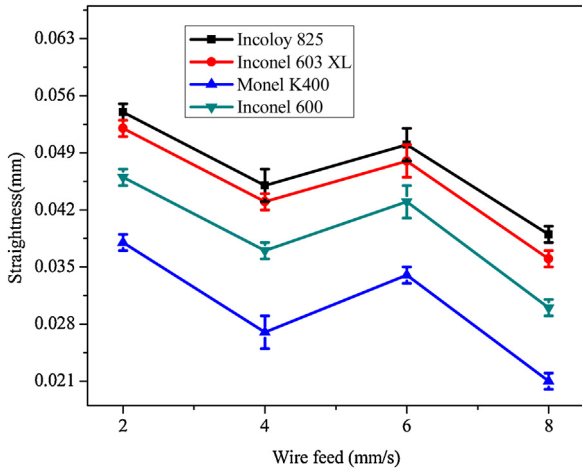


Fig. 4 – Wire feed over straightness.

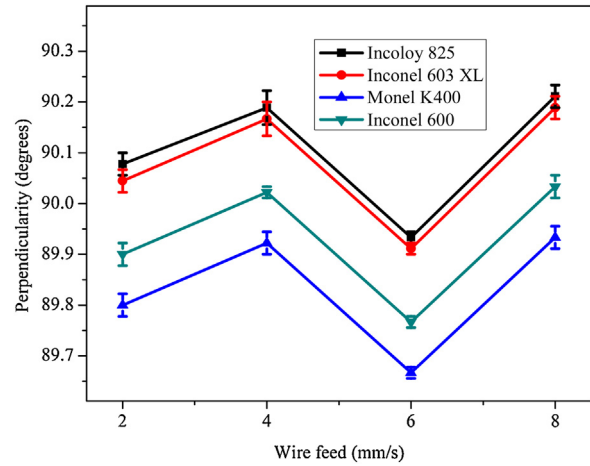


Fig. 7 – Wire feed over perpendicularity.

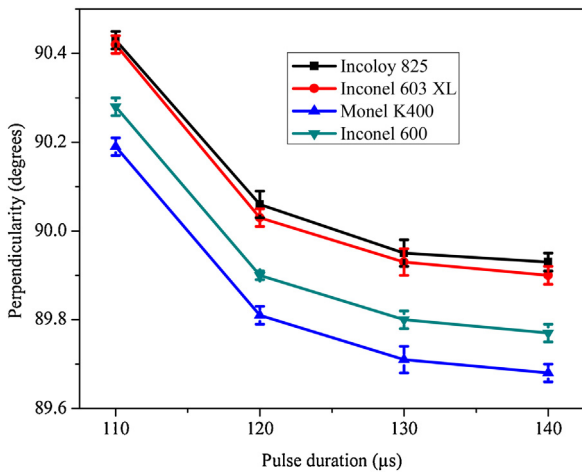


Fig. 5 – Pulse duration over perpendicularity.

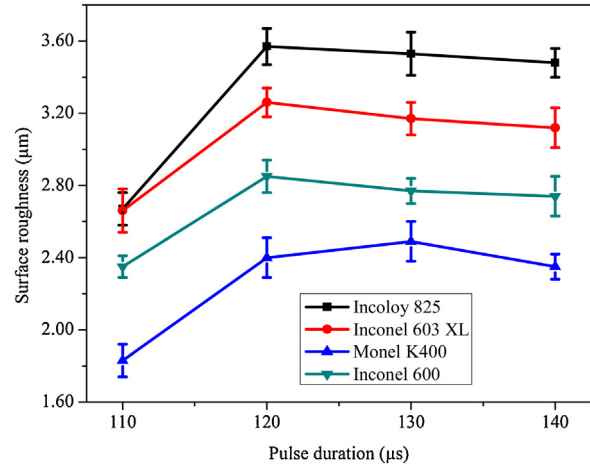


Fig. 8 – Pulse duration over SR.

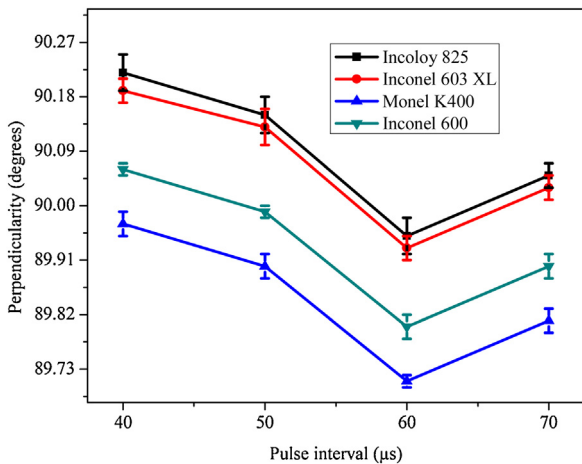


Fig. 6 – Pulse intervals over perpendicularity.

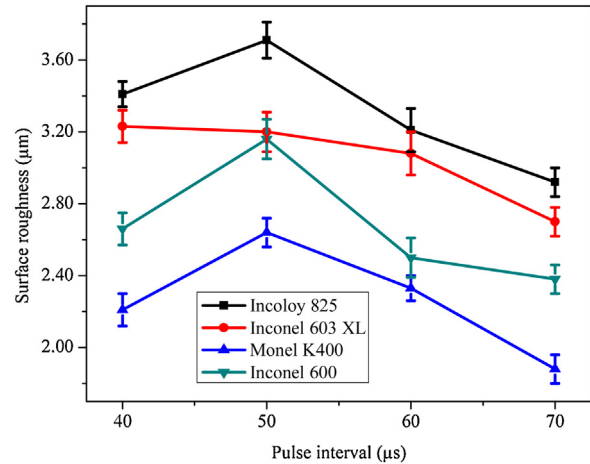


Fig. 9 – Pulse intervals over SR.

For all the selected superalloys, the surface straightness varied by increasing the wire feed. For overall trend graphs analysis, surface straightness decreased by increasing the wire feed. This was due to the discharge gap widened and discharge frequency decreased [31].

3.2. Perpendicularity analysis

The perpendicularity comparisons were made based on pulse duration and it is shown the Fig. 5. The minimum perpendicularity was observed in the Monel K400 at 140 µs pulse duration.

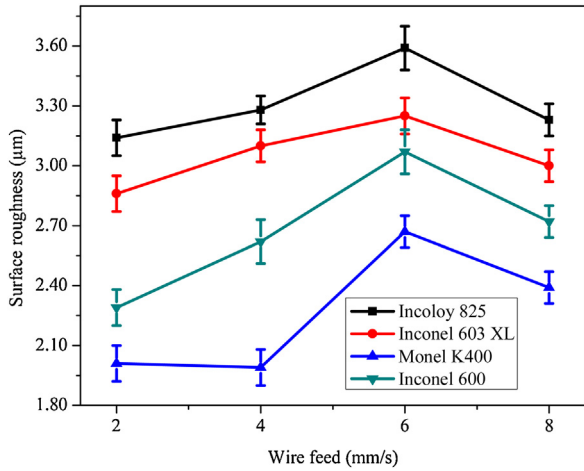


Fig. 10 – Wire feed over SR.

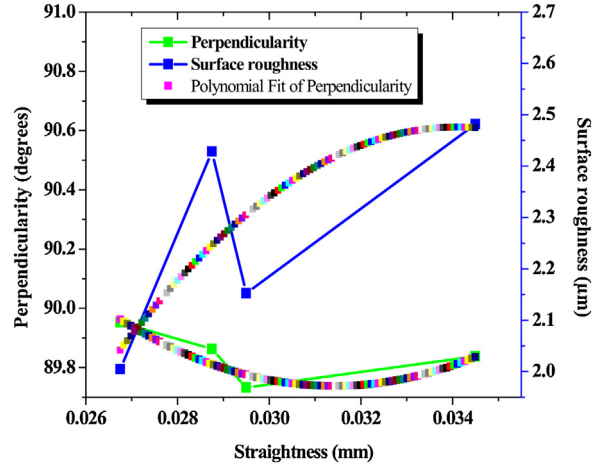


Fig. 11 – Straightness over surface roughness and perpendicularity.

It was observed that less perpendicularity when machining of Monel K400 compared to Incoloy 825, Inconel 603 XL, and Monel K400. The perpendicularity was approximately reduced of 0.56% for all selected superalloys by increasing the pulse duration. The surface perpendicularity for Incoloy 825, Inconel 603 XL, Monel K400, and Inconel 600 were gradually decreased.

The surface perpendicularity was related to the MRR from the side surface. The duration of the pulse was directly affecting MRR because of heat energy striking on the work. Therefore, the more surface perpendicularity was observed using low pulse duration because of less sparking time and insufficient

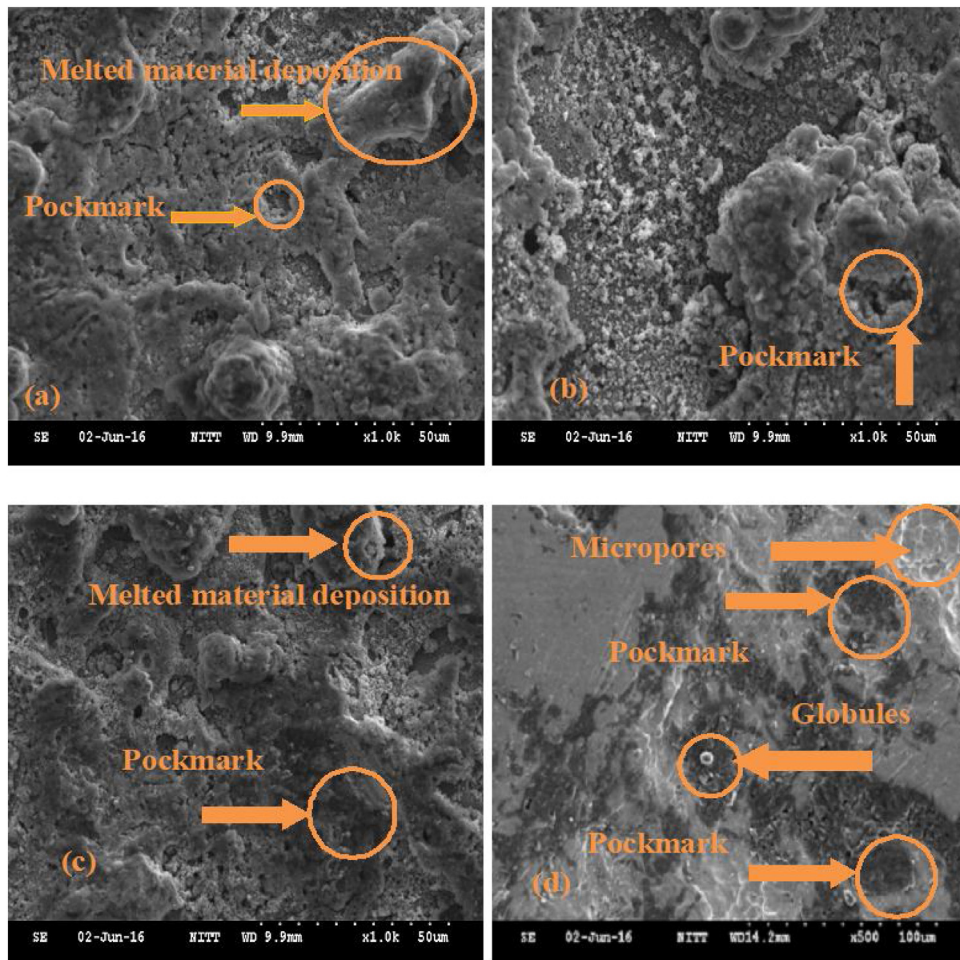


Fig. 12 – SEM images of machined surfaces of Incoloy 825: (a) Exp. No. 4, (b) Exp. No. 8, (c) Exp. No. 12 and (d) Exp. No. 16.

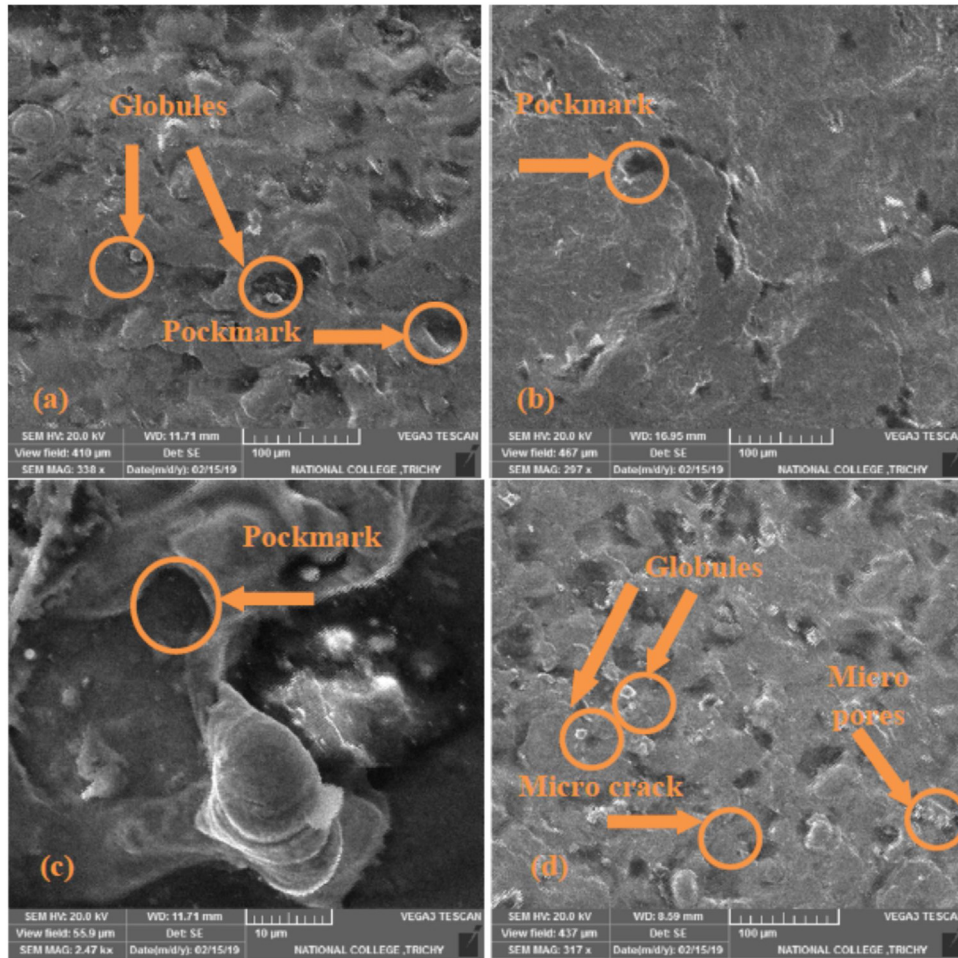


Fig. 13 – SEM images of machined surfaces of Inconel 603 XL: (a) Exp. No. 4, (b) Exp. No. 8, (c) Exp. No. 12 and (d) Exp. No. 16.

heat energy passed [23]. With the increase in pulse duration, the MRR gradually increases. Therefore, less surface perpendicularity was observed using a high pulse duration and because of adequate spark discharge time and a high amount of material removal. Consequently, the surface perpendicularity was slightly reduced from 90° surface. The perpendicularity analyses found that it was varying from 0.505 to 0.512° for selected pulse duration.

The perpendicularity comparisons were made based on pulse interval and it is shown the Fig. 6. The minimum perpendicularity was observed in the Monel K400 using $60 \mu\text{s}$ pulse interval. It was observed that less perpendicularity during machining of Monel K400 compared to Incoloy 825, Inconel 603 XL and Monel K400. The perpendicularity was gradually decreased and then increased by raising the pulse interval. The perpendicularity was approximately decreased of 0.29% for all selected superalloys by increasing the pulse interval. The effects of higher pulse duration and lower pulse interval combinations were increased material removal rates. Therefore, the more surface perpendicularity was observed using a low pulse interval because of more sparking time [23]. With the increase in pulse interval, the MRR gradually decreases. Therefore, less surface perpendicularity was observed using a high pulse interval because of reduced spark discharge time and

less amount of material removal. Consequently, the surface perpendicularity was decreased from 90° surface.

The perpendicularity comparisons were made based on the wire feed and it is shown the Fig. 7. The minimum perpendicularity was observed in the Monel K400 at 6 mm/s wire feed. It was observed that perpendicularity less during machining of Monel K400 compared to Incoloy 825, Inconel 603 XL and Monel K400. The surface perpendicularity was gradually decreased and increased. The perpendicularity was approximately decreased of 0.27% for all selected superalloys by increasing the selected wire feed range.

3.3. Surface roughness analysis

The SR comparisons were made based on the pulse duration and it is shown the Fig. 8. The minimum SR was observed in the Monel K400 at $110 \mu\text{s}$ pulse duration. It was observed that less SR during machining of Monel K400 compared to Incoloy 825, Inconel 603 XL and Monel K400. The SR was increased of 26% (from $1.826 \mu\text{m}$ to $2.495 \mu\text{m}$) for Monel K400, 17% (from $2.349 \mu\text{m}$ to $2.848 \mu\text{m}$) for Inconel 600, 18% (from $2.657 \mu\text{m}$ to $3.256 \mu\text{m}$) for Inconel 603 XL and 25% (from $2.673 \mu\text{m}$ to $3.567 \mu\text{m}$) for Incoloy 825 by increasing the pulse duration. The reason for

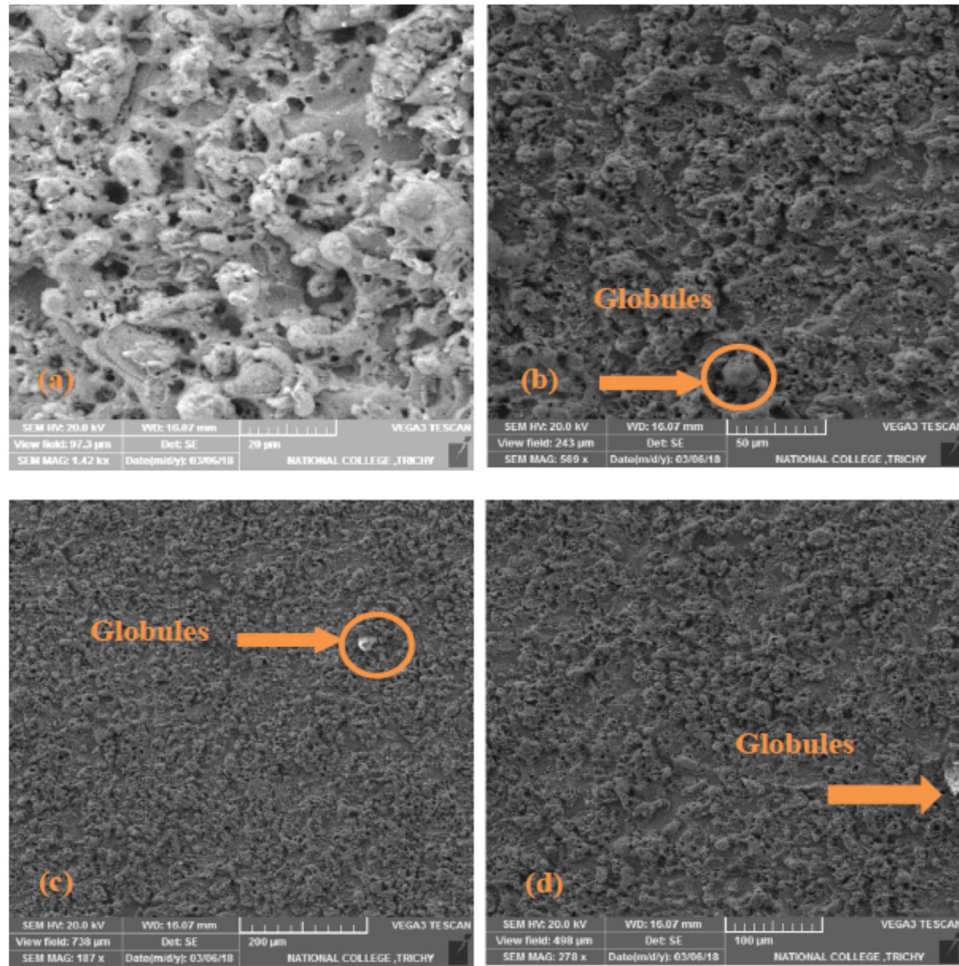


Fig. 14 – SEM images of machined surfaces of Monel K400: (a) Exp. No. 4, (b) Exp. No. 8, (c) Exp. No. 12 and (d) Exp. No. 16.

increased SR was due to the more powerful explosion occurred in the machining zone which produced deep crater.

The SR comparisons were made based on the pulse interval and it is shown the Fig. 9. The minimum SR was observed in the Monel K400 at 70 μ s pulse interval. It was observed that less SR during machining of Monel K400 compared to Incoloy 825, Inconel 603 XL and Monel K400. The SR was decreases of 28% (from 2.64 μ m to 1.88 μ m) for Monel K400, 24.68% (from 3.163 μ m to 2.383 μ m) for Inconel 600, 16% (from 3.230 μ m to 2.697 μ m) for Inconel 603 XL and 21.426% (from 3.713 μ m to 2.917 μ m) for Incoloy 825 when pulse interval was increased. The reason for decreased SR was due to the dielectric fluid effectively removing the debris from the molten material and adequate heat transfer to work material [32].

The SR comparisons were made based on the wire feed and it is shown the Fig. 10. The minimum SR was observed using 4 mm/s wire feed for Monel K400 and 2 mm/s wire feed for remaining superalloys. It was observed that less SR during machining of Monel K400 compared to Incoloy 825, Inconel 603 XL and Inconel 600. The SR was decreased of 25% (from 2.674 μ m to 1.992 μ m) for Monel K400, 25% (from 3.069 μ m to 2.295 μ m) for Inconel 600, 12% (from 3.252 μ m to 2.858 μ m) for Inconel 603 XL and 12.485% (from 3.592 μ m to 3.144 μ m) for Incoloy 825 when wire feed was increased. The similar results

were observed by author [33]. The reason for SR increase was due to the vibration of wire electrode and resolidification of molten material.

In Figs. 3 to 10, it can be identified that the Monel K 400 has produced minimum straightness, perpendicularity and surface roughness. Therefore, Monel K 400 was produced better performance than the Incoloy 825, Inconel 603 XL and Inconel 600. In order to arrive the correlation between the straightness, perpendicularity and surface roughness, the new trend graph is drawn based on the pulse duration which is shown in Fig. 11. The new trend curve found that the pulse duration has directly proportional to surface straightness of Monel superalloys. Also, the surface straightness has directly proportional to surface roughness and indirectly proportional to perpendicularity.

3.4. Machined surface defect analysis

Scanning Electron Microscope (SEM) was used to examine the machined surface defects after WEDM processes. The major microstructural changes in the machined surface of Incoloy 825, Inconel 603 XL, Monel K400 and Inconel 600 superalloys were observed. The various machined surface defects are shown in Figs. 12–15. The pockmarks on the machined sur-

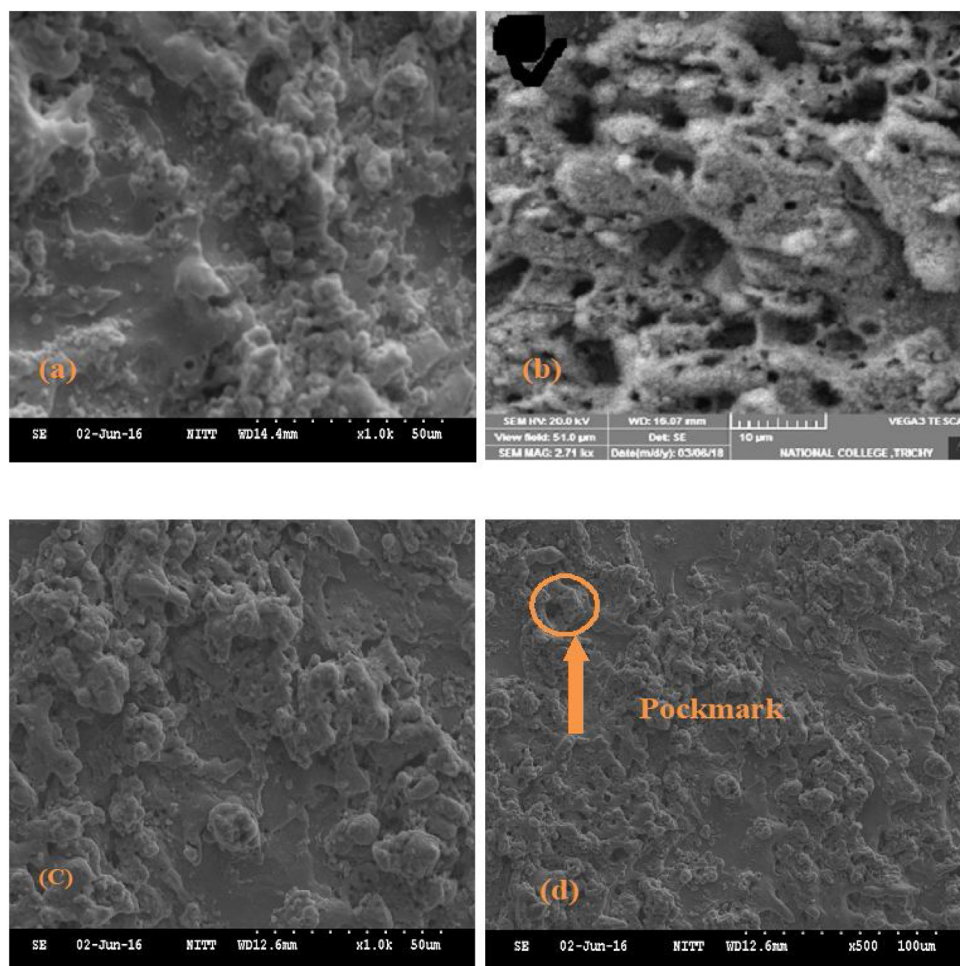


Fig. 15 – SEM images of machined surfaces of Inconel 600: (a) Exp. No. 4, (b) Exp. No. 8, (c) Exp. No. 12 and (d) Exp. No. 16.

face of all superalloys are shown in Figs. 12–15. The Monel K400 produced small craters. The thermal conductivity was the reason for the small crater size. Also, the reason for obtaining small sized craters on the machined surface was due to the low melting temperature, 1300–1350 °C, compared to the other superalloys. The globules, micro pores and micro cracks are mostly observed in the high pulse duration for all the selected superalloys. The reason for micro crack on the machined surface was because of the thermal stresses. Micro cracks and deviations also observed because of the heat generation and thermal expansion. Mechanical strength also plays an important role in arriving the results. The reason for globule on the machined surface was because of the presence of surface tension which is present in the liquid metal. The huge numbers of pockmarks are formed on the all machined superalloys surface. The reason for pockmark on the machined surface was due to that entrapped gases were released from the machined zone during solidification.

4. Conclusions

The machinability of Incoloy 825, Inconel 603 XL, Monel K400 and Inconel 600 superalloys were successfully com-

pared while during WEDM. The following points are drawn.

- The Monel K400 produced the lower straightness, perpendicularity and surface roughness compared to Incoloy 825, Inconel 603 XL, and Inconel 600 superalloys based on the experimental results.
- The pulse duration produced the highest improvement percentage of straightness in Monel K400 compared to other process parameters and other superalloys.
- Pulse duration and pulse interval has most significant factor that affects all the responses.
- The selected superalloys produced smaller standard error based on the error bar analysis.
- The pulse duration and surface roughness are directly proportional to straightness and indirectly proportional to perpendicularity.
- The pock marks, globules and micropores have affecting the functionality of the components.

Conflict of interest

The authors declare no conflicts of interest.

REFERENCES

- [1] Mogra A, Verma SK, Thomas T. Fabrication of square microchannel for experimental investigation of two phase flow using conventional machining process. *Perspect Sci* 2016;8:231-3.
- [2] Habib SS. Study of the parameters in electrical discharge machining through response surface methodology approach. *Appl Math Model* 2009;33(12):4397-407.
- [3] Parthiban A, Chandrasekaran M, Muthuraman V, Sathish S. Optimization of CO₂ laser cutting of stainless steel sheet for curved profile. *Proceedings of the Materials Today* 2018;5(6):14531-8.
- [4] Pawar PJ, Vidhate US, Khalkar MY. Improving the quality characteristics of abrasive water jet machining of marble material using multi-objective artificial bee colony algorithm. *J Comput Des Eng* 2018;5(3):319-28.
- [5] Xu Z, Liu J, Zhu D, Qu N, Wu X, Chen X. Electrochemical machining of burn-resistant Ti40 alloy. *Chinese J Aeronaut* 2015;28(4):1263-72.
- [6] Dhanabalan S, Sivakumar K, Sathiya Narayanan C. Optimization of machining parameters of EDM while machining Inconel 718 for form tolerance and orientation tolerance. *Indian Journal of Engineering and Materials Sciences* 2013;20:391-7.
- [7] Dhanabalan S, Sivakumar K, Sathiya Narayanan C. Analysis of form tolerances in electrical discharge machining process for inconel 718 and 625. *Mater Manuf Process* 2014;29(3):253-9.
- [8] Subramanian, Dhanabalan, Sivakumar K, Chinnaiyan Sathiya Narayanan. Form tolerances investigation in EDM process for super alloys using multiple hole electrodes. *Indian Journal of Engineering and Materials Sciences* 2019;26:200-4.
- [9] Ramakrishnan R, Karunamoorthy L. Modeling and multi-response optimization of Inconel 718 on machining of CNC WEDM process. *J Mater Process Technol* 2008;207(1-3):343-9.
- [10] Muthukumar V, Suresh babu A, Venkatasamy R, Raajenthiren M. Optimization of the WEDM parameters on machining Incoloy 800 super alloy with multiple quality characteristics. *Int J Eng Sci Technol* 2010;2:1538-47.
- [11] Selvakumar Gurusamy, Soumya Sarkar, Mitra, Souren. Experimental analysis on WEDM of monel 400 alloys in a range of thicknesses. *International Journal of Modern Manufacturing Technologies* 2012;4:113-20.
- [12] Rajyalakshmi G. Modeling and Multi-Objective Optimization of WEDM of Commercially Monel Super Alloy considering Multiple Users Preferences. *Journal of Pharmaceutical Sciences and Research* 2016;8(8):902-8.
- [13] Selvakumar G, Thirupathi Kuttalingam K, Selvaraj M, Manohar J. Enhancing die corner accuracy using path modification strategy in wire electrical discharge machining of Monel 400. *Arch J Mech Eng Sci* 1959-1982 2016;232(2):207-16.
- [14] Tejas Ajay B, Mayur Vitthal P, Rajyalakshmi G. WEDM machining on aerospace materials for improving material properties. *Proceedings of the Materials Today* 2017;4(8):9107-16.
- [15] Torres A, Luis CJ, Puertas I. Analysis of the influence of EDM parameters on surface finish, material removal rate, and electrode wear of an INCONEL 600 alloy. *Int J Adv Manuf Technol* 2015;80(1-4):123-40.
- [16] Gowthman PS, Jeyakumar S. Review on Machining of High Temperature Aeronautics Super – Alloys using WEDM. *Proceedings of the Materials Today* 2019;18(7):4782-91.
- [17] Aldrin Raj J, Balasubramanian K, Palanisamy D, Emmanuel AGS. Experimental investigations on WEDM process for machining High Manganese steel. *Mater Manuf Process* 2020;10:1-10.
- [18] Shiyas Muhammed, Rahul M, Kareem Muhammed, Shyam Krishnan PR, Rameez Mohammed NN. Experimental study on the effects of process parameters on MRR in Incoloy 825 using wire EDM process. *Int J Res Appl Sci Eng Technol* 2018;6:829-39.
- [19] Archana G, Dharma Reddy K, Venkataramaiah P. Study on machining response in wire EDM of inconel 625. *Int J Appl Eng Res Dev* 2018;13(21):15270-7.
- [20] Dwaipayana D, Titas N, Asish B. Parametric study for wire cut electrical discharge machining of sintered titanium. *Strojnický Casopis – Journal of Mechanical Engineering* 2019;69(1):17-38.
- [21] Dabade UA, Karidkar SS. Analysis of response variables in WEDM of inconel 718 using taguchi technique. *Procedia Cirp* 2016;41:886-91.
- [22] Caydas Ulas, Ay Mustafa. WEDM cutting of Inconel 718 nickel-based super alloy effects of cutting parameters on the cutting quality. *Mater Technol* 2016;50(1):117-25.
- [23] Unune DR, Mali HS. Experimental investigation on low-frequency vibration assisted micro-WEDM of Inconel 718. *Engineering Science and Technology. Int J* 2017;20(1):222-31.
- [24] Devarasiddappa D, Chandrasekaran M, Sambandam MT. Multi performance optimization in wire cut EDM of inconel 825 using desirability function coupled with analytical hierarchy process. *Mater Today Proc* 2018;5(5):11531-47.
- [25] Kumar SS, Erdemir F, Varol T, Kumaran ST, Uthayakumar M, Canakci A. Investigation of WEDM process parameters of Al-SiC-B4C composites using response surface methodology. *Int J Lightweight Mater Manuf* 2020;3(2):127-35.
- [26] Ishfaq K, Ahmad N, Jawad M, Ali MA, M Al-Ahmari A. Evaluating material's interaction in wire electrical discharge machining of stainless steel (304) for simultaneous optimization of conflicting responses. *Materials* 2019;12(12):1940.
- [27] Kumar Vinod, Jangra Kamal Kumar, Kumar Vikas. Effect of process parameters on surface roughness of nickel based alloys in WEDM. *Int J Recent Adv Mech Eng* 2015;4(4):85-93.
- [28] Bisaria Himanshu, Shandilya Pragya. Experimental investigation on wire electric discharge machining(WEDM) of Nimonic C – 263. *Superalloy* 2019;34(1):83-92.
- [29] Singh T, Arya RK, Dvivedi A. Fabrication of micro-slits using W-ECDM process with textured wire surface an experimental investigation on kerf overcut reduction and straightness improvement. *Precis Eng* 2019; 59:211-23.
- [30] Sanchez J, Ortega N. Wire electrical discharge machines. In: Lopez de Lacalle L, Lamikiz A, editors. *Machine tools for High performance machining*. Springer; 2009. Chapter 9.
- [31] Chalisgaonkar R, Kumar J. Parametric optimization and modelling of rough cut WEDM operation of pure titanium using grey-fuzzy logic and dimensional analysis. *Cogent Eng* 2014;1(1).
- [32] Goyal A. Investigation of material removal rate and surface roughness during wire electrical discharge machining (WEDM) of Inconel 625 super alloy by cryogenic treated tool electrode. *J King Saud Univ - Sci* 2017;29(4):528-35.
- [33] Goswami A, Kumar J. Optimization in wire-cut EDM of Nimonic-80A using Taguchi's approach and utility concept. *Eng Sci Technol Int J* 2014;17(4):236-46.

Laser Surface Modification of Materials

By Natarajan Jeyaprakash, Che-Hua Yang and Durairaj Raj Kumar

Submitted: July 22nd 2020 Reviewed: October 12th 2020 Published: October 31st 2020

DOI: 10.5772/intechopen.94439

Abstract

The metallic materials such as steel, iron, titanium and nickel alloys etc., are extensively used in the automobile, marine, biomedical, aerospace, chemical industry and power generation sector. However, the poor surface properties restricted their wide usage in many applications. Therefore, the surface properties need to be enhanced through novel treatments without affecting the bulk. In recent years, laser surface modification attracts more due to their inherent properties. The laser based surface altering process is appropriate to modify the metallic surfaces in terms of their flexibility, simple operation and process economy. Laser surface modification includes; surface hardening, melting, alloying, cladding and texturing. Thus, from a process engineering, metallurgical reasons and tribologist view point, the laser surface modification process can be recognized as an important topic.

Keywords

laser hardening

melting

alloying

cladding and texturing



Investigation on laser square hole drilling of AA7475/SiC/ZrSiO₄ composites

V. Senthil Kannan¹ · K. Lenin² · D. Srinivasan² · D. Raj Kumar³

Received: 18 March 2021 / Accepted: 2 July 2021
© Springer Nature B.V. 2021

Abstract

Compared with other machining processes, laser machining is seen as one of the time and cost effective processes in machining of metal matrix composites (MMCs). Hence, this work more focuses on analysis of laser machining parameters, namely, laser trepanning speed, laser power and standoff distance, various weight percentages of SiC and ZrSiO₄ are selected for investigation. Laser machining experiments were performed on SiC and ZrSiO₄ reinforced with Aluminium Alloy (AA7475). The performance measures, hole size at entry, surface roughness and taper angle of MMCs were evaluated. Preference Ranking Organization METHod for Enrichment of Evaluations (PROMETHEE II) was used for finding optimum process parameters. PROMETHEE II based Adaptive Network Based Fuzzy Inference System (ANFIS) was used for modelling the responses. The main contribution of this work is the analysis of the impact of reinforcement particles of the composites and laser machining parameters on the responses. The results showed that hole size at entry, surface roughness and taper angle of unreinforced alloy was less than the composite for all the processing conditions. PROMETHEE II algorithm produced a consistent result. PROMETHEE II based ANFIS model produces closer predicted value to experimental value. Scanning electron microscope is used to identify the machined defects such as recast layer, spatter and dross.

Keywords Aluminium · Silicon carbide · Zirconium silicate · Laser

1 Introduction

Metal matrix composites (MMCs) have recently developed as composite materials through addition of aluminium with silicon carbide. Compared to other metals and alloys, the major

benefits of MMCs are improved properties such as superior wear properties, better strength to wear ratio, high modulus, high-temperature resistance and better corrosion resistance [1]. These properties have enabled the use of aerospace, automotive, electronics and consumer goods. MMCs have limited applications due to low machinability [2]. Different hard reinforcement particles were added to the matrix for the improvement of properties/machinability of MMCs. Reinforcement particles including silicon nitride, boron, silicon carbide, silica sand, magnesium oxide, glass beads, titanium carbide and boron carbide were added to the matrix. B₄C, SiC and Al₂O₃ were mixed effectively to the molten aluminium. Hence, SiC was selected as one of the reinforced material. Among the various reinforcement particles, Zircon is identified as promising reinforced due to its high melting point and refractoriness and its high resistance to abrasion, impact and sudden volume changes at elevated temperatures. ZrSiO₄ was selected as another reinforced to the matrix. For getting the desired shape, Tool based machining and non-contact machining was used. Tool based machining of MMCs is difficult owing to the high abrasive nature of silicon carbide. High tool wear and burr formation was observed in the tool based

✉ V. Senthil Kannan
vsktgp@gmail.com

K. Lenin
leninnaga@yahoo.com

D. Srinivasan
principal@krce.ac.in

D. Raj Kumar
profdrajumar@gmail.com

¹ Department of Mechanical Engineering, Paavai Engineering College, Namakkal, Tamil Nadu 637018, India

² Department of Mechanical Engineering, K. Ramakrishnan College of Engineering, Trichy, Tamil Nadu 621112, India

³ Department of Mechanical Engineering, MAM School of Engineering, Trichy, Tamil Nadu 620216, India

machining on MMCs [3]. Hence, non-contact machining was selected for processing on MMCs [4]. In the abrasive water jet process on 7075 Aluminium based MMC, 1.77 μm surface roughness and 0.17° taper angle was obtained [5]. Similarly, in the electrical discharge machining on AA6351/ 5 %SiC/ 10 %B₄C MMC, 4.54 μm surface roughness was obtained [6]. The laser machining of Aluminium Alloy Metal Matrix Composite (AMMC) is a difficult process due to alterations in the physical properties [7]. Hence, laser based machining process on AMMC was selected. SiC and ZrSiO₄ was selected as reinforcement in the AMMC fabrication. Al₂O₃ was added to aluminium alloy for improving the surface quality of composite. The results showed that improvement in the surface quality of composite due to the increase in wear resistance of composite [8]. Addition of Al₂O₃ and SiC reinforcement was made to the matrix for obtaining the hole diameter of MMC. The results showed that increase in laser power from 800 to 2000 W, the diameter varied from 0.692 mm to 0.741 mm due to the millisecond continuous wave laser drilling [9]. The selection of laser sources also greatly affected the quality characteristics of machined dimension and surface due to the different metal removal phenomenon. Hence, previous researchers used a variety of laser sources such as pulsed wave (PW), continuous wave (CW), nanosecond (ns), picosecond (ps) and femtosecond (fs) lasers for improving the machined dimension and surface. With an addition of 25 % SiC particulates to aluminium, the 0.27 μm surface roughness was achieved by machining [10]. Some of the related works were presented in the following. In pulsed mode, an addition of 20 % SiC to molten AA2618, the 9 mm laser drilled hole results showed that 5.28 μm surface roughness and 2.42° taper angle was obtained using 1600 W power, 400 mm/min scanning speed, and 1.3 MPa nitrogen gas pressure [11]. A pulsed Nd:YAG laser parameters, 230 W pulse power, 250 Hz pulse frequency, 9 kg/cm² assistance of gas pressure, and 0.4 ms pulse width were used for obtaining the 3.5° taper in the drilling on Al7075/10 %SiC [12]. In another pulsed Nd:YAG laser processing on alumina, the 2.72° taper angle was observed through use of optimum parameters such as 19 amp lamp current, 4.2 kHz pulse frequency, 2 kg/cm² air pressure and 7 % pulse width [13]. In another alumina–aluminium system processing by pulsed Nd:YAG laser parameter such as 20.31 amp lamp current, 0.66 kHz pulse frequency and 0.66 kg/cm² assisted air pressure was used for obtaining a minimum taper of 0.0251 [14]. During Tin/Al₂O₃ composites pulsed Nd:YAG machining, the parameters including 23.12 amp lamp current, 2.30 kHz pulse frequency, 3.162 % pulse width, 1.800 kg/cm² assisted air pressure and 475.68 micron focal length were used for obtaining the hole taper of 1.54° [15]. With variation in the pulsed Nd:YAG laser parameters such as low pulse frequency, a large number of pulse and moderate pulse width was used for obtaining the greater circularity of steel [16]. In the neodymium–yttrium aluminium

Table 1 Chemical composition of AA7475

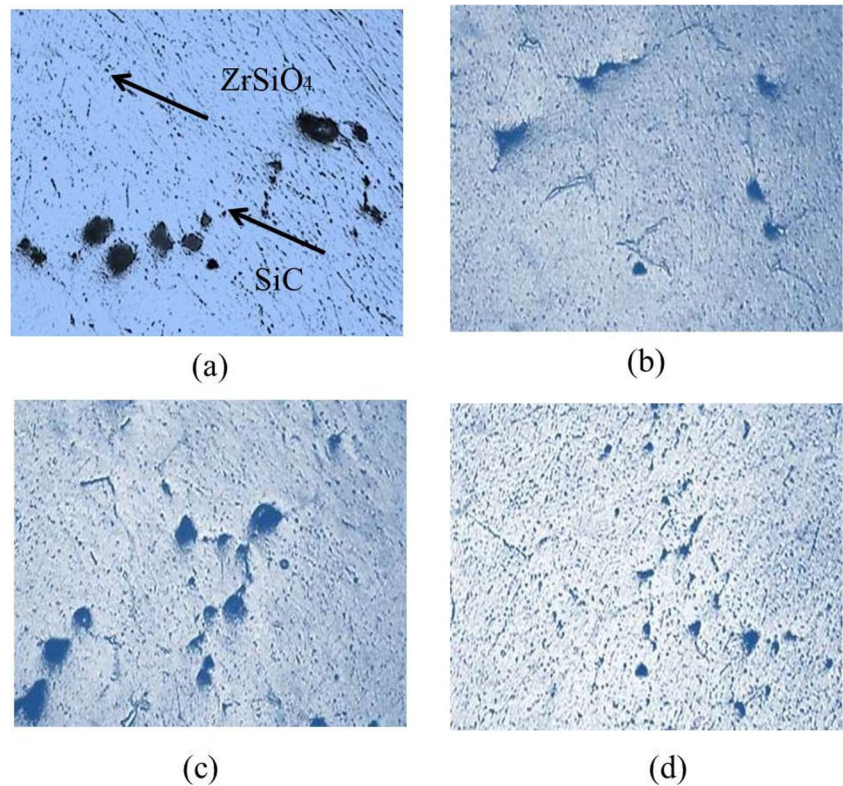
Element	AA	Si	Mg	Cr	others
Wt. %	90.3	1.5	2.3	0.22	Bal.

garnet (Nd:YAG) laser drilling, the 0.196° taper was observed with the use of the 600 μs pulse width, 2 pulses and 10 % wt. SiC in the laser drilling of Al/SiCp composite. With increase in SiC concentrations to aluminium, variations were made in the taper due to the non-uniform pressure generated in the processing [17]. Ultrasonic assistance pulsed Nd:YAG laser drilling was used for improvement to the surface roughness and reduces the taper angle of superalloy [18]. Millisecond pulsed and continuous wave lasers were used to produce 0.7 mm hole size in the aluminum MMC by using the 2 ms laser pulse and 2.5 kW peak power. The results showed that with an increase in laser power from 500 to 1000 W, the surface roughness varied from 6.57 to 7.00 μm [19]. During the CW laser cutting of Al₂O₃ reinforced Al MMC, the 3 μm surface roughness was observed with the use of the 1700 W power and 13 bar nitrogen gas pressure [20]. Variation in the continuous wave (CW) laser parameters such as laser power and working distance did not affect the hole diameter and increases in the hole depth of steel [21]. The addition of 15 % Wt. silicon carbide reinforced Ti6Al4V MMC by using direct metal CW laser sintering process. The results found that low density and high hardness were observed in the Ti6Al4V MMC [22]. The taper angle of 2.3° was observed in the steel by using the ultrasonic vibration-assisted CW CO₂ laser surface drilling [23]. Ultra short pulse laser machining is a promising technology for producing the diameters of less than 100 μm [24]. Hence, the performance of ultra-short pulse laser and micro-EDM was carried out on steel. The results found that ultra-short pulse lasers produced better roughness compared to micro-EDM [25]. The performance of direct cutting and helical cutting was carried out on steel and copper with the use of ultra-short pulse laser. The results found that less than 1 μm surface roughness was obtained in helical cutting [26]. The 20 to 40 μm hole diameter ranges were observed in Al, Ni, Cu and Ti alloy with the use of laser energy of 2 μJ from the ultra-short pulse laser [27]. In the ultra-short pulse laser was used for producing less taper angle in copper and it is found that the taper angle is highly related on the repetitions [28].

Table 2 Materials properties

Materials	AA7475	SiC	ZrSiO ₄
Melting point (°C)	546	2730	2550
Thermal conductivity (W/m.K)	138	490	3.5

Fig. 1 Microstructure of (a) AA7475/0 % SiC/15 % ZrSiO₄, (b) AA7475/5 % SiC/15 % ZrSiO₄, (c) AA7475/10 % SiC/15 % ZrSiO₄, and (d) AA7475/15 % SiC/15 % ZrSiO₄



To sum up, laser based machining is difficult to process on AMMC due to its hard reinforcement ceramic particles. Laser processing on micron level blind square holes has not yet been presented in the addition of 15 % ZrSiO₄ to AA7475/ xSiC (x = 0, 5, 10 and 15 % wt.). The primary aim of this work is to explore the machinability in the laser processing of various combinations of AA7475/SiC/ZrSiO₄ MMCs. A study of laser parameters effects on the machining characteristics is important. Laser parameters such as laser trepanning speed, power and standoff distance are selected as inputs. The performance measures such as hole size at entry (HS), surface roughness (SR) and taper angle (TA) were selected as outputs. More researches are focused on improving microstructure and mechanical properties of AMMCs [29–31] and analysis of

circular hole profile geometry [32–34] by laser processing. In this research work, an effort has made to minimize the hole size at entry, surface roughness and taper angle of AA7475/0 % SiC/15 % ZrSiO₄, AA7475/5 % SiC/15 % ZrSiO₄, AA7475/10 % SiC/15 % ZrSiO₄ and AA7475/15 % SiC/15 % ZrSiO₄ MMCs. Taguchi method is widely used for improving productivity with low cost. Hence, it was used in finding single optimum parameters [35]. Preference Ranking Organization METHod for Enrichment of Evaluations (PROMETHEE II) was selected for multiple criteria optimum problem [36]. The reasons for selecting the PROMETHEE II are complete outranking, real-life planning and user-friendly. The PROMETHEE II based Adaptive Network Based Fuzzy Inference System (ANFIS) was used for modelling the

Fig. 2 (a) Schematic view of laser and (b) SEM images of laser processed composite

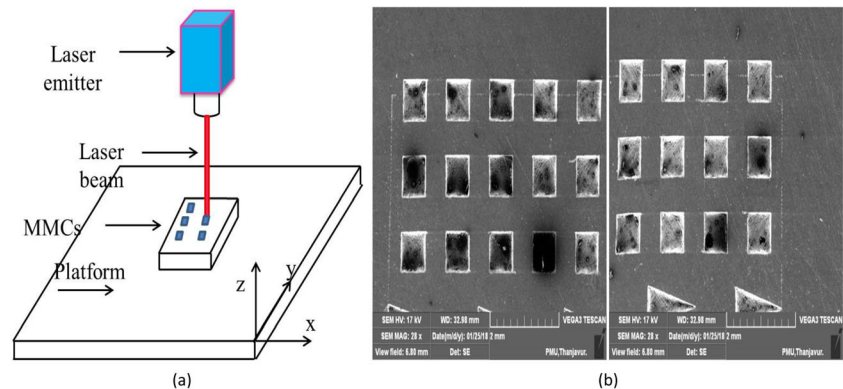


Table 3 Selection of machining parameters and its levels

Machining parameters	unit	code	Levels						
			Below lower limit	1	2	3	4	5	Above upper limit
Laser trepanning speed	mm/s	A	low MRR	15	30	45	60	75	High SR
Laser power	W	B	low MRR	70	75	80	85	90	High taper angle
Standoff distance	mm	C	Poor surface integrity	190	192	194	196	198	Better surface integrity

responses. The research methodology, experimental procedure, results and discussions, microstructural analysis and compared with previous works are presented in the sections below.

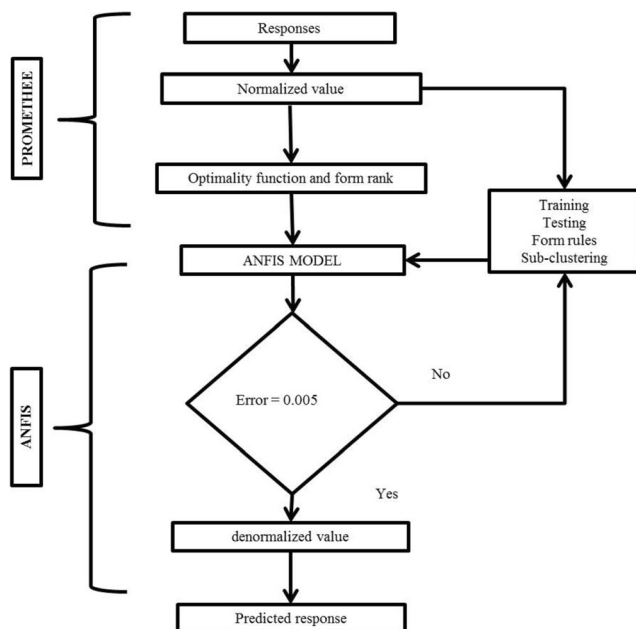
2 Materials and Methods

2.1 Fabrication of MMCs and Experimental Setup

Aluminium alloy (AA7475) was considered as the matrix. The chemical composition of matrix is shown in Table 1. Silicon carbide xSiC ($x = 5\%$, 10% and 15% in weight) and zirconium silicate (15% Wt. $ZrSiO_4$) were used as reinforcement. The material properties are shown in Table 2. The $64\ \mu\text{m}$ particle size of SiC and $87\ \mu\text{m}$ particle size of $ZrSiO_4$ were selected for fabricating composites. AMMCs were fabricated using the stir casting root. During the fabrications, AA7475 was melted in an electrically operated crucible furnace and heated up to 550°C for molten stage. In another furnace, the SiC and $ZrSiO_4$ were preheated to a limit of 750°C at 60 min. During the process, 20 gram of magnesium was

added for removing the absorbed hydroxide and improving wet ability. The molten matrix, SiC and $ZrSiO_4$ were uniformly mixed with stirrer speed of 450 rpm at 20 min. The hexachloroethane of 5 g was added in the casting process for slag removal. The microscopy images of AA7475/0 %SiC/15 %ZrSiO₄, AA7475/5 %SiC/15 %ZrSiO₄, AA7475/10 %SiC/15 %ZrSiO₄ and AA7475/15 %SiC/15 %ZrSiO₄ composites are shown in Fig. 1. In these microstructure results, the presence of SiC and $ZrSiO_4$ particles in the composites and their uniform distributions were seen. Ytterbium fiber laser process was selected (Meera Laser in Chennai, India) for the experimental work. The schematic view of laser system and SEM images of laser processed material is shown in Fig. 2. Laser speed, power and standoff distance was selected as input parameters. As per design of experiment, the L25 was selected for three factors and five levels.

The limits of laser machining factors were selected from a sample tests and machine limits. There were some problems raised in the selection of process parameters during the machining of selected AAMMC combinations by trial and error methods. The parameters and their levels are shown in Table 3. The depth of cut is an important response. The selection of process parameters for machining MMCs are greatly affected the depth of cut due to the thermal properties differences between the matrix and hard reinforced particles. Also, low MRR, High SR, High taper angle and poor surface integrity is raised in the machining AA7475/0 %SiC/15 %ZrSiO₄, AA7475/5 %SiC/15 %ZrSiO₄, AA7475/10 %SiC/15 %ZrSiO₄ and AA7475/15 %SiC/15 %ZrSiO₄ MMCs. The square hole size at entry, surface roughness and taper angle were decided as outputs. 1074 nm wavelength and 25 kHz pulse frequency were fixed for processing in laser machine. Scanning electron microscope was used for measuring outputs.

**Fig. 3** Research methodology

2.2 Methodology

Selection of the design of the experiment used for conducting the experiment was done considering its structured approach and use in process improvement, process development and

Table 4 Design and responses for composites

No	A	B	C	Hole size at entry (mm)				Surface roughness (μm)				Taper angle (degree)			
				x=0	x=5	x=10	x=15	x=0	x=5	x=10	x=15	x=0	x=5	x=10	x=15
1	1	1	1	0.913	0.924	0.932	0.943	2.198	2.682	3.121	3.363	0.237	0.265	0.289	0.315
2	1	2	2	0.910	0.921	0.929	0.940	2.112	2.577	2.999	3.231	0.231	0.259	0.282	0.307
3	1	3	3	0.906	0.917	0.925	0.936	2.199	2.683	3.123	3.364	0.249	0.279	0.304	0.331
4	1	4	4	0.900	0.910	0.918	0.929	2.096	2.557	2.976	3.207	0.223	0.250	0.272	0.297
5	1	5	5	0.900	0.911	0.919	0.930	2.256	2.752	3.204	3.452	0.234	0.262	0.285	0.311
6	2	1	2	0.901	0.913	0.922	0.932	2.223	2.734	3.179	3.423	0.256	0.289	0.315	0.343
7	2	2	3	0.896	0.908	0.917	0.926	2.287	2.813	3.270	3.522	0.259	0.293	0.319	0.347
8	2	3	4	0.900	0.911	0.920	0.930	2.457	3.022	3.514	3.784	0.258	0.292	0.318	0.346
9	2	4	5	0.902	0.914	0.923	0.933	2.123	2.611	3.036	3.269	0.242	0.273	0.298	0.324
10	2	5	1	0.911	0.923	0.932	0.942	1.696	2.086	2.425	2.612	0.212	0.240	0.261	0.284
11	3	1	3	0.884	0.894	0.903	0.913	2.256	2.797	3.204	3.452	0.276	0.315	0.337	0.367
12	3	2	4	0.891	0.901	0.910	0.920	2.157	2.675	3.063	3.300	0.270	0.307	0.329	0.359
13	3	3	5	0.891	0.901	0.910	0.920	2.145	2.660	3.046	3.282	0.256	0.292	0.312	0.340
14	3	4	1	0.901	0.912	0.921	0.931	1.944	2.411	2.760	2.974	0.243	0.277	0.296	0.323
15	3	5	2	0.898	0.909	0.917	0.927	1.792	2.222	2.545	2.742	0.224	0.255	0.273	0.298
16	4	1	4	0.883	0.895	0.903	0.913	2.124	2.655	3.037	3.271	0.289	0.332	0.355	0.387
17	4	2	5	0.883	0.895	0.903	0.913	2.321	2.901	3.319	3.574	0.312	0.359	0.384	0.418
18	4	3	1	0.897	0.909	0.917	0.927	1.832	2.290	2.620	2.821	0.254	0.292	0.312	0.340
19	4	4	2	0.897	0.909	0.917	0.927	2.024	2.530	2.894	3.117	0.278	0.320	0.342	0.373
20	4	5	3	0.894	0.907	0.915	0.925	1.698	2.123	2.428	2.615	0.229	0.263	0.282	0.307
21	5	1	5	0.883	0.893	0.902	0.914	1.989	2.427	2.824	3.083	0.332	0.372	0.405	0.448
22	5	2	1	0.888	0.899	0.908	0.919	1.848	2.255	2.624	2.864	0.289	0.324	0.353	0.390
23	5	3	2	0.887	0.898	0.907	0.918	1.992	2.430	2.829	3.088	0.298	0.334	0.364	0.402
24	5	4	3	0.888	0.899	0.908	0.919	1.954	2.384	2.775	3.029	0.287	0.321	0.350	0.387
25	5	5	4	0.888	0.899	0.908	0.919	1.872	2.284	2.658	2.902	0.326	0.365	0.398	0.440

product development. The benefits were lower development cost, lower operating cost and lower cost for poor quality. Taguchi method was selected for finding the single process parameters. More factors were considered to enable achievement of additional quality characteristics of the product. Hence, a multi objective optimization tool is used. Normally, grey relational analysis, desirability functional analysis, tabu search and etc., are used for solving multiple response problems. Hence, the Preference Ranking Organization METHod for Enrichment of Evaluations (PROMETHEE II) was used for finding optimum parameters. Integration of two methods is more beneficial than a single method. The PROMETHEE II based Adaptive Network Based Fuzzy Inference System (ANFIS) was selected for predicting the responses. The research methodology is shown in Fig. 3.

2.2.1 PROMETHEE II

PROMETHEE I was used for finding partial outranking of alternatives (responses). Hence, PROMETHEE II is

developed in order to find the complete outranking of alternatives and also avoiding errors in the decision making problems. The method is normally applied to the selection of a robot, water management, environmental management, financial management, energy management, logistics and transportation. The application of the PROMETHEE method is gradually increasing in the material processing field. The responses, hole size at entry, surface roughness and taper angle were considered as criteria. The experimental conditions selected were Alternatives (A). Hence, alternatives are forming from A1 to A25. There are two types of criteria, namely, beneficial criteria and non-beneficial criteria. Maximization is considered as the beneficial criterion whereas a non-beneficial criterion is considered to be minimization. Hence, hole size at entry and surface roughness was selected as non-beneficial criteria. Taper angle was selected as the beneficial criteria. The steps were following as.

Step 1: Normalization of responses using max min normalization method

Table 5 ANOVA for hole size, surface roughness and taper angle

Source	DF	Seq SS	Adj SS	Adj MS	F	P	Contribution percentage
Hole size at entry (mm)							
Trepanning speed	4	0.001211	0.001211	0.000303	20.78	0	62.79
Laser power	4	0.000123	0.000123	3.08E-05	2.12	0.142	6.40
Standoff distance	4	0.00042	0.00042	0.000105	7.2	0.003	21.76
Error	12	0.000175	0.000175	1.46E-05			9.06
Total	24	0.001929					100.00
S=0.00381750 R-Sq=90.94% R-Sq(adj)=81.87 %							
Surface roughness (μm)							
Trepanning speed	4	0.432	0.432	0.108	2.53	0.096	19.80
Laser power	4	0.71903	0.71903	0.17976	4.21	0.023	32.96
Standoff distance	4	0.5179	0.5179	0.12948	3.03	0.061	23.74
Error	12	0.51256	0.51256	0.04271			23.50
Total	24	2.1815					100.00
S=0.206672 R-Sq=76.50% R-Sq(adj)=53.01 %							
Taper angle (deg)							
Trepanning speed	4	0.031362	0.031362	0.00784	15.62	0	64.56
Laser power	4	0.006241	0.006241	0.00156	3.11	0.057	12.85
Standoff distance	4	0.004949	0.004949	0.001237	2.46	0.101	10.19
Error	12	0.006024	0.006024	0.000502			12.40
Total	24	0.048576					100
S=0.0224048 R-Sq=87.60% R-Sq(adj)=75.20%							

Fig. 4 The effect of trepanning speed over: (a) hole size, (b) surface roughness and (c) taper angle of various composites

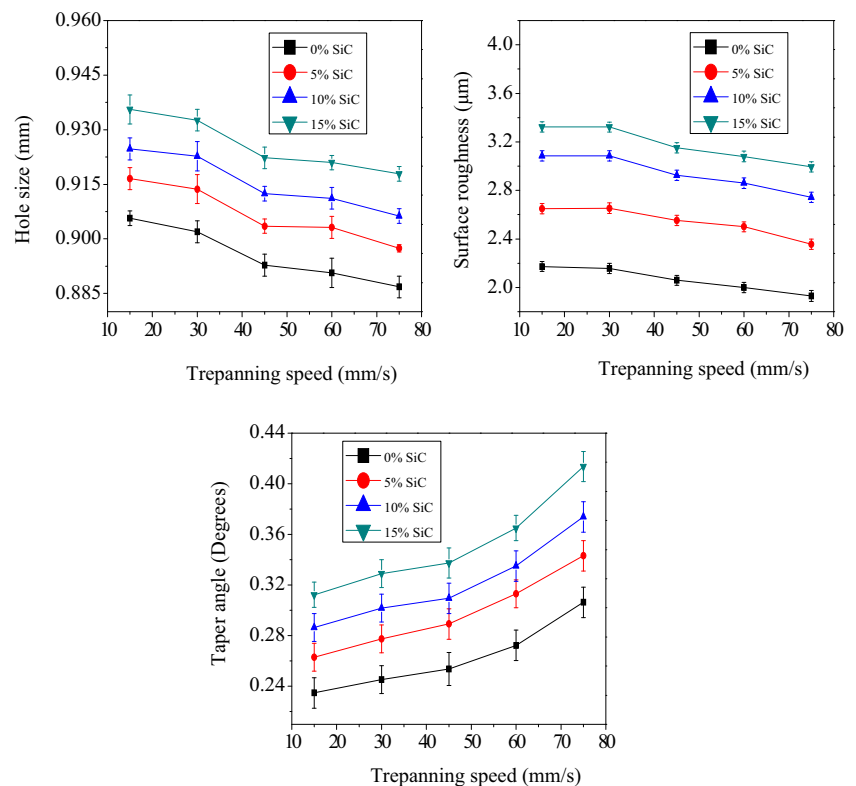
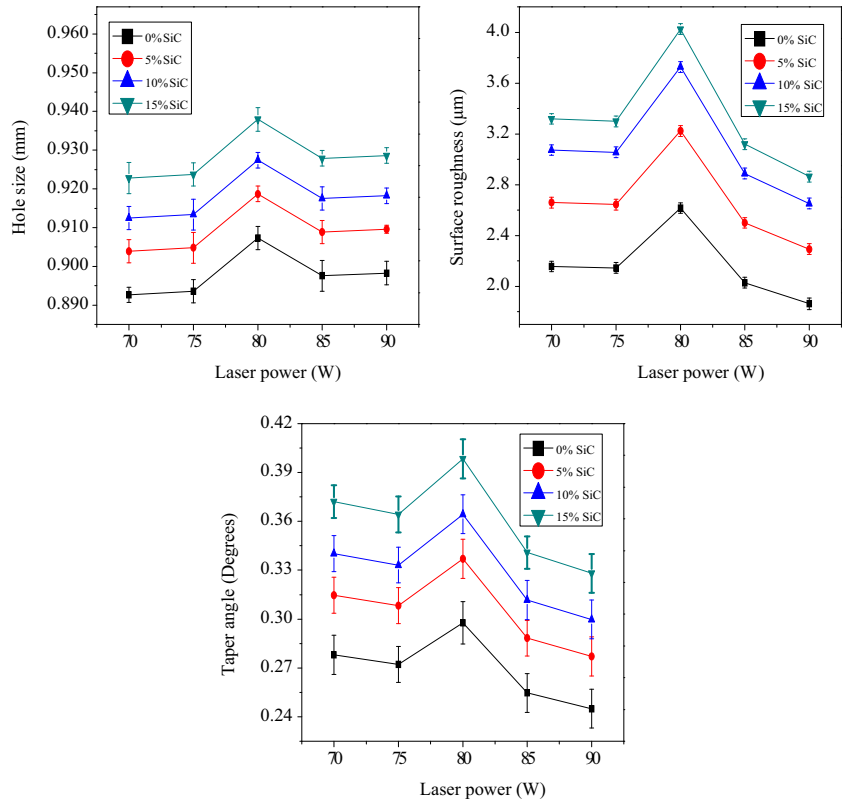


Fig. 5 The effect of laser power over hole size, surface roughness and taper angle of various composites



$$Z_{ij} = \frac{y_{ij} - (y_{ij}, i = 1, 2, , n)}{(y_{ij}, i = 1, 2, , n) - (y_{ij}, i = 1, 2, , n)} \quad (1)$$

(For larger the better)

$$Z_{ij} = \frac{(y_{ij}, i = 1, 2, , n) - y_{ij}}{(y_{ij}, i = 1, 2, , n) - (y_{ij}, i = 1, 2, , n)} \quad (2)$$

(For smaller the better)

Y is considered the responses.

Step 2: Preference function $P_j(a,b)$ was assigned to each j criteria by difference value of two alternatives (a, b). The difference in values obtained between positive and negative values was obtained. The negative value was changed into zero value. The positive value was kept as it was.

$$P_j(a, b) = 0, \text{ if } P_a \leq P_b \quad (3)$$

$$P_j(a, b) = 0, \text{ if } P_a > P_b \quad (4)$$

Step 3: Calculate the aggregated preference function

$$\pi(a, b) = \sum_{j=1}^k W_j P_j(a, b), \left(\sum_{j=1}^k W_j = 1 \right) \quad (5)$$

W_j is weight assigned in the criterion.

Step 4: Determine the leaving and entering outranking flow.

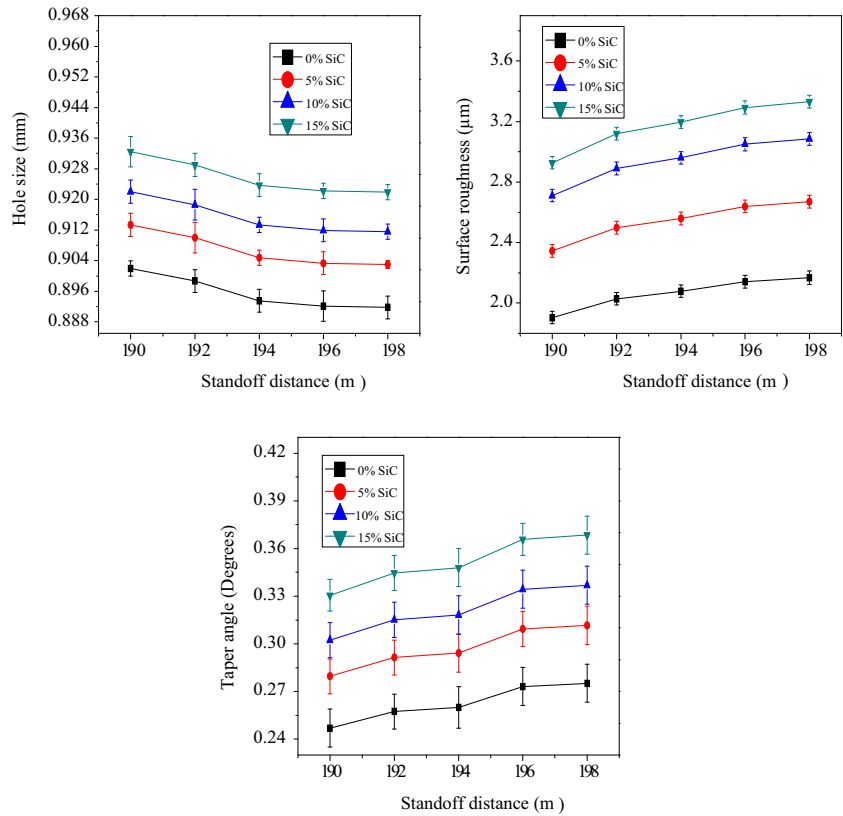
Step 5: Determine the net outranking flow for each alternative

$$\phi^+(a) = \frac{1}{n-1} \sum_{x \in A} \pi(a, x) \quad (6)$$

$$\phi^-(a) = \frac{1}{n-1} \sum_{x \in A} \pi(a, x) \quad (7)$$

$$\phi(a) = \phi^+(a) - \phi^-(a) \quad (8)$$

Fig. 6 The effect of standoff distance over hole size, surface roughness and taper angle of various composites



Step 6: Form the rank based on the net outranking and considered as optimum parameters.

2.2.2 Adaptive Neuro-Fuzzy Inference System (ANFIS)

ANFIS is one of hybrid artificial intelligence models and is an integration of fuzzy logic with Artificial neural network. This type of integration produces an excellent result based on the robustness and accuracy and reduces the drawback of fuzzy logic and ANN. Takagi–Sugeno inference technique was employed and is forming nonlinear mapping between input and output using fuzzy IF–THEN rules. In the ANFIS model, five layers were used.

The first layer was used for obtaining new output O_{li} by supplying inputs x , y and z to the first layer using the generalized gaussian membership function μ . It is expressed in the following equations.

$$O_{1i} = \mu A_i(x), i = 1, 2, 3 O_{2i} = \mu B_{i-2}(y), i = 4, 5, 6 O_{3i} = \mu C_{i-3}(z), i = 7, 8, 9 \tag{9}$$

$$\mu(x) = e^{-(x-\frac{\mu_i}{\sigma_i})^2} \tag{10}$$

Where, A_i , B_i and C_i denoted as membership values of μ . The σ_i and ρ_i are denoted as sets of hypothesis parameters. The output for each node was found as follows.

$$O_{2i} = \mu A_i(x) \times \mu B_{i-2}(y) \times \mu C_{i-3}(z) \tag{11}$$

The output for second layer was normalized in the layer three by following equation

$$O_{3i} = \frac{w_i}{\sum_{i=1}^2 w_i} \tag{12}$$

Then, output for layer three was transformed using the adaptive layer four.

$$O_{4,i} = -w_i f_i = -w_i(p_i x + q_i y + r_i z + s_i) \tag{13}$$

Where, p , q , r and s denoted the associated parameters of i node.

Table 6 Decision matrix

Criterion Criterion type	Hole size at entry (mm) Non-beneficial attributes	Surface roughness (μm) Non-beneficial attributes	Taper angle (degree) Beneficial attributes
Weight	0.3	0.3	0.4
A1	0.943	3.363	0.315
A2	0.94	3.231	0.307
A3	0.936	3.364	0.331
A4	0.929	3.207	0.297
A5	0.93	3.452	0.311
A6	0.932	3.423	0.343
A7	0.926	3.522	0.347
A8	0.93	3.784	0.346
A9	0.933	3.269	0.324
A10	0.942	2.612	0.284
A11	0.913	3.452	0.367
A12	0.92	3.3	0.359
A13	0.92	3.282	0.34
A14	0.931	2.974	0.323
A15	0.927	2.742	0.298
A16	0.913	3.271	0.387
A17	0.913	3.574	0.418
A18	0.927	2.821	0.34
A19	0.927	3.117	0.373
A20	0.925	2.615	0.307
A21	0.914	3.083	0.448
A22	0.919	2.864	0.39
A23	0.918	3.088	0.402
A24	0.919	3.029	0.387
A25	0.919	2.902	0.44

The output of the model is as following

$$O_5 = \sum_i -w_i f_i \quad (14)$$

The drawbacks of ANFIS are slow convergence in training and trapping in local optima. Hence, hybrid modelling is developed by integrating two methods.

3 Results and Discussion

L25 design layout and recorded responses are shown in Table 4. The primary purpose of this work is the reinforcement of the influence of 5 %, 10 %, 15 % SiC and 15 % ZrSiO₄ to AA7475 for preparing AMMCs were using stir casting. Laser processing was carried out on AA7475/0 % SiC/ 15 % ZrSiO₄, AA7475/5 % SiC/ 15 % ZrSiO₄, AA7475/10 % SiC/ 15 % ZrSiO₄ and AA7475/15 % SiC/ 15 % ZrSiO₄ MMCs as per the design of experiment. The hole

size at entry, surface roughness and taper angle of MMCs were measured. Addition of 15 % SiC and 15 % ZrSiO₄ reinforced to AA7475 produced better result compared to other combination results. Hence, AA7475/15 % SiC/ 15 % ZrSiO₄ MMC was selected for a further study. The most influential laser factors were identified using Analysis of Variance (ANOVA). A study of the effects of laser trepanning speed, power and standoff distance on hole size at entry, surface roughness and taper angle of MMCs was made. PROMETHEE II method was used for finding optimum value. Integration of PROMETHEE based ANFIS model was developed for prediction. Finally, the microstructural defects of composites are studied.

3.1 Analysis of Variance

The experimental results used for the construction of the ANOVA table using statistical software are shown in Table 5. ANOVA tests have carried out in 95 % confidence

Table 7 Ranking for alternative

Rank	Alternative	Ranking flows		
		φ^+	φ^-	φ
25	A1	0.020	0.224	-0.204
24	A2	0.032	0.199	-0.167
21	A3	0.041	0.162	-0.121
20	A4	0.055	0.174	-0.119
22	A5	0.033	0.168	-0.135
23	A6	0.054	0.192	-0.137
17	A7	0.083	0.166	-0.083
18	A8	0.060	0.152	-0.092
19	A9	0.045	0.144	-0.098
13	A10	0.146	0.146	0.001
8	A11	0.204	0.138	0.065
12	A12	0.147	0.139	0.007
15	A13	0.128	0.133	-0.004
16	A14	0.099	0.148	-0.049
10	A15	0.148	0.130	0.018
5	A16	0.245	0.146	0.100
3	A17	0.303	0.144	0.159
14	A18	0.156	0.158	-0.003
11	A19	0.154	0.144	0.009
9	A20	0.189	0.144	0.046
1	A21	0.406	0.156	0.250
4	A22	0.278	0.159	0.119
6	A23	0.267	0.169	0.098
7	A24	0.236	0.164	0.072
2	A25	0.377	0.171	0.206

Table 8 Rank comparison based on the GRA, DFA and proposed algorithm

S. No.	GRA [51]	DFA [52]	Proposed algorithm
1	25	23	25
2	24	22	24
3	23	19	21
4	18	21	20
5	22	20	22
6	19	16	23
7	17	15	17
8	21	23	18
9	20	18	19
10	10	23	13
11	5	11	8
12	13	10	12
13	14	12	15
14	16	14	16
15	11	17	10
16	4	6	5
17	3	9	3
18	12	8	14
19	15	7	11
20	6	13	9
21	1	1	1
22	7	3	4
23	8	4	6
24	9	5	7
25	2	2	2

interval. The inference from the ANOVA calculation, it was that hole size at entry and taper angle was primarily influenced by trepanning speed [37]. The contribution of trepanning speed was greater than the standoff distance and power. This was identified by p value lesser than 0.05. Surface roughness was insignificant by selected factors due to its p value. The experimental error for hole size at entry was better than the surface roughness. The surface roughness was insignificant by selected paper due to the higher variability in the responses. The R-squared and R-squared (Adjusted) for surface roughness was lower than hole size at entry and the taper angle. The low R-squared value shows the higher variability in the surface roughness value [38]. Normally, the R-squared and R-squared (Adjusted) are linearly related. On increasing the number of input process parameters, R-squared and R-squared (Adjusted) may be increased. The surface roughness results were in agreement with other works [39]. But, there was not agreement of the taper angle with other works [40]. This is because of laser power's influential factor in spite of laser speed.

3.2 Laser Trepanning Speed

Deviations were seen in the hole size at entry, surface roughness and taper angle of different MMCs by increasing the trepanning speed. Details are presented in Fig. 4. On increasing the trepanning speed of laser, there was a decrease in hole size of composites for all the combinations of the composites. This was due to shorter laser processing time on composite resulting in a decrease in the metal removal rate. In another mechanism, as a result of reducing the processing time, the lesser laser power was used for strike on the composite. Hence, heat affected zone was reduced. This was also reason for decreasing the hole size. A lower hole size was observed in the 0% SiC. This was due to the lesser heat required for melting the AA7475 and ZrSiO₄. Similar mechanisms were observed in the previous works [41]. With increase in the addition of SiC particles to aluminium alloy, the hole size at entry was increased due to the change in reinforced particles in the cutting front dynamics [42]. There was a decrease in surface roughness of composites through increase in the

Table 9 Training parameters for the ANFIS integrated with PROMETHEE II model

Description	values
No. of membership function at each input level	3 (Hole size), 3 (surface roughness) and 3 (taper angle)
Type of membership function for input	trapmf
Type of membership function for output	Constant
Method of optimization	Backpropagation
Error tolerance	0.005
No. of epochs	500

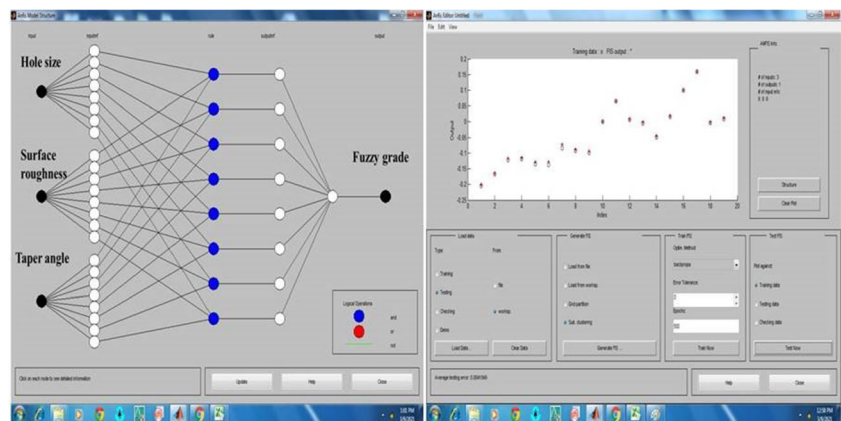
trepanning speed of laser for all the combinations of composites. This was due to the combinational laser factor effects on composites and sufficient energy deposited in the machining zone for clear cut. Similar results were seen in the earlier works [43]. An increase in the addition of SiC particles to aluminium alloy, resulted in an increase in the surface roughness due to the change in reinforced particles in the cutting front dynamics. There was an increase in taper angles of holes, following an increase in the trepanning speed of laser. This was due to the relational between hole size at entry and exit. The reason for increasing taper was due to the variation in the entry and exit of hole size and difference in metal removal

rate. The feed rate of laser beam was highly related to the heat affected zone formation on the hole. Hence, damage is reduced using the higher laser speed [44].

3.3 Laser Power

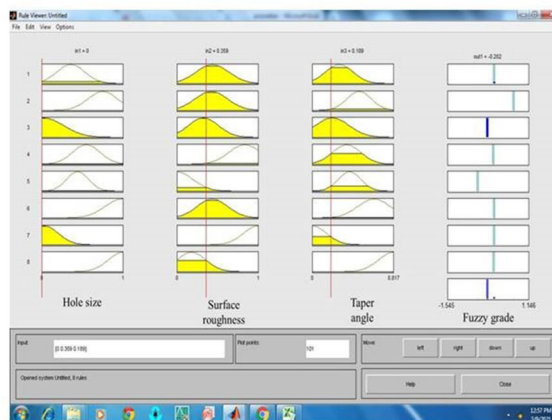
The effects of laser power on hole size at entry, surface roughness and taper angle of different MMCs are shown in Fig. 5. Increment in hole size up to the power of 80 W was observed followed by a decrease. Increase in hole size was due to increase in the energy per pulse. The hard ceramic particles restricted molten metal formation following

Fig. 7 (a) ANFIS Structure, (b) Training error and (c) Rules viewer



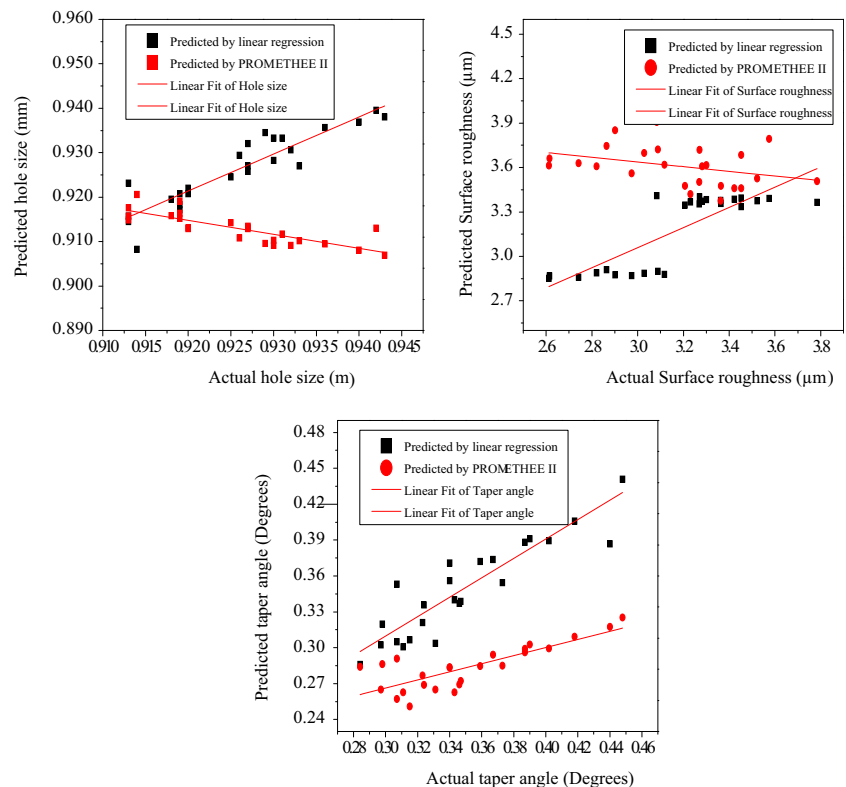
(a)

(b)



(c)

Fig. 8 Experimental and predicted value for 15 %SiC



the supply of 80 W power due to the presence of re-solidified molten metal. Therefore, hole size was reduced. There was an increase in the thermal damages seen on the machined holes. Increment in hole sizes were observed with the addition of SiC particles to the aluminium alloy. This was due to the unburnt SiC particles presented in the state and improper thermal reaction between the matrix and ceramic particles. Differences in the melting point of matrix and ceramic particles were the reason. Similar results were observed in the works [45]. Surface roughness had a similar behaviour. With increase in the laser power, surface roughness increased due to the striation developed on the machined surface for increasing the surface roughness and unburnt SiC and ZrSiO₄ presented in the machined surfaces [46]. An increase in the addition of SiC particles to the aluminium alloy, was followed by a decrease in the taper angle due to the variations in the entry and exit of hole size and difference in melting point. Compared to hole size at entry, hole size at exit was less. Hence, taper angle was reduced by raising the power. Similar results were observed in the works [47, 48].

3.4 Standoff Distance

Variations in the hole size at entry, surface roughness and taper angle of different MMCs were made by increasing the standoff distance. Details are presented in Fig. 6. On increasing the standoff distance, there was a decrease in the

hole size owing to the focal plane set being closer to the composite resulting in beam diameter reduced. Hence, a higher hole size was seen with the use of low standoff distance. An increase in the standoff distance, was followed by an increase in the surface roughness due to the unburnt SiC and ZrSiO₄ present in the machined surfaces. Similarly, an increase in the standoff distance, was followed by an increase in taper angle due to the higher thermal interaction between the laser beam and composite and as a result, more melting [49]. The standoff distance had a big effect on the thermal stress developed and heat affected zone formation in the machined hole. A reduction in the standoff distance has a big effect on the taper hole formation due to changes in laser beam shape. Figures 4, 5 and 6 shows the addition of reinforcement to aluminium alloy making considerable variations in the hole size at entry, surface roughness and taper angle. In this case, the addition of SiC percentage to aluminium alloy, responses also increased. The 546 °C melting point and 138 W/m k thermal conductivity of AA7475 restricted the heat input for melting and vaporizing the material. SiC and ZrSiO₄ retained the heat input due to the poor thermal conductivity. SiC and ZrSiO₄ melting points were 2730 °C and 2550 °C respectively. More melting point deviations were observed between the matrix and reinforcement creates heterogeneity in melting. A rise in the heat input to the aluminium composites, resulted in the aluminium alloy melts in the beginning and holding the heat input retained for melting

Table 10 Experimental and numerical results of hole size, surface roughness and taper angle

S.No.	Predicted by linear regression			Predicted by PROMETHEE II			Deviation in % between Actual vs. linear regression			Deviation in % between Actual vs. PROMETHEE II		
	HS	SR	TA	HS	SR	TA	HS	SR	TA	HS	SR	TA
1	0.938	3.379	0.306	0.907	3.375	0.251	0.522	-0.476	2.705	3.824	-0.364	20.358
2	0.937	3.368	0.305	0.908	3.420	0.257	0.332	-4.249	0.632	3.396	-5.843	16.253
3	0.936	3.358	0.304	0.910	3.476	0.265	0.034	0.190	8.266	2.829	-3.331	19.947
4	0.934	3.347	0.302	0.910	3.477	0.265	-0.590	-4.362	-1.758	2.094	-8.426	10.727
5	0.933	3.336	0.301	0.909	3.461	0.263	-0.353	3.355	3.280	2.244	-0.255	15.484
6	0.931	3.387	0.340	0.909	3.461	0.263	0.148	1.052	0.857	2.454	-1.105	23.369
7	0.929	3.376	0.339	0.911	3.527	0.272	-0.369	4.137	2.409	1.638	-0.149	21.573
8	0.928	3.366	0.337	0.910	3.507	0.269	0.191	11.057	2.538	2.116	7.314	22.157
9	0.927	3.355	0.336	0.910	3.504	0.269	0.641	-2.628	-3.642	2.441	-7.179	17.024
10	0.940	2.853	0.286	0.913	3.612	0.284	0.263	-9.215	-0.697	3.078	-38.300	-0.019
11	0.923	3.395	0.374	0.915	3.685	0.294	-1.113	1.651	-1.809	-0.205	-6.749	19.833
12	0.922	3.384	0.372	0.913	3.617	0.285	-0.213	-2.555	-3.682	0.747	-9.607	20.695
13	0.921	3.374	0.371	0.913	3.609	0.284	-0.083	-2.791	-9.059	0.769	-9.968	16.588
14	0.933	2.871	0.321	0.912	3.562	0.277	-0.243	3.450	0.625	2.072	-19.755	14.261
15	0.932	2.861	0.320	0.913	3.629	0.286	-0.546	-4.329	-7.235	1.465	-32.333	3.920
16	0.916	3.403	0.407	0.916	3.720	0.299	-0.296	-4.035	-5.225	-0.304	-13.739	22.695
17	0.915	3.392	0.406	0.918	3.792	0.309	-0.164	5.084	2.919	-0.505	-6.108	26.022
18	0.927	2.890	0.356	0.913	3.608	0.283	0.000	-2.449	-4.700	1.522	-27.891	16.644
19	0.926	2.879	0.355	0.913	3.618	0.285	0.129	7.623	4.944	1.493	-16.081	23.627
20	0.925	2.869	0.353	0.914	3.662	0.291	0.043	-9.702	-15.029	1.158	-40.045	5.205
21	0.908	3.411	0.441	0.921	3.908	0.325	0.630	-10.639	1.607	-0.718	-26.744	27.377
22	0.921	2.909	0.391	0.916	3.745	0.303	-0.189	-1.564	-0.251	0.283	-30.754	22.414
23	0.920	2.898	0.390	0.916	3.721	0.299	-0.168	6.150	3.095	0.240	-20.508	25.549
24	0.918	2.887	0.388	0.915	3.699	0.296	0.072	4.675	-0.295	0.411	-22.110	23.480
25	0.917	2.877	0.387	0.919	3.851	0.318	0.202	0.872	12.109	-0.014	-32.716	27.840

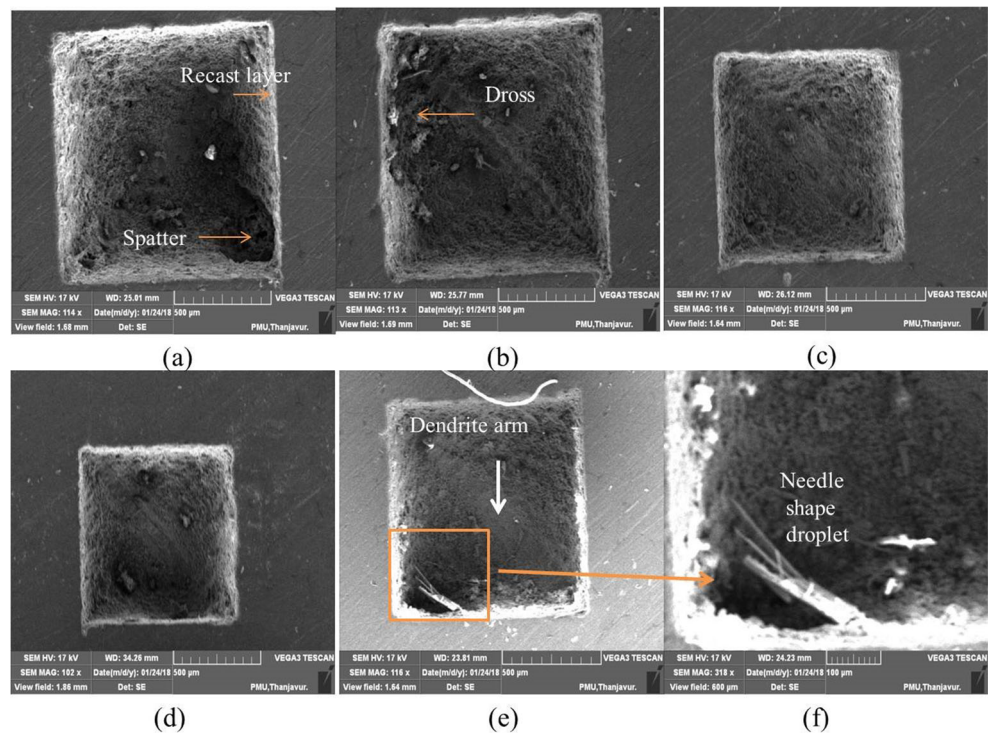
of the reinforcements due to the higher percentage of aluminium in the composites. The higher thermal interaction formed the oxide layer, heat-affected zone and dross inclusions. The dimensional deviations of holes were obtained due to the differences in optical absorption between the matrix and reinforcement [50]. The addition of heat input and SiC reinforced with aluminium alloy caused an increase in the higher thermal damages. Compared to reinforcement aluminium composites, the aluminium alloy was produced the minimum hole size, surface roughness and taper angle due to the induced minimum thermal stress. Therefore, higher hole size, surface roughness and taper angle for aluminium hybrid composite is obtained compared to aluminium alloy.

3.5 PROMETHEE II

The responses, hole size at entry (weight = 0.3), surface roughness (weight = 0.3), and taper angle (weight = 0.4) were considered as criteria. The weights were assigned

by an industrial expert. The decision matrix for PROMETHEE II is shown in Table 6. The first step was normalization of responses using the min max normalization method. The second step was calculation of preference function $P_j(a,b)$. The third step was calculation of the aggregated preference function. The fourth step was used for finding the leaving and entering outranking flow. The fifth step was used to find the net outranking flow of each alternative. Finally, the sixth step was used for forming rank of alternatives and identified optimum process parameters. Details of the ranking for alternatives are shown in Table 7. The 21st experimental number produced the optimum process parameters (trepanning speed = 75 mm/s, laser power = 70 W and standoff distance = 198 mm). In order to check the consistent of proposed algorithm result with grey relational analysis and desirability function analysis results and it is found that rank of the proposed algorithm, grey relational analysis and desirability function analysis is similar and it is shown in Table 8.

Fig. 9 Microstructure of the laser drilled surface hole for 15 %SiC



3.6 PROMETHEE II Based ANFIS Modelling

The experimental value for hole size at entry, surface roughness and taper angle were converted into normalized form using min-max normalization method based on the objective of the responses. The ANFIS models were developed using the MATLAB tool box. In the PROMETHEE II based ANFIS model, 19 experimental values for training and 6 experimental values for testing was considered. The hole size at entry, surface roughness and taper angle were considered as inputs to sugeno ANFIS model whereas net outranking was considered as output. Details relating to the ANFIS training are shown in Table 9. The ‘trapmf’ membership functions with 25 rules for ANFIS architecture are generated to the input data. Normalization of hole size at entry, surface roughness and taper angle were input to ANFIS model for achieving errors lesser than 0.005. The fuzzy grade was converted to a denormalized form. Details of ANFIS model structure, editor for training error and rule viewer are shown in Fig. 7. Based on the normalized value of hole size at entry, surface roughness and taper angle, ANFIS training conditions, fuzzy grade were observed and converted into denormalized values. Regression model, PROMETHEE II based ANFIS modelling showed the experimental values and predicted values as closer. Details are shown in Fig. 8. Table 10 shows experimental and numerical results of hole size, surface roughness and taper angle and found that percentages of deviations are less in linear regression.

3.7 Microstructural Analysis

Figure 9 shows the scanning electron microstructure for 1st, 5th, 10th, 15th and 25th experimental conditions. Recast layer, spatter, dross and dendrite arm were seen in the laser processed 15 % SiC composite. Dendrite arm was seen in the machined surface for confirmation of aluminium based metal matrix composite. Formation of a thin recast layer was seen on the micro square hole rims of the laser processed composite due to the molten materials quickly re-solidified on the machined composites adhered in the sidewalls of the hole surface. Formation of a recast layer has also been in the earlier works [53]. Spatter formation observed was due to the incomplete expulsion of ejected molten materials from the hole surface [54]. A needle shape droplet was found in the machined surface due to the increasing laser power. The 25th experimental result showed the needle shape droplet caused by an increase in the laser power. The magnified view of needle shape droplet was also seen in the machined surface. Inclusions/dark inclusions are a common problem in metal matrix casting during casting. An inclusion is a participle of distinct composition embedded in a processed material. In the metal casting industry, the term has a specific meaning – referring to unwanted particles of dross, refractory materials, sand or deoxidation products trapped in metal castings. Inclusions can be caused by various factors, including impurities from the metal ingot or interaction of the other metal with the mould surfaces or the outside atmosphere. In shortly,

Table 11 Comparison of present results with published literatures

R. No.	Type of laser sources/Materials	Conditions used	Hole size (mm)	SR (μm)	TA ($^\circ$)
[11]	Pulsed mode/ AA2618/20%SiC	Power = 400 W Scanning speed=40 mm/s Pressure = 1.3 kg/cm ² Power=230/210 W Pressure = 9/12 kg/cm ² Lamp current=19 amp Pulse frequency=4.2 kHz, air pressure=2 kg/cm ² Lamp current=20.31 amp Pulse frequency=0.66 kHz	9 (Through Hole)	5.28	2.42
[12]	Pulsed Nd:YAG/ AA7075/10%SiC	Air pressure=0.66 kg/cm ² Lamp current = 23.12 amp Pulse frequency = 2.30 kHz Air pressure=1.800 kg/cm ² Power = 500–1000 W	Circularity = 0.978 (Through Hole)	-	3.5
[13]	Pulsed Nd:YAG/Alumina	Power = 1700 W Pressure=13 bar Laser energy=2 μJ	0.42 (Blind hole)	-	2.72
[14]	Pulsed Nd:YAG Al ₂ O ₃ - Al	Laser speed=2000 mm/min Power=1500 W SiC particles = 10 wt% Standoff distance=1.5 mm Pressure=10 bar Laser speed=3000 mm/min Power=2000 W	Not mentioned (Through Hole)	-	0.0251
[15]	Pulsed Nd:YAG /Ti/Al ₂ O ₃	SiC particles = 10 wt% Standoff distance=2.0 mm Pressure=14 bar Laser speed=75 mm/s Power=90 W standoff distance=96 mm	Circularity at entry=0.949, circularity at exit=0.9426 (Through Hole)	-	1.546
[19]	Millisecond pulsed and CW /Aluminum MMC		Not mentioned 0.7	6.57 to 7.00	-
[20]	CW laser / Al ₂ O ₃ +Al MMC		-	3	-
[27]	Ultra-short pulse laser		0.02–0.04 (blind hole)	-	-
[55]	CO ₂ laser / AA5052 + SiC		Kerf width = 0.228 mm	-	Kerf angle = 0.310
[38]	CO ₂ laser / AA5052 + SiC		-	1.21	-
Present results	Ytterbium fiber laser/ AA7475/10% SiC/ 15% ZrSiO ₄		0.919 (blind hole)	2.902	0.44

the dark inclusions formed on the all the machined surfaces were due to the oxide impurities formed by overheat.

3.8 Comparison with Previous Studies

Comparative studies were made in-between the previous published works and current study which is shown in Table 11. There were many factors affecting the performance measures of AA MMCs. Among the many factors, scanning speed, power and standoff distance were significantly affecting the performance measures. Hence, the factors were selected for processing. The laser machining of AA7475/15 % SiC/ 15 % ZrSiO₄ MMCs was a new observation in this work. Also, the MMCs have different melting temperatures and two different constituents. Therefore, it is essential to monitor how the SiC and ZrSiO₄ particles react with thermal processes for square profile cutting in nature. Normally, the geometry of any machined shape can be defined in a number of ways such as circularity, feret's diameter, squareness and aspect ratio. Hence, all the above names were purely based on the metal removal. The laser trepanning speed, laser power and standoff distance is a major affecting the hole size. The sample tests identified that the low MRR is obtained by lowering below the trepanning speed of 15 mm/s and higher surface roughness is obtained by increasing above the trepanning speed of 75 mm/s. Similarly, the low MRR is obtained by lowering below the power of 70 W and higher taper angle is obtained by increasing above the power of 90 W. The variations are due to the melting point and thermal conductivity of matrix and reinforcement. Similarly the standoff distance greatly affected the surface integrity of the machined surface. Laser speed of 75 mm/s, power of 90 W and standoff distance of 96 mm for current results are producing the hole size of 0.919 in the MMCs. The hole size obtained in the current study is better than the previous studies [12, 15]. The perfect hole sizes are denoted normally as above 0.9 values. This is due to the fact that the thermal properties of AA7075/10 %SiC and Tin/Al₂O₃ composites are approximately closer with AA7475/10 % SiC/ 15 % ZrSiO₄. The SR obtained in the current study is lower than the previous studies [11, 19] and higher than the previous studies [20, 38]. This is due to the variations in the selection of process parameters. The taper obtained in the current study is lower than the previous studies [14] and higher than the previous studies [11–13, 15]. This is also due to the variations in the selection of process parameters.

4 Conclusions

Micron level blind square holes have been processed on AA7475/SiC/ZrSiO₄. The effects of laser process parameters and various percentages of SiC addition to AA7475/ ZrSiO₄

composites using stir casting to study the hole size, surface roughness and taper angle are also shown. Conclusions are:

- Among the various process input parameters, the laser trepanning speed has more effect on the all responses.
- The addition of SiC percentage to aluminium alloy causes an increase in all the responses.
- PROMETHEE II algorithm produces consistent results with grey relational analysis and desirability functional analysis.
- PROMETHEE II based ANFIS modelling has produces good predictions.
- Low power is suggested for minimizing thermal damages in the machined surfaces.

Acknowledgements The authors thank the MEERA laser solutions at Chennai for providing laser machining facilities. They are also thankful to Periyar Maniammai Institute of Science & Technology at Vallam for providing scanning electron microscopy facilities.

Author Contributions V. Senthil Kannan: Conceptualization, Methodology, Writing Reviewing discussion and Editing. K. Lenin: computation, Methodology, Software, Writing discussion and D. Srinivasan: Conceptualization and analysis, Writing-review, writing manuscript, Methodology, Software, and writing – discussion, D. Raj Kumar: review manuscript language,

Funding The authors declare that no firm was supported in this research and own fund was used for completing the doctorate degree.

Data Availability The available data and material had been used and discussed in the manuscript.

Declarations

Conflict of Interest The authors declare that they have no conflict of interest.

Consent to Participate All persons named as authors in this manuscript have participated in the planning, design and performance of the research, and in the interpretation of the results.

Consent for Publication All authors have endorsed the publication of this research.

Ethics Declarations The manuscript has not been published elsewhere and it has not been submitted simultaneously for publication elsewhere.

Declaration of Competing Interest The authors declare that they have no known competing financial interests or personal relationships that could have appeared to influence the work reported in this paper.

References

1. Thirukkumaran K, Mukhopadhyay CK (2021) Analysis of acoustic emission signal to characterization the damage mechanism during drilling of Al-5 %SiC. *Metal Matrix Compos Silicon* 13:309–325

2. Manna A, Bhattacharayya B (2003) A study on machinability of Al/SiC-MMC. *J Mater Process Technol* 140:1–3
3. Kılıçkap E, Cakır O, Aksoy M, Inan A (2005) Study of tool wear and surface roughness in machining of homogenised SiC-p reinforced aluminium metal matrix composite. *J Mater Process Technol* 164:862–867
4. Balasubramaniam V, Rajkumar D, Ranjithkumar P, Narayanan CS (2021) Comparative study of mechanical technologies over laser technology for drilling carbon fiber reinforced polymer materials. *Indian J Eng Mater Sci (IJEMS)* 27(1):19–32
5. Maity KP, Choubey M (2019) A review on vibration-assisted EDM, micro-EDM and WEDM. *Surf Rev Lett* 26:05
6. Suresh Kumar S, Uthayakumar M, Thirumalai Kumaran S, Parameswaran P, Mohandas E (2014) Electrical discharge machining of Al (6351)-5 % SiC-10 % B4C hybrid composite: a grey relational approach. *Model Simul Eng* 2014
7. Baburaja K, Teja SS, Sri DK, Kuldeep J, Gowtham V (2017) Manufacturing and machining challenges of hybrid aluminium metal matrix composites. In: *IOP Conference Series: Materials Science and Engineering*, vol. 225, No. 1. IOP Publishing, Bristol, p 012115
8. Wang Y, Yang LJ, Wang NJ (2002) An investigation of laser-assisted machining of Al₂O₃ particle reinforced aluminum matrix composite. *J Mater Process Technol* 129(1–3):268–272
9. Marimuthu S, Dunleavy J, Smith B (2019) Laser based machining of aluminum metal matrix composites. *Procedia CIRP* 85:243–248
10. Umesh K, Sudarsan G, Krishnaswamy H (2016) Optimization of machining parameters for satisfying the multiple objectives in machining of MMCs. *Mater Manuf Process* 32(10):1082–1093
11. Müller F, Monaghan J (2000) Non-conventional machining of particle reinforced metal matrix composite. *Int J Mach Tools Manuf* 40(9):1351–1366
12. Yunus M, Alsoufi MS (2019) Mathematical modeling of multiple quality characteristics of a laser microdrilling process used in Al7075/SiCp metal matrix composite using genetic programming. *Model Simul Eng* 2019
13. Kuar AS, Acherjee B, Ganguly D, Mitra S (2012) Optimization of Nd: YAG laser parameters for microdrilling of alumina with multiquality characteristics via grey-Taguchi method. *Mater Manuf Process* 27(3):329–336
14. Kuar AS, Paul G, Mitra S (2006) Nd: YAG laser micromachining of alumina-aluminium interpenetrating phase composite using response surface methodology. *Int J Mach Mach Mater* 1(4):432–444
15. Biswas R, Kuar AS, Biswas SK, Mitra S (2010) Effects of process parameters on hole circularity and taper in pulsed Nd: YAG laser microdrilling of Tin-Al₂O₃ composites. *Mater Manuf Process* 25(6):503–514
16. Ghoreishi M, Low DKY, Li L (2002) Comparative statistical analysis of hole taper and circularity in laser percussion drilling. *Int J Mach Tools Manuf* 42(9):985–995
17. Padhee S, Pani S, Mahapatra SS (2012) A parametric study on laser drilling of Al/SiCp metal-matrix composite. *Proc Inst Mech Eng B J Eng Manuf* 226(1):76–91
18. Wang H, Xu G, Zhu S, Zhou W, Ren N, Xia K (2018) Comparison of percussion laser drilling quality with and without water-based ultrasonic assistance. *J Manuf Process* 36:175–180
19. Marimuthu S, Dunleavy J, Liu Y, Smith B, Kiely A, Antar M (2019) Characteristics of hole formation during laser drilling of SiC reinforced aluminium metal matrix composites. *J Mater Process Technol* 271:554–567
20. Marimuthu S, Dunleavy J, Liu Y, Antar M, Smith B (2019) Laser cutting of aluminium-alumina metal matrix composite. *Opt Laser Technol* 117:251–259
21. Alavi SH, Cowell C, Harimkar SP (2017) Experimental and finite element analysis of ultrasonic vibration – assisted continuous-wave laser surface drilling. *Mater Manuf Process* 32(2):216–225
22. Misra S, Hussain M, Gupta A, Kumar V, Kumar S, Das AK (2019) Fabrication and characteristic evaluation of direct metal laser sintered SiC particulate reinforced Ti6Al4V metal matrix composites. *J Laser Appl* 31(1):012005
23. Alavi SH, Harimkar SP (2016) Evolution of geometric and quality features during ultrasonic vibration-assisted continuous wave laser surface drilling. *J Mater Process Technol* 232:52–62
24. Tönshoff HK, Momma C, Ostendorf A, Nolte S, Kamlage G (2000) Microdrilling of metals with ultrashort laser pulses. *J Laser Appl* 12(1):23–27
25. Romoli L, Rashed CAA, Fiaschi M (2014) Experimental characterization of the inner surface in micro-drilling of spray holes: A comparison between ultrashort pulsed laser and EDM. *Opt Laser Technol* 56:35–42
26. He C, Zibner F, Fornaroli C, Ryll J, Holtkamp J, Gillner A (2014) High-precision helical cutting using ultra-short laser pulses. *Phys Procedia* 56:1066–1072
27. Zhao W, Liu H, Shen X, Wang L, Mei X (2020) Percussion drilling hole in Cu, Al, Ti and Ni alloys using ultra-short pulsed laser ablation. *Materials* 13(1):31
28. Büttner H, Hajri M, Roth R, Wegener K (2018) High aspect ratio microstructuring of copper surfaces by means of ultrashort pulse laser ablation. *Procedia Cirp* 68:190–195
29. Panwar RS, Pandey OP (2013) Analysis of wear track and debris of stir cast LM13/Zr composite at elevated temperatures. *Mater Charact* 75:200–213
30. Sharma V, Kumar S, Panwar RS, Pandey OP (2012) Microstructural and wear behavior of dual reinforced particle (DRP) aluminum alloy composite. *J Mater Sci* 47(18):6633–6646
31. Das S, Das K, Das S (2009) Abrasive wear behavior of Al-4.5 wt% Cu/(zircon sand + silicon carbide) hybrid composite. *J Compos Mater* 43(22):2665–2672
32. Du X, Rahaman A, Kar A, Chase M, Wolfe D, Mathy J, Yu X (2021) Laser processing over a large area by wavefront-controlled scanning. *J Laser Appl* 33(1):012052
33. Xia K, Wang H, Ren N, Ren X, Liu D, Shi C, Li T, Tian J (2021) Laser drilling in nickel super-alloy sheets with and without ultrasonic assistance characterized by transient in-process detection with indirect characterization after hole-drilling. *Opt Laser Technol* 134:106559
34. Wang R, Dong X, Wang K, Sun X, Fan Z, Duan W, Jun MBG (2021) Polarization effect on hole evolution and periodic microstructures in femtosecond laser drilling of thermal barrier coated superalloys. *Appl Surf Sci* 537:148001
35. Raj Kumar D, Jeyaprakash N, Yang C-H, Ramkumar KR (2020) Investigation on drilling behavior of CFRP composites using optimization technique. *Arab J Sci Eng* 45:8999–9014
36. Abdullah L, Chan W, Afshari A (2019) Application of PROMETHEE method for green supplier selection: a comparative result based on preference functions. *J Ind Eng Int* 15(2):271–285
37. Morar N, Roy R, Mehnen J, Nicholls JR, Gray S (2017) The effect of trepanning speed of laser drilled acute angled cooling holes on the high temperature low cycle corrosion fatigue performance of CMSX-4 at 850 C. *Int J Fatigue* 102:112–120
38. Sharma V, Kumar V (2016) Multi-objective optimization of laser curve cutting of aluminium metal matrix composites using desirability function approach. *J Braz Soc Mech Sci Eng* 38(4):1221–1238
39. Elango M, Annamalai K (2020) High speed machining and optimisation of Al/SiC/Gr hybrid metal matrix composites using ANOVA and grey relational analysis. *Aust J Mech Eng*
40. Bharatish A, Murthy HN, Anand B, Madhusoodana CD, Praveena GS, Krishna M (2013) Characterization of hole circularity and heat

- affected zone in pulsed CO₂ laser drilling of alumina ceramics. *Opt Laser Technol* 53:22–32
41. Chien WT, Hou SC (2007) Investigating the recast layer formed during the laser trepan drilling of Inconel 718 using the Taguchi method. *Int J Adv Manuf Technol* 33(3):308–316
 42. Lamikiz A, de Lacalle LL, Sanchez JA, Del Pozo D, Etayo JM, Lopez JM (2005) CO₂ laser cutting of advanced high strength steels (AHSS). *Appl Surf Sci* 242(3–4):362–368
 43. Dong GA, Kyung WB (2009) Influence of cutting parameters on surface characteristics of cut section in cutting of Inconel 718 sheet using CW Nd:YAG laser. *Trans Non Ferrous Metal Soc* 19:32–39
 44. Tagliaferri V, Visconti IC, Dillio A (1987) Machining of fiber reinforced material with laser beam: Cut quality evaluation. In: *Proceedings of the Sixth International Conference on Composite Materials*, pp 1190–1198
 45. Mahamani A, Anantha VV (2017) Investigation on laser drilling of AA6061-TiB₂/ZrB₂ in situ composites. *Mater Manuf Processes* 32(15):1700–1706
 46. Sharma A, Yadava V (2013) Modelling and optimization of cut quality during pulsed Nd:YAG laser cutting of thin Al-alloy sheet for curved profile. *Opt Lasers Eng* 51:77–88
 47. Wang CJ, Chen G, Luan D, Zhang P (2014) Effect of laser power on the quality of drilled micro hole using Cu₅₀Zr₅₀ amorphous alloys foils. *Micromachines* 5:1061–1068
 48. Pak AM, Moradi M (2015) Hole geometry features analysis in fiber laser percussion drilling process. *Int J Adv Mech Automobile Eng* 2:18–21
 49. Leone C, Pagano A, Lopresto V, Iorio ID. Solid state Nd: YAG laser cutting of CFRP sheet: Influence of process parameters on kerf geometry and HAZ. In *Proceedings of ICCM-17 Conference*, Edinburgh, July, 2009, 1–10
 50. Grabowski A, Nowak M, Śleziona J (2005) Optical and conductive properties of AlSi-alloy/SiCp composites: Application in modeling CO₂ laser processing of composites. *Opt Lasers Eng* 43:233–246
 51. Jeyaprakash N, Yang CH, Raj Kumar D (2020) Machinability study on CFRP composite using Taguchi based grey relational analysis. *Mater Today Proc* 21(3):1425–1431
 52. Rajkumar D, Ranjithkumar P, Narayanan CS (2017) Optimization of machining parameters on microdrilling of CFRP composites by Taguchi based desirability function analysis
 53. Morar NI, Roy R, Mehnen J, Marithumu S, Gray S, Roberts T, Nicholls J (2018) Investigation of recast and crack formation in laser trepanning drilling of CMSX-4 angled holes. *Int J Adv Manuf Technol* 95(9):4059–4070
 54. Low DKY, Li L, Corfe AG (2001) Characteristics of spatter formation under the effects of different laser parameters during laser drilling. *J Mater Process Technol* 118(1–3):179–186
 55. Sharma V, Kumar V (2018) Investigating the quality characteristics of Al₅₀Si₅₀/SiC metal matrix composites machined by CO₂ laser curve cutting. *Proc Inst Mech Eng L J Mater Des Appl* 232(1):3–19

Publisher's Note Springer Nature remains neutral with regard to jurisdictional claims in published maps and institutional affiliations.



ISSN-1671-4512

CERTIFICATE

OF PUBLICATION

This is to certify that

Punitha. A



Professor, Department of Mechatronics Engineering, M.A.M School of Engineering,
Trichy, Tamilnadu, India

Published a paper entitled

"IMPLEMENTATION OF AUTOMATIC GARMENTS FOLDING MACHINE USING SERVO MOTOR"

in

Journal of Huazhong University of Science and Technology

VOLUME 50 ISSUE 05 - 2021

PAPER ID: HST-0521-115

<http://hxstxxjns.asia>

T. Suresh

Chief Editor



DOAJ DIRECTORATE OF OPEN ACCESS JOURNALS



IMPLEMENTATION OF AUTOMATIC GARMENTS FOLDING MACHINE USING SERVO MOTOR

Punitha. A¹, Ahmed Rifath. S², Mohamed Ithyas.I³, MohammedHussain.M. R⁴,

¹Professor, Department of Mechatronics Engineering, M.A.M School of Engineering, Trichy, Tamilnadu, India

^{2,3,4}Student, Department of Mechatronics Engineering, M.A.M School of Engineering, Trichy, Tamilnadu, India

¹ sweetpunitha@gmail.com ,

² rifath142@gmail.com , ³ mohamedithyas@gmail.com , ⁴ msdhussain514655@gmail.com .

ABSTRACT

Automatic Garment Folding Machine (AGFM) is a simple and valuable cycle in this universe. The reason for this paper is to overlay shirt simply by squeezing a switch. The AGFM is completely programmed where one need to simply put the shirt on the board and press the beginning switch and inside part of seconds the shirt will get folded. This thought will certainly be a useful for Textile industries, Laundry, etc. This energy and time can be saved by this programmed AGFM and can be utilized in some other work. By large individuals get exhausted for collapsing the garments in the wake after sewing so they dump them for what it's worth in the cabinet. This prompts wreck in cabinet and makes troublesome in discovering garments in crisis case. To survive above expressed issue, a savvy machine will design that will identify the shirt and crease. This AGFM will require less human contribution.

Keywords: AGFM, Laundry, Garments, sewing, savvy.

1.INTRODUCTION

Nowadays, many industries were pushed on the basis of the boundaries of autonomous vision and processing of supple materials like fibers, textiles, and garments. The textile industry hasn't seen much advancement in terms of technology, which will help it reach the gold standard in mechanism supply in the foreign market, which is entirely automation in the textile industry's manufacturing sector. The primary goal is to automate the cloth folding process used in the fabric manufacturing industry. In addition to the automatic folding process of the cloth, this aims to implement greater automation through the design of an automated sorting mechanism based entirely on the color of the fabric. This will ensure the complete automation of the textile enterprise that was missing. With the existing substances and parts, the device could be built as a good way to add simplicity and most significantly, price efficiency to the machine. The implementation of the whole assembly will be integrated without difficulties with the modern-day equipment being used inside the modern-day machine being used inside the industry without any major adjustments.

2. LITERATURE SURVEY

Yuliyanto agung prabowo et.al [13] proposed the identification of the Flip Folder Folding Machine Using Artificial Neuro Network Method with NARX (Nonlinear Auto Regressive Exogenous) Structure-I. As Folding

machine is a tool that is needed in the small and medium scale laundry industry that has a goal for the efficiency of production time. The flip folder is the main component of this tool, which functions to fold the clothes by moving to form a certain deflection angle where the movement process is controlled by the controller. The system modelling process is the first step to study the characteristics of the system. In a dynamic system, the form of linear modelling is approved difficult to obtain a model that represents the actual physical model. Selecting the structure of the NARX (Nonlinear Autoregressive exogenous) model was chosen to obtain the dynamic nature of the system. An estimation method to obtain parameter values from the system used Artificial Neural Networks (ANN), which is a trading scheme to be able to predict the output of a system that uses input data and output.

David Estevez et.al [1] proposed towards Robotic Garment Folding. In this, a Vision Approach for Fold Detection method is utilised as a current trend in robotics. Previously to folding clothes, they have to be unfolded. It is not realistic to perform model-based unfolding, as every garment has a different shape, size, colour, texture, etc. In this paper we present a garment-agnostic algorithm to unfold clothes that works using 3D sensor information. The depth information provided by the sensor is converted into a grayscale image.

J. Stria et.al [7] described the paper as Garment perception and its folding using a dual-arm robot. Assistive robots need to be able to perform a large number of tasks that imply some type of cloth manipulation. These tasks include domestic chores such as laundry handling or bed-making, among others, as well as dressing assistance to disabled users. Due to the deformable nature of fabrics, this manipulation requires a strong perceptual feedback, common perceptual skills that enable robots to complete their cloth manipulation tasks are reviewed here, mainly relying on vision, but also resorting to touch and force. The use of such basic skills is then examined in the context of the different cloth manipulation tasks, be them garment-only applications in the line of performing domestic chores, or involving physical contact with a human as in dressing assistance.

3.IMPLEMENTATION

The Framework used by the author to carry out this research using foam sheet the main frame that will later house the Arduino Atmega Servo 1, Servo 2, Servo 3, LCD display, Power supply and other components. All other Components mentioned above are attached to a Foam sheet so that its functionality is more usable. The output module structure is shown in Fig1.

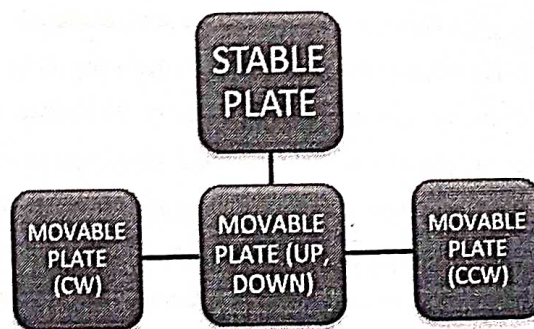


Fig 1. Output module structure

Regarding this, the placement of components on the frame, there are components such as Arduino Atmega, Servo 1, Servo 2, Servo 3, LCD display, Power supply and other components. All of the components mentioned above are attached behind this foam axis, starting from the power supply which provides electricity to the Arduino

Atmega and then connected to several components such as lcd display, IR sensors, servo 1, servo 2, servo 3. So that the function can run smoothly by using this order.

The process of connecting tools and applications that will be created. the tool and application Arduino IDE is an abbreviation of integrated development environment which is a software writing programs, compiling and uploading programs to the Arduino board. For basic applications using the Arduino IDE, the tools and materials used are: Computer, Arduino board, USB cable.

4.METHODOLOGY

First of all, the clothes are spread on the plate manually. This operation includes the way of placing the clothes in the correct alignment in the plate. The alignment depends upon the type of fabric. Using the three movable plates the cloths are folded. The movable plates are rotated to the certain degree for the process of folding the cloth.

However, the operations are influenced by fabric properties and state of making accuracy and reliability. This system transfers, clothes from the plate along with the other phase of the plate, followed by turning clockwise, counter clockwise and downward-up. The positioning plate is grasped by the servomotor. The placed cloth on the plate is folded and turns as per the programme feeded to the microcontroller. As the left plates and right plate turns 120degree and the downward up plate turns 90degree to complete the folding process. Then the folded cloth are collected in conveyer belt to the packaging department in the industry. Then it accesses the data from the AGFM that how many clothes are folded and uploads to the server.

Process of this AGFM will start once the button is pressed the servomotor are started to rotate as per the given position specified. Once it reached the final set in the program, it will stop automatically. The no.of. clothes folded are displayed in LCD and the cloth folded are uploaded automatically to IOT. Then it can be accessible from anywhere in the world with the help of IOTThe block diagram of methodology is shown in Fig2.

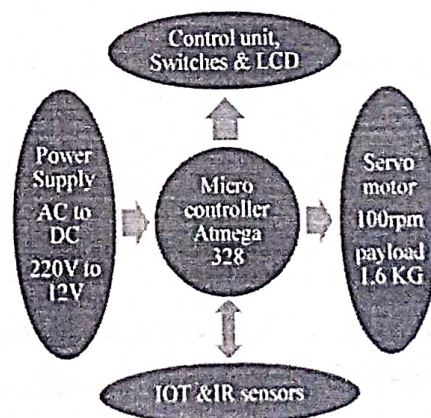


Fig 2 Block diagram of Methodology

5.RESULT AND ANALYSIS

An analysis has wrapped up for testing and the consequences of the ends incorporate the get together of a AGFM as a microcontroller with a servo drive that should be possible with 3servo relying upon the size necessities of the garments, for garments that are over burden, introduced on each contrary side of the current servo arrangement. The AGFM can encourage textile industries, laundries, etc. specifically in crafted by folding garments to be more productive on schedule and energy also by collecting the data of the folded garments from AGFM for the warehouse storage purpose. The implementation of Arduino IDE is shown in fig 3 and fig 4.

```

FBRADUTWEO3060 | Arduino 1.8.13 (Windows Store 1.8.42.0)
File Edit Sketch Tools Help
FBRADUTWEO3060
#include <Servo.h>

Servo servo_pin_12;
Servo servo_pin_7;
Servo servo_pin_5;

int buttonmode = 0;

void setup()
{
  pinMode(3, INPUT);
  digitalWrite(3, HIGH); // button
  servo_pin_12.attach(12); // servo motor
  servo_pin_7.attach(7); // servo motor
  servo_pin_5.attach(5); // servo motor
  Serial.begin(9600);
}

void loop()
{
  Serial.println(digitalRead(3));

  if (digitalRead(3) == HIGH) {
    if (buttonmode == 0) {
      buttonmode = 1;
    } else if (buttonmode == 1) {
      buttonmode = 0; // button (turn on, turn off)
    }
  }
}

```

Fig 3 Implementation of Arduino IDE

```

FBRADUTWEO3060 | Arduino 1.8.13 (Windows Store 1.8.42.0)
File Edit Sketch Tools Help
FBRADUTWEO3060
Serial.println(digitalRead(3));

if (digitalRead(3) == HIGH) {
  if (buttonmode == 0) {
    buttonmode = 1;
  } else if (buttonmode == 1) {
    buttonmode = 0; // button (turn on, turn off)
  }
  delay(500);
}

if (buttonmode == 1)
{
  Serial.println("button");
  servo_pin_12.write(0);
  delay(1500);
  servo_pin_12.write(180);
  delay(1000);
  servo_pin_7.write(0);
  delay(1500);
  servo_pin_7.write(180);
  delay(1000);
  servo_pin_5.write(180);
  delay(1500);
  servo_pin_5.write(0);
  delay(1000); //above are the rotation of servo motor
  //the degrees of the rotation can be changed if the degrees above didn't match the rotation angle of your servo motor
  buttonmode = 0; // the operation will stop once the rotation finish
}
}

Done uploading.
Sketch uses 240 bytes (11%) of program storage space. Maximum is 32256 bytes.
Global variables use 248 bytes (11%) of dynamic memory, leaving 1803 bytes for local variables. Maximum is 2048 bytes.

```

Fig 4 Implementation of Arduino IDE

Automatic folding machine will be more efficient in the time and energy. It will be automated the operation. The step-by-step procedure for T shirt folded as shown in fig 5.

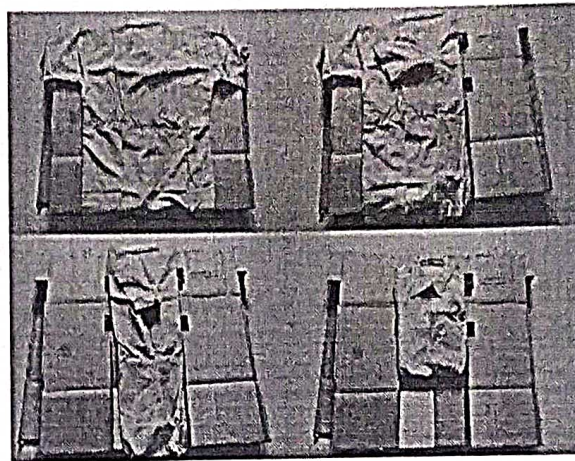


Fig 5 step by step procedure for shirt folded

The step-by-step procedure for T shirt folded as shown in fig 6.

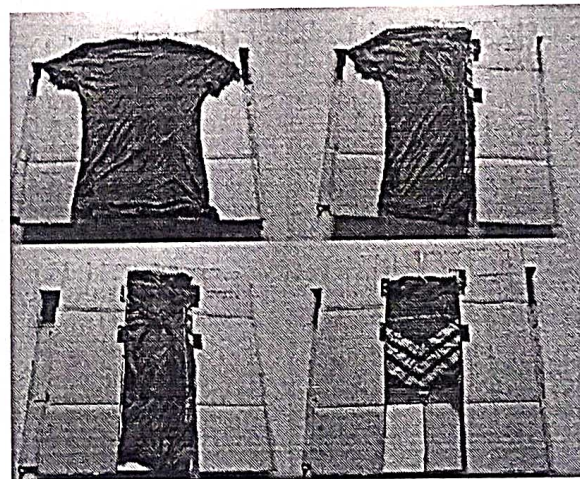


Fig 6 step by step procedure for shirt folded

6.CONCLUSION AND FUTURE SCOPE

When the cloth folding machine is used the time required to fold the cloth is reduced to half of the time compared to manual. Also, it is a step to increase in production to the sales market as early as possible compared to manual folding also saves man-power

In future, the robotic arm will be used to place the fabric on to the folding plate. By using cam shaft mechanism with single Industrial servo motor, it can be able to operated. With using IOT the whole machine will be able to control at one time while using several AGFM at a time from the control room.

REFERENCES

- [1] David Estevez, Juan G, Victores, Santiago Towards Robotic Garment Folding: A Vision Approach for Fold Detection is Proposed in 2016.
- [2] Dourmanoglou, A., Stria, J., Peleka, G., Mariolis, I., Petrik, V., Kargakos, A., ... & Malassiotis, S. Folding Clothes Autonomously: A Complete Pipeline. In 2016 Ieee Transactions on Robotics, 2016 32(6), 1461-1478.
- [3] Erlangga, M. Automation of Arduino-Based Clothes Folding Machines Based on Patent No. 2,758,761 (In 2019 Doctoral Dissertation, University of Muhammadiyah Malang), 2019, Pp 1-6.
- [4] Fred, H. U.S. Patent No. 2,071,257. Washington, Dc: U.S. Patent and Trademark Office, 2013, Pp 45-52.
- [5] Hafis, A. S. A. Design of Semi-Automatic Clothes Folding Machine Based on Arduino Uno (In 2019 Doctoral Dissertation, University of Muhammadiyah Malang), 2019.
- [6] Hariyanti, E., Tambunan, G., Saputra, R. A., Basjaruddin, N. C., & Rakhman, E. Automatic clothes folding device with three microcontroller-based folding modes. In 2020 Proceedings of Industrial Research Workshop and National Seminar, 2020, Vol. 11, No. 1, Pp. 205-210
- [7] Jan stria, Daniel prusa, Vaclav Hlavac, Libor Wagner, Vladimir Petrik. Garment perception and its folding using a dual-arm robot- in 2014.
- [8] Kido .M, and H. Takahashi, "Clothing Model Fitting for Laundry Folding Assistance," 2019 Nicograph International (NicoInt), Yangling, China, 2019, pp. 37-40, doi: 10.1109/NICOInt.2019.00015.
- [9] Miller.S, Fritz. M, Darrell.T, and P. Abbeel, "Parametrized shape models for clothing," 2011 IEEE International Conference on Robotics and Automation, Shanghai, 2011, pp. 4861-4868, doi: 10.1109/ICRA.2011.5980453.
- [10] Nurkholis, A. M., & Alfi, I. Automatic F-Cloth Smart Solution for Folding Clothes Practically Based on Arduino Uno (In 2018 Doctoral Dissertation, University of Technology Yogyakarta), 2018.
- [11] Osawa, F., Seki, H., & Kamiya, Y. Clothes Folding Task by Tool-Using Robot. Journal of Robotics and Mechatronics, 2006, 18(5), 618-625.
- [12] Satya Baktiar, I. K., & Nugroho, P. W. Automatic clothes folding machine based on PLC (Programmable Control Logic) as an alternative to help clothing activities. Final Project of Mechanical Engineering Department- Faculty of Engineering UM, 2017, Pp. 86-89
- [13] Yuliyanto Agung Prabowo & Wahyu Setyo Pambudi, Lmi Rizki Imaduddin. Flip Folder Folding Machine Using Artificial Neuro Network Method with NARX (Nonlinear Auto Regressive Exogenous) Structure- In 2020.



Browse My Settings Help

Institutional Sign In

Institutional Sign In

All



ADVANCED SEARCH

Conferences > 2021 International Conference...

Smart Method for Tollgate Billing System Using RSSI

Publisher: IEEE

Cite This

PDF

Punitha A ; Raghupathi S All Authors

21 Full Text Views



Alerts

Manage Content Alerts

Add to Citation Alerts

More Like This

Research on the Relationship between the Investment in Transportation and Medical Industry and Road Traffic Safety in China

2020 5th International Conference on Information Science, Computer Technology and Transportation (ISCTT)

Published: 2020

On-Board Unit Big Data: Short-term Traffic Forecasting in Urban Transportation Networks

2020 IEEE 7th International Conference on Data Science and Advanced Analytics (DSAA)

Published: 2020

Show More

Abstract



Download PDF

Document Sections

I. Introduction

II. RELATED WORK

III. SYSTEM ARCHITECTURE

IV. IMPLEMENTATION AND RESULT ANALYSIS

V. CONCLUSION

Show Full Outline

Authors

Figures

References

Keywords

Metrics

More Like This

Abstract: Toll gates are commonly regarded by travelers as an annoyance not just for the cost for tolls, but also for toll booth delays, toll roads and bridges. With a view to main... [View more](#)

Metadata

Abstract:

Toll gates are commonly regarded by travelers as an annoyance not just for the cost for tolls, but also for toll booth delays, toll roads and bridges. With a view to maintaining a Steady traffic flow, both workers and drivers need quick access to effective communication system that covers the particular requirements of toll gates. Toll Gate Payment systems have become very effective in reducing the over-congestion that has become part of the process. It is one of the simple ways to navigate the great traffic flow of travelers passing by. In this method of travel, their transport helps them to be aware of the money that has been paid into the account.

Published In: 2021 International Conference on Advance Computing and Innovative Technologies in Engineering (ICACITE)

Date of Conference: 4-5 March 2021 **INSPEC Accession Number:** 20632491

Date Added to IEEE Xplore: 20 April 2021 **DOI:** 10.1109/ICACITE51222.2021.9404596

ISBN Information:

Publisher: IEEE

Conference Location: Greater Noida, India

IEEE websites place cookies on your device to give you the best user experience. By using our websites, you agree to the placement of these cookies. To learn more, read our [Privacy Policy](#).

Accept & Close

INFOKARA RESEARCH

An UGC-CARE Approved Group 2 Journal



INFOKARA

An ISO : 7021 - 2008 Certified Journal

Certificate ID - IK-4350

ISSN NO: 1021-9056 / web : <http://infokara.com/>
e-mail : editor.infokara@gmail.com

Certificate of Publication

This is to certify that the paper entitled
Smart Sewage Water System Using GSM Enabled Sensor

Authored by
M.SUBA PRADHA

From
M.A.M School of Engineering, Trichy

Has been published in
INFOKARA RESEARCH, VOLUME 10, ISSUE 5, MAY - 2021



H. Mathew
Mathew Hull, Editor-In-Chief, INFOKARA RESEARCH



Smart Sewage Water System Using GSM Enabled Sensor

M.Suba Pradha¹, A.Balaji², M. Deepak³, M.E.Mohamed Fahees⁴

¹Assistant Professor, Department of Mechatronics Engineering, M.A.M School of Engineering, Trichy.

^{2,3,4}Student, Department of Mechatronics Engineering, M.A.M School of Engineering, Trichy.

¹cool.pradha@gmail.com, ²alagarbalal1999@gmail.com, ³mpajaydeepak007@gmail.com, ⁴fahees770@gmail.com

Abstract— In recent days the sewage management is the big problem in our country and it is cleaned by the manpower, due to that so many diseases are caused .In India sewage cleaning from manholes and drains are difficult and risky job for everyone, but those people/workers are forced to do all jobs to earn for their family. It is mainly used for metropolitan cities and highly populated areas. To develop this such a device which would monitor the health of the person/worker entering the sewage and provide the health parameters in real time to the officials outside or the control room. The Normal Sewage system are changed into useful water system. All the sewage pipe lines are interconnected and are discharged into water power plant. Sometimes impurities are stroked like block. This block will be released easily and used for recycling and also re-use the water for many useful ways like plantation, gardening etc.

Keywords— Sewages, parameters, pipelines,ditch holes, subway pipes

I. INTRODUCTION

A large number of sanitation workers will die every year due to their erratic and lack of facilities which are available, and the harmful toxic gases will be released while cleaning the sewage. The Manholes will not designed for anyone to work in regular, but the workers may also need to enter inside their manhole to complete the jobs such as cleaning, repair, inspection etc. A better of knowledge related to hazards in their surroundings was necessary for their prevention of poison of gases. All These gases will have to be keep on the track so that enormous rise in their normal level of effluents which should be known and corrective measure can be taken. If the drainage system is not properly managed then pure water gets contaminate with drainage water and infectious diseases may get spread. It is fully automated process. This reduce the human effort and save the life of common People's after that Flow sensors are used to detect the blocks. This can easily controlled by microcontroller and send the SMS by using GSM Technology.

II. LITERATURE SURVEY

Subash Guptaz et al [13] Sewage Management system, 2020 we use one water pump to pump the sewages into receiving chamber. Then from the sewages which are passed to the screening and grit chamber which will consists of net, where the plastics and solid wastes are blocked. After that, sewages are passed in to skimming tank in which oil and greases will be removed. After this, sewages are passed to primary sedimentation tank, here particles which are not settle down in receiving chamber are settled here. From there , sewages will passed into aeration tank where there is an air flow due to which air bubbles will be formed and biological organic matter are removed . After this, sewages are passed to secondary sedimentation tank where scums are removed. After that it was passed in to filtration chamber where the gravels are present for the purification and after that sewage is passed into disinfection chamber where the microorganisms were removed by UV-rays , chlorination and after this it is finally somewhat can be used for drinkable purpose

G. Sunitha, P. Sujatha, D. Lalitha Bhaskari et al [11] today's drainage system is not high-tech. whenever there was blockage it is difficult to figure out their exact location of blockage. Also, alerts the blockage which are not received immediately. Hence the detection and reconstruction of their blockage will become time -consuming. It also becomes a very difficult to handle their situation when the pipes

were clogged completely. Due to their failure of drainage line people will face a lot of problems.

S. Ramanathan, R. Sudharshan, Karthik B, A. Mohammed Suhail, sewage cleaning machine, 2016 et al [12] In the earliest form of sewer cleaning machine which was hand excavation by labourers which loaded sediment into barrows were also moved down the sewer and then lifted out at the manholes by bucket. The work was not only dirty, which was unpleasant and dangerous. The major problem is manual scavenging in the health issues which is faced by the workers and more over the cleaning was done by the human beings because of their earning. Nowadays even though the automation which plays an important role in all the industrial applications, also the proper disposal of sewage from the industries and commercials will have a challenging task. Drainage cleaning system was proposed to overcome their real time problems. In the project their aim was to replace their manual work in the drainage which was cleaned by introducing a semi-automated system in an efficient way to control their disposal of wastages and with their regular filtration of wastages. In that model, a pneumatic piston was connected by the wire rope which was in turn and is coupled with the kinematic of linkages. The linkage from their frame was to be submerged with the sewage. When the pneumatic piston was actuated, the grippers were provided at the bottom which is expanded and collected their solid wastes from the sewage. Ultimately their motto is to fabricate the machine which was cost effective as well as efficient in working

III. IMPLEMENTATION

During rainy day, rainwater results in an overflow of combined sewage systems in poor wastewater management systems. Monitoring the inflow of water with the help of GSM Micro Control can help water utilities to detect overflows in real-time and take appropriate actions to reduce water wastage. For instance, their administrators which can control their valves and provide more water flow to their areas for a specific time interval to prevent the combined sewage overflow. Administrators can also automate the control of valves with the help of GSM technology so that the valves adjust themselves according to the inflow of water and also, algorithms can help to predict the inflow of water and prevent the combined sewage overflow

Regarding this, the placement of components on the frame, there are components such as Arduino ATMEGA, Flow Sensor 1, Flow Sensor 2, Vacuum Motor 3, LCD display Flow Sensor 1, Flow Sensor 2, Vacuum Motor 3, LCD display GSM Module, Water Motor, Power supply and other components. All of the components mentioned above are attached behind this foam axis, starting from the power supply which provides electricity to the Arduino at mega and then connected to several components such as LCD display, Flow Sensors 1, Flow Sensors 1, Water Motor, GSM module, So that the function can run smoothly by using this order.

The process of connecting tools and applications that will be created. The tool and application Arduino IDE is an abbreviation of integrated development environment which is a software writing programs, compiling and uploading programs to the Arduino board. For basic applications using the Arduino IDE, the tools and materials used are: Computer, Arduino board, USB cable.

IV. METHODOLOGY

In this section, the sewage management procedure is explained briefly. ATMEGA328P is a high performance, low power controller from Microchip. It is an 8-bit microcontroller based on AVR RISC architecture. It is one of the most popular of all their AVR controllers was used in the ARDUINO boards. ATMEGA328 is used similar to any other controller. All there to do is programming. Controller was

simply execute their program which is provided by us at any of their instant. Without programming the controller it was simply stays and put without doing anything. As of said, first we have to program their controller and that was done by writing their appropriate program file in the ATMEGA328P FLASH memory. After that dumping their program code, the controller will execute their code and provides the appropriate response

A flow sensor (more commonly referred to as a "flow meter") was an electronic device that will measures or regulates their flow rate of liquids and gasses within the pipes and tubes. It was generally connected to the gauges to render their measurements, but it can also be connected to their computers and digital interfaces. It was commonly used in the HVAC systems, medical devices, chemical factories, and septic systems. Flow sensors were able to detect their leaks, blockages, pipe bursts, and changes in the liquid concentration due to their contamination or pollution.

Ultrasonic flow sensors was the most popular type of their non-contact flow sensor. This sensors will send their pulses of high frequency sound which was across the flowing liquid or gas medium. All these sensors will measure the time between their emission of sound and also it contact with their sensor's receiver to determine their flow rate of gas or liquid.

The display unit comprises of an OLED display, buttons, LED's and a vibration motor. It consists of 3 LED's. The green LED signals that all levels are below critical levels. The red LED signals if any parameter is above or below the critical level. The yellow LED signals when the emergency switch is pressed. The display set communicates with the sensor set via an UART communication [9]. The OLED display works in sunlight better than other available technologies.

A suction motor will creates vacuum pressure and suction by rotating a motor fan. The impeller rotates at an incredibly high speed of about 30,000 RPM. A suction motor's power is measured by multiplying the rate of air flow and the vacuum pressure, which induces air flow from the brush through the hose. Rating the motor for its ability to produce suction with air flow is one of the most misrepresented and misunderstood aspects of vacuum cleaner technology. This confusion have been accentuated by their many manufacturers in all the attempts to make their products which was appear in superior to others

GSM is a mobile communication modem; it stands for global system for mobile communication (GSM). It was widely used by the mobile communication system in all the world. GSM is an open and digital cellular technology used for transmitting mobile voice and data services operate at the particular frequency bands. Administrators can also automate the control of valves with the help of GSM technology. It will predict the inflow of water and prevent the combined sewage overflow.

The below diagram is the methodology of sewage management system is shown in Fig1

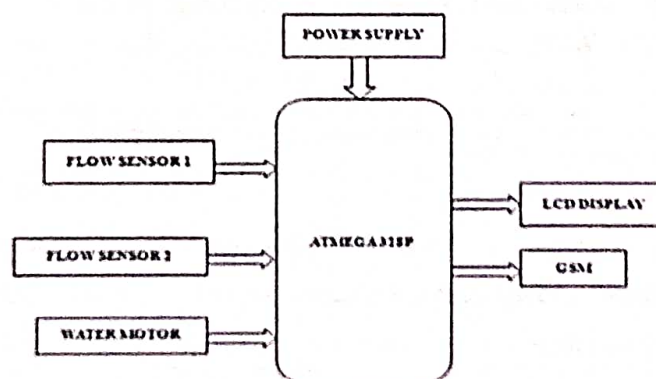


Fig. 1 Block diagram of Methodology

V. RESULTS AND ANALYSIS

This will result in an overflow of combined sewage systems in poor wastewater management systems. Monitoring the inflow of water with the help of GSM Micro Control can help water utilities to detect overflows in real-time and take appropriate actions to reduce water wastage. For instance, the administrators which control all the valves and provide more water flow to their areas for a specific time interval to prevent their combined sewage overflow. Administrators can also automate the control of valves with the help of GSM technology so that the valves adjust themselves according to the inflow of water and also, algorithms can help to predict the inflow of water and prevent the combined sewage overflow.

VI. CONCLUSION AND FUTURE SCOPE

A leak in the distribution pipes is distributed the water regionally which can result in the heavy loss of water. Hence, these pipes need to be changed regularly according to the necessity. Micro Control collects data like type of sand that pipes rest on, topography, and weather records. And then AI can help to analyze these data to find patterns that offer clues to the water utilities about which pipes are at risk of leakage. GSM-enabled sensors and AI-driven analytics in smart wastewater systems are not the only technologies that can help water utilities to improve the management and treatment of wastewater across the facilities. Other technologies like big data analytics can help to improve the accuracy of insights into wastewater management processes and also improve their management. Governments of smart cities play a vital role in their collaboration of most of the technologies. It can take initiatives to educate all the citizens about their benefits of using all technologies for their mainstream of adoption. Also, governments can plan and build the infrastructure for the implementation of systems created with the help of these technologies.

REFERENCES

- [1] Ganesh U L, et al. "Semi-Automatic Drain For Sewage Water Treatment Of Floating Materials", International Journal of Research in Engineering and Technology, Vol No- 05, Jul- 2016.
- [2] James C. Conwell, G.E. Jhonson, "Design, Construction and Instrumentation of a Machine to Measure Tension and Impact Forces in Roller Chain Drives", December 1989.
- [3] S D Rahul Bharadwaj, Shraddha R Jogdhanekar, "Automatic Wastewater treatment process to reduce global warming" International Journal of Environmental Science: Development and Monitoring, Vol No- 2 (2013).
- [4] Dr. K. Kumaresan et al., "Automatic Sewage Cleaning Equipment", International Conference on Explorations and Innovations in Engineering and Technology, 2016.
- [5] R. Sathiyakala et al., "Smart Sewage Cleaning System" International Journal of Innovative Research in Computer and Communication Engineering, Vol No- 4, February 2016
- [6] Arduino, Web article on different types of Arduino Board and its features, <https://www.arduino.cc/>, (Accessed on 10th January 2019).
- [7] Mo Kaidong, Analysis on the Management of Urban Road Manhole Cover and Its Countermeasures [J]. Construction Engineering Technology and Design, 2015, (36): 1963. (in Chinese)
- [8] Zhao Shipeng, Design of Intelligent Manhole Cover Remote Monitoring System Based on ZigBee and GPRS [J]. Electronic World, 2016, (17): 158-159. (in Chinese)
- [9] Wu Xiaobin, Design of remote monitoring system for manhole cover and underground working condition based on NB-IoT [D]. North University of China, 2018. (in Chinese)
- [10] T. Li, W. Zhang, C. Feng, J. Shen, 2014 WATER SCI TECHNOL 69, 422.
- [11] G. Sunitha, P. Sujatha, D. Lalitha Bhaskari, Smart Underground Sewage and Solid Waste Management System Implementation based on IoT, 2018
- [12] S. Ramanathan, R. Sudharshan, Karthik B, A. Mohammed Suhail, et al sewage cleaning machine, 2016
- [13] Subash Guptaz et al [13], Sewage Management system, 2020

A. References

The heading of the References section must not be numbered. All reference items must be in 8 pt font. Please use Regular and Italic styles to distinguish different fields as shown in the References section. Number the reference items consecutively in square brackets (e.g. [1]).

When referring to a reference item, please simply use the reference number, as in [2]. Do not use "Ref. [3]" or "Reference [3]" except at the beginning of a sentence, e.g. "Reference [3] shows ...". Multiple references are each numbered with separate brackets (e.g. [2], [3], [4]–[6]).

Examples of reference items of different categories shown in the References section include:

- example of a book in [1]
- example of a book in a series in [2]
- example of a journal article in [3]
- example of a conference paper in [4]
- example of a patent in [5]
- example of a website in [6]
- example of a web page in [7]
- example of a databook as a manual in [8]
- example of a datasheet in [9]
- example of a master's thesis in [10]
- example of a technical report in [11]
- example of a standard in [12]

VII. CONCLUSIONS

The version of this template is V2. Most of the formatting instructions in this document have been compiled by Causal Productions from the IEEE LaTeX style files. Causal Productions offers both A4 templates and US Letter templates for LaTeX and Microsoft Word. The LaTeX templates depend on the official IEEEtran.cls and IEEEtran.bst files, whereas the Microsoft Word templates are self-contained. Causal Productions has used its best efforts to ensure that the templates have the same appearance.

Causal Productions permits the distribution and revision of these templates on the condition that Causal Productions is credited in the revised template as follows: "original version of this template was provided by courtesy of Causal Productions (www.causalproductions.com)".

ACKNOWLEDGMENT

The heading of the Acknowledgment section and the References section must not be numbered.

Causal Productions wishes to acknowledge Michael Shell and other contributors for developing and maintaining the IEEE LaTeX style files which have been used in the preparation of this template. To see the list of contributors, please refer to the top of file IEEETran.cls in the IEEE LaTeX distribution.

REFERENCES

- [1] S. M. Metev and V. P. Veiko, *Laser Assisted Microtechnology*, 2nd ed., R. M. Osgood, Jr., Ed. Berlin, Germany: Springer-Verlag, 1998.
- [2] J. Breckling, Ed., *The Analysis of Directional Time Series: Applications to Wind Speed and Direction*, ser. Lecture Notes in Statistics. Berlin, Germany: Springer, 1989, vol. 61.
- [3] S. Zhang, C. Zhu, J. K. O. Sin, and P. K. T. Mok, "A novel ultrathin elevated channel low-temperature poly-Si TFT," *IEEE Electron Device Lett.*, vol. 20, pp. 569–571, Nov. 1999.
- [4] M. Wegmuller, J. P. von der Weid, P. Oberson, and N. Gisin, "High resolution fiber distributed measurements with coherent OFDR," in *Proc. ECOC'00*, 2000, paper 11.3.4, p. 109.
- [5] R. E. Sorace, V. S. Reinhardt, and S. A. Vaughn, "High-speed digital-to-RF converter," U.S. Patent 5 668 842, Sept. 16, 1997.
- [6] (2002) The IEEE website. [Online]. Available: <http://www.ieee.org/>
- [7] M. Shell. (2002) IEEEtran homepage on CTAN. [Online]. Available: <http://www.ctan.org/tex-archive/macros/latex/contrib/supported/IEEEtran/>
- [8] *FLEXChip Signal Processor (MC68175/D)*, Motorola, 1996.
- [9] "PDCA12-70 data sheet," Opto Speed SA, Mezzovico, Switzerland.
- [10] A. Karnik, "Performance of TCP congestion control with rate feedback: TCP/ABR and rate adaptive TCP/IP," M. Eng. thesis, Indian Institute of Science, Bangalore, India, Jan. 1999.

- [11] J. Padhye, V. Firoiu, and D. Towsley, "A stochastic model of TCP Reno congestion avoidance and control," Univ. of Massachusetts, Amherst, MA, CMPSCI Tech. Rep. 99-02, 1999.
- [12] *Wireless LAN Medium Access Control (MAC) and Physical Layer (PHY) Specification*, IEEE Std. 802.11, 1997.

Integration of 3D MEMS Accelerometer Sensor

M.Suba pradhan ¹, J.Roselin Suganthi ², C.Malarvizhi ³, S.Susiladevi ⁴

¹Assistant Professor, M.A.M School of Engineering, Trichy, Tamilnadu, India

²Assistant Professor, K.Ramakrishnan College of Engineering, Trichy, Tamilnadu, India

³Assistant Professor, Rajalakshmi Institute of Technology, Chennai, Tamilnadu, India

⁴Assistant Professor, Sri Bharathi Engineering College for Women, Pudukkottai, Tamilnadu, India

Abstract— A methodology which tracks the hand gesture depends on the integration of custom-built Micro Electro Mechanical Systems (MEMS)-based inertial sensor (measurement unit), the low-resolution imaging (i.e., vision) sensor. A 2-D gesture recognition changes in to a motion tracking gesture recognition in three dimensions. Essentially, it will show the inertial data sampled at 100 Hz and vision data sampled at 5frames/s. An Extended Kalman filter, which provides accurate human hand gesture recognition as well as tracking. The novel adaptive algorithm measures noise covariance, acceleration and angular rotational rates. The proposed method may reduce the velocity of error and also position drift by using MEMS Accelerometer sensor. To compensate for the time delay, the moving average filter used to reduce the frequency noise and then propagate the inertia of signal. A dynamic of time wrapping with DCT provides extracted feature and it gives exact value of 92.3% also individual numerical recognition with 100 ms.

Index Terms—fusion sensor, gesture and recognition, MEMS related motion tracking, trajectory algorithm

1. Introduction

The up-gradation of micro electromechanical system (MEMS) technology, leads to various applications with low cost of MEMS-global positioning system (GPS) which is integrated with the navigation system is being popularly researched. The MEMS-based inertial sensor which is integrated with GPS and it also provides a reliable positioning solution in GPS which was commonly occurs in the urban areas [2]. Especially, a low cost of the MEMS-GPS integrated navigated system is used for mobile robot, an unmanned aerial vehicle, a micro-aerial vehicle and also a pedestrian navigated system. Gestures are used for the communication system between the people and also a machine. Then Building the interaction between the human and computers are also required for an accurate hand gesture recognized system also an interface for an easy human computer interaction (HCI) system, a recognized gesture is used for the controlling robot also conveying meaningful information.

The expansion of human machine interaction technologies reduces the size, dimension and weight of the consumer electronic products such as smart phones, handheld computers. It increases the day-to-day convenience. An attractive and alternative, inertial sensor projected body will sense the activities of the human movement, it also captures the motion of trajectory information from the accelerations of recognizing gestures. The main advantage of the inertial sensors for motion sensing that can be operated without any of the external reference and also the limitation in operating the conditions. However, the recognition of motion trajectory is very difficult for the users and also, they have a different speeds or styles to generate a various motion of trajectories. [5] The researchers looking forward to get rid of the issues in increasing the accuracy of the recognition system. By the process of miniaturization, the MEMS accelerometer based recognized system which will acknowledge the gestures in a 3-D is constructed by using this digital format.

Gestures may be static (posture) or dynamic (sequence of more postures). The Static gestures are required less computational, complexity and dynamic gestures which are all complex. It is suitable for the real time environments.

Acquired data available in the recognition system can be obtained either by using spare devices such as instrument data glove devices, or used the virtual image, and both mentioned methods [18, 19].

which are used to extract the gesture features. The Vision based method will approach easy, natural and a less cost comparing with gloves and the approaches are required by users will wear their special device and it was connected to their computer it will hinder their naturalness of the communication between all users and computers. There are a lot of reviews were discussed in the gesture of recognition system also its application was using different no of tools. This work has been demonstrated their advancement of gesture of recognition systems and was represent the starting point of the investigators in the human gesture recognition field. The readers should note that it will aim to provide a broad and introduction of subjects of the inertial methods of navigation, it will be focused mainly on the strap down type of the inertial method of navigation system using micro-machined electromechanical systems (MEMS) devices. MEMS technology have an interest on this current time. Also it was offered a rugged, low no of cost, small and light weighted inertial sensors and which is relative to their technologies. Also, the performance of the MEMS inertial device is for improvement. Due to their inertial navigation system (INS) it was developed which is based on MEMS device.

2. Gesture Tracking

To propose their automatic systems, we could recognize the isolated gesture in the real-time system from stereo the sequences of motion and trajectory by a single human using HMMs [1]. In a proposed system it was consists of three main stages; automatic method of segmentation process, tracking method, also feature extraction and classification.

- (1) Pre-processing; means it localizes and also finds the human to reproduce their motion of trajectory path.
- (2) Feature extraction; means the Clustering which is extract and its feature will be generated their discrete no of vectors, which is given as input to the HMMs recognizer.
- (3) Classification; means their gesture path and it would be recognized by the discrete vectors and also Left-Right Banded of topology.

The two types of the gesture path recognition methods are vision-based and also accelerometer-based sensor. Due to their some of the limitations which was ambient of noise, slower dynamic responses, also large no of data collections/processing of the vision-based methods. The recognized system will be implemented which was based on the inertial measurement unit of the MEMS accelerometer sensor. If accelerometer sensors are used for the inertial measurements it will cause a heavy computational burden, in our system it is based on the MEMS accelerometers only and gyroscope sensors which was not implemented. Many of the researchers is focus by the developed effective of algorithms for an error compensation of the inertial sensor and will improved their recognition system of accuracy. An effective acceleration and errors of compensative algorithm was based on the zero no of velocity of compensated and it would also develop to decrease their acceleration of the error by acquiring in the reconstructed method of trajectory. A Kalman filter with all of the magnetometers (micro inertial of measurement unit (μ IMU) with magnetometers), is employed to the compensate of orientated proposed digital of the instrument.[4] when oriented instrument is estimated, the motion of trajectory and the instruments was also be reconstructed with accurately. An optical method of tracking was calibrated which was based on optical of tracking method system (OTS) it was calibrated by a 3-D of acceleration method, the angular velocity, and spaced attitude of motion. Then OTS is developed by these two goals: 1) Also obtained the acceleration of proposed and ubiquitous of digitized instrument by a calibrated 3-D trajectory and 2) also obtained an accurate of attitude angle by the multiples of calibrated method. In order to recognize and reconstructed their motion of trajectory was accurately mentioned, and approaches to introduce all the sensors which are gyroscopes and magnetometers it was obtained by the précised method of orientations. This will increase their cost of motion of trajectories and recognized system which also a

commutated of burden.

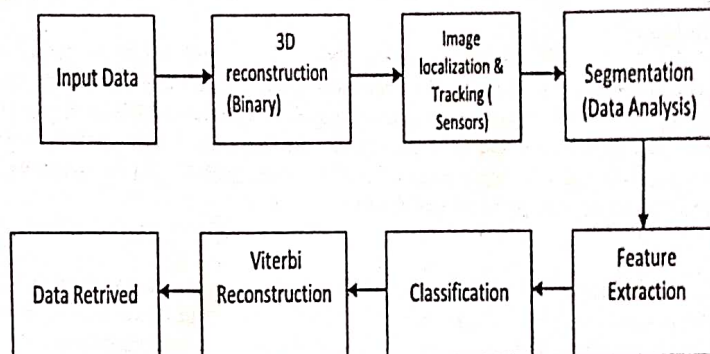


Figure 1: Block diagram

2.1 Segmentation and Tracking

A method of detection and segmentation is a complex and its background was described by the motion of segmented and tracking which will take place by using a 3D depth of map of information. Segmentation of regions will become a robust and if there was a chrominance is used in all analysis. We should ignore all the channels will reduce all their effects of a bright of variation and will use their chrominance fully and will represent a movement of information. A large database will be used for training up the Gaussian of models. This Gaussian Mixture of Models will begin with the models of database and where having a variant method of k-means clustering method algorithm which will perform their model of training and will determine an initial configuration of the GMM of parameters. A depth of an information which will solve all the overlapping problems, then it was obtained by the passive methods of stereo of measuring which is based by the cross correlated of the known calibrated of data's. All the clusters which are composed of resulted a 3D-points.[8] The clustered of algorithm which was considering as a kind of the regions and is grown in a 3D which was used in two methods; skin as well as Euclidean method. Those all methods are very robust to their disadvantage of light and partial occlusions, it was occurred in a real-time of environment. In their analysis which was used to derive their boundary of areas of method, which also bounding boxes of body with centroid point.

After the localization of human target from the segment. We can find their best of matches in a hand of target in a sequential no of frames which was used for measuring their similarity of maximize the Bayes error and arises from their comparisons of targets and also their candidate. Due to their consideration of mean depth of the value which was computed from their frame of the regions to solve their overlapped between their motions. The mean is defined as recursive and will perform their optimization to reduce their strength. This mean-shift optimizations will give their measurement no of locations of hand target method, also uncertain of estimation which was computed and it was followed by the Kalman filter, it will derive their predicted positions of hand target, the hand of gesture path was obtained by took their correspondence of the detect movement and also the successive frames. The frames which are fused together to detect their movement of human body by accelerometer sensor.

2.2. Feature Extraction

To select a nice features and to recognize their hand gestures of path which also played a significant role in the systems performance. The three basic features; are locations, orientated method and velocity. We also analyzed their effective features which are extracted by the trajectories is also combined them to test their recognition rate. A 3D

dynamic feature will divided into two category that are featured in Cartesian space (x; y) and featured in the Polar space (r; θ).

2.2.1 Features in Cartesian Space

A gesture of path is a spatio-temporal pattern which was consists of centroids (x hand and y hand). All there coordinates in the Cartesian space it was extracted by gestures frame. We also considered two types of locations space. First of location space is Lc and it measure the distant from centroid point of all points in the gesture of path because there are different types of location space was generated by same gesture (Eq 1). Second of location feature is Lsc, which was from start point to current point of gesture of path (Eq 3)

$$Lc = \sqrt{(x_{t+1} - c_x)^2 + (y_{t+1} - c_y)^2}$$

$$(c_x, c_y) = 1/n (\sum_{t=1}^n x_t, \sum_{t=1}^n y_t) \quad (2)$$

$$Lsct = \sqrt{(x_{t+1} - x_1)^2 + (y_{t+1} - y_1)^2} \quad (3)$$

A second time basic feature was orientation, it will gives the direction of the hand when it traverses along their space during their gesture process. This orientation feature was based on the calculation method of human displacement vector and in every point it was represented by orientated according to the centroid path of gesture.

A third basic feature was velocity, and it plays more important role in gesture recognition phase which was particularly at the most of the situation. The velocity which was based on their fact in each of the gesture was made by different speeds and the velocity of gesture will decreases by the point of gesture path. The velocity will be calculated at Euclidean distance from two successive points and was divided by all time the number of frames as follows;

$$Vt = \sqrt{(x_{t+1} - x_t)^2 + (y_{t+1} - y_t)^2} \quad (4)$$

In the Cartesian coordinate of system, we also use their different combination of variety of featured vectors. For example, all featured vector is at the frame t + 1 is also provided by the union of locations and features (Lct; Lsct), the location features with the velocity of feature (Lct; Lsct; Vt). Each of the frame will contains a set of vectored at the time t and all dimensions space was proportional to their size of feature vector method. In their manner, a gestures will represent as ordered sequences of featured vectors, it is projected by clusters in the space dimensions to obtain their discrete code word which is used by input to HMMs. It was done by using their k-means clustered algorithm.

2.2.2 Features of Polar Space

The Polar of coordinate system is directly find out by the Cartesian coordinates which is generated from the gesture of images. It also obtained a normalized polar coordinate, which will used a radius from their center point of the gesture path, the radius of start and current point. In Polar space, a different no of combinations of features will obtained a variety of featured vectors.[6] For example, the featured vectors at the frame t + 1 was obtained by the union of location features from centroid point with velocity of feature (pct; φct; Vt), the locations feature will started and the current points with their velocity feature (psct; φsct; Vt), and the combination of all vectors (pct; φct; psct; φsct; Vt).

2.2.3 Vectored Quantization

The extract of features will quantized by obtaining a discrete no of symbols. If the featured locations or velocity which is used as separate, all the features will normalized which was multiplied by different scalars ranged by 10 to 30. The normalization of orientated features was divided by 10, 20, 30 and 40 to obtain a code word. In addition to their combination of features by both Cartesian and Polar coordinate system, it also used the k-mean clustered algorithm to divide their gesture features in K clusters on all featured space. The algorithm was based on the minimum no of distance between their center of clusters and featured points. We would divide all their set featured

vectors into set clusters. It will allowed the human trajectories in featured space by clusters. This was find out by clustered index and was used as input to the HMMs. [11]

2.3. Classification

Markov model is one of the mathematical model of stochastically process, it will generated a random no of sequences and outcomes for certain probabilities. A stochastically process was the sequence of feature code words, all outcome will being the classification of their gesture of path. The Evaluated, Decoded and Trained are the main problem of HMMs and it also being solved by using their Forward- Backward, Viterbi and Baum-Welch (BW) algorithms respectively.

3. MEMS based Accelerometer

Micro-machined of silicon accelerometers also used their principle of mechanical and also a solid state of sensors. If the two classes of MEMS accelerometer. First class will consisted of mechanical accelerometers (i.e: devices which is used to measured their displacement of mass) [3]and it is manufactured by using their MEMS technique. A second time the class will consisted of devices which will measure their change in their frequency of vibration and it is caused the change in tension, it is in the accelerometers.[12] . An advantage of the MEMS devices is listed which was small, very light and having low powered consumption, start-up times have their performance of MEMS device which was improved rapidly.

3.1. MEMS Accelerometer of Error Characteristics

We should also examined their errors and it is a raised in the MEMS type accelerometers. These types of errors are mentioned below in the analogous form of sensor feature, and also therefore represented by the less details .An important difference was the errors which is arises from the accelerometers which was integrated with twice their order to track a position[9], i.e the rate-gyro signals which was only their integrated with once to tracked their orientation.

3.1.1 Constant of Bias

The biases of an accelerometer were offset and it also provides the output of signal from the true value, which is m/s^2 . A constant bias of error is ϵ , it was two times integrated, and caused by an error in the position it will grow by a quadratic in all time. The accumulated error was available at that point was

$$s(t) = \epsilon (t^2/2) \quad (1)$$

Where t is time of integration.

3.1.2 Flicker Noises / Bias Stability

MEMS accelerometer sensor was subjected to flickered noise, it was caused by a bias to wonder over their time. The fluctuation was modeled as biases random walk. The flickered of noise and it will be created by a second order random walk in the velocity which was uncertain and it will grow proportionally by $t^3/2$, which also a third ordered random walk on the positions was grow proportionally by $t^5/2$.

3.1.3 Temperature Effects

The temperature change will be caused the fluctuations on the bias without put of signal. The relation between bias, temperatures will also depend on their specific of the devices, which is also a very highest nonlinear method. A residual bias system will be caused by an error in their position it was grow very quadratically with in a time [7]. An IMU contained the temperature of sensor and it was possible for applying the correction of output of the signal which was ordered and compensate the temperatures of the dependent of effects.

3.1.4 Calibration Errors

The Calibrated errors will appear on the bias of errors it was only a visible to all devices which was undergone by the accelerated method. It shown that the 'temporary' bias error was observed and it was even though fall devices was stationary, it was due to their gravitational of acceleration.

4. Conclusion and future work

The main goal which is demonstrating successfully tracking the body motions and extract an accuracy of 92.3%. The system can recognize the body movement components and the program tracks the motion of human and whatever the left hand moves over a predefined area, it recognizes the motion and receives the next predefined area. The main focus is creating a modern device that can record and recognize the human gestures. Our system provides sufficient data and accurate feedback to the user. The algorithm was developed by the tracks and real-time of positions. Application of all systems can use an education tool for learner as well as facilitate communication.

References

- [1] N. C. Krishnan, C. Juillard, D. Colbry, and S. Panchanathan, "Recognition of hand movements using wearable accelerometers," *J. Ambient Intell. Smart Environ.*, vol. 1, no. 2, pp. 143–155, Apr. 2009.
- [2] C. Ding and X. He, "K-means Clustering via Principal Component Analysis", *International Conference on Machine Learning*, pp. 225-232, 2004.
- [3] R. Karlsson: Particle Filtering for Positioning and Tracking Applications. Thesis No. 9242005. ISBN 91-85297-34-8.
- [4] T. Kanungo, D. M. Mount, N. Netanyahu, C. Piatko, R. Silverman, and A. Y. Wu, "An Efficient k-means Clustering Algorithm: Analysis and Implementation", *IEEE Transaction on PAMI*, Vol. 24, pp. 881-892, 2002.
- [5] G. Bleser, M. Becker, and D. Stricker. Real-time vision-based tracking and reconstruction. *Journal of Real-Time Image Processing*, 2(2–3):161–175, Nov. 2007.
- [6] F. Kendoul, I. Fantoni, and G. Dherbomez. Three Nested Kalman Filters-Based Algorithm for Real-Time Estimation of Optical Flow, UAV Motion and Obstacles Detection. In *IEEE International Conference on Robotics and Automation (ICRA)*, 2007.
- [7] E. Mouragnon, F. Dekeyser, P. Sayd, M. Lhuillier, and M. Dhome. Real time Localization and 3D Reconstruction. In *Conference on Computer Vision and Pattern Recognition (CVPR)*, pages 363–370, 2006.
- [8] Y. Luo, C. C. Tsang, G. Zhang, Z. Dong, G. Shi, S. Y. Kwok, W. J. Li, P. H. W. Leong, and M. Y. Wong, "An attitude compensation technique for a MEMS motion sensor based digital writing instrument," in *Proc. IEEE Int. Conf. Nano/Micro Eng. Mol. Syst.*, 2006, pp. 909–914.
- [9] Pavlovic, V. I., Sharma, R. & Huang, T. S. (1997) "Visual Interpretation of Hand Gestures for Human-Computer Interaction: A Review". *IEEE Transactions on Pattern Analysis And Machine Intelligence*, Vol. 19, No. 7, pp 677- 695, doi; 10.1109/34.598226
- [10] J. A. Corrales Ramón, F. A. Candelas Herías, and F. Torres Medina, "Kalman filtering for sensor fusion in a human tracking system," 2010.
- [11] S. Rajapriya G. Gomathi, "Energy Improved Node Disjoint Multipath Routing Protocol for Wireless Sensor Network", 2018
- [12] A. RUBY SANGEETHA, "An Efficient Approach In WSN Design And Implementation For Energy Saving," 2014
- [13] C Bhuvaneshwari, G Saranyadevi, R Vani, A Manjunathan Development of High Yield Farming using IoT based UAV IOP Conference Series: Materials Science and Engineering 1055 (1), 012007
- [14] A Manjunathan, C Bhuvaneshwari Design of smart shoes *Materials Today: Proceedings* 21, 500-503
- [15] C Bhuvaneshwari, SK Beevi, A Abhinaya Smart and Secure Industrial Environmental Pollution and Faults Identification Control System 2020
- [16] C Bhuvaneshwari, A Manjunathan Reimbursement of sensor nodes and path optimization *Materials Today:*

Proceedings

- [17] Bhuvaneshwari C, Manjunathan A Advanced gesture recognition system using long-term recurrent convolution network Proc. ICONEEEE, 2019 pp. 1-8.
- [18] Viswanathan T, Mathankumar M, Ramya R, "Gesture identification based on neural network", International Journal of Engineering and Advanced Technology (IJEAT), Volume-8, Issue-2S, pp. 418-420, December 2018.
- [19] Rajkanna U, Mathankumar M, & Gunasekaran K, "Hand Gesture Based Mobile Robot Control Using PIC Microcontroller", IEEE International Conference on Circuit, Power and Computing Technologies (ICCPCT), pp. 1687-1691, 2014.

PAPER • OPEN ACCESS

Investigation of Tensile and wear properties of aluminium metal matrix composite

To cite this article: M. Arumugasamy *et al* 2020 *IOP Conf. Ser.: Mater. Sci. Eng.* 923 012060

View the [article online](#) for updates and enhancements.

EXTENDED ABSTRACT DEADLINE: DECEMBER 18, 2020

239th ECS Meeting



with the 18th International Meeting on Chemical Sensors (IMCS)



May 30-June 3, 2021

SUBMIT NOW →

Investigation of Tensile and wear properties of aluminium metal matrix composite

M.Arumugasamy¹, M. Suba pradha² and V.Vaitheeswari³

¹ Assistant Professor, M.A.M School of Engineering, Siruganur, Tamilnadu, India

² Assistant Professor, M.A.M School of Engineering, Siruganur, Tamilnadu, India

³ U.G Student, M.A.M School of Engineering, Siruganur, Tamilnadu, India

E-mail: cool.pradha@gmail.com

Abstract. The recent development of piston materials in internal combustion engines has contributed to the overall improvement in terms of durability and operation reliability. R&D and scientific centers both at home and abroad are conducting studies aimed at increasing the net power, torque and reducing the fuel consumption. The main function of piston is to convert thermal energy into mechanical work. Therefore selection of best material for piston plays a vital role in terms of extending its life, engine efficiency and low fuel consumption. Recent research has come up with a concept of composite materials, which shows that it has good mechanical properties compared to existing materials.

Keywords: automobiles, heavy transport, light transport, medium transport.

1. INTRODUCTION:

Materials that are most commonly used for manufacturing pistons include cast iron, alloy steel and Aluminium alloys, Aluminium-silicon (Al- Si) alloys and Aluminium-copper Aluminium alloys are distinguished by good formability during casting and good machinability (machine cutting). (1) The major drawbacks of these alloys include: a large thermal expansion coefficient, low hardness and low strength indices at elevated temperatures. (2) Cast-iron pistons are less and less often used. They can be found in low-speed self-ignition engines. They are characterized by the slide properties, retaining good mechanical properties at the elevated temperatures, and a small thermal expansion coefficient. The main disadvantage is that limit the use of cast-iron piston in contemporary high-speed engines a low thermal conductivity coefficient and high density .It results in a large piston mass and considerable inertia forces. (3) Due to high strength and low thermal expansion, pistons are increased oftenly and made of alloy steels. In spite of high density of steel, to take advantage of good mechanical properties of the material, designers give pistons appropriate shapes with small overall dimensions, which reduces the piston mass and make it compare to the mass of Aluminium alloy pistons.(4). The main objective of the study is to understand the suitability of Aluminium alloy (8090). The properties of Al alloy (8090) shows that it has better resistive properties to withstand the thermal stress in combustion chamber.

2. PISTON FAILURES

The most frequently occurring engine breakdowns are the failure of the engine pistons. The Engine piston occur at various mileage and due to different cause. This failure is caused by the material defect and engineering operational error.

The common causes of piston failures include: their insufficient cooling, insufficient lubrication of the piston guiding part, thermal fatigue of the piston head surface, failures due to an incorrect combustion process, and mechanical damage. During the engine operation, piston attain higher temperature than the cylinder, which will result in different thermal expansion of piston and cylinder. The thermal expansion of piston is much larger than the cylinder. In addition, the thermal expansion coefficient of Aluminium alloys is two times greater than the grey cast iron.



2.1 TYPES OF FAILURES

Cracked piston: Detonation is most likely caused of a cracked or broken piston. The hammer- like blow of detonation is literally beat a piston to death. It causes similar to those that can burn a piston: the lean fuel mixture, the over- advanced spark timing, bad knock sensor, a low octane fuel that cause the engine to run hotter.

Scuffed piston: Scuffed pistons is caused by too much heat in the combustion chamber, the engine overheat or inadequate lubrication. The piston-to- cylinder clearance is late-model engines which is much less and they are used to reduce piston rock and noise. If the piston or cylinder get too hot, the clearance will go away and get metal-to-metal contact.

Destroyed piston: If the piston is shattered and self-destructed, it will hit a valve. On interference engines, there is not enough clearance between piston and valves to avoid direct contact, the timing belt breaks. In most instance, the piston will survive a timing belt failure but bend it valves. But, some instance, the impact of a valve against a piston is more than casting can handle the piston to shatter like hand grenade. The debris goes into crankcase and it cause additional damage to bearings or piston.

2.2 WEAR PROPERTY OF A MATERIAL

Wear is progressive loss of material from operating surface of solid occurring as a result of relative motion between two surfaces. It appears as it occurs due to the relative motion between two bodies which are solid. There can be different mode or form of wear such as abrasion, adhesion, erosion and fatigue. When the two surface appears smooth macroscopically are brought together then the contact occurs at the isolated asperities on the surface. In general, wear can be classified into following types and it is explained in the following sections.

Abrasive wear, Fretting wear, Corrosive wear, Adhesive wear, Fatigue wear

3. PROPOSED METHOD

The in-depth study is carried out to understand the performance of Al alloy (8090) reinforced with the fly ash and zirconia under various test (tensile and wear). The comparative analysis of study between Al alloys (8090) reinforced with different compositions of zirconium and fly ash has been carried in this project work.

3.1 MATERIAL SELECTIONS

A composite material is the material made from two or more constituent material with significantly different physical or chemical properties, when combined, produce the material with characteristics different from individual components. The individual components remains separate and distinct with the finished structure. The new material is preferred for many reasons: common examples include materials which are stronger, lighter, or less expensive when compared to traditional material. Composites is made up of individual material referred to as constituent materials. There are two main categories of the constituent materials: matrix and reinforcement. At least one portion of type is required. The matrix material surrounds and support the reinforcement materials by maintaining the relative position. The reinforcements impart their special mechanical and physical property to enhance the matrix properties. A synergism produces the material properties unavailable from the individual constituent materials, the wide variety of matrix and strengthening materials allow the designer of product or structure to choose an optimum combination.

3.2 METAL MATRIX COMPOSITES (MMCs)

Metal matrix composites (MMCs) are consist of a metal or an alloy as continuous matrix and a reinforcement that can be a particle, short fiber or whisker, or continuous fiber. There are three kind of MMCs such as particle reinforced MMCs, short fiber or whisker reinforced MMCs, continuous fiber or sheet reinforced MMCs. Important metallic matrices are aluminium alloys, titanium alloys, magnesium alloys, copper etc. Many process for fabricating the metal matrix composites are available. For most of the part, these processes involve processing in the liquid and solid state.

3.2.1 MATRIX

The matrix is the material in which the reinforcement is embedded, and is completely continuous. This means that it is a path through the matrix to any point in the material, unlike two materials sandwiched together. In structural application, the matrix is usually lighter metal such as aluminium magnesium and it provides a compliant support for reinforcement. In high- temperature application, cobalt and cobalt-nickel alloy matrices both are common.

3.2.2 REINFORCEMENT

The reinforcement material is embedded with a matrix. It does not always serve purely structural task (reinforcing the compound), but is also used to change the physical properties such as coefficient, or. The reinforcement. It can be either continuous, or discontinuous. Discontinuous MMCs can be worked with the standard metalworking techniques, such as extrusion, forging, or rolling. In addition, it may be machined using conventional techniques, but commonly need the use of polycrystalline diamond tooling (PCD).

3.2.3 ALUMINIUM ALLOY 8090 (MATRIX)

Aluminium 8090 alloy is a lithium-based wrought alloy. Addition of lithium to aluminum will helps to reduce the density and increase stiffness. When it is properly alloyed, aluminum- lithium alloys can have an excellent combination of strength and toughness. The alloy has an excellent mechanical properties and is designed to promote the less density with increased stiffness. It is used for an advanced material in the design of high technology parts for the aerospace sector. It is used in the defense and weaponry systems.

Density	2540 kg/m ³
Melting Point	600-655 °C
Elastic Modulus	77 GPa
Tensile Strength	450 MPa
Yield Strength	370 MPa
Percent Elongation	7%
Thermal Expansion Coefficient	$21.4 \times 10^{-6}/K$

Table 3.1 Properties of Aluminium Alloy 8090

CONSTITUENT	PERCENTAGE
Aluminum, Al	93 - 96.2
Lithium, Li	2.2 - 2.7
Copper, Cu	1- 1.6
Magnesium, Mg	0.60 - 1.3
Iron, Fe	≤ 0.30
Zinc, Zn	≤ 0.25
Silicon, Si	≤ 0.20
Titanium, Ti	≤ 0.10
Chromium, Cr	≤ 0.10
Manganese, Mn	≤ 0.10
Zirconium, Zr	0.040 - 0.16

Table 3.2 Compositions of Aluminium Alloy 8090

3.2.4 ZIRCONIA (REINFORCEMENT)

Zirconia has an excellent resistance to the chemicals and corrosion without typical brittleness common in technical ceramics. When compared to the other advanced ceramic materials, zirconia has exceptional strength at room temperature. The principal properties of the material include high fracture toughness, high density, high hardness and wear resistance, good frictional behavior, high temperature capability up to 2400°C, non-magnetic, low thermal conductivity, electrical insulation, coefficient of the thermal expansion is similar to iron, and modulus of elasticity which is similar to steel.

3.2.5 FLY ASH (REINFORCEMENT)

The preference is to use fly ash as a filler or reinforcement in metal and polymer matrices is Fly ash which is a byproduct of coal combustion, available in very large quantities (80 million tons per year) at very low cost since much of it is currently land filled. Currently, the use of the manufactured glass microspheres has limited applications due to their high cost of production. Therefore, the material costs of composites can be reduced significantly by the incorporating fly ash into matrices of polymers and metallic alloys. However, very little information is available on aid in the design of the composite materials, even though the attempt is made to incorporate the fly ash in both polymer and metal matrices. Cenosphere fly ash has a lower density than the talc and calcium carbonate, but it slightly higher than hollow glass. The cost of the cenosphere is likely to be much lower than the hollow glass.

Cenosphere may be turn out to be one of the lowest cost fillers in terms of cost per volume. The high electrical resistivity, the low thermal conductivity and low density of fly- ash may be helpful for making the light weight insulating composites. Fly ash is a filler in Al casting which reduces cost, decreases density and increase hardness, stiffness, wear and abrasion resistance. It also improve the Mach inability, damping capacity, coefficient of friction etc. which are needed in the various industries like automotive etc. As the production of Al is reduced by utilization of fly ash. It reduces the generation of greenhouse gases as they are produced during the bauxite processing and the alumina reduction.

COMPOSITION	BITUMINOUS	SUB BITUMINUOS	LIGNITE
SiO ₂ %	20-60	40-60	15-45
Al ₂ O ₃ %	5-35	20-30	20-25
Fe ₂ O ₃ %	10-40	4-10	4-15
CaO%	1-12	5-30	15-40
LOI%	0-15	0-3	0-5

Table 3.3 Chemical Composition of Fly Ash

4. METHODOLOGY

4.1 COMPOSITE MATERIAL PREPARATION

Recent trends in the fabricating metal matrix composite is stir casting. Stir casting is a liquid state method of the composite material fabrication, in which a dispersed phase (ceramic particles, short fibers) mixed with the molten matrix metal by means of the mechanical stirring. Stir casting is simple and the most cost effective method of the liquid state fabrication. The liquid composite material is cast by the conventional casting methods and it may also be processed by the conventional Metal forming technologies.

4.1.1 STIR CASTING PROCESS

- Pre- heating time of die- 500°C for 90 minutes.
- Pre- heating time of reinforcement- 600°C for 90 minutes.
- Temperature of the furnace- 800°C.
- Stirring speed- 700 rpm to 1200 rpm for 10 minutes.
- Weight of the matrix material- 650 grams per sample.

4.1.2 DIFFERENT COMPOSITIONS OF SPECIMENS

- Specimen 1: Al+3% fly ash
650ams of Al +19.5 grams fly ash
- Specimen 2: Al+5% fly ash
650 grams Al+32.5 grams fly ash
- Specimen 3: Al+ 5% zirconia
650 grams Al+32.5 grams zirconia
- Specimen 4: Al+3% fly ash +3%
Zirconia
650 grams Al+19.5 grams fly ash+19.5 grams zirconia
- Specimen 5: Al+ 5% fly ash+5% zirconia
650 grams Al+ 32.5 grams fly ash+ 32.5 grams zirconia

Experimental setup

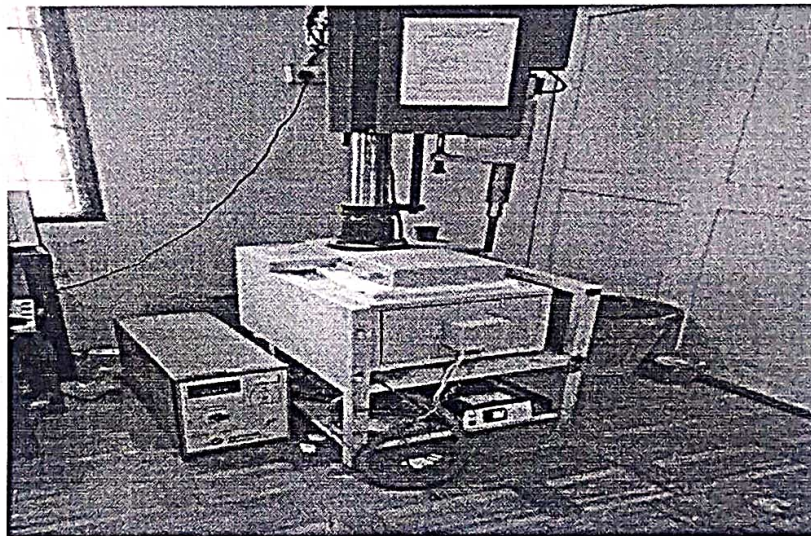


Figure.4.1 Pre- Heating Furnace

Muffle furnace is used to heat the material to the desired temperatures by conduction, convection, Or Black body radiation from the electrical resistance of heating elements. A muffle furnace is a Furnace in which the subject material is isolated from fuel and all the products of combustion is including gases and flying ash. This furnace has a capacity to achieve the maximum temperature of 1000°C, which is shown in the Figure.4.1

4.2 STIRRING PROCES

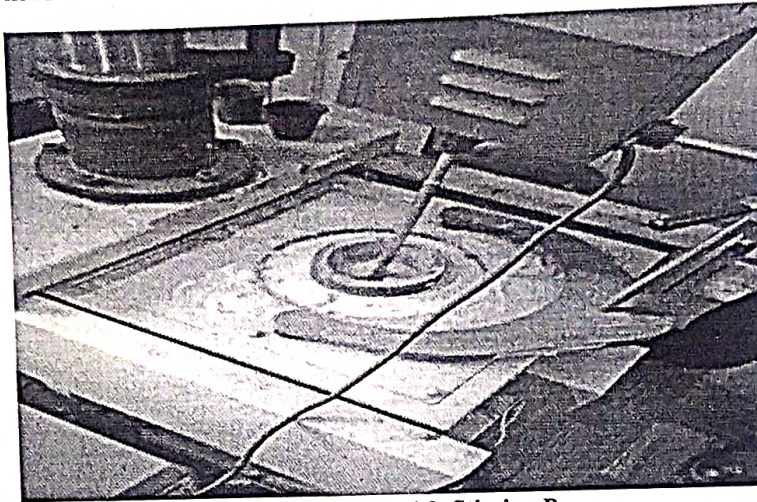


Figure.4.2. Stirring Process

The stirrer used in the process is made of stainless steel. Because of the high temperature the crucible, the stirrer should be capable of withstanding the temperature. Hence the stainless steel is used for making the stirrer in Figure.4.2 A crucible container that can withstand at very high temperatures and is used for the metal, glass, and pigment production as well as number of modern laboratory processes is used. The crucible is used here and is made up of graphite.

4.3 SPECIMEN PREPARATION

Pure Al 8090 of 650 grams placed in the graphite of crucible and is kept in an electric Resistance furnace. The furnace is set to the maximum temperature of 800°C. The melting point of Aluminum starts at 750°C after an elapsed time of 90 minutes. The furnace is kept at untouched for more than one hour at 800°C. 3% Fly Ash is taken and preheated to temperature of 600°C in order to ensure the moisture of free surface. The die is also placed in the separate furnace at a temperature of 500°C for pouring the molten metal. Then Fly Ash is added to the molten metal and the mixture is stirred for 10 to 15 minutes at 700 rpm using stirrer. Then the slurry is poured to the die and allowed to solidify. After solidification, the die is opened and the casted piece is also taken out. The above said procedure is repeated for the casting and for remaining specimens. The casted piece is 180mm in length and 20 mm in diameter. The fabricated specimens are shown in the Figure 4.3 below

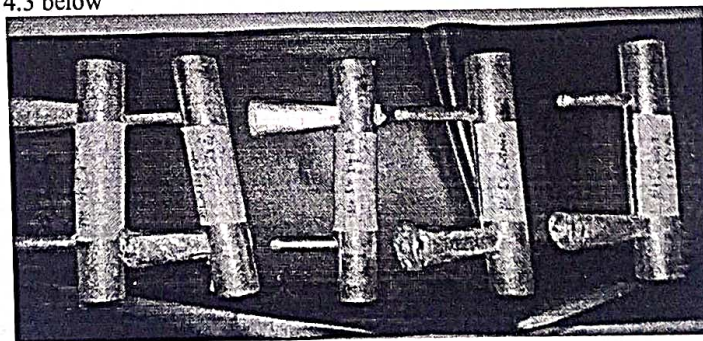


Figure.4.3. Casted Specimens

4.4 MATERIAL TESTING PROCEDURE

Tensile Testing

The specimen for tensile testing is prepared from casted specimen. This specimen has a length of 180 mm and diameter 20mm. The Tensile testing specimen should have gauge length of $5 \cdot D$ of the casted specimen. So the length of 100 mm is taken as gauge length where the elongation takes place. Knurling is done on remaining portion of the specimen on both sides to hold the specimen in Universal Testing Machine (UTM), which is shown in the Figure.4.4.

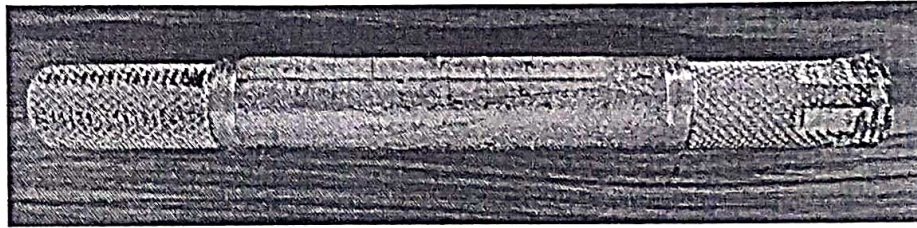


Figure.4.4 Specimen for Tensile Test

Four specimens are casted in stir casting is subjected to tensile test one by one. The specimen should be mounted on machine carefully by rotating the wheels placed here. After the confirmation of the correct placement of specimen, the machine is switched ON. The UTM setup is shown in the Figure.4.5

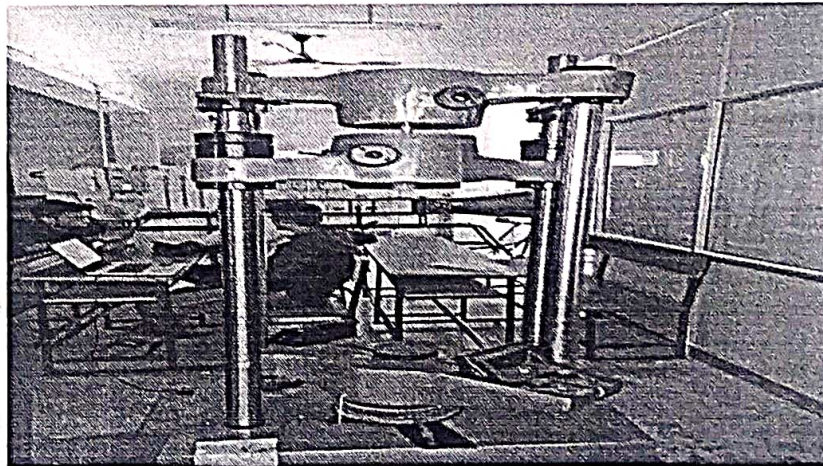


Figure.4.5 Specimen Mounted in Universal Testing Machine

4.4.1.UTM SETUP

The initial load in the machine is kept as the tare load. From the tare load it starts to increase as the load is applied in the specimen gets increased. At a certain point the load slightly decreases and increases which will represent the breaking point of the specimen. The specimen gets destructed at the point and the damaged pieces are collected which is shown below Figure.4.6. The change in the length after the tensile testing is measured for percentage elongation of specimen.

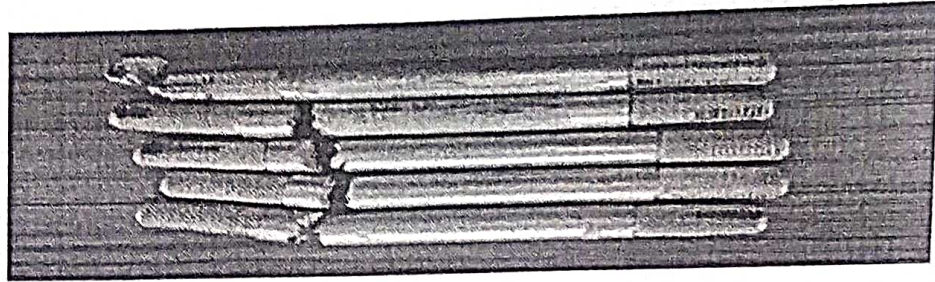


Figure.4.6 Specimens after tensile test

4.5.WEAR TESTING

For testing the wear in the specimen, a pin from the specimen and a disc of suitable material is required. In this work, the composite material is proposed for the piston application. So it is important to select the disc material for application. The piston is in the cylinder reciprocates from TDC to BDC during the Combustion process. Due to the movement, wear occurs between the piston and cylinder walls. Most of the cylinders in the Internal Combustion engines are made of the cast iron. Hence in this work the composite material is used for making Pin while the cast iron is used to make the disc to perform wear test. The pin is made with dimensions of length 50mm and diameter 7mm. The disc is made with dimensions of diameter 30 mm which is shown above in Figure.4.7.



Figure.4.7 Pin on Disc Apparatus

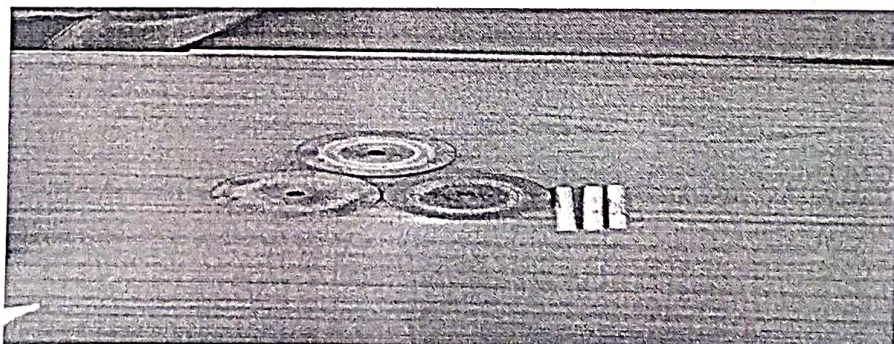


Figure.4.8 Disc and Pin for Wear Test

Load Balancing For Hybrid LIFI And WIFI Networks

J.Roselin Suganthi¹, M.Suba Pradha², S.Sivaranjani³, S.Susiladevi⁴, S.S.Sathya⁵, S.Saravanan⁶

¹Assistant Professor, K.Ramakrishnan College of Engineering, Trichy, Tamilnadu, India

²Assistant Professor, M.A.M School of Engineering, Trichy, Tamilnadu, India

³Assistant Professor, M.Kumarasamy College of Engineering, Karur, Tamilnadu, India

⁴Assistant Professor, Sri Bharathi Engineering College for Women, Pudukkottai, Tamilnadu, India

⁵Assistant Professor, Dhanalakshmi Srinivasan Engineering College, Perambalur, Tamilnadu, India

⁶Professor, Muthayammal Engineering College, Namakkal, Tamilnadu, India

ABSTRACT

The number of nodes in the world is rapidly increasing as the day-to-day communications are entirely depending on the wireless medium. This leads to the main issue of load balancing in the network. To combat this issue, mixture of LIFI and WIFI organizations are mainly emerging criteria in the wireless world. This is called hybrid LIFI and WIFI Networks which improves the framework limit of indoor remote communications. In this task, a joint advancement issue is formed, to decide an organization level determination for every client over a time of time. The proposed approach can improve framework throughput and accomplishing extremely low computational complexity. Burden adjusting turns into a difficult issue because of a total cover between the inclusion spaces of LIFI and WIFI. Shortest path algorithm and hybrid WIFI and LIFI algorithm, is formulated to determine a network-level selection for each user. The proposed approach can improve framework throughput and furthermore to stay away from the information traffic problem. Hybrid LIFI and WIFI organizations (HLWNets) are as of late proposed to improve the framework limit of indoor remote interchanges.

Keywords: Hybrid LIFI and WIFI Networks, Shortest path algorithm, load balancing algorithm.

1. INTRODUCTION

The term remote correspondence was presented in the nineteenth century and remote correspondence innovation has created over the resulting years. It is perhaps the main modes of transmission of data from one gadget to different gadgets. In this innovation, the data can be communicated through the air without requiring any link or wires[2].In the current days, remote correspondence framework has become a fundamental piece of different sorts of remote specialized devices, that grants client to convey even from far off worked zones. There are numerous gadgets utilized for remote correspondence like mobiles. Cordless phones, zigbee wireless innovation, GPS, WI-FI, satellite TV and remote PC parts. Current remote telephones incorporate 3G and 4G organizations, Bluetooth and WI-FI innovations [1]. Versatile information traffic increment between 2016 and 2021 reaching 48.3 hexa bytes each month before the finish of 2021.an indoor remote organization will represent over 80%. This will make a weight on existing WIFI, due its restricted data transfer capacity and thick business. To conquer these issues proposed to consolidate WIFI and LIFI [7]. This is known as hybrid LIFI and WIFI organizations [3]. There are numerous benefits in LIFI over WIFI.LIFI implies light devotion it sends and gets the data through light [6]. LIFI is quick transmission of information and quick web association around multiple times quicker than speeds reachable by WIFI.to stay away from load adjusting issues we join LIFI and WIFI [10][23].Load adjusting is the way toward appropriating network traffic across different servers, this guarantees no single worker bear, too much interest by spreading the work equally by improve application [11].

2. METHODOLOGY

2.1 SHORTEST PATH ALGORITHM

For significant distance remote correspondence information sends from source to objective as parcel. Here in this calculation tracking down the most limited way between the sources to objective [4].

STEPS

1. Introduce the distance as per the calculation
2. Pick first node and figure distance to neighbouring node
3. Pick the following node with negligible distance
4. Rehash adjoining node distance estimation and track down the most limited way.[8]

2.2 HYBRID LIFI AND WIFI LOAD BALANCING ALGORITHM

This calculation looks for lightest worker in the organization and hence assigns Proper burden on it .This method conquers the heterogeneity versatile to dynamic Climate amazing in open minded and has a decent adaptability consequently help in improve the presentation of the framework.[5]

3. PROPOSED SYSTEM

In proposed system, there are 3 sorts of organization access, i) LIFI only, ii) WIFI only, LIFI or WIFI.

During the transmission of information through WIFI is feasible, only when impedance happen in that way. In the proposed work WIFI switches over to LIFI during obstruction and make the information transmission without any problem [9]. In WIFI networks, it arrives at the edge level it switches over to LIFI [10]. In proposed system, there are 3 kinds of association access, LIFI only, WIFI only, LIFI or WIFI during the transmission of data through WIFI there is practical for impedance occur in that manner[13]. In the proposed work WIFI is switch over to LIFI during impediment and make the data transmission with no issue [14]. In WIFI networks it shows up at the edge level it switch over to LIFI[15].

3.1 NETWORK MODEL

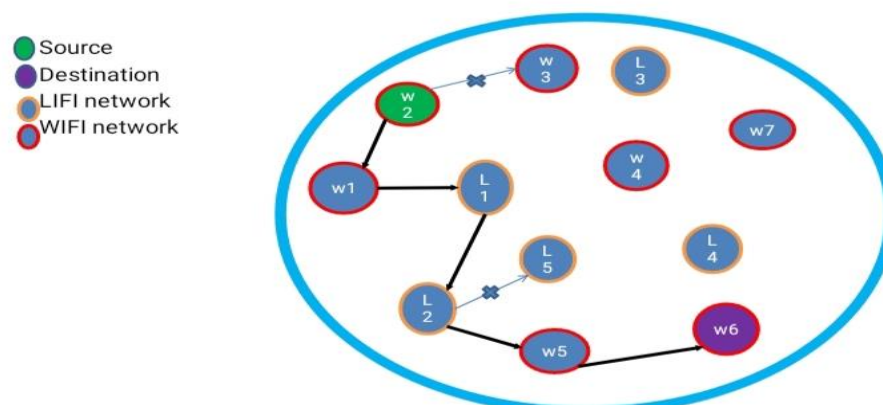


Fig1. Network Model

This figure1 shows Hybrid LIFI WIFI network model is contains combination of two types of networks such LIFI and WIFI.WIFI is higher area coverage network and LIFI is high speed network [16]. When interference occurs in WIFI network LIFI network will combine and reaches the destination [17]. It is used to determine a network level selection for each over a period of time.

3.2 FLOW CHART

Fig.2 shows the work flow of information from source to destination. This flowchart clearly explains the selection of network for transmission without affecting the load and the traffic.

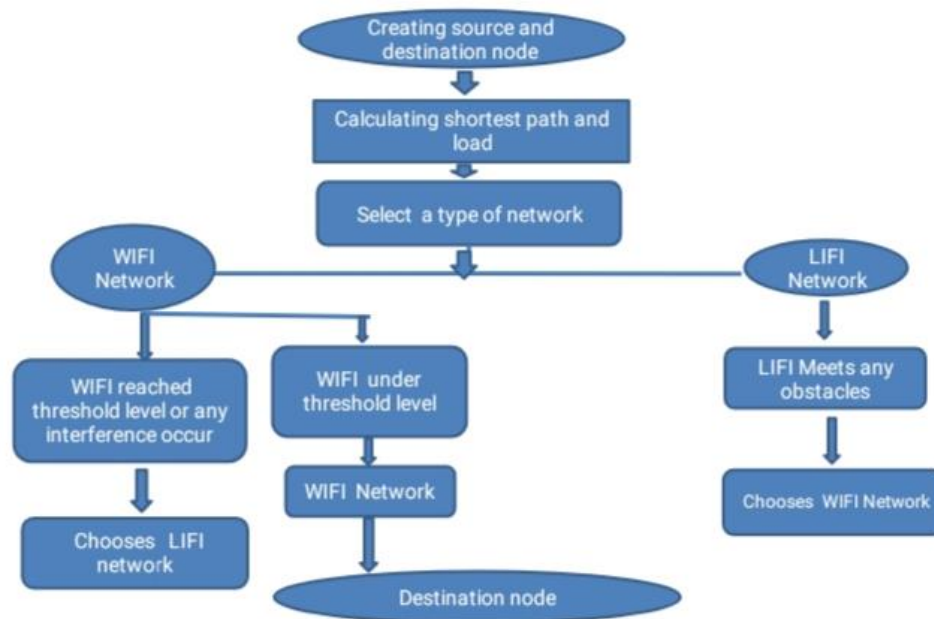


Fig2. Flow Chart

In this process it creates the source node and destination node, and calculating the distance and load based on algorithm .There are two type of networks such as LIFI and WIFI network .when it select WIFI network it has two conditions when WIFI reached the threshold level or any interference the WIFI network chooses the LIFI network [12] .when the WIFI under threshold level it chooses WIFI and reaches the destination node. The LIFI node meets any light path blockage it chooses the WIFI network.

4. RESULTS AND DISCUSSIONS

4.1 NODE ALLOCATION

The First Step of the process is node allocation, enter number of nodes and destination.it allocates the node based on the network availability and shortest path algorithm.

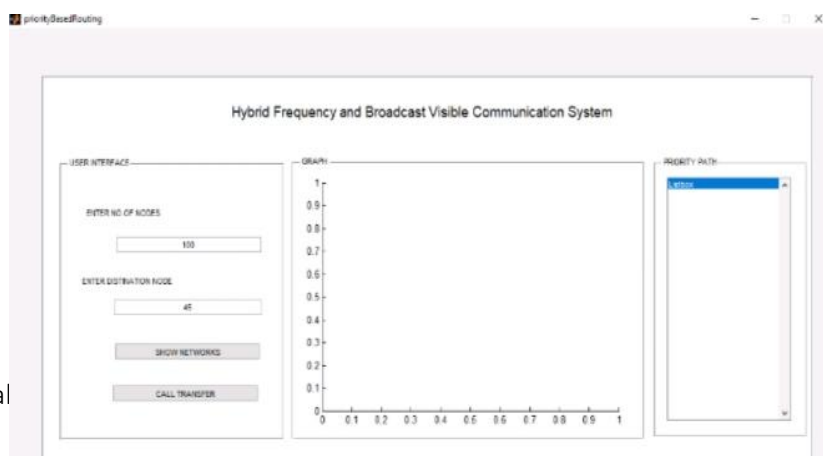


Fig 3. Node Allocation

This figure 3 shows node allocation it means it creates the source node and destination node. First enter number of the nodes and run the select network. Number of node is 75 and destination node is 50.then it find priority path.

4.2 PRIORITY PATH SELECTION

The second step of the process is priority path selection. It finds the shortest path for source and destination. It uses hybrid load balancing LIFI and WIFI algorithm. First it Initializes distances according to the algorithm. Pick first node and calculate distances to adjacent nodes [20][25]. Pick next node with minimal distance, repeat adjacent node distance calculations. Final result of shortest-path tree.

This Figure 4.2 shows priority path selection based on shortest path algorithm. For long distance wireless communication data send from source to destination in he form of packet.it shows priority path for all source node.

4.3 OUTPUT OF HLWNETWORKS

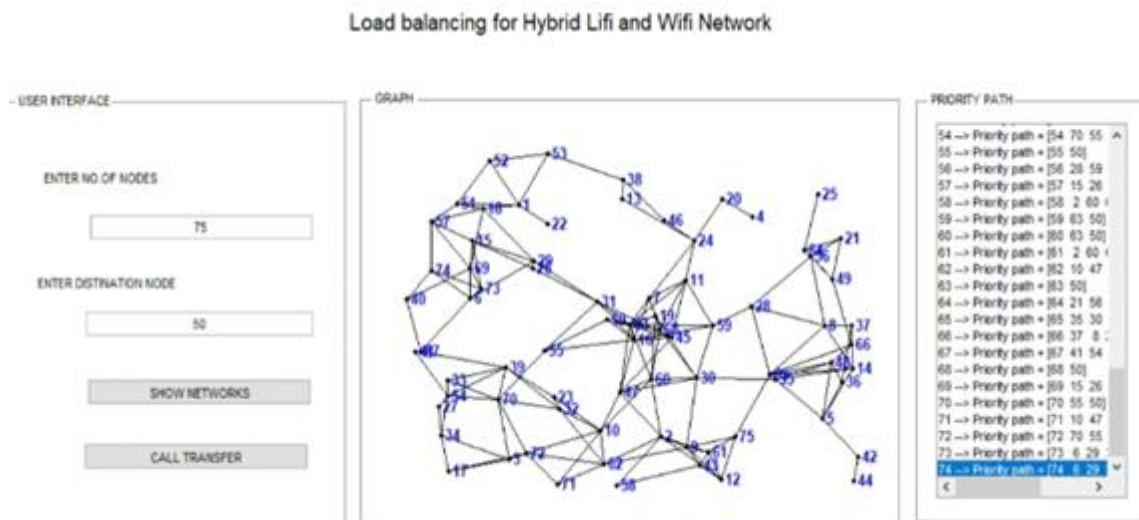


Fig4. Priority Path Selection

This is the output of the load balancing for hybrid LIFI and WIFI networks. Here dark line represents LIFI networks and other colour represents WIFI networks.in this project throughput is increased and delay is reduced.

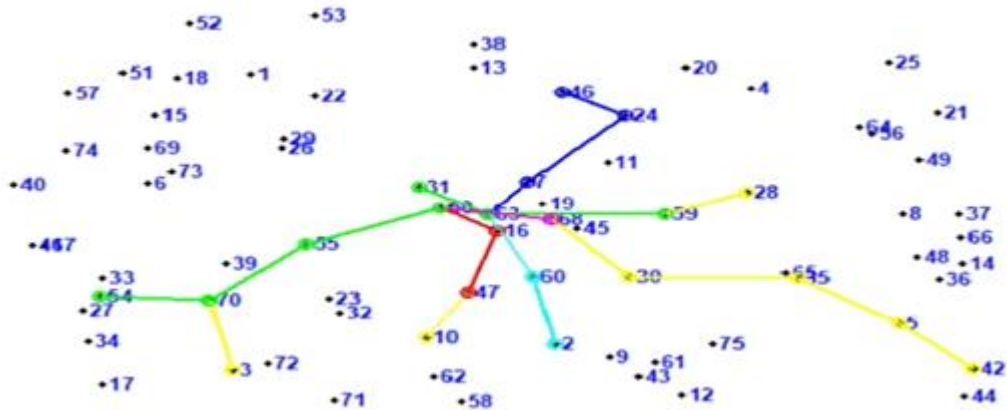


Fig5. Output of the HLWN

The figure 5 shows the output of HLWN by using shortest path and hybrid LIFI and WIFI algorithm. When WIFI reached threshold level it switches over to LIFI. When LIFI meets any obstacles, it switches over to WIFI network. It transfers the data without any interference [21].50th node is the destination node and 54th node is source node when interference occurs in 70th is the WIFI node it switches over to 3 LIFI nodes.

4.4 DELAY ANALYSIS

This is the delay analysis of proposed system,the graph is drawn between packet and time.the delay of proposed system is reduced than existing system.it takes lesser time than other systems.

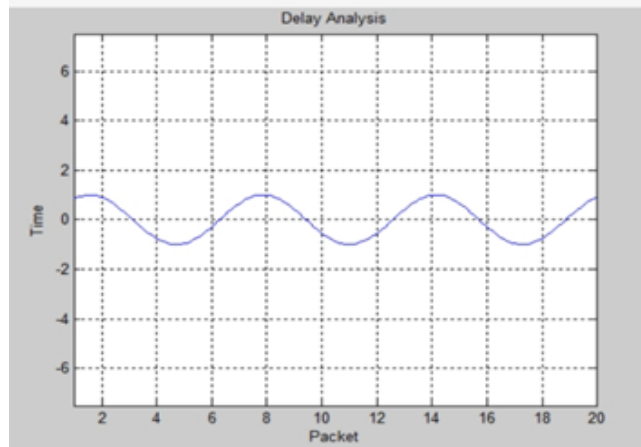


Fig 6 Delay Analysis

Figure 6 shows delay analysis of HLW networks by using shortest path and hybrid LIFI and WIFI algorithm [22]. The waveform represents decreases in delay. It reduces the amount of time taking longer than expected time.

4.5 THROUGHPUT ANALYSIS

This is the throughput analysis of the proposed system; this graph is drawn between packet and time. Packet takes lesser time than other and without any interference so it increases the throughput.

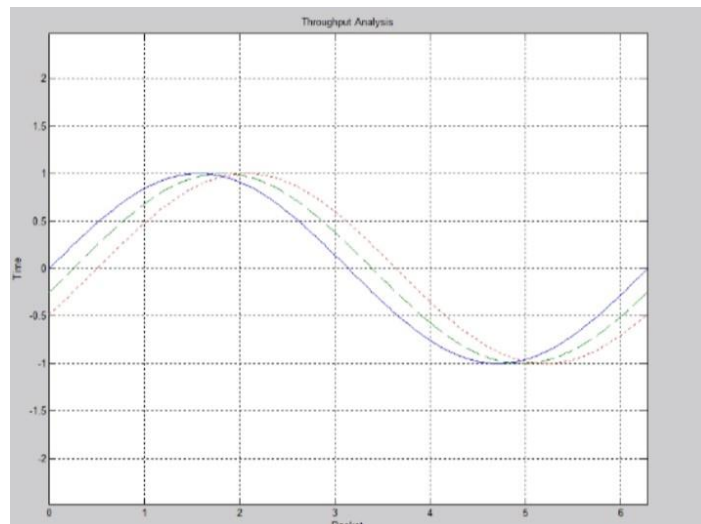


Fig7. Throughput Analysis

The figure 7 Shows Throughput analysis Of HLW networks. Throughput is the actual amount of data that can be successfully delivered over a communication channel. The throughput increased than existing system. The graph represents increases in the throughput.

5. CONCLUSION & FUTURE SCOPE

In the rapid increase of the communication nodes in the network. The demand of increase of the population of network makes demand in the spectrum allocation of the network in the transmission. The technique employed in this paper is an appreciable way for managing the load traffic in the network. Load balancing will help in making the network in a comfortable way so that spectrum is allocated in an efficient way by choosing the appropriate network with respect to obstacles. The throughput is achieved in the accepting way and delay has been reduced in the 50% in case of delay.

REFERENCES

- [1] Y. Wang and H. Haas, "Dynamic load balancing with handover in hybrid Li-Fi and Wi-Fi networks," *J. Lightw. Technol.*, vol. 33, no. 22, pp. 4671–4682, Nov. 15, 2015.
- [2] X. Li, R. Zhang, and L. Hanzo, "Cooperative load balancing in hybrid visible light communications and WiFi," *IEEE Trans. Commun.*, vol. 63, no. 4, pp. 1319–1329, Apr. 2015
- [3] Xiping Wu, Member, IEEE, and Harald Haas , Fellow, IEEE," Load Balancing for Hybrid LiFi and WiFi Networks: To Tackle User Mobility and Light-Path Blockage", *IEEE Transactions On Communications*, Vol. 68, No. 3, March 2020
- [4] Harald Haas," LiFi is a paradigm-shifting 5G technology, *Review in physics*," Volume3, November 2018, Pages 26-31
- [5] Hou H.W, Zhou,Tian, Shi J.L,and Vucetic.B, "Radio environment map aided Doppler shift estimation in LTE railway," *IEEETrans. Veh. Tech.*, to be published, doi: 10.1109/TVT.2016.2599558.
- [6] S.Susiladevi M Subapradha .J Roselin Suganthi C.Malarvizhi," Integration Of 3d Mems Accelerometer Sensor", *Annals Of The Romanian*,3, 2021
- [7] Sun.N, Zhao, "Distributed and dynamic resource management for wireless service delivery to high-speed trains," *IEEEAccess*, vol. 5, pp. 620-632, 2017.
- [8] J. Roselin Suganthi , " Efficient Channel Utilisation in Ultra Dense Networks", *International Journal of Latest Technology in Engineering, Management & Applied Science*

- (IJLTEMAS), Volume VII, Issue V, May 2018 | ISSN 2278-2540
- [9] Wu.J and Fan.P, “A survey on high mobility wireless communications: Challenges, opportunities and solutions” IEEE Access, vol. 4,pp. 450-476, 2016.
 - [10] J Roselin Suganthi, J Swapna,”Vehicle Control System Using VANET”, International Journal of Modern Agriculture, 2020
 - [11] C Bhuvaneshwari, A Manjunathan, “Reimbursement of sensor nodes and path optimization”, Materials Today: Proceedings, 2020.
 - [12] Bhuvaneshwari C, Manjunathan A, “Advanced gesture recognition system using long-term recurrent convolution network”, Materials Today: Proceedings, vol. 21, pp.731-733, 2020.
 - [13] M Ramkumar, C Ganesh Babu, K Vinoth Kumar, D Hepsiba, A Manjunathan, R Sarath Kumar, “ECG Cardiac arrhythmias Classification using DWT, ICA and MLP Neural Network”, Journal of Physics: Conference Series, vol.1831, issue.1, pp.012015, 2021
 - [14] K Balachander, G Suresh Kumaar, M Mathankumar, A Manjunathan, S Chinnapparaj, “Optimization in design of hybrid electric power network using HOMER”, Materials Today: Proceedings, 2020.
 - [15] M.D.Udayakumar, G.Anushree, J.Sathyaraj, A.Manjunathan, “The impact of advanced technological developments on solar PV value chain”, Materials Today: Proceedings, 2020.
 - [16] C.Vivek, S.Palanivel Rajan, "Z-TCAM : An Efficient Memory Architecture Based TCAM", Asian Journal of Information Technology, ISSN No.: 1682-3915, Vol. No.: 15, Issue : 3, pp. 448-454, 2016.
 - [17] Jothimani.S, Suganya.A, “Estimating Securities Exchange Utilizing Profound Neural Networks” International Journal of Grid and Distributed Computing Vol. 12, No. 3, 2019.
 - [18] S.Palanivel Rajan, S.Vijayprasath, “Performance Investigation of an Implicit Instrumentation Tool for Deadened Patients Using Common Eye Developments as Paradigm”, International Journal of Applied Engineering Research, Vol.10, Issue 1, pp.925-929, 2015.
 - [19] P T Sivagurunathan, P Ramakrishnan, “A Survey on Wearable health sensor – based system design”, International Journal of pure and applied mathematics, vol.118, issue.08, page no.383-385, 2018.
 - [20] A Manjunathan, A Lakshmi, S Ananthi, A Ramachandran, C Bhuvaneshwari, “Image Processing Based Classification of Energy Sources in Eatables Using Artificial Intelligence”, Annals of the Romanian Society for Cell Biology,vol.25, issue.3, pp.7401-7407, 2021.
 - [21] A Manjunathan, C Bhuvaneshwari, “Design of smart shoes”, Materials Today: Proceedings 21, 500-503
 - [22] P Matheswaran, C Navaneethan, S Meenatchi, S Ananthi, K Janaki, A Manjunathan,” Image Privacy in Social Network Using Invisible Watermarking Techniques”, Annals of the Romanian Society for Cell Biology, vol.25, issue.5, pp.319-327, 2021
 - [23] C Bhuvaneshwari, G Saranyadevi, R Vani, A Manjunathan, “Development of High Yield Farming using IoT based UAV”, IOP Conference Series: Materials Science and Engineering 1055 (1), 012007
 - [24] Manjunathan A, Suresh Kumar A, Udhayanan S, Thirumarai Selvi C, Albert Alexander Stonier, “Design of Autonomous Vehicle Control using IoT”, IOP Conference Series: Materials Science and Engineering, vol:1055, pp:012008
 - [25] Manjunathan A, Indumathi K, Balasundhari G, Dharani M, “IoT technology for remote controlled watering system”, International Journal of Engineering Research & Technology, vol.5, issue 13, pp. 1-3,2017.

MONITORING SOLID WASTE IN SMART CITIES USING IOT FOR GREEN AND SAFE ENVIRONMENT

Saravanan S¹, Sudha P², Suba Pradha M³

^{1,2,3} Assistant Professor

^{1,2,3} Dept of Mechatronics Engineering, M.A.M School of Engineering, Trichy, Tamilnadu, India.

ABSTRACT:-

Today, the inspection and disposal of the dustbin in the cities becomes a challenging task for the municipal corporation in the whole world. Dust bins are placed in open spaces, due to the daily increase in garbage will cause pollution to the environment. We have proposed a wireless solid waste management system for smart cities that allows municipal corporations to remotely monitor the condition of the dustbin from a web server and keep cities clean very effectively. IoT based Solid Waste Management System as an Ideological Approach with Architectural Solutions as a Smart City Application.

KEYWORD: Relay, Ultrasonic sensor, Atmega328 controller, Accelerometer sensor, Gas Sensor, ESP8266, Internet of things, LCD Display,

I. INTRODUCTION

The universal truth is that the waste of anything is harmful to society. The ultimate need of the developing nation for an effective ecological factor of "smart city" may include hazardous pollution, effects on human health so the Internet of Things (IoT) offers new opportunities to make cities smarter by introducing smart waste management system. We have trash cans that are overflowing and it is being checked by the local authorities that all kinds of garbage are being disposed of in bins and dumped all at once. So we have created a new concept of waste management disposal using automatic waste levels from ultrasonic sensors and Accelerometer sensor will provide real time information about the dustbin that is located in the city.

When Trash is filled, the information can be sent to the relevant authority to clean the dustbin through GSM Module. GSM is now the backbone of a communication system that is low cost and high performance device and easy to implement. The main goal of this project is to save time, money and fuel and also reduce exhaust gas emissions.

II. SENSOR CONCEPT

The Wi-Fi module is a spontaneous SOC with an integrated TCP / IP protocol stack that can provide access to any microcontroller let in your Wi-Fi network. This wi fi is capable of either hosting an application or loading all Wi-Fi networking functions to another application processor.

The Wi-Fi module is a low-cost component with which manufacturers are building wireless networkable microcontroller modules. The Wi-Fi module is a chip on the system that has capabilities for the 2.4GHz range. It is based on TCP / IP (Transfer Control Protocol). It is the most important component of the system as it performs IoT operations.

The Wi-Fi unit performs IOT operations by sending data to a web page that can be accessed by IP address. TX, RX pin, connected to pins 7 and 8 of Arduino microcontroller.

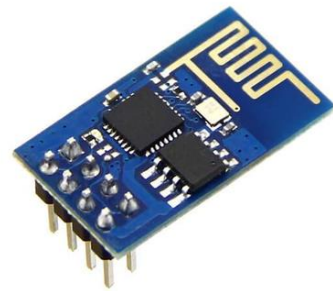


Figure.1. wifi module

III. GARBAGECONTAINER:

Garbage waste is a temporary waste storage container and is usually made of metal or plastic. There are three types: trash, dumpster, wheel barrow.



IV. ATmega328Controller:

The Atmega 328 controller is an open source controller board based on the microchip developed by Arduino. The board is equipped with a set of digital and analog input / output (I / O) pins that can be interfaced in various extension boards and other circuits. It is similar to Arduino Nano and Leonardo. Atmega 328 pre programs with a boot loader that will allow to upload a new code without using all the external hardware programmer.

V. ULTRASONIC SENSOR:

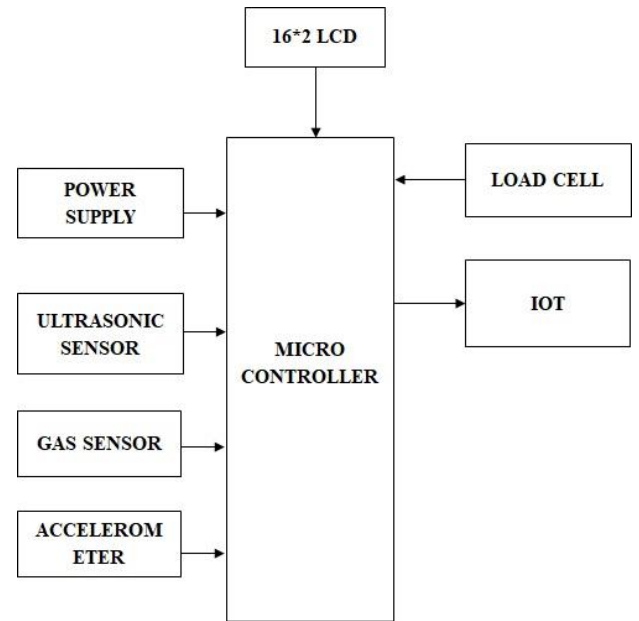
Special transducers are used for ultrasonic proximity sensors, which allow for optional transmission and reception of sound waves. The waves emitted by the transducer are reflected by an object and return to the transducer.



Fig 2: HC-SR04 Ultrasonic Sensor

VI. SOFTWARE DETAILS:

It includes GPRS. The module is a block diagram of the central server, database server and web server, web center software system. The central theme of this work is to develop on the intellectual supervision system for proper management of MSL. The municipal authority can customize this type of system and monitor the waste collection status of the system based on the recorded information, including the provision of the system, which gives customers the option to register their complaints if there are discrepancies.



APPLICATIONS

It can be used by municipal corporation to improve their management of their waste collections. With the help of their proper technology we can also guide the trucks to choose their shortest route. It also favors "Smart City" project and "Digital India"

IX. ADVANTAGES

Trucks Consume less time and fuel as the truck only moves to the filled container. The sensors installed in the container provide real-time information on the filling level. Thus the proposed system provide safe and clean environment to the society.

IX. CONCLUSION

We have implemented a real time waste management system using smart dustbin containers to check the filling level of the smart container whether the dustbin is full or not. The information of all the smart dustbins in this system can be accessed anywhere and anytime by the concerned person and he can decide accordingly. Through the implementation of this proposed system cost reduction, tool optimization, efficient use of smart dustbin can be achieved.

REFERENCES

- [1] Twinkle sinha, K. Mugeshkumar , P. Saishan an,(2015).
“Smart Dustbin“. International journal of Industrial electronics & electrical engineering, ISSN: 2347-6982, Volumee-3,issue-5.
- [2] Glossary of Environment statics: series F, No.67/Department for Economic and Social Information and policy Analysis, United Nations. New York : UN,1997.
- [3] R.Narayanmoorthi, Shubham Thakker: smart and wireless waste management system. System that gives prior information of the filling of bin that alerts the municipality and propose a “Smart Garbage Bin”, which will inform the authorized person when the garbage bin is about to fill. NIT spectroscopy is used for separation of biodegradable waste.
- [4] “GSM Global system for mobile communication”. 4 G Americas. Retrieved 2014-03-22.

SMART SPEED BREAKING SYSTEM FOR EMERGENCY VEHICLE USING RFID

Chandrasekar.M¹, Mohamed Ashib. N², Niyas Ahamed.S³, Mohammed Nowfull.N⁴, Mageshwaran. N⁵

¹Assistant Professor, Department of Mechatronics Engineering, M.A.M School of Engineering, Trichy.

^{2,3,4,5}Student, Department of Mechatronics Engineering, M.A.M School of Engineering, Trichy.

¹mchandrasekar1983@gmail.com, ²mohamedashib777@gmail.com, ³niyasahmedn12@gmail.com,

⁴vsnavfal@gmail.com, ⁵mageshrio460@gmail.com

ABSTRACT

India has a large network of road throughout the country. India faces the highest number of accidents and accidental fatalities in the world. To prevent the accidents caused due to over speeding of vehicles, speed breakers are used. But, the accidents are caused due to both presence and absence of speed breakers. Particularly at the night time the driver of vehicle not has known the presence of speed break on road. Due to this accident will happen. During day time, the speed breakers are necessary to avoid the accident. But the presence of speed breaks on the road will increase the travelling time of the emergency vehicle like ambulance. The proposed system solves the above problem by controlling the speed break automatically as per requirement by using RF detector and it is controlled using arduino controller.

1. INTRODUCITON

Road shipping is crucial mode of shipping in India. India has second largest road network in the world. Out of total stretch of 5.4 million km of road network, almost 97,991 km is covered by national highways. But India faces the largest number of accidents and accidental fatalities in the world.

The Ministry of Road Transport and Highways report reveals that 1, 51, 113 deaths were occurred in the year of 2019. Road accidents continue to be a leading cause of death, disabilities and hospitalization. India ranks first in the number of road accident deaths across the 199 countries and

accounts for almost 11% of the accident related deaths in the World.

Ministry of Road Transport and Highways has been taking multiple initiatives including those related to vehicular and road engineering as well as educational measures for raising awareness in the field of Road Safety. The year 2019 saw the culmination of our efforts in the field of Road safety through the enactment of the Motor Vehicle Amendment Act 2019, which among other things, provides for a stiff hike in penalties for traffic violations with the aim of bringing in discipline and a responsible attitude amongst road users.

The government also placed speed breakers on the road through the ministry of road transport and highway to prevent the accidents caused due to over speeding of vehicles. In India 3,409 deaths occurred in the year of 2015 due to speed breakers which is more than the number of total deaths occurred due to accidents in Australia and UK. The presence of speed breakers also causes some difficulties to the patients travelling in emergency vehicles and also it increases the travelling time. Because of increasing travelling time, the death rate of patient is increased.

All the above problems have been avoided by proposing smart speed breakers. In a proposed system the speed breakers can be used only when it is needed. During night time, speed breakers are not necessary. So the speed breaker flattens during night time. It reduces accident at night time due to presence of speed break. During day time the speed breakers get flattens, whenever the emergency

vehicle cross the speed breaks. It reduces the travelling time for emergency and VIPs vehicles.

2. LITERATURE SURVEY

Vamsee Krishna Kiran M commented that when the user uses the Google maps, an android service begins in the Background. The device collects speed breaker latitude and Longitude data. The proposed system is built in such a way That speed breakers don't need any person to tell. When a Consumer encounters a speed breaker the sudden amplitude Shift is noted.

Shivam Gaikwad explains to develop Today's traffic safety Solution requires all cars to slow down without realizing the Speed of the ongoing vehicle, which raises the traffic issue. To prevent this, the device must work according to the speed of the car. In this assembly, the bumps of the smart speed Breaker lower into the road surface are elevated above the Physical residue.

Dr.Raafiya Gulmeher addressed that Smart Speed Breaker system with IOT that will surface and only display if The speed of the vehicle is greater than those limits. Arduino Board activates a motor to surface the speed breaker Mechanism for control of the speed breaker, for use of RTC in Real time. The Arduino board sends a signal to the buzzer to Start the beep sound to warn the driver according to the Speed and distance of the breaker.

Ajay S addressed that to have an automatic speed breaker On time demand according to the specifications The breaker Disappears when there is no need for a speed breaker and When there is a need then the breaker comes on the road by Spinning itself and begins to work slowing the vehicles Speed. In implementing this definition, we use a hemi cylinder speed breaker made from iron

M. Suresh discusses that the ambulance does not decrease the speed in order to save the patient from injury. As the Ambulance approaches the speed breaker, the motor rotates After getting the signal. The speed breaker is flat. The speed Breaker returns to normal after the speed programmed in the Arduino. The proximity sensor is located to avoid

the rotation In the exact speed breaker location. The control circuit Consists of Arduino, which processes the RF signal and transmits it to the RF receiver via the RF transmitter. The RF transmitter circuit shall be placed on the ambulance. The Speed breaker lets the ambulance reduce speed, but this new Flat speed breaker device plays a major role in protecting Human lives by making the speed breaker flat.

3. PROPOSED METHODOLOGY

India has a large network of road throughout the country. India faces the highest number of accidents and accidental fatalities in the world. To prevent the accidents caused due to over speeding of vehicles, speed breakers are used. But, the accidents are caused due to both presence and absence of speed breakers. During night time, the road user may not aware of the availability of the speed breaker. So the accident may cause. To solve this problem the speed breaker is flattening in the night time and it come backs to the original position in day time.

Patients travelling in emergency vehicles face many difficulties due to speed breakers. I.e. the speed break in the road will increase the travelling time of ambulance and other emergency vehicles. It will cause some serious problem like increasing death rate and increase the difficulty in the treatment process of the patient. They need a smooth ride. In these situations, speed breakers are not needed.

To solve the entire above problem, we proposed a automatic speed breaking system on road based on RFID and Arduino controller. The block diagram of the proposed system is shown in the below figure. The figure-a show the module which is placed on the vehicle and the figure-b shows the module which is placed on the road and it control the movement of the speed breaker.

Here Temperature/LDR sensor is used to sense the available temperature/Light and RFID is used to sense the vehicles. In rainy days many accidents will occur due to low friction during breaking, so the speed breaker is not necessary

during rain. Many luxurious cars are struggling to move over a speed breaker. So, in this paper we are controlling the speed breakers automatically based on the requirement by using RF detector and it is controlled controller.

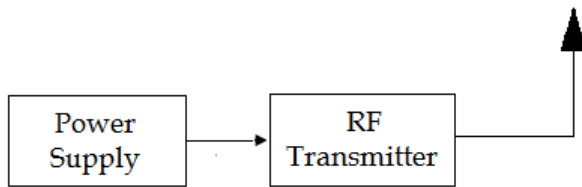


Fig-A Block diagram of module used in vehicle

The RF transmitter is placed on the entire emergency vehicle. It will transmit the RF signal periodically. Whenever the RF receiver receives the RF signal from the vehicle it sends the control signal to the microcontroller. Then the microcontroller makes the speed breaker flattening. After crossing of the emergency vehicle, again the speed breaker comes to the original position. The DC motor and their driver module control the movement of the speed breaker on the road.

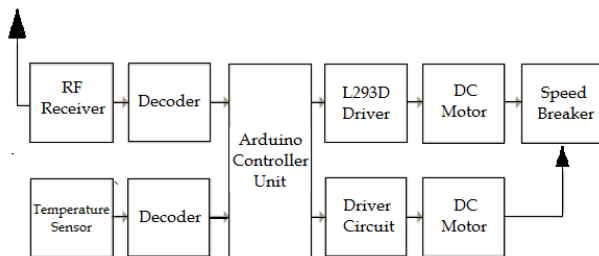


Fig-B Block diagram of the automatic speed breaker on road

Here Temperature/LDR sensor is used to sense the available temperature/Light. The reading of the temperature sensor is decoded by the decoder. If the temperature sensor value is below the threshold value, the microcontroller is moved down the speed breaker and makes the smooth road at night time.

4. HARDWARE COMPONENTS

The proposed system recommends a cost-effective solution that controls the up/down

movements of the speed breaker on the highways. The major components used in the proposed system are as follows:

ARDUINO CONTROLLER

Arduino is an open-source platform used for building electronics projects. Arduino consists of both a physical programmable circuit board (often referred to as a microcontroller) and a piece of software, or IDE (Integrated Development Environment) that runs on your computer, used to write and upload computer code to the physical board.

The Arduino platform has become quite popular with people just starting out with electronics, and for good reason. Unlike most previous programmable circuit boards, the Arduino does not need a separate piece of hardware (called a programmer) in order to load new code onto the board, you can simply use a USB cable. Additionally, the Arduino IDE uses a simplified version of C++, making it easier to learn to program. Finally, Arduino provides a standard form factor that breaks out the functions of the microcontroller into a more accessible package.

DC MOTOR

DC motor is an electrical motor which transforms direct current electric energy in the form of rotation into mechanical energy. The movement is brought about by the electromagnetism's physical behavior. Within DC motors have inductors which generate the movement-generating magnetic field.

When a current-carrying conductor is placed in a magnetic field, it experiences a torque and has a tendency to move. In other words, when a magnetic field and an electric field interact, a mechanical force is produced. The DC motor or direct current motor works on that principle. This is known as motoring action.

RF TRANSMITTER AND RECEIVER

Radio frequency (RF) radiation is a subset of electromagnetic radiation, with wavelengths ranging from 100 km to 1 mm, and frequencies

from 3 KHz to 300 GHz, respectively. The range of electromagnetic radiation constitutes the radio frequency spectrum and corresponds to the frequency of the alternating current signal used to generate and detect radio waves. RF can refer to electromagnetic oscillations in circuits or radiation through air and space. Similar to other subsets of electromagnetic radiation, RF travels at the speed of light.

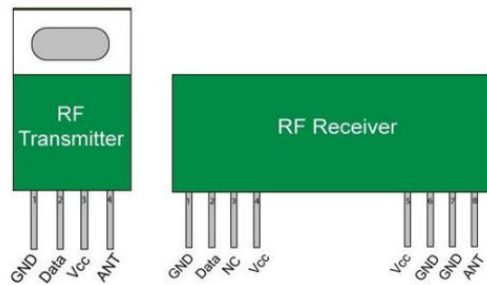


Fig-C Pin Diagram of RF Module

An RF receiver is attached in the speed breaker module and corresponding RF receiver is attached to the emergency vehicle. The RF transmitter attached to the vehicle will continuously send signals with the radius of signal strength. If the RF receiver attached to the speed breaker will detect and receive signals from the transmitter, upon receiving the signal, it can be concluded that an emergency is come nearby. Arduino IDE is used for monitoring and implementing this wireless form of communication between the transmitter and the receiver. After receiving the control signal from the RF receiver, the Arduino microcontroller will rotate the speed breaker and make the flattening road. The wired communication is not possible between a moving vehicle and a static speed breaker, hence wireless form of communication in the form of an RF module is being used in the proposed system.

TEMPERATURE SENSOR

The Temperature Sensor LM35 series are precision temperature detecting devices in the form of integrated-circuit with an output voltage linearly proportional to the Centigrade temperature.

The LM35 device has an advantage over linear temperature sensors calibrated in Kelvin, as

the user is not required to subtract a large constant voltage from the output to obtain convenient Centigrade scaling. The LM35 device does not require any external calibration or trimming to provide typical accuracies of $\pm 1/4^\circ\text{C}$ at room temperature and $\pm 3/4^\circ\text{C}$ over a full -55°C to 150°C temperature range.

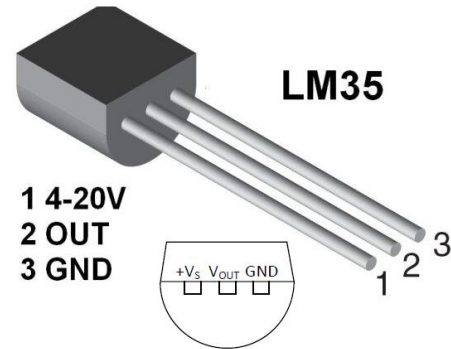


Fig D Pin Diagram of LM35

6. CONCLUSION AND FUTURE SCOPE

The Braking system, if implemented can reduce number of accidents and might save invaluable human lives and property. The complete system is widely open and can work with various sensors and actuators. The proposed system can have different subsystem such as sensors, actuators and etc. Now, this system is designed as a paper work at small level however can adopt this system at industry level in future, So that we can prevent lots of accidents and human lives. The Future of automotive safety is depends on the development of new Technology for preventing accidents.

The future scope is to design and develop a control system Based on an smart braking system is called —smart speed Braking System. The radio Frequency Sensor identification sensor in the smart speed Braking System will alert the driver, if the distance between vehicle and obstacle is not within the sensing range Zone. After receiving alert, the diver has to apply break; if not the brakes are applied automatically by smart breaking system. This is the new function in this prototype design that could be possibly used for all vehicles. By making this safer, this system will provide better Guarantee for people lives and avoid losses. It is

verily useful to public sector and users. It is also avoids the accidents in large or metropolitan cities. So we feel it is a better idea for Smart speed breaking system of emergency vehicle with moderate cost.

REFERENCES

[1] Navaneetha Varier, Abhishek Sehgal, T. Balachander, "Smart Speed Breaker System Using Internet of Things" International Journal of Pure and Applied Mathematics Vol 118 No.22 2018, 415-419.

[2] Shivam Gaikwad, Sumeet Shinde, Shridhar Desai, Prof. Sanjay Deodas "Design and Development of Smart Speed Breaker" International Journal of Advance Research and Innovative Ideas in Education (ISSN (0)- 2395-4396) 2018.

[3] Janardhana Reddy. P, Pavan Kumar, G Reddy Basha, P Janardhana "Intelligent Traffic Light and Speed Breaker Flatten System" p janardhana Reddy.et.al. Int. Journal of Engineering Research and Application (ISSN: 2248- 9622) November 2017.

[4] Mohit Raj, Prof S. D. Ghodmare, Rakesh Kumar Choubey "Comparison of Automated Speed breakers with Conventional Speed breakers" International Journal of Advance Research, Ideas and Innovations in Technology ISSN: 2454-132X Volume 5, Issue 3.

[5] Anchal Dewangan and Dr. N. K. Saikhedkar, "Experimental analysis of Different Types of Speed Breakers" 2018 IEEE.

[6] AravindKaruppaiah, Gansh.S, Dileepan.T, Jayabharathi.S, "Fabrication and Analysis of Automatic speed breakers" 2019 IEEE.

[7] Mohit Raj, Prof. S. D. Ghodmare, Rakesh Kumar Choubey "Review on Speed Breakers for Traffic Calming Roads "International Journal of Innovations in Engineering and science (ISSN: 2456-3463) 2019.

[8] Vengadesh. A, K. Sekar, "Automatic Speed Control of Vehicle in Restricted Areas using RF and GSM" International Research Journal of

Engineering Research and Technology (IRJET)
Volume: 02 Issue: 09 Dec-2015.

[9] Zer-Ming Jeng, Sheng Chung Tzeng, Bo-Jun Yang and YiChun Li, "Design Manufacture and Performance Test of the Speed Breaker System" 2017 IEEE.



Influence of trivalent lanthanides substitution on the thermoelectric properties of nanostructured $\text{Ca}_{1-x}\text{Ln}^{3+}_x\text{MnO}_{3-\delta}$ ($\text{Ln}^{3+} = \text{Sm, Ce, La}$; $x = 0, 0.1$)

S. Berbeth Mary¹ · A. Leo Rajesh¹

Received: 6 December 2019 / Accepted: 4 March 2020
© Springer Science+Business Media, LLC, part of Springer Nature 2020

Abstract

Mesoporous $\text{Ca}_{1-x}\text{Ln}^{3+}_x\text{MnO}_3$ ($\text{Ln}^{3+} = \text{Sm, Ce, La}$; $x = 0, 0.1$) nanoparticles were prepared by sol–gel hydrothermal method followed by annealing under oxygen atmosphere at 950 °C. The systematic analysis revealed that due to the influence of lanthanides substitution, significant changes were occurring on the electrical and thermoelectric properties of the material. The synthesized nanopowders were characterized by XRD, Raman analysis, SEM with EDAX, HRTEM and thermoelectric measurement. Structural analysis confirmed the orthorhombic perovskite structure without distortions and the cell volume increased with a rise in the ionic radius of the Ln^{3+} ions. Microstructure and EDAX analysis demonstrated the grain size and stoichiometry of all the samples. HRTEM analysis is used to measure the size and shape of the nanoparticles. The physical properties of $\text{Ca}_{0.9}\text{Ln}^{3+}_{0.1}\text{MnO}_3$ nanoparticles exhibit metallic behavior with increasing temperature whereas undoped CaMnO_3 shows semiconducting behavior. The electrical and thermoelectric measurements proved that $\text{Ca}_{0.9}\text{Sm}_{0.1}\text{MnO}_3$ nanoparticle showed high Seebeck coefficient value, large electrical resistivity, and significant power factor, indicating a potential n-type thermoelectric material at elevated temperature.

1 Introduction

Perovskite oxides have received much attention due to its electrical, electronic, ionic, electrochemical, superconducting, magnetic, and thermoelectric properties in the fields of solid oxide fuel cells, oxygen sensors, catalysts, super capacitors, electrodes, superconductors and thermoelectric devices [1–5]. These incomparable properties make them as a potential candidate in various energy storage applications. From this perspective, the perovskite oxides are studied as promising material for thermoelectric (TE) applications which convert the irrecoverable heat energy directly into electricity via Seebeck effect and vice versa. Material used for thermoelectric applications should possess high-electrical conductivity and low-thermal conductivity with significant Seebeck coefficient [6]. Bi_2Se_3 , Sb_2Te_3 , and PbTe are highly efficient state of art thermoelectric materials at low temperature but toxicity, scarcity, and instability at higher

temperature confined them in large-scale production. The oxide thermoelectric materials are the solutions for this problem and the discovery of Na_2CoO_2 in the year 1997 stimulated the researchers to find the new novel thermoelectric oxide materials for high-temperature applications. Compared to other oxides, CaMnO_3 is one of the high-temperature potential n-type thermoelectric materials due to its oxidation resistance in air atmosphere and stability at higher temperatures [7].

Due to carrier mobility, the undoped CaMnO_3 nanoparticles exhibit poor TE performance. On the contrary, lanthanides substitution at Ca-site of CaMnO_3 can improve the electrical conductivity, which enhances the TE performance [8–11]. Wang et al. reported the improved TE properties of $\text{Ca}_{1-x}\text{Ln}_x\text{MnO}_3$ ($\text{Ln} =$ trivalent lanthanides) in the composition range $0.02 \leq x \leq 0.1$ [12, 13]. In this scenario, the TE study of $\text{Ca}_{1-x}\text{Ln}^{3+}_x\text{MnO}_3$ where $\text{Ln}^{3+} = \text{La, Ce}$ and Sm ; and $x = 0.0$ and 0.1 have been focused. Reducing thermal conductivity to enhance the TE power factor can be achieved by introducing mesoporous structure and nanostructuring the materials [14]. The synthesis conditions, additives and post heat treatments also improve the efficiency of the material by obtaining pure, nanostructured systems with controlled size and shape. Phase purity, controlled particle size,

✉ A. Leo Rajesh
aleorajesh@gmail.com

¹ Department of Physics, St. Joseph's College (Autonomous),
620 002 Tiruchirappalli, Tamil Nadu, India

monodispersity, homogeneous, predictable surface morphology, and large-scale production are the combined advantages of hydrothermal and sol-gel techniques [15]. Nanostructured mesoporous materials maximize the TE power factor by lowering thermal conductivity. Simultaneously this structure reduces the TE efficiency by increasing the oxygen deficiency. Annealing under oxygen atmosphere removes the oxygen deficiency and improves the thermopower [16–19].

In this research paper, electron-doped $\text{Ca}_{1-x}\text{Ln}^{3+}_x\text{MnO}_3$ ($\text{Ln}^{3+} = \text{Sm}, \text{Ce}, \text{and La}; x = 0, \text{ and } 0.1$) nanoparticles were synthesized by sol-gel hydrothermal method and the temperature dependence thermoelectric properties were measured and analyzed. The influence of rare earth metals on structural, morphological, electrical and thermoelectric properties of $\text{Ca}_{1-x}\text{Ln}^{3+}_x\text{MnO}_3$ ($\text{Ln}^{3+} = \text{Sm}, \text{Ce}, \text{and La}; x = 0, \text{ and } 0.1$) were investigated and optimized for the application of thermoelectrics.

2 Experimental procedure

2.1 Synthesis

AR grade Calcium nitrate tetrahydrate ($\geq 99.0\%$), Manganese (II) nitrate hexahydrate ($\geq 98.0\%$), Lanthanum (III) nitrate hydrate (99.9%), Cerium (III) nitrate hexahydrate (99%), Samarium (III) nitrate hexahydrate (99.9%), Citric acid, polyvinyl pyrrolidone (PVP), and ammonium hydroxide solution were used as precursors without further purification. Citric acid and PVP were used as a chelating and capping agent. Stoichiometric amount of metal nitrates of $\text{Ca}(\text{NO}_3)_2 \cdot 4\text{H}_2\text{O}$ and $\text{Mn}(\text{NO}_3)_2 \cdot 6\text{H}_2\text{O}$ were dissolved in distilled water and citric acid solution were added to the mixture in the molar ratio of 1:1 (citric acid: metal ion) with 2 g of PVP solution added. Homogeneous solution was obtained after stirring for 30 minutes and ammonium hydroxide solution was added dropwise till its pH reached 9.2, then it was heated at 80°C to obtain reduced compound and the sol was transferred into a Teflon-lined stainless steel autoclave, placed in a preheated hot-air oven at 200°C for 20 h. The product was cleaned with distilled water and ethanol to remove the organic substances, then dried and annealed at 950°C under oxygen atmosphere to acquire undoped CaMnO_3 and $\text{Ca}_{0.9}\text{Ln}^{3+}_{0.1}\text{MnO}_3$ compound with a desirable oxygen stoichiometry.

2.2 Characterization

Structural characterization of $\text{Ca}_{1-x}\text{Ln}^{3+}_x\text{MnO}_3$ ($\text{Ln}^{3+} = \text{Sm}, \text{Ce}, \text{and La}; x = 0, \text{ and } 0.1$) samples were carried out using Bruker D8 advance diffractometer equipped with Cu $K\alpha$ radiation ($\lambda = 1.5406 \text{ \AA}$) with 2θ ranging between 10 and 80 degrees with a step size of 0.02° and an exposition

time of 3 s at each step. Raman spectroscopy measurement was performed using LABRAM-HR visible spectrometer equipped with micro-optics, where He-Ne laser was used as a source with an excitation wavelength of 632.8 nm at room temperature. The surface morphology of the samples was analyzed using a JEOL JSM 5600 scanning electron microscope and its elemental analysis accomplished by Energy Dispersive X-ray analysis (EDAX). High-resolution transmission electron microscopy (HRTEM-JEOL JEM 2100) was used to further examine the size, shape and pore structure of $\text{Ca}_{1-x}\text{Ln}^{3+}_x\text{MnO}_3$ nanoparticles. For thermoelectric studies, the annealed powders were compacted with 3 wt% of paraffin wax as a binder at 50 Mpa and sintered at 850°C with a heating rate of $10^\circ\text{C}/\text{min}$ for 4 h by a conventional sintering process. The thermoelectric properties such as Seebeck coefficient (S), electrical conductivity (σ) and the power factor ($S^2\sigma$) of undoped and lanthanides substituted CaMnO_3 nanoparticles were investigated between ambient temperature and 600°C where $\Delta T = 50^\circ\text{C}$ with highly pure helium atmosphere by LSR-3 Seebeck, Linseis, Germany.

3 Results and discussion

3.1 Structural properties

Powder XRD pattern of $\text{Ca}_{1-x}\text{Ln}^{3+}_x\text{MnO}_3$ ($\text{Ln}^{3+} = \text{La}, \text{Ce}, \text{Sm}; x = 0, 0.1$) nanoparticles are shown in Fig. 1a. All the peaks are matched and indexed with the standard JCPDS card 76-1132. It can be seen from the diffractogram, all the samples are of single-phased orthorhombic perovskite structure of CaMnO_3 with a space group of Pnma, indicating that the Ca substitution by the rare earth metals do not affect the crystal structure of the material. The patterns reveal that the samples are crystalline in nature without impurity by sharper peaks with the absence of secondary peaks and also annealing under oxygen atmosphere removed the oxygen deficiency and directed towards stoichiometric CaMnO_3 nanoparticles. Cell parameters of undoped and electron doped samples are calculated by least square fit method and are in good agreement with the reported data [11]. Table 1 shows the comparison between the reported and calculated cell parameters and cell volume of the material. The unit cell volume of the electron-doped CaMnO_3 nanoparticles is increased as compared to the undoped due to the incorporation of higher ionic radii rare earth metals in the compound as dopants. Rare earth metals are doped at the Ca-site of CaMnO_3 nanoparticles, where the ionic radius of the doped materials ($\text{La}^{3+} = 1.17 \text{ \AA}$, $\text{Ce}^{3+} = 1.14 \text{ \AA}$, $\text{Sm}^{3+} = 1.08 \text{ \AA}$) are higher than that of Calcium ($\text{Ca}^{2+} = 1.12 \text{ \AA}$). As a result of the inclusion of larger ionic radius rare earth metals in the structure and the reduction mechanism of Mn^{4+}

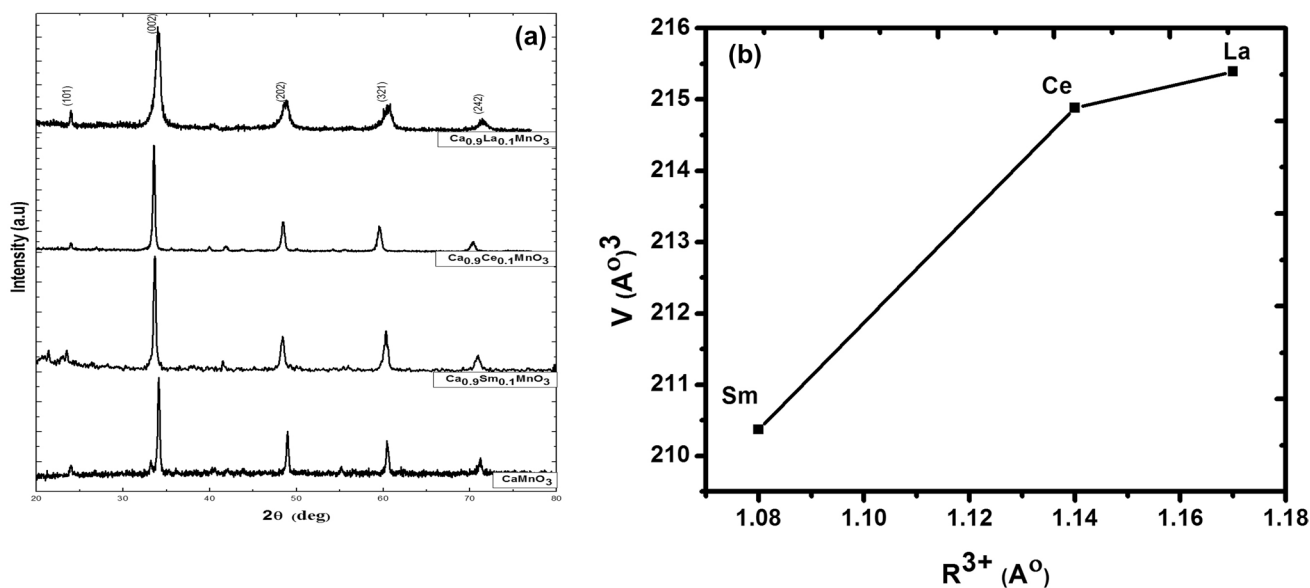


Fig. 1 **a** Powder XRD pattern of $\text{Ca}_{1-x}\text{Ln}^{3+}_x\text{MnO}_3$ ($\text{Ln}^{3+} = \text{Sm}, \text{Ce}, \text{and La}; x = 0, 0.1$) nanoparticles. **b** expansion of unit cell volume with respect to the ionic radii of rare earth ions

Table 1 Lattice parameters and its unit cell volume with average crystallite size of undoped and electron-doped CaMnO_3 nanoparticles

Sample	Ionic radii	Lattice parameters			Cell volume	Average particle size
Units	Å	Å			Å ³	nm
CaMnO_3 JCPDS :761132 reported	1.12	$a=5.279$	$b=7.448$	$c=5.264$	207.027	15
CaMnO_3 calculated	1.12	$a=5.278$	$b=7.443$	$c=5.267$	206.90	42
$\text{Ca}_{0.9}\text{Sm}_{0.1}\text{MnO}_3$	1.08	$a=5.307$	$b=7.451$	$c=5.320$	210.37	56
$\text{Ca}_{0.9}\text{Ce}_{0.1}\text{MnO}_3$	1.14	$a=5.355$	$b=7.502$	$c=5.349$	214.88	78
$\text{Ca}_{0.9}\text{La}_{0.1}\text{MnO}_3$	1.17	$a=5.361$	$b=7.479$	$c=5.372$	215.39	83

(0.53 Å) to Mn^{3+} (0.645 Å) contributes to the increase of unit cell volume [9, 11, 20, 21]. With increasing the ionic radii of rare earth ions the lattice parameters a and c are increasing but not b . This may be due to negligible Jahn–Teller (JT) distortion which in turn causes the MnO_6 octahedron expansion along the ab plane. Figure 1b represents the expansion of unit cell volume with respect to the ionic radii of rare earth ions from Sm^{3+} to La^{3+} . These results confirm that the substitution of Ln^{3+} ions at Ca^{2+} site induces the expansion of the unit cell. The unit cell volume increases with increasing the ionic radii of trivalent lanthanides from Sm^{3+} to La^{3+} [11] and these results are tabulated in Table 1. The average crystallite size of the nanoparticles was found using Scherrer relation $D = 0.94\lambda / \beta \cos\theta$, where λ is the X-ray wavelength, θ is the Bragg angle and β is the FWHM of the XRD peaks of the

samples [22]. The calculated average crystallite sizes of the compounds are presented in Table 1.

Raman spectroscopy is a powerful tool used to study the crystal symmetry, structural disorder with phase transformations and the spectra for $\text{Ca}_{1-x}\text{Ln}^{3+}_x\text{MnO}_3$ ($\text{Ln}^{3+} = \text{Sm}, \text{Ce}, \text{and La}; x = 0, 0.1$) and is shown in Fig. 2. Three broad bands are available for the substituted manganites near the strongest Raman lines of the undoped CaMnO_3 nanoparticles due to two phonon scattering instead of one phonon. Stretching, bending and rotational oxygen vibrations obtained at $669 \text{ cm}^{-1}(\text{B}_{2g})$, $475 \text{ cm}^{-1}(\text{A}_g)$, and $267 \text{ cm}^{-1}(\text{A}_g)$ for the undoped CaMnO_3 nanoparticles. The absence of Jahn–Teller (JT) distortion is due to the low-symmetric stable structure of the perovskite oxides like CaMnO_3 and LaMnO_3 . Structural distortion occurs in metal oxides owing to symmetry breaking at the surface and the rearrangement

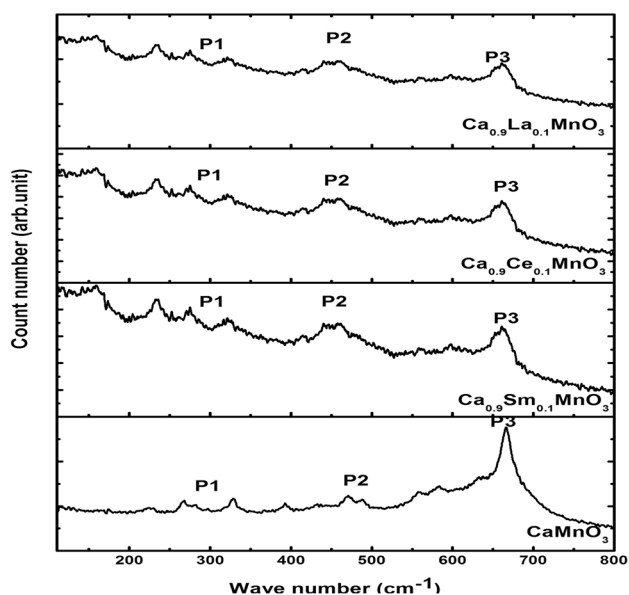


Fig. 2 Raman spectra of $\text{Ca}_{1-x}\text{Ln}^{3+}_x\text{MnO}_3$ ($\text{Ln}^{3+} = \text{Sm}, \text{Ce}, \text{and La}; x=0, 0.1$) nanoparticles

of the MnO_6 octahedron [23]. Doped manganites have change only in magnetic order but not in the structural and electronic reconstruction which could cause stronger JT distortion while doping [24]. And also the disorderness of rare earth-doped CaMnO_3 nanoparticle depends on the concentration level of doping and temperature [25]. The observed unchanged width and peak positions imply that the stoichiometric sample does not have a significant JT disorder which is consistent with the reported results [26, 27]. The distortion ratio (t) of MnO_6 octahedron is almost same for the rare earth-substituted manganites though the ionic radii vary and the coexistence of Mn^{3+} and Mn^{4+} in the crystal structure is the reason for the obtained shift in peaks and is in good agreement with the reported data [28].

3.2 Microstructural properties

Figure 3a, c, e, g gives SEM images and Fig. 3b, d, f, h shows EDAX spectrum of undoped and electron-doped CaMnO_3 nanoparticles. SEM images of as prepared samples having foamy and porous structure but annealed samples at 950°C under oxygen atmosphere show spherical-shaped nanoparticles with a continuous network. High surface mesoporous material is achieved by the addition of citric acid which in turn lowers the thermal conductivity due to its network structure, at the same time reduces the electrical conductivity also. In such a case, citric acid and PVP are used as a chelating agent and capping agent for obtaining shape and size controlled mesoporous material without agglomeration. The measured average crystallite size is in nanometer range which is consistent with the XRD data.

The average particle size decreases with increasing the ionic radii of the rare earth-substituted samples which reveals the vital role of the ionic radii in these perovskite manganites [16, 29, 30]. The chemical composition of the samples are analyzed by the EDAX technique and these results show the existence of cationic composition Ca; ($\text{Ca}_{0.9}\text{Ln}_{0.1}$): Mn is 1:1, which implies the presence of a pure form of undoped and electron-doped CaMnO_3 nanoparticles [31]. The compositional value of undoped and electron-doped CaMnO_3 nanoparticles are listed in Table 2. HRTEM and EDS analyses of undoped CaMnO_3 nanoparticles are carried out and the results are shown in Fig. 4a,b,c,d. Figure 4a and b show the HRTEM images with low and high resolution. The size of the nanoparticles ranging from 10–25 nm and the microscopic image reveal the presence of evenly distributed pores which are in nanometer range. Selected Area Electron Diffraction (SAED) pattern confirms the polycrystalline nature of the nanostructured CaMnO_3 and is shown in Fig. 4c. The observation of the elemental peaks in the EDS results confirm the composition of the CaMnO_3 nanoparticles [32, 33].

3.3 Electrical studies

The measured electrical resistivity as a function of temperature $\rho(T)$ for undoped and electron doped samples is shown in Fig. 5. In this context, the undoped CaMnO_3 is classified as n-type semiconductor due to localized valance band and a collective conduction band which has high-electrical resistivity at room temperature. Hopping conduction with small activation energy is the reason for the negative temperature coefficient ($-d\sigma/dT$) which implies the metallic conduction of perovskite metal oxides at room temperature. For hopping conduction, the electrical conductivity (σ) is given as $\sigma = (C/T) e^{-E_a/KT}$, where K is Boltzmann constant, E_a is the activation energy, (C/T) is thermally activated energy carriers. The above equation predicts a linear relationship between $\log\sigma T$ and $1/T$ for electrical conductivity instead of the usual Arrhenius plots. This equation is applicable for the undoped and highly conducting trivalent-doped CaMnO_3 samples up to 800°C caused by the extension of the extrinsic region due to dopants. The above results reveal a hopping conduction mechanism in CaMnO_3 oxides [34, 35]. The undoped CaMnO_3 nanoparticle shows high-electrical resistivity ($\rho = 10.6 \Omega \text{ cm}$) at room temperature attributable to the porous nature of the sample which is consistent with the reported results [36, 37]. The results confirm that the ρ value of undoped CaMnO_3 is higher than that of the substituted samples. The significant reduction of resistivity by the doping of rare earth ions is due to the change in the valance state of Mn ions. Electrical resistivity increases with increasing temperature for the electron-doped samples due to the metallic behavior whereas it decreases with increasing temperature due to semiconducting behavior of

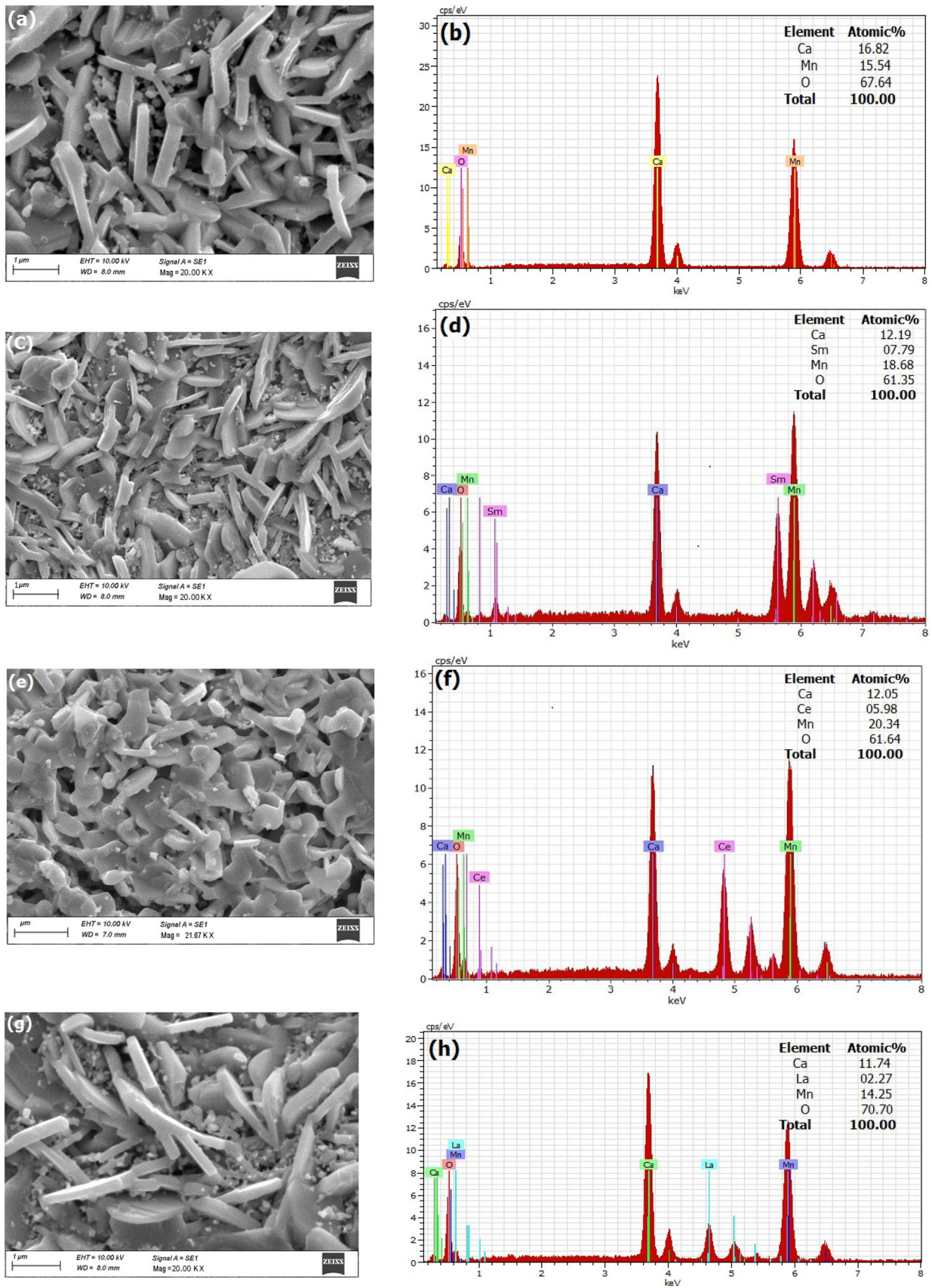


Fig. 3 SEM and EDAX pattern of $\text{Ca}_{1-x}\text{Ln}^{3+}_x\text{MnO}_3$ ($\text{Ln}^{3+} = \text{Sm}, \text{Ce}, \text{and La}; x=0, 0.1$) nanoparticles

Table 2 Elemental composition of $\text{Ca}_{1-x}\text{Ln}^{3+}_x\text{MnO}_3$ ($\text{Ln}^{3+} = \text{Sm}, \text{Ce}, \text{and La}; x = 0, 0.1$) nanoparticles

Sample code	Element/series	Weight %	Atomic %
CaMnO_3	Ca K	25.67	17.04
	Mn K	34.47	16.69
	O K	39.86	66.27
$\text{Ca}_{0.9}\text{Sm}_{0.1}\text{MnO}_3$	Ca K	16.08	12.19
	Sm L	12.42	7.79
	Mn K	33.73	18.68
	OK	37.77	61.35
$\text{Ca}_{0.9}\text{Ce}_{0.1}\text{MnO}_3$	Ca K	14.10	12.05
	Ce L	24.46	5.98
	Mn K	32.63	20.34
	O K	28.80	61.64
$\text{Ca}_{0.9}\text{La}_{0.1}\text{MnO}_3$	Ca K	18.68	12.78
	La L	10.45	2.27
	Mn K	28.56	14.25
	O K	41.26	70.70

the undoped sample [20, 38]. Rare earth doping at Ca-site induces the Mn^{3+} ions and generate electron carriers, which moves the carriers by the hopping mechanism, as a result, electrical resistivity value decreases. The electrical resistivity value is increasing with increasing the ionic radii of the rare earth-substituted samples. In contrary, the observed ρ value for Ce-doped CaMnO_3 nanoparticle is higher than La-substituted and Sm-substituted though the ionic radii lies between these two. This is because Ce^{4+} atom occupies both Ca-site as well as Mn-site and hence induces more number of electrons responsible for the high resistivity of the Ce-substituted sample [21, 39, 40]. The electrical conductivity of the trivalent-substituted samples increases with increasing ionic radii of the cations at room temperature, which implies the increment of mobility because of the larger intersite distances for hopping. Increased electron carrier concentration induced the higher electrical conductivity of Sm^{3+} substituted CaMnO_3 nanoparticle.

3.4 Thermoelectric studies

Figure 6 depicts the temperature dependence of Seebeck coefficient $S(T)$ for $\text{Ca}_{0.9}\text{Ln}^{3+}_{0.1}\text{MnO}_3$ ($\text{Ln}^{3+} = \text{Sm}, \text{Ce}, \text{and La}; x = 0, 0.1$) nanoparticles. Negative Seebeck coefficient values indicating that all the samples are n-type materials. Absolute Seebeck coefficient values for all the samples at room temperature are listed in Table 3. Absolute Seebeck coefficient value decreases with increasing temperature due to the increased carrier concentration and semiconducting behavior is observed for the undoped sample whereas S value increases with increasing temperature [41]. The S value for highly conducting samples increases linearly with

increasing temperature up to 800 °C. The increase in charge carriers lowers the S value of doped samples and is increasing with increasing temperature due to the metallic behavior of the samples. Though the S value is small for the highly conducting samples, it is high for metallic conduction. High resistivity of Ce-substituted samples significantly reduces the Seebeck value and hence thermopower decreases [42].

According to Mott's adiabatic small polaron conduction model, the transport properties can be described as $\rho = \rho_0 T \exp(E_a/k_B T)$, where ρ , E_a , k_B are resistivity, activation energy and Boltzman's constant, respectively. Figure 7 represents the activation energy of the undoped and doped samples using the Arrhenius plot of $\ln(\sigma T)$ versus $1000/T$. The linear fitting method is used to find the slope value for the samples within the measured temperature range due to the non-linearity of the graph and activation energy of undoped and electron-doped CaMnO_3 nanoparticles is calculated and listed in Table 3. The substitution of rare earth ions at Ca-site lowered the activation energy and high activation energy confirms that the sample is highly resistive in nature. The above results indicate that Sm-doped CaMnO_3 nanoparticles have high-electrical conductivity with low activation energy.

Power factor ($\text{PF} = S^2 \sigma$) of the samples are obtained by the product of measured values of S and ρ of the samples and is shown in Fig. 8. The thermoelectric power factor is large for larger cation-substituted CaMnO_3 nanoparticles, whereas it is low for smaller cation-substituted oxides. The calculated power factor for all the samples are listed in Table 3 and the value increases with increasing temperature for all the samples. The rare earth-doped samples show higher power factor and it decreases with increasing the ionic radii but the Ce-doped shows contrary result. This is because of the high resistivity and low Seebeck coefficient value of the Ce-doped sample. The maximum power factor is obtained for the Sm-doped sample at 600 °C is $311 \mu\text{Wm}^{-1}\text{K}^{-2}$. The electrical conductivity and Seebeck coefficient values are high and these oxides are stable at high temperatures because they sintered at higher temperature. These factors imply that these oxides are promising for thermoelectric applications at elevated temperatures.

4 Conclusion

Orthorhombic perovskite structured electron-doped CaMnO_3 nanoparticles were synthesized by sol-gel hydrothermal method at 200 °C, and the influence of trivalent rare earth elements substitution were studied. The lattice parameter and the unit cell volume were increased with increasing the ionic radii of trivalent rare earth elements. Sintered samples were used for thermoelectric studies due to the low diffusion of oxygen atoms in the material which in turn increases the electrical conductivity by reducing the

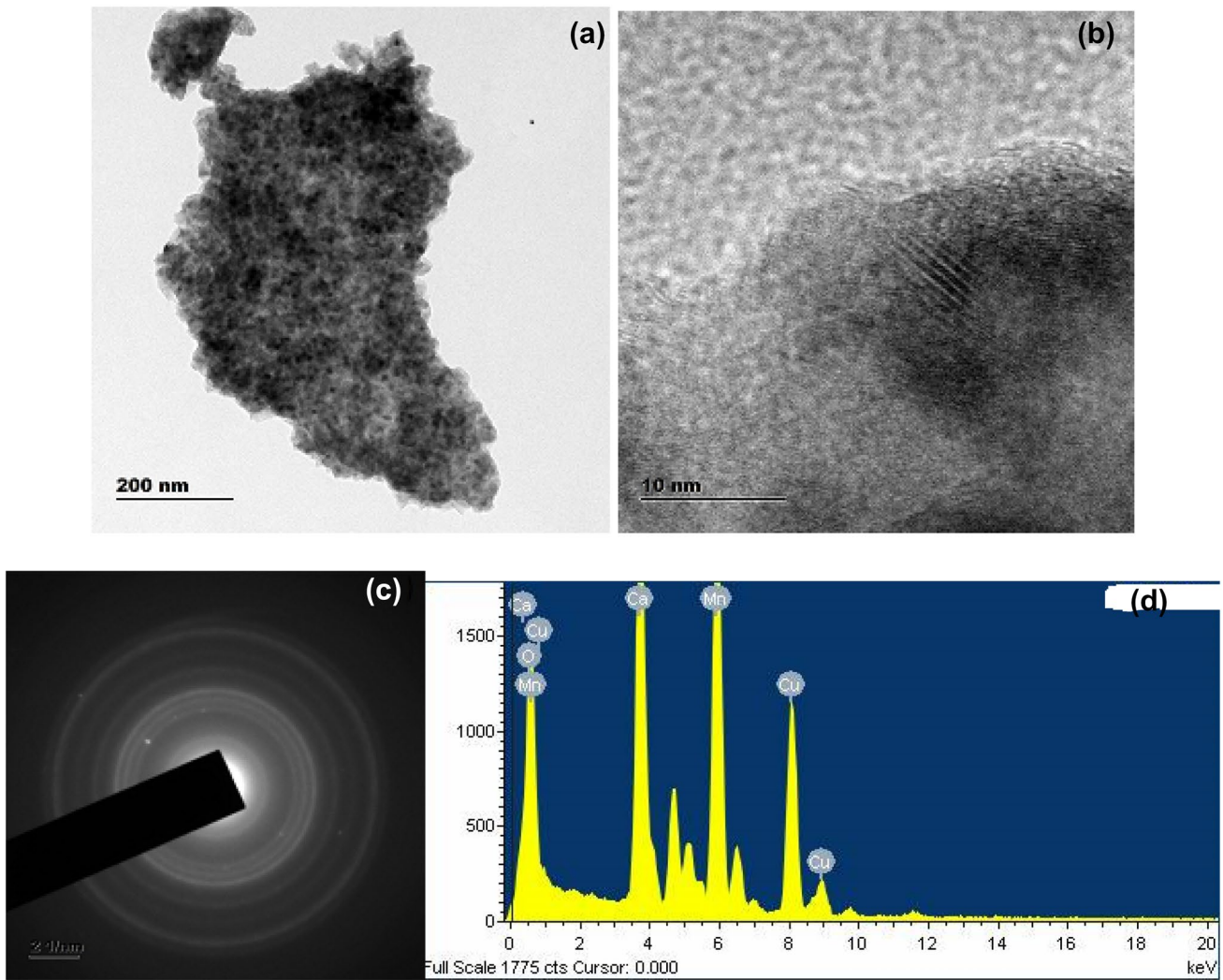


Fig. 4 a, b lower and higher resolution image c SAED pattern d EDS spectrum of CaMnO_3 nanoparticles

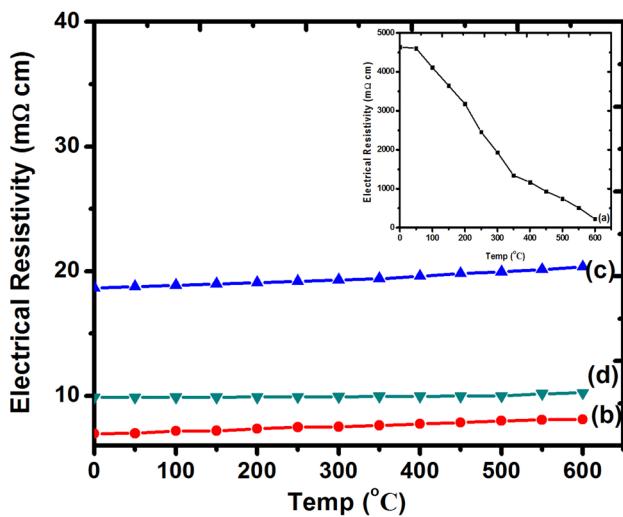


Fig. 5 Electrical resistivity of $\text{Ca}_{1-x}\text{Ln}^{3+}_x\text{MnO}_3$ ($\text{Ln}^{3+} = \text{Sm}, \text{Ce}, \text{and La}; x = 0, 0.1$) nanoparticles

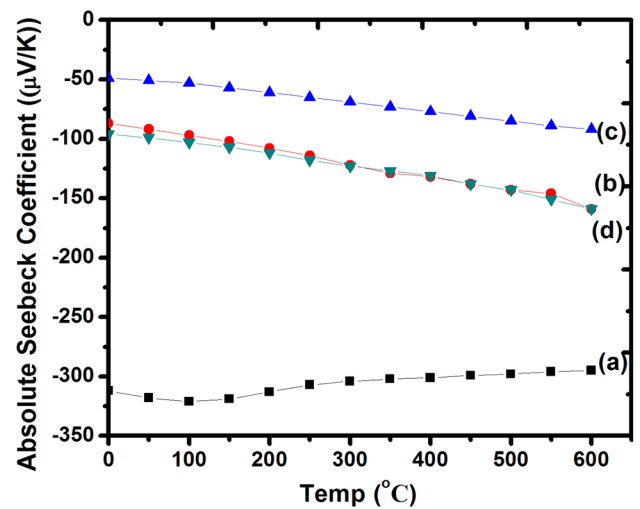
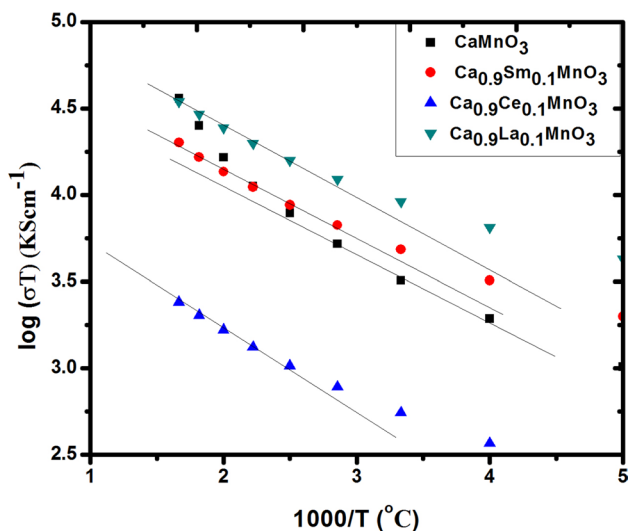
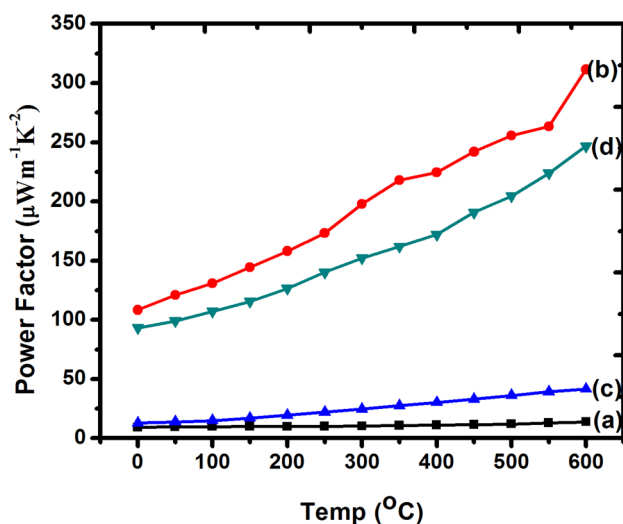


Fig. 6 Absolute Seebeck coefficient of $\text{Ca}_{1-x}\text{Ln}^{3+}_x\text{MnO}_3$ ($\text{Ln}^{3+} = \text{Sm}, \text{Ce}, \text{and La}; x = 0, 0.1$) nanoparticles

Table 3 Physical parameters of $\text{Ca}_{1-x}\text{Ln}^{3+}_x\text{MnO}_3$ ($\text{Ln}^{3+} = \text{Sm}, \text{Ce},$ and $\text{La}; x=0, 0.1$) nanoparticles at room temperature

Sample	ρ ($\text{m}\Omega \text{ cm}$)	S (μVK^{-1})	E_a (eV)	Power factor at 600 °C ($\mu\text{Wm}^{-1} \text{K}^{-2}$)
CaMnO_3	4640	− 312	0.057	38.85
$\text{Ca}_{0.9}\text{Sm}_{0.1}\text{MnO}_3$	6.99	− 87	0.029	311.61
$\text{Ca}_{0.9}\text{Ce}_{0.1}\text{MnO}_3$	18.67	− 49	0.038	46.58
$\text{Ca}_{0.9}\text{La}_{0.1}\text{MnO}_3$	9.89	− 96	0.034	246.78

**Fig. 7** Relation between $\ln(\sigma T)$ vs $1000/T$ of $\text{Ca}_{1-x}\text{Ln}^{3+}_x\text{MnO}_3$ ($\text{Ln}^{3+} = \text{Sm}, \text{Ce},$ and $\text{La}; x=0, 0.1$) nanoparticles**Fig. 8** Power factor of $\text{Ca}_{1-x}\text{Ln}^{3+}_x\text{MnO}_3$ ($\text{Ln}^{3+} = \text{Sm}, \text{Ce},$ and $\text{La}; x=0, 0.1$) nanoparticles

oxygen deficiency. Temperature-dependent Seebeck coefficient value decreases with increasing the temperature for undoped CaMnO_3 nanoparticles due to semiconducting behavior whereas Seebeck value decreases with increasing temperature in trivalent-substituted CaMnO_3 nanoparticles owing to metallic behavior. The samples were highly resistive, and it gradually decreases with increasing temperature. Large Seebeck coefficient, high-electrical conductivity, and low activation energy with high-power factor suggest that $\text{Ca}_{0.9}\text{Sm}_{0.1}\text{MnO}_3$ nanoparticle is a potential n-type thermoelectric material for feasible thermoelectric devices at elevated temperature.

References

- H. Choi, A. Fuller, J. Davis, C. Weilgus, U.S. Ozkan, Ce-doped strontium cobalt ferrite perovskites as cathode catalysts for solid oxide fuel cells: effect of dopant concentration. *Appl. Catal. B* **127**, pp. 336–341, (2012). <https://doi.org/10.1016/j.apcatb.2012.08.027>.
- H. C. Wang, W.B.Su, J. Liu, C.Wang. Recent development of n-type perovskite thermoelectrics. *J Mater.* **2**(3), 225–236 (2016). Doi:<https://doi.org/10.1016/j.jmat.2016.06.005>
- Stephen J. Skinner, Recent advances in Perovskite-type materials for solid oxide fuel cell cathodes. *Int. J. Inorgan. Mater.* **3**(2), 113–121 (2001). Doi:[https://doi.org/10.1016/S1466-6049\(01\)00004-6](https://doi.org/10.1016/S1466-6049(01)00004-6)
- W. Menesklou, H. J. Schreiner, K. H. Härdtl, E. I. Tiffée, High temperature oxygen sensors based on doped SrTiO_3 . *Sens Actuators B* **59**, 2–3 (1999). Doi:[https://doi.org/10.1016/S0925-4005\(99\)00218-X](https://doi.org/10.1016/S0925-4005(99)00218-X). 184–189.
- L.F. Schneemeyer, J.V. Waszczak, S.M. Zahorak, R.B. van Dover, T.Siegrist, Superconductivity in rare earth cuprate perovskites. *Materials Research Bulletin*. **22**(11), 1467–1473 (1987). Doi:[https://doi.org/10.1016/0025-5408\(87\)90211-X](https://doi.org/10.1016/0025-5408(87)90211-X)
- D.M. Rowe. *Thermoelectrics handbook: macro to nano*, pp. 1-3, 1st edn. (CRC Press, Boca Raton, FL, 2006), pp. 1–7
- J.G. Noudem, D. Kenfaui, S. Quetel Weben, C.S. Sanmathi, R. Retoux, M. Gomina, Spark plasma sintering of n-type thermoelectric $\text{Ca}_{0.95}\text{Sm}_{0.05}\text{MnO}_3$. *J. Am. Chem. Soc.* **94**(8), 2608–2612 (2011). Doi:<https://doi.org/10.1111/j.1551-2916.2011.04465.x>
- M.E. Melo Jorge, M.R. Nunes, R. Silva Maria, D. Sousa, Metal–insulator transition induced by Ce doping in CaMnO_3 . *Chem. Mater.* **17**(8), 2069–2075 (2005). Doi: <https://doi.org/10.1021/cm040188b>
- Y. Wang, Y. Sui, H. Fan, X. Wang, Y. Su, W. Su, X. Liu High Temperature thermoelectric response of electron-doped CaMnO_3 . *Chem. Mater.* **21**, 4653–4660 (2009). Doi: <https://doi.org/10.1021/cm901766y>
- D. Flahaut, T. Mihara, R. Funahashi, N. Nabeshima, K. Lee, H. Ohta, K. Koumoto, Thermoelectrical properties of A-site substituted $\text{Ca}_{1-x}\text{Re}_x\text{MnO}_3$ system. *J. Appl. Phys.* **100**(8), 084911 (2006). Doi:<https://doi.org/10.1063/1.2362922>
- B.S. Nagaraja, P. Ashok Rao, G.S. Poornesh, Okram, Effect of rare earth ionic radii on structural, electric, magnetic and thermoelectric properties of REMnO_3 ($\text{RE} = \text{Dy}, \text{Gd}, \text{Eu}$ and Sm) manganites. *J.Supercond. Novel Magn.* **31**: 2271 (2018). Doi: <https://doi.org/10.1007/s10948-017-4505-7>
- Y. Wang, Y. Sui, X. Wang, W. Su, Correlation of structural distortion with magnetic properties in electron-doped $\text{Ca}_{0.9}\text{R}_{0.1}\text{MnO}_3$ perovskites ($\text{R} = \text{rare-earth}$). *J. Appl. Phys.* **108**(6) (2010) 063928-063928-9. Doi: <https://doi.org/10.1063/1.3481419>

13. Y. Li, S. Hao, X. Xia, Preparation, structure, and electrical properties of $\text{Ca}_{1-x}\text{Er}_x\text{MnO}_3$ Powders. *J. Electron. Mater.* **42**, 745–751 (2013). Doi:<https://doi.org/10.1007/s11664-012-2445-3>
14. C.S. Park, M.H. Hong, S. Shin, H.H. Cho, H.H. Park, Synthesis of mesoporous $\text{La}_{0.7}\text{Sr}_{0.3}\text{MnO}_3$ thin films for thermoelectric materials. *J. Alloys Compd.* **632**, 246–250 (2015). Doi:<https://doi.org/10.1016/j.jallcom.2015.01.188>
15. T.M.H. Dang, V.D. Trinh, D. H. Bui, M. H. Phan, D. C. Huynh, Sol-gel hydrothermal synthesis of strontium hexaferrite nanoparticles and the relation between their crystal structure and high coercivity properties. *Adv. Nat. Sci.: Nanosci Nanotechnol.* **3**, 025015 (7 pp) (2012). Doi:<https://doi.org/10.1088/2043-6262/3/2/025015>
16. C.-S. Park, WooJe Han, D.I. Shim, H.H. Cho, H.-H. Park, The effect of mesoporous structure on the thermoelectric properties of nonstoichiometric La-doped SrTiO_3 . *J. Electrochem. Soc.* **163**(6), E155–E158 (2016). Doi:<https://doi.org/10.1149/2.0441606jes>
17. Y.-J. Chou, B.-J. Hong, Y.-C. Lin, C.-Y. Wang, S.-J. Shih, The correlation of pore size and bioactivity of spray-pyrolyzed mesoporous bioactive glasses. *Materials* (Basel). 2017 May; 10(5): 488. Doi: <https://doi.org/10.3390/ma10050488>
18. P. Thiel, J. Eilertsen, S. Populoh, G. Saucke, M. Döbeli, A. Shkablo, L. Sagarna, L. Karvonen, A. Weidenkaff, Influence of tungsten substitution and oxygen deficiency on the thermoelectric properties of $\text{CaMnO}_{3-\delta}$. *J. Appl. Phys.* **114**, 243707 (2013). Doi:<https://doi.org/10.1063/1.4854475>
19. S. BerbethMary, M. Francis, V.G. Sathe, V. Ganesan, A. Leo Rajesh, Enhanced thermoelectric property of nanostructured CaMnO_3 by sol-gel hydrothermal method. *Physica B* **575**, 411707 (2019). Doi:<https://doi.org/10.1016/j.physb.2019.411707>
20. M. Mouyane, B. Itaalit, J. Bernarda, D. Houivet, J.G. Noudem, Flash combustion synthesis of electron doped- CaMnO_3 thermoelectric oxides. *Powder Technol.* **264**, 71–77 (2014). Doi:<https://doi.org/10.1016/j.powtec.2014.05.022>
21. J. Dukic, S. Boskovic, B. Matovic, Crystal structure of Ce-doped CaMnO_3 perovskite. *Ceram. Int.* **35**, 787–790 (2009). Doi:<https://doi.org/10.1016/j.ceramint.2008.02.023>
22. B.D. Guly, *Elements of X-ray diffraction*, 2nd edn. (Addition–Wesley, USA, 1987)
23. S. Merten, V. Bruchmann-Bamberg, B. Damaschke, K. Samwer, V. Moshnyaga, abn-Teller reconstructed surface of the doped manganites shown by means of surface-enhanced Raman spectroscopy. *Phys. Rev. Mater.* **3**, 060401(R) (2019). Doi: <https://doi.org/10.1103/PhysRevMaterials.3.060401>
24. S. Keshavarz, Y.O. Kvashnin, D.C.M. Rodrigues, M. Pereira, I. Di Marco, C. Autieri, L. Nordström, I.V. Solovyev, B. Sanyal, O. Eriksson, Exchange interactions of CaMnO_3 in the bulk and at the surface. *Phys. Rev. B* **95**, 115120 (2017)
25. M. Abrashev, J. Bäckström, L. Börjesson, M. Pissas, N. Kolev, M. Iliev. Raman spectroscopy of the charge- and orbital-ordered state in $\text{La}_{0.5}\text{Ca}_{0.5}\text{MnO}_3$. *Phys. Rev. B* **64**(14) (2001). Doi:<https://doi.org/10.1103/physrevb.64.144429>
26. M.N. Iliev, M.V. Abrashev, V.N. Popov, V.G. Hadjiev, Role of Jahn-Teller disorder in Raman scattering of mixed-valence manganites. *Phys. Rev. B* **67**, 212301–2003. Doi: <https://doi.org/10.1103/PhysRevB.67.212301>
27. M.V. Abrashev, J. Bäckström, L. Börjesson, V.N. Popov, R.A. Chakalov, N. Kolev, R.-L. Meng, M.N. Iliev, Raman spectroscopy of CaMnO_3 : Mode assignment and relationship between Raman line intensities and structural distortions. *Phys. Rev. B* **65**, 184301. Doi: <https://doi.org/10.1103/PhysRevB.65.184301>
28. T. Mori, N. Kamegashira, K. Aoki, T. Shishido, T. Fukuda, Crystal growth and crystal structures of the LnMnO_3 perovskites: Ln = Nd, Sm, Eu and Gd. *Mat. Lett.* **54**(2–3), 238–243 (2002). Doi:[https://doi.org/10.1016/s0167-577x\(01\)00569-9](https://doi.org/10.1016/s0167-577x(01)00569-9)
29. J. Niu, J. Deng, W. Liu, L. Zhang, G. Wang, H. Dai, H. He, X. Zi, Nanosized perovskite-type oxides $\text{La}_{1-x}\text{Sr}_x\text{MO}_{3-\delta}$ (M = Co, Mn; x = 0, 0.4) for the catalytic removal of ethylacetate. *Catal. Today* **126**, 420–429 (2007). Doi:<https://doi.org/10.1016/j.cattod.2005.07.06.027>
30. M.G. Naseri, E. Saion, N.K. Zadeh, The amazing effects and role of PVP on the crystallinity, phase composition and morphology of nickel ferrite nanoparticles prepared by thermal treatment method. *Int. Nano Lett.* **3**, 19 (2013). Doi:<https://doi.org/10.1186/2228-5326-3-19>
31. W. Xiaa, L. Lia, H. Wua, P. Xuea, X. Zhua, Structural, morphological, and magnetic properties of sol-gel derived $\text{La}_{0.7}\text{Ca}_{0.3}\text{MnO}_3$ manganite nanoparticles, *Ceram. Int.* **43** (2017) 3274–3283, Doi:<https://doi.org/10.1016/j.ceramint.2016.11.160>
32. Lee, S.Y., Kim, D.H., Choi, S.C., Lee, D.J., Choi, J.Y., Kim, H.D., Porous multi-walled carbon nanotubes by using catalytic oxidation via transition metal oxide. *Microporous Mesoporous Mater.* **194**, 46–51 (2014). Doi:<https://doi.org/10.1016/j.micromeso.2014.03.040>
33. J. Lee, H. Zhu, G.G. Yadav, J. Caruthers, Y. Wu, Porous ternary complex metal oxide nanoparticles converted from core/shell nanoparticles. *Nano Res.* **9**, 996–1004 (2016). Doi:<https://doi.org/10.1007/s12274-016-0987-z>
34. M. Ohtaki, H. Koga, T. Tokunaga, Koichi Eguchi, Hiromichi Arai, Electrical transport properties and high-temperature thermoelectric performance of $(\text{Ca}_{0.9}\text{M}_{0.1})\text{MnO}_3$ (M = Y, La, Ce, Sm, In, Sn, Sb, Pb, Bi), *J. Solid State Chem.* **120** (1) (1995) 105–111. Doi: <https://doi.org/10.1006/jssc.1995.1384>
35. A. Jiamprasertboon, Y. Okamoto, Z. Hiroi, T. Siritanon, Thermoelectric properties of Sr and Mg double-substituted LaCoO_3 at room temperature. *Ceram. Int.* doi: <https://doi.org/10.1016/j.ceramint.2014.04.123>
36. G. Xu, R. Funahashi, Q. pu, B. Liu, R. Tao, G. Wang, Z. Ding, High-temperature transport properties of Nb and Ta substituted CaMnO_3 system. *Solid State Ion.* **171**, 147–151 (2004)
37. F.C. Fonseca, J.A. Souza, R.F. Jardim, R. Muccillo, E.N.S. Muccillo, D. Gouvea, M.H. Jung, A.H. Lacerda, Transport properties of $\text{La}_{0.6}\text{Y}_{0.1}\text{Ca}_{0.3}\text{MnO}_3$ compounds with different interfaces. *J. Eur. Ceram. Soc.* **24**, 1271–1275 (2004). Doi:[https://doi.org/10.1016/S0955-2219\(03\)00446-1](https://doi.org/10.1016/S0955-2219(03)00446-1)
38. J.W. Park, D.H. Kwakb, S.H. Yoonb, S.C. Choi, Thermoelectric properties of Bi, Nb co-substituted CaMnO_3 at high temperature. *J. Alloys Compd.* **487**, 550–555 (2009). Doi:<https://doi.org/10.1016/j.jallcom.2009.08.012>
39. B. Gröger, J. Kulawik, D. Szwagierczak, A. Skwarek, Influence of various lanthanides on the properties of $\text{Sr}_{0.8}\text{Ce}_{0.1}\text{Ln}_{0.1}\text{MnO}_{3-\delta}$ and $\text{Sr}_{0.9}\text{Ce}_{0.05}\text{Ln}_{0.05}\text{CoO}_{3-\delta}$ ceramics and thick film electrodes. *Solid State Ion.* **180**, 872–877 (2009). Doi:<https://doi.org/10.1016/j.ssi.2009.02.012>
40. Y. Wang, Y. Sui, X. Wang, W/ Su, Effects of substituting La^{3+} , Y^{3+} and Ce^{4+} for Ca^{2+} on the high temperature transport and thermoelectric properties of CaMnO_3 . *J. Phys. D* **42**, 055010 (10 pp) (2009). Doi:<https://doi.org/10.1088/0022-3727/42/5/055010>
41. M. Ohtaki, H. Koga, T. Tokunaga, K. Eguchi, H. Arai, Electrical transport properties and high-temperature thermoelectric performance of $(\text{Ca}_{0.9}\text{M}_{0.1})\text{MnO}_3$ (M = Y, La, Ce, Sm, In, Sn, Sb, Pb, Bi), *J. Solid State Chem.* **120** (1):105–111 (1995). Doi: <https://doi.org/10.1006/jssc.1995.1384>
42. X.H. Zhang, J.C. Li, Y.L. Du, F.N. Wang, H.Z. Liu, Y.H. Zhu, J. Liu, W.B. Su, C.L. Wang, L.M. Mei, Thermoelectric properties of A-site substituted Lanthanide $\text{Ca}_{0.75}\text{R}_{0.25}\text{MnO}_3$. *J. Alloys Compd.* **634**, 1–5 (2015). Doi:<https://doi.org/10.1016/j.jallcom.2015.02.074>

Publisher's Note Springer Nature remains neutral with regard to jurisdictional claims in published maps and institutional affiliations.

Incidence of Fatal Pedestrian Collision And Vehicle Speeds Control

Chandrasekar. M¹, Hasan Harun. A², Praveen. S³, Subash Chandran. R⁴

¹Professor Department of Mechatronics Engineering, M.A.M School of Engineering, Trichy.
^{2,3,4} Student, Department of Mechatronics Engineering, Trichy.

Received Date: 16 June 2021

Revised Date: 16 July 2021

Accepted Date: 27 July 2021

OBJECTIVE

- The main aim of the project is reducing the accidents while school zone, hospital zone.
- Reduce the speed of the vehicle to control the accidents using hardware.

Abstract

The point of this investigation was to gauge the reasonable impact of decreased travel speeds on the frequency of person on foot fatalities in Adelaide, Australia. The examination depended on the aftereffects of itemized examinations of 176 lethal passer by crashes in the Adelaide region somewhere in the range of 1983 and 1991. The strategy created to assess the impact of diminished voyaging speed is portrayed and upheld by references to the distributed writing. A decrease in as far as possible from 60 to 50 km/h was one of four speed decrease situations considered. The littlest assessed decrease in deadly common crashes in the determination introduced was 13%, for a situation wherein all drivers submitted to the current speed limit. The biggest assessed decrease was 48% for a situation wherein all drivers were voyaging 10 km/h more slow. The assessed decreases in fatalities acquired in this examination are contrasted and those saw in where the metropolitan region speed limit has been brought down.

Keywords : Vehicle Speeds, Fatal Pedestrian Collision

Introduction

Vehicle is the one of the fundamental piece of our life. The vehicle utilization is expansion in India from 2000. Because of vehicle utilization and over speed causes numerous mishaps. All the mishaps are in various manners for various explanation and government has a factual report for the majority of mishaps in India. There are numerous distinction starting with one then onto the next. There are increment a utilization of vehicle. The Indian Government has not the street expecting level aside from parkways street.

The motivation behind the proposed work is to recognize the variables adding to lethal mishaps. This is accomplished by breaking down street mishaps utilizing Convolutional Neural

Networks by considering proper highlights and adequately bunching the records. A few blends of qualities of huge datasets are investigated to find covered up designs that are the main driver for mishaps. The odds of mishap event could be distinguished by considering different standards like speed breaking point and injury seriousness, season of mishaps and plastered driver, month and climate during the mishap, gentility and speed limit, human factors, surface and light conditions. The exploratory outcomes on street mishap informational collection FARS (Fatality Analysis Reporting System) produced hazard factors that cause deadly mishaps which will be useful in creating more secure driving standards.

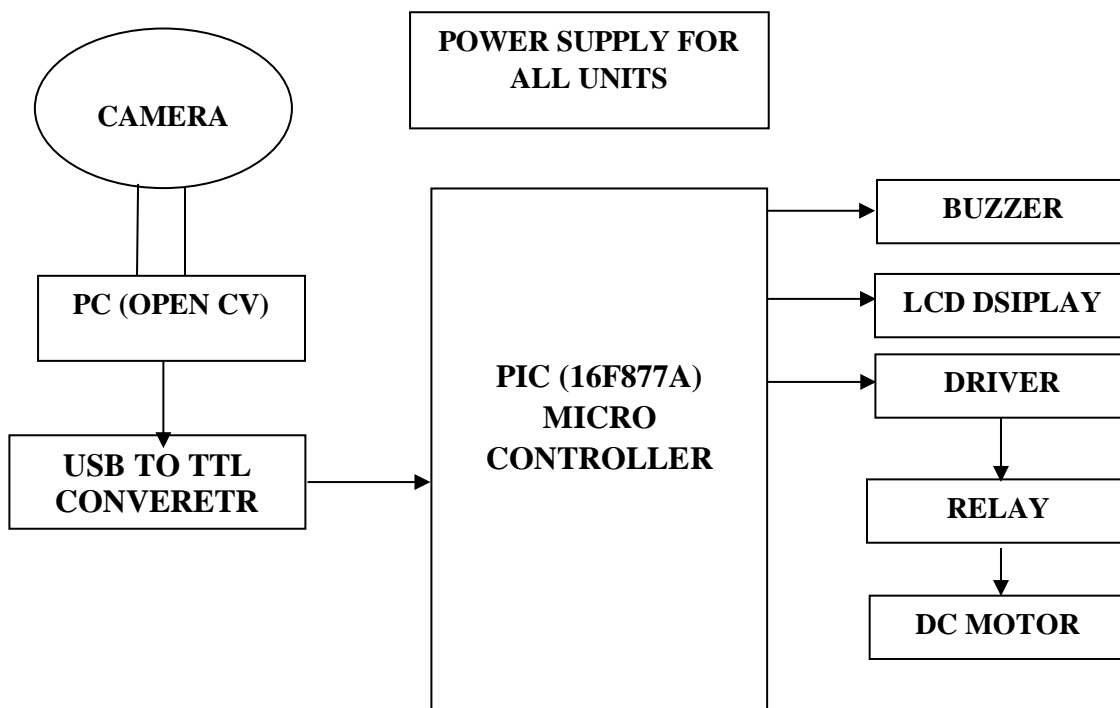
Street traffic is the significant issue nowadays. Expansion in number of vehicles continuing on streets sped up the danger of mishaps. Of them, deadly mishaps is the significant issue where individuals lose their lives. Additionally, these mishaps are capricious that they might happen anyplace, whenever. As an individual we should save the existences of individuals and keep away from these mishaps. A protected street development is a significant worry for both transportation regulating associations and normal nationals. Remembering these realities, the point of this work is to give safe driving guidelines to individuals continuing on the streets and crisis administrations to individuals affected in the mishap zone. Thus, factors like climate conditions, impact way, surface condition, light condition, speed, intoxicated driver, etc were thought of and analysed. Dissected information can be utilized to give more secure driving ideas and decrease the mishap rate. Likewise, crisis administrations can be given to individuals influenced at clumsy region. Information mining is one of the significant instruments utilized in Information Technology from past occasions. Information mining strategies best works in preparing information and recognizing the relationship among information. Affiliation rule mining is a technique utilized for finding fascinating examples among factors from colossal data sets. To discover relationship among information, backing and certainty are determined by setting a limit esteem. Discovering related information utilizing affiliation rules helps in successive thing set mining.



Arrangement is performed on information utilizing some grouping model reasonable to the given arrangement of information. The object is to discover the successive thing sets. During characterization a model is developed in which various records of informational collection with undefined class marks are isolated without any problem. Guileless Bayesian grouping is one of the probabilistic strategies used to predicate the freedom among variable sets. It emphatically accepts and auto associates the data. In some cases these presumptions might turn out badly. Along these lines, a superior arrangement method proposed to proficiently order the information is Convolution Neural Network. It expects

information dependent on the region. The arrangement strategy proposed can be applied on the information to get powerful outcomes. The affiliation rule mining calculation at any point utilized is Apriori. The calculation productively works dependent on pertinent affiliation rules for successive thing set mining. It utilizes a granular perspective. The property followed by this calculation says any subset of successive thing set should be continuous. It utilizes bigger thing sets and can be executed without any problem. This calculation is applied on street traffic deadly mishap dataset to test the information.

BLOCK DIAGRAM:



A tremendous arrangement of qualities structure the information dataset. The work chiefly conveyed dependent on this information. Information Construction is otherwise called Data Preparation. At first information will be cleaned by eliminating clamor, missing qualities, and textures. Missing qualities are supplanted by NULL qualities. Information will be chosen and changed dependent on the prerequisite. It could be either in mathematical or ostensible structure. Information will be in ostensible structure in the dataset, it very well may be changed over into mathematical information while performing procedure on it. Major ascribes chose in this investigation are mishap conditions like, way of impact, light condition, climate condition, street surface condition, speed cutoff points and tanked driver. Additionally, these traits hold a few qualities recorded beneath. Speed Limits: 5, 10, 15, 20, 25, 35, 45, 55, 60, 65, 70, 80, 85, 95, 99 (kmph). Tippy Driver: It has two

conditions either yes or no. Every one of these components influence the pace of mishap event and were utilized to decide if it is dangerous for individuals continuing on streets during these conditions.

Implementation

Convolutional neural organization is a class of profound learning and valuable for a few examinations. They envision representations and mathematical information. It very well may be a distinction of multi-facet perceptron intended to require insignificant pre-handling. Complete organization very still verbalizes to accomplish the capacity from the crude info information toward one side to accomplish the class at the opposite end. It can clarify theory that the data sources permit. To execute convolutional neural organizations a preparation dataset is considered as info. The

dataset contains mathematical qualities that relate to some ostensible information.

The preparing of preparing informational index utilizing Convolutional Neural Networks brought about figuring the danger factor in a productive way. Different components contributed for lethal mishaps were distinguished utilizing this characterization method in a most probabilistic methodology. The outcomes got were utilized to indicate lethal conditions for a mishap. In this manner, security measures can be given to individuals continuing on streets in such conditions. During the interaction, different properties like crash type, light conditions, climate conditions, surface conditions, speed, intoxicated driver or not were thought about to discover the danger factor. The danger factor indicated the potential outcomes of lethal mishaps at various regions. The outcomes acquired in figuring the danger factor utilizing Convolutional Neural Networks can be displayed underneath. Proficiency of the order calculation, Convolutional Neural Networks can be known by computing exactness, accuracy, review and f-measure on came about information. Precision characterizes the certainty of happened result. The entertainer exactness and review indicate the event of significant cases over recovered examples and all out number pertinent occurrences separately. These three measures can be determined dependent on after factors.

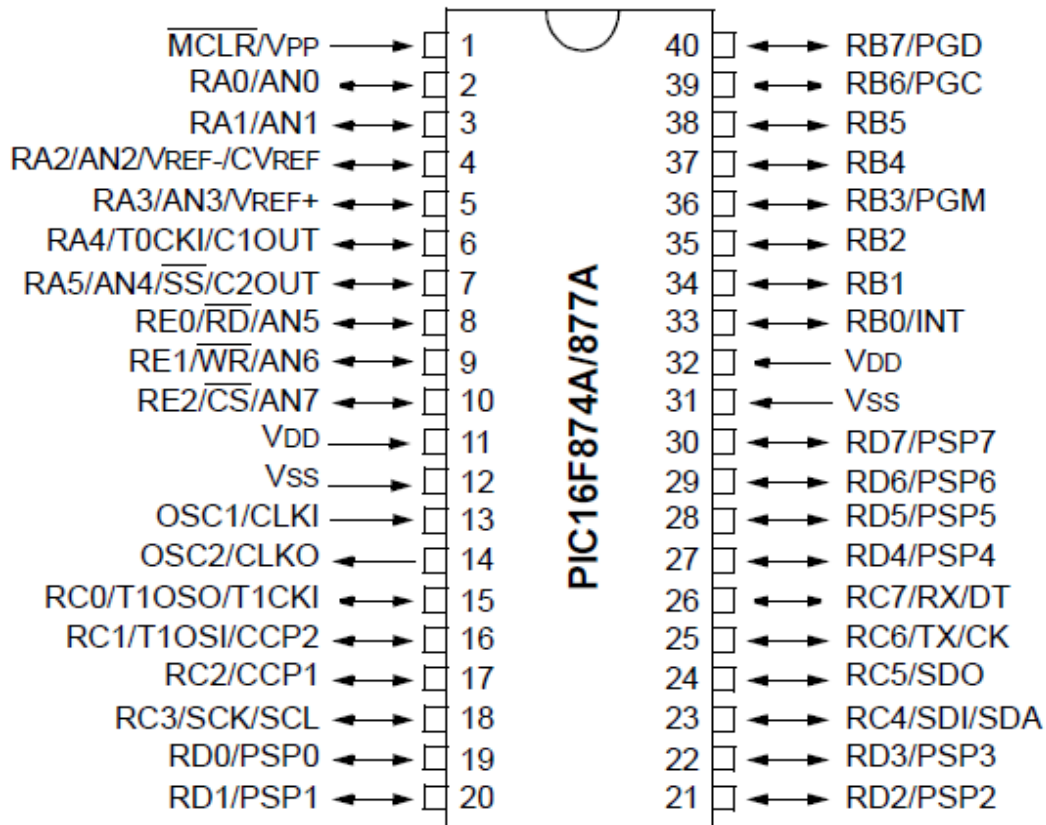
- True positive (TP): If the given combination matches with at least one record in base dataset along with result, that particular result corresponds to TP value.
- True Negative (TN): If the given combination matches with at least one record in base dataset but the rate doesn't match, it defines TN.
- False positive (FP): If the given combination doesn't match with any record in base dataset but the fatality rate is High, it comes under FP.
- False negative (FN): If neither the record matches nor the rate is High, its FN.

The above values TP, TN, FP and FN are compared and incremented on matching basis. Final counts of every case are jotted and following formulae calculates the values respectively.

Efficiency based Result for the classification techniques Naïve Bayes And Convolutional Neural Networks can be given in the below tabular for based on above calculations.

Pin Description:

PIC16F877A consists of 40 pins enclosed in 5 ports. Each port holds 8 pins which are bidirectional input/output pins. Pin diagram of PIC 16F877 is represented in Fig.



TIMER MODULES

The PIC16F877A incorporates timer modules for the purpose of producing software interrupts. These interrupts are part and parcel of microcontroller programming. There are three timers available. They are:

- Timer0 module
- Timer1 module
- Timer2 module

ADVANTAGES

- The programmed vehicle speed control framework is a substantially more common sense and wellbeing highlights for a person on foot and it is practical and execution.
- There is no delay for the yield to the arrive at engine.
- The normal time taken to deal with input and yields by the Arduino.
- The framework ends up being exceptionally viable in limiting over speeding and undesirable mishaps in confined zone.
- In current framework, there independent speed limitation in the vehicle keeps away from mishaps.
- Hence further investigated and advancement of the programmed vehicle speed control due to permit to us carry out in vehicle for further develop wellbeing street side person on foot, travellers, other street clients.
- Vehicle speed controls contributes, limiting mishaps.

APPLICATION

The given framework generally required for school zones and emergency clinic zones and limited high velocity zones. The given framework given limiting street mishaps reasons for drivers botches. It's defeated an errors of driver.

The framework can be utilized in street security regions and lessen the mishaps.

RESULTS AND DISCUSSION

- We propose a computer vision based system for real-time robust Road sign detection and recognition, especially developed for intelligent vehicle.
- Here we proposed a model to predict the Road signs and school, hospital zones using convolution neural network.
- After predicting the required sign, serial communication done by USB to UART converter. Send the serial data to PIC microcontroller.

- The controller will control all the applications like relay, driver motor.

CONCLUSION

In this work, an arrangement procedure named Convolution Neural Networks has been utilized that successfully distinguished the conditions adding to deadly mishaps. Utilizing these conditions, people in general could distinguish hazardous zones and take measures to stay away from mishaps. Exploratory outcomes have shown that CNN is more productive than Naïve Bayes classifier in recognizing the danger factor and furthermore vehicle speed will be decreased with no development. Later on it very well may be wanted to make examination on street mishap dataset by considering more highlights and more groups and to utilize profound learning strategies.

REFERENCES

- [1] K. Jayasudha and C. Chandrasekar, An overview of data mining in road traffic and accident analysis, *Journal of Computer Applications*, 2(4) (2009) 32–37.
- [2] Eric M Ossiander and Peter Cummings, Freeway speed limits and traffic fatalities in Washington state, *Accident Analysis & Prevention*, 34(1) (2002) 13–18.
- [3] William M Evanco, The potential impact of rural mayday systems on vehicular crash fatalities, *Accident Analysis & Prevention*, 31(5) (1999) 455–462.
- [4] KMA Solaiman, Md Mustafizur Rahman and Nashid Shahriar, AVRA Bangladesh collection, analysis & visualization of road accident data in Bangladesh, In *Proceedings of International Conference on Informatics, Electronics & Vision*, (2013) 1-6 IEEE.
- [5] Sachin Kumar and Durga Toshniwal, Analysing road accident data using association rule mining, In *Proceedings of International Conference on Computing, Communication and Security*, (2015) 1–6.
- [6] S. Krishnaveni and M. Hemalatha, A perspective analysis of traffic accident using data mining techniques, *International Journal of Computer Applications*, 23(7) (2011) 40–48.
- [7] Amira A El Tayeb, Vikas Pareek, and Abdelaziz Araar, Applying association rules mining algorithms for traffic accidents in Dubai, *International Journal of Soft Computing and Engineering*, (2015).
- [8] L. Li. S. Shrestha and G. Hu, Analysis of road traffic fatal accidents using data mining techniques, *IEEE 15th International Conference on Software Engineering Research Management and Applications (SERA)*, (2017) 363-370.
- [9] Sami Ayramo, Pasi Pirtala, Janne Kauttonen, Kashif Naveed and Tommi Karkkainen, Mining road traffic accidents, *Reports of the Department of Mathematical Information Technology Series C. Software and Computational Engineering*, University of Jyväskylä, (2009) 1-53.
- [10] S. Shanthi and R. Geetha Ramani, Classification of Vehicle Collision Patterns in Road Accidents using Data Mining Algorithms, *International Journal of Computer Applications* (0975–8887), 35(12) (2011) 30-37.
- [11] S. Shanthi, R. Geetha Ramani, Feature Relevance Analysis and Classification of Road Traffic Accident Data through Data Mining Techniques, *Proceedings of the World Congress on Engineering and Computer Science*, 1(2012).
- [12] Dharmendra Sharma and Suresh Jain, Evaluation of Stemming and Stop Word Techniques on Text Classification Problem, *International Journal of Scientific Research in computer Science and Engineering*, 3(2) (2015).

- [13] Mohnish Patel, Aasif Hasan, Sushil Kumar, Preventing Discovering Association Rules For Large Data Base, International Journal of Scientific Research in computer Science and Engineering 1(3) (2013).
- [14] Neeraj Chhabra, Comparative Analysis of Different Wireless Technologies, International Journal of Scientific Research in Network Security and Communication, 1(5) (2013).
- [15] V. Kapoor, A New Cryptography Algorithm with an Integrated Scheme to Improve Data Security, International Journal of Scientific Research in Network Security and Communication. 1(2) (2013).

Efficient Intrusion Detection System of Botnet Command and Control Traffic

A.Kavitha

UG Student

Department of Computer
Science and Engineering

MAM School of

Engineering

Tiruchirappalli, India

arumugam951997@gmail.com

A.Magesh

UG Student

Department of Computer
Science and Engineering

MAM School of

Engineering

Tiruchirappalli, India.

magesharjun8365@gmail.com

G.Rajeshkumar

Assistant Professor

Department of Computer
Science and Engineering

MAM School of

Engineering

Tiruchirappalli, India.

grkresearch@gmail.com

Abstract— Nowadays high-speed computer networking and the Internet brought great convenience, a number of security issues also emerged with these technologies. Unfortunately, a new type of crime has also emerged along with the Internet: cybercrime and computer network security threats such as viruses and worms, botnets have become one of the most malicious threats over the Internet. Criminal attacks are launched from bots. Every single Internet-connected computer, containing: Personal Computers, mobile phones, network printers, embedded devices, and industrial process controllers, can be twisted into a bot by malware infection. In this project, we describe the issue in developing effective intrusion detection systems for botnet command and control traffic detection. Each detection method analyzes the network traffic to detect one technique used for command and control communications detection and block the connections. The three discovery methods are initially examined, these are: Untrusted Destination by Identifier (UDI), malicious SSL certificate, Traffic Flow Causality (TFC).

Keywords— Cyber attacks, malware, botnet, server, intrusion detection system.

I. INTRODUCTION

Botnets ^[1] ^[2] play an important role in cybercrime. A botnet consists of a large group of remotely controllable computers or bots. The bots are controlled by an individual or organization, referred to as the botmaster. Although there are some rare examples of botnets that perform legitimate tasks, most botmasters have malicious objectives and deploy bots exclusively for criminal operations. Without the knowledge or consent of the owner, computers are recruited as a bot by malware infection and subsequently deployed in diverse criminal activities, such as DDoS (Distributed Denial of Service) attacks, spam, click fraud, theft of sensitive information, and even cyber terrorism. In this work the word botnet refers exclusively to malicious botnets. The botmaster communicates with the bots in a special communication infrastructure, referred to as the C&C (Command and Control) Infrastructure. The botmaster ^[3] is separated from the attacking bots by intermediate computers or stepping stones that complicate the trace back from discovered bots towards the botmaster by the C&C communication. The

trace back complexity is further increased when the stepping stones are distributed over several countries with different legislation. Experts believe that approximately 16-25% of the computers connected to the Internet are members of botnets. One of the biggest recent distributed denial-of service (DDoS) assaults the Internet has ever witnessed against KrebsOnSecurity.com shows that the Internet of Things (IoT) is becoming a key target for attackers. The IoT botnet malware, dubbed 'Mirai', spreads to vulnerable connected devices by continuously scanning the Internet for easily hackable IoT systems protected by hard-coded passwords or factory defaults. It is difficult to accurately define a botnet. Although it is evident that a botnet is a set of bots, connected to a botmaster, this definition is not satisfactory without the definition of a bot. Communication plays an important role, but the sole ability of malware to connect to other malicious instances is not a sufficient condition to classify an infected computer as a bot. Modern malware is practically always a combination of different components for: infection, attack, concealment, adaption, and communication. Not only popular media, but even scientific literature, often refers to the same malware instances with different terms, such as: virus, root kit, backdoor, RAT, or trojan.

II. LITERATURE SURVEY

Most existing detection approaches in networks, it have limited results against botnet traffic that carefully imitates user originated visits to popular social websites, due to the close resemblance to legitimate traffic.

^[1] **Sana Belguith** et al., proposed PAbAC, a novel privacy preserving Attribute-based framework, that combines attribute-based encryption and attribute-based signature mechanisms for securely sharing outsourced data via the public cloud. Our proposal is multifold. First, it ensures fine-grained cryptographic access control enforced at the data owner's side, while providing the desired expressiveness of the access control policies. Second, PAbAC preserves users' privacy, while hiding any identifying information used to satisfy the access control. Third, PAbAC is proven to be highly scalable and efficient

for sharing outsourced data in remote servers, at both the client and the cloud provider side.

^[2]**Sana Belguith** et al., introduced PHOABE, a Policy-Hidden Outsourced ABE scheme. Our construction presents several advantages. First, it is a multi-attribute authority ABE scheme. Second, the expensive computations for the ABE decryption process is partially delegated to a Semi Trusted Cloud Server. Third, users' privacy is protected thanks to a hidden access policy. Fourth, PHOABE is proven to be selectively secure, verifiable and policy privacy preserving under the random oracle model. Five, estimation of the processing overhead proves its feasibility in IoT constrained environments.

^[3]**Ibrahim ghafir** et al., proposed a novel approach, called BotDet, for botnet Command and Control (C&C) traf_c detection to defend against malware attacks in critical Ultra structure systems. There are two stages in the development of the proposed system: it has developed four detection modules to detect different possible techniques used in botnet C&C communications and 2) we have designed a correlation framework to reduce the rate of false alarms raised by individual detection Modules. Evaluation results show that BotDet balances the true positive rate and the false positive rate with 82.3% and 13.6%, respectively. Furthermore, it proves BotDet capability of real time detection.

^[4]**Prerika Agarwal**, Implementation of signature-based detection system using snort in windows, Snort is a signature-based IDS capable of monitoring and analyzing network traffic to match signatures of known botnets. Snort consists of many components working together in order to detect malicious patterns in the traffic. Packets from network interfaces are captured by the packet decoder and they are prepared to be pre processed or sent to the detection engine. Then, packets are checked against specific plugins by a processor, and if anomalies are found, the processor raises an alert.

User traffic profile for traffic reduction and effective botnet C&C detection, Host-based approach for botnet C&C communication detection. This approach analyses suspicious flows produced by filtering out benign traffic from the traffic created by a host. A normal profile of the host traffic is used for the filtering. The behavioral pattern of flows to all destinations is examined in a bid to generate the host profile. This approach achieved a detection rate of 100% and false positives of 8%.

^[5]**Banf** Detection and classification of different botnet C&C channels, Host-based detection method able to detect the existence of botnet C&C traffic on the observed machine, and also categorize the type of C&C communication used by the bot, e.g., peer-to-peer (P2P) based, HTTP-based or IRC-based. As it does not examine the packets payloads, their detection method is independent of the content of the C&C messages. Their method for detecting and categorizing

botnet C&C connections is based on three hypotheses: (1) it is possible to distinguish between botnet C&C communication and botnet non-C&C communication, (2) it is possible to distinguish between botnet C&C communication and valid communication and (3) there are shared characteristics between different styles of C&C and different botnet families.

Exploiting temporal persistence to detect covert botnet channels, Host-based detection method for botnet C&C traffic detection. This method is based on the fact that the infected machines should stay in contact with C&C servers to be instructed and controlled by the botmaster. It is assumed that those connections

III. EXISTING WORK

Recently many countermeasures have been deployed against botnets. Apparently there has been no decisive countermeasure, because botnets are since many years the most important instrument of Internet related crime and massive numbers of computers are part of botnets. The continuous media attention also indicates that botnets are still a real and unsolved threat. According to the recent research in worldwide there is still a spam rate of 69% of all mail. Spam is almost exclusively sent by botnets.

A. Disadvantages

- Most of detection method uses signature-based detection, it can be used for detecting only known botnets.
- Botnet C&C traffic detection uses honey nets. However, honey nets are not always capable of detecting bot infection.
- There is no flexible and extensible intrusion detection system.

Lack of handling network traffic in the real-time.

IV. PROPOSED WORK

In this project focused on network-based detection and host based detection of bots in Internet-connected networks with regard to the botnet threat and botnet detection. Invisibility is an important factor in botnet survivability; fortunately the invisibility of a botnet has practical limitations. Important causes that limit the invisibility are attack traffic, malware installation, limited resources and other survivability measures. The proposed work based on three major detection methods such as Untrusted Destination by Identifier (UDI) malicious SSL certificate, Traffic Flow Causality (TFC) and it is used to analyze and detect the malicious network traffic in real time.

A. Advantages

- The framework that analyzes and detects hidden botnet C&C.
- Botnet C&C traffic is detected by the observation of direct causes of traffic flows.

- To reduce the rate of false alarms raised by individual detection modules.

B. Objective

- Identify the method that are used in existing network-based C&C detection approaches and identify specific new approaches of networks that may lead to new detection approaches.
- Estimate the detection performance of these new approaches.
- To reduce the attacks such as ransomware or bot malware in real time network.

phase’s communication. To this end, three detection modules have been proposed: Botnet C & C by SSL certificate detection module, Botnet C & C by untrusted destinations detection module and Botnet C & C by causal analysis of traffic flows detection module. Each detection module is independent of the other modules and aims to detect one technique that can be used in C&C communication. The outputs of these detection modules should be submitted to the second phase where they are correlated to raise an alert and block on botnet C&C traffic detection. In the second phase, the correlation framework takes events (the outputs of our detection modules) as an input and correlates them to raise an alert and block on botnet C&C traffic detection. The correlation method is based on voting between the detection methods to make the final decision about the detection.

A. ALGORITHM FOR IP BASED DETECTION

- **Input** : Message from NN;
- for each new flow NN_IP do
- Read the NN_IP;
- X= NN_IP;
- if X.equals.BOTN_IP
- X .Status = ANOMALOUS;
- signalAnomaly(X);
- Show(x);
- else
- X .Status = getStatusOfAssociatedFlow(X);
- if X .Status = NORMAL then
- extractForwardReferences(X);
- end if
- end if
- end for

B. ALGORITHM FOR DNS BASED DETECTION

- **Input** : Message from NN;
- for each new flow NN_DNS do
- Read the NN_DNS;
- Y= NN_IP;
- Estimate the detection performance of these new approaches.
- To reduce the attacks such as ransomware or bot malware in real time network.

V. SYSTEM ARCHITECTURE

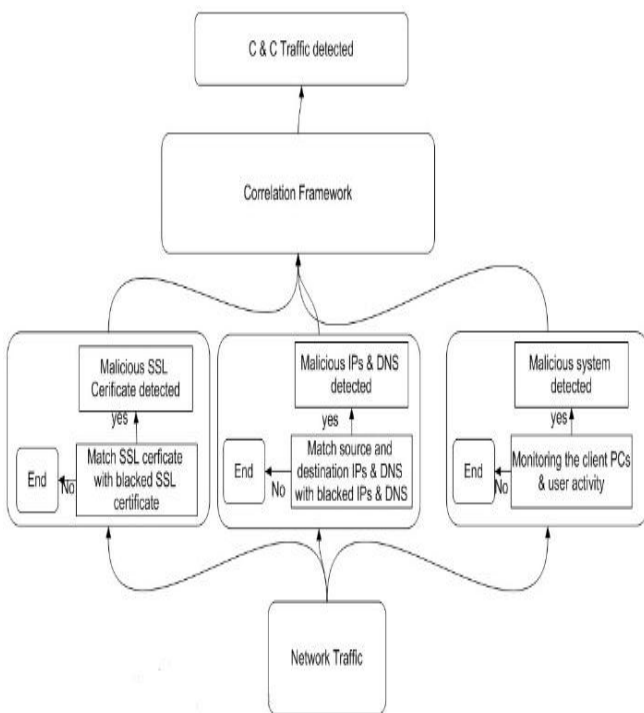


Fig. 1. System Architecture

Our proposed approach for botnet C&C traffic detection is outlined. This approach is based on the correlation between the events, which are the outputs of the detection modules. Fig 1 shows the two main

V. CONCLUSION

In this work, we propose a method that can recognize web-based bots in supervised network by modeling the network behavior of bots. On statement of activities for plenty of web-based bots, we notice that connections carrying C&C communication or other actions for a web-based bot are parallel in statistical meaning and these similar connections also appear periodicity despite the parameters of the features are different. Our work goals extracting this common network behavior shared by web-based bots and making detection models spontaneously. The proposed methodology does not rely on either payload evidence or bots' group-activities. Consequently, we can notice web-based bots with encrypted communication and the single infested bot in supervised network. The evaluation shows that our proposed methodology can discover web-based bots with a low false ratio.

REFERENCES

[1] Sana Belguith, Nesrine Kaaniche “pabac: A Privacy Preserving Attribute based Framework for Fine Grained Access Control in Clouds“, 2016.

[2] Sana Belguith , “PHOABE: Securely outsourcing multi-authority attribute based encryption with policy hidden for cloud assisted IOT”, 2018.

[3] Ibrahim Ghafir ^{1,2}, Vaclav Prenosil¹, Mohammad Hammoudeh ³, Thar Baker ⁴, Sohail Jabbar ⁵, Shehzad Khalid ⁶ , And Sardar Jaf 2 “botdet: A System for Real Time Botnet Command and Control Traffic Detection”, 2019.

[4] Prerika Agarwal,“Implementation of Signature-based Detection System using Snort in Windows”, 2014.

[5] Banff “Detection and Classification of Different Botnet C&C Channels”, 2019.

[6] Ibrahim Ghafir, Vaclav Prenosil and Mohammad Hammoudeh “Botnet Command and Control Traffic Detection Challenges: A Correlation-based Solution” International Journal of Advances in Computer Networks and Its Security– IJCNS Volume 7: Issue 1,ISSN : 2250-3757, 2017.

[7] Xingguo Li , Junfeng Wang , and Xiaosong Zhang “Botnet Detection Technology Based on DNS” Future Internet, 9, 55; doi:10.3390/fi9040055, 2017.

[8] Pieter Burghouwt, Marcel Spruit and Henk Sips “Detection of Botnet Command and Control Traffic by the Identification of Untrusted Destinations” International Conference on Security and Privacy in Communication Networks, pp 174-182,2015.

[9] Sunny Behal1, Amanpreet Singh Brar2, Krishan Kumar “Signature-based Botnet Detection and

Prevention” Proceedings of International Journal,2015.

[10] Sean Miller, Curtis Busby-Earle “The impact of different botnet flow feature subsets on prediction accuracy using supervised and unsupervised learning methods” Journal of Internet Technology and Secured Transactions (JITST), Volume 5, Issue 2, June 2016.

[11] Khattak, Sheharbano, et al. "A taxonomy of botnet behavior, detection, and defense." IEEE communications surveys & tutorials 16.2, 898-924. (2014).

[12] Alieyan, K., Kadhun, M. M., Anbar, M., Rehman, S. U., & Alajmi, N. K. (2016, October). An overview of DDoS attacks based on DNS. In Information and Communication Technology Convergence (ICTC), 2016 International Conference on (pp. 276-280). IEEE.

[13] Gross, G. (2016). Detecting and destroying botnets. Network Security, 2016(3), 7-10.

[14] Koliass, C., Kambourakis, G., Stavrou, A., & Voas, J. (2017). DDoS in the IoT: Mirai and other botnets. Computer, 50(7), 80-84.

Theft Identification System Based on Face Recognition Using Iot

K.Senthamizhselvi
UG Student
Department of Computer
Science and Engineering
MAM School of
Engineering
Tiruchirappalli, India
Jenidani99@gmail.com

M.Alexpandian
UG Student
Department of Computer
Science and Engineering
MAM School of
Engineering
Tiruchirappalli, India.
Alexpandian2799@gmail.com

S.Murugavalli
Assistant Professor
Department of Computer
Science and Engineering
MAM School of
Engineering
Tiruchirappalli, India
Vallisangilimuthu201
2@gmail.com

ABSTRACT:

Intelligent surveillance systems are widely used in several critical areas such as airports, ATM, and bank agencies to ensure more security and more safety. The need for an intelligent behavior recognition system is still increasing. Traditional approaches based on access to restricted places or suspected actions as theft, scam, loitering are insufficient to identify suspect behavior. These actions do not represent area key of suspects. Novel trends attempt to extract behaviors from involuntary actions as face gestures, face characteristics, and feeling features. This paper is motivated not only by the limits of the traditional approaches but also by the complexity of is challenged by the Real-Time exigencies. For this purpose, a Raspberry PI3 board is used in relation to Raspbian Operating System to ensures Real-Time criteria. The proposed is trained according to CKC dataset. In this paper, contributions attempt to ensure not only a high recognition rate using a non-complex algorithm but also guarantee a real-time computation. Results reveal that the proposed algorithm has the advancement in computer vision which are observed as an important trend in video surveillance leads to dramatic efficiency gains. We propose a CCTV based theft detection along with tracking of thieves. We use suspicious individual committing burglary using Real-time analysis of the movement of any human

intelligent algorithms .In this context, the present paper uses face features to recognize the feeling of fear like a suspect behavior. Indeed, this feeling represents the main characteristic of a suspicious person under crime as announced by several psychologist scientists. The fear feeling is usually followed by an increase in heart rate beats. This paper describes the recognition of fear feeling using a camera as a contactless sensor. Frequencies associated with face based-video are used to estimate the heart rate according to the fusion of three techniques: band pass filter, Eulerian transformer, and Lagrangian transformer. The proposed algorithm benefits from the advantages of each technique, but it

best heart rate estimation in comparison with traditional methods. Hardware results justify the success of the proposed design in terms of resource requirements. The job is very challenging as the video contains a lot of information with large differences and difficulties. Human supervision is still required in all surveillance systems. New

image processing to detect theft and motion of thieves in CCTV footage, without the use of sensors. This system concentrates on object detection. The security personnel can be notified about the from CCTV footage and thus gives a chance to avert the same.

I.

NTRODUCTION:

Nowadays, safety and security became an important objective for humanity. Video surveillance system

I

historic starts in1960 by using analogy CCTV. In this phase, the surveillance system serves for storage and

did not provide intelligent processing. Then, the second phase starts in 1980 by using digital CCTV. This evolution helps the researcher to exploit briefly the automation. The third phase starts in 2000. It is highlighted by the evolution of the digital camera that serves for the semi-automation of video-surveillance systems [1]. The automated surveillance needs to be intelligent. For this reason, systems should be able to identify threats and dangerous state from video streaming. System using video processing identifies suspicious behavior when a person is accessing to restricted places or is committing actions as theft, scam and loitering [2]–[4]. The position of the object under surveillance is performed using frame succession (at different point of time). The position is exploited to identify the human behavior as trajectory, gesture, and event. In the case of surveillance, tracking must be accurate which not the case is. The abnormal behavior based on the tracking method results in a poor recognition rate [5] and is not really related to a suspect action. Existing surveillance systems suffer from the following shortcomings: (1) This section focuses mainly on the techniques used in involuntarily suspicious behavior including face gesture and fear feeling. Indeed, working on feeling behavior related to suspect like fear represents a great challenge. Psychologists prove that any offender feels fear under doing a crime [6]. This is accompanied by the increasing of the heart beat. Authors in [7]–[9] as psychological scientists, prove that high dominance and low trustworthiness as morphological features represent a signal of high criminality. These features could be extracted from face expression [10], [11]. Other works attempt to recognize suspicious behavior by the feeling of fear using face video streaming. These studies could be classified into two main groups: facial expression methods and heart rate estimation methods. The first group methods [5] attempt to identify feeling from basic emotions as anger, disgust, fear, joy, sorrow, and surprise from face's expression. Authors in [5] use Support Vector Machine (SVM) classifier to extract eye movements from facial expression then compared with CKC and MUG datasets. Results related to fear sensing is often misclassified (only 42

% of expression are well recognized as fear feeling Authors in [12] propose Local Binary Patterns on Three Orthogonal Planes (LBP-TOP) method to identify fear from face expression. The true recognition rate (about 79 %) in this case is better than previous work but suffers from the increased response time. SVM classifier is performed. The accuracy is lower than LBP-TOP method (about 71%) and the time response does not respect the real-time exigence (about 1 minute). Authors in [14] use High-order Joint Derivative Local Binary Pattern (HJDLBP), Local Binary Pattern (LBP) histogram, and SVM algorithms to extract facial expression. According to results related to the feeling of fear, the accuracy Closed circuit television systems (CCTV) are winding up increasingly famous and are deployed in numerous banks. As the human factors limit the number of camera views of a single operator, this makes for an immeasurable load for the CCTV operators. Another problem when one thinks about the situations of banks is that the system to alert security people in charge are manually triggered [10] and in case of a damaged situation it may not be possible for the people present to activate the trigger [9]. A image-processing and algorithms to the CCTV footage, which will replace the human operatives and alert the security officials if a terrible situation is found [9]. But in some countries, it is allowed to carry firearms freely and openly, and in such cases, it is still wise to grasp the attention of CCTV operatives in order to evaluate such conditions or scenarios [9]. In the previous few years, deep learning and Convolutional Neural Networks (CNNs) have accomplished best results to all the classical machine learning methods in image detection, classification and clustering, etc. Deep learning CNNs automatically discover more and more higher-level features from data, instead of manually selecting features. [3].

II. LITERATURE REVIEW

A great deal of research has been performed for automatic object detection and curbing the situations such as bank robberies and ATM tampering. A significant amount of literature was reviewed for the

same. Michał Grega, Andrzej Matiola have aimed on the two tasks of recognition of suspicious situations and automated detection. They have put forward, some algorithms for the detection of harmful tools. A knife or a gun (most common weapon used in committing crimes) held in someone's hand is an instance of a sign of danger. The sensitivity and specificity of the detection algorithm are 81.18% and 94.93%, respectively. These outcomes are better than the ones published by others recently. His solution can handle poor and low-quality images. This is very important as most of the CCTV footage are of such low quality. The algorithm was performed in real time. For the fire arm detection algorithm, they accomplished a sensitivity of 36.9% and a specificity of 96.7% for the footage having suspicious objects, and they noticed a specificity of 100% for the footage not containing threatening objects [9]. The set of computer instructions creates no false alarms, though it skips few frames with harmful objects this way becoming a practical CCTV aid. The image frame undergoes background subtraction and the foreground image is selected which will then undergo canny edge detection instead of applying it on to the original image. The detection of an object depends on how far it is and requires a value for the sliding window. So they have calculated a value for sliding window which will only need to be increased thereby getting the optimum solution with very alterations. The neural network used here contains 560 (Five hundred and sixty) neurons in the input layer, 200 (Two hundred) neurons in the intermediate layer and 8 (Eight) neurons in the output layer which gives us the result whether the image contains a fire armor a knife [1]. Tasriva Sikandar and Kamarul Hawari Ghazali have addressed image processing techniques in the ATM CCTV footage for analyses of human motion to provide alert to the security officials. In this paper, they have attempted to examine human detection methods which can be proved helpful in CCTV surveillance. They have also examined ATM environment factors that affects human detection process and gave an overall view of various human detection methods.

In motion segmentation, a footage or photo is break down in background and moving object region. For clear image we sketch out the algorithms under some categories arranged in a manner conforming with to their basic idea of the approach which has 1) Background Subtraction 2) Statistical methods 3) Temporal Differencing and 4) Optical flow. Then the object is classified on the basis of shape and motion Thus, after evaluating all existing procedure it is obvious that, for accomplishing the desired detection of human in the ATM environment the applied algorithms need to be strong against critical factors such as, shadows, slow movement, inner and outer illumination variance, and constant and/or repetitive movement of user, camouflage, thief hidden behind another object and noise in the ATM environment [2] Face is detected and the ROI for expression using Viola-Jones AdaBoost method on color filtered image algorithm to detect people's faces, noses, eyes, mouth, or upper body, as these parts have higher entropy for emotion detection. This paper presents a mobile application for real time facial expression recognition running on a smart phone with a camera. The proposed system uses a set of Support Vector Machines (SVMs) for classifying 6 basic emotions and neutral expression along with checking mouth status. It is based on the phenomenon that the color and motion variations in the face video are closely related to the heart beat. The variations also contain the noise due to facial expressions, respiration, eye blinking and environmental factors which are handled by the proposed system. It used the Center-Loss Face and Sphere Face methods as the bases for constructing such feature extractors and fine-tuned them with face images extracted from real surveillance videos.

III. PROPOSED METHOD:

Proposed system focuses on implementing a Smart Cam which monitors suspicious behavior, and the thieves would be tracked on the basis of motion. In this system it consists of camera and IOT module. The System has to capture live stream with camera. is used to take detected camera footage, the system uses image processing to detect an exact area of motion occurrence and highlights it accordingly. The system

now transmits the images of the occurrence over IOT to be viewed by the user online and also this system display the details about the thief based on captured image.

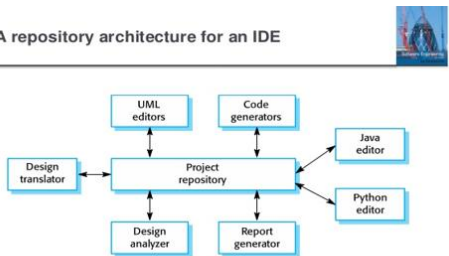
IV. PROBLEM IDENTIFICATION:

Our system focuses on implementing a Smart Cam which monitors the activity in the banks, it can detect any sort of suspicious behavior, and the thieves would be tracked on the basis of motion and the presence of weapons. If any such suspicious weapons or action is detected, the Smart Cam will automatically send an alert message to the security department. The message mentions what type of alert is generated; it also contains the type of weapon and number of weapons detected with a web link where the live image is stored, so that the security can come with appropriate preparation.

V. ALGORITHM:

The second phase estimates the heart rate. The ROI is transformed from the spatial domain to the frequency domain using Fast Fourier Transformer, see equation 1. $F(u; v) = \int \int f(x; y) e^{-j2\pi(ux+vy)} dx dy$ (1)

A repository architecture for an IDE



where u and v are spatial

frequencies. Then, we apply the band pass filter using equation 2. This filter tries to remove the unwanted frequencies which are superior to 150 Hz and inferior to 50 Hz. This filter maintains only the useful signal $F_{bf}(u;v) = \int \int_{D_0-w}^{D_0+w} \int \int_{D_0-Cw}^{D_0+Cw} F(u;v) dx dy$ (2) where w is the bandwidth of the filter Eulerian transformer, defined by equation 3, analyzes the signal to determine the common behavior. This step selects the useful signal. $E = \int \int_{x_1 x_2} F_{bf}(u; v(x); v_0(x)) dx$ (3) The Lagrangian transformer is applied to the obtained signal issued from Eulerian transformer

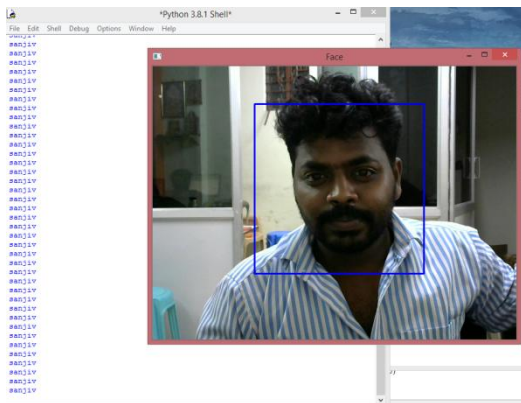
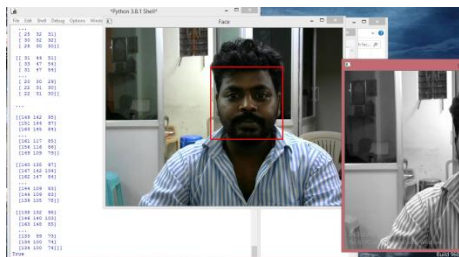
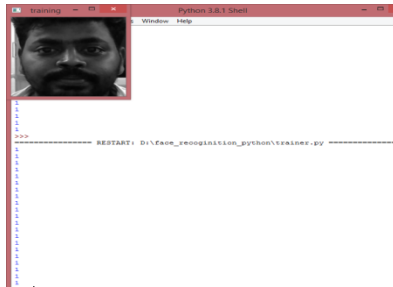
to compute accurately the frequency related to the signal which corresponds to the heart rate, as shown in equation 4. $F_L(u;D) = \int \int_{x@FE@u} @x@FE@u C@ @y@FE@u(4)$ The third phase computes the variation of the heart rate estimation found by a successive video sequence with 5 duration. If the variation of the heart rate (VHR) is superior to 30 Beats Per Minute (BPM) a suspicious behavior based on fear is expected. This VHR is computed through samples of fear emotion described in CKC dataset [23] which is publicly available. As shown in figure 1, the system detects the face then localizes the forehead which represents the ROI. After the detection of the face using the standard function supported by the Open CV library, the algorithm divides the face-image into matrix 3 x 3. The ROI corresponds to the (1,2) position. *A. False Positive Rate (FPR)* It is the ratio of the number of false positive to the sum of the number of false positive and true negative. It measures how well the system can correctly reject false positive.

VI. IMPLEMENTATION:

CPython is the reference implementation of Python. It is written in C, meeting the C89 standard with several select C99 features. It compiles Python programs into an intermediate byte code which is then executed by its virtual machine. CPython is distributed with a large standard library written in a mixture of C and native Python. It is available for many platforms, including Windows and most modern Unix-like systems. Platform portability was one of its earliest priorities.

VII. RESULTS:

This section describes the validation phase for the proposed method. The first section discusses the simulation results then the second provides details about the implementation phase. The investigations were carried out following the rules of the Declaration of Helsinki of 1975 and approved by the Committee for the Ethics of Scientific Research at Majmaah University.



VIII.

CONCLUSION:

The research work that will be carried out in this thesis would be mainly focused to design and develop efficient and convenient motion detection surveillance. The system will capture images only when the motions exceed a certain threshold that is pre-set in the system. It thus reduces the volume of data that needs to be reviewed. It will be applicable for both office and home uses. After successfully implementing the project,

it can be apply for the motion detection for smart home security system which would be very much helpful in auto theft detection for security purpose. It can also be useful in bank, museum and street at mid-night.

IX.

REFERENCES:

- 1.Olmos, SihamTabik, and Francisco Herrera ,Soft Computing and Intelligent Information Systems research, Automatic Handgun Detection Alarm in Videos Using Deep Learning.
- 2.AfzalGodil Roger Bostelman Will ShacklefordTsaiHongMShneier Performance Metrics for Evaluating Object and Human Detection and Tracking System
- 3.PubS. Ren, K. He, R.Girshick, and J. Sun,“FasterRCNN:TowardsRealTimeObject DetectionwithRegionProposalNetworks”, MicrosoftResearch Paper . Apr.-2016lished 2014.
- 4.MichałGrega *, Andrzej Matiolański , Piotr Guzik and MikołajLeszczuk (2016). AGH University of Science and Technology, Article Automated Detection of Firearms and Knives in a CCTV Image.
- 5.M. S. Munagekar, “Smart Surveillance system for theft detection using image processing ”, International Research Journal of Engineering and Technology. Aug.-2018.
- 6.S. Xie and H. Hu, “Facial expression recognition using hierarchical features with deep comprehensive multipatchesaggregation convolutionalneural networks,” *IEEE Trans. Multimedia*, vol. 21, no. 1, pp. 211–220,Jan. 2019.
- 7.M. Sajjada, M. Nasir, F. U. M. Ullaha, K. Muhammadb, A. K. Sangaiah,

- and S. W. Baik, “Raspberry Pi assisted facial expression recognition framework for smart security in law-enforcement services,” *Inf. Sci.*,
- 8.W. Heng, T. Jiang, W. Gao, “How to assess the quality of compressed surveillance videos using face recognition,” *IEEE Trans. Circuits Syst. Video Technol.*, vol. 29, no. 8, pp. 2229–2243, Aug. 2019.
- 9.T. Kanade, J. F. Cohn, and Y. Tian, “Comprehensive database for facial expression analysis,” in *Proc. 4th IEEE Int. Conf. Autom. Face Gesture Recognit. (FG)*, Mar. 2000, pp. 46–53.M.
- 10.T. Pursche, J. Krajewski, and R. Moeller, “Video-based heart rate measurement from human faces,” in *Proc. IEEE Int. Conf. Consum. Electron.(ICCE)*, Jan. 2012, pp. 544–545
- 11.T. Pursche, J. Krajewski, and R. Moeller, “Video-based heart rate measurement from human faces,” in *Proc. IEEE Int. Conf. Consum. Electron. (ICCE)*, Jan. 2012, pp. 544–545.
- 12.K.-Y. Lin, D.-Y. Chen, and W.-J. Tsai, “Face-based heart rate signal decomposition and evaluation using multiple linear regression,” *IEEE Sensors J.*, vol. 16, no. 5, pp. 1351–1360, Mar. 2016.
- 13.U. N. Mahesh and R. Hanumantha, “Hybrid approach for facial expression recognition using HJDLBP and LBP histogram in video sequences,” *Int. J. Image, Graph. Signal Process.*, vol. 10, no. 2, pp. 1–9, 2018.
- 14.T. Chandan, H. Madasu, and V. Shantaram, “Suspicious face detectionbased on eye and other facial features movement monitoring,” in *Proc.IEEE Appl. Imag. Pattern Recognit. Workshop (AIPR)*, Oct. 2018, pp. 1–8.
- 15.N. N. Oosterhof, A. and Todorov, “The functional basis of face evaluation,” *Proc. Nat. Acad. Sci. USA*, vol. 105, no. 32, pp. 11087–11092, 2008.

Comparative study of mechanical technologies over laser technology for drilling carbon fiber reinforced polymer materials

Vellaisamy Balasubramaniam^a, Durairaj Rajkumar^{b*}, Poovaraj Ranjithkumar^c, & Chinnaiyan Sathiya Narayanan^d

^aDepartment of Mechanical Engineering, Kurinji College of Engineering and Technology, Trichy 620009, India

^{b,c}Department of Mechanical Engineering, M.A.M. School of Engineering, Trichy 621 105, India

^dDepartment of Production Engineering, National Institute of Technology, Trichy 620 015, India

Received: 13 August 2018; Accepted: 9 July 2019

More researchers have been worked to increase the quality of the machined composite materials. In this paper, a comparative experimental study of mechanical techniques over the laser techniques has been performed in the drilling process by using the carbon fiber reinforced polymer (CFRP). In order to identify the best process among the mechanical drilling (MD) and laser drilling (LD) technology various analysis methods like normality analysis, control chart analysis, and process capability analysis have been performed. Process capability index analysis for case study 1 and interval plot analysis for case study 2 have been employed to evaluate the best process comparatively. Experiments have been performed in a vertical machining center (VMC) and CO₂ laser. The final results revealed that the MD process is the best technology for drilling CFRP. Therefore, this work has been important for small-scale industries.

Keywords: Mechanical drilling, Laser drilling, Carbide drill, Carbon fiber reinforced polymer, Process capability

1 Introduction

Light weight composite materials are an advanced material group and are shaped by the arrangement of two or more materials in order to get distinctive properties of materials. The CFRP is an extremely strong and light fiber-reinforced polymer which contains carbon fibers and epoxy resin as matrix materials. Applications and development of advanced composite materials are booming in various manufacturing sector such as aerospace sector, structural sector, electronics sector, automobile sector¹. The CFRP composites having several superior properties such as high strength, lower weight, lower coefficient expansion, higher strength-to-weight, stiffness-to-weight ratios, excellent anti-thermal shock ability, and good vibration absorption². The CFRP is one of the polymer matrix composites that widely performed in various domains like aerospace, electronics, structural industries and automotive due to their outstanding properties such elevated strength to wear ratio, corrosion resistance, and superior wear resistance and high modulus. Machining is an important manufacturing process. Machining is defined as the process of removing material from a

workpiece. Tool based machining and energy based machining are important two types of machines. Machining is a most necessary process where tight tolerances on dimensions and surface finishes are required for assembling of components. Normally the available conventional machining processes are turning, milling and drilling, shaping while non-conventional machining is laser machining and abrasive water jet machining. The manufacturing industries are struggling to select the best cutting technology and select the optimum machining process among the various machining process for machining CFRP composites economically. The damages that occur during conventional processing in polymer composites are many such as matrix cracking, fiber pull in/out, spalling, fuzzing, tool wear, delamination, thermal degradation, high dust generation. This is due to the fact of inherent heterogeneity & anisotropy of materials³⁻⁵.

Minimizing the machining damages becomes pivotal for structural integrity of the part. In order to solve the conventional processing problems, non-conventional machining processes have been developed. Among the non-conventional machining processes, laser beam machining and abrasive water jet machining have received sizeable awareness.

*Corresponding author (E-mail: profdrjkumar@gmail.com)

While abrasive water jet machining has been applied in recent days, the employ of water is difficult. Because the polymer composites are naturally absorbing water and it results in reduced strength of parts. Due to the non-contact nature of the process and the high degree of flexibility, the laser beam machining has sizeable awareness as an alternate option to conventional processes. The necessity of creating micro-hole on carbon-fiber reinforced polymer materials are found in the applications like a printed circuit board, printed wiring board, laptop upper panel, access doors, satellite antenna, bridges, pipes and walkways, panels, wheel chairs and body panels. Therefore, these applications of are components demand the micro-hole drilling process on CFRP plate with accurate dimensions⁶. The diameters of the micro-hole required in CFRP component are less than 1 mm^{7,8}. Therefore, Mechanical Drilling (MD) and Laser Drilling (LD) are chosen for this work. The major problems in mechanical drilling are delamination, circularity error, overcut, taper angle⁹⁻¹⁶.

The major problems in laser drilling are heat affected zone, kerf width, taper angle¹⁷⁻²¹. Damages caused in MD are due to the improper selection of drilling parameter, tool geometry, and selection of tool material. LD damages are caused by the improper selection of laser mode, assist gas, sample materials, environment, a focusing lens, selection of workpiece material. It is important to identify the causes prior to machining²². In order to control the problems in MD and LD and to achieve the desired qualities in the machined micro-holes, it is necessary to know the mechanisms of material removal and kinetics of machining processes. In this work, the process capability of CFRP in the MD process and LD process is studied. Prior to the analysis of process capability, the observed experimental data that the normality test and control chart are checked. In the previous research works, drilling of holes having the size below 0.5 mm in CFRP composite in mechanical drilling and laser drilling processes has never been successfully attempted. Therefore, in this work, the holes of size in CFRP 0.5 mm have been drilled by a

mechanical drilling process and the process has been analyzed in different aspects.

2 Design of Experiments

The function of the Design of Experiments (DoE) requires aware of planning, the prudent layout of the experiments, and analysis of results. Taguchi Orthogonal Approach (OA) has universally accepted and standardized approach for each of this experimental design application. The beneficiary of DoE is used to develop the most affecting process parameter and DoE can radically reduce the 'n' number of tests required to meet necessary data. Therefore, the DoE approach has become a more fashionable tool for engineers and researchers. In this case study, the two parameters namely spindle speed and feed rate in MD and the three parameters namely power, cutting velocity and argon pressure in LD were chosen as the controlling factors respectively and each parameter is designed to have four levels denoted by 1, 2, 3 and 4 and are shown in Table 1 and Table 2, respectively.

3 Normality Test, Control Chart and Process Capability

A normality test is used to check whether a sample or any groups of data satisfy normal distribution and it is performed either mathematically or graphically. The most important application of the normality tests is to find the residuals of a linear regressions model. The normality test or probability plot is carried out to evaluate how well the continuous data follows the normal distribution. In this work, Minitab 17 statistical software is used for this purpose. The plot report of AD values and p-values are used to justify whether the observed continuous data are with a 95% confidence interval either follow the normal

Table 1— Mechanical Drilling parameters and their levels.

Control parameters	symbol	Levels			
		1	2	3	4
Spindle speed (V), rpm	V	1000	1500	2000	2500
feed rate (f), mm/rev	f	0.01	0.03	0.06	0.09

Table 2 — Laser Drilling parameters and their levels.

Control parameters	symbol	Levels			
		1	2	3	4
Power (P), W	P	15	30	45	60
Cutting velocity (v), mm/min	v	20	40	60	80
Argon pressure (p), kpa	p	200	300	400	500

distribution or non-normal distribution. The well fit data must have a low AD value (less than one) and high p-value (greater than 0.05).

Quality is the grade to which finished services or products fulfill the requirement of customers. The aims of quality specialist are minimizing defect rates, fabricating the products within design/customer requirement and economical time. Minitab has the broad number of process available to assess quality based on the objective. In a quantitative manner: quality planning tools, process capability, control charts, measurement analysis, and reliability analysis are the methods. In order to study the stability of a process, the control charts are required. Depending upon data type and subgroup size, the control chart is chosen for analysis to find whether the observed data are in control or out of control. There are two types of data such as continuous data (quality characteristics such as surface roughness and hole size) and attribute data (defective item and defects/unit). The I-MR chart was chosen for this study. The reason for choosing the I-MR chart is that the type of data is continuous data and subgroup size is one. The Upper Control Limit (UCL) and Lower Control Limit (LCL) are employed as the control limits for the I-MR charts in Statistical Process Control (SPC). Therefore, the UCL and LCL are calculated from I-MR charts by employing the following expressions.

Control Limit for I Chart:

$$UCL = \bar{x} + 3 \frac{\overline{MR}}{1.128} \quad \dots (1)$$

$$CL = \bar{x} \quad \dots (2)$$

$$LCL = \bar{x} - 3 \frac{\overline{MR}}{1.128} \quad \dots (3)$$

Control Limit for MR Chart:

$$UCL = 3.267\overline{MR} \quad \dots (4)$$

$$CL = \overline{MR} \quad \dots (5)$$

$$LCL = 0 \quad \dots (6)$$

$$\bar{x} = \frac{x_1 + x_2 + \dots + x_m}{m} \quad \dots (7)$$

$$MR = |x_i - x_{i-1}| \quad \dots (8)$$

$$\overline{MR} = \frac{MR_1 + MR_2 + \dots + MR_m}{m} \quad \dots (9)$$

Where, x_i is the measured quality characteristic obtained from the drilling tests.

Process control is defined as the ability of the process to keep a state of good statistical control. Prior to process capability evaluation, the obtained experimental data have some quality characteristics such as statistically within control, normally distributed and data independent. Process capability is also defined as the measure of degree that a process achieves specifications. The main purpose of the process capability is to find the variations spread and find the impact of the quality characteristic on both the average and spread. Obtained results are further utilized for new inspection planning, evaluation techniques, and design applications. The following three steps are carryout to find out the process capability of attributes criterion²³. In this work, hole size at entry (D) and exit (d), delamination factor at entry (F_{dent}) and exit (F_{dext}), taper angle (\emptyset) and aspect ratio (AR_{MD}) are the attribute in MD whereas kerf width at entry (K_{went}) and exit (K_{wext}), heat affected zone entry (HAZ_{ent}) and exit (HAZ_{ext}), kerf angle (K_a) and aspect ratio (AR_{LD}) are the attributes in LD.

Step 1: Calculation of mean (X): calculation of mean is ascertained for every trial run by using following equation.

$$X = \sum_{i=1}^N \frac{x_i}{N} \quad \dots (10)$$

Here, x_i = response parameter value for i^{th} replicate trial, N = number of replicates.

Step 2: Computation of standard deviation (α): Following equation was used to compute Standard deviation (α).

$$\alpha = \sqrt{\frac{\sum_{i=1}^N (x_i - X)^2}{N}} \quad \dots (11)$$

Here,

x_i = Response parameter value for i^{th} replicates of a distinct trial, X = Mean of the N replicates for the trial.

Step 3: Process capability index (c_{pi}): following equation was used to calculate process capability index (c_{pi}) for each experimental run.

$$C_{pi} = \min \left\{ \frac{X - LSL}{3\alpha}, \frac{USL - X}{3\alpha} \right\} \quad \dots (12)$$

Here, USL= Upper Specification Limit for individual attributes, LSL = Lower Specification Limit for individual attributes. USL and LSL actually are a destination value. Specification limits are typically provided from outside which depends on production

necessities, market pre-requisites. It can be either one-sided or two-sided.

4 Running Experiment

A CFRP composite with 55 percent of carbon fibers reinforcement in a total of 12 layers and having 3 mm thickness along a fiber orientation of $0/90^\circ$ with epoxy matrix is chosen and it is shown in Fig. 1. This composite was fabricated by autoclave method and was supplied by M/s GALARK Industry. The chemical composition of CFRP plate has been tested by EDX analysis and composition is as follows: 84.12% C, 14.92% O, 0.20% Na, 0.20% Si, 0.28% Cl, 0.10% K and 0.21% Ca. Hardness of CFRP is most commonly measured by the shore-D (Durometer) test. The Shore-D hardness number is in range 64 to 88. Tensile strength of CFRP is 1200 MPa and elastic modulus of CFRP is 145000 MPa⁶. The composite was laminated rectangular sheet of dimension $120 \times 60 \times 3 \text{ mm}^3$. The MD tests were carried out using computer numerical controlled vertical machining center under dry condition as per design (Make: HARDINGE, Model: VMC 800II machine) and specifications are shown in Table 3.

Prior to drilling, a micro-tool holder, ER32 collect with drill was held in main spindle drive of VMC setup shown in Fig. 2. In order to conduct experiments, the laminate was fastened to the rigid fixture which was mounted on the worktable. Equal spacing was maintained between successive drilled holes in the plate. The standard solid carbide twist drills of 0.5 mm diameter with constant point angle 130 degrees, helix angle 30 degrees and number of flutes 2 were used for the experimental work and overall photograph of the used drill bit with a magnified view of the drill tip region shown in Fig. 3. After drilling, the hole size at entry and exit,

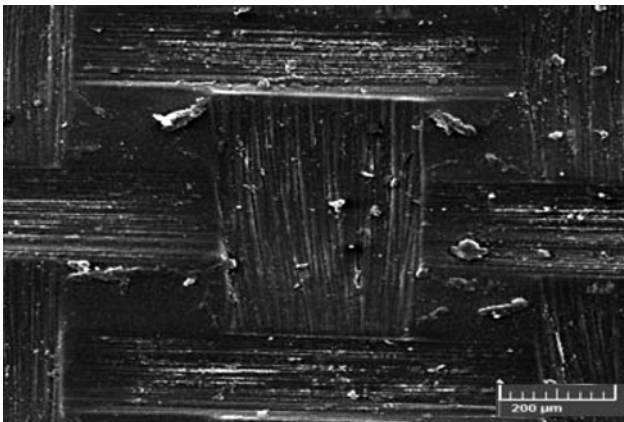


Fig. 1— Image of CFRP composite laminated plate.

delamination factor (F_d) at entry and exit, taper angle (θ) and aspect ratio (AR_{MD}) were measured using a non contact video measuring system (VMS) and it is shown in Fig. 4. The LD tests were carried out using computer numerical controlled 1640W CW CO₂ laser drilling machine (Make: Rofinsinar, Model: OEM 65 iX). The specification is shown in Table 4. The CO₂ laser setup is shown in Fig. 5. Equal spacing was maintained between successive drilled holes in the plate. The spot diameter of 0.5 mm diameters were used for the experimental work. The heat affected

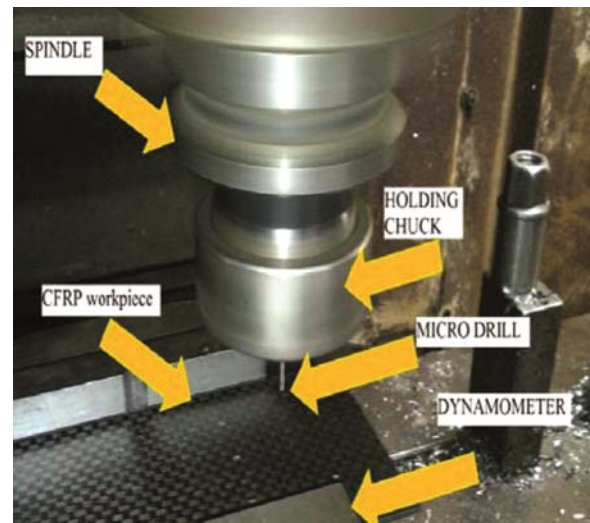


Fig. 2 — Photograph of VMC.

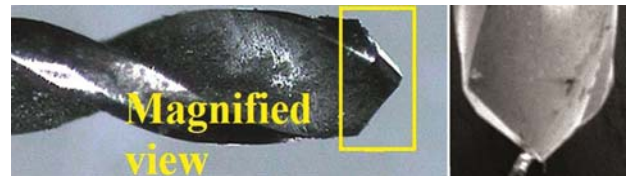


Fig. 3 — Solid carbide drill with 0.5 mm diameter.



Fig. 4 — Setup of video measurement system.

Table 3 — Specifications of the VMC.

Type of machine	Vertical machine center
Brand	HARDING
Model	VMC-800 II
Control	Fanuc series 18-M
Maximum Speed	12000 rpm
Travel length	500 x 800 x 500 mm
Table size	920 x 510 mm

Table 4 — Specifications of the CO₂ laser.

Parameters	Specification
Operating mode	CW
Wavelength	10.6 μm
Peak Laser output power	1640W
Pulse Width/Frequency	2-400μs/0-130KHz
Spot size at focus	0.5 mm
Beam quality M ²	1.7
Assist gas	argon
Stand-off	1.5 mm
Focus position	surface
Maximum power	650 W

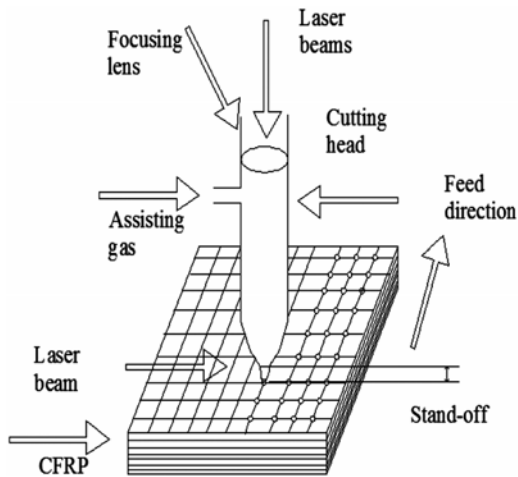


Fig. 5 — Schematic experimental setup of CO₂ laser.

zone (HAZ), Kerf width (K_w), kerf angle (K_a) and aspect ratio (AR_{LD}) were measured using a non contact video measuring system (VMS). Three trials were taken for each set of parameters and the average values of responses were taken for further analysis.

5 Mechanical Drilling and Laser Drilling Calculation

The delamination factor (F_d) was calculated using the formula given below

$$F_d = D_{max}/D \quad \dots (13)$$

where, D_{max} is maximum damaged diameter and D is drill diameter.

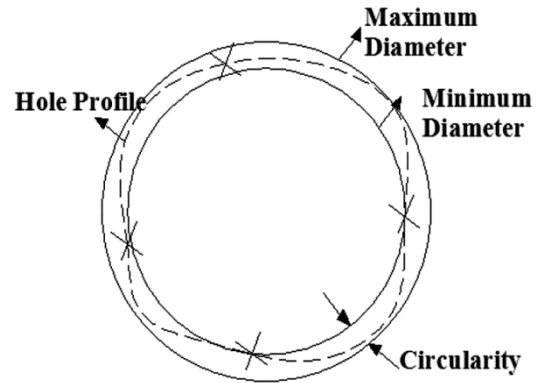


Fig. 6 — Schematic representation of circularity error.

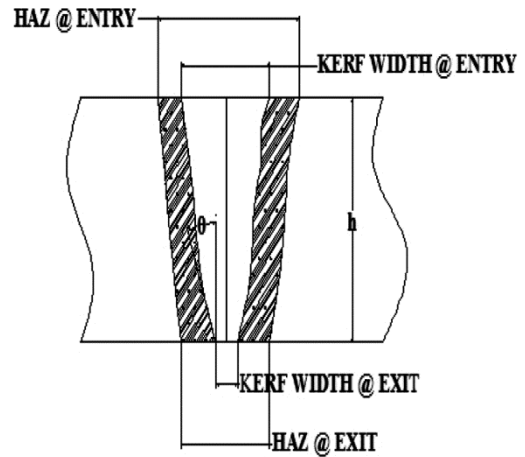


Fig. 7 — Geometry of the laser cut.

The circularity error (C) was also calculated using the formula given below and schematic representation was shown in Fig. 6 and geometry of laser cut is shown in Fig. 7.

$$C = (D_{max} - D_{min})/2 \quad \dots (14)$$

The taper angle (θ) was calculated using the formula given below

$$\theta = \tan^{-1}(D - d)/2t \quad \dots (15)$$

Where, D is mean entrance diameter, d is mean exit diameter and t is thickness of sample.

6 Results and Discussion

Composite materials applied in aerospace and structural applications were machined at Shri Angalamman industry, Thuvagudi in MD and Nano marker, Srirangam in LD. The aim was to find the best process among the two in one through microscopic analysis. Sixteen experiments were performed out using CFRP. Tests were conducted as

per the design of experiment using MINITAB version 17. After performing MD and LD test, the computer aided video measurement system was used to take the photo shot of machined hole. From the MD photo shot Fig. 8 and Fig. 9, the hole size at entry, hole size at exit, maximum damaged surface diameter were measured whereas from the LD photo shot Fig. 10 and Fig. 11, the heat affected zone at entry and the heat affected zone at exit and kerf width were measured. The MD and LD experimental values are shown in Table 5 and Table 6, respectively.

The guideline procedures are followed to evaluate the process capability.

1. Checking the type of data is given for process capability analysis (*e.g.* continuous data or attribute data).
2. Checking the normality of process by normal probability plot.
3. Selecting the control chart depends on data type and examine whether the process in control or out

of control (*e.g.* I-MR chart, X bar-R chart, X bar- S chart, P chart, U chart).

4. Calculating the process capability.

To effectively estimate the process capability and to consistently predict the process capability in the future, the quality characteristics must have the properties such as stable, normal.

6.1 Normality analysis

The statistical assumption of the null hypothesis following as the data distribution law was normal and alternative hypothesis: the data distribution law was non-normal. The normality test for hole size at entry and exit, delamination factor at entry and exit, taper angle and aspect ratio in MD while kerf width at entry and exit, heat affected zone entry and exit, kerf angle and aspect ratio in LD were with 95% confidence interval. The experimental data are presented in Fig. 12 and it closely presents the straight line. In all the cases of probability plot, an obtained value from Anderson-Darling test value and p-value were



Fig. 8 — Machined hole at the entry side in MD.

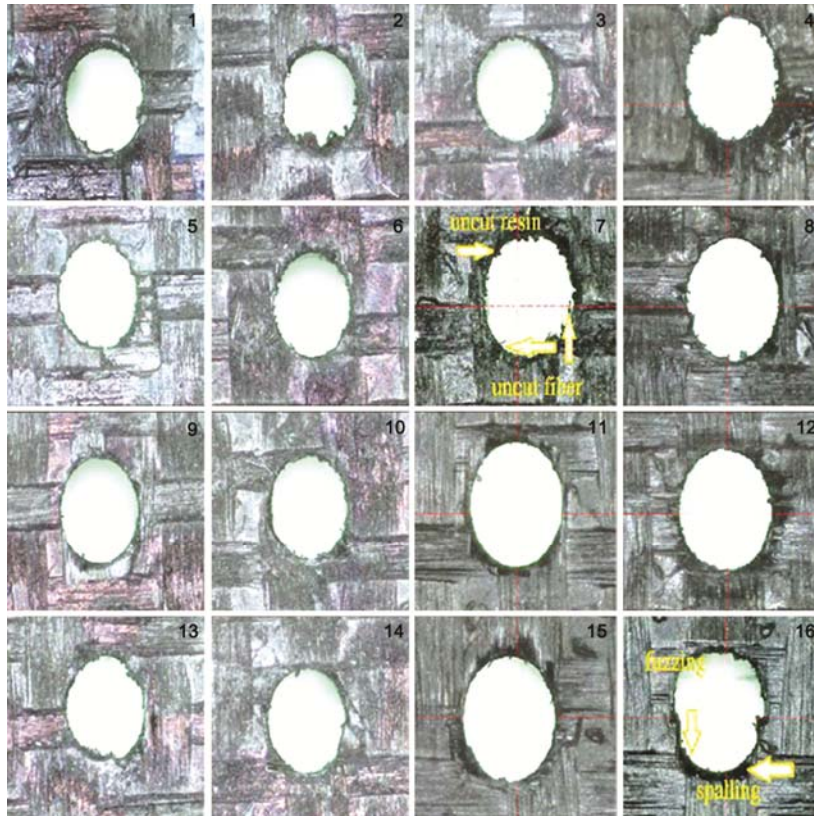


Fig. 9 — Machined hole at the exit side in MD.

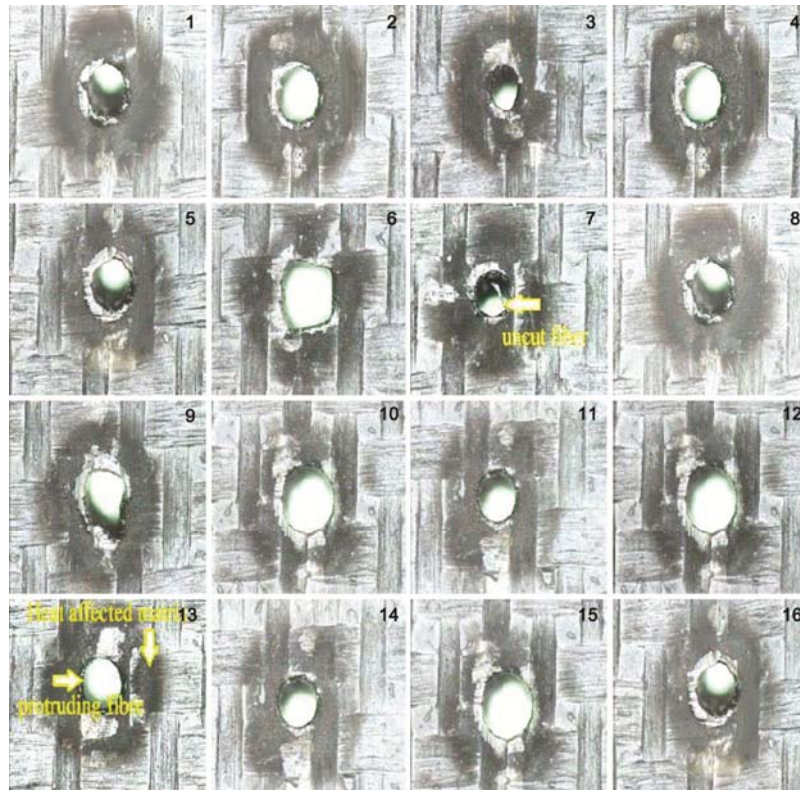


Fig. 10— Machined hole at the entry side in LD.



Fig. 11 — Machined hole at the exit side in LD.

Table 5 — Experimental data in MD

Exp. No.	OA/Process parameters		MD responses					
	Spindle speed (rpm)	Feed rate (mm/rev)	D (mm)	D (mm)	F _{dent}	F _{dext}	Ø (Degrees)	AR _{MD}
1	1000	0.01	0.541	0.549	1.115	1.122	0.081	5.507
2	1000	0.03	0.520	0.531	1.112	1.118	0.106	5.709
3	1000	0.06	0.518	0.526	1.122	1.135	0.072	5.749
4	1000	0.09	0.517	0.523	1.128	1.142	0.063	5.772
5	1500	0.01	0.538	0.544	1.091	1.101	0.057	5.550
6	1500	0.03	0.528	0.532	1.126	1.125	0.043	5.663
7	1500	0.06	0.518	0.526	1.119	1.124	0.076	5.747
8	1500	0.09	0.519	0.527	1.138	1.149	0.076	5.742
9	2000	0.01	0.534	0.539	1.101	1.109	0.048	5.597
10	2000	0.03	0.528	0.536	1.124	1.133	0.076	5.644
11	2000	0.06	0.521	0.527	1.135	1.134	0.057	5.731
12	2000	0.09	0.521	0.526	1.138	1.149	0.048	5.736
13	2500	0.01	0.534	0.541	1.115	1.126	0.067	5.587
14	2500	0.03	0.530	0.539	1.141	1.137	0.086	5.618
15	2500	0.06	0.527	0.530	1.142	1.140	0.029	5.682
16	2500	0.09	0.525	0.527	1.141	1.152	0.019	5.709
MIN			0.517	0.523	1.091	1.101	0.019	5.507
MAX			0.541	0.549	1.142	1.152	0.106	5.772

Table 6 — Experimental data in LD.

Exp. No.	OA/Process parameters			LD responses					
	Power (W)	Cutting velocity (mm/min)	Pressure (kpa)	K _{went} (mm)	K _{wext} (mm)	HAZ _{ent} (mm)	HAZ _{ext} (mm)	K _a (Degrees)	AR _{LD}
1	15	20	200	0.558	0.352	1.251	0.497	1.967	6.593
2	15	40	300	0.471	0.274	1.190	0.439	1.881	8.054
3	15	60	400	0.415	0.219	1.151	0.402	1.872	9.464
4	15	80	500	0.385	0.205	1.071	0.363	1.719	10.169
5	30	20	300	0.582	0.407	1.259	0.504	1.671	6.067
6	30	40	200	0.483	0.306	1.213	0.455	1.690	7.605
7	30	60	500	0.432	0.258	1.152	0.411	1.662	8.696
8	30	80	400	0.383	0.218	1.118	0.372	1.576	9.983
9	45	20	400	0.586	0.447	1.282	0.512	1.327	5.808
10	45	40	500	0.492	0.349	1.216	0.438	1.366	7.134
11	45	60	200	0.471	0.312	1.191	0.412	1.518	7.663
12	45	80	300	0.402	0.253	1.142	0.379	1.423	9.160
13	60	20	500	0.663	0.521	1.333	0.526	1.356	5.068
14	60	40	400	0.589	0.461	1.261	0.452	1.222	5.714
15	60	60	300	0.523	0.407	1.239	0.435	1.108	6.452
16	60	80	200	0.482	0.372	1.181	0.411	1.050	7.026
MIN				0.383	0.205	1.071	0.363	1.050	5.068
MAX				0.663	0.521	1.333	0.526	1.967	10.169

less than one and greater than 0.05 respectively. Therefore, the measured continuous data distributed were normal.

6.2 Control chart analysis

I-MR charts were employed to calculate the upper control limit and lower control limit. The control limits were utilized to control and monitor the process capability of the quality characteristics. The top portion of the graph was represented as an Individual (I) chart that plots the response values of each individual observation data and provides a means to assess the process center. The bottom portion of the graph represented as Moving Range (MR) chart that plots machining process variation as calculated from the ranges of two or more successive observations. The green line on each chart was indicating the mean and the red line was indicating the upper and lower control limits. Process capability was a group of calculations used to assess whether process performances characteristics statistically capable to meet the design specifications. In order to achieve and assess the quality characteristics of process and/or machines specification and within control limit except for LD kerf angle as shown in Fig. 13. In the MR chart of LD kerf angle, the machining response variations were in control. Therefore MR chart was in control. I chart having the process variation which

was out of control. The reasons for this out of control were due to the variation of standard deviations and center line. Minitab was regenerated up to an eight special-cause machining response variation tests for I chart and indicates problem observations with a red symbol and number of failed test.

Test Results for I Chart of LD Kerf angle discussed below:

TEST 1 reported that one point more than 3.00 standard deviations from the center line. Therefore the experimental test number failed at points: 1, 2, 3, 14, 15, and 16.

TEST 2 reported that 7 points in a row on the same side of center line. Therefore the experimental test number failed at points: 7, 8, 15, and 16.

TEST 5 reported that 2 out of 3 points more than 2 standard deviations from the center line (on one side of CL). Therefore the experimental test number failed at points: 2, 3, 4, 6, 10, 14, 15, and 16.

TEST 6 reported that 4 out of 5 points more than 1 standard deviation from the center line (on one side of CL). Therefore the experimental test number failed at points: 4, 5, 6, 7, 13, 14, 15, and 16.

This was the LD strongest evidence test report that responses were out of control. Therefore, the drilling process was found to be stable based on the I-MR (Individual-Moving range) chart. Mechanical drilling

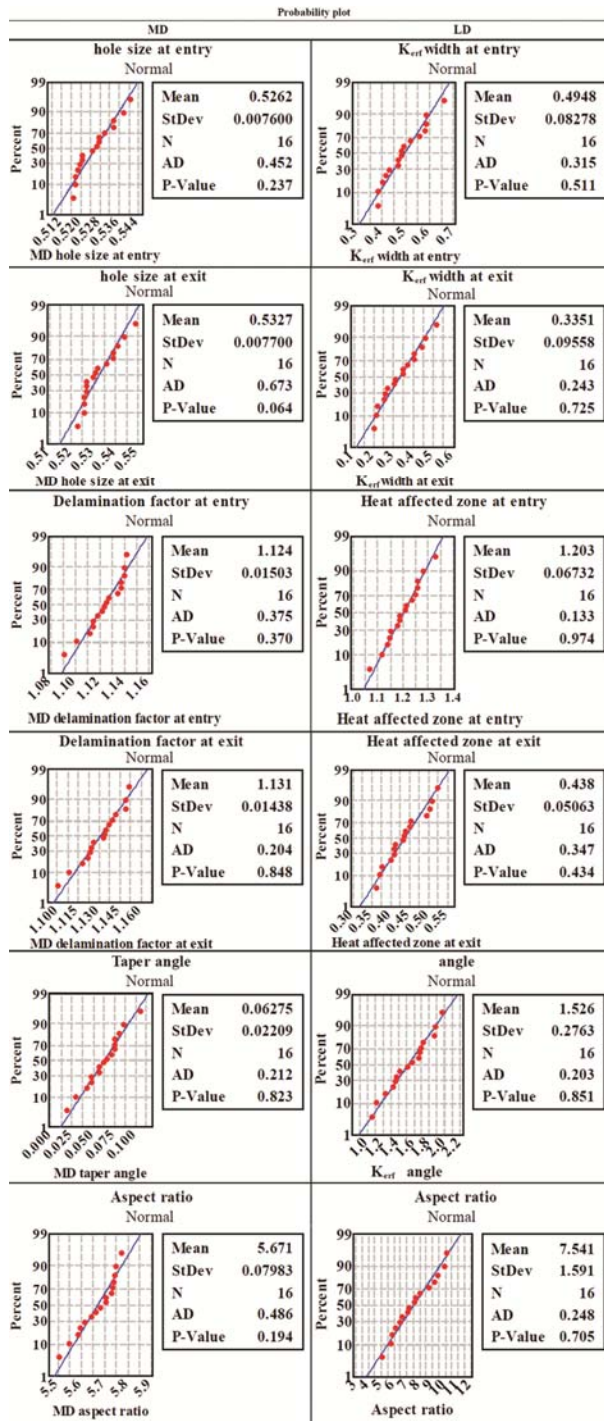


Fig. 12 — Normality graphs of MD and LD.

test showed the best within the I-MR control chart as clearly shown in Fig. 13.

6.3 Process capability analysis – Case I

After confirming that the machining process was in statistically control, it was necessary to find either the process was capable or not and can be meet the design

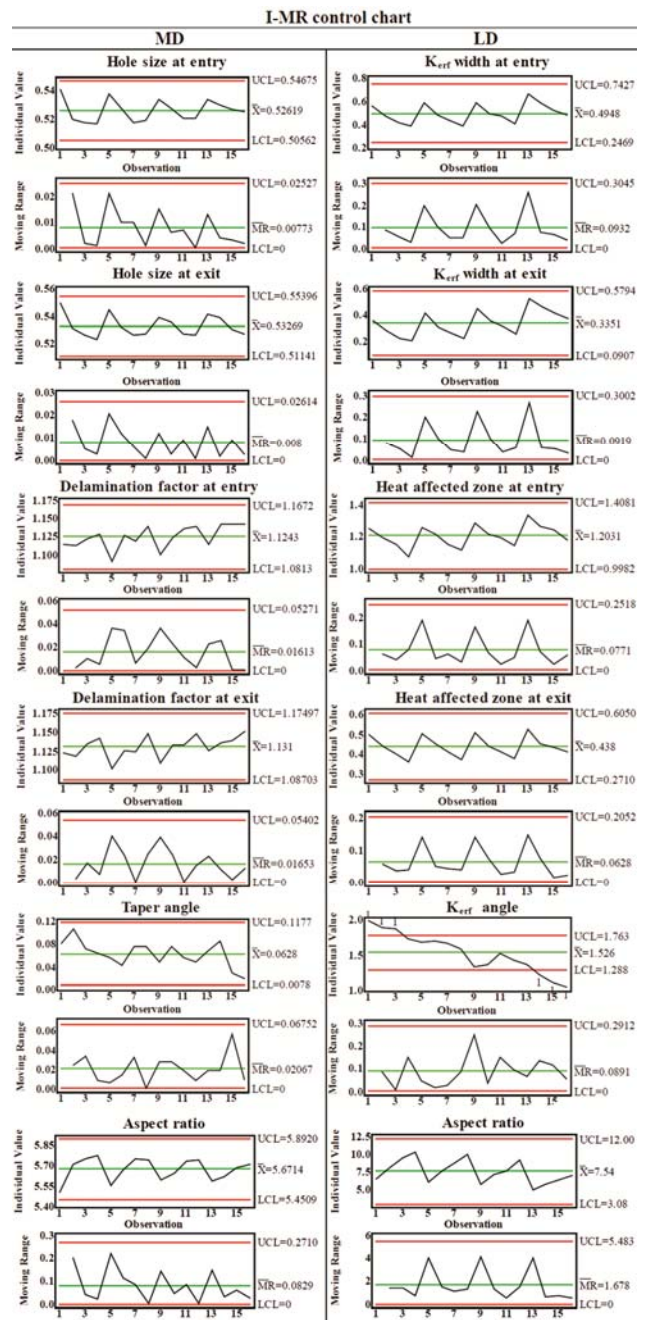


Fig. 13 — I-MR control charts of MD and LD.

specifications and generate “good” hole in MD and LD. Then, the process capability was found by comparing the response data spread in process variation with the width of specification limits. In case, the process responses were not in control, it led to an incorrect estimation of process capability. In Minitab, the process capability can be evaluated by graphically. These graphs were used to evaluate the distribution of the response data and verify either the

process was in control or not. Capabilities indices were used to find the way to assess process capability and process information was reduced to a single number and comparing the process capability of one process to others. Minitab has capability analysis in many distribution forms such as weibull, normal, exponential, poisson, gamma, and binomial. Normal distribution was taken for this analysis and subgroup size one was taken for this analysis. The upper specification limits (USL), lower specification limits (LSL), target value and calculated C_p and C_{pk} for each quality characteristics are given in Table 7. The target value itself was taken as LSL except for aspect ratio. The maximum experimental values of quality characteristic were taken as upper specification limits. Based on the constrained limit of an upper specification and lower specification the process capability of MD and LD were calculated as shown in Fig. 14 and the best was identified. The C_p value of hole size at entry and exit, delamination at entry and exit, taper angle and aspect ratio in MD were one or greater than one. It represented the MD process was capable of achieving the target set for all the above-said quality characteristics. The C_{pk} value for hole size at entry, aspect ratio in MD were greater than one and that for other qualities characteristics studied were less than one. But comparatively better than that in LD. Whereas C_p value and C_{pk} value for all quality characteristics in LD were found to be less than one except for kerf angle. Therefore, it was concluded that the MD process was comparatively better than the LD process for micro-drilling of CFRP.

6.4 Process capability analysis – Case II

In addition process capability studies, Interval plots were drawn based on mean line value of each

response and individual standard deviation of each response as shown in Fig. 15. Hole size obtained in MD || kerf width obtained in LD, delamination factor obtained in MD || HAZ obtained in LD, taper angle obtained in MD || kerf angle obtained in LD, aspect ratio obtained in MD || aspect ratio obtained in LD are assumed to be studied quality characteristics. When were compared the MD & LD based on similar characteristics. The hole size obtained both at entry and exit in MD was found to be nearer to 0.5 mm which means the size of the drill. The SD of this was very less. The kerf width obtained at the entry in LD was found to be nearer to 0.5 mm with high SD whereas the same at the exit was deviating more with high SD. Hence, it was concluded that the MD was superior to the LD for micro-drilling CFRP composites. The delamination factor obtained both at entry and exit in MD was found to be nearer to 1 which means the damage diameter was less. The SD of this was very less.

The HAZ obtained at the entry in LD was found to be nearer to 1 with less SD whereas the same at the exit was deviating more with less SD. Hence, it was concluded that the MD was superior to the LD for micro-drilling CFRP composites. The taper angle obtained in MD was found to be nearer to zero which means the taper angle of holes were minimal. The SD of this was very less. The kerf angle obtained in LD was found to be higher (i.e. 1.5) with high SD. Hence, it was concluded that the MD was superior to the LD for micro-drilling CFRP composites. The aspect ratio obtained in MD was found to be nearer to 5 which means that the deviations of in diameter for the given length of hole. The SD of this was very less. The aspect ratio obtained in LD was found to be higher

Table 7— Specifications limits of process capability.

Quality characteristics	USL (mm)	LSL (mm)	Target value (mm)	C_p	C_{pk}
MD					
Hole size @ entry (mm)	0.555	0.500	0.500	1.34	1.27
Hole size @ exit (mm)	0.555	0.500	0.500	1.29	1.05
Delamination @ entry	1.152	1.000	1.000	1.77	0.65
Delamination @ exit	1.152	1.000	1.000	1.73	0.48
Taper angle (Degrees)	0.11°	0°	0°	1.00	0.86
Aspect ratio in MD	6	5	6	2.27	1.49
LD					
Kerf width @ entry (mm)	0.555	0.500	0.500	0.11	-0.02
Kerf width @ exit (mm)	0.555	0.500	0.500	0.11	-0.68
Heat affected zone @ entry (mm)	1.340	1.000	1.000	0.83	0.67
Heat affected zone @ exit (mm)	1.340	1.000	1.000	1.02	-3.36
Kerf angle (Degrees)	2°	0°	0°	4.22	2.00
Aspect ratio in LD	11	5	11	0.67	0.57

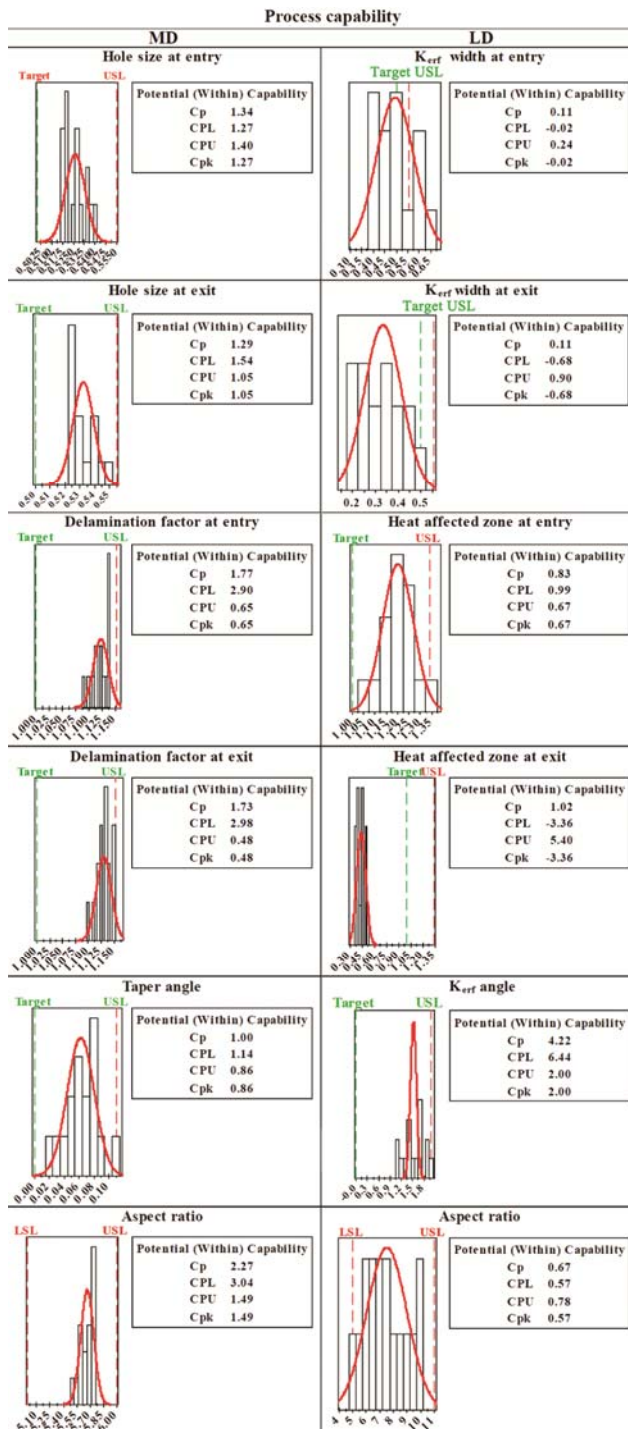


Fig. 14 — Process capabilities for both MD and LD.

(i.e. 7.5) with high SD. Hence, it was concluded that the MD was superior to the LD for micro-drilling CFRP composites. The reason for higher SD may be due to the effects of laser process parameter on quality characteristics and may be an improper selection of process parameter.

6.5 The technical reason for rejection of laser drilling

In laser drilling, high process temperature results were in significant damage to the composite material. The damages were characterized by micro-structural changes such as matrix melting and fiber swelling around the hole area and elliptical hole formation. This was due to the preferential heat conduction along the fiber direction. It was also observed that the carbon fiber-reinforced composite material was losses both tensile and compressive strength in laser drilling. This was also due to the damage around the hole. There were various factors that have to be taken into account when was lasers used as drilling tools, the main considerations were including the absorption of the energy and how this were varies with the temperature of the material, the thermal diffusivity of the material (as this controls how rapidly the heat is conducted away from the cutting zone) and thirdly the reaction temperature (of melting/vaporization/decomposition). There were other considerations such as the dimensions of the heat-affected zone, which was the zone where the capability of stress transfer from the matrix to the fibers was reduced or absent. Further concerns include the formation of burrs and dross, thermal expansion of the material and consideration of the tolerances were required, reaction products, the assist gas and finally safety. All of these elements must be considered.

Another problem with the laser drilling of composites has occurred because the constituents of the material were completely different. Because of the properties of various fibers and resins, there was a vast range of temperatures at which the materials melt (or soften or decompose). The laser beam has a certain power and thus has a defined heat input into the material. However, because of the different properties of the fiber and matrix, the two components can react very differently to the thermal input. In general, the energy was needed for the vaporization of the fibers was higher than that required for the matrix, the instance where this was most noticeable being when cutting carbon fiber composites. Carbon fibers were good conductors of heat and so a large amount of the thermal energy introduced in laser cutting was conducted away. The disassociation temperature of carbon was also very high. These factors combine to make the cutting of carbon fiber reinforced composites very difficult. When a laser was employed to cut these composites, a large volume of resin was vaporized in the process also, since so much heat was required to vaporize the fibers and overcome the

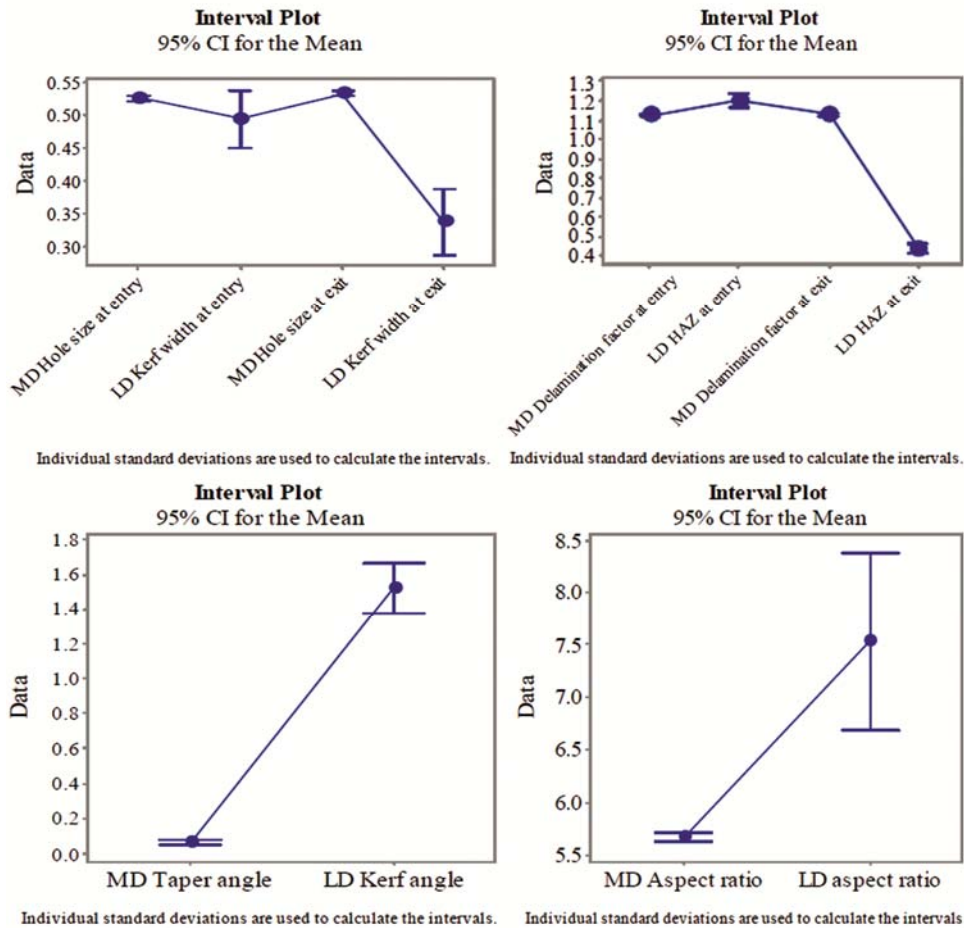


Fig. 15 — Interval plot for MD and LD.

thermal diffusion effects: this can cause delamination of the composite. This was also the reason for rejection of LD of CFRP.

6.6 Structural damages

The local structures around the holes drilled by MD process such as delamination factor, burrs, sub surface damages, cracks propagation, matrix debonding, adhesive fracture, cohesive fracture, fiber pulled out/in, rough and serrated failure surface, matrix cracking, spalling, fuzzing and concave surfaces, will reduce the quality of the component due to the increased stress concentration and will lead to service failure. The local structures around the holes drilled by LD process such as heat affected zone, kerf width, kerf angle, matrix recession, fiber burnout, sideways burning at the bottom edge of the workpiece delamination also reduce the quality of the component and lead to service failure because of increased stress concentration. These local structures around the holes of CFRP mostly influence the stress intensity factor of the hole.

7 Conclusions

The process capability of MD and LD were successfully evaluated while micro-drilling CFRP composites. In order to evaluate the best hole making process normality test, control chart, evaluation of process capability and interval plot were used. From the above analysis, the following conclusion was drawn

- (i) The micro-holes with diameter 0.5 mm were precisely drilled using MD process.
- (ii) The quality characteristics of MD and LD were normal and are in control. The kerf angle obtained in LD was exceptional.
- (iii) The SD values are high in the LD process and therefore it can be concluded to be an inferior process.
- (iv) Based on the selection of machining condition, specifications limit and target values the MD is found to be the best process for processing CFRP composites.

- (v) The C_p and C_{pk} value is very useful to identify the process capability of the different machine.
- (vi) This experimental result is only applicable for CFRP with the following material specification: 3 mm thickness, 55% carbon fiber, 45% epoxy resin, 12 layers, and 0°/90° fiber orientation. However if the sample specification is slightly varied. These results can be used. If the variation in sample specification is large, the user can develop their own model taking this work an example.

References

- 1 Samuel Raj D & Karunamoorthy L, *Mater Manuf Processes*, 5 (2016) 587.
- 2 Wang X, Kwon, P Y, Sturtevan C, (Dae-Wook) Kim D & Lantrip J, *J Manuf Process*, 1 (2013) 127.
- 3 Huang H M, Du S & Wu L Z, *Acta Mat Compos Sin*, 3 (2001) 76.
- 4 Davim J P & Reis P, *Compos Struct*, 59 (2003) 481.
- 5 Houjiang Z, Wuyi C & Dingchang C, *Chin J Mech Eng*, 7 (2004) 150.
- 6 Krishnamoorthy A, *Some Studies on Modeling and Optimization in Drilling Carbon Fiber Reinforced Plastic Composites*, Ph.D. Thesis, Anna University, Chennai, 2011.
- 7 Sahoo S, Thakur A & Gangopadhyay S, *Mater Manuf Processes*, 14 (2016) 1927.
- 8 Hinds B K & Treanor M, *PI Mech Eng B-J Eng*, 1 (2000) 35.
- 9 Karpat Y, Deger B & Bahtiyar O J, *Mater Process Technol*, 10 (2012) 2117.
- 10 An Q, Cai X, Xu J & Chen M, *Int J Abras Technol*, 3 (2014) 183.
- 11 Isbilir O & Ghassemieh E, *Compos Struct*, 105 (2013) 126.
- 12 Anand RS, Patra K & Steiner M, *Prod Engineer*, 3 (2014) 301.
- 13 Akshay, Dilpreet S, Sagar K, Dinesh K & Suhasini G, *Compos Part A*, 82 (2016) 42.
- 14 Xu J, An Q, Cai X & Chen M, *Int J Pr Eng Man*, 14 (2013) 1687.
- 15 Xu J, An Q & Chen M, *Proc Inst Mech Eng B J Eng Manuf*, 231 (2017) 1931.
- 16 Xu J, Li C, Mi S, An Q & Chen M, *Compos Struct*, 201 (2018) 1076.
- 17 Adel S, Yinzhou Y, Lin L, Paul M, David W & Ahmad S, *Mater Des*, 5 (2016) 461.
- 18 Nagesh S, Narasimha Murthy, H N, Ratna Pal, Krishna M & Satyanarayana B S, *Opt Laser Technol*, 69 (2015) 23.
- 19 Dirk H, Matthias S, Max O, Marten C, Markus R & Claus E, *Mater Des*, 92 (2015) 742.
- 20 Di Ilio A, Tagliaferri V & Veniali F, *Mater Manuf Processes*, 4 (1990) 591.
- 21 Davim J P, Barricas N, Conceicao M & Oliveira C, *J Mater Process Technol*, 198 (2008) 99.
- 22 Goeke A & Emmelmann C, *Physcs Proc*, 5 (2010) 253.
- 23 Abhijit S & Himadri M, *J King Saud Univ Eng Sci*, 30 (2016) 377.



Investigation on Drilling Behavior of CFRP Composites Using Optimization Technique

D. Raj Kumar¹ · N. Jeyaprakash² · Che-Hua Yang^{2,3} · K. R. Ramkumar⁴

Received: 29 August 2019 / Accepted: 17 May 2020
© King Fahd University of Petroleum & Minerals 2020

Abstract

Carbon fiber-reinforced polymers (CFRPs) have been applied to various fields such as electronic printed circuit boards, aircraft brakes, automobile forks, and machine tool-damped structures due to their low density and high tensile strength. These application components required micro-hole and macro-hole in it for joining. In this research work, a comparison of the experimental investigation on micro- and macro-drill on CFRP using a vertical machining center has been carried out. The input machining control factors were spindle speed and rate of feed, whereas the quality characteristics of drilling CFRP were considered as thrust force, delamination, and overcut. Analysis of variance (ANOVA) and gray relational analysis were employed to identify the most significant factor and optimum process parameters, respectively. Microstructural defects of micro-hole and macro-hole were studied using scanning electron microscopy. Results showed that the rate of feed linearly affected the thrust force and delamination and is inversely proportional to overcut.

Keywords CFRP · Micro- and macro-drill · Thrust force · Delamination · Overcut · Optimization

1 Introduction

Compared to the various fiber-reinforced composites, the adaptability of carbon fiber-reinforced polymer (CFRP) in various fields like electronic industries fabricating the printed circuit boards, aircraft brakes, automobile forks, and machine tools-damped structure is increased because

of its properties such as low density and high tensile strength [1]. The CFRP material is applied for various parts such as PCBs, satellite antenna, wheelchairs, computer body panels, and these components need micro- and macro-drill in it. Therefore, micro-drilling and macro-drilling on CFRP material have been attempted in this work. The micro-hole and macro-hole making process on CFRP can be performed by employing mechanical drilling, laser drilling, and abrasive water jet machining. In mechanical drilling, the CFRPs have various defects on machined surface such as fiber pullout, delamination, fuzzing, spalling, and fiber breakout due to the nature of material properties, improper selection of drilling condition, tool geometry, and tool materials [2]. Similarly, problems in laser drilling are thermal damage (both fiber and matrix), taper angle, and heat-affected zone in the cut surface because of thermal effects on the selection of process conditions. The problems in abrasive water jet machining are jet-lag, kerf taper angle, and surface roughness because of lack of information in an inadequate selection of condition and carbon fiber absorbs water [3]. The measurement of micron-level features is also a difficult task because of the inadequate development of micrometeorology. The X-ray, ultrasonic C-scan, optical microscope, and digital photograph are commonly used to find the delamination. The delamination is a major problem in CFRP composite,

✉ N. Jeyaprakash
prakash84gct@gmail.com; prakash@ntut.edu.tw

D. Raj Kumar
profdraj कुमार@gmail.com

Che-Hua Yang
chyang@ntut.edu.tw

K. R. Ramkumar
get2raam@gmail.com

¹ Department of Mechanical Engineering, MAM School of Engineering, Tiruchirappalli, India

² Additive Manufacturing Center for Mass Customization Production, National Taipei University of Technology, Taipei 10608, Taiwan, ROC

³ Institute of Manufacturing Technology, National Taipei University of Technology, Taipei 10608, Taiwan, ROC

⁴ Department of Metallurgical and Materials Engineering, Indian Institute of Technology Madras, Chennai, India



and its rejection rate is 60%. Hence, the selection of proper process parameters is necessary for the drilling process. It was revealed that adequate information on the machine tool is required for the processing of the CFRP composites [4]. In conventional CFRP machining, the higher hole surface quality was obtained by increasing spindle speed and decreasing the rate of feed. Also, it was found that the minimum delamination factor was obtained by reducing the cutting force and feed rate [5]. The delamination was achieved in the range of 12.8–25.7% on the CFRP micro-hole by adopting the rotary ultrasonic helical machining [6]. In another way, by changing the tool geometry, tool types, providing backup plate and high-speed drilling, the delamination of CFRP was reduced [7]. Also, the laminate orientation and workpiece constituents of CFRP were also related to delamination on CFRP [8]. The cryo-treated WC drill produced better delamination than untreated drill [9]. Besides, the chilled air environment produced a better delamination factor compared to dry air [10]. The circular drilling strategy decreased the delamination factor compared to grinding [11]. The performance of high-speed steel, tipped carbide, and solid carbide drill on CFRP was evaluated based on the thrust force and torque. The result found that the solid carbide drill produced better performance over other drills [12]. Therefore, various strategies were followed by many researchers to improve the hole quality. The selection of cutting conditions for the machining of CFRP was important to work smoothly without defects. Because of the processing of CFRP composite, drilling variables such as drill velocity and drill feed were greatly influencing delamination, thrust force, and an overcut. It was revealed that the minimum delamination was achieved by increasing the spindle speed and lowering the rate of feed. The quality of the drilled hole in CFRP composite was better by using the spindle speed ranges from 800 to 3000 rpm and feed rate ranges from 100 to 1000 mm/min [13]. The drilling of CFRP laminates using twist drills found that enlargement of drill diameter increased the thrust force. Drilling trials were performed on CFRP laminates using different twist drills. It was found that the diameter of the drill contributes to the improvement in overall machining performance and recognized as the most predominantly influencing factor which affects the delamination and thrust force. Drilling experiment was performed on CFRP/Al stacks using carbide drills in various drill sizes. It was observed that there was an increase in thrust force during drill with lesser diameter than larger diameter of drill bits [14]. Drilling on carbon fiber-reinforced polypropylene composite resulted that a feed rate mainly affected the thrust force and torque [15]. Investigations made on drilling characteristics of CFRP composite found that there was a remarkable increase in the thrust force as the diameter of drill increased. It was suggested that smaller diameter drills reduced the thrust force during drilling process.

From the above literature, it is clear that the influences of micro-drill parameters have studied metals and composites. However, there is no literature on the comparison of micro- and macro-drill process parameters on CFRP using Taguchi-based gray relational analysis. As drilling operation becomes more extensive in the industry, the research and development of these applications in the field of aerospace, electronic, and automobile have changed their attention to improving the drilling quality. The comparison of two various drill (micro and macro) has given a better understanding in terms of delamination, thrust force, and overcut. In the present study, experimental investigation has been proposed for analyzing the micro-hole and macro-hole quality on CFRP using vertical machining center (VMC). The relations between thrust force, delamination, and overcut for various drill diameters have been analyzed. Taguchi's experimental approach has been followed to minimize the experiment trails, and L_9 orthogonal array has been used to perform the experimental runs. Besides, ANOVA has been performed to find out the significance of process variables. Optimum levels were found using gray relational analysis (GRA), and roughness of machined hole has been analyzed.

2 Materials and Methods

The CFRP sample in the form of the plate by having the dimensions of $100 \times 60 \times 3$ mm was used in the present study. The CFRP sample which is considered for the present study has 55% of carbon fibers; epoxy matrix, 12 layers; 0° and 90° of fiber orientation. This composite was designed and fabricated using the autoclave method. The model picture of CFRP plate with dimensions, SEM images of CFRP plate [16], and schematic representation of CFRP plate with fiber orientation is shown in Fig. 1a–c. The HARDINGE VMC 800II was used for conducting the experiments. The considered input variables for this investigation are spindle speed and rate of feed. Two factors and three levels were used to run the experiments. The process conditions were selected based on the available literature and present trial test. The selected process variables and levels are shown in Table 1. The schematic diagram of the experimental setup is shown in Fig. 2. The micro- and macro-drill geometrical dimensions have been measured using an optical microscope as shown in Fig. 3, and the details are presented in Table 2. Table 3 exhibits the measurement of performance characteristics. Before the drilling process, drill collet with micro-drill bit has been fixed in main spindle drive and work material is fixed on digital strain gauge dynamometer. The machining experiments have been performed under dry conditions. During drilling, thrust force (F_y) for each trial has been measured using a digital strain

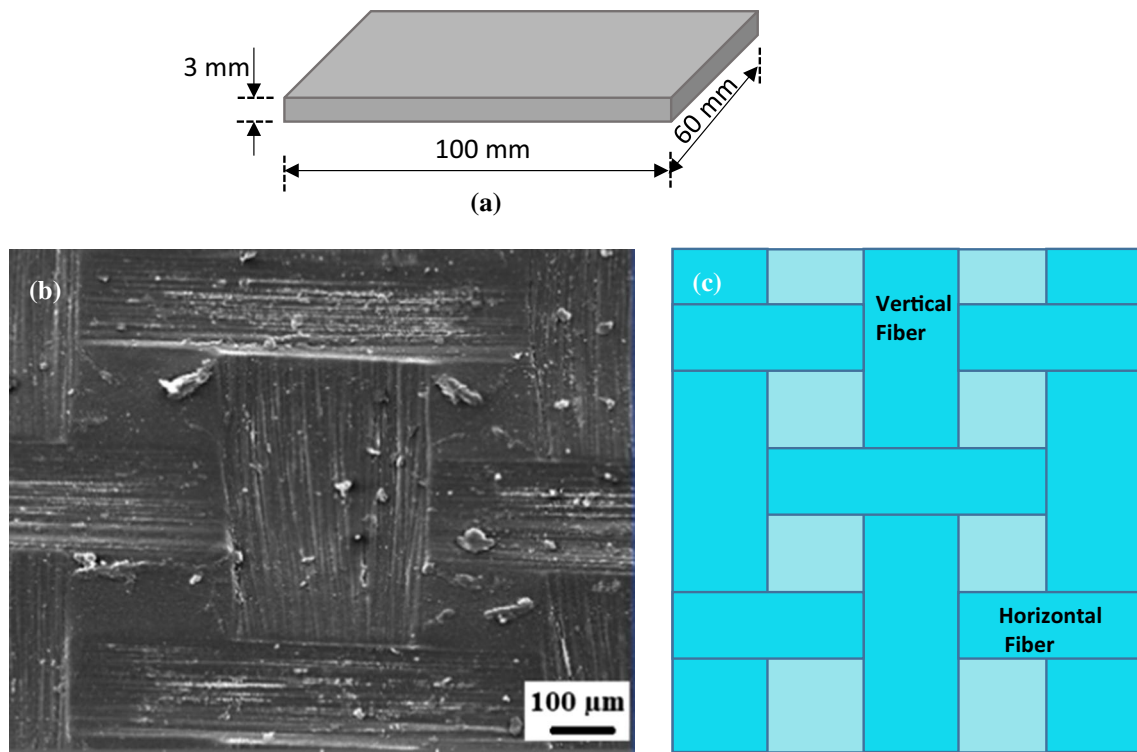


Fig. 1 Model picture of CFRP plate with dimensions (a), SEM images of CFRP plate (b) [16], schematic representation of CFRP plate with fiber orientation (c)

Table 1 Levels and parameters

Parameters	Levels		
	1	2	3
Spindle speed (<i>V</i>) (rpm)	2000	2500	3000
Rate of feed (<i>F</i>) (mm/rev)	0.01	0.03	0.05
Micro-drill diameter (mm)	0.3	0.4	0.5
Macro-drill diameter (mm)	1	2	3

gauge dynamometer. After drilling, hole quality evaluation has been processed on a non-contact video measuring system (VMS). The CFRP sample delamination (F_d) and an overcut (OC) were evaluated by applying Eqs. (1) and (2), respectively:

$$F_d = \frac{D_{max}}{D} \tag{1}$$

where D_{max} is the maximum damaged diameter (mm) and D is the drill diameter (mm).

$$OC = \frac{d_o - d_t}{2} \tag{2}$$

In this connection, d_o is the diameter of hole (mm) and d_t is the diameter of the tool (mm).

3 Results and Discussion

3.1 Thrust Force

The significance of spindle speed and rate of feed on thrust force for three different micro- and macro-drill diameters is illustrated in Fig. 4. In Fig. 4a, it was noticed that thrust force decreases with the increase in spindle speed for selected tool diameter. The reason for the decrease in the thrust force during the increase in the spindle speed was due to the temperature effects on resin and carbon fiber. Also, in Fig. 4b, it was noticed from the results that thrust force raises with the increase in the rate of feed for the selected tool diameter. The reason for increased thrust force based on the rate of feed was owing to an increase in cutting depth per revolution and thus the elevated shear area. The reason for increased thrust force was owing to more impact on cutting edge of drill, and the thrust force increases based on the selected tool diameter. That is, the thrust force increases when the drill diameter increases (F_y of \varnothing 0.5-mm drill $>$ F_y of \varnothing 0.4-mm drill $>$ F_y of \varnothing 0.3-mm drill for micro-drill and F_y of \varnothing 3-mm drill $>$ F_y of \varnothing 2-mm drill $>$ F_y of \varnothing 1-mm drill for macro-drill). Therefore, it was noticed that the increase in drill diameter results in increased thrust force for macro- and micro-drill. Moreover, the material removal rate was more at a higher rate of feed which results in increased

Fig. 2 Schematic representation of experimental setup utilized

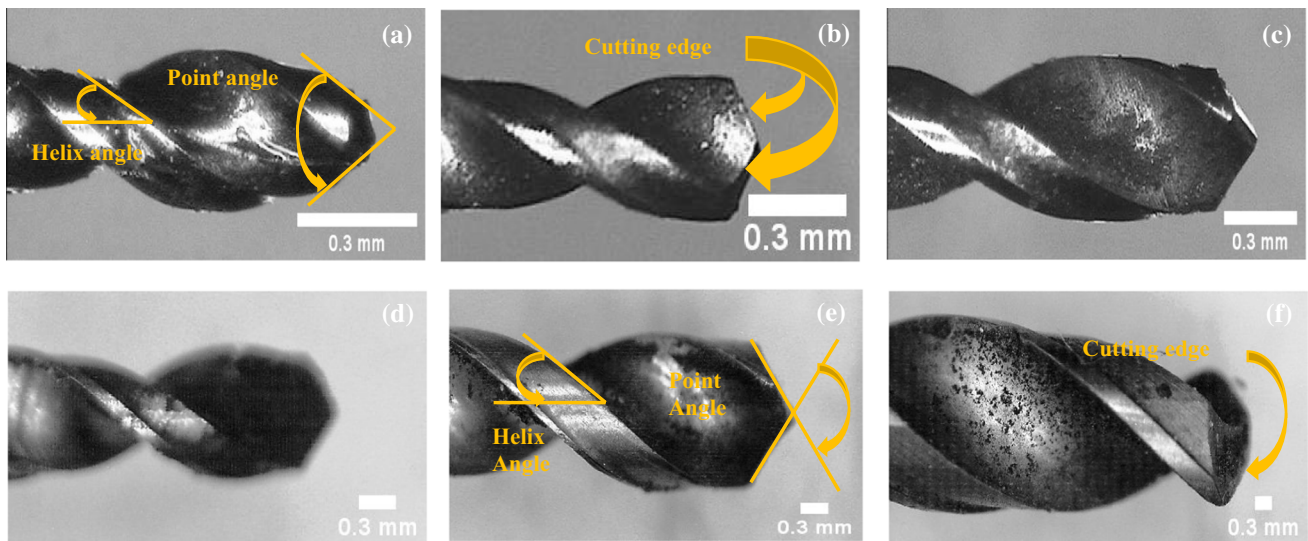
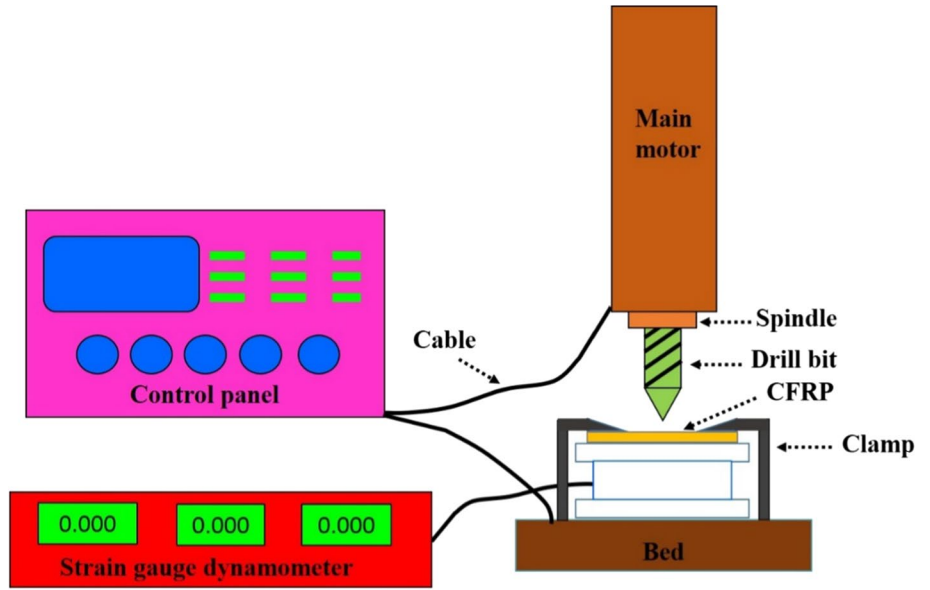


Fig. 3 Drill bit images before machining: micro-drill bits: **a** 0.3 mm, **b** 0.4 mm, **c** 0.5 mm and macro-drill bits: **d** 1 mm, **e** 2 mm and **f** 3 mm

Table 2 Specification of micro-drill and macro-drill

Drill diameter (mm)	0.3	0.4	0.5	1	2	3
Drill name	Multifaceted drill	Twist drill	Twist drill	Twist drill	Twist drill	Multifaceted drill
Drill materials	Carbide	Carbide	Carbide	Carbide	Carbide	Carbide
Shank type	Cylindrical	Cylindrical	Cylindrical	Cylindrical	Cylindrical	Cylindrical
Number of flutes	2	2	2	2	2	2
Point angle (°)	64	128	101	166	130	109
Helix angle (°)	28	26	27	30	43	40
Total length (mm)	38	38	38	38	38	38

Table 3 Measured responses for micro- and macro-drilling

Runs	V	F	Thrust force (N)			Delamination			Overcut (mm)		
			Drill diameter (mm)			Drill diameter (mm)			Drill diameter (mm)		
			0.3	0.4	0.5	0.3	0.4	0.5	0.3	0.4	0.5
<i>Micro-drill</i>											
1	2000	0.01	0.98	1.52	1.92	1.058	1.035	1.019	0.027	0.032	0.037
2	2000	0.03	1.52	1.92	2.36	1.084	1.076	1.060	0.022	0.023	0.025
3	2000	0.05	1.89	2.16	2.54	1.094	1.085	1.069	0.014	0.016	0.018
4	2500	0.01	0.96	1.50	1.91	1.064	1.036	1.020	0.028	0.033	0.036
5	2500	0.03	1.49	1.84	2.35	1.089	1.078	1.062	0.023	0.025	0.024
6	2500	0.05	1.85	2.03	2.49	1.099	1.086	1.068	0.016	0.017	0.019
7	3000	0.01	0.94	1.48	1.89	1.069	1.037	1.021	0.031	0.034	0.035
8	3000	0.03	1.45	1.82	2.26	1.092	1.089	1.073	0.026	0.028	0.029
9	3000	0.05	1.78	2.01	2.41	1.101	1.108	1.070	0.017	0.018	0.020
Runs	V	F	Thrust force (N)			Delamination			Overcut (mm)		
			Drill diameter (mm)			Drill diameter (mm)			Drill diameter (mm)		
			1	2	3	1	2	3	1	2	3
<i>Macro-drill</i>											
1	2000	0.01	2.35	2.65	2.99	1.045	1.026	1.010	0.034	0.036	0.041
2	2000	0.03	2.85	3.14	3.36	1.073	1.064	1.050	0.026	0.028	0.038
3	2000	0.05	2.92	3.26	3.54	1.081	1.073	1.058	0.019	0.021	0.024
4	2500	0.01	2.34	2.62	2.98	1.051	1.025	1.011	0.036	0.038	0.042
5	2500	0.03	2.84	3.11	3.35	1.076	1.065	1.051	0.026	0.029	0.033
6	2500	0.05	2.82	3.12	3.49	1.084	1.072	1.057	0.021	0.025	0.026
7	3000	0.01	2.36	2.67	2.98	1.057	1.025	1.012	0.037	0.039	0.041
8	3000	0.03	2.78	3.09	3.34	1.085	1.074	1.062	0.026	0.031	0.036
9	3000	0.05	2.80	3.11	3.41	1.092	1.095	1.058	0.025	0.027	0.028

thrust force. Among the various micro-drills, 0.3-mm drill produced lesser thrust force in the range of 0.96–1.84 N and 3-mm drill produced higher thrust force in the range of 2.98–3.48 N. The reason for the lesser thrust force in 0.3-mm drill was the lower shear area [17]. Also, the induced thrust force was indirectly proportional to the drill diameter and directly proportional to the rate of feed. In addition, the following formula was used to find the thrust force reduction percentage which is expressed in Eq. (3).

$$\text{Thrust force reduction \%} = \frac{(\text{high drill diameter} - \text{small drill diameter})}{\text{high drill diameter}} \times 100 \quad (3)$$

The thrust force reduction (36%) was observed between 0.3-mm drill and 0.4-mm drill combination which is less compared to 0.4-mm drill and 0.5-mm drill combination using the rate of feed of 0.01 mm/rev. The thrust force reduction (11.285%) was observed between 2-mm drill and 3-mm drill combination which is less compared to 1-mm drill and 2-mm drill combination using the feed of 0.01 mm/

rev. Normally, the twist drill with low point angle produced lesser thrust force in the FRP drilling. The present results of 0.3-mm drill with 64° point angle produced lesser thrust force. Therefore, the point angle was affecting the induced thrust force for 0.3-mm drill because of interlaminar fracture toughness, Poisson’s ratio, and Young’s modulus of material.

3.2 Delamination Factor

The significance of spindle speed and rate of feed on the delamination factor for various micro- and macro-drill diameters is illustrated in Fig. 5. In Fig. 5a, it was noticed that delamination increases with the increase in spindle speed for selected tool diameter. Also, in Fig. 5b, as the rate of feed increases, delamination also increases for all the diameters. The low spindle speed and rate of feed produced minimum delamination owing to the heating of epoxy resin. Also, the minimum delamination effect was involved to reduce the stiffness of machined work material. Throughout the depth of the hole, the minimum delaminations were also observed in the inner circumferences hole. The delamination

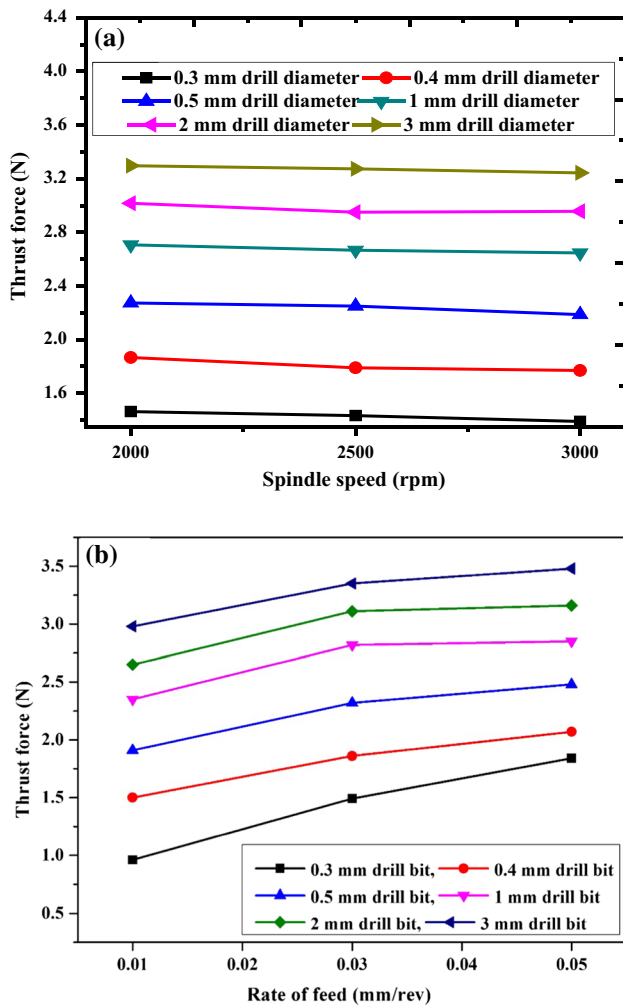


Fig. 4 Thrust force analysis based on a spindle speed, b rate of feed

was increasing with the increase in the rate of feed, and various thrust forces were observed with the increase in the rate of feed. The reason for increasing the delamination was because a higher rate of feed produced higher thrust force. Therefore, more delamination was observed by using a higher rate of feed. Among the different micro-drills, a 0.3-mm drill produced maximum delamination on the CFRP in the range of 1.064–1.098. The induced delamination was reduced by changing drill diameter from 0.4 to 0.5 mm and a changing point angle from 128° to 101°. But, the drill diameter of 0.3 mm produced greater delamination than 0.4-mm drill (1.036–1.093) and 0.5-mm drill (1.020–1.069). Normally, the drill diameter increases with an increase in delamination because the higher contact area of drill produced higher delamination. But, the current results were reversely observed. This may be due to the measurement differences and tool geometrical differences. Hence, the delamination range is calculated by the difference between the maximum delamination and minimum delamination of

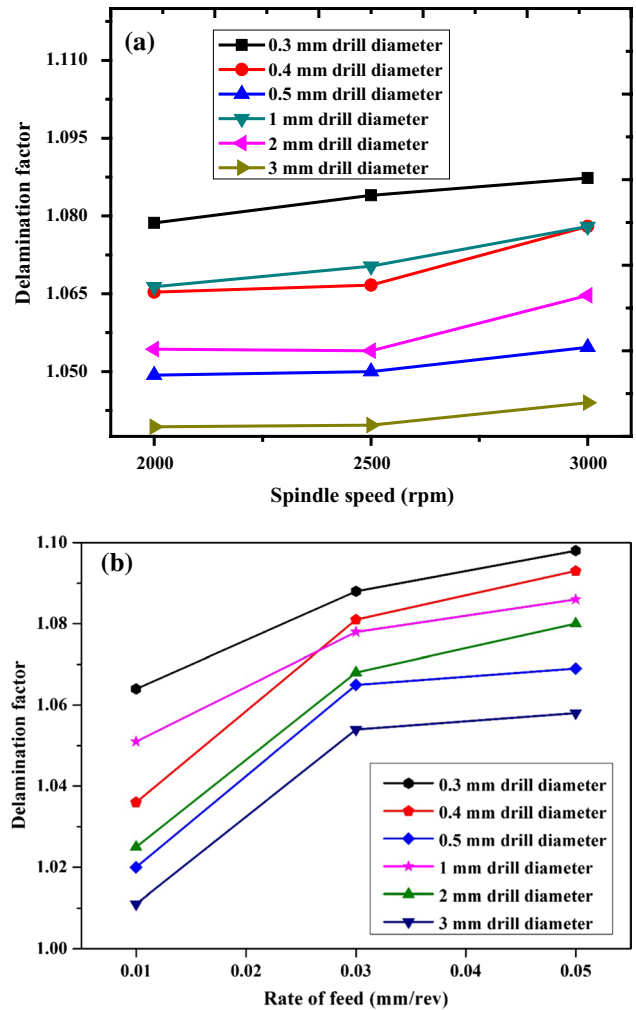


Fig. 5 Delamination factor analysis based on a spindle speed, b rate of feed

each drill diameter. The delamination of 0.3-mm drill, 0.4-mm drill, and 0.5-mm drill was found to be 0.034, 0.057, and 0.049, respectively. The delamination range differences were observed in the micron levels. Similarly, in macro-drill, a 1-mm drill produced delamination in the range of 1.051–1.086. The induced delamination was reduced by changing drill diameter from 1 to 3 mm and a changing point angle from 166° to 109°. But, the 1-mm drill provided higher delamination than a 2-mm drill (1.025–1.080) and a 3-mm drill (1.011–1.058). Similar results were observed in the micro-drill. The 0.5-mm drill and 3-mm drill produced minimum delamination in the range of 1.02–1.069 and 1.011–1.058, respectively. This may be due to the increases in solid carbide drill size; the thermal stability and hot hardness of solid carbide drill also increased simultaneously [18]. Finally, the delamination was indirectly proportional to the drill diameter and directly proportional to the rate of

feed. In addition, the delamination reduction percentage is calculated by using Eq. (4).

Delamination reduction %

$$= \frac{(\text{small drill diameter} - \text{high drill diameter})}{\text{small drill diameter}} \times 100 \quad (4)$$

The delamination reduction (2.601%) was observed between 0.3-mm drill and 0.4-mm drill combination which is a higher reduction compared to 0.4-mm drill and 0.5-mm drill combination using the rate of feed of 0.01 mm/rev. The delamination reduction (2.442%) was observed between the 1-mm drill and 2-mm drill combination which is a higher reduction compared to 2-mm drill and 3-mm drill combination using the rate of feed of 0.01 mm/rev. The fiber interface bonding and fiber orientation were the major reason in variations of delamination reduction [19].

3.3 Overcut

The effect of spindle speed and rate of feed on overcut for the various macro- and micro-drills is presented in Fig. 6. In Fig. 6a, it was noticed that overcut increases with the increase in spindle speed for selected tool diameter. The reason for the increased overcut was the vibration of the drill bit based on the increase in spindle speed. Also, in Fig. 6b, it was noticed that overcut decreases with the increase in the rate of feed for selected tool diameter. That is, by changing the drill diameter from 3 mm to 1 mm and 0.5 mm to 0.3 mm, overcut decreased in the range from 0.041 to 0.026 mm and 0.028 to 0.015 mm, respectively. This was due to the higher rate of feed that increases the penetration rate which led to a decrease in machining time. So, decreases in machining time result in an overcut reduction. During CFRP drilling, an increase in temperature is due to frictional heating and results in variation in drill diameters. The overcut of 0.3-mm drill was lower than 0.4- and 0.5-mm drill as shown in Fig. 6. Similarly, overcut of 1-mm drill was lower than 2- and 3-mm drill. While comparing the performance of all the selected ranges of diameter, minimum overcut was obtained for 0.3-mm micro-drill and 1-mm macro-drill. In another word, overcut was defined by obtained variations in hole diameter. Hence, 0.3- and 1-mm drills provide minimum overcut due to less thrust force generation. The 0.5- and 3-mm drills provided the maximum overcut due to the higher thrust force generation. In addition, obtained hole diameter has a minimum deviation at a high rate of feed and maximum deviation at the low rate of feed. Finally, the overcut was indirectly proportional to the drill diameter and rate

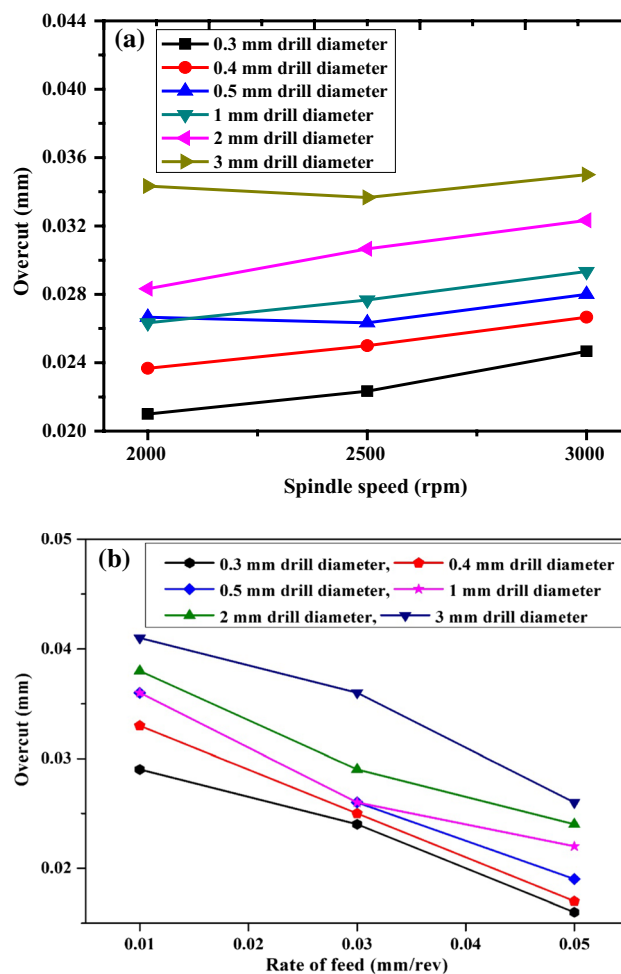


Fig. 6 Overcut analysis based on a spindle speed, b rate of feed

of feed. In addition, the overcut reduction percentage is expressed in Eq. (5).

Overcut reduction %

$$= \frac{(\text{high drill diameter} - \text{small drill diameter})}{\text{high drill diameter}} \times 100 \quad (5)$$

The overcut reduction (13.131%) was observed between 0.3-mm drill and 0.4-mm drill combination which is less compared to 0.4-mm drill and 0.5-mm drill combination using the rate of feed of 0.01 mm/rev. The overcut reduction (17.757%) was observed between 2-mm drill and 3-mm drill combination which is less compared to 1-mm drill and 2-mm drill combination using the rate of feed of 0.03 mm/rev. The minimum overcut was achieved by using a lower drill diameter with a lower point angle due to the geometrical differences.

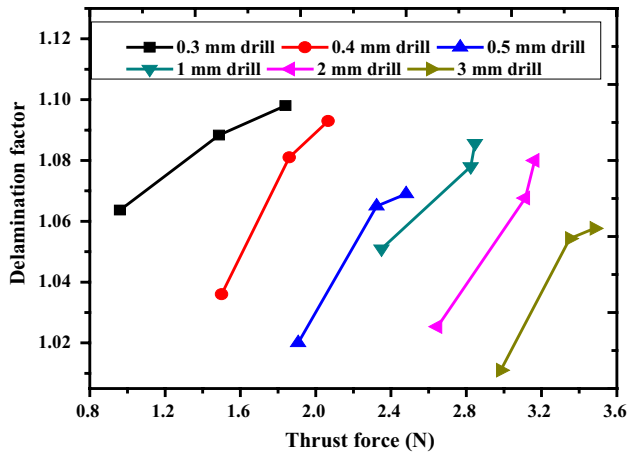


Fig. 7 Thrust force against delamination

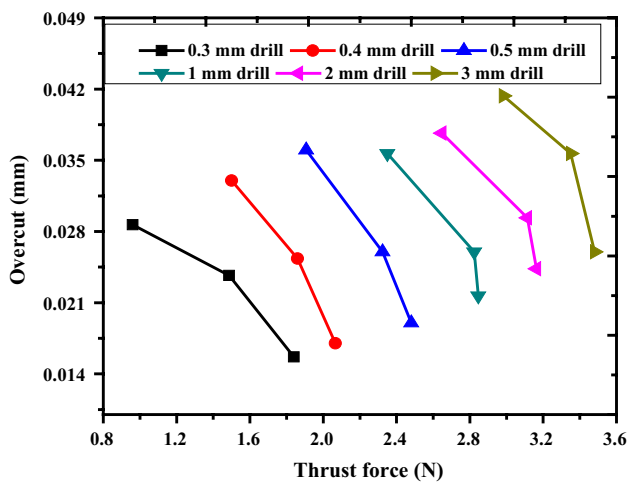


Fig. 8 Thrust force against overcut

3.4 Influence of Thrust Force on Delamination and Overcut

Figures 7 and 8 show the graph of thrust force on delamination and overcut, respectively, for all six drills. It can be noticed that thrust force increases and delamination also increases for all the six drills. The induced thrust force of 0.3-mm drill increased from 0.96 to 1.84 N as shown in Fig. 7. Therefore, a 0.3-mm drill produced maximum delamination among the remaining drill diameter. Similarly, the induced thrust force increased when the drill diameter increases. Therefore, it can be identified that the minimum induced thrust force of all the drill diameter was observed at minimum delamination factor. Among three different micro-drills, a 0.5-mm drill provided a 1.91 N thrust force with the least delamination factor (1.02). Similarly, a 3-mm drill provided 2.98 N thrust force with the least delamination factor (1.011). Velayudham and Krishnamurthy [20] found

that the thrust force increased from 120 to 390 N with the increases in delamination. The thrust force increased from 40 N to 80 N with the increases in delamination from 1.0 to 1.11 for tripod drilling and 1.21–1.23 for WT drill of polymeric composites. The minimum delamination was found with a higher diameter of drill and a lower rate of feed. The supportive result found that the linear fitting curve was observed between the thrust force and the delamination factor [21]. In Fig. 8, it can be noticed that there is an increase in thrust force and a decrease in overcut for all the six drills. The induced thrust force of 0.3-mm drill diameter was ranging from 0.96 to 1.84 N, and it is shown in Fig. 8. Therefore, a 0.3-mm drill produced minimum overcut among the remaining drill diameters. Similarly, the induced overcut increased when the drill diameter increases. The overcut ratio increased from minimum to maximum while increasing the drill diameter in the order of 0.3-mm, 0.4-mm, 0.5-mm, 1-mm, 2-mm, and 3-mm drill.

Among various micro-drills, 0.3-mm drill provided a 1.84 N thrust force with maximum delamination (1.098) and minimum overcut (0.016 mm). Similarly, among various macro-drills, a 1-mm drill provided a 2.98 N thrust force with maximum delamination (1.086) and minimum overcut (0.022 mm). The minimum overcut was observed in the lower diameter, and a higher rate of feed was preferred in this condition. The maximum overcut was observed in the lower rate of feed because unwanted lateral vibrations of all drills also increase [22].

3.5 Analysis of Variables

The significance of input process variables was determined using ANOVA as shown in Tables 4, 5, 6, 7, 8, and 9. The rate of feed has a significant effect on F_y , F_d , and overcut. Based on the ‘ P ’ value, the rate of feed was identified as the significant process variable for all the micro- and macro-drills.

3.6 Optimum Analysis

In order to enhance the production quality, multiple quality characteristics are considered and gray relational theory was employed. In normalization of desired quality characteristics, thrust force, delamination, and overcut were considered as lower the better. The weightage of thrust force, delamination, and overcut was 0.5%, 0.25%, and 0.25%, respectively. The reason for more weightage was considered to thrust force due to tool geometry. It creates more problem on hole quality, and the tool diameter is directly proportional to thrust force. Therefore, 0.5% weightage was assigned to thrust force and 0.25% weightage was assigned to both delamination and overcut. In GRA, the observed results are normalized to the limit of 0–1 and gray coefficients

Table 4 Analysis of variance—0.3-mm drill

Thrust force						
<i>S</i>	DF	Seq-SS	Adj-SS	Adj-MS	<i>F</i>	<i>P</i>
<i>V</i>	2	0.0081	0.0081	0.00408	12.4	0.019
<i>F</i>	2	1.1766	1.1766	0.58831	1794.8	0
<i>E</i>	4	0.0013	0.0013	0.00033		
<i>T</i>	8	1.1860				
<i>S</i> =0.0181046 <i>R</i> -Sq=99.89% <i>R</i> -Sq(adj)=99.78%						
Delamination @ entry						
<i>V</i>	2	0.0001	0.0001	5.73E-05	49	0.002
<i>F</i>	2	0.0018	0.00188	0.00094	806	0
<i>E</i>	4	4.7E-06	4.7E-06	1.2E-06		
<i>T</i>	8	0.001				
<i>S</i> =0.00108012 <i>R</i> -Sq=99.8% <i>R</i> -Sq-(adj)=99.5%						
Overcut @ entry						
<i>V</i>	2	2E-05	2E-05	1E-05	31.1	0.004
<i>F</i>	2	0.0002	0.00025	0.000129	387	0
<i>E</i>	4	1.3E-06	1E-06	3E-07		
<i>T</i>	8	0.0003				
<i>S</i> =0.000577350 <i>R</i> -Sq=99.52% <i>R</i> -Sq(adj)=99.05%						

S—source, *V*—spindle speed, *F*—rate of feed, *E*—error, *T*—total, DF—degree of freedom

Table 5 Analysis of variance—0.4-mm drill

Thrust force						
<i>S</i>	DF	Seq-SS	Adj-SS	Adj-MS	<i>F</i>	<i>P</i>
<i>V</i>	2	0.0156	0.0156	0.00781	7.73	0.042
<i>F</i>	2	0.4934	0.4934	0.24671	244	0
<i>E</i>	4	0.0040	0.0040	0.00101		
<i>T</i>	8	0.5130				
<i>S</i> =0.0317980 <i>R</i> -Sq=99.21% <i>R</i> -Sq(adj)=98.42%						
Delamination @ entry						
<i>V</i>	2	0.00029	0.000290	0.000145	3.95	0.113
<i>F</i>	2	0.00541	0.00541	0.002709	73.55	0.001
<i>E</i>	4	0.0001	0.000147	3.68E-05		
<i>T</i>	8	0.0058				
<i>S</i> =0.00606905 <i>R</i> -Sq=97.5% <i>R</i> -Sq-(adj)=95%						
Overcut @ entry						
<i>V</i>	2	1.36E-05	0.000013	6.8E-06	8.71	0.035
<i>F</i>	2	0.00038	0.000384	0.000192	247	0
<i>E</i>	4	3.1E-06	0.000003	8E-07		
<i>T</i>	8	0.00040				
<i>S</i> =0.000881917 <i>R</i> -Sq=99% <i>R</i> -Sq-(adj)=98%						

were developed to represent the relation between ideal and observed values. The gray relational grade values are estimated by taking the average of GRC values. The highest GRG with the corresponding factor combination indicates the optimal setting. Tables 10 and 11 show the evaluated GRG for micro-drill and macro-drill. The 0.3-, 0.4-, 0.5-, 1-, and 3-mm drills achieved the highest GRG with the corresponding optimum factors in experimental number one.

The 2-mm drill achieved the highest GRG with the corresponding optimum factors in experimental number four. Among the micro- and macro-drills, the best-obtained hole was evaluated based on the GRG value. Therefore, 0.3-mm and 2-mm drills make the best hole among the three different micro- and macro-drills, respectively. Confirmation tests were performed for 0.3-mm and 2-mm drills with the corresponding optimum setting on CFRP. The confirmation

Table 6 Analysis of variance—0.5-mm drill

Thrust force						
<i>S</i>	DF	Seq-SS	Adj-SS	Adj-MS	<i>F</i>	<i>P</i>
<i>V</i>	2	0.0120	0.0120	0.0060	7.87	0.041
<i>F</i>	2	0.5268	0.5268	0.2634	343.61	0
<i>E</i>	4	0.0030	0.0030	0.0007		
<i>T</i>	8	0.542				
<i>S</i> =0.0276887 <i>R</i> -Sq=99% <i>R</i> -Sq-(adj)=99%						
Delamination @ entry						
<i>V</i>	2	5.07E-05	5.07E-05	2.53E-05	1.97	0.253
<i>F</i>	2	0.00444	0.00444	0.00222	173.06	0
<i>E</i>	4	5.13E-05	5E-05	1.28E-05		
<i>T</i>	8	0.0045				
<i>S</i> =0.00358236 <i>R</i> -Sq=99% <i>R</i> -Sq-(adj)=98%						
Overcut @ entry						
<i>V</i>	2	4.7E-06	4.7E-06	2.3E-06	0.7	0.549
<i>F</i>	2	0.00043	0.00043	0.00021	65.7	0.001
<i>E</i>	4	1E-05	1E-05	3E-06		
<i>T</i>	8	0.00045				
<i>S</i> =0.00182574 <i>R</i> -Sq=97.08% <i>R</i> -Sq-(adj)=94.15%						

Table 7 Analysis of variance—1 mm drill

Thrust force						
<i>S</i>	DF	Seq-SS	Adj-SS	Adj-MS	<i>F</i>	<i>P</i>
<i>V</i>	2	0.0056	0.005	0.002	1.95	0.25
<i>F</i>	2	0.4712	0.4712	0.2356	164.4	0
<i>E</i>	4	0.0057	0.00573	0.0014		
<i>T</i>	8	0.482				
<i>S</i> =0.0378594 <i>R</i> -Sq=98.81% <i>R</i> -Sq-(adj)=97.62%						
Delamination @ entry						
<i>V</i>	2	0.00021	0.00021	0.00010	111.65	0
<i>F</i>	2	0.0019	0.00199	0.00099	1053.29	0
<i>E</i>	4	3.8E-06	3.8E-06	9E-07		
<i>T</i>	8	0.00220				
<i>S</i> =0.000971825 <i>R</i> -Sq=99.83% <i>R</i> -Sq-(adj)=99.66%						
Overcut @ entry						
<i>V</i>	2	1.36E-05	1.36E-05	6.8E-06	2.77	0.16
<i>F</i>	2	0.00030	0.00030	0.00015	63.05	0.001
<i>E</i>	4	9.8E-06	9.8E-06	2.4E-06		
<i>T</i>	8	0.000332				
<i>S</i> =0.00156347 <i>R</i> -Sq=97.05% <i>R</i> -Sq-(adj)=94.10%						

results are shown in Tables 12 and 13. The optimized parameters show a significant improvement in performance.

In the initial condition, to position the drill bit on the desired point of CFRP was a little difficult. However, the drill bit was positioned on the desired point with micron-level deviation. The produced micro-holes on the CFRP were not properly identified either it's through or blind hole. Figure 9 shows the picture of produced micro-hole on CFRP. During the machining time, carbon fiber and

resins were sticking on drill flute as shown in Fig. 10. This may affect drill functionality and hole accuracy. Besides, the collected powders were showing the carbon fiber with resins as shown in Fig. 11. The reason for discontinuous chip and powder form of CFRP produced in the machining was the brittleness of materials and brittle fracture mechanism. The tool wears were not observed in all the drills because of the less material thickness and a number of



Table 8 Analysis of variance—2-mm drill

Thrust force						
<i>S</i>	DF	Seq-SS	Adj-SS	Adj-MS	<i>F</i>	<i>P</i>
<i>V</i>	2	0.0080	0.0080	0.0040	1.9	0.263
<i>F</i>	2	0.4872	0.4872	0.2436	114.49	0
<i>E</i>	4	0.0085	0.0085	0.0021		
<i>T</i>	8	0.5038				
<i>S</i> =0.0461278 <i>R</i> -Sq=98.31% <i>R</i> -Sq(adj)=96.62%						
Delamination @ entry						
<i>V</i>	2	0.00022	0.00022	0.0001	2.47	0.2
<i>F</i>	2	0.00493	0.00493	0.00246	55.22	0.001
<i>E</i>	4	0.00017	0.00017	4.47E-05		
<i>T</i>	8	0.00533				
<i>S</i> =0.00668331 <i>R</i> -Sq=96.65% <i>R</i> -Sq(adj)=93.30%						
Overcut @ entry						
<i>V</i>	2	2.42E-05	2.42E-05	1.21E-05	12.82	0.018
<i>F</i>	2	0.00027	0.00027	0.00013	144.12	0
<i>E</i>	4	3.8E-06	3.8E-06	9E-07		
<i>T</i>	8	0.0003				
<i>S</i> =0.000971825 <i>R</i> -Sq=98.74% <i>R</i> -Sq(adj)=97.48%						

Table 9 Analysis of variance—3 mm drill

Thrust force						
<i>S</i>	DF	Seq-SS	Adj-SS	Adj-MS	<i>F</i>	<i>P</i>
<i>A</i>	2	0.0042	0.0042	0.0021	1.87	0.26
<i>B</i>	2	0.3980	0.3980	0.1990	173.89	0
<i>E</i>	4	0.0045	0.0045	0.0011		
<i>T</i>	8	0.4068				
<i>S</i> =0.0338296 <i>R</i> -Sq=98.87% <i>R</i> -Sq(adj)=97.75%						
Delamination @ entry						
<i>A</i>	2	4.07E-05	4.07E-05	2.03E-05	1.61	0.30
<i>B</i>	2	0.004067	0.00406	0.00203	160.53	0
<i>E</i>	4	5.07E-05	5.07E-05	1.27E-05		
<i>T</i>	8	0.004158				
<i>S</i> =0.00355903 <i>R</i> -Sq=98.78% <i>R</i> -Sq(adj)=97.56%						
Overcut @ entry						
<i>A</i>	2	2.71E-06	2.71E-06	1.31E-06	0.29	0.76
<i>B</i>	2	0.000361	0.00036	0.0001	38.64	0.00
<i>E</i>	4	1.87E-05	1.87E-05	4.7E-06		
<i>T</i>	8	0.000382				
<i>S</i> =0.00216025 <i>R</i> -Sq=95.11% <i>R</i> -Sq(adj)=90.23%						

experiments. The non-contact roughness measurement was used to measure the surface roughness of 0.5-mm micro-hole. Figure 12 shows the roughness of 1.48 μm for a 0.3-mm drilled hole. Figure 13a–f shows the microstructural defects of produced holes which are fiber overcut, fiber pull-in, fiber pull-in at the exit, resin melting, uneven hole rim at entry, uncut fiber, and long uncut fiber.

4 Conclusions

An experimental investigation was conducted for analyzing the micro-hole and macro-hole quality on CFRP. The relations between thrust force, delamination, and overcut for various drill diameters were analyzed. Taguchi-based gray relational analysis was followed to minimize the

Table 10 Evaluated gray relational grade for micro-drill

Run	Normalized values			Reference sequence			Gray relational coefficient			GRG	Rank
	F_y	F_d	OC	F_y	F_d	OC	F_y	F_d	OC		
0.3-mm drill											
1	0.96	1.000	0.235	0.04	0.000	0.765	0.92	1.000	0.246	0.723	1
2	0.39	0.395	0.529	0.61	0.605	0.471	0.45	0.293	0.347	0.363	7
3	0.00	0.163	1.000	1.00	0.837	0.000	0.33	0.230	1.000	0.521	4
4	0.98	0.860	0.176	0.02	0.140	0.824	0.96	0.642	0.233	0.611	2
5	0.42	0.279	0.471	0.58	0.721	0.529	0.46	0.257	0.321	0.347	8
6	0.04	0.047	0.882	0.96	0.953	0.118	0.34	0.208	0.680	0.410	5
7	1.00	0.744	0.000	0.00	0.256	1.000	1.00	0.494	0.200	0.565	3
8	0.46	0.209	0.294	0.54	0.791	0.706	0.48	0.240	0.262	0.328	9
9	0.12	0.000	0.824	0.88	1.000	0.176	0.36	0.200	0.586	0.382	6
0.4-mm drill											
1	0.94	1.00	0.11	0.06	0.000	0.889	0.89	1.000	0.220	0.705	1
2	0.35	0.44	0.61	0.65	0.562	0.389	0.44	0.308	0.391	0.378	7
3	0.00	0.32	1.00	1.00	0.685	0.000	0.33	0.267	1.000	0.534	4
4	0.97	0.99	0.06	0.03	0.014	0.944	0.94	0.948	0.209	0.701	2
5	0.47	0.41	0.50	0.53	0.589	0.500	0.49	0.298	0.333	0.372	8
6	0.19	0.30	0.94	0.81	0.699	0.056	0.38	0.264	0.818	0.488	5
7	1.00	0.97	0.00	0.00	0.027	1.000	1.00	0.901	0.200	0.700	3
8	0.50	0.26	0.33	0.50	0.740	0.667	0.50	0.253	0.273	0.342	9
9	0.22	0.00	0.89	0.78	1.000	0.111	0.39	0.200	0.692	0.428	6
0.5-mm drill											
1	0.95	1.000	0.000	0.05	0.000	1.000	0.92	1.000	0.200	0.705	1
2	0.28	0.241	0.632	0.72	0.759	0.368	0.41	0.248	0.404	0.354	8
3	0.00	0.074	1.000	1.00	0.926	0.000	0.33	0.213	1.000	0.515	4
4	0.97	0.981	0.053	0.03	0.019	0.947	0.94	0.931	0.209	0.694	3
5	0.29	0.204	0.684	0.71	0.796	0.316	0.41	0.239	0.442	0.365	7
6	0.08	0.093	0.947	0.92	0.907	0.053	0.35	0.216	0.826	0.464	5
7	1.00	0.963	0.105	0.00	0.037	0.895	1.00	0.871	0.218	0.696	2
8	0.43	0.000	0.421	0.57	1.000	0.579	0.47	0.200	0.302	0.323	9
9	0.20	0.056	0.895	0.80	0.944	0.105	0.38	0.209	0.704	0.433	6

experiment trails and find the optimum levels. The following conclusions were drawn based on the outcomes.

- From the analysis, micro- and macro-drills linearly affect the thrust force and delamination and are inversely proportional to overcut. A rapid decrease was observed on overcut for the rate of feed above 0.01 mm/rev.
- Among the micro-drill, a 0.3-mm drill produced the best hole at lower levels of spindle speed and rate of feed. Similarly, a 2-mm macro-drill produced the best hole at medium spindle speed and a lower rate of feed. The measured surface roughness on the drilled hole was found as a minimum.
- From the statistical analysis, the rate of feed was identified as a major process variable which influences the desired performance measures such as thrust force, delamination, and overcut for all the selected ranges of micro- and macro-drill parameters.
- The proposed Taguchi-based gray relational approach enhances the multi-performance drilling characteristics for the micro- and macro-drilling processes.
- The micro-drilling performance could be analyzed using a laser processing method and abrasive water jet machining in the future.

Table 11 Evaluated gray relational grade for macro-drill

	Normalized values			Reference sequence			Gray relational coefficient			GRG	Rank
	F_y	F_d	OC	F_y	F_d	OC	F_y	F_d	OC		
1-mm drill											
1	0.98	1.000	0.167	0.02	0.000	0.833	0.97	1.000	0.231	0.732	1
2	0.12	0.404	0.611	0.88	0.596	0.389	0.36	0.296	0.391	0.350	6
3	0.00	0.234	1.000	1.00	0.766	0.000	0.33	0.246	1.000	0.526	4
4	1.00	0.872	0.056	0.00	0.128	0.944	1.00	0.662	0.209	0.624	2
5	0.14	0.340	0.611	0.86	0.660	0.389	0.37	0.275	0.391	0.344	7
6	0.17	0.170	0.889	0.83	0.830	0.111	0.38	0.232	0.692	0.433	5
7	0.97	0.745	0.000	0.03	0.255	1.000	0.94	0.495	0.200	0.543	3
8	0.24	0.149	0.611	0.76	0.851	0.389	0.40	0.227	0.391	0.339	8
9	0.21	0.000	0.667	0.79	1.000	0.333	0.39	0.200	0.429	0.338	9
2-mm drill											
1	0.95	0.986	0.167	0.05	0.014	0.833	0.91	0.946	0.231	0.697	2
2	0.19	0.443	0.611	0.81	0.557	0.389	0.38	0.310	0.391	0.361	6
3	0.00	0.314	1.000	1.00	0.686	0.000	0.33	0.267	1.000	0.534	4
4	1.00	1.000	0.056	0.00	0.000	0.944	1.00	1.000	0.209	0.736	1
5	0.23	0.429	0.556	0.77	0.571	0.444	0.40	0.304	0.360	0.353	7
6	0.22	0.329	0.778	0.78	0.671	0.222	0.39	0.271	0.529	0.397	5
7	0.92	1.000	0.000	0.08	0.000	1.000	0.86	1.000	0.200	0.688	3
8	0.27	0.300	0.444	0.73	0.700	0.556	0.41	0.263	0.310	0.326	9
9	0.23	0.000	0.667	0.77	1.000	0.333	0.40	0.200	0.429	0.341	8
3-mm drill											
1	0.98	1.000	0.056	0.02	0.000	0.944	0.97	1.000	0.209	0.725	1
2	0.32	0.231	0.222	0.68	0.769	0.778	0.42	0.245	0.243	0.304	8
3	0.00	0.077	1.000	1.00	0.923	0.000	0.33	0.213	1.000	0.515	4
4	1.00	0.981	0.000	0.00	0.019	1.000	1.00	0.929	0.200	0.710	2
5	0.34	0.212	0.500	0.66	0.788	0.500	0.43	0.241	0.333	0.335	7
6	0.09	0.096	0.889	0.91	0.904	0.111	0.35	0.217	0.692	0.421	5
7	1.00	0.962	0.056	0.00	0.038	0.944	1.00	0.867	0.209	0.692	3
8	0.36	0.000	0.333	0.64	1.000	0.667	0.44	0.200	0.273	0.303	9
9	0.23	0.077	0.778	0.77	0.923	0.222	0.39	0.213	0.529	0.379	6

Table 12 Confirmation test results for 0.3-mm drill

Setting level	Initial setting	Optimal process parameters	
		Prediction	Experiment
	V1F1	V1F1	V1F1
F_y	0.98		0.92
F_d	1.058		1.042
OC	0.027		0.024
GRG	0.723	0.697	0.766
Improvement in gray relational grade=0.043			

Table 13 Confirmation test for 2-mm drill

Setting level	Initial setting	Optimal process parameters	
		Prediction	Experiment
	V1F1	V2F1	V2F1
F_y	2.65		2.51
F_d	1.026		1.020
OC	0.036		0.018
GRG	0.697	0.744	0.736
Improvement in gray relational grade=0.039			

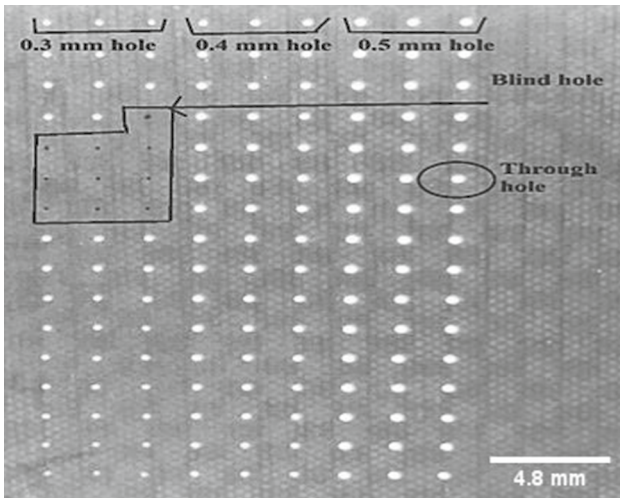


Fig. 9 Optical micrograph of micro-holed CFRP

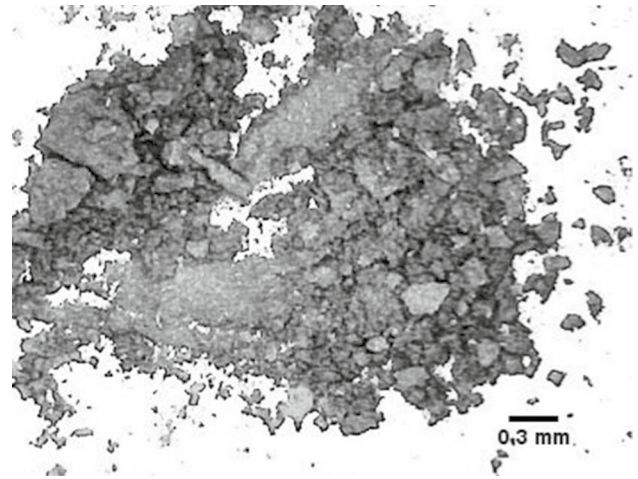


Fig. 11 Optical micrograph of sticking powder of carbon fiber with resin

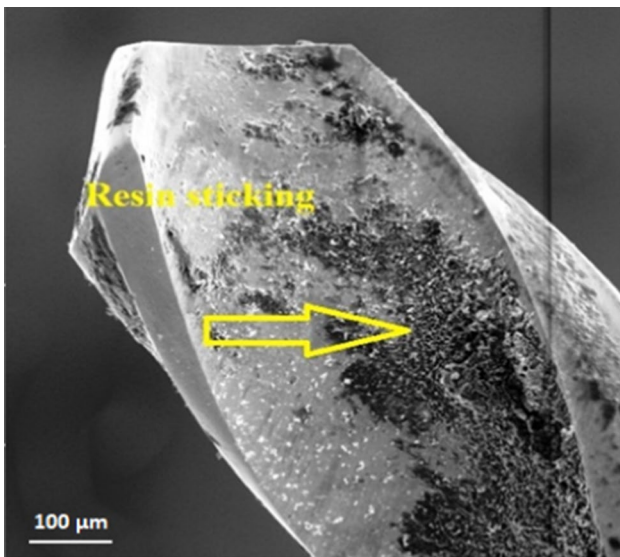


Fig. 10 SEM picture of sticking resin to 0.4-mm drill

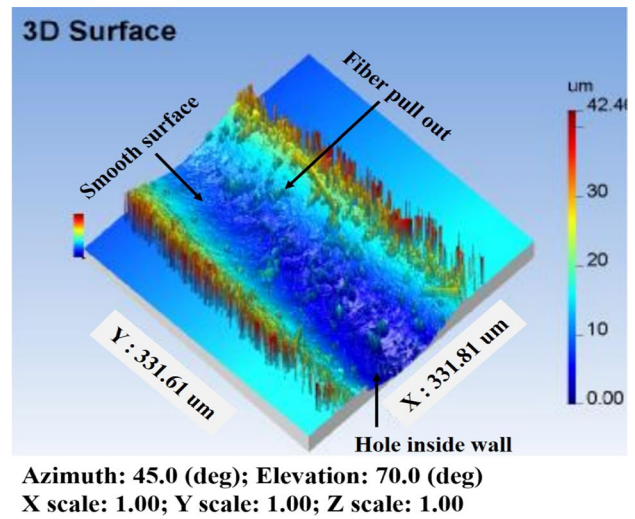
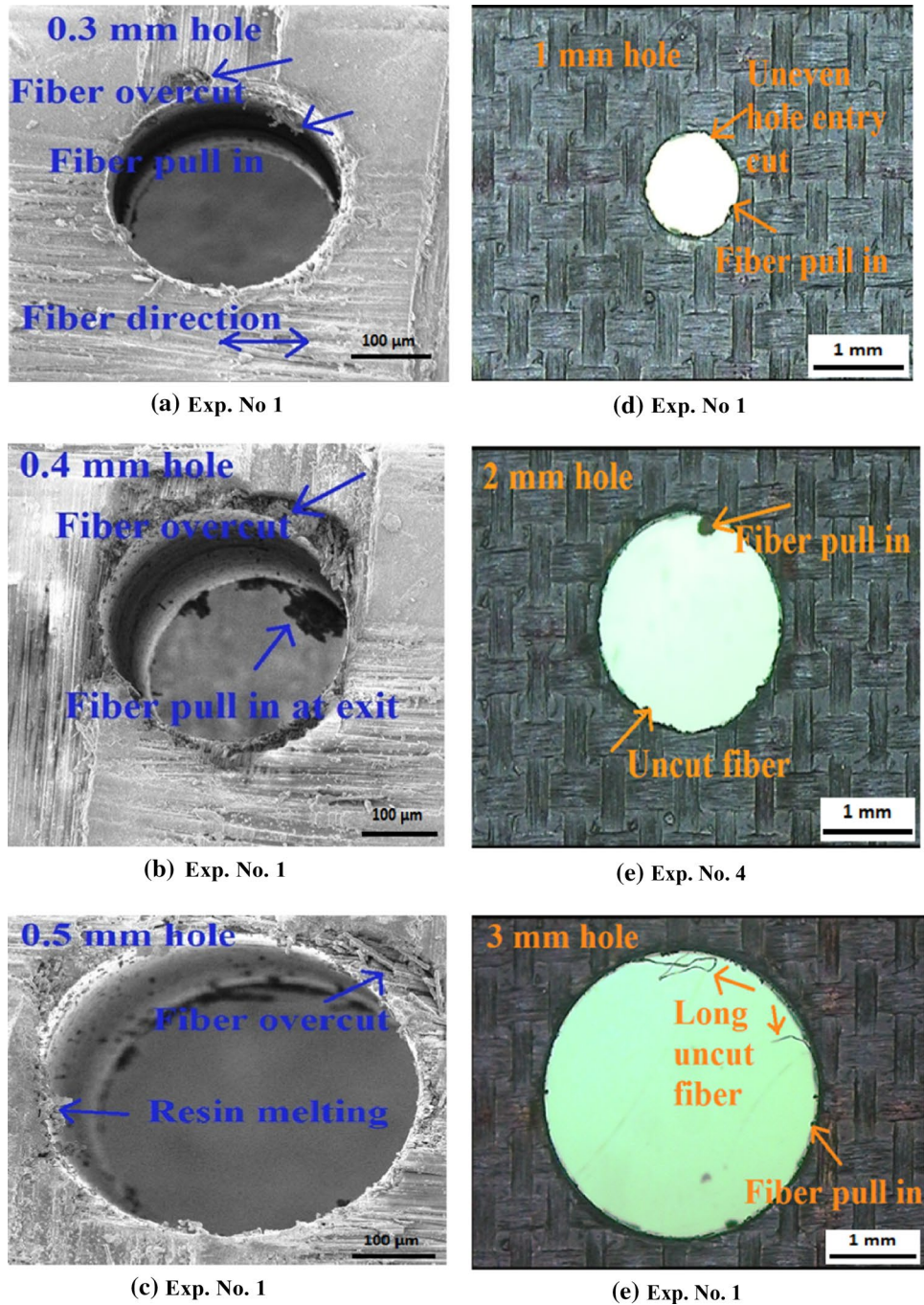


Fig. 12 Roughness inside the wall of 0.3-mm hole

Fig. 13 Structure of holes
a 0.3 mm [16], **b** 0.4 mm, **c**
 0.5 mm, **d** 1 mm, **e** 2 mm, **f**
 3 mm



Acknowledgements The authors wish to thank National Taipei University of Technology, Taipei-10608, Taiwan, ROC, Indian Institute of Technology Madras, India, and MAM School of Engineering, Tiruchirappalli, India, for all support required to carry out this research.

References

1. Raj, D.S.; Karunamoorthy, L.: Study of the effect of tool wear on hole quality in drilling CFRP to select a suitable drill for multi-criteria hole quality. *Mater. Manuf. Process.* **31**, 587–592 (2015). <https://doi.org/10.1080/10426914.2015.1004713>
2. Tan, C.L.; Azmi, A.I.; Muhammad, N.: Delamination and surface roughness analyses in drilling hybrid carbon/glass composite. *Mater. Manuf. Process.* **31**, 1366–1376 (2016). <https://doi.org/10.1080/10426914.2015.1103864>
3. Krishnaraj, V.; Prabukarthi, A.; Ramanathan, A.; Elanghovan, N.; Senthil Kumar, M.; Zitoune, R.; Davim, J.P.: Optimization of machining parameters at high speed drilling of carbon fiber reinforced plastic (CFRP) laminates. *Compos. Part B Eng.* **43**, 1791–1799 (2012). <https://doi.org/10.1016/j.compositesb.2012.01.007>

4. Eneyew, E.D.; Ramulu, M.: Experimental study of surface quality and damage when drilling unidirectional CFRP composites. *J. Mater. Res. Technol.* **3**, 354–362 (2014). <https://doi.org/10.1016/j.jmrt.2014.10.003>
5. Du, J.; Zhang, H.; Geng, Y.; Ming, W.; He, W.; Ma, J.; Cao, Y.; Li, X.; Liu, K.: A review on machining of carbon fiber reinforced ceramic matrix composites. *Ceram. Int.* **45**, 18155–18166 (2019). <https://doi.org/10.1016/j.ceramint.2019.06.112>
6. Daxi, G.; Yunda, T.; Yihang, L.; Zhenyu, S.; Xinggang, J.; Deyuan, Z.: Experimental study on drilling load and hole quality during rotary ultrasonic helical machining of small-diameter CFRP holes. *J. Mater. Process. Technol.* **270**, 195–205 (2019). <https://doi.org/10.1016/j.jmatprotec.2019.03.001>
7. John, K.M.; Thirumalai Kumaran, S.; Rendi, K.; Park, Ki M.; Byeon, J.H.: Review on the methodologies adopted to minimize the material damages in drilling of carbon fiber reinforced plastic composites. *J. Reinf. Plast. Compos.* **38**, 351–368 (2019). <https://doi.org/10.1177/0731684418819822>
8. Panchagnula, K.K.; Palaniyadi, K.: Drilling on fiber reinforced polymer/nanopolymer composite laminates: a review. *J. Mater. Res. Technol.* **7**, 180–189 (2018). <https://doi.org/10.1016/j.jmrt.2017.06.003>
9. Samuel Raj, D.; Karunamoorthy, L.: Performance of cryogenically treated WC drill using tool wear measurements on the cutting edge and hole surface topography when drilling CFRP. *Int. J. Refract. Met. Hard Mater.* **78**, 32–44 (2019). <https://doi.org/10.1016/j.ijrmhm.2018.08.011>
10. Manno Rajkumar, G.; Bhardwaj, D.; Kannan, C.; Oyyaravelu, R.; Balan, A.S.S.: Effect of chilled air on delamination, induced vibration, burr formation and surface roughness in CFRP drilling: a comparative study. *Mater. Res. Express* (2018). <https://doi.org/10.1088/2053-1591/aaf47d>
11. Durante, M.; Boccarusso, L.; De Fazio, D.; Langella, A.: Circular cutting strategy for drilling of carbon fiber-reinforced plastics (CFRPs). *Mater. Manuf. Process.* **34**, 554–566 (2019). <https://doi.org/10.1080/10426914.2019.1566615>
12. Mudhukrishnan, M.; Hariharan, P.; Palanikumar, K.; Latha, B.: Optimization and sensitivity analysis of drilling parameters for sustainable machining of carbon fiber-reinforced polypropylene composites. *J. Thermoplast.* **32**, 1485–1508 (2018). <https://doi.org/10.1177/0892705718799816>
13. Qiu, X.; Li, P.; Niu, Q.; Chen, A.; Ouyang, P.; Li, C.; Jo, K.T.: Influence of machining parameters and tool structure on cutting force and hole wall damage in drilling CFRP with stepped drills. *Int. J. Adv. Manuf. Technol.* **97**, 857–865 (2018). <https://doi.org/10.1007/s00170-018-1981-2>
14. Zitoune, R.; Krishnaraj, V.; Collombet, F.: Study of drilling of composite material and aluminium stack. *Compos. Struct.* **92**, 1246–1255 (2010). <https://doi.org/10.1016/j.compstruct.2009.10.010>
15. Heisel, U.; Pfeifroth, T.: Influence of point angle on drill hole quality and machining forces when drilling CFRP. *AIP Proc. CIRC* **1**, 471–476 (2012). <https://doi.org/10.1016/j.procir.2012.04.084>
16. Raj Kumar, D.; Ranjithkumar, P.; Jenarathanan, M.P.; Sathiyarayanan, C.: Experimental investigation and analysis of factors influencing delamination and thrust force during drilling of carbon-fibre reinforced polymer composites. *Pigment Resin Technol.* **46**(6), 507–524 (2017)
17. Karnik, S.R.; Gaitonde, V.N.; Rubio, J.C.; Correia, A.E.: Delamination analysis in high speed drilling of carbon fiber reinforced plastics (CFRP) using artificial neural network model. *Mater. Des.* **29**, 1768–1776 (2008). <https://doi.org/10.1016/j.matdes.2008.03.014>
18. Abish, J.; Samal, P.; Narenther, M.S.; Kannan, C.; Balan, A.S.S.: Assessment of drilling-induced damage in CFRP under chilled air environment. *Mater. Manuf. Process.* **33**, 1361–1368 (2018). <https://doi.org/10.1080/10426914.2017.1415452>
19. Ravi Shankar, A.; Karali, P.: Cutting force and hole quality analysis in micro-drilling of CFRP. *Mater. Manuf. Process.* **33**, 1369–1377 (2018). <https://doi.org/10.1080/10426914.2017.1401715>
20. Velayudham, A.; Krishnamurthy, R.: Effect of point geometry and their influence on thrust and delamination in drilling of polymeric composites. *J. Mater. Process. Technol.* **185**, 204–209 (2007). <https://doi.org/10.1016/j.jmatprotec.2006.03.146>
21. Liu, L.; Qi, C.; Wu, F.; Xu, J.; Zhu, X.: Experimental thrust forces and delamination analysis of GFRP laminates using candlestick drills. *Mater. Manuf. Process.* **33**, 695–708 (2018). <https://doi.org/10.1080/10426914.2017.1376072>
22. Anwar, S.; Nasr, M.M.; Pervaiz, S.; Al-Ahmari, A.; Alkahtani, M.; El-Tamimi, A.: A study on the effect of main process parameters of rotary ultrasonic machining for drilling BK7 glass. *Adv. Mech. Eng.* (2018). <https://doi.org/10.1177/1687814017752212>





Contents lists available at ScienceDirect

Materials Today: Proceedings

journal homepage: www.elsevier.com/locate/matpr

Minimum cutting thickness and surface roughness achieving during micromachining of aluminium 19000 using CNC machine

N. Jeyaprakash^{a,b,*}, Che-Hua Yang^a, D. Raj Kumar^c

^a Centre of Mass Customization Additive Manufacture, National Taipei University of Technology, Taiwan, ROC

^b Institute of Manufacturing Technology, National Taipei University of Technology, Taiwan, ROC

^c Department of Mechanical Engineering, MAM School of Engineering, Tiruchirappalli, India

ARTICLE INFO

Article history:

Received 26 June 2019

Accepted 30 June 2019

Available online xxx

Keywords:

Minimum cutting thickness
Minimum uncut chip thickness
Surface integrity
Aluminium
Micromachining

ABSTRACT

In this experimental work, a comparison between analytical model and experimental analysis on minimum cutting thickness and surface roughness in a CNC micro turning of aluminium 19000 alloys has been investigated. Prior to machining, a 30 μm thick electroplating was done on the work samples. Machining parameters such as cutting speed, feed and depth of cut were taken as the input parameters while the minimum cutting thickness and surface roughness were the output responses. The machined surfaces of electroplated samples were examined for surface topology, initial and final diameter was also measured. Taguchi techniques were used to optimize the machining parameter. It was found that for the same machining conditions and tool geometry, the minimum cutting thickness and surface roughness were less for the electroplated materials compared with that of unplated material. In addition, the variation results of analytical model and experimental run were within the acceptable range. The analytical results were in a close tolerance with that of experimental results.

© 2019 Elsevier Ltd. All rights reserved.

Peer-review under responsibility of the scientific committee of the International Conference on Recent Trends in Nanomaterials for Energy, Environmental and Engineering Applications.

1. Introduction

The micromachining is to produce microcomponent or to remove material from workpieces in micron levels. Generally in micromachining processes, the metal removal from the component varies within in the limit of 1 μm –999 μm thickness [1]. The micro-components or the micromachined parts are generally produced with a very fine surface finish. The micromachining can be achieved using different types of machine tools namely multipurpose miniature machine tool and dedicated micromachining tool, Ultra precision CNC machine and dedicated unconventional machine tools like micro-EDM, micro-ECM and laser machine tool etc. The fabricated micro pin is having diameter in the range of 475 μm to 276 μm using multipurpose miniature micromachining [2,3]. This machine tool was applied for micromachining process [4,5]. The micromachined hole process was studied using multipurpose miniature micromachine machine tool [6]. They have achieved a

metal removal in a range 0.4 μm to 1 μm . The numerical analysis was performed to analysis the tool design, machining conditions, and fabricated microgroove with size of 11 μm [7]. The mathematical model developed and applied micro turning process using DT-110 integrated multi process micromachine tool. The minimum thickness of cut achieved was in the range 5 μm to 15 μm in their work [4]. High precision CNC machine tool and/or dedicated CNC machine tool are costlier and required at controlled room temperature, constant atmospheres with dirt free air filtration. An ultra-fine surface finish also is achieved in micromachining. The maximum surface roughness of 2 μm and average roughness of 0.25 μm are achieved in one of the works. Even CNC ultra-precision lathes have been used for micromachining. A partial list of the works in which high precision CNC machine tools or dedicated micromachining tool used has been presented in the Table 1. In the above said works, the micromachining has been successfully achieved when cutting tools with very little nose radius i.e. either less than 100 μm or equal are used. Micromachining is applied for producing automobile components and aerospace components in the recent days [25]. In micro turning, the minimum depth of metal removal is known as Minimum Cutting Thickness (MCT). The depth which is remain uncut or which is deforming plastically during the metal cutting operation

* Corresponding author at: Centre of Mass Customization Additive Manufacture, National Taipei University of Technology, Taiwan, ROC.

E-mail addresses: prakash@ntut.edu.tw (N. Jeyaprakash), chyang@ntut.edu.tw (C.-H. Yang).

<https://doi.org/10.1016/j.matpr.2019.06.753>

2214-7853/© 2019 Elsevier Ltd. All rights reserved.

Peer-review under responsibility of the scientific committee of the International Conference on Recent Trends in Nanomaterials for Energy, Environmental and Engineering Applications.

Table 1
List of Micromachining process using Advanced CNC machine tool.

Name and model of advanced CNC machine tool	Material Used	Workpiece Form	Machining Conditions used	MCT(μm) achieved/ Reference
CNC ultra precision machine tool	Aluminium single crystal material	Cylindrical \varnothing 12.7 mm	V = 3000 rpm, f = 20 mm/min d = 10 μm , $\alpha = 0^\circ$, $r_e = 0.774$ mm	5 μm /[8]
CNC	low alloy, heat treated steel	Cylindrical \varnothing 65 mm	V = 125–250 m/min f = 0.03–0.06 mm/rev, d = 5 μm	5 μm /[9]
Two-axis CNC ultra-precision lathe	polycrystalline Al 6061, copper and copper nickel	Cylindrical \varnothing 12.7 mm	V = 3000 rpm, f = 20 mm/min d = 5 μm , $\alpha = 0^\circ$, $r_e = 0.5$ mm	5 μm /[10]
CNC lathe	Aluminium-based MMC reinforced with SiC particles.	Cylindrical \varnothing 32 mm	$r_e = 0.8$, $\alpha = 0^\circ$	1 μm /[11]
CNC ultra-precision lathe	A6061-T6 aluminium alloy	Cylindrical \varnothing 40 mm	V = 2000–3000 rpm, f = 0.02–0.10 mm/rev, d = 0.04–0.12 mm $\alpha = 5^\circ$, $r_e = 0.05$ mm	40 μm /[12]
Two axis CNC ultra-precision lathe	cylindrical Al6061/15 SiCp composite	Cylindrical	V = 4500–8500 rpm, f = 15–55 mm/min, d = 0.5–5.6 μm $\alpha = 25^\circ$, $r_e = 0.762$ mm	1 μm /[13]
Advanced CNC ultra precision machine	Al6060	Flat surface \varnothing 10 mm	V = 100 rpm, f = 1 mm/min d = 5 μm	5 μm /[14]
CNC lathe	16MnCr55 (AISI 5115) steel	Cylindrical	V = 150 m/min, f = 100 μm /rev d = 100 μm , $\alpha = -30^\circ$, $r_e = 100$ –1200 μm	10 μm /[15]
Lathe CNC	Tungsten Carbide (V60)	Cylindrical \varnothing 60 mm	V = 10–30 m/min, f = 0.05–0.3 mm/rev, d = 0.01–0.3 mm, $\alpha = 0^\circ$	10 μm /[16]
CNC turning center	AISI 4340 Steel	Cylindrical \varnothing 25 mm	V = 125 m/min, f = 0.05 mm/rev d = 5 μg , $r_e = 0.4$ mm	5 μg /[17]
CNC lathe	pure aluminium and aluminium alloy AU4G	Cylindrical \varnothing 35 mm	V = 800 rpm, f = 10 μm /rev d = 5–20 μm , $\alpha = 5^\circ$	5 μm /[18]
High-precision CNC lathe	AISI 4340 steel	(8 mm X 1 mm) size workpiece	V = 100 m/min, f = 0.03–0.14 mm, d = 0.02–0.2 mm	20 μm /[19]
CNC turning center	aluminium alloys 7075-T6, 6061-T6, and 2024-T351	Tubular form \varnothing 50mm, thickness of 3 mm	V = 200, 350, and 500 m/min d = 0.0022–0.2222 mm	2 μm /[20]
CNC lathe	Tungsten	Cylindrical \varnothing 15 mm	V = 15 m/min f = 0.0254 mm/rev, d = 0.025–0.229 mm	25 μm /[21]
CNC ultra-precision lathe	A6061-T6 aluminium alloy	Cylindrical \varnothing 40 mm	V = 2000–3000 rpm, f = 0.02–0.10 mm/rev, d = 0.04–0.12 mm	40 μm /[22]
ultra-precision two-axis CNC diamond turning	Al 6061	Spherical surfaces with \varnothing 76 mm	V = 1500 rpm, f = 5 mm/min d = 6 μm , $\alpha = 0^\circ$, $r_e = 0.5$ mm	6 μm /[23]
CNC ultra precision Machine	AISI 420 stainless steel	Cylindrical \varnothing 15 mm	V = 44 m/min, f = 5 μm /rev d = 20 μm	20 μm /[24]

is known as Minimum Uncut Chip Thickness (MUCT) and this is also called as ploughing effect. The MCT is depending upon nose radius, rake angle and MUCT. The metal removal will not take place or chip will not be formed during the machining while set the depth of cut value lesser than critical value. Therefore, it is necessary for designing and finds the MUCT and MCT to ensure micro turning to occur. In order to control the machining accurately, a fast tool servo system and actuator are used as accessories in the conventional CNC machine tool. The fast tool servo system designed for accurately controlling the tool position in conventional CNC machine [9,26–27]. From the literature, it is also clear that only limited authors were involving in the micromachining using conventional CNC machine tool. In the present work, it is attempted to perform the micromachining using conventional CNC machine. It is also attempted to decrease the MCT without changing nose radius for removal of metal in the range of few micro meters as in the case of micromachining. It is also attempted for determining the better machining condition to attain minimum roughness of the machined surface.

2. Material and methods

Al 19000 alloy (IS: 733) in the form cylindrical rod having mean diameter 9.164 mm was taken as workpiece with the following chemical composition 0.7% Fe, 0.5% Si, 0.2% Mg, 0.1% Cu, 0.1% Zn, 0.1% Mn and balance %Al. The mechanical properties of aluminium alloy are such as tensile strength of 147 N/mm², elongation of 13.2% and its Vickers hardness number is 42. Cermet insert with a rake angle (α) of 10° and a nose radius (r_e) of 100 μm was used as cutting tool. A CNC turning centre was used for conducting the experiments. The workpiece was electroplated with nickel for a thickness of 30 μm in order to remove the metal as minimum as possible in microns level. This is explained in the next section, under the heading of “Stages of micromachining process”. The plain workpiece and electroplated workpiece are shown in Fig. 1.

The turning experiments were designed using Design of Experiment (DOE) with help of Minitab 14.0. A L9 orthogonal array was chosen for conducting experiments based on Taguchi method. The



Fig. 1. Aluminium rod a) After Electroplating b) Before Electroplating.

Table 2
Machining parameters and levels.

Parameter	Designation	Level 1	Level 2	Level 3
Cutting speed (m/min)	V	23	35	46
Feed ($\mu\text{m}/\text{rev}$)	f	0.07	0.14	0.21
Depth of cut (μm)	h	120	130	140

input variables considered for this investigation are cutting speed, feed and depth of cut. The considered input machining parameters and their levels and values are presented in Table 2.

After each experiment, the final diameters of workpiece and surface roughness were measured at three places and average value has been considered for the analysis. Using Taguchi method, cutting parameters were optimized for minimum surface roughness. The experimental data were also used for proving that micromachining is achieved by this procedure using CNC machine in single pass.

2.1. Micromachining process stages:

Step 1: In this stage, the MUCT and MCT of unplated aluminium rod was determined using theoretical model [28]. Based on the model, the relationship between parameters in micromachining was derived and it is shown Fig. 2.

Using this theoretical model as given in following Eqs. (1)–(4), the stagnant angle (θ_m), Minimum Uncut Chip Thickness (MUCT/

h_m) and Minimum Cutting Thickness (MCT) were found out for unplated aluminium rod.

$$\alpha = \pi/2 - \theta_m \quad (1)$$

$$\text{MUCT}/h_m = r_e(1 - \cos\theta_m) \quad (2)$$

$$\text{MCT} = (h - h_m) \quad (3)$$

$$\text{MCT}_e = (h - h_m - T) \quad (4)$$

where, MUCT = Minimum Uncut Chip Thickness (μm), MCT = Minimum Cutting Thickness (μm), MCT_e = effective Minimum Cutting Thickness (μm), θ_m = Stagnate Angle ($^\circ$), A = Stagnate point, r_e = nose radius (μm), α = rake angle ($^\circ$), h = depth of cut (μm), T = Plating Thickness (μm). The MUCT was found to be $82.63 \mu\text{m}$ metal using this model. As per the model, MUCT is constant of all depth of cuts while the MCT varies with the depth of cut. The MCT values found using this model for various depth of cut values are given in Table 3. For metal cutting to be taken place by avoiding ploughing effect, the depth of cut given should be more than MUCT, which is $82.63 \mu\text{m}$ in this case. The objective of the work is to remove material less than $82.63 \mu\text{m}$. Therefore an aluminium rod is electroplated and then metal cutting is carried out. When the rod is machined after electroplating the effective base material removed (MCT_e) will be less than the MUCT $82.63 \mu\text{m}$ ($\text{MCT}_e = \text{MCT} - \text{plating thickness}$).

Step 2: Electroplating process

The chosen rod was electroplated for $30 \mu\text{m}$ thickness. In the electrolytic plating process, the aluminium and nickel bar are connected to cathode and anode terminal respectively. The mechanical stirrer was used for uniform metal deposition on aluminium. The details of electrolyte and operating conditions are shown in Table 3. Before electroplating, the following pre-treatment steps were done.

1. Sinking in the NaOH solutions at 3 min.
2. Washing with distilled water thoroughly.
3. Sinking in zincoating solutions at 3 min.
4. Again washing with distilled water.
5. Finally, the aluminium rod was kept in the electrolytic bath for electroplating.
6. The operating conditions are selected depending on the plating thickness that is $30 \mu\text{m}$.
7. Electroplating was done.

Step 3. Measurement of Nickel plating thickness

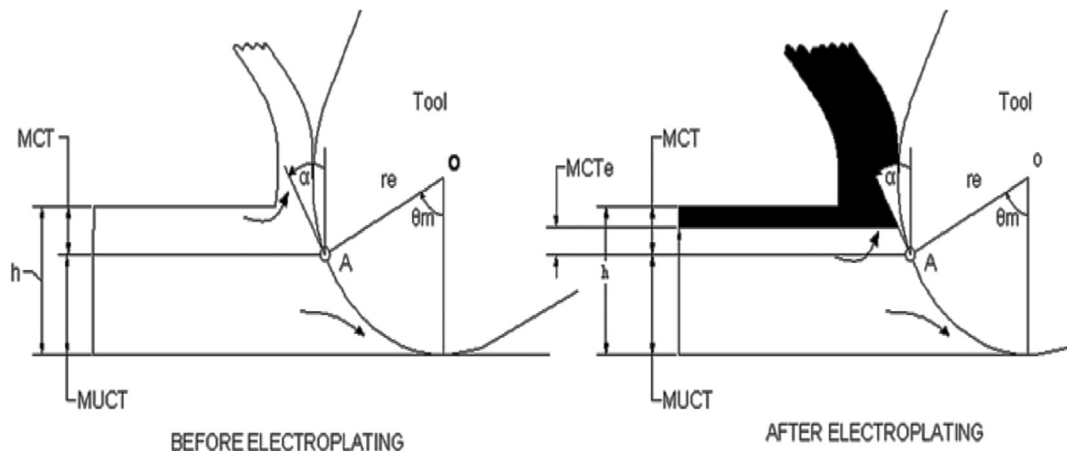


Fig. 2. Relationship of parameters in Micromachining.

Table 3
Electrolyte and operating conditions of the Nickel electroplating baths.

Ingredients	Percentage/value
Nickel sulphate (M)	0.2
Boric acid (M)	0.4
Cobalt sulphate (M)	0.06
Ferrous sulphate (M)	0.06
Ammonium chloride (M)	0.3
Ascorbic acid (g/l)	0.5
Ph	3.5
Temperature (°C)	25
Current (amps)	1
Time (min)	30
Surface area (cm ²)	18.24
Rate of Plating (µm/min)	1.12

The nickel plating thicknesses were measured by a gauge for coating thickness (MAKE: Metrix 25 FN). The plating thickness of rod is along the circumference at a regular interval of 45°. This measurement was repeated for the entire length of rod and plating profile was plotted as shown in Fig. 3.

Step 4: The micro turning was carried out on the electroplated aluminium rod as per the experimental design. The MCT_e and MUCT values for electroplated aluminium rod were predicted using the analytical model developed [28].

The MCT_e value was also determined experimentally. The diameter of aluminium rod before plating and diameter of aluminium rod after machining were measured using Coordinates Measuring Machines (CMM). The lower plating thickness has been considered for analysis. The diameters were measured three times at various places and average value taken for analysis. The values predicted by the model and the values determined using experiments were compared. The values are shown in Table 4.

3. Results and discussion

3.1. Micromachining analysis and variations

When using the analytical model [28], the MUCT while turning the bare aluminium rod is predicted as 82.63 µm. This portion of material is plastically deformed and flows under the tool surface. The remaining material which is called as MCT is removed by the tool.

The MCT and MCT_e are predicted by the model while turning bare unplated rod and plated rod while turning with different depth of cut are given in Table 4. The actual MCT_e measured by the experiment are also given in Table 4. From these values, it is proved that using conventional CNC machine tool, it is possible to avoid the ploughing effect and it is also possible to achieve metal

removal in the order of few micrometres. Above all, differences between the actual depths of cut given and the (MCT -plating thickness) is the actual metal removal (MCT_e) from the parent metal. In the Table 4, the fifth column shows the MCT_e values achieved experimentally are less than the plated thickness. Hence it is also proved that very little amount of metal (in the order of few µm) can be removed from actual parent metal using CNC machine by this way. It is also shown that the variance between the theoretical MCT_e and the experimental MCT_e is very less and in the acceptable range. This actual metal is removal from the parent metal matches with the metal removal by micromachining. The averages of actual minimum metal removal from parent metals are 6.4 µm, 14.98 µm and 24.97 µm for the depth of cut values of 120 µm, 130 µm and 140 µm respectively [26].

3.2. Optimization of surface roughness

The calculated S/N ratio of surface roughness is shown in Table 5. The S/N ratio graph is shown in Fig. 4. The Fig. 4 shows the variation of surface roughness against the process parameters. The cutting speed was increased with decrease surface roughness and increased. The feed rate was increased with increase surface roughness. The depth of cut was increased with increase the surface roughness. The increasing surface roughness was due to the tool vibration and insufficient time to get desired quality finish. ANOVA is a statistical tool employed to determine the influence of process variables on the desired performance measures. ANOVA is computed using statistical software Minitab 18.0. The characteristic of surface roughness is taken as smaller the best and it is calculated equation as shown in following Equation (5).

$$S/N\text{Ratio} = -10 \log_{10} 1/n \text{ (sum of mean of square of surface roughness)} \quad (5)$$

The ANOVA for surface roughness is calculated and presented in Table 6. From the outcomes of ANOVA, it is revealed that feed rate (81.07%) is the most influencing factor and it is followed by cutting speed (15.47%) and depth of cut (3.46) respectively. The results of ANOVA analysis is shown in Table 6. Taguchi's single objective optimization approach is employed for analysing the surface roughness. The Taguchi's response is shown in Table 7 and it is make known that the best possible set of machining variables is $V_2 f_1 h_1$ which means the cutting speed is 35 m/min, feed is 0.07 µm/rev and depth of cut is 120 µm. From the Taguchi's response analysis, it is demonstrated that the results have close relationship with ANOVA analysis.

3.3. Surface integrity

A surface of Aluminium 19000 rod produced by micromachining by the present method is discussed here. During machining,

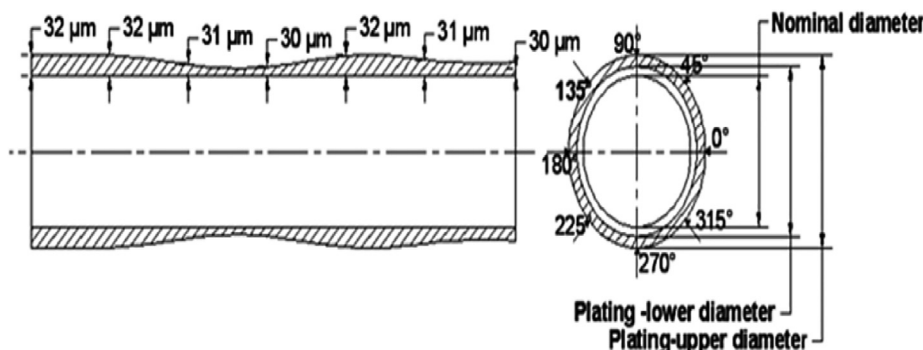


Fig. 3. Profile of plating thickness.

Table 4
Minimum Cutting Thickness Details.

No	h (μm)	Model		Experimental MCT _e (μm)	Variation (%)	Final diameter of rod (mm)
		Before plating MCT (μm)	After plating Theoretical MCT _e (μm)			
1	120	37.37	7.37	6.26	-15.06	9.151
2	130	47.37	17.37	13.94	-19.76	9.136
3	140	57.37	27.37	24.55	10.30	9.115
4	130	47.37	17.37	16.59	4.45	9.131
5	140	57.37	27.37	24.54	-10.35	9.115
6	120	37.37	7.37	6.38	-13.47	9.151
7	140	57.37	27.37	25.82	5.67	9.112
8	120	37.37	7.37	6.57	10.88	9.151
9	130	47.37	17.37	14.42	16.98	9.135

Table 5
Signal to Noise ratios of experimental results for surface roughness.

No.	V	f	h	Surface Roughness (μm)	Calculated S/N Ratio for surface roughness (dB)
1	1	1	1	0.89	1.012
2	1	2	2	2.34	-7.384
3	1	3	3	4.25	-12.567
4	2	1	2	0.96	0.354
5	2	2	3	1.38	-2.797
6	2	3	1	3.75	-11.480
7	3	1	3	2.96	-9.425
8	3	2	1	2.37	-7.495
9	3	3	2	4.18	-12.423
Mean				2.56	-6.911

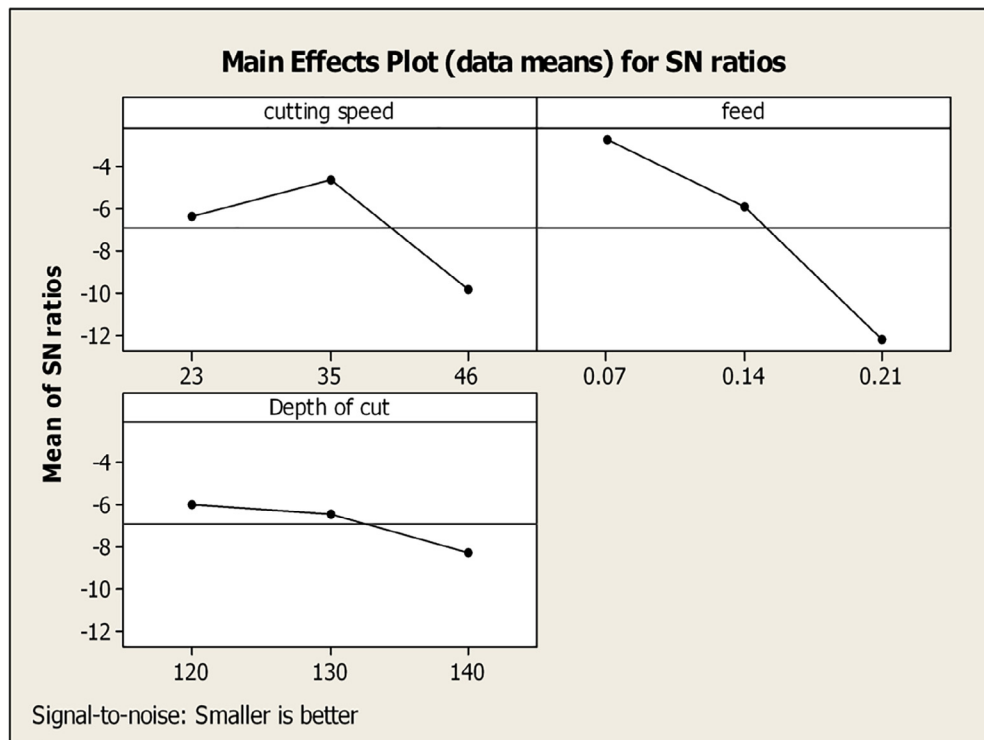


Fig. 4. The graphic of mean S/N ratio versus factor level.

the associated surface structures are subjected to changes which are the result of plastic deformation. The surface integrity depends on the conditions and environments of machining. The topography of machined work sample surface was assessed using SE Microscopy (SEM). From Figs. 5 to 7, it is clear that the surface produced in the present work is on par with surface

produced in specialized micromachining. The present work produces surface with cavities, grooves and flaws. The cavities of diameter are ranging from 11 μm to 17 μm and short grooves width ranging from 1.8 μm to 2 μm and length ranging from 3.7 μm to 3.9 μm are also shown. The flaw of diameter is 18 μm . These surface integrity is good agreement with other

Table 6
ANOVA for Surface Roughness.

Source	DF	SS	MS	F	P	CP
V	2	1.972	0.986	1.74	0.365	15.47
f	2	10.338	5.169	9.12	0.099	81.07
h	2	0.438	0.219	0.39	0.721	3.46
Error	2	1.133	0.566			
Total	8	13.882				100

S = 0.752 R-Sq = 91.84% R-Sq(adj) = 67.35%.

Table 7
Taguchi analysis for mean Signal to Noise Ratios.

level	1	2	3	Rank
V	-6.313	-2.686*	-5.988	2
f	-4.641*	-5.892	-6.484	1
h	-9.781*	-12.157	-6.264	3

* Bold values indicate the optimal point.

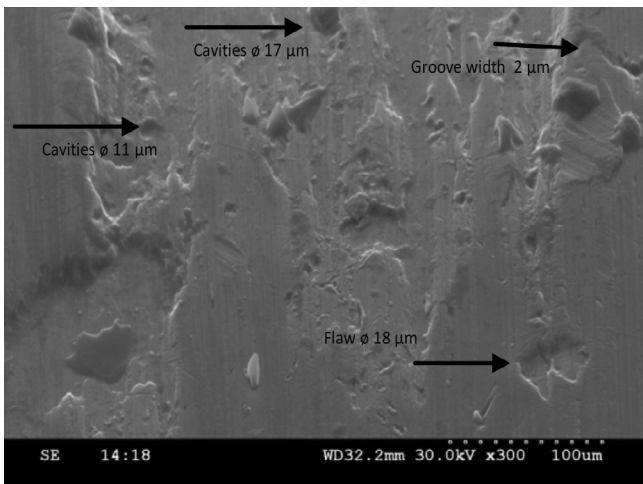


Fig. 5. SEM micrograph (h = 120 µm, f = 0.14 µm/rev, V = 35 m/min).

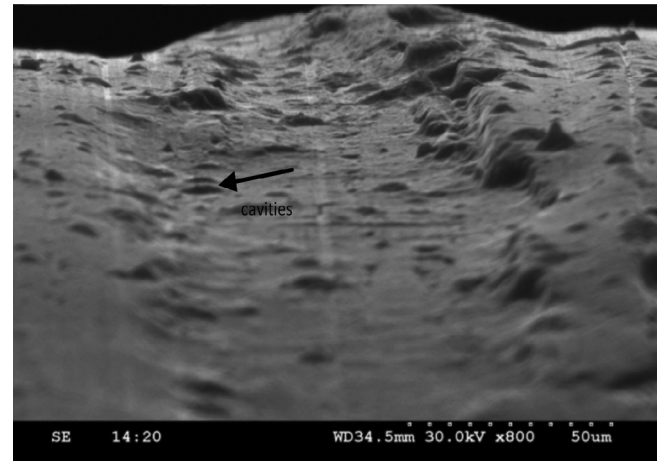


Fig. 6. SEM micrograph (h = 120 µm, f = 0.07 µm/rev, V = 46 m/min).

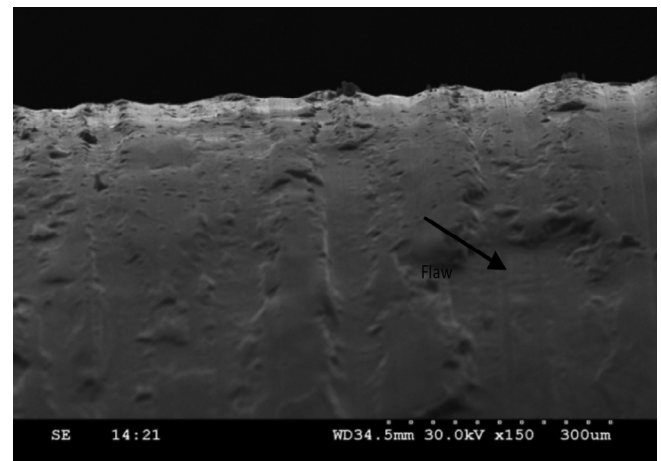


Fig. 7. SEM micrograph (h = 130 µm, f = 0.14 µm/rev, V = 23 m/min).

researcher results studied [3,24] and used while dedicated micromachine tool and ultra-precision machine tool.

3.4. Confirmation tests

Confirmation test is used to find whether the considered machining variables have the ability of producing better results than outcomes obtained in the primary part of the experiment. The optimal value of S/N ratio is to determined best possible set of process variables on performance characteristics. V2f1h1 is an optimum parameter for aluminium. The assessed S/N ratio, (S/N)_{pred} using the best possible level of the input process variables can be estimated by Equations (6)–(8).

$$(S/N)_{pred} = \eta + \sum_{i=1}^p (\eta_{opt} - \eta) \tag{6}$$

$$\eta = 1/n_t \sum_{i=1}^{n_t} \eta_i \tag{7}$$

where η_{opt} is the mean S/N ratio for i-th parameter at the optimal level, p is the number of parameters that significantly affect the quality characteristic, η is the total mean S/N ratio, n_t is the total number of trials, and η_i is the S/N ratio in i-th trial in the OA.

$$\eta = -6.911 \text{ dB}$$

$$(S/N)_{pred} = -3.286 \text{ dB}$$

However, in order to statistically judge the closeness of predicted to observed data, the confidence interval was determined. Confidence interval for the expected results from the confirmation experiment is calculated using the Eq. (8).

$$CI = \pm \sqrt{F_{\alpha}(1, f_e) V_e [1/n + 1/R]} \tag{8}$$

where, $F_{\alpha}(1, f_e)$ is the F-ratio at a significance level of $\alpha\%$, α is the risk, f_e is the error degrees of freedom, v_e is the error mean square, n is the effective total number of tests and R is the number of confirmation tests.

$$n = \text{Total number of observations} / (1 + \text{Total degree of freedoms associated with items used})$$

$$F_{0.05(1,2)} = 18.5 \text{ (tabulated)}$$

$$V_e = 0.566 \text{ (from Table 6)}$$

Table 8
Results of the confirmation experiment for surface roughness.

	Initial Cutting Condition	Optimal Cutting Parameters	
		Prediction	Experiment
Level	V2f1h2	V2f1h1	V2f1h1
Surface Roughness (μm)	0.96	1.46	0.95
S/N ratio (dB)	0.354	-3.286	0.445

$$n = 9/(1 + 6) = 1.28$$

$$R = 1$$

$$CI = \pm 4.32$$

The 95% confidence interval of the predicted optimal value of S/N ratio for surface roughness is:

$$((S/N)_{\text{pred}} - CI) < (S/N)_{\text{pred}} < ((S/N)_{\text{pred}} + CI)$$

$$1.034 < (S/N)_{\text{pred}} < -7.606$$

Optimal value of the surface roughness can be calculated as:

$$SR_{c, \text{opt}} = 10^{((S/N)_{\text{pred}}/20)}$$

$$SR_{c, \text{opt}} = 1.46 \mu\text{m}$$

Table 8 shows the results of the confirmation experiment using the optimal cutting parameters of surface roughness. Good agreement between the predicted machining performance and actual machining performance is shown.

4. Conclusions

Thus, micromachining has been achieved by CNC machine on Al 19000 rod without altering tool dimension and optimal machining parameters were determined. Taguchi's techniques and ANOVA were used for optimizing the process parameters.

- The metal removal of 15 μm is achieved using CNC turning center without changing tool geometry/avoids ploughing.
- The difference in theoretical MCT_e and experimental MCT_e is in the acceptable range.
- It is revealed from the results of confirmation test that the selected optimal combination machining variables were confirmed the improvement in performance characteristics.

- The SEM images of micromachined surface showed the cavities, flaw, groove and also proves that surface quality produced by other micromachining.

Acknowledgements

All authors wish to thank NTUT, Taiwan, MAM School of Engineering, Tiruchirappalli and Sri Angalamman Industries, Thuvakudi, Tiruchirappalli for all support required to carry out this research.

References

- [1] S.P. Leo Kumar, J. Jerald, S. Kumanan, R. Prabakaran, Mater. Manuf. Process. 29 (11–12) (2014) 1291–1337.
- [2] M. Azizur Rahman, M. Rahman, A. Senthil Kumar, H.S. Lim, Int. J. Mach. Tools Manuf. 6 (45, 2005,) 631–639.
- [3] M. Azizur Rahman, M. Rahman, A. Senthil Kumar, H.S. Lim, A.B.M.A. Asad, Int. J. Adv. Manuf. Technol. 27 (9) (2006) 939–944.
- [4] P. Ranjith Kumar, A.S.S. Balan, S. Gowri, Int. J. Precis. Eng. Manf.-Green Technol. 1 (3–4) (2010) 343–355.
- [5] A. Gupta, S.V. Ramagopal, A. Batish, A. Bhattacharya, Mater. Manuf. Process. 29 (5) (2014) 606–613.
- [6] A. Kadirvel, P. Hariharan, S. Gowri, Mater. Manuf. Process. 28 (4) (2013) 390–396.
- [7] D. Chang, P. Shen, J. Hung, S. Lee, H. Tsui, Mater. Manuf. Process. 26 (12) (2011) 1451–1458.
- [8] W.B. Lee, C.F. Cheung, Int. J. Mech. Sci. 43 (4) (2001) 961–991.
- [9] Wen-Hong Zhu, Martin B. Jun, Yusuf Altintas, Int. J. Mach. Tools Manuf. 41 (7) (2001) 953–965.
- [10] Y.K. Sze, W.B. Lee, C.F. Cheung, S.S. To, J. Mater. Process. Technol. 180 (1–3) (2006) 305–309.
- [11] Z.W. Zhong, G. Lin, Int. J. Mach. Tools Manuf. 27 (11) (2006) 1077–1081.
- [12] C.C. Chen, K.T. Chiang, Int. J. Mach. Tools Manuf. 57 (2011) 1101–1116.
- [13] S. Shekhar Roy, J. Mater. Process. Technol. 173 (3) (2006) 337–344.
- [14] L.B. Kong, C.F. Cheung, Comput. Ind. EngComput. Ind. Eng 61 (1) (2011) 216–225.
- [15] R. Meyer, J. Köhler, B. Denkena, Int. J. Mach. Tools Manuf. 58 (9) (2012) 933–940.
- [16] H.S. Jung, KSME Int. J. 18 (5) (2004) 770–779.
- [17] A. Woronko, J. Huang, Y. Altintas, Precis. Eng. 27 (4) (2003) 335–345.
- [18] P. Revel, H. Khanfir, R.Y. Fillit, J. Mater. Process. Technol. 178 (1–3) (2006) 154–161.
- [19] W.B. Rashid, S. Goel, X.C. Luo, J.M. Ritchie, Wear 302 (1–2) (2013) 1124–1135.
- [20] N. Fang, Q. Wu, Int. J. Mach. Tools Manuf. 45 (10) (2005) 1178–1187.
- [21] J. Schoop, M. Effgen, T.J. Balk, I.S. Jawahir, Procedia CIRP 8 (2013) 357–362.
- [22] C.C. Chen, K.T. Chiang, C.C. Chou, Y.C. Liao, Int. J. Mach. Tools Manuf. 54 (5) (2011) 465–478.
- [23] M. Zhou, B.K.A. Ngoi, X.J. Wang, Tribol. Lett. 15 (3) (2003) 211–216.
- [24] W.Y.H. Liew, Y.G. Lu, X. Ding, B.K.A. Ngoi, S. Yuan, Tribol. Lett. 17 (4) (2004) 851–857.
- [25] I. Piotrowska, C. Brandt, H.R. Karimi, P. Maas, Int. J. Mach. Tools Manuf. 1 (45, 2009,) 33–40.
- [26] H.C. Yahya, Mater. Manuf. Process. 28 (10) (2013) 1053–1060, <https://doi.org/10.1080/10426914.2013.773015>.
- [27] K. Izzet, A. Gokhan, A. Kerim, Mater. Manuf. Process. 27 (5) (2012) 538–544.
- [28] M. Malekian, M.G. Mostofa, S.S. Park, M.B.G. Jun, J. Mater. Process. Technol. 212 (3) (2012) 553–559.



Contents lists available at ScienceDirect

Materials Today: Proceedings

journal homepage: www.elsevier.com/locate/matpr

Machinability study on CFRP composite using Taguchi based grey relational analysis

N. Jeyaprakash^{a,b,*}, Che-Hua Yang^{a,b}, D. Raj Kumar^c

^a Centre of Mass Customization Additive Manufacture, National Taipei University of Technology, Taiwan, ROC

^b Institute of Manufacturing Technology, National Taipei University of Technology, Taiwan, ROC

^c Department of Mechanical Engineering, MAM School of Engineering, Tiruchirappalli, India

ARTICLE INFO

Article history:

Received 27 June 2019

Received in revised form 28 July 2019

Accepted 23 August 2019

Available online xxx

Keywords:

Micro drilling

CFRP

Taguchi design

Grey relational analysis

Multi response optimization

ABSTRACT

This paper describes the effects of operating parameters for micro drilling of the carbon fibre reinforced polymer. An effect of cutting speed and feed rate on the entrance diameter, exit diameter, entrance circularity and taper angle are analysed. Taguchi array was used to conducting an experiment. Analysis of variance was used to find the most influence factors. Grey relational analysis was used to find optimum levels. The results indicating that feed rate was most influencing factor than cutting speed.

© 2019 Elsevier Ltd. All rights reserved.

Selection and peer-review under responsibility of the scientific committee of the International Conference on Mechanical and Energy Technologies.

1. Introduction

The necessity of making micro hole in Carbon-Fibre Reinforced Polymer (CFRP) in applications like PCBs, doors in flight, bridges and walkways in structural application, satellite antenna, computer body panels and hence these applications demands the micro drilling process with an accurate dimension [1]. The hole diameter in these components are generated by micro drilling process which various from 0.3 mm to 1 mm. Therefore, an attempted has been made in micro drilling of CFRP material. In recent years, many challenges are involved through the manufacturing industries to making the micro-holes in the CFRP components which involves adequate machining condition, tool geometry, tool material and dimensional tolerance of machined components. Due to the presence of high strength carbon fibres the micro drilling of CFRP components becomes more difficult which leads to damages like improper hole size, overcut, delamination, circularity error, matrix thermal degradation and fibre pull-out. Therefore, selection of process parameters, tool material with its geometry and drill size are important consideration when prior to material processing [2]. While conducting the micro drilling process, thrust forces is devel-

oped which is causing problems like improper hole dimension in both entry and exit, entrance circularity, delamination, overcut, taper angle and resin or fibre pull-out. Therefore, this is essential to know the mechanisms and the kinetics of drilling processes to avoid these difficulties and to obtain the required quality of the drilled micro-hole [3]. The stability in machined hole dimension and interface quality is achieved by a very precise and accurate micro drilling. Krishnamoorthy et al. [4] have used 12 mm, 8 mm and 4 mm drill diameters and it made of solid carbide tool material to cut CFRP. A mathematical model developed on delamination factor using artificial neural network. An error between an experimental value and a predicted value has calculated and it is an acceptable limit. Krishnaraj et al. [5] used 5 mm drill diameter to cut CFRP composites. The thrust force, circularity, hole size, delamination is considered for analysis. It is concluded that the rate of feed has an impact on thrust force, hole size, delamination and cutting speed is impact on the circularity. Xu et al. [6] carried out that the machinability study on CFRP composite. Authors found that the minimum hole defects were produced at high spindle speed and low feed rate. The following authors [7–14] reported that the hole diameter, circularity, taper angle were highly depending on cutting parameters, tool material and its geometry. In order to obtain nominal hole size, minimum circularity and minimum taper angle, it is necessary to perform optimization techniques using design of experiment to find optimal machining parameters. In many manu-

* Corresponding author at: Centre of Mass Customization Additive Manufacture, National Taipei University of Technology, Taiwan, ROC.

E-mail addresses: prakash@ntut.edu.tw (N. Jeyaprakash), chyang@ntut.edu.tw (C.-H. Yang).

<https://doi.org/10.1016/j.matpr.2019.08.212>

2214-7853/© 2019 Elsevier Ltd. All rights reserved.

Selection and peer-review under responsibility of the scientific committee of the International Conference on Mechanical and Energy Technologies.

facturing industries the Taguchi method employed for enhancing the quality of product [15]. Taguchi method focuses on optimizing single response for given problem. To get better quality product more responses is considered and addresses the multiple response problems. In this paper, grey relational analysis is used to solve multi response optimizations of drilling parameters of micro drilling CFRP by the Taguchi method. Tosun [16] used the GRA for resolving the optimal drilling parameters. The surface roughness and burr heights were considered as the output. Lin et al. [17] used the GRA method for optimization of the electrical discharge machining process parameter. The GRA is used for finding the multiple responses [18]. Finally, analysis of variance (ANOVA) is used to point out the most influential parameters and test has been conducted to confirm and the test result is validated.

2. Material and method

2.1. Material

The CFRP made of carbon/epoxy fibre laminated composite. The CFRP composites were commonly fabricated using auto clave method. This fabrication method gave defects free quality samples and also this method was used by most previous researchers. As per the mixture rule, 55% fibre weight used as epoxy resin, 0°/90° fibre orientation with 12 alternative carbon fibre layers with 3 mm sheet thickness. The composites are manufactured by M/s GALARK industry.

2.2. Grey relational analysis

The desired quality characteristics for hole diameter, circularity and taper angle are considered as lower the better. Therefore, the normalization of experimental value was calculated by using Eq. (1).

$$Z_{ij} = \frac{\max y_i(k) - y_i(k)}{\max y_i(k) - \min y_i(k)} \quad (1)$$

where Z_{ij} was the normalized data, $\max y_i(k)$ was the largest value of $y_i(k)$ for the k th response. $y_i(k)$ was the k th response of the i th experiment and $\min y_i(k)$ was the smallest value of $y_i(k)$ for the k th response. The grey relational coefficient (GRC) was calculated by using Eq. (2).

$$\gamma_i(k) = \frac{\Delta_{\min} + \zeta \Delta_{\max}}{\Delta_{oi}(k) + \zeta \Delta_{\max}} \quad (2)$$

where $\gamma_i(k)$ is the grey relational coefficient of the i th experiment for the k th responses, $\Delta_{oi} = \|y_o(k) - y_i(k)\|$ that is the difference between $y_i(k)$ and $y_o(k)$ is denote the absolute value. $y_o(k)$ is denoting the reference sequence. Δ_{\max} denote the largest value of $\Delta_{oi}(k)$, Δ_{\min} is the smallest value of $\Delta_{oi}(k)$. The grey relational grade (GRG) $\bar{\gamma}_j$ is calculated and shown in Eq. (3).

$$\bar{\gamma}_j = \frac{1}{k} \sum_{i=1}^m \gamma_{ij} \quad (3)$$

where $\bar{\gamma}_j$ is the grey relational grade for the each experiment and k denotes the number of performance characteristics.

2.3. Experimental procedure

Drilling tests were conducted using HARDINGE VMC 800II based on L9 orthogonal array. Cutting speed and feed rate were varied as per design. The drill tools were made of solid carbide with round cross section of 0.3 mm. The overall length of the tool is 38 mm. The machining was carried out by dry condition. In the

present study, two factors (cutting speed and feed rate) and three levels were selected by Minitab 18 statistical software. The minimum number of experiments is sufficient to produce the accurate results than L27. It will reduce the time consumption, material usage etc. Also, L9 orthogonal array was recommended by most of the authors. Therefore, the three-level and two factor Taguchi method have been used for this experiment. The machining conditions were selected based on the previous literature and machine specification [19,5]. The parameters that are identified and their levels are given in Table 1. The CFRP laminates is shown in Fig. 1. It was chosen for this study. These composites were produced by autoclave method. The specification of vertical machining centre was used is given in Table 2. The profile of the holes was measured using non-contact video measuring system (Make: Rational Precision Instruments, Model: VMS 2010F, Japan) and it is shown in Fig. 2. Schematic representation of circularity is shown in Fig. 3. The calculated entrance circularity is the distance between the minimum circumscribing circle diameter and the maximum inscribing circle diameter. The hole taper angle was calculated using Eq. (4).

$$\text{Taper angle } (\theta) = \tan^{-1}(D - d)/2t \quad (4)$$

3. Results and discussions

3.1. Entrance diameter

From the graph of main effects, the entrance hole diameter is shown in Fig. 4(a). It shows that the entrance diameter of hole increases with speed. This is due to the reason the frictional heating the machining temperature increases in which the larger hole diameter results obtained at high speed. At slow speed, the machining temperature reduced which results obtained in smaller hole diameter near to nominal diameter.

Fig. 4(a) also shows the influence of feed rate on entrance diameter of hole. The feed rate was significantly affecting the entrance hole diameter. The significance is proved from the ANOVA table. This is due to the selected feed rates lower than the cutting depth. The self-generated vibration in the drill was decreased with increase feed rate. Due to this effect the obtained holes were nearer to nominal diameter [5]. The level of contribution percentage of cutting speed and feed rate on entrance hole diameter is identified by using ANOVA. It is presented in Table 4(a). The results of Table 4 (a) found that it can be seen that the P value of feed rate is less than 0.05. Thus, feed rate has highly contributing towards drilling performance measures. Also, the ANOVA got the same order of importance. The feed rate is contributing more for entrance hole diameter and it is followed by cutting speed. From Table 5(a), optimum conditions were found as cutting speed: 2000 rpm, feed rate: 0.05 mm/min. The L9 orthogonal arrays with experimental results are shown in Table 3.

3.2. Exit diameter

Main effects graph for exit hole diameter are illustrated in Fig. 4 (b). It shows that the exit diameter of hole increases with speed. This is due to the reason the frictional heating the machining tem-

Table 1
Factors and levels in drilling test.

Process parameters	Notation	Levels		
		Low	Medium	High
Cutting speed (rpm)	A	2000	2500	3000
Feed rate (mm/min)	B	0.01	0.03	0.05

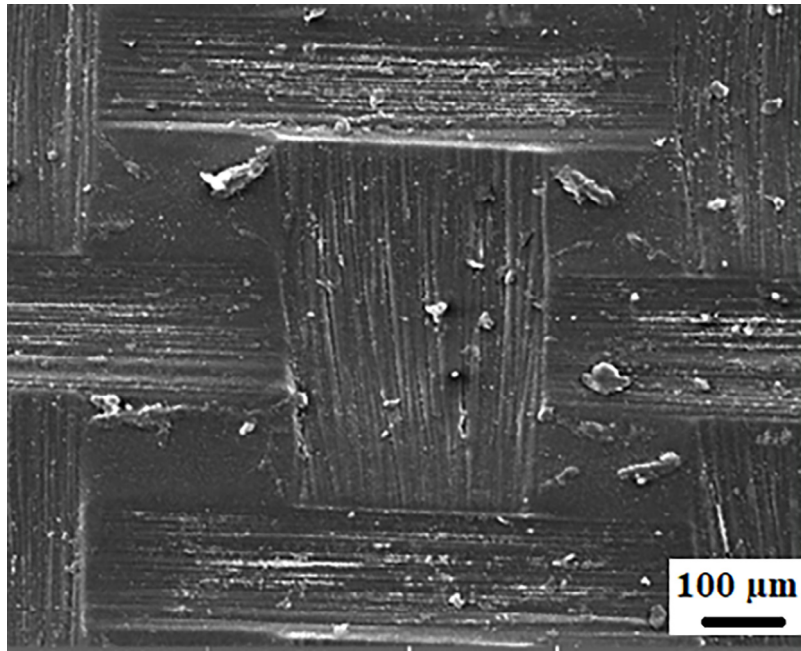


Fig. 1. SEM picture of CFRP composite.

Table 2
Specification of the vertical machining center.

Type of machine	Vertical machine center
Brand	HARDING
Model	VMC-800 II
Control	Fanuc series 18-M
Maximum Speed	12 000 rpm
Travel length	500 × 800 × 500 mm
Table size	920 × 510 mm



Fig. 2. Experimental setup of video measurement system.

perature increases which the larger hole diameter results obtained at high speed. At slower speed, the machining temperature reverse in which results obtained in smaller hole diameter near to nominal diameter [5]. Fig. 4(b) also shows the influence of feed rate on exit

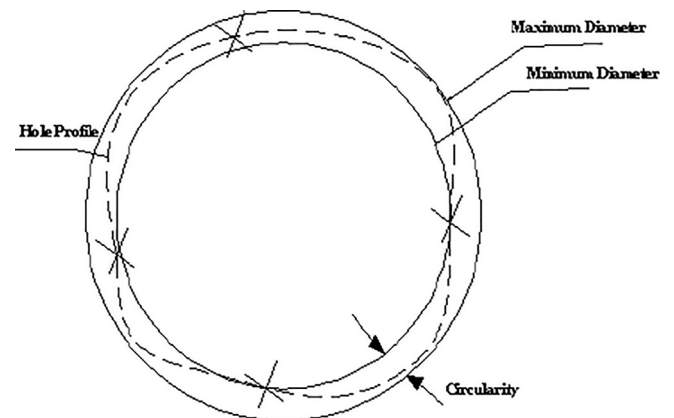


Fig. 3. Schematic representation of circularity.

diameter of hole. In general, CFRP composite has spring back properties. This may be the reason for decrease the exit hole diameter after level 2. The feed rate is also significantly affecting the exit hole diameter. It is confirmed by the results of ANOVA. It shows that the exit diameter of hole increases first then decreases with increases speed. ANOVA for exit diameter is shown in Table 4(b). From Table 5(b), optimum conditions were found as cutting speed: 2000 rpm, feed rate: 0.05 mm/min.

3.3. Entrance circularity

The main effects for entrance circularity are illustrated in Fig. 4 (c). From this figure, it is clear that the entrance circularity decreases with speed. The stability of drill is improved at higher speed than the lower speed. It denotes the lesser entrance circularity at high speed whereas at low feed rate makes higher entrance circularity. This is due to the reason of frictional heating and ploughing effect. Fig. 4(c) also shows the influence of feed rate on entrance circularity of hole. The feed rate is significantly affecting the entrance circularity. ANOVA table also got the same results. This is due to the reason that the feed rates are greater than the

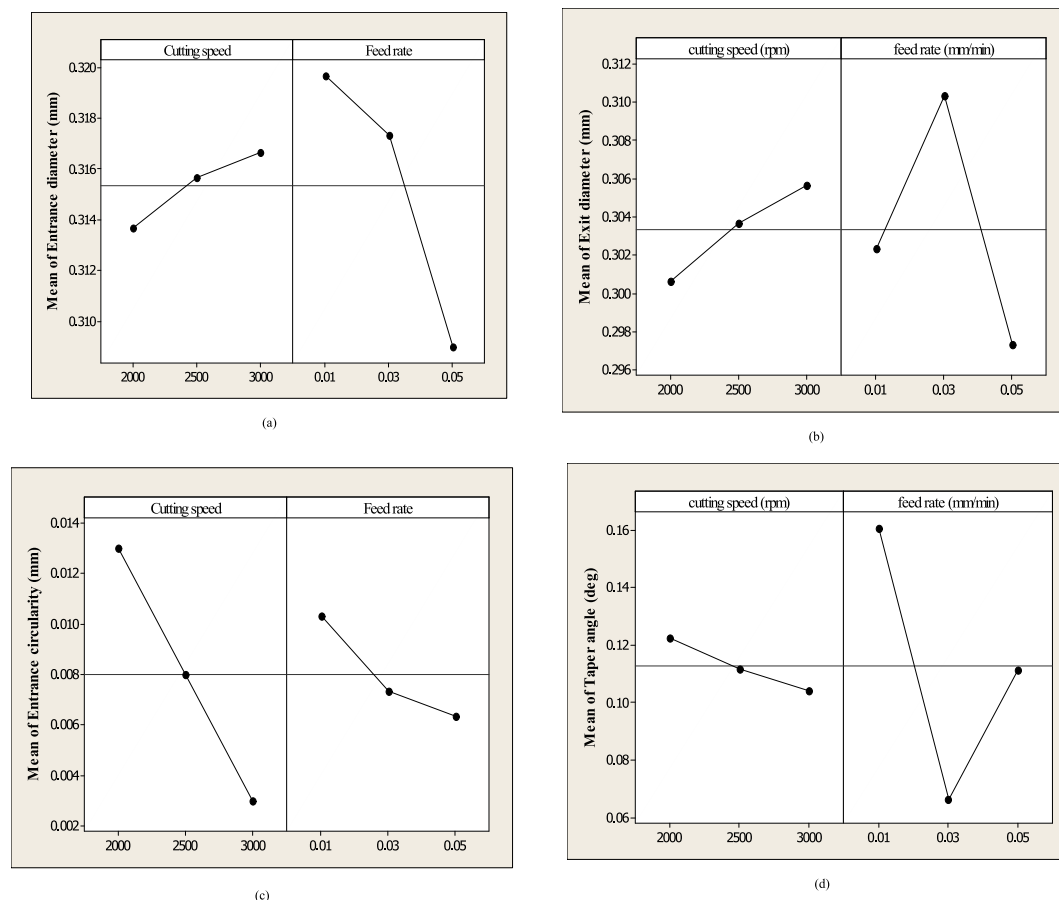


Fig. 4. Main effects plot for (a) entrance diameter, (b) exit diameter, (c) entrance circularity, (d) taper angle.

Table 3

Experimental observation based on L9 orthogonal array.

Run	A	B	D (mm)	D (mm)	C (mm)	T (deg)
1	1	1	0.317	0.297	0.016	0.182
2	1	2	0.315	0.308	0.012	0.068
3	1	3	0.309	0.297	0.011	0.118
4	2	1	0.320	0.303	0.011	0.158
5	2	2	0.318	0.311	0.007	0.066
6	2	3	0.309	0.297	0.006	0.111
7	3	1	0.322	0.307	0.004	0.142
8	3	2	0.319	0.312	0.003	0.065
9	3	3	0.309	0.298	0.002	0.105

cutting depth and self-generated vibration decreases with increases feed rate. The obtained result of entrance circularity is lesser while at high feed rate and at high speed used [5]. The level of contribution percentage of cutting speed and feed rate on entrance circularity is determined by using ANOVA. It is presented in Table 4(c). In the Table 4(c), it can be seen that the feed rate is significantly contributing to performance measures. The ANOVA also got the same results. The cutting speed is higher contributing percentage for entrance circularity and it is followed by the feed rate. In the Table 5(c), optimum conditions were noted as cutting speed: 3000 rpm, feed rate: 0.05 mm/min.

3.4. Taper angle

The main effects graph for taper angle is illustrated in Fig. 4(d). From the figure, it is clear that the taper angle decreases with cutting speed. This is because of the lower feed rate (0.01 mm/min),

the entrance side is showing to take higher time to machine and therefore the obtained machined holes are prone to higher taper angle. At higher feed rate (0.05 mm/min), dynamic instability is being the reason for larger taper angle. Fig. 4(d) also shows the influence of feed rate on taper angle. The feed rate is significantly affecting the taper angle. It is proved by the ANOVA table. It is showed that the angle of taper was reduced with increase cutting speed. This is owing to the stability of rotation in drill at higher speeds. The level of contribution percentage of cutting speed and feed rate on taper angle is calculated by ANOVA. It is presented in Table 4(d). In the Table 4(d), it is found that the feed rate P value is less than 0.05. Thus, representing the feed rate is significantly contributing to drilling performance measures. ANOVA also got same the results. The feed rate is higher contribution for taper angle and it is followed by cutting speed. From Table 5(d), optimum conditions were found as cutting speed: 3000 rpm, feed rate: 0.03 mm/min [20].

3.5. Multi response optimization

In the Grey relational analysis calculation, all the responses have considered as equal weightage, Therefore, the 0.25 weightage has been assigned to each response. Each response has been converted into normalized form depending upon the quality characteristics. The normalization of responses was calculated by using Eq. (1). The normalized data were converted into grey relational coefficient by using Eq. (2). The grey relational coefficients were converted into grey relational grade by using Eq. (3). Based the GRG value, the ranking of nine experimental conditions were provided. The highest GRG represents the higher relational between

Table 4
ANOVA for all responses.

S	DF	SS	V	F	P	CP
a) Entrance diameter						
V	2	0.000014	0.000007	3.82	0.118	6.67
f	2	0.000189	9.43E-05	51.45	0.001	89.86
E	4	7.3E-06	1.8E-06			3.48
T	8	0.00021				100.00
S = 0.00135401 R-Sq = 96.51% R-Sq(adj) = 93.02%						
b) Exit diameter						
V	2	0.000038	0.000019	3.45	0.134	11.95
f	2	0.000258	0.000129	23.45	0.006	81.13
E	4	0.000022	5.5E-06			6.92
T	8	0.000318				100.00
S = 0.000577350 R-Sq = 96.30% R-Sq(adj) = 92.59%						
c) Entrance circularity						
V	2	0.00015	0.000075	75	0.001	83.33
f	2	0.000026	0.000013	13	0.018	14.44
E	4	0.000004	0.000001			2.22
T	8	0.00018				100.00
S = 0.001 R-Sq = 97.78% R-Sq(adj) = 95.56%						
d) Taper angle						
V	2	0.000528	0.000264	2.84	0.171	3.70
f	2	0.013358	0.006679	71.86	0.001	93.68
E	4	0.000372	9.29E-05			2.61
T	8	0.014258				100.00
S = 0.00964077 R-Sq = 97.39% R-Sq(adj) = 94.78%						

Table 5
Taguchi analysis all response table by S/N ratio.

Level	Cutting speed	Feed rate
a) Entrance diameter		
1	10.071*	9.906
2	10.016	9.97
3	9.989	10.201*
Delta	0.082	0.295
Rank	2	1
b) Exit diameter		
1	10.44*	10.39
2	10.35	10.16
3	10.3	10.54*
Delta	0.14	0.37
Rank	2	1
c) Entrance circularity		
1	37.84	41.02
2	42.24	43.99
3	50.8*	45.86*
Delta	12.96	4.85
Rank	1	2
d) Taper angle		
1	18.9	15.93
2	19.58	23.57*
3	20.09*	19.08
Delta	1.19	7.64
Rank	2	1

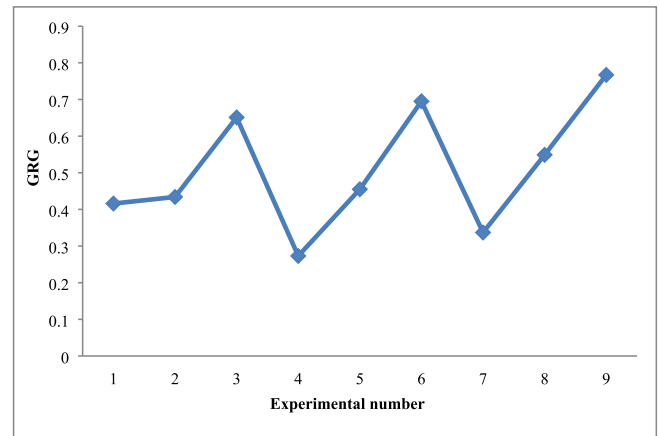


Fig. 5. Grey relational grades for the experiments.

the process parameters and responses. The GRA calculation is shown in Table 6. The graph is drawn between the numbers of experiments against the GRG. It is shown in Fig. 5. In the Figure, the ninth experiments got the optimum process parameters. The average grey relational grade value for every level of the input parameters have been computed by taking mean for every group

Table 6
Evaluated grey relational grade for the responses for machining of CFRP composites.

Run	Normalized values				Grey relational analysis				Grey relational coefficient				GRG	Rank
	D	d	C _{ent}	Θ	D	d	C _{ent}	Θ	D	d	C _{ent}	Θ		
1	0.385	1.000	0.036	0.000	0.615	0.000	0.964	1.000	0.289	1.000	0.176	0.200	0.416	7
2	0.538	0.267	0.286	0.974	0.462	0.733	0.714	0.026	0.351	0.254	0.222	0.907	0.434	6
3	1.000	1.000	0.393	0.547	0.000	0.000	0.607	0.453	1.000	1.000	0.250	0.356	0.651	3
4	0.154	0.600	0.364	0.205	0.846	0.400	0.636	0.795	0.228	0.385	0.242	0.239	0.273	9
5	0.308	0.067	0.679	0.991	0.692	0.933	0.321	0.009	0.265	0.211	0.375	0.967	0.455	5
6	1.000	1.000	0.702	0.607	0.000	0.000	0.298	0.393	1.000	1.000	0.390	0.389	0.695	2
7	0.000	0.333	0.893	0.342	1.000	0.667	0.107	0.658	0.200	0.273	0.599	0.275	0.337	8
8	0.231	0.000	0.964	1.000	0.769	1.000	0.036	0.000	0.245	0.200	0.749	1.000	0.549	4
9	1.000	0.933	1.000	0.658	0.000	0.067	0.000	0.342	1.000	0.789	0.856	0.422	0.767	1

levels of machining parameters and the values are given in Table 7. From the Table 7, the optimal process parameter is A3B3. The optimum level for machining of CFRP composites is cutting speed: 3000 rpm, feed rate; 0.05 mm/min. The ANOVA on all responses are given in Table 8. From the Table 8, the feed rate P value is less

Table 7
Optimum level selection CFRP composites.

Level	Cutting speed (A)	Feed rate (B)
1	0.500	0.342
2	0.474	0.479
3	0.551	0.704
Delta	0.077	0.362
Rank	2	1

Table 8
ANOVA on GRG.

S	DF	SS	V	F	P	CP
V	2	0.02113	0.01056	5.55	0.07	4.96
f	2	0.3973	0.19865	104.35	0.00	93.26
E	4	0.00761	0.0019			1.79
T	8	0.42604				100.00

Table 9
Results of the confirmation experiment.

Setting level	Raw data	Optimal Process parameters	
		Prediction	Experiment
	A1B1	A3B3	A3B3
D	0.317		0.311
d	0.297		0.301
C _{ent}	0.016		0.004
Θ	0.182		0.068
GRG	0.416	0.747	0.639

Improvement in grey relational grade = 0.223

than 0.05. Thus, representing the feed rate is significantly involving to drilling performance measures. ANOVA also got same results.

3.6. Confirmation test

Confirmation test was performed by utilizing the optimal machining parameters (A3B3) for entrance diameter, exit diameter, entrance circularity and taper angle as shown in Table 9. The optimum process parameters are identified based on the highest GRG value and it shows A3B3 (cutting speed at 3000 rpm and feed rate at 0.05 mm/min). After GRA calculation, the optimum process parameter for confirmation test is identified as the cutting speed at 3000 rpm and feed rate at 0.05 mm/min. Comparing the GRG value between initial and final confirmation test, the optimized parameter shows significant improvement in the performance measure. Fig. 6 exhibits the SEM images of confirmation test. The uncut fibre was observed on confirmative SEM observation.

4. Conclusion

The effects of working parameters such as cutting speed and feed rate was studied in micro drilling of CFRP material. Taguchi based grey relational analysis was used to find the optimum levels. Based on the achieved results, the following conclusions were drawn.

- Effects of cutting speed and feed rate on entrance diameter, exit diameter, entrance circularity and taper angle are analyzed and reported.
- A statistical analysis shows that the cutting speed and feed rate are significantly affecting the diameter at entry by 6.67%, 89.86% respectively.
- The cutting speed and feed rate are affecting the diameter at exit, circularity at entry, taper angle by 11.95%, 81.13% and 83.33%, 14.44% and 3.70%, 93.68%, respectively.
- The application of grey relational analysis was improved the process performance measure. From the ANOVA table, the feed rate is significantly contributing to machining performance measures and followed by cutting speed. Further, some uncut fiber was observed on confirmative SEM observation.

Acknowledgements

All authors wish to thank NTUT, Taiwan, MAM School of Engineering, Tiruchirappalli, India, Sri Angalamman Industries, Tiruchirappalli, India and Nano markers laser works, Tiruchirappalli, India for all support required to carry out this research.

References

- [1] D. Hull, T.W. Clyne, An Introduction to Composite Materials, 2nd ed., Cambridge University Press, Cambridge, 1996.
- [2] J.P. Davim, P. Reis, Compos. Struct. 59 (2003) 481–487.
- [3] P.S. Sreejith, R. Krishnamurthy, S.K. Malhota, K. Narayanasamy, J. Mater. Process. Technol. 104 (2000) 53–58.
- [4] A. Krishnamoorthy, S. Rajendra Boopathy, K. Palanikumar, J. Eng. Sci. Technol. 6 (2011) 191–203.
- [5] V. Krishnaraj, A. Prabukarthi, A. Ramanathan, N. Elanghovan, M. SenthilKumar, R. Zitoune, J.P. Davim, Compos. Part B Eng. 43 (2012) 1791–1799.
- [6] J. Xu, Q. An, X. Cai, M. Chen, Int. J. Precis. Eng. Manuf. 14 (2013) 1687–1696.
- [7] Y. Karpat, B. Deger, O. Bahtiyar, J. Mater. Process. Technol. 212 (2012) 2117–2127.
- [8] Q. An, X. Cai, J. Xu, M. Chen, IJAT 6 (2014) 183–196.
- [9] O. Isbilir, E. Ghassemieh, Compos. Struct. 105 (2013) 126–133.
- [10] R.S. Anand, K. Patra, M. Steiner, Prod. Eng. 8 (2014) 301–307.
- [11] X. Wang, P.Y. Kwon, C. Sturtevan, D. Kim, J. Lantrip, J. Manuf. Process. 15 (2013) 127–135.
- [12] K.K. Panchagnula, K. Palaniyandi, J. Mater. Res. Technol. 7 (2) (2018) 180–189.

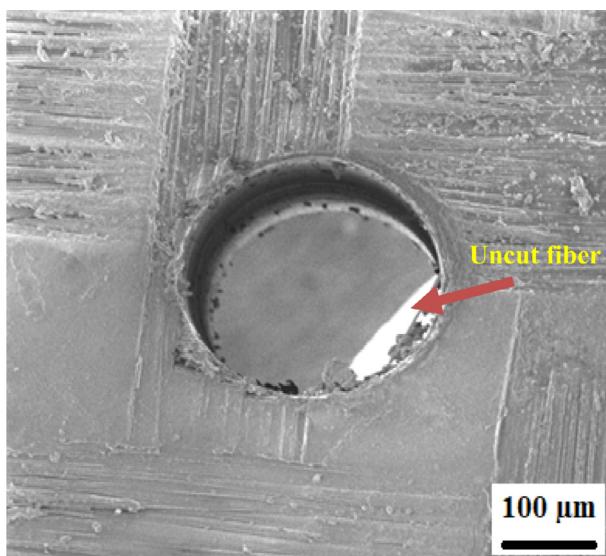
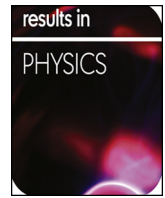


Fig. 6. SEM picture of confirmation test hole.

- [13] D. Rajkumar, P. Ranjithkumar, M.P. Jenarthanan, C. Sathiya Narayanan, *Pigm. Resin. Technol.* 46 (6) (2017) 507–524.
- [14] D. Rajkumar, P. Ranjithkumar, C. Sathiya Narayanan, *Indian J. Eng. Mater.* 24 (5) (2017) 331–338.
- [15] R. Surace, L. Filippis, A. Ludovico, G. Boghetic, *Int. J. Mater. Form.* 3 (2010) 1–5.
- [16] N. Tosun, *Int. J. Adv. Manuf.* 28 (2006) 450–455.
- [17] C.L. Lin, J.L. Lin, T.C. Ko, *Int. J. Adv. Manuf.* 19 (2002) 271–277.
- [18] R. Jeyapaul, P. Shahabudeen, K. Krishnaiah, *Int. J. Adv. Manuf.* 26 (2005) 1331–1337.
- [19] C.C. Tsao, H. Hocheng, *J. Mater. Process. Technol.* 203 (2008) 342–348.
- [20] J. Prasanna, L. Karunamoorthy, M. VenkatRaman, S. Prashanth, D. Raj Chordia, *Measurement* 48 (2014) 346–354.



Investigation of high temperature wear performance on laser processed nodular iron using optimization technique

N. Jeyaprakash^{a,b,*}, Che-Hua Yang^{a,b}, Muthukannan Duraiselvam^c, G. Prabu^c, Sheng-Po Tseng^b, D. Raj Kumar^d

^a Centre of Mass Customization Additive Manufacture, National Taipei University of Technology, Taiwan, ROC

^b Institute of Manufacturing Technology, National Taipei University of Technology, Taiwan, ROC

^c Department of Production Engineering, National Institute of Technology, Tiruchirappalli, India

^d Department of Mechanical Engineering, MAM School of Engineering, Tiruchirappalli, India



ARTICLE INFO

Keywords:

Laser material processing
Microstructure
Wear resistance
Whitelight interferometer
Roughness
Optimization

ABSTRACT

Nodular cast iron (NCI) are used in nuclear energy and transportation industries. Also, NCI are used in gear boxes, camshaft, crank shaft, rolling mill rolls and machine tool beds. The reliability of the NCI under heavy loading condition is affected through several tribological aspects. In the present study, NCI surface has been melted by using an Ytterbium-doped fiber laser. The wear resistances of the substrate and melted surface have been analyzed by using a tribometer. Sliding speed, load and working temperatures have been considered as input parameters to tribometer. From the optimization trials, the applied load was identified as the most significant parameter followed by sliding speed and ambience temperature. The responses of the optimized tribological parameters attained by GRA was confirmed through experimental and agreed closely to the predicted value. Further, the surface of the substrate and laser melted samples were analyzed. The melted surfaces were free from surface deformities and exhibited a noticeable improvement in the wear resistance compared to the substrate.

Introduction

Nodular cast iron (NCI) is an iron-carbon family. In NCI, the graphite shape is nearly spherical that shows unique properties while comparing with other cast iron. NCI has good mechanical properties with low manufacturing cost as compared to steels and it continuous as major emerging cast materials in the world [1]. Due to this reason, NCI is widely used in nuclear energy and transportation industries. Also, NCI are used in gearboxes, camshaft and crankshafts in automotive industry [2]. Some other applications include rolling mill rolls, machine tool beds, cylinders, pistons and sea water pump housings [3,4]. However, the reliability of the material under heavy loading condition is affected through several tribological aspects.

Therefore, NCI surface modification is an essential process to enhance the surface properties of parent material [5,6]. Electron Beam (EB), Thermal Spraying (TS), Laser Treatments (LT), Physical vapor coating, Powder Welding (PW) and Chemical vapor coating are employed in the surface modification techniques. Among those methods, laser treatment has found as a promising technique to modify the

surface properties due to its fast heating and cooling rates [7]. Also, this technology was used widely, especially for steel and cast iron. In laser treatment, there are many techniques such as laser hardening, glazing, cladding, alloying and melting. Among those techniques, laser melting is best surfacing technique which can modify the substrate surface without defects [8]. Zhongqi Wang et al. investigated the cladding process on grey cast iron and reported that 75 ferrosilicon has a significant impact on phase transformation, microhardness, carbon distribution, grain size and corrosion resistance of cladding area [9]. Mohammad Nabhani et al. studied on laser cladding Ti-64 alloy in various corrosive environments. The results indicated that the cladding region was showed a needle like coaxial structure. Fine metallurgical bonding was observed between the substrate and coating [10]. Yongjian Li et al. was studied the heat treatment effects on microstructure and mechanical properties of nodular iron. The cladding layers was increased the mechanical and tribological properties [11]. Liu et al. was performed the nickel laser cladding on cast iron and concluded that enhanced the mechanical properties. S. Zhou et al. [12] was investigated the crack behaviour of nickel based WC composite coatings

* Corresponding author at: Centre of Mass Customization Additive Manufacture, National Taipei University of Technology, Taiwan, ROC.

E-mail addresses: prakash@ntut.edu.tw (N. Jeyaprakash), chyang@ntut.edu.tw (C.-H. Yang), durai@nitt.edu (M. Duraiselvam), tseng3392@gmail.com (S.-P. Tseng).

<https://doi.org/10.1016/j.rinp.2019.102585>

Received 24 July 2019; Received in revised form 10 August 2019; Accepted 12 August 2019

Available online 16 August 2019

2211-3797/© 2019 The Authors. Published by Elsevier B.V. This is an open access article under the CC BY license (<http://creativecommons.org/licenses/by/4.0/>).

Nomenclature

Acronyms

S.V	Sliding Velocity (m/s)
V.L	Volume loss (mm ³)
CoF	Coefficient of friction
W. R	Wear rate in micron
DF	degree of freedom
SS	sum of squares
V	variance
P	percentage of contribution

by laser cladding methods. The outcomes indicate that cracks were produced on interfaces and substrates. Further, laser induction hybrid rapid cladding was produced and it shows free of cracks due to preheat temperature increases. S. Zhou et al. [13] was studied the effect of milling time on oxidation and microstructure formation of NiCrAlY by laser induction hybrid cladding. The results indicating that milling time is most critical parameter on microstructure and oxidation behavior. S. Zhou et al. [14] was investigated on the microstructure and tribological properties of iron based WC cladding. The results indicating that wear rate was maintaining constant with increased sliding distance and identified wear mechanisms are oxidation and abrasion.

Wear is a fashionable mechanical property of any material and it is varied by operating environments. To get a clear understanding of wear mechanism, NCI constituents and operating environments are necessary [15]. Numerous wear calculations were made by many investigators for the abrasive wear [16–21]. These wear equations were expressed volume loss of material as a function of properties such as hardness, reinforcement and operating conditions such as sliding velocity, temperature, applied load and coefficient of friction. Practical investigations of the examiners were indicated that the operating conditions such as supplied load, a sliding distance, the sliding velocity and the temperature were influenced in abrasive wear behavior [22–25]. Therefore, the abrasive wear is a phenomenon which is influenced by material properties coming interaction and the working environments. The major limitation of the archived practical investigations and wear equations are; they have not reported the influence of individual input parameters on the wear behavior.

The conventional and Taguchi technique can be applied while studying the influence of input parameters in single response optimization. However, in the tribo-chemistry issues there is a necessity to optimize the multiple outputs. To find a solution for optimization problems with multiple outputs through the above method, the optimization of each output were determined separately and now overall optimization is calculated over previous engineering knowledge. This method cannot identify the proper solution with multiple responses due to the chances of inaccurate findings [26,27]. To overcome the above issues, Taguchi based grey-relational analysis was used for the multiple output optimization. Taguchi based grey technique was used to solve the multiple responses optimization in flank milling parameters [28], turning parameters [29], welding process parameters [30] and drilling parameters [31]. Pan et al. [32] optimized the Nd: YAG laser welding parameters using Taguchi method and reported that the laser energy and pulse shape were the most influential parameter. Caydas et al. [33] investigated the laser cutting parameters on St-37 steel using grey Taguchi technique and reported that the laser power has more influence on responses rather than cutting speed. Tsao [34] applied Taguchi–Grey analysis to find the optimum milling parameter of A6061PT651 aluminium alloy and reported that the surface roughness was influenced in flank wear decreases.

From the above literature study, it is clear that there are many researchers was investigated on laser cladding, optimization of laser

parameters and mechanical properties. There is no literature study related to optimization of tribological parameters on NCI. In the present work, the surface of the NCI is melted through laser processing technique. The laser melted surfaces were tested for wear resistance under different loading conditions. The test parameters were designed by following L27 orthogonal array with varying input parameters namely applied load in the unit of N, sliding velocity in the unit of m/s, and temperature in the unit of °C. These parameters were optimized using Taguchi based GRA. Further, the cross-section of the laser-processed surface was studied to analyze the XRD, microstructure, hardness and roughness.

Materials and methods

Substrate and laser processing

The elemental composition of the NCI material is illustrated in the Table 1. The surfaces of the substrate are cleaned by SiC grit paper and followed to alumina paste prior to laser processing. The surface of substrate was laser processed with 3kW fiber laser of wavelength 1080 nm. The NCI samples are irradiated by using the argon atmosphere at 3 bar pressure to avoid the oxidation and atmospheric impurity. The selected substrate was laser treated by various working parameters. The final parameter was selected by considering the highest melt depth and defects less. The parameters with 20 mm defocus, 300 mm/min scanning speed and 1 kW power shows the surface crack on the laser processed specimen. Further, with 20 mm defocus, 600 mm/min scanning speed and 1.5 kW power shows the insufficient melt depth. However, the optimized laser parameter which is showing in Table 2 produces maximum melt depth and defect free surfaces. Fig. 1 shows the schematic of laser melting, laser melting set-up and macro picture of cross sectioned laser melted specimen.

Multi objective optimization

Taguchi methods give the different optimum process parameter for different responses. In order to convert the multi optimum process parameters for different responses into single optimum process parameters for different responses is performed by GRA. The GRA steps are described as: 1) The responses are converted into S/N ratio. It depends upon quality loss function 2) S/N ratio responses are converted into normalized form 3) The GRC are calculated from the normalized responses 4) Assign the weightage to each responses 5) The GRG is calculated from the GRC 6) The optimum process parameters are identified by taking average of each response value. It is based on the highest GRG of each response. 7) ANOVA for GRG is performed to find significant parameters. 8) Confirmation test is performed by using predicated optimum process parameters [35].

Wear test

As per ASTM G99-05 standard, the high temperature sliding wear trail was performed using a pin-on-disc tribometer (Model: TR-20LE-PHM 400-CHM 500) [36]. The pin has a cylindrical shape with 6 mm diameter and 30 mm length. The disc is made up of hardened stainless steel with 5 mm thickness and 100 mm diameter. For every test, the pin was weighed before and after the test to calculate the mass loss. The mass loss is measured by using electronic weighing machine with 0.1 mg accuracy. The volume loss and Friction coefficient responses are

Table 1
Chemical Composition of Nodular Cast Iron (SG 450–10).

Element	Fe	C	Si	Mn	P	S	Mg	Cr	Cu
Wt (%)	Bal.	3.69	3.16	0.610	0.0620	0.0220	0.0280	0.0350	0.218

Table 2
Optimized laser parameters.

Specimen	Power (kW)	Scan Speed (mm/min)	Overlapping %	Defocus (mm)
NCI	1.5	600	30	15

calculated by the standard Eqs. (1)–(3) below mentioned. Fig. 2 shows the schematic of pin-on-disc.

$$Volume\ loss\ (mm^3) = \frac{mass\ loss}{density\ (\rho)} \times 1000 \tag{1}$$

where ρ is the density

$$Sliding\ distance\ (m) = \pi DNT \tag{2}$$

Here, D denotes as wear track mean diameter in the unit of m, N denotes as the rotational speed in the unit of rpm, and T denotes as the time in the unit of min.

$$Friction\ coefficient\ (\mu) = \frac{Friction\ Force\ (F)}{Normal\ Load\ (N)} \tag{3}$$

Microstructural characterization

After laser processing, the material is sectioned for microstructure analysis and to examine the microhardness. The laser processed specimens are etched with HNO₃ and ethanol in the ratio of 10:1 to reveal the microstructure. The microhardness is measured with Wolpert

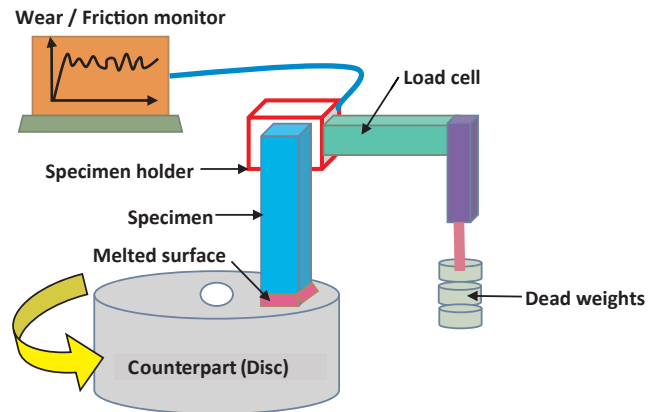


Fig. 2. Schematic of pin-on-disc.

Wilson Vickers microhardness tester by applying load of 300 g and dwell time of 10 s. The microstructure, surface morphology and surface roughness of treated and substrate samples before and after wear test are examined by Optical microscope (OM) (BX41M-LED, Olympus, Japan), scanning electron microscopy (SEM) (TESCAN) and whitelight interferometer (Rtec Instruments, USA). The Phase analysis (XRD) (Ultima IV, Japan) was performed to study the phase changes in surface layer.

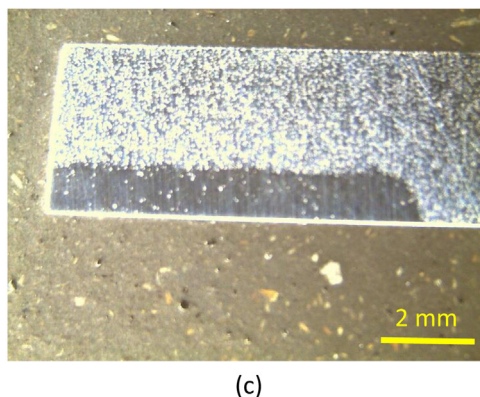
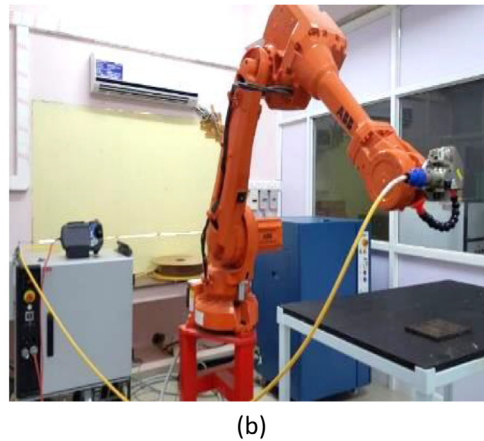
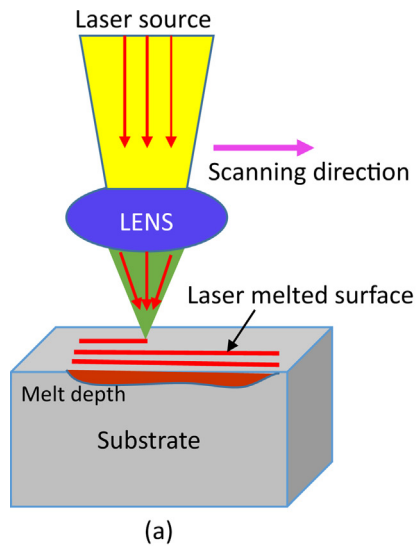


Fig. 1. (a) Schematic of laser melting, (b) photograph of laser melting set-up, (c) macro picture of cross sectioned laser melted specimen with depth.

Find the optimum process parameters

In this section, Taguchi method was used to optimize the tribological parameters for nodular cast iron. Optimized wear test parameters are determined and validated. In the present study, load, sliding velocity and temperature are considered as three levels of process parameters with constant sliding distance of 1000 m. Twenty-seven experiments are conducted to analyze the influence of numerous combinations of wear test criterion on the performance characteristics. Experimental plan for the wear test is exhibited in Table 3.

Multi-response signal-to-noise proportion

S/N proportion formulation is intended to a researcher that can constantly choose the better common level for setting the optimizing of the quality nature of an experiment. The bigger S/N proportion results in improved performance or improved product value.

Grey relational analysis

Stage 1: Smaller – the – better

$$S/N \text{ ratio } (\mu) = -10 \log_{10} \left(\frac{1}{n} \sum_{i=0}^n y_{ij}^2 \right) \tag{4}$$

This type of problem is suitable when characteristic minimization is expected. The S/N proportion as a specified response like volume loss, coefficient of friction (smaller – the – better) is computed using Eq. (1).

Stage 2: The S/N proportion fact is accepted when standardizing input in grey relation analysis.

$$Z_{ij} = \frac{\max(y_{ij}, i = 1, 2, 3 \dots, n) - y_{ij}}{\max(y_{ij}, i = 1, 2, 3 \dots, n) - \min(y_{ij}, i = 1, 2, 3 \dots, n)} \tag{5}$$

(Smaller the better)

where, Z_{ij} = standardized rate of responses.

The S/N proportion rate of volume loss, coefficient of friction is standardized by using Eq. (2). The results are shown in the Tables 4 and 5.

Stage 3:

The grey relational corollary is intended to represent the connection in the actual and best (ideal) experiment outcomes. The grey relational corollary ξ_i (k) is represented as shown below.

$$\gamma(Y_0(k), Y_i(k)) = \frac{(\Delta_{min} + \xi \Delta_{max})}{(\Delta_{oj}(k) + \xi \Delta_{max})} \tag{6}$$

where γ is the grey relational co-efficient

1. j = 1, 2... n; k = 1, 2... m; n is the number of experimental data items and m is the number of responses.
2. Y₀(k) is the reference sequence (Y₀(k) = 1, k = 1, 2, ..., m); Y_i(k) is the specific comparison sequence.
3. Δ_{ij} = ||Y₀(k) – Y_i(k)|| the absolute value of the difference between Y₀(k) and Y_i(k)
4. Δ_{min} = $\min_{j \in i} \min_k ||Y_0(k) - Y_i(k)||$ is the smallest value of Y_i(k)
5. Δ_{max} = $\max_{j \in i} \max_k ||Y_0(k) - Y_i(k)||$ is the biggest value of Y_i(k)
6. ξ Denotes as the distinguishing coefficient. It is defined in the range 0 ≤ ξ ≤ 1.

Stage 4: Generating the grey relational grade

The GRG is finding by using the Eq. (7).

$$\bar{\gamma}_j = \frac{1}{k} \sum_{i=1}^m \gamma_{ij} \tag{7}$$

Here, $\bar{\gamma}_j$ denotes as the grey relational grade of the jth experiment and ‘k’ denotes as the number of performance characteristics.

Stage 5: Determine the optimal levels of the process parameters.

The grey relational grade value of maximum indicates the good output quality. So, in the origin of grey grade, the aspect outcome may act valued and the optimum match for single manageable aspect may be calculated. Being instance, to predict the response of aspect ‘i’, we compute the average of grade values (AGV) for each level ‘j’, represented as AGV_{ij}, then the response, E_i is defined as:

$$E_i = \text{maximum}(AGV_{ij}) - \text{minimum}(AGV_{ij}) \tag{8}$$

With the condition of aspect ‘i’ is manageable, the best level j*, is resolute by

$$j^* = \max_j(AGV_{ij}) \tag{9}$$

The effective parameters of maximum grey relational grade are ranked in Table 6.

Anova

Analysis of variance (ANOVA) is used to focus the most significant process parameter affect the wear test criterion. Generally, the influences of the process parameters on performance characteristics majorly when F rate is bigger. For recognizing the important factor of ANOVA is framed through the grey grade.

Results and discussions

Microstructural examination

The SEM picture of received NCI is illustrated in Fig. 3. The microstructures of nodular graphite are dispersed in a ferritic matrix. Cross sectional image shows semi-circular melt pool geometry of laser melted surface this may be originated due to the Gaussian profile of laser beam irradiated over the surface. The melt depth was confined only to the top layer as shown in Fig. 1(c), where most of the graphite nodules were completely dissolved after laser melting.

The laser melted zone exhibited fine structure containing austenitic dendrites with an interdendritic carbide network as shown in Fig. 4. The dendrites were formed due to rapid heating and solidification of nodular iron during the exposure of laser source [37]. The distribution of dendrites consists of austenite coupled with interdendritic carbide network. Martensite is also present in some of the dendrites. The microstructure shows a long needle like interdendritic region consist of cementite or a lath of martensite with arm spacing of below 3 μm. This showed a great cooling rate through solidification. The high speed laser source heating caused energetic convection thereby resulting in

Table 3
L27 Orthogonal array.

Exp. No	Load (N)	S.V (m/s)	Temperature (°C)	Exp. No	Load (N)	S.V (m/s)	Temperature (°C)
1	10	0.5	RT	15	20	1	300
2	10	0.5	200	16	20	1.5	RT
3	10	0.5	300	17	20	1.5	200
4	10	1	RT	18	20	1.5	300
5	10	1	200	19	30	0.5	RT
6	10	1	300	20	30	0.5	200
7	10	1.5	RT	21	30	0.5	300
8	10	1.5	200	22	30	1	RT
9	10	1.5	300	23	30	1	200
10	20	0.5	RT	24	30	1	300
11	20	0.5	200	25	30	1.5	RT
12	20	0.5	300	26	30	1.5	200
13	20	1	RT	27	30	1.5	300
14	20	1	200				

Table 4
Experimental results for untreated samples using L27 Orthogonal array.

S. No	Substrate sample							
	Responses		S/N ratio(dB)		GRC		Grade	Rank
	V.L	CoF	V.L	CoF	V.L	CoF		
1	25.5019	0.12	-28.13	18.42	0.5477	0.3333	0.494	18
2	30.7061	0.15	-29.74	16.48	0.6280	0.3704	0.564	15
3	49.2069	0.16	-33.84	15.92	1.0000	0.3828	0.846	5
4	12.1569	0.16	-21.70	15.92	0.3628	0.3828	0.368	26
5	10.0139	0.17	-20.01	15.39	0.3333	0.3951	0.349	27
6	21.9083	0.18	-26.81	14.89	0.4959	0.4075	0.474	19
7	11.0250	0.24	-20.85	12.40	0.3473	0.4839	0.381	25
8	12.0889	0.24	-21.65	12.40	0.3619	0.4839	0.392	24
9	22.5000	0.25	-27.04	12.04	0.5043	0.4971	0.502	17
10	34.2778	0.26	-30.70	11.70	0.6877	0.5105	0.643	11
11	30.8889	0.28	-29.80	11.06	0.6309	0.5379	0.608	13
12	42.0806	0.29	-32.48	10.75	0.8357	0.5519	0.765	7
13	11.0861	0.34	-20.90	9.37	0.3482	0.6259	0.418	23
14	10.1750	0.38	-20.15	8.40	0.3356	0.6906	0.424	22
15	22.2639	0.39	-26.95	8.18	0.5009	0.7077	0.553	16
16	13.6250	0.41	-22.69	7.74	0.3827	0.7431	0.473	20
17	10.3056	0.41	-20.26	7.74	0.3374	0.7431	0.439	21
18	23.7083	0.42	-27.50	7.54	0.5216	0.7615	0.582	14
19	48.2150	0.43	-33.66	7.33	0.9751	0.7803	0.926	2
20	48.1750	0.42	-33.66	7.54	0.9741	0.7615	0.921	3
21	47.9909	0.45	-33.62	6.94	0.9695	0.8195	0.932	1
22	30.4444	0.46	-29.67	6.74	0.6238	0.8398	0.678	9
23	32.2972	0.44	-30.18	7.13	0.6540	0.7996	0.690	8
24	40.3972	0.47	-32.13	6.56	0.8014	0.8608	0.816	6
25	25.5889	0.48	-28.16	6.38	0.5490	0.8823	0.632	12
26	28.0944	0.48	-28.97	6.38	0.5868	0.8823	0.661	10
27	40.1094	0.53	-32.06	5.51	0.7957	1.0000	0.847	4

Table 5
Experimental results for Laser treated samples using L₂₇ Orthogonal array.

S. No	Laser processed sample							
	Responses		S/N ratio(dB)		GRC		Grade	Rank
	V.L	CoF	V.L	CoF	V.L	CoF		
1	3.9556	0.32	-11.94	18.42	0.6513	0.3333	0.572	15
2	3.7833	0.35	-11.56	16.48	0.6316	0.3704	0.566	16
3	3.3000	0.38	-10.37	15.92	0.5780	0.3828	0.529	19
4	2.4333	0.37	-7.72	15.92	0.4860	0.3828	0.460	23
5	1.0311	0.38	-0.27	15.39	0.3356	0.3951	0.350	27
6	1.0122	0.39	-0.11	14.89	0.3333	0.4075	0.352	26
7	3.1389	0.39	-9.94	12.40	0.5606	0.4839	0.541	18
8	1.0411	0.40	-0.35	12.40	0.3367	0.4839	0.374	24
9	1.0139	0.41	-0.12	12.04	0.3335	0.4971	0.374	25
10	6.5107	0.45	-16.27	11.70	1.0000	0.5105	0.878	3
11	5.1000	0.49	-14.15	11.06	0.7921	0.5379	0.729	8
12	5.2444	0.48	-14.39	10.75	0.8114	0.5519	0.747	7
13	3.4667	0.49	-10.80	9.37	0.5962	0.6259	0.604	14
14	2.2724	0.51	-7.13	8.40	0.4693	0.6906	0.525	21
15	2.2687	0.52	-7.12	8.18	0.4689	0.7077	0.529	20
16	3.6168	0.54	-11.17	7.74	0.6129	0.7431	0.645	11
17	2.0122	0.52	-6.07	7.74	0.4422	0.7431	0.517	22
18	2.3383	0.57	-7.38	7.54	0.4761	0.7615	0.547	17
19	6.2999	0.59	-15.99	7.33	0.9658	0.7803	0.919	1
20	5.5333	0.58	-14.86	7.54	0.8512	0.7615	0.829	4
21	5.9722	0.60	-15.52	6.94	0.9151	0.8195	0.891	2
22	4.5381	0.61	-13.14	6.74	0.7205	0.8398	0.750	6
23	3.4667	0.63	-10.80	7.13	0.5962	0.7996	0.647	10
24	3.5900	0.60	-11.10	6.56	0.6099	0.8608	0.673	9
25	4.7371	0.65	-13.51	6.38	0.7453	0.8823	0.780	5
26	3.0094	0.67	-9.57	6.38	0.5467	0.8823	0.631	13
27	2.8153	0.68	-8.99	5.51	0.5261	1.0000	0.645	12

homogeneous dendritic formation. Moreover, it is obvious from those micrographs indicate that all the graphite nodules were softened in the heated ferrous material through treatment and high speed self-

Table 6
Main effects on grey grades.

Level	Substrate sample			Laser processed sample		
	V.L	W. R	CoF	V.L	W. R	CoF
1	0.4856	0.7443	0.5571	0.4577	0.7399	0.6833
2	0.5448	0.5299	0.5608	0.6355	0.5433	0.5741
3	0.7893	0.5455	0.7018	0.7516	0.5616	0.5874
Delta	0.3037	0.2144	0.1447	0.2939	0.1966	0.1092
Rank	1	2	3	1	2	3

quenching crushed the re-organization of cast iron in kindness of the white iron evolution. The partial graphite dissolution occurred in the bottom layer and nodules diameter is decreased. The intermediate layer was embraced of a combination of uneven martensite and dendrites. The uneven melt coalesces specified that as the melt layer intruded in to the base for locality of graphite which is melted first. This happens since the carbon enhancement nearby graphite nodules that provincially dropped the melting point of the ferrous metal. At the end, the internal area of laser melted zone contained of fine indeterminate martensite. It is noticed that at the interface of the laser exposed sample representing there is no cracks and blows even though it is held with severe quenching. The creation of porosity due to oxidation between oxygen and carbon elements. During the laser melting process, the porosity can be reduced by evading oxygen percentage. So, the experiment samples were irradiated under argon gas to minimize oxygen elements. Therefore, the porosity investigation was not performed in this work.

Microhardness

Fig. 5 shows indentation of Vickers microhardness and melt depth profile of LSM. Through solidification of the melted area, the material normally drops its real stability tempted by strain hardening. The increase in hardness of separate-phase materials on the melted zone was tempted by residual stress, precipitation hardening effects or microstructural grain refinement owing to rapid cooling of the melted zone. The sufficient interaction time resulted in more amount of hotness absorption in melted area. The rapid cooling caused grain modification in the melt zone [38]. Due to fine grain size, the hardness of the laser melted zone is very high when compared to base material. The higher residual stress, which can be from fast heating and quenching process while laser exposure, could be associated with the microhardness increases. The graph shows the level of melt depth achieved during laser surface melting. The hardness measurement gives the value ranges from 820 to 880 HV_{0.3}. The hardness was almost uniform due to fine and homogeneous structure of laser melted zone. The heat affected zone exhibits higher hardness of about 920 HV_{0.3} due to improper melting of graphite and martensite formation and fine ledeburite structure of the graphite interface. In the melted regions, the obtained hardness shows nearly uniform. This is due to the creation of uniform structure on the melted regions.

X-ray diffraction analysis

X-ray diffraction analysis for substrate and laser treated samples were performed and the resulting x-ray diffraction patterns are shown in Fig. 6. In substrate, the maximum peaks are located at bcc (αFe) phase, graphite and Fe₃C. The αFe lattice parameter is very closer to the Fe equilibrium value. The retained austenite peak was observed in both as received and laser surface melted sample. It is evident that the intensity of as received (αFe) peak was higher than the laser treated sample with considerable peak shift. After laser processing, the produced peaks were broadened and lowered by grains formation as shown in XRD spectra. The rapid cooling of molten pool onto a cooler base

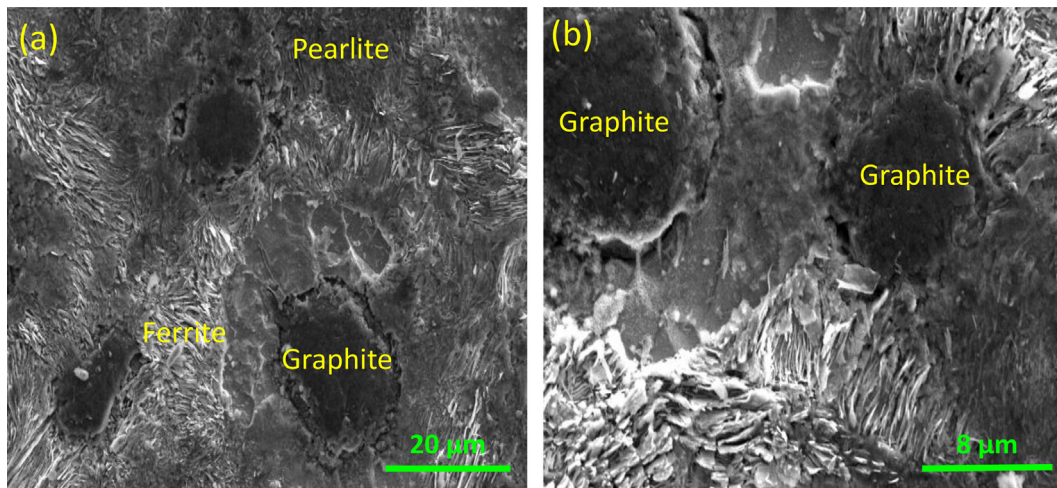


Fig. 3. (a) SEM picture of as-received NCI with lower magnification, (b) with higher magnification.

metal can change the grain structures. The increase in confined austenite peak intensity may be associated to the concerned phase's higher volume fraction, while the peak shift may have attributed due to the dissolution of carbon content [37]. The further investigation of peak intensity in laser surface melted samples reveals that the diminishing of intensity is associated with retained austenite volume fraction reduction and an average lower carbon concentration. In laser treated surfaces, maximum of the peaks was identified in γ phase (fcc) and Fe_3C . The low percentage of carbon content is martensite due to austenite transformation. Laser processed surface indicates higher hardness than substrate material due to Fe_3C formation.

Analysis of factors and ANOVA

In Taguchi technique, the objective role is changed to Signal to Noise (S/N) proportion which is dealt with the multiple factor of unique. In the current task, volume loss is taken as the objective function and Taguchi's "Lower the Better" multiple factor of unique is preferred to decrease the objective function (i.e. volume loss).

To investigate the influencing factor volume loss, the S/N proportion rate of all the tested samples are shown in Tables 4 and 5. From the S/N proportion, the delta rates are calculated for all individual factors as shown in Table 6 and applied load was influencing more and ensued by sliding velocity and temperature. From the main effect graph as shown in Fig. 7, In order to minimize the wear amount, the optimal parameters should be in high exact for applied load (30 N), low level for

sliding velocity (0.5 m/s) and high level for temperature (300 °C) for substrate and high level load (30 N), low level sliding velocity (0.5 m/s) and low level temperature (RT) for laser processed sample. In addition, tested load has more influence on wear rate and ensued by sliding velocity and temperature. The trend of higher wear depth at maximum load observed and reported by several researchers [39–42].

The outcomes of ANOVA are summarized in Table 7 using Minitab 16. From the results of ANOVA, it was understood that applied load (52.45%) influences more on wear and followed by sliding velocity (28.91%) and temperature (13.76%) with computed R-Sq of 95.13% for substrate and applied load (57%) influences more on wear and followed by sliding velocity (30.69%) and temperature (9.19%) with computed R-Sq of 96.95% for the laser processed sample. The multiple performance characteristic is investigated to explore optimization of wear test parameters. Tables 4 and 5 display the grey relation coefficient, grade and the rank for each experiments for substrate and laser processed samples, respectively. The maximum GRG implies that the corresponding experimental results are nearer to the ideal standardized value. Due to this, the experiment 21st the GRG is maximum for substrate and 19th experiment the grey relational grade is maximum for laser processed sample. The maximum grades have the greatest multiple performance characteristics among all experimentation. Table 6 and Fig. 7 shows the main effects of grey relational grade for each parameter at various levels, respectively. Fig. 8 shows the volume loss and CoF of substrate and laser processed samples.

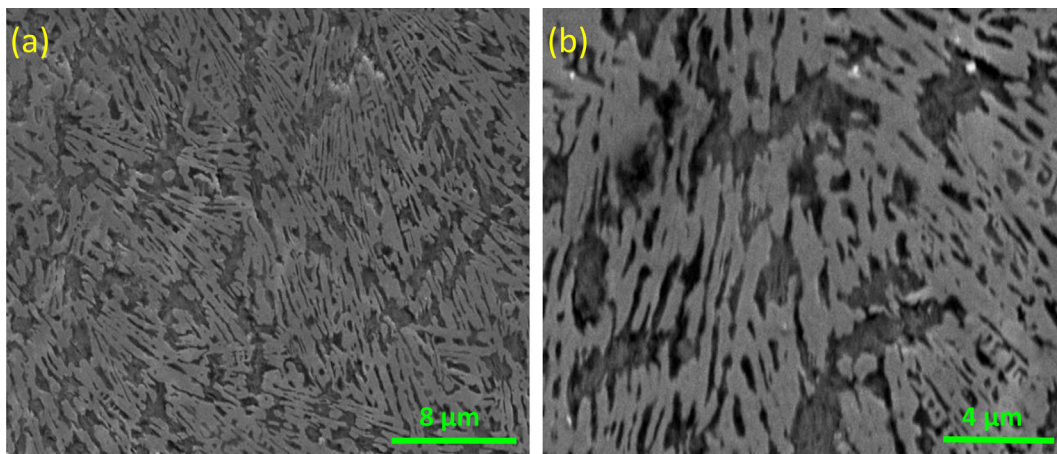


Fig. 4. (a) SEM picture of laser melted surface, (b) magnified view of (a).

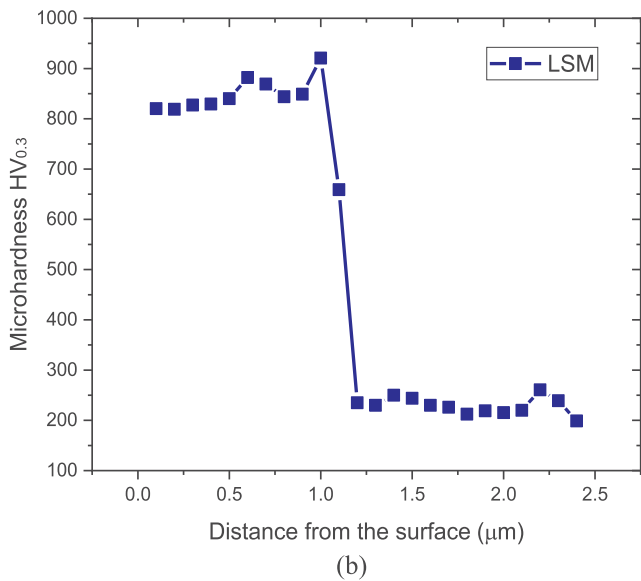
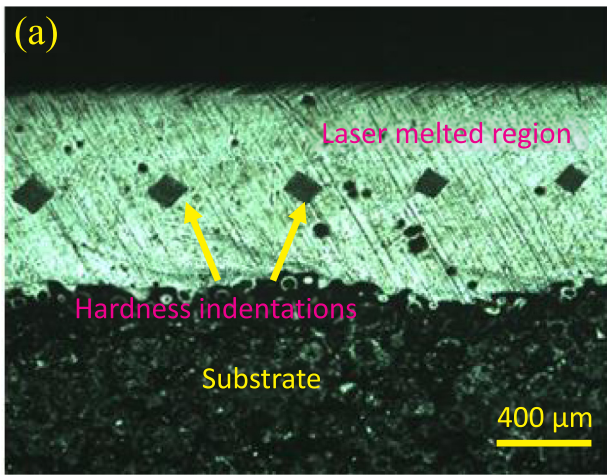


Fig. 5. (a) Optical micrograph of hardness indentation in different region, (b) Microhardness profile of laser melted cross section.

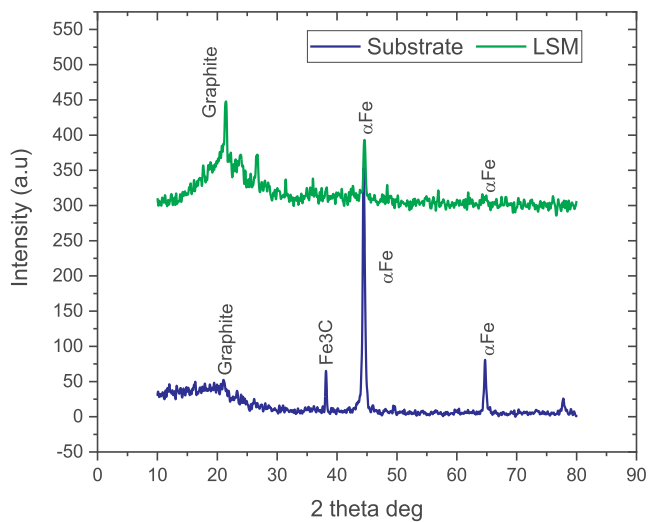


Fig. 6. XRD analysis of substrate and melting surface.

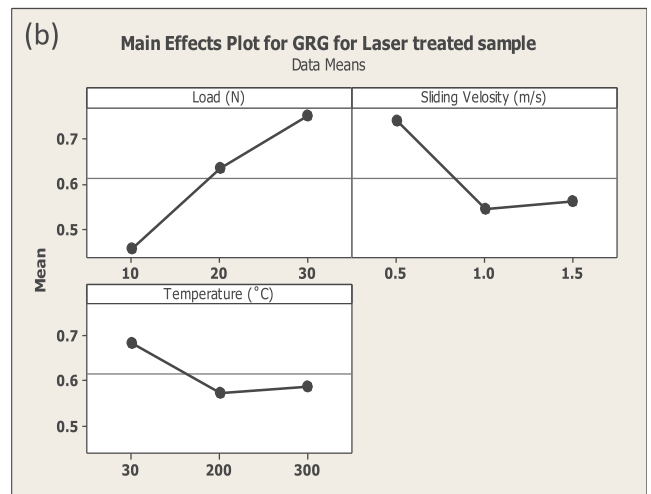
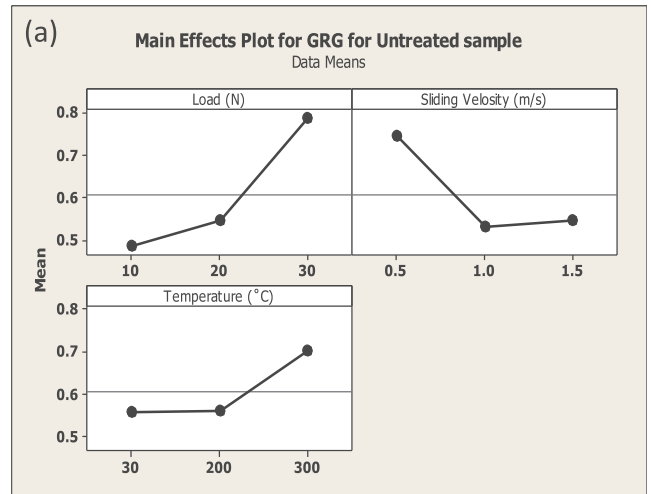


Fig. 7. Main effect graph (a) Untreated sample, (b) Laser treated sample.

Confirmation test

A confirmation experiment was conducted to validate the results of the taguchi based grey relational analysis in order to experimentally verify the optimum levels of selected parameters. The identified optimized parameter was set, and three trials were carried out in this test. The optimum combinations at 95% confidence level are computed such that nearness of the perceived value of S/N proportion with that of the envision value is evaluated. From this confirmation test, the multiple performance characteristics is greatly improved over Taguchi based grey method. Table 8 shows that the volume loss decreased from 49.20 to 47.98 mm³ for substrate and 6.51 to 6.27 mm³ for laser processed sample.

Worn out surface analysis

The worn out surface of optimized sample was analyzed using SEM. The worn out surfaces of specimens tested for optimized parameter for substrate and laser processed sample are shown in Fig. 9. At higher load and low sliding velocity, the wear intensity is more in substrate specimen than laser processed sample. The wear depth is high and pile-ups of material is more on the plow marks. It is clear that the untreated cast iron displays poor wear resistance and plastic deformation is very severe. The delamination principle maintains that crack initiation, plastic distortion and propagation makes to layer by layer delamination. The penetration of harder disc surface on the smoother pin surface might

Table 7
Result of ANOVA on grey grade.

Factor	Substrate sample					Laser processed sample					
	DF	SS	V	F Test	P Test	P %	SS	V	F Test	P Test	P %
Load	2	0.46617	0.23309	107.6	0.000	52.45	0.39504	0.19752	186.9	0.000	57.00
S.V	2	0.25720	0.12860	59.38	0.000	28.91	0.21256	0.10628	100.5	0.000	30.69
Temp	2	0.12267	0.06133	28.32	0.000	13.76	0.06369	0.03184	30.14	0.000	9.19
Error	20	0.04332	0.00217	-	-	4.86	0.02113	0.00106	-	-	3.05
Total	26	0.88936	-	-	-	100	0.69242	-	-	-	100

R-Sq = 95.13% R-Sq (adj) = 93.67% R-Sq = 96.95% R-Sq (adj) = 96.03%.

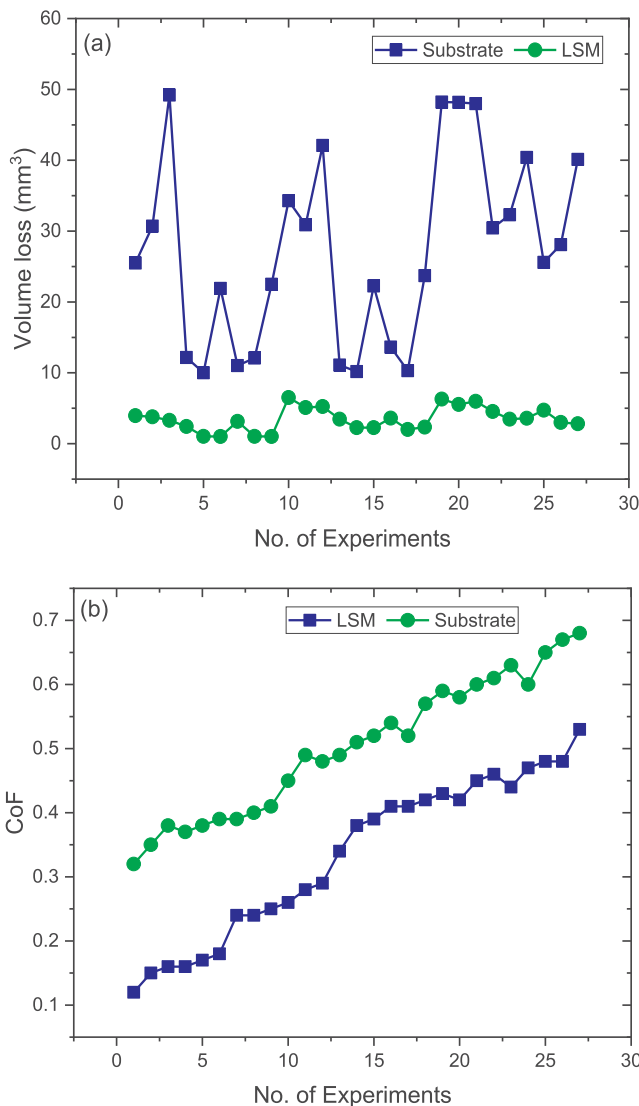


Fig. 8. (a) Volume loss, (b) CoF of substrate and laser processed sample.

have led to the rupture and displacement of the material. The material removal rate progresses by increasing load. In laser treated cast iron, the surface of the specimen damaged very less as compared to untreated cast iron. The harder laser treated surfaces might have influenced to reduce the intensity of the abrasion and increased the wear resistance [43]. It is very clear that the SEM (Fig. 4) images shows the fine structure after laser surface melting does not allow any defects and damages. The occurrence of fine martensite and retained austenite enclosed by strong grid of Fe₃C plays a major role and reduced the wear rate. The laser processed specimen can sustain with various operating environment.

Table 8
Confirmation test.

	Substrate sample			Laser processed sample		
	Initial	Prediction	Experiment	Initial	Prediction	Experiment
Level	A1B1C3	A3B1C3	A3B1C3	A2B1C1	A3B1C1	A3B1C1
V. L	49.20	-	47.98	6.51	-	6.27
CoF	0.16	-	0.45	0.26	-	0.43
GRG	0.846	0.932	0.931	0.682	0.919	0.909

Grade Improvement: 10.04% Grade Improvement: 33.28%.

The coefficient of friction (CoF) was increased in both substrate and laser processed samples. When the temperature crossing more than 100 °C the toughening of graphite film may induce the friction [44,45]. The microstructure changes also may induce the friction in higher level. The dissolution of the graphite nodules in the reinforced outer layer may leads to increase in CoF. Additionally, the surface hardness was increased by laser treatment, owing to the fine microstructure, presence of martensite and Fe₃C may induce to increase the CoF [46].

Surface roughness analysis

Fig. 10 (a and b) shows worn out substrate and laser processed surface roughness. The substrate surface roughness was observed at ~4.3 μm. It was achieved due to lesser hardness and the higher wear rate. The laser processed surface shows less surface roughness of ~0.7 μm due to less wear and high hardness of the material. While relating with substrate specimen, laser processed samples exhibited ~5.14 times reduction in roughness.

Conclusions

The sliding wear test was performed at high temperature employing pin-on-disc tribometer on substrate and laser processed nodular iron using grey-Taguchi technique. The following conclusions were drawn from the experimental results.

- The microstructure of laser processed sample shows that the graphite nodules soften in the molten ferrous material and emerged as very elegant structure consist of austenite dendrites with an interdendritic grid of carbides. The hardness of the laser processed sample increased to ~850 HV_{0.3} from its original hardness value of 220 HV_{0.3}.
- The XRD analysis indicates that the αFe phase changed from bcc to fcc (γFe). Higher carbon content is confined austenite due to disintegration of graphite nodules throughout laser surface melted region.
- The roughness results indicate that higher surface roughness (4.3 μm) on substrate and less surface roughness (0.7 μm) on laser processed specimen.
- The optimum level of combinations for reducing the wear rate was identified as 30 N, 0.5 m/s and 300 °C (i.e. A3B1C3) for substrate

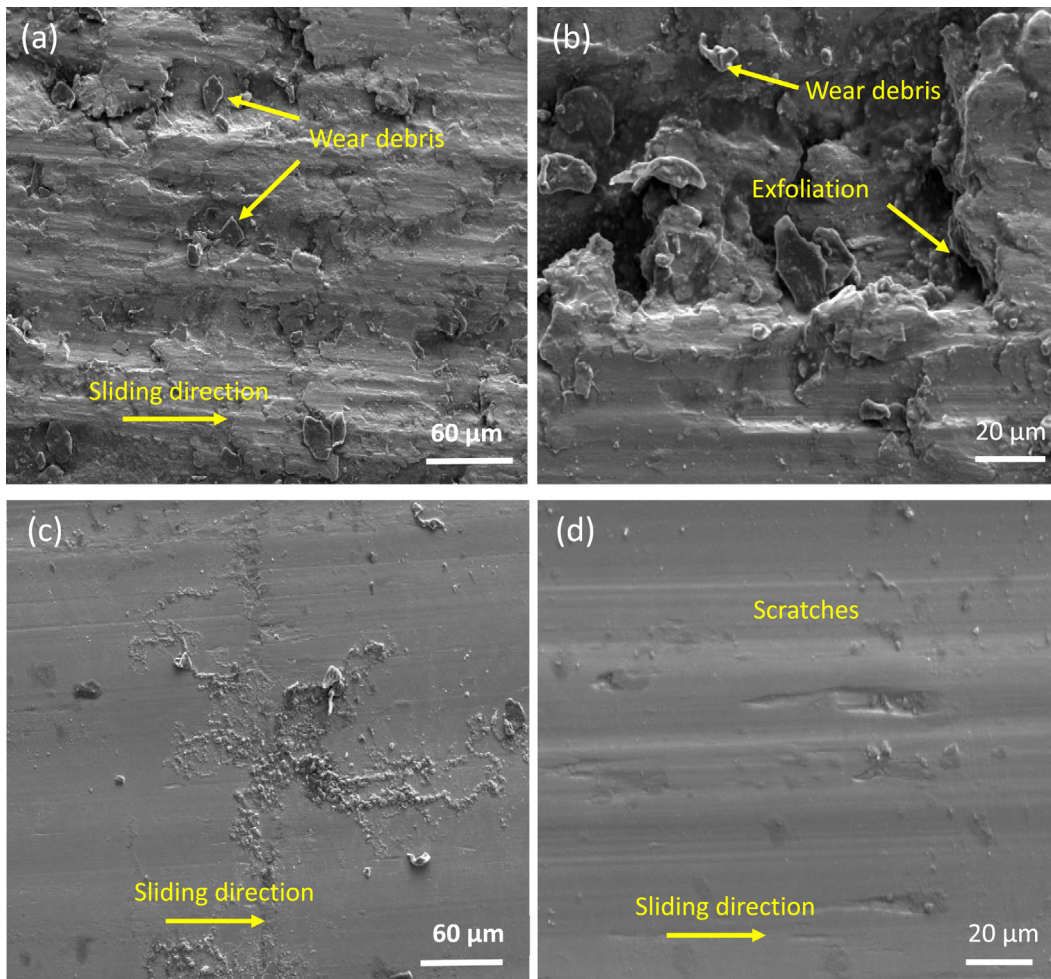


Fig. 9. Worn-out surfaces of (a and b) substrate and (c and d) laser processed samples.

and 30 N, 0.5 m/s and room temperature (i.e. A3B1C1) for laser processed sample.

- Based on the ANOVA results, the most influencing parameter were determined as applied load (52.45%), sliding velocity (28.91%) and

temperature (13.76%) for substrate with R-Sq value of 95.13% and applied load (57%), sliding velocity (30.69%) and temperature (9.19%) for laser processed sample with R-Sq value of 96.95%.

- Finally, the confirmation test was conducted and shows the VL was

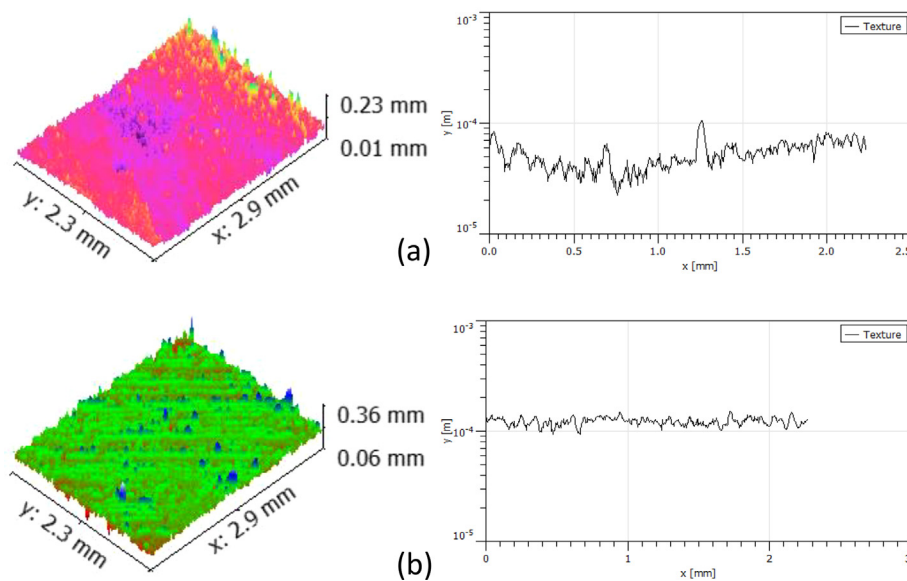


Fig. 10. Roughness of worn-out samples (a) substrate (b) laser processing.

reduced from 49.20 to 47.98 mm³ for substrate and 6.51 to 6.27 mm³ for laser processed sample. Based on the experimental results, the laser processed sample shows better wear resistance than substrate which shows 86.87% improvement.

Acknowledgments

All the authors wish to thank NTUT, Taiwan and NIT-Trichy, India for all support required to carry out this research.

Appendix A. Supplementary data

Supplementary data to this article can be found online at <https://doi.org/10.1016/j.rinp.2019.102585>.

References

- [1] Wilk-Kolodziejczyk Dorota, Regulski Krzysztof, Gumienny Grzegorz. Comparative analysis of the properties of the nodular cast iron with carbides and the austempered ductile iron with use of the machine learning and the support vector machine. *Int J Adv Manuf Technol* 2016;87:1077–93.
- [2] Hutter G, Zybelle L, Kuna M. Micro mechanisms of fracture in nodular cast iron: from experimental findings towards modeling strategies – a review. *Eng Fract Mech* 2015;144:118–41.
- [3] Ceschini Lorella, Campana Giampaolo, Pagano Nunziante, Angelini Valerio. Effect of laser surface treatment on the dry sliding behaviour of the EN-GJS400-12 ductile cast iron. *Tribol Int* 2016;104:342–51.
- [4] Podgornik B, Vizintin J, Thorbjornsson I, Johannesson B, Thorgrimmson JT, Martinez Celis M, et al. Improvement of ductile iron wear resistance through local surface reinforcement. *Wear* 2012;274–5.
- [5] Qi X, Zhu S, Ding H, Zhu Z, Han Z. *Appl Surf Sci* 2013;282:672–9.
- [6] Jeyaprakash N, Yang Che-Hua, Duraiselvam Muthukannan, Prabu G. Microstructure and tribological evolution during laser alloying WC-12%Co and Cr₃C₂–25%NiCr powders on nodular iron surface. *Results Phys* 2019;12:1610–20.
- [7] Benyounis KY, Fakron OMA, Abboud AG, Olabi AG, Hashmi MJS. Surface melting of nodular cast iron by Nd-YAG laser and TiG. *Mater. Process. Technol.* 2005;170:127.
- [8] Vilar R. *Comprehensive Materials Processing*. 2014. p. 163–216.
- [9] Wang Zhongqi, Zhang Jianlong, Zhang Peng, Zhou Hong, Zhou Ti. Effect of the 75 ferrosilicon on the laser cladding on gray cast iron. *Opt Laser Technol* 2019;113:64–71.
- [10] Nabhani Mohammad, Razavi Reza Shoja. Corrosion study of laser clad Ti-6Al-4V alloy in different corrosive environments. *Eng Fail Anal* 2019;97:234–41.
- [11] Li Yongjian, Dong Shiyun, He Peng, Yan Shixing, Li Enzhong, Liu Xiaoting, et al. Microstructure characteristics and mechanical properties of new-type FeNiCr laser cladding alloy coating on nodular cast iron. *J Mater Process Technol.* 2019;269:163–71.
- [12] Zhou Shengfeng, Zeng Xiaoyan, Qianwu Hu, Huang Yongjun. Analysis of crack behavior for Ni-based WC composite coatings by laser cladding and crack-free realization. *Appl Surf Sci* 2008;255:1646–53.
- [13] Zhou Shengfeng, Xiong Zheng, Lei Jianbo, Dai Xiaoqin, Zhang Tianyou, Wang Chunxia. Influence of milling time on the microstructure evolution and oxidation behavior of NiCrAlY coatings by laser induction hybrid cladding. *Corros Sci* 2016;103:105–16.
- [14] Zhou Shengfeng, Dai Xiaoqin, Zheng Haizhong. Microstructure and wear resistance of Fe-based WC coating by multi-trackoverlapping laser induction hybrid rapid cladding. *Opt. Lasers Technol.* 2012;44:190–7.
- [15] Ramesh BN, Suresha B. Optimization of tribological parameters in abrasive wear mode of carbon-epoxy hybrid composites. *Mater Des* 2014;59:38–49.
- [16] Ratner SN, Farberoua II, Radyukeich OV, Lure EG. Correlation between wear resistance of plastics and other mechanical properties. *Sov Plast* 1964;7:37–45.
- [17] Lancaster JK. Abrasive wear of polymers. *Wear* 1969;14:223–39.
- [18] Zum-Gahr KH. Abrasive wear of two-phase metallic materials with a coarse micro structure. Vancouver: ASME; 1985. p. 793.
- [19] Axen N, Jacobson S. A model for abrasive wear resistance of multiphase materials. *Wear* 1994;174:187–99.
- [20] Lee GY, Dharan CKH, Ritchie RO. A physically-based abrasive wear model for composite materials. *Wear* 2002;252:322–31.
- [21] Yen B, Dharan CKH. A model for the abrasive wear of fiber-reinforced polymer composites. *Wear* 1996;195:123–7.
- [22] Bijwe J, Rajesh JJ, Jeyakumar A, Ghosh A, Tewari US. Influence of solid lubricants and fibre reinforcement on wear behaviour of polyethersulphone. *Tribol Int* 2000;33:697–706.
- [23] Patnaik A, Satapathy A, Biswas S. Investigations on three-body abrasive wear and mechanical properties of particulate filled glass epoxy composites. *Malay Polym J* 2010;5:37–48.
- [24] Suresha B, Chandramohan G, Mohanram PV. Role of fillers on three-body abrasive wear of glass fabric reinforced epoxy composites. *Polym Compos* 2009;30:1106–13.
- [25] Suresha B, Siddaramaiah Kishore, Seetharamu S, Sampath Kumaran S. Investigations on the influence of graphite filler on dry sliding wear and abrasive wear behaviour of carbon fabric reinforced epoxy composites. *Wear* 2009;267:1405–14.
- [26] Chang CY, Huang R, Lee PC, Weng TL. Application of a weighted Grey-Taguchi method for optimizing recycled aggregate concrete mixtures. *Cem Concr Compos* 2011;33:1038–49.
- [27] Phadke SM. *Quality engineering using robust design*. Englewood cliffs (NJ): Prentice-Hall; 1989.
- [28] Kopac J, Krajnc P. Robust design of flank milling parameters on Grey-Taguchi method. *J Mater Process Technol* 2007;191:400–3.
- [29] Tzeng C, Lin Y, Yang Y, Jeng M. Optimization of turning operations with multiple performance characteristics using the Taguchi method and grey relational analysis. *J Mater Process Technol* 2009;209:2753–9.
- [30] Targ YS, Juang SC, Chang CH. The use of grey based Taguchi methods to determine submerged arc welding process parameters in hardfacing. *J Mater Process Technol* 2012;28:1–6.
- [31] Rajmohan T, Palanikumar K, Karthivel K. Optimization of machining parameters in drilling hybrid aluminum metal matrix composites. *Trans Nonferr Met Soc China* 2012;22:1286–97.
- [32] Pan LK, Wang CC, Hsiao YC, Haaso KC. *Opt Laser Technol* 2004;37:33–42.
- [33] Caydas U, Hascalik A. *Opt Laser Technol* 2008;40:987–94.
- [34] Tsao CC. *Int J Adv Manuf Technol* 2009;40:41–8.
- [35] Hsiao YF, Targ YS, Huang WJ. Optimization of plasma arc welding parameters by using the taguchi method with the grey relational analysis. *Mater Manuf Processes* 2008;23:51–8.
- [36] *Standard test method for wear testing with a pin-on-disk apparatus, ASTM Standard, 2010, G: 99-05.*
- [37] Alabeedi KF, Abboud JH, Benyounis KY. Microstructure and erosion resistance enhancement of nodular cast iron by laser melting. *Wear* 2009;266:925–33.
- [38] Jeyaprakash N, Muthukannan Duraiselvam, Aditya SV. Numerical modeling of WC-12%Co laser alloyed cast iron in high temperature sliding wear condition using response surface methodology. *Surf Rev Lett* 2019;26:1950009.
- [39] Baskaran S, Anandakrishnan V, Muthukannan Duraiselvam, Investigations on dry sliding wear behavior of in situ casted AA7075–TiC metal matrix composites by using Taguchi technique. *Mater Des* 2014;60:184–92.
- [40] Arik H, Ozcatalbas Y, Turker M. Dry sliding wear behavior of in situ Al–Al4C3 metal matrix composite produced by mechanical alloying technique. *Mater Des* 2006;27:799–804.
- [41] Liu L, Li W, Tang Y, Shen B, Hu W. Friction and wear properties of short carbon fiber reinforced aluminum matrix composites. *Wear* 2009;266:733–8.
- [42] Shorowordi KM, Haseeb ASMA, Celis JP. Tribo-surface characteristics of Al–B4C and Al–SiC composites worn under different contact pressures. *Wear* 2006;261:634–41.
- [43] Jeyaprakash N, Duraiselvam M, Raju R. Modelling of Cr₃C₂-25%NiCr laser alloyed cast iron in high temperature sliding wear condition using response surface methodology. *Arch Metall Mater* 2018;63:1303–15.
- [44] Sugishita J, Fujiyoshi S. The effect of cast iron graphite's on friction and wear performance; II: variables influencing graphite film formation. *Wear* 1981;68:7–20.
- [45] Gadag SP, Srinivasan MN. Dry sliding wear and friction: laser-treated ductile iron. *Wear* 1994;173:21–9.
- [46] Pagano N, Angelini V, Ceschini L, Campana G. Laser remelting for enhancing tribological performances of a ductile iron. *Procedia CIRP* 2016;41:987–91.

Influence of Surfactant Concentrations on N-Type Nanostructured Thermoelectric Oxide $\text{CaMnO}_{3-\delta}$

S. Berbeth Mary

Research Scholar, Department of Physics
St. Joseph's College (Autonomous)
Tiruchirappalli- 620 002
Tamil Nadu, India.

A. Leo Rajesh*

Assistant Professor, Department of Physics
St. Joseph's College (Autonomous),
Tiruchirappalli- 620 002,
Tamil Nadu, India.

Abstract:- Nano crystalline calcium manganite nanoparticles are promising n-type thermoelectric oxides at higher temperatures with perovskite orthorhombic structure have been synthesized by sol-gel hydrothermal method and the influence of surfactant polyvinyl pyrrolidone (PVP) concentration on $\text{CaMnO}_{3-\delta}$ nanoparticles were investigated. Systematic studies revealed that the surfactant concentration induces the average particle size of the nanoparticles. The synthesized nanoparticles were characterized by X-ray diffraction, scanning electron microscope with energy dispersive X-ray analysis and thermoelectric studies were done on the sintered sample between room temperature and 600 °C. Pure and crystalline $\text{CaMnO}_{3-\delta}$ nanoparticles were observed and the average particle size was calculated by Scherrer formula. Vibrational bands between 550-650 cm^{-1} confirms the formation of crystalline $\text{CaMnO}_{3-\delta}$ nanoparticle by FTIR analysis and peak intensity increases with increasing the concentration of PVP. Thermoelectric properties have been obtained for the pure, single phase sample with less average particle size without agglomeration and secondary phase. Optical studies revealed that $\text{CaMnO}_{3-\delta}$ nanoparticles having the absorption in the visible region and the indirect band gap was in the range of 2.14 eV- 2.41 eV using UV-Vis spectroscopy and the thermoelectric analysis showed the negative value of Seebeck coefficient of $-287 \mu\text{VK}^{-1}$ at room temperature.

Key words: Calcium manganite; PVP; sol-gel hydrothermal; electrical resistivity; thermopower.

1. INTRODUCTION

Thermoelectric energy system overcomes the limitations of energy resources and environmental pollution problems by converting the waste heat energy directly into electricity from industrial processes without any greenhouse gas emissions via the Seebeck effect, Peltier effect and vice versa. The energy conversion efficiency is estimated by the dimensionless figure of merit ZT [1]. The state of art alloys such as Bi_2Te_3 , CoSb_3 are not chemically and thermally stable at higher temperatures under air atmosphere, but the discovery of $\text{Na}_x\text{CoO}_{2+\delta}$ by Terasaki et al. in 1997 initiated more research on oxides. Electron doped calcium manganite $\text{Ca}_{1-x}\text{R}_x\text{MnO}_3$ is extensively studied n-type thermoelectric oxide material because of its high electrical conductivity, oxidation resistant, and stability at elevated temperature. However, the undoped $\text{CaMnO}_{3-\delta}$ material has low carrier mobility due to ionic bonding which in turn reduces the thermopower of the material [2]. Materials with high electrical conductivity and

Seebeck coefficient, together with a low thermal conductivity are potential candidates for thermoelectric devices. In bulk materials Seebeck coefficient, electrical conductivity and thermal conductivity are linked together by the electronic structure and they cannot be optimized independently, but band structure and phonon scattering can be engineered by nanostructured systems. Thermal conductivity can be reduced by producing the nanostructures with one or more dimensions smaller than the mean free path of phonons, but larger than that of the electrons without affecting the electrical conductivity. Nanostructuring can effectively enhance the ZT values by suppressing the thermal transport of phonons [3-5].

The product obtained from sol-gel method is amorphous in nature while the yield is very less in hydrothermal method. Sol-gel hydrothermal method is a suitable method for synthesizing the thermoelectric metal oxide nanoparticles due to controlled grain size, morphology, high surface area for large scale application. The parameters such as pH, precursor, addition of surfactants, experimental temperature and duration induces the growth mechanism of the nanoparticles. The expected nanostructures within the range can be achieved by the systematic studies on these parameters [6, 7]. Annealing in air atmosphere at higher temperatures leads to the formation of perovskite oxides, but it affects the growth mechanism, homogeneity, surface area [8].

A surfactant is essential in wet chemical metal oxide synthesis process to form discrete nanoparticles than network and it controls the grain growth by regulating the reaction kinetics. Surfactants are used in aqueous synthesis to reduce the interfacial energy and hence control the growth mechanism in nanoparticles. Particle agglomeration is being avoided by forming an absorption layer by a surfactant on the surface of the nanoparticle and regulates the grain growth of the particle. In metal oxide nanoparticle synthesis process, surfactants are acting as chelating agent, capping agent, template and fuels. Citric acid as a chelating agent modifies the synthesis process and the formation of perovskite oxide occurs at lower annealing temperature [9-12].

Reducing the annealing temperature and duration decreases the size of the nanoparticles that leads to the low thermal conductivity which in turn improves the thermopower [13, 14]. Non-toxic and non-ionic polymer Polyvinyl pyrrolidone (PVP) with the functional groups C=O, C-N, CH_2

is used in synthesizing nanoparticles [15, 16]. PVP as a capping agent initially increases the particle size by forming an absorption layer on the nanoparticle, and then particle size reduces during annealing by burning the PVP polymer [17-19]. The reduction of grain size by nanostructuring and addition of surfactants induces the phonon scattering; as a result the lattice thermal conductivity reduces which will then improves the thermopower of the material [20, 21].

In this research paper, n-type thermoelectric oxide $\text{CaMnO}_{3-\delta}$ nanoparticles have been synthesized by sol-gel hydrothermal method and the role of surfactants as chelating and capping agent are investigated. The influence of polyvinyl pyrrolidone on structural, morphological, electrical and thermoelectric properties has been optimized based on the size, crystallinity and surface morphology of the nanoparticles for the application of thermoelectrics.

2. EXPERIMENTAL PROCEDURE

2.1. Preparation of $\text{CaMnO}_{3-\delta}$ nanoparticles

AR grade calcium nitrate tetrahydrate ($\geq 99\%$), manganese nitrate hydrate ($\geq 98\%$), and ammonium hydroxide solution were used as precursors without further purification. Citric acid and polyvinyl pyrrolidone (PVP, $\text{MW} \approx 40000 \text{ g/m}$) are used as chelating and capping agent respectively. Stoichiometric amounts of metal nitrates of $\text{Ca}(\text{NO}_3)_2 \cdot 4\text{H}_2\text{O}$, $\text{Mn}(\text{NO}_3)_2 \cdot \text{H}_2\text{O}$ were weighed at 1:1 molar ratio and dissolved in distilled water. Citric acid solution was added to the mixture in the mole ratios 1:1 (citric acid: metal ion) and PVP solution was added to the precursor solution with different concentrations of 1g, 2g, and 3g. Homogeneous solution was obtained after stirring for 30 minutes and ammonium hydroxide was added drop wise till its pH reaches 9.2, then it heated at 80°C till it reduced to the half of the amount of it. Then this sol was transferred into a Teflon lined stainless steel autoclave, which is placed it in hot air oven at 200°C for 20 hours. The product was cleaned with distilled water and ethanol to remove the organic substances, then dried and annealed at 950°C to attain $\text{CaMnO}_{3-\delta}$ nanoparticles.

2.2. Characterization Techniques

Structural characterization of the $\text{CaMnO}_{3-\delta}$ samples were carried out by using Bruker D8 advance diffractometer equipped with $\text{Cu K}\alpha$ radiation ($\lambda = 1.5406 \text{ \AA}$) with 2θ ranging between 10° and 80° with a step size of 0.02° . The surface morphology of the samples were analyzed using a JEOL JSM 5600 scanning electron microscope and its elemental analysis was accomplished by Energy Dispersive X-ray analysis (EDAX). Perkin Elmer Fourier Transform Infrared Spectrometer is used to capture the FTIR spectrum of the samples. Optical characterization was done by Bruker Lambda 35 UV-Visible spectrometer and Tauc's relation used to calculate the band gap value. The annealed powders were compacted with 3 wt % of paraffin wax as a binder at 50Mpa and sintered at 850°C with a heating rate of $10^\circ\text{C}/\text{min}$ for 4 h by the conventional sintering process for thermoelectric measurement. LSR-3, Seebeck, Linseis, Germany, investigated thermoelectric properties such as Seebeck coefficient (S), electrical conductivity (σ) and the power factor ($S^2\sigma$) of surfactant assisted $\text{CaMnO}_{3-\delta}$ nanoparticles were investigated

between ambient and 600°C with $\Delta T = 50^\circ\text{C}$ with highly pure helium atmosphere.

3. RESULTS AND DISCUSSION

3.1. Structural analysis of $\text{CaMnO}_{3-\delta}$ nanoparticles

XRD measurement was used to find the purity and crystallinity and influence of PVP on $\text{CaMnO}_{3-\delta}$ nanoparticles. Figure 1(a-d) represents the powder XRD pattern of the pure $\text{CaMnO}_{3-\delta}$ nanoparticles with different concentrations of PVP 0g, 1g, 2g, and 3g. All the diffraction patterns were indexed and matched with the JCPDS card No: 461009. Orthorhombic $\text{CaMnO}_{3-\delta}$ with the space group of Pbam were identified with the lattice parameters $a = 5.424 \text{ \AA}$, $b = 10.23 \text{ \AA}$, $c = 3.735 \text{ \AA}$ and unit cell volume $V = 207.25 \text{ \AA}^3$ [22]. Peaks at $2\theta = 19.00^\circ$, and 31.26° are observed as minor phases of Co_3O_4 (JCPDS card no: 431003) along with the peaks of $\text{CaMnO}_{3-\delta}$ nanoparticles. As surfactant concentration increases, the intermediate phase Co_3O_4 gradually disappears and hence the remaining peaks are attributed to $\text{CaMnO}_{3-\delta}$ nanoparticles. When the surfactant exceeds the limit of saturation i.e, 3g then there was a secondary peak of PVP at $2\theta = 20.23^\circ$ and this could be seen while synthesizing the nanoparticles as precipitation which is good agreement with the reported data [23]. The addition of PVP as a capping agent improves the crystallinity and reduces the average crystallite size of the sample, indicating that this surfactant plays an important role in synthesizing nanoparticles.

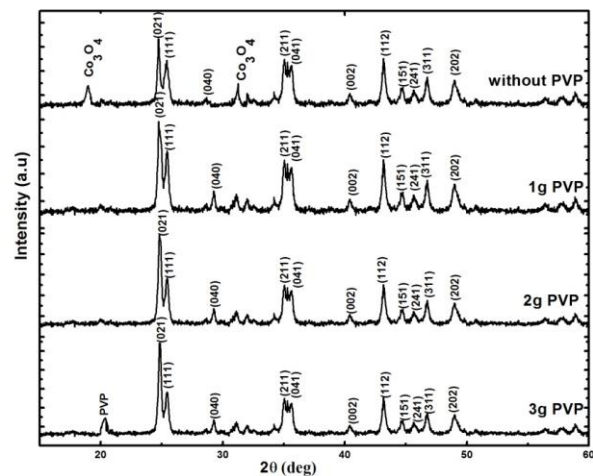


Figure 1. XRD pattern of $\text{CaMnO}_{3-\delta}$ nanoparticles (a) without PVP (b) with 1g PVP (c) with 2g PVP (d) with 3g PVP

The average crystallite size was estimated by Scherrer formula and it is denoted as $D = K\lambda / \beta \cos\theta$, where K , λ , β , θ are the Scherrer constant ($K=0.9$), the wavelength of the radiation $\text{Cu K}\alpha$ ($\lambda = 1.5406 \text{ \AA}$), full width at half maximum of the diffraction peaks, and the Bragg's angle respectively. The size of the nanoparticles decreases with increasing the concentration of PVP and the calculated average particle size of $\text{CaMnO}_{3-\delta}$ nanoparticles with 3g, 2g, 1g of PVP, and without PVP is 11, 15, 42, and 71 nm respectively [24, 25].

3.2. Surface morphology and chemical composition of $\text{CaMnO}_{3-\delta}$ nanoparticles

Figure. 2 represents the surface morphology and EDAX spectrum of surfactant assisted $\text{CaMnO}_{3-\delta}$ nanoparticles

(a, b) without PVP, (c, d) 1g of PVP, (e, f) 2g of PVP, (g, h) 3g of PVP. SEM images shows that the samples have spherical shaped well defined nanoparticles without agglomeration for lower concentration of PVP. When the concentration of PVP exceeds the solubility limit then agglomerated particles are formed [26]. The capping agents form an absorption layer while synthesizing the nanoparticles and then the capped polymer disappear during annealing process and hence the average grain size reduces. The average grain size decreases with increasing the concentration of PVP, due to the burning of more amount of PVP polymer during annealing process.

Elemental composition confirmed the presence of elements with the cationic ratio 1:1 of Ca:Mn is shown in table 1. Oxygen deficient $\text{CaMnO}_{3-\delta}$ nanoparticles are observed for all the samples, indicating that the PVP molecules occupy the vacancy of oxygen. Consequently, we can infer that the synthesized $\text{CaMnO}_{3-\delta}$ nanoparticle is an oxygen deficient material which could be removed to improve the thermopower.

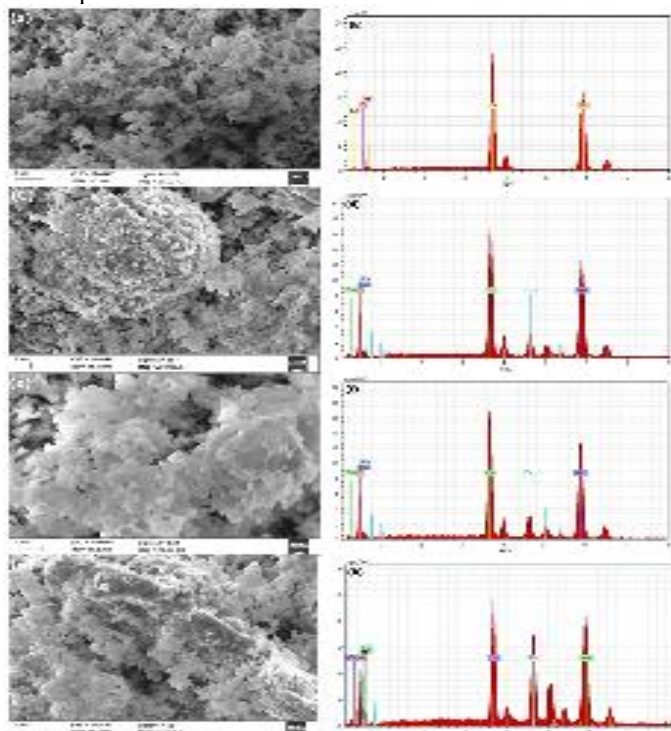


Figure 2. SEM and EDAX pattern of $\text{CaMnO}_{3.6}$ nanoparticles (a, b) without PVP (c, d) with 1g PVP (e, f) with 2g PVP (g, h) with 3g PVP

Table 1. Compositional values of the synthesized $\text{CaMnO}_{3.6}$ nanoparticles based on EDAX analysis

Sample	Element	Series	Atomic %	Ca/Mn
$\text{CaMnO}_{3.6}$ without PVP	Ca	K	24.43	1.03
	Mn	K	23.56	
	O	K	52.01	
$\text{CaMnO}_{3.6}$ with 1g of PVP	Ca	K	22.54	1.10
	Mn	K	20.42	
	O	K	57.04	
$\text{CaMnO}_{3.6}$ with 2g of PVP	Ca	K	21.42	1.05
	Mn	K	20.38	
	O	K	58.20	
$\text{CaMnO}_{3.6}$ with 3g of PVP	Ca	K	22.67	1.21
	Mn	K	18.81	
	O	K	58.52	

3.3. Functional group analysis of $\text{CaMnO}_{3.6}$ nanoparticles

The FTIR spectra of PVP assisted $\text{CaMnO}_{3.6}$ nanoparticles are shown in figure. 3. The OH-stretching and HOH- bending vibrational bands are observed at 3420 cm^{-1} and 1594 cm^{-1} are due to the physically adsorbed water molecule. The peak intensity increases with increasing the concentration of PVP, indicating that the presence of large amounts of carbon in the sample due to excess amount of PVP [27]. Average particle size influences the bands by a small shift which could be attributed to the addition of PVP as a capping agent [28]. Interaction between metal ions and PVP through oxygen C=O group of the polymer is the reason behind the shift in the bands [29]. The symmetric stretching occurs at 855 cm^{-1} indicates the vibration of NO_3 ions and the standard peak of $\text{CaMnO}_{3.6}$ was appeared in the region of $550\text{--}650\text{ cm}^{-1}$ [30].

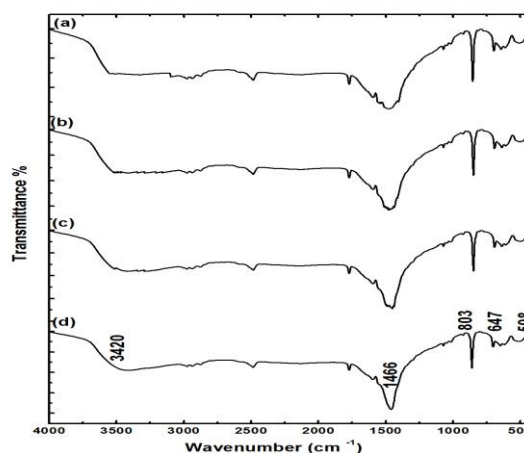


Figure 3. FTIR spectrum of $\text{CaMnO}_{3.6}$ nanoparticles (a) without PVP (b) with 1g PVP (c) with 2g PVP (d) with 3g PVP

3.4. Optical properties of $\text{CaMnO}_{3.6}$ nanoparticles

Figure. 4 (a) represents the absorbance spectra and (b) indirect energy band gap (E_g) of surfactant assisted CaMnO_3 nanoparticles by UV-Vis spectroscopy. Absorption spectra of the samples are recorded in the range of 200-800 nm and it is observed that the absorption spectra shows a wide range of absorption with a broad peak around 300 nm. As PVP concentration increases from 0g to 3g the band gap edges changes between 380 nm and 440 nm and then it sharply moved to lower wavelength regions, indicating that $\text{CaMnO}_{3.6}$ nanoparticle is an indirect band gap material. This absorption spectra shift to a lower wavelength due to the larger band gap of the nanoparticles.

The band gap E_g was calculated from the equation $(\alpha h\nu)^n = B (h\nu - E_g)$, Where α is the absorption coefficient, $h\nu$ is the photon energy, B is dimensional constant, and n is the index representing the transmission order, where $n=2$ for direct band gap and $n=1/2$ for an indirect band gap. The band gap was determined by extrapolating the linear portion of the plot relating $(\alpha h\nu)^{1/2}$ versus $h\nu$ (eV) is shown in figure 4 (b). The calculated band gap energies of $\text{CaMnO}_{3.6}$ nanoparticles at different PVP concentrations of 0g, 1g, 2g and 3g are 2.14 eV, 2.22 eV, 2.30 eV and 2.42 eV. The results indicate that the CaMnO_3 nanoparticle is an indirect, wide band gap semiconducting material. As the concentration of PVP increases, the crystallite size of the material decreases. As a result the band gap energy of the material increases. This

increased band gap due to decreased crystallite size is attributed to the quantum confinement effect of $\text{CaMnO}_{3-\delta}$ nanoparticles.

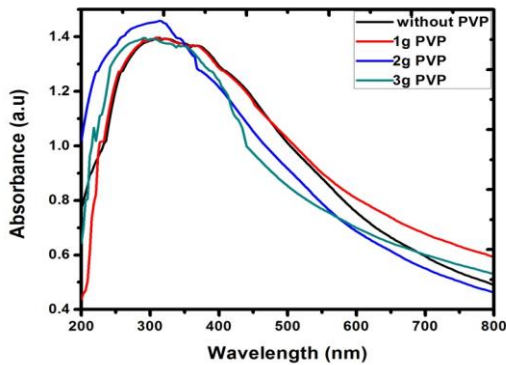


Figure 4 (a) Absorption spectra of $\text{CaMnO}_{3-\delta}$ nanoparticles (a) without PVP (b) with 1g PVP (c) with 2g PVP (d) with 3g PVP

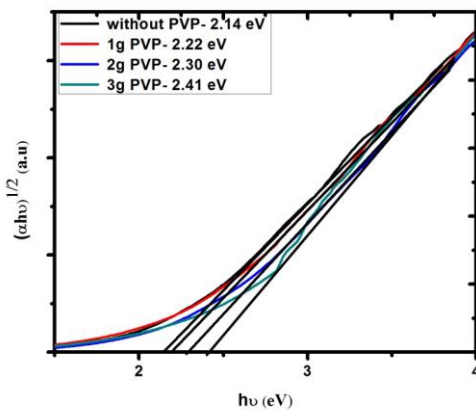


Figure 4 (b) Indirect Band gap of $\text{CaMnO}_{3-\delta}$ nanoparticles (a) without PVP (b) with 1g PVP (c) with 2g PVP (d) with 3g PVP

3.5. Thermoelectric property of $\text{CaMnO}_{3-\delta}$ nanoparticles

Figure 5 depicts the temperature dependence of Seebeck coefficient $S(T)$ and electrical resistivity of surfactant optimized $\text{CaMnO}_{3-\delta}$ nanoparticle annealed at 950°C under air atmosphere with 2g of PVP, where the negative Seebeck coefficient value indicating that the sample is n-type material. The absolute Seebeck coefficient value and electrical resistivity at room temperature is $-287 \mu\text{V/K}$ and $7.4 \Omega \text{ cm}$.

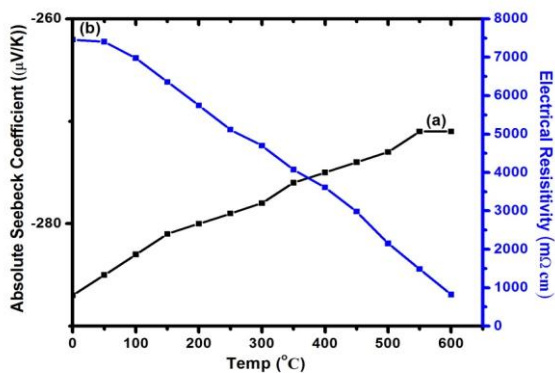


Figure 5. Absolute Seebeck coefficient and electrical resistivity of $\text{CaMnO}_{3-\delta}$ nanoparticles with 2g of PVP annealed at 950°C under air atmosphere

Figure 6 represents the power factor of the $\text{CaMnO}_{3-\delta}$ nanoparticles with 2g of PVP. According to Mott's adiabatic small polaron conduction model the transport properties can be described as $\rho = \rho_0 T \exp(E_a/k_B T)$ where ρ , E_a , k_B are resistivity, activation energy and Boltzman's constant respectively. By using the Arrhenius plot of $\ln(\sigma T)$ versus $1000/T$ and the linear fitting method is used to calculate the activation energy and it was found that 0.08 eV. Power factor increases with increasing temperature.

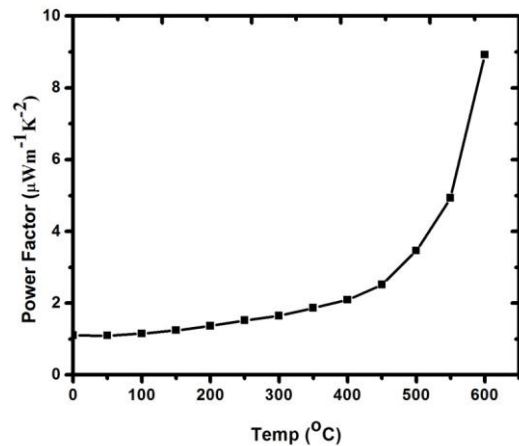


Figure 6. Power factor of $\text{CaMnO}_{3-\delta}$ nanoparticles with 2g of PVP annealed at 950°C under air atmosphere

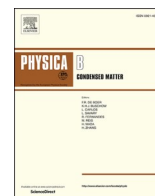
4. CONCLUSION

Orthorhombic perovskite structured $\text{CaMnO}_{3-\delta}$ nanoparticles were synthesized by sol-gel hydrothermal method at 200°C , and the influence of PVP was studied. The average particle size increases with increasing the concentration of PVP, but higher PVP concentration yields the agglomerated nanoparticles with the secondary phase of PVP. FTIR analysis confirmed the formation of crystalline $\text{CaMnO}_{3-\delta}$ nanoparticle with the bands between 550 and 650 cm^{-1} . The Larger amount of carbon in the sample due to excess amount of PVP increased the peak intensity and the shift is due to the interaction between metal ions and PVP molecules. The absolute Seebeck coefficient, electrical resistivity, activation energy and the power factor are obtained for the PVP optimized $\text{CaMnO}_{3-\delta}$ nanoparticle. From the above results, $\text{CaMnO}_{3-\delta}$ nanoparticle with 2g of PVP is a suitable candidate for the fabrication of thermoelectric devices at higher temperature.

REFERENCES

- [1] D.M. Rowe, Thermoelectrics, an environmentally-friendly source of electrical power, *Renew. Ener.*, 16 (1-4) (1999) 1251–1256. Doi : 10.1016/S0960-1481(98)00512-6.
- [2] Mohamed Mouyane, Brahim Itali, Jérôme Bernard, David Houivet, Jacques G. Noudem, Flash combustion synthesis of electron doped- CaMnO_3 thermoelectric oxides, *Powder Tech* 264 (2014) 71–77. Doi: 10.1016/j.powtec.2014.05.022.
- [3] G. J. Snyder, E. S. Toberer, Complex thermoelectric materials, *Nat. Mater.*, 7(2) (2008) 105–114. Doi: 10.1038/nmat2090.
- [4] R. Venkatasubramanian, E. Siivola, T. Colpitts B. Quinn, *Nature.*, 413 (2001) 597–602. Doi: 10.1038/35098012.
- [5] Majumdar A, Thermoelectricity in Semiconductor Nanostructures, *Science.*, 303 (2004) 777–778. Doi: 10.1126/science.1093164.

- [6] Jeroen Spooren Richard, I.Walton, Hydrothermal synthesis of the perovskite manganites $\text{Pr}_{0.5}\text{Sr}_{0.5}\text{MnO}_3$ and $\text{Nd}_{0.5}\text{Sr}_{0.5}\text{MnO}_3$ and alkali-earth manganese oxides CaMn_2O_4 , 4H-SrMnO_3 , and 2H-BaMnO_3 , Hydrothermal synthesis of the perovskite manganites $\text{Pr}_{0.5}\text{Sr}_{0.5}\text{MnO}_3$ and $\text{Nd}_{0.5}\text{Sr}_{0.5}\text{MnO}_3$ and alkali-earth manganese oxides CaMn_2O_4 , 4H-SrMnO_3 , and 2H-BaMnO_3 , *J. Solid State Chem.*, 178 (5) (2005) 1683-1691. Doi:10.1016/j.jssc.2005.03.006.
- [7] Masahiro Yoshimura, Importance of soft processing of advanced materials for sustainable society, *Procedia Engineering.*, 171 (2017) 40-52. Doi: 10.1016/j.proeng.2017.01.308.
- [8] L.M. Fang, X.T. Zu, Z.J. Li, S. Zhu, C.M. Liu, W.L. Zhou, L.M. Wang, Synthesis and characteristics of Fe^{3+} -doped SnO_2 nanoparticles via sol-gel-annealing or sol-gel-hydrothermal route, *J. Alloys Compd.*, 454 (2008) 261–267. Doi: 10.1016/j.jallcom.2006.12.014. 1
- [9] Luminita Predoana, Andrei Jitianu, Silviu Preda, Barbara Malic & Maria Zaharescu, Thermal behavior of Li–Co-citric acid water-based gels as precursors for LiCoO_2 powders, *J. Therm Anal Calorim* (2015) 119:145-153. Doi: 10.1007/s10973-014-4178-4.
- [10] F. Deganello, G. Marci, G. Deganello, Citrate–nitrate auto-combustion synthesis of perovskite-type nanopowders: A systematic approach, *J. Eur. Ceram. Soc.*, 29 (2009) 439–450. Doi: 10.1016/j.jeurceramsoc.2008.06.012.
- [11] A. Mali, A. Ataie, Influence of the metal nitrates to citric acid molar ratio on the combustion process and phase constitution of barium hexaferrite particles prepared by sol–gel combustion method, *Ceram. Int.*, 30 (2004) 1979–1983. Doi: 10.1016/j.ceramint.2003.12.178.
- [12] M. Khazaei, A. Malekzadeh, F. Amini, Y. Mortazavi, A. Khodadadi, Effect of citric acid concentration as emulsifier on perovskite phase formation of nano-sized SrMnO_3 and SrCoO_3 samples, *Cryst. Res. Technol.* 45 (10) (2010) 1064 – 1068. Doi: 10.1002/crat.201000258.
- [13] Mosleh, P. Kamelin, M. Ranjbar, H. Salamatii, Effect of annealing temperature on structural and magnetic properties of $\text{BaFe}_{12}\text{O}_{19}$ hexaferrite nanoparticles, *Ceram. Int.*, 40 (2014) 7279– 7284. Doi: 10.1016/j.ceramint.2013.12.068.
- [14] Phan, C. M, Nguyen, H. M, Role of Capping Agent in Wet Synthesis of Nanoparticles, *J. Phys.Chem. A.*, 121(17) (2017) 3213–3219. Doi:10.1021/acs.jpca.7b02186.
- [15] S. V. Jadhav, D. S. Nikam, V. M. Khot, N. D. Thorat, M. R. Predator, R. S. Ningthoujam, A. B. Salunkhe, S. H. Pawar, Studies on colloidal stability of PVP-coated LSMO nanoparticles for magnetic fluid hyperthermia, *New J. Chem.*, 2013,37, 3121-3130. Doi: 10.1039/C3NJ00554B.
- [16] Tie Liu, Jingyuan Liu, Qi Liu, Yanbo Sun, Xiaoyan Jing, Hongquan Zhang, Jun Wang, Three-dimensional hierarchical Co_3O_4 nano/micro-architecture: synthesis and ethanol sensing properties. *CrystEngComm*, 2019. Doi: 10.1039/C9CE01086F.
- [17] Tongfang Yin, Dawei Liu, Yun Ou, Feiyue Ma, Shuhong Xie, Jing-Feng Li, Jiangyu Li, Nanocrystalline Thermoelectric $\text{Ca}_3\text{Co}_4\text{O}_9$ Ceramics by Sol-Gel Based Electrospinning and Spark Plasma Sintering, *J. Phys. Chem. C* 2010, 114, 10061–10065. Do: 10.1021/jp1024872. Ch. Kanchana Lata, Mucherla Raghasudha, Y. Aparna, Mc. Ramchander, D. Ravinder, Ke.Jaipal, P. Veerasomaiah, D. Shridhar, Effect of Capping Agent on the Morphology, Size and Optical Properties of In_2O_3 Nanoparticles. *Mat. Res.*, 20 (1) (2017) 256–263. Doi:10.1590/1980-5373-mr-2016-0292.
- [18] R. Ma, K. Takada, K. Fukuda, N. Iyi, Y. Bando, T. Sasaki, Topochemical synthesis of monometallic (Co^{2+} - Co^{3+}) layered double hydroxide and its exfoliation into positively charged $\text{Co}(\text{OH})_2$ nanosheets. *Angew. Chem. Int. Ed.* 47 (2008) 86–89. Doi : 10.1002/anie.200703941.
- [19] J.W. Park, D.H. Kwak, S.H. Yoon, S.C. Choi, Thermoelectric properties of Bi, Nb co-substituted CaMnO_3 at high temperature, *J. Alloys Compd.*, 487 (2009) 550–555. Doi: 10.1016/j.jallcom.2009.08.012.
- [20] Ravindra K. Gupta, Eun Yi Kim, Yoo Hang Kim, Chin Myung Whang, Effect of strontium ion doping on structural, thermal, morphological and electrical properties of a co-doped lanthanum manganite system, *J. Alloys Compd.*, 490 (2010) 56–61. Doi: 10.1016/j.jallcom.2009.10.095.
- [21] Yang Wang, Yu Sui, Hongjin Fan, Xianjie Wang, Yantao Su, Wenhui Su, Xiaoyang Liu, High Temperature Thermoelectric response of Electron-Doped CaMnO_3 . *Chem. Mater.* 2009, 21, 4653–4660 4653. Doi:10.1021/cm901766y.
- [22] Jing-Fang Zhu, Guo-Hong Tao, Hang-Yu Liu, Ling He, Qian-Hui Sun, Hai-Chao Liu, Aqueous-phase selective hydrogenation of phenol to cyclohexanone over soluble Pd nanoparticles. *Green chem.*, 02-07. Doi: 10.1039/c0xx00000x.
- [23] B. D. Gultiy, Elements of X-ray diffraction., 2nd ed, Addition –Wesley, USA,(1987).
- [24] Marcela F. Silva, Luiz A. S. de Oliveira, Mariani A. Ciciliati, Michele K. Lima, Flávio F. Ivashita, Daniela M. Fernandes de Oliveira, Ana Adelina W. Hechenleitner, Edgardo A. G. Pineda, The Effects and Role of Polyvinylpyrrolidone on the Size and Phase Composition of Iron Oxide Nanoparticles Prepared by a Modified Sol-Gel Method. *J. Nanomat.*, 2017. Doi: 10.1155/2017/7939727.
- [25] Hang Sun, Jiating He, Jiangyan Wang, Shuang-Yuan Zhang, Cuicui Liu, Thirumany Sritharan, Subodh G Mhaisalkar, Ming-Yong Han, Dan Wang, and Hongyu Chen. Investigating the Multiple Roles of Polyvinylpyrrolidone for A General Methodology of Oxide Encapsulation. *J. Am. Chem. Soc.*, (2013). Doi: 10.1021/ja4035335.
- [26] Marijan Gotic, Svetozar Music, Mo' ssbauer, FT-IR and FE SEM investigation of iron oxides precipitated from FeSO_4 solutions, *J. Molecular Structure.*, 834–836 (2007) 445–453. Doi: 10.1016/j.molstruc.2006.10.059.
- [27] Babu KS, Reddy AR, Reddy KV, Mallika AN. High thermal annealing effect on structural and optical properties of ZnO-SiO_2 nanocomposite. *Mater Sci Semicond Process.*, 2014;27:643–8.
- [28] KV Anasuya, MK Veeraiah, P Hemalatha, Synthesis and Characterization of Poly (Vinylpyrrolidone) -Copper (II) Complexes. *Res.J.chem.sci.*, 5 (2) (2015) 64-69.
- [29] F.P. Zhang, Q.M. Lu, X. Zhang, J.X. Zhang, First principle investigation of electronic structure of CaMnO_3 thermoelectric compound oxide, *J. Alloy Compd.*, 509 (2011) 542–545. doi:10.1016/j.jallcom.2010.09.102.
- [30] A. N. Mallika, A. Ramachandra Reddy, K. Venugopal Reddy. Annealing effects on the structural and optical properties of ZnO nanoparticles with PVA and CA as chelating agents. *J. Advanced Cera.*, 2015, 4(2): 123-129. Doi: 10.1007/s40145- 015-0142-4.



Enhanced thermoelectric property of nanostructured CaMnO_3 by sol-gel hydrothermal method

S. Berbeth Mary^a, M. Francis^a, V.G. Sathe^b, V. Ganesan^b, A. Leo Rajesh^{a,*}

^a Department of Physics, St. Joseph's College (Autonomous), Tiruchirappalli, 620 002, Tamil Nadu, India

^b UGC-DAE Consortium for Scientific Research, University Campus, Khandwa Road, Indore, 452001, India



ARTICLE INFO

Keywords:

Sol-gel hydrothermal
Annealing
Porosity
Oxygen deficiency
Electrical conductivity
Thermopower

ABSTRACT

Perovskite CaMnO_3 nanoparticles were synthesized by sol-gel hydrothermal method at 200 °C, and the samples were annealed at different temperatures between 800 °C and 1000 °C in steps of 50 °C under oxygen (CaMnO_3) and air ($\text{CaMnO}_{2.5}$) atmosphere. The systematic analysis revealed the annealing temperature and atmosphere influenced significant changes in the crystal structure, crystallite size, and oxygen stoichiometry of the material. Powder XRD analysis showed that stable orthorhombic perovskite structure acquired at 950 °C. Microstructure studies confirmed that grains were spherical, and larger grain size was observed for higher annealing temperature. Raman spectra determined orthorhombic domains and the symmetry of Raman lines. Negative values of thermopower were observed, and absolute Seebeck coefficient value for CaMnO_3 and $\text{CaMnO}_{2.5}$ was found to be $-312 \mu\text{VK}^{-1}$ and $-287 \mu\text{VK}^{-1}$ at room temperature. Stoichiometric CaMnO_3 nanoparticle is a suitable material for thermoelectric applications due to low activation energy and high power factor.

1. Introduction

Thermoelectric generation can offer a promising method to acquire a large amount of irrecoverable thermal energy from industries and automobiles by converting the waste heat directly into electricity via Seebeck effect with abundant advantages such as the absence of greenhouse gas, radioactive substances and other emissions with cost-effective and non-movable parts. Potential thermoelectric material should have a large Seebeck coefficient, high electrical conductivity with low thermal conductivity, and the efficiency is measured by a dimensionless figure of merit ZT [1]. Intermetallics like Bi_2Te_3 and CoSb_3 have high ZT value, but unstable in the air at higher temperatures. More research has been done on metal oxides by Terasaki et al. to enhance the efficiency of thermoelectric material at higher temperatures. In 1997 he reported the significant Seebeck coefficient (100 $\mu\text{V/K}$) with high electrical conductivity ($2 \times 10^4 \text{ S/m}$) at 300 K for $\text{Na}_x\text{CoO}_{2+\delta}$ [2,3]. Metal oxides are potential materials for the fabrication of durable thermoelectric devices due to its stability in oxidizing environments at higher temperatures. Oxygen deficient metal oxides show high electrical conductivity, but their thermal stability is relatively poor [4,5]. Compared to other metal oxides, n-type CaMnO_3 compound is thermally stable and oxidation resistant in the air at higher temperatures and

accomplish the need for thermoelectrics [6]. Synthesis techniques like nanostructuring with mesoporous structure can reduce thermal conductivity. Phonon scattering induces the thermal insulation property in mesoporous materials with nanosized pores. This mesoporous structure with nanosized pores is more effective in reducing the thermal conductivity by electron and phonon scattering than the electrical conductivity as nanostructuring changes the band structures, which results in a high Seebeck coefficient. As a consequence, the mesoporous structure is expected to have low thermal conductivity with relatively high electrical conductivity [7–10].

Chemical synthesis methods like hydrothermal, sol-gel, and coprecipitation produce mesoporous nanoparticles with controlled grain size [11,12]. Hydrothermal method has been extensively studied, because of their environmentally friendly nature, monodispersity, morphological control, and highly pure products in the fabrication of ceramics and metal oxides, but the high production cost and failure of large scale production are the limitations of this method. The sol-gel hydrothermal method is a unique method for qualitative as well as quantitative production of metal oxide nanomaterials of high purity, ultra-fine structure, and single phase particles [13,14]. The structure and properties of perovskite manganite depend on its annealing temperature, dwelling time, and atmosphere [15,16]. Smaller grain size

* Corresponding author.

E-mail address: aleorajesh@gmail.com (A.L. Rajesh).

<https://doi.org/10.1016/j.physb.2019.411707>

Received 25 July 2019; Received in revised form 14 September 2019; Accepted 16 September 2019

Available online 20 September 2019

0921-4526/© 2019 Elsevier B.V. All rights reserved.

nanoparticles were achieved by using polyvinyl pyrrolidone as a capping agent which results in high surface to volume ratio, that leads to low thermal conductivity, and hence thermopower of the material has been improved [17–19]. CaMnO_3 is an oxygen storage material due to the availability of a broad range of oxygen content. A significant variation in thermoelectric properties at higher temperature is observed owing to oxygen vacancies compared with air atmosphere. Oxygen deficiency leads to a high amount of Mn^{3+} ions, where this compound has mixed valence states such as Mn^{3+} and Mn^{4+} , which leads to the expansion of the cell. Moreover, the symmetry of the crystal structure and oxygen deficiency depends on the temperature [20–24].

In this present research work, perovskite CaMnO_3 nanoparticles were synthesized by sol-gel hydrothermal method at 200 °C and the samples were annealed at different annealing temperature between 800 °C and 1000 °C in steps of 50 °C under oxygen and air atmosphere. The annealing temperature and atmosphere influenced the crystal structure, crystallite size and oxygen stoichiometry of the material. As the annealing temperature and atmosphere vary, the physical property also gets varied. The formation of perovskite structure and the influence of annealing temperature and oxygen stoichiometry have been investigated and optimized for thermoelectric applications.

2. Experimental procedure

2.1. Synthesis of CaMnO_3 nanoparticles

Metal nitrates of AR grade $\text{Ca}(\text{NO}_3)_2 \cdot 4\text{H}_2\text{O}$ (Sigma–Aldrich, 99%), $\text{Mn}(\text{NO}_3)_2 \cdot \text{H}_2\text{O}$ (Sigma–Aldrich, 99%) and ammonium hydroxide were used as a precursors. Citric acid and Polyvinyl Pyrrolidone (PVP) were used as chelating agent and capping agent respectively. Metal nitrates were weighed according to the stoichiometric value of the composite oxide and dissolved in distilled water to obtain the metal ion solution. Citric acid solution added to the above mixture in the molar ratio 1:1 (citric acid: metal ion) along with PVP solution. A homogeneous solution obtained after stirring it for 30 min and ammonium hydroxide added till its pH reached 9.2, then it is heated till the volume reduced to half of it. This sol transferred into a Teflon lined stainless steel autoclave and placed it in a hot air oven at 200 °C for 20 h. The acquired particles were cleaned with distilled water and ethanol to remove the organic substances, dried and annealed at different temperatures as 800 °C, 850 °C, 900 °C, 950 °C, and 1000 °C under air and oxygen atmosphere for 4 h. The annealing temperature and atmosphere of $\text{CaMnO}_{3-\delta}$ nanoparticles were varied, and structural, morphological, electrical, and thermoelectric properties were investigated and analyzed.

2.2. Characterization

Thermogravimetric (TG) and differential thermal analysis (DTA) were investigated by SDT Q600 TA using an alumina crucible under air atmosphere between room temperature and 1000 °C at a heating rate of 10 °C/min. TG analysis in oxygen atmosphere with the rate of 20 ml/min for $\text{CaMnO}_{3-\delta}$ sample was performed to find the oxygen stoichiometry. To identify the purity, crystallinity, and phase powder, X-ray diffraction (XRD) data were collected by using Bruker D8 advance diffractometer equipped with $\text{Cu K}\alpha$ radiation source ($\lambda = 1.5406 \text{ \AA}$) between 10° and 80° with a step size of 0.02° and a measuring time of 2s. The micro Raman measurement was carried out using Jobin Yvon Horibra LABRAM – HR visible spectrometer connected with micro-optics, where He–Ne laser as source with an excitation wavelength of 632.8 nm at room temperature. The Microstructural observations of the samples were carried out, using a JEOL JSM 5600 scanning electron microscope attached with an Energy Dispersive X-ray spectrometer (EDAX) for determining the chemical composition. For thermoelectric studies, the annealed powders were compacted with 3 wt % of paraffin wax as a binder at 50Mpa and sintered at 850 °C with a heating rate of 10 °C/min for 4 h by conventional sintering process. LSR-3, Seebeck,

Linseis, Germany was used to investigate the thermoelectric properties such as Seebeck coefficient (S), electrical conductivity (σ), activation energy and the power factor ($S^2\sigma$) of CaMnO_3 nanoparticles between room temperature and 600 °C with ΔT as 50 °C in a highly pure helium atmosphere.

3. Results and discussion

3.1. Influence of annealing temperature and atmosphere

3.1.1. Thermal analysis

The result of TG-DTA analysis of the as-prepared CaMnO_3 nanopowders between room temperature and 1000 °C under air atmosphere is shown in Fig. 1. The total weight loss observed in three different temperature regions, where the first weight loss occurs from room temperature to 296 °C, accompanied by an endothermic peak at 238 °C, due to adsorbed water, residual ethanol, and citric acid. The second weight loss occurs in the 296 °C–355 °C temperature range with an endothermic peak at 342 °C and is due to the decomposition of surfactants and nitrates. The third weight loss occurs between 355 °C and 666 °C with a moderate endothermic peak at 451 °C, indicating that the calcination of Ca–Mn–citrate is initiated at 412 °C and completed at 474 °C. Above this temperature, no considerable weight loss was observed due to the complete decomposition of organic compounds and the formation of stable perovskite $\text{CaMnO}_{3-\delta}$ powders. The significant weight loss is due to the removal of lattice oxygen from the sample, indicating that the sample is oxygen deficient ($\delta \sim 0.5$).

TG analysis is used to study the influences of the oxygenation on the chemical composition of the $\text{CaMnO}_{3-\delta}$ nanoparticles. The oxygenation is a single step process where thermogravimetric analysis performed under oxygen atmosphere is depicted in Fig. 2. The above result infers that 2.3% of weight gain occurs between 30 °C and 1000 °C, which is due to the inclusion of oxygen into the structure during the annealing process. In this context, it has been noted that the XRD pattern of the residue sample shows the reflections of $\text{CaMnO}_{3-\delta}$ nanoparticles. Generally, at higher or lower oxygen stoichiometry, stabilization of single phase is a critical task hence two phases are observed instead of single phase and is due to the elimination of only one of each two oxygen along [101] direction. However, single phased orthorhombic structure is observed for the residue of TG measurements which is isostructural phase of $\text{CaMnO}_{2.5}$ nanoparticles. The above results are consistent with the reported data of Luisa Ruiz Gonzalez et al. [25]. They reported that the reduction process of $\text{La}_{0.5}\text{Sr}_{0.5}\text{MnO}_3$ nanoparticles under H_2/He atmosphere leads to oxygen deficiency with the stabilization of the $\text{La}_{0.5}\text{Sr}_{0.5}\text{MnO}_3$ composition. Stabilization of single phased $\text{CaMnO}_{2.5}$ is

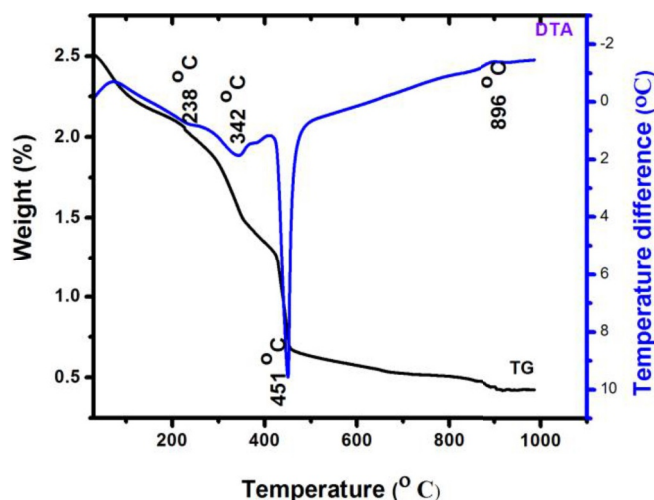


Fig. 1. TG-DTA curves of as prepared $\text{CaMnO}_{3-\delta}$ nanopowder.

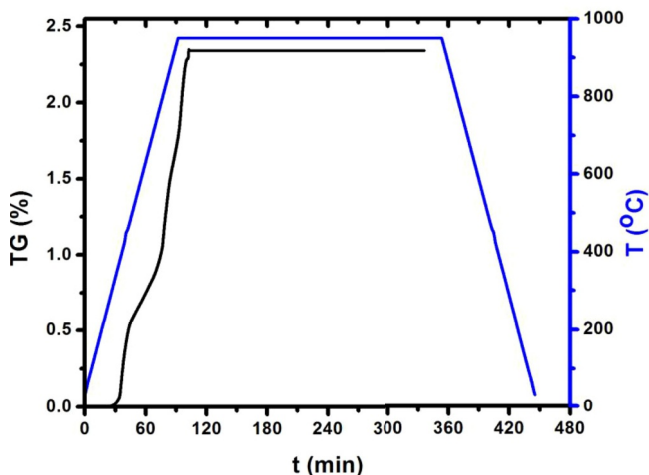


Fig. 2. TG curve of complete oxidation of $\text{CaMnO}_{3-\delta}$ nanoparticles.

possible when the oxygen partial pressure is $P_{\text{O}_2} \leq 5 \times 10^{-4}$ atm at 1273 K [23]. However, oxygen deficiency reduces the thermoelectric power of $\text{CaMnO}_{3-\delta}$ nanoparticles which is not suitable for this application. These problems can be overcome by annealing under oxygen atmosphere, which reduces the oxygen deficiency of the sample and sintering process lowers the oxygen diffusion in the sample. Oxygen loss is active in powdered samples, while sintered samples are used to measure the thermoelectric properties. A moderate exothermic peak at 896 °C implies that the formation of stable orthorhombic $\text{CaMnO}_{3-\delta}$ nanoparticles [26–28].

3.1.2. Morphological analysis

Fig. 3(a)–(f) represents the SEM images and EDAX pattern of $\text{CaMnO}_{3-\delta}$ nanoparticles at different annealing temperatures between 800 °C and 1000 °C in steps of 50 °C under air atmosphere. It can be seen from the results that the samples annealed at lower temperature demonstrates a foamy structure with pores due to the liberation of a large volume of gases during synthesis process. As the annealing temperature increases, the nanoparticles attain uniformly distributed spherical shape with connected pores. However, agglomeration appears when the annealing temperature increased, and the density of the pores gradually moves to nanorange. This porous structure is due to the burning of gases while synthesizing the material. Oxygen deficiency induces the porosity of the sample and hence, the electrical resistivity increases, which in turn reduces the thermopower of the material [29]. The measured average grain size is in the range of nanometer, which is close to the calculated value from XRD analysis. Fig. 3(g) represents the microstructure of CaMnO_3 nanoparticles annealed at 950 °C under oxygen atmosphere for 4 h. Homogeneously dispersed nanoparticles are observed with connected network structure is due to the recovery of oxygen atoms from the atmosphere, and thus stoichiometric CaMnO_3 nanoparticles are obtained, which is consistent with EDAX data. The result reveals that annealing the sample at oxygen atmosphere reduces the oxygen deficiency by recovering the oxygen atoms at higher temperature [30,31]. The surface morphology and EDAX pattern of CaMnO_3 nanoparticles sintered at 850 °C under oxygen atmosphere are shown in Fig. 3(h) and (i). It can be seen from Fig. 3(h), that the sintered sample has less porosity with aggregated grains, and the absorbent range gets reduced to nanometers. Sintering process lowers the oxygen diffusion process, and hence high density material is observed. Nearly spherical shaped particles observed and the grain size is in nanometer range. EDAX spectrum shows the presence of Ca, Mn, and O with the cationic composition as Ca:Mn is 1:1. These results reveal that the pure form of perovskite CaMnO_3 oxide nanoparticles is achieved [32].

3.1.3. Structural analysis

Powder XRD pattern of $\text{CaMnO}_{3-\delta}$ powders with different annealing temperatures from 800 to 1000 °C in steps of 50 °C under air atmosphere is shown in Fig. 4(a)–(e). All the diffraction peaks are indexed and matched with the JCPDS card 46–1009 which confirms the orthorhombic perovskite structure of CaMnO_3 nanoparticles with the space group Pbam. The cell parameters are calculated and tabulated in Table 1, which is consistent with the reported data. However, the calculated lattice parameter along a-axis is larger than the standard one, indicating that the obtained phase is oxygen deficient, which leads to an expansion of the unit cell. The expansion of unit cell is due to the high amount of Mn^{3+} (ionic radius = 0.645 Å) ions over Mn^{4+} (ionic radius = 0.53 Å) ions, though there are two valence states such as Mn^{3+} and Mn^{4+} . The higher amount of Mn^{3+} ions indicates that this perovskite oxide is oxygen-deficient, and this oxygen deficiency generates two five-fold coordinate sites for each oxygen vacancy. Out of six, four of them occupy the rectangular plane site (O1) and two of them octahedral pole site (O2) in MnO_6 octahedron structure. The hybridization of Mn–O1 is higher than Mn–O2 in the conduction process. High electrical resistivity of $\text{CaMnO}_{3-\delta}$ nanoparticles is due to oxygen vacancy of Mn–O1 site. Thus, this oxygen vacancy should be ruled out to obtain high thermopower by enhancing electrical conductivity [21,33]. During synthesis, mixtures of intermediates are transformed into $\text{CaMnO}_{3-\delta}$ at 450 °C, and above this temperature, $\text{CaMnO}_{3-\delta}$ nanoparticle is gradually formed. However, the optimum temperature to obtain a pure, single phase orthorhombic $\text{CaMnO}_{3-\delta}$ nanoparticles is about 900 °C, which is consistent with TG-DTA data.

Fig. 4(f) shows the powder XRD pattern of CaMnO_3 powder annealed at 950 °C under oxygen atmosphere. All the peaks are matched with the standard JCPDS data (CaMnO_3 ; 76-1132), representing that annealing at different atmosphere does not affect the crystal structure of the material. The result shows that the intensity of the peaks of the oxygen annealed sample is stronger than the air annealed sample and the improvement of crystallinity is due to the reduction of oxygen vacancy for oxygen annealed sample which is consistent with the reported data [34]. Least square method is used to calculate the unit cell parameters and cell volume, and the results are tabulated in Table 1, and the calculated values are in good agreement with the reported data. The annealing temperature induces the growth mechanism of nanoparticles; as a result, the average crystallite size increases. Annealing at air atmosphere leads to the reduction process of perovskite oxides, which further leads to oxygen deficiency i.e., $\text{CaMnO}_{3-\delta}$ where $\delta \sim 0.5$ and the Seebeck coefficient decreases enormously due to this oxygen deficiency hence lowers the thermopower of the material. Annealing at air atmosphere produces a less number of Mn–O–Mn bonds which induces the oxygen non-stoichiometry in the samples. However, annealing under oxygen atmosphere leads to stoichiometric CaMnO_3 nanoparticle by recovering the oxygen content from the oxygen atmosphere at higher temperature. Thus all the samples are annealed at oxygen atmosphere for 4 h to overcome the oxygen deficiency to enhance the thermopower [23,35,36]. The average crystallite size is calculated using the Scherrer equation $D = 0.94\lambda / \beta \cos\theta$, where λ , β , and θ are Scherrer constant, the X-ray wavelength, FWHM, and Bragg angle respectively [37–39]. Average crystallite size for the samples annealed at 800 °C, 850 °C, 900 °C, 950 °C, and 1000 °C under air atmosphere is 9, 11, 13, 16 and 27 nm respectively.

One of the effective instrument for structural characterization is Raman spectroscopy in nanomaterials characterization, which detects the symmetry, structural distortions, and phase transformations. The Raman spectra of the samples recorded in the frequency range of 100–800 cm^{-1} at room temperature attached with He–Ne as laser source, and its excitation wavelength is 632 nm. Fig. 5 shows the Raman spectra of CaMnO_3 and $\text{CaMnO}_{2.5}$ nanoparticles with multiple peaks. The observed Raman modes confirm the orthorhombic phase, which is concurrent with the XRD data [40]. The sharp Raman bands substantiate the crystalline nature of CaMnO_3 material, and the observed Raman

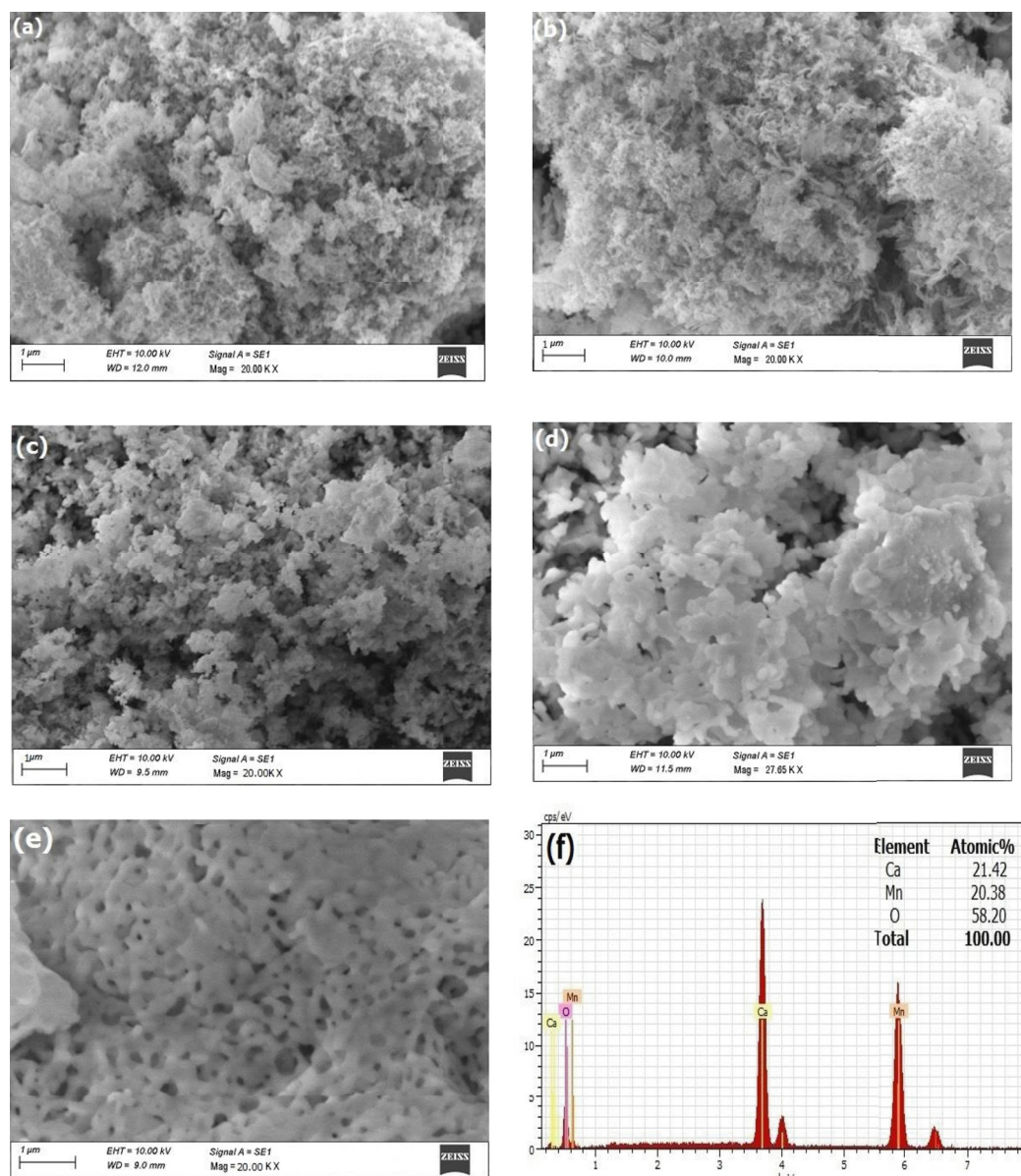


Fig. 3. SEM images and EDAX pattern of $\text{CaMnO}_{3.6}$ nano particles annealed at (a) 800 °C (b) 850 °C (c) 900 °C (d) 950 °C (e) 1000 °C under air atmosphere. SEM images of CaMnO_3 nano particles (g) annealed at 950 °C (h) sintered at 950 °C (i) EDAX spectrum under oxygen atmosphere.

peaks are at 669, 635, 579, 559, 472, 435, 393, 330, 266, 223, and 176 cm^{-1} which are matched with the reported data. Sharp and intensified peaks are observed for CaMnO_3 nanoparticles whereas oxygen deficient nanoparticle shows broadened and low intensified peaks due to two phonon scattering than one phonon. The band can view the symmetric Mn–O stretching vibration of MnO_6 groups that can be seen by the band at 635 cm^{-1} , and the band at 579 cm^{-1} is the fingerprint of Mn–O vibration in MnO_6 layer of the birnessite-type structure. The observed A_g modes are at 266, 223, and 489 cm^{-1} and B_{2g} mode at 635 cm^{-1} . Due to in-plane stretching of Mn–O bonds in MnO_6 octahedra, there was suppression in the peak intensities at 485, and 618 cm^{-1} and this suppression imply that this annealed sample at oxygen atmosphere has low Jahn-Teller distortion. However, broadened peaks infer that air atmosphere annealed sample has high JT distortion due to significant distortion ratio. These results confirm that the sample annealed at air atmosphere has oxygen deficiency [41,42].

3.1.4. Thermoelectric analysis

Figs. 6 and 7 shows the temperature dependence Seebeck coefficient $S(T)$ and electrical resistivity $\rho(T)$ from room temperature to 600 °C. The negative value of thermopower indicates that electrons are the primary charge carriers. Seebeck coefficient depends on charge carriers, which in turn is dependent on the sample nature. The absolute S value for CaMnO_3 and $\text{CaMnO}_{2.5}$ is $-312 \mu\text{VK}^{-1}$ and $-287 \mu\text{VK}^{-1}$ at room temperature. The oxygen annealed sample shows the highest Seebeck coefficient value at 100 °C, which is in good agreement with the previously reported data [43]. The above results are due to the semiconducting behavior and low carrier concentration of the sample. The temperature dependence $S(T)$ value decreases with increasing temperature in the whole temperature range, which is consistent with the reported data [44]. Literature shows different S values and trends for the same range of temperature. M. Mouyane et al. and Cohn et al. measured the Seebeck coefficient as $-460 \mu\text{V K}^{-1}$ and $-550 \mu\text{V K}^{-1}$ for poly crystalline sample at room temperature and the S value decreases with increasing temperature [44,45]. M. Molinari et al. reported the S value for the highly

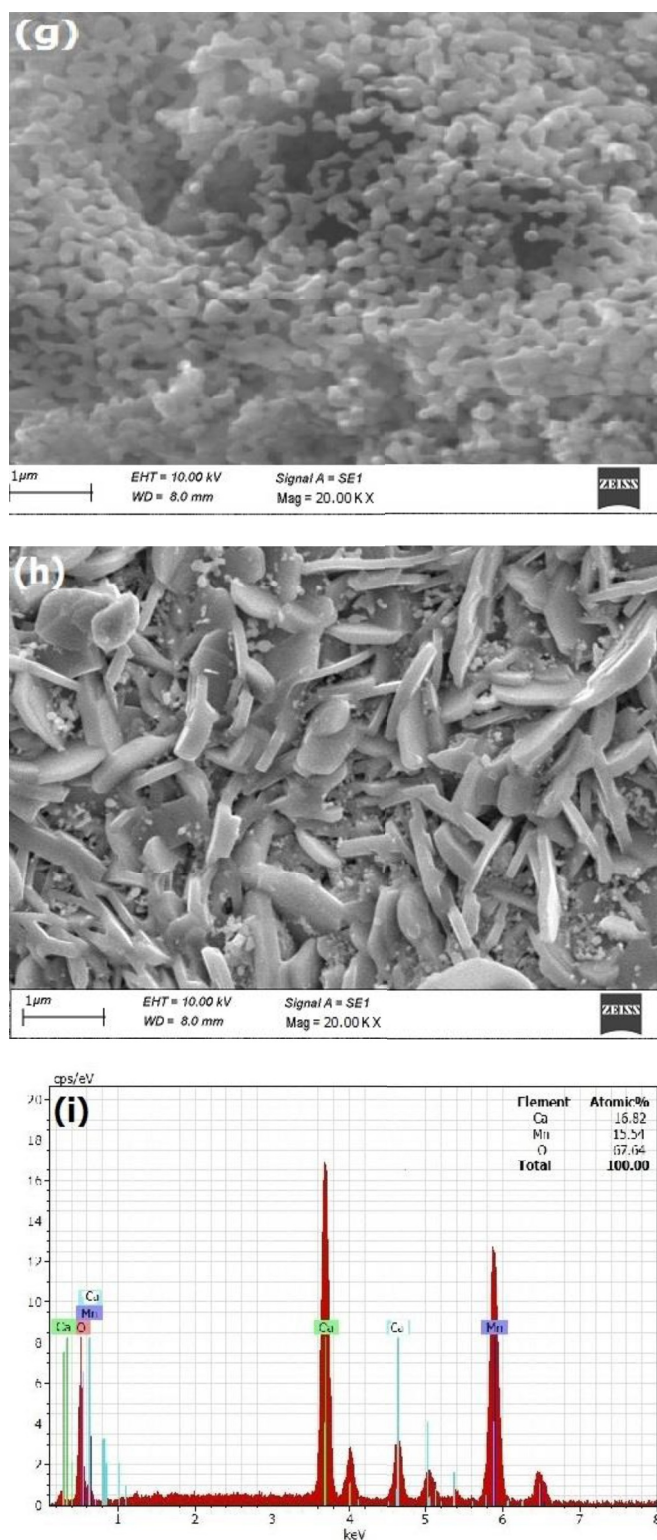


Fig. 3. (continued).

oxidized and highly reduced sample as $-294 \mu\text{VK}^{-1}$ and $-220 \mu\text{VK}^{-1}$ at room temperature [46]. This significant difference may be due to impurities in the samples. However, the absolute Seebeck value of CaMnO_3 is higher than the reduced $\text{CaMnO}_{2.5}$ with a nearly flat curve in the operating temperature range, which reveals that this sample is suitable for thermoelectric applications.

The electrical resistivity (ρ) as a function of temperature is shown in Fig. 7. Non-Stoichiometric and Stoichiometric samples show a high

resistive value of 7.4 and $4.6 \Omega \text{ cm}$ at room temperature, respectively. The above results are similar to the results reported by Xu et al. ($\rho \sim 8 \Omega \text{ cm}$) and Mouyane et al. ($\rho \sim 10 \Omega \text{ cm}$) at room temperature [43, 44]. Highly induced polarons are the critical factors for this high resistive nature of the undoped CaMnO_3 sample, which can then reduce by doping the rare earth metal ions at Ca site. However, the synthesized sample with less oxygen deficiency has higher electrical conductivity than the other one.

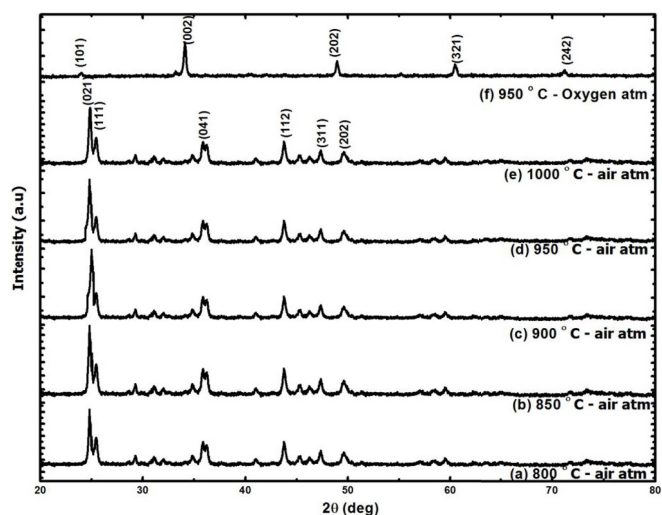


Fig. 4. XRD pattern of $\text{CaMnO}_{3-\delta}$ nano particles with different annealing temperature and atmosphere.

Table 1

Crystallographic parameters with average crystallite size of the CaMnO_3 and $\text{CaMnO}_{2.5}$ nanoparticles.

Sample	Lattice parameters		Cell volume		Average crystallite size
	Calculated	Reported	Calculated	Reported	
Units	\AA		\AA^3		nm
CaMnO_3	$a = 5.278$	$a = 5.279$	206.90	207.027	15
JCPDS: 76-1132	$b = 7.443$	$b = 7.448$			
	$c = 5.2677$	$c = 5.264$			
$\text{CaMnO}_{2.5}$	$a = 5.45$	$a = 5.424$	208.51	207.25	26
JCPDS: 46-1009	$b = 10.23$	$b = 10.23$			
	$c = 3.74$	$c = 3.735$			

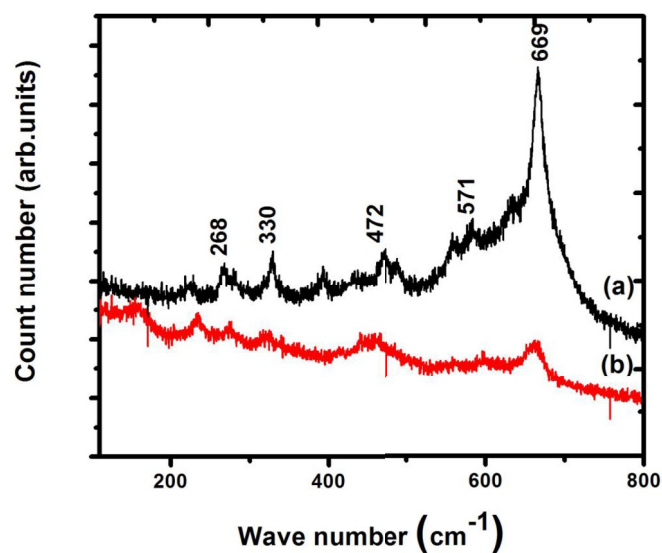


Fig. 5. Raman spectra of CaMnO_3 nanoparticles annealed at 950°C under (a) oxygen atmosphere and (b) air atmosphere.

Fig. 8 represents the activation energy of the samples by using the Arrhenius plot of $\ln(\sigma T)$ versus $1000/T$. The linear fitting method is used to find the slope value for the samples within the measured temperature range due to the non-linearity of the graph and 0.07 eV , and

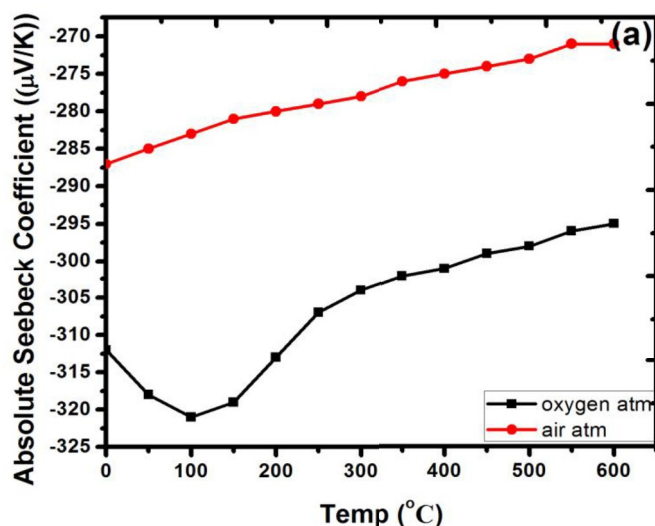


Fig. 6. Seebeck coefficient of CaMnO_3 nanoparticles annealed at 950°C under oxygen and air atmosphere.

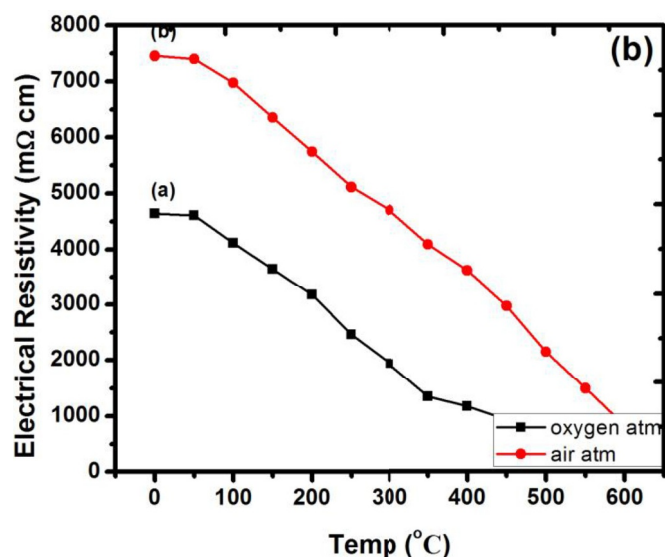


Fig. 7. Electrical resistivity of CaMnO_3 nanoparticles annealed at 950°C under oxygen and air atmosphere.

0.08 eV is the calculated activation energy of CaMnO_3 nanoparticles annealed at oxygen atmosphere and air atmosphere respectively. Larger activation energy implies that the electrical conductivity of the samples is low. CaMnO_3 nanoparticle annealed at oxygen atmosphere shows lower activation energy than at air atmosphere. These results reveal that annealing under oxygen atmosphere at elevated temperature is essential to acquire high electrical conductive CaMnO_3 nanoparticles for thermoelectric devices [45,46].

Temperature-dependent power factor ($\text{PF} = S^2\sigma$) for the stoichiometric and non-stoichiometric samples is shown in Fig. 9. Power factor value increases with increasing temperature for both the samples as expected but the annealed sample under oxygen atmosphere shows higher power factor values due to the absence of oxygen deficiency. These results indicate that the CaMnO_3 nanoparticle annealed at 950°C under oxygen atmosphere is a promising n-type thermoelectric material for feasible thermoelectric devices at elevated temperature [47,48].

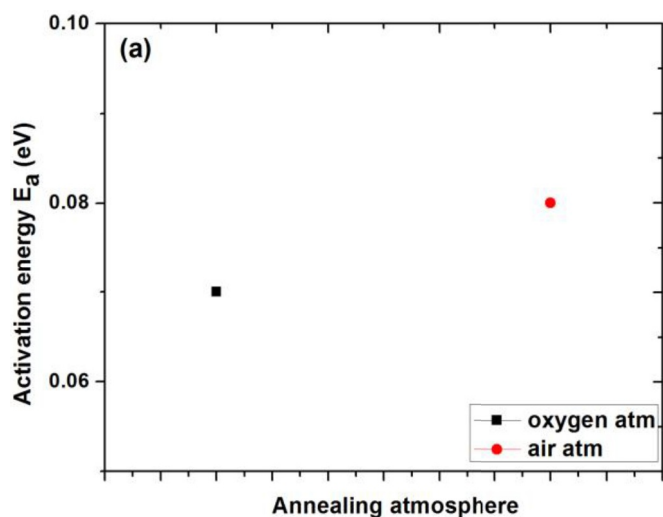


Fig. 8. Activation energy of CaMnO_3 nanoparticles annealed at 950°C under oxygen and air atmosphere.

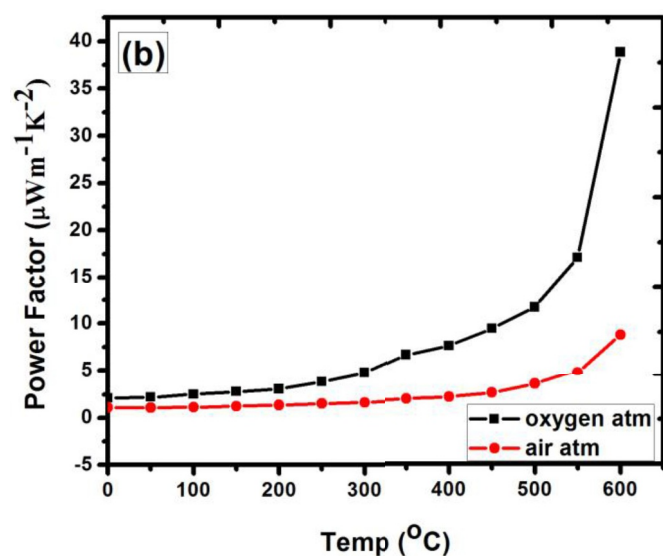


Fig. 9. Power Factor of CaMnO_3 nanoparticles annealed at 950°C under oxygen and air atmosphere.

4. Conclusions

Nanocrystalline CaMnO_3 nanoparticles were synthesized by sol-gel hydrothermal method at 200°C , and the influence of annealing temperature and its oxygen non-stoichiometry were studied. The results indicate that the increase in annealing temperature increases the average crystallite size. Thus the annealing temperature is optimized in such a way that the average crystallite particles get reduced to enhance its physical properties. Mesoporous materials with nanosized pores are introduced in the structure to lower the thermal conductivity. The oxygen deficiency in the samples lead to the expansion of the unit cell. $S(T)$ value decreases with increasing temperature for both CaMnO_3 and $\text{CaMnO}_{2.5}$ nanoparticles due to semiconducting behavior. The Seebeck coefficient value for CaMnO_3 and $\text{CaMnO}_{2.5}$ is $-312 \mu\text{VK}^{-1}$ and $-287 \mu\text{VK}^{-1}$ at room temperature. The samples are highly resistive, and it gradually decreases with increasing temperature. Lower activation energy and high power factor obtained for the stoichiometric sample due to the lower value of resistivity. The above structural, morphological, and thermoelectric results indicate that annealed CaMnO_3 nanoparticles

at 950°C under oxygen atmosphere is a suitable n-type material for thermoelectric applications at a higher temperature.

Declaration of interests

The authors declare that they have no known competing financial interests or personal relationships that could have appeared to influence the work reported in this paper.

Acknowledgment

One of the author Ms. S. Berbeth Mary would like to extend her gratitude to the UGC-DAE Consortium for Scientific Research, Indore for providing the XRD, SEM with EDAX, and Raman instrumentation techniques.

References

- [1] D.M. Rowe (Ed.), *Thermoelectrics Handbook: Macro to Nano, first ed.*, CRC Press, Boca Raton, FL, 2006, 1-3-1-7.
- [2] G. Chen, M.S. Dresselhaus, G. Dresselhaus, J.P. Fleurial, T. Caillat, Recent developments in thermoelectric materials, *Int. Mater. Rev.* 48 (2003) 45, <https://doi.org/10.1179/095066003225010182>.
- [3] I. Terasaki, Y. Sasago, K. Uchinokura, Large thermoelectric power in NaCo_2O_4 single crystals, *Phys. Rev. B* 56 (1997) R12685–R12687, <https://doi.org/10.1103/physrevb.56.R12685>.
- [4] Michitaka Ohtaki, Hisako Koga, Tsutomu Tokunaga, Koichi Eguchi, Hiromichi Arai, Electrical transport properties and high-temperature thermoelectric performance of $(\text{Ca}_{0.9}\text{M}_{0.1})\text{MnO}_3$ ($M = \text{Y, La, Ce, Sm, In, Sn, Sb, Pb, Bi}$), *J. Solid State Chem.* 120 (1995), <https://doi.org/10.1006/jssc.1995.1384>.
- [5] X.H. Zhang, J.C. Li, Y.L. Du, F.N. Wang, H.Z. Liu, Y.H. Zhu, J. Liu, W.B. Su, C. L. Wang, L.M. Mei, Thermoelectric properties of A-site substituted Lanthanide $\text{Ca}_{0.75}\text{R}_{0.25}\text{MnO}_3$, *J. Alloy. Comp.* 634 (2015) 1–5, <https://doi.org/10.1016/j.jallcom.2015.02.074>.
- [6] J.G. Noudem, D. Kenfaui, S. Quetel Weben, C.S. Sanmathi, R. Retoux, M. Gomina, Spark Plasma sintering of n-type thermoelectric $\text{Ca}_{0.95}\text{Sm}_{0.05}\text{MnO}_3$, *J. Am. Chem. Soc.* 94 (8) (2011) 2608–2612, <https://doi.org/10.1111/j.1551-2916.2011.04465.X>.
- [7] X. Han, Y. Hu, J. Yang, F. Cheng, J. Chen, Porous perovskite CaMnO_3 as an electro catalyst for rechargeable LiO_2 batteries, *Chem. Commun. (J. Chem. Soc. Sect. D)* 50 (2014) 1497, <https://doi.org/10.1039/C3CC48207C>.
- [8] Jianrong Niu, Jiguang Deng, Wei Liu, Lei Zhang, Guozhi Wang, Hongxing Dai, He Hong, Xuehong Zi, Nanosized perovskite-type oxides $\text{La}_{1-x}\text{Sr}_x\text{MO}_{3-\delta}$ ($M = \text{Co, Mn}$; $x = 0, 0.4$) for the catalytic removal of ethyl acetate, *Catal. Today* 126 (2007) 420–429, <https://doi.org/10.1016/j.cattod.2007.06.027>.
- [9] C.J. Vineis, T.C. Harman, S.D. Calawa, M.P. Walsh, R.E. Reeder, R. Singh, A. Shakouri, Carrier concentration and temperature dependence of the electronic transport properties of epitaxial PbTe and PbTe/PbSe nanodot superlattices, *Phys. Rev. B* 77 (2008) 235202, <https://doi.org/10.1103/physrevb.77.235202>.
- [10] Jinle Lan, Yuan-Hua Lin, Hui Fang, Mei Ao, Ce-Wen Nan, Yong Liu, Shaoliang Xu, Matthew Peters, High-temperature thermoelectric behaviors of fine-grained Gd-doped CaMnO_3 ceramics, *J. Am. Ceram. Soc.* 93 (8) (2010) 2121–2124, <https://doi.org/10.1111/j.1551-2916.2010.03673.x>.
- [11] Nikhil Satyala, Daryoosh Vashae, The effect of crystallite size on thermoelectric properties of bulk nanostructured magnesium silicide (Mg_2Si) compounds, *Appl. Phys. Lett.* 100 (2012), 073107, <https://doi.org/10.1063/1.3684615>.
- [12] K.G. Kanade, J.O. Baeg, S.K. Apte, T.L. Prakash, B.B. Kale, Synthesis and characterization of nanocrystalline zirconia by hydrothermal method, *Mater. Res. Bull.* 43 (2008) 723–729, <https://doi.org/10.1016/j.materresbull.2007.03.025>.
- [13] K. Sadhana, R.S. Shinde, S.R. Murthy, Synthesis of nano crystalline Yig using microwave-hydrothermal method, *Int. J. Mod. Phys. B* 17 (2009) 3637–3642, <https://doi.org/10.1142/s0217979209063109>.
- [14] Thi Minh Hue Dang, Viet Dung Trinh, Doan Huan Bui, Manh Huong Phan, Dang Chinh Huynh, Sol-gel hydrothermal synthesis of strontium hexaferrite nanoparticles and the relation between their crystal structure and high Coercivity properties, *Adv. Nat. Sci. Nanosci. Nanotechnol.* 3 (2012), 025015, <https://doi.org/10.1088/2043-6262/3/2/025015>.
- [15] Xianwei Meng, Hao Sue, Jialong Li, Qiuyue Fu, Dongsheng Fu, Preparation of $\text{Ca}_{0.8}\text{Sm}_{0.2}\text{MnO}_3$ powders and effects of calcination temperature on structure and electrical property, *Powder Technol.* 224 (2012) 96–100, <https://doi.org/10.1016/j.powtec.2012.02.034>.
- [16] S. Ravia, A. Karthikeyan, Effect of calcination temperature on $\text{La}_{0.7}\text{Sr}_{0.3}\text{MnO}_3$ nanoparticles synthesized with modified sol-gel route, *Phy Proc* 54 (2014) 45–54, <https://doi.org/10.1016/j.phpro.2014.10.035>.
- [17] Marcela F. Silva, Luiz A.S. De Oliveira, Mariani A. Ciciliati, Michele K. Lima, Flávio F. Ivashita, Daniela M. Fernandes de Oliveira, Ana Adelina W. Hechenleitner, Edgardo A.G. Pineda, The effects and role of polyvinyl pyrrolidone on the size and phase composition of iron oxide nanoparticles prepared by a modified sol-gel method, *J. Nanomater.* (2017) 7939727, <https://doi.org/10.1155/2017/7939727>.
- [18] Mahmoud Goodarz Naseri, Saion Elias, Nasrin Khalil Zadeh, The amazing effects and Role of PVP on the crystallinity phase composition and morphology of nickel

- ferrite nanoparticles prepared by thermal treatment method, *Int. Nano Lett.* 3 (2013) 19, <https://doi.org/10.1186/2228-5326-3-19>.
- [19] Hang Sun, Jiating He, Jiangyan Wang, Shuang-Yuan Zhang, Cuicui Liu, Thirumany Sritharan, Subodh G. Mhaisalkar, Ming-Yong Han, Dan Wang, Hongyu Chen, Investigating the multiple roles of polyvinyl pyrrolidone for A general methodology of oxide encapsulation, *J. Am. Chem. Soc.* 135 (2013) 9099–9110, <https://doi.org/10.1021/ja4035335>.
- [20] Philipp Thiel, James Eilertsen, Sascha Populoh, Gesine Saucke, Max Döbeli, Andrey Shkablo, Leyre Sagarna, Lassi Karvonen, Weidenkaff Anke, Influence of tungsten substitution and oxygen deficiency on the thermoelectric properties of $\text{CaMnO}_{3-\delta}$, *J. Appl. Phys.* 114 (2013) 243707, <https://doi.org/10.1063/1.4854475>.
- [21] Atsuko Kosuga, Yuri Isse, Yifeng Wang, Kunihito Koumoto, Ryoji Funahashi, High-temperature thermoelectric properties of $\text{Ca}_{0.9-x}\text{Sr}_x\text{b}_{0.1}\text{MnO}_{3-\delta}$ ($0 \leq x \leq 0.2$), *J. Appl. Phys.* 105 (2009), 093717, <https://doi.org/10.1063/1.3125450>.
- [22] Brajendra Singh, S.S. Manoharan, Structural transformation and magnetic properties of $\text{CaMn}_{1-x}\text{Fe}_x\text{O}_{3-\delta}$ ($0.0 \leq x \leq 0.5$), *Mater. Lett.* 65 (13) (2011) 2029–2031, <https://doi.org/10.1016/j.matlet.2011.04.025>.
- [23] K. Vijayanandhini, Phase conversions in calcium manganites with changing Ca/Mn ratios and their influence on the electrical transport properties, *J. Mater. Sci. Mater. Electron.* 20 (5) (2009) 445–454, <https://doi.org/10.1007/s10854-008-9749-3>.
- [24] Luisa Ruiz-González, Raquel Cortés-Gil, José M. Alonso, José M. González-Calbet, María Vallet-Regí, Revisiting the role of vacancies in manganese related perovskites, *Open Inorg Chem* 1 (2007) 37–46.
- [25] Luisa Ruiz-González, Raquel Cortés-Gil, José M. Alonso, M. José, González-Calbet, María Vallet-Regí, Revisiting the role of vacancies in manganese related perovskites, *Open Inorg. Chem. J.* 1 (2007) 37–46.
- [26] Farnham Craig, Masaki Nakao, Masatoshi Nishioka, Minako Nabeshima, Takeo Mizuno, Effect of water temperature on evaporation of mist sprayed from a nozzle, *J. Heat Island Institute Int.* 10 (2015) 35–44.
- [27] Mahmood M. Barbooti, Dhoab A. Al-Sammerrai, Thermal decomposition of citric acid, *Thermochim. Acta* 98:119–126. DOI: 10.1016/0040-6031(86)87081-2.
- [28] J.W. Park, D.H. Kwak, S.H. Yoon, S.C. Choi, Thermoelectric properties of Bi, Nb co-substituted CaMnO_3 at high temperature, *J. Alloy. Comp.* 487 (1–2) (2009) 550–555, <https://doi.org/10.1016/j.jallcom.2009.08.012>.
- [29] C.S. Sanmathi, Y. Takahashi, D. Sawaki, Y. Klein, R. Retoux, I. Terasaki, J. G. Noudem, Microstructure control on thermoelectric properties of $\text{Ca}_0.96\text{Sm}_0.04\text{MnO}_3$ synthesized by co-precipitation technique, *Mater. Res. Bull.* 45 (5) (2010) 558–563, <https://doi.org/10.1016/j.materresbull.2010.01.023>.
- [30] Chang-Sun Park, woogie Han, Dong Il Shim, Hyung Hee Cho, Hyung-Ho Park, The effect of mesoporous structure on the thermoelectric properties of non-stoichiometric La-doped SrTiO_3 , *J. Electrochem. Soc.* 163 (6) (2016) E155–E158, <https://doi.org/10.1149/2.0441606jes>.
- [31] Ch.S. Park, Min Hee Hong, Sangwoo Shin, Hyung Hee Cho, Hyung Ho Park, Synthesis of mesoporous $\text{La}_{0.7}\text{Sr}_{0.3}\text{MnO}_3$ thin films for thermoelectric Materials, *J. Alloy. Comp.* 632 (2015) 246–250, <https://doi.org/10.1016/j.jallcom.2015.01.188>.
- [32] Weiren Xiaa, Lia Lei, Heng Wua, Piaojie Xuea, Xinhua Zhua, Structural, morphological, and magnetic properties of sol-gel derived $\text{La}_{0.7}\text{Ca}_{0.3}\text{MnO}_3$ manganese nanoparticles, *Ceram. Int.* 43 (2017) 3274–3283, <https://doi.org/10.1016/j.ceramint.2016.11.160>.
- [33] Ravindra K. Guptaa, Eun Yi Kima, Yoo Hang Kimb, Chin Myung Whanga, Effect of Strontium ion doping on structural, thermal, morphological and electrical properties of a co-doped lanthanum manganite system, *J. Alloy. Comp.* 490 (2010) 56–61, <https://doi.org/10.1016/j.jallcom.2009.10.095>.
- [34] Atefeh Jafari, Komail Boustani, Siamak Pilban-Jahromi, Boon Tong Goh, Evolution of structural and magnetic properties of nickel oxide nanoparticles: influence of annealing ambient and temperature, *J. Magn. Magn. Mater.* 469 (2019) 383–390, <https://doi.org/10.1016/j.jmmm.2018.08.005>.
- [35] Z. Zeng, M. Greenblatt, M. Croft, Large magnetoresistance in antiferromagnetic $\text{CaMnO}_{3-\delta}$, *Phys. Rev. B* 13 (1999) 8784–8788, <https://doi.org/10.1103/physrevb.59.8784>.
- [36] P. Thiel, S. Populoh, S. Yoon, A. Weidenkaff, Enhancement of redox and phase stability of Thermoelectric $\text{CaMnO}_{3-\delta}$ by substitution, *J. Solid State Chem.* 229 (2015) 62–67, <https://doi.org/10.1016/j.jssc.2015.05.013>.
- [37] F.P. Zhang, Q.M. Lu, X. Zhang, J.X. Zhang, First principle investigation of electronic structure of CaMnO_3 thermoelectric compound oxide, *J. Alloy. Comp.* 509 (2011) 542–545, <https://doi.org/10.1016/j.jallcom.2010.09.102>.
- [38] M.F. Silva, C.A. Da Silva, F.C. Fogo, E.A.G. Pineda, Anita A.W. Hechenleitner, Thermal and FTIR study of polyvinylpyrrolidone/lignin blends, *J. Therm. Anal. Calorim.* (2005) 367–370, <https://doi.org/10.1007/s10973-005-0066-2>.
- [39] B.D. Cullity, *Elements of X-Ray Diffraction*, second ed., Addison-Wesley, USA, 1987.
- [40] V. Abrashev, J. Backstrom, L. Borjesson, V.N. Popov, R.A. Chakalov, N. Kolev, R.-L. Meng, M.N. Iliiev, Raman spectroscopy of CaMnO_3 : mode assignment and relationship between Raman line intensities and structural distortions, *Phys. Rev. B* 65 (2001) 184301, <https://doi.org/10.1103/physrevb.65.184301>.
- [41] S. Majumdar, H. Huhtinen, P. Patuuri, R. Palai, The effect of oxygen on the Jahn–Teller distortion and magnetization dynamics of $\text{Pr}_{0.9}\text{Ca}_{0.1}\text{MnO}_3$ thin films, *J. Phys. Condens. Matter* 25 (6) (2013), 066005, <https://doi.org/10.1088/0953-8984/25/6/066005>.
- [42] C.H. Shek, G.M. Lin, J.K.L. Lai, Effect of oxygen deficiency on the Raman spectra and hyperfine interactions of nanometer SnO_2 , *Nanostructured Mater.* 11 (7) (1999) 831–835.
- [43] Gaojie Xu, Ryoji Funahashi, Qirong Pu, Biao Liu, Ruhua Tao, Guansheng Wang, Zejun Ding, High-temperature transport properties of Nb and Ta substituted CaMnO_3 system, *Solid State Ion.* 171 (2004) 147–151, [https://doi.org/10.1016/S0167-2738\(03\)00108-5](https://doi.org/10.1016/S0167-2738(03)00108-5).
- [44] Mouyane Mohamed, Brahim Itaait, Jérôme Bernarda, David Houivet, Jacques G. Noudem, Flash combustion synthesis of electron doped- CaMnO_3 thermoelectric oxides, *Powder Technol.* 264 (2014) 71–77, <https://doi.org/10.1016/j.powtec.2014.05.022>.
- [45] J.L. Cohn, C. Chiorescu, J.J. Neumeier, Polaron transport in the paramagnetic phase of electron-doped manganites, *Phys. Rev. B* 72 (2005), 024422, <https://doi.org/10.1103/PhysRevB.72.024422>.
- [46] Marco Molinari, David A. Tompsett, Stephen C. Parker, Feridoon azough, robert freer, structural, electronic and thermoelectric behaviour of CaMnO_3 and $\text{CaMnO}_{3-\delta}$, *J. Mater. Chem.* 2 (2014) 14109, <https://doi.org/10.1039/c4ta01514b>.
- [47] Guangru Zhang, Xueliang Dong, Zhengkun Liu, Wei Zhou, Zongping Shao, Wanqin Jin, Cobalt-site cerium doped $\text{Sm}_x\text{Sr}_{1-x}\text{CoO}_{3-\delta}$ oxides as potential cathode materials for solid-oxide fuel cells, *J. Power Sources* 195 (2010) 3386–3393, <https://doi.org/10.1016/j.jpowsour.2009.12.039>.
- [48] J.W. Parka, D.H. Kwakb, S.H. Yoonb, S.C. Choi, Thermoelectric properties of Bi, Nb co substituted CaMnO_3 at high temperature, *J. Alloys Compd* 487 (2009) 550–555, <https://doi.org/10.1016/j.jallcom.2009.08.012>.

Materials Research Express



PAPER

Microstructural characterization and mechanical properties of Al7075/BN metal matrix composites prepared by conventional casting method

RECEIVED
23 September 2018

REVISED
27 January 2019

ACCEPTED FOR PUBLICATION
18 February 2019

PUBLISHED
6 March 2019

V Vignesh Kumar^{1,5} , K Raja², K Chandrasekaran³ and T Ramkumar⁴ 

¹ Department of Mechanical Engineering, Sree Sowdambika College of Engineering, Aruppukottai, Tamilnadu, India

² Department of Mechanical Engineering, University College of Engineering, Anna University, Dindigul, Tamilnadu, India

³ Department of Mechanical Engineering, MAM School of Engineering, Trichy, Tamilnadu, India

⁴ Department of Mechanical Engineering, Dr Mahalingam College of Engineering and Technology, Pollachi, Tamilnadu, India

⁵ Author to whom any correspondence should be addressed.

E-mail: vigneshed2014@gmail.com, rajagce@gmail.com, kchandrasekaran1984@gmail.com and ramkimech89@gmail.com

Keywords: BN, carbide drill bit, FESEM-EDAX, MM, tensile fractography

Abstract

The research article addresses to improve the mechanical behaviour of the Al 7075 composites like tensile, surface roughness (SR) and thrust force fabricated by conventional stir casting process with a modernized three step stirring method. Boron Nitride particles are reinforced with varying wt% of 3, 6 and 9 respectively. Boron Nitride particles are characterized using metallurgical microscopy (MM), Field Emission Scanning Electron Microscopy (FESEM) & Energy Dispersive x-ray Analysis (EDAX). The density and hardness of the samples are determined using Archimedes principle and micro hardness testing machine. Drilling experiments are conducted for the prepared composites. Fully carbide drill bit is used for the entire experiment with varying input parameters such as (Speed, Feed & Point of angle). The results reveal that the surface roughness is decreased due to the presence of hard ceramic phase. The tensile behaviour of the composites is increased when compared with the base material. Further the tensile fractography and drill worn surface is analyzed using SEM.

1. Introduction

Aluminium based Composite materials are broadly used as an auxiliary for predominant materials because of the light weight, inexpensive and energy efficient. It has some outstanding properties which helps to utilize it for military, automobiles, aircraft and other nuclear applications as depicted by Mahesh L *et al* 2018 [1]. Matrix stipulation is depended upon the key factors to choose the perfect reinforcement and the route of fabrication. The matrix material involves distributing the stress over to the secondary particles, which also keeps and gives shape to the material. The reinforcement affords the feasible mechanical strength to the composite material in a superior path. According to Yanjun Li *et al* 2017 [2] quotes, recently BN has attracted reinforcement of researchers due to low density (2.1 g cm^{-3}), extreme melting point ($2973 \text{ }^\circ\text{C}$) stability; high stiffness; high hardness and good thermal stability. The Boron Nitride (BN) particle is an immersive and strong ceramic material for aluminium matrix composites which acts as an excellent solid-self lubricant and makes the composites tougher. The augmentation of BN particles enhances the machinability and wear resistance bears of the Al-BN composites. Several production routes such as liquid metallurgy (LM) route, Powder Metallurgy (PM) route and infiltration techniques are used to produce AMC composites. Defu Liu *et al* 2012, Ali Çelik *et al* 2015, Harichandran *et al* 2017, Kannan *et al* 2017 [3–6] concluded that, the liquid metallurgy casting method is the cheapest method, of all the available manufacturing techniques for AMCs, with a low-cost benefit; it also offers a varied range of material processing conditions and can manufacture composites with better wt% and vol% of reinforcement particles because of the accomplishment of the stirring action. Samy *et al* 2017 [7] has reported that, the primary recognition of stir casting process is its suitability to mass production; compared to another fabrication processes, stir casting process costs low from 1/3rd to 1/10th with mass production of

Table 1. Chemical composition (wt%) and mechanical properties of Al7075 aluminium alloy.

Al7075	Chemical Composition	Zn	Cr	Cu	Fe	Mg	Mn	Si	Ti	Al
		5.23	0.19	1.23	0.53	2.52	0.18	0.42	0.095	Bal
	Mechanical properties	Ultimate tensile strength			Yield strength		Fatigue strength		Thermal conductivity	
		572 MPa			503 MPa		159 MPa		130 W m ⁻¹ .k	

aluminium matrix composites. Due to all these considerations, stir casting process is employed in the present research for the manufacturing of aluminium composites. Basavarajappa *et al* 2008, Zedan *et al* 2013 [8, 9] depicted that drilling of AMCs is challenging since, hard ceramic particles presence wear in cutting tool during machining processes, and also surface quality cannot be achieved.

Mihai-Bogdan Lazar *et al* 2011, Yahya Altunpak *et al* 2012, Aftab *et al* 2017, D’Orazio *et al* 2017 [10–13] said that, being the final linkage of aircraft structure assembly, drilling is one of the most significant methods in mechanical manufacturing industry. In aircraft riveting assembly, drilling is the main concern to join the components. Palanikumar *et al* 2014, Nanya Li *et al* 2015, Selvakumar *et al* 2016, Xavier Rimpault *et al* 2016, Ergün Ekici *et al* 2017 [14–18] stated that drilling constitutes 40% of all metal cutting operations. There are some parameters that influence the cutting forces and surface quality of the drill hole, such as cutting speed, feed rate, tool type and particle fraction. To optimize these drilling, parameters are needed for improving the efficiency of drilling and surface quality of the drilled hole. Polycrystalline diamond, cubic boron nitride tools are recommended for machining BN-reinforced Aluminium matrix composites. But these cutting tools are very expensive. Owing to their low cost, carbide drill tool material is selected in this research work.

Numerous researchers applied different reinforcement particles using various methods to produce aluminium composites. They are used to different production routes for attaining the desired microstructural and mechanical properties. In the aerospace industries, they met the trouble in making of aircraft structural components with good microstructural and high hardness with less in weight. Usage of secondary particles can act as a ceramic material as well as solid lubricant. Boron nitride particle has fulfilled both the needs. There is still a lack of understanding of the machining of Al-BN composite and it is well known that limited work is reported in the area of machining and microstructural studies of Al7075. The intention of this research work is to investigate the fabrication of Al7075-BN particulate reinforced composites through mechanical assisted stir casting processes. By using carbide drill bit the drilling operation was performed for fabricated samples. As a result, the BN reinforced aluminium composites provides better properties such as, microstructure, mechanical, and surface roughness than un reinforced alloys.

2. Experimental methods

2.1. Materials

The research work carried, Aluminium alloy (Al7075-T6) of peak-aged condition in the form of rod with 20 mm diameter and 100 mm length is used as the base material. Al7075 is a homogenizing alloy which contains zinc and magnesium as the major alloying element. Density of the base Aluminium alloy is 2.81 g cm⁻³. The quality assured Al 7075 material has been purchased from Coimbatore Metal Mart, India. The chemical composition and mechanical properties of the alloy are given in table 1. The industrial quality BN powder has been purchased from Sigma-Aldrich, Germany (98% purity) with an average particle size of 1 μm. The composites samples are prepared by varying the Boron Nitride (BN) wt% such as 3, 6 and 9 respectively.

2.2. Fabrication process

In order to produce the Al 7075/BN composites using stir casting process is used in this study. The base material Aluminium alloy 7075 is cleaned using acetone for removing the lapping rusts. Before casting, the base metal is melted through high performance electric resistance graphite crucible furnace (figure 1) up to 850 °C. 8 kg of Al7075 material is used to fabricate the specimen. Once the base alloy is liquefied fully, degassing process is carried out by adding Potassium Hexafluorotitanate powder; this removes nitrogen, carbon-dioxide and impurities absorbed during the melting process in the furnace, Mahamani A 2014 [19]. Now the 500 °C preheated BN powder particles are dispersed into the matrix and stirred mechanically for 600 RPM for 15 min. The stirring is carried out at inside the molten metal using a stainless-steel twin blade impeller. It supports to disperse the reinforcement material consistently dispersion. The mechanical stirrer is placed closer to the bottom of the graphite crucible, and the impeller blades are tilted at an angle of 45°. It covers a comparatively large area of the crucible bottom. At the end, the molten metal is poured into the preheated EN8 Die steel

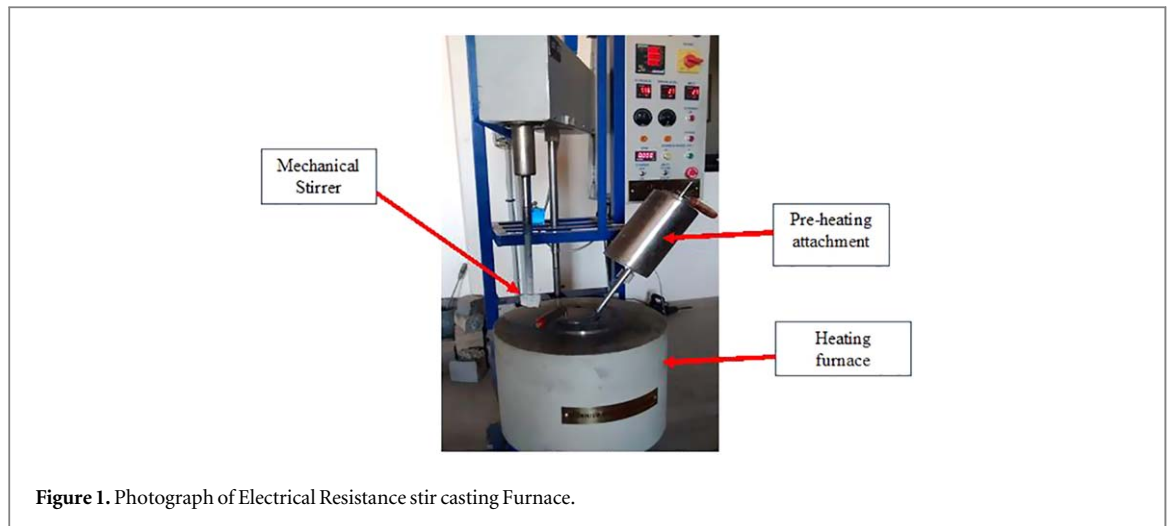


Figure 1. Photograph of Electrical Resistance stir casting Furnace.

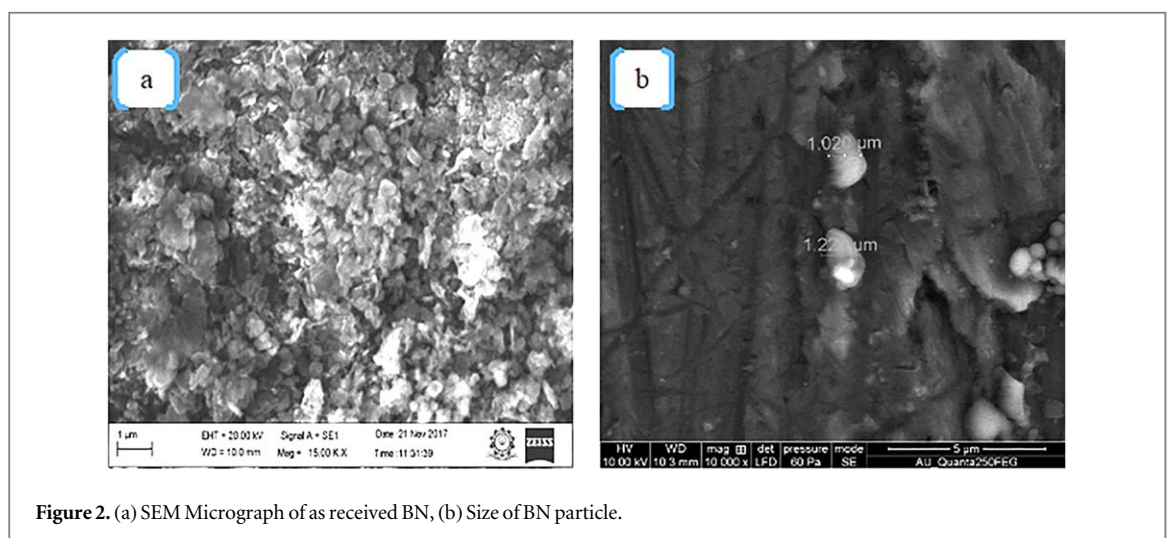


Figure 2. (a) SEM Micrograph of as received BN, (b) Size of BN particle.

(400 °C) rectangular ($100 \times 100 \times 10$ mm). All specimens are fabricated as per ASTM standard to meet the microstructural and mechanical characterization.

2.3. Characterization of material

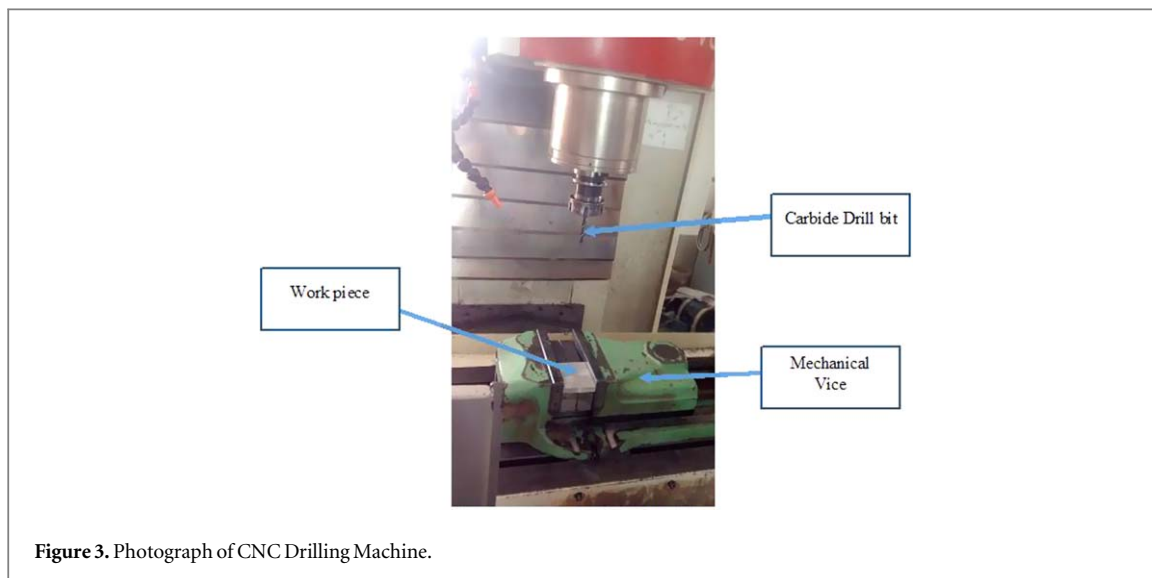
The received BN particle and size of the particle SEM micrographs are shown in figures 2(a) and (b). Microstructure evaluation of a composite exposes the dispersal of the reinforcement particles in the prepared samples. Specimens are analysed using OPTICS Metallurgical microscope and FESEM. It is also assisted in determining the grain structure and the position of the particulates. The specimen is dipped into the 3 ml of hydrochloric acid (HCl) chemical for 30 s which will remove the thin dust layer formed over the specimen. The machined surface of the specimens is etched with a solution of 1 ml Diamond paste. The etching area is polished via disc polishing machine by applying hand load. Then, the microstructure of the composite samples are analysed. Taskesen *et al* 2013 [20] revealed that, Field Emission scanning electron microscopy with energy dispersive x-ray spectroscopy (EDAX) is used to estimate the elemental presentation in the prepared Aluminium matrix composites. Before scanning, samples are cut according to the size of the tray of the machine.

2.4. Hardness and density test

The Hardness of the composites has been measured using Vickers Micro Hardness Testing machine according to the IS 1501:2002 ASTM Standard. Table 2 shows the Density measurement of prepared composites. Hardness of the samples is analyzed using Vickers hardness testing machine having diamond indenter of 10 mm. A load of 60 kgf is used which includes 10 kgf minor load and 50 kgf major load with 30 s of dwell time on the surface of the prepared composites. To avoid the future error, readings have been taken at three different locations. S Suresh *et al* 2014 [21]. The indenter diagonals are measured through reflected light microscope. The test is carried out at the room temperature. Each specimen is indented five times at the peculiar position for the

Table 2. Density measurement on prepared composites.

Sl. no	Description	Theoretical density (g cm^{-3})	Actual density (g cm^{-3})	Relative density	Porosity (%)
1	Sample-1	2.81	2.56	0.911	0.09
2	Sample-2	2.68	2.43	0.906	0.09
3	Sample-3	2.56	2.31	0.902	0.08
4	Sample-4	2.42	2.18	0.901	0.09

**Figure 3.** Photograph of CNC Drilling Machine.

prepared composites and the moderate hardness value is reported. The theoretical density of the composites is measured using Archimedes principle. The average densities of the composites are $\geq 89\%$.

2.5. Tensile behaviour

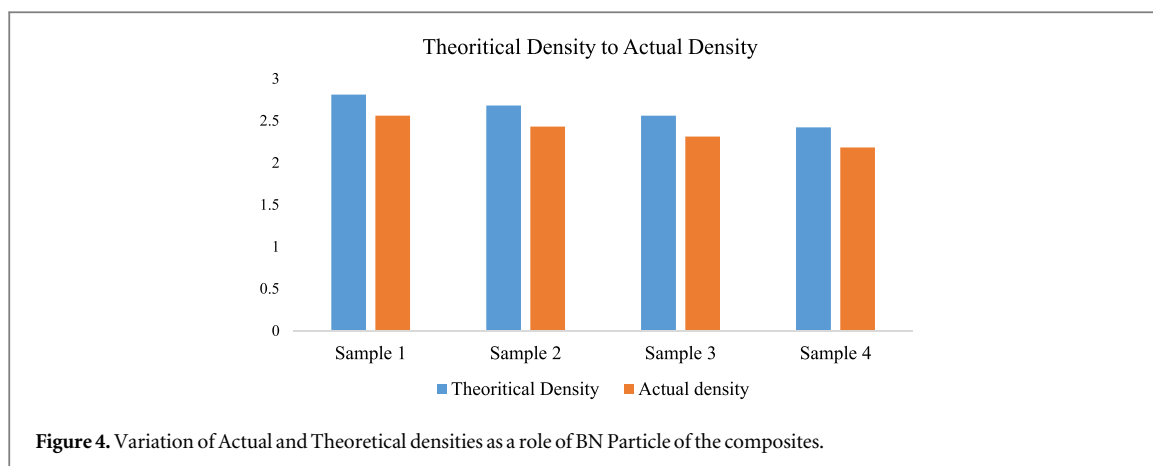
The tensile test is carried out using universal testing machine according to the ASTM E8 standard. Tensile specimens are machined from extruded samples with the tensile axes parallel to the extrusion direction. The tensile test is observed at room temperature with a minimum cross head with the speed of 0.5 mm min^{-1} . The tensile behaviour of Aluminium matrix composites indicate the increase in ultimate tensile strength (UTS) while increasing the secondary particle (Boron Nitride), which is attributed to the presence and relatively good dispersion with matrix. The averages of three tensile tests are carried with all specimens and reported the properties and behaviour.

2.6. Surface roughness (Ra)

The function of Surface Roughness has an important role in many areas, such as its vast consequence in the evaluation of machining accuracy. Surface Roughness measurement is generally a good prediction of the act of mechanical auxiliaries. The Machining parameters such as spindle speed, feed rate, and depth of cut have a significant influence on surface roughness for a given work piece. The surface roughness (Ra) is measured after machining using profilometer. Ra is the most widely used one-dimensional roughness parameter. While using the Probe, it repeats the roughness measurements which are taken in three different places of the sample in order to increase reliability. By using statistical analysis, it helps to predict the value of surface roughness.

2.7. Thrust force measurement

Drilling experiment is conducted on CNC vertical machining centre (figure 3). During the experiment, some vertical force occurred on the work piece is measured frequently by attaching the contact type drill tool dynamometer (piezoelectric). The piezoelectric signals are transmitted to the amplifier and recorded via data storage, which is integrated with a computer unit subsequently. The device consists of a sensors and connector cable. The sensor cables are fixed at the bottom of the work piece. Thrust force directly affects the drill tool and it reflects the chip formation. At the end of the experiment each process chip is collected separately.



3. Result and discussion

3.1. Density and porosity

The theoretical and experimental densities are shown in table 2. Al7075/BN composites, wt% of secondary particle acts as a major function. The noticed experimental values are the densities of the composites which are prepared under 850 °C. The law of composites is, the density of the composites mixture is frequently increased by addition of wt% of the secondary particle as expected. While comparatively direct relationship is observed between the experimental densities and BN wt%. The measured experimental densities are less than that of theoretical densities, Yosra Turki *et al* 2014 [22]. Figure 4 showed that the comparison of actual and theoretical densities. These indicate the presence of some voids in the prepared composites. Particle size also plays a vital role for porosity of the fabricated composites. In this research work, 1 μm BN are used as secondary particles. Hence, the distribution of the secondary particle is uniform and make sufficient angle of wetting is achieved by the liquid phase of the matrix. Therefore, the composites are fabricated with low porosity and results in high density.

3.2. Microstructural characterization

The micro structure of the prepared aluminium matrix composites (AMC's) are shown below. Figure 5(a) illustrates the as-casted microstructure of Al7075 alloy, used as the matrix material. The wt% of the BN was 0, 3, 6 and 9% respectively. Now we can realize, the microstructure consists of α phase and Al-Zn-Mg ternary eutectic phases are distributed in α phase boundaries. The closer observation is done by computerized optical microscopy. The microstructure consists of α -phase and secondary particles (BN) homogenously reinforced in the α region. In these micrographs, BN particles are distinguished as black dots in the α -Phase surrounded by a matrix. As in the view, the contents of BN particle are increased in microstructure that is in accordance with the increasing number of particles in molten aluminium during stir casting. As the stir casting parameters are optimized before production of samples, the minimum fraction of porosities and particle agglomerations are observable. Also, the reinforcement/matrix interfaces are approximately free of voids due to the enhancement of wettability by adding Potassium Hexafluorotitanate and preheating of BN particles just before adding to the melt. Figure 5 illustrates that as-casted Al7075 matrix alloy after the conduction of etching and polishing processes. Figure 5(b) indicates that Mg and Zn are precipitated and formed as a thick layer in the α -Phase grain boundary. FESEM images of as-casted Al7075 composites are represented in figure 5(c), shows in the micrograph are the secondary particle (BN) are also incorporated in microstructure and spread interior and also located over the grain boundaries. Figure 5(d), shows the Secondary particles as a higher magnification and it confirms the size of the ceramic particle. In order to find out the results of reaction between ceramic particle (BN) with molten aluminium, high-magnification FESEM image is shown below (figures 6(a)–(d)). A small amount of agglomeration occurred by adhesion ceramic particles to each other during final stage of solidification. The trace of BN element can be seen in EDAX analysis figures 7(a) and (b) indicates that the marked area shows the presence of BN particle. It is important to note that the high magnification is showed FESEM microstructure of figures 6(a) to (d) illustrates the distribution of BN particles even in the range of 1 μm showed that the reaction between BN and molten aluminium alloy. EDAX analysis shows the trace of oxygen and aluminium enriched zones on the marked area. It can be concluded that these agglomerated BN particles are adhered to each other during stirring after solidification. This EDAX compositional analysis has been used to confirm the elemental presence, Ramkumar *et al* 2017 [23].

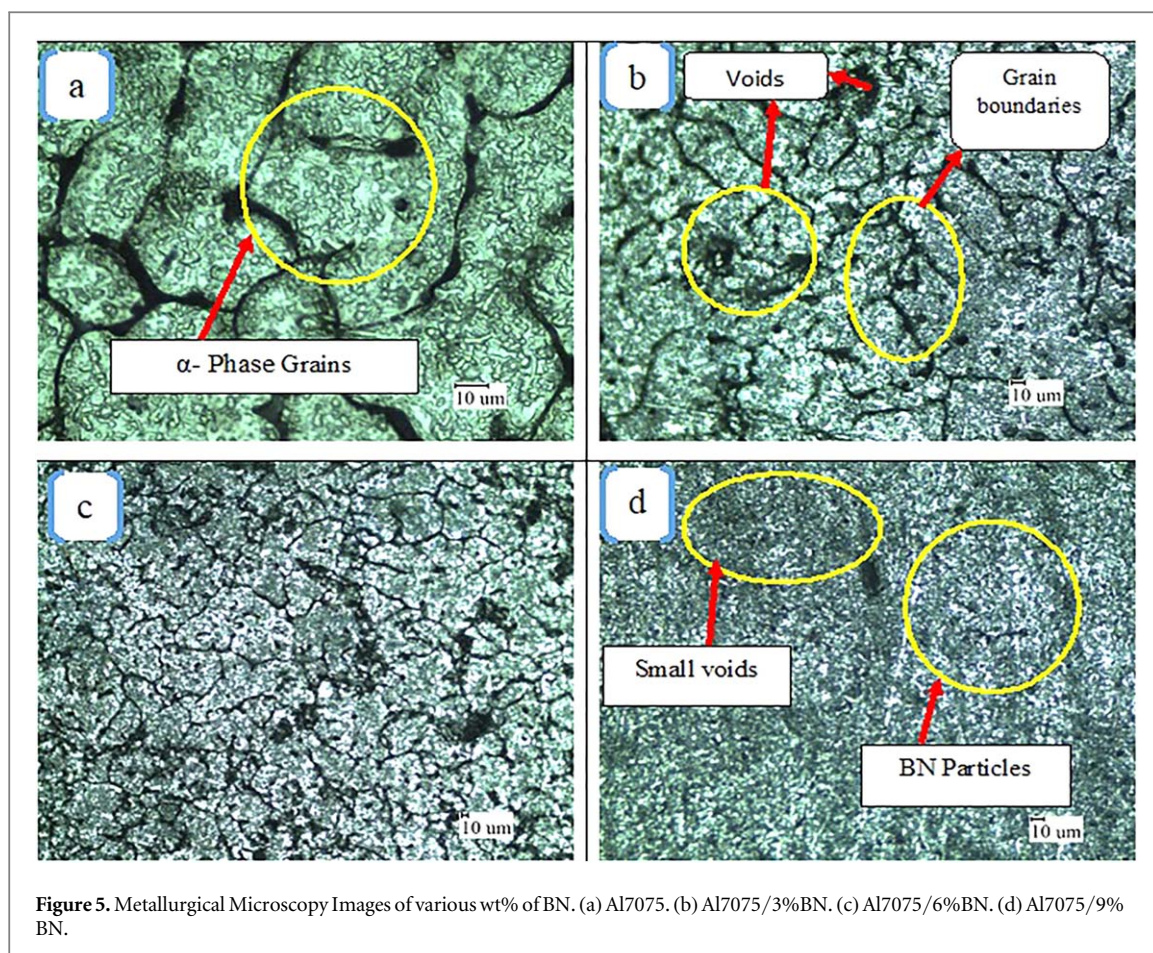


Figure 5. Metallurgical Microscopy Images of various wt% of BN. (a) Al7075. (b) Al7075/3%BN. (c) Al7075/6%BN. (d) Al7075/9% BN.

3.3. Mechanical characterization

3.3.1. Micro hardness

The micro hardness indicates that to increase the hardness with increasing wt% of the secondary particles (BN) in the matrix. At the same time, it helps to prevent the plastic deformation and abrasion between contact surfaces of the composites by the reinforcement particles. Adding BN particles in to Al7075 melt during stir casting provides preferred sites for homogeneous nucleation of matrix grains. Therefore, matrix microstructure is refined by increasing the wt% of BN particles. This is the one of the reasons for increasing hardness with the increase of reinforcement wt%. The other major factor that greatly influences the hardness of composites is the bonding characteristics of reinforcement particles and matrix material, Sumesh Narayan *et al* 2017 [24]. By reinforcing the secondary particle (BN) into the matrix material the hardness has been significantly increased the twin time of the base material because of the wt% of BN. While reinforcing beyond the 9 wt% of the secondary particle the hardness of the composite material was decreased because of agglomeration. It primes to brittle nature of the composites, Ramkumar T *et al* 2018 [25]. Therefore, the saturating perspective between matrix and reinforcement of the interface affect the load transfer capacity of matrix to reinforcement. It is clearly noted that BN particle doesn't make any brittle layer in the composites. Finally, the free Ti occasioned from disintegration of K_2TiF_6 reacts with aluminium to form hard and brittle Al_3Ti intermetallic phase. So that, the formation of Al_3Ti intermetallic is another cause of the improved hardness of Al7075- BN composites compared with Al7075 matrix alloy.

3.3.2. Tensile behaviour

Tensile properties (UTS) prepared of Al/BN composites with different wt% of secondary particle are investigated and compared with pure matrix alloy was shown in figure 8. In order to investigate the tensile properties of Al/BN composites at room temperature, different samples (Al7075, Al/3%BN, Al/6%BN, Al/9% BN) are used to conduct the experiments. Figure 9(a) illustrates an increase in ultimate tensile stress (UTS) when increased in the addition of secondary particle wt%. The typical tensile stress and tensile strain curve is plotted and shown in figures 9(b)–(d) with the increase of strain periodically, the tensile stress promptly increases, reaches the maximum and decreases rapidly. Initially UTS of the composites increases and later declines with enlarging the BN contents. The UTS of the Al/BN composites reaches the ultimate level, when increasing the

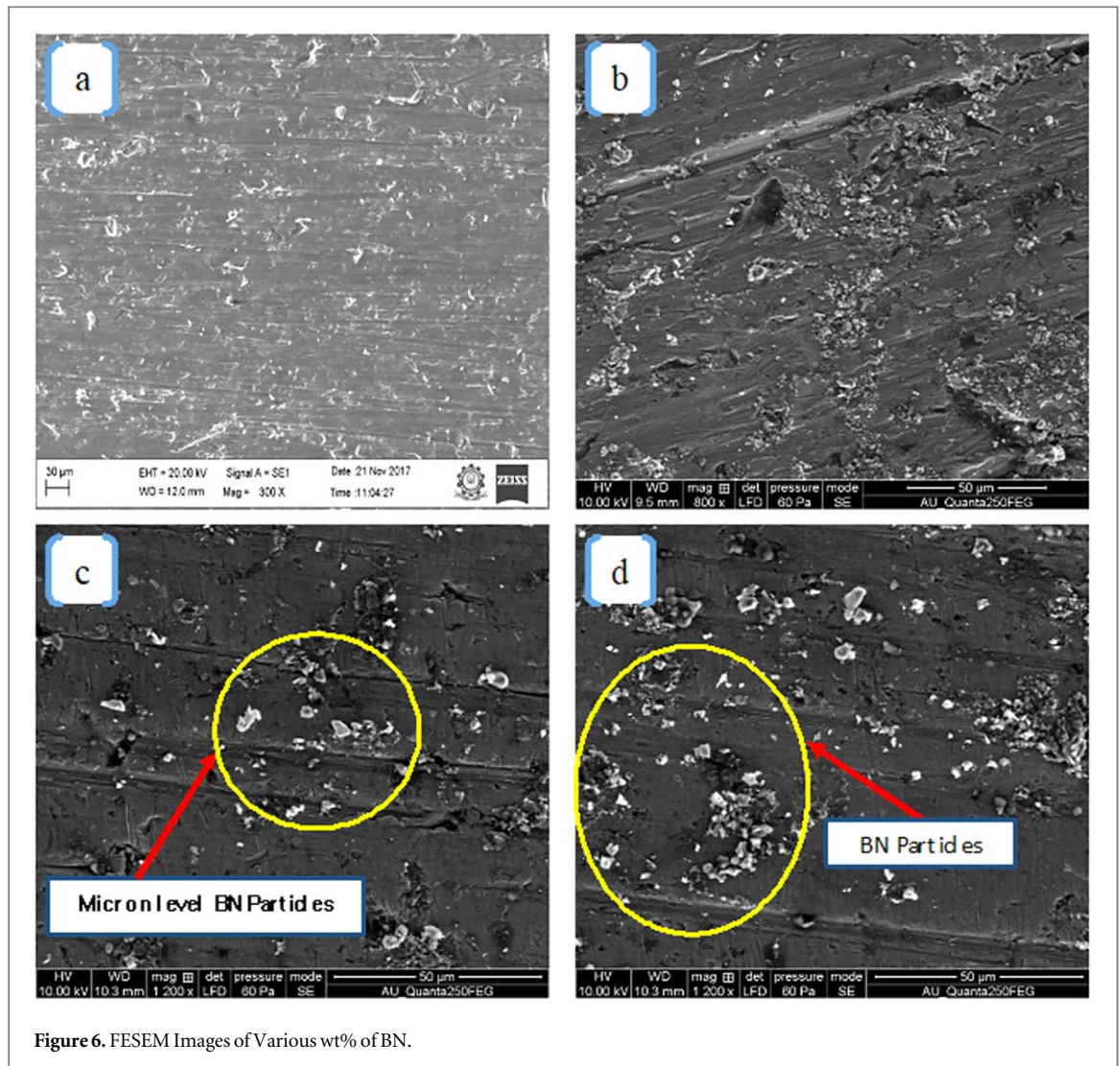


Figure 6. FESEM Images of Various wt% of BN.

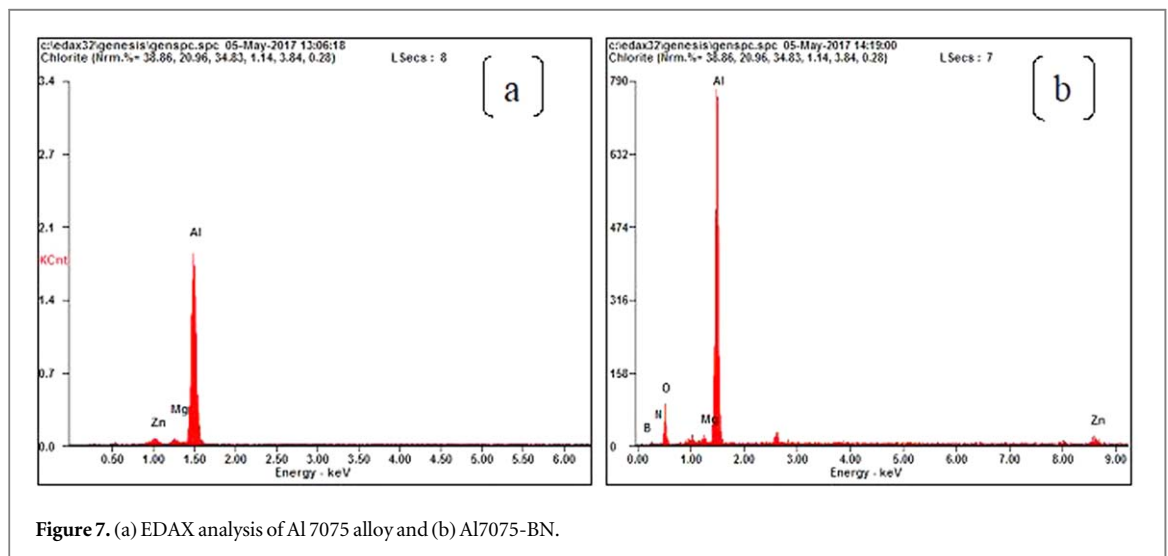


Figure 7. (a) EDAX analysis of Al 7075 alloy and (b) Al7075-BN.

wt% of secondary particle is 9% which results 80.2% higher than that of the unreinforced aluminium alloy is noted. A neck region of the sample could be detected near the crack zone of the sample, which indicates a high necking ductileness of the composites. It could be noticed that the whole gauge part is involved in the deformation process deciding from the Al/BN fractured composites with different gauge parts. As the UTS proceed, the cracks amalgamated with end-to-end, the initial crack leads to fracture failure of the composites. It

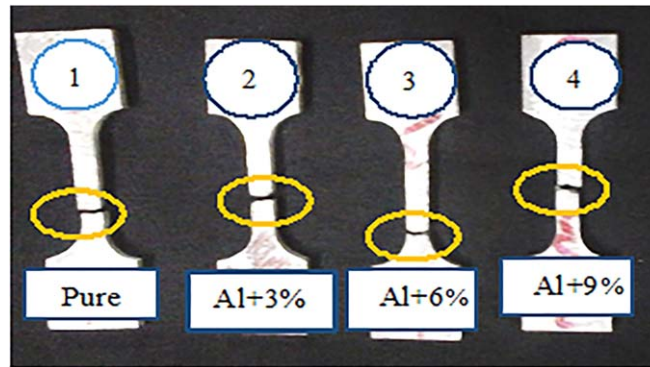


Figure 8. Tensile Specimens after testing.

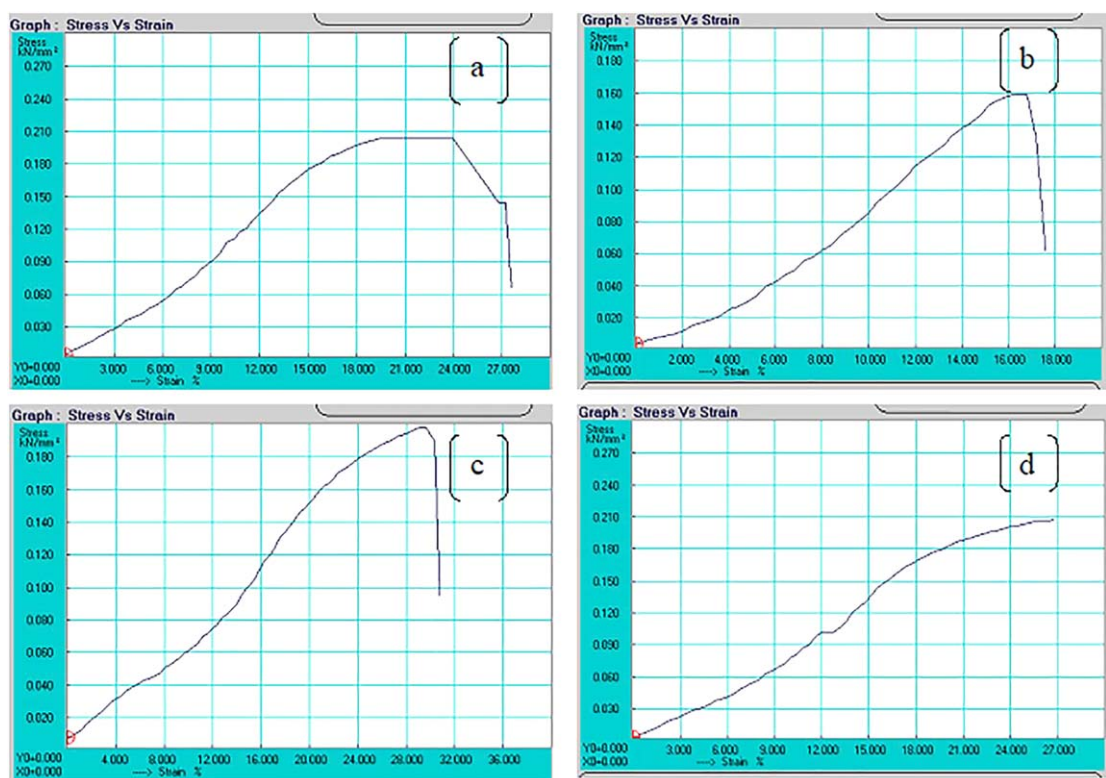


Figure 9. Graphical Images of Specimen after tensile test (a) Al7075, (b) Al7075-3%BN, (c) Al7075 –6% BN and (d) Al7075-9% BN.

might be recognized that BN reinforced composites possessed high yield ratio. The clarification of tensile process proceeds the number of cracks improved, results in the decrease of the cross section of gauge part. The result of the work hardening is virtually responded by the focused cross-sectional area leading to a high yield ratio of the composites. This result demonstrates that BN has enormous potential submissions as the ideal reinforcement in Al matrix composites, was predicted by Palanikumar *et al* 2014 [14].

The tensile fractography of the Al/BN composites with different wt% of BN particles are shown in figures 10(a)–(d). The pure Al fracture surface is rough and a lot of pits exist. With enlarging the BN a particle, the crack surface becomes plane and the number of pits reduces. In 3 wt% Al/BN composite, a lot of crashes and dumps around the α - boundary of Al grains can be found on the crack surface.

3.3.3. Tensile fractography

Figures 9(a)–(d) illustrates that the stress-strain curves and tensile properties of the Al/BN composites tested at room temperature 25 °C. The stress strain is compared with pure aluminium to the wt% in addition to BN particles. During the longitudinal tensile experiments, all fabricated specimens are failed, compared with that of

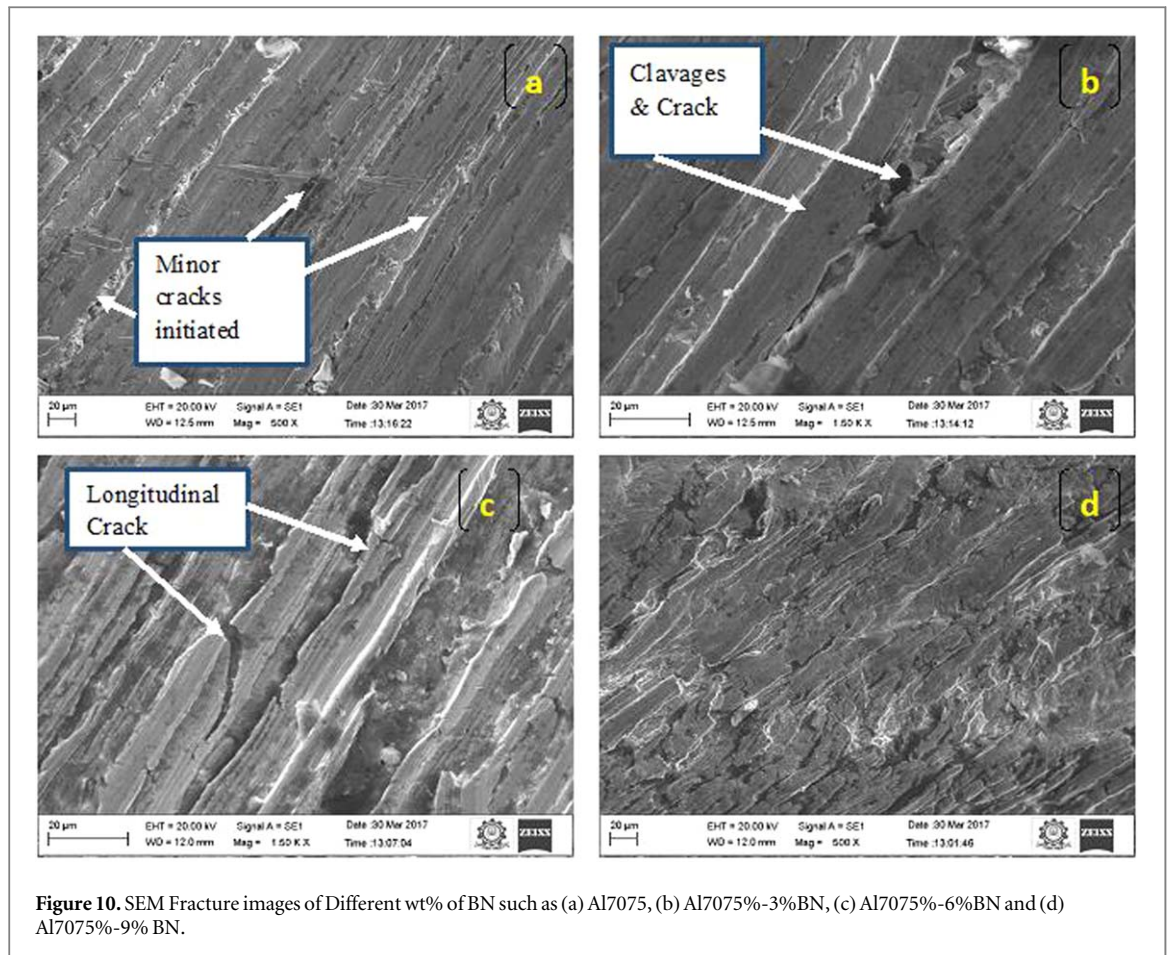
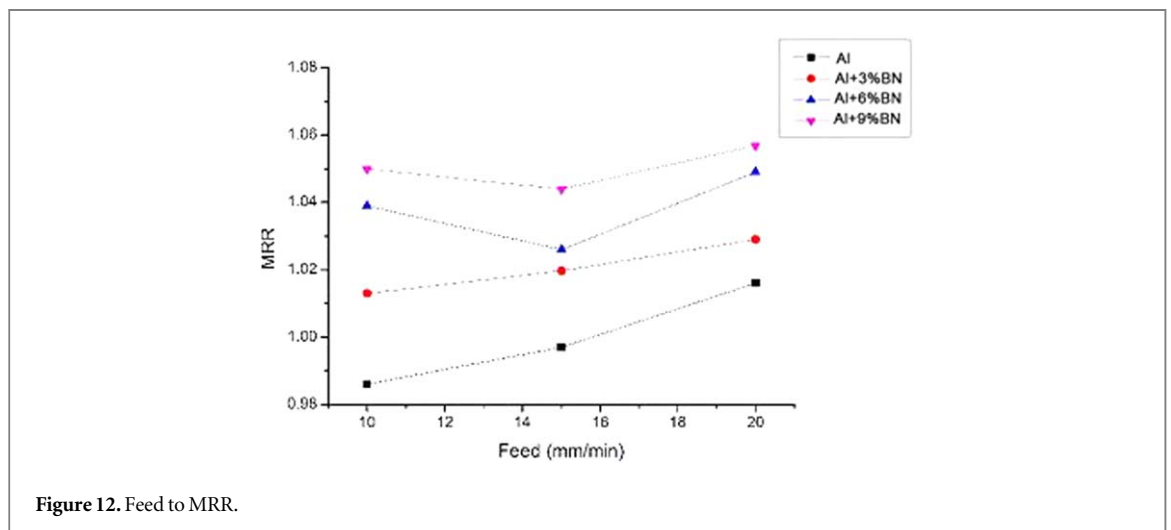
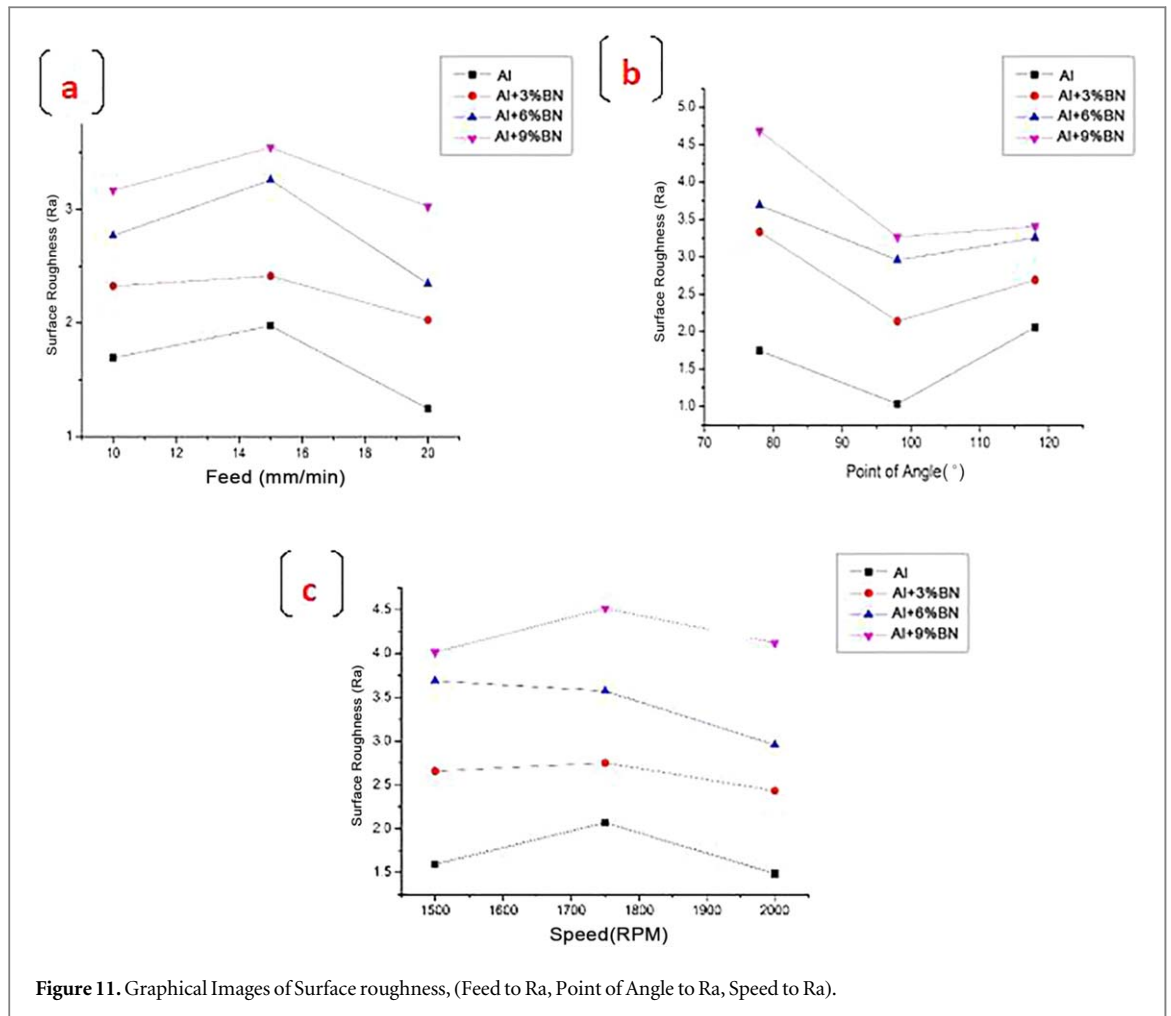


Figure 10. SEM Fracture images of Different wt% of BN such as (a) Al7075, (b) Al7075%-3%BN, (c) Al7075%-6%BN and (d) Al7075%-9% BN.

the parent metal. Al7075 base metal has a naturally raw and fully dendritic microstructure, which leads to low impact toughness and ductility. Thus, the metal is failed before experiencing an outstanding quantity of plastic elongation. Nevertheless, there are numerous discontinuous bands of secondary phases perceived in the SEM morphology. The secondary particle has increased the yield strength and the ultimate strength of the fabricated composite materials. Figures 10(a)–(d) shows the SEM fractography of the tensile fractured surface. SEM fractographs are populated to identify the microscopic voids. The SEM fractograph of the base material revealed non-uniform cleavage facets interspersed with micron BN particles. The presence of secondary particle facilitated brittle mode of fracture resulting in low tensile strength. The longitudinal sectional micrograph of necked region of the specimen shown in figure 10(c) and this region, initial cavities formation starts between the parent and the secondary particle. Fractures occurred in the pure aluminium alloy and Al/3% of BN, Al/6% of BN and Al/9% of BN composites by casted route. It can be realized that the crack surface is self-possessed of regions of cleavage fracture and elastic deformation, Ramkumar *et al* 2017 [23].

3.4. Surface roughness (Ra)

The influence of various input parameters such as spindle speed, feed rate, and rack angle will directly affect the drilled surface. The increased feed rate forms rough surface on the drill hole and maximum spindle speed and rack angle helps to produce good surface finish. The chips that are formed at higher feed rate have increased the shearing action between the cutting tool and workpiece interface. Experiments are conducted in different wt% of secondary particles reinforced Al/BN composites. Figure 11(a) illustrates that the increased surface roughness (Ra) value, because of the feed rate is increased if the speed and feed rate is increased it results in the surface roughness (Ra) and indicates minimum. Further, the increase in speed increases the heat flow in the work piece, which softens the base metal and reduces the surface roughness. If increase in feed rate increases the thrust force, it leads to poor surface finish. The point of angle influenced more on affecting the roughness and hence a proper selection of tool geometry is required. Figure 11(b) indicates that the increase in the point of angle of the tool produced poor finish, which is due to the minimum contact area between the work and tool. Medium rack angle produced better surface finish and it reduces thrust force and minimum tool wear. Figure 11(c) shows that the increase in speed rate will reduce the surface roughness value. Figure 12 indicated that the increase in feed ratio will increase the MRR. Thus, the selection of suitable tool is essential to achieve optimum output performance.



The results designate that maximum feed rate with maximum speed is favoured in drilling of composites, Abdul Nasir *et al* 2015, Selvakumar *et al* 2017, Ravindranath *et al* 2017 [26–28].

3.5. Thrust force analysis

The present investigation is to analyse the process parameters which influence the maximum thrust force occurring on the fabricated Al/BN composites. The thrust force is affected by various aspects such as cutting tool material, workpiece material, machine conditions, machining parameters, tool geometry and cutting fluid etc. This research work aims to investigate the different cutting parameters to the tool geometry. The increase in wt% of the secondary particle increases the hardness and toughness. The selection of suitable machining parameters

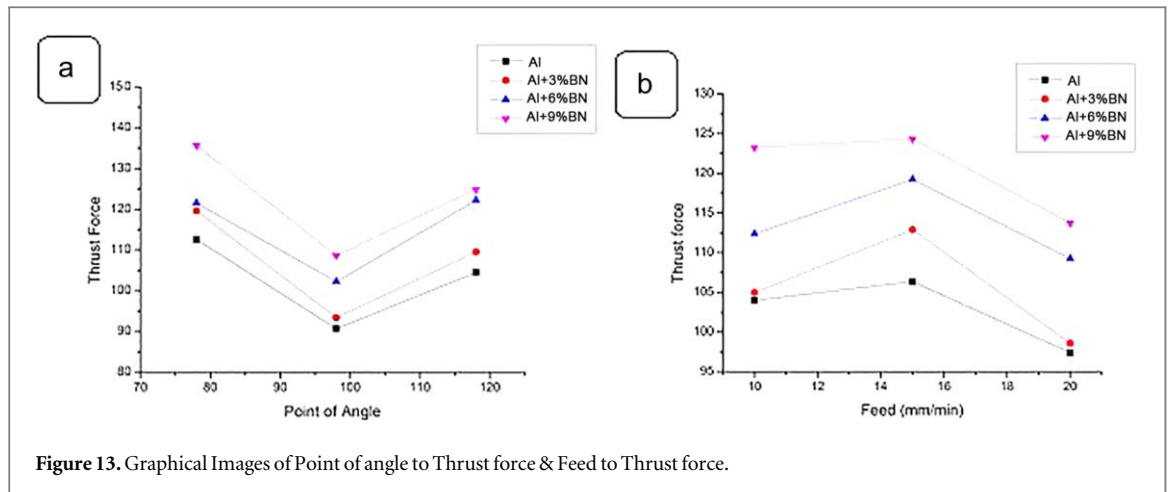


Figure 13. Graphical Images of Point of angle to Thrust force & Feed to Thrust force.

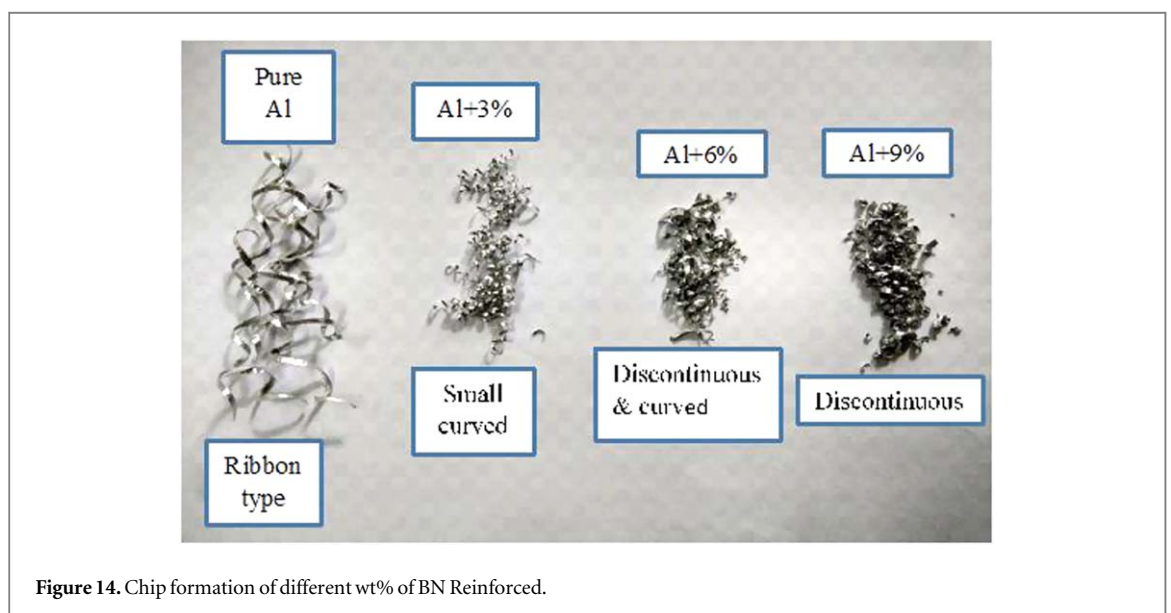


Figure 14. Chip formation of different wt% of BN Reinforced.

and cutting tool material is the most significant role to reduce the error and improve the machinability and tool life, Valarmathi *et al* 2013 [29], Ramkumar T *et al* 2019 [30]. Figure 13(a) illustrates that the thrust force is increased when the point of angle is maximum (118°) with low speed rate and high feed. Figure 13(a) shows that the angle (98°) produces low thrust force in highest feed rate and maximum spindle speed condition. Figure 13(b) illustrates that the highest axial force is developed, when the minimum feed condition and point of angle is reduced to (78°), because of the flank face is interacted with lateral surface of the drill hole. Further, the edge wear will affect the surface quality of the hole. The various forces lead to develop the different kind of chip formation and surface roughness also. In all these considerations, the nominal selection of machining parameters, drill tool material and drill tool geometry here induce the minimum thrust force and surface roughness.

3.6. Chip morphology

The results of the thrust force will directly influence the tool wear and chip formation. Figure 14 shows that the different kind of chip formation in different wt% of secondary particle addition. In the evaluation of chip morphology, it shows different characteristics at different input parameters like cutting speed, feed and point of angle or rack angle. Figure 15(a) indicates that the worn surface of the drill bit. The cutting edge is chipped when the highest thrust force obtained on the work piece, and the figure 15(b) shows that the presence of Aluminium and BN particle in the cutting edge. The decrease in point of angle increases the pressure on the work piece and produce high thrust force at low speed condition. But the contact surface of the tool and work piece increases high temperature. Jenso Eapen *et al* 2017 [31] said that the temperature of the cutting edge is also increased due to the high residual stress. When the point angle is increased, the formation of built-up edge is predominant in the tool region. In addition, the wear formation of the surface quality is also affected. However, the increase in

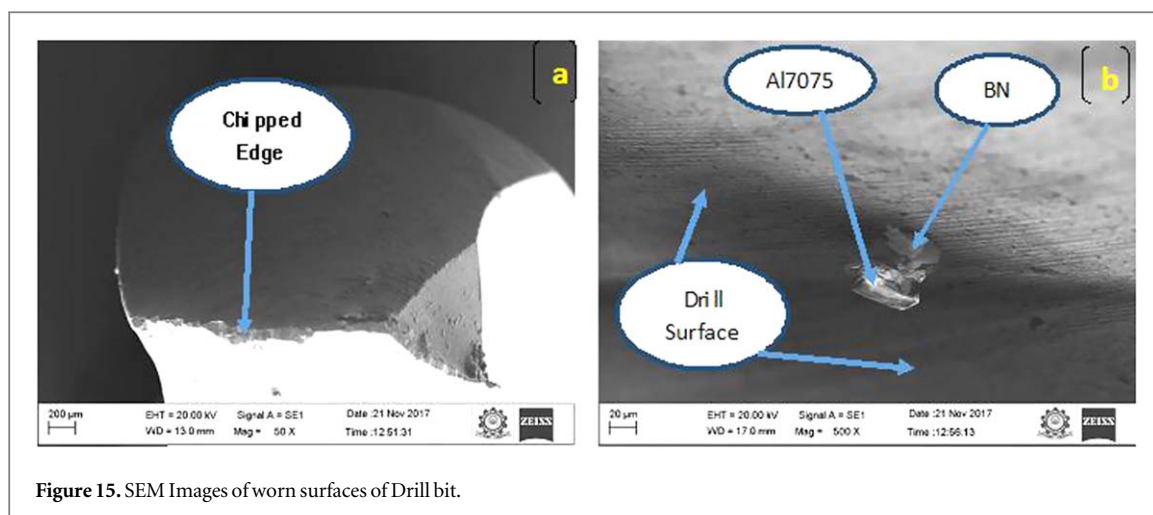


Figure 15. SEM Images of worn surfaces of Drill bit.

feed, point angle and spindle speed results in achieving the maximum MRR with good surface quality. The maximum delamination factor at 118° , 98° and 78° are found to be 1.073, 1.026 and 0.993 respectively.

4. Conclusion

- The microstructural evaluation clearly reveals that the secondary particles are well dispersed in the matrix material.
- FESEM & EDAX results of the fabricated composite materials also confirm the homogeneous distribution of the BN particles in the matrix material and existence of secondary particle.
- To increase the wt% of BN will directly influence the Surface roughness and thrust force of the aluminium composites is often.
- Increase in the wt% of BN particles elevate the composites materials to achieve high ultimate strength when compared to the base aluminium alloy and its greater than that of reinforced composite materials.
- The results indicate that UTS has improved 80.2% higher than that of unreinforced base aluminium alloy when increased 9 wt% of the BN particles.
- The effect of reinforcement influences the fabricated composites, tensile strength, elongation and fracture behaviour of the samples are examined. The highest toughness and strain rate are observed from 9 wt% of secondary particles reinforced composites. The existence of dislocation in aluminium matrix indicates the pile up phenomena during the fracture behaviour of composites

ORCID iDs

V Vignesh Kumar  <https://orcid.org/0000-0001-5720-2250>

T Ramkumar  <https://orcid.org/0000-0003-1654-8022>

References

- [1] Mahesh L, Vinyas M, Sudheer Reddy J and Muralidhara B K 2018 Investigation of the microstructure and wear behaviour of titanium compounds reinforced aluminium metal matrix composites' *Mater. Res. Express* **6** 026516
- [2] Li Y, Ge B, Wu Z, Xiao G, Shi Z and Jin Z 2017 Effects of h-BN on mechanical properties of reaction bonded β -SiAlON/h-BN composites *J. Alloys Compd.* **703** 180–7
- [3] Liu D F, Tang Y J and Cong W L, 2012 A review of mechanical drilling for composite laminates *Compos. Struct.* **94** 1265–79
- [4] Çelik A, Lazoglu I, Kara A and Kara F 2015 Investigation on the performance of SiAlON ceramic drills on aerospace grade CFRP composites *J. Mater. Process. Technol.* **223** 39–47
- [5] Harichandran R and Selvakumar N 2017 Microstructure and mechanical characterization of ($B_4C + h$ -BN)/Al hybrid nanocomposites processed by ultrasound assisted casting *Int. J. Mech. Sci.* **144** 814–26
- [6] Kannan C and Ramanujam R 2017 Comparative study on the mechanical and microstructural characterisation of AA 7075 Nano and hybrid nanocomposites produced by stir and squeeze casting *Journal of Advanced Research* **309**–19
- [7] Samy G S and Thirumalai Kumaran S 2017 Measurement and analysis of temperature, thrust force and surface roughness in drilling of AA (6351)- B_4C composite *Measurement* **103** 1–9

- [8] Basavarajappa S, Chandramohan G and Paulo Davim J 2008 Some studies on drilling of hybrid metal matrix composites based on Taguchi techniques *J. Mater. Process. Technol.* **196** 332–8
- [9] Zedan Y and Alkhatani S 2013 Influence of the microstructure on the machinability of heat-treated Al–10.8% Si cast alloys: role of copper-rich intermetallics *J. Mater. Process. Technol.* **213** 167–79
- [10] Lazar M-B and Xirouchakis P 2011 Experimental analysis of drilling fiber reinforced composites *International Journal of Machine Tools and Manufacture* **51** 937–46
- [11] Altunpak Y, Mustafa A Y and Aslan S 2012 Drilling of a hybrid Al/SiC/Gr metal matrix composites *Int. J. Adv. Manuf. Technol.* **60** 513–7
- [12] Aftab A, Ismail A R, Ibupoto Z H, Akeiber H and Malghani M G K 2017 Nanoparticles based drilling muds a solution to drill elevated temperature wells: a review *Renewable and Sustainable Energy Reviews* **76** 1301–13
- [13] D’Orazio A, Mehtedi E I M, Forcellese A, Nardinocchi A and Simoncini M 2017 Tool wear and hole quality in drilling of CFRP/AA7075 stacks with DLC and nanocomposite TiAlN coated tools *Journal of Manufacturing Processes* **30** 582–92
- [14] Palanikumar K and Muniaraj A 2014 Experimental investigation and analysis of thrust force in drilling cast hybrid metal matrix (Al–15%SiC–4%graphite) composites *Measurement* **53** 240–50
- [15] Li N, Li Y, Zhou J, He Y and Hao X 2015 Drilling delamination and thermal damage of carbon nanotube/carbon fiber reinforced epoxy composites processed by microwave curing *International Journal of Machine Tools and Manufacture* **97** 11–7
- [16] Selvakumar N and Ramkumar T 2016 Effect of high temperature wear behaviour of sintered Ti–6Al–4V reinforced with nano B₄C particle *Trans. Indian Inst. Met.* **69** 1267–76
- [17] Rimpault X, Chatelain J-F, Klemberg-Sapieha J E and Balazinski M 2016 Surface profile topography of trimmed and drilled carbon/epoxy composite *Procedia CIRP* **45** 27–30
- [18] Ekici E, Motorcu A R and Uzun G 2017 An investigation of the effects of cutting parameters and graphite reinforcement on quality characteristics during the drilling of Al/10 B₄C composites *Measurement* **95** 395–404
- [19] Mahamani A 2014 Experimental investigation on drilling of AA2219-TiB₂/ZrB₂ in-situ metal matrix composites *Procedia Materials Science* **6** 950–60
- [20] Taskesen A and Kutukde K 2013 Analysis and optimization of drilling parameters for tool wear and hole dimensional accuracy in B₄C reinforced Al-alloy *Trans. Nonferrous Met. Soc. China* **23** 2524–36
- [21] Suresh S, Shenbaga Vinayaga Moorthi N, Vettivel S C, Selvakumar N and Jinu G R, 2014 Effect of graphite addition on mechanical behavior of Al6061/TiB₂ hybrid composite using acoustic emission *Materials Science & Engineering A* **612** 16–27
- [22] Turki Y, Habak M, Velasco R, Aboura Z, Khellil K and Vantom-me P 2014 Experimental investigation of drilling damage and stitching effects on the mechanical behavior of carbon/epoxy composites *International Journal of Machine Tools and Manufacture* **87** 61–72
- [23] Ramkumar T, Selvakumar M, Narayanasamy P, Ayisha Begam A, Mathavan P and Arun Raj A 2017 Studies on the structural property, mechanical relationships and corrosion behaviour of Inconel 718 and SS 316L dissimilar joints by TIG welding without using activated flux *Journal of Manufacturing Processes* **30** 290–8
- [24] Narayan S and Rajeshkannan A 2017 Hardness, tensile and impact behaviour of hot forged aluminium metal matrix composites *J. Mater. Res. Technol.* **6** 213–9
- [25] Rankumar T, Narayanasamy P, Selvakumar M and Balasundar M 2018 Effect of B₄C reinforcement on the dry sliding wear behaviour of Ti–6Al–4V/B₄C sintered composites using response surface methodology *Arch. Metall. Mater.* **63** 3 1179–200
- [26] Abdul Nasir A A, Azmi A I and Khalil A N M 2015 Measurement and optimization of residual tensile strength and delamination damage of drilled flax fibre reinforced composites *Measurement* **75** 298–307
- [27] Selvakumar N and Ramkumar T 2017 Effect of particle size of B₄C reinforcement on Ti–6Al–4V sintered composite prepared by mechanical milling method *Transactions of the Indian Ceramic Society* **76** 31–7
- [28] Ravindranath V M, Yerriswamy M, Vivek S V and Shiva Shankar G S 2017 Drilling of Al2219/B₄C/Gr metal matrix hybrid composites *Materials Today: Proceedings* **4** 9898–901
- [29] Valarmathi T N and Palanikumar K 2013 Measurement and analysis of thrust force in drilling of particle board (PB) composite panels *Measurement* **46** 1220–30
- [30] Ramkumar T, Selvakumar M, Mohanraj M and Chandrasekar P 2019 Experimental investigation and analysis of drilling parameters of metal matrix (Ti/TiB) composites *Journal of the Brazilian Society of Mechanical Sciences and Engineering* **41** 1–12
- [31] Eapen J, Murugappan S and Arul S 2017 A study on chip morphology of aluminum alloy 6063 during turning under pre-cooled cryogenic and dry environments *Materials Today: Proceedings* **4** 7686–93



SMART ENERGY MONITORING SYSTEM USING IOT

K. Umarani

Associate Professor, M.A.M. School of Engineering,
Siruganur, Trichy, Tamilnadu

Cite This Article: K. Umarani, "Smart Energy Monitoring System Using IOT", International Journal of Computational Research and Development, Volume 4, Issue 1, Page Number 10-15, 2019.

Abstract:

Smart application has become more and more popular in recent years. It aims at helping people manage the various devices freely and build an autonomous environment. This project introduces a wireless solution based on Internet protocol to manage the industrial units easily. Smart application system can connect the various units together and provide a unified interface for users to interact with the monitoring block. Some main features are listed such as motor control, load control, temperature control of motor, security and safety. Based this control the energy has consumed which can be monitored using IOT. As with the development of the Internet, Internet based remote monitoring and control solutions for industry has been proposed.

Key Words: Energy Consumption, Industrial Monitoring, Load Control, Motor Control, Fire Sensor, Aurdino UNO, IOT & Temperature Sensor

1. Introduction:

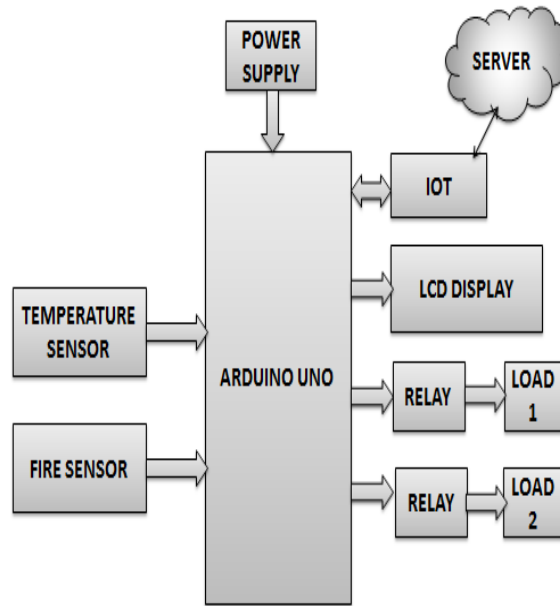
Electricity plays an important role in our life. Every moment of our life depends upon electricity. Electricity has several components and equipment helping human to transfer and regulate the distribution according to usage. The most crucial equipment of transmission and distribution of electric power is transformer. In power systems, an electrical equipment distribution transformer directly distributes power to the low-voltage users and its operation condition is an important criterion of the entire network operation. The majority of these devices have been in service for many years in different (electrical, mechanical and environmental) conditions.

Automation has much more importance in industry because due to automation overall productivity is increases. Quality of the product is also increases due to automation. It also reduces manufacturing cost. There are another several reasons such as lack of availability of skilled person, lack of industrial training centers so that automation got importance. Most of the developed countries suffer from lack of human resources. Those persons who work for their industry from many years they are leaving the industry. If they want to hire new candidate to replace old candidate then first problem is that new candidate is non-experienced. So we have to arrange training session. Candidate may leave the industry if workload is more. In case of developing country skill become important factor. They have more manpower but these peoples are not technically strong. Hence automation is become need.

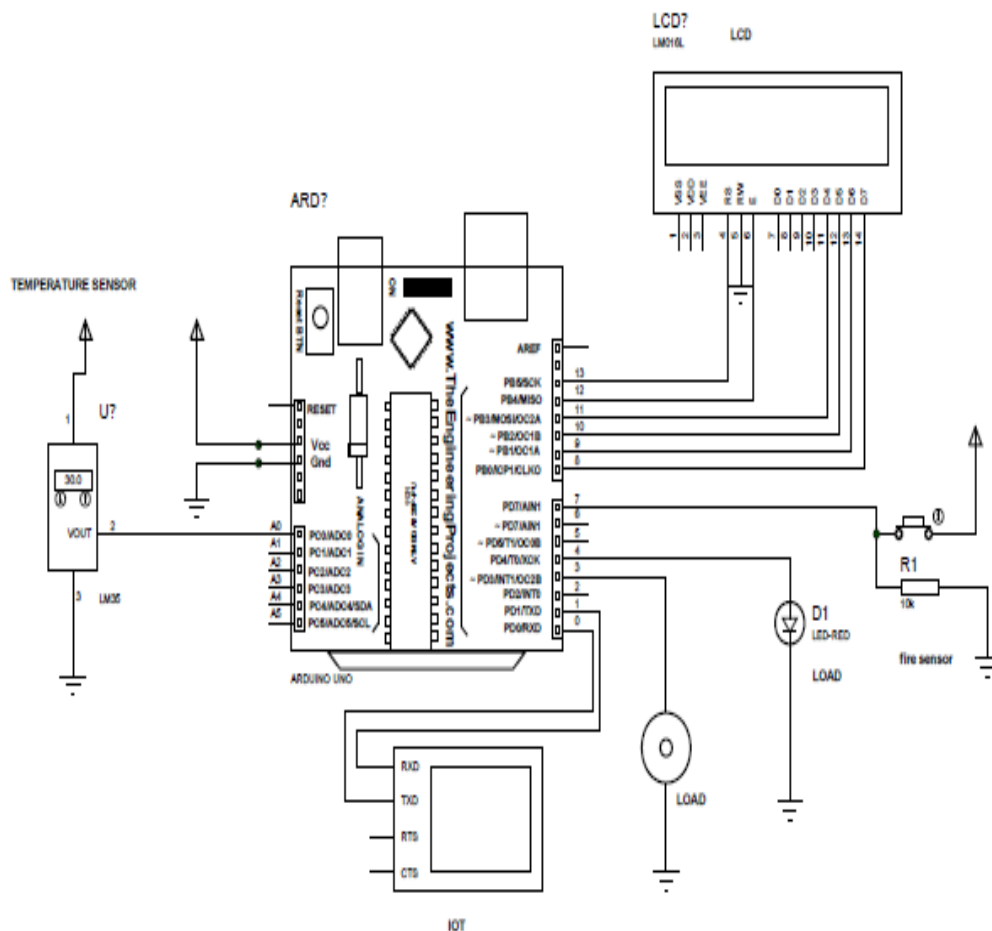
Technologies which are invented for the industrial automation deals with the monitoring and controlling of the various activities and different manufacturing process running in the industry. Machinery used in the industry has its own specification. In industry boilers are used for heating purpose. These boilers have own their operating temperature range. If the temperature of the boiler exceed beyond the threshold level then there is possibility of explosion of the boiler which become more dangerous. Hence controlling of temperature is important. All other parameters such as speed of the motor, torque of the motor, pressure, available light etc. must be monitor and control. In day today life people wants to have world in their fingerprints. That means use of internet is increased in great extent. Internet of things is a new emerging technology which connects all the living or nonliving things of the world using internet. Internet of things allows the communication between the people and thing anytime, anywhere using large internet network. To monitor and control such automation process we can use concept of internet of things. We can also control this parameter by providing appropriate feedback command. For this communication between devices and web page we use controlling device along with IOT.

2. Block Diagram:

This is our proposed system block diagram. Our smart energy monitoring system consists Aurdino uno, temperature and fire sensors, power supply, lcd, load, motor, IOT, server and relays.



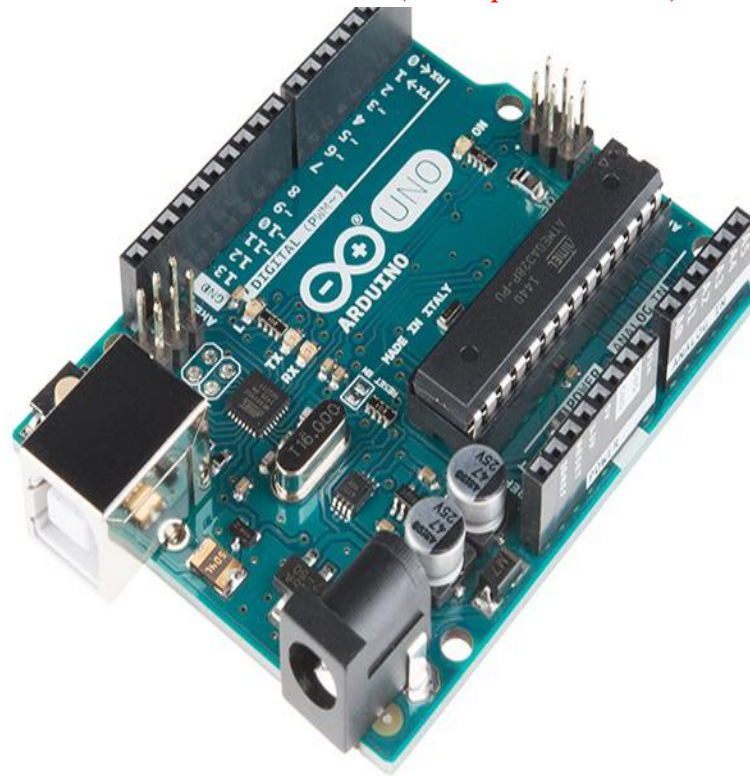
3. Circuit Diagram:



This is the circuit diagram of our proposed system.

4. Components:

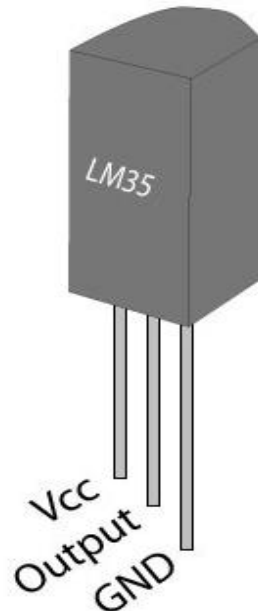
Arduino Uno the hardware system is based on the Arduino Uno is a type of microcontroller component that is used in the development of electronics, computers, robotics and similar devices. It is controlled by software and programmed in such a way that it performs different tasks and controls a generation line.



Each of the 14 digital pins and 6 analog pins on the uno can be used as an input or output, using `pinmode()`, `digital write()`, and `digital read()` functions. They operate at 5 volts. The uno has 6 analog inputs, each of which provide 10 bits of resolution (i.E. 1024 different values).

Temperature Sensor:

LM35 is a precision IC temperature sensor with its output proportional to the temperature (in °c). The sensor circuitry is sealed and therefore it is not subjected to oxidation and other processes. With lm35, temperature can be measured more accurately than with a thermistor. It also possess low self heating and does not cause more than 0.1 °c temperature rise in still air. It is suitable for remote purposes.



Fire Sensor:

IR based flame sensor is used. It is based on the YG1006 sensor which is a high speed and high sensitive NPN silicon phototransistor. It can detect infrared light with a wavelength ranging from 700nm to 1000nm and its detection angle is about 60°. Flame sensor module consists of a photodiode (IR receiver), resistor, capacitor, potentiometer, and LM393 comparator in an integrated circuit.



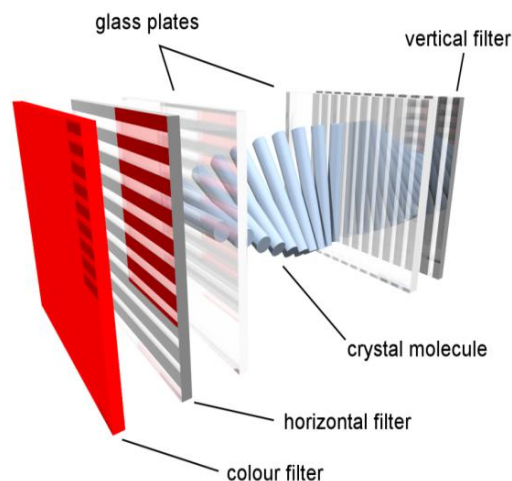
The sensitivity can be adjusted by varying the on board potentiometer. Working voltage is between 3.3v and 5v DC, with a digital output. Logic high on the output indicates presence of flame or fire. Logic low on output indicates absence of flame or fire.

LCD Display:

LCD (Liquid Crystal Display) screen is an electronic display module and find a wide range of applications. A 16x2 LCD display is very basic module and is very commonly used in various devices and circuits. These modules are preferred over seven segments and other multi segment LEDs. The reasons being: LCDs are economical; easily programmable; have no limitation of displaying special & even custom characters (unlike in seven segments), animations and so on. A 16x2 LCD means it can display 16 characters per line and there are 2 such lines.

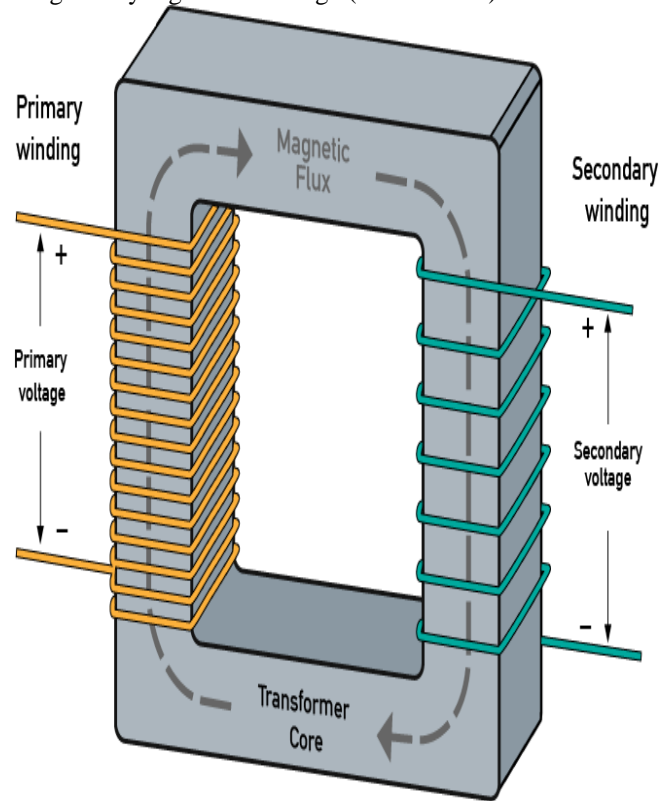


In this LCD each character is displayed in 5x7 pixel matrix. This LCD has two registers, namely, Command and Data. The command register stores the command instructions given to the LCD. A command is an instruction given to LCD to do a predefined task like initializing it, clearing its screen, setting the cursor position, controlling display etc. The data register stores the data to be displayed on the LCD.



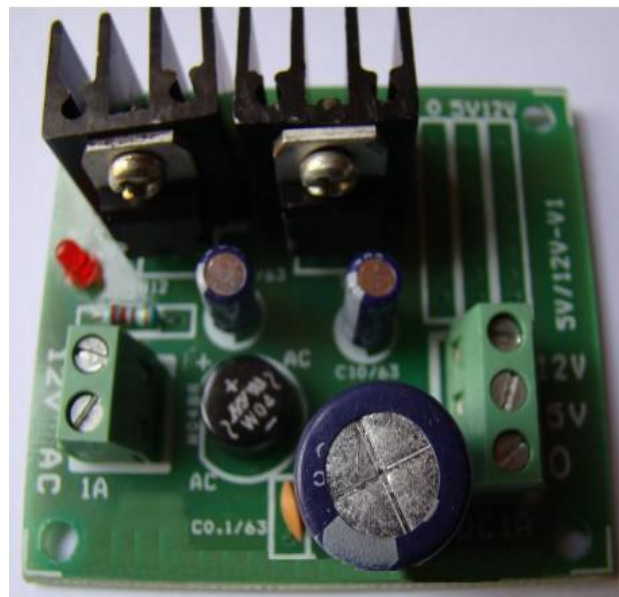
Transformer:

Transformers convert AC electricity from one voltage to another with little loss of power. Transformers work only with AC and this is one of the reasons why main electricity is AC. Step-up transformers increase voltage, step-down transformers reduce voltage. Most power supplies use a step-down transformer to reduce the dangerously high main voltage (230V in UK) to a safer low voltage.



Power Supply:

Power supply is reference to a source of electrical power. A device or system that supplies electrical or other types of energy to an output load or group of loads is called a power supply unit or PSU. This term is most commonly applied to electrical energy supplies, less often to mechanical ones, and rarely to others.



5. Operation:

Temperature sensor is used to monitor the heat condition of the industrial device. The measured detail uploads to IOT. Fire sensor is used for fire detection purpose which is connected to Arduino uno. Lcd display is

used to display the measured details. The industrial devices like motor and load are monitored using temperature sensor and machine speed is controlled using IOT. Then measured parameters will also updated to the IOT website.

6. Conclusion:

Thus we built a system for monitoring and controlling of industrial environment by using new emerging technology of internet of things. This system gives efficient solution than other systems. In this system we collect the data from the sensor and made it available to the user from remote location anytime. Hence it will become low cost, high efficient embedded system. The advantages of the developed system are to have a continuous monitoring over industrial applications and also control them if going beyond their threshold conditions. As sometimes it will be late in this process and it will harm to property as well as life. For this purpose we are developing a system for Industrial Automation using IoT with the help of Artificial Intelligence to make system automated which will take intelligent decisions.

7. References:

1. Kartik Rathod, Nilay Parikh, Aesha Parikh and Prof. Vrushank Shah, 2012. Wireless Automation using Zigbee protocols,
2. Alaparathi Narmada and Parvataneni Sudhakara Rao, 2012. Zigbee Based WSN with IP Connectivity,
3. Ploplys, N.J., P.A. Kawka and A.G. Alleyne, 2004. Closed-Loop Control over Wireless Networks, IEEE Control Systems Magazine
4. Maldar Aman Malikamber, Tamhankar S. G, "Implementing SCADA system for industrial environment using 'IEEE C37.1' standard", IEEE C37.1: IEEE standard for SCADA & Automation system
5. Zafar Aydogmus, Omur Aydogmus, "A Web Based Remote Access Laboratory Using SCADA" IEEE Transactions on Education, Volume 52, No.1, February, 2009.
6. Prof. Jaikaran Singh, Prof. Mukesh Tiwari, Mr. Manish shrivastava," Industrial Automation-A Review", Int. Journal of Advanced Engineering Tends And Technology Vol. 4, Issue 8, August 2013.



ASSESSMENT OF FABRICATED ALUMINIUM ALLOY CHANNELS: PROCESS CAPABILITY INDEX

R. Saravanan ^{a, *}, P. Navaneetha krishnan ^b, D. Raj kumar ^a

^a Assistant professor, Department of Mechanical Engineering, JJ College of Engineering and Technology, Trichy, Tamil Nadu, India.

^b Assistant professor, Department of Mechanical Engineering, University College of Engineering, Trichy, Tamil Nadu, India.

***Corresponding Author**

saravanan040587@gmail.com

(R. Saravanan)

Tel.: 0432 66308194

Received : 29-12-2017

Accepted : 30-01-2018

ABSTRACT: Aluminum (AA8011) is the one of light weight alloy which is widely used in aerospace, automotive, bioengineering, gas turbine blades and electrical component. The main purpose of task is to fabricate micro-channels on AL using specially designed copper foil setup by die sinking EDM (Electrical Discharge Machining) and aiming to achieve design tolerance limit of 0.5 ± 0.2 mm. The application of micro-channels creating on AL in order to increases the cooling efficiency of heat exchanger. The current and pulse on have been considered as input machining factors and the width size and delamination factor have been considered as output machining factors. Taguchi's orthogonal array has been used to perform the experiment.

Keywords: AL, copper foil, width and depth

1 Introduction

The quality of an item is measured as far as total loss to the society because of functional variety and side effects. More loss means lower quality. This loss happens because of the failure of the item to convey the desired performance and because of destructive side effects of it including its expenses. It is impractical to reach zero loss or perfect quality condition, yet utilizing robust design engineering technique we can enhance the quality of an item by minimizing the impact of the reasons for variation without eradicate of the causes. This is accomplished by optimizing the item and process design to make the execution insignificantly sensitive to causes of variation.

Based on the customer's needs and associated costs it is necessary for the supplier to set realistic cost and effective part specifications. Within the given tolerance limits capability studies can assess how well a process is capable of producing components. A viable quality administration framework ought to guarantee the nature of the parts in view of taking suitable corrective activities. If we know the capability of our process, we can choose the most convenient process among competing processes to fulfill the customer expectation. Process

capability analysis helps to summarize process capability in terms of essential metrics and also helps to forecast the extent to which the machining process will be able to hold customer requirements or tolerances. It is an inherent quantitative measurement of a process to fulfill the requirements of the product statistical quality control is an important concept for industrial managers to understand. Process Capability is the capacity of the procedure to understand a characteristic that will fulfill the prerequisites for that characteristic. As of late, process capability investigation has assumed a critical part in guaranteeing nature of fabricated items. The process capability index is generally utilized in industrial process as a part of modern procedure to monitor the product as per the specification limits. This kind of capability index is valuable to decrease the variety in the product. Electrical Discharge Machining (EDM), primitive machining processes in the manufacturing industry, is a basic material removal process which is carried out on a machining center. EDM has the ability to machine the work-piece in a desired shape with the help of electrode at a feed, given speed and at a predefined depth of cut.

Researchers have attempted several approaches to identify multiple process parameter settings that can increase quality, at higher productivity levels; require the turning process to be executed more efficiently. So it is utmost important to identify optimal parameter settings using a process capability index to improve tool life, lessen cutting force, reduce chip thickness and increase surface accuracy in milling process.

Process capability index is outline insights which quantify the real or the potential execution of procedure attributes with respect to the objective and particular points of confinement. It has been the most regularly utilized index as a part of the practice since it gives limits on the procedure division of defectives. It is an important conception under statistical process control which portrays the strength of a process to produce components within tolerance limits.

As of late, to know whether the process can meet the requirements a statistical quality control approach known as Process Capability Analysis (Cpi) has been introduced. Cpi plays a significant part in persuade quality of manufactured products. Several modern businesses these days recommend the process capability index and utilize it as a management tool for measuring products quality (1). Higher the index, very less chance that the item will be outside the specifications. As noted by numerous quality control practitioners and researchers, Process Capability Index is yield-based and is not dependent on target. It is a competent tool which continuously improved quality, productivity and also helps in taking administrative decisions (Rajvanshi and Belokar, 2012) and can measure the internal potential of a process.

Capability index (Cpi) demonstrates that within the range specified by the design limits how well a produced part can fit (3). From this literature overview, it can be seen that as far as process effectiveness, quality of output or economy concern, there has been a basic absence of experimental studies on process capability of milling process. Extensive works has been carried out using Process Capability investigation on different steps of managerial process and also in machining processes like WEDM, grinding, casting but very few works have been done on Turning (4).

In the last few decades, owing to the rapid developments in micro-electronics and biotechnologies, the applied research in micro-coolers, micro-biochips,

micro-reactors, and micro-fuel cells has been expanding at a tremendous pace.

Among these micro-fluidic systems, microchannels have been identified to be one of the essential elements to transport fluid within a miniature area. In addition to connecting different chemical chambers, microchannels are also used for reactant delivery, physical particle separation, fluidic control, chemical mixing, and computer chips cooling. Microchannels are primarily used in biomedical devices and microfluidic applications. Fabrication of microchannels has always been a tough task using conventional manufacturing technologies. Various types of materials are in use for fabricating microchannels in different types of applications including metals, polymers and ceramics. A number of methods are in use for fabricating different types of microchannels.

These processes include both conventional and nonconventional fabrication techniques. Some of the most established techniques include Micro-machining, lithography, Stereolithography, Diffusion Bonding Chemical Etching, LIGA, embossing processes, and laser ablation processing, etc. In this paper we have fabricated microchannels by electro-discharge machining process using copper sheet as electrode. Electro Discharge Machining or EDM is a machining method primarily used for hard metals or those that would be impossible to machine with traditional techniques.

So, Electro Discharge machining (EDM) is one of the most important non-traditional machining processes, which is used for machining difficult to machine materials like composites and inter-metallic materials. In electro discharge machining the erosive action of an electrical discharge between conductive tool and work-piece is used to remove material. Electro-thermal erosion (material melting and evaporation for every spark) creates small craters both in the piece and in the tool during machining progress, and then tool shape is copied in the workpiece with a no contact system. With this technique it is possible to machine not only difficult to cut metals (like hardened steels) or carbides but also semiconductors and conductive ceramics. The discharge results from the application of an electrical voltage between electrodes (tool and workpiece) with a dielectric flushed fluid interposed. We also used Taguchi Method for optimization

of EDM process parameters for surface roughness in the machined microchannels. The main disadvantage of this method is that the results obtained are only relative in nature and do not exactly indicate which parameter has the highest effect on the performance characteristic value. Hence, process capability index is used for finding for which machining conditions suitable for performing desired width and delamination factor. This is a complex process for cutting microchannels using electrode sheets as the complete microchannel is made using only the vertical movement of the electrode.

2. Design of experiment

The application of design-of-experiments (DoE) requires careful planning, prudent layout of the experiments, and expert analysis of results. Taguchi has standardized methods for each of these DoE application steps. This approach in finding factors that affect a product in a DoE can dramatically reduce the number of trials required to gather necessary data. Thus, DoE using Taguchi approach has become a much more attractive tool to practicing engineers and scientists. In this case study, the two parameters namely pulse on and current in EDM and each parameter was designed to have three levels denoted by 1, 2, 3 level.

3. Process capability

Process control is defined as the evaluation of process stability over time or the ability of the process to maintain a state of good statistical control. Before evaluating the process capability, the process must be shown under statistical control i.e. the process must be operating under the influence of only chance causes of variation and also ensure that the process data is normally distributed and observations are independent. Process Capability is defined as the evaluation of how much a process meets specifications or the ability of the process to produce parts that conform to engineering specifications. The main purpose of the process capability study is to determine the variation spread and to find the effect of responses on both the average and the spread. The results are further used for new design applications, inspection planning and evaluation techniques.

The following three steps are carryout to find out the process capability of attributes criterion. In this work width, delamination factor are the attributes.

Step 1: calculation of mean (\bar{X}): calculation of mean is ascertained for every trial run by using following equation.

$$\bar{x} = \frac{\sum_{i=1}^N x_i}{N} \quad (1)$$

Here, x_i = response parameter value for i -th replicate trial, N = number of replicates.

Step 2: Computation of standard deviation (α): Following equation was used to compute Standard deviation (α).

$$\alpha = \sqrt{\frac{\sum_{i=1}^N (x_i - \bar{X})^2}{N}} \quad (2)$$

Here,

x_i = Response parameter value for i -th replicates of a distinct trial, \bar{X} = Mean of the N replicates for the trial.

Step 3: Process capability index (C_{pi}): following equation was used to calculate process capability index (C_{pi}) for each experimental run.

$$C_{pi} = \min \left\{ \frac{\bar{X} - LSL}{3\alpha}, \frac{USL - \bar{X}}{3\alpha} \right\} \quad (3)$$

Here, USL = upper specification limit for individual attributes, LSL = lower specification limit for individual attributes. USL and LSL actually are a destination value. Specification limits are typically provided from outside which depends on production necessities, market pre-requisites. It can either be one-sided or two-sided.

4. Experimental details

Micro-channel fabricating experiments were performed on a die sinking EDM. The workpiece material was aluminium alloy. Square shaped copper foil electrode was used for all the experiments. To minimize the experiments machining operations were carried out following L9 Orthogonal Array (by the help of MINITAB 14 Statistical Software) taking three prevalent input parameters power and pulse on were taken as input criterion. Machining parameters which were considered for experiments are shown in Table 1. After the experiments average width size and delamination factor for all machined surfaces was measured utilizing optical microscope and ImageJ software. Table 2. Machined image observed from ImageJ. The measurement was performed at five different locations on the machined width and average value of width size has been taken for further examination. The foil thickness was measured by optical microscope and its value was 0.736 mm and was shown in Figure 1. The copper foil setup was shown in Figure 2. The observed results were shown in Table 3.

Table 1. Machining conditions used

Factor	level1	level2	level3
Current (amp)	1	2	3
Pulse on (µs)	100	200	300

Table 2. Machined image observed from ImageJ

Current	Pulse on	Optical microscope image
1	100	
1	200	
1	300	
2	100	
2	200	
2	300	
3	100	
3	200	

3	300	
---	-----	--

Formula used:

Delamination factor = maximum damaged diameter (mm)/ foil thickness (mm)

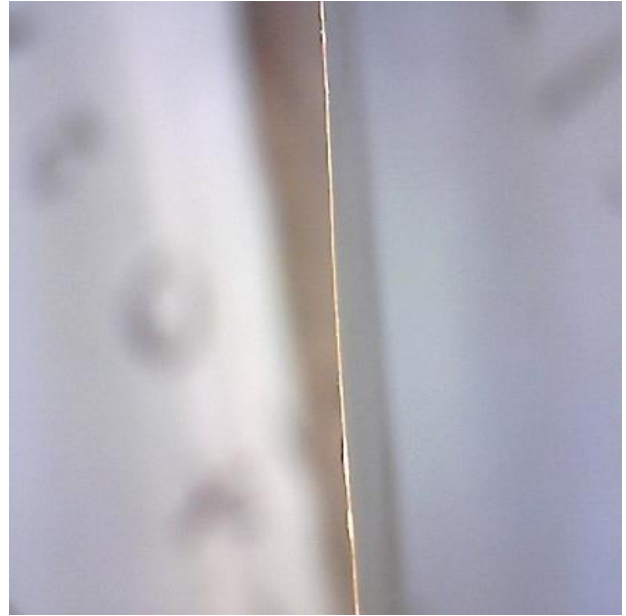


Figure 1. Copper foil thickness



Figure 2. Copper foil setup and machined aluminium

5. Results and discussions

5.1. Effect of machining parameters on obtained width size and delamination factor

Table 3. Taguchi design and observed results

No	I (amp)	T _{on} (µs)	width size (mm)					Delamination factor				
			1	2	3	4	5	1	2	3	4	5
1	1	100	1.003	0.943	1.000	1.022	1.002	1.363	1.281	1.359	1.389	1.361
2	1	200	0.949	1.022	1.015	1.139	0.964	1.289	1.389	1.379	1.548	1.310
3	1	300	1.490	1.586	1.549	1.423	1.417	2.024	2.155	2.105	1.933	1.925
4	2	100	1.409	1.482	1.615	1.606	1.644	1.914	2.014	2.194	2.182	2.234
5	2	200	1.572	1.787	1.659	1.694	1.609	2.136	2.428	2.254	2.302	2.186
6	2	300	1.574	1.547	1.565	1.668	1.607	2.139	2.102	2.126	2.266	2.183
7	3	100	1.298	1.233	1.252	1.237	1.265	1.764	1.675	1.701	1.681	1.719
8	3	200	1.507	1.518	1.573	1.854	1.823	2.048	2.063	2.137	2.519	2.477
9	3	300	1.518	1.675	1.300	1.395	1.660	2.063	2.276	1.766	1.895	2.255

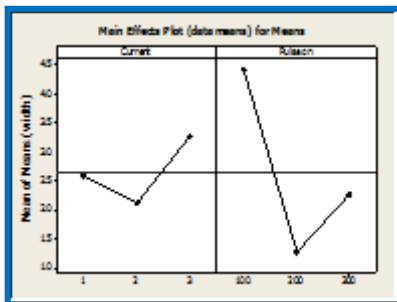


Figure 3. Width size against current and pulse on

Figure 3 shows the width size against current and pulse on graph. From the graph, the width size decreases from level 1 to level 2 and increases from level 2 to level 3 when the current increases. Also, the width size decreases from level 1 to level 2 and increases from level 2 to level 3 when the pulse on increases. The optimum point is level 2 for both current and pulse on (I2P2). The quality character sits lower the better is chosen for this work.

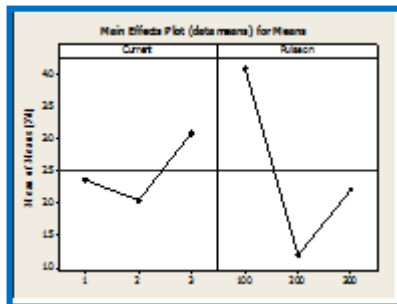


Figure 4. delamination factor against current and pulse on

Figure 4 shows the Fd against current and pulse on graph. From the graph, the Fd decreases from level 1 to level 2 and increases from level 2 to level 3 when the current increases. Also, the Fd decreases from level 1 to level 2 and increases from level 2 to level 3 when the pulse on increases. The optimum point is level 2 for both current

and pulse on (I2P2). The quality character sits lower the better is chosen for this work.

Table 4. Process capability for width size

No	mean	SD	CPL	CPU	CP (WS)
1	0.994	0.027	3.670	12.557	3.670
2	1.018	0.067	1.585	4.898	1.585
3	1.493	0.067	3.943	2.521	2.521
4	1.551	0.090	3.145	1.658	1.658
5	1.664	0.074	4.330	1.508	1.508
6	1.592	0.043	6.979	3.190	3.190
7	1.257	0.023	7.923	10.568	7.923
8	1.655	0.152	2.097	0.758	0.758
9	1.510	0.146	1.844	1.117	1.117

5.2 Process capability study

Table 4 and Table 5 show the process capability of width size and delamination calculation. In order to justify the whether the process is capable or not. The following grade is adopted for this work shown in Table 6. The design tolerance limits chosen for width and delamination are

Width size (WS):

Upper specification limits: 2 mm

Lower specification limits: 0.7 mm

Delamination factor (DF):

Upper specification limits: 2.7 mm

Lower specification limits: 1 mm

From the table 4 and 5 observed that all the process condition is capable for performing micro-channel fabrication on aluminium except 8 conditions. The maximum current is reason for obtained results incapable.

Table 5. Process capability for Delamination factor

No	mean	sd	CPL	CPU	CP (DF)
1	1.351	0.036	3.220	12.397	3.220
2	1.383	0.091	1.405	4.834	1.405
3	2.029	0.091	3.764	2.457	2.457
4	2.108	0.123	3.012	1.611	1.611
5	2.261	0.101	4.169	1.451	1.451
6	2.163	0.058	6.698	3.090	3.090
7	1.708	0.032	7.411	10.386	7.411
8	2.249	0.206	2.018	0.729	0.729
9	2.051	0.199	1.762	1.088	1.088

6. CONCLUSIONS

In this experimental study, process capability index has been researched for machining of aluminium. On the ground of investigation results the accompanying conclusions might be drawn:

References

- [1] K.S. Chen, S.L. Yang, H.T. Chen, Process improvement capability index with cost—a modeling method of mathematical programming, *Applied Mathematical Modelling*, 39 (2015)1577–1586.
- [2] P.K. Rajvanshi, R.M. Belokar, Improving the process capability of a boring operation by the application of statistical techniques, *International Journal of Scientific and Engineering Research*, 3 (2012) 450-455.
- [3] M. Abdolshah, A fuzzy Taguchi loss-based process capability index, *International Journal of Quality Engineering and Technology*, 3 (2013)303–318.
- [4] A.A. Eramah, N.A. Raji, R.O. Durojaye, A.A. Yussouff, Process capability analysis of a centre lathe turning process, *Engineering*, 8 (2016) 79-85

(1) Process Capability Analysis is the most convenient approach to measure the capacity of a process. Though it has some limitations which prevent a deep and flexible analysis because of the crisp movement and specification limits still it is broadly utilized as a part of industrial process to monitor the product according to the specification limits which is helpful to reduce the variation in the product.

Table 6. Grade for process capable

Cp	Grade
Cp > 1.67	A very capable
1.67 > Cp > 1.33	A highly capable
1.33 > Cp > 1.00	A barely capable
1.00 > Cp > 0.67	Not capable
0.67 > Cp	Very not capable

(2) Optimum process parameter settings for process capability index (Cp) of width and delamination were current level 2 and power level.

(3) From the present study, with the proposed optimal parameters it is possible to increase the efficiency of machining process and decrease production cost in an automated manufacturing environment.

(4) The research findings from the process capability analysis will provide effective guidelines and the results would be a good technical database for the aerospace, automobile and military applications in fabrication and machining aspects.

SPECIAL ISSUE PAPER

Energy efficient low-power full-adder by 65 nm CMOS technology in ALU

Suresh Kumar N¹  | Paramasivam K²

¹Department of Electronics and Communication Engineering, MAM School of Engineering, Tamil Nadu 621 105, India
²Department of Electronics and Communication Engineering, Kumaraguru College of Technology, Chinavedampatti, Coimbatore, Tamil Nadu 641049, India

Correspondence

Suresh Kumar N, Department of Electronics and Communication Engineering, MAM School of Engineering, Tamil Nadu 621 105, India.
Email: sureshsaint3@gmail.com

Summary

The arrangement of energy efficient low-power full adder has vital role in VLSI systems. In this paper Energy Efficient Low-power 9T full-adder is proposed. Its functioning basis of Power Delay Product (PDP), Delay, power and area is distinguished in accordance with that current 1 bit full-adder simulated by utilizing various Complementary MOS logic designs. Output provides an average minimization of 99.28% in power usage, 67.87% in area, 99.89% in delay, and 99.99% in Power-Delay Product (PDP) distinguished to the traditional 28 Transistors CMOS logic. The ALU design has been implemented using 9T full adder. These logic gates are analysis at 65 nm technology of CMOS by utilizing Schematic Editor Tool.

KEYWORDS

area, average power, delay, power delay product (PDP)

1 | INTRODUCTION

To demand of VLSI is minimized area, delay and power usage properties raising quickly the utilization of handheld devices such as laptop, tab, notebook, and computers.¹ Full-adder is fundamental of arithmetic and logical circuits also used in compressors, converters, calculators, etc.² so that improvement of full-adder is affect the whole circuit performances.³ In digital the combinational circuit has 2 addition of number is called Half-adder and 3 addition of number is called Full-adder.

Beside the minimizing energy consumption, area and delay also important objective that need to be considered. The delay is depends on amount transistor used in logic gates. The formatting of energy efficient less-power full adder has vital role in VLSI systems.⁴

1.1 | 28 transistor full-adder

Traditional CMOS Full-Adder or mirror full adder⁵ has 28T as depicted in Figure 1. the inputs A, B, and C_{in} outputs are sum and carry out. Consideration of result is in both delay and area. However, it increases high input loads because of substantial number of transistors.

$$C_{out} = AB + BC_{in} + AC_{in} \quad (1)$$

$$Sum = ABC_{in} + CO(A + B + C_{in}) \quad (2)$$

1.2 | 22T Zhuang full-adder

The 22T Zhuang Full-Adder⁶ which minimizes transistor count and the inverter additional which is utilized to create inverter of Xnor (Xor). As contradictory to 22T adder and TG adder enforces gate xor instead of multiplexer for making S_{out} . 22T Full-Adder is as depicted in Figure 2.

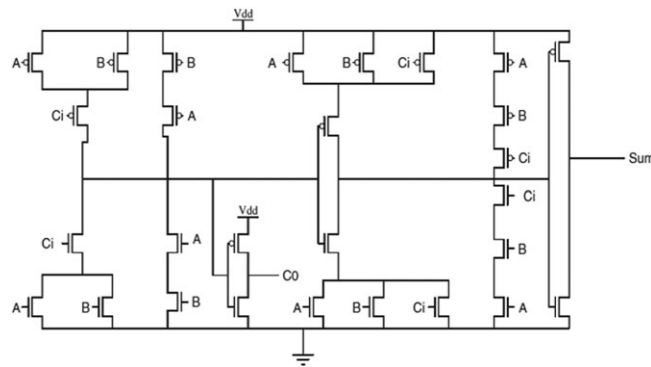


FIGURE 1 28T Full adder

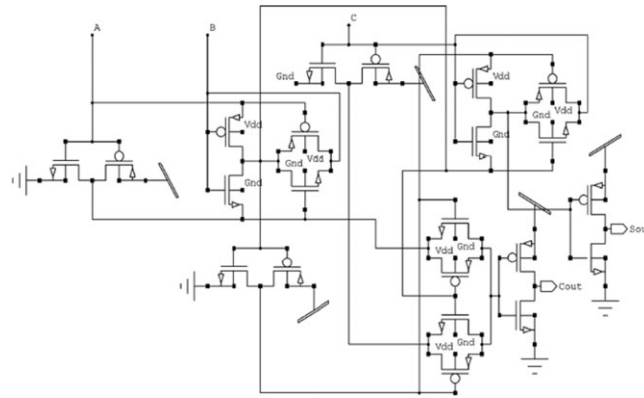


FIGURE 2 22T Zhuang full-adder

1.3 | 20T TG full-adder

20T TG Full-Adder, (TG) which is selectively pass signal from the input to output. It includes transistor of pMOS and nMOS. Complementary manner repression gates are biased so that transistors either on or off.⁷ The transmission gate provides bi-directional connectivity without degradation of input signal. However, it has more power dissipation. 20 Transistor is as depicted in Figure 3.

1.4 | 10T Exclusive-OR full adder

Exclusive-OR gate diffusion full-adder⁸: Exclusive-OR gate diffusion full-adder has inputs three the number one G- Common input state of PMOS and NMOS, number two n input to off flow gradually or source of NMOS and number three P-input to source or off the flow gradually of PMOS.⁹ Exclusive-OR full-adder techniques executed for plan low-energy full-adder and good performance. However need to improve delay and area. Ex-OR gate diffusion full adder as depicted in Figure 4.

1.5 | 8T full-adder

The 8T full-adder¹⁰ created by 1 inverter and 3 selector circuit. The circuit has inverter which gives speed up spreading and balanced C_{out} signal demanding of creating for Sum. The inverter is not required 8T full-adder because the Ex-OR gate substituted by Ex-NOR gate.

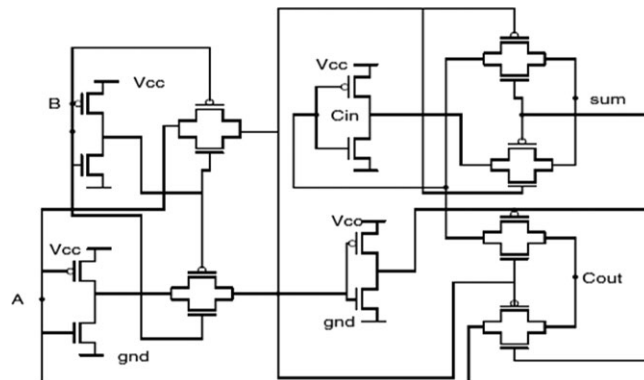


FIGURE 3 20T Transmission gate full adder

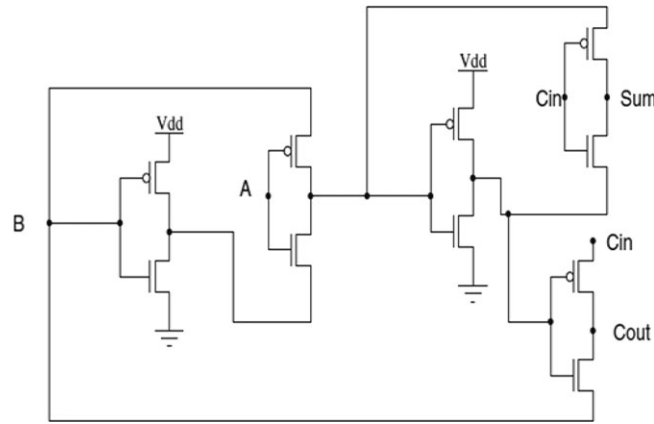


FIGURE 4 Ex-OR full adder

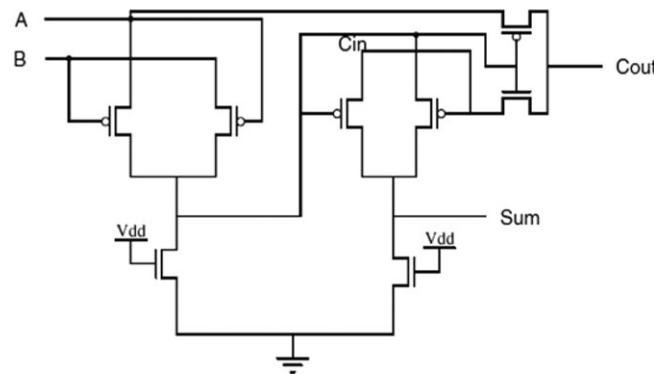


FIGURE 5 8T Full-adder

Hence it's minimized count of transistor to eight. However, need to improve the power dissipation.¹¹ The 8T implementation depicted in Figure 5.

1.6 | 9T proposed full-adder

The 9T proposed full adder is depicted in Figure 6, which has one Xor gate and two 2:1 Mux gate. The proposed 9T full-adder structure, it reduced crucial path delay due to a Xor gate substituted by a multiplexer gate. The crucial path delay is executed by utilizing 2nd Multiplexer and output of Xor as selection line. Minimizing the count of Xor gates it lead to full-adder power usage can be minimized.

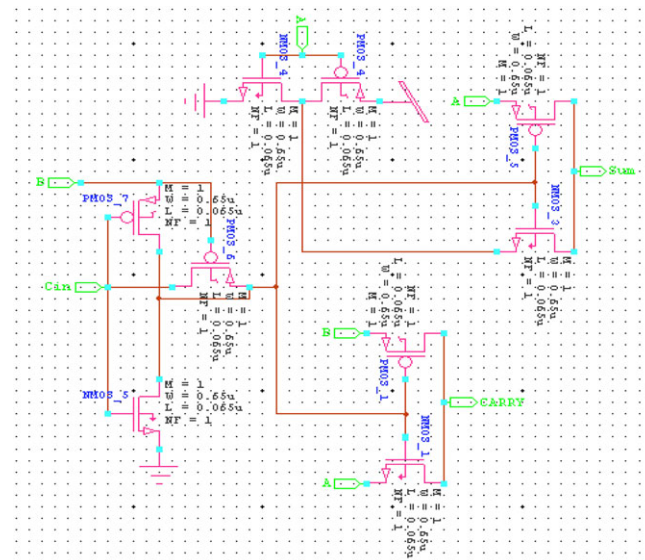


FIGURE 6 Proposed 9T full adder

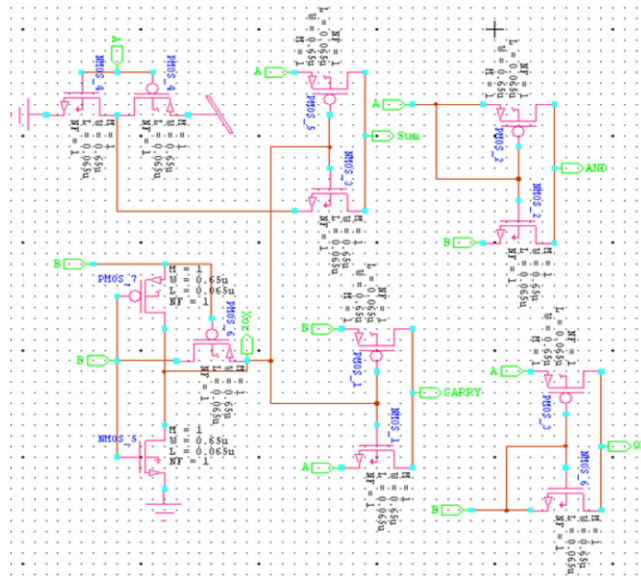


FIGURE 7 Schematic diagram of low-area low-power proposed ALU using 9T full-adder

The 9T proposed full-adder enforced into ALU and array structure multiplier. Figure 7 is low-power and low-area ALU using 9T full adder the total number transistor count is 13. Transistor size minimized using technology library. The vital functions of ALU are arithmetic, logical operations and bit shifting operations these are essential process and processed by CPU. In an array multiplier the partial product has specific levels. In that when there are 3 bits full-adder has to be used. In that 3 input, 2 inputs are given to Xor gate and 1 input given to first mux, the output behave as select

TABLE 1 Functionality Check of 9T Proposed Full-adder compare to Existing Full adders

S.No.	FA	Avg power nW	Area pM	Power Delay Product fJ
1	28T (mirror)	435.1	1.183	9.132
2	22T (Zhuang)	842.6	0.929	17.63
3	20T (TG)	207.1	0.845	4.328
4	10T (E.orfa)	184.7	0.422	3.692
5	8T	89.66	0.338	1.791
6	9T (Proposed)	3.101	0.380	0.069

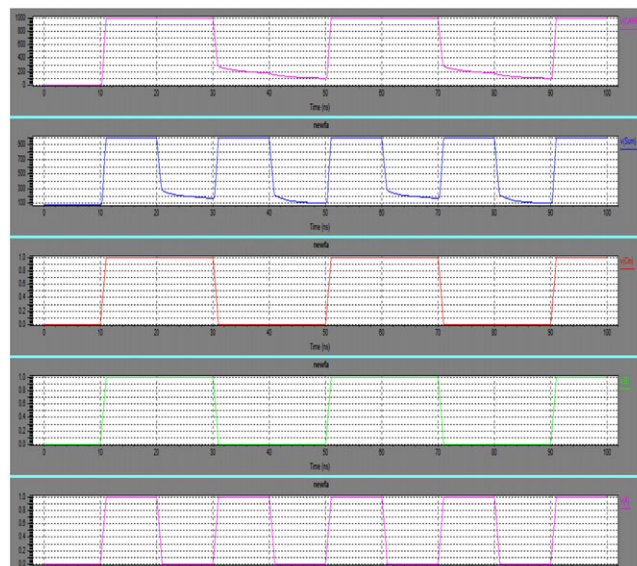


FIGURE 8 Waveform for proposed 9T Full-adder

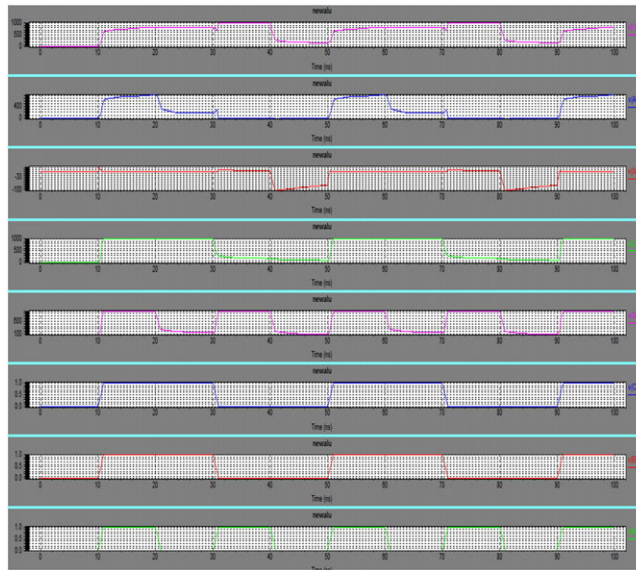


FIGURE 9 Waveform for low-power less-area ALU

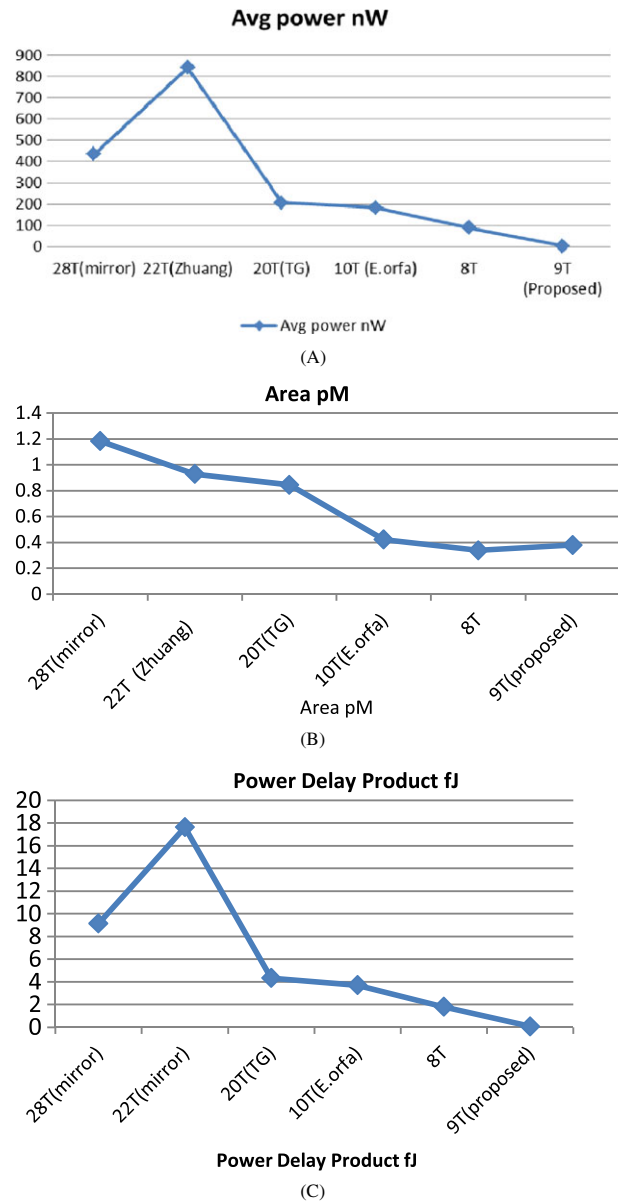


FIGURE 10 Performance metrics

line for both mux. The carry bit given gives as input of 2nd mux. This designing leads to switching activity reduction critical path delay also minimized hence maximizes the speed. The proposed 9T operation can be explained as follows:

- i. When a, b, and c_{in} is one = sum: one, c_{out} : one
- ii. When a, b, and c_{in} is zero = sum: zero; c_{out} : zero
- iii. When Any one input is one = sum: one; c_{out} : zero
- iv. When Any two inputs is one = sum: zero; c_{out} : one

2 | SIMULATION RESULT

The Table 1 has given simulation results for analysis of full-adders. The Table 1 provides Comparison of Average-power, Area and (PDP) power delay product in 28 T Full-adder, Zhuang full-adder, 20T TG, 10T, 8T transistor and 9T proposed full-adder. Full adder and ALU output waveform depicted in Figures 8 and 9 also Average power, Area and PDP performance metrics are shown in Figure 10(a), (b), and (c).

From the results 9T proposed full-adder achieves better performance compared with the existing full adder circuits in terms of Average-power, Area and PDP.

3 | CONCLUSION

In this paper represents 9T proposed full adder. The simulation was carried out Schematic editor tool using 65-nm technology. The proposed 9T full-adder is compared with other existing full-adders in terms of area, delay, power and Power Delay Product (PDP). Using 9T full-adder an attempt has been made to implement low-power and less area Arithmetic Logic Unit (ALU). In this accessibility is earmark for advanced industrial process technology. In future, the hybrid- full adder circuits are required to achieve minimum PDP while maintaining low complexity.

ORCID

Suresh Kumar N  <http://orcid.org/0000-0001-5283-2843>

REFERENCES

1. Senthil Kumar G, Paramasivam K. Test power minimization of VLSI circuits: a survey. IEEE Sponsored 4th International Conference on Computing Communication and Networking Technologies – ICCCNT 2013 at Vivekanandha College of Engineering for Women, Tiruchengode, 4-6th July 2013. The paper is available in IEEE Xplore Portal. <https://doi.org/10.1109/ICCCNT.2013.6726569>. pp. 1-6.
2. Rabaey JM, Chadrakasan A, Nikolic B. Digital integrated circuits: design approach. IEEE International Conference on Power, Control and Embedded System (ICPCES), 28 Nov.-1 Dec. 2010.
3. Bhattacharyya P, Kundu B, Ghosh S, Kumar V, Dandapat A. Performance analysis of a low-power high speed hybrid 1-bit full adder circuit. *IEEE Trans Very Large Scale Integr (VLSI) Syst*. Sep. 2014.
4. Goel S, Kumar A, Bayoumi MA. Design of robust, energy efficient full adders for deep-sub micrometer design using hybrid-CMOS logic style. *IEEE Trans Very Large Scale Integr (VLSI) Syst*. 2006;14(12):1309–1321.
5. Shams AM, Darwish TK, Bayoumi MA. Performance analysis of low-power 1-bit CMOS full adder cells. *IEEE Trans Very Large Scale Integr (VLSI) Syst*. 2002;10(1):20–29.
6. Zhuang N, Wu H. A new design of the CMOS full adder. *JSSC*. May 1992;27(5):840–844.
7. Panda S, Banerjee A, Maji B, Mukhopadhyay AK. Power and delay comparison in between different types of full adder circuits. *Int J Adv Res Electr Electron Instrum Eng*, ISSN: 2278-8875.
8. Mishra SS, Agrawal AK, Nagaria RK. A comparative performance analysis of various CMOS design techniques for XOR and XNOR circuits. *Int J Emerg Technol*. ISSN: 0975-8364.
9. Mishra S, Narendar V, Mishra RA. On the design of high-performance CMOS 1-bit full adder circuits. International Conference on VLSI, Communication and Instrumentation; 2011.
10. Chowdhury SR, Banerjee A, Roy A, Saha H. A high speed 8 transistor full adder design using novel 3 transistor XOR gates. *Int J Electron Circuits Syst*. 2008;2:218
11. Kalamani C, Paramasivam K. Survey of low power testing using compression techniques. *Int J Electron Commun Technol*. 2013;4(4).

How to cite this article: N SK, K P. Energy efficient low-power full-adder by 65 nm CMOS technology in ALU. *Concurrency Computat Pract Exper*. 2019;31:e4741. <https://doi.org/10.1002/cpe.4741>



iJRASET

International Journal For Research in
Applied Science and Engineering Technology



INTERNATIONAL JOURNAL FOR RESEARCH

IN APPLIED SCIENCE & ENGINEERING TECHNOLOGY

Volume: 5 Issue: XII Month of publication: December 2017

DOI:

www.ijraset.com

Call:  08813907089

E-mail ID: ijraset@gmail.com

Lossless Image Compression using an Efficient Huffman Coding

K. Umarani¹, V M Sriram², N. Logesh Kumar³

^{1, 2, 3} Anna University, Trichy, Tamilnadu, India

Abstract: *Lossless image compression is a technique to reduce the size of image without failure of its originality. It yields all its content while received an output image. There are different well known compression techniques offered to efficiently compress an image. Here an efficient work introduce for lossless compression named Huffman coding which is an efficient lossless compression technique. It is uncomplicated and proficient to implement and need lesser amount of memory space for store an image.*

Keywords: *Image compression, Lossless compression, Lossy compression, Huffman coding, Source Reduction*

I. INTRODUCTION

Lossless compression is a technique to reproduce an accurate image exactly similar to the original. A new lossless method of image compression and Decompression using Huffman coding techniques [1] describes detailed lossless method of compression and decompression using Huffman coding. The execution of this method is easy to implement, simple and use minimum memory space. It describes how an image get compressed and also describes the various redundancy types including coding redundancy, inter pixel and psycho visual redundancy. The implementation of compression and decompression using Huffman coding is provided and the results shows that there is no information can loss while decompressed of image. Compression Using Huffman Coding [2] describes various techniques for compression such as simple repetition, RLE, pattern substitution, Entropy encoding, Shannon-fano algorithm, Huffman and adaptive Huffman coding. The main conception is to explain the basic technique of Huffman coding algorithm. It includes the Huffman coding characteristics, area of applications, advantages and disadvantages. Huffman Based LZW Lossless Image Compression Using Retinex Algorithm [3] proposes two lossless compression methodologies such as Huffman coding and Lempel-Ziv-Welch(LZW) method. Huffman coding method is provide a Huffman tree and performs encoding operation on input symbols.

Then use LZW for compression and finally it use retinex algorithm on compressed image for improve image quality. Energy Aware Lossless Data Compression [4] illustrates various data compression methods for lossless and their performance on image. It can be estimate the compression ratio and also calculate the time for compression and decompression of image when using various compression algorithms. Simple Fast and Adaptive Lossless Image Compression Algorithm [5] explains lossless methods and proposes an algorithm named as an SFALIC.

The compression ratio of SFALIC was examined the similarities and differences between the various image compression algorithms. Lossless Image Compression Technique Using Combination Methods [6] describes lossless method LZW and Bose, Chaudhuri, and Hocquenghem (BCH) and compare those yield compression ratios with RLE and Huffman coding and some other lossless compression method. Lossless image compression algorithm for transmitting over low bandwidth line [7] proposes a new efficient lossless compression algorithm based on Bayer format image. It uses adaptive wavelet decomposition method and explains Huffman coding method. The results shows an adaptive wavelet decomposition is works better than non-adaptive wavelet decomposition. Lossless image compression [8] explains different linearization schemes using Huffman, arithmetic and LZW. It uses the spatial domain algorithms. The experimental results shows the image performance when using various compression methods. Lossless Compression of Continuous-Tone Images [9] describes some current advantages of continuous-tone images than other images. It uses different coders such as JPEG-LS, CALIC and FELICS (Fast, Efficient Lossless Image Compression System). A Literature Survey on Lossless Image Compression [10] describes a basic concept and procedure for a condensed image. Lossy and lossless compression using various algorithms [11] describes the different lossy compression and lossless compression techniques and applies those various algorithms on compound images and calculates Peak Signal to Noise Ratio (PSNR) for those various compound images. Section II defines an image compression and their categories lossy method and lossless compression method. Section III describes the operations of Huffman encoding and decoding. It defines the average length and code efficiency of Huffman code. In Section IV conclusion is drawn.

II. IMAGE COMPRESSION

Image Compression is a technique to diminish the amount of data without any degradation in an image quality. So the image should requires less memory for store, it leads to some more images have stored in those memory space. Image compression is widely used for transmission of image over internet and storage. The necessity of image compression is to decreasing the image transmission time. This means every image took some time for transmitting via internet, but compressed image took less time than uncompressed image transmission time. There are two types of Compression namely lossy compression and lossless compression.

A. Lossy Compression

Lossy image compression is a technique which offers reducing of data efficiently. It does not reproduce an original image. It can only trying to recuperate an approximation of original image. So thus the resultant image should be smaller and has lower quality. It is also known as irreversible compression. It is mostly used in multimedia data.

It consists of the following techniques.

- 1) Predictive Coding
- 2) Transform Coding
- 3) Wavelet Coding

B. Lossless Compression

Lossless image compression is a technique to reproduce a precisely accurate image. so thus the resultant image should be larger and has higher quality. It consists of the following techniques. It is also known as reversible compression.

- 1) Variable Length coding
 - a) Huffman coding
 - b) Arithmetic coding
- 2) Bit Plane coding
- 3) Lempel-Ziv-Welch coding
- 4) Lossless Predictive Coding
- 5) Differential Pulse Code Modulation (DPCM)

III. HUFFMAN CODING

The popular method for eliminating some pixel values more common than others is called Huffman coding. The principle of huffman coding is performs to encode the data presented in an image and those data encodes are stored in a code book.

Huffman encoding algorithms performs encoding operations on an input symbols and their frequency of a list of nodes. The list of nodes having probabilities of $P(X_i)$ where $i=1,2,\dots,L$. A table which has a source symbols and the number of times they occurred is called a frequency table. It can be used to construct a huffman tree having a list of nodes. The encoding process of huffman tree starts from root node to leaf node. Each and every node of huffman tree consisting of input symbols and their respected frequency, a pointer that pointed to the parent node and child nodes. Find the very lowest probabilities of two nodes in a list and going to adding them. The entire huffman tree is involve to encoding process, causes to generates a new node. That the new node has been consider as a parent node to the two child nodes. At last it will eliminate the new node childrens from a tree and including the new parent node. Continue this process and then terminate if there is only one node without a parent node. This one node will play as a root node of the entire tree. The parent node will assign a bit to left and right child node. A bit 0 is assigned to the left child node and a bit 1 is assigned to the right child node. The process of decoding a huffman tree starts from child node to root node.

One example is given here. A list of nodes consists of 0, 2, 14, 136, and 222 symbols. Their frequency occurrences are given in Table 1. The table shows, symbol 0 occurs 50 times in the list. The Huffman tree and their final code are shown in below.

SYMBOLS	FREQUENCY
0	50
2	9
14	8
136	6
222	4

Table 1: Frequency of Input Source Symbols.

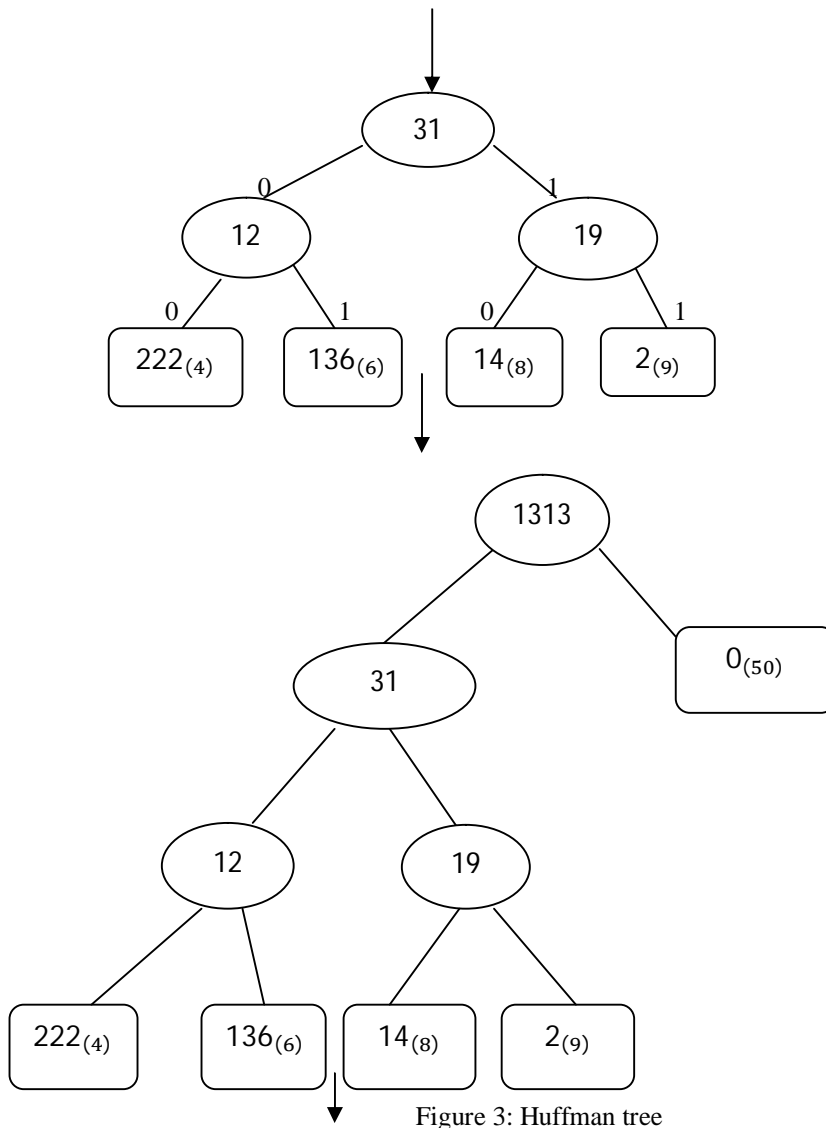


Figure 3: Huffman tree

SYMBOLS	CODE	FREQUENCY
0	1	50
2	011	9
14	010	8
136	001	6
222	000	4

Table 2: Symbols with their Codes

A. Steps In Huffman Coding

- 1) Construct a node list with input symbols and their frequency of symbols .
- 2) Search the two nodes which has lowest probabilities in the list.
- 3) Consider those two nodes as the children of a new node which has a probability by adding those two lowest probabilities.
- 4) These children of a new node has take away from the list of nodes and include the new parent-node.
- 5) Do the same procedure from step 2 to step 4 until the list consists of only one node without a parent node.

An example is given here to explain each steps in Huffman coding algorithm. A list of nodes having symbols and their probability is given. To construct a Huffman table by arrange the given probabilities from very large to small value and adding the least two values. Do this method until a table has two values.

Source		Reduction of Source			
Symbo	Probability	I	II	III	IV
b2	0.4	0.4	0.4	0.4	0.6
b1	0.3	0.3	0.3	0.3	0.4
b3	0.1	0.1	0.2	0.3	
b4	0.1	0.1	0.1		
b6	0.07	0.1			
b5	0.03				

In the above table, first source reduction is done by adding 0.07 and 0.03 i.e., $0.07+0.03=0.1$. So in a I column of Huffman reduction table, write 0.1 instead of 0.07 and 0.03. Then combining 0.1 and 0.1 and write the value in IInd column i.e., $0.1+0.1=0.2$ as a 3rd value. Similarly to do reduction in IIIrd column. In IVth column, there is only two values. So reduction can stop. Next to assign a code for each value. The code assignment procedure table is given below.

Source			Source reduction							
Symbol	Probability	Code	I		II		III		IV	
b2	0.4	1	0.4	1	0.4	1	0.4	1	0.6	0
b1	0.3	00	0.3	00	0.3	00	0.3	00	0.4	1
b3	0.1	011	0.1	011	0.2	010	0.3	01		
b4	0.1	0100	0.1	0100	0.1	011				
b6	0.07	01010	0.1	0101						
b5	0.03	01011								

In above table assign 0 to 0.6 and 1 to 0.4 in Column IV. In column III assign 1 to 0.4 that is already consigned in column IV and allocate 0.6 in column IV is created by 0.3 and 0.3 in column III. So assign 0 to 0.3 and 0.3 and append 0 and 1 after the 0 of two values 0.3 and 0.3. Do the same procedure till Ist column to obtain the Huffman code.

A multiplication of symbols probability and the number of encoded bits is called as the average length of the huffman code (L_{avg}). It can be calculated as beow.

$$L_{avg} = (\text{probability of source symbols}) \times (\text{number of bits})$$

$$= (0.4 \times 1) + (0.3 \times 2) + (0.1 \times 3) + (0.1 \times 4) + (0.07 \times 5) + (0.03 \times 5)$$

$$= 2.2 \text{ bits/symbol}$$

If the source entropy is 3.14 bits/symbol then the code efficiency is,

$$\text{Efficiency} = 3.14 / 2.2 = 1.4272727$$

IV. CONCLUSION

Lossless compression is an efficient method of compressed a given image without any failure of its original information in a resultant image. It will look same as the original. A future work may involve to introduce some other efficient lossless compression method for improving an image code efficiency by reduction of more bits while compressed.



REFERENCES

- [1] Jagadish h. Pujar, lohit m. Kadlaskar, "A new lossless method of image compression and Decompression using huffman coding techniques".
- [2] Mamta Sharma, "Compression Using Huffman Coding" IJCSNS International Journal of Computer Science and Network Security, VOL.10 No.5, May 2010.
- [3] Dalvir Kaur, Kamaljit Kaur, "Huffman Based LZW Lossless Image Compression Using Retinex Algorithm" International Journal of Advanced Research in Computer and Communication Engineering Vol. 2, Issue 8, August 2013.
- [4] Kenneth C. Barr, "Energy Aware Lossless Data Compression" B.S.E. Computer Engineering University of Michigan, April 2000.
- [5] Roman Starosolski, "Simple Fast and Adaptive Lossless Image Compression Algorithm" December 20, 2006.
- [6] A. Alarabeyyat, S. Al-Hashemi, T. Khdour, M. Hjouj Btoush, S. Bani-Ahmad, R. Al-Hashemi, "Lossless Image Compression Technique Using Combination Methods" Journal of Software Engineering and Applications, 2012
- [7] Dr.E.kannan, G.Murugan, "Lossless image compression algorithm for transmitting over low bandwidth line" Volume 2, issue 2, February 2012
- [8] B.C. Vemuri, S.Sahni, F.Chen, C.Kapoor, C.Leonard, "Lossless image compression"
- [9] Bruno Carpentieri, Marcelo J. Weinberger and Gadiel Seroussi "Lossless Compression of Continuous-Tone Images".
- [10] Malwinder Kaur, Navdeep Kaur, "A Literature Survey on Lossless Image Compression" International Journal of Advanced Research in Computer and Communication Engineering, Vol. 4, Issue 3, March 2015
- [11] M.Sundaresan, E.Devika, "Lossy and lossless compression using various algorithms", March 2013.



10.22214/IJRASET



45.98



IMPACT FACTOR:
7.129



IMPACT FACTOR:
7.429



INTERNATIONAL JOURNAL FOR RESEARCH

IN APPLIED SCIENCE & ENGINEERING TECHNOLOGY

Call : 08813907089  (24*7 Support on Whatsapp)



ISSN No. 2321-9653

IJRASET

International Journal for Research in Applied
Science & Engineering Technology

IJRASET is indexed with Crossref for DOI-DOI : 10.22214

Website : www.ijraset.com, E-mail : ijraset@gmail.com

Certificate

It is here by certified that the paper ID : IJRASET11527, entitled
Lossless Image Compression using an Efficient Huffman Coding

by

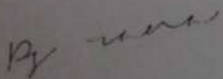
K. Umarani

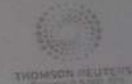
after review is found suitable and has been published in
Volume 5, Issue XII, December 2017

in

International Journal for Research in Applied Science &
Engineering Technology

Good luck for your future endeavors

By 
Editor in Chief, IJRASET





iJRASET

International Journal For Research in
Applied Science and Engineering Technology



INTERNATIONAL JOURNAL FOR RESEARCH

IN APPLIED SCIENCE & ENGINEERING TECHNOLOGY

Volume: 5 Issue: XII Month of publication: December 2017

DOI:

www.ijraset.com

Call:  08813907089

E-mail ID: ijraset@gmail.com

Advanced Autonomous Vehicle Systems and Adaptive Cruise by Using Internet of Things (IOT)

T.Ashok¹, M.Chandrasekar², M.Maruthu³

Abstract: *There has recently been a significant amount of activity in developing supervisory control algorithms for multiple unmanned aerial vehicle operation by a single operator. While previous work has demonstrated the favorable impacts that arise in the introduction of increasingly sophisticated autonomy algorithms, little work has performed an explicit comparison of different types of multiple unmanned vehicle control architectures on operator performance and workload. This paper compares a vehicle-based paradigm (where a single operator individually assigns tasks to unmanned assets) to a task-based paradigm (where the operator generates a task list, which is then given to the group of vehicles that determine how to best divide the tasks among themselves.) The results demonstrate significant advantages in using a task based paradigm for both overall performance and robustness to increased workload. The proposed framework incorporates sensor constraints, such as processing/travel time. These results have implications for the design of future human-UV systems, as well as more general multiple task supervisory control models*

I. INTRODUCTION

The purpose of the project is to implement a multiple unmanned vehicle control system using a single operator from anywhere in the world. The aim of this paper is to reduce the man power with the help of human automation collaboration. There are two sections in this operation. One is the transmitter part and another section is the receiver section. The receiver section consists of the IoT transceiver and PC and the transmitter section consist of Mini car model, PIC microcontroller and Ultrasonic Sensor, Battery's. Thus, the implementation of a complete unmanned vehicle system applied to a robotic exploration vehicle is put forward. The proposed system was tested on the robotic platform an unmanned exploration vehicle specialized in recognition

A. Embedded System

A precise definition of embedded systems is not easy. Simply stated, all computing systems other than general purpose computer (with monitor, keyboard, etc.) are embedded systems. System is a way of working, organizing or performing one or many tasks according to a fixed set of rules, program or plan. In other words, an arrangement in which all units assemble and work together according to a program or plan. An embedded system is a system that has software embedded into hardware, which makes a system dedicated for an application (s) or specific part of an application or product or part of a larger system. It processes a fixed set of pre-programmed instructions to control electromechanical equipment which may be part of an even larger system (not a computer with keyboard, display, etc).

A general-purpose definition of embedded systems is that they are devices used to control, monitor or assist the operation of equipment, machinery or plant. "Embedded" reflects the fact that they are an integral part of the system. In many cases, their "embeddedness" may be such that their presence is far from obvious to the casual observer.

An embedded system is an engineering artifact involving computation that is subject to physical constraints (reaction constraints and execution constraints) arising through interactions of computational processes with the physical world. Reaction constraints originate from the behavioral requirements & specify deadlines, throughput, and jitter whereas execution constraints originate from the implementation requirements & put bounds on available processor speeds, power, memory and hardware failure rates. The key to embedded systems design is to obtain desired functionality under both kinds of constraints.

II. LITERATURE SURVEY

A. Related Work

In recent years, the use of unmanned vehicles (UVs) has become increasingly prominent. Unmanned aerial vehicles (UAVs), ground vehicles (UGVs), surface vehicles (USVs), and undersea vehicles (UUVs) have been used in applications ranging from military operations to border security.

Unmanned ground vehicles (UGVs) have many potential applications, both in military and civilian areas, such as reconnaissance, surveillance, target acquisition, search and rescue, and exploration. Knowledge of UGV behaviors under control commands on different terrain types plays an important role on improving their safety, reliability and autonomy. In this thesis, the complex process involved in a UGV driveline and its interaction with terrain are thoroughly analyzed and a robust low-level control scheme is developed for driving the autonomous vehicle.

Mission and path planning makes use of all known information from prior maps, mission goals, sensory and control structures to generate trajectories, or way points and other actions for the vehicle to execute. However, due to the incomplete knowledge of the world in outdoor missions, the vehicle must use the environment information gathered along the local path to update or rebuild the trajectory.

B. Problem Statement

A significant aspect of the UV control problem is the optimization of a minimum-time trajectory from the UV's starting point to its goal. This trajectory is essentially planar, and is constrained by vehicle dynamics and obstacle avoidance. This optimization problem is difficult because it is non-convex due to the presence of obstacles, and because the spaces of possible control actions over a long trajectory is extremely large. Simplifications that reduce its dimensionality while preserving feasibility and near-optimality are challenging. We can control the Vehicle for particular distance only, because Zigbee having distance limitation respective of particular model. so by using Internet of Things (IoT) we can control the vehicle without any distance limitation.

III. SYSTEM DESIGN

A. Proposed System

This paper focuses on the design and construction of unmanned vehicle with the help of two architecture: A Vehicle-Based Architecture (where a single operator individually assigns tasks to unmanned assets) to a Task-Based Architecture (where the operator generates a task list, which is then given to the group of vehicles that determine how to best divide the tasks among themselves.)

The Unmanned system programming is divided into three main code levels and its hardware was designed with a hierarchical control structure based on modular microcontrollers. The top level program, carried out in C language, is executed in a remote PC and offers to monitor and control the whole robotic vehicle.

The second code level, programmed in C language, runs autonomously on a master PIC16F876A microcontroller. Communication with the remote PC is achieved through the technique IoT for the centralized control of vehicle.

B. System Architecture

1) Block Diagram

a) Receiver Section: Vehicle-2

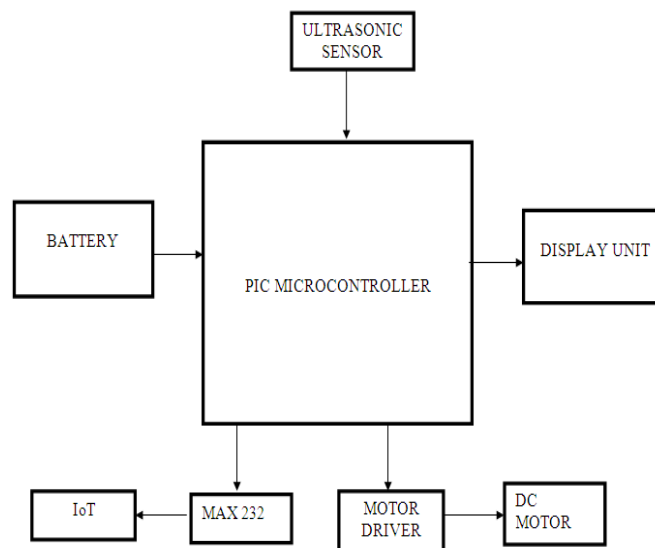


Fig 3.1 Block diagram of this project

b) Transmitter Section

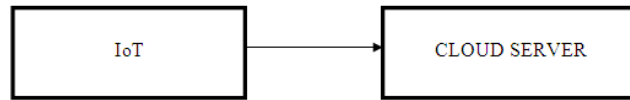


Fig 3.2 Block diagram of this project

2) Circuit Diagram

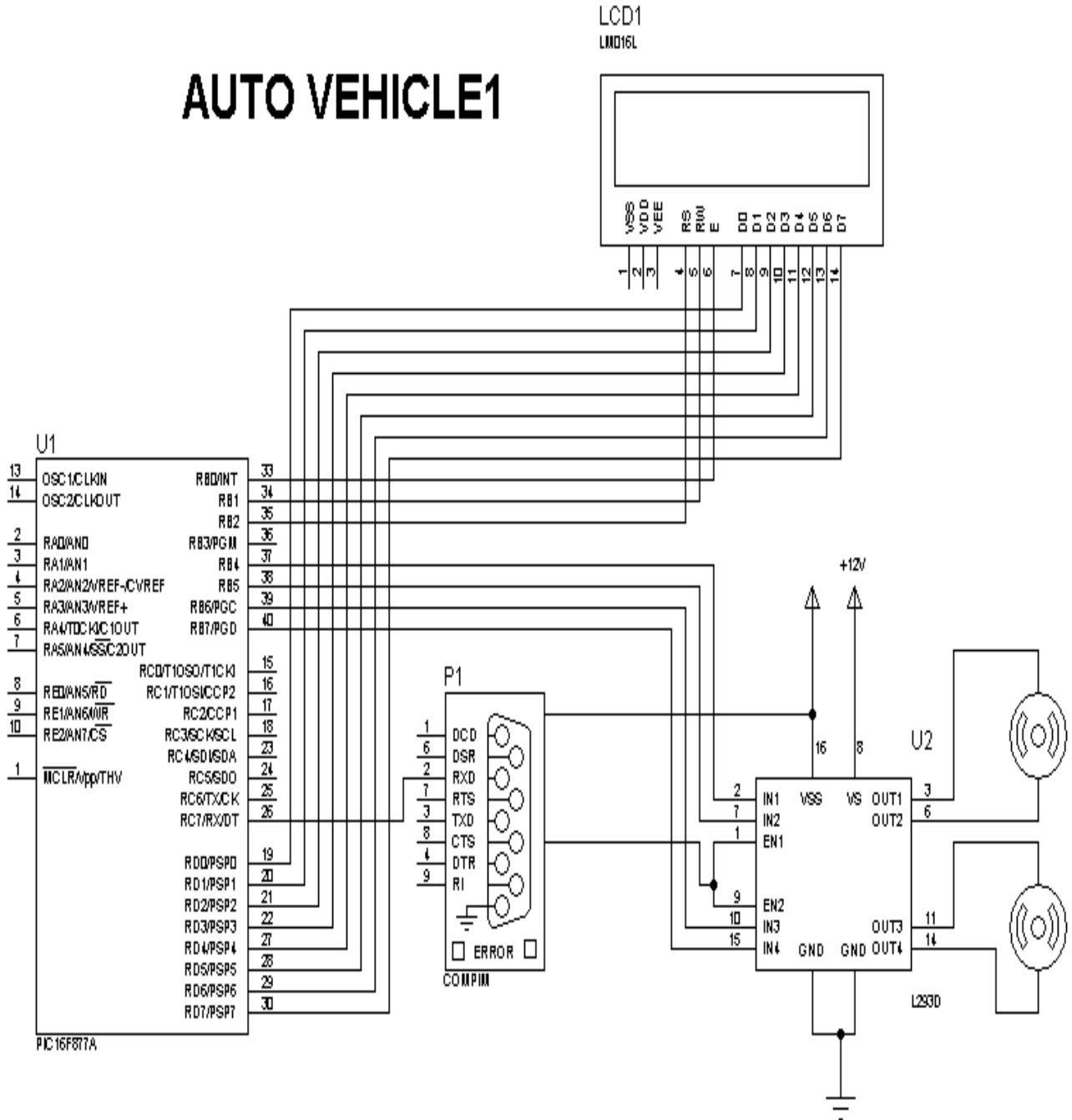


Fig 3.3 Circuit Diagram of this project

3) *Flow Diagram*

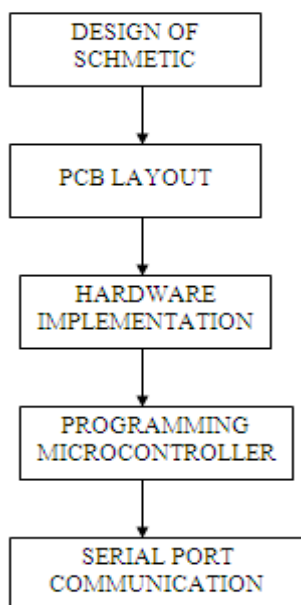


Fig 3.4 Flow Diagram of this project

C. *System Specifications*

1) *Hardware requiriment:*

- a) Microcontroller (PIC16F877A)
- b) Motor Driver IC (L293D)
- c) DC motor
- d) Ultrasonic Sensor
- e) IoT
- f) Lead Acid Battery

2) *Software requiriment:*

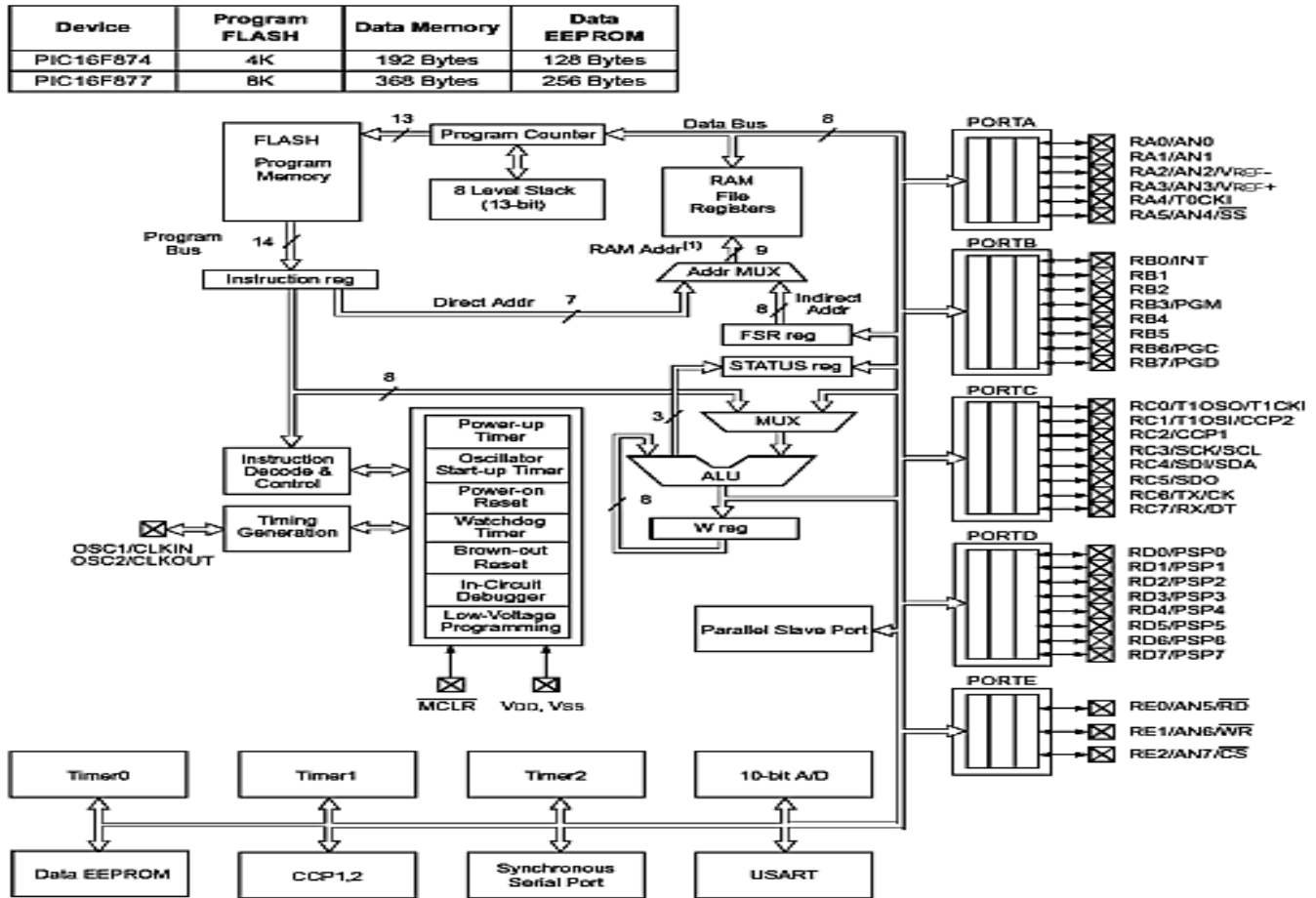
- a) Embedded C
- b) DOTNET
- c) MPLAB IDE (HI-TECH C-COMPILER)
- d) Pic Kit 2
- e) Proteus 7.8 simulator

D. *Microcontroller-Pic16f877a*

1) *Features*

- a) High performance RISC CPU
- b) Only 35 single word instructions to learn
- c) All single cycle instructions except for program branches which are two-cycle
- d) Operating speed: DC - 20 MHz clock input DC - 200 ns instruction cycle
- e) 2K x 14 words of FLASH Program Memory
- f) 128 x 8 bytes of Data Memory (RAM)
- g) 64 x 8 bytes of EEPROM Data Memory
- h) Pin out compatible to the PIC16CXXX 28 and 40-pin devices
- i) Interrupt capability (up to 11 sources)
- j) Eight level deep hardware stack
- k) Direct, Indirect and Relative Addressing modes
- l) Power-on Reset (POR)
- m) Power-up Timer (PWRT) and Oscillator Start-up Timer (OST)

2) Architecture Diagram Of Pic16f877a



Note 1: Higher order bits are from the STATUS register.

FIG 3.5 Architecture Diagram Of Pic16f877a

3) Pin Diagram Of Pic16f877a

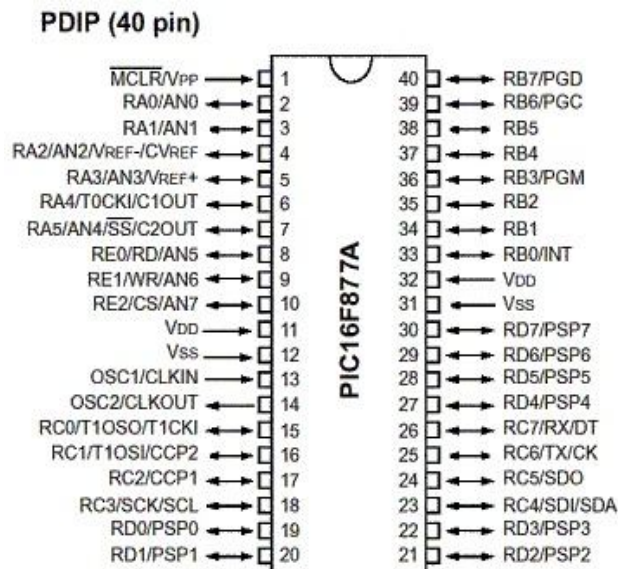


Fig 3.6 Pin Diagram Of Pic16f877a

E. Ultrasonic Sensor

The working of the ultrasonic sensors is quite simple and they are easy to interface with the microcontroller. The sensor module has 4-pins out of which Pin-1 and Pin-4 are +Vcc and Gnd respectively. Pin-2 is Trigger and Pin-3 is Echo pin. The working of sensors can be described from the below figure.

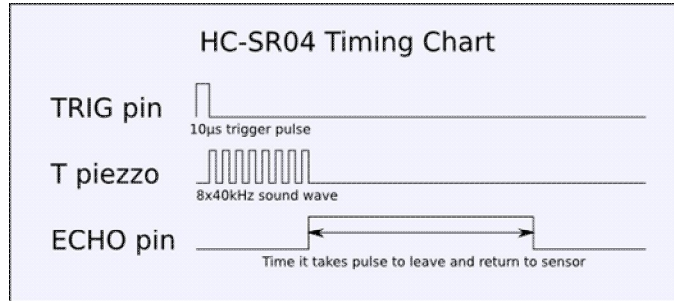


Fig 3.7 Ultrasonic Sensor Timing Diagram

When a High pulse of 10µs is applied at TRIG pin, the ultrasonic transmitter sends 8 consecutive pulses of 40 kHz frequency. As the Eighth pulse is sent the ECHO pin of the sensor becomes HIGH. Now when the ultrasonic waves reflect from any surface and are received by the Receiver, the ECHO pin becomes LOW. The time it takes to leave and return to sensor is used to find the distance from the reflecting surface.

Distance in centimeters = (Time/58) cms

In Inches = (Time/148)

Distance can also be calculated by taking into account the speed of Sound (=340m/s)

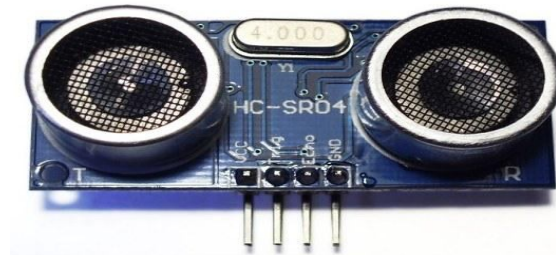


Fig 3.8 Ultrasonic Sensor

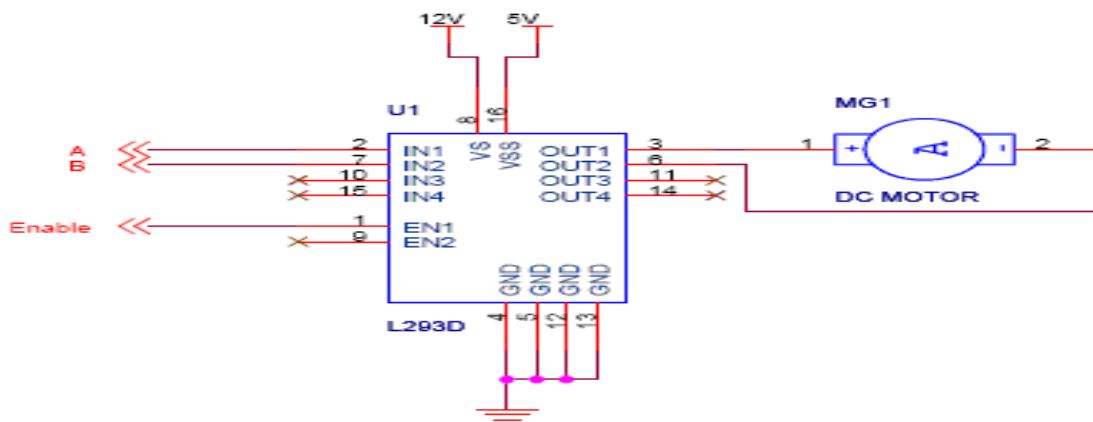
F. Introduction Of Dc Motor

Whenever a robotics hobbyist talk about making a robot, the first thing comes to his mind is making the robot move on the ground. And there are always two options in front of the designer whether to use a DC motor or a stepper motor. When it comes to speed, weight, size, cost... DC motors are always preferred over stepper motors. There are many things which you can do with your DC motor when interfaced with a microcontroller. For example you can control the speed of motor, you can control the direction of rotation, you can also do encoding of the rotation made by DC motor i.e. keeping track of how many turns are made by your motors etc. So you can see DC

Usually H-bridge is proffered way of interfacing a DC motor. These days many IC manufacturers have H-bridge motor drivers available in the market like L293D is most used H-Bridge driver IC. H-bridge can also be made with the help of transistors and MOSFETs etc. rather of being cheap, they only increase the size of the design board, which is sometimes not required so using a small 16 pin IC is preferred for this purpose.

- 1) L293D: L293D is a dual H-Bridge motor driver, So with one IC we can interface two DC motors which can be controlled in both clockwise and counter clockwise direction and if you have motor with fix direction of motion the you can make use of all the four I/Os to connect up to four DC motors. L293D has output current of 600mA and peak output current of 1.2A per channel. Moreover for protection of circuit from back EMF output diodes are included within the IC. The output supply (VCC2) has a wide range from 4.5V to 36V, which has made L293D a best choice for DC motor driver. As you can see in the circuit, three pins are needed for interfacing a DC motor (A, B, Enable). If you want the o/p to be enabled completely then you can

connect Enable to VCC and only 2 pins needed from controller to make the motor work. A simple schematic for interfacing a DC motor using L293D is shown below.



Truth Table

A	B	Description
0	0	Motor stops or Breaks
0	1	Motor Runs Anti-Clockwise
1	0	Motor Runs Clockwise
1	1	Motor Stops or Breaks

For above truth table, the Enable has to be Set (1). Motor Power is mentioned 12V, but you can connect power according to your motors.

Fig 3.9 L293d with Dc Motor

As per the truth mentioned in the image above its fairly simple to program the microcontroller. It's also clear from the truth table of BJT circuit and L293D the programming will be same for both of them, just keeping in mind the allowed combinations of A and B. We will discuss about programming in C as well as assembly for running motor with the help of a microcontroller.

2) Dc Motor Block Diagram

The name "H-Bridge" is derived from the actual shape of the switching circuit which control the motion of the motor. It is also known as "Full Bridge". Basically there are four switching elements in the H-Bridge as shown in the figure below.

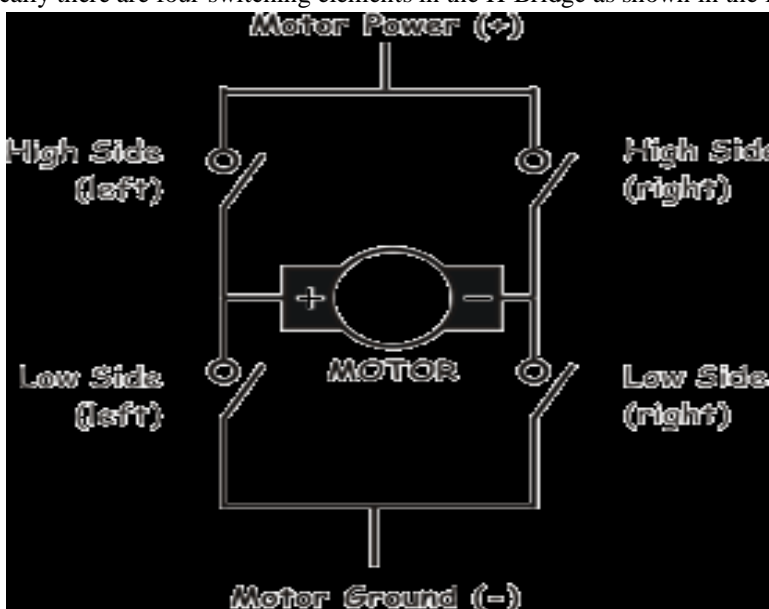


FIG 3.10 H-BRIDGE OF DC MOTOR

As you can see in the figure above there are four switching elements named as "High side left", "High side right", "Low side right", "Low side left". When these switches are turned on in pairs motor changes its direction accordingly. Like, if we switch on High side left and Low side right then motor rotate in forward direction, as current flows from Power supply through the motor coil goes to ground via switch low side right. This is shown in the figure below.

Similarly, when you switch on low side left and high side right, the current flows in opposite direction and motor rotates in backward direction. This is the basic working of H-Bridge. We can also make a small truth table according to the switching of H-Bridge explained above.



Truth Table

High Left	High Right	Low Left	Low Right	Description
On	Off	Off	On	Motor runs clockwise
Off	On	On	Off	Motor runs anti-clockwise
On	On	Off	Off	Motor stops or decelerates
Off	Off	On	On	Motor stops or decelerates

Tab 3.1 Truth Table Of Dc Motor

As already said, H-bridge can be made with the help of transistors as well as MOSFETs; the only thing is the power handling capacity of the circuit. If motors are needed to run with high current then lot of dissipation is there. So heat sinks are needed to cool the circuit.

Now you might be thinking why i did not discuss the cases like High side left on and Low side left on or high side right on and low side right on. Clearly seen in the diagram, you don't want to burn your power supply by shorting them. So that is why those combinations are not discussed in the truth table.

So we have seen that using simple switching elements we can make our own H-Bridge, or other option we have is using an IC based H-bridge driver.

G. IOT

IoT (Internet of Things) can be explained as the networking of physical objects with the use of embedded sensors. These sensors collect information about the objects, their surroundings and communicate this information to other stations, linked through wired or wireless networks. The use of IoT started a movement of taking control of devices and making objects speak to one another. Now, the focus seems to have shifted towards making the things intelligent. Kevin Ashton introduced the term Internet of Things, in context of supply chain management. The initial technical realization of IoT was achieved by utilizing RFID (Radiofrequency Identification) technology, which was limited to identification, object tracking and extracting information of specific objects.

However, the current IoT performs sensing, actuating, data gathering, storing, and processing by connecting physical or virtual devices to the Internet. The recent development in the application of IoT has made it useful in the field of waste management. In Indian cities, waste management is mainly handled by Municipal Corporations/Committees. Many of them often suffer from resource crunch in terms of men and machinery. Moreover, the general public is not ready for cost sharing in this process. Seasonal as well as daily variations in waste generation add up to the problem. This renders the waste collection capacity less than the waste generation capacity, which is visible in form of open dumps and overflowing solid waste containers. These issues have thus resulted in increased collection costs and environmental damage. Many researches into waste management have been conducted, ranging from optimization of routes using GIS to RFID tagging have thus been conducted. IoT based systems are one such proposition. This paper proposes an IoT based solution for effective and efficient waste collection. The solution has main focus on the optimal use of waste collection vehicles. The movement of collection vehicles will be linked to the information from the waste collection bins. The system will notify the waste managers upon filling up of the bins and will provide an optimal and effective collection route. The application can use Cloud Analytics and Machine Learning in order to improve the system upon usage. This will help in handling the variations in waste generation.

Internet and its applications have become an integral part of today's human lifestyle. It has become an essential tool in every aspect. Due to the tremendous demand and necessity, researchers went beyond connecting just computers into the web. These researches led to the birth of a sensational gizmo, Internet of Things (IoT). Communication over the internet has grown from user - user interaction to device - device interactions these days. The IoT concepts were proposed years back but still it's in the initial stage of commercial deployment. Home automation industry and transportation industries are seeing rapid growth with IoT. Yet not many articles have been published in this field of study. This paper aims in structuring a state of the art review on IoT. The technology, history and applications have been discussed briefly along with various statistics. Since most of the process is done through the internet we must have an active high speed internet connection. The technology can be simply explained as a connection between humans-computers-things. All the equipment's we use in our day to day life can be controlled and monitored using the IoT. A majority of process is done with the help of sensors in IoT. Sensors are deployed everywhere and these sensors convert raw physical data into digital signals and transmits them to its control center. By this way we can monitor environment changes remotely from any part of the world via internet. This systems architecture would be based on context of operations and processes in real-time scenarios. Smart collection bin works in the similar manner with the combination of sensors namely weight sensor and IR sensor that indicates its weight and different levels respectively. The IR sensors will show us the various levels of garbage in the dustbins and also the weight sensor gets activated to send its output ahead when its threshold level is crossed. These details are further given of the microcontroller and the controller gives the details to the transmitter module (IoT module). At the receiver section a mobile handset is needed to be connected to the IoT router so the details of the garbage bin are displayed onto the HTML page in web browser of our mobile handset.

The Internet of Things (IoT) is a concept in which surrounding objects are connected through wired and wireless networks without user intervention. In the field of IoT, the objects communicate and exchange information to provide advanced intelligent services for users. Owing to the recent advances in mobile devices equipped with various sensors and communication modules, together with communication network technologies such as Wi-Fi and LTE, the IoT has gained considerable academic interests.

The term Internet of Things was introduced by Kevin Ashton, who was the director of the Auto-ID Center of MIT in 1999. The initial technical realization of IoT was achieved by utilizing RFID technology for the identification and tracking of devices and storing device information. However, IoT utilizing RFID technology was limited to object tracking and extracting information of specific objects.

The current IoT performs sensing, actuating, data gathering, storing, and processing by connecting physical or virtual devices to the Internet. For IoT applications performing these functions, a variety of researches on IoT services including environmental monitoring, object tracking, traffic management, health care, and smart home technology are being conducted.

Internet of Things (IoT) is an environment in which objects, animals or people are provided with unique identifiers and the ability to transfer data over a network without requiring human-to-human or human-to-computer interaction. The IoT allows objects to be sensed and/or controlled remotely across existing network infrastructure, creating opportunities for more direct integration of the physical world into computer-based systems, and resulting in improved efficiency, accuracy and economic benefit. IoT board featured with SIM900 GPRS modem to activate internet connection also equipped with a controller to process all input

UART data to GPRS based online data. Data may be updated to a specific site or a social network by which the user can able to access the data.



Fig.3.11 Block of Iot Sensor

H. Features

- 1) Power Supply: DC +12v 1Amp.
- 2) Auto data updating: 30sec
- 3) Digital Output port Pins: +5V DC
- 4) Message Format: *message or Data # (Start with * and End with #)
- 5) Provided with 3 links
 - a) Data updating to a specific web site
 - b) Device controlling web site
 - c) Data updating to a social network

I. Web Server

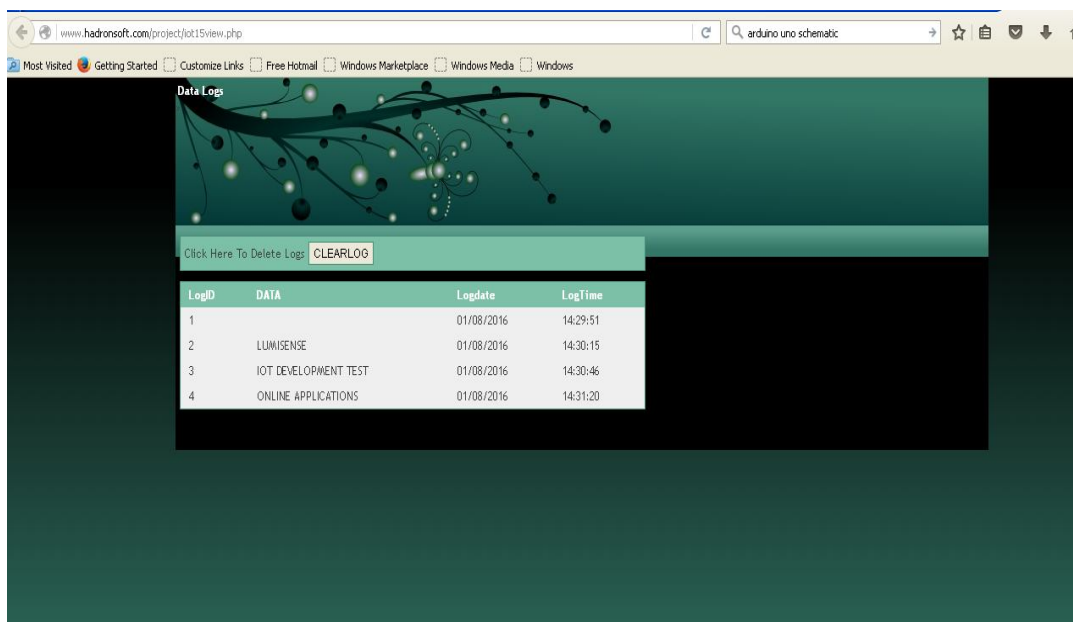


FIG.3.12 WEB SERVER

J. Lcd Display

LCD (Liquid Crystal Display) screen is an electronic display module and find a wide range of applications. A 16x2 LCD display is very basic module and is very commonly used in various devices and circuits. These modules are preferred over seven segments and other multi segment LEDs. The reasons being: LCDs are economical; easily programmable; have no limitation of displaying special & even custom characters (unlike in seven segments), animations and so on.

A 16x2 LCD means it can display 16 characters per line and there are 2 such lines. In this LCD each character is displayed in 5x7 pixel matrix. This LCD has two registers, namely, Command and Data. The command register stores the command instructions given to the LCD. A command is an instruction given to LCD to do a predefined task like initializing it, clearing its screen, setting the cursor position, controlling display etc. The data register stores the data to be displayed on the LCD. The data is the ASCII value of the character to be displayed on the LCD. Click to learn more about internal structure of a LCD.

A. Pin Diagram

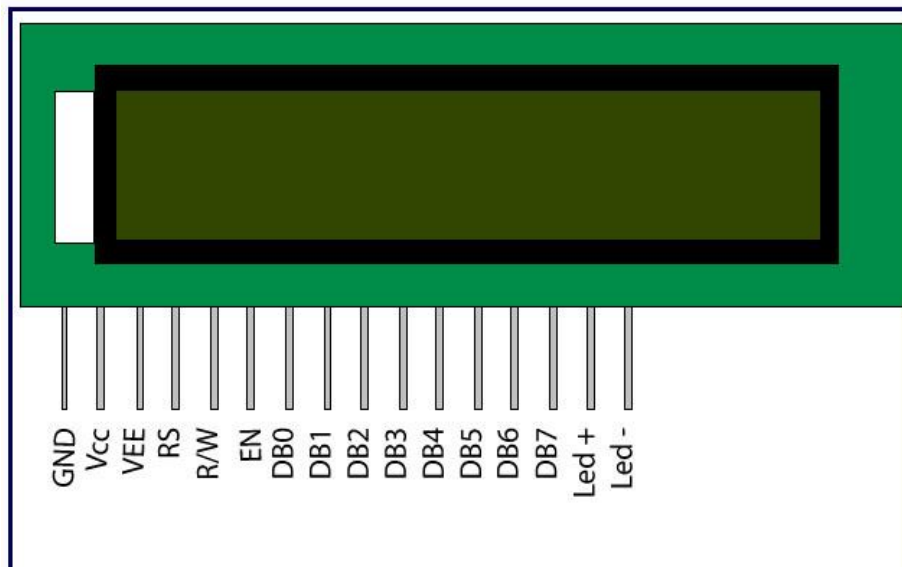


Fig 3.13 Pin Diagram Of Lcd

K. Power Supply

Power Supply is the device that transfers electric power from a source to a load using electronic circuits. Power supplies are used in many industrial and aerospace applications and also in consumer products. Some of the requirements of power supplies are small size, lightweight, low cost, and high power conversion efficiency. In addition to these, some power supplies require the following: Typical application of power supplies is to convert utility's AC input power to a regulated voltage(s) required for electronic equipment. Depending on the mode of operation of power semiconductors power supply can be linear or switching.

1) **Linear Power Supply:** A linear power supply is the oldest and simplest type of power supply. In these power supplies, electrical isolation can only be provided by bulky line frequency transformers. The ac source can be rectified with a bridge rectifier to get an uncontrolled dc, and then a dc-to-dc converter can be used to get a controlled dc output. Figure 4.9 shows the block diagram of the Linear power supply and figure 4.10 shows the circuit diagram of the power supply The output voltage is regulated by dropping the extra input voltage across a series transistor (therefore, also referred to as a series regulator). They have very small output ripple, theoretically zero noise, large hold-up time (typically 1–2 ms), and fast response. The action of a transformer is such that a time-varying (AC) voltage or current is transformed to a higher or lower value, as set by the transformer turns ratio.

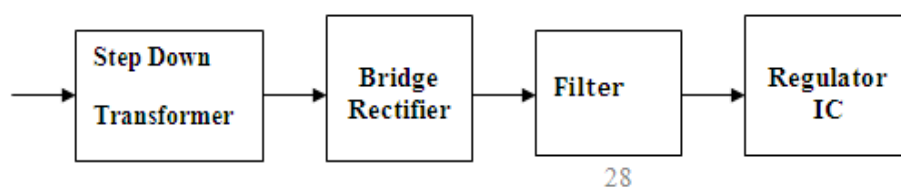


Fig 3.14 Block Diagram of Linear Power Supply

The transformer does not add power, so it follows that the power ($V \times I$) on either side must be constant. That is the reason that the winding with more turns has higher voltage but lower current, while the winding with less turns has lower voltage but higher current. The step down transformer converts the AC input with the higher level to some lower level.

A bridge rectifier converts the AC voltage into DC voltage. A four-transistor converter (Bridge Rectifier) can generate the highest output power than other types of rectifiers. The filter circuit resists the unwanted AC signals. The regulator down-convert a DC voltage to a lower DC voltage of the same polarity.

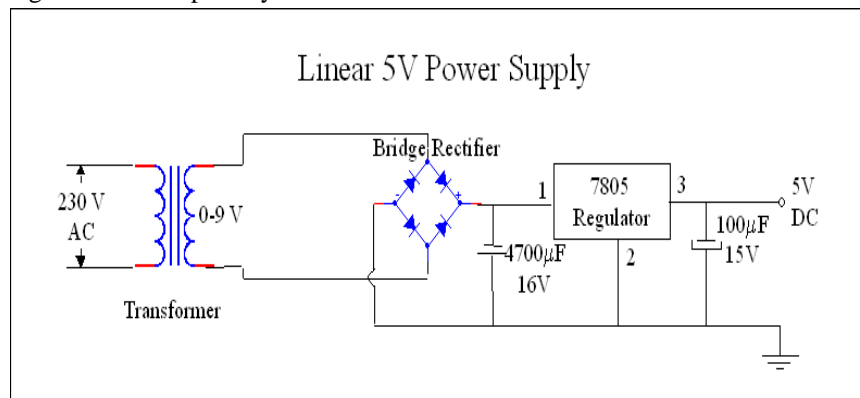


Fig 3.15 Circuit Diagram for 5V power Supply

IV. IMPLEMENTATION AND RESULTS

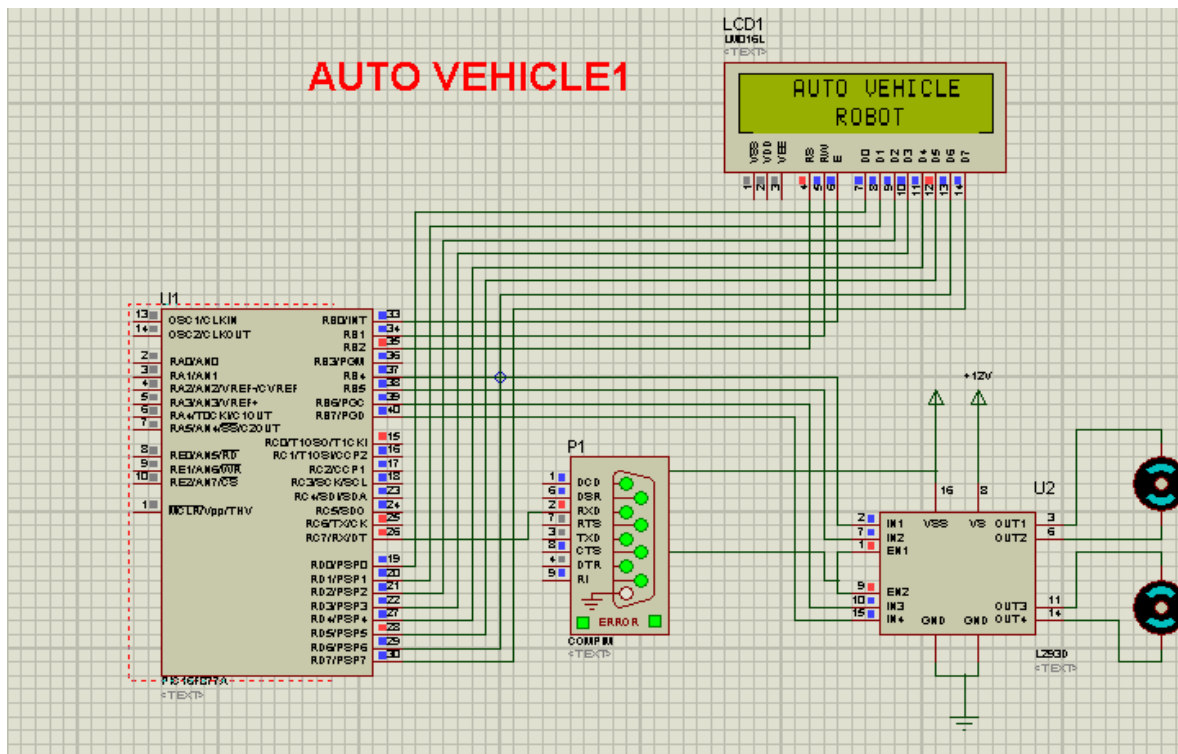


Fig 4.1 Simulation Results of our Project

V. CONCLUSION AND FUTURE ENHANCEMENT

The emergence and performance of the over trusters deserves further attention. Overtrusters ignored the vehicle route replanning functions in both control architectures, effectively over relying on the automation to manage the vehicles appropriately the over trusters, while performing the worst in terms of vehicle damage, performed better than the vehicle based performers in terms of number of targets accurately identified. Information is aggregated for presentation, operators can perform well, but this comes at a loss of control and possibly the ability to manage contingencies and unexpected situations.

A. Future Enhancement

The Proposed system design use ultrasonic sensor to sense the obstacle in V shape but in future the Ultrasonic sensor should be changed to Spherical shape. The distance here we used in our project is 1Km but in future we can use Wi-Fi for high range data transmission.

REFERENCES

- [1] Reuters. US Marines extend K-MAX unmanned helicopter's use in Afghanistan, May 19, 2013.
- [2] T. Chen, D. Campbell, G. Coppin, M. Mooij, and F. Gonzalez, "A capability framework vialisation for multiple heterogeneous UAVS: From a mission commander's perspective," in Proc. 28th Int. Congr. Aeronautical Sci., Brisbane, Australia, 2012, pp. 1–10
- [3] C. A. Miller, R. P. Goldman, H. B. Funk, P. Wu, and B. B. Pate, "A playbook approach to variable autonomy control: Application for control of multiple, heterogeneous unmanned air vehicles," presented at the Am. Helicopter Soc. 60th Annu. Forum, Baltimore, MD, USA, 2004.
- [4] M. L. Cummings, C. E. Nehme, and J. W. Crandall, "Predicting operator capacity for supervisory control of multiple UAVs," in Studies in Computational Intelligence, J. S.Chahk, L. C. Jain,A. Mizutani, andM. Sato-Ilic, Eds. New York, NY, USA: Springer, 2007.
- [5] J. S. Bellingham, "Coordination and control of UAV fleets using mixedinteger linear programming," in Masters, Aeronautics, and Astronautics. Cambridge, MA, USA: MIT, 2002.
- [6] A. Caves, "Human-Automation collaborative RRT for UAV mission path planning," Electrical Engineering and Computer Science, Cambridge, MA, USA: MIT, 2010.
- [7] L. F. Bertuccelli and M. L. Cummings, "Operator choice modeling for collaborative UAV visual search tasks," IEEE Syst., Man, Cybern. A, Syst., Humans, vol. 42, no. 5, pp. 1088–1099, Sep. 2012.
- [8] M. L. Cummings, J. How, A. Whitten, and O. Toupet, "The impact of human-automation collaboration in decentralized multiple unmanned vehicle control," Proc. IEEE, vol. 100, no. 3, pp. 660–671, Mar. 2012.
- [9] M. L. Cummings, "Automation bias in intelligent time critical decision support systems," presented at the AIAA 3rd Intell. Syst. Conf., Chicago, IL, USA, 2004.
- [10] M. L. Cummings and S. Guerlain, "Developing operator capacity estimates for supervisory control of autonomous vehicles," Human Factors, vol. 49, pp. 1–15, 2007.
- [11] B. Donmez, C. Nehme, and M. L. Cummings, "Modeling workload impact in multiple unmanned vehicle supervisory control," IEEE Syst., Man, Cybern. A, Syst. Humans, vol. 40, no. 6, pp. 1180–1190, Nov. 2010.
- [12] W. B. Rouse, Systems Engineering Models of Human–Machine Interaction. New York, NY, USA: North Holland, 1983.
- [13] L. G. Appelbaum, M. S. Cain, E. F. Darling, and S. R. Mitroff, "Action video game playing is associated with improved visual sensitivity, but not alterations in visual sensory memory," Attention, Perception, Psychophysics, vol. 75, no. 6, pp. 1161–1167, 2013.
- [14] A. J. Rowe, K. K. Liggett, and J. E. Davis, Vigilant Spirit Control Station: A Research Testbed For Multi-Uas Supervisory Control Interfaces. H. E. Directorate, Wright-Patterson AFB, OH Air Force Research Laboratory, 2009.



10.22214/IJRASET



45.98



IMPACT FACTOR:
7.129



IMPACT FACTOR:
7.429



INTERNATIONAL JOURNAL FOR RESEARCH

IN APPLIED SCIENCE & ENGINEERING TECHNOLOGY

Call : 08813907089  (24*7 Support on Whatsapp)



ISSN No. : 2321-9653

IJRASET

**International Journal for Research in Applied
Science & Engineering Technology**

IJRASET is indexed with Crossref for DOI-DOI : 10.22214

Website : www.ijraset.com, E-mail : ijraset@gmail.com

Certificate

*It is here by certified that the paper ID : IJRASET11918, entitled
ADVANCED AUTONOMOUS VEHICLE SYSTEMS AND ADAPTIVE
CRUISE BY USING INTERNET OF THINGS (IOT)*

by

Ashok T

*after review is found suitable and has been published in
Volume 5, Issue XII, December 2017*

in

*International Journal for Research in Applied Science &
Engineering Technology*

Good luck for your future endeavors

By [Signature]

Editor in Chief, IJRASET



UGC
and State Support
45.96
INDEX COPERNICUS



THOMSON REUTERS
Researcher ID: A1007-2012

doi
crossref



TOGETHER WE REACH THE GOAL
IMPACT FACTOR : 4.807



ISSN No. : 2321-9653

IJRASET

**International Journal for Research in Applied
Science & Engineering Technology**

IJRASET is indexed with Crossref for DOI-DOI : 10.22214

Website : www.ijraset.com, E-mail : ijraset@gmail.com



UGC
and State Regent



45.98
INDEX COPERNICUS



THOMSON REUTERS
Research & Innovation



10.22214/IJRASET
TOGETHER WE REACH THE GOAL
IMPACT FACTOR : 4.887

Certificate

*It is here by certified that the paper ID : IJRASET11661, entitled
AN Energy Efficient MAC Protocol for WSN based on Quorum Concept*

by

M. Chandrasekar

*after review is found suitable and has been published in
Volume 5, Issue XII, December 2017*

in

*International Journal for Research in Applied Science &
Engineering Technology*

Good luck for your future endeavors

By [Signature]

Editor in Chief, IJRASET



iJRASET

International Journal For Research in
Applied Science and Engineering Technology



INTERNATIONAL JOURNAL FOR RESEARCH

IN APPLIED SCIENCE & ENGINEERING TECHNOLOGY

Volume: 5 Issue: XII Month of publication: December 2017

DOI:

www.ijraset.com

Call:  08813907089

E-mail ID: ijraset@gmail.com

AN Energy Efficient MAC Protocol for WSN based on Quorum Concept

M. Chandrasekar¹, T. Ashok²

Abstract: *The lifetime of each node in a wireless sensor network depends on the durability of the wireless sensor nodes battery resources. Hence, the power consumption of sensor node must be tightly controlled. This can be done by designing energy saving MAC protocols. Most of the existing power-saving protocols achieve power savings by periodically putting sensor nodes to sleep. Such a regular sleep/awake mechanism fails to adjust a sensor node's sleep duration based on its traffic load, thereby reducing its power efficiency and increase the latency. In this paper, we propose a quorum-based medium access control (QMAC) protocol that enables sensor nodes to sleep longer under light loads. Since traffic flows toward the sink node in wireless sensor networks, a new concept, i.e., the next-hop group, is also proposed to reduce transmission latency. Simulation results verify that the proposed QMAC saves more energy and keeps the transmission latency low.*

I. INTRODUCTION

A. Wireless Sensor Networks

Wireless Sensor Networks consists of individual nodes that are able to interact with their environment by sensing or controlling physical parameter; these nodes have to collaborate in order to fulfill their tasks as usually, a single node is incapable of doing so; and they use wireless communication to enable this collaboration. The definition of WSN, according to, Smart Dust program of DARPA is: "A sensor network is a deployment of massive numbers of small, inexpensive, self powered devices that can sense, compute, and communicate with other devices for the purpose of gathering local information to make global decisions about a physical environment".

B. Wireless Sensor Network Model

Unlike their ancestor ad-hoc networks, WSNs are resource limited, they are deployed densely, they are prone to failures, the number of nodes in WSNs is several orders higher than that of ad hoc networks, WSN network topology is constantly changing, WSNs use broadcast communication mediums and finally sensor nodes don't have a global identification tags. The major components of a typical sensor network are:

- 1) *Sensor Field:* A sensor field can be considered as the area in which the nodes are placed.
- 2) *Sensor Nodes:* Sensors nodes are the heart of the network. They are in charge of collecting data and routing this information back to a sink.
- 3) *Sink:* A sink is a sensor node with the specific task of receiving, processing and storing data from the other sensor nodes. They serve to reduce the total number of messages that need to be sent, hence reducing the overall energy requirements of the network. Sinks are also known as data aggregation points.
- 4) *Task Manager:* The task manager also known as base station is a centralized point of control within the network, which extracts information from the network and disseminates control information back into the network. It also serves as a gateway to other networks, a powerful data processing and storage centre and an access point for a human interface. The base station is either a laptop or a workstation.

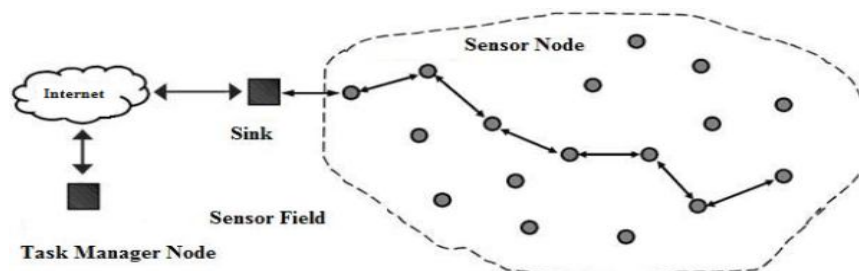


Fig.1.1. Components of Wireless Sensor Networks Data

C. The Sensor Node

A sensor is a small device that has a micro-sensor technology, low power signal processing, low power computation and a short-range communications capability. Sensor nodes are conventionally made up of four basic components a sensor, a processor, a radio transceiver and a power supply/battery. Additional components may include Analog-to-Digital Converter (ADC), location finding systems, mobilizes that are required to move the node in specific applications and power generators. The analog signals are measured by the sensors are digitized via an ADC and in turn fed into the processor. The processor and its associated memory commonly RAM is used to manage the procedures that make the sensor node carry out its assigned sensing and collaboration tasks. The radio transceiver connects the node with the network and serves as the communication medium of the node. Memories like EEPROM or flash are used to store the program code. The power supply/battery is the most important component of the sensor node because it implicitly determines the lifetime of the entire network. Due to size limitations of AA batteries or quartz, cells are used as the primary sources of power. To give an indication of the energy consumption involved, the average sensor node will expend approximately 4.8mA receiving a message, 12mA transmits a packet and 5 μ A sleeping. In addition the CPU uses on average 5.5mA when in active mode.

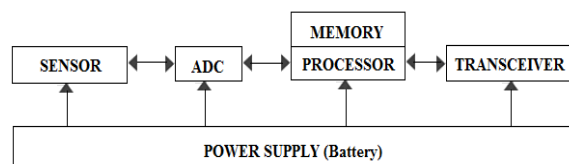


Fig.1.2. Components of a Wireless Sensor Node

D. Characteristics Of Wireless Sensor Networks

1) WSNs have some unique characteristics. These are:

- a) Sensor nodes are small-scale devices with volumes approaching cubic millimeters in the near future. Such small devices are very limited in the amount of energy they can store or harvest from the environment.
- b) Nodes are subject to failures due to depleted batteries or, more generally, due to environmental influences. Limited size and energy also typically means restricted resources (CPU performance, memory, wireless communication bandwidth and range).
- c) Node mobility, node failures, and environmental obstructions cause a high degree of dynamics in WSN. This includes frequent network topology changes and network partitions. Despite partitions, however, mobile nodes can transport information across partitions by physically moving between them.
- d) The resulting paths of information flow might have unbounded delays and are potentially unidirectional. Communication failures are also a typical problem of WSN.

E. Design Factors

1) The following factors are important as a guideline to design a protocol for wireless sensor networks:

- a) **Fault tolerance:** The failure of some sensor nodes must not affect the overall task of the network.
- b) **Scalability:** The protocol must be able to work in dense wireless sensor networks.
- c) **Production costs:** The cost of producing a node must be kept low.
- d) **Hardware constraints:** A sensor node is made up of four basic components: a sensing unit, a processing unit, a transceiver unit, and a power unit. Apart from size, there are some other stringent constraints for sensor nodes. These nodes must consume extremely low power, operate in high volumetric densities, have low production cost, be dispensable and autonomous, operate unattended, and be adaptive to the environment.
- e) **Sensor network topology:** Wireless sensor network protocol must be able to maintain network topology so the network can accomplish its objectives.
- f) **Power consumption:** In a multi-hop wireless sensor network, each node plays the dual role of data originator and data router. The malfunctioning of a few nodes can cause significant topological changes and might require rerouting of packets and reorganization of the network. Hence, power conservation and power management take on additional importance. Our protocol will focus on reducing network energy consumption and latency.

F. Power Saving In Wireless Sensor Network

Generally, the sensor nodes are battery powered, and it is often not feasible to recharge them. Thus, it is important to design energy-efficient protocols for WSNs. Recently, many protocols have been proposed to extend the network lifetime of sensor networks in their deployment protocols, power efficient medium access control (MAC) protocols and routing protocols.

In wireless sensor applications where all sensor nodes constantly report data to a single sink node (a many-to-one communication model), sensor nodes that are closer to the sink deplete their power faster. This is referred to as the energy-hole problem. To solve this, node deployment protocols try to distribute more nodes around the sink. However, due to environment limits, sometimes, only uniform (random) node distribution is possible. In such situations, node-deployment protocols are unable to prolong the network lifetime. One way of prolonging the network lifetime is by designing energy-efficient MAC protocols. Since idle listening has been identified as a major reason for energy wastage, several proposals were made to reduce the time a sensor node spends in idle listening. Some required time synchronization among sensor nodes. Since time synchronization is essential for many sensor applications, it is natural for a synchronous MAC protocol to be used to conserve energy. Generally, synchronous protocols maintain a schedule that indicates when a sensor should be awake to check transmission activity. Energy waste is reduced since nodes keep awake only at a specified time. However, these synchronous protocols either suffer from long latency or fail to adapt to an individual's traffic well. In asynchronous solutions, sensor nodes independently schedule their awake period to periodically check the channel. In transmitting data, the source node sends a preamble that is long enough for the destination node to detect. When the preamble is detected, the destination node will remain awake to receive the data that follows the preamble. For asynchronous sensor applications, these protocols avoid the synchronization overhead. However, long preambles introduce long latency and excess energy consumption. All of the protocols aforementioned, including synchronous and asynchronous ones, do not consider the problem wherein nodes may unexpectedly fail. Unexpected node failures produce link breakage, which prevents data packets from being transmitted smoothly. As a result, the transmission latency is enlarged. The protocol we propose in this paper is also a synchronous MAC protocol. The core of this proposed protocol is a quorum-based wake-up scheme. The wake-up frequency is determined according to each sensor node's traffic load. A node is allowed to sleep longer if less traffic is involved. The concept of quorum has been used to design energy conservation MAC protocols for wireless mobile ad hoc networks. Here, we investigate the effectiveness of using quorum in MAC protocol design for WSNs. Since latency is an important issue, we also provide a scheme that reduces the sensor-to-sink latency. This scheme proves to be robust in an environment where unexpected node failures exist.

Wireless sensor networks are dense networks of small, low-cost sensors, which collect and disseminate data. Wireless sensor networks facilitate monitoring and controlling of physical environments from remote locations. A sensor network is composed of a large number of sensor nodes that are densely deployed either inside the phenomenon or very close to it. The position of sensor nodes need not be engineered or predetermined. This allows random deployment in inaccessible terrains or disaster relief operations. On the other hand, this also means that sensor network protocols and algorithms must possess self-organizing capabilities. Another unique feature of sensor networks is the cooperative effort of sensor nodes. Sensor nodes are fitted with an onboard processor. Instead of sending the raw data to the nodes responsible for the fusion, they use their processing abilities to locally carry out simple computations and transmit only the required and partially processed data.

G. Reasons For Energy Waste

The following reasons are main reason for energy waste.

- 1) *Collision*: When a transmitted packet is corrupted it has to be discarded, and the follow-on retransmissions increase energy consumption. Collision increases latency as well.
- 2) *Overhearing*: Overhearing, meaning that a node picks up packets that are destined to other nodes.
- 3) *Control packet overhead*: Sending and receiving control packets consumes energy too, and less useful data packets can be transmitted.
- 4) *Idle listening*: listening to receive possible traffic that is not sent. However idle listening is the major reason for energy waste. Many measurements have shown that idle listening consumes 50–100% of the energy.

H. Mac Protocols For Wireless Sensor Networks

The MAC is a sub layer of the Data Link Layer of the Open Systems Interconnection (OSI) model. Among other things, this layer is responsible for controlling the access of nodes to the medium to transmit or receive data. In traditional wireless voice or data networks, each user desires equal opportunity and time to access the medium, i.e., sending or receiving packets for their own applications. Per-hop MAC level fairness is, thus, an important issue. However, in sensor networks, all nodes cooperate for a single

common task. At any particular time, one node may have dramatically more data to send than some other nodes. In this case fairness is not important as long as application-level performance is not degraded. In wireless sensor networks, MAC protocols control how sensor nodes access a shared radio channel to communicate with neighbors. Traditionally, this problem is known as the channel allocation or multiple access problems. Though MAC protocols have been extensively studied in traditional areas of wireless voice and data communications (e.g. Time division multiple access (TDMA), frequency division multiple access (FDMA), code division multiple access (CDMA), and carrier sense multiple access (CSMA)), sensor networks require a MAC protocol that differs from those of traditional wireless voice or data networks in several ways. First of all, most nodes in sensor networks are likely to be battery powered and it is often very difficult to change batteries for all the nodes. Second, nodes are often deployed in an ad-hoc fashion rather than with careful pre-planning. Hence, after deployment the sensor nodes must quickly organize themselves into a communication network. Third, many applications employ large numbers of nodes. Finally, most traffic in the network is triggered by sensing events, and it can be extremely burst. All these characteristics suggest that traditional MAC protocols employed in the past wireless networks are not suitable for wireless sensor networks without modifications.

Since our protocol is designed to detect extreme events, the system thus has to remain operational for months or years. Once a flooding is detected, this information must be forwarded to the system management quickly and accurately. Contention based MAC protocols are suitable for wireless sensor networks because the required synchronization allows higher clock drifts; while TDMA requires a tight synchronization. The lifetime of a mobile ad hoc network (MANET) depends on the durability of the mobile hosts' battery resources. In the IEEE 802.11 Power Saving Mode, a host must wake up at every beacon interval, to check if it should remain awake. Such a scheme fails to adjust a host's sleep duration according to its traffic, thereby reducing its power efficiency. This paper presents new MAC protocols for power saving in a single hop MANET. The essence of these protocols is a quorum-based sleep/wake-up mechanism, which conserves energy by allowing the host to sleep for more than one beacon interval, if few transmissions are involved. The proposed protocols are simple and energy-efficient. Simulation results showed that our protocols conserved more energy and Extended the lifetime of a MANET.

The T-MAC [4] is a contention-based Medium Access Control protocol for Wireless sensor networks. Applications for these networks have some characteristics (low message rate, insensitivity to latency) that can be exploited to reduce energy consumption. To handle load variations in time and location, T-MAC [4] introduces an adaptive duty cycle in a novel way: by dynamically ending the active part of it. This reduces the amount of energy wasted on idle listening, in which nodes wait for potentially incoming messages, while still maintaining a reasonable throughput. They discuss the design of T-MAC, and provide a head-to-head comparison with classic CSMA (no duty cycle) and S-MAC (fixed duty cycle) through extensive simulations. Under homogeneous load, T-MAC and S-MAC achieve similar reductions in energy consumption (up to 98 %) compared to CSMA. In a sample scenario with variable load, however, T-MAC outperforms S-MAC by a factor of 5. Preliminary energy-consumption measurements provide insight into the internal workings of the T-MAC protocol.

The S-MAC [5], a MAC protocol designed for wireless sensor networks. Wireless sensor networks use battery-operated computing and sensing devices. A network of these devices will collaborate for a common application such as environmental monitoring. These characteristics of sensor networks and applications motivate a MAC that is different from traditional wireless MAC such as IEEE 802.11 in several ways: energy conservation and self-configuration are primary goals, while per-node fairness and latency are less important. S-MAC uses a few novel techniques to reduce energy consumption and support self-configuration. It enables low-duty-cycle operation in a multi-hop network. Nodes form virtual clusters based on common sleep schedules to reduce control overhead and enable traffic-adaptive wake-up. S-MAC uses in-channel signaling to avoid overhearing unnecessary traffic. Finally, S-MAC applies message passing to reduce contention latency for applications that require in-network data processing. The measurement results of S-MAC performance on a sample sensor node, the UC Berkeley Mote, and reveals fundamental tradeoffs on energy, latency and throughput. The duty cycle is fixed in such protocols, the network throughput can degrade under heavy traffic, while under light loads, unwanted energy consumption can occur. In the proposed Pattern-MAC (PMAC [6]) protocol, instead of having fixed sleep wakeups, the sleep-wakeup schedules of the sensor nodes are adaptively determined. The schedules are decided based on a node's own traffic and that of its neighbors.

II. EXISTING MAC PROTOCOL FOR WSN

A. S-MAC

- 1) *Basic Characteristics:* A wireless sensor network MAC protocol must have the characteristics described below in order to be suitable for applications on these sorts of networks:

- a) Energy efficient in such a way that nodes spend the least amount possible of energy in their communication and computation functions. Communication procedures consume much more energy than those of computation, so this protocol concentrated on communication issues.
- b) Scalable to allow the network which is running it to grow without compromising too much its performance.
- c) Adaptable to changes not only due to new nodes that enter the network but also due to nodes that fail in their normal operation.
- d) Major sources of energy wastage are identified and described below:
- e) Collisions: packets discarded have to be retransmitted, which increase energy consumption.
- f) Overhearing: a node listens to packets destined to other nodes
- g) Control packet overhead: transmission and reception of control packets consumes Energy.
- h) Idle listening: Listening to receive possible packets that are not sent.
- i) Over emitting: Transmission of a packet when destination node is not ready.

S-MAC takes into account characteristics described above taking more emphasis on reducing energy consumption by reducing idle listening and control packet overhead. This protocol trades off energy consumption with latency. Low latency is a desirable feature for traditional networks that do not have the constraint of energy.

- 2) *Synchronization*: To minimize the idle listening energy consumption, S-MAC uses a sleep-listen schedule where a node remains inactive for a long time and then wakes up to transmit or receive packets. When slept, a node turns off its radio saving a lot of energy. Figure 2.1 shows S-MAC sleep-listen schedule. A frame is a complete cycle of listen and sleep times. The duty cycle is defined as the ratio of the listen interval to the frame length.

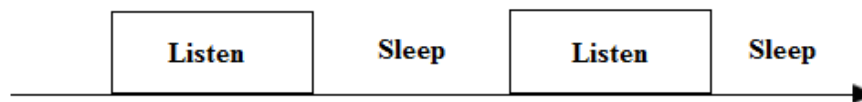


Fig.2.1. Basic Sleep-Listen schedule

Nodes synchronize each other by periodically broadcasting Synchronization (SYNC) packets. A node could follow more than one schedule if received more than one SYNC packet when synchronizing for the first time. In such case, the node follows both schedules. SYNC packets are very short and include the address of the sender and the time of its next sleep. The time of the next sleep is relative to the moment that the sender starts to send its SYNC packet rather than absolute. SYNC packets and data ones are sent on different time slots as shown in Figure 2.2.

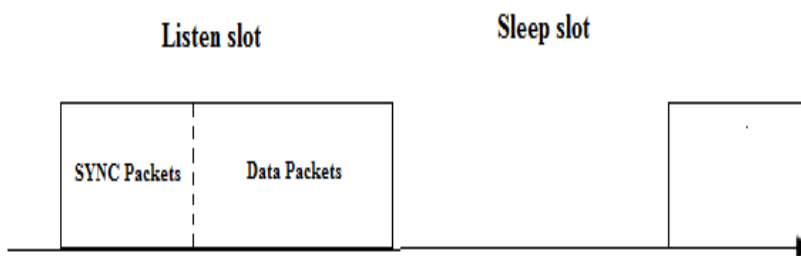


Fig.2.2. The Listen slot is divided

- 3) *Collision Avoidance*: To avoid collisions, S-MAC uses the 802.11 mechanism: RTS/CTS/DATA/ACK. Only broadcast packets do not follow RTS/CTS/DATA/ACK sequence. A second mechanism that S-MAC uses to avoid collision is the vector called Network Allocation Vector (NAV). In such vector, it keeps the duration of transmission of node's neighbors. In this way, the node knows when the medium will be most likely idle to transmit a data packet. This mechanism is called virtual carrier sense. Furthermore, S-MAC uses Carrier Sense (CS) before transmitting a SYNC or data packet to verify if whether there are current transmissions or not, this mechanism is a physical sense. Within a frame, a node can transmit only a SYNC packet, only a data packet or both. This is shown in Figure 2.3. The figure highlights the procedure RTS/CTS/DATA that S-MAC uses to send a data packet by avoiding collisions.

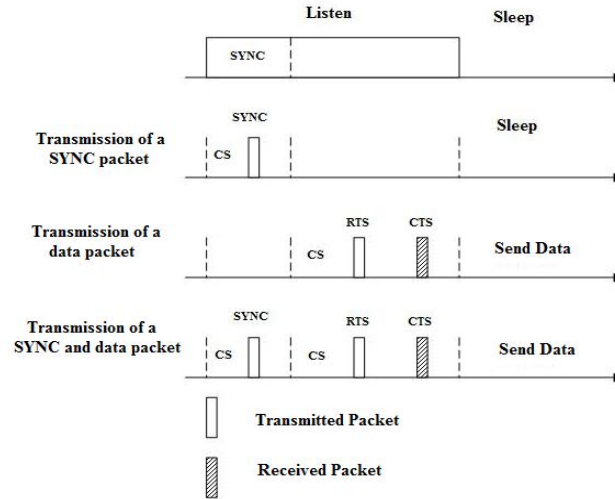


Fig.2.3 Ways to send a data packet and synchronize other nodes.

4) Adaptive Listening

Adaptive listening is a mechanism to turn nodes from low-duty cycle to a more active state to reduce latency trading it off with more energy consumption. The basic idea is to let the node who overhears its neighbor’s transmissions (ideally only RTS or CTS) wake up for a short period of time at the end of the transmission. In this way, if the node is the next-hop node, its neighbor is able to immediately pass the data to it instead of waiting for its scheduled listen time. If the node does not receive anything during the adaptive listening, it will go back to sleep until its next scheduled listen time. If the next-hop node is a neighbor of the sender, it will receive the RTS packet. If it is only a neighbor of the receiver, it will receive the CTS packet from the receiver. Thus, both the neighbors of the sender and receiver will learn about how long the transmission is from the duration field in the Request-to-Send (RTS) and Clear-to-Send (CTS) packets. In this way, they are able to adaptively wake up when the transmission is over.

It should be noted that not all next-hop nodes can overhear a packet from the previous transmission, especially when the previous transmission starts adaptively, i.e., not at the scheduled listen time. So if a sender starts a transmission by sending out an RTS packet during the adaptive listening, it might not get a CTS reply. In this case, it just goes back to sleep and will try again at the next normal listen time.

5) Overhearing Avoidance

Inspired by PAMAS [10], S-MAC tries to avoid overhearing by letting interfering nodes go to sleep after they hear an RTS or CTS packet. Since DATA packets are normally much longer than control packets, the approach prevents neighboring nodes from overhearing long DATA packets and following ACKs. All immediate neighbors of both the sender (node C) and receiver (node D) should sleep after they hear the RTS or CTS until the current transmission is over, as indicated by “X” in Figure 2.4.

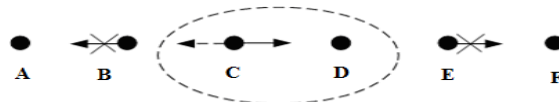


Fig. 2.4. Nodes that should go to sleep when C transmits to D

6) Message Passing: Message Passing consists in fragmenting the long message into many small fragments, and transmitting them in a burst. Only one RTS and one CTS are used. They reserve the medium for transmitting all the fragments. Every time a data fragment is transmitted, the sender waits for an ACK from the receiver. If it fails to receive the ACK, it will extend the reserved transmission time for one more fragment, and re-transmit the current fragment immediately. If a neighboring node hears an RTS or CTS packet, it will go to sleep for the time that is needed to transmit all the fragments. Each data fragment or ACK also has the duration field. In this way, if a node wakes up or a new node joins in the middle of a transmission, it can properly go to sleep no matter if it is the neighbor of the sender or the receiver. If the sender extends the transmission time due to fragment losses or errors, the sleeping neighbors will not be aware of the extension immediately. However, they will learn it from the extended fragments or ACKs when they wake up.

B. T-MAC

Timeout-MAC (T-MAC) is proposed to enhance the performance results of S-MAC protocol under variable traffic load. In T-MAC, listen period ends when no activation event has occurred for a time threshold (TA). This operation makes T-MAC's schedule variable instead of the fixed schedule proposed in S-MAC. Figure 2.5 depicts the basic operation of TMAC.

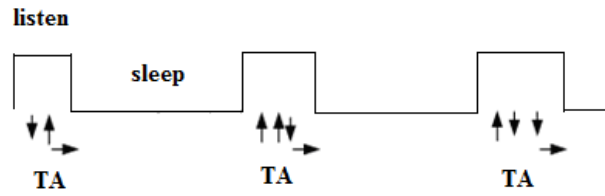


Fig.2.5. T-MAC basic operation

T-MAC synchronization is similar to that of S-MAC. SYNC packets are exchanged between nodes to form virtual clusters that share the same synchronization. A node can run more than one synchronization scheme. The scheme used to contend for the medium is the well known RTS/CTS/DATA/ACK. However, T-MAC proposes a change in this scheme that is used to avoid the early sleep problem. The early sleep problem is the excessive contention for a node that wants to transmit to its neighbors. To avoid this problem T-MAC proposes two solutions: Future request to send and priority on full buffers.

C. D-MAC

The main objective of DMAC is to achieve very low latency and still be energy efficient. For that purpose it is designed to overcome S-MAC problems: increased delivery latency because a packet cannot reach the sink in a single listen period, fixed duty cycles that do not adapt to traffic changes and the increased possibility of collisions due to synchronous duty cycle. It identifies a problem that exists in implicit sleep delay reducing protocols: SMAC and T-MAC. Sleep delay refers to the time that a packet suffers since it is transmitted from originating node to the sink (Base Station). This delay refers to the time that transmitting node has to wait for intended receiving node to wake up and receive the packet. It is shown that S-MAC and T-MAC only solve this problem for a two-hop path. If a network is a multi-hop one with more than 2 hops, the solutions provided by S-MAC and TMAC are not appropriate. This problem is identified as Data forwarding Interruption (DFI). It identified that the limited overhearing range due to radio sensitivity is the origin of this DFI problem.

The solution proposed is a staggered active/sleep schedule shown in Figure 2.6. Low latency is achieved by assigning subsequent slots to nodes that are successive in the data transmission path. With this scheme it is expected that a packets do not suffer from sleep delay at all because the next intended receiving node must always be awake when transmitting node wants to transmit a packet to it.

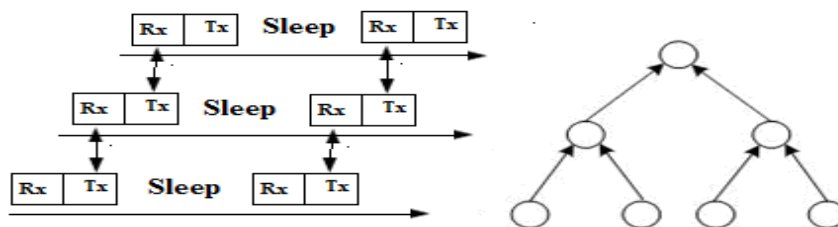


Fig. 2.6. Staggered active/sleep schedule in D-MAC

DMAC staggers the active/sleep schedule of the nodes in the data gathering tree according to its depth in the tree. This allows continuous packet forwarding flow in which all nodes on the multi-hop path can be notified of the data delivery in progress as well as any duty-cycle adjustments.

D. B-MAC

B-MAC is designed for an Ad-Hoc network of nodes with N-sender to 1-receiver transmissions. The basic idea of B-MAC is to keep the protocol simple. That allows very small implementations, an important point because of the limited available memory. Like the other protocols B-MAC uses periodically sleep/wakeup cycles. The mechanism used here is called Low Power Listening. LPL means in the wakeup time the node listens for incoming data transmissions. If there is no data received, called a "false positive", a timeout interrupts the listen state. Otherwise the node waits for complete packet transmission. To ensure that the received packet is

complete from the beginning there is a preamble time of 100ms added after the wakeup. Fairness is not guaranteed by LPL. The sleep periods of the nodes can differ to each other, B-MAC is asynchronous. When there is data to send a node switches the radio mode and starts to send an announcement. This announcement must be long enough to make sure that the receiver notices, even if the receiver starts sleeping at the beginning. Afterwards the sender transmits the target address and starts sending data. Asynchronous networks don't need complicated and expensive synchronization methods. There is no data fragmentation used in B-MAC. This would be more complicated to coordinate and B-MAC expects short messages like the ones commonly used for sensor information's. Another concept to reduce the amount of needed energy is clear channel assessment (CCA). This is used for clear channel detection. For energy reduction a better separation between signals and noise on the channel is useful. Therefore the noise must be analyzed. In case of a false positive a sample was put into a queue. It makes sense to capture and analyses more than one sample because the noise caused by the environment changes continuously. An optional feature is using acknowledgements. B-MAC has an application interface for flexible configuring parameters like this. Other options are for example the check interval. A good value for this sometimes depends on the use case so this can be adjusted by a higher layer application.

E. Wise MAC

Wise MAC [9] is an infrastructure protocol. It assumes there is one central unit with unlimited energy supply and connection to another high speed network e. g. Ethernet to exchange data packets. That is why this unit is called access point. Because of the independence to batteries the access point should manage the network. Therefore it has a table containing the wakeup times for every known node. That reduces the needed listening time. These times are part of acknowledgement packets send from the nodes. If the access point has information for a specific node it can be notified as soon as possible. There must be a little delay before message passing because of the possible clock drift to the nodes. The messages are expected to be short for sensor nodes. The base station handles one message after the other. Synchronized nodes would have to wait except for one node. That is why the wakeup schedules of the nodes are asynchronous. The packet header contains a frame pending bit. It indicates there is more data waiting. After sending an acknowledgement the node stays awake if the bit is set. The sender sends the second packet ongoing to the received ACK-packet.

F. Problem Statement

Existing solutions for the energy-hole problem are dependent on proper node distribution strategies. However, these protocols function in vain in environments where planned node deployment is not possible. In such cases, since network lifetime extension is still necessary, other power-saving protocols (such as S-MAC, T-MAC, and DMAC [7]) should be applied. One of the problems of sensor nodes running S-MAC, T-MAC, or DMAC is that they have to wake up at every time frame to check if there is pending traffic. Since sensor nodes have different traffic loads (nodes that are closer to the sink are the heavy-loaded ones), all nodes adopting the same frequency to listen/sleep are not power efficient. PMAC allows nodes to have different listen/sleep frequencies, but its functionality relies on the correct exchanges of the nodes' schedules. A scheme that lets sensor nodes choose their own wake-up frequencies is desirable, but the challenge is that sensor nodes may not be able to meet each other if they are not well controlled. For example, as shown in Fig.2.7, two nodes, i.e., A and B, with the same wake-up frequency of 0.5 (wake up every two time frames) will never meet if host B always wakes up one time frame later than host A. In other words, what we need is a power efficient protocol that can alleviate the energy-hole problem when intentional node deployment is difficult or not impossible. The solution should not only be able to adjust each sensor node's listen/sleep frequency according to their traffic loads, but it should also guarantee that sensor nodes meet each other.

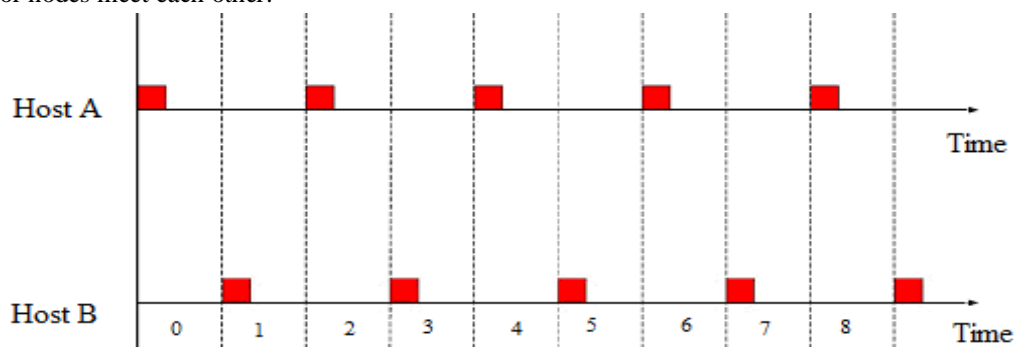


Fig.2.7. Example that two hosts that never meets.

III. QUORUM-BASED ENERGY SAVING MAC PROTOCOL

A. Quorum Concept

A quorum is a request set that enables some actions if permission is granted. There are always nonempty intersections between any two quorum sets. There are many kinds of quorum, such as the majority-based quorum, the tree-based quorum, the grid-based quorum, and others. Here a quorum set represents the time frames wherein a sensor node must wake up. For non-quorum time frames, sensor nodes are allowed to enter sleep mode for the entire time frame to conserve energy. Because quorums are used, any two nodes can wake up and meet each other at some time frame. In a grid-based quorum, one row and one column are picked in an $n \times n$ grid as a quorum set. This concept is shown in Figure 3.1. Host A picks row R_a and column C_a as its quorum, while host B picks row R_b and column C_b . There are two intersections between hosts A and B: one for R_a and C_b and the other for C_a and R_b . As mentioned earlier, sensor nodes must wake up at their chosen quorums. This means that both nodes will wake up at these intersections.

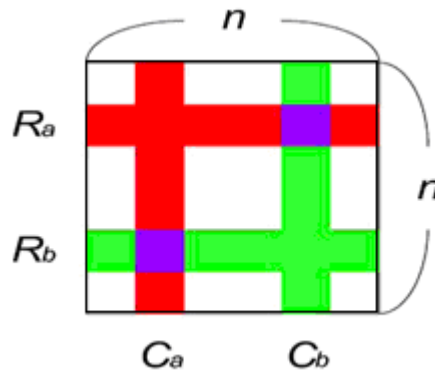


Fig. 3.1 Example of a grid-based quorum.

Fig. 3.2 is an example of quorum time frame selection, where node A picks the third row and the third column as its quorum set, while host B selects the first row and the first column. That is, node A wakes up at time frames 2, 5, 6, 7, and 8, while node B wakes up at time frames 0, 1, 2, 3, and 6. The intersections are frames 2 and 6 when both nodes A and B are awake.

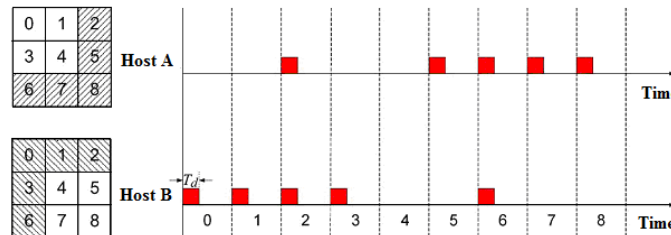


Fig.3.2. Example of intersections. Host A & host B meet each other at intervals 2 and 6.

B. Quorum-Based Wake-Up Schedule

The QMAC protocol aims to reduce power consumption and determine the sleep frequency for each sensor node based on its own traffic load. Each sensor node randomly and independently selects one row and one column as its quorum set. In QMAC, power saving is achieved by reducing the number of wakeup time frames. As mentioned earlier, we use a quorum set to represent the time frames wherein a sensor node must wake up. However, during these wake-up time frames, a sensor node does not always stay awake for the entire time frame. A sensor node can go to sleep whenever it identifies that another transmission that it is not involved in is activated. Furthermore, a sensor node will go to sleep if the channel is idle for duration of Td . In this paper, the value of Td is set to one fifth of the length of a time frame. A sensor node using an $n \times n$ grid will wake up $2n - 1$ out of n^2 time frames. Because they have heavier traffic, sensor nodes located in the inner coronas can use a smaller grid. On the other hand, sensor nodes in outer coronas can pick up a larger grid. By choosing grid sizes based on each sensor node's individual traffic load, QMAC solves the fixed-listen/sleep frequency problem. Note that sensor nodes that use different quorum sizes are still guaranteed to meet each other. Thus, it is feasible for QMAC to operate in WSNs. Furthermore, note that a sensor node with pending traffic will not go to sleep until the traffic is delivered, regardless of whether a quorum time frame is coming or not.

Next, we describe how we decide on the exact grid size for each sensor node. Since we assume a many-to-one and constantly reporting model, it is possible to determine each sensor node’s grid size in advance. A sensor node that is in an inner corona has more traffic because, aside from its own traffic, it has to relay traffic from nodes in outer coronas. To obtain the exact traffic load, we need to know the average number of outer nodes of which an inner node is in charge. Here we describe our QMAC using a four-corona network, as shown in below Fig.3.3.

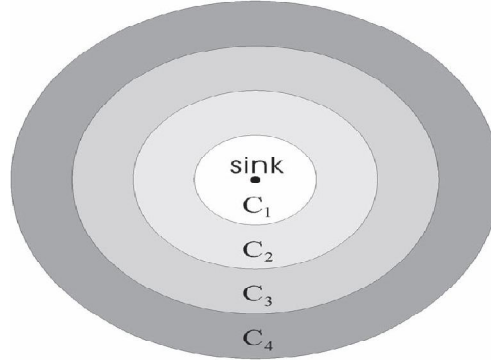


Fig.3.3 Network divided into adjacent coronas centered at the sink node.

The traffic load of the node is depends on the area of the coronas. The ratio of areas for different coronas $C_1 : C_2 : C_3 : C_4$ is $1 : 3 : 5 : 7$. This means that, on the average, a node in C_3 is responsible for relaying traffic for $7/5$ nodes in C_4 , a node in C_2 is responsible for $5/3$ nodes in C_3 , and a node in C_1 will take care of three nodes in C_2 .

Assume that the average hop distance is R . The area of C_1 is πR^2 , and the area of C_2 is $\pi(2R)^2 - \pi R^2 = 3\pi R^2$. Similarly, the areas of C_3 and C_4 are $5\pi R^2$ and $7\pi R^2$, respectively. The area of the corona = $\pi(\text{corona number} * R)^2 - \text{area of previous corona}$

Assuming that each node generates one unit of traffic for each reporting, the sensor nodes in C_4 only have their own traffic to deliver; thus, their traffic load is one. Aside from their own traffic, sensor nodes in C_3 have to forward traffic from C_4 . Each node in C_3 is responsible for $7/5$ nodes in C_4 ; thus, the traffic load in C_3 is $1 + (7/5) \times 1 = 2.4$. Similarly, nodes in C_2 and C_1 have traffic loads of $1 + (5/3) \times 2.4 = 5$ and $1 + 3 \times 5 = 16$, respectively. In general, in a network where sensor nodes generate the same amount of traffic, the traffic load for sensor nodes in C_i can be denoted by TC_i and calculated by

$$T_{C_i} = \{1 + [C_{i+1}] / [C_i]\} * T_{C_{i+1}}$$

Where $|C_i|$ means the area of C_i . In a network with different numbers of coronas, the grid sizes can be calculated in the same way.

It is reasonable to assign a grid size based on a sensor node’s traffic load. If sensor nodes in C_1 use a 2×2 grid, then their ratio of wake-up time frames is 0.75. According to the ratio of traffic loads for different coronas ($C_1 : C_2 : C_3 : C_4 = 16 : 5 : 2.4 : 1$), the ratio of wake-up time frames for the sensor nodes in C_2 , C_3 , and C_4 should be 0.234, 0.112, and 0.047, respectively. This indicates that the quorum sizes used by C_2 , C_3 , and C_4 should be 8×8 , 17×17 , and 42×42 , respectively.

C. Latency Reduction

In allowing sensor nodes to sleep longer than one time frame, QMAC is believed to reduce energy consumption. The price for this saved energy, though, is higher latency. Assuming that sensor node A in corona C_i relies on the help of sensor node B in corona C_{i-1} to relay its data. Longer latency is induced since the quorum of node B may not coincide with that of node A. Thus, node A may take several time frames before it meets node B. To reduce the latency induced when applying QMAC, we introduce the concept of “next-hop group.” Each sensor node, e.g., node X, in C_i randomly selects a set of sensor nodes that are both within C_{i-1} and in the coverage range of node X as its candidate relaying nodes, as shown in Figure 3.4. This set of candidates form the next-hop group of node X. The next-hop group selection for each sensor node can be done in the network-initialization phase, where each node notifies its next-hop group members through a control packet MEMBER_NOTIFY. The basic idea of the next-hop group is to make more sensor nodes in inner coronas, instead of only one, capable of relaying packets for a particular sensor node in outer coronas. Thus, when a sensor node in an outer corona reports its data, it already has multiple candidate next-hop nodes and has a good chance of meeting one faster. It should be noted that only one member in the next-hop group is selected to relay traffic for each data report. A node can reselect its next hop group member by retransmitting a MEMBER_NOTIFY packet whenever the node finds that its next-hop group does not function properly.

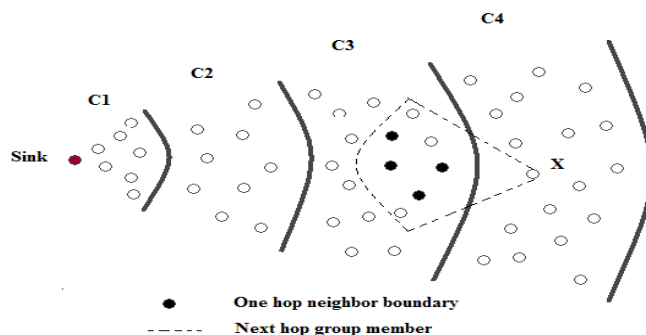


Fig.3.4. Next-hop group

The data reporting of QMAC_LR follows the four-way “request-to-send (RTS)/CTS/DATA/ACK” dialog. When sensor node X reports its data, the relay-node-selection process occurs as follows.

- 1) Sensor node X multicasts an RTS to its next-hop group members. One possible way to implement multicasting is to set the multicast address as the address of the source node. This means that an RTS packet with the same source and destination address will indicate a multicast transmission.
- 2) All the awake members of X that receive the RTS will back off before replying with a CTS packet. The back-off time selection is based on each node’s remaining battery capacity. The ones that have more than half of their remaining battery capacity will randomly distribute their back-off time at the first half of the contention window. On the other hand, the ones that have less than half of their remaining battery capacity will locate their back-off time at the second half of the contention window.
- 3) After node X receives a CTS from one of its next-hop group members, e.g., node Y, it can transmit its data to Y (through unicast). This data transmission also informs the other awake members that the relay node has been selected, and they can cease their back-off processes and go to sleep. Finally, correctly receiving data from node X, node Y will reply with an ACK packet.

We use an example to illustrate the operation of data transmission with latency reduction. As shown in Fig.3.5, sensor node A initiates the dialog with a multicast RTS packet. Sensor nodes B, C, and D, being the next-hop group members of node A, will accept the RTS packet, while sensor node E, which is not a next-hop group member of node A, will simply ignore it and go to sleep. After contention resolution, node C then transmits a CTS packet back to A. Once the DATA packet from node A is received, all nodes other than node C will enter sleep mode.

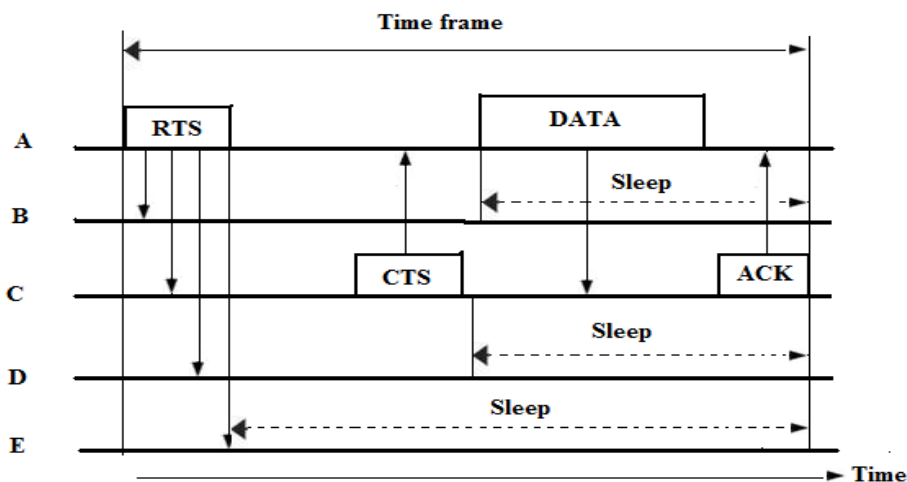


Fig3.5 Example of the operation of latency reduction.

The proper setting of next-hop group sizes is critical to the success of latency reduction. To reduce power consumption, the size should be as small as possible. The drawback of a small next-hop group is longer latency, while a large next-hop group may produce many redundant candidate sensor nodes, which induces energy waste. To find the proper size of a next-hop group, we need to know the probability wherein a sensor node, with the intention to report, meets at least one of its next-hop members.

IV. SIMULATION & DESIGN

A. The Network Simulator (Ns2)

NS is an event driven network simulator developed at University of California at Berkeley, USA, as a REAL network simulator projects in 1989 and was developed at with cooperation of several organizations. Now, it is a VINT project supported by DARPA. NS is not a finished tool that can manage all kinds of network model. It is actually still an on-going effort of research and development. The users are responsible to verify that their network model simulation does not contain any bugs and the community should share their discovery with all. There is a manual called NS manual for user guidance.

NS is a discrete event network simulator where the timing of events is maintained by a scheduler and able to simulate various types of network such as LAN and WPAN according to the programming scripts written by the user. Besides that, it also implements variety of applications, protocols such as TCP and UDP, network elements such as signal strength, traffic models such as FTP and CBR, router queue management mechanisms such as Drop Tail and many more. There are two languages used in NS2. They are C++ and OTcl (an object oriented extension of Tcl). The compiled C++ programming hierarchy makes the simulation efficient and execution times faster. The OTcl script which written by the users the network models with their own specific topology, protocols and all requirements need. The form of output produce by the simulator also can be set using OTcl. The OTcl script is written which creating an event scheduler objects and network component object with network setup helping modules. The simulation results produce after running the scripts can be use either for simulation analysis or as an input to graphical software called Network Animation (NAM).

B. The Network Animation (Nam)

The network animator began in 1990 as a simple tool for animating packet trace data. This trace data is typically derived as output from a network simulator like ns or from real network measurements, e.g., using tcpdump. Steven McCanne wrote the original version as a member of the Network Research Group at the Lawrence Berkeley National Laboratory, and has occasionally improved the design, as he's needed it in his research. Marylou Orayani improved it further and used it for her Master's research over summer 1995 and into spring 1996. The nam development effort was an ongoing collaboration with the VINT project. Currently, it is being developed at ISI by the SAMAN and Conser projects.

C. Parameters Used To Design Qmac Protocol

Simulation of QMAC protocol is performed based on the following parameters.

Nodes = 15

Maximum transmission range = 50m

Circular area = 200m

Channel capacity = 10kbps

CBR payload = 128B @ 2.5s with maximum delay of 100ms

Power mode threshold:

Transmit = 0.66w

Receive = 0.395w

Sleep = 0.35w

Simulation time= 20/40/100 ms

D. Simulation Results

1) Nam For Qmac Protocol

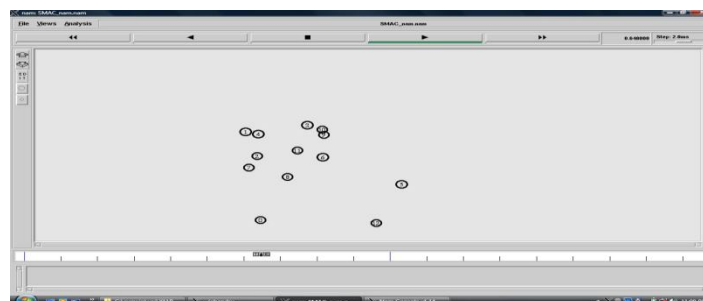


Figure 4.1 NAM for QMAC protocol

2) *Impact On Live Nodes*

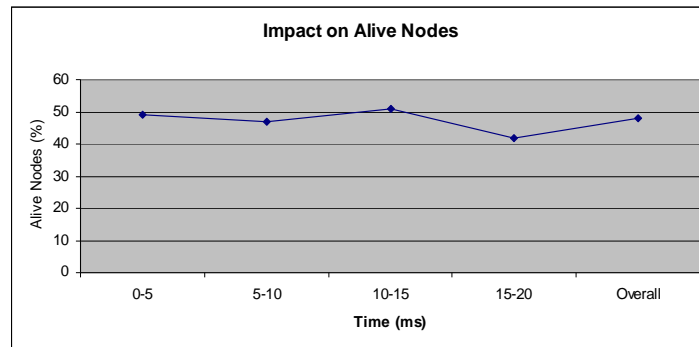


Fig. 4.2 Impact on Live Nodes

The Fig. 4.2 shows the performance of the proposed protocols in terms of how much they can extend network lifetime. The proposed protocol will increase the life time of the node by increasing the sleep duration more than one time interval.

3) *Impact On Transmission Latency*

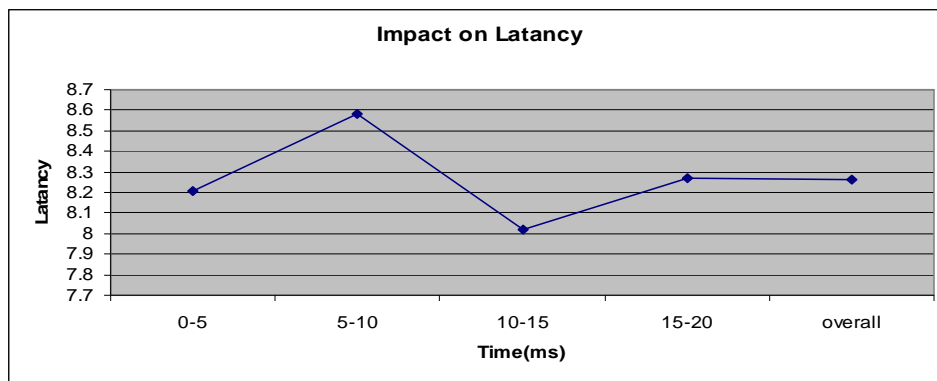


Fig. 4.3 Effect of QMAC protocols on latency.

Transmission latency for QMAC protocols can be found in Fig. 4.3. We separately observed the average latency at durations of 0–5, 5-10, 10-15 and 15-20s, as well as observed the overall average latency.

4) *Impact On The Transmission Success Ratio*

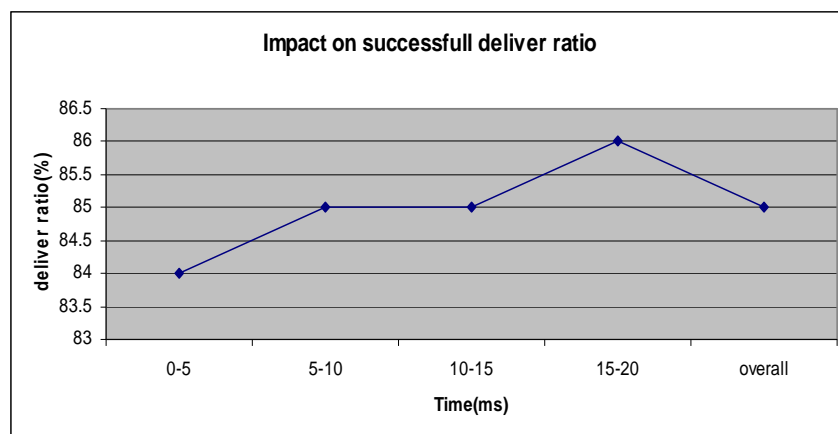


Fig. 4.4. Effect of QMAC protocols on the transmission success ratio.

Transmission success ratio for QMAC protocols can be found in Fig. 4.4. Similar to prior latency experiments, we also separately observed them at 0–5, 5-10, 10-15 and 15-20s, as well as observed the overall average latency.

V. CHAPTER 5 CONCLUSION AND FUTURE WORK

Energy conservation is crucial in wireless sensor network. Typically, sensor nodes closer to the sink run out of energy faster. Most previous solutions have tried to deploy more nodes around the sink. Here we have focused on an environment where planned deployment is difficult, and we have also proposed an energy-conserving MAC protocol. Realizing that sensor nodes have different loads due to their different distances to the sink, we have applied the concept of quorum to enable sensor nodes to adjust their sleep durations based on their traffic loads. To reduce delays induced by longer sleep durations, we have increased each node's transmission opportunity by enabling a group of next-hop nodes to accomplish the packet-relaying job. Such a mechanism also enhances the robustness of the proposed protocol. Simulation results verify that our MAC reduces energy consumption and keeps the latency low. This reveals that MAC is a promising energy-saving protocol for randomly deployed sensor networks. In future I am going to design this MAC protocol with mobility nodes.

REFERENCES

- [1] C.-M. Chao, J.-P. Sheu, and I.-C. Chou, "An adaptive quorum-based energy conserving protocol for IEEE 802.11 ad hoc networks," *IEEE Trans. Mobile Comput.*, vol. 5, no. 5, pp. 560–570, May 2006.
- [2] J.-R. Jiang, Y.-C. Tseng, C.-S. Hsu and T.-H. Lai, "Quorum-based asynchronous power-saving protocols for IEEE 802.11 ad hoc networks," *Mob. Netw. Appl. (MONET)*, vol. 10, no. 1/2, pp. 169–181, Feb. 2005.
- [3] J. Li and P. Mohapatra, "An analytical model for the energy hole problem in many-to-one sensor networks," in *Proc. IEEE 62nd Veh. Technol. Conf.*, Dallas, TX, Sep. 2005, pp.
- [4] T. V. Dam and K. Langendoen, "An adaptive energy-efficient MAC protocol for wireless sensor networks," in *Proc. ACM SenSys*, Los Angeles, CA, Nov. 2003,
- [5] W. Ye, J. Heidemann, and D. Estrin, "An energy-efficient MAC protocol for wireless sensor networks," in *Proc. 21st Int. Annu. Joint Conf. IEEE Comput. Commun. Soc. INFOCOM*, New York, Jun. 2002, pp. 214–226.
- [6] T. Zheng, S. Radhakrishnan, and V. Sarangan, "PMAC: An adaptive energy-efficient MAC protocol for wireless sensor networks," in *Proc. IEEE Int. Parallel Distrib. Process. Symp.*, Denver, CO, Apr. 2005, pp. 65–72.
- [7] G. Lu, B. Krishnamachari, and C. S. Raghavendra, "An adaptive energy efficient and low-latency MAC for tree-based data gathering in sensor networks," in *Proc. 18th Int. Parallel Distrib. Process. Symp.*, Santa Fe, NM, Apr. 2004, pp. 224–231.
- [8] M. Buettner, G. Yee, E. Anderson, and R. Han, "X-MAC: A short preamble MAC protocol for duty-cycled wireless sensor networks," in *Proc. 4th Int. Conf. Embedded Netw. SenSys*, Boulder, CO, Oct. 2006, pp. 307–320.
- [9] A. El-Hoiydi and J.-D. Decotignie, "Low power downlink MAC protocols for infrastructure wireless sensor networks," *Mob. Netw. Appl.*, vol.10, no.5, Oct. 2005.
- [10] S. Singh and C.S. Raghavendra, "PAMAS: Power aware multi-access protocol with signaling for ad hoc networks," *ACM Computer Communication Review*, vol. 28, no. 3, pp. 5–26, July 1998.



10.22214/IJRASET



45.98



IMPACT FACTOR:
7.129



IMPACT FACTOR:
7.429



INTERNATIONAL JOURNAL FOR RESEARCH

IN APPLIED SCIENCE & ENGINEERING TECHNOLOGY

Call : 08813907089  (24*7 Support on Whatsapp)



ISSN No. : 2321-9653

IJRASET

**International Journal for Research in Applied
Science & Engineering Technology**

IJRASET is indexed with Crossref for DOI-DOI : 10.22214

Website : www.ijraset.com, E-mail : ijraset@gmail.com



UGC
उच्च शिक्षा विभाग



45.98
INDEX COPERNICUS



THOMSON REUTERS
Subscriber ID: 51551-2015



Certificate

*It is here by certified that the paper ID : IJRASET11661, entitled
AN Energy Efficient MAC Protocol for WSN based on Quorum Concept
by*

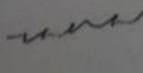
T. Ashok

*after review is found suitable and has been published in
Volume 5, Issue XII, December 2017*

in

*International Journal for Research in Applied Science &
Engineering Technology*

Good luck for your future endeavors

By 

Editor in Chief, IJRASET



ISSN No. : 2321-9653

IJRASET

**International Journal for Research in Applied
Science & Engineering Technology**

IJRASET is indexed with Crossref for DOI-DOI : 10.22214

Website : www.ijraset.com, E-mail : ijraset@gmail.com



UGC
and State Regent



45.98
INDEX COPERNICUS



THOMSON REUTERS
Research & Innovation



10.22214/IJRASET
TOGETHER WE REACH THE GOAL
IMPACT FACTOR : 4.887

Certificate

*It is here by certified that the paper ID : IJRASET11661, entitled
AN Energy Efficient MAC Protocol for WSN based on Quorum Concept*

by

M. Chandrasekar

*after review is found suitable and has been published in
Volume 5, Issue XII, December 2017*

in

*International Journal for Research in Applied Science &
Engineering Technology*

Good luck for your future endeavors

By [Signature]

Editor in Chief, IJRASET

A Technique to Solve Parametric Type Triangular Number Fuzzy Transportation Problem

Faritha Asma A¹ Meena C²

Assistant Professor of Mathematics¹, M.Phil research scholar², Department of Mathematics^{1,2}
Government Arts College, Trichy-22.^{1,2}

Email: asma.faritha@yahoo.com¹, meena95c@gmail.com²

Abstract-This paper discusses an optimization technique to solve Fuzzy Transportation Problem. Initially the cost, demand, supply and allocation in cell are considered as triangular fuzzy numbers. Then those fuzzy numbers are changed into parametric form. Finally this parameterized fuzzy transportation problem is solved, so as to find the Optimum solution.

Keywords-Triangular fuzzy number; Parametric form; IBFS; Optimum solution.

1. INTRODUCTION

Bellman and Zadeh[1] introduced the concept of fuzzy set theory in decision making. In traditional Mathematical formulation of Transportation problem all the parameters are treated as deterministic in nature. However, in real life, uncertainty always exists. Due to this vagueness the concept of fuzzy set theory introduced by zadeh[7] is more suitable in Transportation problem. There are many research articles on fuzzy Transportation problem [4],[6]. Malini et.al [2] used ranking technique to solve trapezoidal number fuzzy Transportation problem. In 2011 Sagaya Roseline et.al [5] proposed a generalized fuzzy modified distribution method for generalized fuzzy transportation problem.

This paper discusses an optimization technique to solve parametric type Triangular number fuzzy Transportation problem. Here, the triangular fuzzy numbers are taken in parametric form. For this, parametric type Fuzzy Transportation problem, the initial basic feasible solution (IBFS) and the optimum solution are found using the proposed method. The model is illustrated with an example.

2. PRELIMINARIES

2.1 Definition

A fuzzy set is characterized by a membership function mapping elements of a domain, space, or universe of discourse X to the unit interval [0,1]. (i.e) $A = \{(x, \mu_A(x)) / x \in X\}$, here $\mu_A: X \rightarrow [0,1]$ is a mapping called the degree of membership function of the fuzzy set A and μ_A is called the membership value of $x \in X$ in the fuzzy set A.

2.2 Definition

It is a fuzzy number, if it satisfies the following:

- A_α is convex (i.e. interval) $\forall \alpha \in [0,1]$

- Normal (there exists $x_0 \in \mathbb{R}$ with $\mu_A(x_0) = 1$)
- A_α is closed interval (with the end points) $\forall \alpha \in (0,1)$

Then \tilde{A} is called fuzzy interval. Moreover if there exists only one $x_0 \in \mathbb{R}$ with $\mu_A(x_0) = 1$ then \tilde{A} is called fuzzy number.

2.3 Definition

Among the various types of fuzzy number, triangular fuzzy number (TFN) is the most popular one. If A is a fuzzy number represented with three points as follows. The triangular fuzzy number A, can be represented by $A(a_1, a_2, a_3; 1)$ with membership function $\mu(X)$ given by

$$\mu_A(x) = \begin{cases} 0 & ; x < a_1 \\ \frac{x-a_1}{a_2-a_1} & ; a_1 \leq x \leq a_2 \\ \frac{a_3-x}{a_3-a_2} & ; a_2 \leq x \leq a_3 \\ 0 & ; x > a_3 \end{cases}$$

2.4 Parametric type Triangular Fuzzy Number

Let $\tilde{\alpha} = (\alpha_1, \alpha_2, \alpha_3)$ be a triangular fuzzy number then the parametric form of the TFN is defined as $\tilde{\alpha} = (\alpha_0, \alpha_*, \alpha^*)$ where $\alpha_* = \alpha_0 - \underline{a}$ and $\alpha^* = \bar{a} - \alpha_0$, $\bar{a}(p) = \alpha_3 - (\alpha_3 - \alpha_2)p$ and $\underline{a}(p) = (\alpha_2 - \alpha_1)p + \alpha_1$, $\alpha_0 = \frac{\underline{a}(p) + \bar{a}(p)}{2}$ when $p=1$, we get $\alpha_0 = \alpha_2$ where $p \in [0,1]$

2.5 Arithmetic Operations on Parametric type Triangular Fuzzy Number

Ming Ma et al.[3] have proposed a new fuzzy arithmetic operation based upon both location index and fuzziness index functions. The location index number is taken in the ordinary arithmetic, whereas the fuzziness index functions are considered to follow the lattice rule which is least upper bound in the

lattice L. That is for $\alpha, \beta \in L$ we define $\alpha \vee \beta = \max\{\alpha, \beta\}$ and $\alpha \wedge \beta = \min\{\alpha, \beta\}$

For arbitrary triangular fuzzy numbers $\tilde{\alpha} = (\alpha_0, \alpha_*, \alpha^*)$ $\tilde{\beta} = (\beta_0, \beta_*, \beta^*)$ and $*$ = {+, -, ×, ÷}, the arithmetic operations are defined as

$$\begin{aligned} \tilde{\alpha} * \tilde{\beta} &= (\alpha_0, \alpha_*, \alpha^*) * (\beta_0, \beta_*, \beta^*) = (\alpha_0 * \beta_0, \alpha_* * \beta_*, \alpha^* * \beta^*) \\ &= (\alpha_0 * \beta_0, \max\{\alpha_* * \beta_*, \max\{\alpha^* * \beta^*\}) \end{aligned}$$

In particular for any two triangular fuzzy numbers $\tilde{\alpha} = (\alpha_0, \alpha_*, \alpha^*)$ and $\tilde{\beta} = (\beta_0, \beta_*, \beta^*)$, we define

$$\begin{aligned} 2.5.1 \quad \text{Addition: } \tilde{\alpha} + \tilde{\beta} &= (\alpha_0, \alpha_*, \alpha^*) + (\beta_0, \beta_*, \beta^*) \\ &= (\alpha_0 + \beta_0, \max\{\alpha_*, \beta_*\}, \max\{\alpha^*, \beta^*\}) \end{aligned}$$

$$\begin{aligned} 2.5.2 \quad \text{Subtraction: } \tilde{\alpha} - \tilde{\beta} &= (\alpha_0, \alpha_*, \alpha^*) - (\beta_0, \beta_*, \beta^*) \\ &= (\alpha_0 - \beta_0, \max\{\alpha_*, \beta_*\}, \max\{\alpha^*, \beta^*\}) \end{aligned}$$

$$\begin{aligned} 2.5.3 \quad \text{Multiplication: } \tilde{\alpha} \times \tilde{\beta} &= (\alpha_0, \alpha_*, \alpha^*) \times (\beta_0, \beta_*, \beta^*) \\ &= (\alpha_0 \times \beta_0, \max\{\alpha_*, \beta_*\}, \max\{\alpha^*, \beta^*\}) \end{aligned}$$

$$\begin{aligned} 2.5.4 \quad \text{Division: } \tilde{\alpha} \div \tilde{\beta} &= (\alpha_0, \alpha_*, \alpha^*) \div (\beta_0, \beta_*, \beta^*) \\ &= (\alpha_0 \div \beta_0, \max\{\alpha_*, \beta_*\}, \max\{\alpha^*, \beta^*\}) \end{aligned}$$

3. ALGORITHM TO SOLVE PARAMETRIC TYPE FUZZY TRANSPORTATION PROBLEM

3.1 Mathematical Formulation of Fuzzy Transportation Problem

Consider a fuzzy transportation with m sources n destinations with triangular fuzzy numbers. Let $\tilde{a}_i \geq \tilde{\delta}$ be the fuzzy availability at source i and $\tilde{b}_j, (\tilde{b}_j \geq \tilde{\delta})$ be the requirement at destination j. Let \tilde{C}_{ij} ($\tilde{C}_{ij} \geq \tilde{\delta}$) be the unit fuzzy transportation cost from source i to destination j. Let \tilde{X}_{ij} denote the number of fuzzy units to be transported from source i to destination j. Now the problem is to find a feasible way of transporting the available amount at each source to satisfy the demand at each destination so that the total transportation cost is minimized.

The mathematical model of fuzzy transportation problem is as follows

$$\begin{aligned} \text{Minimize} \quad & \tilde{Z} \approx \sum_{i=1}^m \sum_{j=1}^n \tilde{C}_{ij} \tilde{X}_{ij} \\ \text{Subject to} \quad & \sum_{j=1}^n \tilde{X}_{ij} \approx \tilde{a}_i, \quad i=1,2,3,\dots,m \\ & \sum_{i=1}^m \tilde{X}_{ij} \approx \tilde{b}_j, \quad j=1,2,3,\dots,n \end{aligned} \quad \text{----(1)}$$

$$\begin{aligned} \sum_{i=1}^m \tilde{a}_i &\approx \sum_{j=1}^n \tilde{b}_j, \quad i=1,2,3,\dots,m; \\ j &= 1,2,3,\dots,n \text{ and } \tilde{X}_{ij} \geq \tilde{0} \text{ for all } i \end{aligned}$$

and j.

Where \tilde{C}_{ij} is the fuzzy unit transportation cost from ith source to the jth destination

3.2 Steps to find IBFS to Parametric type Fuzzy Transportation Problem

Here, IBFS is found using PARAMETRIC TYPE LEAST COST method.

Step 1: Consider the Parametric type fuzzy transportation problem with triangular fuzzy demand and

triangular fuzzy supply.

Step 2: Convert all the triangular fuzzy supply and fuzzy demand into parametric form of Triangular Fuzzy Number,

$$\tilde{\alpha} = (\alpha_0, \alpha_*, \alpha^*) \quad \text{where } \alpha_* = \alpha_0 - \underline{a} \quad \text{and} \\ \alpha^* = \bar{a} - \alpha_0, \quad \bar{a}(p) = \alpha_3 - (\alpha_3 - \alpha_2)p,$$

$$\underline{a}(p) = (\alpha_2 - \alpha_1)p + \alpha_1, \quad \alpha_0 = \frac{\underline{a}(p) + \bar{a}(p)}{2} \quad \text{here}$$

p=1, we get $\alpha_0 = \alpha_2$

Step 3: Similarly convert all the fuzzy cost coefficient into the same Parametric type.

Step 4: Determine the smallest cost in the cost matrix of the transportation table. Let it be \tilde{c}_{ij} , Allocate

$$\tilde{x}_{ij} = \min(\tilde{a}_i, \tilde{b}_j) \text{ in the cell } (i,j)$$

Step 5: If $\tilde{x}_{ij} = \tilde{a}_i$ cross off the ith row of the transportation table and decrease \tilde{b}_j by \tilde{a}_i . Go to step 3.

If $\tilde{x}_{ij} = \tilde{b}_j$ cross off the jth column of the transportation table and decrease \tilde{a}_i by \tilde{b}_j . Go to step 3.

If $\tilde{x}_{ij} = \tilde{a}_i = \tilde{b}_j$ cross off either the ith row or jth column but not both.

step 6: Repeat steps 3 and 4 for the resulting reduced transportation table until all the rim requirements are satisfied.

Whenever the minimum cost is not unique, make an arbitrary choice among the minima.

3.3 Optimum Solution to Parametric type of Fuzzy Transportation Problem

Here, we have used PARAMETRIC TYPE MODI Method to find the Optimum Solution to the Parametric type Fuzzy Transportation Problem. The arithmetic operations proposed in section 2.5 are used to find the optimum solution to the parametric type triangular number fuzzy transportation problem.

4. NUMERICAL EXAMPLE

Parametric form technique to solve fuzzy transportation problem

Solve the following Fuzzy Transportation Problem using Parametric form of Triangular Fuzzy Number.

	D1	D2	D3	D4	Supply
S1	(0,1,2)	(1,2,4)	(0,1,4)	(3,4,7)	(25,30,40)
S2	(1,3,6)	(1,3,4)	(0,2,5)	(0,1,3)	(20,30,50)
S3	(1,4,8)	(1,2,5)	(2,5,9)	(6,9,15)	(15,20,25)
Demand	(10,20,25)	(20,40,50)	(20,30,40)	(5,10,20)	

Solution:

Here each allocation, Demand and Supply are Fuzzy Triangular Number.

Parametric form of Triangular Fuzzy Number

$\tilde{\alpha}=(\alpha_0, \alpha_*, \alpha^*)$ where $\alpha_* = \alpha_0 - \underline{a}$ and $\alpha^* = \bar{a} - \alpha_0$,

$\bar{a}(p)=\alpha_3 - (\alpha_3 - \alpha_2)p$,

$$\underline{a}(p) = (\alpha_2 - \alpha_1)p + \alpha_1, \alpha_0 = \frac{\underline{a}(p) + \bar{a}(p)}{2} \text{ here } p=1,$$

we get $\alpha_0 = \alpha_2$

The parametric form of all triangular fuzzy numbers in the fuzzy transportation table are,

Table 1

	D1	D2	D3	D4	Supply
S1	(1,1-p,1-p)	(2,1-p,2-2p)	(1,1-p,3-3p)	(4,1-p,3-3p)	(30,5-5p,10-10p)
S2	(3,2-2p,3-3p)	(3,2-2p,1-p)	(2,2-2p,3-3p)	(1,1-p,2-2p)	(30,10-10p,20-20p)
S3	(4,3-3p,4-4p)	(2,1-p,3-3p)	(5,3-3p,4-4p)	(9,3-3p,6-6p)	(20,5-5p,5-5p)
Demand	(20,10-10p,5-5p)	(40,20-20p,10-10p)	(30,10-10p,10-10p)	(10,5-5p,10-10p)	

Table 2: Finding IBFS using Parametric type Least cost method

	D1	D2	D3	D4	Supply
S1	(1,1-p,1-p) (10,10-10p,20-20p)	(2,1-p,2-2p)	(1,1-p,3-3p) (20,10-10p,20-20p)	(4,1-p,3-3p)	(30,5-5p,10-10p)
S2	(3,2-2p,3-3p)	(3,2-2p,1-p) (20,10-10p,20-20p)	(2,2-2p,3-3p) (10,10-10p,20-20p)	(1,1-p,2-2p)	(30,10-10p,20-20p)
S3	(4,3-3p,4-4p)	(2,1-p,3-3p) (20,5-5p,5-5p)	(5,3-3p,4-4p)	(9,3-3p,6-6p)	(20,5-5p,5-5p)
S4	(0,3-3p,4-4p) (10,10-10p,20-20p)	(0,2-2p,3-3p)	(0,3-3p,4-4p)	(0,3-3p,6-6p) (10,5-5p,10-10p)	(20,10-10p,20-20p)
Demand	(20,10-10p,5-5p)	(40,20-20p,10-10p)	(30,10-10p,10-10p)	(10,5-5p,10-10p)	

The IBFS in Parametric form is = (150,10-10p,20-20p)

The fuzzy IBFS for different values of p are

Table 3

P	IBFS
0	(150,10,20)
0.5	(150,5,10)
1	(150)

Table 4: Optimum Solution

	D1	D2	D3	D4	Supply
S1	(1,1-p,1-p) (10,10-10p,20-20p)	(2,1-p,2-2p)	(1,1-p,3-3p) (20,10-10p,20-20p)	(4,1-p,3-3p)	$u_1=0$
S2	(3,2-2p,3-3p)	(3,2-2p,1-p) (20,10-10p,20-20p)	(2,2-2p,3-3p) (10,10-10p,20-20p)	(1,1-p,2-2p)	$u_2=(1,2-2p,3-3p)$
S3	(4,3-3p,4-4p)	(2,1-p,3-3p) (20,5-5p,5-5p)	(5,3-3p,4-4p)	(9,3-3p,6-6p)	$u_3=(0,2-2p,3-3p)$
S4	(0,3-3p,4-4p) (10,10-10p,20-20p)	(0,2-2p,3-3p)	(0,3-3p,4-4p)	(0,3-3p,6-6p) (10,5-5p,10-10p)	$u_4=(-1,3-3p,4-4p)$
Demand	$v_1=(1,1-p,1-p)$	$v_2=(2,2-2p,3-3p)$	$v_3=(1,1-p,3-3p)$	$v_4=(1,3-3p,6-6p)$	

$$z_{12}=2+0-2=0, \quad z_{14}=1+0-4=-3, \quad z_{21}=1+1-3=-1, \quad z_{24}=1+1-1=1, \quad z_{31}=1+0-4=-3,$$

$$z_{33}=1+0-5=-4, \quad z_{34}=1+0-9=-8, \quad z_{42}=2-1+0=1, \quad z_{43}=1-1-0=0.$$

Table 5

	D1	D2	D3	D4	Supply
S1	(1,1-p,1-p) (0,10-10p,20-20p)	(2,1-p,2-2p)	(1,1-p,3-3p) (30,10-10p,20-20p)	(4,1-p,3-3p)	$u_1=(-1,2-2p,3-3p)$
S2	(3,2-2p,3-3p)	(3,2-2p,1-p) (20,10-10p,20-20p)	(2,2-2p,3-3p) (0,10-10p,20-20p)	(1,1-p,2-2p) (10,5-5p,10-10p)	$u_2=0$
S3	(4,3-3p,4-4p)	(2,1-p,3-3p) (20,5-5p,5-5p)	(5,3-3p,4-4p)	(9,3-3p,6-6p)	$u_3=(-1,2-2p,3-3p)$
S4	(0,3-3p,4-4p) (20,10-10p,20-20p)	(0,2-2p,3-3p)	(0,3-3p,4-4p)	(0,3-3p,6-6p)	$u_4=(-2,3-3p,4-4p)$
Demand	$v_1=(2,2-2p,3-3p)$	$v_2=(3,2-2p,1-p)$	$v_3=(2,2-2p,3-3p)$	$v_4=(1,1-p,2-2p)$	

$$z_{12}=3-1-2=0, \quad z_{14}=1-1-4=-4, \quad z_{21}=2+0-3=-1, \quad z_{31}=2-1-4=-3, \quad z_{33}=2-1-5=-4,$$

$$z_{34}=1-1-9=-9, \quad z_{42}=3-2=1, \quad z_{43}=2-2=0, \quad z_{44}=1-2=-1.$$

Table 6

	D1	D2	D3	D4	Supply
S1	(1,1-p,1-p) (20,10-10p,20-20p)	(2,1-p,2-2p)	(1,1-p,3-3p) (10,10-10p,20-20p)	(4,1-p,3-3p)	$u_1=(-1,2-2p,3-3p)$

S2	(3,2-2p,3-3p)	(3,2-2p,1-p) (0,10-10p,20-20p)	(2,2-2p,3-3p) (20,10-10p,20-20p)	(1,1-p,2-2p) (10,5-5p,10-10p)	$u_2=0$
S3	(4,3-3p,4-4p)	(2,1-p,3-3p) (20,5-5p,5-5p)	(5,3-3p,4-4p)	(9,3-3p,6-6p)	$u_3=(-1,2-2p,3-3p)$
S4	(0,3-3p,4-4p)	(0,2-2p,3-3p) (20,10-10p,20-20p)	(0,3-3p,4-4p)	(0,3-3p,6-6p)	$u_4=(-3,2-2p,3-3p)$
Demand	$v_1=(2,2-2p,3-3p)$	$v_2=(3,2-2p,1-p)$	$v_3=(2,2-2p,3-3p)$	$v_4=(1,1-p,2-2p)$	

$$z_{12}=3-1-2=0, \quad z_{14}=1-1-4=-4, \quad z_{21}=2+0-3=-1, \quad z_{31}=2-1-4=-3, \quad z_{33}=2-1-5=-4,$$

$$z_{34}=1-1-9=-9, \quad z_{41}=2-3=-1, \quad z_{43}=2-3=-1, \quad z_{44}=1-3=-2.$$

All $z_{ij} \leq 0$ The given table is optimal.

The Optimum Transportation cost in Parametric Form = (120,10-10p,20-20p)

The fuzzy optimal solution in different values of p are

Table 7

P	OPTIMUM TRANSPORTATION COST
0	(120,10,20)
0.5	(120,5,10)
1	(120)

5. CONCLUSION

In this paper, we have presented a Transportation Problem where demand, supply and cost are considered as Triangular Fuzzy Numbers instead of crisp or probabilistic in nature to make the Transportation Problem more realistic. At first, Parametric type Triangular fuzzy numbers are developed. Then it is solved using the proposed method. A numerical example illustrates the proposed method.

REFERENCES

[1] Bellman, R.E.,zadeh,L.A.: Decision-making in a fuzzy environment Management science;(1970);17(4),141164.

[2] Malini.P and Dr.M.Ananthanarayanan: Solving Fuzzy Transportation Problem using Ranking of Trapezoidal Fuzzy Numbers” ISSN 0976-5840.

[3] Ming Ma.; Menahem Friedman and Abraham kandel: A new fuzzy arithmetic, Fuzzy sets and systems,108,83-90,1999.

[4] Nidhi Joshi.; Surject singh chauhan(Gonder): A new Approach for obtaining optimal solution of Unbalanced

Fuzzy Transportation Problem, International Journal of Computer and technology ISSN 2277-3061.

[5] Sagaya Roseline Generalized fuzzy modified distribution method for generalized fuzzytransportation problem, International Multidisciplinary Research Journal, 2011,1(10):12-15. ISSN 2231-6302.

[6] Umamaheswari.P and Ganesan.K, “A Solution approach to Fuzzy Nonlinear Programming problem International Journal of pure and applied mathematics volume 113 No.13 2017,291-300,ISSN:1311-8080.

[7] Zadeh, L.A.;Fuzzy sets. Information and control;8, 338-352.



M.A.M. SCHOOL OF ENGINEERING

(Accredited by NAAC)

(Approved by AICTE, New Delhi & Affiliated to Anna University)

Siruganur, Tiruchirappalli – 621 105.

Academic year (2017-2018)

Department of Electrical and Electronics Engineering

Title of paper	Name of the author/s	Department of the teacher	Name of journal	Year of publication	ISSN number	Link to the recognition in UGC enlistment of the Journal /Digital Object Identifier (doi) number		
						Link to website of the Journal	Link to article/ paper/ abstract of the article	Is it listed in UGC Care list /Scopus/Web of Science/other, mention
Stepped Multicarrier SPWM Techniques for Seven level Cascaded Inverter	M.Meenkshi	EEE	International Journal of Emerging Technology in Engineering Research	2017-2018	ISSN: 2454-6410	https://www.ijeter.everscience.org/Manuscripts/Volume-5/Issue-12/Vol-5-issue-12-M-08.pdf		
Development of Multicarrier SPWM Techniques for Cascaded MLI	M.Dharani Devi	EEE	International Journal of Computational Engineering Research (IJCER)	2017-2018	ISSN (e): 2250 – 3005	https://www.researchgate.net/publication/320867741_Development_of_Multicarrier_SPWM_Techniques_for_Cascaded_MLI		
Implementation of different PWM control strategy for Cascaded MLI	M.Dharani Devi	EEE	Journal of Network Communication and Emerging Technologies	2017-2018	ISSN: 2395-5317	https://www.jncet.org/Manuscripts/Volume-7/Issue-11/Vol-7-issue-11-M-06.pdf		

R. Deep

HOD/EEE

HEAD OF THE DEPARTMENT
ELECTRICAL and ELECTRONICS ENGINEERING
M.A.M. SCHOOL OF ENGINEERING
SIRUGANUR, TRICHY - 621 105.

PRINCIPAL
PRINCIPAL

M.A.M. SCHOOL OF ENGINEERING
SIRIGANUR, TIRUCHIRAPPALLI-621 105.

Stepped Multicarrier SPWM Techniques for Seven - Level Cascaded Inverter

M.Meenakshi ¹, R.Nagarajan ², R. Banupriya ³, M.Dharani Devi ⁴

¹Assistant Professor, Dept. of Electrical and Electronics Engineering, M.A.M. School of Engineering, Trichy, India.

²Professor, Dept. of Electrical and Electronics Engineering, Gnanamani College of Technology, Namakkal, India.

³Assistant Professor, Dept. of Electrical and Electronics Engineering, P.G.P. College of Engineering and Technology, Namakkal, India.

⁴Associate Professor, Dept. of Electrical and Electronics Engineering, M.A.M. School of Engineering, Trichy, India.

Abstract – In this paper, novel multicarrier pulse width modulation technique which uses stepped carrier waveform is proposed for seven-level cascaded inverter. In each carrier waveform different techniques such as phase disposition (PD), inverted phase disposition (IPD), phase opposition disposition (POD) and alternative phase opposition disposition (APOD) are implemented. The fundamental output voltage and harmonics obtained in each method are compared with the output waveform obtained with the triangular carrier waveform. The proposed switching technique enhances the fundamental component of the output voltage and improves total harmonic distortion. The different PWM methodologies adopting the constant switching frequency multicarrier with different modulation indexes are simulated for a 1kW, 3 ϕ inverter using MATLAB/SIMULINK. The effect of switching frequency on the fundamental output voltage and harmonics are also analyzed.

Index Terms – Modulation Index (MI), Stepped Multicarrier SPWM (SMC SPWM), Total Harmonic Distortion (THD) and Triangular Multicarrier SPWM (TMC SPWM).

1. INTRODUCTION

The multilevel inverter is an effective solution for increasing power and reducing harmonics of ac waveform [1]. The elementary concept of a multilevel converter to achieve higher power is to use a series of power semiconductor switches with several lower voltage dc sources to perform the power conversion by synthesizing a staircase voltage waveform. Capacitors, batteries, and renewable energy voltage sources can be used as the multiple dc voltage sources. The commutation of the power switches aggregate these multiple dc sources in order to achieve high voltage at the output; however, the rated voltage of the power semiconductor switches depends only upon the rating of the dc voltage sources to which they are connected [2].

In this paper, constant switching frequency multicarrier pulse width modulation method is used for the multilevel inverter [3]. The control objective is to compare the reference sine wave with multicarrier waves for three phase seven level cascaded inverters. Multilevel voltage source inverter (MVSI) structure is very popular especially in high power DC to AC power

conversion applications. It offers several advantages that make it preferable over the conventional voltage source inverter (VSI). These include the capability to handle higher DC link voltage; the stress on each switching device can be reduced in proportional to the higher voltages [4]. Consequently, in some applications, it is possible to avoid expensive and bulky step-up transformer. Another significant advantage of a multilevel output is better sinusoidal voltage waveform. As a result, a lower total harmonic distortion (THD) is obtained [5], [6].

The concept of multilevel converter has been introduced since 1975 [7]. The term multilevel began with the three-level converter. Subsequently, several multilevel converter topologies have been developed, such as the Diode Clamped Multilevel Inverter (DCMLI) also known as Neutral Point Clamped (NPC) Inverter, Flying Capacitor Multilevel Inverter (FCMLI) and Cascaded Multilevel Inverter (CCMLI) [8], [9]. Among them, CCMLI topology is the most attractive, since it requires the least number of components and increases the number of levels in the inverter without requiring high ratings on individual devices and the power rating of the CCMLI is also increased. It also results in simple circuit layout and is modular in structure. Furthermore, CCMLI type of topology is free of DC voltage balancing problem, which is a common issue facing in the DCMLI and FCMLI topologies [10], [11].

Numerous industrial applications have begun to require higher power apparatus in recent years. Some medium voltage motor drives and utility applications require medium voltage and megawatt power level. For a medium voltage grid, it is troublesome to connect only one power semiconductor switch directly [12]. As a result, a multilevel power converter structure has been introduced as an alternative in high power and medium voltage situations. A multilevel converter not only achieves high power ratings, but also enables the use of renewable energy sources. Renewable energy sources such as photovoltaic, wind, and fuel cells can be easily interfaced to a multilevel converter system for high power application [13].

In motor applications, high dv/dt in power supply generates high stress on motor windings and requires additional motor

insulation. Further; high dv/dt of semiconductor devices increases the electromagnetic interference (EMI), common-mode voltage and possibilities of failure on motor [14], [15]. By increasing the number of levels in the output waveform, the switching dv/dt stress is reduced in the multilevel inverter [16], [17]. Multilevel inverters are suitable for power electronics applications such as flexible AC transmission systems, renewable energy sources, uninterruptible power supplies, electrical drives and active power filters.

2. CASCADED MULTILEVEL INVERTER

The single-phase structure of three phase seven-level cascaded inverter is illustrated in Figure 1. Each separate dc source is connected to a single-phase full-bridge, or H-bridge, inverter. Each inverter can generate three different outputs voltage level, $+V_{dc}$, 0 and $-V_{dc}$, by connecting the dc source to the ac output by different switching combinations of the four semiconductor switches S1, S2, S3 and S4. To obtain $+V_{dc}$, switches S1 and S2 are tuned on, whereas $-V_{dc}$ can be obtained by tuning on switches S3 and S4. By turning on S1 and S3 or S2 and S4, the output voltage is 0. The ac outputs of each of the full-bridge inverter levels are connected in series such that the synthesized voltage waveform is the sum of the inverter outputs [18], [19].

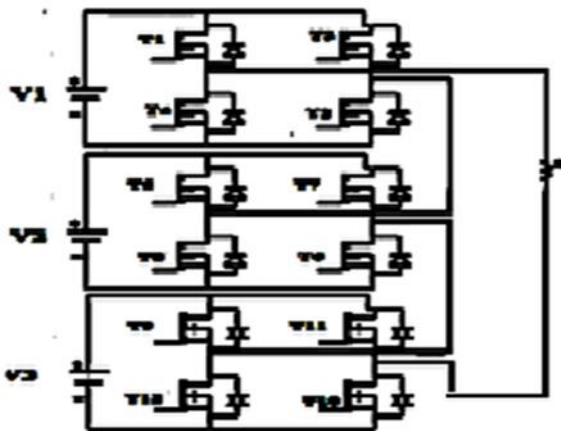


Figure 1 1 ϕ structure of seven-level CCMLI

The CCMLI is producing seven level output and they are $3V_{dc}$, $2V_{dc}$, V_{dc} , 0, $-V_{dc}$, $-2V_{dc}$ and $-3V_{dc}$. This topology is suitable for applications where separate dc voltage sources are available, such as photovoltaic (PV) generators, fuel cells and batteries. The phase output voltage is generated by the sum of two output voltage of the full bridge inverter modules. The circuit in Figure 1 utilizes three independent dc sources and consequently will create an output phase voltage with seven-level. In general, if N is the number of independent dc sources per phase, then the following relations apply [20]:

$$m = 2N + 1 \quad (1)$$

$$q = 2(m - 1) \quad (2)$$

Where m is the number of levels and q is the number of switching devices in each phase

The most well known SPWM which can be applied to a CCMLI is the Phase-Shifted SPWM. This modulation technique is the same as that of the conventional SPWM technique which is applied to a conventional single phase full-bridge inverter, the only difference being that it utilizes more than one carrier. The number of carriers to be used per phase is equal to twice the number of dc voltage sources per phase ($2N$) [21].

3. MODULATION TECHNIQUES

The Pulse Width Modulation (PWM) control strategies development tries to reduce the total harmonic distortion (THD) of the output voltage. Any deviation in the output voltage of the sinusoidal wave shape will result in harmonic currents in the load and this harmonic current produces the electromagnetic interference (EMI), harmonic losses and torque pulsation in the case of motor drives. Increasing the switching frequency of the PWM pattern reduces the lower frequency harmonics by moving the switching frequency carrier harmonic and associated sideband harmonics away from the fundamental frequency component [22]. This increased switching frequency reduces harmonics, which results in a lower THD with high quality output voltage waveforms of desired fundamental RMS value and frequency which are as close as possible to sinusoidal wave shape [23].

The carrier frequency defines the switching frequency of the converter and the high order harmonic components of the output voltage spectrum and the sidebands occur around the carrier frequency and its multiples. The higher switching frequency can be employed for low and medium power inverters, whereas, for high power and medium voltage applications the switching frequency should be low. Harmonic reduction can then be strictly related to the performance of an inverter with any switching strategy [24], [25]. The three phase multi level inverter requires three modulating signals or reference signals which are three sine-waves with 120 degree phase shift and equal in magnitudes. In this paper, new carrier based PWM techniques are developed which are as Stepped Multicarrier Sinusoidal PWM (SMC SPWM).

Each carrier is to be compared with the corresponding modulating sine wave [26], [27]. The reference or modulation waveform has peak amplitude A_r and frequency f_r and it is centered in the middle of the carrier set. The general principle of a carrier based PWM technique is the comparison of a sinusoidal waveform with a carrier waveform, this typically being a triangular carrier waveform. The reference is continuously compared with the carrier signal. If the reference is greater than the carrier signal, then the active device corresponding to that carrier is switched on, and if the reference is less than the carrier signal, then the active device

corresponding to that carrier is switched off [28], [29]. In multilevel inverters, the amplitude modulation index, M_a and the frequency ratio, M_f are defined as,

$$M_a = \frac{A_r}{(m-1)A_c} \tag{3}$$

$$M_f = \frac{f_c}{f_r} \tag{4}$$

Where A_r and A_c are amplitude of reference and carrier signal respectively. f_r and f_c are frequency of reference and carrier signal respectively.

In this paper, modulation indexes used are 0.7, 0.8, 0.9 and 1 for seven-level CCMLI. For multilevel applications, carrier based PWM techniques with multiple carriers are used. The Multicarrier Modulation (MCM) techniques can be divided in to the following categories such as [30], [31],

1. Phase disposition (PD) where all the carriers are in phase.
2. Inverted phase disposition (IPD) where all the carriers are in phase and is inverted.
3. Phase opposition disposition (POD) where the carriers above the zero reference are in phase but shifted by 180 degrees from those carriers below the zero reference.
4. Alternative phase opposition disposition (APOD) where each carrier band is shifted by 180 degrees from the adjacent carrier bands [2].

The above modulation strategies are implemented for stepped carrier wave. The phase voltage and line voltage waveform, harmonic spectrums of the line voltage are shown for different modulation techniques by doing simulation using MATLAB/SIMULINK for seven-level CCMLI and the results obtained are compared.

3.1. Triangular Multicarrier Sinusoidal PWM (TMC SPWM)

The performance of the multilevel inverter is based on the multicarrier modulation technique used. Two-level to multilevel inverters are made using several triangular carrier signals and one reference signal per phase. Carrara [5] developed multilevel sub harmonic PWM (SH-PWM), which is as follows, for m -level inverter, $m-1$ carriers [32] with the same frequency f_c and same amplitude A_c are disposed such that the bands they occupy are contiguous. They are defined as

$$C_i = A_c \left((-1)^i y_c(\omega_c, \varphi) + t - \frac{m}{2} \right), \tag{5}$$

$i = 1, \dots, (m-1)$

Where y_c is a normalized symmetrical triangular carrier defined as,

$$y_c(\omega_c, \varphi) = (-1)^{\lfloor \alpha \rfloor} ((\alpha \bmod 2) - 1) + \frac{1}{2} \tag{6}$$

$$\alpha = \frac{\omega_c t + \varphi}{\pi}, \omega_c = 2\pi f_c \tag{7}$$

φ represents the phase angle of y_c . y_c is a periodic function with the period $T_c = \frac{2\pi}{\omega_c}$. It is shown that using symmetrical

triangular carrier generates less harmonic distortion at the inverters output [33], [34]. The carrier waveforms, output voltage waveforms and %THD chart are shown only for selected PWM techniques in order to restrict the number of figures.

In TMC SPWM, so far only the PD, POD and APOD techniques are discussed earlier in the literature. In this paper, IPD scheme is also applied to TMC SPWM and it is found that this scheme gives the lowest THD among the TMC SPWM schemes. The multicarrier modulation techniques such as PD, IPD, POD and APOD are implemented using triangular multicarrier signals for seven-level CCMLI with different modulation indexes and are shown in Figure 2(a) and 2(b) respectively.

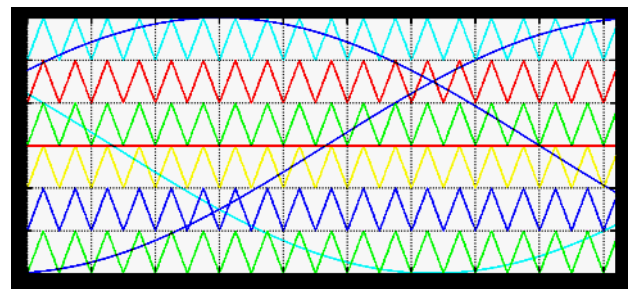


Figure 2(a) PD TMC SPWM with $M_a = 1$

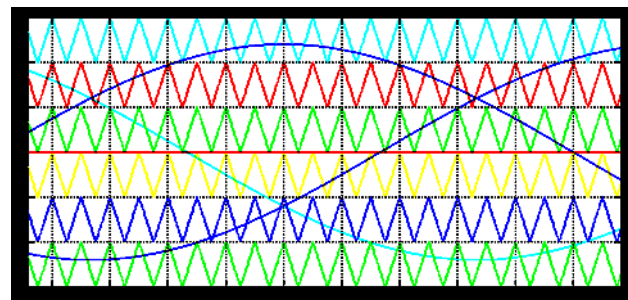


Figure 2(b) IPD TMC SPWM with $M_a = 0.8$

3.2. Stepped Multicarrier Sinusoidal PWM (SMC SPWM)

The Stepped wave is also known as approximated or modified sine wave, refers to a sine wave that instead of looking like a smooth curve where the wave gradually ramps up and down over the course of the cycle, there are a series of "steps" or jumps in wave from one plateau to another. The simulink block provides a step between two definable levels at a specified time. Each cycle constitutes eight steps. Every step is equal in

magnitude and in time. At the beginning and ending of the cycle, the signal has magnitude zero and retains for half the value of the one step time period. The angle of each step is ϕ which is given by.

$$\phi = \frac{360^\circ}{n_s} \tag{8}$$

Where n_s is the number of steps in one cycle, since $n_s = 8$ the angle for each step is 45° .

The multicarrier modulation techniques such as PD, IPD, POD and APOD are implemented using stepped multicarrier signals for seven-level CCMLI with different modulation indexes and are shown in Figure 3(a) and 3(b) respectively.

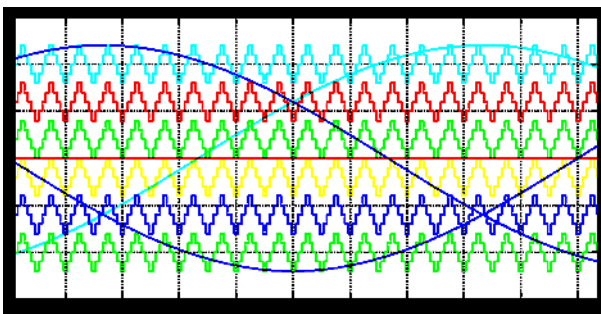


Figure 3(a) PD SMC SPWM with $M_a = 1$

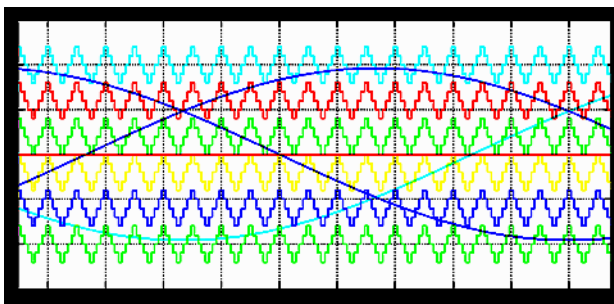


Figure 3(b) IPD SMC SPWM with $M_a = 0.8$

4. SIMULATION RESULTS

The seven-level cascaded multilevel inverter model with different modulation indexes was implemented in MATLAB/SIMULINK software to demonstrate the feasibility of PWM techniques. Phase disposition, inverted phase disposition, phase opposition disposition and alternative phase opposition disposition techniques are used for the various multicarrier SPWM techniques such as

1. Triangular Multicarrier Sinusoidal PWM
2. Stepped Multicarrier Sinusoidal PWM

The line voltage waveform with its harmonic spectrum at fundamental frequency of 50Hz and switching frequency of

2kHz and 10kHz are obtained for the proposed CCMLI. For comparison, the total harmonic distortion (THD) was chosen to be evaluated for all the modulation techniques. In order to get THD level of the waveform, a Fast Fourier Transform (FFT) is applied to obtain the spectrum of the output voltage [35] – [38]. The THD is calculated using the following equation in this work.

$$THD = \frac{\sqrt{\sum_{n=2}^{80} v_n^2}}{v_1} \tag{9}$$

Where n is the harmonic order, v_n is the RMS value of the n^{th} harmonic component and v_1 is the RMS value of the fundamental component. Here the %THD is calculated up to a harmonic order which is twice the switching frequency. For 2kHz switching frequency up to 80th order harmonics is taken in to account for calculating THD and for 10kHz switching frequency up to 400th order harmonics is taken in to account for calculating THD.

Figure 4 presents the simulation model of a three-phase seven-level CCMLI and is developed using MATLAB/SIMULINK. The simulation results are obtained for the output phase voltage and line voltage of the three phase seven-level CCMLI with 1kW, 3 ϕ resistive loads for various PWM techniques.

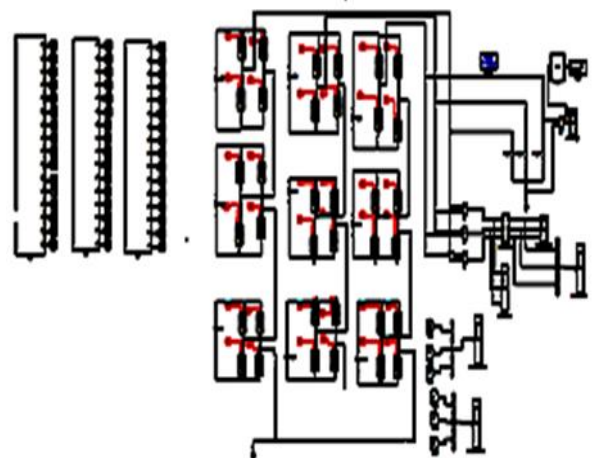


Figure 4 Simulation model of 3 ϕ seven-level CCMLI

4.1. Triangular Multi Carrier SPWM (TMC SPWM)

Figure 5(a) and 5(b) show the line voltage waveforms and the percentage THD of the line voltage for seven level using the phase disposition technique for triangular multi carrier sinusoidal PWM with $M_a=1$.

Table 1 shows the percentage line voltage THD for the seven-level CCML with triangular multicarrier signal with different multicarrier PWM techniques with a switching frequency of 2kHz and 10kHz respectively for different modulation indexes.

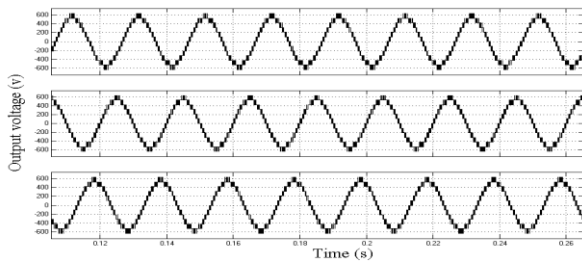


Figure 5(a) Line Voltage for PD SPWM with $M_a = 1$

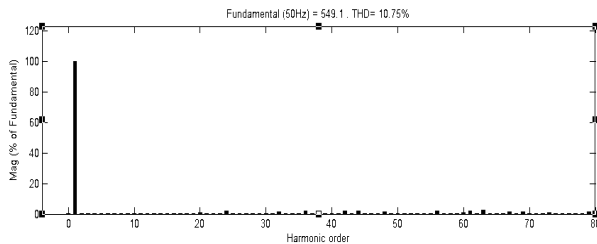


Figure 5(b) Line Voltage %THD for PD SPWM with $M_a = 1$

Table 1: Line voltage %THD for CCMLI with TMC SPWM

Switching frequency	Modulation Technique	Modulation Indexes			
		$M_a=1$	$M_a=0.9$	$M_a=0.8$	$M_a=0.7$
2kHz	PD	10.75	12.69	13.19	16.61
	IPD	10.75	12.69	13.19	16.61
	POD	15.22	20.62	21.98	20.10
	APOD	14.91	18.04	19.65	23.86
10kHz	PD	10.90	12.78	13.40	16.15
	IPD	10.90	12.78	13.40	16.15
	POD	16.25	20.92	22.31	21.41
	APOD	15.09	18.53	20.53	24.65

From the above table, it is observed that, when the switching frequency of the CCMLI is increased, the percentage line voltage THD is reduced for the PD and IPD schemes with modulation index of 0.7 in seven level CCMLI. In the POD and APOD schemes, when the switching frequency of the CCMLI is increased, the percentage line voltage THD is reduced with modulation index of 0.8. If the output voltage level increases the percentage line voltage THD decreases. From the simulation result in the triangular multi carrier SPWM technique PD and IPD PWM schemes, from 3rd order harmonics to 17th order harmonics and higher odd order harmonics (above 17th harmonics) are less than 1%. Few of the even order harmonics from 18th harmonics to 54th harmonics for the above mentioned scheme are less than 2%. The dominant 57th harmonic factor is about 2% for the PD and IPD schemes.

In the POD scheme, from 3rd odd order harmonics to 19th odd order harmonics are less than 1% and all even order harmonics are zero. Few of the odd order harmonics from 21st harmonics to 69th harmonics are 1% to 2%. The dominant 39th and 41st harmonic factor are 5.37% and 5.59% respectively for the POD

scheme. In the APOD scheme, from 3rd odd order harmonics to 25th odd order harmonics are less than 1% and all even order harmonics are 0.01%. Few of the odd order harmonics from 27th harmonics to 69th harmonics are present. The dominant 29th and 51st harmonic factor are 4.70% and 4.59% respectively for the APOD scheme. It is observed that, when the switching frequency of the CCMLI is increased, the percentage line voltage THD, the fundamental phase and line voltage are decreased very slightly for the PD and IPD schemes. In the POD and APOD schemes, if the switching frequency is increased, the percentage line voltage THD is increased very slightly and the fundamental phase and line voltage are decreased very slightly. Also the fundamental line voltage is maximum for POD and APOD schemes and is minimum for PD and IPD schemes.

4.2. Stepped Multi Carrier SPWM (SMC SPWM)

Figure 6(a) and 6(b) show the line voltage waveforms and the percentage THD of the line voltage for seven-level using the inverted phase disposition technique for stepped multicarrier sinusoidal PWM with $M_a=1$.

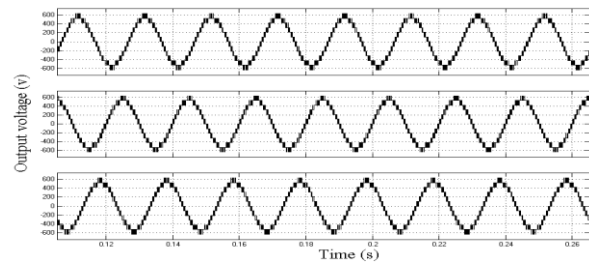


Figure 6(a) Line Voltage for PD SPWM with $M_a = 1$

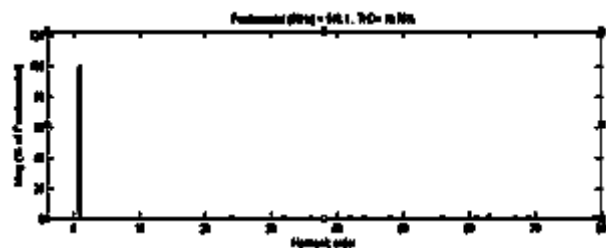


Figure 6(b): Line Voltage %THD for IPD SPWM with $M_a=1$

Table 2 shows the percentage line voltage THD for the seven-level CCML with stepped multicarrier signal with different multicarrier PWM techniques with a switching frequency of 2kHz and 10kHz respectively for different modulation indexes.

Table 2: Line voltage %THD for CCMLI with SMC SPWM

Switching frequency	Modulation Technique	Modulation Indexes			
		$M_a=1$	$M_a=0.9$	$M_a=0.8$	$M_a=0.7$
2kHz	PD	11.18	12.83	13.16	16.62
	IPD	11.18	12.83	13.16	16.62
	POD	17.28	22.02	22.80	23.77
	APOD	15.71	18.69	21.33	25.35

10kHz	PD	11.00	13.13	13.09	16.46
	IPD	11.00	13.13	13.09	16.46
	POD	15.73	20.11	21.46	21.73
	APOD	14.49	17.76	19.35	23.67

From the above table, it is observed that, when the switching frequency of the CCMLI is increased, the percentage line voltage THD is reduced for all PWM schemes, except PD and IPD schemes with modulation index of 0.9. From the simulation result in the stepped multi carrier SPWM technique PD and IPD PWM schemes, from 3rd order harmonics to 54th order harmonics and higher even order harmonics (above 54th harmonics) are less than 1%. Few of the odd order harmonics from 55th harmonics to 79th harmonics for the above mentioned scheme are less than 2%. The dominant 57th harmonic factor is about 2% for the PD and IPD schemes.

In the POD scheme, from 3rd odd order harmonics to 19th odd order harmonics are less than 1% and all even order harmonics are 0.01%. Few of the odd order harmonics from 21st harmonics to 79th harmonics are 1% to 2%. The dominant 39th and 41st harmonic factor are 6.55% and 6.16% respectively for the POD scheme. In the APOD scheme, from 3rd odd order harmonics to 25th odd order harmonics are less than 1% and all even order harmonics are 0.01%. Few of the odd order harmonics from 27th harmonics to 79th harmonics are present. The dominant 29th and 51st harmonic factor are 5.17% and 4.98% respectively for the APOD scheme.

It is observed that, when the switching frequency of the CCMLI is increased, the percentage line voltage THD is decreased very slightly and the fundamental phase and line voltage are increased very slightly for the PD and IPD schemes. In the POD and APOD schemes, if the switching frequency is increased, the percentage line voltage THD is decreased very slightly and the fundamental phase and line voltage are increased very slightly. Also the fundamental line voltage is maximum for POD and APOD schemes and is minimum for PD and IPD schemes.

5. CONCLUSION

In this paper, the performance of different multicarrier PWM techniques which uses triangular multicarrier waveform and stepped multicarrier waveform in multilevel inverters is found out. In all the above PWM techniques, different modulation strategies such as phase disposition (PD), inverted phase disposition (IPD), phase opposition disposition (POD) and alternative phase opposition disposition (APOD) are implemented. The results are verified by doing simulation for a 1kW, 3 ϕ seven-level cascaded inverter in MATLAB/SIMULINK. The output quantities like fundamental phase and line voltage, percentage THD of the line voltage and percentage dominant harmonic factor are measured in the all the above PWM schemes and the results are compared.

REFERENCES

- [1] Mariusz Malinowski, K. Gopakumar, Jose Rodriguez and Marcelo A. Pérez, "A Survey on Cascaded Multilevel Inverters" IEEE Transactions on Industrial Electronics, vol. 57, n. 7, July 2010, pp 2197 – 2206.
- [2] R.Nagarajan and M,Saravanan, "Performance Analysis of Multicarrier PWM Strategies for Cascaded Multilevel Inverter," European Journal of Scientific Research (EJSR), Vol.92 No.4, pp. 608-625, Dec. 2012.
- [3] Jang-Hwan Kim, A carrier-Based PWM Method for Three-Phase Four-Leg Voltage Source Converters", IEEE transactions on power electronics, vol. 19, n.1, January 2004.
- [4] R.Nagarajan and M,Saravanan, "A Carrier - Based Pulse Width Modulation Control Strategies for Cascaded Multilevel Inverter," International Review on Modeling and Simulations (IRMOS), Vol 6.No1, pp-8-19, Feb. 2013.
- [5] G.Carrara, S.Gardella, M.Marchesoni, R.Salutari, G.Sciutto, "A New Multilevel PWM Method: A Theoretical Analysis," IEEE Trans. Power Electronics, vol. 7, n.3, July 1992, pp 497-505.
- [6] R.Nagarajan and M, Saravanan, "Comparison of PWM Control Techniques for Cascaded Multilevel Inverter" International Review of Automatic control (IRACO), Vol.5, No.6, pp. 815-828. Nov. 2012.
- [7] G. Vidhya Krishnan, R.Nagarajan, T. Durka, M.Kalaiselvi, M.Pushpa and S. Shanmuga priya, "Vehicle Communication System Using Li-Fi Technology," International Journal of Engineering And Computer Science (IJECs), Volume 6, Issue 3, pp. 20651-20657, March 2017.
- [8] S.M.Ayob, Z.Salam, "Trapezoidal PWM Scheme for Cascaded Multilevel Inverter" First International Power and Energy Conference, November 2006, pp 368-372.
- [9] M.Dharani Devi and R.Nagarajan, "Implementation of Different PWM Control Strategies for Cascaded MLI," Journal of Network Communications and Emerging Technologies (JNCET), Volume 7, Issue 7, pp. 49- 55, July-2017.
- [10] R.Prabhu, R.Nagarajan, N.Karthick and S.Suresh, "Implementation of Direct Sequence Spread Spectrum Communication System Using FPGA," International Journal of Advanced Engineering, Management and Science (IJAEMS), Vol-3.Issue-5, pp. 488-496, May. 2017
- [11] Rodriguez, Jih-sheng lai, and F.Zheng peng, "Multilevel Inverters; A Survey of Topologies, Controls, and Applications," IEEE Trans.Ind.Electron, vol.49, n. 4, pp724-738, Aug.2002.
- [12] R. Banupriya, R.Nagarajan, M.Malarvizhi and M.Dharani Devi, "Multicarrier - Based PWM Control Strategies for Five - Level CMLI." Journal of Network Communications and Emerging Technologies (JNCET), Vol. 7, Issue 11, November - 2017, pp. 33-39.
- [13] M.Dharani Devi, M.Malarvizhi and R.Nagarajan, "Development of Multicarrier SPWM Techniques for Cascaded MLI." International Journal of Computational Engineering Research (IJCER), Vol. 7, Issue 10, October 2017, pp. 44-52.
- [14] J.Chandramohan, R.Nagarajan, K.Satheeshkumar, N.Ajithkumar, P.A.Gopinath and S.Ranjithkumar, "Intelligent Smart Home Automation and Security System Using Arduino and Wi-fi," International Journal of Engineering And Computer Science (IJECs), Volume 6, Issue 3, pp. 20694-20698, March, 2017.
- [15] Samir koaro, PabloLezana, Mauricio Anguio and Jose Rodriguez, "Multicarrier PWM DC-Link ripple forward compensation for multilevel inverters," IEEE Trans. Power.Electron., vol.123, n.1, pp.52-56, Jan 2008.
- [16] K. Anandhi and Dr. R. Nagarajan, "Mutex-Heart: Fail Safe Dual Chamber Cardiac Pacemaker Device with Rate Responsive Control and Cryptographic Security," IJSD- International Journal for Scientific Research & Development. Vol. 3, Issue- 2, pp. 489-493, 2015.
- [17] Fang.Z. Peng, John W.Mckeever, and Donald J.Adams, "A Power line conditioner using Cascade Multilevel Inverters for Distribution systems" IEEE Transactions on Industrial Applications, vol. 34, n.6, pp 1293-1298, Nov/Dec 1998.
- [18] J.Chandramohan, R.Nagarajan, M.Ashok kumar, T.Dineshkumar, G.Kannan and R.Prakash, "Attendance Monitoring System of Students Based on Biometric and GPS Tracking System," International Journal of

- Advanced Engineering, Management and Science (IAEMS), Vol-3, Issue-3, pp. 241-246, Mar. 2017.
- [19] B.P.Mcgrath, D.G.Holmes, "Multicarrier PWM strategies for multilevel inverters," IEEE Trans. Ind.Electron, vol 49, n.4, pp 858-867, Aug.2002.
- [20] R Rameshkumar and R Nagarajan, "Sine Multicarrier SPWM Technique for Seven Level Cascaded Inverter," CiiT-Programmable Device Circuits and Systems. Vol. 5, Issue- 6, 2013.
- [21] Dr.R.Nagarajan, S.Sathishkumar, K.Balasubramani, C.Boobalan, S.Naveen and N.Sridhar, "Chopper Fed Speed Control of DC Motor Using PI Controller," IOSR- Journal of Electrical and Electronics Engineering (IOSR-JEEE), Volume 11, Issue 3, Ver. I, pp. 65-69, May – Jun. 2016.
- [22] R.Nagarajan and M,Saravanan "Staircase Multicarrier SPWM Technique for Nine Level Cascaded Inverter," 2013 International Conference on Power, Energy and Control (ICPEC), IEEE Press, pp-668-675. 2013.
- [23] Lion M.Tolbert and Thomas.G.Habetler, "Novel Multi Level Inverter Carrier Based PWM methods", IEEE IAS, 1998, pp 1424-1431.
- [24] N.Karthick, R.Nagarajan, S.Suresh and R.Prabhu, "Implementation of Railway Track Crack Detection and Protection," International Journal Of Engineering And Computer Science (IJECS), Volume 6, Issue 5, May 2017, pp. 21476-21481, DOI: 10.18535/ijecs/v6i5.47
- [25] M.Padmavathi and R.Nagarajan, "Smart Intelligent ATM Using LABVIEW," International Journal of Emerging Technologies in Engineering Research (IJETER), Volume 5, Issue 5, pp. 41- 45, May-2017.
- [26] R.Nagarajan and M, Saravanan. "Performance Analysis of a Novel Reduced Switch Cascaded Multilevel Inverter," Journal of Power Electronics, Vol.14, No.1, pp. 48-60, Jan.2014.
- [27] D.G.Holmes and T.A.Lipo, Pulse Width Modulation For Power Converters (Wiley Inter-science, 2003).J. Proakis, Digital Communications. New York: McGraw-Hill, 1995.
- [28] R.Nagarajan, S.Sathishkumar, S.Deepika, G.Keerthana, J.K.Kiruthika and R.Nandhini, "Implementation of Chopper Fed Speed Control of Separately Excited DC Motor Using PI Controller", International Journal of Engineering And Computer Science (IJECS), Volume 6, Issue 3, pp. 20629-20633, March, 2017.
- [29] D.G.Holmes and B.P.Mcgrath, "Opportunities for harmonic cancellation with carrier based PWM for two level and multilevel cascaded inverters", in conf.prec IEEE/IAS Annual meeting, 1999.
- [30] R.Nagarajan, R.Yuvaraj, V.Hemalatha, S.Logapriya, A.Mekala and S.Priyanga, "Implementation of PV - Based Boost Converter Using PI Controller with PSO Algorithm," International Journal of Engineering And Computer Science (IJECS), Volume 6, Issue 3, pp. 20479-20484, March, 2017.
- [31] Ms. C. Hemalatha, Mr. R. Nagarajan, P. Suresh, G. Ganesh Shankar and A. Vijay, "Brushless DC Motor Controlled by using Internet of Things," IJSTE - International Journal of Science Technology & Engineering, Volume -3, Issue-09, pp. 373-377, March- 2017.
- [32] R.Nagarajan, J.Chandramohan, S.Sathishkumar, S.Anantharaj, G.Jayakumar, M.Visnukumar and R.Viswanathan, "Implementation of PI Controller for Boost Converter in PV System," International Journal of Advanced Research in Management, Architecture, Technology and Engineering (IJARMATE). Vol.11, Issue.XII, pp. 6-10, December. 2016.
- [33] M.Elangovan, R.Yuvara, S.Sathishkumar and R.Nagarajan, "Modelling and Simulation of High Gain Hybrid Boost Converter," International Journal of Emerging Technologies in Engineering Research (IJETER), Volume 5, Issue 6, pp. 9- 14, June-2017
- [34] S.Suresh, R.Nagarajan, L.Sakthivel, V.Logesh, C.Mohandass and G.Tamilselvan, "Transmission Line Fault Monitoring and Identification System by Using Internet of Things," International Journal of Advanced Engineering Research and Science (IJAEERS), Vol - 4, Issue - 4, pp. 9-14, Apr- 2017.
- [35] R.Nagarajan, J.Chandramohan, R.Yuvaraj, S.Sathishkumar and S.Chandran, "Performance Analysis of Synchronous SEPIC Converter for a Stand-Alone PV System," International Journal of Emerging Technologies in Engineering Research (IJETER), Vol. 5, Issue - 5, pp. 12-16, May-2017
- [36] M. Sridhar, S.Sathishkumar, R.Nagarajan and R.Yuvaraj, "An Integrated High Gain Boost Resonant Converter for PV System," International Journal of Emerging Technologies in Engineering Research (IJETER), Volume 5, Issue 6, pp. 54- 59, June-2017.
- [37] J.Hamman and F.S.Van Der merwe, "Voltage harmonics generated by voltage fed inverters using PWM natural sampling" IEEE Trans. Power Electron, vol PE-3,n.3, pp.297-302, Jul.1988.
- [38] S.Suresh, R.Nagarajan, R.Prabhu and N.Karthick, "Energy Efficient E0 Algorithm for Wireless Transceivers," International Journal of Engineering and Computer Science (IJECS), Volume 6, Issue 7, July 2017, pp. 21982-21985, DOI: 10.18535/ijecs/v6i7.15.

Authors



M.Meenakshi received her B.E. in Electrical and Electronics Engineering from Anna University, Trichy, India, in 2012. She received her M.E. in Power Electronics and Drives from Anna University, Chennai, India, in 2016. She has worked in the various institution as an Assistant Professor. She is currently working as an Assistant Professor of Electrical and Electronics Engineering at M.A.M.School of Engineering, Trichy, Tamilnadu, India. Her research interest includes Power Electronics and Renewable Energy Sources.



R. Nagarajan received his B.E. in Electrical and Electronics Engineering from Madurai Kamarajar University, Madurai, India, in 1997. He received his M.E. in Power Electronics and Drives from Anna University, Chennai, India, in 2008. He received his Ph.D in Electrical Engineering from Anna University, Chennai, India, in 2014. He has worked in the industry as an Electrical Engineer. He is currently working as Professor of Electrical and Electronics Engineering at Gnanamani College of Technology, Namakkal, Tamilnadu, India. His current research interest includes Power Electronics, Power System, Soft Computing Techniques and Renewable Energy Sources.



R. Banupriya received her B.E. in Electrical and Electronics Engineering from Anna University, Chennai, India, in 2010. She received her M.E. Power Electronics and Drives from Anna University, Chennai, India, in 2012. She has worked in the industry as an Asst. Deputy Manager. She is currently working as an Assistant Professor of Electrical and Electronics Engineering at P.G.P. College of Engineering and Technology, Namakkal, Tamilnadu, India. Her research interest includes Power Electronics and Renewable Energy Sources.



M. Dharani Devi received her B.E. in Electronics and Instrumentation Engineering from Madurai Kamaraj University, Madurai, India, in 2003. She received her M.E. in Process control and Instrumentation Engineering from Annamalai University, Chidambaram, India, in 2005. She has worked in the various institution as an Associate Professor. She is currently working as an Associate Professor of Electrical and Electronics Engineering at M.A.M.School of Engineering, Trichy, Tamilnadu, India. Her research interest includes Process Control, Power Electronics and Renewable Energy Sources.

See discussions, stats, and author profiles for this publication at: <https://www.researchgate.net/publication/320867741>

Development of Multicarrier SPWM Techniques for Cascaded MLI

Article · October 2017

CITATIONS

13

READS

318

3 authors, including:



[Nagarajan Ramalingam](#)

Gnanamani College of Technology

89 PUBLICATIONS 804 CITATIONS

[SEE PROFILE](#)

Some of the authors of this publication are also working on these related projects:



POWER ELECTRONICS [View project](#)

Development of Multicarrier SPWM Techniques for Cascaded MLI

M.Dharani Devi¹, M.Malarvizhi², R.Nagarajan³

¹Asso. Professor, Department of Electrical and Electronics Engineering, M.A.M. School of Engineering, Trichy, India.

²Asso. Professor, Department of Electrical and Electronics Engineering, Gnanamani College of Technology, Namakkal, India.

³Professor, Department of Electrical and Electronics Engineering, Gnanamani College of Technology, Namakkal, India.

Corresponding Author: M.Dharani Devi

ABSTRACT

In this paper, investigates and analysis the performance of the novel pulse width modulation techniques which uses unipolar sine carrier waveform and staircase carrier waveform are proposed for five-level cascaded inverter. In each carrier waveform, different techniques such as phase disposition (PD), inverted phase disposition (IPD), phase opposition disposition (POD) and alternative phase opposition disposition (APOD) are implemented. The fundamental output voltage and harmonics obtained in each method are compared with the output waveform obtained with the triangular carrier waveform. The different PWM methodologies adopting the constant switching frequency multicarrier with different modulation indexes are simulated for a 1kW, 3 ϕ cascaded multilevel inverter using MATLAB/SIMULINK and the effect of switching frequency on the fundamental output voltage and harmonics are also analyzed. The proposed switching technique enhances the fundamental component of the output voltage and reduces the total harmonic distortion.

Keywords: Modulation Index (MI), Staircase Multicarrier SPWM (SCMC SPWM), Total Harmonic Distortion (THD), Triangular Multicarrier SPWM (TMC SPWM), Unipolar Sine Multicarrier SPWM (USMC SPWM)

Date of Submission: 24-10-2017

Date of acceptance: 04-11-2017

I. Introduction

The multilevel inverter is an effective solution for increasing power and reducing harmonics of ac waveform [1]. The elementary concept of a multilevel converter to achieve higher power is to use a series of power semiconductor switches with several lower voltage dc sources to perform the power conversion by synthesizing a staircase voltage waveform. Capacitors, batteries, and renewable energy voltage sources can be used as the multiple dc voltage sources. The commutation of the power switches aggregate these multiple dc sources in order to achieve high voltage at the output; however, the rated voltage of the power semiconductor switches depends only upon the rating of the dc voltage sources to which they are connected [2].

In this paper, constant switching frequency multicarrier pulse width modulation method is used for the multilevel inverter [3]. The control objective is to compare the reference sine wave with multicarrier waves for three phase five level cascaded inverters. Multilevel voltage source inverter (MVSI) structure is very popular especially in high power DC to AC power conversion applications. It offers several advantages that make it preferable over the conventional voltage source inverter (VSI). These include the capability to handle higher DC link voltage; the stress on each switching device can be reduced in proportional to the higher voltages [4]. Consequently, in some applications, it is possible to avoid expensive and bulky step-up transformer. Another significant advantage of a multilevel output is better sinusoidal voltage waveform. As a result, a lower total harmonic distortion (THD) is obtained [5], [6]. The concept of multilevel converter has been introduced since 1975 [7]. The term multilevel began with the three-level converter [6]. Subsequently, several multilevel converter topologies have been developed, such as the Diode Clamped Multilevel Inverter (DCMLI) also known as Neutral Point Clamped (NPC) Inverter, Flying Capacitor Multilevel Inverter (FCMLI) and Cascaded Multilevel Inverter (CCMLI) [8], [9]. Among them, CCMLI topology is the most attractive, since it requires the least number of components and increases the number of levels in the inverter without requiring high ratings on individual devices and the power rating of the CCMLI is also increased. It also results in simple circuit layout

and is modular in structure. Furthermore, CCMLI type of topology is free of DC voltage balancing problem, which is a common issue facing in the DCMLI and FCMLI topologies [10], [11].

Numerous industrial applications have begun to require higher power apparatus in recent years. Some medium voltage motor drives and utility applications require medium voltage and megawatt power level. For a medium voltage grid, it is troublesome to connect only one power semiconductor switch directly [12]. As a result, a multilevel power converter structure has been introduced as an alternative in high power and medium voltage situations. A multilevel converter not only achieves high power ratings, but also enables the use of renewable energy sources. Renewable energy sources such as photovoltaic, wind, and fuel cells can be easily interfaced to a multilevel converter system for high power application [13]

In motor applications, high dv/dt in power supply generates high stress on motor windings and requires additional motor insulation. Further; high dv/dt of semiconductor devices increases the electromagnetic interference (EMI), common-mode voltage and possibilities of failure on motor [14], [15]. By increasing the number of levels in the output waveform, the switching dv/dt stress is reduced in the multilevel inverter [16], [17]. Multilevel inverters are suitable for power electronics applications such as flexible ac transmission systems, renewable energy sources, uninterruptible power supplies, electrical drives and active power filters.

II. Cascaded Multilevel Inverter

The single-phase structure of three phase five-level cascaded inverter is illustrated in Figure 1. Each separate dc source is connected to a single-phase full-bridge, or H-bridge, inverter. Each inverter can generate three different outputs voltage level, $+V_{dc}$, 0 and $-V_{dc}$, by connecting the dc source to the ac output by different switching combinations of the four semiconductor switches S1, S2, S3 and S4. To obtain $+V_{dc}$, switches S1 and S2 are tuned on, whereas $-V_{dc}$ can be obtained by tuning on switches S3 and S4, By turning on S1 and S3 or S2 and S4, the output voltage is 0, The ac outputs of each of the full-bridge inverter levels are connected in series such that the synthesized voltage waveform is the sum of the inverter outputs [18], [19].

The CCMLI is producing five level output and they are $2V_{dc}$, V_{dc} , 0, $-V_{dc}$ and $-2V_{dc}$. This topology is suitable for applications where separate dc voltage sources are available, such as photovoltaic (PV) generators, fuel cells and batteries. The phase output voltage is generated by the sum of two output voltage of the full bridge inverter modules. The circuit in Figure1 utilizes two independent dc sources and consequently will create an output phase voltage with five-level. In general, if N is the number of independent dc sources per phase, then the following relations apply [20]:

$$m = 2N + 1 \tag{1}$$

$$q = 2(m - 1) \tag{2}$$

Where m is the number of levels and q is the number of switching devices in each phase

The most well known SPWM which can be applied to a CCMLI is the Phase-Shifted SPWM. This modulation technique is the same as that of the conventional SPWM technique which is applied to a conventional single phase full-bridge inverter, the only difference being that it utilizes more than one carrier. The number of carriers to be used per phase is equal to twice the number of dc voltage sources per phase (2N) [21]. Figure 2 presents the simulation model of a three-phase five-level CCMLI and is developed using MATLAB/SIMULINK. The simulation results are obtained for the output phase voltage and line voltage of the three phase five-level CCMLI with 1kW, 3φ resistive loads for various PWM techniques.

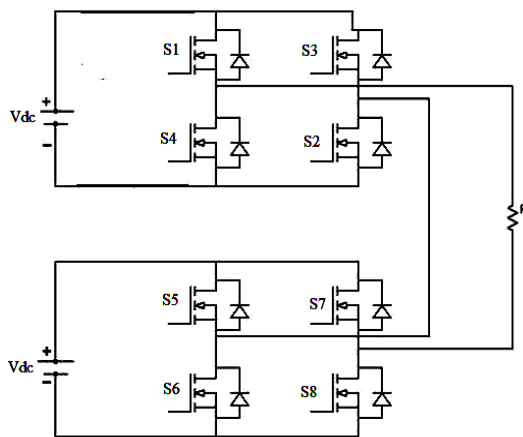


Figure 1 1φ structure of five-level CCMLI

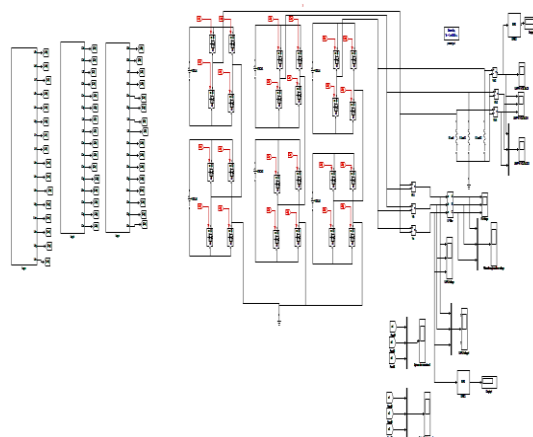


Figure 2 Simulation model of 3φ five-level CCMLI

III. Modulation Techniques

The Pulse Width Modulation (PWM) control strategies development tries to reduce the total harmonic distortion (THD) of the output voltage. Any deviation in the output voltage of the sinusoidal wave shape will result in harmonic currents in the load and this harmonic current produces the electromagnetic interference (EMI), harmonic losses and torque pulsation in the case of motor drives. Increasing the switching frequency of the PWM pattern reduces the lower frequency harmonics by moving the switching frequency carrier harmonic and associated sideband harmonics away from the fundamental frequency component [22]. This increased switching frequency reduces harmonics, which results in a lower THD with high quality output voltage waveforms of desired fundamental RMS value and frequency which are as close as possible to sinusoidal wave shape [23]. The carrier frequency defines the switching frequency of the converter and the high order harmonic components of the output voltage spectrum and the sidebands occur around the carrier frequency and its multiples. The higher switching frequency can be employed for low and medium power inverters, whereas, for high power and medium voltage applications the switching frequency should be low. Harmonic reduction can then be strictly related to the performance of an inverter with any switching strategy [24], [25]. The three phase multi level inverter requires three modulating signals or reference signals which are three sine-waves with 120 degree phase shift and equal in magnitudes. In this paper, new carrier based PWM techniques are developed which are as, Unipolar Sine Multicarrier Sinusoidal PWM (USMC SPWM) and Staircase Multicarrier Sinusoidal PWM (SCMC SPWM). Each carrier is to be compared with the corresponding modulating sine wave [26], [27]. The reference or modulation waveform has peak amplitude A_r and frequency f_r and it is centered in the middle of the carrier set. The general principle of a carrier based PWM technique is the comparison of a sinusoidal waveform with a carrier waveform, this typically being a triangular carrier waveform. The reference is continuously compared with the carrier signal. If the reference is greater than the carrier signal, then the active device corresponding to that carrier is switched on, and if the reference is less than the carrier signal, then the active device corresponding to that carrier is switched off [28], [29]. In multilevel inverters, the amplitude modulation index, M_a and the frequency ratio, M_f are defined as,

$$M_a = \frac{A_r}{(m-1)A_c} \quad (3)$$

$$M_f = \frac{f_c}{f_r} \quad (4)$$

Where A_r and A_c are amplitude of reference and carrier signal respectively. f_r and f_c are frequency of reference and carrier signal respectively.

In this paper, modulation indexes used are 0.6, 0.7, 0.8, 0.9 and 1 for five-level CCMLI. For multilevel applications, carrier based PWM techniques with multiple carriers are used. The Multicarrier Modulation (MCM) techniques, can be divided in to the following categories such as [30], [31],

1. Phase disposition (PD) where all the carriers are in phase.
2. Inverted phase disposition (IPD) where all the carriers are in phase and is inverted.
3. Phase opposition disposition (POD) where the carriers above the zero reference are in phase but shifted by 180 degrees from those carriers below the zero reference.
4. Alternative phase opposition disposition (APOD) where each carrier band is shifted by 180 degrees from the adjacent carrier bands [2].

The above modulation strategies are implemented for different carriers such as unipolar sine wave and staircase wave. The phase voltage and line voltage waveform, harmonic spectrums of the line voltage are shown for different modulation techniques by doing simulation using MATLAB/SIMULINK for five-level CCMLI and the results obtained are compared.

3.1. Triangular Multicarrier Sinusoidal PWM (TMC SPWM)

The performance of the multilevel inverter is based on the multi carrier modulation technique used. Two-level to multilevel inverters are made using several triangular carrier signals and one reference signal per phase. Carrara [5] developed multilevel sub harmonic PWM (SH-PWM), which is as follows, for m-level inverter, m-1 carriers [32] with the same frequency f_c and same amplitude A_c are disposed such that the bands they occupy are contiguous. They are defined as

$$C_i = A_c \left((-1)^{f(i)} y_c(\omega_c, \varphi) + t - \frac{m}{2} \right), \quad (5)$$

$$i = 1, \dots, (m-1)$$

Where y_c is a normalized symmetrical triangular carrier defined as,

$$y_c(\omega_c, \varphi) = (-1)^{[\alpha]} \left((\alpha \bmod 2) - 1 \right) + \frac{1}{2} \quad (6)$$

$$\alpha = \frac{\omega_c t + \varphi}{\pi}, \omega_c = 2\pi f_c \quad (7)$$

φ represents the phase angle of y_c . y_c is a periodic function with the period $T_c = \frac{2\pi}{\omega_c}$. It is shown that using

symmetrical triangular carrier generates less harmonic distortion at the inverters output [33], [34]. The carrier waveforms, output voltage waveforms and %THD chart are shown only for selected PWM techniques in order to restrict the number of figures.

In TMC SPWM, so far only the PD, POD and APOD techniques are discussed earlier in the literature. In this paper, IPD scheme is also applied to TMC SPWM and it is found that this scheme gives the lowest THD among the TMC SPWM schemes. The multicarrier modulation techniques (PD, IPD, POD and APOD) are implemented using triangular multicarrier signals for five-level CCMLI with different modulation indexes and are shown in Figure 3(a) and 3(b) respectively.

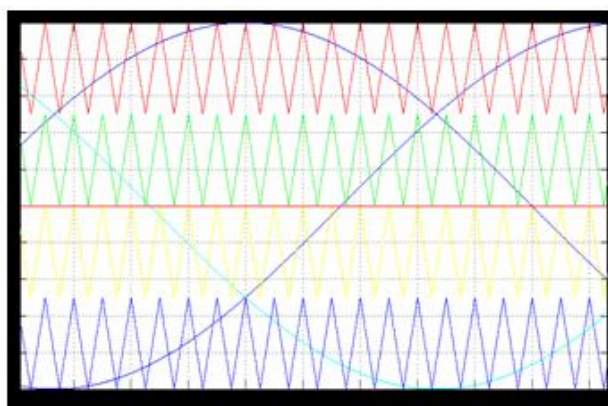


Figure 3(a): IPD TMC SPWM with $M_a=1$

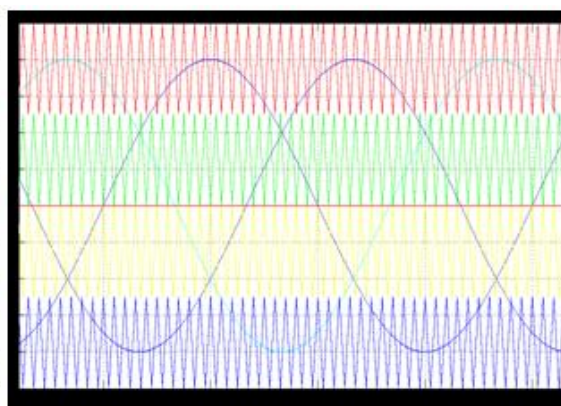


Figure 3(b): POD TMC SPWM with $M_a=0.8$

3.2. Unipolar Sine Multicarrier Sinusoidal PWM (USMC SPWM)

In this PWM technique, the sinusoidal signal is converted in to the unipolar sinusoidal signal [35]. The entire negative half cycles in the waveform is converted into positive half cycles with the same amplitude and frequency. This signal is same as that of the full wave rectifier output. That is the signal has only continuous positive half cycles. This is called unipolar sine wave. The control strategy uses the same reference (synchronized sinusoidal signal) as the conventional SPWM while the carrier triangle is a modified one. The control scheme uses a high frequency sine carrier that helps to maximize the output voltage for a given modulation index [36]-[38]. The multicarrier modulation techniques (PD, IPD, POD and APOD) are implemented using unipolar sine multicarrier signals for five level CCMLI with different modulation indexes and are shown in Figure 4(a) and 4(b) respectively.

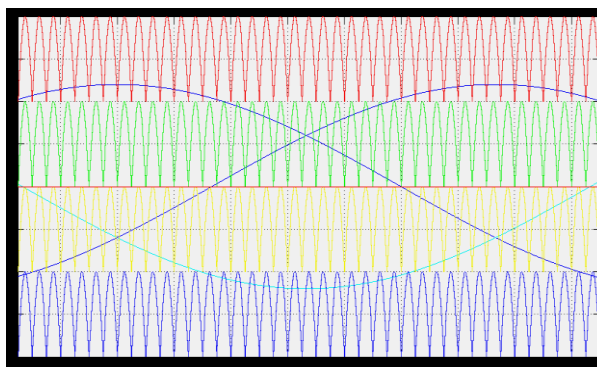


Figure 4(a): PD USMC SPWM with $M_a=0.6$

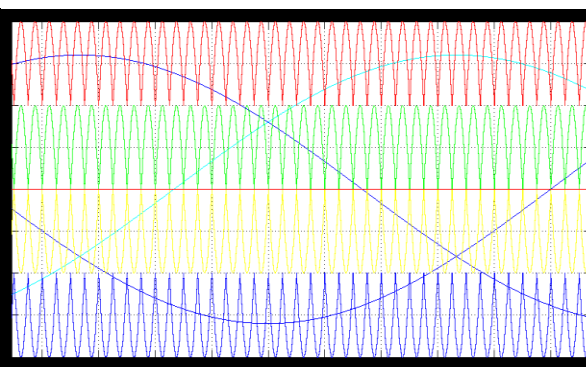


Figure 4(b): POD USMC SPWM with $M_a=0.8$

3.3. Staircase Multicarrier Sinusoidal PWM (SCMC SPWM)

Staircase wave is also known as approximated or modified triangular wave and is obtained from the repeated sequence carrier wave by limiting its magnitude to A_c ; it is obtained from simulink block, Stair case wave is the periodic signal which passes its input signal through a stair-step function so that many neighboring points on the input time axis are mapped to one point on the output magnitude axis. The effect is to make a smooth stair-step signal. The output is computed using the round-to-nearest method, which produces an output that is symmetric about zero.

$$y_q = q \times \left(\frac{u}{n} \right), (0 \leq t \leq \frac{T}{2}) \quad (8)$$

$$y = 2\left(1 - \frac{t}{T}\right), \left(\frac{T}{2} \leq t \leq T\right) \quad (9)$$

Where q is the step number = 1, 2... 8, n is the max number of steps = 8, y is the output, u is the peak voltage and T is the period of staircase waveform. After the maximum step (magnitude), the magnitude reduces linearly and comes to zero and the process repeats. The number of steps for each stair case wave is nine.

The multicarrier modulation techniques (PD, IPD, POD and APOD) are implemented using staircase multicarrier signals for five level CCMLI with different modulation indexes and are shown in Figure 5(a) and 5(b) respectively.

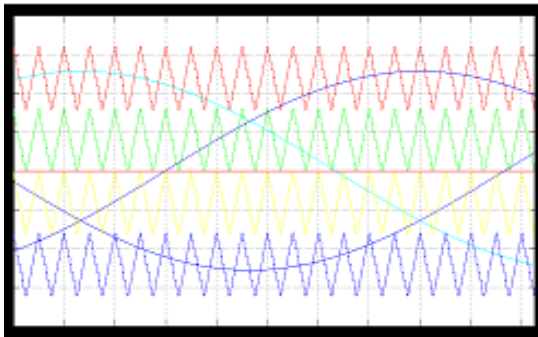


Figure 5(a): IPD SCMC SPWM with Ma=0.8

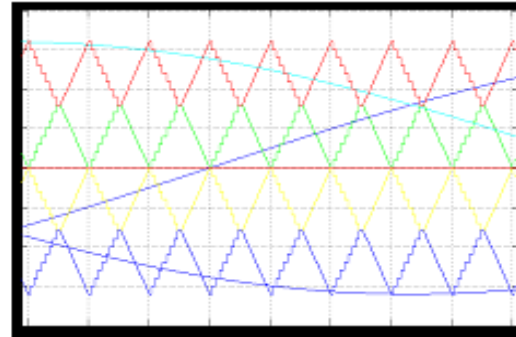


Figure 5(b): APOD SCMC SPWM with Ma=1

IV. Simulation Results

The five level cascaded multilevel inverter model with different modulation indexes was implemented in MATLAB/SIMULINK software to demonstrate the feasibility of PWM techniques. Phase disposition, inverted phase disposition, phase opposition disposition and alternative phase opposition disposition techniques are used for the various multicarrier SPWM techniques such as

1. Triangular Multicarrier Sinusoidal PWM
2. Unipolar Sine Multicarrier Sinusoidal PWM
3. Staircase Multicarrier Sinusoidal PWM

The line voltage waveform with its harmonic spectrum at fundamental frequency of 50Hz and switching frequency of 2kHz and 10kHz are obtained for the proposed CCMLI. For comparison, the total harmonic distortion (THD) was chosen to be evaluated for all the modulation techniques. In order to get THD level of the waveform, a Fast Fourier Transform (FFT) is applied to obtain the spectrum of the output voltage. The THD is calculated using the following equation in this work.

$$THD = \frac{\sqrt{\sum_{n=2}^{80} v_n^2}}{v_1} \quad (10)$$

Where n is the harmonic order, v_n is the RMS value of the n^{th} harmonic component and v_1 is the RMS value of the fundamental component. Here the %THD is calculated up to a harmonic order which is twice the switching frequency. For 2kHz switching frequency up to 80th order harmonics is taken in to account for calculating THD and for 10kHz switching frequency up to 400th order harmonics is taken in to account for calculating THD.

4.1. Triangular Multi Carrier SPWM (TMC SPWM)

Figure 6(a) and 6(b) show the line voltage waveforms and the percentage THD of the line voltage for five level using the inverted phase disposition technique for triangular multi carrier sinusoidal PWM with Ma=1.

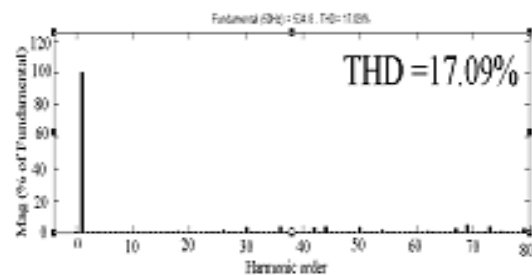
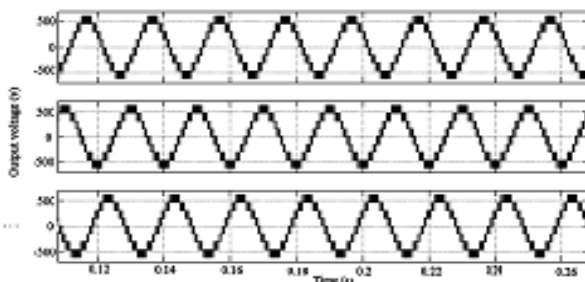


Figure 6(a): Line Voltage for IPD SPWM with Ma=1 Figure 6(b): Line Voltage %THD for IPD SPWM with Ma=1

Table 1 shows the percentage line voltage THD for the five-level CCML with triangular multicarrier signal with different multicarrier PWM techniques with a switching frequency of 2kHz and 10kHz respectively for different modulation indexes.

Table1: Line voltage %THD for TMC SPWM

Modulation Technique	Line voltage %THD									
	2kHz					10kHz				
	$M_a=1$	$M_a=0.9$	$M_a=0.8$	$M_a=0.7$	$M_a=0.6$	$M_a=1$	$M_a=0.9$	$M_a=0.8$	$M_a=0.7$	$M_a=0.6$
PD	17.11	17.55	21.73	24.14	25.62	17.58	17.77	21.81	24.21	28.03
IPD	17.09	17.55	21.73	24.14	25.62	17.56	17.77	21.81	24.21	28.03
POD	21.89	29.94	35.48	38.65	38.42	23.91	31.42	36.45	38.63	37.68
APOD	25.66	28.75	29.75	28.04	25.93	27.07	29.57	30.46	28.85	29.33

From the above table, it is observed that, when the switching frequency of the CCMLI is increased, the percentage line voltage THD is increased for the PD and IPD schemes with all modulation indexes. In the POD scheme, if the switching frequency is increased, the percentage line voltage THD is reduced with modulation index of 0.7 and 0.6. In the APOD scheme, when the switching frequency is increased, the percentage line voltage THD is increased with all modulation indexes, in five-level CCMLI. From the simulation result in the triangular multicarrier SPWM technique PD and IPD PWM schemes, from 3rd order harmonics to 25th order harmonics are less than 1%. Few of the odd and even order harmonics from 26th harmonics to 79th harmonics are present. The dominant 69th harmonic factor is about 5% for the PD and IPD schemes. In the POD scheme, from 3rd odd order harmonics to 27th odd order harmonics are less than 1% and all even order harmonics are zero. Few of the odd order harmonics from 29th harmonics to 79th harmonics are 1% to 3%. The dominant 39th and 41st harmonic factor are 10.29% and 10.46% respectively for the POD scheme. In the APOD scheme, from 3rd odd order harmonics to 31st odd order harmonics are less than 1% and all even order harmonics are 0.03%. Few of the odd order harmonics from 33rd harmonics to 79th harmonics are present. The dominant 35th and 45th harmonic factor are 11.94% and 11.87% respectively for the APOD scheme.

It is observed that, when the switching frequency of the CCMLI is increased, the percentage line voltage THD is increased very slightly and the fundamental phase and line voltage are decreased for the PD and IPD schemes. In the POD and APOD schemes, if the switching frequency is increased, the percentage line voltage THD is increased and the fundamental phase and line voltage are decreased very slightly. Also the fundamental line voltage is maximum for APOD scheme and is minimum for PD and IPD schemes.

4.2. Unipolar Sine Multi Carrier SPWM (USMC SPWM)

Figure 7(a) and 7(b) show the line voltage waveforms and the percentage THD of the line voltage for five-level using the inverted phase disposition technique for unipolar sine multicarrier sinusoidal PWM with $M_a=0.9$.

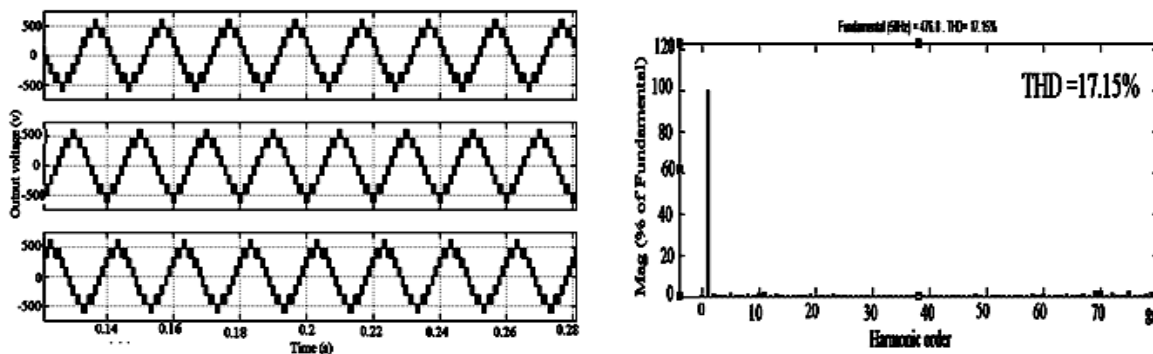


Figure 7(a): Line Voltage for IPD SPWM with $M_a=0.9$ Figure 7(b): Line Voltage %THD for IPD SPWM with $M_a=0.9$

Table 2 shows the percentage line voltage THD for the five and three level CCML with unipolar sine multicarrier signal with different multicarrier PWM techniques with a switching frequency of 2kHz and 10kHz respectively for different modulation indexes.

Table 2: Line voltage %THD for USMC SPWM

Modulation Technique	Line voltage %THD									
	2kHz					10kHz				
	$M_a=1$	$M_a=0.9$	$M_a=0.8$	$M_a=0.7$	$M_a=0.6$	$M_a=1$	$M_a=0.9$	$M_a=0.8$	$M_a=0.7$	$M_a=0.6$
PD	17.67	17.15	20.49	23.38	26.24	18.09	16.89	19.82	23.21	27.24
IPD	17.67	17.15	20.49	23.38	26.24	18.09	16.89	19.82	23.21	27.24
POD	27.89	36.16	39.83	41.02	41.68	28.39	35.17	41.86	43.56	49.48
APOD	26.70	28.81	30.14	29.80	27.44	30.48	29.00	27.90	34.10	29.38

From the above table, it is observed that, when the switching frequency of the CCMLI is increased, the percentage line voltage THD is increased for the PD and IPD schemes with modulation index of 1 and 0.6. In the POD scheme, if the switching frequency of the CCMLI is increased, the percentage line voltage THD is reduced with modulation index of 0.9. In the APOD scheme, when the switching frequency of the CCMLI is increased, the percentage line voltage THD is reduced with modulation index of 0.8, in five-level CCMLI. If the output voltage level increases the percentage line voltage THD decreases. From the simulation result in the unipolar sine multi carrier SPWM technique PD and IPD PWM schemes, from 3rd order harmonics to 66th order harmonics are less than 1%. Few of the higher odd order harmonics and even order harmonics from 67th harmonics to 79th harmonics for the above mentioned scheme are less than 3%. The dominant 76th harmonic factor is about 3% for the PD and IPD schemes. In the POD scheme, from 3rd odd order harmonics to 5th order harmonics are less than 1% and all even order harmonics are zero. Few of the odd order harmonics from 7th harmonics to 79th harmonics are 1% to 2%. The dominant 73rd and 79th harmonic factor are 6.82% and 15.00% respectively for the POD scheme. In the APOD scheme, from 3rd odd order harmonics to 5th odd order harmonics are less than 1% and all even order harmonics are zero. Few of the odd order harmonics from 7th harmonics to 79th harmonics are present. The dominant 73rd and 75th harmonic factor are 6.56% and 10.50% respectively for the APOD scheme.

It is observed that, when the switching frequency of the CCMLI is increased, the percentage line voltage THD is increased very slightly and the fundamental phase and line voltage are decreased for the PD and IPD schemes. In the POD scheme, if the switching frequency is increased, the percentage line voltage THD, the fundamental phase and line voltage are increased. In the APOD scheme, when the switching frequency is increased, the percentage line voltage THD is increased and the fundamental phase and line voltage are decreased. Also the fundamental line voltage is maximum for APOD scheme and is minimum for PD and IPD scheme.

4.3. Staircase Multi Carrier SPWM (SCMC SPWM)

Figure 8(a) and 8(b) show the line voltage waveforms and the percentage THD of the line voltage for five-level using the phase disposition technique for staircase multicarrier sinusoidal PWM with $M_a=0.9$.

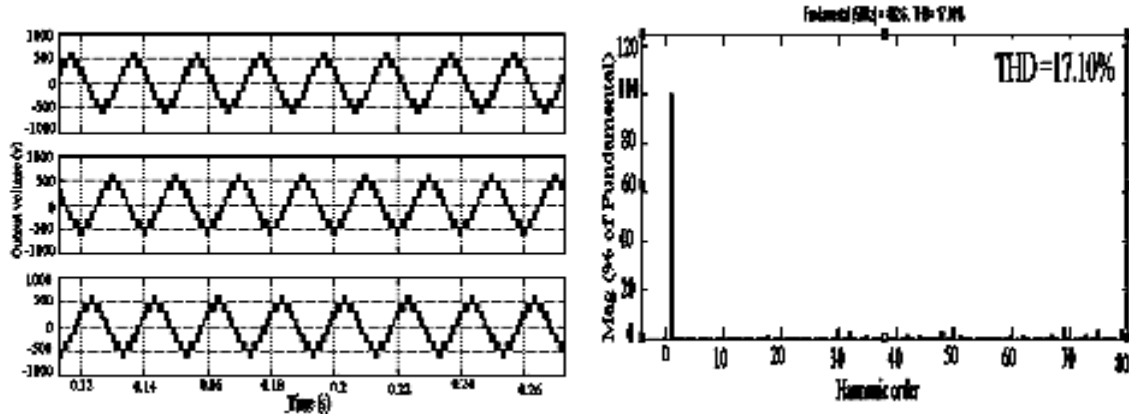


Figure 8(a): Line Voltage for PD SPWM with $M_a=0.9$ Figure 8(b): Line Voltage %THD for PD SPWM with $M_a=0.9$

Table 3 shows the percentage line voltage THD for the five-level CCML with staircase multicarrier signal for different multicarrier PWM techniques with a switching frequency of 2kHz and 10kHz respectively for different modulation indexes.

Table 3: Line voltage %THD for SCMC SPWM

Modulation Technique	Line voltage %THD									
	2kHz					10kHz				
	$M_a=1$	$M_a=0.9$	$M_a=0.8$	$M_a=0.7$	$M_a=0.6$	$M_a=1$	$M_a=0.9$	$M_a=0.8$	$M_a=0.7$	$M_a=0.6$
PD	17.22	17.10	21.38	24.04	25.38	17.18	17.15	21.75	24.18	26.54
IPD	17.20	17.10	21.38	24.04	25.38	17.16	17.15	21.75	24.18	26.54
POD	21.71	29.42	35.56	38.88	39.14	23.24	29.28	35.74	39.24	39.56
APOD	25.90	28.78	30.17	28.53	26.55	26.74	28.41	30.18	28.82	27.13

From the above table, it is observed that, when the switching frequency of the CCMLI is increased, the percentage line voltage THD is reduced for the PD and IPD schemes with modulation index of 1. In the POD and APOD schemes, if the switching frequency is increased, the percentage line voltage THD is reduced with modulation index of 0.9 in five level CCMLI. If the output voltage level increases the percentage line voltage

THD decreases. From the simulation result in the proposed staircase multi carrier SPWM technique PD and IPD PWM schemes, from 3rd order harmonics to 25th order harmonics are less than 1% and are negligible. Few of the odd and even order harmonics from 26th harmonics to 79th harmonics are 1% to 3%. The dominant 69th harmonic factor is about 5% for the PD and IPD schemes. In the POD PWM scheme, from 3rd odd order harmonics to 27th odd order harmonics are less than 1% and all even order harmonics are 0.03%. Few of the odd order harmonics from 29th harmonics to 79th harmonics are present. The dominant 39th and 41st harmonic factor are 10.05% and 9.97% respectively for the POD scheme. In the APOD PWM scheme, from 3rd odd order harmonics to 31st odd order harmonics are less than 1% and all even order harmonics are 0.03%. Few of the odd order harmonics above 33rd harmonics are present. The dominant 35th and 45th harmonic factor are 11.61% and 11.43% respectively for the APOD scheme.

It is observed that when the switching frequency of the CCMLI is increased, the percentage line voltage THD, the fundamental voltage for phase and line are decreased very slightly for the PD and IPD schemes. In the POD and APOD schemes, if the switching frequency is increased, the percentage line voltage THD is increased very slightly and the fundamental voltage for phase and line voltage are decreased very slightly. Also the fundamental line voltage is maximum for POD and APOD schemes and is minimum for PD and IPD schemes.

V. Conclusion

In this paper, the performance of different multicarrier PWM techniques which uses triangular multicarrier waveform, unipolar sine multicarrier waveform and staircase waveform in multilevel inverters are found out. In all the above PWM techniques, different modulation strategies such as phase disposition (PD), inverted phase disposition (IPD), phase opposition disposition (POD) and alternative phase opposition disposition (APOD) are implemented. The results are verified by doing simulation for a 1kW, 3 ϕ five-level cascaded inverter in MATLAB/SIMULINK. The output quantities like fundamental phase and line voltage, percentage THD of the line voltage and percentage dominant harmonic factor are measured in the all the above PWM schemes and the results are compared.

References

- [1] Mariusz Malinowski, K. Gopakumar, Jose Rodriguez and Marcelo A. Pérez, "A Survey on Cascaded Multilevel Inverters" IEEE Transactions on Industrial Electronics, vol. 57, n. 7, July 2010, pp 2197 – 2206.
- [2] R.Nagarajan and M.Saravanan, "Performance Analysis of Multicarrier PWM Strategies for Cascaded Multilevel Inverter," European Journal of Scientific Research (EJSR), Vol.92 No.4, pp. 608-625, Dec. 2012.
- [3] Jang-Hwan Kim, "A carrier-Based PWM Method for Three-Phase Four-Leg Voltage Source Converters", IEEE transactions on power electronics, vol. 19, n.1, January 2004.
- [4] R.Nagarajan and M.Saravanan, "A Carrier - Based Pulse Width Modulation Control Strategies for Cascaded Multilevel Inverter," International Review on Modeling and Simulations (IRMOS), Vol 6.No1, pp-8-19, Feb. 2013.
- [5] G.Carrara, S.Gardella, M.Marchesoni, R.Salutari, G.Sciutto, "A New Multilevel PWM Method: A Theoretical Analysis," IEEE Trans. Power Electronics, vol. 7, n.3, July 1992, pp 497-505.
- [6] R.Nagarajan and M. Saravanan, "Comparison of PWM Control Techniques for Cascaded Multilevel Inverter" International Review of Automatic control (IRACO), Vol.5, No.6, pp. 815-828. Nov. 2012.
- [7] G. Vidhya Krishnan, R.Nagarajan, T. Durka, M.Kalaiselvi, M.Pushpa and S. Shanmuga priya, "Vehicle Communication System Using Li-Fi Technology," International Journal of Engineering And Computer Science (IJECS), Volume 6, Issue 3, pp. 20651-20657, March 2017.
- [8] S.M.Ayob, Z.Salam, "Trapezoidal PWM Scheme for Cascaded Multilevel Inverter" First International Power and Energy Conference, November 2006, pp 368-372.
- [9] M.Dharani Devi and R.Nagarajan, "Implementation of Different PWM Control Strategies for Cascaded MLI," Journal of Network Communications and Emerging Technologies (JNCET), Volume 7, Issue 7, pp. 49- 55, July-2017.
- [10] R.Prabhu, R.Nagarajan, N.Karthick and S.Suresh, "Implementation of Direct Sequence Spread Spectrum Communication System Using FPGA," International Journal of Advanced Engineering, Management and Science (IJAEMS), Vol-3.Issue-5, pp. 488-496, May. 2017
- [11] Rodriguez, Jih-sheng lai, and F.Zheng peng, "Multilevel Inverters; A Survey of Topologies, Controls, and Applications," IEEE Trans.Ind.Electron, vol.49, n. 4, pp724-738, Aug.2002.
- [12] A.Mahendran, K.Muthulakshmi and R.Nagarajan, "Triangular Multicarrier SPWM Technique for Nine Level Cascaded Inverter," International Journal of Scientific & Engineering Research, Vol.4, No.5, pp. 269-275, May-2013.
- [13] C.Mallika devi and R.Nagarajan, "High-Power Transformer-Less Wind Energy Conversion System with three phase Cascaded Multilevel Inverter," International Journal of Scientific & Engineering Research. Vol. 4, Issue- 5, pp. 67-70, May-2013.
- [14] J.Chandramohan, R.Nagarajan, K.Satheeshkumar, N.Ajithkumar, P.A.Gopinath and S.Ranjithkumar, "Intelligent Smart Home Automation and Security System Using Arduino and Wi-fi," International Journal of Engineering And Computer Science (IJECS), Volume 6, Issue 3, pp. 20694-20698, March, 2017.
- [15] Samir koaro, PabloLezana, Mauricio Anguio and Jose Rodriguez, "Multicarrier PWM DC-Link ripple forward compensation for multilevel inverters," IEEE Trans. Power.Electron., vol.123, n.1, pp.52-56, Jan 2008.
- [16] K. Anandhi and Dr. R. Nagarajan, "Mutex-Heart: Fail Safe Dual Chamber Cardiac Pacemaker Device with Rate Responsive Control and Cryptographic Security," IJSRD- International Journal for Scientific Research & Development. Vol. 3, Issue- 2, pp. 489-493, 2015.
- [17] Fang.Z. Peng, John W.McKeever, and Donald J.Adams, "A Power line conditioner using Cascade Multilevel Inverters for Distribution systems" IEEE Transactions on Industrial Applications, vol. 34, n.6, pp 1293-1298, Nov/Dec 1998.

- [18] J.Chandramohan, R.Nagarajan, M.Ashok kumar, T.Dineshkumar, G.Kannan and R.Prakash, "Attendance Monitoring System of Students Based on Biometric and GPS Tracking System," International Journal of Advanced Engineering, Management and Science (IJAEMS), Vol-3.Issue-3, pp. 241-246, Mar. 2017.
- [19] B.P.Mcgrath, D.G.Holmes, "Multicarrier PWM strategies for multilevel inverters," IEEE Trans. Ind.Electron, vol 49, n.4, pp 858-867, Aug.2002.
- [20] R Rameshkumar and R Nagarajan, "Sine Multicarrier SPWM Technique for Seven Level Cascaded Inverter," CiiT-Programmable Device Circuits and Systems. Vol. 5, Issue- 6, 2013.
- [21] Dr.R.Nagarajan, S.Sathishkumar, K.Balasubramani, C.Boobalan, S.Naveen and N.Sridhar. "Chopper Fed Speed Control of DC Motor Using PI Controller," IOSR- Journal of Electrical and Electronics Engineering (IOSR-JEEE), Volume 11, Issue 3, Ver. I, pp. 65-69, May – Jun. 2016.
- [22] R.Nagarajan and M,Saravanan "Staircase Multicarrier SPWM Technique for Nine Level Cascaded Inverter," 2013 International Conference on Power, Energy and Control (ICPEC), IEEE Press, pp-668-675. 2013.
- [23] Lion M.Tolbert and Thomas.G.Habetler, "Novel Multi Level Inverter Carrier Based PWM methods", IEEE IAS, 1998, pp 1424-1431.
- [24] N.Karthick, R.Nagarajan, S.Suresh and R.Prabhu, "Implementation of Railway Track Crack Detection and Protection," International Journal Of Engineering And Computer Science (IJECS), Volume 6, Issue 5, May 2017, pp. 21476-21481, DOI: 10.18535/ijecs/v6i5.47
- [25] M.Padmavathi and R.Nagarajan, "Smart Intelligent ATM Using LABVIEW," International Journal of Emerging Technologies in Engineering Research (IJETER), Volume 5, Issue 5, pp. 41- 45, May-2017.
- [26] R.Nagarajan and M, Saravanan. "Performance Analysis of a Novel Reduced Switch Cascaded Multilevel Inverter," Journal of Power Electronics, Vol.14, No.1, pp. 48-60, Jan.2014.
- [27] D.G.Holmes and T.A.Lipo, Pulse Width Modulation For Power Converters (Wiley Inter-science, 2003).J. Proakis, Digital Communications. New York: McGraw-Hill, 1995.
- [28] R.Nagarajan, S.Sathishkumar, S.Deepika, G.Keerthana, J.K.Kiruthika and R.Nandhini, "Implementation of Chopper Fed Speed Control of Separately Excited DC Motor Using PI Controller", International Journal of Engineering And Computer Science (IJECS), Volume 6, Issue 3, pp. 20629-20633, March, 2017.
- [29] D.G.Holmes and B.P.Mcgrath, "Opportunities for harmonic cancellation with carrier based PWM for two level and multilevel cascaded inverters", in conf.prec IEEE/IAS Annual meeting, 1999.
- [30] R.Nagarajan, R.Yuvaraj, V.Hemalatha, S.Logapriya, A.Mekala and S.Priyanga, "Implementation of PV - Based Boost Converter Using PI Controller with PSO Algorithm," International Journal of Engineering And Computer Science (IJECS), Volume 6, Issue 3, pp. 20479-20484, March, 2017.
- [31] Ms. C. Hemalatha, Mr. R. Nagarajan, P. Suresh, G. Ganesh Shankar and A. Vijay, "Brushless DC Motor Controlled by using Internet of Things," IJSTE - International Journal of Science Technology & Engineering, Volume -3.Issue-09, pp. 373-377, March-2017.
- [32] R.Nagarajan, J.Chandramohan, S.Sathishkumar, S.Anantharaj, G.Jayakumar, M.Visnukumar and R.Viswanathan, "Implementation of PI Controller for Boost Converter in PV System," International Journal of Advanced Research in Management, Architecture, Technology and Engineering (IJARMATE). Vol.11, Issue.XII, pp. 6-10, December. 2016.
- [33] M.Elangovan, R.Yuvara, S.Sathishkumar and R.Nagarajan, "Modelling and Simulation of High Gain Hybrid Boost Converter," International Journal of Emerging Technologies in Engineering Research (IJETER), Volume 5, Issue 6, pp. 9- 14, June-2017
- [34] S.Suresh, R.Nagarajan, L.Sakthivel, V.Logesh, C.Mohandass and G.Tamilselvan, "Transmission Line Fault Monitoring and Identification System by Using Internet of Things," International Journal of Advanced Engineering Research and Science (IJAERS), Vol - 4.Issue - 4, pp. 9-14, Apr- 2017.
- [35] R.Nagarajan, J.Chandramohan, R.Yuvaraj, S.Sathishkumar and S.Chandran, "Performance Analysis of Synchronous SEPIC Converter for a Stand-Alone PV System," International Journal of Emerging Technologies in Engineering Research (IJETER), Vol. 5, Issue - 5, pp. 12-16, May-2017
- [36] M. Sridhar, S.Sathishkumar, R.Nagarajan and R.Yuvaraj, "An Integrated High Gain Boost Resonant Converter for PV System," International Journal of Emerging Technologies in Engineering Research (IJETER), Volume 5, Issue 6, pp. 54- 59, June-2017.
- [37] J.Hamman and F.S.Van Der merwe, "Voltage harmonics generated by voltage fed inverters using PWM natural sampling" IEEE Trans. Power Electron, vol PE-3,n.3, pp.297-302, Jul.1988.
- [38] S.Suresh, R.Nagarajan, R.Prabhu and N.Karthick, "Energy Efficient E0 Algorithm for Wireless Transceivers," International Journal of Engineering and Computer Science (IJECS), Volume 6, Issue 7, July 2017, pp. 21982-21985, DOI: 10.18535/ijecs/v6i7.15.

International Journal of Computational Engineering Research (IJCER) is UGC approved
Journal with Sl. No. 4627, Journal no. 47631.

M.Dharani Devi Development of Multicarrier SPWM Techniques for Cascaded MLI."
International Journal of Computational Engineering Research (IJCER), vol. 7, no. 10, 2017, pp.
44-52.

Multicarrier - Based PWM Control Strategies for Five - Level CMLI

R. Banupriya¹, R.Nagarajan², M.Malarvizhi³, M.Dharani Devi⁴

¹Assistant Professor, Department of Electrical and Electronics Engineering, P.G.P. College of Engineering and Technology, Namakkal, India.

²Professor, Department of Electrical and Electronics Engineering, Gnanamani College of Technology, Namakkal, India.

³Associate Professor, Department of Electrical and Electronics Engineering, Gnanamani College of Technology, Namakkal, India.

⁴Associate Professor, Department of Electrical and Electronics Engineering, M.A.M. School of Engineering, Trichy, India.

Abstract – In this paper, performance analysis of different multicarrier pulse width modulation techniques which uses sine (regular) carrier waveforms are carried out for five-level cascaded inverter. In each carrier waveform, different techniques such as phase disposition (PD), inverted phase disposition (IPD), phase opposition disposition (POD) and alternative phase opposition disposition (APOD) are implemented. The fundamental output voltage and harmonics obtained in each method are compared with the output waveform obtained with the triangular carrier waveform. The different PWM methodologies adopting the constant switching frequency multicarrier with different modulation indexes are simulated for a 1kW, 3 ϕ cascaded multilevel inverter using MATLAB/SIMULINK and the effect of switching frequency on the fundamental output voltage and harmonics are also analyzed.

Index Terms – Modulation Index (MI), Sinusoidal Pulse Width Modulation (SPWM), Total Harmonic Distortion (THD),

1. INTRODUCTION

Multilevel inverter is an effective solution for increasing power and reducing harmonics of AC waveform [1]. The elementary concept of a multilevel converter to achieve higher power is to use a series of power semiconductor switches with several lower voltage DC sources to perform the power conversion by synthesizing a staircase voltage waveform. Capacitors, batteries, and renewable energy voltage sources can be used as the multiple DC voltage sources. The commutation of the power switches aggregate these multiple DC sources in order to achieve high voltage at the output; however, the rated voltage of the power semiconductor switches depends only upon the rating of the DC voltage sources to which they are connected [2].

In this paper, constant switching frequency multicarrier pulse width modulation method is used for the multilevel inverter [3]. The control objective is to compare the reference sine wave with multicarrier waves for three phase five level

cascaded inverters. Multilevel voltage source inverter (MVSI) structure is very popular especially in high power DC to AC power conversion applications. It offers several advantages that make it preferable over the conventional voltage source inverter (VSI). These include the capability to handle higher DC link voltage; the stress on each switching device can be reduced in proportional to the higher voltages [4], [5]. Consequently, in some applications, it is possible to avoid expensive and bulky step-up transformer. Another significant advantage of a multilevel output is better sinusoidal voltage waveform. As a result, a lower total harmonic distortion (THD) is obtained [6].

The concept of multilevel converter has been introduced since 1975. The term multilevel began with the three-level converter. Subsequently, several multilevel converter topologies have been developed, such as the Diode Clamped Multilevel Inverter (DCMLI) also known as Neutral Point Clamped (NPC) Inverter, Flying Capacitor Multilevel Inverter (FCMLI) and Cascaded Multilevel Inverter (CCMLI) [7], [8]. Among them, CCMLI topology is the most attractive, since it requires the least number of components and increases the number of levels in the inverter without requiring high ratings on individual devices and the power rating of the CCMLI is also increased [9], [10]. It also results in simple circuit layout and is modular in structure. Furthermore, CCMLI type of topology is free of DC voltage balancing problem, which is a common issue facing in the DCMLI and FCMLI topologies.

Numerous industrial applications have begun to require higher power apparatus in recent years. Some medium voltage motor drives and utility applications require medium voltage and megawatt power level. For a medium voltage grid, it is troublesome to connect only one power semiconductor switch directly [11]. As a result, a multilevel power converter structure has been introduced as an alternative in high power and medium voltage situations. A multilevel converter not only

achieves high power ratings, but also enables the use of renewable energy sources. Renewable energy sources such as photovoltaic, wind, and fuel cells can be easily interfaced to a multilevel converter system for high power application [12]

In motor applications, high dv/dt in power supply generates high stress on motor windings and requires additional motor insulation. Further; high dv/dt of semiconductor devices increases the electromagnetic interference (EMI), common-mode voltage and possibilities of failure on motor. By increasing the number of levels in the output waveform, the switching dv/dt stress is reduced in the multilevel inverter [13], [14]. Multilevel inverters are suitable for power electronics applications such as flexible AC transmission systems, renewable energy sources, uninterruptible power supplies, electrical drives and active power filters [15], [16].

2. CASCADED MULTILEVEL INVERTER

The single-phase structure of three phase five-level cascaded inverter is illustrated in Figure 1. Each separate DC source is connected to a single-phase full-bridge, or H-bridge, inverter. Each inverter can generate three different outputs voltage level, $+V_{dc}$, 0 and $-V_{dc}$, by connecting the DC source to the AC output by different switching combinations of the four semiconductor switches S1, S2, S3 and S4. To obtain $+V_{dc}$, switches S1 and S2 are tuned on, whereas $-V_{dc}$ can be obtained by tuning on switches S3 and S4. By turning on S1 and S3 or S2 and S4, the output voltage is 0. The AC outputs of each of the full-bridge inverter levels are connected in series such that the synthesized voltage waveform is the sum of the inverter outputs [17], [18].

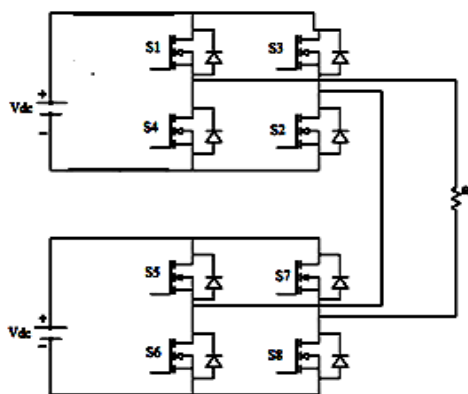


Figure 1, 1 ϕ Structure of Five-Level Cascaded Inverter

The CCMLI is producing five level output and they are $2V_{dc}$, V_{dc} , 0, $-V_{dc}$ and $-2V_{dc}$. This topology is suitable for applications where separate DC voltage sources are available, such as photovoltaic (PV) generators, fuel cells and batteries. The phase output voltage is generated by the sum of two output voltage of the full bridge inverter modules. The circuit in Figure 1 utilizes two independent DC sources and

consequently will create an output phase voltage with five-level. In general, if N is the number of independent DC sources per phase, then the following relations apply [19]:

$$m = 2N + 1 \quad (1)$$

$$q = 2(m - 1) \quad (2)$$

Where m is the number of levels and q is the number of switching devices in each phase. The most well known SPWM which can be applied to a CCMLI is the Phase-Shifted SPWM. This modulation technique is the same as that of the conventional SPWM technique which is applied to a conventional single phase full-bridge inverter, the only difference being that it utilizes more than one carrier. The number of carriers to be used per phase is equal to twice the number of DC voltage sources per phase ($2N$) [20]. The simulation results are obtained for the output phase voltage and line voltage of the three phase five-level CCMLI with 1kW, 3 ϕ resistive loads for various PWM techniques.

3. MODULATION TECHNIQUES

The Pulse Width Modulation (PWM) control strategies development tries to reduce the total harmonic distortion (THD) of the output voltage. Any deviation in the output voltage of the sinusoidal wave shape will result in harmonic currents in the load and this harmonic current produces the electromagnetic interference (EMI), harmonic losses and torque pulsation in the case of motor drives. Increasing the switching frequency of the PWM pattern reduces the lower frequency harmonics by moving the switching frequency carrier harmonic and associated sideband harmonics away from the fundamental frequency component [21], [22]. This increased switching frequency reduces harmonics, which results in a lower THD with high quality output voltage waveforms of desired fundamental RMS value and frequency which are as close as possible to sinusoidal wave shape. The carrier frequency defines the switching frequency of the converter and the high order harmonic components of the output voltage spectrum and the sidebands occur around the carrier frequency and its multiples. The higher switching frequency can be employed for low and medium power inverters, whereas, for high power and medium voltage applications the switching frequency should be low. Harmonic reduction can then be strictly related to the performance of an inverter with any switching strategy [23], [24].

The three phase multilevel inverter requires three modulating signals or reference signals which are three sine-waves with 120 degree phase shift and equal in magnitudes. In this paper, new carrier based PWM techniques are developed which are as Sine Multicarrier Sinusoidal PWM (SMC SPWM).

Each carrier is to be compared with the corresponding modulating sine wave [25], [26]. The reference or modulation

waveform has peak amplitude A_r and frequency f_r and it is centered in the middle of the carrier set. The general principle of a carrier based PWM technique is the comparison of a sinusoidal waveform with a carrier waveform, this typically being a triangular carrier waveform. The reference is continuously compared with the carrier signal. If the reference is greater than the carrier signal, then the active device corresponding to that carrier is switched on, and if the reference is less than the carrier signal, then the active device corresponding to that carrier is switched off [27], [28]. In multilevel inverters, the amplitude modulation index, M_a and the frequency ratio, M_f are defined as,

$$M_a = \frac{A_r}{(m-1)A_c} \quad (3)$$

$$M_f = \frac{f_c}{f_r} \quad (4)$$

Where A_r and A_c are amplitude of reference and carrier signal respectively. f_r and f_c are frequency of reference and carrier signal respectively.

In this paper, modulation indexes used are 0.6, 0.7, 0.8, 0.9 and 1 for five-level CCMLI. For multilevel applications, carrier based PWM techniques with multiple carriers are used. The Multicarrier Modulation (MCM) techniques, can be divided in to the following categories [29], [30] such as,

1. Phase disposition (PD) where all the carriers are in phase.
2. Inverted phase disposition (IPD) where all the carriers are in phase and is inverted.
3. Phase opposition disposition (POD) where the carriers above the zero reference are in phase but shifted by 180 degrees from those carriers below the zero reference.
4. Alternative phase opposition disposition (APOD) where each carrier band is shifted by 180 degrees from the adjacent carrier bands [2].

The above modulation strategies are implemented for sine multicarrier waveform. The phase voltage and line voltage waveform, harmonic spectrums of the line voltage are shown for different modulation techniques by doing simulation using MATLAB/SIMULINK for a five level CCMLI and the results obtained are compared.

3.1. Triangular Multicarrier Sinusoidal PWM (TMC SPWM)

The performance of the multilevel inverter is based on the multicarrier modulation technique used. Two-level to multilevel inverters are made using several triangular carrier signals and one reference signal per phase. Carrara [5] developed multilevel sub harmonic PWM (SH-PWM), which is as follows, for m -level inverter, $m-1$ carriers [31] with the same frequency f_c and same amplitude A_c are disposed such

that the bands they occupy are contiguous. They are defined as

$$C_i = A_c \left[(-1)^{f(i)} y_c(\omega_c t + \varphi) + t - \frac{m}{2} \right], \quad (5)$$

$$i = 1, \dots, (m-1)$$

Where y_c is a normalized symmetrical triangular carrier defined as,

$$y_c(\omega_c t + \varphi) = (-1)^{[\alpha]} ((\alpha \bmod 2) - 1) + \frac{1}{2} \quad (6)$$

$$\alpha = \frac{\omega_c t + \varphi}{\pi}, \omega_c = 2\pi f_c \quad (7)$$

φ represents the phase angle of y_c . y_c is a periodic function with the period $T_c = \frac{2\pi}{\omega_c}$. It is shown that using symmetrical triangular carrier generates less harmonic distortion at the inverters output [32]-[34].

In TMC SPWM, so far only the PD, POD and APOD techniques are discussed earlier in the literature. In this paper, IPD scheme is also applied to TMC SPWM and it is found that this scheme gives the lowest THD among the TMC SPWM schemes.

The multicarrier modulation techniques (PD, IPD, POD and APOD) are implemented using triangular multicarrier signals for five-level CCMLI with different modulation indexes and are shown in Figure 2.

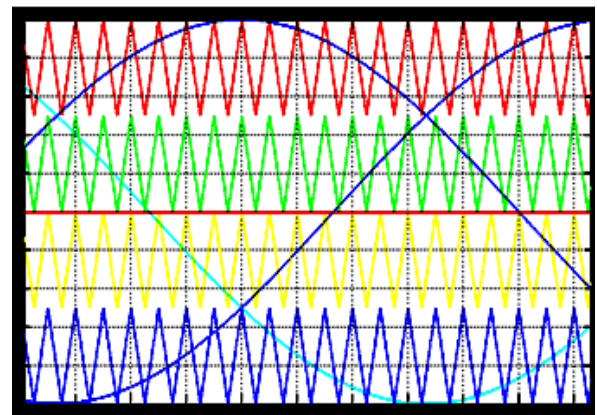


Figure 2 IPD TMC SPWM with $M_a = 1$ for five-level CCMLI

3.2. Sine Multicarrier Sinusoidal PWM (SMC SPWM)

In this PWM technique, the PWM pulses are generated due to the interference of sinusoidal modulating and carrier signals. Here both the modulating and carrier signal are sine wave. The output of the sine wave block in simulink is determined by:

$$y = a \times \sin(f \times t + \phi) + b \quad (8)$$

Where y is the output, a is the amplitude, f is the frequency, t is the time, ϕ is the phase shift and b is the bias. In the gating pulse generation of the proposed SMC SPWM scheme, the triangular carrier waveform of SPWM is replaced by sine waveform. In that the amplitude and frequency of both the signals are differed. The pulses are generated when the amplitude of the modulating signal is greater than that of the carrier signal. The proposed control strategy has a better spectral quality and a higher fundamental output voltage without any pulse dropping.

The multicarrier modulation techniques (PD, IPD, POD and APOD) are implemented using sine multicarrier signals for five-level CCMLI with different modulation indexes and are shown in Figure 3 respectively.

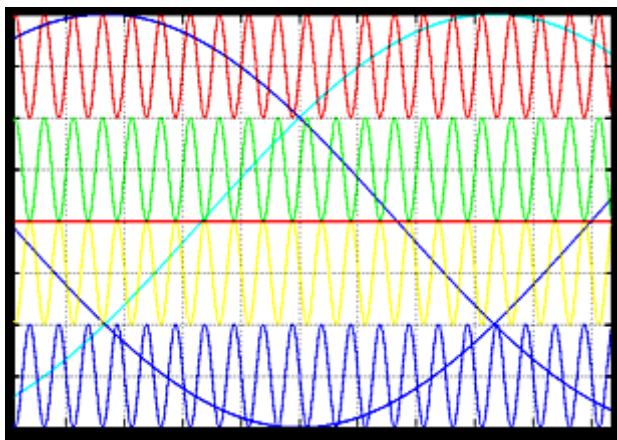


Figure 3 POD SMC SPWM with Ma=1 for five-level CCMLI

4. SIMULATION RESULTS

The five level cascaded multilevel inverter model with different modulation indexes was implemented in MATLAB/SIMULINK software to demonstrate the feasibility of PWM techniques. Phase disposition, inverted phase disposition, phase opposition disposition and alternative phase opposition disposition techniques are used for the various multicarrier SPWM techniques such as;

1. Triangular Multicarrier Sinusoidal PWM
2. Sine Multicarrier Sinusoidal PWM

The line voltage waveform with its harmonic spectrum at fundamental frequency of 50Hz and switching frequency of 2kHz and 10kHz are obtained for the proposed CCMLI. For comparison, the total harmonic distortion (THD) was chosen to be evaluated for all the modulation techniques. In order to get THD level of the waveform, a Fast Fourier Transform (FFT) is applied to obtain the spectrum of the output voltage. The THD is calculated using the following equation in this work [35]-[38].

$$THD = \frac{\sqrt{\sum_{n=2}^{80} v_n^2}}{v_1} \quad (9)$$

Where n is the harmonic order, v_n is the RMS value of the nth harmonic component and v_1 is the RMS value of the fundamental component. Here the %THD is calculated up to a harmonic order which is twice the switching frequency. For 2kHz switching frequency up to 80th order harmonics is taken in to account for calculating THD and for 10kHz switching frequency up to 400th order harmonics is taken in to account for calculating THD.

4.1. Triangular Multi Carrier SPWM (TMC SPWM)

Figure 4(a) and 4(b) show the line voltage waveforms and the percentage THD of the line voltage for five level using the inverted phase disposition technique for triangular multi carrier sinusoidal PWM with Ma=1.

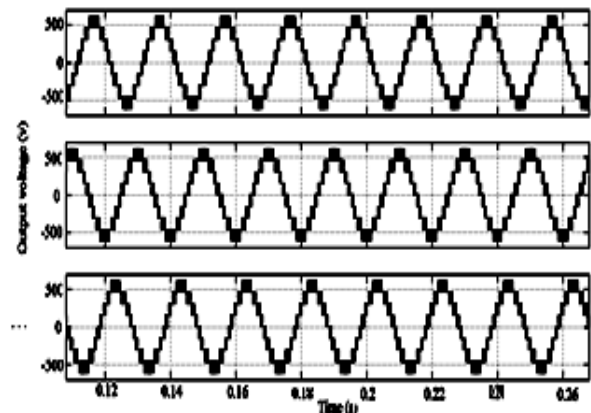


Figure 4(a) Line Voltage for IPD SPWM with Ma=1

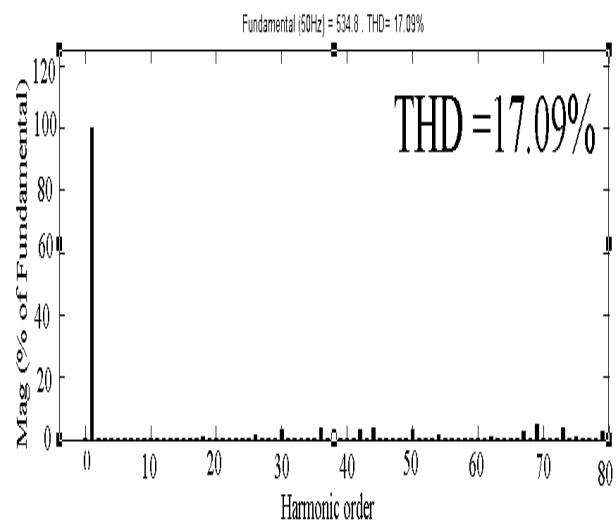


Figure 4(b): Line Voltage %THD for IPD SPWM with Ma=1

Table 1: Line voltage %THD for CCMLI with TMC SPWM

Switching frequency	Modulation Technique	Modulation Indexes				
		$M_a=1$	$M_a=0.9$	$M_a=0.8$	$M_a=0.7$	$M_a=0.6$
2KHz	PD	17.11	17.55	21.73	24.14	25.62
	IPD	17.09	17.55	21.73	24.14	25.62
	POD	21.89	29.94	35.48	38.65	38.42
	APOD	25.66	28.75	29.75	28.04	25.93
10KHz	PD	17.58	17.77	21.81	24.21	28.03
	IPD	17.56	17.77	21.81	24.21	28.03
	POD	23.91	31.42	36.45	38.63	37.68
	APOD	27.07	29.57	30.46	28.85	29.33

Table 1 shows the percentage line voltage THD for the five-level CCMLI with triangular multicarrier signal with different multicarrier PWM techniques with a switching frequency of 2 KHz and 10 KHz respectively for different modulation indexes.

From the above table, it is observed that, when the switching frequency of the CCMLI is increased, the percentage line voltage THD is increased for the PD and IPD schemes with all modulation indexes. In the POD scheme, if the switching frequency is increased, the percentage line voltage THD is reduced with modulation index of 0.7 and 0.6. In the APOD scheme, when the switching frequency is increased, the percentage line voltage THD is increased with all modulation indexes, in five-level CCMLI.

From the simulation result in the triangular multicarrier SPWM technique PD and IPD PWM schemes, from 3rd order harmonics to 25th order harmonics are less than 1%. Few of the odd and even order harmonics from 26th harmonics to 79th harmonics are present. The dominant 69th harmonic factor is about 5% for the PD and IPD schemes. In the POD scheme, from 3rd odd order harmonics to 27th odd order harmonics are less than 1% and all even order harmonics are zero. Few of the odd order harmonics from 29th harmonics to 79th harmonics are 1% to 3%. The dominant 39th and 41st harmonic factor are 10.29% and 10.46% respectively for the POD scheme. In the APOD scheme, from 3rd odd order harmonics to 31st odd order harmonics are less than 1% and all even order harmonics are 0.03%. Few of the odd order harmonics from 33rd harmonics to 79th harmonics are present. The dominant 35th and 45th harmonic factor are 11.94% and 11.87% respectively for the APOD scheme.

4.2 Sine Multi Carrier SPWM (SMC SPWM)

Figure 5(a) and 5(b) show the line voltage waveforms and the percentage THD of the line voltage for five level using the phase disposition technique for sine multi carrier sinusoidal

PWM with $M_a=0.9$.

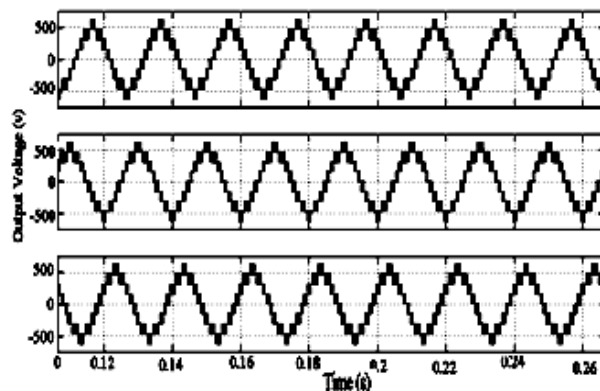


Figure 5(a) Line Voltage for PD SPWM with $M_a=0.9$

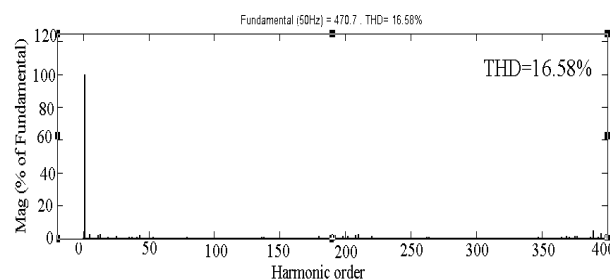


Figure 5(b) Line Voltage %THD for PD SPWM with $M_a=0.9$

Table 2 shows the percentage line voltage THD for the five-level CCMLI with sine multicarrier signal with different multicarrier PWM techniques with a switching frequency of 2kHz and 10kHz respectively for different modulation indexes.

Table 2: Line voltage %THD for CCMLI with SMC SPWM

Switching frequency	Modulation Technique	Modulation Indexes				
		$M_a=1$	$M_a=0.9$	$M_a=0.8$	$M_a=0.7$	$M_a=0.6$
2kHz	PD	17.93	17.25	20.26	23.17	26.68
	IPD	17.93	17.25	20.26	23.17	26.68
	POD	26.34	33.74	38.13	41.82	44.92
	APOD	29.18	31.72	31.57	30.06	27.64
10kHz	PD	18.27	16.58	20.46	22.65	28.68
	IPD	18.27	16.58	20.46	22.65	28.68
	POD	26.15	34.35	37.86	41.14	43.82
	APOD	29.83	32.22	32.19	29.65	29.43

From the above table, it is observed that, when the switching frequency of the CCMLI is increased, the percentage line voltage THD is reduced for the PD and IPD schemes with modulation index of 0.9 and 0.7. In the POD scheme, if the switching frequency is increased, the percentage line voltage THD is reduced with all PWM schemes except for the modulation index of 0.9. In the APOD scheme, when the switching frequency is increased, the percentage line voltage THD is increased with all PWM schemes except for the modulation index of 0.7 in five level CCMLI.

From the simulation result in the PD and IPD PWM scheme, from 3rd order harmonics to 9th order harmonics and higher odd order harmonics (above 9th harmonics) are less than 1%. Few of the even order harmonics from 24th harmonics to 56th harmonics for the above mentioned scheme are less than 2%. The dominant 69th harmonic factor is about 4% for the PD and IPD scheme.

In the POD scheme, from 3rd odd order harmonics to 9th odd order harmonics are less than 1% and all even order harmonics are zero. Few of the odd order harmonics from 11th harmonics to 79th harmonics are 1% to 2%. The dominant 39th and 41st harmonic factor are 13.74% and 13.95% respectively for the POD scheme. In the APOD scheme, from 3rd odd order harmonics to 9th odd order harmonics are less than 1% and all even order harmonics are zero. Few of the odd order harmonics from 11th harmonics to 79th harmonics are present. The dominant 35th and 45th harmonic factor are 12.58% and 12.45% respectively for the APOD scheme.

It is observed that, when the switching frequency of the CCMLI is increased, the percentage line voltage THD, the fundamental phase and line voltage are increased very slightly for the PD and IPD scheme. In the POD and APOD schemes, if the switching frequency is increased, the percentage line voltage THD is decreased very slightly and the fundamental phase and line voltage are increased. Also the fundamental line voltage is maximum for POD and APOD scheme and is minimum for PD and IPD scheme.

5. CONCLUSION

In this paper, the performance of different multicarrier PWM techniques which uses triangular multicarrier waveform, sine multicarrier waveform in multilevel inverters is found out. In all the above PWM techniques, different modulation strategies such as phase disposition (PD), inverted phase disposition (IPD), phase opposition disposition (POD) and alternative phase opposition disposition (APOD) are implemented. The results are verified by doing simulation for a 1kW, three-phase five-level cascaded inverter in MATLAB/SIMULINK. The output quantities like fundamental phase and line voltage, percentage THD of the line voltage and percentage dominant harmonic factor are

measured in the all the above PWM schemes and the results are compared.

REFERENCES

- [1] Mariusz Malinowski, K. Gopakumar, Jose Rodriguez and Marcelo A. Pérez, "A Survey on Cascaded Multilevel Inverters" IEEE Transactions on Industrial Electronics, vol. 57, n. 7, July 2010, pp 2197 – 2206.
- [2] R.Nagarajan and M,Saravanan, "Performance Analysis of Multicarrier PWM Strategies for Cascaded Multilevel Inverter," European Journal of Scientific Research (EJSR), Vol.92 No.4, pp. 608-625, Dec. 2012.
- [3] Jang-Hwan Kim, "A carrier-Based PWM Method for Three-Phase Four-Leg Voltage Source Converters", IEEE transactions on power electronics, vol. 19, n.1, January 2004.
- [4] R.Nagarajan and M,Saravanan, "A Carrier - Based Pulse Width Modulation Control Strategies for Cascaded Multilevel Inverter," International Review on Modeling and Simulations (IRMOS), Vol 6.No1, pp-8-19, Feb. 2013.
- [5] G.Carrara, S.Gardella, M.Marchesoni, R.Salutari, G.Sciutto, "A New Multilevel PWM Method: A Theoretical Analysis," IEEE Trans. Power Electronics, vol. 7, n.3, July 1992, pp 497-505.
- [6] R.Nagarajan and M, Saravanan, "Comparison of PWM Control Techniques for Cascaded Multilevel Inverter" International Review of Automatic control (IRACO), Vol.5, No.6, pp. 815-828. Nov. 2012.
- [7] G. Vidhya Krishnan, R.Nagarajan, T. Durka, M.Kalaiselvi, M.Pushpa and S. Shanmuga priya, "Vehicle Communication System Using Li-Fi Technology," International Journal of Engineering And Computer Science (IJECs), Volume 6, Issue 3, pp. 20651-20657, March 2017.
- [8] S.M.Ayob, Z.Salam, "Trapezoidal PWM Scheme for Cascaded Multilevel Inverter" First International Power and Energy Conference, November 2006, pp 368-372.
- [9] R.Prabhu, R.Nagarajan, N.Karthick and S.Suresh, "Implementation of Direct Sequence Spread Spectrum Communication System Using FPGA," International Journal of Advanced Engineering, Management and Science (IJAEMS), Vol-3.Issue-5, pp. 488-496, May. 2017
- [10] Rodriguez, Jih-sheng lai, and F.Zheng peng, "Multilevel Inverters; A Survey of Topologies, Controls, and Applications," IEEE Trans.Ind.Electron, vol.49, n. 4, pp724-738, Aug.2002.
- [11] A.Mahendran, K.Muthulakshmi and R.Nagarajan, "Triangular Multicarrier SPWM Technique for Nine Level Cascaded Inverter." International Journal of Scientific & Engineering Research, Vol.4, No.5, pp. 269-275, May-2013.
- [12] M.Dharani Devi, M.Malarvizhi and R.Nagarajan, "Development of Multicarrier SPWM Techniques for Cascaded MLI." International Journal of Computational Engineering Research (IJCER), vol. 7, no. 10, 2017, pp. 44-52.
- [13] J.Chandramohan, R.Nagarajan, K.Satheeshkumar, N.Ajithkumar, P.A.Gopinath and S.Ranjithkumar, "Intelligent Smart Home Automation and Security System Using Arduino and Wi-fi," International Journal of Engineering And Computer Science (IJECs), Volume 6, Issue 3, pp. 20694-20698, March, 2017.
- [14] Samir koaro, PabloLezana, Mauricio Anguio and Jose Rodriguez, "Multicarrier PWM DC-Link ripple forward compensation for multilevel inverters," IEEE Trans. Power.Electron., vol.123, n.1, pp.52-56, Jan 2008.
- [15] K. Anandhi and Dr. R. Nagarajan, "Mutex-Heart: Fail Safe Dual Chamber Cardiac Pacemaker Device with Rate Responsive Control and Cryptographic Security," IJSRD- International Journal for Scientific Research & Development. Vol. 3, Issue- 2, pp. 489-493, 2015.
- [16] Fang.Z. Peng, John W.McKeeever, and Donald J.Adams, "A Power line conditioner using Cascade Multilevel Inverters for Distribution systems" IEEE Transactions on Industrial Applications, vol. 34, n.6, pp 1293-1298, Nov/Dec 1998.
- [17] J.Chandramohan, R.Nagarajan, M.Ashok kumar, T.Dineshkumar, G.Kannan and R.Prakash, "Attendance Monitoring System of Students Based on Biometric and GPS Tracking System," International Journal

- of Advanced Engineering, Management and Science (JJAEMS), Vol-3, Issue-3, pp. 241-246, Mar. 2017.
- [18] B.P.Mcgrath, D.G.Holmes, "Multicarrier PWM strategies for multilevel inverters," IEEE Trans. Ind.Electron, vol 49, n.4, pp 858-867, Aug.2002.
- [19] R Rameshkumar and R Nagarajan, "Sine Multicarrier SPWM Technique for Seven Level Cascaded Inverter," CiiT-Programmable Device Circuits and Systems. Vol. 5, Issue- 6, 2013.
- [20] Dr.R.Nagarajan, S.Sathishkumar, K.Balasubramani, C.Boobalan, S.Naveen and N.Sridhar, "Chopper Fed Speed Control of DC Motor Using PI Controller," IOSR- Journal of Electrical and Electronics Engineering (IOSR-JEEE), Volume 11, Issue 3, Ver. I, pp. 65-69, May - Jun. 2016.
- [21] R.Nagarajan and M,Saravanan "Staircase Multicarrier SPWM Technique for Nine Level Cascaded Inverter," 2013 International Conference on Power, Energy and Control (ICPEC), IEEE Press, pp-668-675. 2013.
- [22] Lion M.Tolbert and Thomas.G.Habetler, "Novel Multi Level Inverter Carrier Based PWM methods", IEEE IAS, 1998, pp 1424-1431.
- [23] N.Karthick, R.Nagarajan, S.Suresh and R.Prabhu, "Implementation of Railway Track Crack Detection and Protection," International Journal of Engineering And Computer Science (IJECS), Volume 6, Issue 5, May 2017, pp. 21476-21481, DOI: 10.18535/ijeecs/v6i5.47
- [24] M.Padmavathi and R.Nagarajan, "Smart Intelligent ATM Using LABVIEW," International Journal of Emerging Technologies in Engineering Research (IJETER), Volume 5, Issue 5, pp. 41- 45, May-2017.
- [25] R.Nagarajan and M, Saravanan. "Performance Analysis of a Novel Reduced Switch Cascaded Multilevel Inverter," Journal of Power Electronics, Vol.14, No.1, pp. 48-60, Jan.2014.
- [26] D.G.Holmes and T.A.Lipo, Pulse Width Modulation For Power Converters (Wiley Inter-science, 2003).J. Proakis, Digital Communications. New York: McGraw-Hill, 1995.
- [27] R.Nagarajan, S.Sathishkumar, S.Deepika, G.Keerthana, J.K.Kiruthika and R.Nandhini, "Implementation of Chopper Fed Speed Control of Separately Excited DC Motor Using PI Controller", International Journal of Engineering And Computer Science (IJECS), Volume 6, Issue 3, pp. 20629-20633, March, 2017.
- [28] D.G.Holmes and B.P.Mcgrath, "Opportunities for harmonic cancellation with carrier based PWM for two level and multilevel cascaded inverters", in conf.prec IEEE/IAS Annual meeting, 1999.
- [29] R.Nagarajan, R.Yuvaraj, V.Hemalatha, S.Logapriya, A.Mekala and S.Priyanga, "Implementation of PV - Based Boost Converter Using PI Controller with PSO Algorithm," International Journal of Engineering And Computer Science (IJECS), Volume 6, Issue 3, pp. 20479-20484, March, 2017.
- [30] Ms. C. Hemalatha, Mr. R. Nagarajan, P. Suresh, G. Ganesh Shankar and A. Vijay, "Brushless DC Motor Controlled by using Internet of Things," IJSTE - International Journal of Science Technology & Engineering, Volume -3.Issue-09, pp. 373-377, March- 2017.
- [31] R.Nagarajan, J.Chandramohan, S.Sathishkumar, S.Anantharaj, G.Jayakumar, M.Visnukumar and R.Viswanathan, "Implementation of PI Controller for Boost Converter in PV System," International Journal of Advanced Research in Management, Architecture, Technology and Engineering (IJARMATE). Vol.11, Issue.XII, pp. 6-10, December. 2016.
- [32] M.Elangovan, R.Yuvara, S.Sathishkumar and R.Nagarajan, "Modelling and Simulation of High Gain Hybrid Boost Converter," International Journal of Emerging Technologies in Engineering Research (IJETER), Volume 5, Issue 6, pp. 9- 14, June-2017
- [33] S.Suresh, R.Nagarajan, L.Sakthivel, V.Logesh, C.Mohandass and G.Tamilselvan, "Transmission Line Fault Monitoring and Identification System by Using Internet of Things," International Journal of Advanced Engineering Research and Science (JJAERS), Vol - 4.Issue - 4, pp. 9-14, Apr- 2017.
- [34] R.Nagarajan, J.Chandramohan, R.Yuvaraj, S.Sathishkumar and S.Chandran, "Performance Analysis of Synchronous SEPIC Converter

for a Stand-Alone PV System," International Journal of Emerging Technologies in Engineering Research (IJETER), Vol. 5, Issue - 5, pp. 12-16, May-2017

- [35] M. Sridhar, S.Sathishkumar, R.Nagarajan and R.Yuvaraj, "An Integrated High Gain Boost Resonant Converter for PV System," International Journal of Emerging Technologies in Engineering Research (IJETER), Volume 5, Issue 6, pp. 54- 59, June-2017.
- [36] J.Hamman and F.S.Van Der merwe, "Voltage harmonics generated by voltage fed inverters using PWM natural sampling" IEEE Trans. Power Electron, vol PE-3,n.3, pp.297-302, Jul.1988.
- [37] S.Suresh, R.Nagarajan, R.Prabhu and N.Karthick, "Energy Efficient E0 Algorithm for Wireless Transceivers," International Journal of Engineering and Computer Science (IJECS), Volume 6, Issue 7, July 2017, pp. 21982-21985, DOI: 10.18535/ijeecs/v6i7.15.
- [38] M.Dharani Devi and R.Nagarajan, "Implementation of Different PWM Control Strategies for Cascaded MLI," Journal of Network Communications and Emerging Technologies (JNCET), Volume 7, Issue 7, July 2017, pp. 49-55.

Authors



R. Banupriya received her B.E. in Electrical and Electronics Engineering from Anna University, Chennai, India, in 2010. She received her M.E. Power Electronics and Drives from Anna University, Chennai, India, in 2012. She has worked in the industry as an Asst. Deputy Manager. She is currently working as an Assistant Professor of Electrical and Electronics Engineering at P.G.P. College of Engineering and Technology, Namakkal, Tamilnadu, India. Her research interest includes Power Electronics and Renewable Energy Sources.



R. Nagarajan received his B.E. in Electrical and Electronics Engineering from Madurai Kamarajar University, Madurai, India, in 1997. He received his M.E. in Power Electronics and Drives from Anna University, Chennai, India, in 2008. He received his Ph.D in Electrical Engineering from Anna University, Chennai, India, in 2014. He has worked in the industry as an Electrical Engineer. He is currently working as Professor of Electrical and Electronics Engineering at Gnanamani College of Technology, Namakkal, Tamilnadu, India. His current research interest includes Power Electronics, Power System, Soft Computing Techniques and Renewable Energy Sources.



M. Malarviathi received her B.E. in Electronics and Electronics Engineering from Bharathiyar University, Coimbatore, India. She received her M.E. in Power Electronics and Drives from Anna University, Chennai, India, She received her Ph.D in Electrical Engineering from Anna University, Chennai, India, She has worked in the various institution as an Associate Professor. She is currently working as an Associate Professor of Electrical and Electrical Engineering in Gnanamani College of Technology, Namakkal, Tamilnadu, India. Her research interest includes Power Systems, Power Electronics and Soft Computing.



M. Dharani Devi received her B.E. in Electronics and Instrumentation Engineering from Madurai Kamarajar University, Madurai, India, in 2003. She received her M.E. in Process control and Instrumentation Engineering from Annamalai University, Chidambaram, India, in 2005. She has worked in the various institution as an Associate Professor. She is currently working as an Associate Professor of Electrical and Electronics Engineering at M.A.M.School of Engineering, Trichy, Tamilnadu, India. Her research interest includes Process Control, Power Electronics and Renewable Energy Sources.



ALIGNMENT TEST ON PORTABLE TABLETOP MINI LATHE

*Kannan T TM¹, Ranjith Kumar P², Ramanathan R³ and Chandrasekaran K⁴

^{1,3,4}Associate Professor, Department of Mechanical Engineering, M.A.M.School of Engineering, Trichy-621 105, Tamilnadu, India.

² Professor, Department of Mechanical Engineering, M.A.M.School of Engineering, Trichy-621 105, Tamilnadu, India

ABSTRACT

Tabletop mini lathes are preferred by some professional such as Locksmith, Goldsmith, Watch maker and prototyping Engineers. The idea of Table top lathe was initiated in the concept of Micro factory in Japan in 1990. The main Objectives of Miniature of lathes are greater saving of power, space, materials, Time and other resources. Micro machining is the foundation of technology to produce miniature of components with relative accuracy requirements in 3 dimensional features are made in the wide range of engineering applications. Usually three directional forces to improve the working accuracy are applied to micro machine parts such as Spindle, Bed and Cross slide of Tabletop mini lathe. In this experimental work deals with alignment test was conducted on various micro machine parts using dial test indicator. The maximum and minimum values of alignment tests are compared with mini machine tool guide. The alignment values of Machine bed, Spindle and Cross slide are within allowed limit of design of machine elements guide and Indicate table top mini lathe is suitable for micro machining process.

Keywords: Table top Mini Lathe, Alignment test, Dial test Indicator, Accuracy, Micro machining

1. Introduction

Micro factory is a small dimensioned factory which is capable for small production system. Micro factory was a concept of future Manufacturing system which was proposed in Japanese national R&D project in 1990. Microfactory was able to perform a series of Fabrication and assembly with a small table top machine [1,2] Metrology and Inspection system are the basis for ultra precision mini machines to be widely applied in Industry which is used to analyze performance of micro machines [3] Design Strategy is developed with the aim of getting a very high dynamic analysis of tabletop micro machines [4] The development of Precision manufacturing has greatly changed our lives in terms of increased living standards. High precision manufacturing offers quality and reliability for conventional products. Usually Table top mini lathe accuracy will improve by inherent reductions of machine component Inertia, Negligible thermal drift and larger Eigen frequencies[5] Spindle is a key component of precision machine tool because the spindle motion error will have significant effects on the surface quality and accuracy of machine component[6] Steel or Cast iron are most widely used material for the machine bed and slide ways because their good wear resistance, low stress caused deformation and vibration damping capacity[7,8] Three important principle parts

like machine bed, cross slide and spindle performance are measured by dial test indicator. It indicates the errors and tolerance limit of alignment of small tabletop machines [9]. The performance of micro machine was analyzed by Gap sensor method and finite element analysis method and then conduct experimental work on different materials [10] Previous researchers were conducted performance test in different conventional machines but we conduct performance test on tabletop mini lathe using dial test indicator and values are compared with design of machine elements data book.

2. Specifications

Net weight = 3.20 kg
Motor specification = 1/12 hp
Bed length = 165 mm
Centre height = 65mm
Spindle speed = 3000-9000 rpm
Longitudinal feed = 80mm
Cross feed = 30mm
Pitch of lead screw = 2mm
Distance between the centres = 92.5 mm
Mode of Operation – Manual

*Corresponding Author - E- mail: ttmk_8@rediffmail.com

3. Alignment test on Tabletop Mini lathe.

3.1. Rotational Accuracy of Chuck

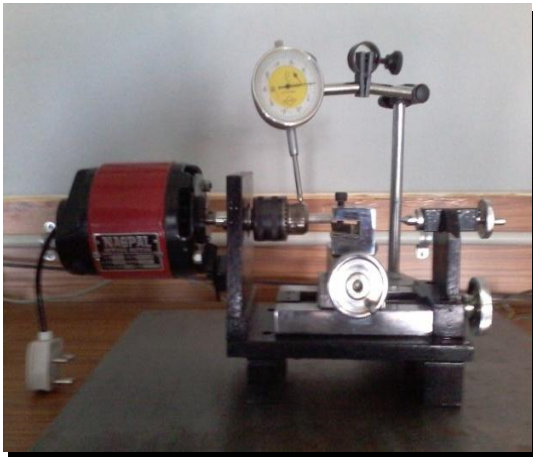


Fig.1 Alignment test on chuck

Table 1. Alignment test result of chuck

Test Trial No	Chuck Alignment position (degrees)	Deviation division in Dial test indicator	Amount of Deviation (mm)
1	0	2	0.02
2	90	1	0.01
3	180	1	0.01
4	270	2	0.02

Table top mini lathe carryout machining by means of rotational force of Chuck. The accuracy of chuck affects the roundness and surface roughness of the work piece. The final product accuracy depends upon the chuck accuracy and spindle speed. In general the chuck accuracy is measured by Dial gauge at very low speed. This method is simple and easy to analyze the chuck alignment and also measure the performance of table top mini lathe.

The maximum and minimum values are tabulated in Table 1. The average value of chuck roundness is 0.015 mm and within allowable limit as per design of mini machine tool guide. Fig 2 shows that Deviation values of different position of rotation of spindle chuck through the Radar diagram.

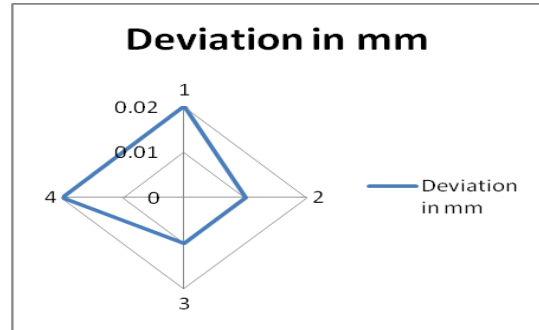


Fig 2 Radar diagram for chuck alignment values

3.2. Movement accuracy of cross slide



Fig.3 Alignment test on cross slide

Table 2. Alignment test results of Cross slide

Test Trial No	Alignment distance In mm	Deviation division in Dial test indicator	Amount of Deviation In mm
1	10	2	0.02
2	15	3	0.03
3	20	1	0.01
4	25	3	0.03

Cross slide movement of mini lathe is based on screw mechanism and adjusted by clamping nut. The final product accuracy, surface finish, metal removal rate, tool wear, heat generation and tool vibrations are controlled by correct alignment of cross slide. The cross slide movement accuracy is measured by dial gauge and values are tabulated in Table 2. It shows that average value of cross slide movement is 0.02 mm and also within allowable limit as per design of mini machine tool guide. Fig 3 shows that Amount of deviation of cross slide movement during alignment test on Mini

lathe and also give graphical representation through Scatter Diagram

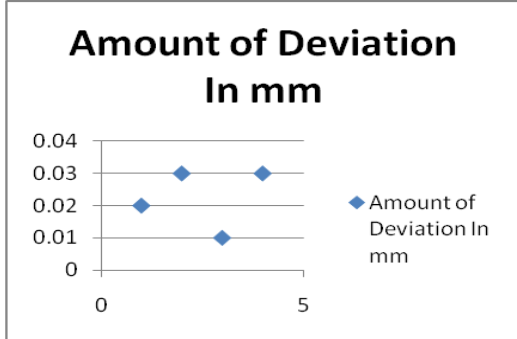


Fig.3 Scatter diagram for Cross slide alignment values

3.3 Alignment Test on Machine bed

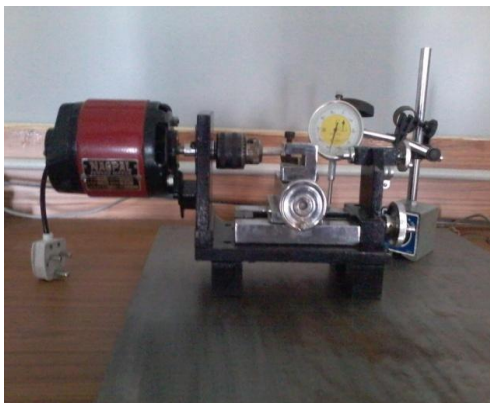


Fig 4 Alignment test on Machine bed

Carriage mechanism and tool post arrangement are placed on machine bed and allow moving between head stock to tail stock by actuating lead screw. The accuracy of machine bed lead to observe cutting force vibration and tool vibrations developed during machining process. The machine bed alignment has been conducted on top surface of machine body by using dial gauge. The maximum and minimum values of Alignment test of machine bed are measured by dial gauge and tabulated in Table 3.

Table 3. Alignment test results of Lathe Bed.

Test Trial No	Chuck Alignment position (distance)	Deviation division in Dial test indicator	Amount of Deviation (mm)
1	10	2	0.02
2	20	2	0.02

3	40	1	0.01
4	60	2	0.02

It shows that average value of machine bed in 0.02 mm and also within allowable limit as per design of mini machine tool guide. Fig 3 shows that amount of deviation of machine bed during alignment test through Scatter Diagram. Fig 5 shows that deviation of machine bed of mini lathe which represent there is no deviation in alignment test. So the machine produces best accuracy in plain turning process.

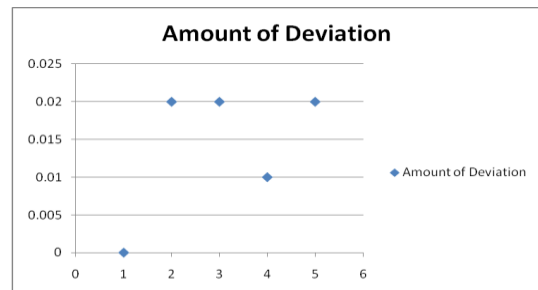


Fig 5 Scatter diagram for Alignment values of Bed

4. Conclusion

The performance test was conducted on various principle parts such as Machine spindle chuck, lathe bed and cross slide of Tabletop mini lathe. Dial gauge was used to check the values of Alignment test which the maximum and minimum values are within allowed limit. Hence Table top mini lathe is suitable for micro machining process and it can be implement the micro factory concept.

References

1. Kawahara N, Suto, Teheran, Ishikawa Y, Kitahara T, Ooyama T and Aka T (1997), "Technical Papers; Micro system Technologies Micro factories; new applications of micro machine technology to the Manufacture of small products", Springer-Verlag, 37-41.
2. Kussul E, Baidyk T, Ruiz Huerta L, Caballero Ruiz A, Velasco G and Kasatkina (2002), "Development of micro machine tool prototypes for micro factories", Journal of Micromechanics and Micro engineering, Vol.12, 795-812.
3. Trusty J (2013), "System and methods of testing of machine tools" micro technique, 162-173
4. Dai Gil Lee, Jung Do Suh, Hak Sung Kim and Jong Min Kim (2014), "Design and manufacture of composite high speed small machine tool structures", In Composites Science and Technology", Vol.64, 1523-1530.
5. Vogler M P, Liu X, Kapoor S G, Devor R E and Ehmann K F (2008), "Development of meso-scale machine tool (mMT) systems", Society of Manufacturing Engineers, 02-18, 1-9.

6. Heikkilä R, Järvenpää E & Tuokko R (2010), "Advances in the TUT Micro factory Concept", Vol.5, 290-296.
7. Elter J and Uswari Y (2014), "Micro machines mechanics and design", Precision machine design, Prentice-Hall, 223-234.
8. Okazaki Y and Kitahara T (2014), "Development and Evaluation of a Micro-Lathe Equipped with Numerical Control", Journal of the JSPE, Vol.67(11), 123-129
9. Ashida K (2012), "Development of a micro press machine", Journal of Mechanical Engineering lab, Vol.54 (6), 16-20.
10. Kitahara T, Ishikawa Y, Terada K, Nakajima N and Furuta K (2006), "Development of Micro-lathe and analysis", Journal of Mechanical Engineering Lab, Vol.50, 117-123.
11. Kondoh S, Masui K, Mishima N, and Matsumoto M (2012), "Total performance Analysis of Product life cycle considering product value", Proceedings of Care Innovation, Austria, 197-203.

TRIBOLOGICAL BEHAVIOUR FOR STIR CAST Al5086/Gr/Al₂O₃ HYBRID MATRIX COMPOSITE

K.CHANDRASEKARAN^{*1}, S.AJITH², P.ABBAS³, A.YASAR ARAFATH⁴, K.VINOTHKUMAR⁵

Department of Mechanical Engineering, MAM School of Engineering, Trichy, Tamilnadu, India.

**Corresponding author Email: kchandrusekaran1984@gmail.com, Mobile +919942042664.*

ABSTRACT

Aluminum Hybrid Reinforcement Technology is a reaction to the dynamic regularly expanding administration necessities of ventures, for example, Transportation, Aerospace, Automobile, Marine, and so forth since they are bendable, profoundly conductive, light weight and have a high quality to weight proportion. In this development, an endeavour has been made to research the wear rate of Al5086 hybrid metal matrix composite strengthened with the hard earthenware Alumina (4, 8, 12 wt. % of Al₂O₃) and delicate strong oil of graphite (2, 4, 6 wt. % of Gr) manufactured by utilizing mix throwing technique. The un-greased up pins on plate wear tests were directed to look at the wear conduct of Al5086/12 wt. % of Al₂O₃/Gr composites. The sliding wear tests were completed at different heaps of (15, 30, 45 N), sliding speed (1.25, 2.50, 3.25 m/sec), and diverse graphite wt. % (2, 4, 6 wt. %).

Keywords: Al5083; Al₂O₃; Graphite; Taguchi techniques; wear rate.

I. INTRODUCTION

Aluminum Hybrid Matrix Composites are becoming better substitutes for the conventional Aluminum Alloys because of the characteristics like improved strength to weight ratio, energy saving, better wear resistance etc [1]. Interest in particulate reinforced aluminum hybrid matrix composites for the use in the automotive industry and other structural applications has increased because of the physical and mechanical properties they possess [2]. Aluminum based hybrid matrix composites with a variety of particulate reinforcements such as Al₂O₃, TiC, Ti₂B, B₄C, TiN, Si₃N₄, graphite and industrial waste by-product have been conceived and developed for various potential applications [3]. Aluminum hybrid matrix composites are developed by the researchers and they are used in many commercial and industrial applications [4]. Newer compositions have been continuously explored and the related valuable studies presented by the past researchers are discussed. Veeresh Kumar et al [5] have conducted the experiment on Al6061/SiC and Al7075/Al₂O₃ metal matrix composites and present the experimental results of the studies regarding hardness, tensile strength and wear resistance properties of Al6061/SiC and Al7075/Al₂O₃ composites. The SiC and Al₂O₃ resulted in improving the hardness and density of their respective composites. Wang and Yan [6] investigated the feasibility of machining Al6061/Al₂O₃ composite materials by electro discharge machining for blind hole drilling and evaluated the material removal rate, tool wear rate and surface roughness with various input parameters. Yan and Wang [7] observed that material removal rate increased with peak current and was erratic with pulse duration. The material removal rate, tool wear rate and surface

roughness increases with flushing pressure during machining of Al6061/Al₂O₃ composites using rotary electro discharge machining with a tube electrode. Yan et al [8] found that in case of rotary electro discharge machining process, the main challenge is of using a disk like electrode for machining Al6061/Al₂O₃ composites. Veeresh kumar et al [9] investigated the influence of reinforcement on mechanical properties when different matrix materials that is Al6061 and Al7075 and reinforcements such as SiC and Al₂O₃ are used and they observed micro hardness of the composite were increased with the increase of filler content.

While many researchers have carried out on the mechanical, wear properties and machining characteristics of aluminum metal matrix composites with graphite and Al₂O₃ as reinforcing materials. In the case of hybrid Al5086/Gr/Al₂O₃ composites, limited literatures is available, encompassing various aspects such as mechanical properties and wear behaviour and conduct the machining study of the composites. Aluminum based Al₂O₃ particle reinforced composite material have become useful engineering materials due to their properties such as low weight, heat resistant, wear resistant and low cost. These are found in various engineering applications such as cylinder block liners, vehicle drive shafts, automotive pistons, bicycle frames etc.

II. EXPERIMENTAL DETAILS

The stir casting technique is the simplest and the most economical process for producing particulate reinforced composites available for particulate reinforced metal

matrix composites. In this technique, in order to accomplish the optimum property of the hybrid composite, the distribution of the reinforced particles in the base material sought to be homogeneous and the wet ability among the olden materials and particulates ought to be optimized. The moisture level with cast composite must be minimized and the element reactions between the particle material and the base material have to be avoided. The whirlpool method is individual of the enhanced recognized approaches used to build a high quality allocation of the reinforced material in the base matrix. During this, once the base material is melted, it is stirred forcefully by automatic agitator to form a whirlpool at the face of liquefy, and the particle material is subsequently introduced at the region of the vortex.

A. Material fabrication

The chemical composition of Al5086 alloy is given in Table 1 and Al5086 alloy was melted in a crucible in a generation type of furnace at 725°C. Subsequent to melting and degassing by nitrogen, an alumina coated stainless steel stirrer was meant for stirring at 600 rpm used for 20 min time duration. During stirring, it is preheated at 600°C, particles alumina and MoS₂ powder was added. After that the composite alloy was roll poured into the pre heated (250°C) permanent mould. The Al5086 alloy with different wt. % of hybrid composites is produced and test specimens were machined.

TABLE I

Chemical composition of Al5086 alloy

Si	Fe	Cu	Mn	Mg	Cr	Zn	Ti	Al
0.6	0.	0.2	0.1	0.	0.0	0.2	0.1	Remaini
5	7	5	5	8	7	5	5	ng

B. Mechanical behaviour

The hardness tests were carried out according to ASTM E10-07 standards using Brinell hardness testing machine with a 10 mm ball indenter and 500 kg load for 30 s. The test was conducted at room temperature (30°C) and the measurement of hardness was taken at three different places on each sample to obtain an average value of hardness. As per the ASTM E08-8 standard, the tensile strength was evaluated on the cylindrical rod of casted composites. The 1200 grit grindings silicon carbide paper was used to polish the test specimens in order to decrease the machining scratches and the effects of surface defects on the sample. The universal testing machine was loaded with 10 KN, load cell was used to conduct the tensile test. The affecting factors and levels selected for mechanical behaviour Al5086/Gr/Al₂O₃ are given in Table 2.

TABLE II

Affecting factors and levels selected for tensile strength Al5086/Gr/Al₂O₃

Factors /levels	1	2	3
X- wt. % Al ₂ O ₃ (wt. %)	4	8	12
Y- wt. % Graphite (wt. %)	2	4	6

C. Tribological behaviour

The pin on disc test apparatus is used to investigate the dry sliding wear behaviour of Al5086/12 wt. % Al₂O₃/ Gr hybrid composites. Pin specimens of 6 mm diameter and 15 mm height for wear test was prepared from the above composites were machined and polished. The test was conducted with various loads of 15 N, 30 N and 45 N at a sliding speed of 125, 2.50, 3.25 m/s and 2, 4, 6 Gr wt. %. The test was conducted at room temperature (30°C) and relative humidity of 60–65%. The affecting factors and levels selected for Tribology Al5086/12 wt. % Al₂O₃/ Gr is given in Table 3.

Table III

Affecting factors and levels selected for Tribology Al5086/12 wt. % Al₂O₃/ Gr

Factors /levels	1	2	3
A-Load (N)	15	30	45
B-Sliding velocity (m/s)	1.25	2.50	3.25
C-wt. % of Gr (wt. %)	2	4	6

III. RESULT AND DISCUSSION

A. Optimum setting for TS & BHN of Al5086/Al₂O₃/ Gr

The tensile strength and hardness of the Al5086/4, 8, 12 wt. % Al₂O₃/2, 4 wt. % Gr hybrid composites is shown in Figure 1(a) and Figure 1 (b). It is observed that an addition of alumina particles improve the tensile strength and hardness of hybrid composites. It is evident that tensile strength and hardness clearly increases with the addition of alumina particles. The tensile strength and hardness of the Al5086/4, 8, 12 wt. % Al₂O₃/6 wt. % Gr hybrid composites is shown in Figure 1(c). Increase in content of graphite the tensile strength and hardness of hybrid composite is decreased.

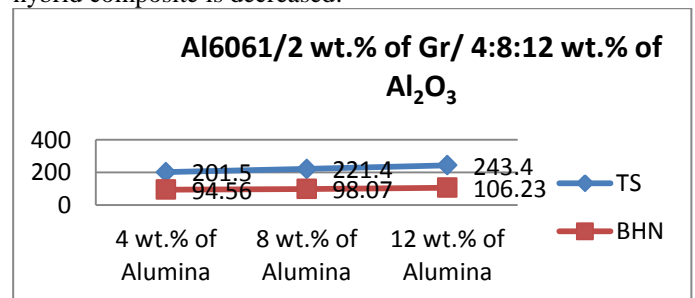


Fig. 1 (a) Mechanical behaviour of Al5086/2 wt. % of Gr/4:8:12 wt. % of Al₂O₃

TABLE VI

Taguchi Analysis: TS & BHN versus X, Y of Al₅₀₈₆/Al₂O₃/ Gr

Level	TS		BHN	
	X	Y	X	Y
1	46.42	46.91	33.33	33.42
2	47.19	47.54	33.48	33.54
3	48.00	47.16	33.63	33.47
Delta	1.58	0.64	0.29	0.12
Rank	1	2	1	2

**Al6061/4 wt.% of Gr/ 4:8:12 wt.%
of Al₂O₃**

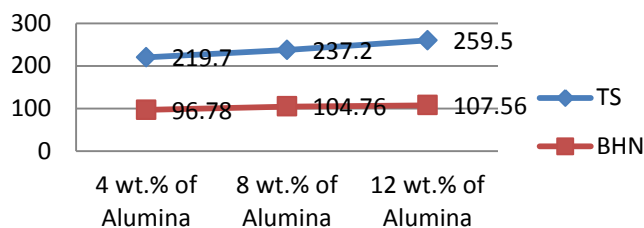


Fig. 1 (b) Mechanical behaviour of Al₅₀₈₆/4 wt. % of Gr/ 4:8:12 wt. % of Al₂O₃

**Al6061/6 wt.% of Gr/ 4:8:12
wt.% of Al₂O₃**

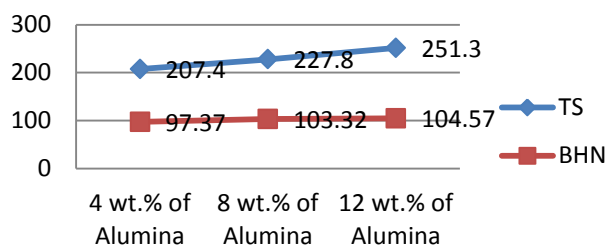


Fig. 1 (c) Mechanical behaviour of Al₅₀₈₆/6 wt. % of Gr/ 4:8:12 wt. % of Al₂O₃

TABLE V

Experimental result for tensile strength of Al₅₀₈₆/Al₂O₃/ Gr

X	Y	Al ₂ O ₃ (wt. %)	Mo S ₂ (wt. %)	TS (N/mm ²)	S/N Ratio	BHN	S/N Ratio
1	1	4	2	201.5	46.08 55	94.5 6	33.27 13
1	2	4	4	219.7	46.83 66	96.7 8	33.41 17
1	3	4	6	207.4	46.33 62	97.3 7	33.31 84
2	1	8	2	221.4	46.90 36	98.6 7	33.42 41
2	2	8	4	237.2	47.50 23	104. 76	33.53 43
2	3	8	6	227.8	47.15 11	103. 32	33.46 98
3	1	12	2	243.4	47.72 64	106. 23	33.57 52
3	2	12	4	259.5	48.28 27	107. 56	33.67 58
3	3	12	6	251.3	48.00 38	104. 57	33.62 55

The measured values of tensile strength and BHN for Al₅₀₈₆/Al₂O₃/ Gr under different wt. % and corresponding signal to noise ratio for all experimental runs are given in Table 5. The Taguchi analysis of tensile strength and BHN for Al₅₀₈₆/Al₂O₃/Gr under different wt. % is given in Table 6. It clearly shows the maximum tensile strength is obtained at 12 wt. % of Al₂O₃ and 2 wt. % of Gr and the maximum BHN is obtained at 12 wt. % of Al₂O₃ and 4 wt. % of Gr. Table 7 shows that the results of ANOVA for tensile strength and BHN on Al₅₀₈₆/Al₂O₃/ Gr hybrid composite. It is observed that Al₂O₃ is the most significant parameter affected the tensile strength of Al₅₀₈₆/Al₂O₃/ Gr with F: P value of 1092.26: 0.000 and Al₂O₃ is significantly affecting the BHN of Al₅₀₈₆/Al₂O₃/ Gr with F: P value of 480.69: 0.000.

B. Tribological behaviour of Al₅₀₈₆/Al₂O₃/ Gr

The variation of wear rate for Al₅₀₈₆/Al₂O₃/ Gr hybrid composite with respect to different sliding velocity and applied load is given in Table 8. The applied load affects the wear rate of hybrid composites significantly. The wear rate varies with applied load is an indicative of Archard's law and significantly lower in the case of hybrid composites. The wear rate increases with increasing applied load and it is less at 6 wt. % of Gr hybrid composites as compared to 2 wt. % of Gr. This is mainly due to the presence of Al₂O₃ in Al₅₀₈₆. However, at all load conditions are considered the wear resistance of the hybrid composites were superior to the matrix alloy. The wear rate is increased with increase in sliding speed Al₅₀₈₆/12 wt. % Al₂O₃/ Gr hybrid composite. Increasing sliding speed temperature is raised to the sliding surfaces this leads to softening of the matrix and composite pin surfaces and it is due to the enhancement in the hardness. The increase in hybrid composite hardness results in improvement of wear resistance. The presence of Gr and Al₂O₃ particles in the hybrid composite will lead to further reduction of wear rate. The coefficient of friction for Al₅₀₈₆/12 wt. % Al₂O₃/ MoS₂ hybrid composites under varying load and sliding velocity is given in Table 8. The coefficient of friction is decreased with increasing wt. % of Graphite and increasing the due to load. The Al₂O₃ particles act as load bearing elements in the hybrid composites and also it results in formation of more stable lubricating film on the Tribo surface of the hybrid composites. The decreased coefficient of friction of hybrid composite with Graphite content can be credited to the

collective effects of Graphite and Al₂O₃ particles in formation of a more resistant Tribo layer on the contact surface. The graphite Tribo film minimize the degree of shear stress transferred to the sliding material underneath the sliding contact area which results in less plastic deformation in the sub surface region and reduces the wear rate in the hybrid composites. The experimental values of wear rate and coefficient of friction for Al5086/12 wt. % Al₂O₃/ Graphite under different parameters and corresponding signal to noise ratio for all experimental runs are given in Table 8. The Taguchi analysis for

Al5086/12 wt. % Al₂O₃/ Graphite under different load, sliding velocity and wt. % of Graphite is given in Table 9. It clearly shows the minimum wear rate and coefficient of friction is obtained at 15N of load, 3.25 m/sec of sliding velocity and 6 wt. % of Graphite. Table 10 shows that the results of ANOVA for wear rate and coefficient of friction on Al5086/12 wt. % Al₂O₃/ Graphite hybrid composite. It is observed that load is the most significant parameter affecting the wear rate and coefficient of friction of Al5086/12 wt. % Al₂O₃/ Graphite with F: P value of 29.06: 0.033 and 756.27:0.001.

TABLE VII

Analysis of Variance for TS & BHN of Al6061/Al₂O₃/ MoS₂

Source	DF	TS				BHN			
		Seq SS	Adj MS	F	P	Seq SS	Adj MS	F	P
X	2	2634.78	1317.39	1092.26	0.000	3.7691	1.8845	480.69	0.000
Y	2	423.56	211.78	175.59	0.000	0.6125	0.3063	78.12	0.001
Error	4	4.82	1.21			0.0157	0.0039		
Total	8	3063.17				4.3973			
R-Sq = 99.84%; R-Sq(adj) = 99.69%					R-Sq = 99.64% ; R-Sq(adj) = 99.29%				

TABLE VIII

Experimental results for Al6061/12 wt. % Al₂O₃/ Graphite of wear study

Trial	A	B	C	Load (N)	Sliding velocity (m/s)	wt. % of Gr (Wt. %)	Wear rate (mm ³ /min) X 10 ⁻³	S/N	Coefficient of friction	S/N
1	1	1	1	15	1.25	2	1.346	-2.580	0.487	6.249
2	1	2	2	15	2.50	4	1.250	-1.938	0.455	6.839
3	1	3	3	15	3.25	6	0.966	0.300	0.423	7.473
4	2	1	2	30	1.25	4	2.344	-7.399	0.523	5.629
5	2	2	3	30	2.50	6	2.576	-8.218	0.496	6.090
6	2	3	1	30	3.25	2	2.133	-6.579	0.537	5.400
7	3	1	3	45	1.25	6	2.756	-8.805	0.568	4.913
8	3	2	1	45	2.50	2	3.813	-11.625	0.603	4.393
9	3	3	2	45	3.25	4	3.245	-10.224	0.579	4.746

TABLE XI

Taguchi Analysis: Wear rate and coefficient of friction versus A, B, C of Al5086/12 wt. % Al₂O₃/ Graphite

Level	Wear rate			Coefficient of friction		
	A	B	C	A	B	C
1	-1.406	-6.262	-6.929	6.854	5.597	5.348
2	-7.399	-7.261	-6.521	5.707	5.775	5.739
3	-10.218	-5.501	-5.575	4.684	5.873	6.159
Delta	8.812	1.760	1.354	2.170	0.276	0.811
Rank	1	2	3	1	3	2

TABLE X

Analysis of Variance for Wear rate of Al5086/12 wt. % Al₂O₃/ Graphite

Source	DF	Wear rate				Coefficient of friction			
		Seq SS	Adj MS	F	P	Seq SS	Adj MS	F	P
A	2	6.5442	3.2721	29.06	0.033	0.0247047	0.0123523	756.27	0.001
B	2	0.3456	0.1728	1.53	0.395	0.0002580	0.0001290	7.90	0.112
C	2	0.1651	0.0826	0.73	0.577	0.0032667	0.0016333	100.00	0.010
Error	2	0.2252	0.1126			0.0000327	0.0000327		
Total	8	7.2801				0.0282620			
R-Sq = 96.91% R-Sq(adj) = 87.63%					R-Sq = 99.88% R-Sq(adj) = 99.54%				

IV. CONCLUSION

In the present investigation, the Al5086/Al₂O₃/ Graphite hybrid composite was successfully fabricated using stir casting process. The mechanical behaviour and tribological behaviour were evaluated. The obtained results can be summarized as follows:

- Mechanical properties of hybrid composites increase with an increase in weight fraction of alumina particles. An increase in weight fraction of molybdenum disulphide reinforcement decreases the mechanical properties like tensile strength and BHN. The optimum parameter for maximization of tensile strength is obtained at 12 wt. % of Al₂O₃ and 2 wt. % of Graphite and the maximum BHN is obtained at 12 wt. % of Al₂O₃ and 4 wt. % of Graphite
- The incorporation of Al₂O₃ reinforcement to Al5086 increases the wear resistance of the composites. The addition Graphite reinforcement in Al5086/Al₂O₃ composites as a hybrid reinforcement further increases the wear and friction resistance of the composite. This is attributed to the stable and Graphite rich mechanically mixed layer, which prevents metal to metal contact and reduces the wear of the composite. The unstable mechanically mixed layer in the absence of the lubricant phase leads to lower wear resistance in Al5086/Al₂O₃/ Graphite hybrid composite. The optimum parameter for minimization wear rate and coefficient of friction is obtained at 15N of load, 3.25 m/sec of sliding velocity and 6 wt. % of MoS₂.

REFERENCES

- [1] L. Poovazhagan, K. Kalaichelvan, A. Rajadurai, and V. Senthilvelan, "Characterization of hybrid silicon carbide and boron carbide nano particles-reinforced aluminum alloy composites", *Procedia Engineering*, vol.64, pp.681 – 689, 2013.
- [2] A.M. Al Qutub, A. Khalil, N. Saheb, and A.S. Hakeem, "Wear and friction behaviour of Al6061 alloy reinforced with carbon nanotubes", *Wear*, vol.297, pp.752–761, 2013.
- [3] K. Umanath, S.T. Selvamani, and K. Palanikumar, "Analysis of dry sliding wear behaviour of Al6061/SiC/Al₂O₃ hybrid metal matrix composites", *International Journal of Composite Part-B Engineering*, vol.53, pp.159-168, 2013.
- [4] K. Umanath, S.T. Selvamani, and K. Palanikumar, "Friction and wear behaviour of Al6061 alloy (SiCp/Alp) Hybrid composites", *International Journal of Engineering Science and Technology*, vol.03, no.7, pp.5441-5551, 2011.
- [5] G.B. Veeresh Kumar, C.S.P. Rao, N.Selvaraj, and M.S. Bhagyashekar, "Studies on Al6061/SiC and Al7075/Al₂O₃ Metal Matrix Composites", *Journal of*

Minerals & Materials Characterization & Engineering, vol. 9, no.1, pp.454-461, 2010.

[6] C.C. Wang, and B.H. Yan, "Blind-hole drilling of Al₂O₃/6061Al composite using rotary electro discharge machining", *Journal of Material Processing Technology*, vol. 102, pp.90-102, 2000.

[7] B.H. Yan, and C.C Wang, "The machining characteristics of Al6061 composite using rotary electro-discharge machining with a tube electrode", *Journal of Material Processing Technology*, vol. 95, pp.222-231, 1999.

[8] B.H. Yan, C.C. Wang, W.D. Liu, and F.Y. Huang, "Machining characteristics of Al₂O₃/6061Al composite using rotary EDM with a disk like electrode", *International Journal of Advanced Manufacturing and Technology*, vol. 16, pp.322-333, 2000.

[9] G.B. Veeresh Kumar, C.S.P. Rao, N. Several, and M.S. Bhagyshakar, "Studies on Al6061-SiC and Al7075-Al₂O₃ Metal Matrix Composites", *Journal of Minerals & Materials Characterization & Engineering*, vol.09, pp.43-55, 2010.

Biographies and Photographs



Dr.K.Chandrasekaran, M.E., PhD, MISTE, IRED obtained his Bachelor degree in Mechanical Engineering and Master Degree in Manufacturing Engineering from Anna University Chennai and Anna University of Technology Tiruchirappalli, India. He was completed PhD in the area of Machining science from Anna University, Chennai. He had served in many Institutions at various positions as Lecturer, Assistant Professor and Associate Professor. Now he is working as a professor in MAM School of Engineering, Trichy. He had published more number of papers in refereed International Journals and Conferences. His research areas include Manufacturing, Composites, Machining Science, Modeling and optimization. He is guiding PhD scholars in different areas. He is active Doctoral committee member for PhD scholars and Examiner for various autonomous Institutions and Universities.

Fabrication and Optimization of MEMS based Micro Grinder

^[1] TTM.Kannan, ^[2] K.Chandrasekaran, ^[3] R.Ramanathan, ^[4] S.Surya

^[123] Associate Professor, Department of Mechanical Engineering, M.A.M.School of Engineering, Trichy-621 105.
India

^[4] UG student, Department of Mechanical Engineering, M.A.M.School of Engineering, Trichy-621 105. India.

Abstract: -- Microfabrication technologies have been steadily advancing in recent years. Research and development are being vigorously conducted with a view towards the implementation of micromachines. Miniature of components with micro scaled features are increasing required in many industries including biomedical, Consumer electronics, automotive and defense. Mems has been identified as one of the most promising technology for 21 st Century has the potential revolutionize both industrial and consumer products. MEMS is a technology used to create tiny integrated chips that combine mechanical and electrical components. Micro grinding has a competitive edge over microfabrication processes are generally used as finishing process and generated very high surface finish. In this experimental work, fabrication of mems based micro grinding machine for the purpose of producing a very high surface finish on micro components. Dimensions of Micro grinder are 10mm x 2mm x 2mm and provide the speed of 10,000 rpm. Optimize the material removal rate of micro grinding process parameters are selected by L9 orthogonal array using 3 levels and 2 factors. Main objectives of the MEMS based micro grinder are saving energy, space, material, time and other resources. The sustainability of miniaturized production is discussed from three perspectives such as Economics, Environment and social.

Keywords - Micro Fabrication, MEMS, Micro Grinder, DOE, Analysis.

I. INTRODUCTION

A. Micro grinder

Mems is a process technology used to create tiny integrated devices combines mechanical and electrical components. Mems consist of micro actuator, micro sensor and micro electronics and integrated on same silicon chip. Mems devices are very small and their components are usually microscopic levers, gears, actuators and motors have fabricated by MEMS technology. Micro grinder is a small sized grinding machine which is used to ground micro sized components in degree of accuracy.(Fig1) The micro grinder is made of Mems devices and controlled by actuator. It is tiny machine to remove the material from micro component from 1 micron into 999 micron. Micro grinding is the machining processes which improve surface quality and dimensional accuracy. Various process parameters affect the micro grinding operations are depth of cut, spindle speed, feed and wheel grain size are adverse impact of surface roughness and material removal rate are the influencing parameters of micro grinding process

II-APPLICATIONS

MEMS based Micro grinder is very much useful for dental mechanic, micro valve lapping, micro cutting, tool grinding. Micro electronics and automotive applications.

III-EXPERIMENTAL DETAILS

Work material: AISI 1020
Tool Material: SiC
Designation of Grinding Wheel
W A 36 K 5 R 17
W-Manufacture's Abrasive symbol
A- Aluminium oxide
36- Medium grain
K-Medium Grade
5-Dense Structure
R-Rubber Bond
17- Manufacture's type symbol
A-Experiment Design

The micro grinding process of AISI 1020 has been optimized by Taguchi design of experiment and analyzed by Signal to noise ratio. L9 type of design is utilized to conduct

experiments. There are 3 levels and 2 Factors are conducted in this experiment. The spindle speed and depth of cut are the input parameters of micro grinding process and Material removal rate is selected as a response parameter is shown in Table 1.

Table 1 Levels and Factors of Micro grinding process parameters

Sl.no	Levels	Spindle speed(rpm)	Depth of Cut(mm)
1	Low	1000	0.01
2	Medium	2000	0.02
3	High	3000	0.03

Fig 1 MEMS based Micro grinder

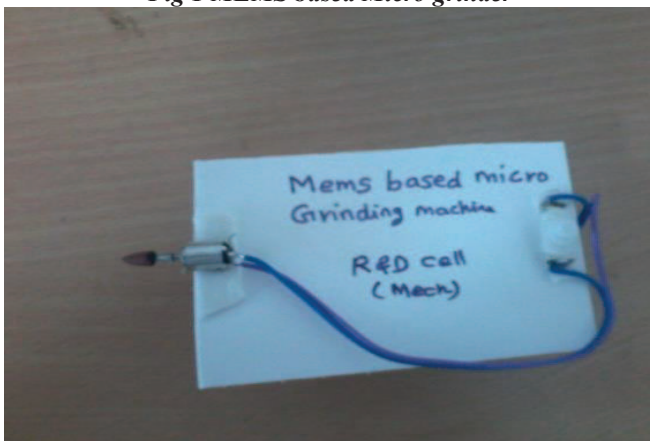


Fig 1 MEMS based Micro grinder

B. Design of Experiments via Taguchi methods

The Taguchi method involves reducing the variation in a process through robust design of experiments. The overall objective of the method is to produce high quality product at low cost to the manufacturer. The Taguchi method was developed by Dr. Genichi Taguchi of Japan who maintained that variation. Therefore, poor quality in a process affects not only the manufacturer but also the society. He developed a method for designing experiments to investigate how different parameters affect the mean and variance of a process performance characteristics that defines how well the process is functioning. The experimental design proposed by Taguchi involves using orthogonal arrays to organize the parameters affecting the process and the levels at which they should be varied and it allows for the collection of the necessary data to determine which factors most affect product quality with a

minimum amount of experimentation, thus saving time and resources.

IV- OPTIMIZATION OF MEMS BASED MICRO GRINDING MACHINE.

Table 2 Micro grinding parameters of AISI-1020

Spindle speed(rpm)	Depth of cut(mm)	MRR(gram/min)
1	1	0.30
1	2	0.34
1	3	0.28
2	1	0.48
2	2	0.46
2	3	0.70
3	1	0.90
3	2	0.94
3	3	0.92

Table 2 shows that optimum parameter of micro grinding process for achieving larger material removal rate of AISI 1020 are 3 rd level of spindle speed and 2 nd Level of depth of cut

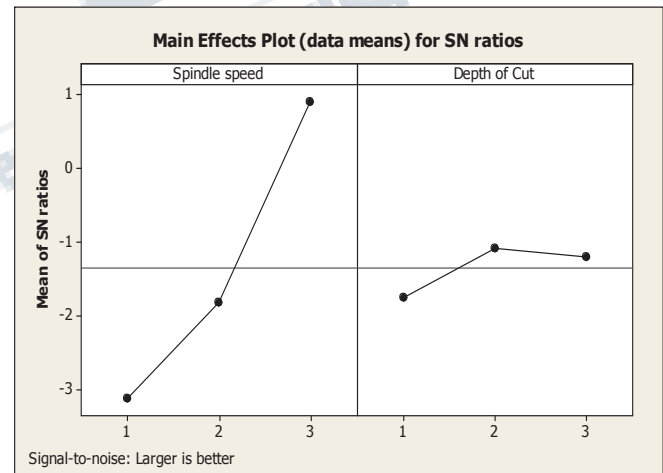


Fig 2 Main effect plot for Micro grinding process

Fig 2 shows that the signal to noise ratio of micro grinding process of AISI 1020 and represent thirdrd level of spindle speed and second level of depth of cut is an optimum parameter of micro grinding process in Mems based micro Grinding machine

**Table 3 Response Table for Signal to noise ratio
(Larger is better)**

Level	Spindle speed	Depth of cut
1	-3.1034	-1.7520
2	-1.8190	-1.0829
3	0.8988	-1.1886
Delta	.0021	0.6691
Rank	1	2

Table 3 shows that Spindle speed is a dominating parameter of micro grinding process of MEMS based micro grinding machine

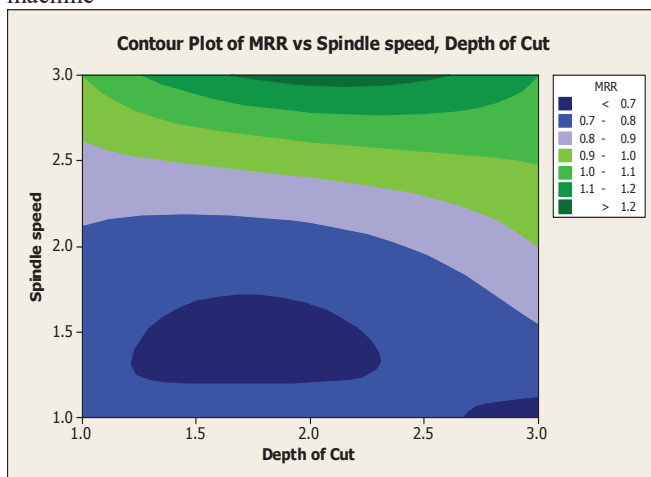


Fig3 Contour plot for micro grinding process

Fig 3 Contour plot for micro Grinding process parameter of AISI 1020 which indicate the optimum setting of micro grinding process of MEMS based Micro grinding machine are third level of spindle speed and second level of depth of cut for achieving Larger material removal rate.

V-CONCLUSION

The micro grinder has been fabricated successfully using MEMS devices and suitable for micro components. The larger material removal rate of micro grinding process are Third level of spindle speed and Second level of depth of cut. The micro grinder is saving energy, space, material, time and other resources. The sustainability of miniaturized production are discusses from three perspective such as economic, environment and social.

REFERENCES

- Breguet, J.M., C. Schmitt and R. Clavel (2010) Micro/ Nano factory: Concept and State of the Art. Micro robotics and Micro assembly II, Proceedings of SPIE, 4194, 1-5.
- Clévy, C., A. Hubert and N. Chaillet (2008) Flexible micro-assembly system equipped with an automated tool changer. Journal of Micro - Nano Mechatronics,4, 59-72.
- Fruta, K. (2005) The Experimental micro factory system in Japanese national R&D project. Singapore-Japan forum on MEMS, 23 November 2000, Singapore.
- Heikkilä, R., E. Järvenpää and R. Tuokko (2011) Micro factories: New applications of micro machine technology for small products. Manufacture 2011 conference, October 24, 78-84.
- Heikkilä, R., I. Karjalainen, J. Uusitalo, A. Vuola, and R. Tuokko (2012) Possibilities of a Micro factory in the Assembly of Small Parts and Products. First Results of the M4-project, ISAM, Japan, 166-171.
- Heikkilä, R., I. Karjalainen, J. Uusitalo, A. Vuola, and R. Tuokko (2007) Possibilities of a Micro factory in the Assembly of Small Parts and Products – First Results of the M4-project. Proceedings of the ISAM 2007, IEEE International symposium on assembly and manufacturing, Ann Arbor, Michigan, USA, 166-171.
- Heikkilä, R., J. Uusitalo, R. Heikkilä and R. Tuokko (2010) A Micro factory Concept for Laser-Assisted Manufacturing of Personalized Implants. IWMP, 77-80.
- Hofmann, A., B. Hummel, O. Firat, G. Bretthauer, M. Bär and M. Meyer (2011) Micros FLEX - A New Concept to Address the Needs for Adaptable Meso and Micro Assembly Lines. ISAM 2011,123-127.
- Kawahara, N, T. suto, T. Hirano, Y. Ishikawa, itahara, N. Ooyama, & T. Ataka (2007) icrofactories: New applications of micro machine technology to manufacture of small products. Journal of Micro system Technologies, 3, 37-41.
- Kondoh.S., K. Masui, N. Mishima, and M. Matsumoto (2012) Total performance Analysis of Product life cycle considering product value. Proceedings of CARE INNOVATION, Austria, 2012:2.101.

**International Journal of Engineering Research in Mechanical and Civil Engineering
(IJERMCE)**

Vol 2, Issue 12, December 2017

11. Okazaki. Y. (2010) Micro factories - A New Methodology for Sustainable Manufacturing. International Journal of Automation Technology, 4, 82-87.
12. Park, J.K., N.K. Lee, D.W. Lee and J. Song (2012) Development of Micro factory Systems for the Next Generation. 3rd Year Report, 3rd International Workshop on Micro factory Technology, 5-12.
13. Ashida, K., M.Mishima and T.Tanikawa (2000) Development of desktop machining microfactory-Trail production of miniature of machine products Japan, USA Flexible automation conference ,Ann Arbor, Michigan.3,123-129.
14. Kawakara, N., T.suto and T.Hirano (1997) Micro factories: New applications of micro machine technology to the manufacture of small products. Micro system technologies. 37-41.
15. Rahman, M.A., M.Rahman and A.Senthil kumar (2003) Fabrication of Miniature of components using micro machining. Proceedings of International conference on Mechanical Engineering (ICME 2003), 1-6.
16. Kussul,E.,D.Rachkovskij and T.Baldyk (2014) A basis for low cost manufacturing of mechanical micro devices using Micro equipment. J of Micro mechanics and Micro engineering. 6 , 410-425.
17. Shimizu, S., (2014) Reduction of machine tools in size and weight. J of JSPE.,920-925.
18. Ikawa, N., R.R. Donaldson., R.Kormanduri., W.Konig and T.H,Aachen (1991) Ultra precision metal cutting-past –present and Future, Annals of CIRP. 40, 587-594.
19. Heikkilä, R., Järvenpää, E. & Tuokko, R., (2010) Advances in the TUT Micro factory Concept, 5, 290-296.
- 20.Kannan,TTM., P.Ranjith Kumar., Chandrasekaran(2017)Development of MEMS based Pocket factory for Sustainable manufacturing system-Lambert Academic publishing,65-75

ISSN (Online) : 2456 - 1290

**The Board of
International Journal of
Engineering Research in Mechanical and Civil Engineering
(IJERMCE)**

is hereby awarding this certificate to

K.Chandrasekaran

in recognition of the publication of the paper entitled

Fabrication and Optimization of MEMS based Micro Grinder

Published in IJERMCE Journal, Volume 2, Issue 12, December 2017

Srinivas P.C.
Chief Editor

creal
Director

 **IFERP**
connecting engineers...developing research



TAGUCHI AND RESPONSE SURFACE METHODOLOGIES ENGAGED FOR SURFACE ROUGHNESS IN CNC TURNING AISI 316 BY MULTILAYERED COATED TOOL

*Chandrasekaran K¹, Ramanathan R², Kannan T T M³ and Ranjithkumar P⁴

^{1,2,3,4} Department of Mechanical Engineering, M.A.M.School of Engineering, Trichy, Tamilandu, India.

ABSTRACT

This paper examines about the utilization of Taguchi and reaction surface techniques (RSM) for minimizing the surface roughness (SR) in CNC turning austenitic stainless steel (AISI 316) by multilayered coated with TiCN/Al₂O₃ tool. The trials have been led utilizing Taguchi exploratory outline system. The cutting parameters utilized are cutting pace, encourage and profundity of cut. The impact of cutting parameters on SR is assessed and the ideal cutting condition for limiting the SR is resolved. In the first place and second request demonstrate are built up between the cutting parameters and SR utilizing RSM. The test comes about uncover that the most huge tuning parameter for SR is sustain trailed by cutting rate. The predicted values and measured values are fairly close, which indicates that the developed model can be effectively used to predict the SR in turning of AISI 316. Analysis of variance (ANOVA) is used for identifying the significant parameters affecting the responses. Finally the residual analysis is employed for verify the regression model.

Keywords: CNC tuning – surface roughness – Taguchi technique – Response surface method – ANOVA.

1. Introduction

Machining process is very important in manufacturing technology. These processes are applied for manufacturing the mechanical parts because of these processes have efficient and economical. There are many parameters to be considered for affecting the surface quality [1, 2]. SR is one of the imperative reactions for machined item quality. SR is influencing the useful conduct of the mechanical items. The mechanism of SR formation depends on various uncontrollable parameters that make its estimation difficult [3, 4]. AISI 316 are generally regarded as being more difficult to machine material compare to carbon and other alloy steels due their high strength, ductility and high work hardening tendency [5]. Stainless steels are having different grades and different properties under variation of chemical compositions. Therefore, these variations in their properties have an influence on their machinabilities [6]. Tool wear is broadly viewed as a standout amongst the most difficult part of causing poor surface quality in machining. Coated carbides are essentially an established carbide coated with at least one daintily layers of wear safe materials, for example, titanium nitride, titanium

carbide and aluminum oxide [7, 8]. It is outstanding that covering can diminish tool wear and enhance the SR [9, 10]. Hence, a large portion of the carbide apparatuses utilized as a part of the metal cutting enterprises is covered while covering realizes an additional cost [11, 12].

In order to get good SR and dimensional properties, it is necessary to employ optimization techniques to find optimal cutting parameters and theoretical models to do predictions. Taguchi and RSM can be conveniently used for these purposes [13]. Taguchi and RSM are applied for optimizing geometric errors in surface grinding process [14]. RSM is more practical, economical and relatively easy to use [15]. Researcher have used many methods to predict responses, but combination of these methods not been done for CNC turning on AISI 316 by multilayered tool. In this paper Taguchi method is used to optimize the performance characteristics of process parameters and first and second order models are developed for predicting the SR. The predicted and measured values are fairly close to each other.

*Corresponding Author - E- mail: kchandrasekaran1984@gmail.com

2. Material and methods

The work material used for the present investigation is AISI 316. The diameter of the material is 32 mm and machined length is 60mm for all trials. The chemical composition of the work material is given in Table 1.

Table 1 Chemical composition of AISI 316.

C	Si	Mg	P	S	Ni	Cr	Mo
0.04	0.49	1.56	0.03	0.01	10.4	16.7	2.11
0	8	0	6	7	5	1	2

2.1 Taguchi method

This paper uses Taguchi method for optimization of machining parameters in turning AISI 316, which is very attractive and effective method to deal with responses influenced by number of variables. In this method, main parameters are assumed to have influence on process results, which are located at different rows in a designed orthogonal array. With such an arrangement completely randomized experiments can be conducted. This method is useful for studying the interactions between the parameters, and also it is a powerful design of experiments tool, which provides a simple, efficient and systematic approach to determine optimal cutting parameters. Compared to the conventional approach of experimentation, this method reduces significantly the number of experiments that are required to model the response functions [16, 17]. There are three categories of quality characteristic in the analysis of the S/N ratio, (1) the-lower-the-better, (2) the-higher-the-better and (3) the-nominal-the-better. Since the quality characteristic is to be minimized, the-lower-the-better category is used to calculate the S/N ratio for SR. Equation (1) shows the smaller the better characteristic.

$$\eta = -10 \log_{10} \left\{ \frac{1}{n} \sum_{i=1}^n y_i^2 \right\} \quad (1)$$

Where:

η = Signal to noise ratio

n = Number of repetitions of experiment

y = Measured value of quality characteristic

Minitab14 statistical software has been used for the analysis of the experimental work. The software studies the experimental data and then provides the calculated results of signal-to-noise ratio. In this work, the software has given the signal-to-noise ratio for SR.

2.2 Response surface methodology

The surface finish of machined AISI 316 part is critical in assembling applications which have extensive impact on a few properties, for example, superb corrosive resistance. While machining, quality of the parts can be achieved only through proper cutting conditions. Keeping in mind the end goal to know the surface quality and dimensional properties ahead of time, it is important to utilize hypothetical models making it conceivable to do expectation in capacity of operation conditions. RSM is a collection of mathematical and statistical techniques that are useful for the modeling and analysis of problems in which a response of interest is influenced by several variables and the objective is to optimize this response. In many engineering fields, there is a relationship between an output variable of interest 'y' and a set of controllable variables $\{x_1, x_2, \dots, x_n\}$. In some systems, the nature of the relationship between y and x values might be known. Then, a model can be written in the form

$$Y = f(x_1, x_2, \dots, x_n) + \varepsilon \quad (2)$$

Where ε represents noise or error observed in the response y. If we denote the expected response be $f(x_1, x_2, \dots, x_n) = \hat{y}$ then the surface represented by

$$\hat{Y} = f(x_1, x_2, \dots, x_n) \quad (3)$$

In most of the RSM problems, the form of relationship between the response and the independent variable is unknown. Thus the first step in RSM is to find a suitable approximation for the true functional relationship between y and set of independent variables employed. Usually a second order model is utilized in response surface methodology [18].

3 Experimental details

The experiments are planned using Taguchi's orthogonal array in the design of experiments, which helps in reducing the number of

experiments. The experiments were conducted according to orthogonal array. The three machining parameters selected for the present investigation is cutting speed (v), feed (f) and depth of cut (d). Since the considered factors are multi-level variables and their outcome effects are not linearly related, it has been decided to use three level tests for each parameter. The machining parameters used and their levels chosen are given in Table 2. Taguchi's orthogonal array of L_{27} is most suitable for this experiment. This needs 27 runs and has 26 degrees of freedoms. It can conduct three levels of parameters. To check the degrees of freedom (DOF) in the experimental design, for the three levels test, the three main factors take 6 ($3 \times (3-1)$) DOFs. Square effects and interaction between parameters take the remaining DOFs. The values of machining parameters and S/N ratio for SR are presented in Table 3. The experiments were conducted on Fancu CNC lathe. Multilayered CNMG 120408 coated with $TiN+Al_2O_3$ of 14 μm is used as the insert for all machining operation. The range of cutting parameters were selected based on past experience, data book and available resources. SR is measured by the mitutoyo surface roughness tester.

Table 2 Machining parameters and levels.

Process parameter	Level 1	Level 2	Level 3
Cutting speed (m/min)	110	160	210
Feed(mm/rev)	0.1	0.2	0.3
Depth of cut (mm)	0.7	1.4	2.1

4 Results and discussions

4.1 Effect of control parameters on SR

In Taguchi method, the term signal represents the desirable value and noise represents the undesirable value. The objective of using S/N ratio is a measure of performance to develop products and processes insensitive to noise parameters. The S/N ratio indicates the degree of the predictable performance of a process in the presence of noise parameters. Table 4 shows the S/N ratios obtained for different parameter levels. The calculated S/N ratio for three factors on the SR in turning of AISI 316 for each level is shown in Fig. 4. As shown in Table 4 and Fig. 4 feed is a dominant parameter on the SR followed by depth of cut. The

cutting speed had a lower effect on the SR. Lower SR is always preferred. The quality characteristic considered in the investigation is lower-the better characteristics. The SR observed at low cutting speed is more than the SR observed at higher cutting speed. In the present investigation, when the cutting speed is set at 110 m/min is applied the SR is minimized. From the experimental results, it is observed that at high depth of cut the SR is minimal. Here feed is increased with head generation and tool wear so the SR is increased. The increase in feed also increases the chatter, and it produces incomplete machining of work piece, which led to higher SR. The results shown prove that the roughness of the machined surface is highly influenced by the feed, based on the above discussion and also evident from Fig. 4.

It is emphasized that these conditions only provide best SR among the cutting conditions tested. From Table 6 ANOVA for SR. It can be found that depth of cut and feed are the significant cutting parameters for affecting SR. The change of the cutting speed range given in Table 3 has an insignificant effect on SR (p -value = 0.98).

Table-3 Experimental results for SR versus v,f,d.

Trial	v	f	d	SR(μm)	S/N for SR
1	110	0.1	0.7	0.64	3.87
2	110	0.1	1.4	0.61	4.29
3	110	0.1	2.1	0.56	5.03
4	110	0.2	0.7	1.39	-2.86
5	110	0.2	1.4	1.14	-1.13
6	110	0.2	2.1	1.11	-0.90
7	110	0.3	0.7	1.66	-4.40
8	110	0.3	1.4	1.44	-3.16
9	110	0.3	2.1	1.02	-0.17
10	160	0.1	0.7	1.49	-3.46
11	160	0.1	1.4	0.92	0.72
12	160	0.1	2.1	0.7	3.09
13	160	0.2	0.7	1.33	-2.47
14	160	0.2	1.4	1.43	-3.10
15	160	0.2	2.1	1.38	-2.79
16	160	0.3	0.7	1.17	-1.36
17	160	0.3	1.4	1.23	-1.79
18	160	0.3	2.1	1.33	-2.47
19	210	0.1	0.7	1.83	-5.24
20	210	0.1	1.4	0.64	3.87
21	210	0.1	2.1	0.74	2.61
22	210	0.2	0.7	1.51	-3.57
23	210	0.2	1.4	1.43	-3.10
24	210	0.2	2.1	1.23	-1.79
25	210	0.3	0.7	1.7	-4.60

26	210	0.3	1.4	1.47	-3.34
27	210	0.3	2.1	1.39	-2.86

Table-4 Taguchi Analysis: SR versus v,f,d.

Level	v	f	d
1	0.06220	1.64526	-2.68090
2	-1.51796	-2.41895	-0.75213
3	-2.00636	-2.68843	-0.02909
Delta	2.06856	4.33369	2.65180
Rank	3	1	2

Table-5 Analysis of Variance for SR versus v,f,d.

Source	DF	SS	MS	F	P
v	2	0.315	0.15790	2.62	0.098
f	2	1.226	0.61338	10.17	0.001
d	2	0.635	0.31774	5.27	0.015
Error	20	1.206	0.06034		
Total	26	3.384			

S = 0.245637 R-Sq = 64.35% R-Sq (adj) = 53.65%

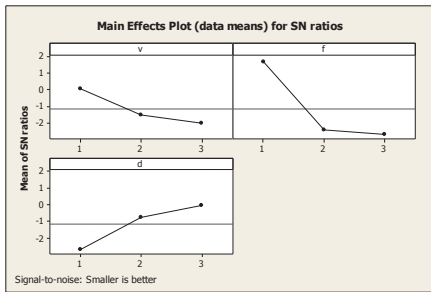


Fig.1. The Main effect of plot for S/N ratio for SR

4.2 Response surface analysis

4.2.1 First order regression model

The first order response surface representing the SR can be expressed as a function of cutting parameters. The relation between the SR and machining parameters has been expressed as follows

$$SR = \beta_0 + \beta_1 (v) + \beta_2 (f) + \beta_3 (d) + \beta_7 (v f) + \beta_8 (v d) + \beta_9 (f d) \quad (4)$$

From the observed data for SR, the response function has been determined is un coded unit as

$$SR = 0.941 + 0.132 v + 0.238 f - 0.181 d + 0.0372 vf - 0.0228 vd - 0.0717 df \quad (5)$$

The β coefficients, used in the above model can be calculated by means of using least square method. The first -order model is normally used when the response function is not known or nonlinear. The estimated first order regression coefficient the least squares method is as shown in table 6. Result of ANOVA for the function SR is presented in table 7. The analysis is carried of 5%, ie, for a level of confidence of 95%. To verify the regression model, we performed residual analysis. The normal plot and residual histogram from this analysis are depicted in Fig 2 and 3 respectively. As shown in Fig 2, the departures are scattered. It indicates the abnormalities in the residual distribution. Alternatively, the residual histogram shows that frequency of the residual is not satisfied with the normal distribution.

Table 6 First order regression coefficient

	Coef.	Coef.SE	T	P
β_0	0.9411	0.3028	3.11	0.006
β_1	0.13167	0.06096	2.16	0.043
β_2	0.23778	0.06096	3.90	0.001
β_3	-0.18111	0.06096	-2.97	0.008
β_4	0.03722	0.06096	0.61	0.548
β_5	-0.02278	0.06096	-0.37	0.711
β_6	-0.07167	0.06096	-1.18	0.254

Table 7 ANOVA for first order regression model

Source	D	SS	MS	F	P
Regression	6	2.04689	0.34115	5.10	0.003
Residual	20	1.33791	0.06690		
Error					
Total	26	3.38480			

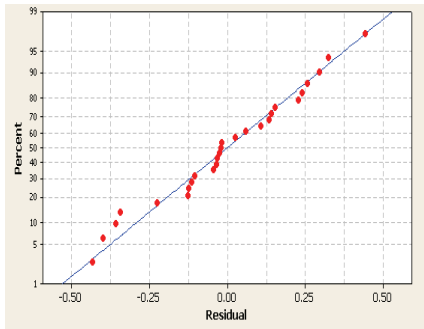


Fig 2 .Normal probability plot for the residuals

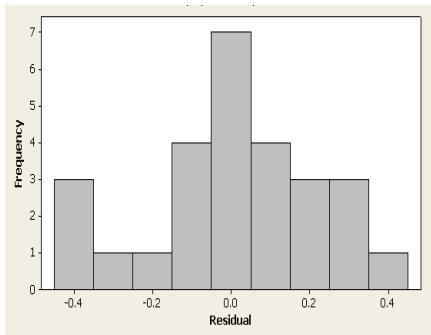


Fig 3.Histogram of the residuals.

4.2.2 Second order regression model

The second order response surface representing the SR can be expressed as a function of machining parameters. The relation between the SR and machining parameters has been expressed as follows

$$SR = \beta_0 + \beta_1 (v) + \beta_2 (f) + \beta_3 (d) + \beta_4 (v^2) + \beta_5 (f^2) + \beta_6 (d^2) + \beta_7 (v f) + \beta_8 (v d) + \beta_9 (f d) \quad (6)$$

From the observed data for SR, the response function has been determined is un coded unit as

$$SR = 0.889 + 0.132v + 0.238f - 0.181d + 0.0372v^2 - 0.0228f^2 - 0.0717d^2 + 0.0800vf + 0.0200vd - 0.0739fd \quad (5)$$

The second order estimated coefficient is shown in table 8. Result of ANOVA for the second order regression model is shown in table 9. Fig 5 and

6 show the results of normal probability and histogram of the residuals. As shown in Fig 5, the result is enhanced more than the first order regression model. Also, the frequency of the residual was satisfied with the normal distribution as shown if Fig 6 and the second order regression model is suitable for explaining the machining errors.

Table 8 The second order regression coefficient

	Coef.	Coef.SE	T	P
β_0	0.8889	0.3659	2.43	0.026
β_1	0.13167	0.06042	2.18	0.044
β_2	0.23778	0.06042	3.94	0.001
β_3	-0.18111	0.06042	3.00	0.008
β_4	0.03722	0.06042	0.62	0.546
β_5	-0.02278	0.06042	-0.38	0.711
β_6	-0.07167	0.06042	-1.19	0.252
β_7	0.08000	0.06042	1.32	0.203
β_8	0.02000	0.06042	0.33	0.745
β_9	-0.07389	0.06042	-1.22	0.238

Table 9 ANOVA for second order regression model

Source	DF	SS	MS	F	P
Regression	9	2.2675	0.25195	3.83	0.008
Residual	17	1.1172	0.06572		
Error					
Total	26	3.384			

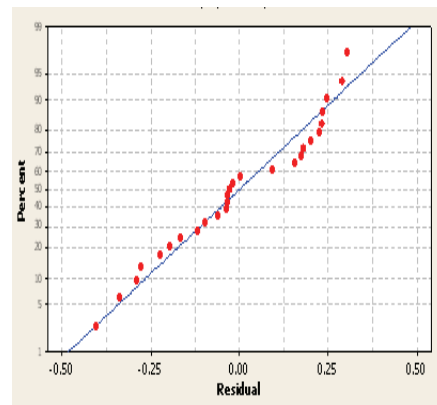


Fig 3 Normal probability plot for the residuals

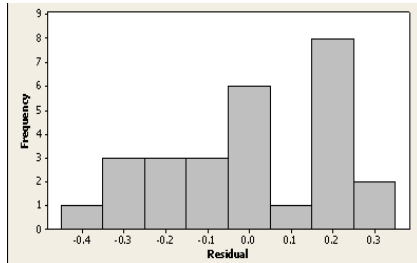


Fig 4. Histogram of the residuals.

5 Conclusions

The SR in the turning procedure is measured for machining of AISI 316 under various cutting conditions with multilayer of TiCN/Al₂O₃ tool utilizing Taguchi orthogonal array. In view of the trial and diagnostic outcomes, the accompanying conclusions drawn.

- The impact of machining parameters on the SR has been assessed the assistance of Taguchi strategy and ideal machining conditions to limit the SR have been resolved.
- The feed is the predominant parameter for SR took after by the depth of cut. Cutting speed demonstrated negligible impact on SR contrasted with different parameters.
- For accomplishment of good SR on AISI 316 low cutting speed, low feed and high depth of cut are favored.
- The second order regression model demonstrate is more appropriate than the primary order regression model show for portraying the turning procedure, from the view purpose of ANOVA and residual analysis.
- The second order response surface model for SR is created from the watched information the anticipated and measured esteem are genuinely close, which shows that the created model can be adequately used to foresee the SR.

References

1. Tosun N and Ozler L (2000), "A study of tool life in hot machining using artificial neural network and regression analysis", *J. mat.proc.Technol.* 124, 99-104.

2. Wardancy, T.I.E., Elestawi, M.A., 1997, "Prediction of tool failure rate in turning hardened steels" *Int.J.manuf.Technol.* 13, 1-16.

3. Selvam, M.S., 1975, "Tool vibration and its influence on surface roughness in turning", 35, 149-157.

4. Lasota, A., Rusek, P., 1983, "Influence of random vibrations on the roughness of turned surfaces", *J. Mech Work Technol.* 7, 277-284.

5. Trent EM. 1989. *Metal cutting*. London, Butterworths Press. New York.

6. Paro, J., Hanninen, H., Kauppinen, V., 2001, "Tool wear and machinability of X5 CrMnN18 18 stainless steels", *J.Mater. Process. Technol.* 119, 14-20.

7. Sarwar, M., Zhang, X., Gillibrand, D., 1997, "Performance of titanium nitride coated carbide tipped circular saws when cutting stainless steel and mild steel", *Surf.Coat.Technol.* 94, 617-21.

8. Groover, M.P., 1996, "Fundamentals of modern manufacturing—materials, processes and systems", New Jersey: Prentice-Hall Inc.

9. DeGarmo, E.P., Black, J.T., Kohser, R.A., 1997, "Materials and processes in manufacturing", New Jersey: Prentice-Hall Inc.

10. Lim, C.Y.H., Lim, S.C., Lee, K.S., 1999, "The performance of TiN-coated high speed steel tool inserts in turning", *Tribol Int* 32, 393-8.

11. Ezugwu, E.O., Okeke, C.I., 2001, "Tool life and wear mechanisms of TiN coated tools in an intermittent cutting operation", *J. Mater. Process. Technol.* 116, 10-15.

12. Nouari, M., List, G., Girot, F., Coupard, D., 2003, "Experimental analysis and optimization of tool wear in dry machining of aluminum alloy". 255, 1359-68.

13. Suresh, P.V.S., Venkathwara rao, K., Desmukh, S.G., 2002 "A genetic algorithmic approach for optimization of the surface roughness prediction model", *Int J Mach Tools Manuf.* 42, 675-680.

14. Kwak, J.S., 2005, "Application of Taguchi and response surface methodologies for geometric error in surface grinding process", *Int J Mach Tool Manuf.* 45, 327-334.

15. Sahin, Y., Motorcu, A.R., 2004, "Surface roughness model for machining mild steel", *Mater Des-article in press.*

16. George, P.M., Raghunath, B.K., Manochac, L.M., Warriar, A.M., 2004, "EDM machining of carbon-carbon composite-a Taguchi approach", *J Mater Process Technol.* 145, 66-71.

17. Ross, P.J., 1996, *Taguchi techniques for quality engineering*. McGraw-Hill, New York.

18. Montgomery, D.C., 1991, *Design and analysis of experiments*. John Wiley and Sons, NewYork.



Controller General of Patents, Designs and Trademarks
Department of Industrial Policy and Promotion
Ministry of Commerce and Industry

Application Details

APPLICATION NUMBER	201741027566
APPLICATION TYPE	ORDINARY APPLICATION
DATE OF FILING	03/08/2017
APPLICANT NAME	1 . Dr.P.Ranjith Kumar 2 . Dr. TTM. Kannar. 3 . Dr.K.Chandrasekaran 4 . Mr.R.Ramanathan
TITLE OF INVENTION	ACRYLIC OPEN TYPE MICRO DRILL JIG
FIELD OF INVENTION	MECHANICAL ENGINEERING
E-MAIL (As Per Record)	
ADDITIONAL-EMAIL (As Per Record)	ranjjith@gmail.com
E-MAIL (UPDATED Online)	
PRIORITY DATE	NA
REQUEST FOR EXAMINATION DATE	28/12/2017
PUBLICATION DATE (U/S 11A)	18/08/2017

Application Status

APPLICATION STATUS

Application Awaiting Examination

[View Documents](#)

(12) PATENT APPLICATION PUBLICATION

(19) INDIA

(22) Date of filing of Application :03/08/2017

(21) Application No.201741027566 A

(43) Publication Date : 18/08/2017

(54) Title of the invention : ACRYLIC OPEN TYPE MICRO DRILL JIG

(51) International classification	:B24B3/24; B24B41/02	(71)Name of Applicant :
(31) Priority Document No	:NA	1)Dr.P.Ranjith Kumar
(32) Priority Date	:NA	Address of Applicant :99, SANKAR NAGAR, MANGAMMANAGAR EXTENSION, SRIRANGAM, TRICHY - 620006, TAMIL NADU. Tamil Nadu India
(33) Name of priority country	:NA	2)Dr. TTM. Kannan
(86) International Application No	:NA	3)Dr.K.Chandrasekaran
Filing Date	:NA	4)Mr.R.Ramanathan
(87) International Publication No	: NA	(72)Name of Inventor :
(61) Patent of Addition to Application Number	:NA	1)Dr.P.Ranjith Kumar
Filing Date	:NA	2)Dr.TTM.Kannan
(62) Divisional to Application Number	:NA	3)Dr.K.Chandrasekaran
Filing Date	:NA	4)Mr.R.Ramanathan

(57) Abstract :

ABSTRACT Micro drill jig is a special work holding device for holding, supporting and locating the Micro work pieces and also guide the micro drills from 0.2 mm -1.5 mm in micro hole production system. As the efficient running of micro manufacturing company which demand prompt and simple work positioning strategy for correct operations depends largely on the interchange ability system. This led to demand for a better cost effective work holding devices which will ensure better quality products, reduces lead time and also increase throughput. Micro fabrication Technology has been steadily advances in recent times. Miniaturization of various devices with present changes in many areas such as machine design, equipment design, jig and fixture design. Acrylic is a versatile material having the superior properties such as good impact strength, good dimensional accuracy, Excellent Optical Clarity and good rigidity with lesser weight. In this work, we have fabricated Acrylic open type micro drill jig for micro hole production system. Acrylic Jig performs well in harsh weather condition and also provides the property of excellent fabrication. Acrylic open type micro drill is a special type jig which top of the drill jig is open and micro work piece are placed on top and micro drill is passed through the drill bush. This Acrylic micro drill jig which eliminates marking system also facilitating the micro hole production in larger quantities without circularity error occur in the micro holes. Over all dimensions of Acrylic open type micro drill is 60 X 35 X 40 mm. This Acrylic micro drill jig may be implemented in micro manufacturing system and Micro factory concept It is specially designed to concept of Small jig for small components.

No. of Pages : 8 No. of Claims : 10

18

PATENT OFFICE
 INTELLECTUAL PROPERTY BUILDING
 G.S.T. Road, Guindy, Chennai-600032
 Tel.No. (091)(044) 22502081-84 Fax No. 044 22502066
 E-mail : Chennai-patent@nic.in
 Web Site : www.ipindia.gov.in



सत्यमेव जयते
 GOVERNMENT OF INDIA



INTELLECTUAL
 PROPERTY INDIA
 PATENTS | DESIGNS | TRADE MARKS
 GEOGRAPHICAL INDICATIONS

CHALLAN : TR-5
 DOCKET NO : 80963

Date/Time : 28/12/2017 11:12:59

To,
 DR. P. RANJITH KUMAR
 99, SANKAR NAGAR, MANGAMMANAGAR EXTENSION, SRIRANGAM, TRICHY - 620006, TAMIL NADU INDIA.
 ranjjith@gmail.com

Agent Number:

Sr. No.	CBR No.	Reference Number / Application Type	Application Number	Title/Remarks	Amount Paid
1	39759	ORDINARY APPLICATION	201741046967	AUTOMATION IN MICRO TURNING PROCESS USING SENSITIVE CONTROLLED MOTOR	1750
2		E-2/4001/2017-CHE	201741046967	Form2	0
3		E-3/30139/2017-CHE	201741046967	Form3	0
4		E-5/1635/2017-CHE	201741046967	Form5	0
5	39759	E-12/1164/2017-CHE	201741046967	Form9	2750
Total :					4500

Received a sum of Rs. 4500 (Rupees Four Thousand Five Hundred only) through

Payment Mode	Bank Name	Cheque/Draft Number	Cheque/Draft Date	Amount in Rs
Cash	---	---	---	4500

Note: This is electronically generated receipt hence no signature required.

(12) PATENT APPLICATION PUBLICATION

(21) Application No.201741046967 A

(19) INDIA

(22) Date of filing of Application :28/12/2017

(43) Publication Date : 05/01/2018

(54) Title of the invention : AUTOMATION IN MICRO TURNING PROCESS USING SENSITIVE CONTROLLED MOTOR

(51) International classification

:G01D5/24

(31) Priority Document No

:NA

(32) Priority Date

:NA

(33) Name of priority country

:NA

(86) International Application No

:NA

Filing Date

:NA

(87) International Publication No

:NA

(61) Patent of Addition to Application Number

:NA

Filing Date

:NA

(62) Divisional to Application Number

:NA

Filing Date

:NA

(71)Name of Applicant :

1)Dr.P.Ranjith Kumar

Address of Applicant :99, Sankar Nagar, Mangammanagar
Extension, Srirangam, Trichy-620006, Tamilnadu, India Tamil
Nadu India

2) Dr.K.Chandrasekaran

3)Dr.TTM.Kannan

4)Prof.R.Ramanathan

(72)Name of Inventor :

1)Dr.P.Ranjith Kumar

2)Dr.K.Chandrasekaran

3)Dr.TTM.Kannan

4)Prof.R.Ramanathan

(57) Abstract :

ABSTRACT In the Manufacturing Industry keen and useful assessments are normal for the new century. Miniaturized scale creation advancements have been relentlessly progressing as of late. Innovative works are by and large vivaciously led with a view towards the usage of smaller scale machines. The micro lathe is a little measured machine that performs the vast majority of the round and hollow operations. Micro lathe are favored over bigger machines by a few experts, regularly bolt smiths, Jewelers and designers for prototyping or manufacture work. The specialists have been created manual worked micro lathe with high minimal effort however low exactness and expend high electrical power. Presently days computer numerical controlled (CNC) micro lathe are utilized to create the round and hollow jobs with high precision and high cost. This research work is mainly focused on development of automation for micro machine using sensitive controlled motor in manufacturing system which leads to high accuracy. The created automated micro lathe using sensitive controlled motor which works effectively without bargaining machining resistances. From the monetary perspective, the robotized micro lathe will decrease all assets, for example, space, time, material, vitality and power. It can be actualized in little scale industry and cabin industry for social advancement.

No. of Pages : 7 No. of Claims : 5



ALIGNMENT TEST ON PORTABLE TABLETOP MINI LATHE

*Kannan T TM¹, Ranjith Kumar P², Ramanathan R³ and Chandrasekaran K⁴

^{1,3,4}Associate Professor, Department of Mechanical Engineering, M.A.M.School of Engineering, Trichy-621 105, Tamilnadu, India.

² Professor, Department of Mechanical Engineering, M.A.M.School of Engineering, Trichy-621 105, Tamilnadu, India

ABSTRACT

Tabletop mini lathes are preferred by some professional such as Locksmith, Goldsmith, Watch maker and prototyping Engineers. The idea of Table top lathe was initiated in the concept of Micro factory in Japan in 1990. The main Objectives of Miniature of lathes are greater saving of power, space, materials, Time and other resources. Micro machining is the foundation of technology to produce miniature of components with relative accuracy requirements in 3 dimensional features are made in the wide range of engineering applications. Usually three directional forces to improve the working accuracy are applied to micro machine parts such as Spindle, Bed and Cross slide of Tabletop mini lathe. In this experimental work deals with alignment test was conducted on various micro machine parts using dial test indicator. The maximum and minimum values of alignment tests are compared with mini machine tool guide. The alignment values of Machine bed, Spindle and Cross slide are within allowed limit of design of machine elements guide and Indicate table top mini lathe is suitable for micro machining process.

Keywords: Table top Mini Lathe, Alignment test, Dial test Indicator, Accuracy, Micro machining

1. Introduction

Micro factory is a small dimensioned factory which is capable for small production system. Micro factory was a concept of future Manufacturing system which was proposed in Japanese national R&D project in 1990. Microfactory was able to perform a series of Fabrication and assembly with a small table top machine [1,2] Metrology and Inspection system are the basis for ultra precision mini machines to be widely applied in Industry which is used to analyze performance of micro machines [3] Design Strategy is developed with the aim of getting a very high dynamic analysis of tabletop micro machines [4] The development of Precision manufacturing has greatly changed our lives in terms of increased living standards. High precision manufacturing offers quality and reliability for conventional products. Usually Table top mini lathe accuracy will improve by inherent reductions of machine component Inertia, Negligible thermal drift and larger Eigen frequencies[5] Spindle is a key component of precision machine tool because the spindle motion error will have significant effects on the surface quality and accuracy of machine component[6] Steel or Cast iron are most widely used material for the machine bed and slide ways because their good wear resistance, low stress caused deformation and vibration damping capacity[7,8] Three important principle parts

like machine bed, cross slide and spindle performance are measured by dial test indicator. It indicates the errors and tolerance limit of alignment of small tabletop machines [9]. The performance of micro machine was analyzed by Gap sensor method and finite element analysis method and then conduct experimental work on different materials [10] Previous researchers were conducted performance test in different conventional machines but we conduct performance test on tabletop mini lathe using dial test indicator and values are compared with design of machine elements data book.

2. Specifications

Net weight = 3.20 kg
Motor specification = 1/12 hp
Bed length = 165 mm
Centre height = 65mm
Spindle speed = 3000-9000 rpm
Longitudinal feed = 80mm
Cross feed = 30mm
Pitch of lead screw = 2mm
Distance between the centres = 92.5 mm
Mode of Operation – Manual

*Corresponding Author - E- mail: ttmk_8@rediffmail.com

3. Alignment test on Tabletop Mini lathe.

3.1. Rotational Accuracy of Chuck

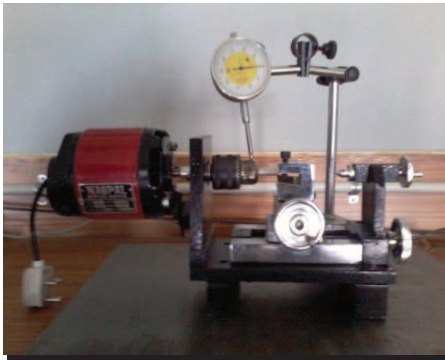


Fig.1 Alignment test on chuck

Table 1. Alignment test result of chuck

Test Trial No	Chuck Alignment position (degrees)	Deviation division in Dial test indicator	Amount of Deviation (mm)
1	0	2	0.02
2	90	1	0.01
3	180	1	0.01
4	270	2	0.02

Table top mini lathe carryout machining by means of rotational force of Chuck. The accuracy of chuck affects the roundness and surface roughness of the work piece. The final product accuracy depends upon the chuck accuracy and spindle speed. In general the chuck accuracy is measured by Dial gauge at very low speed. This method is simple and easy to analyze the chuck alignment and also measure the performance of table top mini lathe.

The maximum and minimum values are tabulated in Table 1. The average value of chuck roundness is 0.015 mm and within allowable limit as per design of mini machine tool guide. Fig 2 shows that Deviation values of different position of rotation of spindle chuck through the Radar diagram.

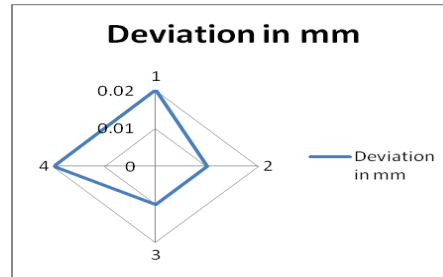


Fig 2 Radar diagram for chuck alignment values

3.2. Movement accuracy of cross slide

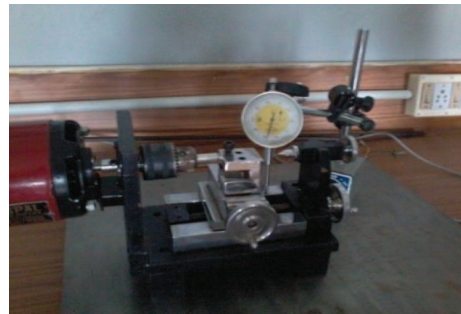


Fig.3 Alignment test on cross slide

Table 2. Alignment test results of Cross slide

Test Trial No	Alignment distance In mm	Deviation division in Dial test indicator	Amount of Deviation In mm
1	10	2	0.02
2	15	3	0.03
3	20	1	0.01
4	25	3	0.03

Cross slide movement of mini lathe is based on screw mechanism and adjusted by clamping nut. The final product accuracy, surface finish, metal removal rate, tool wear, heat generation and tool vibrations are controlled by correct alignment of cross slide. The cross slide movement accuracy is measured by dial gauge and values are tabulated in Table 2. It shows that average value of cross slide movement is 0.02 mm and also within allowable limit as per design of mini machine tool guide. Fig 3 shows that Amount of deviation of cross slide movement during alignment test on Mini

lathe and also give graphical representation through Scatter Diagram

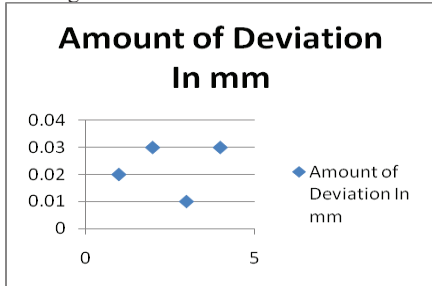


Fig.3 Scatter diagram for Cross slide alignment values

3.3 Alignment Test on Machine bed



Fig 4 Alignment test on Machine bed

Carriage mechanism and tool post arrangement are placed on machine bed and allow moving between head stock to tail stock by actuating lead screw. The accuracy of machine bed lead to observe cutting force vibration and tool vibrations developed during machining process. The machine bed alignment has been conducted on top surface of machine body by using dial gauge. The maximum and minimum values of Alignment test of machine bed are measured by dial gauge and tabulated in Table 3.

Table 3. Alignment test results of Lathe Bed.

Test Trial No	Chuck Alignment position (distance)	Deviation division in Dial test indicator	Amount of Deviation (mm)
1	10	2	0.02
2	20	2	0.02

3	40	1	0.01
4	60	2	0.02

It shows that average value of machine bed in 0.02 mm and also within allowable limit as per design of mini machine tool guide. Fig 3 shows that amount of deviation of machine bed during alignment test through Scatter Diagram. Fig 5 shows that deviation of machine bed of mini lathe which represent there is no deviation in alignment test. So the machine produces best accuracy in plain turning process.

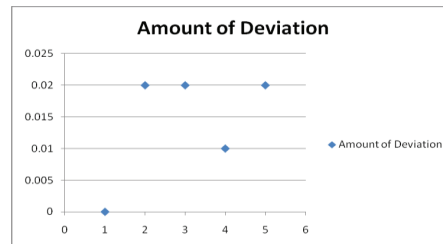


Fig 5 Scatter diagram for Alignment values of Bed

4. Conclusion

The performance test was conducted on various principle parts such as Machine spindle chuck, lathe bed and cross slide of Tabletop mini lathe. Dial gauge was used to check the values of Alignment test which the maximum and minimum values are within allowed limit. Hence Table top mini lathe is suitable for micro machining process and it can be implement the micro factory concept.

References

1. Kawahara N, Suto, Teheran, Ishikawa Y, Kitahara T, Ooyama T and Aka T (1997), "Technical Papers; Micro system Technologies Micro factories; new applications of micro machine technology to the Manufacture of small products", Springer-Verlag, 37-41.
2. Kussul E, Baidyk T, Ruiz Huerta L, Caballero Ruiz A, Velasco G and Kasatkina (2002), "Development of micro machine tool prototypes for micro factories", Journal of Micromechanics and Micro engineering, Vol.12, 795-812.
3. Trusty J (2013), "System and methods of testing of machine tools" micro technique, 162-173
4. Dai Gil Lee, Jung Do Suh, Hak Sung Kim and Jong Min Kim (2014), "Design and manufacture of composite high speed small machine tool structures", In Composites Science and Technology", Vol.64, 1523-1530.
5. Vogler M P, Liu X, Kapoor S G, Devor R E and Ehmman K F (2008), "Development of meso-scale machine tool (mMT) systems", Society of Manufacturing Engineers, 02-18, 1-9.

6. Heikkilä R, Järvenpää E & Tuokko R (2010), "Advances in the TUT Micro factory Concept", Vol.5, 290-296.
7. Elter J and Usuari Y (2014), "Micro machines mechanics and design", Precision machine design, Prentice-Hall, 223-234.
8. Okazaki Y and Kitahara T (2014), "Development and Evaluation of a Micro-Lathe Equipped with Numerical Control", Journal of the JSPE, Vol.67(11), 123-129
9. Ashida K (2012), "Development of a micro press machine", Journal of Mechanical Engineering lab, Vol.54 (6), 16-20.
10. Kitahara T, Ishikawa Y, Terada K, Nakajima N and Furuta K (2006), "Development of Micro-lathe and analysis", Journal of Mechanical Engineering Lab, Vol.50, 117-123.
11. Kondoh S, Masui K, Mishima N, and Matsumoto M (2012), "Total performance Analysis of Product life cycle considering product value", Proceedings of Care Innovation, Austria, 197-203.

TRIBOLOGICAL BEHAVIOUR FOR STIR CAST Al5086/Gr/Al₂O₃ HYBRID MATRIX COMPOSITE

K.CHANDRASEKARAN^{*1}, S.AJITH², P.ABBAS³, A.YASAR ARAFATH⁴, K.VINOTHKUMAR⁵

Department of Mechanical Engineering, MAM School of Engineering, Trichy, Tamilnadu, India.

**Corresponding author Email: kchandrusekaran1984@gmail.com, Mobile +919942042664.*

ABSTRACT

Aluminum Hybrid Reinforcement Technology is a reaction to the dynamic regularly expanding administration necessities of ventures, for example, Transportation, Aerospace, Automobile, Marine, and so forth since they are bendable, profoundly conductive, light weight and have a high quality to weight proportion. In this development, an endeavour has been made to research the wear rate of Al5086 hybrid metal matrix composite strengthened with the hard earthenware Alumina (4, 8, 12 wt. % of Al₂O₃) and delicate strong oil of graphite (2, 4, 6 wt. % of Gr) manufactured by utilizing mix throwing technique. The un-greased up pins on plate wear tests were directed to look at the wear conduct of Al5086/12 wt. % of Al₂O₃/Gr composites. The sliding wear tests were completed at different heaps of (15, 30, 45 N), sliding speed (1.25, 2.50, 3.25 m/sec), and diverse graphite wt. % (2, 4, 6 wt. %).

Keywords: Al5083; Al₂O₃; Graphite; Taguchi techniques; wear rate.

I. INTRODUCTION

Aluminum Hybrid Matrix Composites are becoming better substitutes for the conventional Aluminum Alloys because of the characteristics like improved strength to weight ratio, energy saving, better wear resistance etc [1]. Interest in particulate reinforced aluminum hybrid matrix composites for the use in the automotive industry and other structural applications has increased because of the physical and mechanical properties they possess [2]. Aluminum based hybrid matrix composites with a variety of particulate reinforcements such as Al₂O₃, TiC, Ti₂B, B₄C, TiN, Si₃N₄, graphite and industrial waste by-product have been conceived and developed for various potential applications [3]. Aluminum hybrid matrix composites are developed by the researchers and they are used in many commercial and industrial applications [4]. Newer compositions have been continuously explored and the related valuable studies presented by the past researchers are discussed. Veeresh Kumar et al [5] have conducted the experiment on Al6061/SiC and Al7075/Al₂O₃ metal matrix composites and present the experimental results of the studies regarding hardness, tensile strength and wear resistance properties of Al6061/SiC and Al7075/Al₂O₃ composites. The SiC and Al₂O₃ resulted in improving the hardness and density of their respective composites. Wang and Yan [6] investigated the feasibility of machining Al6061/Al₂O₃ composite materials by electro discharge machining for blind hole drilling and evaluated the material removal rate, tool wear rate and surface roughness with various input parameters. Yan and Wang [7] observed that material removal rate increased with peak current and was erratic with pulse duration. The material removal rate, tool wear rate and surface

roughness increases with flushing pressure during machining of Al6061/Al₂O₃ composites using rotary electro discharge machining with a tube electrode. Yan et al [8] found that in case of rotary electro discharge machining process, the main challenge is of using a disk like electrode for machining Al6061/Al₂O₃ composites. Veeresh kumar et al [9] investigated the influence of reinforcement on mechanical properties when different matrix materials that is Al6061 and Al7075 and reinforcements such as SiC and Al₂O₃ are used and they observed micro hardness of the composite were increased with the increase of filler content.

While many researchers have carried out on the mechanical, wear properties and machining characteristics of aluminum metal matrix composites with graphite and Al₂O₃ as reinforcing materials. In the case of hybrid Al5086/Gr/Al₂O₃ composites, limited literatures is available, encompassing various aspects such as mechanical properties and wear behaviour and conduct the machining study of the composites. Aluminum based Al₂O₃ particle reinforced composite material have become useful engineering materials due to their properties such as low weight, heat resistant, wear resistant and low cost. These are found in various engineering applications such as cylinder block liners, vehicle drive shafts, automotive pistons, bicycle frames etc.

II. EXPERIMENTAL DETAILS

The stir casting technique is the simplest and the most economical process for producing particulate reinforced composites available for particulate reinforced metal

matrix composites. In this technique, in order to accomplish the optimum property of the hybrid composite, the distribution of the reinforced particles in the base material sought to be homogeneous and the wet ability among the olden materials and particulates ought to be optimized. The moisture level with cast composite must be minimized and the element reactions between the particle material and the base material have to be avoided. The whirlpool method is individual of the enhanced recognized approaches used to build a high quality allocation of the reinforced material in the base matrix. During this, once the base material is melted, it is stirred forcefully by automatic agitator to form a whirlpool at the face of liquefy, and the particle material is subsequently introduced at the region of the vortex.

A. Material fabrication

The chemical composition of Al5086 alloy is given in Table 1 and Al5086 alloy was melted in a crucible in a generation type of furnace at 725°C. Subsequent to melting and degassing by nitrogen, an alumina coated stainless steel stirrer was meant for stirring at 600 rpm used for 20 min time duration. During stirring, it is preheated at 600°C, particles alumina and MoS₂ powder was added. After that the composite alloy was roll poured into the pre heated (250°C) permanent mould. The Al5086 alloy with different wt. % of hybrid composites is produced and test specimens were machined.

TABLE I
Chemical composition of Al5086 alloy

Si	Fe	Cu	Mn	Mg	Cr	Zn	Ti	Al
0.6	0.	0.2	0.1	0.	0.0	0.2	0.1	Remaini
5	7	5	5	8	7	5	5	ng

B. Mechanical behaviour

The hardness tests were carried out according to ASTM E10-07 standards using Brinell hardness testing machine with a 10 mm ball indenter and 500 kg load for 30 s. The test was conducted at room temperature (30°C) and the measurement of hardness was taken at three different places on each sample to obtain an average value of hardness. As per the ASTM E08-8 standard, the tensile strength was evaluated on the cylindrical rod of casted composites. The 1200 grit grindings silicon carbide paper was used to polish the test specimens in order to decrease the machining scratches and the effects of surface defects on the sample. The universal testing machine was loaded with 10 KN, load cell was used to conduct the tensile test. The affecting factors and levels selected for mechanical behaviour Al5086/Gr/Al₂O₃ are given in Table 2.

TABLE II

Affecting factors and levels selected for tensile strength Al5086/Gr/Al₂O₃

Factors /levels	1	2	3
X- wt. % Al ₂ O ₃ (wt. %)	4	8	12
Y- wt. % Graphite (wt. %)	2	4	6

C. Tribological behaviour

The pin on disc test apparatus is used to investigate the dry sliding wear behaviour of Al5086/12 wt. % Al₂O₃/ Gr hybrid composites. Pin specimens of 6 mm diameter and 15 mm height for wear test was prepared from the above composites were machined and polished. The test was conducted with various loads of 15 N, 30 N and 45 N at a sliding speed of 1.25, 2.50, 3.25 m/s and 2, 4, 6 Gr wt. %. The test was conducted at room temperature (30°C) and relative humidity of 60–65%. The affecting factors and levels selected for Tribology Al5086/12 wt. % Al₂O₃/ Gr is given in Table 3.

Table III

Affecting factors and levels selected for Tribology Al5086/12 wt. % Al₂O₃/ Gr

Factors /levels	1	2	3
A-Load (N)	15	30	45
B-Sliding velocity (m/s)	1.25	2.50	3.25
C-wt. % of Gr (wt. %)	2	4	6

III. RESULT AND DISCUSSION

A. Optimum setting for TS & BHN of Al5086/Al₂O₃/ Gr

The tensile strength and hardness of the Al5086/4, 8, 12 wt. % Al₂O₃/2, 4 wt. % Gr hybrid composites is shown in Figure 1(a) and Figure 1 (b). It is observed that an addition of alumina particles improve the tensile strength and hardness of hybrid composites. It is evident that tensile strength and hardness clearly increases with the addition of alumina particles. The tensile strength and hardness of the Al5086/4, 8, 12 wt. % Al₂O₃/6 wt. % Gr hybrid composites is shown in Figure 1(c). Increase in content of graphite the tensile strength and hardness of hybrid composite is decreased.

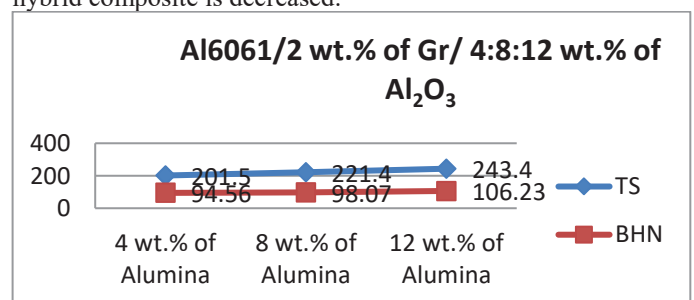


Fig. 1 (a) Mechanical behaviour of Al5086/2 wt. % of Gr/4:8:12 wt. % of Al₂O₃

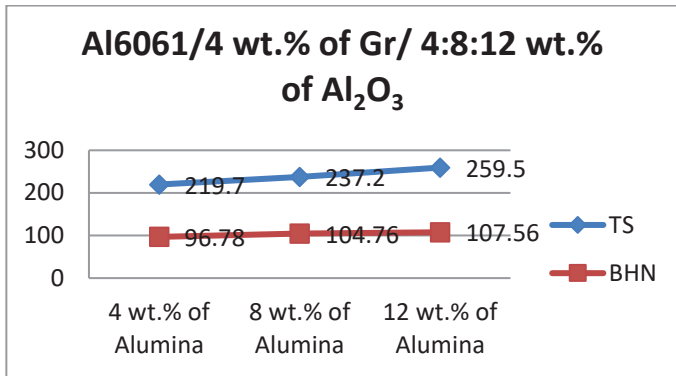


Fig. 1 (b) Mechanical behaviour of Al5086/4 wt. % of Gr/ 4:8:12 wt. % of Al₂O₃

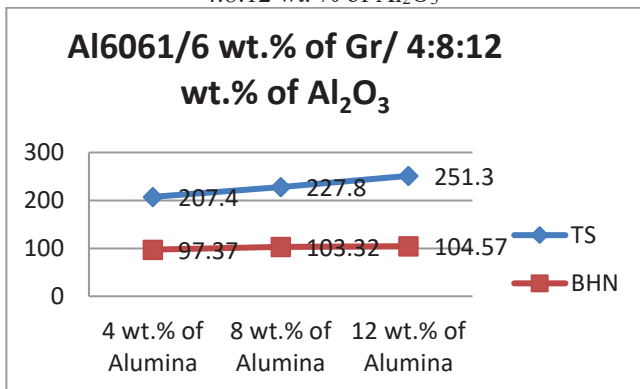


Fig. 1 (c) Mechanical behaviour of Al5086/6 wt. % of Gr/ 4:8:12 wt. % of Al₂O₃

TABLE V
 Experimental result for tensile strength of Al5086/Al₂O₃/ Gr

X	Y	Al ₂ O ₃ (wt. %)	Mo S ₂ (wt. %)	TS (N/mm ²)	S/N Ratio	BHN	S/N Ratio
1	1	4	2	201.5	46.08 55	94.5 6	33.27 13
1	2	4	4	219.7	46.83 66	96.7 8	33.41 17
1	3	4	6	207.4	46.33 62	97.3 7	33.31 84
2	1	8	2	221.4	46.90 36	98.6 7	33.42 41
2	2	8	4	237.2	47.50 23	104. 76	33.53 43
2	3	8	6	227.8	47.15 11	103. 32	33.46 98
3	1	12	2	243.4	47.72 64	106. 23	33.57 52
3	2	12	4	259.5	48.28 27	107. 56	33.67 58
3	3	12	6	251.3	48.00 38	104. 57	33.62 55

TABLE VI
 Taguchi Analysis: TS & BHN versus X, Y of Al5086/Al₂O₃/ Gr

Level	TS		BHN	
	X	Y	X	Y
1	46.42	46.91	33.33	33.42
2	47.19	47.54	33.48	33.54
3	48.00	47.16	33.63	33.47
Delta	1.58	0.64	0.29	0.12
Rank	1	2	1	2

The measured values of tensile strength and BHN for Al5086/Al₂O₃/ Gr under different wt. % and corresponding signal to noise ratio for all experimental runs are given in Table 5. The Taguchi analysis of tensile strength and BHN for Al5086/Al₂O₃/Gr under different wt. % is given in Table 6. It clearly shows the maximum tensile strength is obtained at 12 wt. % of Al₂O₃ and 2 wt. % of Gr and the maximum BHN is obtained at 12 wt. % of Al₂O₃ and 4 wt. % of Gr. Table 7 shows that the results of ANOVA for tensile strength and BHN on Al5086/Al₂O₃/ Gr hybrid composite. It is observed that Al₂O₃ is the most significant parameter affected the tensile strength of Al5086/Al₂O₃/ Gr with F: P value of 1092.26: 0.000 and Al₂O₃ is significantly affecting the BHN of Al5086/Al₂O₃/ Gr with F: P value of 480.69: 0.000.

B. Tribological behaviour of Al5086/Al₂O₃/ Gr

The variation of wear rate for Al5086/Al₂O₃/ Gr hybrid composite with respect to different sliding velocity and applied load is given in Table 8. The applied load affects the wear rate of hybrid composites significantly. The wear rate varies with applied load is an indicative of Archard's law and significantly lower in the case of hybrid composites. The wear rate increases with increasing applied load and it is less at 6 wt. % of Gr hybrid composites as compared to 2 wt. % of Gr. This is mainly due to the presence of Al₂O₃ in Al5086. However, at all load conditions are considered the wear resistance of the hybrid composites were superior to the matrix alloy. The wear rate is increased with increase in sliding speed Al5086/12 wt. % Al₂O₃/ Gr hybrid composite. Increasing sliding speed temperature is raised to the sliding surfaces this leads to softening of the matrix and composite pin surfaces and it is due to the enhancement in the hardness. The increase in hybrid composite hardness results in improvement of wear resistance. The presence of Gr and Al₂O₃ particles in the hybrid composite will lead to further reduction of wear rate. The coefficient of friction for Al061/12 wt. % Al₂O₃/ MoS₂ hybrid composites under varying load and sliding velocity is given in Table 8. The coefficient of friction is decreased with increasing wt. % of Graphite and increasing the due to load. The Al₂O₃ particles act as load bearing elements in the hybrid composites and also it results in formation of more stable lubricating film on the Tribo surface of the hybrid composites. The decreased coefficient of friction of hybrid composite with Graphite content can be credited to the

collective effects of Graphite and Al₂O₃ particles in formation of a more resistant Tribo layer on the contact surface. The graphite Tribo film minimize the degree of shear stress transferred to the sliding material underneath the sliding contact area which results in less plastic deformation in the sub surface region and reduces the wear rate in the hybrid composites. The experimental values of wear rate and coefficient of friction for Al5086/12 wt. % Al₂O₃/ Graphite under different parameters and corresponding signal to noise ratio for all experimental runs are given in Table 8. The Taguchi analysis for

Al5086/12 wt. % Al₂O₃/ Graphite under different load, sliding velocity and wt. % of Graphite is given in Table 9. It clearly shows the minimum wear rate and coefficient of friction is obtained at 15N of load, 3.25 m/sec of sliding velocity and 6 wt. % of Graphite. Table 10 shows that the results of ANOVA for wear rate and coefficient of friction on Al5086/12 wt. % Al₂O₃/ Graphite hybrid composite. It is observed that load is the most significant parameter affecting the wear rate and coefficient of friction of Al5086/12 wt. % Al₂O₃/ Graphite with F: P value of 29.06: 0.033 and 756.27:0.001.

TABLE VII

Analysis of Variance for TS & BHN of Al6061/Al₂O₃/ MoS₂

Source	DF	TS				BHN			
		Seq SS	Adj MS	F	P	Seq SS	Adj MS	F	P
X	2	2634.78	1317.39	1092.26	0.000	3.7691	1.8845	480.69	0.000
Y	2	423.56	211.78	175.59	0.000	0.6125	0.3063	78.12	0.001
Error	4	4.82	1.21			0.0157	0.0039		
Total	8	3063.17				4.3973			
R-Sq = 99.84%; R-Sq(adj) = 99.69%					R-Sq = 99.64%; R-Sq(adj) = 99.29%				

TABLE VIII

Experimental results for Al6061/12 wt. % Al₂O₃/ Graphite of wear study

Trial	A	B	C	Load (N)	Sliding velocity (m/s)	wt. % of Gr (Wt. %)	Wear rate (mm ³ /min) X 10 ⁻³	S/N	Coefficient of friction	S/N
1	1	1	1	15	1.25	2	1.346	-2.580	0.487	6.249
2	1	2	2	15	2.50	4	1.250	-1.938	0.455	6.839
3	1	3	3	15	3.25	6	0.966	0.300	0.423	7.473
4	2	1	2	30	1.25	4	2.344	-7.399	0.523	5.629
5	2	2	3	30	2.50	6	2.576	-8.218	0.496	6.090
6	2	3	1	30	3.25	2	2.133	-6.579	0.537	5.400
7	3	1	3	45	1.25	6	2.756	-8.805	0.568	4.913
8	3	2	1	45	2.50	2	3.813	-11.625	0.603	4.393
9	3	3	2	45	3.25	4	3.245	-10.224	0.579	4.746

TABLE XI

Taguchi Analysis: Wear rate and coefficient of friction versus A, B, C of Al5086/12 wt. % Al₂O₃/ Graphite

Level	Wear rate			Coefficient of friction		
	A	B	C	A	B	C
1	-1.406	-6.262	-6.929	6.854	5.597	5.348
2	-7.399	-7.261	-6.521	5.707	5.775	5.739
3	-10.218	-5.501	-5.575	4.684	5.873	6.159
Delta	8.812	1.760	1.354	2.170	0.276	0.811
Rank	1	2	3	1	3	2

TABLE X

Analysis of Variance for Wear rate of Al5086/12 wt. % Al₂O₃/ Graphite

Source	DF	Wear rate				Coefficient of friction			
		Seq SS	Adj MS	F	P	Seq SS	Adj MS	F	P
A	2	6.5442	3.2721	29.06	0.033	0.0247047	0.0123523	756.27	0.001
B	2	0.3456	0.1728	1.53	0.395	0.0002580	0.0001290	7.90	0.112
C	2	0.1651	0.0826	0.73	0.577	0.0032667	0.0016333	100.00	0.010
Error	2	0.2252	0.1126			0.0000327	0.0000327		
Total	8	7.2801				0.0282620			
R-Sq = 96.91% R-Sq(adj) = 87.63%					R-Sq = 99.88% R-Sq(adj) = 99.54%				

IV. CONCLUSION

In the present investigation, the Al5086/Al₂O₃/ Graphite hybrid composite was successfully fabricated using stir casting process. The mechanical behaviour and tribological behaviour were evaluated. The obtained results can be summarized as follows:

- Mechanical properties of hybrid composites increase with an increase in weight fraction of alumina particles. An increase in weight fraction of molybdenum disulphide reinforcement decreases the mechanical properties like tensile strength and BHN. The optimum parameter for maximization of tensile strength is obtained at 12 wt. % of Al₂O₃ and 2 wt. % of Graphite and the maximum BHN is obtained at 12 wt. % of Al₂O₃ and 4 wt. % of Graphite
- The incorporation of Al₂O₃ reinforcement to Al5086 increases the wear resistance of the composites. The addition Graphite reinforcement in Al5086/Al₂O₃ composites as a hybrid reinforcement further increases the wear and friction resistance of the composite. This is attributed to the stable and Graphite rich mechanically mixed layer, which prevents metal to metal contact and reduces the wear of the composite. The unstable mechanically mixed layer in the absence of the lubricant phase leads to lower wear resistance in Al5086/Al₂O₃/ Graphite hybrid composite. The optimum parameter for minimization wear rate and coefficient of friction is obtained at 15N of load, 3.25 m/sec of sliding velocity and 6 wt. % of MoS₂.

REFERENCES

- [1] L. Poovazhagan, K. Kalaichelvan, A. Rajadurai, and V. Senthilvelan, "Characterization of hybrid silicon carbide and boron carbide nano particles-reinforced aluminum alloy composites", *Procedia Engineering*, vol.64, pp.681 – 689, 2013.
- [2] A.M. Al Qutub, A. Khalil, N. Saheb, and A.S. Hakeem, "Wear and friction behaviour of Al6061 alloy reinforced with carbon nanotubes", *Wear*, vol.297, pp.752–761, 2013.
- [3] K. Umanath, S.T. Selvamani, and K. Palanikumar, "Analysis of dry sliding wear behaviour of Al6061/SiC/Al₂O₃ hybrid metal matrix composites", *International Journal of Composite Part-B Engineering*, vol.53, pp.159-168, 2013.
- [4] K. Umanath, S.T. Selvamani, and K. Palanikumar, "Friction and wear behaviour of Al6061 alloy (SiCp/Alp) Hybrid composites", *International Journal of Engineering Science and Technology*, vol.03, no.7, pp.5441-5551, 2011.
- [5] G.B. Veeresh Kumar, C.S.P. Rao, N.Selvaraj, and M.S. Bhagyashekar, "Studies on Al6061/SiC and Al7075/Al₂O₃ Metal Matrix Composites", *Journal of*

Minerals & Materials Characterization & Engineering, vol. 9, no.1, pp.454-461, 2010.

[6] C.C. Wang, and B.H. Yan, "Blind-hole drilling of Al₂O₃/6061Al composite using rotary electro discharge machining", *Journal of Material Processing Technology*, vol. 102, pp.90-102, 2000.

[7] B.H. Yan, and C.C Wang, "The machining characteristics of Al6061 composite using rotary electro-discharge machining with a tube electrode", *Journal of Material Processing Technology*, vol. 95, pp.222-231, 1999.

[8] B.H. Yan, C.C. Wang, W.D. Liu, and F.Y. Huang, "Machining characteristics of Al₂O₃/6061Al composite using rotary EDM with a disk like electrode", *International Journal of Advanced Manufacturing and Technology*, vol. 16, pp.322-333, 2000.

[9] G.B. Veeresh Kumar, C.S.P. Rao, N. Several, and M.S. Bhagyshakar, "Studies on Al6061-SiC and Al7075-Al₂O₃ Metal Matrix Composites", *Journal of Minerals & Materials Characterization & Engineering*, vol.09, pp.43-55, 2010.

Biographies and Photographs



Dr.K.Chandrasekaran, M.E., PhD, MISTE, IRED obtained his Bachelor degree in Mechanical Engineering and Master Degree in Manufacturing Engineering from Anna University Chennai and Anna University of Technology Tiruchirappalli, India. He was completed PhD in the area of Machining science from Anna University, Chennai. He had served in many Institutions at various positions as Lecturer, Assistant Professor and Associate Professor. Now he is working as a professor in MAM School of Engineering, Trichy. He had published more number of papers in refereed International Journals and Conferences. His research areas include Manufacturing, Composites, Machining Science, Modeling and optimization. He is guiding PhD scholars in different areas. He is active Doctoral committee member for PhD scholars and Examiner for various autonomous Institutions and Universities.

See discussions, stats, and author profiles for this publication at: <https://www.researchgate.net/publication/331345783>

TAGUCHI AND RESPONSE SURFACE METHODOLOGIES ENGAGED FOR SURFACE ROUGHNESS IN CNC TURNING AISI 316 BY MULTILAYERED COATED TOOL

Article · December 2017

CITATIONS

0

READS

38

2 authors:



Kamaraj Chandrasekaran

MAM School of Engineering, Tamilnadu, India.

43 PUBLICATIONS 168 CITATIONS

SEE PROFILE



Ttm.Kannan Mahadevan

PRIST University

75 PUBLICATIONS 92 CITATIONS

SEE PROFILE

Some of the authors of this publication are also working on these related projects:



Dr.TTM,kannan [View project](#)



Welding [View project](#)



TAGUCHI AND RESPONSE SURFACE METHODOLOGIES ENGAGED FOR SURFACE ROUGHNESS IN CNC TURNING AISI 316 BY MULTILAYERED COATED TOOL

*Chandrasekaran K¹, Ramanathan R², Kannan T T M³ and Ranjithkumar P⁴

^{1,2,3,4}Department of Mechanical Engineering, M.A.M.School of Engineering, Trichy, Tamilandu, India.

ABSTRACT

This paper examines about the utilization of Taguchi and reaction surface techniques (RSM) for minimizing the surface roughness (SR) in CNC turning austenitic stainless steel (AISI 316) by multilayered coated with TiCN/Al₂O₃ tool. The trials have been led utilizing Taguchi exploratory outline system. The cutting parameters utilized are cutting pace, encourage and profundity of cut. The impact of cutting parameters on SR is assessed and the ideal cutting condition for limiting the SR is resolved. In the first place and second request demonstrate are built up between the cutting parameters and SR utilizing RSM. The test comes about uncover that the most huge tuning parameter for SR is sustain trailed by cutting rate. The predicted values and measured values are fairly close, which indicates that the developed model can be effectively used to predict the SR in turning of AISI 316. Analysis of variance (ANOVA) is used for identifying the significant parameters affecting the responses. Finally the residual analysis is employed for verify the regression model.

Keywords: CNC tuning, surface roughness, Taguchi technique, Response surface method and ANOVA.

1. Introduction

Machining process is very important in manufacturing technology. These processes are applied for manufacturing the mechanical parts because of these processes have efficient and economical. There are many parameters to be considered for affecting the surface quality [1, 2]. SR is one of the imperative reactions for machined item quality. SR is influencing the useful conduct of the mechanical items. The mechanism of SR formation depends on various uncontrollable parameters that make its estimation difficult [3, 4]. AISI 316 are generally regarded as being more difficult to machine material compare to carbon and other alloy steels due their high strength, ductility and high work hardening tendency [5]. Stainless steels are having different grades and different properties under variation of chemical compositions. Therefore, these variations in their properties have an influence on their machinabilities [6]. Tool wear is broadly viewed as a standout amongst the most difficult part of causing poor surface quality in machining. Coated carbides are essentially an established carbide coated with at least one daintily layers of wear safe materials, for example, titanium nitride, titanium

carbide and aluminum oxide [7, 8]. It is outstanding that covering can diminish tool wear and enhance the SR [9, 10]. Hence, a large portion of the carbide apparatuses utilized as a part of the metal cutting enterprises is covered while covering realizes an additional cost [11, 12].

In order to get good SR and dimensional properties, it is necessary to employ optimization techniques to find optimal cutting parameters and theoretical models to do predictions. Taguchi and RSM can be conveniently used for these purposes [13]. Taguchi and RSM are applied for optimizing geometric errors in surface grinding process [14]. RSM is more practical, economical and relatively easy to use [15]. Researcher have used many methods to predict responses, but combination of these methods not been done for CNC turning on AISI 316 by multilayered tool. In this paper Taguchi method is used to optimize the performance characteristics of process parameters and first and second order models are developed for predicting the SR. The predicted and measured values are fairly close to each other.

*Corresponding Author - E- mail: kchandrasekaran1984@gmail.com

2. Material and methods

The work material used for the present investigation is AISI 316. The diameter of the material is 32 mm and machined length is 60mm for all trials. The chemical composition of the work material is given in Table 1.

Table 1 Chemical composition of AISI 316.

C	Si	Mg	P	S	Ni	Cr	Mo
0.04	0.49	1.56	0.03	0.01	10.4	16.7	2.11
0	8	0	6	7	5	1	2

2.1 Taguchi method

This paper uses Taguchi method for optimization of machining parameters in turning AISI 316, which is very attractive and effective method to deal with responses influenced by number of variables. In this method, main parameters are assumed to have influence on process results, which are located at different rows in a designed orthogonal array. With such an arrangement completely randomized experiments can be conducted. This method is useful for studying the interactions between the parameters, and also it is a powerful design of experiments tool, which provides a simple, efficient and systematic approach to determine optimal cutting parameters. Compared to the conventional approach of experimentation, this method reduces significantly the number of experiments that are required to model the response functions [16, 17]. There are three categories of quality characteristic in the analysis of the S/N ratio, (1) the-lower-the-better, (2) the-higher-the-better and (3) the-nominal-the-better. Since the quality characteristic is to be minimized, the-lower-the-better category is used to calculate the S/N ratio for SR. Equation (1) shows the smaller the better characteristic.

$$\eta = -10 \log_{10} \left\{ \frac{1}{n} \sum_{i=1}^n y_i^2 \right\} \quad (1)$$

Where:

η = Signal to noise ratio

n = Number of repetitions of experiment

y = Measured value of quality characteristic

Minitab14 statistical software has been used for the analysis of the experimental work. The software studies the experimental data and then

provides the calculated results of signal-to-noise ratio. In this work, the software has given the signal-to-noise ratio for SR.

2.2 Response surface methodology

The surface finish of machined AISI 316 part is critical in assembling applications which have extensive impact on a few properties, for example, superb corrosive resistance. While machining, quality of the parts can be achieved only through proper cutting conditions. Keeping in mind the end goal to know the surface quality and dimensional properties ahead of time, it is important to utilize hypothetical models making it conceivable to do expectation in capacity of operation conditions. RSM is a collection of mathematical and statistical techniques that are useful for the modeling and analysis of problems in which a response of interest is influenced by several variables and the objective is to optimize this response. In many engineering fields, there is a relationship between an output variable of interest 'y' and a set of controllable variables $\{x_1, x_2, \dots, x_n\}$. In some systems, the nature of the relationship between y and x values might be known. Then, a model can be written in the form

$$Y = f(x_1, x_2, \dots, x_n) + \varepsilon \quad (2)$$

Where ε represents noise or error observed in the response y. If we denote the expected response be $f(x_1, x_2, \dots, x_n) = \hat{y}$ then the surface represented by

$$\hat{Y} = f(x_1, x_2, \dots, x_n) \quad (3)$$

In most of the RSM problems, the form of relationship between the response and the independent variable is unknown. Thus the first step in RSM is to find a suitable approximation for the true functional relationship between y and set of independent variables employed. Usually a second order model is utilized in response surface methodology [18].

3 Experimental details

The experiments are planned using Taguchi's orthogonal array in the design of experiments, which helps in reducing the number of experiments. The experiments were conducted according to orthogonal array. The three machining parameters selected for the present investigation is cutting speed (v), feed (f) and depth of cut (d). Since

the considered factors are multi-level variables and their outcome effects are not linearly related, it has been decided to use three level tests for each parameter. The machining parameters used and their levels chosen are given in Table 2. Taguchi's orthogonal array of L_{27} is most suitable for this experiment. This needs 27 runs and has 26 degrees of freedoms. It can conduct three levels of parameters. To check the degrees of freedom (DOF) in the experimental design, for the three levels test, the three main factors take 6 ($3 \times (3-1)$) DOFs. Square effects and interaction between parameters take the remaining DOFs. The values of machining parameters and S/N ratio for SR are presented in Table 3. The experiments were conducted on Fanuc CNC lathe. Multilayered CNMG 120408 coated with $TiN+Al_2O_3$ of 14 μm is used as the insert for all machining operation. The range of cutting parameters were selected based on past experience, data book and available resources. SR is measured by the mitutoyo surface roughness tester.

Table 2 Machining parameters and levels.

Process parameter	Level 1	Level 2	Level 3
Cutting speed (m/min)	110	160	210
Feed(mm/rev)	0.1	0.2	0.3
Depth of cut (mm)	0.7	1.4	2.1

4 Results and discussions

4.1 Effect of control parameters on SR

In Taguchi method, the term signal represents the desirable value and noise represents the undesirable value. The objective of using S/N ratio is a measure of performance to develop products and processes insensitive to noise parameters. The S/N ratio indicates the degree of the predictable performance of a process in the presence of noise parameters. Table 4 shows the S/N ratios obtained for different parameter levels. The calculated S/N ratio for three factors on the SR in turning of AISI 316 for each level is shown in Fig. 4. As shown in Table 4 and Fig. 4 feed is a dominant parameter on the SR followed by depth of cut. The cutting speed had a lower effect on the SR. Lower SR is always preferred. The quality characteristic considered in the investigation is lower-the better characteristics. The SR observed at low cutting speed

is more than the SR observed at higher cutting speed. In the present investigation, when the cutting speed is set at 110 m/min is applied the SR is minimized. From the experimental results, it is observed that at high depth of cut the SR is minimal. Here feed is increased with head generation and tool wear so the SR is increased. The increase in feed also increases the chatter, and it produces incomplete machining of work piece, which led to higher SR. The results shown prove that the roughness of the machined surface is highly influenced by the feed, based on the above discussion and also evident from Fig. 4.

It is emphasized that these conditions only provide best SR among the cutting conditions tested. From Table 6 ANOVA for SR. It can be found that depth of cut and feed are the significant cutting parameters for affecting SR. The change of the cutting speed range given in Table 3 has an insignificant effect on SR (p-value = 0.98).

Table 3 Experimental results for SR versus v,f,d.

Trial	v	f	d	SR(μm)	S/N for SR
1	110	0.1	0.7	0.64	3.87
2	110	0.1	1.4	0.61	4.29
3	110	0.1	2.1	0.56	5.03
4	110	0.2	0.7	1.39	-2.86
5	110	0.2	1.4	1.14	-1.13
6	110	0.2	2.1	1.11	-0.90
7	110	0.3	0.7	1.66	-4.40
8	110	0.3	1.4	1.44	-3.16
9	110	0.3	2.1	1.02	-0.17
10	160	0.1	0.7	1.49	-3.46
11	160	0.1	1.4	0.92	0.72
12	160	0.1	2.1	0.7	3.09
13	160	0.2	0.7	1.33	-2.47
14	160	0.2	1.4	1.43	-3.10
15	160	0.2	2.1	1.38	-2.79
16	160	0.3	0.7	1.17	-1.36
17	160	0.3	1.4	1.23	-1.79
18	160	0.3	2.1	1.33	-2.47
19	210	0.1	0.7	1.83	-5.24
20	210	0.1	1.4	0.64	3.87
21	210	0.1	2.1	0.74	2.61
22	210	0.2	0.7	1.51	-3.57
23	210	0.2	1.4	1.43	-3.10
24	210	0.2	2.1	1.23	-1.79
25	210	0.3	0.7	1.7	-4.60
26	210	0.3	1.4	1.47	-3.34
27	210	0.3	2.1	1.39	-2.86

Table-4 Taguchi Analysis: SR versus v,f,d.

Level	v	f	d
1	0.06220	1.64526	-2.68090
2	-1.51796	-2.41895	-0.75213
3	-2.00636	-2.68843	-0.02909
Delta	2.06856	4.33369	2.65180
Rank	3	1	2

Table-5 Analysis of Variance for SR versus v,f,d.

Source	DF	SS	MS	F	P
v	2	0.315	0.15790	2.62	0.098
f	2	1.226	0.61338	10.17	0.001
d	2	0.635	0.31774	5.27	0.015
Error	20	1.206	0.06034		
Total	26	3.384			

S = 0.245637 R-Sq = 64.35% R-Sq (adj) = 53.65%

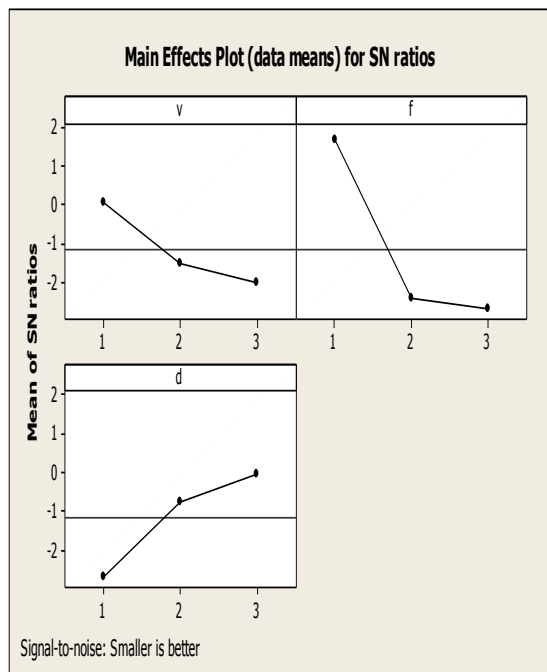


Fig.1 The main effect of plot for S/N ratio for SR

4.2 Response surface analysis

4.2.1 First order regression model

The first order response surface representing the SR can be expressed as a function of cutting parameters. The relation between the SR and machining parameters has been expressed as follows

$$SR = \beta_0 + \beta_1 (v) + \beta_2 (f) + \beta_3 (d) + \beta_7 (v f) + \beta_8 (v d) + \beta_9 (f d) \quad (4)$$

From the observed data for SR, the response function has been determined is un coded unit as

$$SR = 0.941 + 0.132 v + 0.238 f - 0.181 d + 0.0372 vf - 0.0228 vd - 0.0717 df \quad (5)$$

The β coefficients, used in the above model can be calculated by means of using least square method. The relationship between S/N ratio and SR is given in the graphical plot in Fig.1. The first -order model is normally used when the response function is not known or nonlinear. The estimated first order regression coefficient the least squares method is as shown in table 6. Result of ANOVA for the function SR is presented in table 7. The analysis is carried of 5%, ie, for a level of confidence of 95%. To verify the regression model, we performed residual analysis. The normal plot and residual histogram from this analysis are depicted in Fig 2 and 3 respectively. As shown in Fig 2, the departures are scattered. It indicates the abnormalities in the residual distribution. Alternatively, the residual histogram shows that frequency of the residual is not satisfied with the normal distribution.

Table 6 First order regression coefficient

	Coef.	Coef.SE	T	P
β_0	0.9411	0.3028	3.11	0.006
β_1	0.13167	0.06096	2.16	0.043
β_2	0.23778	0.06096	3.90	0.001
β_3	-0.18111	0.06096	-2.97	0.008
β_4	0.03722	0.06096	0.61	0.548
β_5	-0.02278	0.06096	-0.37	0.711
β_6	-0.07167	0.06096	-1.18	0.254

Table 7 ANOVA for first order regression model

Source	D	SS	MS	F	P
Regression	6	2.04689	0.34115	5.10	0.003
Residual	20	1.33791	0.06690		
Error					
Total	26	3.38480			

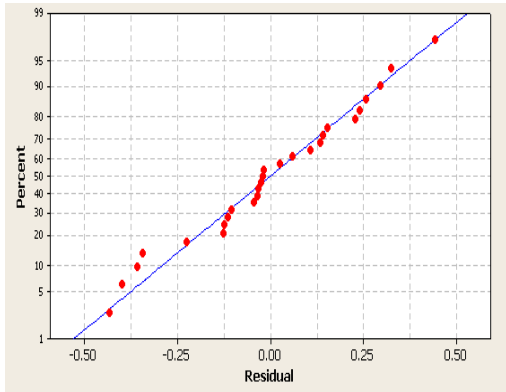


Fig 2 Normal probability plot for the residuals

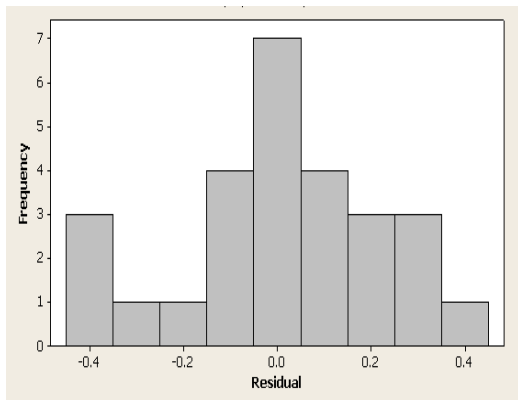


Fig. 3 Histogram of the residuals

4.2.2 Second order regression model

The second order response surface representing the SR can be expressed as a function of machining parameters. The relation between the SR and machining parameters has been expressed as follows

$$SR = \beta_0 + \beta_1 (v) + \beta_2 (f) + \beta_3 (d) + \beta_4 (v^2) + \beta_5 (f^2) + \beta_6 (d^2) + \beta_7 (v f) + \beta_8 (v d) + \beta_9 (f d) \quad (6)$$

From the observed data for SR, the response function has been determined is un coded unit as

$$SR = 0.889 + 0.132v + 0.238f - 0.181d + 0.0372v^2 - 0.0228f^2 - 0.0717d^2 + 0.0800vf + 0.0200vd - 0.0739fd \quad (5)$$

The second order estimated coefficient is shown in table 8. Result of ANOVA for the second order regression model is shown in table 9. Fig 2 and

3 show the results of normal probability and histogram of the residuals. As shown in Fig 4, the result is enhanced more than the first order regression model. Also, the frequency of the residual was satisfied with the normal distribution as shown if Fig 5 and the second order regression model is suitable for explaining the machining errors.

Table 8 The second order regression coefficient

	Coef.	Coef.SE	T	P
β_0	0.8889	0.3659	2.43	0.026
β_1	0.13167	0.06042	2.18	0.044
β_2	0.23778	0.06042	3.94	0.001
β_3	-0.18111	0.06042	3.00	0.008
β_4	0.03722	0.06042	0.62	0.546
β_5	-0.02278	0.06042	-0.38	0.711
β_6	-0.07167	0.06042	-1.19	0.252
β_7	0.08000	0.06042	1.32	0.203
β_8	0.02000	0.06042	0.33	0.745
β_9	-0.07389	0.06042	-1.22	0.238

Table 9 ANOVA for second order regression model

Source	DF	SS	MS	F	P
Regression	9	2.2675	0.25195	3.83	0.008
Residual Error	17	1.1172	0.06572		
Total	26	3.384			

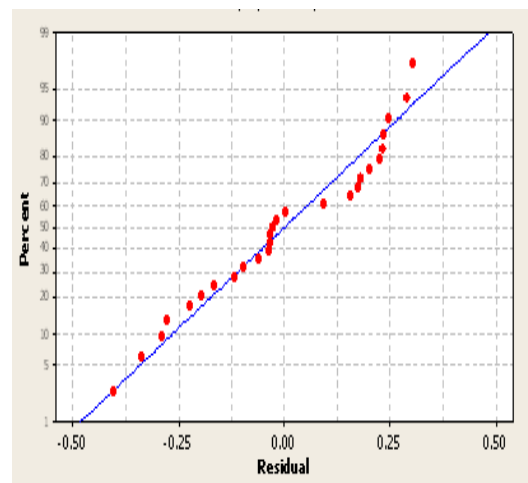


Fig. 4 Normal probability plot for the residuals

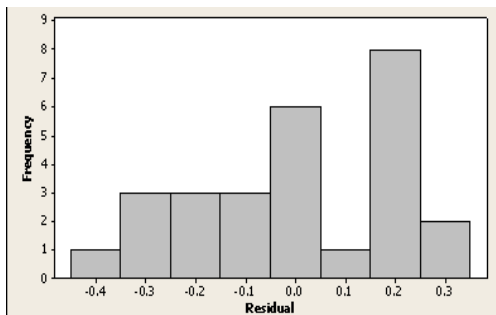


Fig. 5 Histogram of the residuals.

5 Conclusions

The SR in the turning procedure is measured for machining of AISI 316 under various cutting conditions with multilayer of TiCN/Al₂O₃ tool utilizing Taguchi orthogonal array. In view of the trial and diagnostic outcomes, the accompanying conclusions drawn.

- The impact of machining parameters on the SR has been assessed the assistance of Taguchi strategy and ideal machining conditions to limit the SR have been resolved.
- The feed is the predominant parameter for SR took after by the depth of cut. Cutting speed demonstrated negligible impact on SR contrasted with different parameters.
- For accomplishment of good SR on AISI 316 low cutting speed, low feed and high depth of cut are favored.
- The second order regression model demonstrate is more appropriate than the primary order regression model show for portraying the turning procedure, from the view purpose of ANOVA and residual analysis.
- The second order response surface model for SR is created from the watched information the anticipated and measured esteem are genuinely close, which shows that the created model can be adequately used to foresee the SR.

References

1. Tosun N and Ozler L (2000), "A study of tool life in hot machining using artificial neural network and regression analysis", *J. mat.proc.Technol.* 124, 99-104.
2. Wardancy T I E, Elestawi M A (1997), "Prediction of tool failure rate in turning hardened steels" *Int.J.manuf,Technol.* Vol. 13, 1-16.
3. Selvam M S (1975), "Tool vibration and its influence on surface roughness in turning", *Vol. 35*, 149-157.
4. Lasota A, Rusek P (1983), "Influence of random vibrations on the roughness of turned surfaces", *J. Mech Work Technol.* Vol. 7, 277-284.
5. Trent E M (1989), "Metal cutting", London, Butterworths Press. New York.
6. Paro J, Hanninen H and Kauppinen V (2001), "Tool wear and machinability of X5 CrMnN18 18 stainless steels", *J.Mater. Process. Technol.* Vol. 119, 14-20.
7. Sarwar M, Zhang X and Gillibrand D (1997), "Performance of titanium nitride coated carbide tipped circular saws when cutting stainless steel and mild steel", *Surf.Coat.Technol.*,Vol. 94, 617-21.
8. Groover, M P (1996), "Fundamentals of modern manufacturing—materials, processes and systems", New Jersey: Prentice-Hall Inc.
9. DeGarmo E P, Black J T and Kohser R A (1997), "Materials and processes in manufacturing", New Jersey: Prentice-Hall Inc.
10. Lim C Y H, Lim S C, Lee K S (1999), "The performance of TiN-coated high speed steel tool inserts in turning", *Tribol Int.*, Vol.32, 393-398.
11. Ezugwu, E.O., Okeke, C.I., 2001, "Tool life and wear mechanisms of TiN coated tools in an intermittent cutting operation", *J. Mater. Process. Technol.* 116, 10-15.
12. Nouari M, List G, Girot F and Coupard D (2003), "Experimental analysis and optimization of tool wear in dry machining of aluminum alloy", *Vol. 255*, 1359-1368.
13. Suresh P V S, Venkatehara Rao K and Desmukh S G "A genetic algorithmic approach for optimization of the surface roughness prediction model", *Int J Mach Tools Manuf.* Vol. 42, 675-680.
14. Kwak J S 2005, "Application of Taguchi and response surface methodologies for geometric error in surface grinding process", *Int J Mach Tool Manuf.*, Vol. 45, 327-334.
15. Sahin, Y., Motorcu, A.R., 2004, "Surface roughness model for machining mild steel", *Mater Des-article in press.*
16. George P M, Raghunath B K, Manochac L M and Warriar A M (2004), "EDM machining of carbon-carbon composite-a Taguchi approach", *J Mater Process Technol.*, Vol. 145, 66-71.
17. Ross P J (1996), "Taguchi techniques for quality engineering". McGraw-Hill, New York.
18. Montgomery D C (1991), "Design and analysis of experiments". John Wiley and Sons, NewYork.

Mechanics and Mechanical Engineering

Vol. 21, No. 2 (2017) 207–216

© Lodz University of Technology

Workability Behavior of Hybrid Copper Matrix Composites Synthesized by Powder Metallurgy Technique

K. ILAYARAJA

*Department of Mechanical Engineering
Ariyalur Engineering College
Ariyalur, India
Ilayarajakaruppiah14@gmail.com*

P. RANJITH KUMAR

*Department of Mechanical Engineering
MAM School of Engineering
Tiruchirappalli, India
ranjjith@mamce.org*

V. ANANDAKRISHNAN

S. SATHISH

*Department of Production Engineering
National Institute of Technology
Tiruchirappalli, India
krishna@nitt.edu
sadish.kss@gmail.com*

M. RAVICHANDRAN

*K. Ramakrishnan College of Engineering, Trichy, India
smravichandran@hotmail.com*

R. RAVIKUMAR

*Department of Mechanical Engineering
Ariyalur Engineering College
Ariyalur, India
ravikumar_mech@yahoo.com*

Received (13 December 2016)

Revised (16 January 2017)

Accepted (17 February 2017)

Copper based hybrid composite materials with 5wt.% of titanium dioxide and 0wt.%, 2wt.% and 4wt.% of graphite were produced using powder metallurgy technique. The presence and distribution of titanium dioxide and graphite reinforcements were examined in the copper matrix using scanning electron microscopic and energy dispersive spectroscopic analysis. To investigate the workability behavior of the sintered composite preforms, cold upset tests were conducted and various stresses and forming parameters were determined and using that various stress ratio parameters such as the true axial stress versus the true effective stress, the true hoop stress versus the true effective stress, the true hydrostatic stress versus the true effective stress and the true hoop stress versus the true hydrostatic stress were calculated and correlated with the true axial strain. From the studies, the workability of the composite is found to increase with increasing graphite content due to increase in lubricating affect by graphite addition.

Keywords: hybrid copper composite, Powder metallurgy, workability.

1. Introduction

In the field of automotive, aerospace, marine and defense industries [1] there is a prerequisite of innovation in material with enriched properties to use in diverse environments. Metal matrix composites have a wide range of scope to design and build materials with desired properties by reinforcing with hard and/or soft materials. Ceramic is one among the reinforcement which plays major role in the composite materials due to its outstanding mechanical properties, tremendous strength and better chemical stability even at elevated temperatures [2]. There are several modes of composite fabrication which includes solid phase or liquid phase processing and each has its own assets and faults in distribution of reinforcement and interfacial bonding of reinforcement with the matrix material. Powder metallurgy is one of the best and cost effective fabrication techniques which fabricate the required component at desired geometry with uniform distribution of reinforcement and ease of control in microstructure [3–6]. Further the properties of the material produced through powder metallurgy technique may be improved with the secondary processing and heat treatment [7]. Copper is the material which has extensive application due its remarkable properties such as electrical conductivity [8, 9], thermal conductivity [8, 9], ductility [9] and corrosion resistance [9]. Copper composites have exposed a superior combined properties of conductivities, mechanical and tribology [10]. Cu-Fe₃Al composite was effectively fabricated at varying volume fractions of Fe₃Al by powder metallurgy and investigated its wear behavior [11]. Mechanical and wear properties of copper tin composites with copper coated and uncoated lubricant of graphite and molybdenum disulfide was investigated [12] and found that the addition of copper coated lubricant shows an adverse effect on the material properties. Steel composite reinforced with TiC particles was produced through powder metallurgy and studied the workability of the produced composite during hot forging [13]. Workability of the copper composite produced by powder metallurgy with silicon carbide was studied and examined the different stress ratio parameter under trial stress state [14]. Hybrid copper composite with TiC and graphite was successfully fabricated and its tribological properties was investigated [15]. Al₂₀₂₄-SiCp composite was synthesized by powder metallurgy technique and investigated the workability behavior of the produced composite [16].

Copper composites with carbon nanotubes were fabricated and the tribological property of the composites were examined [17]. Aluminium composite with ti-

tanium carbide particles was synthesized through powder metallurgy route and explored its forming behavior under triaxial stress state condition [18]. Hybrid aluminium composite with 5wt. % TiO_2 and 6wt. % graphite using powder metallurgy technique was produced and its forming behavior was studied [19]. Three copper based composite by precipitation, dispersion and multiple hardening using powder metallurgy was produced and the strengthening effects at room temperature and elevated temperature were studied [20]. The effect of copper addition on the mechanical properties of Acorsteel 85 HP alloy was studied and reported that there is an increase in density and toughness [21]. Mechanically mixed the copper powder was mixed with aluminium silicon alloy, produced the composite by liquid phase hot pressing and observed that the addition of copper led to the formation of Al_2Cu , which enhanced the mechanical properties by precipitation and solid solution hardening [22]. With reference to the earlier findings discussed above, it was identified that there is research gap in the synthesis and workability studies of copper composites with TiO_2 and graphite as reinforcement. Therefore an attempt is made to produce a hybrid copper composite with 5wt.% TiO_2 and at varying weight percentage of graphite (0, 2 and 4) through powder metallurgy technique. To identify the reinforcement's presence and distribution the copper composite were subjected to scanning electron microscopic along with energy dispersive spectroscopy. Further the hybrid composites workability behavior is investigated during cold upset.

2. Experimental details

Copper powder of 150 μm with 99% of purity was chosen as the matrix material, TiO_2 and graphite powder of 10 μm with 99% of purity was taken as reinforcements to fabricate the hybrid copper composite material with 5wt.% TiO_2 and at different weight percentages of graphite (0, 2 and 4) using powder metallurgy techniques. In order to obtain the required composite composition, copper, TiO_2 and graphite powders were weighed accurately using 0.0001 g accurate digital weighing balance and then the mix were blended in a ball mill for 15 hrs at 300rpm using a ball to powder ratio of 10:1. After the blending process, the powders were compacted in a hydraulic press using a punch and die setup with zinc stearate as die wall lubricant. Green compacts were further sintered at 900°C temperature for a duration of 2 hours under argon environment in a muffle furnace and then it is allowed to cool in the furnace. Samples were prepared from the sintered preforms for metallurgical characterization through scanning electron microscopic analysis along with energy dispersive spectroscopy analysis. During the pilot experiments, reduction of hardness was observed beyond 10wt.% TiO_2 addition and also agglomeration of graphite particles were observed beyond 6wt.% addition of graphite. Hence the hybrid copper composite for the workability study were constrained to Cu-5wt.% TiO_2 -0wt.% Gr, Cu-5wt.% TiO_2 -2wt.%Gr, and Cu-5wt.% TiO_2 -4wt.%Gr.

Initially the dimensions of the sintered hybrid copper composite preforms were measured, and cold upsetted with 20 kN compressive load was applied in an incremental manner using flat fine polished dies till the appearance of crack on the surface. At the end of the each incremental loading, the dimensions such as bottom contact diameter (D_{BC}), top contact diameter (D_{TC}), bulged diameter (D_B) and height (H_d) of the upset preforms were documented to quantify the deformation. With all

the measured values, relating the plasticity theory as explained elsewhere [13, 14, 19, 23, and 24], the various stresses and forming parameters were determined. From that the stress ratio parameters such as the true axial stress versus the true effective stress (σ_z/σ_{eff}), the true hoop stress versus the true effective stress ($\sigma_\theta/\sigma_{eff}$), the true hydrostatic stress versus the true effective stress (σ_m/σ_{eff}) and the true hoop stress versus the true hydrostatic stress (σ_θ/σ_m) were calculated and correlated with the true axial strain (ε_z).

3. Results and discussion

3.1. Scanning electron microscopic analysis

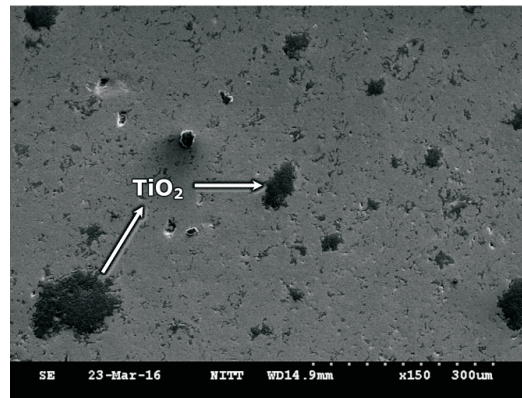
Fig. 1(a)–(c) shows the scanning electron microscopic image of hybrid copper composite with 5wt.% TiO₂ and varying graphite content. The microscopic image clearly visualizes and differentiates the matrix phase and reinforcement phase and also shows the even distribution of reinforcements in the copper matrix. From the energy dispersive spectroscopic analysis it is observed that in all three compositions, the presence of TiO₂ is found equal whereas the intensity for graphite are found to be increasing with increase in graphite content of 2 and 4 weight percentages as shown in Fig. 2 (a)–(c).

3.2. Workability behavior

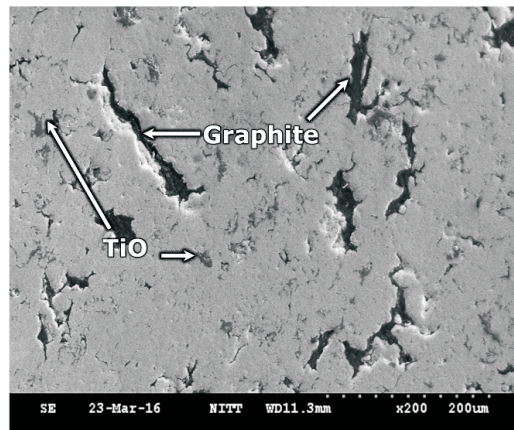
Workability of a material highly depends on the ductility and its process parameters [46], which can be evaluated using the stress ratio parameters. Fig. 3–6 depicts the relationship of the stress ratio parameters (σ_z/σ_{eff}), ($\sigma_\theta/\sigma_{eff}$) with the true axial strain (ε_z) for Cu hybrid sintered composites during cold upsetting. Fig. 3 shows that stress ratio parameter (σ_z/σ_{eff}) increases with increase in graphite particles in the hybrid copper composite. Among the various composites tested the higher stress ratio parameter (σ_z/σ_{eff}) is observed for Cu-5% TiO₂-2% Gr composite and this may be due to the addition of 2wt.% of soft graphite particles which promotes densification in the axial direction and hence the axial stress (σ_z) is relatively more than that of the effective stress (σ_{eff}). But for higher content of graphite such as 4wt.% , the material gets self-lubricated and due to which the axial stress (σ_z) is relatively less than that of the effective stress (σ_{eff}) thereby the stress ratio parameter (σ_z/σ_{eff}) for 2wt.% is higher than that of 4wt.%.

In the present study, the stress ratio parameter decreases for the increase in true axial strain which is due to the rate of increase in true effective stress (σ_{eff}) which is higher than that of increase in true axial strain (ε_z). Due to similar reasons the stress ratio parameter ($\sigma_\theta/\sigma_{eff}$) and (σ_m/σ_{eff}) as shown in Figs. 4 and 5 represents similar trend which is observed in Fig. 3.

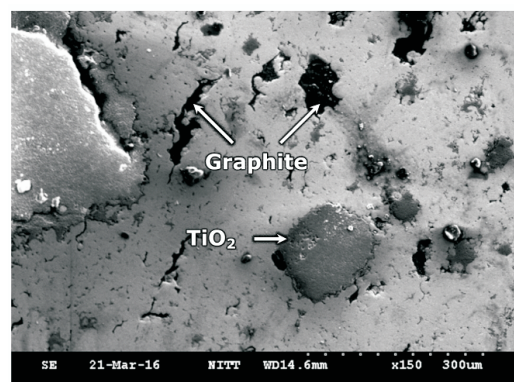
Fig. 6 represents the variation of stress ratio parameter (σ_θ/σ_m) with true axial strain (ε_z) during cold upsetting of copper hybrid composites. In the early conditions of axial strain the composite without graphite exhibits lower stress ratio parameter (σ_θ/σ_m) as the pore size is relatively larger which leads to lower hoop stress whereas the composite with higher graphite content having very fine pores leads to higher hoop stresses. Later after deformation the larger pores get closed and decreased in size which makes the stress ratio parameter (σ_θ/σ_m) uniform for all the composites tested.



a)

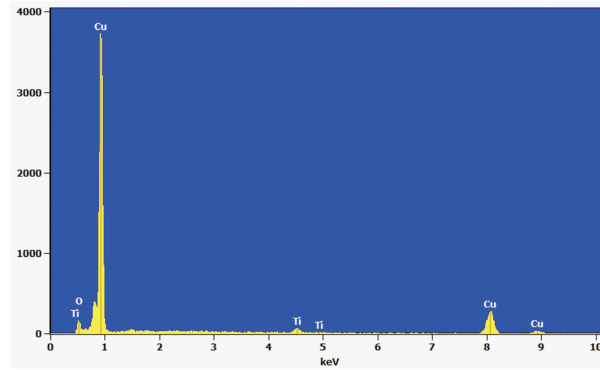


b)

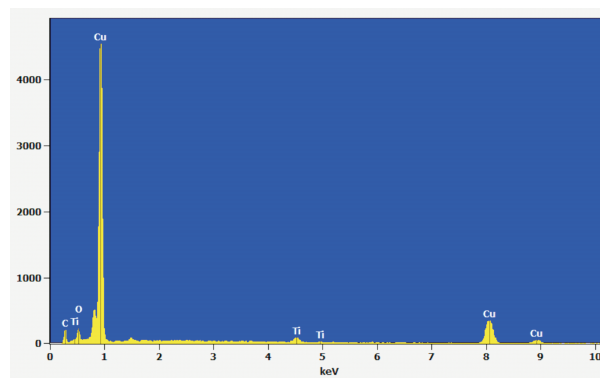


c)

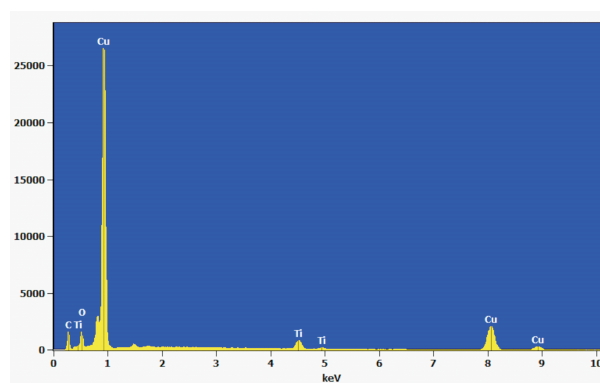
Figure 1 Scanning electron microscopic images of (a) Cu-5wt.% TiO₂-0wt.% Gr, (b) Cu-5wt.% TiO₂-2wt.% Gr, and (c) Cu-5wt.% TiO₂-4wt.% Gr



(a)



(b)



(c)

Figure 2 EDS spectral analysis for hybrid copper composite a) Cu-5wt.% TiO₂-0wt.% Gr, b) Cu-5wt.% TiO₂-2wt.% Gr, and c) Cu-5wt.% TiO₂-4wt.% Gr

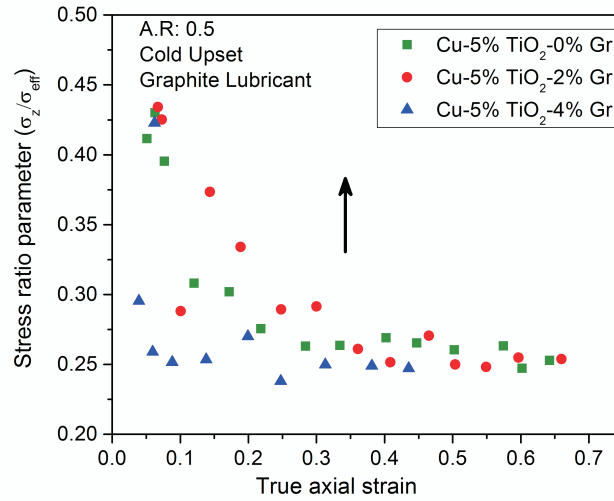


Figure 3 Stress ratio parameter (σ_z/σ_{eff}) versus True axial strain (ϵ_z)

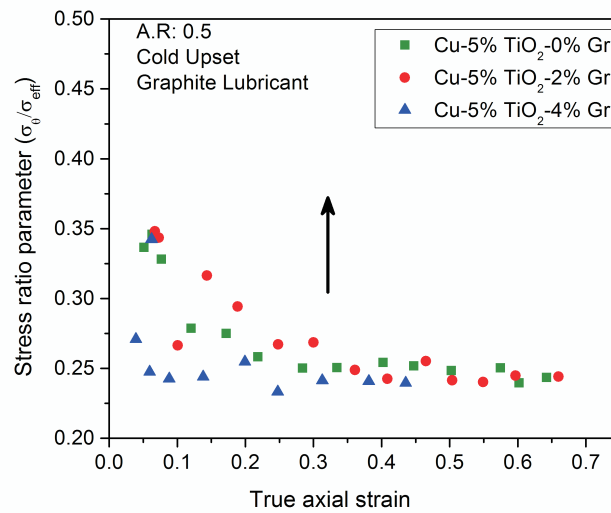


Figure 4 Stress ratio parameter ($\sigma_\theta/\sigma_{eff}$) versus True axial strain (ϵ_z)

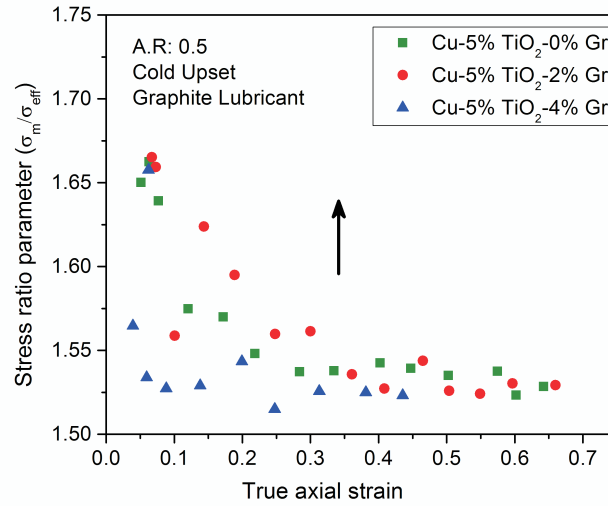


Figure 5 Stress ratio parameter (σ_m/σ_{eff}) versus True axial strain (ϵ_z)

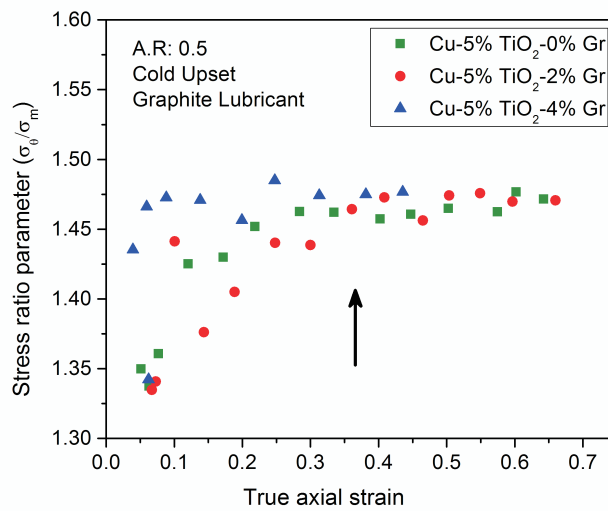


Figure 6 Stress ratio parameter (σ_θ/σ_m) versus True axial strain (ϵ_z)

4. Conclusions

Hybrid copper composites with 5 weight percentage of TiO₂ and varying weight percentage of graphite namely 0, 2 and 4% was successfully synthesized through powder metallurgy technique and following are the conclusions drawn based on the characterization and formability studies. Scanning electron microscopic analysis with Energy Dispersive Spectroscopy shows the presence and uniform distribution of TiO₂ and Graphite reinforcements. Workability of the composite is found to increase with increasing graphite content due to lubricating property of graphite.

References

- [1] **Derakhshandeh, R. and Jenabali Jahromi, H. A.:** An investigation on the capability of equal channel angular pressing for consolidation of aluminum and aluminum composite powder, *Mater. Design*, 32, 3377–3388, **2011**.
- [2] **Sadık Ünlü, B.:** Investigation of tribological and mechanical properties Al₂O₃–SiC reinforced Al composites manufactured by casting or P/M method, *Mater. Design*, 29, 2002–2008, **2008**.
- [3] **Zhangwei Wang, Min Song, Chao Sun, Daihong Xiao, Yuehui He:** Effect of extrusion and particle volume fraction on the mechanical properties of SiC reinforced Al–Cu alloy composites, *Mat. Sci. Eng., A*, 527, 6537–6542, **2010**.
- [4] **Hailong Wang, Rui Zhang, Xing Hu, Chang-An Wang, Yong Huang:** Characterization of a powder metallurgy SiC/Cu–Al composite, *J. Mater. Process. Tech.*, 197, 43–48, **2008**.
- [5] **Moazami-Goudarzi, M. and Akhlaghi, F.:** Effect of nanosized SiC particles addition to CP Al and Al–Mg powders on their compaction behavior, *Powder Technol.*, 245, 126–133, **2013**.
- [6] **Abouelmagd, G.:** Hot deformation and wear resistance of P/M aluminium metal matrix composites, *J. Mater. Process. Tech.*, 155–156, 1395–1401, **2004**.
- [7] **Izadi, H., Nolting, A., Munro, C., Bishop, D. P., Plucknett, K. P. and Gerlich, A. P.:** Friction stir processing of Al/SiC composites fabricated by powder metallurgy, *J. Mater. Process. Tech.*, 213, 1900–1907, **2013**.
- [8] **Selvakumar, N. and Vettivel, S. C.:** Thermal, electrical and wear behavior of sintered Cu–W nanocomposite, *Mater. Des.*, 46, 16–25, **2013**.
- [9] **Samal, C. P., Parihar, J. S. and Chaira, D.:** The effect of milling and sintering techniques on mechanical properties of Cu-graphite metal matrix composite prepared by powder metallurgy route, *Journal of Alloys and Compounds*, 569, 95–101, **2013**.
- [10] **Tu, J. P., Meng, L. and Liu, M. S.:** Friction and wear behavior of CuFe₃Al powder metallurgical composites in dry sliding, *Wear*, 220, 1, 72–79, **1998**.
- [11] **Tu, J. P., Meng, L. and Liu, M. S.:** Friction and wear behavior of Cu–Fe₃Al powder metallurgical composites in dry sliding, *Wear*, 1648, 72–79, **1997**.
- [12] **Kato, H., Takama, M., Iwai, Y., Washida, K. and Sasaki, Y.:** Wear and mechanical properties of sintered copper–tin composites containing graphite or molybdenum disulfide, *Wear*, 255, 573–578, **2003**.
- [13] **R. Narayanasamy, V. Senthilkumar, K. S. Pandey.:** Some aspects of workability studies on sintered high strength P/M steel composite preforms of varying TiC contents during hot forging, *J. Mater. Sci.*, 43, 102–116, **2008**.
- [14] **Sumathi, M., Selvakumar, N. and Narayanasamy, R.:** Workability studies on sintered Cu–10SiC preforms during cold axial upsetting, *Mater. Design*, 39, 1–8, **2012**.

- [15] **Rajkumar, K. and Aravindan, S.:** Tribological performance of micro wave sintered copper-TiC-graphite hybrid composites, *Tribol. Int.*, 44, 347–358, **2011**.
- [16] **Shao, J. C., Xiao, B. L., Wang, Q. Z., Ma, Z. Y., Liu, Y. and Yang, K.:** Constitutive flow behavior and hot workability of powder metallurgy processed 20 vol.% SiCP/2024Al composite, *Mater. Sci. Engg.*, A, 527, 7865–7872, **2010**.
- [17] **Wei, X. U., Rui, H. U., Jin-shan, L. I. and Heng-zhi, F. U.:** Effect of electrical current on tribological property of Cu matrix composite reinforced by carbon nanotubes, *Trans. Nonferrous Met. Soc. China*, 21, 2237–2241, **2011**.
- [18] **Anandakrishnan, V., Baskaran, S. and Sathish, S.:** Synthesis and Forming Behavior of In-Situ AA 7075 - TiC Composites, *Advanced Materials Research*, 651, 251–256, **2013**.
- [19] **Ravichandran, M., Vidhya, V. S. and Anandakrishnan, V.:** Study of the Characteristics of AL+ 5 wt.% TiO₂+ 6 wt.% GR Hybrid P/M Composite Powders Prepared by the Process of Ball Milling, *Mater. Sci.*, 51, 4, 589–597.
- [20] **Ruzic, J., Stašić, J., Rajkovic, V. and Bozic, D.:** Strengthening effects in precipitation and dispersion hardened powder metallurgy copper alloys, *Materials and Design*, 49, 746–754, **2013**.
- [21] **Wong-Angel, W. D., Tellez-Jurado, L., Chavez-Alcala, J. F., Chavira-Martinez, E. and Verduzco-Cedeno, V. F.:** Effect of copper on the mechanical properties of alloys formed by powder metallurgy, *Materials and Design*, 58, 12–18, **2014**.
- [22] **Zhiyong Cai, Chun Zhang, Richu Wang, Chaoqun Peng, Xiang Wu:** Effect of copper content on microstructure and mechanical properties of Al/Sip composites consolidated by liquid phase hot pressing, *Materials and Design*, 110, 10–17, **2016**.
- [23] **Ravichandran, M. and Anandakrishnan, V.:** Optimization of powder metallurgy parameters to obtain maximum strength coefficient in Al-MoO₃ composite, *J. Mater. Res.*, 30, 2380–2387.
- [24] **Ravichandran, M., Naveen Sait, A. and Anandakrishnan, V.:** Effect of TiO₂ in aluminum matrix on workability behavior of powder metallurgy composites during cold upsetting, *Int. J. Mater. Res.*, 105 4, 358–364.

Should you have **institutional access?** [Here's how to get it ...](#)

Requires Authentication Published by [De Gruyter](#) July 5, 2017

Synthesis, characterization and forming behavior of hybrid copper matrix composites produced using powder metallurgy

Ilyaraja Karuppiah, Ranjith Kumar Poovaraj, Anandkrishnan Veeramani, Sathish Shanmugam, Ravichandran Manickam and Ravikumar Rangasamy

From the journal [International Journal of Materials Research](#)

<https://doi.org/10.3139/146.111510>

Cite this

Citations

3

You currently have no access to view or download this content. Please log in with your institutional or personal account if you should have access to this content through either of these. Showing a limited preview of this publication:

Abstract

Hybrid copper matrix composites containing 5 wt.% of titanium dioxide and varying graphite content (0 wt.%, 2 wt.% and 4 wt.%) were synthesized using powder metallurgy. Metallurgical studies were carried out to examine the presence and distribution of reinforcements in the copper matrix. To investigate the forming behavior of the sintered composite preforms, cold upset tests were conducted from which the true axial stress, the true hoop stress, the true hydrostatic stress and the true effective stress were evaluated and their relationship with the true axial strain was analyzed and presented. It is observed that the increase in addition of weight percentage of graphite into the copper matrix increases the true axial, the true hoop, the true hydrostatic and the true effective stresses. The variation of hardness, strength coefficient and strain hardening with respect to the addition of graphite content is also evaluated and reported.

Keywords: [Cold working](#); [Composite](#); [Powder metallurgy](#)

*Correspondence address, K. Ilyaraja, Assistant Professor, Department of Mechanical Engineering, Ariyalur Engineering College, NH 227, Trichy – Chithambaram Main Road, Ariyalur – 621707, India, Tel.: +91-9965457711, Fax: +91-9965457711, E-mail: ilyarajakaruppiah14@gmail.com, Web: www.ariyalurengineeringcollege.com

References

- [1] F.Akhlaghi, S.A.Pelaseyyed: Mater. Sci. Eng. A385 (2004) 258. [10.1016/j.msea.2004.06.050](https://doi.org/10.1016/j.msea.2004.06.050) [Search in Google Scholar](#)
- [2] J.Oñoro: J. Rare Met.30 (2011) 200. [10.1007/s12598-011-0224-6](https://doi.org/10.1007/s12598-011-0224-6) [Search in Google Scholar](#)
- [3] R.Derakhshandeh, H.A. JenabaliJahromi: Mater. Des.32 (2011) 3377. [10.1016/j.matdes.2011.02.015](https://doi.org/10.1016/j.matdes.2011.02.015) [Search in Google Scholar](#)
- [4] B.S.Ünlü: Mater. Des.29 (2008) 2002. [10.1016/j.matdes.2008.04.014](https://doi.org/10.1016/j.matdes.2008.04.014) [Search in Google Scholar](#)
- [5] Z.W.Wang, M.Song, C.Sun, D.H.Xiao, Y.H.He: Mater. Sci. Eng. A527 (2010) 6537. [10.1016/j.msea.2010.07.017](https://doi.org/10.1016/j.msea.2010.07.017) [Search in Google Scholar](#)

- [6] H.L.Wang, R.Zhang, X.Hu, C.A.Wang, Y.Huang: J. Mater. Process. Technol.197 (2008) 43. [10.1016/j.jmatprotec.2007.06.002](https://doi.org/10.1016/j.jmatprotec.2007.06.002) [Search in Google Scholar](#)
- [7] M.Moazami-Goudarzi, F.Akhlaghi: Powder Technol.245 (2013) 126. [10.1016/j.powtec.2013.04.025](https://doi.org/10.1016/j.powtec.2013.04.025) [Search in Google Scholar](#)
- [8] G.Abouelmagd: J. Mater. Process. Technol.155 (2004) 1395. [10.1016/j.jmatprotec.2004.04.223](https://doi.org/10.1016/j.jmatprotec.2004.04.223) [Search in Google Scholar](#)
- [9] C.Ghit, I.N.Popescu: Comput. Mater. Sci.64 (2012) 136. [10.1016/j.commatsci.2012.05.031](https://doi.org/10.1016/j.commatsci.2012.05.031) [Search in Google Scholar](#)
- [10] M.Rahimian, N.Parvin, N.Ehsani: Mater. Sci. Eng. A527 (2010) 1031. [10.1016/j.msea.2009.09.034](https://doi.org/10.1016/j.msea.2009.09.034) [Search in Google Scholar](#)
- [11] M.A.Baghchesara, H.Abdizadeh: J. Mech. Sci. Technol.26 (2012) 367. [10.1007/s12206-011-1101-9](https://doi.org/10.1007/s12206-011-1101-9) [Search in Google Scholar](#)
- [12] J.K.Chen, I.S.Huang: Composites Part B Eng.44 (2013) 698. [10.1016/j.compositesb.2012.01.083](https://doi.org/10.1016/j.compositesb.2012.01.083) [Search in Google Scholar](#)
- [13] X.Q.Zhang, Y.H.Peng, M.Q.Li, S.C.Wu, X.Y.Ruan: J. Mater. Eng. Perform.9 (2000) 164. [10.1361/105994900770346114](https://doi.org/10.1361/105994900770346114) [Search in Google Scholar](#)
- [14] H.Izadi, A.Nolting, C.Munro, D.P.Bishop, K.P.Plucknett, A.P.Gerlich: J. Mater. Process. Technol.213 (2013) 1900. [10.1016/j.jmatprotec.2013.05.012](https://doi.org/10.1016/j.jmatprotec.2013.05.012) [Search in Google Scholar](#)
- [15] R.E.D.Mann, R.L.HexemerJr, I.W.Donaldson, D.P.Bishop: Mater. Sci. Eng. A528 (2011) 5476. [10.1016/j.msea.2011.03.081](https://doi.org/10.1016/j.msea.2011.03.081) [Search in Google Scholar](#)
- [16] R.Narayanasamy, V.Senthilkumar, K.S.Pandey: J. Mater. Sci.43 (2008) 102. [10.1007/s10853-007-2124-6](https://doi.org/10.1007/s10853-007-2124-6) [Search in Google Scholar](#)
- [17] J. AppaRao, J. BabuRao, S.Kamaluddin, M.M.M.Sarcar, N.R.M.R.Bhargava: Mater. Des.30 (2009) 2143. [10.1016/j.matdes.2008.08.028](https://doi.org/10.1016/j.matdes.2008.08.028) [Search in Google Scholar](#)
- [18] R.Narayanasamy, V.Senthilkumar, K.S.Pandey: J. Mater. Sci.43 (2008) 102. [10.1007/s10853-007-2124-6](https://doi.org/10.1007/s10853-007-2124-6) [Search in Google Scholar](#)
- [19] J.C.Shao, B.L.Xiao, Q.Z.Wang, Z.Y.Ma, Y.Liu, K.Yang: Mater. Sci. Eng. A527 (2010) 7865. [10.1016/j.msea.2010.08.080](https://doi.org/10.1016/j.msea.2010.08.080) [Search in Google Scholar](#)
- [20] M.A.Taha, N.A.El-Mahallawy, A.M.El-Sabbagh: J. Mater. Process. Technol.202 (2008) 380. [10.1016/j.jmatprotec.2007.07.047](https://doi.org/10.1016/j.jmatprotec.2007.07.047) [Search in Google Scholar](#)
- [21] M.Sumathi, N.Selvakumar, R.Narayanasamy: Mater. Des.39 (2012) 1. [10.1016/j.matdes.2012.02.004](https://doi.org/10.1016/j.matdes.2012.02.004) [Search in Google Scholar](#)
- [22] K.Rajkumar, S.Aravindan: Tribol. Int.44 (2011) 347. [10.1016/j.triboint.2010.11.008](https://doi.org/10.1016/j.triboint.2010.11.008) [Search in Google Scholar](#)
- [23] S.Rathod, O.P.Modi, B.K.Prasad, A.Chrysanthou, D.Vallauri, V.P.Deshmukh, A.K.Shah: Mater. Sci. Eng. A502 (2009) 91. [10.1016/j.msea.2008.10.002](https://doi.org/10.1016/j.msea.2008.10.002) [Search in Google Scholar](#)

- [24] W.Xu, R.Hu, J.S.Li, H.Z.Fu: Trans. Nonferrous Met. Soc. China 21 (2011) 2237. [10.1016/S1003-6326\(11\)61001-7](https://doi.org/10.1016/S1003-6326(11)61001-7) [Search in Google Scholar](#)
- [25] Y.H.Liang, Q.Zhao, Z.H.Zhang, X.J.Li, L.Q.Ren: Int. J. Refract. Met. Hard Mater. 46 (2014) 71. [10.1016/j.ijrmhm.2014.05.017](https://doi.org/10.1016/j.ijrmhm.2014.05.017) [Search in Google Scholar](#)
- [26] X.Zhou, K.Q.Feng, S.F.Wei, R.Zhang, J.Xiong, H.Y.Fan: Int. J. Refract. Met. Hard Mater. 31 (2012) 109. [10.1016/j.ijrmhm.2011.09.013](https://doi.org/10.1016/j.ijrmhm.2011.09.013) [Search in Google Scholar](#)
- [27] K.Raza, F.A.Khalid: J. Alloys Compd. 615 (2014) 111. [10.1016/j.jallcom.2014.06.139](https://doi.org/10.1016/j.jallcom.2014.06.139) [Search in Google Scholar](#)
- [28] S.Oh, M.Kim, J.Choe, D.G.Lee: Compos. Struct. 147 (2016) 294. [10.1016/j.compstruct.2016.03.048](https://doi.org/10.1016/j.compstruct.2016.03.048) [Search in Google Scholar](#)
- [29] R.R.Jiang, X.F.Zhou, Q.L.Fang, Z.P.Liu: Mater. Sci. Eng. A 645 (2016) 124. [10.1016/j.msea.2015.12.039](https://doi.org/10.1016/j.msea.2015.12.039) [Search in Google Scholar](#)
- [30] F.Y.Chen, J.M.Ying, Y.F.Wang, S.Y.Du, Z.P.Liu, Q.Huang: Carbon 96 (2016) 836. [10.1016/j.carbon.2015.10.023](https://doi.org/10.1016/j.carbon.2015.10.023) [Search in Google Scholar](#)
- [31] J.Grzonka, M.J.Kruszewski, M.Rosiński, Ł.Ciupiński, A.Michalski, K.J.Kurzydłowski: Mater. Charact. 99 (2015) 188. [10.1016/j.matchar.2014.11.032](https://doi.org/10.1016/j.matchar.2014.11.032) [Search in Google Scholar](#)
- [32] Q.D.Qin, B.W.Huang, W.Li, F.Shao: J. Alloys Compd. 672 (2016) 590. [10.1016/j.jallcom.2016.02.174](https://doi.org/10.1016/j.jallcom.2016.02.174) [Search in Google Scholar](#)
- [33] A.K.Shukla, NirajNayan, S.V.S.N.Murty, S.C.Sharma, P.Chandran, S.R.Bakshi, K.M.George: Mater. Sci. Eng. A 560 (2013) 365. [10.1016/j.msea.2012.09.080](https://doi.org/10.1016/j.msea.2012.09.080) [Search in Google Scholar](#)
- [34] V.Rajkovic, D.Bozic, J.Stasic, H.W.Wang, M.T.Jovanovic: Powder Technol. 268 (2014) 392. [10.1016/j.powtec.2014.08.051](https://doi.org/10.1016/j.powtec.2014.08.051) [Search in Google Scholar](#)
- [35] D.D.Zhang, Z.J.Zhan: J. Alloys Compd. 654 (2016) 226. [10.1016/j.jallcom.2015.09.013](https://doi.org/10.1016/j.jallcom.2015.09.013) [Search in Google Scholar](#)
- [36] Q.Liu, X.He, S.Ren, C.Zhang, T.T.Liu, X.H.Qu: J. Alloys Compd. 587 (2014) 255. [10.1016/j.jallcom.2013.09.207](https://doi.org/10.1016/j.jallcom.2013.09.207) [Search in Google Scholar](#)
- [37] H.Bai, N.G.Ma, J.Lang, Y.Jin, C.X.Zhu, Y.Ma: Mater. Des. 46 (2013) 740. [10.1016/j.matdes.2012.09.053](https://doi.org/10.1016/j.matdes.2012.09.053) [Search in Google Scholar](#)
- [38] H.J.Yang, R.Y.Luo, S.Y.Han, M.D.Li: Wear 268 (2010) 1337. [10.1016/j.wear.2010.02.007](https://doi.org/10.1016/j.wear.2010.02.007) [Search in Google Scholar](#)
- [39] N.Nemati, R.Khosroshahi, M.Emamy, A.Zolriasatein: Mater. Des. 32 (2011) 3718. [10.1016/j.matdes.2011.03.056](https://doi.org/10.1016/j.matdes.2011.03.056) [Search in Google Scholar](#)
- [40] Y.H.Liang, Q.Zhao, Z.Han, Z.H.Zhang, X.J.Li, L.Q.Ren: Corros. Sci. 93 (2015) 283. [10.1016/j.corsci.2015.01.029](https://doi.org/10.1016/j.corsci.2015.01.029) [Search in Google Scholar](#)
- [41] V.Anandakrishnan, S.Baskaran, S.Sathish: Adv. Mater. Res. 651 (2013) 251. [10.4028/www.scientific.net/AMR.651.251](https://doi.org/10.4028/www.scientific.net/AMR.651.251) [Search in Google Scholar](#)

- [42] M.Ravichandran, V.S.Vidhya, V.Anandakrishnan: Mater. Sci.51 (2016) 589. [10.1007/s11003-016-9880-x](https://doi.org/10.1007/s11003-016-9880-x) [Search in Google Scholar](#)
- [43] S.Sivasankaran, K.Sivaprasad, R.Narayanasamy, V.K.Iyer: Powder Technol.201 (2010) 70. [10.1016/j.powtec.2010.03.013](https://doi.org/10.1016/j.powtec.2010.03.013) [Search in Google Scholar](#)
- [44] D.R.Kumar, R.Narayanasamy, C.Loganathan: Mater. Des.34 (2012) 120. [10.1016/j.matdes.2011.07.062](https://doi.org/10.1016/j.matdes.2011.07.062) [Search in Google Scholar](#)
- [45] S.Sivasankaran, R.Narayanasamy, T.Ramesh, M.Prabhakar: Comput. Mater. Sci.47 (2009) 46. [10.1016/j.commatsci.2009.06.013](https://doi.org/10.1016/j.commatsci.2009.06.013) [Search in Google Scholar](#)
- [46] T.Ramesh, M.Prabhakar, R.Narayanasamy: Int. J. Adv. Manuf. Technol.44 (2009) 389. [10.1007/s00170-008-1880-z](https://doi.org/10.1007/s00170-008-1880-z) [Search in Google Scholar](#)
- [47] R.Narayanasamy, T.Ramesh, K.S.Pandey: Mater. Sci. Eng. A391 (2005) 418. [10.1016/j.msea.2004.09.018](https://doi.org/10.1016/j.msea.2004.09.018) [Search in Google Scholar](#)
- [48] G.H.A.Bagheri: J. Alloys Compd.676 (2016) 120. [10.1016/j.jallcom.2016.03.085](https://doi.org/10.1016/j.jallcom.2016.03.085) [Search in Google Scholar](#)

Received: 2016-12-07

Accepted: 2017-03-31

Published Online: 2017-07-05

Published in Print: 2017-07-14

© 2017, Carl Hanser Verlag, München

Authenticate or login to

Download ↓

— or —

PDF **30,00 €**

Buy Article

From the journal



International Journal of Materials Research

Volume 108 Issue 7

Journal and Issue

Search journal



This issue All issues

Articles in the same Issue

[Contents](#)

[A modified parallel constitutive model for elevated temperature flow behavior of Ti-6Al-4V alloy based on multiple regression](#)

[Simulation of directional solidification furnace with bottom opening insulation to grow quality mc-Si ingot for PV applications](#)

[Dependence of corrosion properties of AISI 304L stainless steel on the austenite grain size](#)

[Tensile behavior and microstructural evolution for AZ31 magnesium alloys sheet at high strain rate](#)

[Equal-strength precision diffusion bonding of AA6063 aluminum alloy with the surface passivated by a self-assembled monolayer](#)

[Effect of grain size on hydration and rheological behavior of calcium aluminate cements containing spinel](#)

[Synthesis, characterization and forming behavior of hybrid copper matrix composites produced using powder metallurgy](#)

[Synthesis of binary bismuth–cadmium oxide nanorods with sensitive electrochemical sensing performance](#)

[Improving the productivity and purity of vaterite produced via a refined bubbling method](#)

[See more...](#)

Contact us

[Customer Service](#)
[Human Resources](#)
[Press](#)
[Contacts for authors](#)

Career

[How to join us](#)
[Current Vacancies](#)
[Working at De Gruyter](#)

Open Access

[Articles](#)
[Books](#)
[Funding & Support](#)

For Authors

[Publish your book](#)
[Publish your journal article](#)
[Abstracting & Indexing](#)

For Libraries & Trade Partners

[Electronic Journals](#)
[Ebooks](#)
[Databases & Online Reference](#)
[Metadata](#)

Our Partner Publishers

Rights & Permissions

[Repository Policy](#)
[Free Access Policy](#)

About De Gruyter

[De Gruyter Foundation](#)
[Our locations](#)

[Help/FAQ](#)
[Privacy Policy](#)
[Terms & Conditions](#)
[Legal Notice](#)

© Walter de Gruyter GmbH 2021



iJRASET

International Journal For Research in
Applied Science and Engineering Technology



INTERNATIONAL JOURNAL FOR RESEARCH

IN APPLIED SCIENCE & ENGINEERING TECHNOLOGY

Volume: 5 Issue: XII Month of publication: December 2017

DOI:

www.ijraset.com

Call:  08813907089

E-mail ID: ijraset@gmail.com

Design and Fabrication of Smart Stair Climbing and Stuff Delivering Robot

Chandra Mohan M¹

¹Assistant Professor, Department of Mechatronics Engineering, M.A.M School of Engineering, Trichy, India.¹

Abstract: People who work in office, school, colleges, industries etc. are often running from ground floor to all floors to deliver files or some other stuff. Due to this their works has been interrupt and disturbed. So we plan to design and fabricate a bot which climbs stairs and delivers the stuff. In this project we use microcontroller (Arduino) as a heart of bot, then wheels with belt driver unit to climb the stairs, which was controlled by high torque D.C motors unit. For path finding, we using wireless A.V camera which is an vision unit for robot and which will be controlled by computer using RF modules for serial communication between robot and computer. And the Transmitter (Tx) unit connected to computer will transmit the encode to Receiver unit (Rx) where decoded process takes place and makes the bot to move as per the received signal from computer. And for locating bot position, we used GPS module as an advantage. Thus via computer we could control the bot and delivers the stuff.

Keywords: Stair climbing, wireless camera, Arduino and RF unit.

I. INTRODUCTION

The main objective of this project is to deliver stuffs such as files, documents, e-components etc. from one place to another with the help of robot, controlling wirelessly via computer. This project describes the planning, design and implementation of a wirelessly controlled robot for material delivering from one location to another via laptop or computer. So that human work load and their tension at busy works may avoid. The main advantage of this bot is that it can climb any stairs and run smoothly on all surfaces which will easy to delivers things from any other place to anywhere else. We are replacing old bots with high range wireless communication via RF and wireless camera for vision system which makes the robot to do its task faster. There are many ways to climb stairs but to make the mechanical design simple and easier we adopt belt drive unit over the wheels which easily climbs on all stairs and surfaces. This model consists of high torqued.c motor unit where the motor is controlled by motor driver unit with Arduino uno.

For vision system wireless camera with large range has been mounted on front portion of the bot for clear vision which can be viewed in laptop or T.V. To a saw view in laptop, TV tuner card can be installed on laptop. This entire robot is user control interface so it can be easily operated by anyone else with some knowledge on s/w. The data are send via laptop through serial port on Arduino software. Bot can also be controlled by remote as per user wish. But for vision system we prefer it to control via laptop.

II. METHODOLOGY

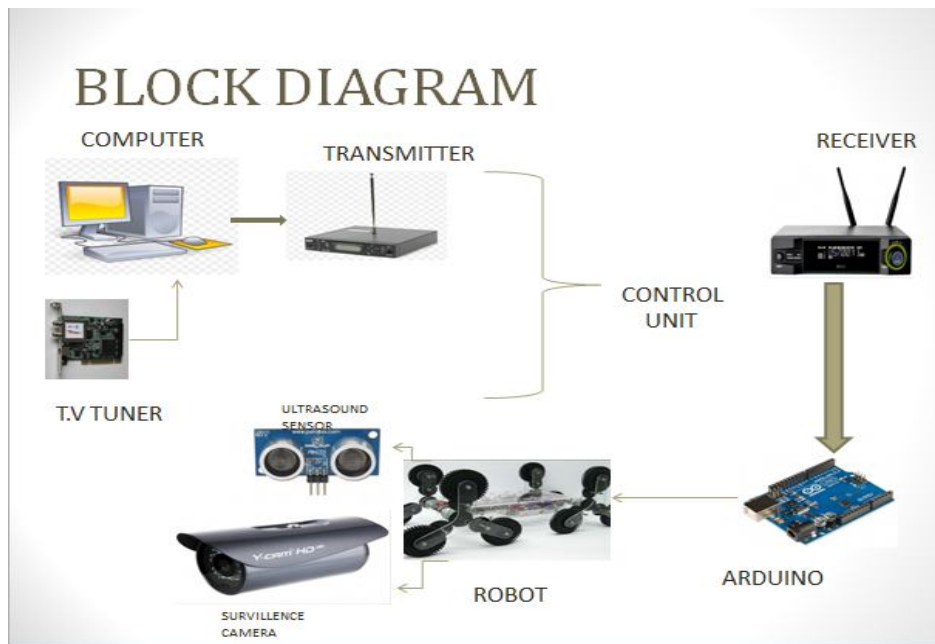
The vision system of the robot i.e. wireless a.v camera turn on, the power supply for the camera is supplied by 9v external power supply which will mount on front portion of the bot. Thus view will be displayed on laptop or t.v monitor so that path can be obtained to move the bot in desired direction to its destination place. Open Arduino ide s/w-> select ports->com 6 and then select board ->Arduino uno. Then open serial monitor for serial communication to send data. As the commands type in serial monitor, the required function will be transmitted over bot wirelessly via RF modules. The transmitter unit is connected to laptop via Arduino uno board, which send the encoded to receiver unit in robot. On receiver unit the received signals decoded and respond according to its function. The bot will move forward if the signal received from the transmitter is “f”, which will decode at receiver section. The vision system for robot is given by wireless a.v camera for path finding via laptop, Such that bot will move backward, right, left when signal received as

“b” – backward direction

“r” – right direction

“l” – left direction

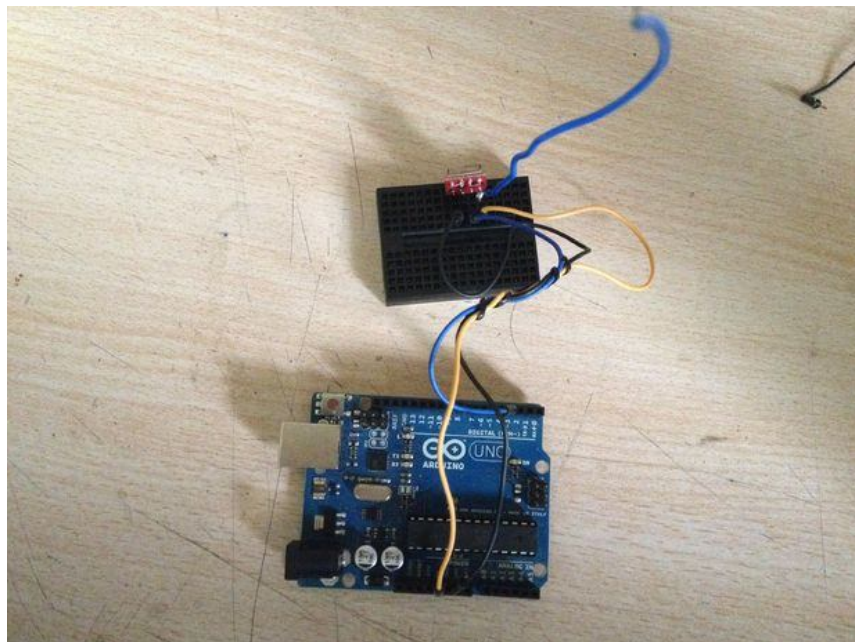
The robot will stop when the code is received as “s” and even if something went wrong during the operation. The belt drive mounted over wheel makes bot to climb stairs due to its robust gripness and high torque motor rotation continuously in which power is supplied by 12v external power supply. Due to this mechanism robot can sustain and run over on all surfaces and terrain.



(A).Project Working Diagram

III.ARDUINO CONNECTIONS

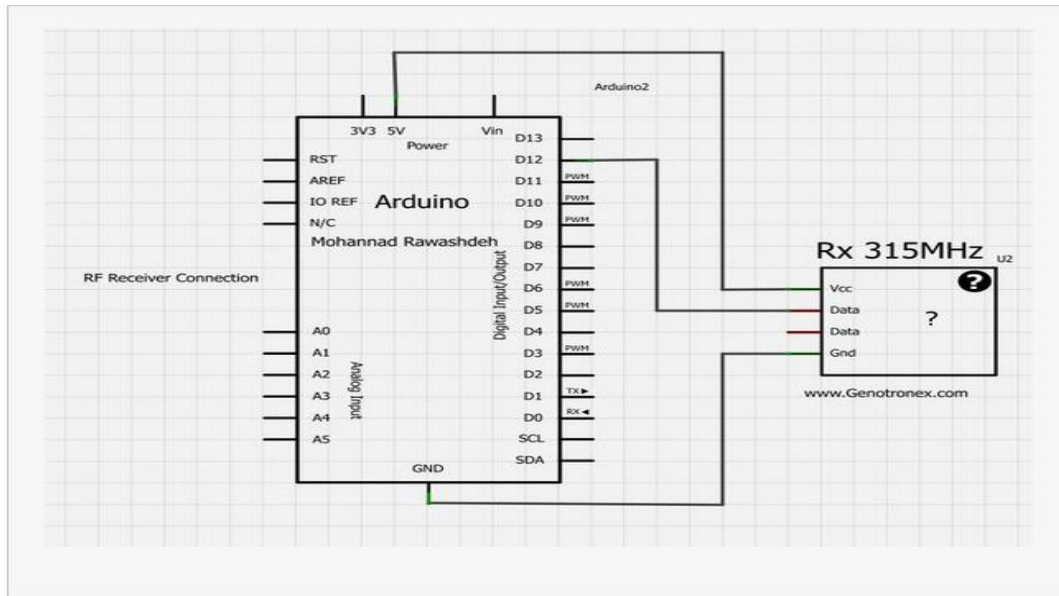
A. Transmitter Connection



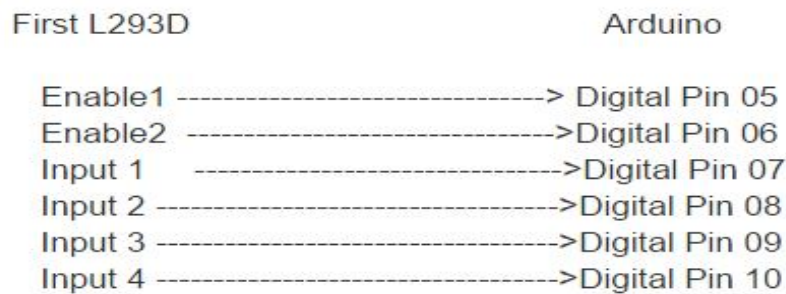
B. The transmitter is the smaller module having 4 pins:

- 1) Ant.....>Antenna
- 2) Vcc.....>power supply, in this case 5V from the Arduino at the Tx end.
- 3) Data>data pin, Transmits the data in bytes.
- 4) Gnd.....>ground pin, connected to Arduino ground.

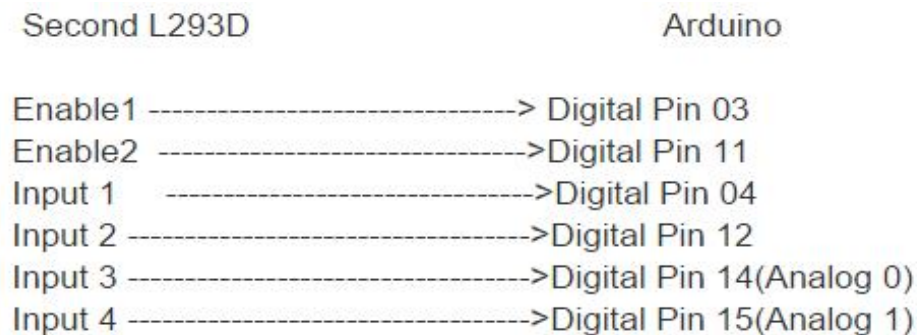
C. Receiver connection



D. First L293d Connection With Arduino



E. Second l293d connection with arduino



IV.CONCLUSION

The intention of the project is to develop a robot that can deliver the stuffs from one place to another so that the people who work in office, school, colleges, industries etc. can be free from their miscellaneous works and concentrate on their on-going work and to reduce the human work. The overall project was successful and it can be useful in many industries for material transferring. It can also be used as spy robot in defense field in borders.

In the future, user control option should be neglected. This can be done by taking the bot from smaller controllers to high level artificial intelligence sector [AI]. So that it can think itself and take decision of his own and act according to it without any human interface. Vision system of robot can be replaced by mat lab interface using image processing techniques to find the path as its own.

V. SNAPSHOTS



REFERENCES

- [1] Nan Li, Shugen Ma, "An Online Stair-Climbing Control Method for a Transformable Tracked Robot," Senior Member, IEEE, Bin Li, Minghui Wang, and Yuechao Wang, 2012.
- [2] P. Ben-Tzvi, S. Ito, and A. A. Goldenberg, "Autonomous stair climbing with reconfigurable tracked mobile robot," in Proc. IEEE Workshop Robot. Sens. Environ, 2007, pp.1–6.
- [3] Shatnawi, A. Abu-El-Haija, A. Elabdalla, "A Digital Receiver for Dual-Tone Multi frequency (DTMF) Signals", Technology Conference, Ottawa, CA, May1997.
- [4] <http://seminarprojects.com/Thread-mobile-controlledrobot-usingdtmf-technology>.
- [5] Basil Hamed, "Design and Implementation of Stair-Climbing Robot for Rescue Applications," in International Journal of Computer and Electrical Engineering, Vol. 3, No. 3, June 2011
- [6] Saleh Ahmad, Hongwei Zhang, and Guangjun Liu, Senior Member, IEEE "Multiple Working Mode Control of Door-Opening With a Mobile Modular and Reconfigurable Robot" IEEE/ASME TRANSACTIONS ON MECHATRONICS, 2012.
- [7] http://www.nxp.com/documents/data_sheet/LPC2141_42_44_46_48.pdf
- [8] Junke Li1, YujunWang2, TingWan3Department of C&IS, Southwest University, Chongqing, China "Design of AHexapod Robot".2008.
- [9] R. C. Luo, K. L. Su, "Amultiagentmulti sensor based realtime sensory control system for intelligent security robot"IEEE International Conference on Robotics and Automation, vol. 2, 2003,pp.2394 –2399.
- [10] Nicolai Dvinge, Ulrik P. Schultz, and David Christensen Maersk Institute University of Southern Denmark. "Roles and Self-Reconfigurable Robots"2010 IEEE.
- [11] Arduino Robotics by John David Warren
- [12] www.instructables.com/wireless-control-a-robot-with-arduino-using-rf-module.



10.22214/IJRASET



45.98



IMPACT FACTOR:
7.129



IMPACT FACTOR:
7.429



INTERNATIONAL JOURNAL FOR RESEARCH

IN APPLIED SCIENCE & ENGINEERING TECHNOLOGY

Call : 08813907089  (24*7 Support on Whatsapp)

M.A.M SCHOOL OF ENGINEERING

Siruganur, Tiruchirapalli – 621 105

(Accredited by NAAC)

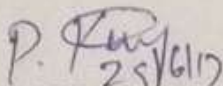
Department of Aeronautical Engineering

Academic Year: 2016-2017

Journal Details

Date: 29.06.2017

Sl.No	Name of the author/s	Department of the teacher	Name of journal	Year of publication	ISSN number
1	P.Kaviyarasu	Aeronautical	International Journal of Current and Innovative Research	2016	2395-5775
2	P.Kaviyarasu	Aeronautical	International Journal of Advanced and Innovative Research	2016	2278-7844
3	T.Uma sankari	Aeronautical	Imperial Journal of Interdisciplinary Research	2016	2454-1362
4	S.Anand	Aeronautical	International Journal of Advanced and Innovative Research	2016	2278-7844


25/6/17
HOD/AERO

Head of the Department
Aeronautical Engineering
M.A.M.School of Engineering
Siruganur, Trichy - 621 105


PRINCIPAL

PRINCIPAL
M.A.M. SCHOOL OF ENGINEERING
SIRUGANUR, Tiruchirapalli-621 105.

Emission control in modified KIRLOSKER TV-1 diesel engine by Aqua silencer

S.Maniamramasamy¹, P.Kaviyarasu¹, B.Ravish kumar², R.Ranjith kumar², M.Ramar²

1-Assistant Professor, MAM School of Engineering, Trichy, Tamil nadu,

2- UG Student, MAM School of Engineering, Trichy, Tamil nadu,

rksmaniam@gmail.com, aerokaviyarasu@gmail.com, ravish510@gmail.com

Abstract— In the modern world Diesel engines are playing a vital role in Road and sea transport, agriculture, mining and many other industries. Considering the available fuel resources and the present technological development, Diesel fuel is evidently indispensable. In general, the consumption of fuel is an index for finding out the economic strength of any country. This paper is an attempt to reduce the toxic content of diesel exhaust, before it is emitted to the atmosphere. This system Reduction of obnoxious Exhaust particulates The principle involved is by bubbling the exhaust gas through the scrubber tank containing an alkaline solution, here the temperature of the gases are reduced, while most of the oxides of nitrogen in the exhaust are rendered non-toxic. The highly dangerous carbon monoxide is not such a menace in diesel exhaust, as it does not exceed 0.2 percent by volume, where as in petrol engines the CO content may be as high as 10 %. A lime stone container in the scrubber tank reduces the considerable percentage of sulphur – di – oxide presents in the exhaust. The provision of suitable baffles in the scrubber tank aids the turbulence so that, thorough scrubbing takes place. The bell – mouth solution, while reducing the back pressure.

Keywords: alkaline solution, aqua silencer, Emission control, scrubber tank etc...

I. INTRODUCTION

The exhaust gas contains carbon – di – oxide, sulphur – di – oxide, carbon monoxide and other oxides of nitrogen. At full load, the temperature of the exhaust gas will lie anywhere between 500°C to 700°C. The pressure of the exhaust gas depend upon so many factors viz.,

1. The design of exhaust gas manifold
2. Magnitude of valve overlap
3. Engine speed
4. Number of cylinders
5. The length of the exhaust gas flow path, etc,

The design of exhaust gas manifold is very important in case of high speed diesel engines. In order to maintain the exhaust gas pressure within required limits, the exhaust gas manifold is designed so that, the gases which come out of the cylinder flows very smoothly, before it is let out to the atmosphere.

II. CONSTRUCTIONAL FEATURES

A. Outlet Pipe From the Engine (or) Inlet to the Scrubber Tank

The outlet pipe from the engine was connected to the scrubber tank. The nominal bore of the pipe is 50mm, which is also the

inlet diameter of the scrubber tank. The shape and length of the pipe is decided according to the space availability to keep the flow resistance to a minimum.

B. Scrubber – Tank Assembly

The scrubber tank is fabricated in three stages and it contains the following sub assemblies.

1. Tank.
2. Bell – Mouth.
3. Lime stone container
4. Level plug – Drain Assembly.

C. Tank Fabrication

The tank is made of standard steel plates of 3mm thickness of quality structural steel conforming to BIS: 226, Designation ST 42S. The tank is fabricated using Electric Arc Welding process to withstand a maximum pressure of 0.8N/mm^2 [8Kg/Cm^2], with leak – proof.

Design considerations: The tank is 5 liters capacity keeping in view the size of Bell-mouth and lime stone container, which are to be accommodated inside. The maximum water content of the tank is about 3 liters, corresponding to 115mm of water level from the bottom of the scrubber tank. Suitable baffles are provided which will encourage through scrubbing of the exhaust gas. The baffles also prevent entry of water into the stone container to a considerable extent.

D. Bell – Mouth Fabrication

The bell – mouth is made of standard steel plates of 3mm thickness of quality structural steel conforming to BIS: 226, Designation ST 42S.

E. Level Plug cum Drain

Fabrication: The level plug cum drain is fabricated using 12.7mm nominal bore pipes fittings and conforming to BIS: 1369 where, fabricated using electric arc welding. The surface is rough ground in order to have better finish.

Design consideration: The level plug is designed to maintain a level of 115mm inside the tank. Instead of providing a separate drain plug, a tee welded at the bottom of the level pipe to accommodate the drain plug. The whole assembly can be unscrewed and taken out of the tank for periodic maintenance and repair by unscrewing the thread, which is fastening it to the boss, which is welded to the bottom of the tank. Water level indicator is fixed in the tee joint, which shows the level of water in the scrubber tank. During the

evaporation period this will be useful to maintain the level of water.

F. Outlet Pipe from the Scrubber Tank

The outlet pipe from the scrubber tank is fabricated using standard medium duty pipes, which are conforming to BIS 1369. The nominal bore of the pipe is 60mm, which is also the diameter of the inlet pipe. The flange at the end is to suit the flange on the outlet of the lime stone container. The shape and length of the pipe are to keep the flow resistance to a minimum.

III. WORKING PRINCIPLE

The problems that arise from the Diesel utilization in inflammable environment may be listed as follows:

1. Gases and particulate in engine emission
2. Heat and Humidity
3. Risk of explosion and fires
4. Transportation and storage of fuel
5. High speed in long hauls
6. Risk of trackless vehicles entering inadequately ventilated areas
7. Noise

This section examines the first two of these problems and suggests means by which they may be reduced or overcome.

A. Gases and Particulates in Diesel Exhaust

In addition to heat and water vapor, the pollutants in diesel exhaust are,

- a) Carbon monoxide (CO)
- b) Carbon dioxide (CO₂)
- c) Oxides of Nitrogen (NO_x)
- d) Sulphur dioxide (SO₂)
- e) Particulate and Unburned Hydrocarbons (UBHC)
- f) Respirable Combustible Dust (RCD)

The above polluting contents in the diesel engine exhaust are to be controlled by the scrubbing method, details of which are followed.

B. Expansion and Scrubbing

The high temperature high pollutant exhaust gas is allowed to pass through the bell – mouth assembly of the scrubber in the first phase. The bell – mouth at the inlet/outlet is approximately 2 ½ times more in an area is that of the inlet. This allows the exhaust gas to expand considerably. This expansion allows the gas to cool, because the temperature is a function of pressure. This considerable reduction of backpressure allows for the additional involved due to the introduction of water and lime stone container. The venture effect of the bell – mouth is minimized because the exhaust gas escapes out of the bell – mouth randomly along the periphery. After expansion, the emission comes in contact with water; (which could be otherwise being any alkaline solution) where the obnoxious products of combustion are scrubbed when bubbled through it. The bell – mouth also allows for more contact area with water, so that effective cooling takes place within the short span of time available for the gas to pass through the water. The length of bubbling can be increased by the water level in the scrubber tank, as shown in fig.1.

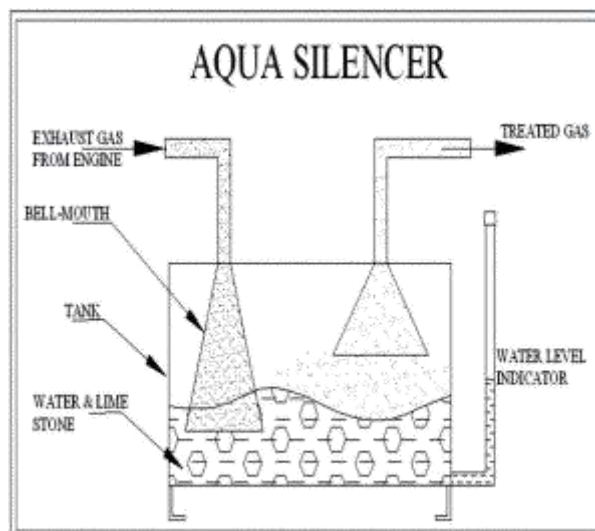


Fig.1. Aqua silencer



Fig.2. Fabricated Aqua silencer

But this will be increased result in an abnormal backpressure, which inadvertently affect the performance of the engine. And for this reason the bell – mouth is a multipurpose component, to allow for reduction in back pressure, and provides for an increased contact area with the scrubbing agent. After bubbling through the water, it comes in contact with baffles, which encourage turbulence of the exhaust gas within and below the water surface without unduly increasing the back pressure of the exhaust. This allows for the thorough scrubbing of the emission, so that more obnoxious product is absorbed in the allowed time. As our fabricated aqua silencer shown in Fig.2. The baffles are of invaluable help to reduce the carryover of water particles which are converted into steam, which otherwise will escape out of the system. A lime stone container, which is provided above the baffles, allows the exhaust emission to pass through limestone radically. Now due to high temperature of the exhaust gas and the high chemical reaction prone lime stone, the products of combustion to go through a series of chemical reactions. The chemical reactions in their different phases are explained later in this topic. The extent of scrubbing can be analyzed by using an ORSAT apparatus very easily. The procedure and results are explained in the subsequent chapter. The area at any particular and results are explained in the subsequent topics.

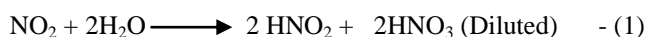
The area at any particular section in the whole system is more than the outlet of exhaust manifold of the engine, which contributes to the reduction of backpressure of the system as a whole.

IV. DETAILS OF CHEMICAL REACTIONS

In the scrubber tank water is used as a alkaline solution mainly to dissolve the Unburned Hydro Carbons (UBHC). By this method, the UBHC, even if it is in glowing conditions, it is dissolved in water; thereby it is suppressing a spark which could escape from the engine to the inflammable environment.

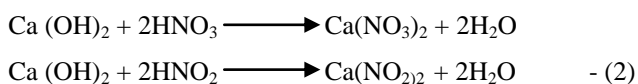
A. Chemical Reaction-I

The obnoxious product of combustion is NO_x – the oxides of Nitrogen. Water will absorb the oxides of Nitrogen to a larger extent. The following chemical reaction will enhance the proof, for the above statement.



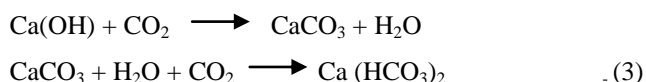
B. Chemical Reaction-II

If a small amount of limewater is added to scrubber tank, further reaction takes place as below.



C. Chemical Reaction-III

When the carbon-di-oxide present in the exhaust gas comes in contact with the limewater, calcium carbonate will precipitate. The calcium carbonate when further exposed to carbon-di-oxide, calcium-bi-carbonate will be precipitated. The following is the chemical reaction,



D. Chemical Reaction-IV

The sulphur-di-oxide present in the Diesel Exhaust also reacts with the limewater. But the small trace of sulphur-di-oxide makes it little difficult to measure the magnitude of the chemical reaction, accurately. The following equation gives the chemical reaction and calcium sulphite will precipitate.



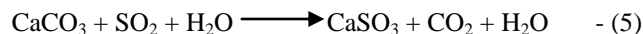
Because CO is chemically balanced and stable, it will not readily react with water or with any by – products, which is resulted from the above reactions. Also the negligible volume (0.2%) of CO present in the Diesel emission is not such a menace, when compared to the petrol engine exhaust which as high as 10% of CO.

Even though, the limewater absorbs a part of the oxides of Nitrogen, carbon-di-oxide, the time limitation for the reaction take place allows a considerable percentage to escape. But, the stone container, which is provided with limestone or calcium carbonate, (CaCO₃), encourages further chemical reaction, in the presence of steam, which evaporates from the scrubber tank due to the high exhaust temperature (400°C -

700° C). The following are the chemical reactions for the oxides of Nitrogen (NO_x) Carbon-di-oxide (CO₂) and Sulphur-di-oxide (SO₂).

E. Chemical reaction-V

From calcium carbonate, calcium sulphite will precipitate and CO₂ will be by-product. Because of the small percentage and SO₂ presence, the liberation of Carbon dioxide is very less. But the liberated CO₂ will again combine with CaCO₃ to form calcium bicarbonate as mentioned in equation 5.



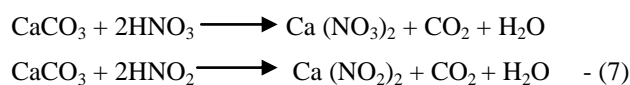
F. Chemical reaction-VI

The presence of steam makes it possible to have a preliminary reaction with oxides of nitrogen, in the following manner;



G. Chemical reaction-VII

The resultant products when come in contact with calcium carbonate the following reaction takes place



[i.e.,] calcium Nitrate Ca (NO₃)₂ and calcium Nitrite Ca(NO₂)₂ are the by products, and CO₂ is liberated. The liberated CO₂ again combines with calcium carbonate to form calcium bicarbonate

H. Analysis of Exhaust Emission

Emissions from diesel engines can be classified in same categories as those from the gasoline engines but the level of emission in these categories varies considerably. A sample of diesel exhaust may be free from smoke, odorless, and have no unburned hydrocarbons (UBHC) or it may be heavily smoke laden, highly mal-odorous and can have heavy concentration of UBHC.

It shows the approximately the possible variations in concentration of different constituents of diesel exhaust. The concentration is deceptively low in diesel engines, as compared to petrol engines. However, as the specific air consumption in diesel engines is always high due to excess air, the total amount of pollutants is nearly same in diesel and petrol engine exhaust. Hence, diesel exhaust emissions are as great concern as of petrol engines. Engine type and the mode of operation are two main factors, which influence the exhaust emissions from a diesel engine.

Table.1. Range of concentration of different constituents of Diesel Exhaust

S.No	Constituent	Min.	Max.
1.	Hydrocarbon,(HC)	A few ppm	1000 ppm
2.	NO _x	100ppm	2000 ppm
3.	RCD	few	100 ppm
4.	CO	zero	2 percent

Table.2. Emission levels of 4 – stroke normally aspirated engine at medium speed & high speed

S.No	Emission	Medium Speed	High Speed
1.	Hydrocarbon	Low	High
2.	NOx	Low	Low
3.	RCD	Low	High
4.	SMOKE	High	High

Effect of mode of operation on diesel exhaust idle, full load at rated speed, and acceleration at full rack are the three modes of operation which have been found to significantly affect the emission levels in diesel exhaust as can be seen.

During the idle mode the concentration of HC, NOx and aldehyde emissions are lower than other modes the emissions at idle are less significant than during any other mode. The acceleration mode has profound influence on odor. Highest odor occurred when full rack acceleration was encountered. Smoke levels are also high during acceleration emissions at full load relative to emissions at other operational modes very significantly with engine type. Four – stroke normally aspirated engines smoke very much at rated full load.

V. RESULTS AND DISCUSSIONS

KIRLOSKER TV 1 diesel engine has been selected to test the aqua silencer for controlling sound and emission from engine exhaust. At first, impure and non-treated exhaust from the engine was tested in the AVI apparatus.

Then, the treated exhaust gas coming through the scrubber tank was tested in the AVI apparatus. The AVI apparatus observations of before and after treatment of exhaust gases are shown in the following two separate observation tables.

The results obtained from the observations are given in percentage reduction of gases. The variation in the percentage gives amount of pollutants control by this paper.

SPECIFICATIONS: Scrubber Tank

- Alkaline solution -Lime Water (Ca (OH)₂)
- Water level from bottom - 100mm
- Chemical -Lime stone (CaCO₃)

Bell mouth bottom portion

- Submerged in the alkaline solution - 25mm

Engine Details

- Engine - KIRLOSKER TV 1
- Type - vertical 4 stroke
- No. of cylinder - One
- Cylinder Dia. - 0.0875mm
- Stroke - 0.11 mm
- Speed - 1500 rpm
- Power - 5.2 kW

Table.3. Result Tabulation

% of load Applying	NOx (ppm)		Amount of PM (g/min)		Smoke Density (HSU)	
	With out AQUA Silencer	With AQUA Silencer	With out AQUA Silencer	With AQUA Silencer	With out AQUA Silencer	With AQUA Silencer
0	65.93	38.82	0.010	0.003	7.2	2.35
24.57	175.76	112.60	0.012	0.008	15.15	5.25
49.13	295.20	223.45	0.016	0.010	16.65	7.3
73.71	406.88	311.90	0.022	0.014	22.9	8.6
100	618.70	433.68	0.026	0.019	26.85	15.55

Table.4. Tabulation for Percentage of Reduction

% of load Applying	% of NOx Reduction		Amount of PM		Smoke Density	
	ppm	%	g/min	%	HSU	%
0	27.11	41.11	0.007	70	4.85	67.36
24.57	63.16	35.93	0.004	33.33	9.9	65.34
49.13	71.75	24.30	0.006	37.5	9.35	56.15
73.71	94.98	23.34	0.008	36.36	14.3	62.4
100	185.02	29.90	0.007	26.92	11.3	42.8

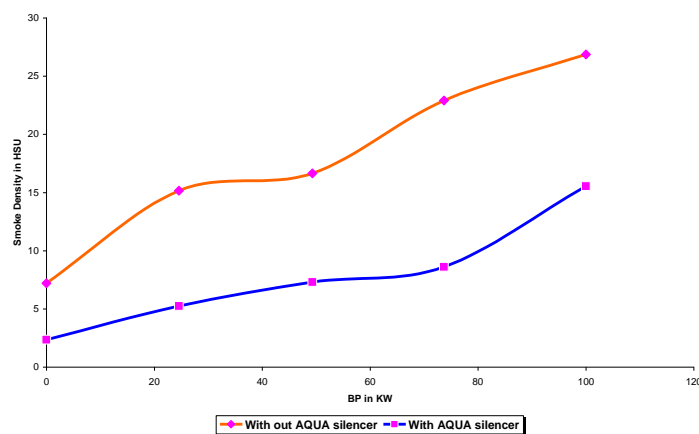


Fig .3. BP Vs Smoke Density

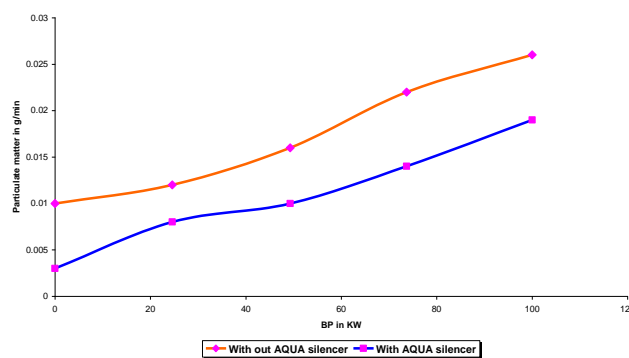


Fig.4. BP Vs Particulate Matter

VI. CONCLUSION

The aqua silencer is more effective in the reduction of emission gases from the engine exhaust gas using perforated tube. By using perforated tube the back Pressure. Will remain constant and the sound level is reduced. Using the perforated tube the fuel consumption remains same as conventional system. By using water as a medium the sound can be lowered and also by using activated charcoal in water. We can control the exhaust emission to a greater level. The water contamination is found to be negligible in aqua silencer, because the amount of acidity level in aqua silencer is expected to be below the dangerous acidity. i.e. 250mg/lit. It is smokeless and pollution free emission and also very cheap. The aqua silencer’s performance is almost equivalent to the conventional silencer. In No load condition, by using AQUA Silencer the NOx will be reduced to 29.9%, the Particulate Matter will be reduced to 70%. In the Smoke Density will be reduced to 67.36%.

REFERENCES

[1] HsiehaWD, ChenRH, WuTL, LinTH .Engine performance and pollutant emission of an SI engine using ethanol–gasoline blended fuels. Atmos Environment (2002) ; Vol-36, pp 403–410.
 [2] C. A. Okoronkwo , C. C. Dr. Nwachukwu, L.C. Dr. Ngozi and J.O. Igbokwe, "The Effect of Electromagnetic Flux Density on the Ionization and the Combustion of Fuel (An Economy Design Project)" American Journal of Scientific and Industrial Research, ISSN: 2153-649X doi:10.5251/ajsir. (2010).Vol 1, Issue 3, pp 527-531.
 [3] P. Govindasamy, S. Dhandapani, "Experimental Investigation of the Effect of MagnetiC Flux to Reduce Emissions and Improve Combustion Performance in a Two Stroke, Catalytic-Coated Spark-Ignition Engine" International Journal of Automotive Technology, (2007) Vol. 8, No. 5, , pp. 533-542
 [4] RezanianA, Rosendahl LA. Thermal effect of a thermo electric generator on parallel micro channel heat sink Energy (2012) Vol-3, Issue 7, pp 220–227.
 [5] Martinez JG, VianD, AstrainA, Rodriguez Berriol. “Optimization of the heat exchangers electric generation system”, Journal of Electron Mater (2010) Vol-39 , pp 1463–1468.

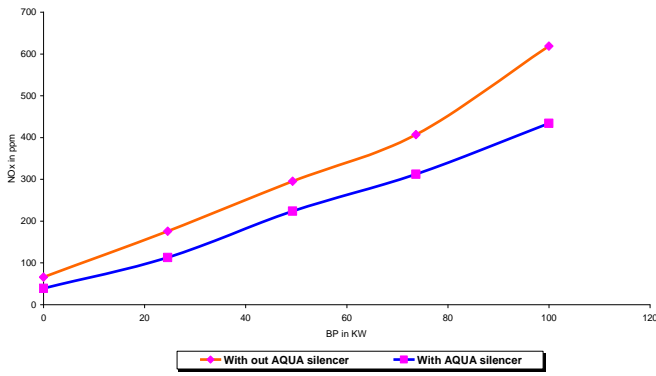


Fig.5. BP Vs NOx

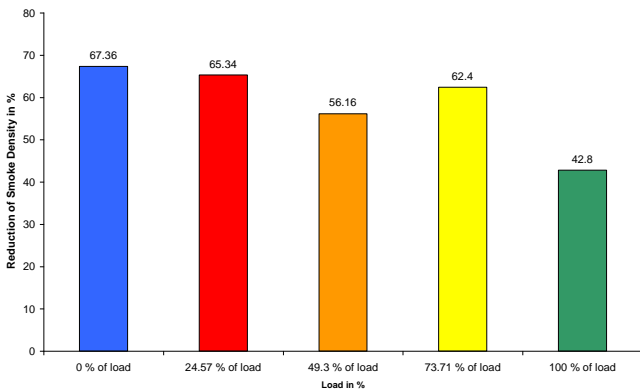


Fig.6. Load Vs Reduction of Smoke Density

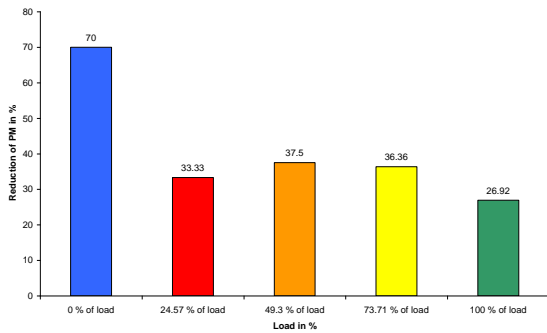


Fig.7. Load Vs Reduction of Particulate Matter

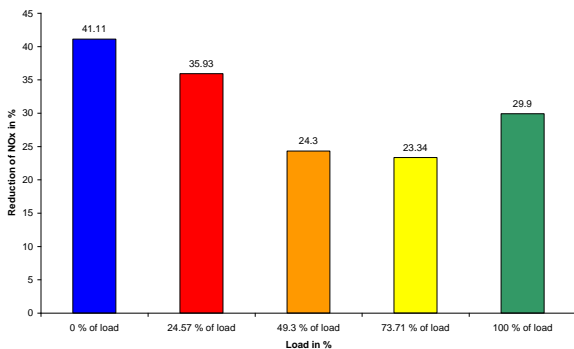


Fig.8. Load Vs Reduction of NOx

Effect of Geometric Twist on Wind Turbine Blade

S.Sharmila a S.Anand b.

Assistant Professor

M.A.M School Of Engineering,Trichy, India.

Sharmilasharmi047@gmail.com

Abstract: Increasing need for fundamental research in rotor aerodynamics and practical aspects, constraints were imposed on the design. An important part of this work is to conduct a study of the design trade-offs to determine the effect of the geometric twist on the wind turbine and its energy capture of the rotor. Another objective was to determine the necessary modifications to the blade geometry and twist in aerofoil for a three-bladed rotor configuration. This project aims to describe the approach and process used to design a tapered/twisted blade, and to provide performance predictions for the conventional wind turbine blade and the updated model with geometric twist. The aerodynamic performance of the blade with and without geometric twist is analysed by using Computational Fluid Dynamics and to increase the lift of the blade and to prevent over speed of the rotor. Additionally, twisted blades tested for its stall delaying characteristics.

Keywords—twisted blade, tapered, stall, CFD, oscillation and over pressure.

I. INTRODUCTION

The Wind it might seem obvious, but an understanding of the wind is fundamental to wind turbine design. The power available from the wind varies as the cube of the wind speed, so twice the wind speed means eight times the power. This is why sites have to be selected carefully: below about 5m/s (10mph) wind speed there is not sufficient power in the wind to be useful. Conversely, strong gusts provide extremely high levels of power, but it is not economically viable to build machines to be able to make the most of the power peaks as their capacity would be wasted most of the time. So the ideal is a site with steady winds and a machine that is able to make the most of the lighter winds whilst surviving the strongest gusts. As well as varying day-to-day, the wind varies every second due to turbulence caused by land features, thermals and weather. It also blows more strongly higher above the ground than closer to it, due to surface friction. All these effects lead to varying loads on the blades of a turbine as they rotate, and mean that the aerodynamic and structural design needs to cope with conditions that are rarely optimal. By extracting power, the turbine itself has an effect on the wind; downwind of the turbine the air moves more slowly than upwind. The wind starts to slow down even before it reaches the blades, reducing the wind speed through the “disc” (the imaginary circle formed by the blade tips, also called the swept area) and hence reducing the available power. Some of the wind that was heading for the disc diverts around the slower-moving air and misses the blades entirely. So there is an optimum amount of power to extract from a given disc diameter: try to take too much and the wind will slow down too much, reducing the available power. In fact the ideal is to

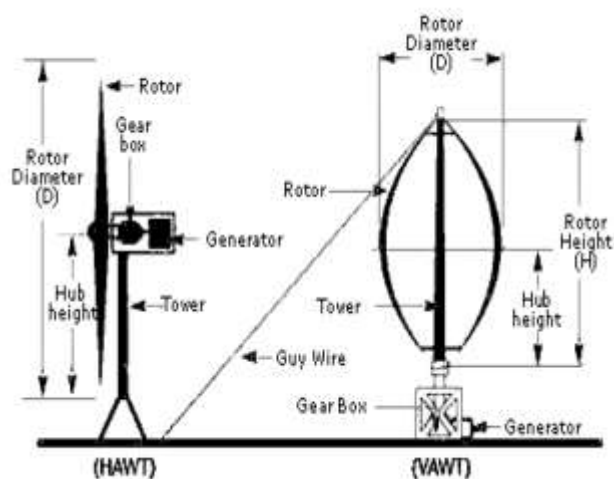
reduce the wind speed by about two thirds downwind of the turbine, though even then the wind just before the turbine will have lost about a third of its speed. This allows a theoretical maximum of 59% of the wind’s power to be captured (this is called Betz’s limit). In practice only 40-50% is achieved by current designs.

1.5 WIND TURBINE TYPE

The horizontal wind turbine is a turbine in which the axis of the rotor’s rotation is parallel to the wind stream and the ground. Most HAWTs today are two- or three-bladed, though some may have fewer or more blades. There are two kinds of Horizontal Axis Wind Turbines: the upwind wind turbine and the downwind wind turbine. The HAWT works when the wind passes over both surfaces of the airfoil shaped blade but passes more rapidly at the upper side of the blade, thus, creating a lower-pressure area above the airfoil. The difference in the pressures of the top and bottom surfaces results in an aerodynamic lift. The blades of the wind turbine are constrained to move in a plane with a hub at its center, thus, the lift force causes rotation about the hub. In addition to the lifting force, the drag force which is perpendicular to the lift force impedes rotor rotation.

1.8 COMPONENT OF A WIND TURBINE

Wind turbine usually has six main components the rotor, the generator, the gear box, the control and protection system, the tower and the foundation. This main component can be seen in figure.



1.8.1 Rotor: the rotor is an elegant aero foil shaped blade which takes the wind and aerodynamically converts its kinetic energy into mechanical energy through a connected shaft.

1.8.2 Generator: the generator is a device that produces electricity when mechanical work is given to the system. Control and protection system: the protection system is like a safety feature that makes sure that the turbine will not be working under dangerous condition. This includes a break system triggered by the signal of higher wind speeds to stop the rotor from movement under excessive wind gusts.

1.8.3 Gear box: Gear box used in wind energy systems to change low speed high torque power coming from a rotor blade to high speed low torque power which is used for generator. It is connected in between main shaft and generator shaft to increase rotational speeds from about 30 to 60 rotations per minute (rpm) to about 1000 to 1800 rpm. Gearboxes used for wind turbine are made from superior quality aluminum alloys, stainless steel, cast iron etc.

1.8.4 Nacelle: A housing which contains all the components which is essential to operate the turbine efficiently is called a nacelle. It is fitted at the top of a tower and includes the gear box, low- and high-speed shafts, generator, controller, and brakes. A wind speed anemometer and a wind vane are mounted on the nacelle.

1.8.5 Tower: the tower is the main shaft that connects the rotor to the foundation. It also raises the rotor high in the air where we can find stronger winds. With horizontal axis wind turbines, the tower houses the stair to allow for maintenance and inspection.

1.8.6 Foundation: The foundation or the base supports the entire wind turbine and make sure that it is well fixed onto the ground or the roof for small household wind turbine. This is usually consisting of a solid concrete assembly around the tower to maintain its structural integrity.

III INTRODUCTION TO CFD

CFD provides numerical approximation to the equations that govern fluid motion. Application of the CFD to analyze a fluid problem requires the following steps. First, the mathematical equations describing the fluid flow are written. These are usually a set of partial differential equations. These equations are then discretized to produce a numerical analogue of the equations. The domain is then divided into small grids or elements. All CFD codes contain three main elements: (1) a pre-processor, which is used to input the problem geometry, generate the grid, and define the flow parameter and the boundary conditions to the code. (2) A flow solver, which is used to solve the governing equations of the flow subject to the conditions provided. There are four different methods used as a flow solver: (i) finite difference method; (ii) finite element method, (iii) finite volume method, and (iv) Spectral method. (3)

A post-processor, which is used to massage the data and show the results in graphical and easy to read format.

Due to the nonlinear behavior of the Navier-Stokes equations, solving a whole 3D turbulent flow model of a wind turbine rotor with finest details in a time dependent way is extremely

difficult based on methods such as direct numerical simulation (DNS). Other options like large eddy simulation (LES) and detached eddy simulation (DES) methods are also applied in wind turbine aerodynamics by some researchers. However, to be computationally cost-efficient, RANS equations are most widely used to model the change of flow domain caused by turbulence around wind turbine blades. To obtain a reasonable accurate solution for wind turbine aerodynamics, three key elements are involved:

- (1) A good mesh quality.
- (2) An advanced turbulence model.
- (3) An accurate solve scheme.

4.3 GEOMETRY AND MESH

To model a wind turbine rotor using the CFD method, an exact 3D geometry of the wind turbine rotor is needed in a digitized format, usually in a "computer aided design" (CAD) format. A small wind turbine blade is generally twisted and tapered. The sectional airfoil of the blade is a shape often with a small rounded leading edge, and a sharp trailing edge or thin blunt trailing edge. A sufficient resolution of the boundary layer mesh is needed to solve the boundary layer around the blade surfaces. To secure an accurate solution in the boundary flow, the dimensionless cell wall distance Y^+ should be below or at least approximated to 1. Additionally, a large-enough flow domain is needed to avoid disturbances from the domain boundary surfaces, and a fine enough time step is preferable to generate a good result. However, a good match between mesh refinement, mesh quality, domain size and time step refinement is very important to produce a quality result, i.e. accurate solution and reasonable computation cost.

4.4 TURBULENCE AND TRANSITION

To explore the flow field near rotating wind turbine blades, there are several turbulence models presented with good results for wind turbine airfoil and rotor aerodynamics analysis: Spalart-Allmaras (S-A) model, standard k-epsilon ($k-\epsilon$) model, k-omega ($k-\omega$) model, Shear Stress Transport (SST) $k-\omega$ model, and transition SST model. The details of these models can be found. In Villalpando's research, it was reported that, the SST $k-\omega$ model has a better agreement with experimental results than other turbulence models such as the S-A model, the $k-\epsilon$ model and the Reynolds Stress Model (RSM).

However, when stall occurs, the conclusion was drawn that the transition location is crucial for the simulation and the Menter's SST transition model was claimed to have better agreement with experiment results than other models. In the transition SST model, the transition equations (i.e. one is for the intermittency γ and the other is for the transition momentum thickness Reynolds number $Re\theta^*$) interact with the SST $k-\omega$ turbulence model. Due to two additional transport equations involved, it is apparent that the transition model is more time-consuming and more sensitive to converge than the SST $k-\omega$ model. Some research works aimed to find a middle way. Catalano performed a RANS analysis using the SST $k-\omega$

model with an imposed transition location which is 10% offset downstream from the predicted point of a fully turbulence model. However, the offset is based on experience in this approach. Instead of using imposed variables to catch the transition phenomenon like turbulence models and without imposing transition location, the transition SST model was reported to have a promising accuracy in predicting transition flows. Many research works have been done regarding to the transition model. The Menter's transition model was investigated on the 2D S809 airfoil and better agreements have been achieved for angle of attack from 0° to 9° , and it was indicated that the difference at high angle of attacks was more possibly caused by the 3D flow effects which 2D simulation model cannot capture. A full 3D wind turbine rotor which uses the S809 airfoil were accomplished in Langtry's research, the transition model was reported to be compatible with modern CFD techniques such as unstructured grids and massively parallel execution, and the transition model was claimed to be well suited to predict wind turbine rotor aerodynamics.

IV DERIVATION OF RANS EQUATION

Applying the fundamental laws of mechanics to a fluid gives the governing equations for a fluid. The conservation of mass equation is

$$\frac{\partial \rho}{\partial t} + \nabla \cdot (\rho \vec{V}) = 0$$

Momentum equation,

$$\rho \frac{\partial \vec{V}}{\partial t} + \rho (\vec{V} \cdot \nabla) \vec{V} = -\nabla p + \rho \vec{g} + \nabla \cdot \tau_{ij}$$

The equations governing the fluid motion are the three fundamental principles of mass, momentum, and energy conservation.

$$\text{Continuity} \quad \frac{\partial \rho}{\partial t} + \nabla \cdot (\rho \vec{V}) = 0$$

$$\text{Momentum} \quad \rho \frac{D\vec{V}}{Dt} = \nabla \cdot \tau_{ij} - \nabla p + \rho \vec{F}$$

$$\text{Energy} \quad \rho \frac{De}{Dt} + p(\nabla \cdot \vec{V}) = \frac{\partial Q}{\partial t} - \nabla \cdot \mathbf{q} + \Phi$$

4.7.1 Elliptic:

Laplace equation is a familiar example of an elliptic type equation.

$$\nabla^2 u = 0$$

Where u is the fluid velocity. The incompressible irrotational flow (potential flow) of a fluid is represented by this type of equation. Another practical example of this equation is the steady state pure heat conduction in a solid, i.e., $\nabla^2 T = 0$, as can be readily obtained from equation.

4.7.2 Hyperbolic:

Qualitative properties of hyperbolic equations can be explained by a wave equation.

$$\frac{\partial^2 u}{\partial t^2} = c^2 \frac{\partial^2 u}{\partial x^2}$$

Where c is the wave speed. In this case, values of solution depend locally on the initial conditions. The propagation signal speed is finite. Continuous boundary and initial values can give rise to discontinuity. Solution is no more continuous and therefore shocks can be observed and captured in this class of equations. Depending on the flow, the governing equations of fluid motion can exhibit all three classifications.

4.8 BOUNDARY CONDITIONS:

The governing equation of fluid motion may result in a solution when the boundary conditions and the initial conditions are specified. The form of the boundary conditions that is required by any partial differential equation depends on the equation itself and the way that it has been discretized. Common boundary conditions are classified either in terms of the numerical values that have to be set or in terms of the physical type of the boundary condition.

For steady state problems there are three types of spatial boundary conditions that can be specified

Dirichlet boundary condition

$$\phi = f_1(x, y, z)$$

$$\frac{\partial \phi}{\partial n} = f_2(x, y, z)$$

Neuman boundary condition:

Mixed type boundary condition:

The physical boundary conditions that are commonly observed in the fluid problems are as follows

$$a\phi + b \frac{\partial \phi}{\partial n} = f_3(x, y, z)$$

4.8.1 Solid walls: Many boundaries within a fluid flow domain will be solid walls, and these can be either stationary or moving walls. If the flow is laminar then the velocity components can be set to be the velocity of the wall. When the flow is turbulent, however, the situation is more complex.

4.8.2 Inlets: At an inlet, fluid enters the domain and, therefore, its fluid velocity or pressure, or the mass flow rate may be known. Also, the fluid may have certain characteristics, such as the turbulence characterizes which needs to be specified.

4.8.3 Symmetry boundaries: When the flow is symmetrical about some plane there is no flow through the boundary and the derivatives of the variables normal to the boundary are zero.

4.8.4 Cyclic or periodic boundaries: These boundaries come in pairs and are used to specify that the flow has the same

values of the variables at equivalent positions on both of the boundaries.

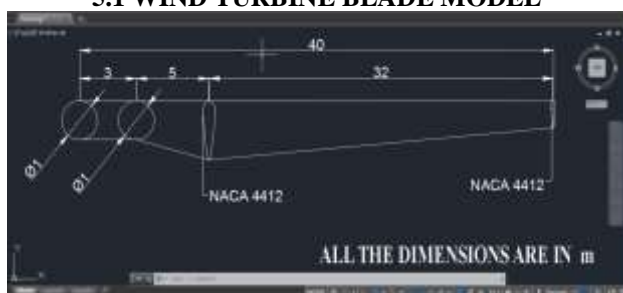
4.11 UNSTRUCTURED GRID

Unstructured grids have the advantage of generality in that they can be made to conform to nearly any desired geometry. This generality, however, comes with a price. The grid generation process is not completely automatic and may require considerable user interaction to produce grids with acceptable degrees of local resolution while at the same time having a minimum of element distortion. Unstructured grids require more information to be stored and recovered than structured grids (e.g., the neighbor connectivity list), and changing element types and sizes can increase numerical approximation errors.

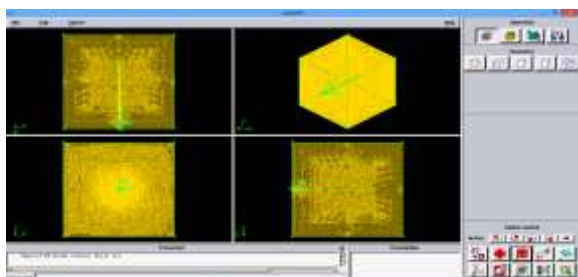
A popular type of unstructured grid consists of tetrahedral elements (Fig. 15). These grids tend to be easier to generate than those composed of hexahedral.

V WIND TURBINE BLADE MODEL

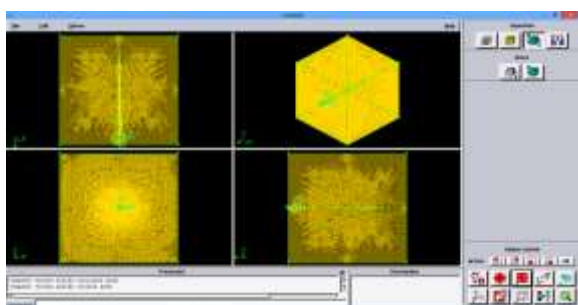
5.1 WIND TURBINE BLADE MODEL



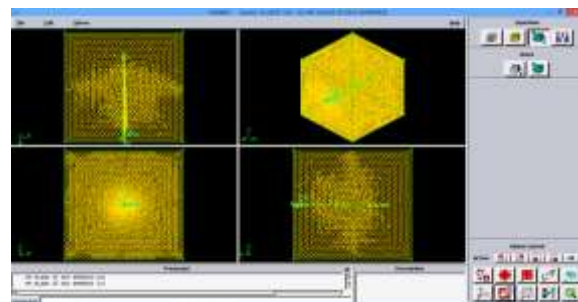
5.2 TAPERED WIND TURBINE BLADE WITHOUT TWIST .



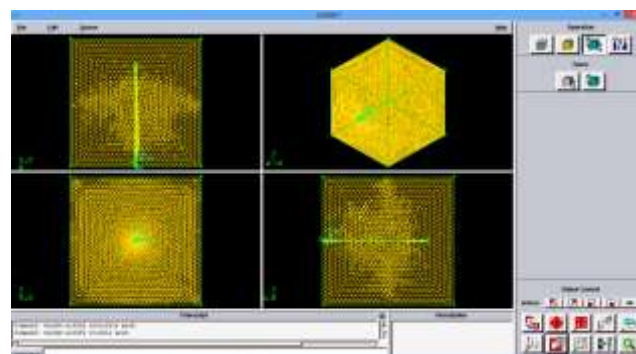
5.3 WIND TURBINE BLADE WITH TWIST IN 25 DEGREE WASH IN



5.4 WIND TURBINE BLADE WITH TWIST IN 45 DEGREE WASH IN



5.5 WIND TURBINE BLADE WITH TWIST IN 25 DEGREE WASHOUT



VI ANALYSIS OF WIND TURBINE BLADE MODEL

6.1 TAPERED BLADE WITHOUT TWIST

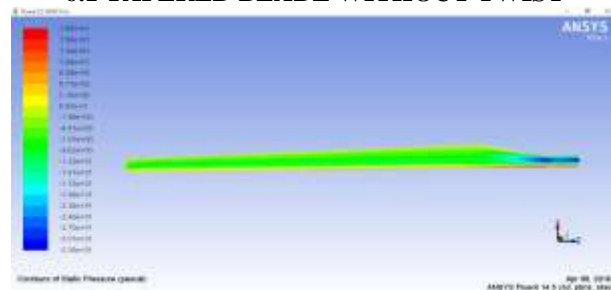


Figure 6.1: static pressure top view



Figure 6.2: static pressure bottom view

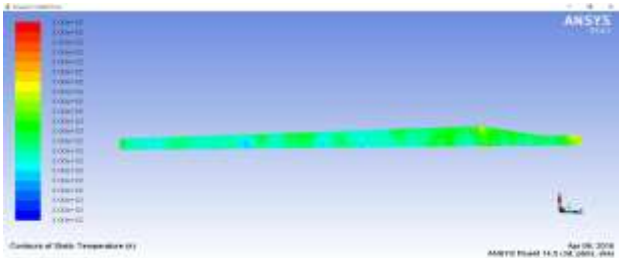


Figure 6.3: static temperature top view

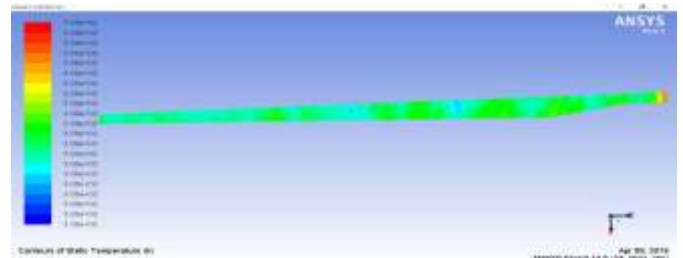


Figure 6.8: static temperature bottom view

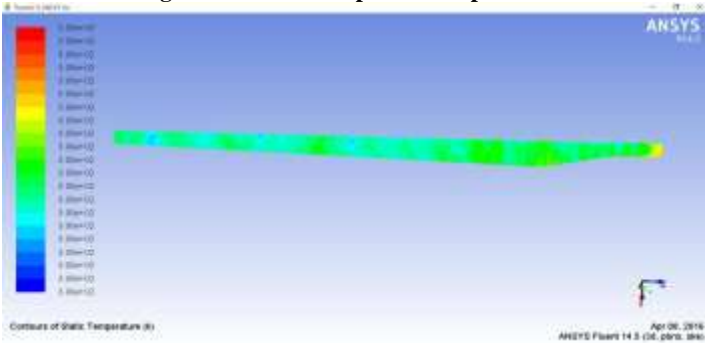


Figure 6.4: static temperature bottom view



6.3 TAPERED BLADE WITH TWIST 45 DEGREE WASH IN

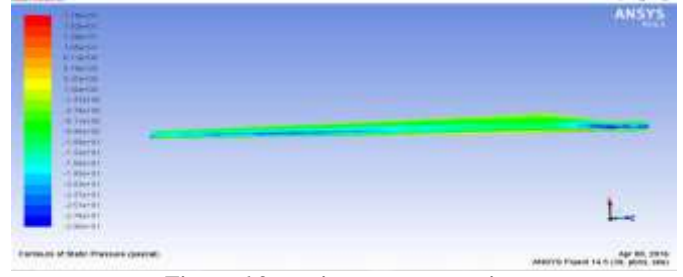


Figure 6.9: static pressure top view

6.2 TAPERED BLADE WITH TWIST 25 DEGREE WASH IN

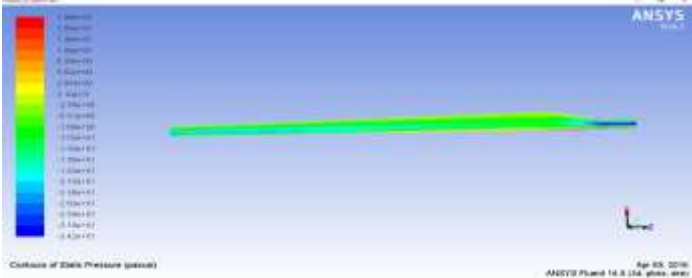


Figure 6.5: static pressure top view

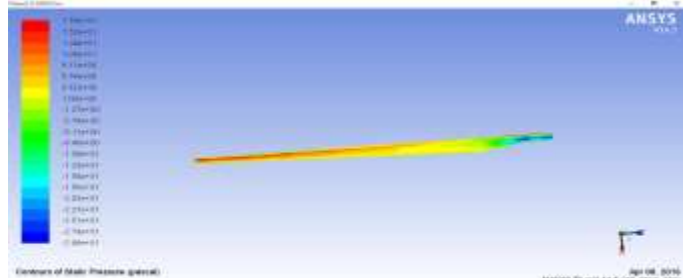


Figure 6.10: static pressure bottom view

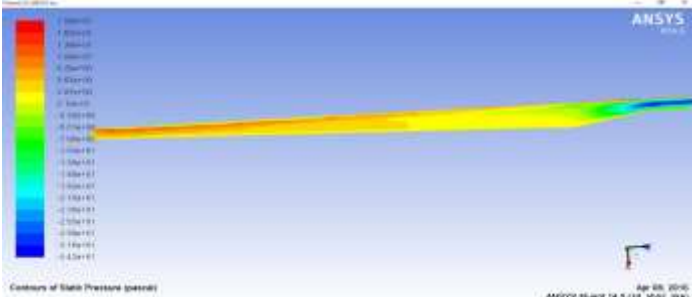


Figure 6.6: static pressure bottom view

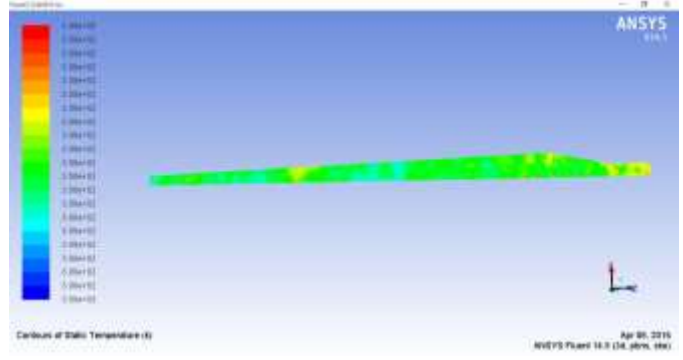


Figure 6.11: static temperature top view

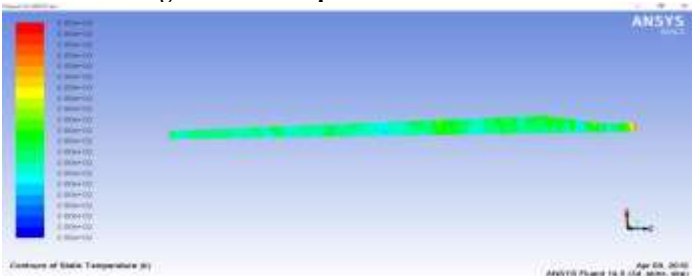


Figure 6.7: static temperature top view

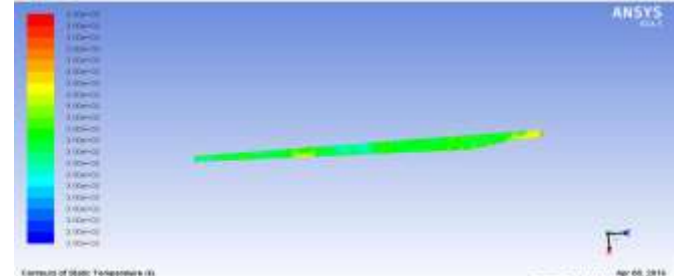


Figure 6.12: static temperature bottom view

6.4 TAPERED BLADE WITH TWIST 25 DEGREE WASH OUT

6.5 TAPERED BLADE WITH TWIST 45 DEGREE WASH OUT

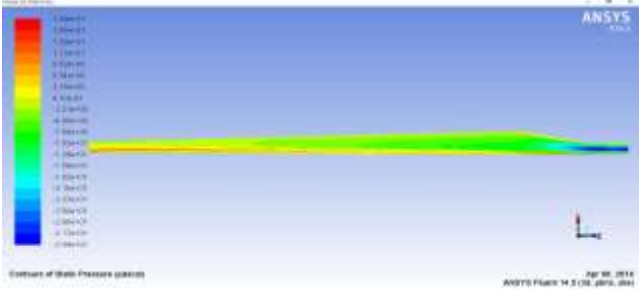


Figure 6.13: static pressure top view

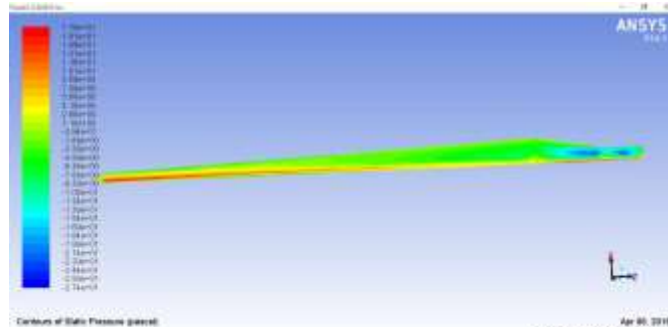


Figure 6.17: static pressure top view

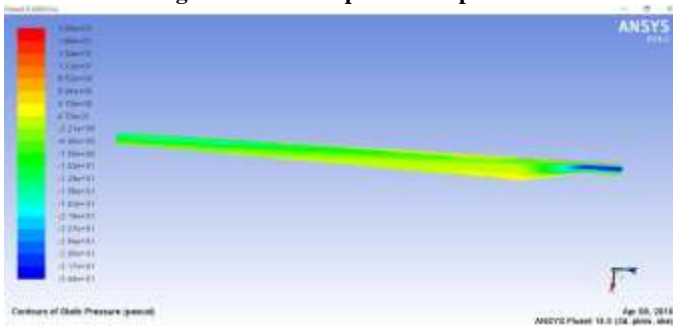


Figure 6.14: static pressure bottom view

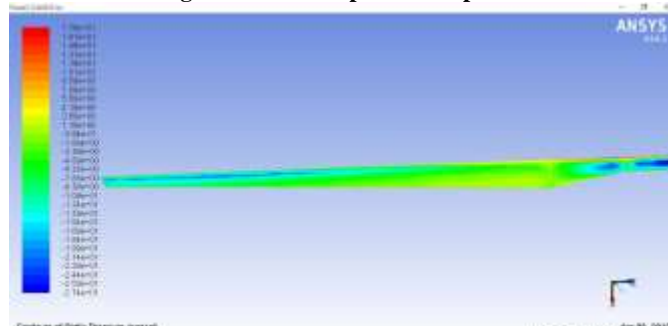


Figure 6.18: static pressure bottom view

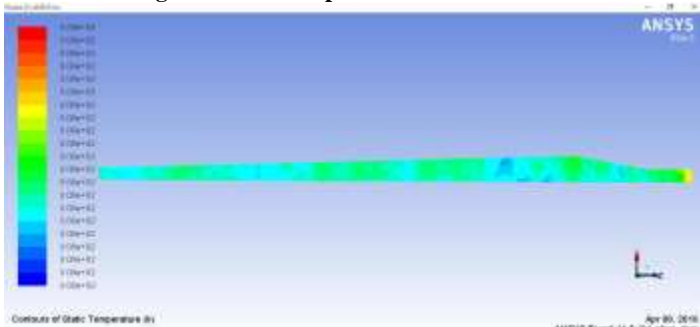


Figure 6.15: static temperature top view

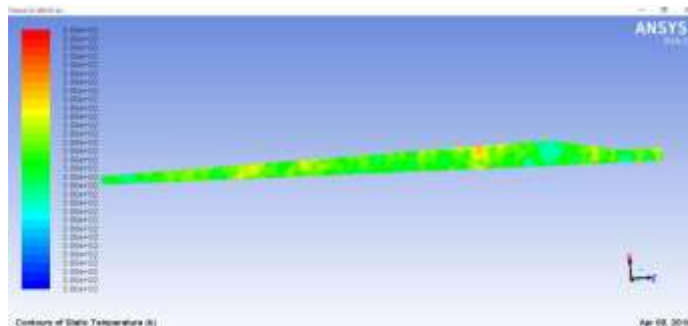


Figure 6.19: static temperature top view

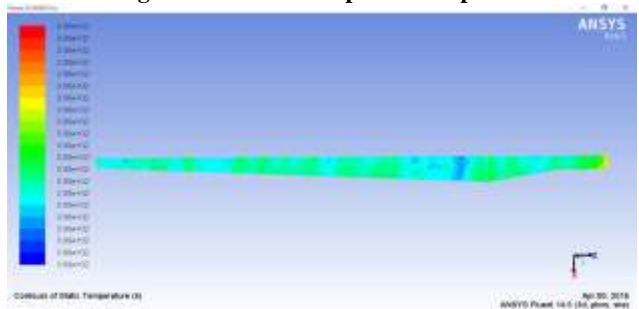


Figure 6.16: static temperature bottom view

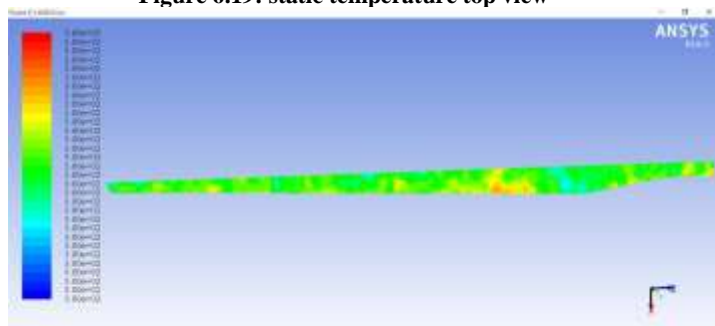


Figure 6.20: static temperature bottom view

VII RESULTS AND DISCUSSION

7.1 DETERMINATION OF LIFT TO DRAG RATIO

Table 7.1: Determination Lift to Drag Ratio L/D

BLADE TYPE	LIFT	DRAG	LIFT/DRAG RATIO
CONVENTIONAL TAPERED BLADE	14.02	7.10	1.97
25° DOWN	-14.6	12.78	-1.14
25° UPWARD	49.54	13.38	3.70
45° DOWN	-28.02	23.57	-1.19
45° UPWARD	56.89	23.18	2.45

VIII CONCLUSION

The lift to drag ratio of the wind turbine blade with and without geometric twist is analysed by using Computational Fluid Dynamics. We are selected the twist angles 25, 45 in wash out and wash in condition to analyse the lift to drag ratio. In this analysis 25 degree wash in condition is gives the result of 46 % higher than conventional blade and to increase the lift of the blade and prevented the over speed of the rotor. Finally the increase the stall delay of the rotor.

REFERENCES

- 1) Hardikpatel, Sanatdamania "Performance Prediction of Horizontal Axis Wind Turbine Blade" - May 2013.
- 2) Farooq Ahmad Najar, G A Harmain "Blade Design and Performance Analysis of Wind Turbine" - June 2013.
- 3) G.Sivaraj, Mr. M Gokul raj "Optimum Aerodynamic Design in Wind Mill Blades using Winglet function" Prof, - May 2012.
- 4) L.Wanga, X. Tanga, X. Liub "Optimized chord and twist angle distributions of wind turbine blade considering Reynolds number effects" - 2012.
- 5) Mohammad Shamsavarifard, Eric Louis Bibeau n,"Effect of shroud on the performance of horizontal axis hydrokinetic turbines" - 21 January 2015.
- 6) H. V. Mahawadiwar, V.D. Dhopte, P.S.Thakare, Dr. R. D. Askhedkar"Cfd Analysis of Wind Turbine Blade"Vol-2, Issue-3, pp-3188-3194, 2012
- 7) R.S. Amano, R.J. Malloy "CFD Analysis on Aerodynamic Design Optimization of Wind Turbine Rotor Blade", pp 71-75 2009
- 8) kentaro hayashi, hiroshi nishino, hiroyuki hosoya, koji fukami, tooru matsuo, takao kuroiwa "Low- noise Design for Wind Turbine Blades", Vol-49, pp-74-772012
- 9) Horia dumitrescu, Vladimir Cardos Florin Frunzulica, Alexandru DUMITRACHE "Determination of angle of attack for rotating blades"Volume-4, Issue-2, 2012
- 10) s. rajakumar, dr.d.ravindran "computational fluid dynamics of wind turbine blade at various angles of attack and low reynolds number", vol-2(11), 2010 55

Nd-YAG Laser cutting on Stainless steel

M.P.Tamizhmani¹, T.Uma sankari² & R.Ramanathan³

^{1,2&3}Assistant Professor, Mechanical Engineering, M.A.M School of Engineering, Trichy, India

Abstract- This project deals with the cutting parameter of Nd-yag laser cutting of stainless steel sheets by a pulsed Nd: YAG laser at the optimum process parameter ranges. In this project many attempts are being made for test pieces to predict the surface quality and dimensional accuracy of Nd-yag laser cutting for getting maximum best mechanical properties and minimum HAZ with various parameters. The responses considered are the heat-affected zone (HAZ) and mechanical properties analysis. The effect of the process parameters on the output responses is also investigated through mechanical properties.

Index Terms - Nd-yag laser, stainless steel sheets, laser cutting, surface quality.

I. Introduction

A laser is a device that emits light through a process of optical amplification based on the stimulated emission of electromagnetic radiation. The term "laser" originated as an acronym for Light Amplification by Stimulated Emission of Radiation. Spatial coherence allows a laser to be focused to a tight spot, enabling applications like laser cutting and lithography. Spatial coherence also allows a laser beam to stay narrow over long distances (collimation), enabling applications such as laser pointers. Lasers can also have high temporal coherence which allows them to have a very narrow spectrum, i.e., they only emit a single color of light.

Laser cutting is classified as a typical thermal process that has special advantages over other known thermal processes due to the high quality and very smooth cut surface, narrow width, small heat affected zone (HAZ), small metal deformation, perpendicular and sharp cut sides, square corners of cut edges and little or no oxide layer.

Neodymium-doped yttrium aluminum garnet; Nd:Y₃Al₅O₁₂) is a crystal that is used as a lasing medium for solid-state lasers. Nd:YAG lasers are optically pumped using a flashtube or laser diodes. These are one of the most common types of

laser, and are used for many different applications. Solid state Nd:YAG lasers have the advantages of less floor space, simple maintenance requirements, easy beam alignment, easy sharing, smaller wavelength (1.06 μ m) that can cut materials having greater reflectivity to CO₂ lasers. Using diode pumped Nd: YAG lasers increase their efficiency up to 20–30%. Moreover, Nd: YAG laser beam can be delivered and shared by using optical fibers to multiple and far work stations.

Laser can be emitted in continuous, constant and steady power (CW mode) or in the form of very short and intense burst of energy (pulsed mode). There are specific areas where either a pulsed laser or CW laser is more suitable. Peak pulse powers for pulsing Nd: YAG lasers can reach values of over 30 times greater than the maximum average power levels. This allows low-to-medium power lasers to achieve enough energy to reach vaporization temperatures for most materials.

Laser type	Nd: Yag laser
Class	4 Type laser
Emission wave length	1064nm
Operating system	Glavo scanner operating system
Operation	Cutting, Engraving, Embossing & Marking
Cooling system	water cooling system embedded
Precision	0.001mm cutting kerf of laser
Cutting Material	wood to diamond (highest hardness of material)

Table no: 1.1. Specification of Nd: YAG Laser

II. Material Selection

SS is a heat treatable martensitic chromium stainless steel. Melt practice is controlled to develop a surface nearly free from defects. It contains 12 and 25% of chromium, together with carbon contents ranging from 0.1 to 1.5%. The presence of carbon restores the α to γ transition. These compositions can be heated to the austenitic range of temperatures and will transform to martensite upon cooling at suitable rates.

SS 410 is a heat treatable martensitic chromium stainless steel. Melt practice is controlled to develop a surface nearly free from defects.

It provides the best combination of wear resistance and corrosion resistance, and is used in demanding medical accessories.

MATERIAL COMPOSITION

COMPOSITION	PERCENTAGE %
Chromium	11.8%
Nickel	20%
Manganese	40%
Carbon	14%
Silicon	30%
Iron	Balance

Table no: 3.1 Material compositions

TYPICAL MECHANICAL PROPERTIES:

PROPERTIES	VALUE
Ultimate Tensile Strength	483 MPa
Yield Strength	275 MPa
Hardness	450 DPH
Modulus of Elasticity	29×10^6 Psi
Poisson's Ratio	0.24

III. Specimen Preparation

In all cases, the thickness of the specimen should be at least 1:5 the diagonal of the indent. In the case of uncounted specimens, there should be no bulging or surface distortion on the surface opposite to the indent. In the case of laminated specimens, the top layer should conform to the 1:5X relationship.

The analysis surface must be finished such that the diagonals are clearly defined and can be measured with $\pm 5\%$ or half a micron accuracy, whichever is larger. Cold-finishing is necessary as

to not temper or work harden the surface during preparation.

In the case that a self-leveling support is not available, the specimen should have the surface opposite to the indentation surface parallel within 1° .

IV. Hardness Testing Of Machine

A hardness test is a robust method of correlating materials to mechanical Properties. However, there are minimum equipment checks, specimen preparation procedures and indentation placement.

The indentation centers should be placed at least 2:5xa diagonal apart. This is done to avoid the indentation-affected zone that surrounds each indent from interfering with results. Indentation sites should be in regions that are free of defects, scratches and surface contamination as this will also affect the result. For very hard materials, the 2:5x rule may be reduced first creating a grid of indents that are slightly less than 5x apart, and then placing indents directly between them to see if the hardness is affected and the latter point must be validated via statistical methods.

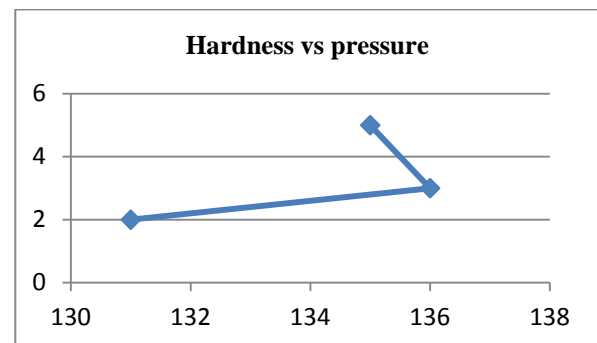


Figure: 4.1 Hardness Vs pressure

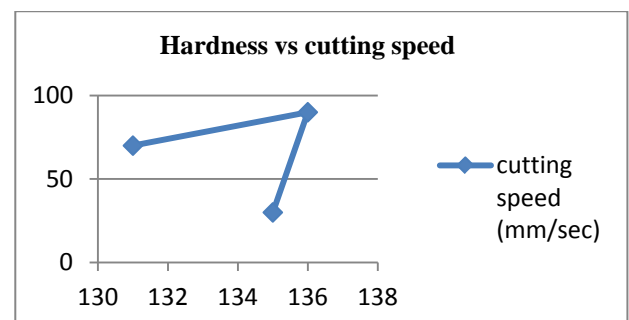


Figure: 4.2 Hardness Vs Cutting speed

V. Thermal Analysis Of Specimen In Ansys

Thermal analyses are used to calculate the temperature distribution and related thermal quantities in an object. It uses a heat balance equation obtained from the principle of

conservation energy as the basis for thermal analysis.

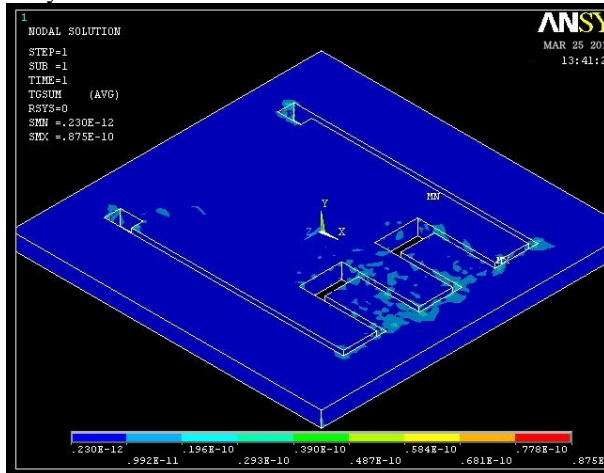
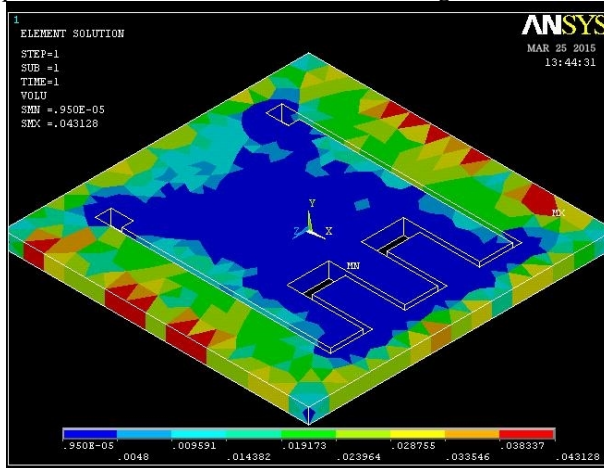


Fig 5.1 Thermal gradation analysis

All three primary modes of heat transfer conduction, convection, and radiation are handled by the program. In addition to the three modes of heat transfer, for special effects such as change of phase and internal heat generation.



VOLUME ANALYSIS

VI. PARAMETER SELECTION

Selection of parameters

Laser Power = 25.5 Watt
 Cutting Speed = upto 100 mm/sec
 Type and pressure of assist gas = argon (upto 5bar)
 Material thickness = 0.5 mm (SS 410 sheet)

S.n	Material	Thickne ss mm	Gas Pressu re Bar	Cutti ng speed mm/s	Cutti ng time Min
A	Stainle ss steel	0.5	2	70	32
B	Stainle ss steel	0.5	2.5	30	25
C	Stainle ss steel	0.5	3	90	20

INPUT PARAMETERS

S.N	Material	Thicknes s mm	Gas Pressur e Bar	Cuttin g speed mm/se c
A	Stainles s steel	0.5	2	70
B	Stainles s steel	0.5	2.5	30
C	Stainles s steel	0.5	3	90

OUTPUT RESPONSE

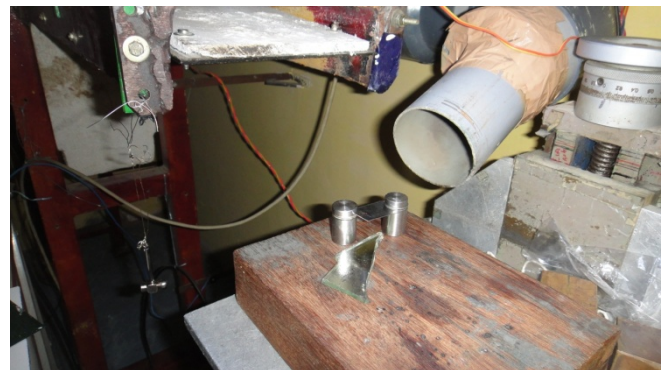


Figure: 6.1 ND: YAG laser machine

ND: YAG laser machine set up used to cut the stainless steel specimen is displayed.



Figure: 6.2 Cutting stainless steel in ND: YAG laser machine

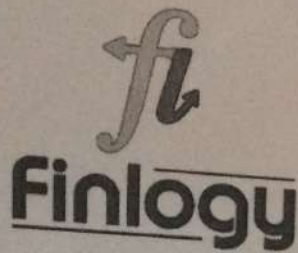
CONCLUSION

In order to achieve to high degree cutting surface as well as minimum nodes and minimum heat affected zone these machining parameters will be used. Thus cutting stainless steel by pulsed and CW Nd:YAG laser, it was shown that the laser cutting quality depends mainly on the cutting speed, cutting mode, laser power and pulse

frequency and focus position. The cutting parameters that provided dross-free and sharp cut surface during pulsed laser mode were: power=25W, cutting speed 90mm/sec, gas pressure =3 bar, time duration 20 min. The maximum hardness value obtained after machining in terms of Vickers hardness number is 136HV.

REFERENCES

- [1] B.D.Prajapati, R.J.Patel, and B.C.Khatri. "Parametric Investigation of CO2 Laser Cutting of Mild Steel and Hardox-400 Material." *IJETAE*, 3(4):204–208, 2013.
- [2] Avanish Kumar Dubey and Vinod Yadava, "Laser beam machining review, "International Journal of Machine Tools & Manufacture, vol. 48, pp.609– 628",2008.
- [3] K. Abdel Ghany, M. Newishy, "Cutting of 1.2mm thick austenitic stainless steel sheet using pulsedNd: YAG laser and CW."2005.
- [4] Han et al"The experiment in CW mode on H13 tool steel and stainless steel 304."2005.
- [5] Grevey and Desplats "The cutting performance of continuous wave (CW) and pulsed Nd: YAG laser beam for cutting bare and coated metal plates (0.8–2.0mm thick)." 1994.
- [6] Tahmouch et al"The experimental study for cutting stainless steel sheets (up to 2 cm thick) from a long distance (1 m) without using any assist gas in pulsed mode."1997.
- [7] Kaebernick et al"The experiments on mild steel and stainless steel sheets (0.5 and 0.9mm thick) in pulsed mode using oxygen assist gas."1999.
- [8] Matthew Roy"Vickers Hardness Measurements" 2010.



Imperial Journal of Interdisciplinary Research

CERTIFICATE OF PUBLICATION
ISSN : 2454-1362 website : www.onlinejournal.in/IJIR

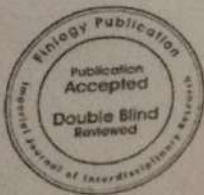


Is hereby awarding this certificate to
T.Uma sankari



In recognition of the publication of the paper entitled
Nd-YAG Laser cutting on Stainless steel

Published in: Vol-2, Issue-3, 2016



Signature
(Managing Editor)

: Dr. M.N.Ansari



DESIGN AND ANALYSIS OF MECHANICAL AND THERMAL BEHAVIOUR OF SHAPE MEMORY ALLOY IN ENGINE'S INTAKE AND EXHAUST

Monoj N¹ and Kaviyarasu P²

Abstract

Most of shape memory alloys are functional inter metallic's. Recent developments within nearly 10 years on shape memory alloys and martensitic transformations, on which shape memory effect and super elasticity are based, were concisely reviewed. Since TiNi alloys are the best practical shape memory alloys, we mostly discussed on the alloys, but we discussed more general problems as well. This paper summarizes the design and analysis of Aircraft engine's intake and blade, on which CATIA V5 is used for deign of solid model of these parts with the help of the Ansys software is used analysis of finite element model generated by meshing of these parts and thereby applying the boundary condition. This project specifies the effective use of the Ansys to analyse the complex engine geometries and apply boundary conditions to examine thermal and structural performance of the intake and exhaust for Nickel-Titanium Alloy. Finally stating the best suited material among the different alloys from the report generated after analysis. From this the results are stated and reported.

Key Words: shape memory alloys, martensitic, Nickel-Titanium Alloy etc...

INTRODUCTION

The F-14 Tomcat was designed as both an air superiority fighter and a long-range naval interceptor. The F-14 has a two-seat cockpit with a bubble canopy that affords all-round visibility. It features variable geometry wings that swing automatically during flight. For high-speed intercept, they are swept back and they swing forward for lower speed flight. It was designed to improve on the F-4 Phantom's air combat performance in most respects.

The F-14's fuselage and wings allow it to climb faster than the F-4, while the twin-tail arrangement offers better stability. The F-14 is equipped with an internal 20 mm M61 Vulcan Gatling cannon mounted on the left side, and can carry AIM-54 Phoenix, AIM-7 Sparrow, and AIM-9 Sidewinder anti-aircraft missiles. The twin engines are housed in nacelles, spaced apart by 1 to 3 ft (0.30 to 0.91 m). The flat area of the fuselage between the nacelles is used to contain fuel and avionics systems such as the wing-sweep mechanism and flight controls, and the underside used to carry the F-14's complement of Phoenix or Sparrow missiles, or assorted bombs. By itself, the fuselage provides approximately 40 to 60 percent of the F-14's aerodynamic lifting surface depending on the wing sweep position.

LITERATURE REVIEW

Sergey Belyaev was discussed that the main factors in a variation in the shape memory alloy properties under insonation are heating of the material and alternate stresses action.

Dimensional analysis and the finite element method are applied by **Wenyi Yan** to study spherical indentation of super elastic shape memory alloys. The scaling relationships derived from dimensional analysis bridge the indentation response and the mechanical properties of a super elastic shape memory alloy. Several key variables of a super elastic indentation curve are revealed and examined. We prove that the bifurcation force in a super elastic indentation curve only relies on the forward transformation stress and the elastic properties of the initial austenite; and the return force in a super elastic indentation curve only relies on the reverse transformation stress and the elastic properties of the initial austenite.

Most of shape memory alloys are functional inter metallic's. They are now practically being used for couplings, actuators, medical guide wires etc., and are hopeful candidates for smart materials, which already exist. **Kazuhiro Otsuka** focused that, recent developments within nearly 10 years on shape memory alloys and martensitic: transformations, on which shape memory effect and super elasticity are based, were concisely reviewed.

¹Jay Shriram Group Of Institutions, Tirupur Tamilnadu, ² MAM School of Engineering, Trichy, Tamilnadu.
Correspondence and Reprint Requests: Monoj N and Kaviyarasu P

Since TiNi alloys are the best practical shape memory alloys, we mostly discussed on the alloys, but we discussed more general problems as well. Furthermore, we discussed the ductility and densities of point defects in inter-metallic, since they are important problems in inter metallic's in general.

In order to increase the efficiency of jet engines, **M. Zeis** was concluded that it is hard to machine nickel-based and titanium-based alloys are in common use for aero engine components such as blades and blisks (blade integrated disks). Here Electrochemical Machining (ECM) is a promising alternative to milling operations. Due to lack of appropriate process modelling capabilities beforehand still knowledge based and a cost intensive cathode design process is passed through. Therefore this paper presents a multi-physical approach for modelling the ECM material removal process by coupling all relevant conservation equations. The resulting simulation model is validated by the example of a compressor blade. Finally a new approach for an inverted cathode design process is introduced and discussed.

A unique dovetail fretting fatigue fixture was designed and evaluated by **Patrick J. Golden** for testing turbine engine materials at room or elevated temperatures. Cold section and hot section materials from military turbojet engines were chosen for testing. These included Ti-6Al-4V, Rene'88DT, and Rene'N5. The new fixture was improved over a previously used dovetail fretting fatigue fixture by including instrumentation for direct measurement of the normal contact force, alignment control, and elevated temperature capability. Measurement of the shear component of the contact force was validated through an alternative instrumentation method. Investigation of the thermal gradient in the specimen and pads was conducted. Initial test results revealed interesting variability in the behaviour of the nickel based super alloy specimens at elevated temperature.

Shape Memory Alloy

A shape-memory alloy (SMA, smart metal, memory metal, memory alloy, muscle wire, smart alloy) is an alloy that "remembers" its original, cold-forged shape: returning to the pre-deformed shape when heated. This material is a lightweight, solid-state alternative to conventional actuators such as hydraulic, pneumatic, and motor-based systems. Shape-memory alloys have applications in industries including medicine and aerospace.

Shape Memory Effect

One-Way Memory Effect

When a shape-memory alloy is in its cold state (below A_s), the metal can be bent or stretched and will hold those shapes until heated above the transition temperature. Upon heating, the shape changes to its

original. When the metal cools again it will remain in the hot shape, until deformed again.

With the one-way effect, cooling from high temperatures does not cause a macroscopic shape change. A deformation is necessary to create the low-temperature shape. On heating, transformation starts at A_s and is completed at A_f (typically 2 to 20 °C or hotter, depending on the alloy or the loading conditions). A_s is determined by the alloy type and composition and can vary between 150 °C and 200 °C.

One-Way Memory Effect

The two-way shape-memory effect is the effect that the material remembers two different shapes: one at low temperatures, and one at the high-temperature shape. A material that shows a shape-memory effect during both heating and cooling is called two-way shape memory. This can also be obtained without the application of an external force (intrinsic two-way effect). The reason the material behaves so differently in these situations lies in training. Training implies that a shape memory can "learn" to behave in a certain way. Under normal circumstances, a shape-memory alloy "remembers" its low-temperature shape, but upon heating to recover the high-temperature shape, immediately "forgets" the low-temperature shape. However, it can be "trained" to "remember" to leave some reminders of the deformed low-temperature condition in the high-temperature phases. There are several ways of doing this. A shaped, trained object heated beyond a certain point will lose the two-way memory effect, this is known as "amnesia".

Pseudo-Elasticity

One of the commercial uses of shape-memory alloy exploits the pseudo-elastic properties of the metal during the high-temperature (austenitic) phase. The frames of reading glasses have been made of shape-memory alloy as they can undergo large deformations in their high-temperature state and then instantly revert to their original shape when the stress is removed. This is the result of pseudo elasticity; the martensitic phase is generated by stressing the metal in the austenitic state and this martensite phase is capable of large strains. With the removal of the load, the martensite transforms back into the austenite phase and resumes its original shape.

This allows the metal to be bent, twisted and pulled, before reforming its shape when released. This means the frames of shape-memory alloy glasses are claimed to be "nearly indestructible" because it appears no amount of bending results in permanent plastic deformation. The martensite temperature of shape-memory alloys is dependent on a number of factors including alloy chemistry. Shape-memory alloys with

transformation temperatures in the range of 60–1450 K have been made.

Response Time And Response Symmetry

SMA actuators are typically actuated electrically, where an electric current results in Joule heating. Deactivation typically occurs by free convective heat transfer to the ambient environment. Consequently, SMA actuation is typically asymmetric, with a relatively fast actuation time and a slow deactivation time. A number of methods have been proposed to reduce SMA deactivation time, including forced convection, and lagging the SMA with a conductive material in order to manipulate the heat transfer rate. Novel methods to enhance the feasibility of SMA actuators include the use of a conductive "lagging".

This method uses a thermal paste to rapidly transfer heat from the SMA by conduction. This heat is then more readily transferred to the environment by convection as the outer radii (and heat transfer area) is significantly greater than for the bare wire. This method results in a significant reduction in deactivation time and a symmetric activation profile. As a consequence of the increased heat transfer rate, the required current to achieve a given actuation force is increased. In fig.1. shows Comparative force-time response of bare and lagged Ni-Ti shape memory alloy.

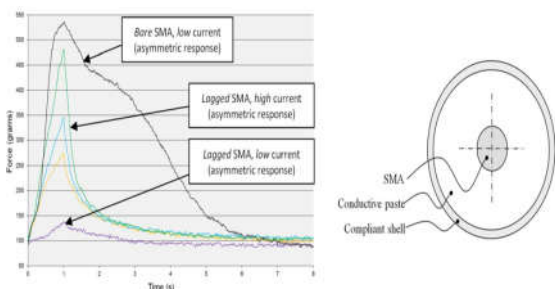


Fig 1. Comparative force-time response of bare and lagged Ni-Ti shape memory alloy.

Classifications

Table .1 Classification of SMA

S. No	ALLOY	% of Concentration
1.	Ag-Cd	44/49 at.% Cd
2.	Au-Cd	46.5/50 at.% Cd
3.	Cu-Al-Ni	14/14.5 wt.% Al and 3/4.5 wt.% Ni
4.	Cu-Sn	approx. 15 at.% Sn
5.	Cu-Zn	38.5/41.5 wt.% Zn
6.	Cu-Zn-X (X = Si, Al, Sn)	in various concentrations
7.	Fe-Pt	approx. 25 at.% Pt
8.	Mn-Cu	5/35 at.% Cu
9.	Fe-Mn-Si	in various concentrations
10.	Pt alloys	in various concentrations
11.	Co-Ni-Al	in various concentrations
12.	Co-Ni-Ga	in various concentrations
13.	Ni-Fe-Ga	in various concentrations
14.	Ti-Pd	in various concentrations
15.	Ni-Ti	~55% Ni
16.	Ni-Ti-Nb	in various concentrations
17.	Ni-Mn-Ga	in various concentrations

Geometric Modelling

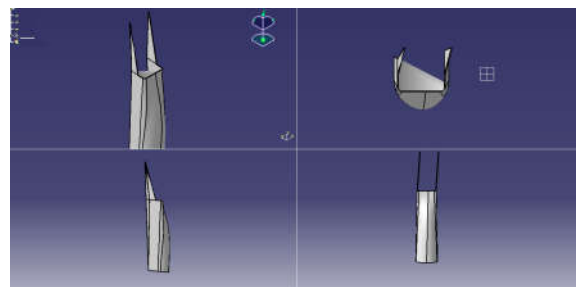


Fig 2 Design of Engine Air intake

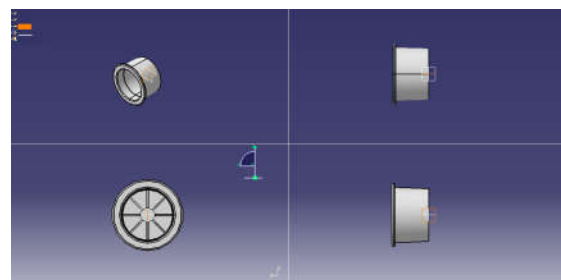


Fig 3 Design of Engine exhaust

RESULTS AND DISCUSSIONS

Engine Exhaust

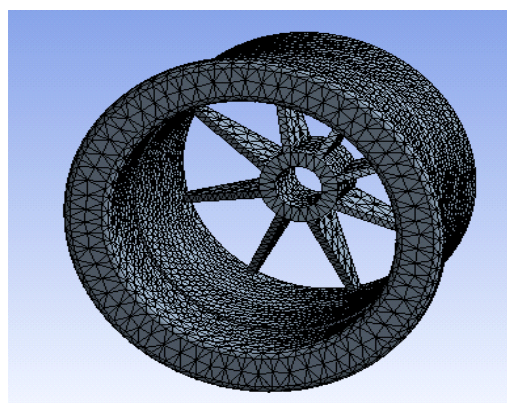


Fig 4. Meshing of Engine exhaust

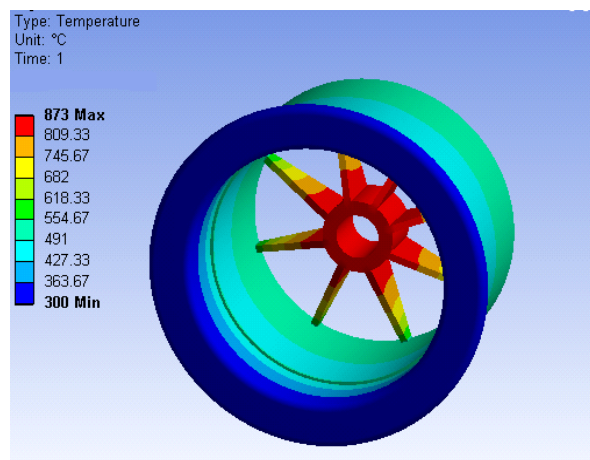


Fig 5. Thermal analysis of Engine exhaust

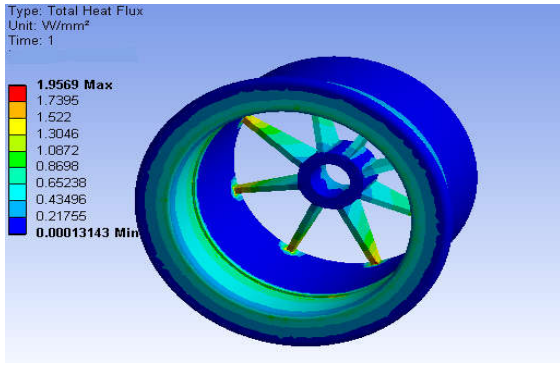


Fig 6. Heat flux analysis of Engine exhaust

Structural Analysis

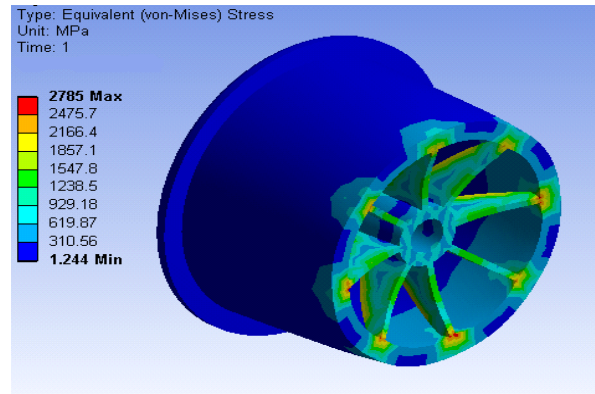


Fig 10. Equivalent stress of Engine exhaust

Engine Intake

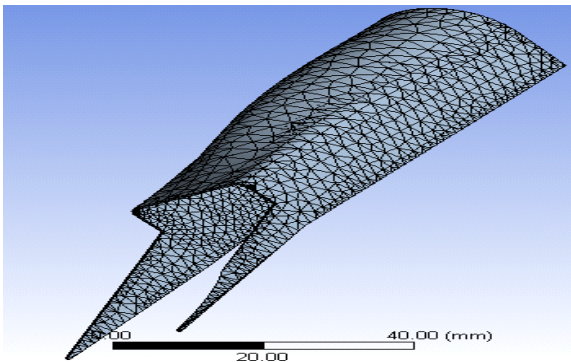


Fig 7 Meshing of Engine intake

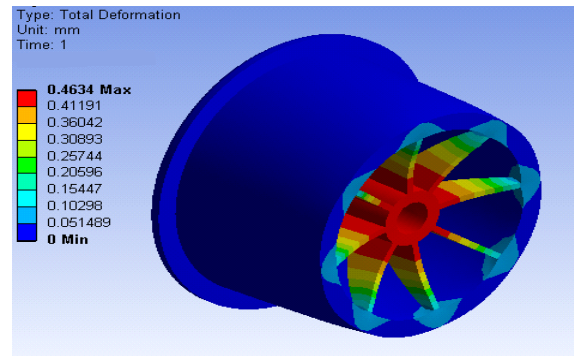


Fig 11. Total deformation of Engine exhaust

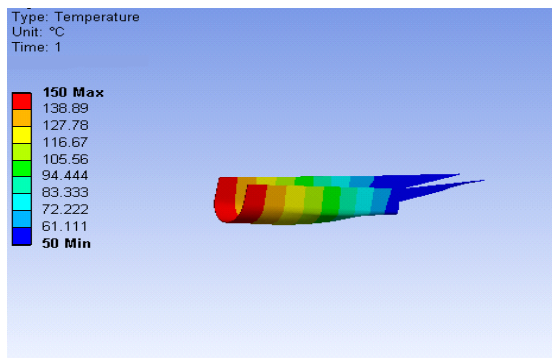


Fig 8 Thermal analysis of Engine intake

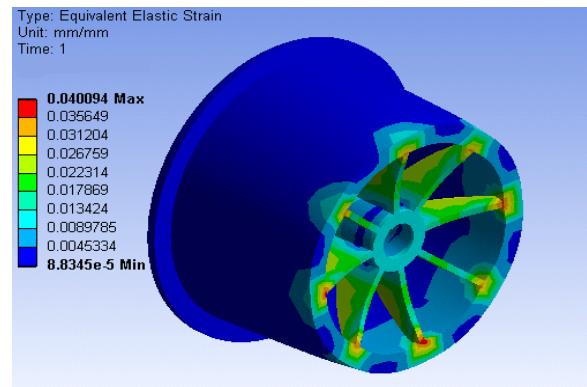


Fig 12. Equivalent elastic strain of Engine exhaust

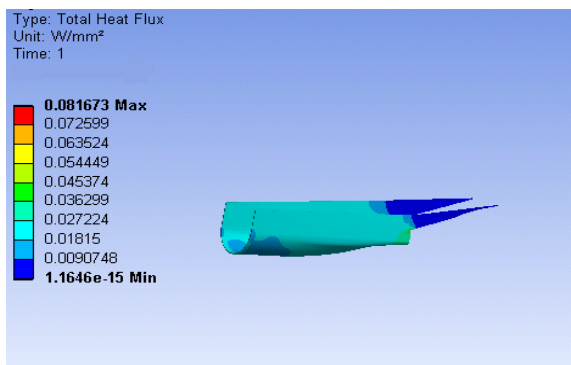


Fig 9. Heat flux analysis of Engine intake

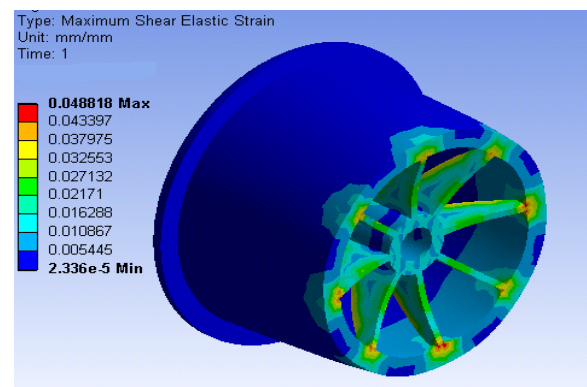


Fig 13. Maximum shear elastic strain of Engine exhaust

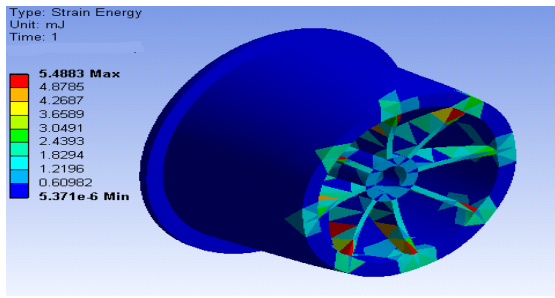


Fig 14. Strain energy of Engine exhaust

Model Analysis -Engine Exhaust

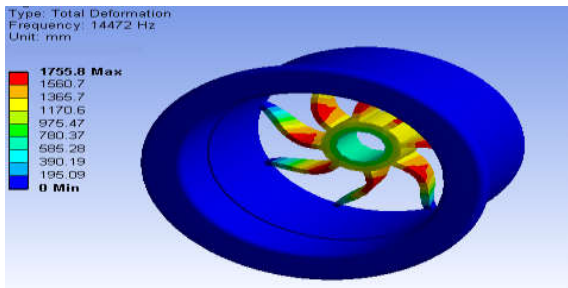


Fig 15. Model analysis of Engine exhaust (14472 Hz)

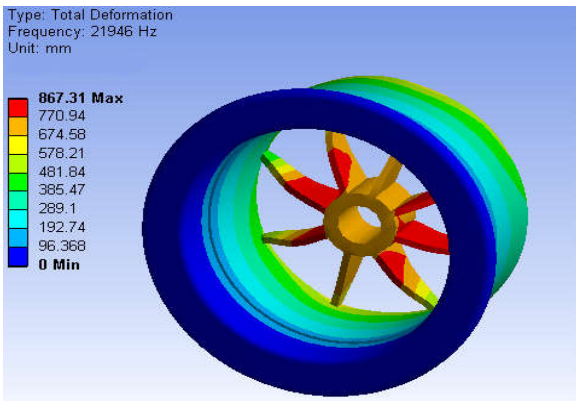


Fig 16. Model analysis of Engine exhaust (21946 Hz)

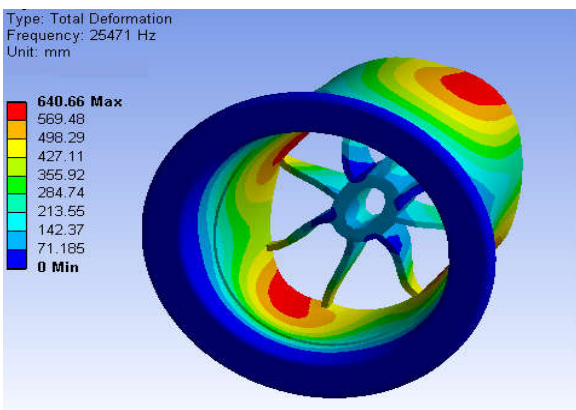


Fig 17 Model analysis of Engine exhaust (25471 Hz)

Model Analysis -Engine Intake

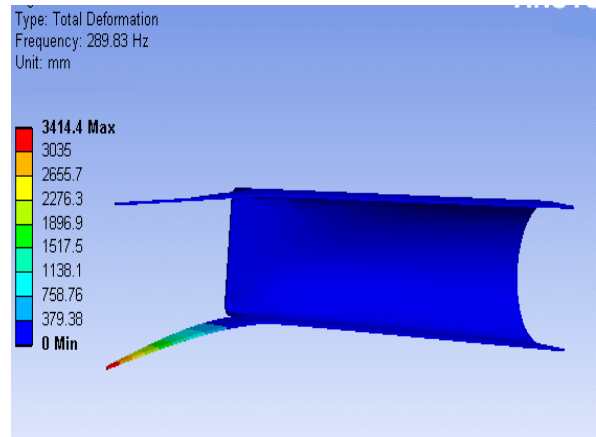


Fig 18. Model analysis of Engine intake (289.83 Hz)

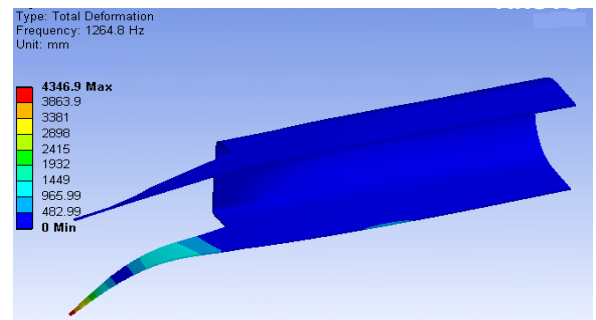


Fig 19. Model analysis of Engine intake (1264.8 Hz)

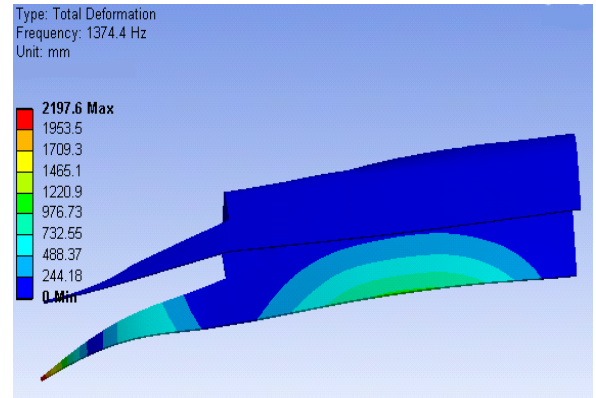


Fig 20. Model analysis of Engine intake (1374.4 Hz)

MATERIAL SELECTION

Material Used

The material used for this design process is made of Nickel-Titanium Alloy.

NICKEL

Nickel is a chemical element with the chemical symbol Ni and atomic number 28. It is a silvery-white lustrous metal with a slight golden tinge. Nickel belongs to the transition metals and is hard and ductile. Pure nickel shows a significant chemical activity that can be observed when nickel is powdered to maximize the exposed surface area on which reactions can occur, but larger pieces of the metal are slow to react with air at

ambient conditions due to the formation of a protective oxide surface. Even then, nickel is reactive enough with oxygen that native nickel is rarely found on Earth's surface, being mostly confined to the interiors of larger nickel-iron meteorites that were protected from oxidation during their time in space. On Earth, such native nickel is always found in combination with iron, a reflection of those elements' origin as major end products of supernova nucleosynthesis. An iron-nickel mixture is thought to compose Earth's inner core.

Extraction and Purification

Nickel is recovered through extractive metallurgy. Nickel is extracted from its ores by conventional roasting and reduction processes that yield a metal of greater than 75% purity. In many stainless steel applications, 75% pure nickel can be used without further purification, depending on the composition of the impurities. Most sulphide ores have traditionally been processed using pyro metallurgical techniques to produce a matte for further refining. Recent advances in hydrometallurgy have resulted in significant nickel purification using these processes. Most sulphide deposits have traditionally been processed by concentration through a froth flotation process followed by pyro metallurgical extraction. In hydrometallurgical processes, nickel sulphide ores undergo flotation (differential flotation if Ni/Fe ratio is too low) and then smelted. After producing the nickel matte, further processing is done via the Sherritt-Gordon process. First, copper is removed by adding hydrogen sulphide, leaving a concentrate of only cobalt and nickel. Then, solvent extraction is used to separate the cobalt and nickel, with the final nickel concentration greater than 99%.

Titanium

Titanium is a chemical element with the symbol Ti and atomic number 22. It is a lustrous transition metal with a silver color, low density and high strength. It is highly resistant to corrosion in sea water, aqua regia and chlorine. Titanium was discovered in Cornwall, Great Britain, by William Gregor in 1791 and named by Martin Heinrich Klaproth for the Titans of Greek mythology. The element occurs within a number of mineral deposits, principally rutile and ilmenite, which are widely distributed in the Earth's crust and lithosphere, and it is found in almost all living things, rocks, water bodies, and soils. The metal is extracted from its principal mineral ores via the Kroll process or the Hunter process. Its most common compound, titanium dioxide, is a popular photocatalyst and is used in the manufacture of white pigments. Other compounds include titanium tetrachloride (TiCl₄), a component of smoke screens and catalysts; and titanium trichloride (TiCl₃), which is used as a catalyst in the production of polypropylene.

Titanium can be alloyed with iron, aluminium, vanadium, molybdenum, among other elements, to produce strong lightweight alloys for aerospace (jet engines, missiles, and spacecraft), military, industrial process (chemicals and petro-chemicals, desalination plants, pulp, and paper), automotive, agri-food, medical prostheses, orthopedic implants, dental and endodontic instruments and files, dental implants, sporting goods, jewellery, mobile phones, and other applications.

The two most useful properties of the metal are corrosion resistance and the highest strength-to-weight ratio of any metal. In its unalloyed condition, titanium is as strong as some steels, but 45% lighter. There are two allotropic forms and five naturally occurring isotopes of this element, ⁴⁶Ti through ⁵⁰Ti, with ⁴⁸Ti being the most abundant (73.8%). Titanium's properties are chemically and physically similar to zirconium, as both of them have the same number of valence electrons and are in the same group in the periodic table.

Applications

Titanium is used in steel as an alloying element (Ferro-titanium) to reduce grain size and as a deoxidizer, and in stainless steel to reduce carbon content. Titanium is often alloyed with aluminium (to refine grain size), vanadium, copper (to harden), iron, manganese, molybdenum, and with other metals. Applications for titanium mill products (sheet, plate, bar, wire, forgings, castings) can be found in industrial, aerospace, recreational, and emerging markets. Powdered titanium is used in pyrotechnics as a source of bright-burning particles.

CONCLUSION

In this conceptual design phase work has been done on the study of turbofan engine air intake and exhaust part's materials that are used at present. The exhaust made up of titanium alloy is taken under study. Nosecone, engine's air intake and exhaust are modelled using CATIA. The outputs for these parts are shown in different views.

The engine parts that are generated using CATIA V5 are had been imported to the Ansys software. After finite element modelling by meshing and applying the boundary conditions, the stress distribution for these parts have been calculated. The maximum von Mises stress obtained for mechanical and thermal load stresses are compared with material allowable stress. The calculated reserve factors for the models are more than the required value of one. Hence the component is safe from static strength criteria.

References

1. Crosby, Francis, Fighter Aircraft. London: Lorenz Books, 2002.
2. Stevenson, J.P. Grumman F-14, Vol. 25. New York: Tab Books, 1975.

3. Greenwood, N.N. Earnshaw, A. (1997). *Chemistry of the Elements* (2nd ed.). Oxford: Butterworth-Heinemann.
4. Barksdale, Jelks (1968), "Titanium", In Clifford A. Hampel (editor). *The Encyclopedia of the Chemical Elements*. New York: Reinhold Book Corporation. pp. 732–738.
5. Derek G. E. Kerfoot (2005), "Nickel", *Ullmann's Encyclopedia of Industrial Chemistry*, Weinheim: Wiley-VCH.
6. Davis, Joseph R (2000). "Uses of Nickel". *ASM Specialty Handbook: Nickel, Cobalt, and Their Alloys*. ASM International. pp. 7–13
7. Jenkins, Dennis R. *Grumman F-14 Tomcat: Leading US Navy Fleet Fighter*. London: Aerofax, 1997.
8. Wilson, Stewart. *Combat Aircraft since 1945*. Fyshwick, Australia: Aerospace Publications, 2000.
9. S. Pfirrmann et al. (2009). "A Dinuclear Nickel(I) Dinitrogen Complex and its Reduction in Single-Electron Steps". *Angewandte Chemie International Edition*.



**INTERNATIONAL JOURNAL OF CURRENT INNOVATION
RESEARCH**

ISSN:2395 – 5775

www.journalijcir.com

Certificate For Publication

Is hereby awarding this certificate to

Monoj N and Kaviyarasu P



In recognition of the publication of the paper entitled

**DESIGN AND ANALYSIS OF MECHANICAL AND THERMAL BEHAVIOUR OF SHAPE MEMORY
ALLOY IN ENGINE'S INTAKE AND EXHAUST**

Published in International Journal of Current Innovation Research
(Vol. 2, Issue 09, pp 467-473, September 2016)

Date: 28/09/2016



Signature: _____
Managing Editor

www.journalijcir.com
E-mail: journalijcir@gmail.com



M.A.M. SCHOOL OF ENGINEERING

(Accredited by NAAC)

(Approved by AICTE, New Delhi & Affiliated to Anna University)

Siruganur, Tiruchirappalli – 621 105.

Academic year (2016-2017)

Department of Electrical and Electronics Engineering

Title of paper	Name of the author/s	Department of the teacher	Name of journal	Year of publication	ISSN number	Link to the recognition in UGC enlistment of the Journal /Digital Object Identifier (doi) number		
						Link to website of the Journal	Link to article/paper/abstract of the article	Is it listed in UGC Care list/Scopus/Web of Science/other, mention
Innovative Method to Secure ECG Signal using ECC in Wireless Communication	Dr.R.Ilango	EEE	International Journal for Modern Trends in Science and Technology Volume: 03, Issue No: 05	2016-2017	ISSN: 2455-3778	https://www.ijmtst.com/vol3issue5/IJMTSTTRPEE1039.pdf		
Innovative Method to Secure ECG Signal using ECC in Wireless Communication	N.Karthika	EEE	International Journal for Modern Trends in Science and Technology Volume: 03, Issue No: 05	2016-2017	ISSN: 2455-3778	https://www.ijmtst.com/vol3issue5/IJMTSTTRPEE1039.pdf		
Asymmetrical Half Bridge Flyback Converter with Wind Energy	V.Sivashankari	EEE	Imperial Journal of Interdisciplinary Research (IJIR) Vol-3, Issue-1	2016-2017	ISSN: 2454-1362	http://www.onlinejournal.in/IJIRV3I1/201.pdf		
Asymmetrical Half Bridge Flyback Converter with Wind Energy	M.Sasikala	EEE	Imperial Journal of Interdisciplinary Research (IJIR) Vol-3, Issue-1	2016-2017	ISSN: 2454-1362	http://www.onlinejournal.in/IJIRV3I1/201.pdf		
Asymmetrical Half Bridge Flyback Converter with Wind Energy	R.Raghavi	EEE	Imperial Journal of Interdisciplinary Research (IJIR) Vol-3, Issue-1	2016-2017	ISSN: 2454-1362	http://www.onlinejournal.in/IJIRV3I1/201.pdf		

R. Shree
HOD/EEE

HEAD OF THE DEPARTMENT
ELECTRICAL and ELECTRONICS ENGINEERING
M.A.M. SCHOOL OF ENGINEERING
SIRUGANUR, TRICHY - 621 105.

[Signature]
PRINCIPAL
PRINCIPAL

M.A.M. SCHOOL OF ENGINEERING
SIRIGANUR, TIRUCHIRAPPALLI-621 105.

Innovative Method to Secure ECG Signal using ECC in Wireless Communication

G.Purushothaman¹ | Dr. R.Ilango² | N.Karthika³ | N.Ajith⁴

^{1,2,3,4} Assistant Professor, Department of EEE, M.A.M.S.E, Tamilnadu, India.

To Cite this Article

G.Purushothaman, Dr. R.Ilango, N.Karthika and N.Ajith, "Innovative Method to Secure ECG Signal using ECC in Wireless Communication", *International Journal for Modern Trends in Science and Technology*, Vol. 03, Issue 05, May 2017, pp. 99-103.

ABSTRACT

Mobile based healthcare is one of the fastest growing area of health care computing. One of the important social problems we are facing now is the increasing percentage of the aged in the population and also modern people face much more financial and society pressure than before, living and working in a rapid rhythm, the health status can't get often monitoring, sudden death occurs without any medical symptom. To deal with these challenges, it is necessary to research the automated health care (ECG) service with maximum data security in order to lay the foundation for its successful application on Mobile Cloud. In a mobile care system setting, wearable electrocardiogram ECG sensors can give a continuously monitoring over days or weeks anywhere anytime over the Bluetooth to mobile. The proposed system using SPIHT for compression the ECG data and the best encryption mechanism provides a simple and yet effective security solution for an ECG sensor-based communication platform, where end-to-end encryption of entire ECG data encrypting using ECC algorithm which is based on public key cryptography as a lightweight algorithm in Mobile Cloud. This part of the encrypted data is essential to ECG data quality and it saves significant additional energy saving due to its unequal investment of communication energy to the outcomes of the lightweight encryption, and thus, it maintains a high ECG data transmission quality.

KEYWORDS: ECG, BASNs, CDC.

Copyright © 2017 International Journal for Modern Trends in Science and Technology
All rights reserved.

I. INTRODUCTION

With the technological advancement in body area sensor networks (BASNs), low cost high quality electrocardiographic (ECG) diagnosis systems have become important equipment for healthcare service providers. However, energy consumption and data security with ECG systems in BASNs are still two major challenges to tackle. In this study, we investigate the properties of compressed ECG data for energy saving as an effort to devise a selective encryption mechanism and a two rate unequal error protection (UEP) scheme. The selective encryption mechanism provides a simple and yet effective security solution for man ECG sensor based communication platform, where only

one percent of data is encrypted without compromising ECG data security. This part of the encrypted data is essential to ECG data quality due to its unequally important contribution to distortion reduction. The two-rate UEP scheme achieves a significant additional energy saving due to its unequal investment of communication energy to the outcomes of the selective encryption, and thus, it maintains a high ECG data transmission quality. Their results show the improvements in communication energy saving of about 40%, and demonstrate a higher transmission quality and security measured in terms of wavelet based weighted percent root-mean-squared difference.

A. ECG In Existing System

Electrocardiographic (ECG) information reveals essential heart condition for heart illness diagnosing such as heart attacks, arterial blockages, enlarged heart muscle, etc., and it has been widely used in healthcare. According to statistical data collected by the Centres for Disease Control and Prevention (CDC), heart illnesses have been identified as the leading cause of death at least since 1980 in the United States. The fast increase in the number of heart illness patients, most of them technological progress in wireless sensing and wearable sensors has made body area sensor networks (BASNs) technology a promising solution to help us to meet this growing demand. For example, a miniature ECG monitoring device has been developed with a size as small as 55 × 23 mm. This device adopts ultra-low power circuitry using efficient system level power management, promising a long battery life. In addition, many sophisticated architectures for wireless ECG transmission have also been developed. According to their studies, the sensors are becoming increasingly smaller and more wearable. The new ECG sensor uses textile-structured electrodes, which are embedded inside clothes. In addition, numerous communication protocols such as 8011.15.4, Bluetooth, and TDA5250 have been designed and implemented in BASNs to lower power consumption. It is seen from all those pilot research and development projects that BASN has become a realistic and promising tool for implementation of wireless ECG diagnosis systems. It is seen that although the aforementioned research works can be utilized to solve the energy problem in BASNs to some extent, the improvement is still quite limited. In this paper, we are motivated to investigate the properties of the compressed ECG data, based on which we will show that a big room is still left for us to save more energy. In particular, we will propose a selective encryption algorithm and a two rate UEP scheme, as an effort to further improve energy saving, transmission quality, and security.

B. Selective ECG Encryption

Based on the previous discussions on the SPIHT compression algorithm, both the values and positions are recorded in the output from a compression codec. In a particular subset, value information is dependent on position information, i.e., value information is useless if the position information is not reliable. Among different subsets, position information is not independent

either. In fact, two lists, i.e., the list of insignificant points (LIP) and the list of insignificant sets (LIS), record the position information. The current-partition-sorting step performs the searches in both LIP and LIS of the previous bitplane. Therefore, the position information in the current bit-plane is dependent on the previous position information.

C. Two-Rate UEP Scheme

In ECG signals, several important features for cardiac disease diagnosis are well defined. It is worth noting how these features are allocated in the wavelet domain, where we apply the SPIHT compression algorithm. The QRS complex is a significant feature in the ECG signal, which is characterized by sharp slopes. Most of its frequency spectrum is located between 1 to 40 Hz and centered around 17 Hz. The T wave always appears after the QRS complex, and it can appear in various shapes. Its frequency distribution is typically less than 6 Hz. The P wave normally appears before the QRS complex, and its frequency is usually below 10 Hz. ST segments often occupying a lower frequency range.

II. EXSISTING ALGORITHMAM SPIHT-AES

- i. A small amount of data (about 1%) is to be encrypted, thereby significantly reducing the encryption burden. At the same time, the encrypted parts are the coefficients in the first bit-plane, which is more robust to the brute-force attacks than state-of-the-art encryption standards. Therefore, the determining factor for the achievable level of security in their scheme depends entirely on the level of security of the employed encryption algorithm itself, such as Advanced Encryption Standard (AES). Furthermore, their security scheme is independent and it works compatible to almost all existing encryption algorithms.
- ii. The ECG feature distribution in the wavelet domain is studied in this study. In addition, the unequal importance in set partitioning in hierarchical trees (SPIHT) coded bits is investigated. Based on these studies, a two-rate UEP scheme is proposed. Using this proposed scheme, we can save additional 40% energy without compromising ECG transmission quality on top of the compression energy saving (using 20:1 compression rate with about 6.3% PRD).



Figure 1: Existing ECG Transmission

III. DISADVANTAGES OF EXISTING SYSTEM

Recent technological progress in wireless sensing and wearable sensors has made BASNs technology a promising solution to help us to meet this growing demand.

- i. ECG signals contain sensitive and private health information about patients, and it is required by law that this individual physiological data should be kept strictly confidential for all times.
- ii. Existing schemes uses only AES algorithm to encrypt ECG signal but there is no assurance of ECG signal security.
- iii. Key distribution is problem in existing scheme because of this Symmetric algorithm.

IV. PROPOSED ALGORITHM: SPIHT-ECC

A. SPIHT

The main purpose of compression is to represent an ECG image with the smallest possible number of bits. It can assist the transmission and processing of image. Among many medical signal sources, the compression of electrocardiogram (ECG) is in great demand. Many types of ECG recordings generate a vast amount of data. These include up to 48 hour. Halter recordings, telemetry recordings, continuous ECG performed in intensive care units and stress test ECG. With the growing use of these ECG signals to detect and diagnose heart disorders, ECG compression becomes mandatory to efficiently store and retrieve this data from medical database. Other practical importance includes transmitting real time ECG over the mobile communication network and storing patient data in a medical smart card. In this paper, we treated ECG signal as image recorded on an ECG paper. ECG paper is traditionally divided into 1mm squares. Vertically, ten blocks usually correspond to 1 mV, and on the horizontal axis, the paper speed is usually 25mm/s, which makes one block 0.04s (or 40ms). We also have "big blocks" which are 5mm on their side. Knowing the paper speed, it's easy to work out heart rate. If the number of big block is 1, the rate is 300, if it is 2, the rate is 150 and so on. Rates in between these numbers are easy to interpolate. In recent years,

wavelet based embedded image coder is quite attractive in modern applications. Wavelet transform, bit plane coding and other techniques make embedded image coders practically, which not only provide efficient compression performance, distortion scalability, resolution scalability, but the efficiency of a wavelet based compression scheme relies on the efficiency of specifying to the decoder which coefficients to quantize before which others, and of the corresponding bit allocation. Said and Pearlman developed an algorithm, called set partitioning in hierarchical trees (SPIHT) based on the same basic concepts. It was more effective in transmission of significance information to the decoder. Both the schemes relied on partial magnitude ordering of the wavelet coefficients, followed by progressive refinement, and produced embedded bit streams. The transmission of ordering information is achieved by a subset partitioning approach that is duplicated at the decoder. The refinement is based on ordered bit plane transmission of the magnitudes of the coefficients previously ascertained as significant. In this work, a low bit rate image coder of modified SPIHT algorithm without arithmetic coder has been demonstrated for High speed ECG compression. The modifications of the SPIHT compressor have been presented combining the sorting and refinement phase. With the elimination of List of Significant Pixels (LSP) and List of insignificant pixels (LIP) lists, the memory requirement has been reduced tremendously.

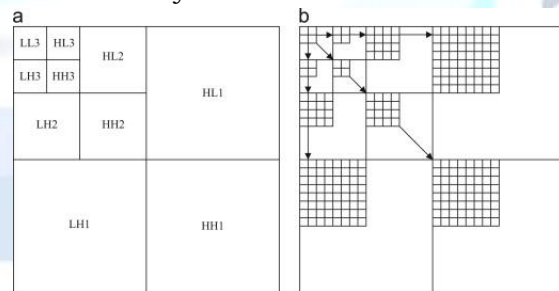


Figure 2: SPIHT structure (a, b)

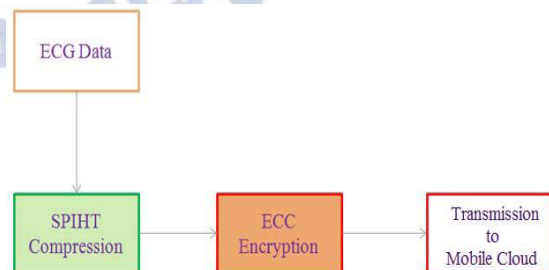


Figure 3: Proposed Security Enhanced ECG Transmission

B. Elliptic Curve Cryptography (ECC)

Elliptic curve cryptography [ECC] is a public-key cryptosystem just like RSA. Analysis of ECC with other Cryptosystems

- i. RSA – Integer Factorization
- ii. ECC - Elliptic Curve Discrete Logarithm problem

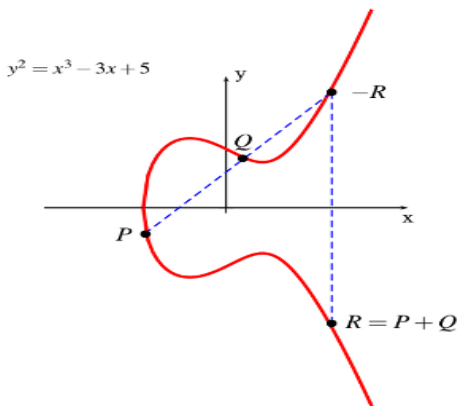


Figure 4: ECC Encryption

Elliptic curve cryptography (ECC) was proposed by Koblitz and Miller in 1985. Compared with other commonly used public key cryptosystems such as RSA and discrete logarithm, claims have been made that ECC offers a smaller key length, better security, and a smaller hardware realization than other methods. ECC is particularly suitable for embedded applications, the benefits being

- i. ECC offers the highest security per bit of any known public key cryptosystem so a smaller memory can be used
- ii. ECC hardware implementations use less transistors, as an example, a VLSI implementation of 155-bit ECC has been reported which uses only 11,000 transistors compared with an equivalent strength 512-bit RSA processor which used 50,000 transistors.
- iii. ECC is probably more secure than RSA, the largest and RSA and ECC challenges solved being 512-bit and 97-bit respectively. In cracking the 97-bit ECG problem, approximately twice the computing power of the RSA problem was used.

V. ADVANTAGES OF PROPOSED SYSTEM

The proposed scheme going to use lightweight ECC (Ecliptic Curve Cryptography) to secure the ECG Signal.

- i. ECC is best suited for energy efficient devices like wireless sensors, Mobile, etc.
- ii. MD5 algorithm going to use ensuring the security of ECG signal.
- iii. In addition, this scheme uses SPIHT for compressing the ECG signal to save energy.

- iv. Simultaneous compression and encryption will save energy and secure the signal, Its equivalent to dual encryption like security.

VI. RESULT AND COMPARATION

In this section, MATLAB simulations are conducted to evaluate the proposed ECC based encryption. In our experiments, the raw ECG data are first source encoded by SPIHT and then processed with the help of the ECC security algorithm. The SPIHT encoded bit-stream is split into equal-sized packets that are first encrypted by ECC algorithm and then signed by private key of sender, and then send to receiver. Once received by the receiver decrypted by ECC with using private key of receiver and then verified by senders public key. Instead of obtaining bit-error-rate through testing, we have done public key cryptography technique with using digital signature concepts (Figure 4,5& 6).

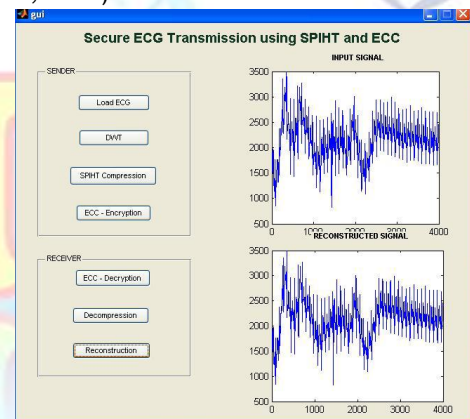


Figure 4: Proposed Mat Lab Implementation

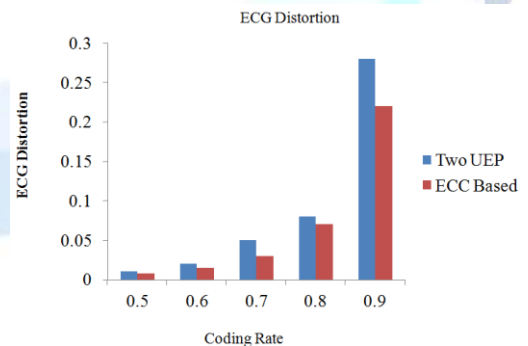


Figure 5: ECG Distortion Comparison

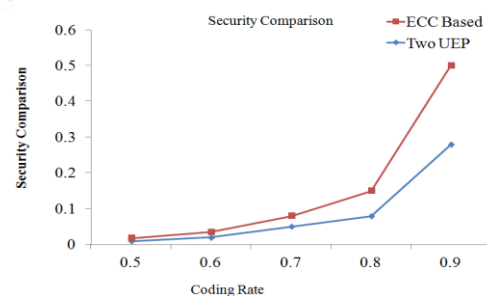


Figure 6: Security Comparison

VII. CONCLUSION

Energy saving and security are the two most critical issues for ECG transmission in BASNs. In this project, an energy efficient and lightweight secure scheme for ECG transmissions in BASNs would be presented. Characteristics of compressed ECG are extensively explored and the unequal ECG quality distribution among the output bits of the compression codec is studied. In this study, I proposed a simple and yet effective encryption scheme in which only 1% of the compressed ECG data needs to be encrypted using ECC. This ECC algorithm greatly reduces the burden of ECG encryption, while also providing a significant energy saving. This proposed simulation results showed that this scheme would be able to provide more than 40% additional energy saving at 0.099 after compression that maintains a high quality of the ECG data, while providing desired security in medical applications.

REFERENCES

- [1] A.Boskovic and M. Despotovic, "An efficient approach to ECG signal transmission via GPRS," in Proc. Int.Conf. Comput. Tool (EUROCON), 2005, vol. 1, pp. 76-79.
- [2] Adrian D. C. Chan, Mohyeldin M. Hamdy, Armin Badre and VesalBadee, "Wavelet Distance Measure for Person Identification
- [3] C. P. Wu, and C. C. J. Kuo, "Design of Integrated Multimedia Compression and Encryption Systems", IEEE Transactions on Multimedia, VOL. 7, No. 5, Oct. 2005, pp. 829-839
- [4] Chan, M. Hamdy, A. Badre, andV. Badee, "Wavelet distance measure for person identification using electrocardiograms," IEEE Trans. Instrum. Meas., vol. 57, no. 2, pp. 248-253, Feb. 2008.
- [5] DR Stinson, Cryptography, Theory and Practice, 2nd edition, Chapman & Hall, CRC Press, Boca Raton (2002).
- [6] G.H Jeong and I.S Lee, "Wavelet-based ECG compression using dynamic multi-stage vector quantization," 4th IEEE Conference on Industrial Electronics and Applications, pp.2100-2105, 2009
- [7] G.Nave and A. Cohen, "ECG compression using long-term prediction," IEEE Trans. Biomed. Eng., vol. 40, no.9, pp. 877- 885, Sep. 1993. Health Insurance Portability Accountability Act (HIPAA).
- [8] H. Wang, D. Peng, W. Wang, H. Sharif, H. H. Chen, and A.Khoynezhad, "Resource-aware secure ECG healthcare monitoring through body sensor networks," IEEE Wireless, vol. 17, no. 1, pp. 12-19, Feb. 2010.
- [9] H.Kim, Y. Kim, and H. J. Yoo, "A low cost quadratic level ECG compression algorithm and its hardware optimization for body sensor network system," in Proc.Int. Conf. Eng. Med. Biol. Soc., 2008, pp. 5490-5493.
- [10] Health Insurance Portability Accountability Act of 1996 (HIPAA), Centers for Medicare and Medicaid Services (1996)
- [11] Health Insurance Portability and Accountability Act of 1996, 104th Congress, Public Law 104-191, 1996
- [12] M. Blount et al, "Remote health-care monitoring using Personal Care Connect", IBM Systems Journal, Vol. 46, No. 1, 2007, pp. 95-113

Asymmetrical Half Bridge Flyback Converter with Wind Energy

S.Chandravadivu¹, V.Sivashankari², M.Sasikala³ & R.Raghavi⁴
^{1,2,3,4}Assistant Professor, M.A.M School of Engineering, Trichy.

Abstract--*The main aim of the project is to analyze the performance of an asymmetrical half bridge flyback converter under variation in wind speed. The wind turbine uses a permanent magnet synchronous generator to perform low speed and high speed of wind .It develops low amount of mechanical stress. As per wind speed the output power is also varied. The switching frequency is maintained as constant as 300Khz.The feedback controller is employed to provide speed control mechanism on permanent magnet brushless dc motor and it tend to achieve an high efficiency rating. The pwm technique is used to provide a gate signal for an 3phase inverter circuit. The BLDC motor speed may vary from 1500rpm to maximum 7000rpm. Simulation work is carried in MATLAB/simulink model.*

Index terms- *Wind turbine, Flyback converter, Permanent magnet synchronous generator, Feedback controller, Permanent magnet brushless dc motor.*

I.INTRODUCTION

The renewable energy sources are the biggest concern in our times. Wind power is good renewable, clean and free source of energy for power production. The Reduce dependence on fossil fuels and imported oils tend to increase use wind energy. It Reduce the emission of greenhouse gas and other pollutant. One major concern is the noise, Intermittency and variability of the wind. The resonant topologies clearly have good potential on wind power. Power generation from wind has emerged as one of the most successful programs in the renewable energy sector, and has started making meaningful contributions to the overall power requirements of some States. Wind turbines today are up to the task of producing serious amounts of electricity. Turbines vary in size from small 1 kW structures to large machines rated at 2 MW or more.

Therefore, renewable are expected to play a key role in accelerating development and sustainable growth in the second half of the next century, accounting then to 50 to 60% of the total global

energy supply. Wind energy production may, however, vary from hour to hour, just as demand from electricity customers will vary from hour to hour. Second to second or minute to minute variations in wind energy production are rarely a problem for installing wind power in a grid [1].

In wind turbine the permanent magnet synchronous generator (PMSG) is preferred because of its simpler design and it doesn't require any external magnetization. Hence PMSG excitation avoids field current supply or reactive power compensation facilities and the slip rings which are preferred on wound rotor synchronous generator or induction generator. The two mass drive train models are chosen to reduce time consumption problems and it include turbine and shaft model.

The flyback converter has special feature as it can operate at both buck-boost mode with constant switching frequency as 300 KHz and variable duty cycle is possible. The design and test of solid state lamp driver with asymmetrical half bridge flyback converter had been described with large input voltage variations in input with higher efficiency without any harmonics [2] but it has no improvement on output power and it can be applicable for low power applications. The integrated buck-boost converter [3] is more efficient as compared with pwm solution but there is the current limiting device at input which increases the circuit complexity. The buck converter(step down) are used at led replacement lamps since its used for charging the batteries but the current ripples are high [4],it was an transformer less design and provides an surge protection to an equipment connected to it.

The LLC converter [4] can perform both buck and boost mode operation and are most widely used to control the wide range of output power with only narrow variation in operating frequency, but it's not easy to optimize under large input voltage variations and require an variable frequency control. The steady state analysis of LLC converter [5] had higher transformer turns ratio and there is a semi empirical approach is necessary to perform an analytical function. The series resonant topologies are proposed [6] with led lamp driver hence it requires a high magnetizing inductance which

negatively impacts on magnetic component design (relevant number of primary turns, high volume occupation).

At final analysis the asymmetrical half bridge flyback converter is ideal to provide good properties of series resonant topologies with addition of fixed frequency and variable duty cycle. This paper is organized with following section such as flyback design, wind turbine design analysis, feedback technique with PID controller and a three phase inverter with simulation analysis.

II.AHB FLYBACK CONVERTER

The operation of flyback converter is briefly reviewed in fig1 it represents the schematic diagram of this paper. Hence input voltage from wind turbine is fed to an uncontrolled rectifier; pitch angle control, two mass drive train models and a permanent magnet synchronous generator are used to afford essential input supply from wind energy.

The flyback converter can be operated at two types of mode as continuous and discontinuous .the continuous mode has drawback as switch is turned on before secondary current falls to zero so there is overlapping occurs in addition the feedback control is so difficult to execute .In order to overcome the drawbacks the discontinuous mode is chosen so the secondary current becomes zero after a time interval switch is turned on and it has easy implementation of feedback control.

With the design choice, the typical converter waveforms are shown in fig 2.Hence it neglects the short intervals corresponding to the charge and discharge of switch output capacitance, each switching period can be subdivided into up to three modes. There is no need of blocking capacitor because of an single controllable switch S1.the direct current flows at an output side and its easy way to operate an dc motor appliances with reduced harmonic order. The harmonic standard as EN6100-3-2 is chosen on converter to reduce voltage ripples on the dc-link.

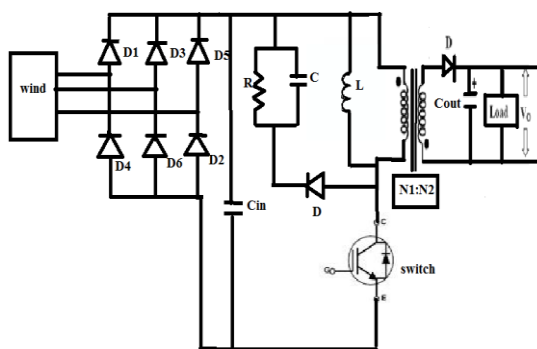


Fig 1.schematic diagram of proposed circuit

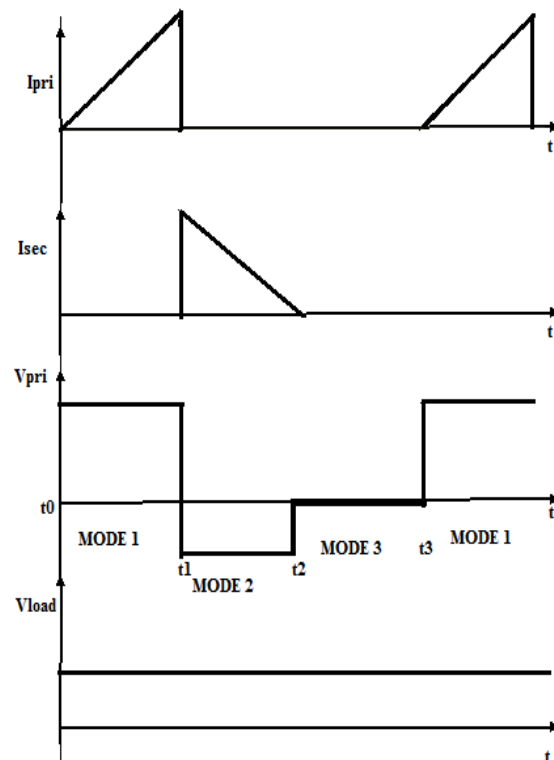


Fig 2. waveforms for modes of operation for a flyback converter

Model1:

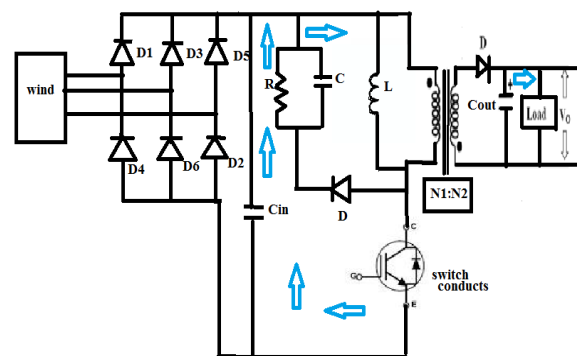


Fig 3. Operating mode 1

During the time interval t_0-t_1 switch S1 is turned on and the primary winding of transformer get connected to input supply. Diode D_r at output side becomes reverse biased and the primary current rises linearly. Diode at input becomes reverse biased and snubber capacitor becomes charged. The output capacitor discharges the stored energy for continuous regulation of load.

$$V_{in} = L_{pri} \times \frac{d}{dt} i_{pri} \quad (1)$$

At the end of mode 1, the magnetic field energy rises in the primary winding as $(1/2) L_{pri} I_p^2$.

And the primary winding voltage and secondary winding voltage are (2) and (3).

$$V_{pri} = V_{in} \quad (2)$$

$$V_{sec} = V_{in} \times \left(\frac{N_2}{N_1} \right) \quad (3)$$

Mode2:

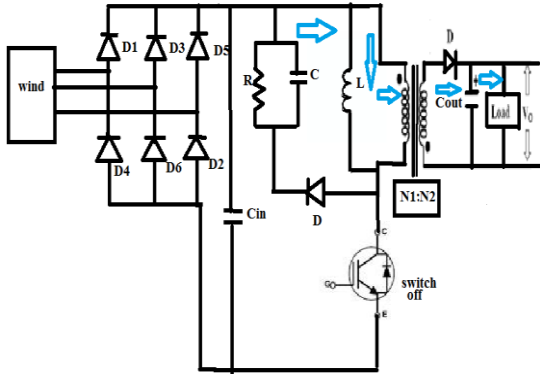


Fig 4. Operating mode 2

During t_1 - t_2 time interval the switch S1 is turned off and the voltage polarities across the primary winding becomes reversed. Diode D becomes forward biased and snubber capacitor starts to dissipate at slow rate because of parallel connection of snubber resistor. Diode Dr at output side is forward biased and the supply current to load, the output capacitor C0 gets charged. At the end of this mode the complete transfer of magnetic field to the output is done and the secondary winding emf as well the current falls to zero. The diode Dr Stops conducting. At the end of mode 2 the primary winding and secondary winding voltage are (4) and (5).

$$V_{Pri} = V_0 \times \left(\frac{N_1}{N_2} \right) \quad (4)$$

$$V_{sec} = V_0 \quad (5)$$

Mode3:

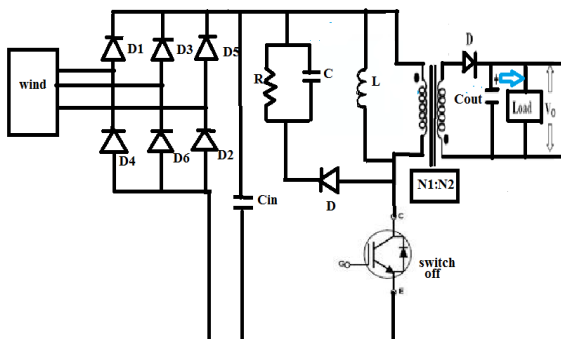


Fig 5. Operating mode 3

During the time interval t_2 - t_3 the switch S1 still at turned off condition and the diode Dr is also at zero conducting state. The output capacitor however discharges the energy to supply

uninterrupted voltage at the load. This method then again follows the 1st mode.

III.AHB FLYBACK DESIGN PROCEDURE

The typical specification of an asymmetrical half bridge flyback converter with BLDC motor as shown in Table 1. The switching frequency of a soft switch IGBT is set to 300 kHz. The proper design of snubber results in high reliability, high efficiency and low EMI. The switching stresses are high because of parasitic inductance. To suppress the peak voltage the typical RC snubber is attached and the snubber capacitor must be small enough as 50uf in order to keep a power dissipation of the resistor to a minimum.

Table 1
Converter specifications

Input voltage range from wind energy, V_{in}	240V-270V
Permanent magnet BLDC motor speed	1500-7000 rpm
Output power	>200 watts
Output current, I_o	3A
Efficiency	>90%

A. Transformer Design

In designing the isolation transformer for the flyback converter, one needs to consider the worst condition as mode 3. The minimum input voltage and maximum duty cycle (d_{max}) is taken with an assumption of voltage balance across magnetizing inductance (L_m), it gives the following expressions:

$$V_m(t) = \frac{(1-d_{max})V_{in min}}{1+\lambda} d_{max} T_s - \frac{V_0}{n_{21}} (1 - d_{max}) T_s = 0 \quad (6)$$

$$M_{max} = \frac{V_0}{V_{in min}} = \frac{n_{21}}{1+\lambda} d_{max} \quad (7)$$

The magnetizing current peak and valley values are expressed as

$$I_{pk} = I_m + \frac{V_0}{2n_{21}L_m f_s} (1 - d_{max}) = n_{21} I_0 \left(1 + \frac{1-d_{max}}{\gamma} \right) \quad (8)$$

$$I_{vl} = I_m - \frac{V_0}{2n_{21}L_m f_s} (1 - d_{max}) = n_{21} I_0 \left(1 - \frac{1-d_{max}}{\gamma} \right) \quad (9)$$

Where $\gamma = 2 \frac{L_m f_s}{R_0} n_{21}^2$ is a dimensional parameter, n_{21} is the transformer ratio and T_s is the sampling time period.

B. PWM design of three phase inverter

For higher switching frequency, the pwn inverter is considered as the voltage source inverter. SPWM are applied to inverter in order to obtain sinusoidal output voltage with reduced harmonics. The three-phase switching state functions S_a, S_b, S_c of the inverter are used to calculate the line output voltage of PWM inverter.

$$[U_{AB} \ U_{BC} \ U_{CA}]^T = [T_{AV} \ T_{BV} \ T_{CV}]^T U_{dc} \quad (10)$$

Where,

$$\begin{bmatrix} T_{AV} \\ T_{BV} \\ T_{CV} \end{bmatrix} = \frac{1}{2} \begin{bmatrix} 1 & -1 & 0 \\ 0 & 1 & -1 \\ -1 & 0 & 1 \end{bmatrix} \begin{bmatrix} S_a \\ S_b \\ S_c \end{bmatrix} \quad (11)$$

These are the switching values for the gate pulses of three phase inverter.

IV. CONTROL STRATEGY

The speed control mechanism of BLDC motor is achieved by the closed loop method .in closed loop technique we prefer a feedback type to achieve an high efficiency rate with reduced distortion rate. The PID controller is used for fast response, high stability and zero steady state error. The transfer function of PID controller as expressed

$$PID(s) = K_p + \frac{K_i}{s} + sK_d \quad (12)$$

From the PID controller the comparator is used to calculate the pulse signal for an soft switch.the values of PID controller as

$$K_p = 0.1$$

$$K_i = 0.001$$

$$K_d = 0$$

V. SIMULATION RESULTS

The AHB flyback converter is analyzed and experimental results are obtained through a matlab tool.

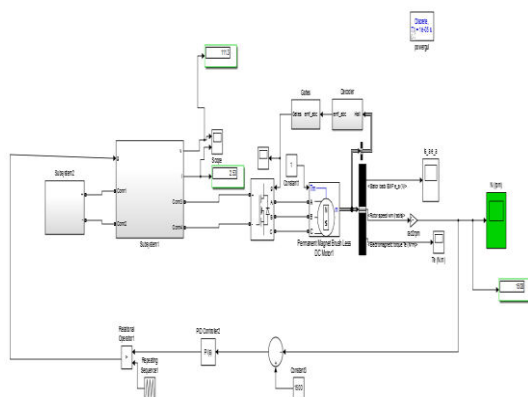


Fig 6 .Overall simulation of proposed circuit.

The source current and source voltage are shown in fig 8.the source voltage is rectified by an uncontrolled diode bridge rectifier to obtain an direct current and it's supplied to an flyback converter circuit.the gate pulses are generated through a feedback control mechanism for an converter switch. The gate pulse generation is shown in fig 7.

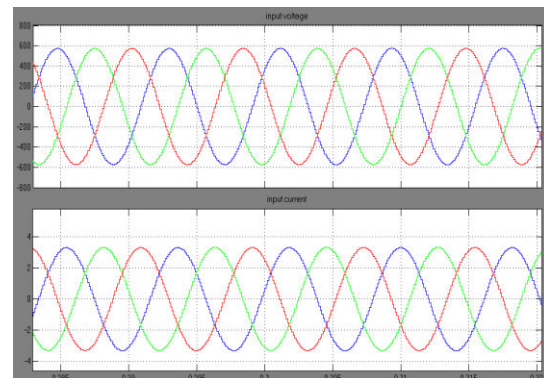


Fig 7.The source voltage and source current from the wind energy.

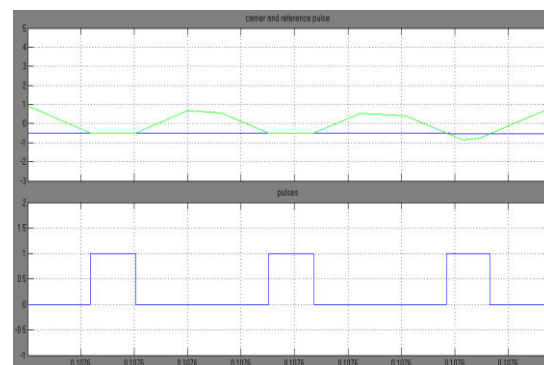


Fig 8 comparison of actual signal and reference signal to obtain pulses for converter switch S1.



Fig 9. pulses of three phase inverter by an SPWM technique

The speed of permanent magnet BLDC motor obtained from flyback converter is shown in fig 7.for a constant 1500 the speed rate as 1495-

1505 rpm is achieved. The torque has been calculated with an stator emf current from the BLDC Motor

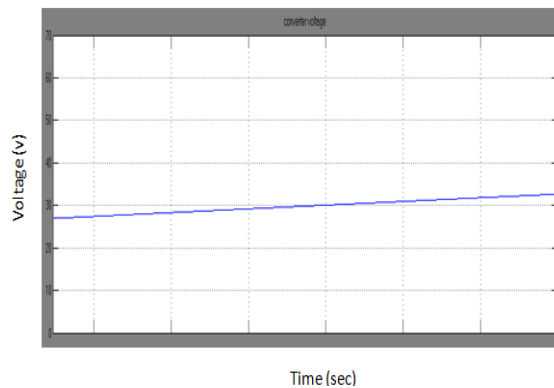


Fig 10. Flyback converter voltage

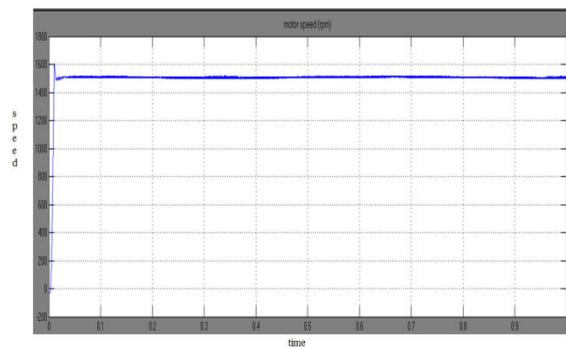
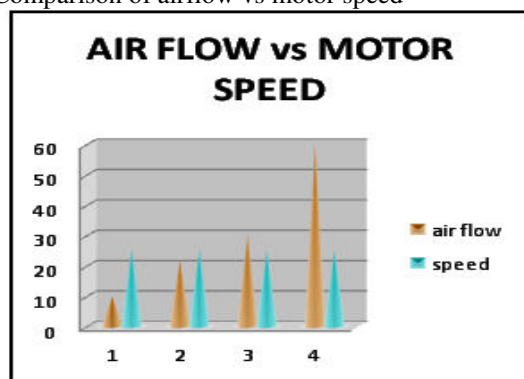


Fig 11. The speed of BLDC motor that ranges from 1495-1510 rpm

Finally converter efficiency is calculated based on the input and output power relation. It's nearly above 90%.

Comparison of airflow vs motor speed



Air flow	Motor speed(rps)
10	25.2
22	25.13
30	25.11
60	25.15

Fig 12.comparison of wind flow and BLDC motor speed

VI. CONCLUSION

The paper presents the application of the asymmetrical half bridge (AHB) flyback converter as a wind energy power for high speed BLDC motor. Based on the advantage of discontinuous conduction mode the converter analysis performed for high frequency operation.

The results of simulation models are tested to confirm the good properties of the circuit and to adopt the model to run a various dc motor with certain specification.

References

- [1] Shuhui Li, Timothy A. Haskew, Richard P. Swatloski and William Gathings senior member "Optimal And Direct-Current Vector Control Of Direct-Driven PMSG Wind Turbines" *IEEE TRANS, VOL. 27, NO. 5, MAY 2012*
- [2] Driver S. Buso, Member, IEEE, G. Spiazzi, Member, IEEE, and F. Sichirollo Member, "Study of the Asymmetrical Half Bridge Flyback Converter as an Effective Line Fed Solid State Lamp" *IEEE- TRANS -2014*.
- [3]J.M. Alonso, J. Vina, D.G. Vaquero, G. Martinez, R. Osorio, "Analysis and Design of the Integrated Double Buck–Boost Converter as a High- Power-Factor Driver for Power-LED Lamps," *IEEE Trans. Ind.Electron., Vol. 59, No. 4, pp. 1689–1697, Apr 2012*.
- [4]Q. Xiaohui, S. Wong, C. K. Tse, "Resonance-Assisted Buck Converter for Offline Driving of Power LED Replacement Lamps," *IEEE Trans.Power Electron., Vol. 26, No. 2, pp. 532–540, Feb. 2011*.
- [5] G. Sauerländer, D. Hente, H. Radermacher, E. Waffenschmidt, J. Jacobs, "Driver Electronics for LEDs," IEEE Industry Application Society Annual Meeting (IAS), 2006, pp. 2621–2626.
- [6] C. Adragna, S. De Simone, C. Spini, "A Design Metodology for LLC Resonant Converters Based on Inspection of Resonant Tank Currents," IEEE Applied Power Electronics Conf. (APEC), February 2008, pp. 1361–1367.
- [7] W. Y. Choi, J. M. Kwon, B. H. Kwon, "Efficient LED Back-light Power Supply for Liquid-Crystal Display," IET Electric Power Applications., Vol. 1, 2007, pp. 133–142.

[8] T.-F. Wu, J.-C. Hung, S.-Y. Tseng, and Y.-M. Chen, "A Single-Stage Fast Regulator With PFC Based on an Asymmetrical Half-Bridge Topology," *IEEE Trans. Power Electron.*, Vol. 52, No. 1, pp. 139–150, February 2005

[9] J.F. Lazar, R. Martinelli, "Steady-State Analysis of the LLC Series Resonant Converter," *IEEE Applied Power Electronics Conf. (APEC)*, 2001, pp. 728–735

[10] R. Oruganti, P. C. Heng, J. T. Kian Guan, L. A. Choy, "Soft-Switched DC/DC Converter with PWM Control," *IEEE Trans. Power Electron.*, Vol. 13, No. 1, pp. 102–114, January 1998.



International Journal of Advance Engineering and Research Development

National Conference On Nanomaterials, (NCN-2017)

Volume 4, Special Issue 6, Dec.-2017 (UGC Approved)

Effect of pH on Thermoelectric Oxide $\text{Ca}_3\text{Co}_4\text{O}_9$

S. Berbeth Mary¹, D. Edward Christy², A. Panithra Amuthini¹, A. Leo Rajesh^{1*}

¹Department of Physics, St. Joseph's College (Autonomous), Tiruchirappalli-620 002, Tamil Nadu, India.

²Research Scholar, Research and Development Centre, Bharathiyar University, Coimbatore – 641046, Tamil Nadu, India.

Abstract The misfit layered cobalt oxide $\text{Ca}_3\text{Co}_4\text{O}_9$ is a promising thermoelectric material prepared through different potential of hydrogen (pH) ranging from 8 – 10 by citric acid complexing coupled with hydrothermal method by varying the pH level of the solution followed by annealing at 800°C. The effect of PH variation on the structural, morphological, compositional and optical properties of $\text{Ca}_3\text{Co}_4\text{O}_9$ nanoparticles were characterized by using X - ray diffractometer, Scanning Electron Microscopy, Fourier Transform Infrared Spectroscopy and UV-Visible Spectroscopy. Identical crystal phases were obtained from XRD analysis and the average crystallite size decreased with increasing pH level, it was found to be 78, 61, 56 nm by using Scherrer formula. Morphological studies confirmed the increment of crystallite size due to rapid nucleation of larger pH value and the porous nature of the samples also found. Strong peak identified at 564 cm^{-1} revealed the formation of metal oxides by FTIR spectroscopy. The results of the optical absorption studies showed that the indirect band gap energy values of the calcium cobaltite nanoparticles decreased from 3.22 eV to 2.41 eV with increasing pH values

Key words: layered cobaltite, potential of hydrogen, thermoelectric oxide, rapid nucleation

1. Introduction

The development of environmental friendly and cost effective power sources overcomes the problems of energy crises and global warming. Thermoelectric devices can directly convert waste heat into electricity. This technology can recover natural energy such as solar and geothermal energy, but also waste heat from industries. These devices can operate for longer durations without maintenance due to its non moving parts and it is free from global warming gas emission. The efficiency of a thermoelectric material depends on the thermoelectric figure of merit ZT [1-2]. Efficient thermoelectric materials must show high thermo power (S) to obtain a high voltage and electrical conductivity (σ) to reduce the internal resistance of the material combined with a low thermal conductivity (κ) to introduce the large temperature difference between both ends of the material. These three parameters S, σ , κ depends on each other since they are closely related to the scattering of charge carriers and lattice vibrations. The electronic, magnetic and electromagnetic properties of these oxides depend strongly on crystallite size and the oxidation state of the metal centers. Modified band structure can enhance the electrical conductivity (σ) and Seebeck coefficient (S) at the same time nanostructure reduces the thermal conductivity by increasing the phonon scattering consequently ZT gets improved. So the addition of dopants and substitutions can increase ZT values [3-8]. Intermetallics, Skutterudites, half-Heusler and chalcogenide compounds are some of the promising thermoelectric materials. However, these materials are not attractive when operating at higher temperatures due to decomposing, vaporizing and melting nature at higher temperatures. But metal oxides have attracted much attention at higher temperature on the basis of their potential advantages over heavy metallic alloys. Due to high thermal and chemical stability in air, the metal oxides are widely used as thermoelectric materials at higher temperatures [9-11]. The structure of $\text{Ca}_3\text{Co}_4\text{O}_9$ is similar to NaCo_2O_4 , with the misfit structure of CdI_2 - type CoO_2 layers stacked up with triple rock salt - type layers alternately along the c-axis. These two kinds of layers have similar a, c and β lattice parameters but different b parameter. To accentuate the inadequate nature of the structure, $\text{Ca}_3\text{Co}_4\text{O}_9$ has two monoclinic subsystems, $[\text{Ca}_2\text{CoO}_3]_{(b_2/b_1)} [\text{CoO}_2]$, where b_1 and b_2 are two different lattice parameters of the rock salt system and the CoO_2 subsystem respectively. The edge sharing CoO_2 octahedral layers are charge reservoir to supply charge carriers into the CoO_2 layers [12-14].

Citric acid complexing with hydrothermal method is very simple and easy to prepare $\text{Ca}_3\text{Co}_4\text{O}_9$ (CCO) nanoparticles. This method is prominently and most effective because of compositional modification, microstructure control using capping chelating agents, doping can be controlled. The amount of H^+ and OH^- ions decides the morphology by influencing the polymerization of the metal oxygen bonds during sol formation while the hydrolysis and condensation of the solution affected by the pH during gel formation. The phase formation, particle size and morphology of the structure during solution method are the consequences of varying pH of the solution [15]. This research article reports the influence of pH on

structural, morphological, compositional and optical properties of $\text{Ca}_3\text{Co}_4\text{O}_9$ by hydrothermal method for thermoelectric applications.

2. Materials and Methods

AR Grade Calcium nitrate tetrahydrate, cobalt nitrate hexahydrate, citric acid monohydrate and ammonia solution were used without further purification. Calcium Cobalt Oxide (CCO) nanopowders were prepared using the citric acid complexing coupled with hydrothermal method. Stoichiometric amounts of nitrates of calcium, cobalt and equal amount of citric acid were dissolved in deionized water so that the metal ions can be consistently complexed together. A certain amount of ammonia solution was added drop wise to the above mixed solution and part of ammonia added to defuse the unreacted citric acid. pH value of the solution was adjusted to 8, 9, and 10 respectively by adding ammonia solution, hence a sol was obtained and then this sol was transferred to a 150 ml autoclave and the autoclave was placed into an oven for hydrothermal treatment at 200 °C for 20h. The obtained precursors were in turn filtered, washed with deionized water and ethanol and then dried at 120 °C over night. The dried powders were calcined in air in a furnace at 800 °C for 4h [16].

Powder X-ray diffraction pattern has been recorded in order to identify the Phase and the crystal structure, using a XRD diffractometer (D8 Advanced) with $\text{Cu K}\alpha$ radiation. Microstructural observations were performed on powder samples, using scanning electron microscopy (SEM, JEOL JSM-6700F) at 20 kV and images were obtained. The composition was characterized by FTIR spectrophotometer in the range of 4000-400 cm^{-1} . The optical property of the CCO nanoparticles and band gap was determined by using a Lambda 35 UV-vis spectrometer.

3. Results and discussion

X-ray diffraction (XRD) patterns of the CCO samples at selected pH values 8, 9 and 10 are shown in Fig. 1. Amorphous nature was perceived for the sample prepared at pH 8 and the pattern synthesized at pH 9 agreed well with that of the $\text{Ca}_3\text{Co}_4\text{O}_9$ (JCPDS card no 23-0110) while the sample synthesized at pH 10 concurred with $\text{Ca}_9\text{Co}_{12}\text{O}_{28}$ (JCPDS card no 21-0139). These two substances were identical in crystal phases, whereas oxygen content is differs to some extent. The composition $\text{Ca}_9\text{Co}_{12}\text{O}_{28}$ varied by one oxygen atom, results higher oxidation state for Co [17]. This may be attributable to the reduction of more Co cations from higher to lower valences accompanied by increased ionic radius and the formation of more oxygen vacancies since the average oxidation state for Co ions in $\text{Ca}_9\text{Co}_{12}\text{O}_{28}$ is higher than that of $\text{Ca}_3\text{Co}_4\text{O}_9$ [18]. The average crystallite size of the synthesized samples was calculated from the major diffraction peaks using the Scherrer formula $D = K\lambda / \beta \cos\theta$, Where K is a constant ($K = 0.94$), λ is the wavelength (1.5418 Å), θ is the Bragg angle and β is full width half maximum that is, broadening due to the crystalline dimensions [19]. The average particle size of the prepared samples at pH 8, pH 9 and pH 10 were calculated as 78, 61 and 56 nm respectively. The presence of the $\text{Ca}_3\text{Co}_4\text{O}_9$ phase prepared at pH 9 had a strong influence on the electrical and thermoelectric properties of CCO nanoparticles [20]. The surface to volume ratio of nanoparticles gradually increased with decreasing particle size has been observed in metal oxides with perovskite structure as of $\text{Ca}_3\text{Co}_4\text{O}_9$.

Fig. 2 signifies the surface morphology of $\text{Ca}_3\text{Co}_4\text{O}_9$ nanoparticles revealed by SEM analysis. It can be seen that the samples were composed of rod-like grains with different sizes. The grains demonstrated randomly oriented structure as expected for the typical structure of $\text{Ca}_3\text{Co}_4\text{O}_9$ ceramic materials. The relatively high degree of porosity nature was observed for the sample prepared at pH 9 due to the solid state synthetic methods. It can be seen from 3(c) that the plate like grains were more pronounced for the sample prepared at pH 10 because of rapid nucleation. Enhanced Seebeck effect and low thermal conductivity observed for the porous nanograined materials henceforth the sample prepared at pH 9 will be optimized for thermoelectric application due to its $\text{Ca}_3\text{Co}_4\text{O}_9$ phase purity and porous nature of the sample [21].

The formation of $\text{Ca}_3\text{Co}_4\text{O}_9$ phase from the precursor was further ascertained by FTIR spectroscopy as shown in fig 3. The band around 3400 cm^{-1} represented the O-H mode of vibration and the peak broadened when there was an increment in the pH level of the solution and its movement played an important role in the structure formation where the phase changes from $\text{Ca}_3\text{Co}_4\text{O}_9$ to $\text{Ca}_9\text{Co}_{12}\text{O}_{28}$. The strong asymmetric stretching mode of vibration of C=O was observed at around 1500 cm^{-1} . As the pH value increased by the addition of alkali ammonia solution, the vibration peak of C=O shifted from up and down which implied the phase change. The symmetric stretching occurred at 850 cm^{-1} confirmed the vibration of NO_3^{-1} ions. The standard peak of CCO nanoparticles was observed at 564 cm^{-1} [22-24].

The optical properties of $\text{Ca}_3\text{Co}_4\text{O}_9$ nanoparticles were characterized by UV-vis spectroscopy. Fig.4 (a) shows the UV-visible spectrum of $\text{Ca}_3\text{Co}_4\text{O}_9$ nanoparticles. The optical band gap of $\text{Ca}_3\text{Co}_4\text{O}_9$ was strongly influenced by the size, shape, and dimension of materials. There absorption peaks in the spectrum at 208, 247 and 277 nm confirmed the formation of CCO nanoparticles at different pH values. The band gap E_g can be calculated from the equation $(\alpha h\nu)^n = B (h\nu - E_g)$, Where α is the absorption coefficient, $h\nu$ is the photon energy, B is constant, and n can be either 1/2 or 2 for indirect and direct transition respectively [25]. From the $(\alpha h\nu)^{1/2}$ versus $h\nu$ curve, the band gap was found to be 3.22, 2.86, 2.41 eV respectively. The determined band gap value showed that larger band gap for the lower pH value [26].

4. Conclusion

Ca₃Co₄O₉ nanoparticles have been synthesized by using citric acid complexing coupled with hydrothermal method at different pH levels. Amorphous, good and low crystalline fine powders were achieved with identical phase of Ca₃Co₄O₉ perovskite oxide nanoparticles and there was a slight change in composition due to the different oxidation state of Co cation. pH variation altered the crystallite size as it reduced when pH increased. SEM Micrograph showed well dispersed and porosity nature sample. The peak at 564 cm⁻¹ established the formation of Ca₃Co₄O₉ phase. The estimated band gap reduced from 3.22 to 2.41 eV while the pH of the solution increased. The Ca₃Co₄O₉ nanoparticles prepared at pH 9 will be optimum for thermoelectric applications.

References

1. J. P. Heremans, V. Jovovtha, E. S. Toberer, A. Saramat, K. Kurosaki, A. Charoenphakdee, S. Yamanaka, G. Snyder, *J.Sci.*, 321,554 (2008)
2. J. Pei, G. Chen, N. Zhou, D. Q. Lu, F. Xiao, *Physica B.*, 406, 571 (2011)
3. S. Malkhandi, B. Yang, A. K. Manohar, A. Manivannan, G. K. Surya Prakash, S.R. Narayanan, *J. Phys. Chem. Lett.*, 3, 967 (2012)
4. C. Gayner, K. K. Kar, *Prog. Mater. Sci.*, 83, 330 (2016)
5. S. Walia, S. Balendran, H. Nili, S. Zhuiykov, G. Rosengarten, Q. H. Wang, M. Bhaskaran, S. Sriram, M. S. Strano, K. Kalanta/r Zadeh, *Prog. Mater. Sci.*, 58, 1143 (2013)
6. W. Liu, Q. Jie, H. Kim, Z. Ren, *Acta Mater.*, 87, 357 (2015)
7. F. Delorme, C. Fernandez Martin, P. Marudhachalam, O. Ovono Ovono, G. Guzman, *J. Alloys. Compd.*, 509, 2311 (2011)
8. M. Ohtaki, H. Koga, T. Tokunga, K. Eguchi, H. Arai, *J. Solid State Chem.*, 120, 105 (1995)
9. G. Mahan, B. Sales, *J. Phys. Today.*, 50, 42 (1997)
10. K. F. Hsu, S. Loo, F. Guo, W. Chen, J. S. Dyck, C. Uher, T. Hogen, E. K. Polychroniadis, M. G. Kanatzidis, *Science.*, 303, 818 (2004)
11. B. Abeles, R. Cohen, *J. Appl. Phys.*, 35, 247 (1964)
12. Hirmochi Ohta, Kenji Sugiura, Kunihito Koumoto, *Inorg. Chem.*, 47, 8429 (2008)
13. Yang Wang, Yu Sui, Fang Li, Luxiang Xu, Xianjie Wang, Wenhui Su, Xiaoyang Liu, *J. Nanoen.*, 1, 456 (2012)
14. W. Koshibae, K. Tsutsui, S. Maekawa, *Phys. Rev B.*, 62, 6869 (2000)
15. Rizwan Wahab, Young soon Kim, Hyung Shik Shin, *Mater. Trans.*, 50, 2092 (2009)
16. Jianrong Niu, Jiguang Deng, Wei Liu, Lei Zhang, Guozhi Wang, Hongxing Dai, Hong He, Xuehong Zi, *catal. Today.*, 126, 420 (2007)
17. H. Tran, T. Metha, M. Zellar, R. H. Jarman, *Mater. Sci. Bull.*, 48, 2450 (2013)
18. K. T. Lee, A. Manthiram, *Chem. Mat.*, 18, 1621 (2012)
19. S. Enzo, G. Fagherazzi, A. Benedetti, S. Polizzi, *J. Appl. Cryst.*, 21 536 (1988)
20. Masahiro Tahashi, Kiyoshi Ogawa, Makoto Takahashi, Hideo Goto, *J. Cera. Soc. Jap.*, 121, 444 (2013)
21. Hohyun Lee, Daryoosh Vasahee, Wang DZ, Mildred S Dresselhaus, Ren ZF, Gang Chen, *J. Appl. Phys.*, 107, 94308 (2010)
22. Rizwan Wahab, Young-Soon Kim, Hyung-Shik Shin, *Mater. Trans.*, 50, 2092 (2009)
23. R. Wahab, S. G. Ansari, H. K. Seo, Y. S. Kim, E. K. Suh, H. S. Shin, *Solid State Sci.*, 11, 439 (2009)
24. L. Wu, Y. Wu, L. Wei, *Phys. E.*, 28, 76 (2005)
25. M. C. Santhosh Kumar, B. Pradeep, *Indian J. Phys.*, 85, 401 (2011)
26. Mohamed Hamid Elsheikh, Dhafer Abdulameer Ahnawah, Mohd Faizul Mohd Sabri, Shuhana Binti Mohd Said, Masjuki Haji Hassan, Mohammed Bashir Ali Basher, Mahazani Mohamad, *Ren. Sust. Ener. Rews.*, 30, 337 (2014)

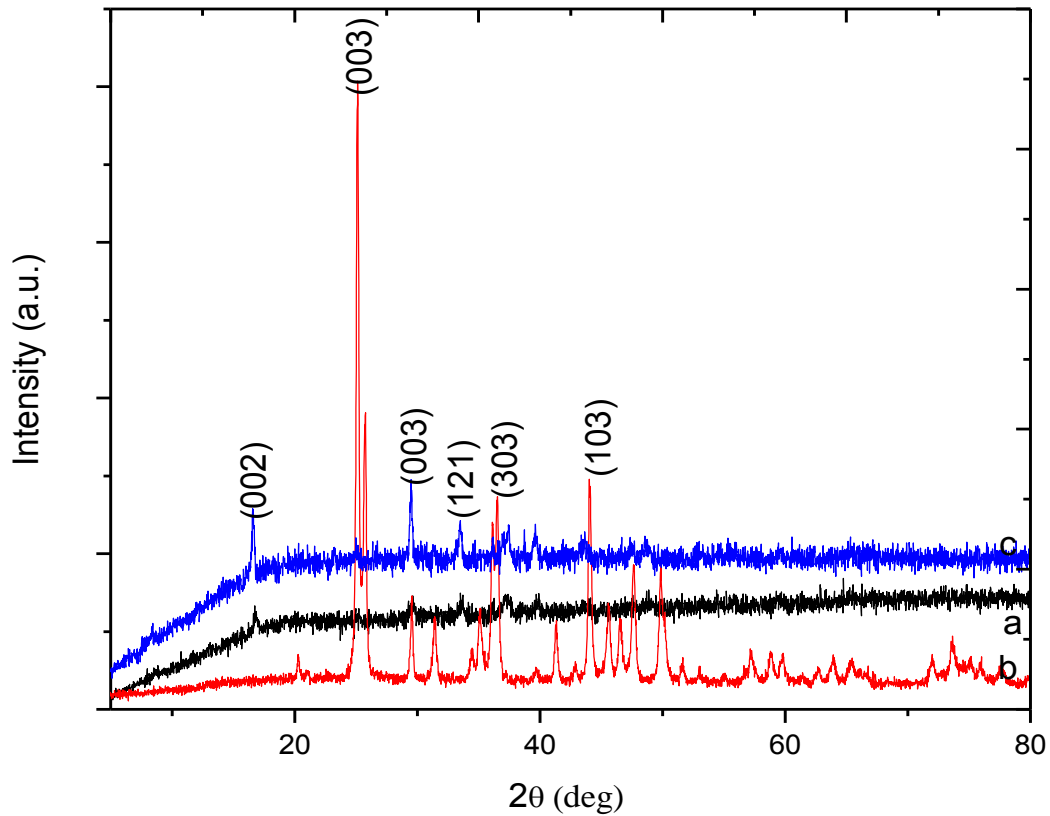


Fig.1. Powder XRD Patterns for $\text{Ca}_3\text{Co}_4\text{O}_9$ nanoparticles at (a) pH 8 (b) pH 9 (c) pH 10

Effect of pH on Thermoelectric Oxide $\text{Ca}_3\text{Co}_4\text{O}_9$
S. Berbeth Mary¹, D. Edward Christy², A. Panithra Amuthini¹, A. Leo Rajesh^{1*}

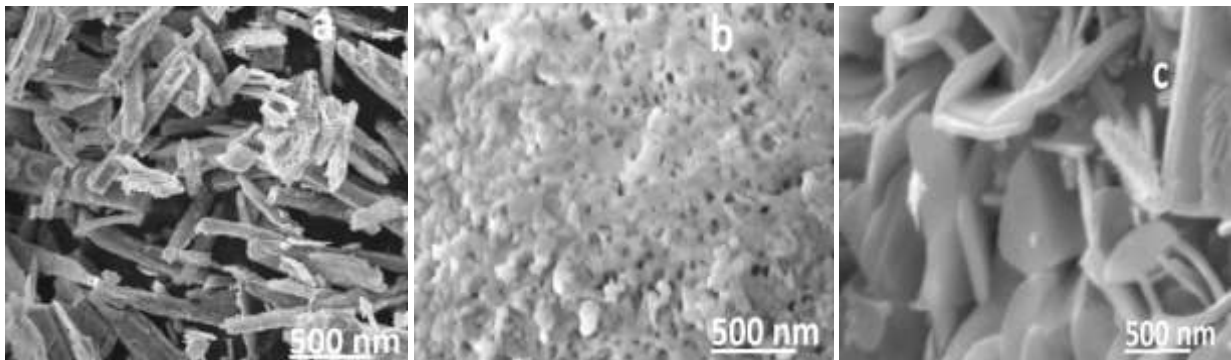


Fig.2. SEM Micrograph of $\text{Ca}_3\text{Co}_4\text{O}_9$ nanoparticles at (a) pH 8 (b) pH 9 (c) pH 10

Effect of pH on Thermoelectric Oxide $\text{Ca}_3\text{Co}_4\text{O}_9$
S. Berbeth Mary¹, D. Edward Christy², A. Panithra Amuthini¹, A. Leo Rajesh^{1*}

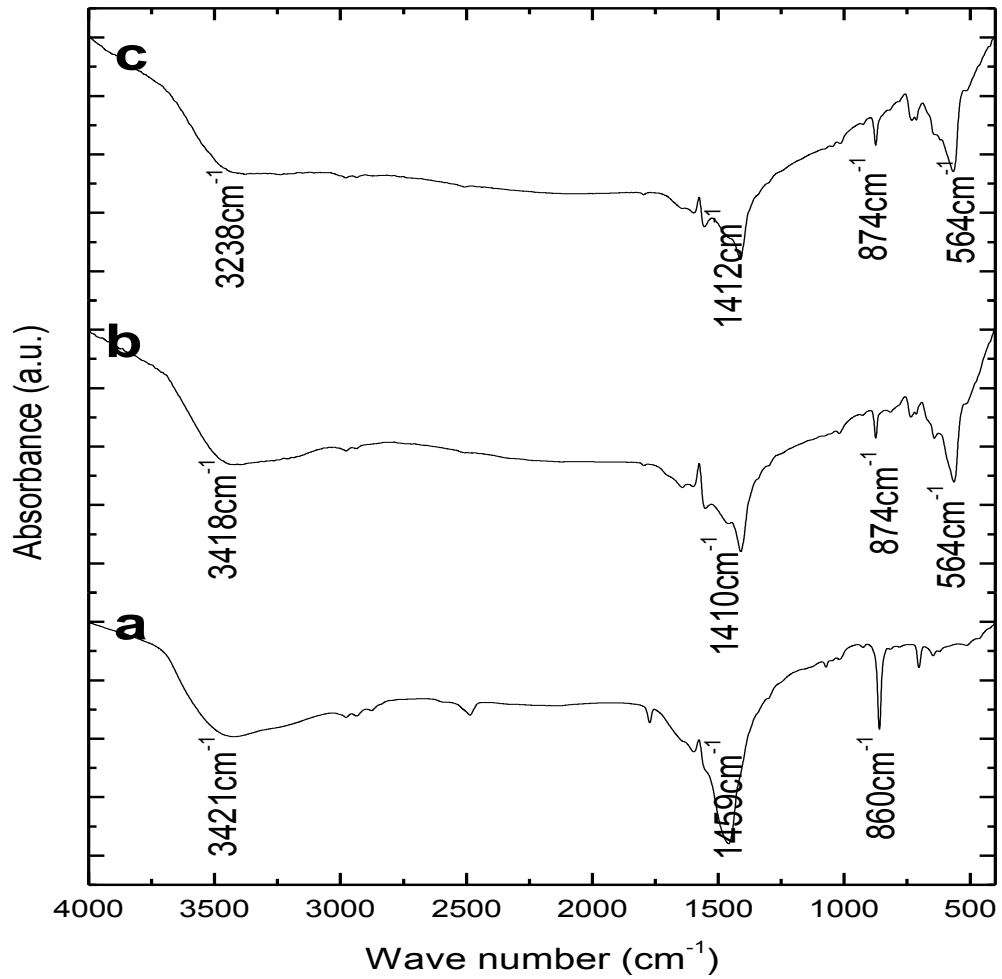
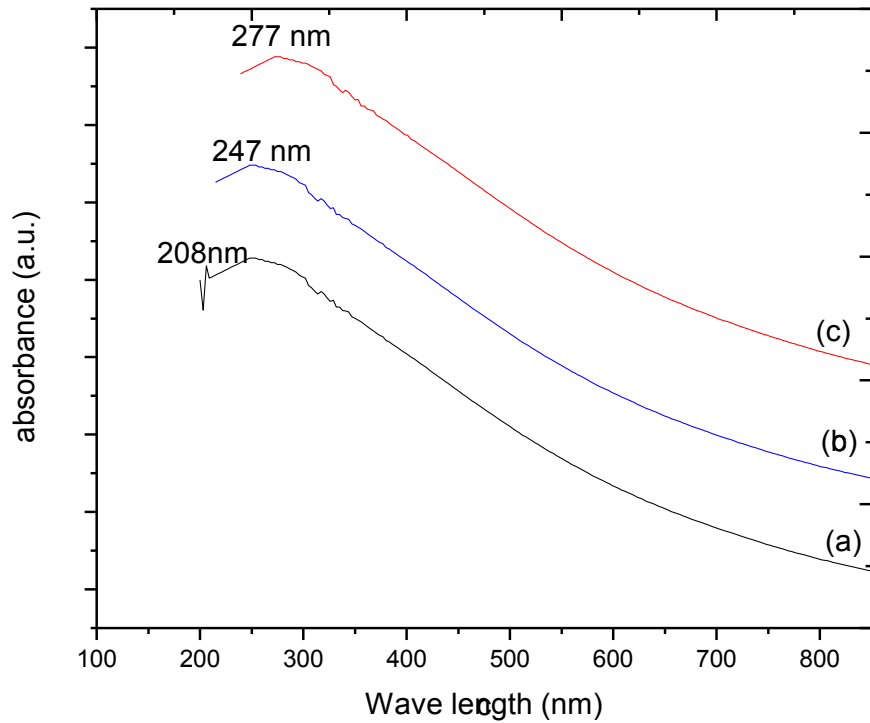


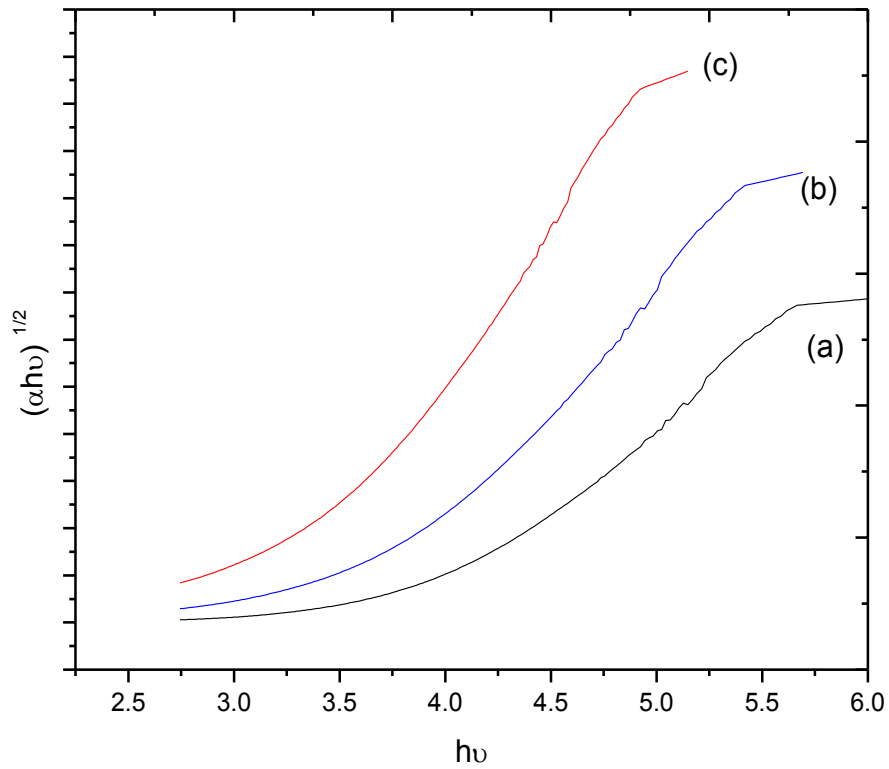
Fig.3. FTIR Spectra of Ca₃Co₄O₉ nanoparticles at (a) pH 8 (b) pH 9 (c) pH 10

Effect of pH on Thermoelectric Oxide Ca₃Co₄O₉
S. Berbeth Mary¹, D. Edward Christy² A. Panithra Amuthini¹, A. Leo Rajesh^{1*}



4 (a)

Effect of pH on Thermoelectric Oxide $\text{Ca}_3\text{Co}_4\text{O}_9$
S. Berbeth Mary¹, D. Edward Christy² A. Panithra Amuthini¹, A. Leo Rajesh^{1*}



4(b)
Fig. 4(a) UV –Vis spectra of $\text{Ca}_3\text{Co}_4\text{O}_9$ Nanoparticle 4(b) Band gap determination

Effect of pH on Thermoelectric Oxide $\text{Ca}_3\text{Co}_4\text{O}_9$
S. Berbeth Mary¹, D. Edward Christy² A. Panithra Amuthini¹, A. Leo Rajesh^{1*}

**Hydrothermal Synthesis of Perovskite Oxides CaMnO_3 and SrMnO_3** **S. Berbeth Mary¹, D.Edward Christy², S. Selvakumari¹, A. Leo Rajesh^{1*}**¹*Department of Physics, St. Joseph's College (Autonomous),
Tiruchirappalli-620 002, Tamil Nadu, India.*²*Research Scholar, Research and Development Centre,
Bharathiyar University, Coimbatore – 641046, Tamil Nadu, India.*

Abstract:-Calcium Manganite (CaMnO_3) and Strontium Manganite (SrMnO_3) nanostructured perovskite oxides were prepared by cost effective and size controllable hydrothermal method at pH 9.2 with and without chelating agent. The as-prepared samples were annealed under air at 800°C. Single phase and crystalline material was observed by X-Ray diffraction and the average crystallite size was in the range of 40-60 nm. SEM Micrograph showed the homogeneously dispersed nanomaterials without agglomeration. Strong doublet peak around 550 cm^{-1} confirmed the formation of perovskite oxides by Fourier Transform Infrared Spectroscopy. The absorption peaks were observed by using UV- Visible spectroscopy and the band gap was estimated from Tauc's relation. The indirect band gap increased for the chelating agent used sample where it influenced by the crystallite size of the nanomaterials.

Key words: chelating agent, hydrothermal method, perovskite oxide, indirect band gap

1. Introduction

Perovskite type oxide materials (ABO_3 where A is larger cation and B is a smaller cation) have received much attention due to their interesting electrical, electrochemical, superconducting, magnetic and thermoelectric properties [1-4]. These exceptional properties make them potential candidates in various novel electronic devices for energy storage applications. The development of environmental friendly and cost effective power sources overcomes the problems of energy crises and global warming. Thermoelectric power generation is a promising method of converting waste heat directly into electricity without any greenhouse gas emission. The efficiency of this thermoelectric material is determined by the figure of merit ZT. Dimensionless figure of merit is directly proportional to Seebeck coefficient (S), electrical conductivity (σ) and inversely proportional to thermal conductivity (κ) and absolute temperature (T). Good thermoelectric materials should have a large Seebeck coefficient, high electrical conductivity and low thermal conductivity where large electrical conductivity minimizes joule heating while low thermal conductivity maintains a temperature gradient between the hot and cold sides in the thermoelectric device. The intermetallic materials such as Bi_2Te_3 and CoSb_3 have a high ZT at low temperatures. However, they are toxic, rare and degrade at high temperatures under air [5]. Besides, thermoelectric materials are required to be stable at higher temperatures. Oxides are one of the best candidate materials for this requirement, but most oxides with high stability at high temperature in air are unsuitable for thermoelectric applications due to high electrical resistivity. These limitations were over welcomed by the discovery of Na_xCoO_2 with a high Seebeck coefficient (100MV/K at 300 K) and a low electrical resistivity (0.2 $\text{m}\Omega$ at 300K) by Terasaki et al in 1997 [6]. Due to its chemical, thermal stability and oxidation resistance in the air, CaMnO_3 (CMO) and SrMnO_3 (SMO) compounds are stable at higher temperatures [7].

Energy efficiency, environmentally friendly, recycling of unused components, high purity products, access of metastable and new phases, control of crystal size, morphology, composition, and polymorphism of the synthesized phases are the recompenses of hydrothermal method in synthesizing metal oxide nanocrystals. Experimental parameters such as temperature and pressure, pH, oxidation-reduction potential, concentration of chemical species, and the use of inorganic additives for homogeneous and heterogeneous nucleation can also be carefully controlled [8-10]. Homogeneous distribution of metal ions, reduced segregation, reduction of external temperature to form the required phase and large surface area were obtained when citric acid used as chelating agent [11 -13]. In this work CMO and SMO nanomaterials were prepared by hydrothermal method. The structural, morphological, functional and optical properties were analyzed.

2. Materials and Methods

AR Grade Calcium Nitrate tetra hydrate, Strontium Nitrate, Manganese (II) Nitrate hydrate, Citric acid anhydrous and Ammonia Solution (28%) were used without any further purification. CMO and SMO nanocrystals were prepared by hydrothermal method. Stoichiometric amounts of nitrates of calcium, strontium, manganese and equivalent amount of citric acid were dissolved in deionized water so that the metal ions can be consistently complexed together. Ammonia solution was added drop wise to the above mixed solution in which part of ammonia used to neutralize the unreacted citric acid. A sol was obtained when the pH value of the solution reached 9.2, then this sol was transferred to a 150 ml autoclave and the autoclave was placed into an oven for hydrothermal treatment at 200 °C for 20 h. The obtained precursors were centrifuged, washed with deionized water and ethanol for many times in order to remove the byproducts and dried at 120 °C overnight. The dried powders were calcined in air in a furnace at 800 °C for 4 h [14].

Crystal structure and phase purity were determined by Powder X-ray diffraction (XRD) and data were collected using a X-ray diffractometer (D8 Advanced) with Cu K α radiation with a step up of 0.02° ($\lambda=0.15406$ nm). The surface morphology was observed by Scanning electron microscopy (SEM) with low and high magnifications. Fourier transform infrared (FTIR) spectra of the powder samples were recorded from 4000 to 400 cm⁻¹ using a Perkin Elmer Fourier transform infrared spectrometer. The optical properties and the band gap were determined by using a Lambda 35 UV-Vis spectrometer.

3. Results and Discussion

Starting from the yellowish of the manganese nitrate solution, the suspension was bluish when pH reached 9.2. After hydrothermal treatment the powder became darkish due to the presence of different manganese valence states [15]. The XRD pattern of CMO and SMO nanomaterials prepared by hydrothermal method (a) by using a chelating agent (b) without chelating agent is shown in Fig. 1. Low crystalline powders were obtained for precursor whereas crystalline peaks were acquired from citric acid used sample. The results showed that the high quality crystalline and fine powders were achieved for the sample prepared with citric acid as chelating agent [16]. They clearly prove the single phase of the orthorhombic perovskite structure of CaMnO₃ with JCPDS Card no 46-1009. The subgroup was Pbam and the lattice parameters were a= 5.424 Å, b= 10.23 Å, c= 3.735 Å. Hexagonal structured crystalline peaks were observed for SrMnO₃ and the lattice parameters were a= 5.44 Å, c= 9.080 Å was matched with the JCPDS card no 24-1213. The average crystallite sizes of the synthesized samples were estimated from the major diffraction peaks using the Scherrer formula $D = K\lambda / \beta \cos\theta$, where K is constant (K = 0.94), λ is the wavelength (1.5418 Å), θ is the Bragg angle and β is full width half maximum (FWHM) that is, broadening due to the crystallite dimensions. The average crystallite size of the prepared CMO and SMO samples by hydrothermal method with and without citric acid were 41, 53 nm and 52, 61 nm respectively where citric acid as chelating agent controlled the size of the nanomaterials [17].

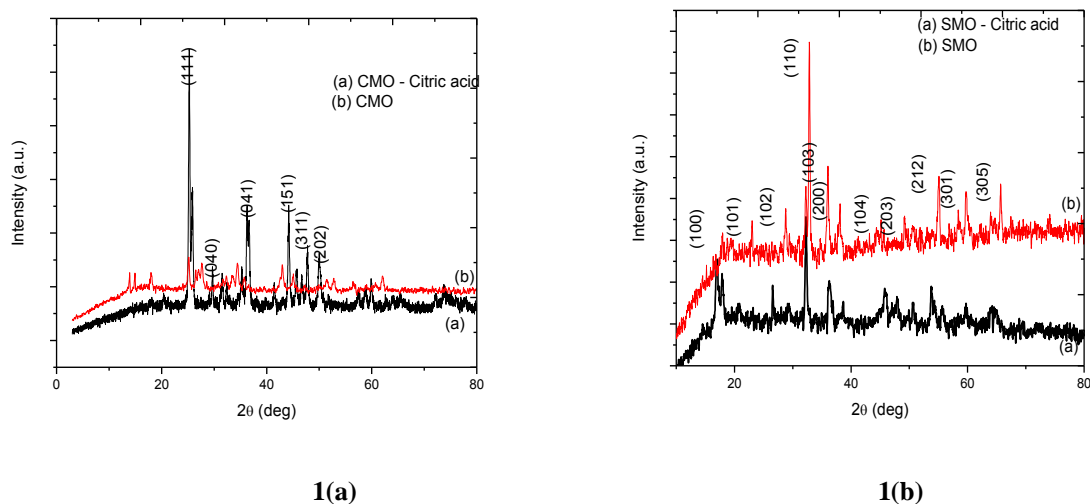


Fig. 1. XRD Pattern of (a) CMO and (b) SMO nanomaterials

Fig 2(a, b) exhibits the surface morphology of CMO and SMO nanomaterials. The grains were agglomerated while homogeneously dispersed grains found in the samples where citric acid was used as chelating agent. The samples were in

porous nature where it was generated due to the evolution of carbon dioxide during the decomposition of doped manganese oxide nanoparticles. The prepared samples in the presence of citric acid were quite uniform and mono dispersed, whereas the samples prepared in the absence of chelating agent were agglomerated and poly dispersed. Randomly oriented grains were attained as expected for the typical structure of CMO and SMO nanomaterials and the average grain size was seemed to be in the range of a few nanometers as determined by using Scherrer formulae from X-ray diffraction analysis[18].

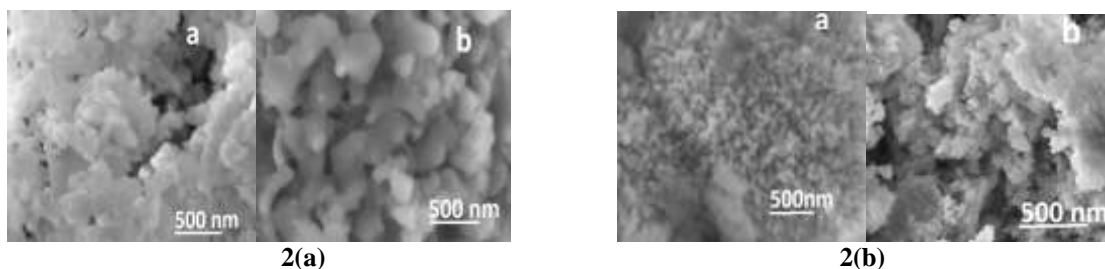
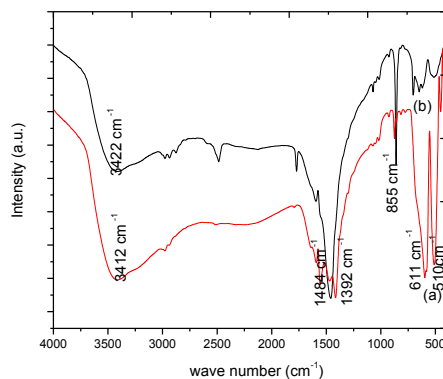
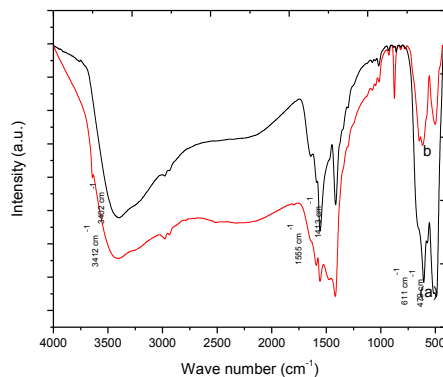


Fig. 2. SEM Micrograph of (a) CMO and (b) SMO nanocrystals

The formation of CMO and SMO nanomaterials were further established by FTIR spectroscopy as shown in fig 3(a, b). The band around 3500 cm^{-1} corresponds to the O-H mode of vibration and the strong asymmetric stretching mode of vibration of C=O was scrutinized at around 1450 cm^{-1} . The symmetric stretching occurs at 850 cm^{-1} indicates the vibration of NO_3^{-1} ions and the standard peak of CMO and SMO nanocrystals was appeared in the region of 550 cm^{-1} [19]. The sharp peaks have been observed for the samples prepared with citric acid as chelating agent.



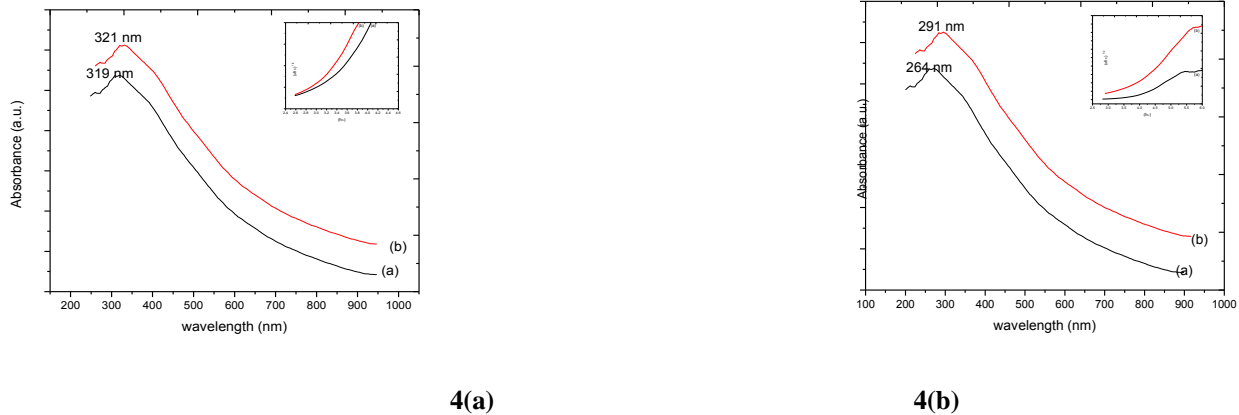
3(a)



3(b)

Fig. 3. FTIR Spectra of (a) CMO Nanocrystals (b) SMO Nanocrystals

The optical properties of CMO and SMO nanocrystals were characterized by UV-vis spectroscopy as shown in fig.4 (a, b). The formation of CMO and SMO nanomaterials were indicated by the absorption peaks at 319, 321 nm and 264, 292 nm. The band gap E_g was calculated from the equation $(\alpha h\nu)^n = B(h\nu - E_g)$, Where α is the absorption coefficient, $h\nu$ is the photon energy, B is dimensional constant, and n is the index representing the transmission order, where $n=2$ for an direct band gap and $n=1/2$ for indirect band gap [20]. The band gap was determined by extrapolating the linear portion of the plot relating $(\alpha h\nu)^{1/2}$ versus $h\nu$ to the value of $\alpha=0$. The band gap of the prepared samples were 2.64, 2.51 eV and 2.91, 2.7 eV for CMO and SMO nanomaterials respectively. The higher band gap value could be ascribed to a smaller crystallite size of the nanomaterials [21].



4(a) **4(b)**
Fig.4. UV – Visible Spectra of (a) CMO and (b) SMO Nanomaterials

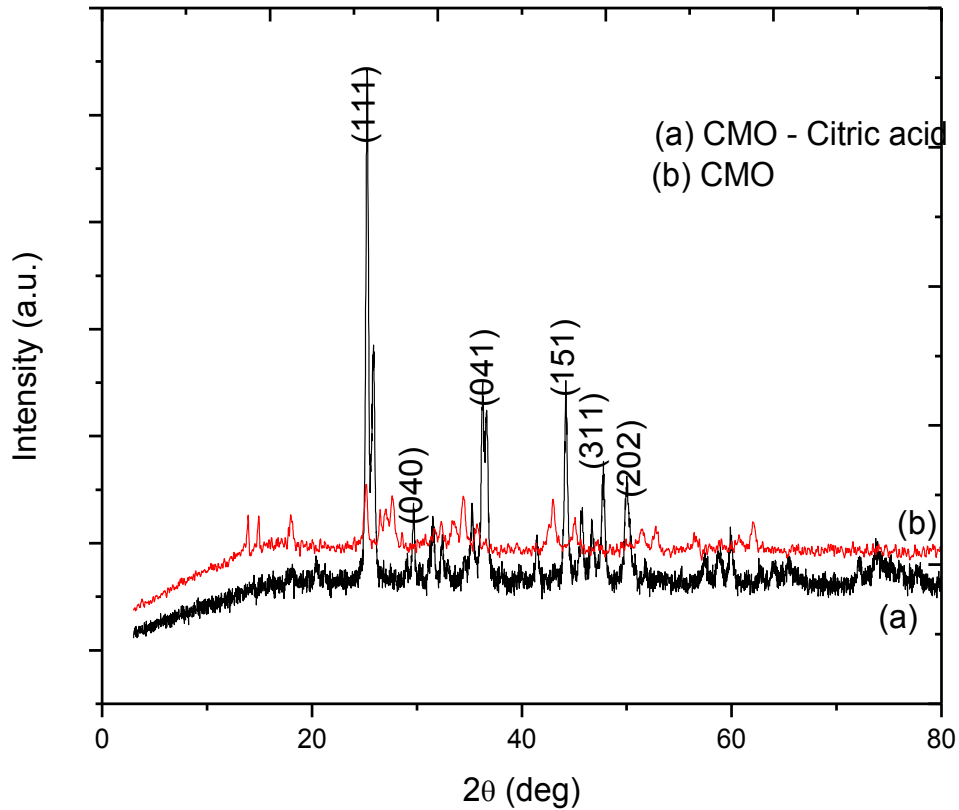
4. Conclusion

CMO and SMO nanomaterials were synthesized by using hydrothermal method at pH 9.2 with and without citric acid as chelating agent. The XRD analysis confirmed that good crystalline material obtained for the sample prepared with citric acid. The addition of citric acid enhanced the crystallization process at low temperature and reduced the average crystallite size. SEM Micrograph showed a high degree of homogeneously dispersed and non agglomerated nanograins observed for the same sample. The formations of CMO and SMO nanomaterials have been signified by FTIR spectroscopy. From the absorption peak, band gap increased for the smaller crystallite size of the nanomaterials and it was found to be 2.64 eV and 2.91 eV for CMO and SMO nanomaterials. These results suggest that there might be the scope for improving n – type materials for high temperature thermoelectric applications.

References

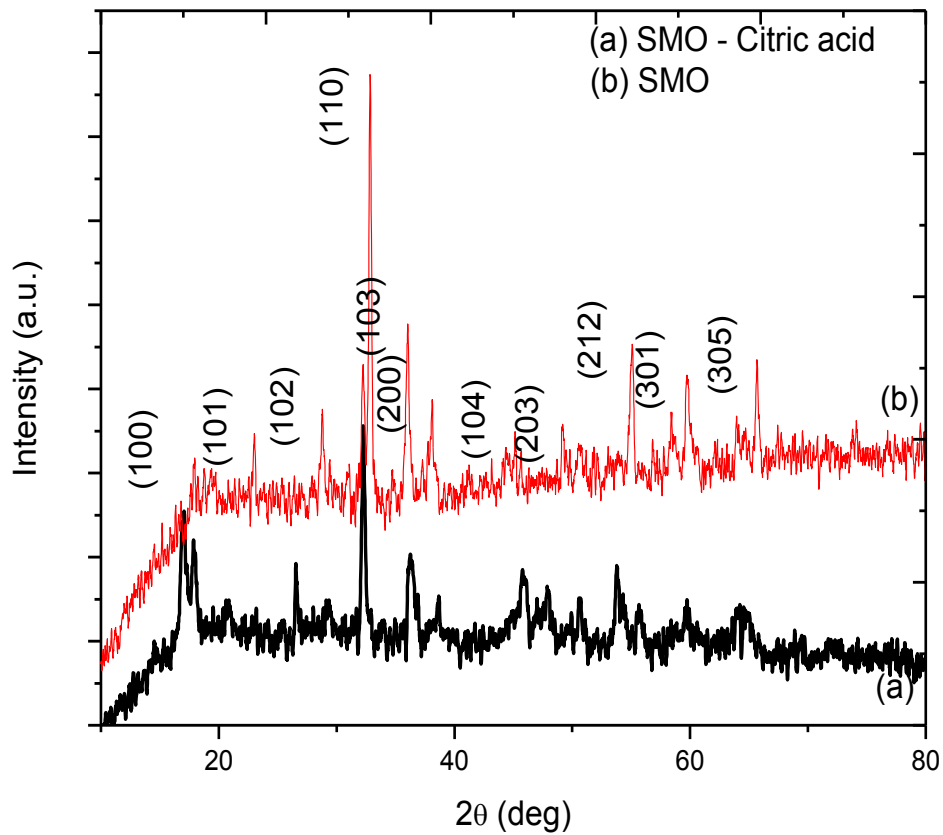
1. M. A. Pena, J. L. G. Fierro, Chem. Rev., 101, 1981 (2001)
2. R. Chiba, H. Orui, T. Komatsu, Y. Tabata, K. Nozawa, M. Arakawa, K. Sato, H. B. Arai, J. Electro chem. Soc., 155, 575 (2008)
3. L. Abdul Khalam, H. Sreemoolanathan, R. Ratheesh, P. Mohanan, M. T. Sebastian, Mater. Sci. Eng., 107,264 (2004)
4. J. Dho, W. S. Kim, E. O. Chi, N. H. Hur, S. H. Park, H. C. R, Solid State Commun., 125, 143 (2003)
5. G. Chen, M. S. Dresselhaus, D. Dresselhaus, J. P. Fleurial, T. Caillat, Int. Mater. Rev., 48, 45 (2003)
6. J. Pei, G. Chen, N. Zhou, D. Q. Lu, F. Q. Xiao, Physica B., 406, 571 (2011)
7. J. F. Nakahara, T. Takeshita, M. J. Tschetter, B. J. Beaudry, J. K. A. Gshneider, J. Appl. Phys., 63, 2331 (1998)
8. M. Yoshimura, S. E. Yoo, M. Hayashi, N. Ishizawa, J. Appl. Phys., 28, 2007 (1989)
9. S. Komarneni, S. Roy, Mater. Lett., 3,165 (1985)
10. Sridhar Komarneni, Young Dong Noh, Joo Young Kim, Seok Han Kim, Hiroaki Katsuki, Z. Naturforsch., 65b, 1033 (2010)
11. A. Pathak, P. Pramanik, Pansa., 67, 47 (2001)
12. D. J. Anderton, F. R. Sale, Powder Metall., 22, 14 (1979).
13. M. S. G. Baythoun, F. R. Sale, J. Mater. Sci., 17, 2757 (1982).
14. Jianrong Niu, Jiguang Deng, Wei Liu, Lei Zhang, Guozhi Wang, Hongxing Dai, Hong He, Xuehong Zi, catal.Today., 126, 420 (2007)
15. R. Ma, K. Takada, K. Fukuda, N. Iyi, Y. Bando, T. Sasaki, Angew. Chem. Int. Ed., 47, 86 (2008)

16. Hohyun Lee, Daryoosh Vasahee, Wang DZ, Mildred S Dresselhaus, Ren ZF, Gang Chen, *J. Appl. Phys.*, 107, 94308 (2010)
17. A. Shalaby, A. Bachvarova-Nedelcheva, R. Iordanova, Y. Dimitriev, *J. Chem. Tech. Metay.*, 48, 585 (2013)
18. Provas Pal, Sandip K. Pahari, Arnab Kanti Giri, Sagar Pal, Hari C. Bajaj, Asit Baran Panda, *J. Mater. Chem. A.*, 1, 10251 (2013)
19. R. Wahab, S. G. Ansari, H. K. Seo, Y. S. Kim, E. K. Suh, H. S. Shin, *Solid State Sci.*, 11, 439 (2009)
20. R. Wahab, S. G. Ansari, Y. S. Kim, H. K. Seo, G. S. Kim, G. Khang, H. S. Shin, *Mater. Res. Bull.*, 42, 1640 (2007)
21. X. M. Lu, J. S. Zhu, W. Y. Zhang, G. Q. Ma and Y. N. Wang, *Thin Solid Films.*, 274, 165 (1996)



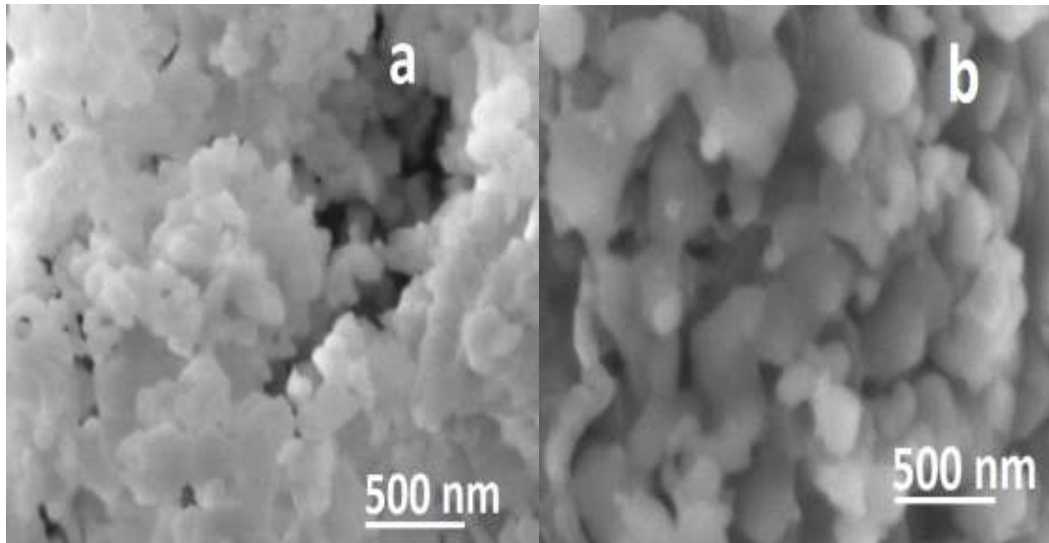
1(a)

Fig. 1. XRD Pattern of (a) CMO and (b) SMO nanomaterials
Hydrothermal Synthesis of Perovskite Oxides CaMnO_3 and SrMnO_3
S. Berbeth Mary¹, D. Edward Christy², S. Selvakumari¹, A. Leo Rajesh^{1*}



1(b)

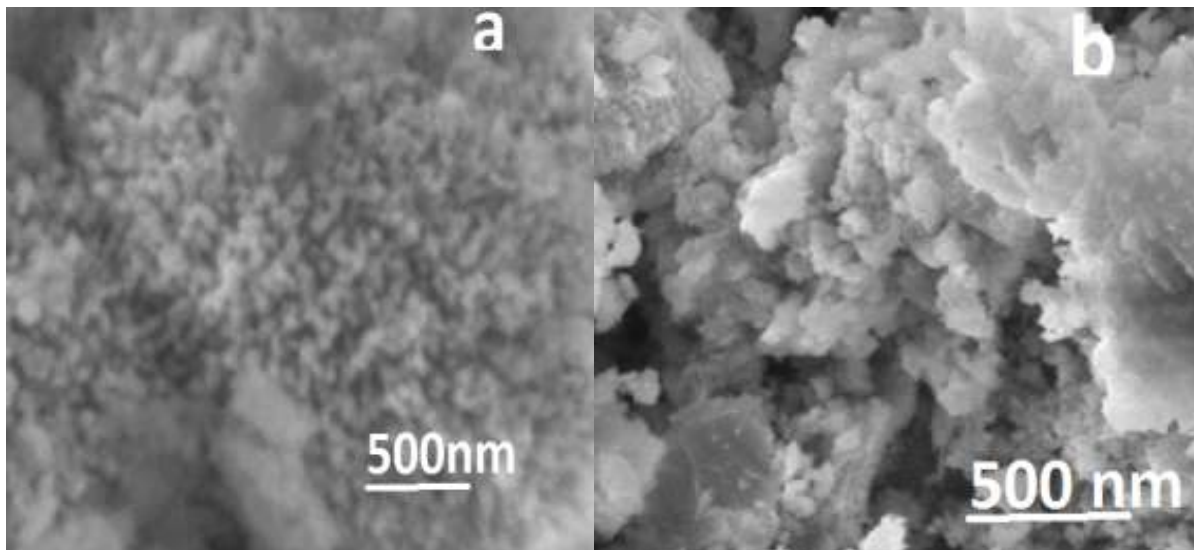
Fig. 1. XRD Pattern of (a) CMO and (b) SMO nanomaterials
Hydrothermal Synthesis of Perovskite Oxides CaMnO_3 and SrMnO_3
S. Berbeth Mary¹, D.Edward Christy², S. Selvakumari¹, A. Leo Rajesh^{1*}



2(a)

Fig. 2. SEM Micrograph of (a) CMO and (b) SMO nanocrystals

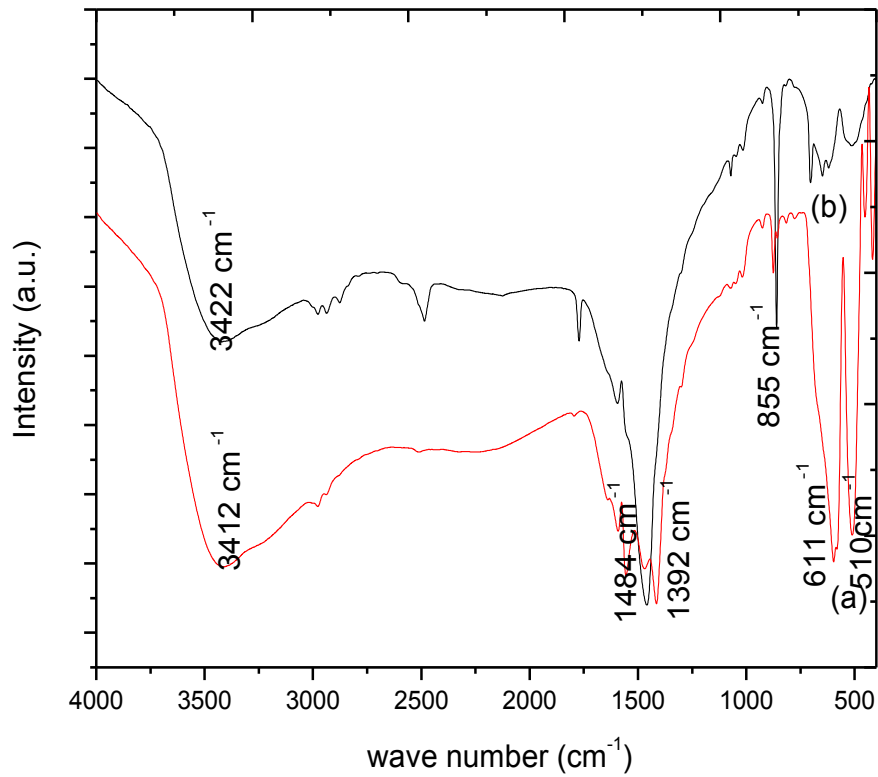
Hydrothermal Synthesis of Perovskite Oxides CaMnO_3 and SrMnO_3
S. Berbeth Mary¹, D.Edward Christy², S. Selvakumari¹, A. Leo Rajesh^{1*}



2(b)

Fig. 2. SEM Micrograph of (a) CMO and (b) SMO nanocrystals

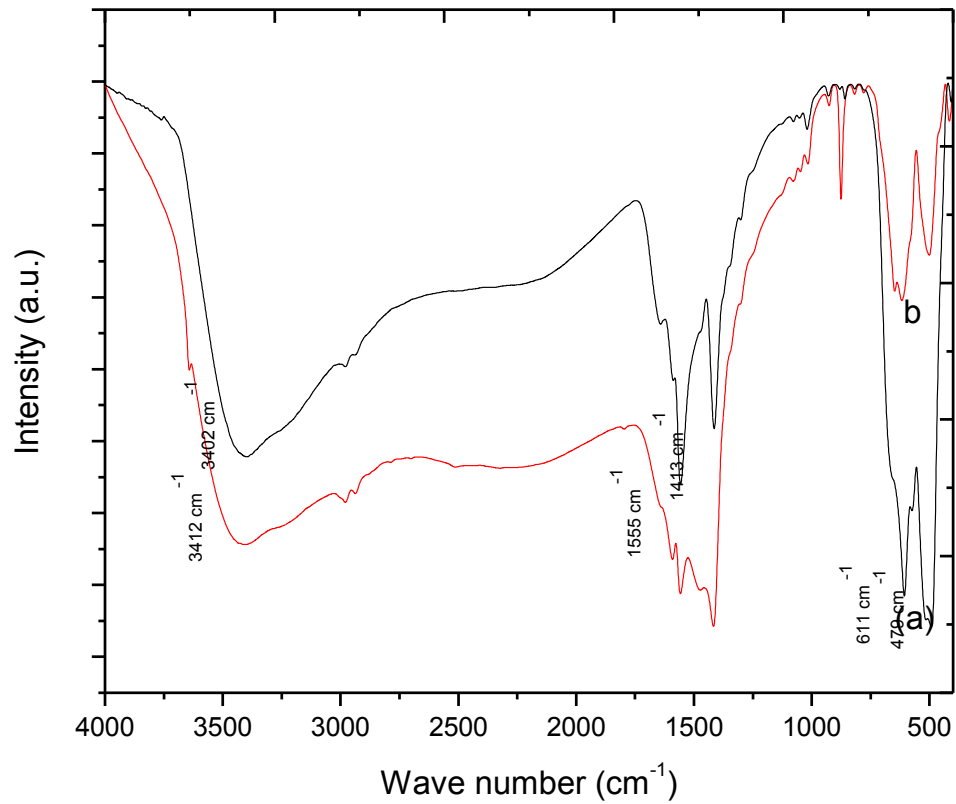
Hydrothermal Synthesis of Perovskite Oxides CaMnO_3 and SrMnO_3
S. Berbeth Mary¹, D.Edward Christy², S. Selvakumari¹, A. Leo Rajesh^{1*}



3(a)

Fig. 3. FTIR Spectra of (a) CMO Nanocrystals (b) SMO Nanocrystals

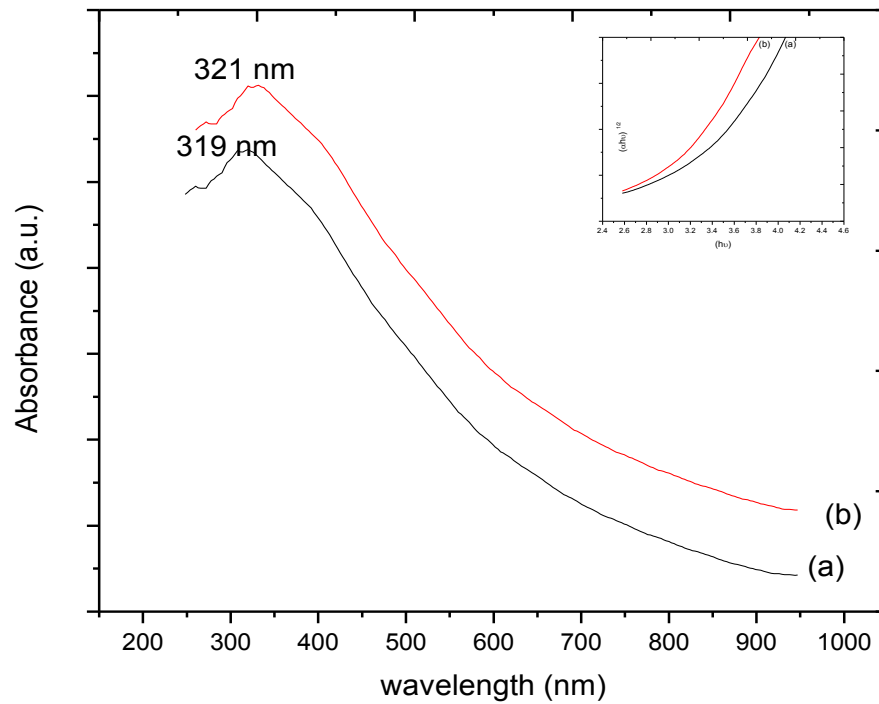
Hydrothermal Synthesis of Perovskite Oxides CaMnO₃ and SrMnO₃
S. Berbeth Mary¹, D.Edward Christy², S. Selvakumari¹, A. Leo Rajesh^{1*}



3(b)

Fig. 3. FTIR Spectra of (a) CMO Nanocrystals (b) SMO Nanocrystals

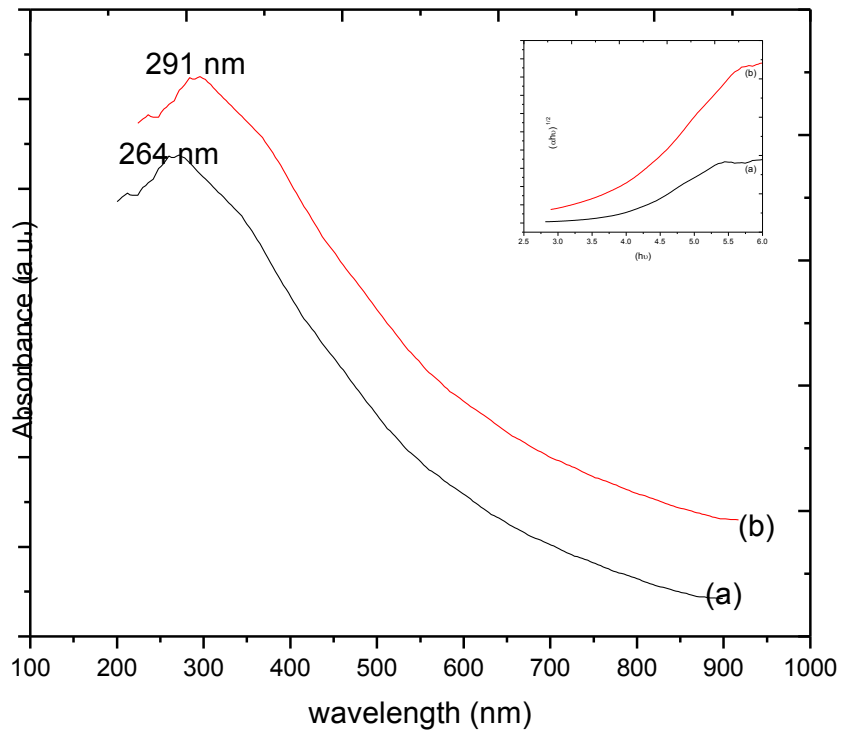
Hydrothermal Synthesis of Perovskite Oxides CaMnO₃ and SrMnO₃
S. Berbeth Mary¹, D.Edward Christy², S. Selvakumari¹, A. Leo Rajesh^{1*}



4(a)

Fig.4. UV – Visible Spectra of (a) CMO and (b) SMO Nanomaterials

Hydrothermal Synthesis of Perovskite Oxides CaMnO_3 and SrMnO_3
S. Berbeth Mary¹, D.Edward Christy², S. Selvakumari¹, A. Leo Rajesh^{1*}



4(b)

Fig.4. UV – Visible Spectra of (a) CMO and (b) SMO Nanomaterials

Hydrothermal Synthesis of Perovskite Oxides CaMnO_3 and SrMnO_3
S. Berbeth Mary¹, D.Edward Christy², S. Selvakumari¹, A. Leo Rajesh^{1*}



Synthesis and Characterization of Cerium doped CaMnO_3 Nanoparticles

S. Berbeth Mary, A. Leo Rajesh*

Department of Physics, St. Joseph's College (Autonomous), Tiruchirappalli-620 002, Tamil Nadu, India

*corresponding author: E-mail address: aleorajesh@gmail.com;

Tel.:+91-944412207

Abstract

Nanostructured cerium doped calcium manganite $\text{Ca}_{1-x}\text{Ce}_x\text{MnO}_3$ ($x=0.0, 0.1, 0.2, 0.3, 0.4, 0.5$) samples were synthesized successfully using the citric acid complexing coupled with hydrothermal method followed by annealing at 900°C . Powder X-ray diffraction (XRD) analysis showed that the single phases of orthorhombic perovskite structure of CaMnO_3 and the cell volume increased from undoped to cerium doped CaMnO_3 structure due to the ionic radius of added R^{3+} cations. The crystallinity decreased with increased concentration of Ce^{3+} doping and the average crystallite size was about 10-20 nm. Sphere like nanoparticles observed by the scanning electron microscopy. FTIR analysis showed a strong peak around 600 cm^{-1} revealed the formation of perovskite oxides and the obtained band gap was 3.56 eV.

Keywords: calcium manganite, hydrothermal, single phase, perovskite oxide

1. Introduction

The development of environmental friendly and cost effective power sources overcomes the problems of energy crises and global warming. Thermoelectric power generation is a promising method by converting waste heat directly into electricity without any greenhouse gas emission. The conversion efficiency is measured by the dimensionless figure of merit

$$ZT = \left(\frac{S^2 \sigma}{k} \right) T$$

where S , σ , K , T are seebeck coefficient, electrical conductivity, thermal conductivity and absolute temperature respectively. Good thermoelectric materials should have large seebeck coefficient, high electrical conductivity and low thermal conductivity where large electrical conductivity minimize joule heating while low thermal conductivity maintains temperature gradient between the hot and cold sides in thermoelectric device. The intermetallic materials such as Bi_2Te_3 and CoSb_3 have high ZT at low temperatures. However, they are toxic, rare and degrade at high temperatures under air [1]. Besides, thermoelectric materials are required to be stable at higher temperatures. Oxides are one of the best candidate materials for this requirement but most oxides with high stability at high temperature in air are unsuitable for thermoelectric applications due to high electrical resistivity. These limitations were overcome by the discovery of Na_xCoO_2 with a high seebeck coefficient (100mV/K at 300 K) and a low electrical resistivity ($0.2\text{ m}\Omega$ at 300K) by Terasaki et al in 1997 [2].

The interesting physical properties such as electrical, electrochemical, magnetic, superconducting and thermoelectrical make them great candidates in various energy storage applications like supercapacitor, solid oxide fuel cells and thermoelectric devices [3-5]. Several perovskite type oxides are well known as highly conductive ceramics whereas CaMnO_3 based oxides are the major n-type thermoelectric oxide which produces granular fine particles with high chemical and thermal stability. The undoped

CaMnO_3 has poor TE property due to the high electrical resistivity whereas calcium substitution with various rare earth elements can enhance the carrier mobility which progress the electrical conductivity [6]. The thermoelectric performance of perovskite type oxides can be enhanced by doping, band engineering and nanostructuring [7]. Reduction of thermal conductivity can be accomplished by nanotailoring with controlled grain size. $\text{Ca}_{1-x}\text{Re}_x\text{MnO}_3$ can be successfully synthesized by various bottom up methods such as chemical combustion, sol-gel, coprecipitation, hydrothermal method and so on [8-11]. Here citric acid complexing coupled with hydrothermal method has been employed to obtain high purity, homogenous, environmental friendly and fine particles with controlled grain size [12 -14].

CaMnO_3 based thermoelectric materials has high seebeck coefficient but the dimensionless figure of merit is low because of low electrical conductivity. N- type doping at A-site (Ca), B-site (Mn) and dual doping at both sites has been done to improve the TE property, while A- site rare earth elements doping shows the enhancement in ZT values [15-18]. In rare earth doped manganite, dopant occupies either A-site or B-site depending on its radius. Doping cerium in CaMnO_3 , Ce occupies the A-site and raises the Thermoelectric (TE) performance by strongly reducing the resistivity [19]. In this paper, the effects of Ce substitution on nanostructured n-type thermoelectric oxide $\text{Ca}_{1-x}\text{Ce}_x\text{MnO}_3$ (CCMO) samples are systematically studied.

2. Materials and Methods

$\text{Ca}_{1-x}\text{Ce}_x\text{MnO}_3$ ($x=0.0, 0.1, 0.2, 0.3, 0.4, 0.5$) powders were prepared using the strategy of citric acid complexing coupled with hydrothermal

method. Stoichiometric amounts of nitrates such as cerium, calcium, manganese and equal amount of citric acid (metal/citric acid molar ratio = 1/1) were dissolved in deionized water to obtain homogeneity in the metal ions. A certain amount of ammonia solution was added drop wise to the above mixed solution. Part of ammonia added to neutralize the unreacted citric acid. When the pH value of the solution reached around 9.2 a sol was obtained. This sol was transferred to a 150 ml stainless steel autoclave was placed it in hot air oven at 200 °C for 20 hr. once the assigned time was over the oven was switched off and allowed to cool down to room temperature. The obtained products were in turn filtered, washed with deionized water and ethanol, filtered again, and dried around 120 °C overnight. The dried powders were well ground and annealed in air at 900 °C for 4 hr.

Crystal structure and phase identification were determined by Powder X-ray diffraction (XRD) and data were collected using a XRD diffractometer (D8 Advanced) with $\text{CuK}\alpha$ radiation ($\lambda = 0.15406$ nm). The surface morphology was observed with scanning electron microscopy (SEM). Fourier transform infrared (FTIR) spectra of the powder samples were recorded from 4000 to 400 cm^{-1} using a Fourier transform infrared spectrometer (Perkin Elmer) equipped with a KBr beam splitter. The optical properties of the nanoparticles were characterized by UV-Vis spectroscopy Lambda 35 UV-Vis spectrometer.

3. Results and Discussion

The yellowish colour of the manganese nitrate solution is turned into bluish when pH value of the solution reached to 9.2. After centrifugation and drying, the powder is darkish due to the presence of different manganese valance states [20]. Figure 1

represents the XRD patterns of annealed undoped and doped CaMnO_3 powders. They clearly demonstrate the single phase of orthorhombic pervoskite structure of CaMnO_3 which is matching with JCPDS Card no 76-1133 with space group Pnma , indicating that annealing under oxygen atmosphere leads to the formation of CaMnO_3 structure [21]. The strong doublet of the main pervoskite peak in the 2θ region, 33° of the CCMO nanostructure exhibited a tendency to unify with increasing the doping concentration [22, 23]. Fig 1(d) shows that there is shift in peaks due to the release of large volume of gases while annealing.

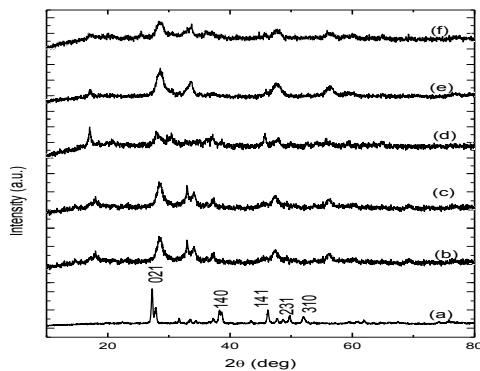


Figure 1. XRD Pattern of $\text{Ca}_{1-x}\text{Ce}_x\text{MnO}_3$ ($x = 0.0, 0.1, 0.2, 0.3, 0.4, 0.5$) samples

The average grain size of the synthesized samples are calculated from the major diffraction peaks using the Scherrer formula $D = K\lambda/\beta\cos\theta$, where K is constant ($K = 0.94$), λ is the wavelength (1.5406 \AA). θ is the Bragg angle; β is full width half maximum that is, broadening due to the crystallite dimensions [24]. The average grain size of the prepared samples is in the range of 10-20 nm. Partial substitution of Ce^{3+} (Ln^{3+}) for Ca^{2+} decreases the average grain size with increasing the cerium concentration [25-27].

Figure 2 shows SEM images of undoped and cerium doped CaMnO_3 samples. It can be seen that all the samples shows a porous nature. This porous

morphology is attributed to the release of a large volume of gases during the synthetic process due to the addition of citric acid as chelating agent and post heating treatment. The majority of the particles are nearly round shaped and the others are elongated. The average size of spherical particles deduced from SEM lies in the range of few nanometers. Microstructures of cerium doped samples are downgraded, which is associated with the most decrease of electrical conductivity. The decrease of electrical conductivity leads to a decrease of κ_e , which is due to the partial substitution of Ce^{3+} for Ca^{2+} , the decrease of κ_{total} can be mainly attributed to the reduction of lattice contribution arising from incorporation of heavier Ce^{3+} ions in the structure as compared to Ca^{2+} ions [28] ($\kappa_{\text{total}} = \kappa_{\text{ph}} + \kappa_e$, where κ_e and κ_e are the thermal conductivity due to lattice and electronic contribution) which leads to the enhancement in thermo power S .

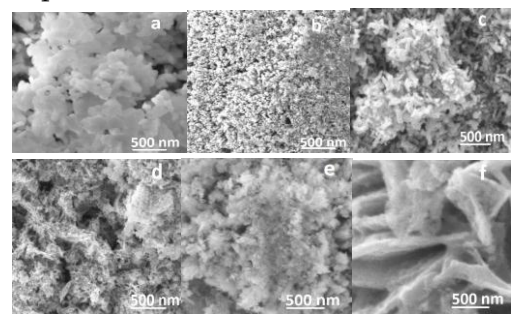


Figure 2. SEM Micrograph of $\text{Ca}_{1-x}\text{Ce}_x\text{MnO}_3$ ($x = 0.0, 0.1, 0.2, 0.3, 0.4, 0.5$) samples

The FTIR study is carried out to correlate the relative change in the high frequency stretching mode and mid frequency bending mode with the bond lengths and consequently to the unit cell volume [29, 30]. Figure 3 shows the FTIR spectra of CCMO nanoparticles. The typical peak of CCMO nanoparticle is observed around $500\text{-}600 \text{ cm}^{-1}$. The symmetric stretching occurs about 800 cm^{-1} indicates the vibration of NO_3^{-1} ions. The strong

asymmetric stretching mode of vibration of C=O is observed around 1300-1500 cm^{-1} . The band at 3500 cm^{-1} corresponds to O-H mode of vibration [31,32].

These results show that this material it is suitable for thermoelectric application.

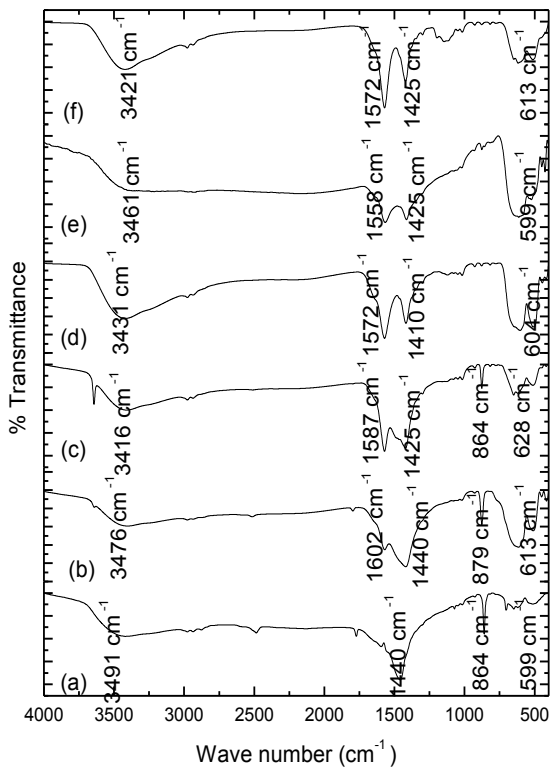


Figure 3. FTIR Spectra of $\text{Ca}_{1-x}\text{Ce}_x\text{MnO}_3$ ($x = 0.0, 0.1, 0.2, 0.3, 0.4, 0.5$) samples

Figure 4(a) shows UV-Visible spectra of $\text{Ca}_{1-x}\text{Ce}_x\text{MnO}_3$ nanoparticles. The absorption peaks are around 300 cm^{-1} . When the concentration of cerium increases peak value also increases. The band gap E_g can be calculated from the equation

$$(\alpha h\nu)^n = B (h\nu - E_g)$$

where α is absorption coefficient, $h\nu$ is the photon energy, B is constant, and n can be either 1/2 or 2 for indirect and direct transitions respectively [33]. The $(\alpha h\nu)^2$ versus $h\nu$ curve is shown in figure 4(b) and it is found to be 3.56 eV which is good agreement with the optimum value.

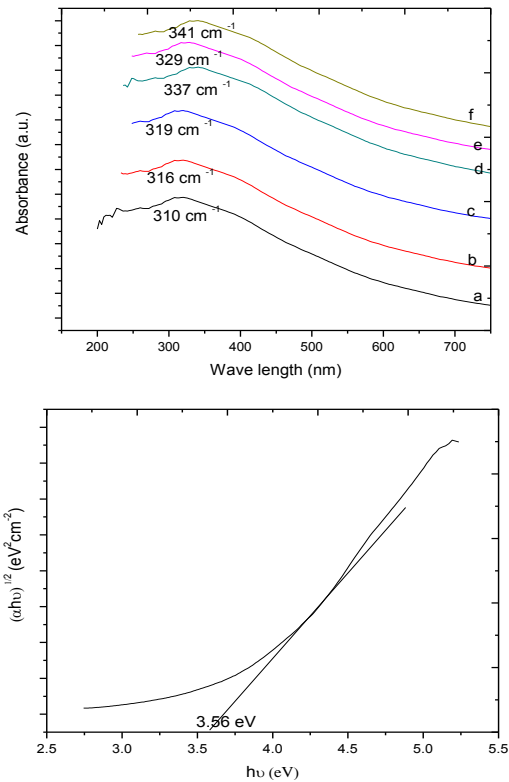


Figure 4(a). UV- Visible Spectra of $\text{Ca}_{1-x}\text{Ce}_x\text{MnO}_3$
(b) Band gap determination

4. Conclusion

This work exhibited that Cerium is a suitable alternative material for Ca in $\text{Ca}_{1-x}\text{Ce}_x\text{MnO}_3$, here the concentration was ($x \leq 0.5$) in which there is no change in the crystal structure and the improved thermoelectric properties were obtained using citric acid complexing coupled with hydrothermal method. Crystalline and single phase structure of the nanoparticle was observed for all the samples. The observed porous nanoparticles lead to the connectivity in microstructure due to chelating reagent. The peaks at 600 cm^{-1} concluded the presence of Cerium doped CaMnO_3 nanoparticle and the band gap energy was calculated to be 3.56 eV. The crystalline nature, porosity and low band

gap nature of these samples confirms that it is suitable for thermoelectric application. Sphere shaped surface morphology was observed for majority of the samples. The chelating agent played major role obtains the reduced particle size and good porous nature of the material.

References

- [1] G. Chen, M. S. Dresselhaus, D. Dresselhaus, J.P. Fleurial, T. Caillat, *Int. Mater. Rev.*, **48**, 45 (2003).
- [2] J. Pei, G. Chen, N. Zhou, D.Q. Lu, F.Q. Xiao, *Physica B.*, **406**, 571 (2011)
- [3] M.A. Pena, J.L.G. Flerro, *Chem. Rev.*, **101**, 7 (2001)
- [4] E. Konyshova, J.T.S. Irvine, *J. Mater. Chem.*, **18**, 5147 (2008).
- [5] F. Azough, C. Leach, R. Freer, *J. Eur. Ceram. Soc.*, **26**, 10 (2006).
- [6] J. Dho, W.S. Kim, E.O. Chi, N.H. Hur, S.H. Park, H.-C. Ri, *Solid State Commun.*, **125**, 143 (2003)
- [7] Michitaka Ohtaki, Hisako Koga, Tsutomu Tokunaga, Koichi Eguchi, Hiromichi Arai, *J. Solid State Chem.*, **120**, 105 (1995)
- [8] R.V. Mangalaraja, J. Mouzon, P. Hedström, I. Kero, K.V.S. Ramam, C.P. Camurri, M. Odén, *J. Mater. Process. Technol.*, **208** 415 (2008)
- [9] N.P. Bansal, *J. Mater. Sci.* **27**, 2922 (1992)
- [10] C.S. Sanmathi, Y. Takahashi, D. Sawaki, Y. Klein, R. Retoux, I. Terasaki, J.G. Noudem, *Mater. Res. Bull.*, **45**, 558 (2010)
- [11] Jianrong Niu, Jiguang Deng, Wei Liu, Lei Zhang, Guozhi Wang, Hongxing Dai, Hong He, Xuehong Zi, *Catal. Today.*, **126**, 420 (2007)
- [12] Yoshimura M, Yoo S. E, Hayashi M, Ishizawa N, *J. Appl. Phys.*, **28**, 2007 (1989)
- [13] Sridhar Komarneni, Young Dong Noh, Joo Young Kim, Seok Han Kim, Hiroaki Katsuki, *Naturforsch.*, **65b**, 1033 (2010)
- [14] A. Pathak, P. Pramanik, *Pinsa.*, **67**, 47 (2001)
- [15] T. Okuda, Y. Fujii, *J. Appl. Phys.*, **108**, 103702 (2010)
- [16] D. Sousa, M.R. Nunes, C. Silveira, I. Matos, A.B. Lopes, M.E. Jorge, *Mater. Chem. Phys.*, **109**, 311 (2008)
- [17] G. Xu, R. Funahashi, Q. Pu, B. Liu, R. Tao, G. Wang, Z. Ding, *Solid State Ionics.*, **171**, 147 (2004).
- [18] Y.H. Zhu, C.L. Wang, W.B. Su, J.C. Li, J. Liu, Y.L. Du, L.M. Mei, *Ceram. Int.*, **40**, 15531 (2014)
- [19] Mohamed Mouyane, Brahim Itaalit, Jérôme Bernard, David Houivet, Jacques G. Noudem, *Powder Technology.*, **264**, 71 (2014)
- [20] Ma R, Takada K, Fukuda K, Iyi N, Bando Y, Sasaki T, *Angew. Chem. Int. Ed.*, **47**, 86 (2008)
- [21] Mohamed Mouyane, Brahim Itaalit, Jerome Bernad, David Houivet, Jacques G Noudem, *Powder Tech.*, **264**, 71 (2014)
- [22] Millini R, Gagliardi MF, Piro G, *J. Mater. Sci.*, **29**, 4065 (1994)
- [23] Gaudon M, Laberty-Robert C, Ansart F, Stevens P, Rousset A, *Solid State Sci.*, **4**, 125 (2002)
- [24] S. Enzo, G. Fagherazzi, A. Benedetti, S. Polizzi, *J. Appl. Cryst.*, **21**, 536 (1988)
- [25] N.V. Nong, Chia Jyi Liu, M. Othaki, *J. Alloys. Compds.*, **509**, 977 (2011)
- [26] W. Koshibae, K. Tsutsui, S. Maekawa, *Phys. Rev. B.*, **62**, 6869 (2000)



**International Journal of
Scientific Research in Science and Technology (IJSRST)**

Print ISSN : 2395-6011, Online ISSN : 2395-602X

International Conference on Advanced Materials

Held on 14, 15 December 2017, Organized by Department of Physics,
St. Joseph's College, Trichy, Tamilnadu, India



- [27] R. Asahi, J. Sugiyama, T. Tani, Phys. Rev. B.,
66, 155103 (2002)
- [28] R. K. Gupta, C.M. Whang, Solid State Ionics.,
178, 1617 (2007)
- [29] M. Daturi, G. Busca, R. J. Willey, Chem.
Mater., 7, 2115 (1995)
- [30] Rizwan Wahab, Young-Soon Kim, Hyung-Shik
Shin, Mater.Trans., 50, 2092 (2009)
- [31] G. De Marzi, Z. V. Popovic, A. Cantarero, Z.
Dohcevic-Mitrovic N.Paunovic, J. Bok, F.
Sapina, Phys. Rev. B., 68, 064302 (2003)
- [32] K. Rekha, M. Nirmala, Manjula G.Nair, A.
Anukaliani, Physica B, Cond Matr., 405, 3180
(2010)
- [33] K. Omri, J. El Ghouli, O. M. Lemine, M.
Bououdina, B. Zhang, L. El Mir, Superlattices and
Microstructures., 60, 139 (2013)

MULTI-OBJECTIVE OPTIMIZATION OF ELECTRIC DISCHARGE MACHINING OF HYBRID COPPER COMPOSITE USING TAGUCHI GREY RELATIONAL ANALYSIS

[K. Ilayaraja](#), [P. Ranjithkumar](#), [A. Veeramani](#), [S. Sathish](#), [M. Ravichandran](#), [R. Ravikumar](#) [less](#) • Published 10 January 2017 • Materials Science • Journal of Advances in Chemistry

Hybrid copper composite of Cu-5wt.% TiO₂-0wt.%Gr, Cu-5wt.% TiO₂-2wt.%Gr and Cu-5wt.% TiO₂-4wt.%Gr were successfully fabricated through powder metallurgy technique. Samples from the composites were analyzed through scanning electron microscopy to study the microstructure. Electric discharge machining with Taguchi's L₂₇ orthogonal design was carried out to measure the responses material removal rate and surface roughness. Multi response optimization was performed in order to achieve the higher material removal rate and lower surface roughness with grey relational analysis. From the main effect plot the optimal level of parameter combination was obtained. The parameter significance is obtained through the analysis of variance and the process is validated with a confirmation test. [Collapse](#)

Optimization Kerf Width and Surface Roughness in Wirecut Electrical Discharge Machining Using Brass Wire

M. PANNER SELVAM
P. RANJITH KUMAR

*Department of Mechanical Engineering
MAM School of Engineering
Tirchy, Tamilnadu, India
mpselvam65@gmail.com*

Received (21 November 2016)
Revised (6 December 2016)
Accepted (11 December 2016)

Wire Electric Discharge Machining (WEDM) is one of the important non-traditional machining process used for machining difficult to machine materials like composites and inter-metallic materials, Intricate profiles. In the present work, the study has been made to optimize the process parameters during machining of Hastelloy -C-276 by wire-cut electrical discharge machining (WEDM). This paper presents an effective approach to optimize process parameters for Wire electric discharge machining (WEDM) is extensively used in tool and die industries. Precision and intricate machining are the strengths. While machining, time and surface quality still remains as major challenges. The input parameters are pulse on time (Ton), pulse off time (Toff), wire feed rate and current and voltage were changed during the process. The optimization of analysis is performed by using Genetic Algorithm (GA) method L-27 orthogonal array.

Keywords: kerf, Wire Electric Discharge Machining, optimization.

1. Introduction

1.1. Introduction of Wire-cut EDM

There is always a demand for alloy materials having high strength, impact resistance, hardness, toughness. Nevertheless, such materials are difficult to be machined by traditional methods. Hence, non-traditional machining methods including ultrasonic machining, electrical discharge machining and electrochemical machining etc. are used to machine such materials. Wire-cut electrical discharge machining (WEDM) technology has grown tremendously since it was applied more than 45 years ago. In 1974, D.H. Dulebohn applied the optical-line follower system to automatically control the shape of the components to be machined by the

PARAMETRIC OPTIMIZATION OF ASPECT RATIO ON CARBON FIBER REINFORCED POLYMER BY USING TAGUCHI METHOD

^aD. Rajkumar, ^bP. Ranjithkumar, and ^cC. Sathiya Narayanan

Address for Correspondence

^aAssistant professor, Department of Production Engineering, JJ College of Engineering and Technology, Tiruchirappalli, Tamilnadu, INDIA.

^bPrincipal and Professor, Department of Mechanical Engineering, MAM School of Engineering, Sriganur, Tamilnadu, India

^cAssistant professor, Department of Production Engineering, National Institute of Technology, Tiruchirappalli, Tamilnadu, INDIA.

ABSTRACT

This article presents the influence of machining parameter are cutting speed, feed rate and drill diameter in obtained aspect ratio of drilled microhole. In this work, optimum machining parameters were found out for carbide drilling tool in micro-drilling processes in CFRP composite. Drilling of micro-holes with 0.3 mm, 0.4 mm and 0.5 mm drill tools were performed with various cutting speeds and feed rates. It has been decided to find a relationship among the considered parameters namely cutting speed, feed rate and drill diameter with the induced aspect ratio in composites. The relationship has been attained by linear regression and the values are compared with experimental outcomes. From the analysis found that the aspect ratio is mostly influenced by small drill diameter.

KEYWORDS: microdrilling, carbon fibre reinforced polymer, solid carbide, aspect ratio.

1. INTRODUCTION

Due to the nature and properties of the material, CFRP composites is used in various applications like aerospace, automobile, chemical, sport goods, industries etc (1). The purpose of making micro-holes on CFRP is to facilitate the assembly of components, for making printed circuit board and for facilitating the uses of fasteners in structural joints like screws, bolts and rivets. The micro-holes are produced by various processes such as laser beam drilling, Micro Electrical Discharge Machining process, multi-purpose miniature machine tool, Micro Electro Chemical Machining and computer numerical controlled drilling processes (2). Among these processes, the cost of CNC controlled micro drilling is less to produce micro holes. However, micro drilling of CFRP composites is very difficult because of the non-homogeneous structure, anisotropic and an abrasive property of CFRP composites (3). Therefore, appropriate for finding of drill conditions is crucial for attaining high-quality in micro-holes. Various aspect ratio achieved by various authors using different machines/processes are listed in Table 1. The observation from the literature survey the majority of the experiments made micro-holes using laser beam machining, dedicated micromachining equipment and unconventional machines. During laser beam machining, the problem of resin melting is taking place. The cost of micromachining setup and unconventional machining process are higher than CNC controlled machining center. The CFRP composites can be used Printed Circuit.

Table 1 - List of various aspect ratio achieved using different machine/process

S. no.	Machine Used	Workpiece Material, Tool Material, (Length of Hole to Drill Diameter used)	AR Achieved/ Reference
1	Drilling machine	PCB, cemented carbide micro-drills, 2.6/0.1	26 (4)
2	laser drilling	AISI 316L, 45/1.5	30 (5)
3	Drilling experimental	PCB, tungsten carbide (WC) tips., 4.7/0.4	12 (6)
4	Micromachining center	PCB, WC-Co, 2.5/0.4	6 (7)

5	vertical type machining center	SUS304, ultra-fine cemented carbide, 100/90	1 (8)
6	Micro EDM	stainless steel, tungsten 1/0.125	8 (9)
7	CNC Machining centre	C45, carbide 200/100	2 (10)
8	Multipurpose Micro-Machine	Brass, HSS 10/0.5	20 (11)
9	High speed drilling process.	PCB, Carbide 4.8/0.7	7 (12)
10	CNC tapping machine	CFRP, cemented carbide, 1.6/0.6	3 (13)
11	Ultra-precision CNC Machining center	tempered steel AISI 1045, Carbide 200/100	2 (14)
12	Water Jet Machining Centre	aluminum 6061-T6 and stainless steel 316L	3 (15)
13	micro ECDCM experimental setup	glass slide, Tungsten carbide rod 1.2/0.11	11 (16)

Table 2 - Factors and levels in drilling test

Process parameters	Units	Levels		
		-1	0	1
Cutting speed	rpm	1300	1400	1500
Feed rate	mm/min	1	2	3
Drill diameter	mm	0.3	0.4	0.5

Board (PCB). The drilling on CFRP materials has been attempted by many researchers. But nobody has attempted drilling micro-holes on these materials using micro-drills and conventional CNC VMC. Therefore, it is aimed to make microhole on CFRP material using micron level tools. In this work, the quality characteristic of microhole is evaluated by aspect ratio of microhole obtained. None of the researchers have not been studied the aspect ratio of micro-holes on CFRP laminates. The aspect ratio of micro-holes values are depending on the input machining parameters namely cutting speed, rate of feed and diameter of drill. The relationship aspect ratio achieved and machining parameters are analysed by linear regression model and the obtained results are compared with the experimental results. A regression model was also developed to predict the aspect ratio achieved. The factors and its levels in

drilling experiments are shown in Table 2. The main aim of the paper is to making high aspect ratio microhole on CFRP using carbide microdrill.

2. DESIGN OF EXPERIMENT

Carrying out experiments as per traditional experimental design procedures are complex to solve the problems, taking more time and high cost consuming methods. In order to overcome these, Taguchi developed the special design of orthogonal array to study the whole parameters with least number of experiments (17, 18). Taguchi approach analyzes the variation in responses using S/N ratio which results in obtaining maximization of quality characteristics. In this present investigation, the aspect was selected as the desired performance characteristic, which has the quality characteristics of “larger the better”.

3. EXPERIMENTAL PROCEDURE

The CFRP composites used in this work was fabricated using autoclave method with 55 percent of carbon fiber reinforced in epoxy matrix. The CFRP composites have 3 mm thickness and consisting of 12 alternating layers of fibres along the 0/90° fibre orientation. Holes were drilled using a HARDINGE VMC 800II vertical machining center. The entry and exit diameter microhole were measured by non-contact video measurement system (VMS). The photograph of drilling set-up is shown in Fig. 1. Solid carbide drills having diameter of 0.3 mm, 0.4 mm and 0.5 mm were performed in this study. The conditions of cutting were chosen from previous literature and trial experiments. All experiments were conducted under dry drilling conditions. The aspect ratio of holes made is calculated as the ratio of the length of hole to the average diameter of the machined hole which is given as ((diameter of the hole at entry + diameter of the hole at the exit)/2).



Figure 1. Drilling set-up

4. EXPERIMENTAL RESULTS

Relationship between aspect ratio achieved and cutting parameters

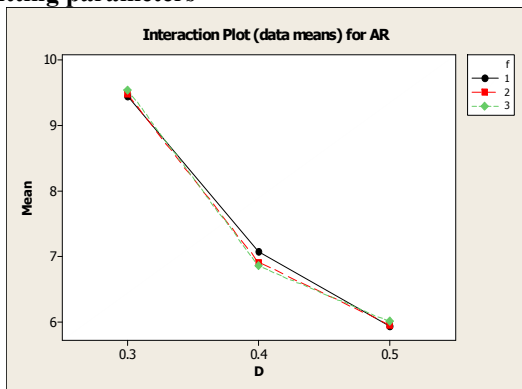


Figure 2. Effect of Tool Diameter on Aspect ratio

The cutting speed, rate of feed and drill diameter were have been considered for the evolvement of mathematical models for aspect ratio. The relationship between input factors and output factors

were established by using linear regression equations. The statistical analysis software MINITAB 14.0 was employed to obtain the regression models.

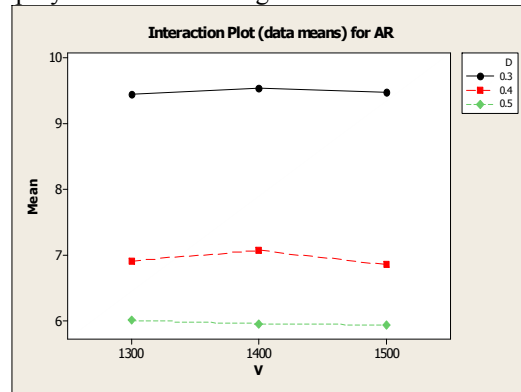


Figure 3. Effect of cutting speed on Aspect ratio

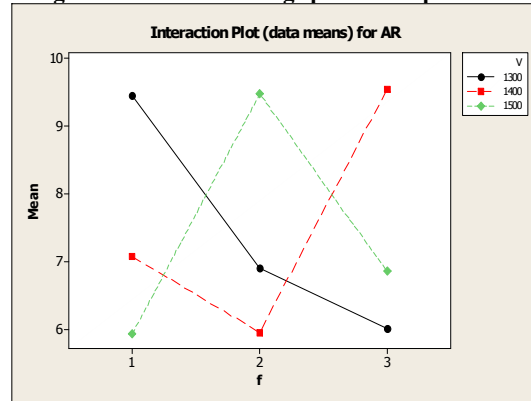


Figure 4. Effect of feed rate on Aspect ratio

The model developed for aspect ratio is given as below Eq. (1)

$$AR = 14.8 - 0.00017 * V - 0.008 * f - 17.7 * D \quad (1)$$

R-Sq = 93.7% R-Sq (adj) = 89.9%

In this linear regression analysis, R-Sq is the regression coefficient (R-Sq>0.90) for the developed models, which specify that the experimental data are fit with the model satisfactory.

Effects of drilling conditions on aspect ratio

The effect of drill diameter on the obtained aspect ratio is shown in Fig. 2. Generally, when using macro size drills as the tool diameter decreases the mean obtained aspect ratio value increases. This is also found to be correct when using micro tools in this paper. The mean obtained aspect ratio values drill diameters as 0.5 mm, 0.4 mm and 0.3 mm are 5.96, 6.94 and 9.49 respectively. The maximum variation in the obtained aspect ratio is 8.65%. The effect of cutting speed on obtained aspect ratio is shown in Fig. 3. As the cutting speed increases while the mean obtained aspect ratio is almost constant for all drill diameters. The effect of feed rate on obtained aspect ratio is shown in Fig. 4. As the feed rate increases the mean obtained aspect ratio values is fluctuating.

Analysis of variance

Table 3 - L9 orthogonal array and values of aspect ratio

No	V	f	D	Theoretical Aspect ratio	Obtained Aspect ratio	Variation (%)
1	1300	1	0.3	10	9.45	5.48
2	1300	2	0.4	7.5	6.91	7.82
3	1300	3	0.5	6	6.00	0.06
4	1400	1	0.4	7.5	7.07	5.73
5	1400	2	0.5	6	5.95	0.84
6	1400	3	0.3	10	9.55	4.50
7	1500	1	0.5	6	5.93	1.24
8	1500	2	0.3	10	9.48	5.18
9	1500	3	0.4	7.5	6.85	8.65

The theoretical aspect ratio and the experimental results of the obtained aspect ratio are shown in Table 3. The S/N of obtained aspect ratio was shown in Table 4. Based on the taguchi analysis, the optimum machining parameters for the optimum obtained aspect ratio are at medium cutting speed 1400 rpm, low feed rate 1 mm/min and low drill diameter 0.3 mm.

Table 4 - Taguchi analysis for S/N ratio of aspect ratio versus V, f, D

Level	Cutting speed	Feed rate	Drill diameter
1	17.29	17.32*	19.55*
2	17.36*	17.27	16.83
3	17.24	17.29	15.50
Delta	0.12	0.05	4.04
Rank	2	3	1

*optimum level

Table 5 - ANOVA for aspect ratio

	DF	SS	MS	F	P	% CP
V	2	0.01	0.008	1.11	0.47	0.08
f	2	0.01	0.001	0.13	0.88	0.01
D	2	19.9	9.976	1328	0.00	99.87
E	2	0.01	0.007			0.08
T	8	19.98				100

S = 0.0866667 R-Sq = 99.92%
R-Sq(adj) = 99.70%

These optimum machining parameters were chosen as the parameter corresponding to high S/N ratio from Table 4. In the Table 5, it is found that the drilling is the most influencing drill diameter with a P= 0.001. This depicts the physical and statistical significance in microdrilling of CFRP. The cutting speed and feed rate are found to have no significance aspect ratio.

5. Confirmation test

Table 6 depicts the conditions of machining which is employed for confirmation test. The aspect ratio predicted by the model developed in this study and the aspect ratio obtained by experiments is given in Table 7. The percentage error between the predicted values and experimental results are obtained within 5% as given in Table 7. Hence, the developed model is said to be a feasible and an effectual method for the assessing the drilling process.

Table 6 - Cutting conditions in confirmation tests

Trails	V	f	D
	rpm	mm/min	mm
1	1300	1	0.3
2	1300	1	0.5
3	1400	1	0.3
4	1400	1	0.5
5	1500	1	0.3
6	1500	1	0.5

Table 7 - Experimental confirmation and comparison with model

Trails	Aspect Ratio		
	Experimental value	Predicted value	Variation (%)
1	9.32	9.26	0.64
2	5.45	5.72	4.74
3	9.67	9.24	4.61
4	5.71	5.70	0.11
5	9.34	9.22	1.22
6	5.67	5.68	0.30

CONCLUSIONS

The CFRP material was drilled using drills having diameter 0.3 mm, 0.4 mm and 0.5 mm by varying cutting speed and feed rate. The parameters were optimized using taguchi method. A model for aspect ratio was developed. From this analysis the following conclusions were drawn.

- The drill diameter has larger contribution to the aspect ratio.
- A high average aspect ratio 9 was achieved where using 0.3 mm drill diameters with less deviation of obtained hole diameter. This result is in good agreement with the confirmation test
- The confirmation tests verify this method for the evaluation of aspect ratio and error within 5 % while drilling of CFRP composite material.

REFERENCES

1. Hull, D., and Clyne, T. W., 1996, "An Introduction to Composite Materials," 2nd ed., Cambridge University Press, Cambridge.
2. Rahamathullah, I., Shunmugam, M. S., 2013, "Analyses of forces and hole quality in micro-drilling of carbon fabric laminate composites," *Journal of Composite Materials*, Vol. 47, pp. 1129-1140.
3. Faraz, A., Biermann, D., and Weinert, K., 2009, "Cutting edge rounding: an innovative tool wear criterion in drilling CFRP composite laminates," *International Journal of Machine Tools & Manufacture*, vol. 49, pp.1185-1196.
4. Zheng, L., Wang, C., Yang, L., Song, Y., and Fu, L., 2012, "Characteristics of chip formation in the micro-drilling of multi-material sheets," *International Journal of Machine Tools & Manufacture*, vol. 52, pp. 40-49.
5. Zabel, A., and Heilmann, M., 2012, "Deep hole drilling using tools with small diameters-Process analysis and process design," *CIRP Annals - Manufacturing Technology*, vol. 61, pp.111-114.
6. Bhandari, B., Sun H, Y., Sung Y, H., Seol M, J., Quan P, M., Bong L, G., Huang, Y., Linke, B, S., D.A. Dornfeld, D, A., and Hoon, A, S., 2014, "Development of a micro-drilling burr-control chart for PCB drilling," *Precision Engineering*, vol. 38, pp. 221- 229.
7. Lei, X., Shen, B., Cheng, L., Sun, F., and Chen, M., 2014, "Influence of pretreatment and deposition parameters on the properties and cutting performance of NCD coated PCB micro drills," *International Journal of Refractory Metals and Hard Materials*, vol. 43, pp. 30-41.
8. Aziz, M., Ohnishi, O., and Onikura, H., 2012, "Innovative micro hole machining with minimum burr formation by the use of newly developed micro compound tool," *Journal of Manufacturing Processes*, vol. 14, pp. 224-232.
9. Yahagi, Y., Koyano, T., Kunieda, M., and Yang, X., 2012, "Micro Drilling EDM with High Rotation Speed of Tool Electrode Using the Electrostatic Induction Feeding Method," *Procedia CIRP*, vol.1, pp.162 - 165.
10. Abouridouane, M., Klocke, F., Lung, D., and Adams, O., 2012, "Size Effects in Micro Drilling Ferritic-Pearlitic Carbon Steels," *Procedia CIRP*, vol. 3, pp.91-96.
11. Rahman, A, A., Mamat, A., and Wagiman, A., 2009, "Effect of Machining Parameters on Hole Quality of Micro Drilling for Brass," *Modern Applied Science*, Vol. 3, pp. 221-230.
12. Prajapati, H, B., and Pillai, B., 2014, "Process optimization of PCB Micro-Drilling Process," *International Journal of Engineering Development and Research*, Vol. 2, Issue. 2, ISSN: 2321-9939.
13. Ogawa, K., Nakagawa, H., Hirogaki, T., and Aoyama, E., 2012, "Micro-drilling of CFRP Plates Using a High-speed Spindle," *Key Engineering Materials*, Vol. 523-524, pp.1035-1040.
14. Klocke, F., and Gerschwile, K., 2009, Abouridouane, M., 2009, "Size effects of micro drilling in steel," *Production Engineering Research and Development*, Vol. 3, pp. 69-72.
15. Haghbin, N., Spelt, J, K., and Papini, M., 2015, "Abrasive water jet micro-machining of channels in metals: Model to predict high aspect-ratio channel profiles for submerged and unsubmerged machining," *Journal of Materials Processing Technology*, vol. 222, pp. 399-409.
16. Jui, S, K., Kamaraj, A, B., and Sundaram, M, M., 2013, "High aspect ratio micromachining of glass by electrochemical discharge machining (ECDM)," *Journal of Manufacturing Processes*, vol. 15, pp. 460-466.
17. Yang, W, H., and Tarnq, Y, S., 1999, "Design optimization of cutting parameters for turning operations based on the Taguchi method," *Journal of Material Processing Technology*, Vol. 84, pp. 122-129.
18. Taguchi, G., 1990, "Introduction of quality engineering," Asian Productivity Organization, Tokyo, 1990.



Asian Research Consortium

Asian Journal of Research in Social Sciences and Humanities
Vol. 6, No. 12, December 2016, pp. 768-774.

ISSN 2249-7315

A Journal Indexed in Indian Citation Index

DOI NUMBER:10.5958/2249-7315.2016.01327.7

Category: Science and Technology

Asian Journal
of Research in
Social Sciences
and
Humanities

www.ajsh.com

Experimental Investigation of Machining Parameters in Electrical Discharge Machining using OHNS Material

M. Panneer Selvam*; R. Ravi Kumar**; P. Ranjith Kumar***

*Research Scholar,

Karpagam University,

Coimbatore, India.

**Professor,

Department of Mechanical Engineering,

CMS College of Engineering,

Namakkal, India.

***Professor,

Department of Mechanical Engineering,

MAM School of Engineering,

Tiruchirappalli, India.

Abstract

In this project experimental investigation and analysis of process parameters of EDM process is carried on using Response Surface Methodology. The output process parameters are measured in terms of Machining time and surface roughness. Optimization of EDM process is carried out using OHNS (Oil hardened Non-shrinking Steel) material. Copper is taken as the electrode for machining. Diesel is used as dielectric medium. Experiment is done by varying the gap between the material and electrode, peak voltage and spark timing and other input parameters. The various input parameters considered are current, pulse ON, pulse OFF and tool lift. A set of 27 readings are taken by varying the process parameters. The design of elements considered in response surface method is Box - Behnken Design (BBD). Analysis and optimization is carried out under this design in RSM. This leads to a set of optimized values that indicate a certain parametric factors produce a good surface finish. The main objective is to investigate the surface finish of the drilled holes in the work piece with reference to the machining time and other process variables.

Keywords: OHNS, RSM,, Pulse ON, EDM.



EXPERIMENTAL INVESTIGATION OF MACHINING PARAMETERS IN ELECTRICAL DISCHARGE MACHINING USING EN36 MATERIAL

M. Panneer Selvam¹, Ravikumar. R², Ranjith Kumar.P¹ and Deepak. U¹

¹Department of Mechanical Engineering, MAM School of Engineering, Trichy, Tamilnadu, India

²Department of Mechanical Engineering CMS Engineering College, Namakkal, Tamilnadu, India

E-Mail: mpselvam7565@gmail.com

ABSTRACT

The quality of a product is the main factor for showing growth of a company. The quality of the product mainly depends upon the material and process parameters. Optimization technique plays a vital role to increase the quality of the product. Hence, many authors have presented their works on the optimization of process parameters for various machining processes. EDM process optimization with multiple performance characteristics based on orthogonal array with copper electrode. The process parameters such as gap current, pulse on time and pulse off time were optimized with the considerations of multiple performance characteristics such as material removal rate, tool wear rate and surface roughness value on the work material

Keywords: EDM, MRR, SR, EN36.

INTRODUCTION

Electrical Discharge Machining (EDM) is an important manufacturing process for machining hard metals and alloys. This process is widely used for producing dies, molds, and finishing parts for aerospace, automotive, and surgical components. The process is capable of getting required dimensional accuracy and surface finish by controlling the process parameters. EDM performance is generally evaluated on the basis of Material Removal Rate (MRR), Tool Wear Rate (TWR), Relative Wear Ratio (RWR), and Surface Roughness (SR).

The important EDM parameters affecting to the performance measures of the process are discharge current, pulse on time, pulse off time, arc gap, and duty cycle. In EDM, for optimum machining performance measures, it is an important task to select proper combination of machining parameters. Generally, the machining parameters are selected on the basis of operator's experience or data provided by the EDM manufactures.

LITERATURE REVIEW

Rajneesh Kumar Singh and D.K. Singh

Control parameters optimization of wire – EDM by using genetic algorithm to improve and optimize the responses of a WIRE - EDM machining process.

Raghuraman S, Thirupathi K, Panneerselvam T, Santosh S

Optimization of EDM parameters using Taguchi method and grey relational analysis. Optimization is one

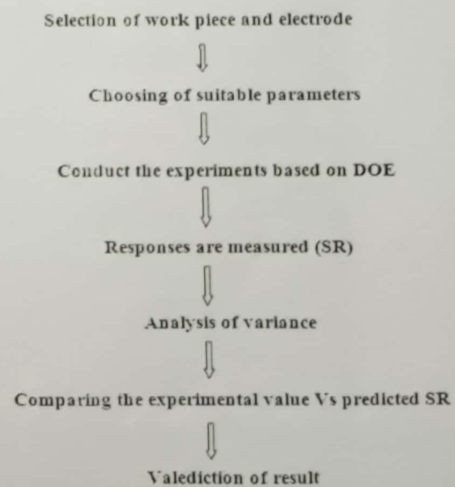
of the techniques used in manufacturing sectors to arrive for the best manufacturing Conditions.

R.A. Mahdavejad

EDM process optimization via predicting a controller model

Dr Navdeep Malhotra, Dr. Sona Rani and Khalid Sheikh
 Optimization of control parameters for surface roughness in side flushing form of die sink EDM

EXPERIMENTAL METHODOLOGY



Research Article

Al6061 Hybrid Metal Matrix Composite Reinforced with Alumina and Molybdenum Disulphide

G. Pitchayapillai,¹ P. Seenikannan,¹ K. Raja,² and K. Chandrasekaran³

¹Department of Mechanical Engineering, Sethu Institute of Technology, Kariapatti, Tamil Nadu, India

²Department of Mechanical Engineering, University College of Engineering, Anna University, Dindigul, Tamil Nadu, India

³Department of Mechanical Engineering, MAM School of Engineering, Trichy, Tamil Nadu, India

Correspondence should be addressed to G. Pitchayapillai; gp-pillai05@yahoo.com

Received 1 September 2016; Accepted 12 October 2016

Academic Editor: Luigi Nicolais

Copyright © 2016 G. Pitchayapillai et al. This is an open access article distributed under the Creative Commons Attribution License, which permits unrestricted use, distribution, and reproduction in any medium, provided the original work is properly cited.

Aluminum Hybrid Reinforcement Technology is a response to the dynamic ever-increasing service requirement of industries such as transportation, aerospace, automobile, and marine, due to its attractive properties like high ductility, highly conductivity, light weight, and high strength to weight ratio. In this evolution, an attempt has been made to investigate the wear rate of Al6061 hybrid metal matrix composite reinforced with the hard ceramic alumina (4, 8, and 12 wt.% of Al_2O_3) and soft solid lubricant of molybdenum disulphide (2, 4, and 6 wt.% of MoS_2) is fabricated by using stir casting method. The unlubricated pins on disc wear tests were conducted to examine the wear behaviour of Al6061/12 wt.% of Al_2O_3 / MoS_2 composites. The sliding wear tests were carried out at various loads of 15, 30, and 45 N, sliding velocity (1.25, 2.50, and 3.25 m/sec), and different MoS_2 wt.% (2, 4, and 6 wt.%). In addition, the CNC turning experiments were conducted on Al6061/12 wt.% Al_2O_3 /6 wt.% MoS_2 using CNMG 120408 uncoated carbide cutting tool under cutting of 100, 150, and 200 m/min, feed of 0.1, 0.2, and 0.3 mm/rev, and depth of cut of 1, 1.5, and 2 mm.

1. Introduction

Aluminum hybrid matrix composites have become better substitutes for the conventional aluminum alloys because of their characters like improved strength to weight ratio, energy saving, and better wear resistance [1]. Reinforced aluminum hybrid matrix, a composite for the use of the automotive industry and other structural applications, has been increased because of the physical and mechanical properties it possesses [2]. Aluminum based hybrid matrix composites with a variety of particulate reinforcements such as Al_2O_3 , TiC, Ti_2B , B_4C , TiN, Si_3N_4 , graphite, and industrial waste byproduct have been conceived and developed for various potential applications [3]. Researchers have developed aluminum hybrid matrix composites and they are used in many commercial and industrial applications [4]. Newer compositions have been continuously explored and the related valuable studies presented by the past researchers were discussed. Veeresh Kumar et al. [5] conducted the experiment on Al6061/SiC

and Al7075/ Al_2O_3 metal matrix composites and presented the experimental results of the studies regarding hardness, tensile strength, and wear resistance properties of Al6061/SiC and Al7075/ Al_2O_3 composites. The SiC and Al_2O_3 resulted in improving the hardness and density of their respective composites.

Anilkumar et al. [6] have conducted the mechanical properties of fly ash reinforced Al6061 composites and found that the tensile strength, compressive strength, and hardness of the Al6061 composites decrease with the increase in particle size of reinforced fly ash. Increase in the weight fractions of the fly ash particles increases the ultimate tensile strength, compressive strength, and hardness and decreases the ductility of the composite. Asif et al. [7] have investigated the development of aluminum based hybrid metal matrix composites for heavy duty applications and investigated the dry sliding wear behaviour of aluminum alloy based composites, reinforced with silicon carbide particles and solid lubricants such as graphite/antimony trisulphide. The results

revealed that wear rate of hybrid composites is lower than the binary composite. The wear rate decreases with the increasing load and increases with increasing speed.

Singh et al. [8] have conducted an experimental investigation on mechanical behaviour of aluminum by adding SiC and alumina. This work was focused on studying the change in behaviour of aluminum by adding a different percentage age amount of SiC and Al_2O_3 composite and it was concluded that the mechanical properties such as hardness, yield strength, and ultimate strength increasing with a weight percentage of reinforcement increase. But at the same time elongation is decreased and the behaviour of material is changed from ductile to brittle. Gaitondel et al. [9] have done an experiment on wear and corrosion properties of Al/ Al_2O_3 /graphite hybrid composites. The effects of reinforcement, time duration, and particle size on prepared samples of composites have been studied on slurry erosive wear. The static and accelerated corrosion tests have been performed and the microhardness of the developed composites was also investigated. The experimental results on Al5083/ Al_2O_3 /graphite hybrid composites revealed that the addition of reinforcement improves the hardness and reduces corrosion and wear rates.

Sharanabasappa and Motgi [10] were conducting experiments on mechanical properties of fly ash and alumina reinforced aluminum alloy composites. The mechanical properties of fly ash and alumina reinforced aluminum alloy (LM25) composite samples, processed by stir casting route, were reported. It was found that the tensile strength and hardness of the aluminum alloy composites increase with the increase in %wt. of Al_2O_3 . Kuma and Singh [11] investigated a comparative investigation of mechanical properties of aluminum based hybrid metal matrix composites. The result indicated that there is an increase in the value of tensile strength, ultimate tensile strength, hardness value, and flexural strength of newly developed composite having SiC and B_4C particulates in comparison to the SiC, graphite reinforced composite.

Wang and Yan [12] investigated the feasibility of machining Al6061/ Al_2O_3 composite materials by electro discharge machining for blind hole drilling and evaluated the material removal rate, tool wear rate, and surface roughness with various input parameters. Yan and Wang [13] observed that material removal rate is increased with peak current and was erratic with pulse duration. The material removal rate, tool wear rate, and surface roughness are increased with flushing pressure during machining of Al6061/ Al_2O_3 composites using rotary electro discharge machining with a tube electrode. Yan et al. [14] found that, in case of rotary electro discharge machining process, the main challenge is using a disk like electrode for machining Al6061/ Al_2O_3 composites. The influence of reinforcement of SiC and Al_2O_3 in different matrix of Al6061 and Al7075 on mechanical properties was investigated by Veeresh kumar et al. [15] and they found that microhardness of the composites was increased linearly with the increase of filler content. The surface roughness increases with increase in volume fraction of Al_2O_3 particles reinforced with aluminium metal matrix composites when machined by carbide coated tools [16].

The cutting velocity has 20.8% influences on the surface roughness during machining of A356/20/SiC/T6 composite [17]. Better surface finish was achieved while machining aluminum metal matrix composites with 5% SiCp at higher cutting speed produces [18]. Metin Kok [19] concluded that while machining Al2024/ Al_2O_3 composites using coated and uncoated carbide cutting tools the surface roughness of the work piece was mostly affected by cutting speed. The machined surfaces of Al-Si alloy-graphite composites tend to be rougher than the surfaces machined at identical conditions on matrix material without reinforcement because of the presence of deeper holes or valleys [20]. The surface roughness value decreases with increasing cutting speed.

However many researchers have carried out the mechanical and wear properties and machining characteristics of aluminum metal matrix composites with SiC and Al_2O_3 as reinforcing materials. In the case of hybrid Al6061/ Al_2O_3 /MoS₂ composites, limited literature is available, encompassing various aspects such as mechanical properties and wear behaviour and conducting the machining study of the composites. Aluminum based Al_2O_3 composite material has properties such as low weight, heat resistant, wear resistant, and low cost. These are found in various engineering applications such as cylinder block liners, vehicle drive shafts, automotive pistons, and bicycle frames. These materials are known as difficult to machine materials, because of the hardness and abrasive nature of reinforcement element like alumina particle [21]. The addition of MoS₂ reinforcement in composites as a hybrid reinforcement further increases the wear resistance of the composite. This is attributed to the stable and MoS₂ rich mechanically mixed layer, which prevents metal to metal contact and reduces the wear of the composite. The unstable mechanically mixed layer in the absence of the lubricant phase leads to lower wear resistance in hybrid composite [22]. So an attempt was made to study the tribological, mechanical, and machining characteristics on Al6061/ Al_2O_3 /MoS₂ hybrid composite.

2. Experimental Details

The stir casting method is simple and the most economical way of fabricating particulate reinforced composites. In this technique, to accomplish the optimum properties of the hybrid composites, the distribution of the reinforced particles in the base material should be homogeneous and the wettability among the olden materials and particulates ought to be optimized. The moisture level in the cast composite must be reduced and the element reactions among the particles and the base material have to be avoided. The whirlpool method is one of the enhanced recognized tactics used to build a high quality allocation of the reinforced material in the base matrix. In this method, the base material is melted followed by a forceful stirring by automatic agitator to form a whirlpool at the face of dissolve, and the particle is subsequently introduced at the region of the vortex.

2.1. Material Fabrication. The chemical composition of Al6061 alloy is given in Table 1 and Al6061 alloy was

TABLE 1: Chemical composition of Al6061 alloy.

Si	Fe	Cu	Mn	Mg	Cr	Zn	Ti	Al
0.65	0.7	0.25	0.15	0.8	0.07	0.25	0.15	Remaining

TABLE 2: Affecting factors and levels selected for tensile strength Al6061/Al₂O₃/MoS₂.

Factors/levels	1	2	3
X: wt.% Al ₂ O ₃ (wt.%)	4	8	12
Y: wt.% MoS ₂ (wt.%)	2	4	6

melted in a crucible furnace at 725°C. Subsequent to melting and degassing by nitrogen, the molten metal was stirred by an alumina coated stainless steel stirrer at 600 rpm for 20 min time duration. During stirring, it is preheated at 600°C; particles alumina and MoS₂ powder were added. After the addition of MoS₂, the composite was poured into the preheated (250°C) permanent mould. The Al6061 alloy with different wt.% of hybrid composites is produced and test specimens were machined according to ASTM standards.

2.2. Mechanical Behaviour. The hardness tests were carried out according to ASTM E10-07 standards using Brinell hardness testing machine with a 10 mm ball indenter and 500 kg load for 30 sec. The test was carried out at atmospheric temperature (30°C) and the measurement of hardness was taken at three different locations on each sample to obtain an average value of hardness. As per the ASTM E08-8 standard, the tensile strength was evaluated on the cylindrical rod of casted composites. The 1200 grit grindings silicon carbide paper was used to polish the test specimens in order to decrease the machining scratches and the effects of surface defects on the sample. The universal testing machine was loaded with 10 KN; load cell was used to conduct the tensile test. The affecting factors and levels selected for mechanical behaviour Al6061/Al₂O₃/MoS₂ are given in Table 2.

2.3. Tribological Behaviour. Dry sliding wear behaviour of Al6061/12 wt.% Al₂O₃/MoS₂ hybrid composites is studied in pin on disc test apparatus. Pin specimens of 6 mm diameter and 15 mm height, for wear test, were prepared from the above composites and the composites were machined and polished. The test was conducted with various loads of 15 N, 30 N, and 45 N at a sliding speed of 125, 2.50, and 3.25 m/s and 2, 4, and 6 MoS₂ wt.%. It was conducted at room temperature (30°C) and relative humidity of 60–65%. The affecting factors and levels selected for Tribology Al6061/12 wt.% Al₂O₃/MoS₂ are given in Table 3.

2.4. CNC Turning Test. The work material used for the present investigation is Al6061/12 wt.% Al₂O₃/6 wt.% MoS₂ and diameter of the material is 20 mm and machined length is 60 mm for all trials. The experiments were conducted on Fanuc CNC lathe and CNMG 120408; uncoated carbide cutting tool is used as the insert for all machining operations. The affecting factors and levels selected for turning properties Al6061/12 wt.% Al₂O₃/6 wt.% MoS₂ are given in Table 4. SR

is measured by the Mitutoyo surface roughness tester. The three cutting parameters selected for the present investigation are cutting speed, feed, and depth of cut. Minitab14 statistical software has been used for the analysis of the experimental work.

3. Result and Discussion

3.1. Optimum Setting for TS and BHN of Al6061/Al₂O₃/MoS₂. The tensile strength and hardness of the Al6061/4, 8, and 12 wt.% Al₂O₃/2, 4 wt.% MoS₂ hybrid composite are shown in Figures 1(a) and 1(b). It is observed that an addition of alumina particles improves the tensile strength and hardness of hybrid composites. It is evident that tensile strength and hardness clearly increase with the addition of alumina particles. The tensile strength and hardness of the Al6061/4, 8, and 12 wt.% Al₂O₃/6 wt.% MoS₂ hybrid composites are shown in Figure 1(c). The tensile strength and hardness of hybrid composites were decreased with increasing content of molybdenum disulphide.

The measured values of tensile strength and BHN for Al6061/Al₂O₃/MoS₂ under different wt.% and corresponding signal to noise ratio for all experimental runs are given in Table 5. The Taguchi analyses of tensile strength and BHN for Al6061/Al₂O₃/MoS₂ under different wt.% are given in Table 6. It clearly shows the maximum tensile strength is obtained at 12 wt.% of Al₂O₃ and 2 wt.% of MoS₂ and the maximum BHN is obtained at 12 wt.% of Al₂O₃ and 4 wt.% of MoS₂. Table 7 shows the results of ANOVA for tensile strength and BHN on Al6061/Al₂O₃/MoS₂ hybrid composite. It is observed that Al₂O₃ is the most significant parameter affecting the tensile strength of Al6061/Al₂O₃/MoS₂ with $F: P$ value of 1092.26 : 0.000 and Al₂O₃ is significantly affecting the BHN of Al6061/Al₂O₃/MoS₂ with $F: P$ value of 480.69 : 0.000.

3.2. Tribological Behaviour of Al6061/Al₂O₃/MoS₂. The variation of wear rate for Al6061/12 wt.% Al₂O₃/MoS₂ hybrid composite with respect to different sliding velocity and applied load is shown in Figures 2(a), 2(b), and 2(c). The applied load affects the wear rate of hybrid composites significantly. The wear rate varying with applied load is an indicative of Archard's law and significantly lower in the case of hybrid composites. The wear rate increases with increasing applied load and it is less at 6 wt.% of MoS₂ hybrid composites as compared to 2 wt.% of MoS₂ [23]. This is mainly due to the presence of Al₂O₃ in Al6061. However, at all load conditions

TABLE 3: Affecting factors and levels selected for Tribology Al6061/12 wt.% Al₂O₃/MoS₂.

Factors/levels	1	2	3
A: load (N)	15	30	45
B: sliding velocity (m/s)	1.25	2.50	3.25
C: wt.% of MoS ₂ (wt.%)	2	4	6

TABLE 4: Affecting factors and levels selected for turning properties Al6061/12 wt.% Al₂O₃/6 wt.% MoS₂.

Factors/levels	1	2	3
V (cutting speed (m/min))	100	150	200
F (feed (mm/rev))	0.1	0.2	0.3
D (depth of cut (mm))	1	1.5	2

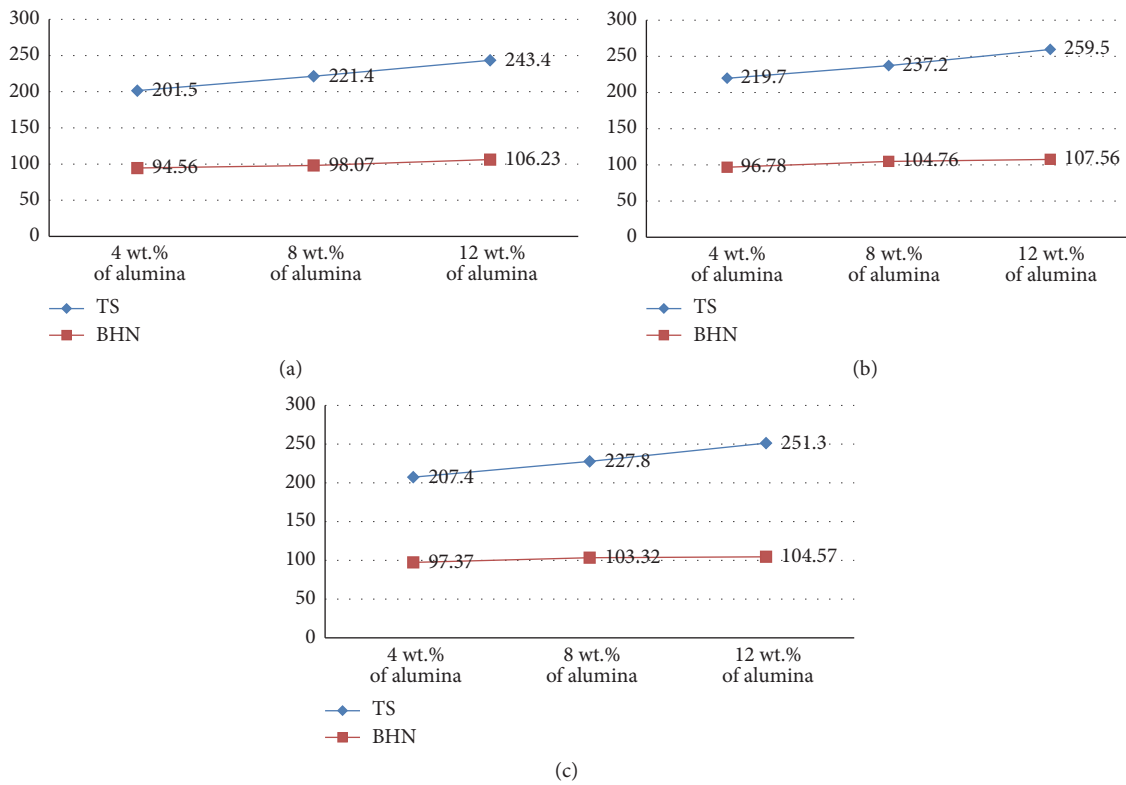


FIGURE 1: (a) Mechanical behaviour of Al6061/2 wt.% of MoS₂/4 : 8 : 12 wt.% of Al₂O₃. (b) Mechanical behaviour of Al6061/4 wt.% of MoS₂/4 : 8 : 12 wt.% of Al₂O₃. (c) Mechanical behaviour of Al6061/6 wt.% of MoS₂/4 : 8 : 12 wt.% of Al₂O₃.

TABLE 5: Experimental result for tensile strength of Al6061/Al₂O₃/MoS₂.

Trial	X	Y	Al ₂ O ₃ (wt.%)	MoS ₂ (wt.%)	TS (N/mm ²)	S/N ratio	BHN	S/N ratio
1	1	1	4	2	201.5	46.0855	94.56	33.2713
2	1	2	4	4	219.7	46.8366	96.78	33.4117
3	1	3	4	6	207.4	46.3362	97.37	33.3184
4	2	1	8	2	221.4	46.9036	98.67	33.4241
5	2	2	8	4	237.2	47.5023	104.76	33.5343
6	2	3	8	6	227.8	47.1511	103.32	33.4698
7	3	1	12	2	243.4	47.7264	106.23	33.5752
8	3	2	12	4	259.5	48.2827	107.56	33.6758
9	3	3	12	6	251.3	48.0038	104.57	33.6255

TABLE 6: Taguchi analysis: TS & BHN versus X, Y of Al6061/Al₂O₃/MoS₂.

Level	TS		BHN	
	X	Y	X	Y
1	46.42	46.91	33.33	33.42
2	47.19	47.54	33.48	33.54
3	48.00	47.16	33.63	33.47
Delta	1.58	0.64	0.29	0.12
Rank	1	2	1	2

TABLE 7: Analysis of variance for TS & BHN of Al6061/Al₂O₃/MoS₂.

Source	DF	TS				BHN			
		Seq SS	Adj MS	F	P	Seq SS	Adj MS	F	P
X	2	2634.78	1317.39	1092.26	0.000	3.7691	1.8845	480.69	0.000
Y	2	423.56	211.78	175.59	0.000	0.6125	0.3063	78.12	0.001
Error	4	4.82	1.21			0.0157	0.0039		
Total	8	3063.17				4.3973			

$R^2 = 99.84\%$; R^2 (adj) = 99.69%
 $R^2 = 99.64\%$; R^2 (adj) = 99.29%

considered, the wear resistance of the hybrid composites is superior to the matrix alloy. The wear rate is increased with increase in sliding speed Al6061/12 wt.% Al₂O₃/MoS₂ hybrid composite. Increasing sliding speed temperature is raised to the sliding surfaces; this leads to softening of the matrix and composite pin surfaces and it is due to the enhancement in the hardness. The increase in hybrid composite hardness results in improvement of wear resistance. The presence of MoS₂ and Al₂O₃ particles in the hybrid composite will lead to further reduction of wear rate [24].

The coefficient of friction for Al6061/12 wt.% Al₂O₃/MoS₂ hybrid composites under varying load and sliding velocity is shown in Figures 3(a), 3(b), and 3(c). The coefficient of friction is decreased with increasing wt.% of MoS₂ and increasing the due to load. The Al₂O₃ particles act as load bearing elements in the hybrid composites and also this results in formation of more stable lubricating film on the tribosurface of the hybrid composites. The decreased coefficient of friction of hybrid composite with MoS₂ content can be credited to the collective effects of MoS₂ and Al₂O₃ particles in formation of a more resistant tribolayer on the contact surface. The graphite tribofilm minimizes the degree of shear stress transferred to the sliding material underneath the sliding contact area which results in less plastic deformation in the subsurface region and reduces the wear rate in the hybrid composites [25].

3.3. Effect of Alumina and Molybdenum Disulfide Content in Al6061. The wear surface of the Al6061/12 wt.% Al₂O₃/6 wt.% MoS₂ under sliding velocity of 2.50 m/sec is given in Figures 4(a) and 4(b). It clearly reveals the formation of tribolayer on the contact surfaces of aluminum composites tested at 15 N and 45 N conditions. Figure 4(a) reveals that the tribolayer is formed only to a limited extent in Al6061/12 wt.%

Al₂O₃/4 wt.% MoS₂ hybrid composite at 15 N load, 2.50 m/s sliding speed. At a higher load of 45 N and 2.50 m/s sliding speed the tribolayer that is formed increases, due to squeezing out of solid lubricant from the hybrid composites. The extent of tribolayer formation also increases with increasing percentage of molybdenum disulphide located immediately below the contact surface.

The experimental values of wear rate and coefficient of friction for Al6061/12 wt.% Al₂O₃/MoS₂ under different parameters and corresponding signal to noise ratio for all experimental runs are given in Table 8. The Taguchi analysis for Al6061/12 wt.% Al₂O₃/MoS₂ under different load, sliding velocity, and wt.% of MoS₂ is given in Table 9. It clearly shows the minimum wear rate and coefficient of friction is obtained at 15 N of load, 3.25 m/sec of sliding velocity, and 6 wt.% of MoS₂. Table 10 shows the results of ANOVA for wear rate and coefficient of friction on Al6061/12 wt.% Al₂O₃/MoS₂ hybrid composite. It is observed that load is the most significant parameter affecting the wear rate and coefficient of friction of Al6061/12 wt.% Al₂O₃/MoS₂ with $F : P$ value of 29.06 : 0.033 and 756.27 : 0.001.

3.4. Optimum Setting for CNC Tuning Al6061/12 wt.% Al₂O₃/6 wt.% MoS₂. The experimental results of arithmetic mean value for turning Al6061/12 wt.% Al₂O₃/6 wt.% MoS₂ under different cutting conditions and corresponding signal to noise ratio for all experimental runs are given in Table 11. The Taguchi analysis for Al6061/12 wt.% Al₂O₃/6 wt.% MoS₂ using uncoated carbide cutting tool is given in Table 12. It clearly shows the minimum surface roughness is obtained at 100 m/min of cutting speed, 0.1 mm/rev of feed, and 1.5 mm of depth of cut for tuning Al6061/12 wt.% Al₂O₃/6 wt.% MoS₂. Table 13 shows the results of ANOVA for surface roughness on Al6061/12 wt.% Al₂O₃/6 wt.% MoS₂ hybrid

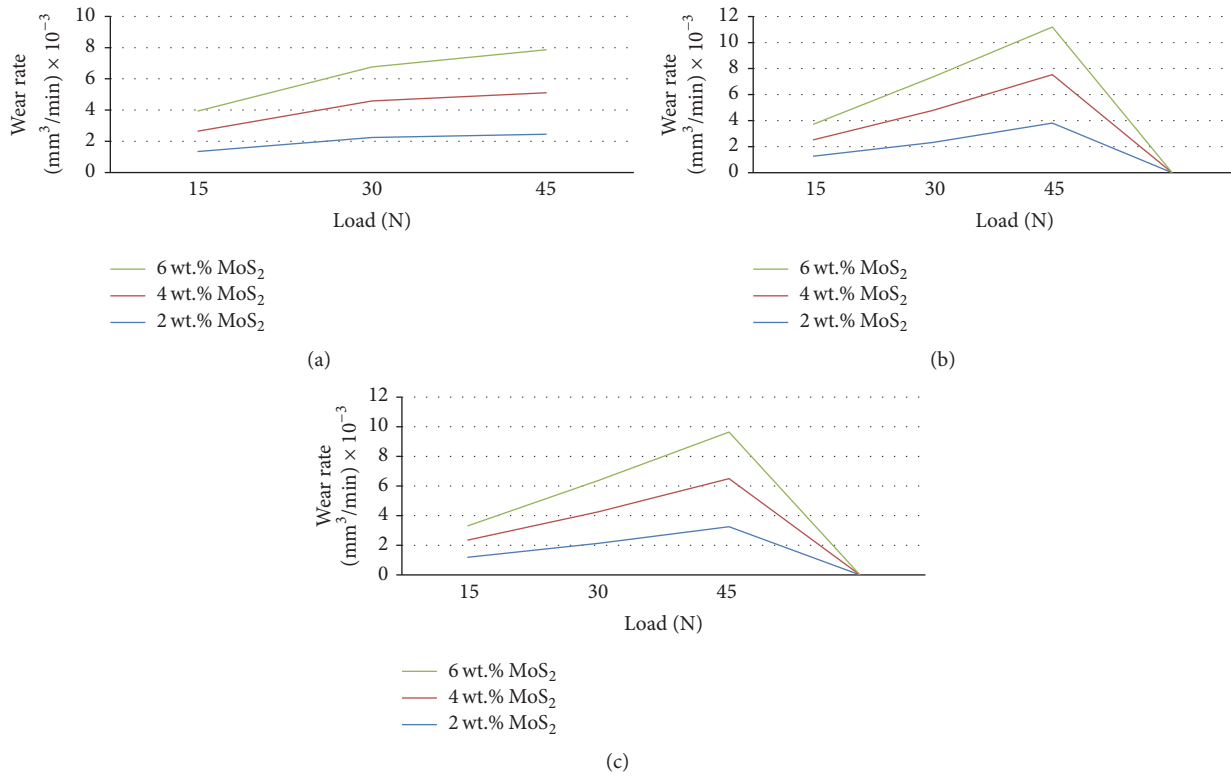


FIGURE 2: (a) Wear rate of Al6061/12 wt.% Al₂O₃/MoS₂ during sliding velocity of 1.25 m/sec. (b) Wear rate of Al6061/12 wt.% Al₂O₃/MoS₂ during sliding velocity of 2.50 m/sec. (c) Wear rate of Al6061/12 wt.% Al₂O₃/MoS₂ during sliding velocity of 3.25 m/sec.

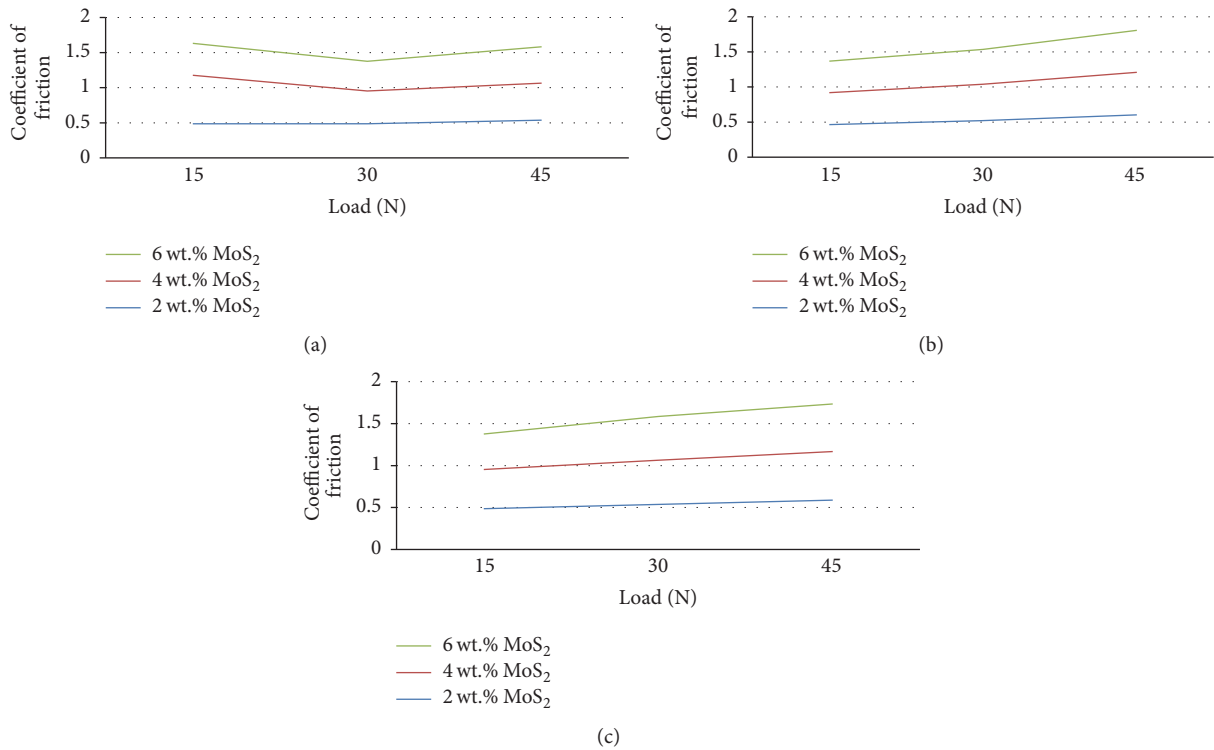


FIGURE 3: (a) Coefficient of friction of Al6061/12 wt.% Al₂O₃/MoS₂ during sliding velocity of 1.25 m/sec. (b) Coefficient of friction of Al6061/12 wt.% Al₂O₃/MoS₂ during sliding velocity of 2.50 m/sec. (c) Coefficient of friction of Al6061/12 wt.% Al₂O₃/MoS₂ during sliding velocity of 3.25 m/sec.

TABLE 8: Experimental results for Al6061/12 wt.% Al₂O₃/MoS₂ of wear study.

Trial	A	B	C	Load (N)	Sliding velocity (m/s)	wt.% of MoS ₂ (wt.%)	Wear rate (mm ³ /min) × 10 ⁻³	S/N	Coefficient of friction	S/N
1	1	1	1	15	1.25	2	1.346	-2.580	0.487	6.249
2	1	2	2	15	2.50	4	1.250	-1.938	0.455	6.839
3	1	3	3	15	3.25	6	0.966	0.300	0.423	7.473
4	2	1	2	30	1.25	4	2.344	-7.399	0.523	5.629
5	2	2	3	30	2.50	6	2.576	-8.218	0.496	6.090
6	2	3	1	30	3.25	2	2.133	-6.579	0.537	5.400
7	3	1	3	45	1.25	6	2.756	-8.805	0.568	4.913
8	3	2	1	45	2.50	2	3.813	-11.625	0.603	4.393
9	3	3	2	45	3.25	4	3.245	-10.224	0.579	4.746

TABLE 9: Taguchi analysis: wear rate and coefficient of friction versus A, B, and C of Al6061/12 wt.% Al₂O₃/MoS₂.

Level	Wear rate			Coefficient of friction		
	A	B	C	A	B	C
1	-1.406	-6.262	-6.929	6.854	5.597	5.348
2	-7.399	-7.261	-6.521	5.707	5.775	5.739
3	-10.218	-5.501	-5.575	4.684	5.873	6.159
Delta	8.812	1.760	1.354	2.170	0.276	0.811
Rank	1	2	3	1	3	2

TABLE 10: Analysis of variance for wear rate of Al6061/12 wt.% Al₂O₃/MoS₂.

Source	DF	Seq SS	Wear rate			Seq SS	Coefficient of friction			
			Adj MS	F	P		Adj MS	F	P	
A	2	6.5442	3.2721	29.06	0.033	0.0247047	0.0123523	756.27	0.001	
B	2	0.3456	0.1728	1.53	0.395	0.0002580	0.0001290	7.90	0.112	
C	2	0.1651	0.0826	0.73	0.577	0.0032667	0.0016333	100.00	0.010	
Error	2	0.2252	0.1126			0.0000327	0.0000327			
Total	8	7.2801				0.0282620				
			$R^2 = 96.91\%$; R^2 (adj) = 87.63%						$R^2 = 99.88\%$; R^2 (adj) = 99.54%	

TABLE 11: Experimental result of surface roughness for Al6061/12 wt.% Al₂O₃/6 wt.% MoS₂.

Trial	V	F	D	V	F	D	Ra (μm)	S/N ratio
1	1	1	1	100	0.1	1	2.21	-6.887
2	1	2	2	100	0.2	1.5	2.35	-7.421
3	1	3	3	100	0.3	2	3.56	-11.029
4	2	1	2	150	0.1	1.5	2.48	-7.889
5	2	2	3	150	0.2	2	2.65	-8.464
6	2	3	1	150	0.3	1	3.62	-11.174
7	3	1	3	200	0.1	2	2.88	-9.187
8	3	2	1	200	0.2	1	3.02	-9.600
9	3	3	2	200	0.3	1.5	3.87	-11.754

TABLE 12: Taguchi analysis: Ra versus V, F, and D for Al6061/12 wt.% Al₂O₃/6 wt.% MoS₂.

Level	V	F	D
1	-8.446	-7.988	-9.221
2	-9.176	-8.495	-9.022
3	-10.181	-11.319	-9.561
Delta	1.735	3.331	0.539
Rank	2	1	3

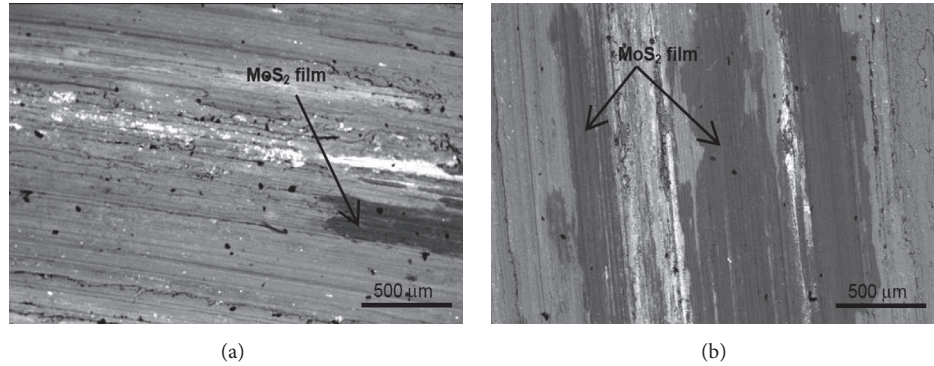


FIGURE 4: (a) Wear surface of Al6061/12 wt.% Al₂O₃/6 wt.% MoS₂ tested at 15 N load. (b) Wear surface of Al6061/12 wt.% Al₂O₃/6 wt.% MoS₂ tested at 45 N load.

TABLE 13: Analysis of variance for Ra of Al6061/12 wt.% Al₂O₃/6 wt.% MoS₂.

Source	DF	Seq SS	Adj SS	Adj MS	F	P
V	2	0.46220	0.46220	0.23110	24.85	0.039
F	2	2.38820	2.38820	1.19410	128.40	0.008
D	2	0.02580	0.02580	0.01290	1.39	0.419
Error	2	0.01860	0.01860	0.00930		
Total	8	2.89480				

S = 0.0964365; R² = 99.36%; R² (adj) = 97.43%

composite. It is observed that feed is the most significant parameter affecting the surface roughness of Al6061/12 wt.% Al₂O₃/6 wt.% MoS₂ with $F : P$ value of 128.40 : 008.

4. Conclusion

In the present investigation, the Al6061/Al₂O₃/MoS₂ hybrid composite is successfully fabricated using stir casting process. The mechanical behaviour, tribological behaviour, and machinability behaviour are evaluated. The obtained results can be summarized as follows:

- (i) Mechanical properties of hybrid composites increase with an increase in weight fraction of alumina particles. An increase in weight fraction of molybdenum disulphide reinforcement decreases the mechanical properties like tensile strength and BHN. The optimum parameter for maximization of tensile strength is obtained at 12 wt.% of Al₂O₃ and 2 wt.% of MoS₂ and the maximum BHN is obtained at 12 wt.% of Al₂O₃ and 4 wt.% of MoS₂.
- (ii) The incorporation of Al₂O₃ reinforcement to Al6061 increases the wear resistance of the composites. The addition of MoS₂ reinforcement in Al6061/Al₂O₃ composites as a hybrid reinforcement further increases the wear and friction resistance of the composite. This is attributed to the stable and MoS₂ rich mechanically mixed layer, which prevents metal to metal contact and reduces the wear of the composite. The unstable mechanically mixed layer in the absence of the lubricant phase leads to lower wear resistance in Al6061/Al₂O₃/MoS₂ hybrid composite.

The optimum parameter for minimization wear rate and coefficient of friction are obtained at 15 N of load, 3.25 m/sec of sliding velocity, and 6 wt.% of MoS₂.

- (iii) The optimum parameter for minimization surface roughness is obtained at 100 m/min of cutting speed, 0.1 mm/rev of feed, and 1.5 mm of depth of cut for CNC turning Al6061/12 wt.% Al₂O₃/6 wt.% MoS₂ hybrid composite.

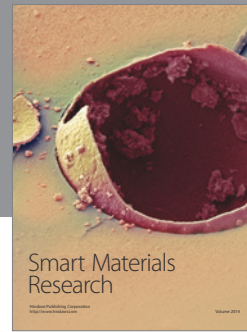
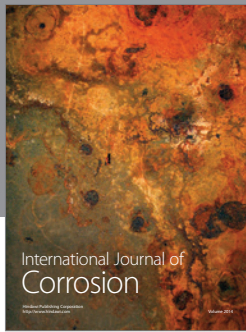
Competing Interests

The authors declare that they have no competing interests.

References

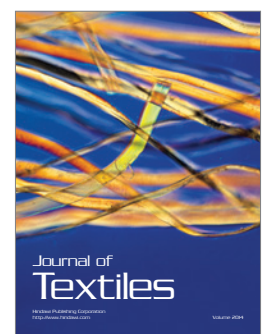
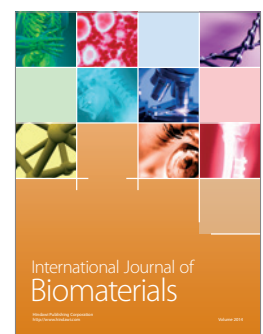
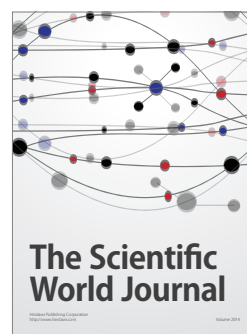
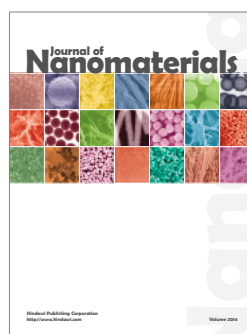
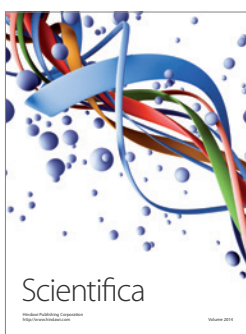
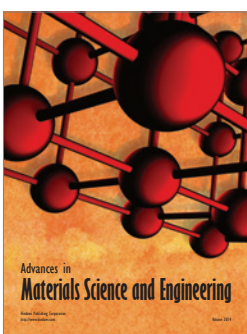
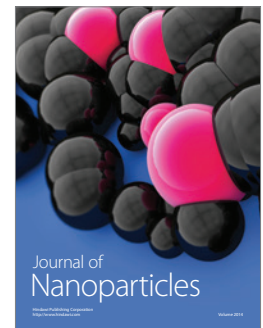
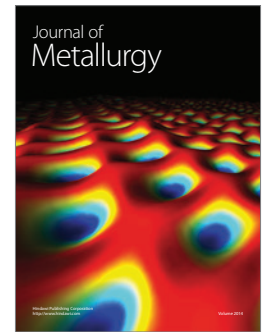
- [1] L. Poovazhagan, K. Kalaichelvan, A. Rajadurai, and V. Senthilvelan, "Characterization of hybrid silicon carbide and boron carbide nano particles reinforced aluminum alloy composites," *Procedia Engineering*, vol. 64, pp. 681–689, 2013.
- [2] A. M. Al-Qutub, A. Khalil, N. Saheb, and A. S. Hakeem, "Wear and friction behavior of Al6061 alloy reinforced with carbon nanotubes," *Wear*, vol. 297, no. 1-2, pp. 752–761, 2013.
- [3] K. Umanath, K. Palanikumar, and S. T. Selvamani, "Analysis of dry sliding wear behaviour of Al6061/SiC/Al₂O₃ hybrid metal matrix composites," *Composites Part B: Engineering*, vol. 53, pp. 159–168, 2013.
- [4] K. Umanath, ST. Selvamani, and K. Palanikumar, "Friction and wear behaviour of Al6061alloy (SiCp/Alp) hybrid composite," *International Journal of Engineering Science and Technology*, vol. 3, pp. 5441–5551, 2011.
- [5] G. B. Veeresh Kumar, C. S. P. Rao, N. Selvaraj, and M. S. Bhagyashekar, "Studies on Al6061/SiC and Al7075/Al₂O₃ metal

- matrix composites," *Journal of Minerals Materials Characterization Engineering*, vol. 9, pp. 454–461, 2010.
- [6] H. C. Anilkumar, H. S. Hebbar, and K. S. Ravishankar, "Mechanical properties of fly ash reinforced aluminum alloy composites," *International Journal of Mechanical and Materials Engineering*, vol. 6, pp. 225–233, 2011.
- [7] M. Asif, K. Chandra, and P. S. Misra, "Development of aluminum based hybrid metal matrix composites for heavy duty applications," *Journal of Minerals and Materials Characterization and Engineering*, vol. 10, pp. 115–134, 2011.
- [8] D. Singh, H. Singh, S. Kumar, and G. Singh, "An Experimental investigation of Mechanical behaviour of aluminum by adding SiC and Alumina," *International Journal on Emerging Technologies*, vol. 3, pp. 178–184, 2012.
- [9] V. N. Gaitonde, S. R. Karnik, and M. S. Jayaprakash, "Some studies on wear and corrosion properties of Al5083/Al₂O₃/graphite hybrid composites," *Journal of Minerals and Materials Characterization and Engineering*, vol. 11, pp. 695–703, 2012.
- [10] R. Sharanabasappa and B. S. Motgi, "A study on mechanical properties of fly ash and alumina reinforced aluminum alloy (LM25) composites," *IOSR Journal of Mechanical and Civil Engineering*, vol. 7, pp. 14–21, 2013.
- [11] D. Kuma and J. Singh, "Comparative Investigation of Mechanical Properties of aluminum based hybrid metal matrix composites," *International Journal of Engineering Research and Applications*, vol. 1, pp. 31–36, 2014.
- [12] C. C. Wang and B. H. Yan, "Blind-hole drilling of Al₂O₃/6061Al composite using rotary electro-discharge machining," *Journal of Materials Processing Technology*, vol. 102, no. 1, pp. 90–102, 2000.
- [13] B. H. Yan and C. C. Wang, "Machining characteristics of Al₂O₃/6061 Al composite using rotary electro-discharge machining with a tube electrode," *Journal of Materials Processing Technology*, vol. 95, no. 1–3, pp. 222–231, 1999.
- [14] B. H. Yan, C. C. Wang, W. D. Liu, and F. Y. Huang, "Machining characteristics of Al₂O₃/6061Al composite using rotary EDM with a disklike electrode," *International Journal of Advanced Manufacturing Technology*, vol. 16, no. 5, pp. 322–333, 2000.
- [15] G. B. Veeresh Kumar, C. S. P. Rao, N. Several, and M. S. Bhagyshekar, "Studies on Al6061-SiC and Al7075-Al₂O₃ metal matrix composites," *Journal of Minerals and Materials Characterization & Engineering*, vol. 9, pp. 43–55, 2010.
- [16] Y. Sahin, M. Kok, and H. Celik, "Tool wear and surface roughness of Al₂O₃ particle-reinforced aluminium alloy composites," *Journal of Materials Processing Technology*, vol. 128, no. 1–3, pp. 280–291, 2002.
- [17] J. P. Davim, "Design of optimisation of cutting parameters for turning metal matrix composites based on the orthogonal arrays," *Journal of Materials Processing Technology*, vol. 132, no. 1–3, pp. 340–344, 2003.
- [18] E. Kiliçkap, O. Çakir, M. Aksoy, and A. Inan, "Study of tool wear and surface roughness in machining of homogenised SiC-p reinforced aluminium metal matrix composite," *Journal of Materials Processing Technology*, vol. 164–165, pp. 862–867, 2005.
- [19] A. Metin Kok, "A study on the machinability of Al₂O₃ particle reinforced aluminum alloy composite," in *Proceedings of the 11th Inorganic Bonded Fiber Composites Conference*, vol. 1, pp. 272–281, Madrid, Spain, November 2008.
- [20] C. A. Brown and M. K. Surappa, "The machinability of a cast aluminium alloy-graphite particle composite," *Materials Science and Engineering*, vol. 102, no. 1, pp. 31–37, 1988.
- [21] M. Kök and K. Özdin, "Wear resistance of aluminium alloy and its composites reinforced by Al₂O₃ particles," *Journal of Materials Processing Technology*, vol. 183, no. 2–3, pp. 301–309, 2007.
- [22] H. Kato, M. Takama, Y. Iwai, K. Washida, and Y. Sasaki, "Wear and mechanical properties of sintered copper-in composites containing graphite or molybdenum disulfide," *Wear*, vol. 255, no. 1–6, pp. 573–578, 2003.
- [23] A. Baradeswaran, S. C. Vettivel, A. Elaya Perumal, N. Selvakumar, and R. Franklin Issac, "Experimental investigation on mechanical behaviour, modelling and optimization of wear parameters of B₄C and graphite reinforced aluminium hybrid composites," *Materials and Design*, vol. 63, pp. 620–632, 2014.
- [24] A. Baradeswaran and A. Elaya Perumal, "Study on mechanical and wear properties of Al 7075/Al₂O₃/graphite hybrid composites," *Composites Part B: Engineering*, vol. 56, pp. 464–471, 2014.
- [25] S. Mahdavi and F. Akhlaghi, "Effect of the graphite content on the tribological behavior of Al/Gr and Al/30SiC/Gr composites processed by in situ powder metallurgy (IPM) method," *Tribology Letters*, vol. 44, no. 1, pp. 1–12, 2011.



Hindawi

Submit your manuscripts at
<http://www.hindawi.com>



Soft Structures on Fuzzy Version of Soft INT G-Modules

R.Nagarajan¹, S. Saleem Abdullah², K.Balamurugan³

1.Associate Professor, Department of Mathematics, J J College of Engg& Tech,Trichirappalli-09

2.Associate Professor, Department of Mathematics, Hazara University, Pakistan

3. Assistant Professor, M.A.M School of Engineering, Trichirappalli-105

Abstract: In this paper, we introduce fuzzy version of soft int-G-modules of a vector space with respect to soft structures, which are fuzzy soft int-G-modules (IFSG-module) .These new concepts show that how a soft set affects on a G-module of a vector space in the mean of intersection, union and inclusion of sets and thus, they can be regarded as a bridge among classical sets, fuzzy soft sets and vector spaces. We then investigate their related properties with respect to soft set operations, soft image, soft pre-image, soft anti image, α -inclusion of fuzzy soft sets and linear transformations of the vector spaces. Furthermore, we give the applications of these new G-module on vector spaces.

Keywords: Soft set, IFSG-module, , fuzzy soft image, fuzzy soft anti image, α -inclusion,trivial,whole.

1.Introduction: Most of the problems in economics, engineering, medical science, environments etc. have various uncertainties. We cannot successfully use classical methods to solve these uncertainties because of various uncertainties typical for those problems. Hence some kinds of theories were given like theory of fuzzy sets [44], rough sets [17], i.e., which we can use as mathematical tools for dealing with uncertainties. However, all of these theories have their own difficulties which are pointed out in [15]. Soft set theory was introduced by Molodtsov [29] for modeling vagueness and uncertainty and it has been received much attention since Maji et al [27], Ali et al [6] and Sezgin and Atagun [34] introduced and studied operations of soft sets. Soft set theory has also potential applications especially in decision making as in [10,11,27]. This theory has started to progress in the mean of algebraic structures, since Aktas, and Cagman [5] defined and studied soft groups. Since then, soft substructures of rings, fields and modules [8], union soft substructures of near-rings and near-ring modules [35], normalistic soft groups [32] are defined and studied in detailed. Soft set has also been studied in the following papers [1,2,3,25,26,45].The theory of G-modules originated in the 20th century. Representation theory was developed on the basis of embedding a group G in to a linear group GL (V).

The theory of group representation (G module theory) was developed by Frobenius G [1962]. Soon after the concept of fuzzy sets was introduced by Zadeh [44] in 1965. Fuzzy subgroup and its important properties were defined and established by Rosenfeld [31] in 1971. After that in the year 2004 Shery Fernandez [36] introduced fuzzy parallels of the notions of G-modules. This study is of great importance since IFSG-modules show how a fuzzy soft set affect on a G-module of a vector space in the mean of intersection, union and inclusion of sets, so it functions as a bridge among classical sets, soft sets and vector spaces. In this paper, we introduce intersection fuzzy soft G-modules of a vector space that is abbreviated by IFSG- module and investigate its related properties with respect to fuzzy soft set operations. Then we give the application of fuzzy soft image, fuzzy soft pre image, upper α -inclusion of fuzzy soft sets, linear transformations of vector spaces on vector spaces in the mean of IFSG-modules. Moreover, we apply soft pre image, soft anti-image, lower α -inclusion of soft sets, linear transformations of vector spaces on these fuzzy soft G-modules. The work of this paper is organized as follows. In the second section as preliminaries, we give basic concepts of soft sets and fuzzy soft G-modules. In Section 3, we introduce IFSG-modules and study their characteristic properties. In Section 4, we give the applications of IFSG-modules .

2.Preliminaries:In this section as a beginning, the concepts of G-module[36] soft sets introduced by Molodsov [29] and the notions of fuzzy soft set introduced by Maji et al. [26] have been presented.

2.1 Definition [36]: Let G be a finite group. A vector space M over a field K (a subfield of C) is called a G-module if for every $g \in G$ and $m \in M$, there exists a product (called the right action of G on M) $m.g \in M$ which satisfies the following axioms.

1. $m.1_G = m$ for all $m \in M$ (1_G being the identify of G)
2. $m.(g.h) = (m.g).h, m \in M, g, h \in G$
3. $(k_1 m_1 + k_2 m_2).g = k_1 (m_1.g) + k_2(m_2.g), k_1, k_2 \in K, m_1, m_2 \in M$ &

$g \in G$. In a similar manner the left action of G on M can be defined.

2.2. Definition [36]:Let M and M^* be G-modules. A mapping $\emptyset: M \rightarrow M^*$ is a G-module homomorphism if

1. $\emptyset(k_1 m_1 + k_2 m_2) = k_1 \emptyset(m_1) + k_2 \emptyset(m_2)$
2. $\emptyset(gm) = g \emptyset(m), k_1, k_2 \in K, m, m_1, m_2 \in M$ & $g \in G$.

2.3. Definition [36]: Let M be a G -module. A subspace N of M is a G -sub module if N is also a G -module under the action of G .

Let U be a universe set, E be a set of parameters, $P(U)$ be the power set of U and $A \subseteq E$.

2.4. Definition [29]: A pair (F, A) is called a soft set over U , where F is a mapping given by $F : A \rightarrow P(U)$.

In other words, a soft set over U is a parameterized family of subsets of the universe U . Note that a soft set (F, A) can be denoted by F_A . In this case, when we define more than one soft set in some subsets A, B, C of parameters E , the soft sets will be denoted by F_A, F_B, F_C , respectively. On the other case, when we define more than one soft set in a subset A of the set of parameters E , the soft sets will be denoted by F_A, G_A, H_A , respectively. For more details, we refer to [11,17,18,26,29,7].

2.5. Definition [6] : The relative complement of the soft set F_A over U is denoted by F_A^r , where $F_A^r : A \rightarrow P(U)$ is a mapping given as $F_A^r(a) = U \setminus F_A(a)$, for all $a \in A$.

2.6. Definition [6]: Let F_A and G_B be two soft sets over U such that $A \cap B \neq \emptyset$. The restricted intersection of F_A and G_B is denoted by $F_A \Psi G_B$, and is defined as $F_A \Psi G_B = (H, C)$, where $C = A \cap B$ and for all $c \in C$, $H(c) = F(c) \cap G(c)$.

2.7. Definition [6]: Let F_A and G_B be two soft sets over U such that $A \cap B \neq \emptyset$. The restricted union of F_A and G_B is denoted by $F_A \cup_R G_B$, and is defined as $F_A \cup_R G_B = (H, C)$, where $C = A \cap B$ and for all $c \in C$, $H(c) = F(c) \cup G(c)$.

2.8. Definition [12]: Let F_A and G_B be soft sets over the common universe U and ψ be a function from A to B . Then we can define the soft set $\psi(F_A)$ over U , where $\psi(F_A) : B \rightarrow P(U)$ is a set valued function defined by $\psi(F_A)(b) = \cup\{F(a) \mid a \in A \text{ and } \psi(a) = b\}$,

if $\psi^{-1}(b) \neq \emptyset$, $= 0$ otherwise for all $b \in B$. Here, $\psi(F_A)$ is called the soft image of F_A under ψ . Moreover we can define a soft set $\psi^{-1}(G_B)$ over U , where $\psi^{-1}(G_B) : A \rightarrow P(U)$ is a set-valued function defined by $\psi^{-1}(G_B)(a) = G(\psi(a))$ for all $a \in A$. Then, $\psi^{-1}(G_B)$ is called the soft pre image (or inverse image) of G_B under ψ .

2.9. Definition [13]: Let F_A and G_B be soft sets over the common universe U and ψ be a function from A to B . Then we can define the soft set $\psi^*(F_A)$ over U , where $\psi^*(F_A) : B \rightarrow P(U)$ is a set-valued function defined by $\psi^*(F_A)(b) = \cap\{F(a) \mid a \in A \text{ and } \psi(a) = b\}$, if $\psi^{-1}(b) \neq \emptyset$, $= 0$ otherwise for all $b \in B$. Here, $\psi^*(F_A)$ is called the soft anti image of F_A under ψ .

2.1.Theorem [13]: Let F_H and T_K be soft sets over U , F_H^r , T_K^r be their relative soft sets, respectively and ψ be a function from H to K . then, i) $\psi^{-1}(T_K^r) = (\psi^{-1}(T_K))^r$,
 ii) $\psi(F_H^r) = (\psi^*(F_H))^r$ and $\psi^*(F_H^r) = (\psi(F_H))^r$.

2.10.Definition[14]: Let F_A be a soft set over U and a be a subset of U . Then upper α -inclusion of F_A , denoted by $F_A^{\supseteq\alpha}$, is defined as $F_A^{\supseteq\alpha} = \{x \in A / F(x) \supseteq \alpha\}$. Similarly, $F_A^{\subseteq\alpha} = \{x \in A \mid F(x) \subseteq \alpha\}$ is called the lower α -inclusion of F_A . A nonempty subset U of a vector space V is called a subspace of V if U is a vector space on F . From now on, V denotes a vector space over F and if U is a subspace of V , then it is denoted by $U < V$.

3. IFSG-modules: In this section, we first define intersection fuzzy soft G-modules of a vector space, abbreviated as IFSG-modules. We then investigate its related properties with respect to soft set operations.

Let G be a non-empty set. A fuzzy subset μ on G is defined by $\mu : G \rightarrow [0,1]$ for all $x \in G$.

3.1.Definition: Let G be a group. Let M be a G -module of V and A_M be a fuzzy soft set over V . Then A_M is called Intersection Fuzzy Soft G -module of V (IFSG-m), denoted by $A_M \widetilde{\prec}_l V$ if the following properties are satisfied

$$(IFSG-m_1) \quad A(ax + by) \geq A(x) \cap A(y)$$

$$(IFSG-m_2) \quad A(\alpha x) \geq A(x), \text{ for all } x, y \in M, a, b, \alpha \in F.$$

Example: Let $G = \{1, -1\}$, $M = \mathbb{R}^4$ over \mathbb{R} . Then M is a G -module.

Define A on M by,

$$A(x) = \begin{cases} 1, & \text{if } x_i = 0 \forall i. \\ 0.5, & \text{if at least } x_i \neq 0. \end{cases}$$

Where $x = \{x_1, x_2, x_3, x_4\}$; $x_i \in \mathbb{R}$. Then A is a fuzzy soft G -Module.

3.1.Proposition: If $A_M \widetilde{\prec}_l V$, then $A(0_V) \supseteq A(x)$ for all $x \in M$.

Proof: Since A_M is an IFSG-module of V , then $A(ax+by) \supseteq A(x) \cap A(y)$ for all $x, y \in M$ and since $(M, +)$ is a group, if we take $ay = -ax$ then, for all $x \in M$,

$$A(ax-ax) = A(0_V) \supseteq A(x) \cap A(x) = A(x).$$

3.2.Proposition: If $A_{M_1} \widetilde{\prec}_l V$ and $B_{M_2} \widetilde{\prec}_l V$, then $A_{M_1} \cap B_{M_2} \widetilde{\prec}_l V$.

Proof: Since M_1 and M_2 are G -modules of V , then $M_1 \cap M_2$ is a G -module of V . By

definition 2.6, let $A_{M_1} \cap B_{M_2} = (A, M_1) \cap (B, M_2) = (T, M_1 \cap M_2)$, where

$T(x) = A(x) \cap B(x)$ for all $x \in M_1 \cap M_2 \neq \emptyset$. Then for all $x, y \in M_1 \cap M_2$ and $\alpha \in F$.

$$\begin{aligned} \text{(IFSG-}m_1\text{)} \quad T(ax+by) &= A(ax+by) \cap B(ax+by) \supseteq (A(x) \cap A(y)) \cap (B(x) \cap B(y)) \\ &= (A(x) \cap B(x)) \cap (A(y) \cap B(y)) = T(x) \cap T(y), \end{aligned}$$

$$\text{(IFSG-}m_2\text{)} \quad T(\alpha x) = A(\alpha x) \cap B(\alpha x) \supseteq A(x) \cap B(x) = T(x).$$

There fore $A_{M_1} \cap B_{M_2} = T_{M_1 \cap M_2} \lesssim_l V$.

3.2.Definition: Let (A, M_1) and (B, M_2) be two IFSG-modules of V_1 and V_2 respectively, the product of IFSG-modules (A, M_1) and (B, M_2) is defined as $(A, M_1) \times (B, M_2) = (Q, M_1 \times M_2)$, where $Q(x,y) = A(x) \times B(y)$ for all $(x,y) \in M_1 \times M_2$.

3.1.Theorem: If $A_{M_1} \lesssim_l V$ and $B_{M_2} \lesssim_l V$, then $A_{M_1} \times B_{M_2} \lesssim_l V_1 \times V_2$.

Proof: Since M_1 and M_2 are G -modules of V_1 and V_2 respectively, then $M_1 \times M_2$ is a G -module of $V_1 \times V_2$. By definition 3.2, let

$$\begin{aligned} A_{M_1} \times B_{M_2} &= (A, M_1) \times (B, M_2) \\ &= (Q, M_1 \times M_2), \text{ where } Q(x,y) = A(x) \times B(y) \text{ for all } (x,y) \in M_1 \times M_2. \end{aligned}$$

Then for all $(x_1, y_1), (x_2, y_2) \in M_1 \times M_2$ and $(\alpha_1, \alpha_2) \in F \times F$,

$$\begin{aligned} \text{(IFSG-}m_1\text{)} \quad Q \{(ax_1, by_1) + (ax_2, by_2)\} &= Q (ax_1 + ax_2, by_1 + by_2) \\ &= A (ax_1 + ax_2) \times B(by_1 + by_2) \\ &\supseteq (A (x_1) \cap A (x_2)) \times (B (y_1) \cap B (y_2)) \\ &= Q(x_1, y_1) \cap Q(x_2, y_2) \end{aligned}$$

$$\begin{aligned} \text{(IFSG-}m_2\text{)} \quad Q ((\alpha_1, \alpha_2)(x_1, y_1)) &= Q (\alpha_1 x_1 + \alpha_2 y_1) \\ &= A (\alpha_1 x_1) \times B (\alpha_2 y_2) \supseteq A (x_1) \cap B (y_2) = Q(x_1, y_1). \end{aligned}$$

Hence $A_{M_1} \times B_{M_2} = Q_{M_1 \times M_2} \lesssim_l V_1 \times V_2$.

3.3.Definition: Let A_{M_1} and B_{M_2} be two IFSG-module's of V . If $M_1 \cap M_2 = \{0_V\}$, then the sum of IFSG-module's A_{M_1} and B_{M_2} is defined as $A_{M_1} + B_{M_2} = T_{M_1 + M_2}$ where $T(ax+by) = A(x)+B(y)$ for all $ax+by \in M_1 + M_2$.

3.2.Theorem: If $A_{M_1} \lesssim_l V$ and $B_{M_2} \lesssim_l V$ where $M_1 \cap M_2 = \{0_V\}$, then $A_{M_1} + B_{M_2} \lesssim_l V$.

Proof: Since M_1 & M_2 are G -modules of V , then $M_1 + M_2$ is a G -modules of V . By definition: 3.3, let $A_{M_1} + B_{M_2} = (A, M_1) + (B, M_2) = (T, M_1 + M_2)$, where

$T(ax+by) = A(x)+B(y)$ for all $ax+by \in M_1 + M_2$. It is obvious that since $M_1 \cap M_2 = \{0_V\}$, then the sum is well defined. Then for all $ax_1 + by_1, ax_2 + by_2 \in M_1 + M_2$ and $\alpha \in F$,

$$T ((ax_1 + by_1)+(ax_2 + by_2)) = T((ax_1 + ax_2)+(by_1 + by_2))$$

$$\begin{aligned}
 &= A(a(x_1 + x_2)) + B(b(y_1 + y_2)) \\
 &\supseteq (A(x_1) \cap A(x_2)) + (B(y_1) \cap B(y_2)) \\
 &= (A(x_1) + B(y_1)) \cap (A(x_2) + B(y_2)) \\
 &= T(ax_1 + by_1) \cap T(ax_2 + by_2)
 \end{aligned}$$

$$\begin{aligned}
 T(\alpha(x_1 + y_1)) &= T(\alpha x_1 + \alpha y_1) \\
 &= A(\alpha x_1) + B(\alpha y_1) \supseteq A(x_1) + B(y_1) \\
 &= T(x_1 + y_1)
 \end{aligned}$$

Thus, $A_{M_1} + B_{M_2} \lesssim_l V$.

3.4. Definition : Let A_M be an IFSG-module of V . Then,

- (i) A_M is said to be trivial if $A(x) = \{0_V\}$ for all $x \in M$.
- (ii) A_M is said to be whole if $A(x) = V$ for all $x \in M$.

3.3. Proposition: Let A_{M_1} and B_{M_2} be two IFSG-modules of V , then

- (i) If A_{M_1} and B_{M_2} are trivial IFSG-modules of V , then $A_{M_1} \cap B_{M_2}$ is a trivial IFSG-module of V .
- (ii) If A_{M_1} and B_{M_2} are whole IFSG-modules of V , then $A_{M_1} \cap B_{M_2}$ is a whole IFSG-module of V .
- (iii) If A_{M_1} is a trivial IFSG-module of V and B_{M_2} is a whole IFSG-modules of V , then $A_{M_1} \cap B_{M_2}$ is a trivial IFSG-module of V .
- (iv) If A_{M_1} and B_{M_2} are trivial IFSG-modules of V where $M_1 \cap M_2 = \{0_V\}$, then $A_{M_1} + B_{M_2}$ is a trivial IFSG-module of V .
- (v) If A_{M_1} and B_{M_2} are whole IFSG-modules of V where $M_1 \cap M_2 = \{0_V\}$, then $A_{M_1} + B_{M_2}$ is a whole IFSG-module of V .
- (vi) If A_{M_1} is a trivial IFSG-module of V and B_{M_2} is a whole IFSG-modules of V where $M_1 \cap M_2 = \{0_V\}$, then $A_{M_1} + B_{M_2}$ is a whole IFSG-module of V .

Proof: The proof is easily seen by definition2.6, definition3.3, definition3.4, theorem3.1 and theorem3.3.

3.4. Proposition: Let A_{M_1} and B_{M_2} be two IFSG-modules of V_1 and V_2 respectively. Then

- (i) If A_{M_1} and B_{M_2} are trivial IFSG-modules of V_1 and V_2 respectively, then $A_{M_1} \times B_{M_2}$ is a trivial IFSG-module of $V_1 \times V_2$.
- (ii) If A_{M_1} and B_{M_2} are whole IFSG-modules of V_1 and V_2 respectively, then $A_{M_1} \times B_{M_2}$ is a whole IFSG-module of $V_1 \times V_2$.

Proof: The proof is easily seen by definition3.2, definition3.4 and theorem3.3

4. Applications of IFSG-modules: In this section, we give the applications of soft image, soft pre image, upper α -inclusion of fuzzy soft sets and linear transformation of vector spaces on vector space with respect to IFSG-modules.

4.1.Theorem: If $A_M \lesssim_l V$, then $M_G = \{x \in M / A(x) = A(0_V)\}$ is a G -module of M .

Proof: It is obvious that $0_V \in M_G$ and $\emptyset \neq M_G \subseteq M$. We need to show that $ax+by \in M_G$ and $\alpha x \in M_G$ for all $x, y \in M_G$ and $\alpha \in F$, which means that $A(ax+by) = A(0_V)$ and $A(\alpha x) = A(0_V)$ have to be satisfied. Since $x, y \in M_G$ and A_M is an IFSG-Module of V , then $A(x) = A(y) = A(0_V)$, $A(ax+by) \supseteq A(x) \cap A(y) = A(0_V)$, $A(\alpha x) \supseteq A(x) = A(0_V)$ for all $x, y \in M_G$ and $\alpha \in F$. Moreover, by Proposition 3.1, $A(0_V) \supseteq A(ax+by)$ and $A(0_V) \supseteq A(\alpha x)$ which completes the proof.

4.2.Theorem: Let A_M be a fuzzy soft set over V and α be a subset of V such that $A(0_V) \supseteq \alpha$. If A_M is an IFSG-module of V , then $A_M^{\supseteq \alpha}$ is a G -module of V .

Proof:

Since $A(0_V) \supseteq \alpha$, then $0_V \in A_M^{\supseteq \alpha}$ and $\emptyset \neq A_M^{\supseteq \alpha} \subseteq V$. Let $x, y \in A_M^{\supseteq \alpha}$, then $A(x) \supseteq \alpha$ and $A(y) \supseteq \alpha$. We need to show that $x + y \in A_M^{\supseteq \alpha}$ and $nx \in A_M^{\supseteq \alpha}$ for all $x, y \in A_M^{\supseteq \alpha}$ and $n \in F$. Since A_M is an IFSG-module of V , it follows that

$$A(ax + by) \supseteq A(x) \cap A(y) \supseteq \alpha \cap \alpha = \alpha.$$

Furthermore, $A(nx) \supseteq A(x) \supseteq \alpha$, which completes the proof.

4.3.Theorem: Let A_M and T_W be fuzzy soft sets over V , where M and W are G -modules of γ and Ψ be a linear isomorphism from M to W . If A_M is an IFSG-Module of V , then so is $\Psi(A_M)$.

Proof: Let $w_1, w_2 \in W$. Since Ψ is a surjective linear transformation. Then there exists $m_1, m_2 \in M$ such that $\Psi(m_1) = w_1$, $\Psi(m_2) = w_2$. Then

$$\begin{aligned} (\Psi(A_M))(aw_1 + bw_2) &= \cup\{A(m): m \in M, \Psi(m) = aw_1 + bw_2\} \\ &= \cup\{A(m): m \in M, m = \Psi^{-1}(aw_1 + bw_2)\} \\ &= \cup\{A(m): m \in M, m = \Psi^{-1}(\Psi(aw_1 + bw_2)) = am_1 + bm_2\} \\ &= \cup\{A(am_1 + bm_2) : m_i \in M, \Psi(m_i) = w_i, i = 1,2\} \\ &\supseteq \cup\{A(m_1) \cap A(m_2) : m_i \in M, \Psi(m_i) = w_i, i = 1,2\} \\ &= (\cup A(m_1): m_1 \in M, \Psi(m_1) = w_1) \cap (\cup A(m_2): m_2 \in M, \Psi(m_2) = w_2) \\ &= (\Psi(A_M))(w_1) \cap (\Psi(A_M))(w_2) \end{aligned}$$

Now let $\alpha \in F$ and $w \in W$. Since Ψ is a surjective linear transformation, there exists $\tilde{m} \in M$ such that $\Psi(\tilde{m}) = w$. Then

$$\begin{aligned} (\Psi(A_M))(\alpha w) &= \cup\{A(m): m \in M, \Psi(m) = \alpha w\} \\ &= \cup\{A(m): m \in M, m = \Psi^{-1}(\alpha w)\} \\ &= \cup\{A(m): m \in M, m = \Psi^{-1}(\Psi(\alpha \tilde{m})) = \alpha \tilde{m}\} \\ &= \cup\{A(\alpha \tilde{m}): \alpha \tilde{m} \in M, \Psi(\tilde{m}) = w\} \\ &= (\Psi(A_M))(w) \end{aligned}$$

Hence, $\Psi(A_M)$ is an IFSG –module of V .

4.4.Theorem: Let A_M and T_W be fuzzy soft sets over V , where M and W are G -modules of γ and Ψ be a linear isomorphism from M to W . If T_W is an IFSG-Module of V , then so is $\Psi^{-1}(T_W)$.

Proof: Let $m_1, m_2 \in M$. Then

$$\begin{aligned} \Psi^{-1}(T_W)(am_1+bm_2) &= T(\Psi(am_1+bm_2)) \\ &= T(\Psi(am_1)+\Psi(bm_2)) \\ &\supseteq T(\Psi(m_1)) \cap T(\Psi(m_2)) \\ &= (\Psi^{-1}(T_W))(m_1) \cap (\Psi^{-1}(T_W))(m_2) \end{aligned}$$

Now let $\alpha \in F$ and $m \in M$. Then,

$$\begin{aligned} \Psi^{-1}(T_W)(\alpha m) &= T(\Psi(\alpha m)) \\ &= T(\alpha \Psi(m)) \\ &\supseteq T(\Psi(m)) = \Psi^{-1}(T_W)(m) \end{aligned}$$

Hence $\Psi^{-1}(T_W)$ is an IFSG –module of V .

4.5.Theorem: Let V_1 and V_2 be two vector spaces and $(A_1, M_1) \lesssim_l V_1, (A_2, M_2) \lesssim_l V_2$.

If $f: M_1 \rightarrow M_2$ is a linear transformation of vector spaces, then

- (i) f is surjective, then $(A_1, f^{-1}(M_2)) \lesssim_l V_1$,
- (ii) $(A_2, f(M_1)) \lesssim_l V_2$,
- (iii) $(A_1, \ker f) \lesssim_l V_1$.

Proof: (i) Since $M_1 < V_1, M_2 < V_2$ and $f: M_1 \rightarrow M_2$ is a surjective linear transformation, then it is clear that $f^{-1}(M_2) < V_1$. Since $(A_1, M_1) \lesssim_l V_1$ and $f^{-1}(M_2) < M_1, A_1(ax+by) \supseteq A(x) \cap A(y)$ and $A_1(\alpha x) \supseteq A(x)$ for all $x, y \in f^{-1}(M_2)$ and $\alpha \in F$. Hence $(A_1, f^{-1}(M_2)) \lesssim_l V_1$.

(ii) Since $M_1 < V_1, M_2 < V_2$ and $f: M_1 \rightarrow M_2$ is a vector space linear transformation, then $f(M_1) < V_2$. Since $f(M_1) \subseteq M_2$, the result is obvious by definition 3.1.

(iii) Since $\ker f < V_1$ and $\ker f \subseteq M_1$, the rest of the proof is clear by definition 3.1.

4.1.Corollary: Let $(A_1, M_1) \lesssim_l V_1, (A_2, M_2) \lesssim_l V_2$. If $f: M_1 \rightarrow M_2$ is a linear transformation, then $(A_2, \{0M_2\}) \lesssim_l V_2$.

Proof: By theorem: 4.5, (iii) $(A_1, \ker f) \lesssim_l V_1$, then $(A_2, f(\ker f)) = (A_2, \{0M_2\}) \lesssim_l V_2$,
By theorem 4.5 (ii).

Conclusion: Throughout this paper, we have dealt with IFSG-modules of a vector space. We have investigated their related properties with respect to soft set operations. Furthermore, we have derived some applications of IFSG-modules with respect to soft image, soft pre image, soft anti image, α -inclusion of soft sets and linear transformations of vector spaces. Further study could be done for fuzzy soft sub structures of different algebras.

REFERENCES

[1] S. Abdullah and N. Amin, Analysis of S-box Image encryption based on generalized fuzzy

- soft expert set, *Nonlinear Dynamics*, (2014),[dx.doi.org/10.1007/s11071-014-1767-5](https://doi.org/10.1007/s11071-014-1767-5).
- [2] S. Abdullah, M. Aslam and K. Ullah, Bipolar fuzzy soft sets and its applications in decision making problem, *J. Intell. Fuzzy Syst.* 27:2, 729-742 (2014).
- [3] S. Abdullah, M. Aslam and K. Hila, A new generalization of fuzzy bi-ideals in semigroups and its Applications in fuzzy finite state machines, *Multiple Valued Logic and Soft Computing*, 27:2, 599-623 (2015).
- [4] U. Acar, F. Koyuncu and B. Tanay, Soft sets and soft rings, *Comput. Math. Appl.* 59, 3458-3463 (2010).
- [5] H. Aktas and N. Çağman, Soft sets and soft groups, *Inform.Sci.* 177, 2726-2735 (2007).
- [6] M.I. Ali, F. Feng, X. Liu, W.K. Min and M. Shabir, On some new operations in soft set theory, *Comput. Math. Appl.* 57, 1547-1553 (2009).
- [7] M. I. Ali, M. Shabir, M. Naz, A structures of soft sets associated with new operations, *Comput. Math. Appl.* 61, 2647-2654 (2011).
- [8] A.O. Atagün and A. Sezgin, Soft substructures of rings, fields and modules, *Comput. Math. Appl.* 61 (3), 592-601 (2011).
- [9] K.V. Babitha and J.J. Sunil, Soft set relations and functions, *Comput. Math. Appl.* 60 (7), 1840-1849 (2010).
- [10] N. Çağman and S. Enginoğlu, Soft matrix theory and its decision making, *Comput. Math. Appl.* 59, 3308-3314 (2010).
- [11] N. Çağman and S. Enginoğlu, Soft set theory and uni-int decision making, *Eur. J. Oper. Res.* 207, 848-855 (2010).
- [12] N. Çağman, F. Çitak and H. Aktas, Soft int-groups and its applications to group theory, *Neural Comput. Appl.* 21, 151-158 (2012).
- [13] N. Çağman, A. Sezgin and A.O. Atagün, Soft uni-groups and its applications to group theory, (submitted).
- [14] N. Çağman, A. Sezgin and A.O. Atagün, α -inclusions and their applications to group theory, (submitted).
- [15] Charles W. Curtis and Irving Reiner, *Representation Theory of finite groups and Associative Algebras*, INC, (1962).
- [16] F. Feng, Y. B. Jun, X. Zhao, Soft semirings, *Comput. Math. Appl.* 56, 2621-2628 (2008).

- [17] F. Feng, X.Y. Liu, V. Leoreanu-Fotea, Y.B. Jun, Soft sets and soft rough sets, Inform. Sci. 181 (6), 1125-1137 (2011).
- [18] F. Feng, C. Li, B. Davvaz and M. I. Ali, Soft sets combined with fuzzy sets and rough sets: a tentative approach, Soft Comput. 14 (6), 899-911 (2010).
- [19] George J. Klir and Bo Yuan, Fuzzy sets and Fuzzy logic, Prentice-Hall of India (2000).
- [20] John N. Mordeson and D.S. Malik, Fuzzy Commutative Algebra, World scientific publishing (1998).
- [21] Y.B. Jun, Soft BCK/BCI-algebras, Comput. Math. Appl. 56, 1408-1413 (2008).
- [22] Y.B. Jun, K.J. Lee and J. Zhan, Soft p -ideals of soft BCI-algebras, Comput. Math. Appl. 58, 2060-2068 (2009).
- [23] O. Kazancı, S. Yılmaz and S. Yamak, Soft sets and soft BCH-algebras, Hacet. J. Math. Stat. 39 (2), 205-217 (2010).
- [24] X. Ma and J. Zhan, Applications of a new soft set to h -hemi regular hemi rings via (M,N) -SI- h -ideals, J. Intell. Fuzzy Syst. 26, 2515-2525 (2014).
- [25] X. Ma and J. Zhan, Characterizations of hemi regular hemi rings via a kind of new soft union sets, J. Intell. Fuzzy Syst. 27, 2883-2895 (2014).
- [26] P.K. Maji, R. Biswas and A.R. Roy, Soft set theory, Comput. Math. Appl. 45, 555-562 (2003).
- [27] P.K. Maji, A.R. Roy and R. Biswas, An application of soft sets in a decision making problem, Comput. Math. Appl. 44, 1077-1083 (2002).
- [28] P. Majumdar and S.K. Samanta, On soft mappings, Comput. Math. Appl. 60 (9), 2666-2672 (2010).
- [29] D. Molodtsov, Soft set theory-first results, Comput. Math. Appl. 37, 19-31 (1999).
- [30] J. N. Mordeson and D. S. Malik., Fuzzy Commutative Algebra, World scientific publishing, (1998).
- [31] A. Rosenfeld, Fuzzy groups, J.M. Anal. and Appli. 35, 512 - 517 (1971).
- [32] A. Sezgin and A. O. Atagun, Soft groups and normalistic soft groups, Comput. Math. Appl. 62 (2), 685-698 (2011).
- [33] A. Sezgin, A. O. Atagun, N. Cagman, Union soft substructures of near-rings and N -groups, Neural Comput. Appl. 21, 133-143 (2012).

- [34] A. Sezgin and A.O. Atagun, On operations of soft sets, *Comput. Math. Appl.* 61 (5), 1457-1467 (2011).
- [35] A. Sezgin, A.O. Atag'un and E. Ayg'un, A note on soft near-rings and idealistic soft near-rings, *Filomat* 25 (1), 53-68(2011).
- [36] Shery Fernandez, Ph.D. thesis "A study of fuzzy g-modules" April 2004.
- [37] Shery Fernadez, Fuzzy G-modules and Fuzzy Representations, *TAJOPAM* 1, 107-114 (2002).
- [38] Souriar Sebastian and S. Babu Sundar, On the chains of level subgroups of homomorphic images and pre-images of Fuzzy subgroups, *Banyan Mathematical Journal* 1,25- 34 (1994).
- [39] Souriar Sebastian and S. Babu Sundar,Existence of fuzzy subgroups of every level cardinality upto H_0 , *Fuzzy sets and Systems*, 67, 365-368(1994).
- [40] Souriar Sebastian and S. Babu Sundar,Generalisations of some results of Das, *Fuzzy sets and Systems*, 71 , 251-253(1995).
- [41] Souriar Sebastian and S. Babu Sundar, Fuzzy groups and group homomorphisms, *Fuzzy sets and Systems*, 81, 397-401(1996).
- [42] Souriar Sebastian and Thampy Abraham, 'A fundamental theorem of Fuzzy Representations' *TAJOPAM* (To appear).
- [43]Thampy Abraham and Souriar Sebastian,Fuzzification of Cayley's and Lagrange's Theorems , *J. Comp. and Math. Sci*, Vol. 1(1), 41-46 (2009).
- [44] L.A. Zadeh, Fuzzy sets, *Information Control* 8, 338 - 353 (1965).
- [45] J. Zhan, N. Cagman, A. Sezgin Sezer, Applications of soft union sets to hemi rings via SU-h-ideals, *J. Intell. Fuzzy Syst.*26, 1363-1370 (2014).
- [46] Y. Zou and Z. Xiao, Data analysis approaches of soft sets under incomplete information, *Knowled-Based Syst.* 21, 941-945 (2008).



• **Dr. R.NAGARAJAN** is Associate Professor and Head of Mathematics at J.J.College of Engineering and Technology, Trichy. He received the Ph.D degree from Bharathidasan University, Trichy. His main research interests are Group theory, Neutrosophic soft group, Near-ring, soft set and its applications and fuzzy decision making.



SOFT UNION FUZZY STRUCTURES OF G-MODULES

R. Nagarajan*, S. Saleem Abdullah** & K. Balamurugan***

* Associate Professor, Department of Mathematics, J J

College of Engineering and Technology, Trichirappalli, Tamilnadu

** Associate Professor, Department of Mathematics, Hazara University, Pakistan

*** Assistant Professor, M.A.M School of Engineering, Trichirappalli, Tamilnadu

Abstract:

In this paper, we introduce fuzzy version of soft uni-G-modules of a vector space with respect to soft structures, which are fuzzy soft uni-G-modules (UFSG-module). These new concepts show that how a soft set affects on a G-module of a vector space in the mean of intersection, union and inclusion of sets and thus, they can be regarded as a bridge among classical sets, fuzzy soft sets and vector spaces. We then investigate their related properties with respect to soft set operations, soft image, soft pre-image, soft anti image, α -inclusion of fuzzy soft sets and linear transformations of the vector spaces. Furthermore, we give the applications of these new G-module on vector spaces.

Key Words: Soft Set, UFSG-Module, Fuzzy Soft Image, Fuzzy Soft Anti Image, A-Inclusion, Trivial & Whole

1. Introduction:

Most of the problems in economics, engineering, medical science, environments etc. have various uncertainties. We cannot successfully use classical methods to solve these uncertainties because of various uncertainties typical for those problems. Hence some kinds of theories were given like theory of fuzzy sets and rough sets [17], i.e., which we can use as mathematical tools for dealing with uncertainties. However, all of these theories have their own difficulties which are pointed out in [15]. Soft set theory was introduced by Molodtsov for modeling vagueness and uncertainty and it has been received much attention since Ali et al [6] and Sezgin and Atagun [34] introduced and studied operations of soft sets. This theory has started to progress in the mean of algebraic structures, since Aktas, and Cagman [5] defined and studied soft groups. Since then, soft substructures of rings, fields and modules [8], union soft substructures of near-rings and near-ring modules, normalistic soft groups are defined and studied in detailed. Soft set has also been studied in the following papers [1, 2, 3, 25, 26]. The theory of G-modules originated in the 20th century. Representation theory was developed on the basis of embedding a group G in to a linear group $GL(V)$.

The theory of group representation (G module theory) was developed by Frobenius G [1962]. Soon after the concept of fuzzy sets was introduced by Zadeh in 1965. Fuzzy subgroup and its important properties were defined and established by Rosenfeld in 1971. After that in the year 2004 Shery Fernandez introduced fuzzy parallels of the notions of G-modules. This study is of great importance since UFSG-modules show how a fuzzy soft set affect on a G-module of a vector space in the mean of intersection, union and inclusion of sets, so it functions as a bridge among classical sets, soft sets and vector spaces. In this paper, we introduce union fuzzy soft G-modules of a vector space that is abbreviated by UFSG- module and investigate its related properties with respect to fuzzy soft set operations. Then we give the application of fuzzy soft image, fuzzy soft pre image, upper α -inclusion of fuzzy soft sets, linear transformations of vector spaces on vector spaces in the mean of UFSG-modules. Moreover, we apply soft pre image, soft anti-image, lower α -inclusion of soft sets, linear transformations of vector spaces on these fuzzy soft G-modules. The work of this paper

is organized as follows. In the second section as preliminaries, we give basic concepts of soft sets and fuzzy soft G-modules. In Section 3, we introduce UFSG-modules and study their characteristic properties. In Section 4, we give the applications of UFSG-modules.

2. Preliminaries:

In this section as a beginning, the concepts of G-module soft sets introduced by Molodsov and the notions of fuzzy soft set introduced by Maji et al. have been presented.

2.1 Definition [36]:

Let G be a finite group. A vector space M over a field K (a subfield of C) is called a G -module if for every $g \in G$ and $m \in M$, there exists a product (called the right action of G on M) $m.g \in M$ which satisfies the following axioms.

1. $m.1_G = m$ for all $m \in M$ (1_G being the identify of G)

2. $m.(g.h) = (m.g).h$, $m \in M$, $g, h \in G$

3. $(k_1 m_1 + k_2 m_2).g = k_1(m_1.g) + k_2(m_2.g)$, $k_1, k_2 \in K$, $m_1, m_2 \in M$ & $g \in G$. In a similar manner the left action of G on M can be defined.

2.2. Definition [36]:

Let M and M^* be G -modules. A mapping $\emptyset: M \rightarrow M^*$ is a G -module homomorphism if

1. $\emptyset(k_1 m_1 + k_2 m_2) = k_1 \emptyset(m_1) + k_2 \emptyset(m_2)$

2. $\emptyset(gm) = g \emptyset(m)$, $k_1, k_2 \in K$, $m, m_1, m_2 \in M$ & $g \in G$.

2.3. Definition [36]:

Let M be a G -module. A subspace N of M is a G -sub module if N is also a G -module under the action of G . Let U be a universe set, E be a set of parameters, $P(U)$ be the power set of U and $A \subseteq E$.

2.4. Definition [29]:

A pair (F, A) is called a soft set over U , where F is a mapping given by $F: A \rightarrow P(U)$. In other words, a soft set over U is a parameterized family of subsets of the universe U . Note that a soft set (F, A) can be denoted by F_A . In this case, when we define more than one soft set in some subsets A, B, C of parameters E , the soft sets will be denoted by F_A, F_B, F_C , respectively. On the other case, when we define more than one soft set in a subset A of the set of parameters E , the soft sets will be denoted by F_A, G_A, H_A , respectively. For more details, we refer to [11, 17, 18, 26, 29, 7].

2.5. Definition [6]:

The relative complement of the soft set F_A over U is denoted by F_A^r , where $F_A^r: A \rightarrow P(U)$ is a mapping given as $F_A^r(a) = U \setminus F_A(a)$, for all $a \in A$.

2.6. Definition [6]:

Let F_A and G_B be two soft sets over U such that $A \cap B \neq \emptyset$. The restricted intersection of F_A and G_B is denoted by $F_A \cap G_B$, and is defined as $F_A \cap G_B = (H, C)$, where $C = A \cap B$ and for all $c \in C$, $H(c) = F(c) \cap G(c)$.

2.7. Definition [6]:

Let F_A and G_B be two soft sets over U such that $A \cap B \neq \emptyset$. The restricted union of F_A and G_B is denoted by $F_A \cup G_B$, and is defined as $F_A \cup G_B = (H, C)$, where $C = A \cap B$ and for all $c \in C$, $H(c) = F(c) \cup G(c)$.

2.8. Definition [12]:

Let F_A and G_B be soft sets over the common universe U and ψ be a function from A to B . Then we can define the soft set $\psi(F_A)$ over U , where $\psi(F_A): B \rightarrow P(U)$ is a set valued function defined by $\psi(F_A)(b) = \cup\{F(a) \mid a \in A \text{ and } \psi(a) = b\}$, if $\psi^{-1}(b) \neq \emptyset$, = 0 otherwise for all $b \in B$. Here, $\psi(F_A)$ is called the soft image of F_A under ψ . Moreover we can define a soft set $\psi^{-1}(G_B)$ over U , where $\psi^{-1}(G_B): A \rightarrow P(U)$ is a set-valued function

defined by $\psi^{-1}(G_B)(a) = G(\psi(a))$ for all $a \in A$. Then, $\psi^{-1}(G_B)$ is called the soft pre image (or inverse image) of G_B under ψ .

2.9. Definition [13]:

Let F_A and G_B be soft sets over the common universe U and ψ be a function from A to B . Then we can define the soft set $\psi^*(F_A)$ over U , where $\psi^*(F_A) : B \rightarrow P(U)$ is a set-valued function defined by $\psi^*(F_A)(b) = \cap \{F(a) \mid a \in A \text{ and } \psi(a) = b\}$, if $\psi^{-1}(b) \neq \emptyset$, otherwise for all $b \in B$. Here, $\psi^*(F_A)$ is called the soft anti image of F_A under ψ .

2.1. Theorem [13]:

Let F_H and T_K be soft sets over U , F_{r_H} , T_{r_K} be their relative soft sets, respectively and ψ be a function from H to K . then,

- i) $\psi^{-1}(T_{r_K}) = (\psi^{-1}(T_K))^r$,
- ii) $\psi(F_{r_H}) = (\psi^*(F_H))^r$ and $\psi^*(F_{r_H}) = (\psi(F_H))^r$.

2.10. Definition [14]:

Let F_A be a soft set over U and a be a subset of U . Then upper α -inclusion of F_A , denoted by $F_A^{\supseteq \alpha}$, is defined as $F_A^{\supseteq \alpha} = \{x \in A \mid F(x) \supseteq \alpha\}$. Similarly, $F_A^{\subseteq \alpha} = \{x \in A \mid F(x) \subseteq \alpha\}$ is called the lower α -inclusion of F_A . A nonempty subset U of a vector space V is called a subspace of V if U is a vector space on F . From now on, V denotes a vector space over F and if U is a subspace of V , then it is denoted by $U < V$.

3. Union Fuzzy Soft G-Modules:

In this section, we first define Union fuzzy soft G-modules of a vector space, abbreviated by UFSG-modules. We then investigate its related properties with respect to soft set operations.

3.1. Definition:

Let G be a group. Let M be a G-module of V and B_M be the fuzzy soft set over V . Then B_M is called Union fuzzy soft G-modules of V , denoted by $B_M \widetilde{<}_u V$ if the following properties are satisfied: $B(ax+by) \subseteq B(x) \cup B(y)$, $B(\alpha x) \subseteq B(x)$, for all $x, y \in M$, and $\alpha \in F$.

3.1. Proposition:

If $B_M \widetilde{<}_u V$, then $B(0_V) \subseteq B(x)$ for all $x \in M$.

Proof:

Since B_M is an UFSG-module of V , then $B(ax+by) \subseteq B(x) \cup B(y)$ for all $x, y \in M$ and since $(M, +)$ is a group, if we take $by = -ax$ then, for all $x \in M$,

$$B(ax-ax) = B(0_V) \subseteq B(x) \cup B(x) = B(x), \text{ for all } x \in M.$$

In section 3, we showed that restricted intersection, the sum and product of two IFSG-modules of V is an IFSG-modules of V . Now, we show that restricted union of two UFSG-modules of V with the following theorem:

3.1. Theorem:

If $A_{M_1} \widetilde{<}_u V$ and $B_{M_2} \widetilde{<}_u V$, then $A_{M_1} \cup_{\mathcal{R}} B_{M_2} \widetilde{<}_u V$.

Proof:

By definition 2.7, let $A_{M_1} \cup_{\mathcal{R}} B_{M_2} = (A, M_1) \cup_{\mathcal{R}} (B, M_2) = (Q, M_1 \cap M_2)$, where $Q(x) = A(x) \cup B(x)$ for all $x \in M_1 \cap M_2 \neq \emptyset$. Since M_1 & M_2 are G-modules of V , then $M_1 \cap M_2$ is a G-modules of V .

Let $x, y \in M_1 \cap M_2$ and $\alpha \in F$. Then

$$\begin{aligned} Q(ax+by) &= A(ax+by) \cup B(ax+by) \subseteq (A(x) \cup A(y)) \cup (B(x) \cup B(y)) \\ &= (A(x) \cup B(x)) \cup (A(y) \cup B(y)) = Q(x) \cup Q(y) \end{aligned}$$

$$Q(\alpha x) = A(\alpha x) \cup B(\alpha x) \subseteq A(x) \cup B(x) = Q(x)$$

There fore $A_{M_1} \cup_{\mathcal{R}} B_{M_2} = Q_{M_1 \cap M_2} \widetilde{<}_u V$.

3.2. Definition:

Let B_M be a UFSG-module of V . Then

(a) B_M is said to be trivial if $B(x) = \{0_V\}$ for all $x \in M$.

(b) B_M is said to be whole if $B(x) = V$ for all $x \in M$.

3.2. Proposition:

Let A_{M_1} and B_{M_2} be UFSG-modules of V , then

(i) If A_{M_1} and B_{M_2} are trivial UFSG-modules of V , then $A_{M_1} \cup_{\mathcal{R}} B_{M_2}$ is a trivial UFSG-module of V .

(ii) If A_{M_1} and B_{M_2} are whole UFSG-modules of V , then $A_{M_1} \cup_{\mathcal{R}} B_{M_2}$ is a whole UFSG-module of V .

(iii) If A_{M_1} is a trivial UFSG-module of V and B_{M_2} is a whole UFSG-modules of V , then $A_{M_1} \cup_{\mathcal{R}} B_{M_2}$ is a whole UFSG-module of V .

Proof:

The proof is easily seen by definition 2.7, definition 3.2, and theorem 3.1.

4. Application of UFSG-Modules:

In this section, first we obtain the relation between IFSG-modules and UFSG-modules and then give the applications of soft pre-image, soft anti-image, lower α -inclusion of soft sets and linear transformation of vector spaces on vector spaces with respect to UFSG-modules.

4.1. Theorem:

Let T_M be a fuzzy soft set over V . Then, T_M is an UFSG-module of V if and only if T_M^r is an IFSG-modules of V .

Proof:

Let T_M be a UFSG-modules of V . Then for all $x, y \in M, a, b, \alpha \in F$,

$$\begin{aligned} T_M^r(ax+by) &= V/T_M(ax+by) \supseteq V/(T_M(x) \cup T_M(y)) \\ &= (V/T(x)) \cap (V/T(y)) = T_M^r(x) \cap T_M^r(y) \end{aligned}$$

$$T_M^r(\alpha x) = V/T_M(\alpha x) \supseteq V/T_M(x) = T_M^r(x)$$

Thus, T_M^r is an IFSG-module of V .

Conversely, let T_M^r be an IFSG-module of V . Then for all $x, y \in M$, and $\alpha \in F$,

$$\begin{aligned} T_M(ax+by) &= V/T_M^r(x+y) \subseteq V/(T^r(x) \cap T^r(y)) \\ &= (V/T^r(x)) \cup (V/T^r(y)) = T(x) \cup T(y) \end{aligned}$$

$$T_M(\alpha x) = V/T_M^r(\alpha x) \subseteq V/T^r(\alpha x) = T(x)$$

Thus, T_M is an UFSG-module of V .

The above theorem shows that if a fuzzy soft set is a UFSG-module of V , then its relative complement is an IFSG-module of V and vice versa.

4.2. Theorem:

If $T_M \lesssim_u V$, then $M_T = \{x \in M / T(x) = T(0_V)\}$ is a G - module of M .

Proof:

It is seen that $0_V \in M_T$ and $\emptyset \neq M_T \subseteq M$. We need to show that $ax+by \in M_T$ and $\alpha x \in M_T$, for all $x, y \in M_T$ and $\alpha \in F$. Since $x, y \in M_T$ and T_M is a UFSG- module of V , then $T(x) = T(y) = T(0_V)$, $T(ax+by) \subseteq T(x) \cup T(y) \subseteq T(0_V)$. $T(\alpha x) \subseteq T(x) = T(0_V)$ for all $x, y \in M_T$ and $\alpha \in F$. Furthermore, $T(0_V) \subseteq T(ax+by)$ and $T(0_V) \subseteq T(\alpha x)$. Thus, the proof is completed.

4.3. Theorem:

Let G_M be a fuzzy soft set over V and α be a subset of V such that $\alpha \supseteq G(0_V)$. If G_M is a UFSG-module of V , then $G_M^{\subseteq \alpha}$ is a G -module of V .

Proof:

Since $\alpha \supseteq G(0_V)$, then $0_V \in G_M^{\subseteq \alpha}$ and $\emptyset \neq G_M^{\subseteq \alpha} \subseteq V$.

Let $x, y \in G_M^{\subseteq \alpha}$ and $a, b, \alpha \in F$, then $G(x) \subseteq \alpha$ and $G(y) \subseteq \alpha$.

We need to show that $ax+by \in G_M^{\subseteq \alpha}$ and $nx \in G_M^{\subseteq \alpha}$ for all $x, y \in G_M^{\subseteq \alpha}$ and $n \in F$. Since G_M is a UFSG -module of V , it follows that $G(ax+by) \subseteq G(x) \cup G(y) \subseteq \alpha \cup \alpha = \alpha$

Therefore, $G(nx) \subseteq G(x) \subseteq \alpha$, which completes the proof.

4.4. Theorem:

Let G_M and T_W be a fuzzy soft set over V , where M and W are G -modules of V and Ψ be a linear transformation from M to W . If T_W is a UFSG-module of V , then so is $\Psi^{-1}(T_W)$.

Proof:

Let T_W be a UFSG-module of V . Then T_W^r is an IFSG- module of V by theorem:6.1 and $\Psi^{-1}(T_W^r)$ is an IFSG- module of V by theorem4.4. Thus, $\Psi^{-1}(T_W^r) = (\Psi^{-1}(T_W))^r$ is an IFSG- module of V by theorem 2.1. Therefore, $\Psi^{-1}(T_W)$ is a UFSG -module of V by theorem 4.1.

4.5. Theorem:

Let G_M and T_W be a fuzzy soft sets over V , where M and W are G - Modules of V and Ψ be a linear isomorphism from M to W . If G_M is a UFSG- Module of V , then so is $\Psi^*(G_M)$

Proof:

Let G_M be a UFSG- module of V . Then G_M^r is an IFSG- module of V by theorem: 6.1 and $\Psi^{(G_M^r)}$ is an IFSG- module of V by theorem4.3. Thus, $\Psi^{(G_M^r)} = (\Psi^*(G_M))^r$ is an IFSG- module of V by theorem 2.1. So, $\Psi^*(G_M)$ is a UFSG- module of V by theorem4.1.

4.6. Theorem:

Let V_1 and V_2 be two vector spaces and $(T_1, M_1) \lesssim_u V_1, (T_2, M_2) \lesssim_u V_2$. If $f: M_1 \rightarrow M_2$ is a linear transformation of vector spaces, then

- (i) If f is surjective, then $(T_1, f^{-1}(M_2)) \lesssim_u V_1$,
- (ii) $(T_2, f(M_1)) \lesssim_u V_2$,
- (iii) $(T_1, \ker f) \lesssim_u V_1$.

Proof:

Follows from theorem 3.1 and theorem 4.5 .Therefore omitted.

4.1. Corollary:

Let $(T_1, M_1) \lesssim_u V_1, (T_2, M_2) \lesssim_u V_2$. If $f: M_1 \rightarrow M_2$ is a linear transformation, then $(T_2, \{0_{M_2}\}) \lesssim_u V_2$.

Proof:

Follows from definition 4.6 (ii) and theorem 4.6 (iii).

Conclusion:

Throughout this paper, we have dealt with UFSG-modules and UFSG-modules of a vector space. We have investigated their related properties with respect to soft set operations obtained the relations on UFSG-modules. Furthermore, we have derived some applications of UFSG-modules with respect to soft image, soft pre image, soft anti image, α -inclusion of soft sets and linear transformations of vector spaces. Further study could be done for fuzzy soft sub structures of different algebras.

References:

1. S. Abdullah and N. Amin, Analysis of S-box Image encryption based on generalized fuzzy soft expert set, Nonlinear Dynamics, (2014), dx.doi.org/10.1007/s11071-014-1767-5.
2. S. Abdullah, M. Aslam and K. Ullah, Bipolar fuzzy soft sets and its applications in decision making problem, J. Intell. Fuzzy Syst. 27:2, 729-742 (2014).

3. S. Abdullah, M. Aslam and K. Hila, A new generalization of fuzzy bi-ideals in semi groups and its Applications in fuzzy finite state machines, *Multiple Valued Logic and Soft Computing*, 27:2, 599-623 (2015).
4. U. Acar, F. Koyuncu and B. Tanay, Soft sets and soft rings, *Comput. Math. Appl.* 59, 3458-3463 (2010).
5. H. Aktas and N. Cagman, Soft sets and soft groups, *Inform. Sci.* 177, 2726-2735 (2007).
6. M.I. Ali, F. Feng, X. Liu, W.K. Min and M. Shabir, On some new operations in soft set theory, *Comput. Math. Appl.* 57, 1547-1553 (2009).
7. M. I. Ali, M. Shabir, M. Naz, A structures of soft sets associated with new operations, *Comput. Math. Appl.* 61, 2647-2654 (2011).
8. A.O. Atagun and A. Sezgin, Soft substructures of rings, fields and modules, *Comput. Math. Appl.* 61 (3), 592-601 (2011).
9. K.V. Babitha and J.J. Sunil, Soft set relations and functions, *Comput. Math. Appl.* 60 (7), 1840-1849 (2010).
10. N. Çağman and S. Enginoğlu, Soft matrix theory and its decision making, *Comput. Math. Appl.* 59, 3308-3314 (2010).
11. N. Çağman and S. Enginoğlu, Soft set theory and uni-int decision making, *Eur. J. Oper. Res.* 207, 848-855 (2010).
12. N. Cagman, F. C, itak and H. Aktas,, Soft int-groups and its applications to group theory, *Neural Comput. Appl.* 21, 151-158 (2012).
13. N. Cagman, A. Sezgin and A.O. Atagun, Soft uni-groups and its applications to group theory, (submitted).
14. N. C, ağman, A. Sezgin and A.O. Atagun, α -inclusions and their applications to group theory, (submitted).
15. Charles W. Curties and Irving Reiner, *Representation Theory of finite groups and Associative Algebras*, INC, (1962).
16. F. Feng, Y. B. Jun, X. Zhao, Soft semi rings, *Comput. Math. Appl.* 56, 2621-2628 (2008).
17. F. Feng, X.Y. Liu, V. Leoreanu-Fotea, Y.B. Jun, Soft sets and soft rough sets, *Inform. Sci.* 181 (6), 1125-1137 (2011).
18. F. Feng, C. Li, B. Davvaz and M. I. Ali, Soft sets combined with fuzzy sets and rough sets: a tentative approach, *SoftComput.* 14 (6), 899-911 (2010).
19. George J. Klir and Bo Yuan, *Fuzzy sets and Fuzzy logic*, Prentice-Hall of India (2000).
20. John N. Mordeson and D.S. Malik, *Fuzzy Commutative Algebra*, World scientific publishing (1998).
21. Y.B. Jun, Soft BCK/BCI-algebras, *Comput. Math. Appl.* 56, 1408-1413 (2008).
22. Y.B. Jun, K.J. Lee and J. Zhan, Soft p-ideals of soft BCIalgebras, *Comput. Math. Appl.* 58, 2060-2068 (2009).
23. O. Kazancı, S. Yilmaz and S. Yamak, Soft sets and soft BCH-algebras, *Hacet. J. Math. Stat.* 39 (2), 205-217 (2010).
24. X. Ma and J. Zhan, Applications of a new soft set to hemi regular hemi rings via (M, N) -SI-h-ideals, *J. Intell. Fuzzy Syst.* 26, 2515-2525 (2014).
25. X. Ma and J. Zhan, Characterizations of hemi regular hemi rings via a kind of new soft union sets, *J. Intell. Fuzzy Syst.* 27, 2883-2895 (2014).
26. P.K.Maji, R. Biswas and A.R. Roy, Soft set theory, *Comput. Math. Appl.* 45, 555-562 (2003).

27. P.K. Maji, A.R. Roy and R. Biswas, An application of soft sets in a decision making problem, *Comput. Math. Appl.* 44, 1077-1083 (2002).
28. P. Majumdar and S.K. Samanta, on soft mappings, *Comput. Math. Appl.* 60 (9), 2666-2672 (2010).
29. D. Molodtsov, Soft set theory-first results, *Comput. Math. Appl.* 37, 19-31 (1999).
30. J. N. Mordeson and D. S Malik., *Fuzzy Commutative Algebra*, World scientific publishing, (1998).
31. A. Rosenfeld, Fuzzy groups, *J.M. Anal. and Appli.* 35,512 - 517 (1971).
32. Sezgin and A. O. Atag'un, Soft groups and normalistic soft groups, *Comput. Math. Appl.* 62 (2), 685-698 (2011).
33. Sezgin, A. O. Atagun, N. Cagman, Union soft substructures of near-rings and N-groups, *Neural Comput. Appl.* 21, 133-143 (2012).
34. Sezgin and A.O. Atagun, On operations of soft sets, *Comput. Math. Appl.* 61 (5), 1457-1467 (2011).
35. Sezgin, A.O. Atag'un and E. Ayg'un, A note on soft near-rings and idealistic soft near-rings, *Filomat* 25 (1), 53-68(2011).
36. Shery Fernandez, Ph.D. thesis "A study of fuzzy g-modules" April 2004.
37. Shery Fernadez, Fuzzy G-modules and Fuzzy Representations, *TAJOPAM* 1, 107-114 (2002).
38. Souriar Sebastian and S. Babu Sundar, On the chains of level subgroups of homomorphic images and pre-images of Fuzzy subgroups, *Banyan Mathematical Journal* 1, 25- 34 (1994).
39. Souriar Sebastian and S. Babu Sundar, Existence of fuzzy subgroups of every level cardinality upto H_0 , *Fuzzy sets and Systems*, 67, 365-368(1994).
40. Souriar Sebastian and S. Babu Sundar, Generalisations of some results of Das, *Fuzzy sets and Systems*, 71, 251-253(1995).
41. Souriar Sebastian and S. Babu Sundar, Fuzzy groups and group homomorphisms, *Fuzzy sets and Systems*, 81, 397-401(1996).
42. Souriar Sebastian and Thampy Abraham, 'A fundamental theorem of Fuzzy Representations' *TAJOPAM* (To appear).
43. L.A. Zadeh, Fuzzy sets, *Information Control* 8, 338 - 353 (1965).



ISSN Print: 2394-7500
 ISSN Online: 2394-5869
 Impact Factor: 5.2
 IJAR 2016; 2(6): 898-901
 www.allresearchjournal.com
 Received: 19-04-2016
 Accepted: 20-05-2016

R Nagarajan
 Associate Professor,
 Department of Mathematics,
 JJ College of Engg & Tech,
 Trichirappalli-09, India.

S Saleem Abdullah
 Associate Professor,
 Department of Mathematics,
 Hazara University, Pakistan.

K Balamurugan
 Assistant Professor, M.A.M
 School of Engineering,
 Trichirappalli-105, India.

Correspondence
R Nagarajan
 Associate Professor,
 Department of Mathematics,
 JJ College of Engg & Tech,
 Trichirappalli-09, India.

Group action on G-invariant fuzzy sub lattice with thresholds of complemented lattices

R Nagarajan, S Saleem Abdullah and K Balamurugan

Abstract

In this paper, we first introduce the concepts of group action on fuzzy sub lattice with thresh hold of a lattice L and listed some properties of them. We define the group action on fuzzy subset of a lattice L and introduce the notion of fuzzy sub lattice with threshold of complemented lattices. Also the notion of G-invariant fuzzy sub lattice with thresh hold of L and homomorphic image, pre-image of fuzzy sub lattice with threshold of L are also studied.

Keywords: Poset, finite group, fuzzy sub lattice, group action, complemented lattice, G-invariant, lattice homomorphism, pre- image

Introduction

The concept of fuzzy sets was first introduced by Zadeh ^[20] in 1965 and the fuzzy sets have been used in the reconsideration of classical mathematics. Recently, yuan ^[19] introduced the concept of fuzzy subgroup with thresholds. A fuzzy subgroups with thresholds λ and μ is also called a (λ, μ) -fuzzy subgroups. Yao ^[16] continued to research (λ, μ) -fuzzy normal subgroups, (λ, μ) - fuzzy quotient subgroups and (λ, μ) - fuzzy subrings in ^[17]. L.A. Zadeh ^[20] in 1965 introduced the concept of fuzzy sets to describe vagueness mathematically in its very abstractness. The notion of L-fuzzy sets in lattice theory and introduced the concepts of fuzzy sub lattices and fuzzy ideals in ^[15]. In particular N. Ajmal and K.V. Thomas ^[2-4] systematically developed the theory of fuzzy sub lattice. Here we give some basic definitions and results related to fuzzy sub lattice which is taken from their work. The concept of group actions in various algebraic structures in ^[9, 13]. Let X be a non-empty set. A mapping $\mu: X \rightarrow [0, 1]$ is called a fuzzy subset of X. Rosenfeld ^[12] applied the concept of fuzzy sets to the theory of groups and defined the concept of fuzzy subgroups of a group. Since then, many papers concerning various fuzzy algebraic structures have appeared in the literature ^[1, 5-7, 11, 18]. In this paper, we first introduce the concepts of fuzzy sub lattice with thresh hold of a lattice L and listed some properties of them. We define the group action on fuzzy subset of a lattice L and introduce the notion of fuzzy sub lattice with threshold of complemented lattices. Many properties of fuzzy sub lattice with threshold of complemented lattice L and G-invariant fuzzy sub lattice with thresh hold of L are studied. The homomorphic image and pre-image of fuzzy sub lattice with threshold of L are also established.

2. Preliminaries

In this section we always use L to stand for a lattice.

Definition 2.1 ^[5]: A nonempty set L together with two binary operations \vee and \wedge on L is called a lattice if it satisfies the following identities: $L_1: (a) x \vee y \approx y \vee x$ (b) $x \wedge y \approx y \wedge x$, $L_2: (a) x \vee (y \vee z) \approx (x \vee y) \vee z$ (b) $x \wedge (y \wedge z) \approx (x \wedge y) \wedge z$, $L_3: (a) x \vee x \approx x$ (b) $x \wedge x \approx x$, $L_4: (a) x \approx x \vee (x \wedge y)$ (b) $x \approx x \wedge (x \vee y)$. The operation \wedge is called meet and the operation \vee is called join. Let L be the set of propositions and let \vee denote the connective "or" and \wedge denote the connective "and". Then, L_1 to L_4 are well-known properties from propositional logic

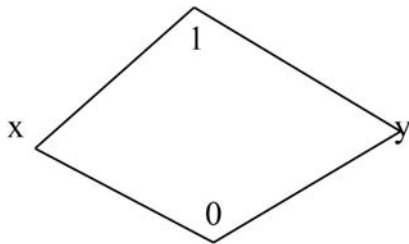
Definition 2.2 [2]: A poset L is a lattice if and only if for every a, b in L both $\sup\{a, b\}$ and $\inf\{a, b\}$ exist in L . One can show that the both definitions of a lattice are equivalent. If L is a lattice by the first condition, then define \leq on L by $a \leq b$ if and only if $a = a \wedge b$, and so $b = a \vee b$. If L is a lattice by the second condition, then define the operations \wedge and \vee by $a \vee b = \sup\{a, b\}$ and $a \wedge b = \inf\{a, b\}$.

Throughout this paper $L = \langle L, \vee, \wedge \rangle$ denotes a lattice and $\langle [0, 1], \vee, \wedge \rangle$ is a complete lattice, where $[0, 1]$ is the set of real's between 0 and 1 and $x \vee y = \max\{x, y\}$, $x \wedge y = \min\{x, y\}$.

An action of G on X is a map $G \times X \rightarrow X$ denoted by $(g, x) \mapsto (gh)x$ for all $x \in X$ and $g, h \in G$. Throughout these notes, G denotes a group and X, Y denote sets. We use symbols g, g_1, g^1, \dots to denote elements of G . Similar x, x_1, x^1, \dots to denote element of X and y, y_1, y^1, \dots to denote elements of Y .

Definition 2.3: A fuzzy subset A of a lattice L is said to be fuzzy sub lattice with thresh hold of L if, for all $x, y \in L$ (FSL1) $A(x \wedge y) \vee \alpha \geq (A(x) \wedge A(y)) \wedge \beta$ and (FSL2) $A(x \vee y) \vee \alpha \geq (A(x) \wedge A(y)) \wedge \beta$ for some time the above definition is recalled as $A(x \wedge y) \wedge A(x \vee y) \vee \alpha \geq (A(x) \wedge A(y)) \wedge \beta$ for all $x, y \in L$ and $\alpha, \beta \in [0, 1]$ and $\alpha \leq \beta$. Let L be a lattice and χ_i is a characteristic function of a subset I of L . Then χ_i is a fuzzy lattice if and only if I is sub lattice.

Example: Suppose L is the following Boolean algebra we define fuzzy subsets A of L as follows



$A(1) = 0, A(x) = 0, A(y) = 1/3, A(0) = 1$. Therefore A is fuzzy sub lattice of L

Let L be the lattice and G a finite group which acts in L (that is for all $g \in G, x \in L, x^g = gxg^{-1}$. The identity of G is denoted by e .

Definition 2.4: A group action of G on a fuzzy set A of a lattice L is denoted by A^g and it is defined by $A^g(x) = A(x^g)$, $g \in G$. From the definition of group action G on a fuzzy set, following results are easy to verify.

Lemma 2.1: Let A and B be two fuzzy sets of L and G a finite group which acts on L . Then

- (i) If A is subset of B , then A^g is also subset of B^g , for all $g \in G$.
- (ii) $(A \cup B)^g = A^g \cup B^g$;
- (iii) $(A \cap B)^g = A^g \cap B^g$;
- (iv) $(A \times B)^g = A^g \times B^g$;
- (v) $A(g_1 g_2) = A g_1 g_2$; for all $g_1, g_2 \in G$.
- (vi) $(A g)^{g^{-1}} = A^e = A$, for all $g \in G$.

Lemma 2.2: Let G be a finite group which acts on all lattice L . Then for every $x, y \in L, g \in G$, we have

- (i) $(x \vee y)^g = x^g \vee y^g$
 - (ii) $(x \wedge y)^g = x^g \wedge y^g$
- Proof; (i) since $(x \vee y)^g = g(x \vee y)g^{-1} = (gxg^{-1}) \vee (gyg^{-1}) = x^g \vee y^g$.
- (ii) $(x \wedge y)^g = g(x \wedge y)g^{-1} = (gxg^{-1}) \wedge (gyg^{-1}) = x^g \wedge y^g$.

3. Homomorphism of G-invariant Fuzzy Sub lattice with thresh hold

In this section, we study the image and pre-image of fuzzy sub lattice with thresh hold under the lattice homomorphism's.

Definition 3.1 [13]: Let A be fuzzy sub lattice with thresh hold of a lattice L and G be a finite group which acts on L . Then A is said to be G -invariant fuzzy sub lattice with thresh hold of L if and only if $A^g(x) = A(x^g) \geq A(x)$ for all $x \in L$ and $g \in G$.

Lemma 3.1: Let $f: L_1 \rightarrow L_2$ be two lattices and let A be fuzzy sub lattice with thresh hold of L_1 and G a finite group which acts on L_1 and L_2 . Let $f: L_1 \rightarrow L_2$ be a mapping defined by $f(x^g) = (f(x))^g$, for all $x \in L, g \in G$. Then f is lattice homomorphism. We call the map f as G -lattice homomorphism.

Proof: Let $x, y \in L, g \in G$. Then we have
 $f(x^g \vee y^g) = (f(x \vee y))^g = (f(x) \vee f(y))^g = (f(x))^g \vee (f(y))^g = f(x^g) \vee f(y^g)$
 $f(x^g \wedge y^g) = (f(x \wedge y))^g = (f(x) \wedge f(y))^g = (f(x))^g \wedge (f(y))^g = f(x^g) \wedge f(y^g)$.
Hence f is G -lattice homomorphism.

Theorem 3.1: Let A be a fuzzy subset of L and G a finite group which acts on L . Then the following are equivalent;

- (i) A^g is a fuzzy sub lattice with thresh hold of L ;
- (ii) A^g is a sub lattice of L for any $p \in [\alpha, \beta]$ where $A^g_{p \neq \Phi}$.

Proof; "(i) implies (ii)"

Let A be a fuzzy sub lattice with thresh hold of L and G a finite group which acts on L .

For any $p \in [\alpha, \beta]$, such that $A_{p \neq \Phi}$.

We need to show that $x^g \wedge y^g \in A_{p^g}$ and $x^g \vee y^g \in A_{p^g}$ for all $x^g, y^g \in A_{p^g}$.

From $x^g \in A_{p^g}$, we know that $A^g(x) = A(x^g) \geq p$. And similarly we obtain that $A(y^g) \geq p$. Thus

$$A^g(x \wedge y) \vee \alpha = A(x \wedge y) \vee \alpha = A(x^g \wedge y^g) \vee \alpha \geq A((x^g) \wedge A(y^g)) \wedge \beta \geq (A^g(x) \wedge A^g(y)) \wedge \beta \geq p.$$

we also know that $\alpha \leq p$. Then we conclude that $A^g(x \wedge y) \geq p$. so $x^g \wedge y^g \in A_{p^g}$.

Similarly, we can be proved $x^g \vee y^g \in A_{p^g}$.

"(ii) implies (i)"

Conversely, Let A_{p^g} be a sub lattice of L . If there exists $x_0, y_0 \in L$ such that $A^g(x_0 \wedge y_0) \vee \alpha < p = A^g(x_0) \wedge A^g(y_0) \wedge \beta < A(x_0^g) \wedge A(y_0^g) \wedge \beta$, then $p \in [\alpha, \beta]$. $A(x_0^g) \wedge A(y_0^g) \geq p$ so $x_0^g \in A_{p^g}$ and $y_0^g \in A_{p^g}$

But $A^g(x_0 \wedge y_0) < p$, that is $x_0^g \wedge y_0^g$ does not belong to A_{p^g} . This is a contradiction with that A_{p^g} is a sub lattice of L . Thus $A^g(x \wedge y) \vee \alpha \geq A((x^g) \wedge A(y^g)) \wedge \beta$ holds for $x^g, y^g \in L$. Similarly we can prove $A^g(x \vee y) \vee \alpha \geq A((x^g) \vee A(y^g)) \wedge \beta$.

Theorem 3.2: A fuzzy subset A of a lattice L , then the following are equivalent

For any $x^g, y^g \in L$ (i) $A^g(x \wedge y) \vee \alpha \geq (A^g(x) \vee A^g(y)) \wedge \beta$ (ii) $x^g \leq y^g$ implies $A^g(x) \vee \alpha \geq A^g(y) \wedge \beta$.

Proof: "(i) implies (ii)"

If $x^g \leq y^g$, then $x^g \wedge y^g = x^g$. Thus $A^g(x) \vee \alpha = A^g(x \wedge y) \vee \alpha \geq A^g(x) \vee A^g(y) \wedge \beta \geq A^g(y) \wedge \beta$. "(ii) implies (i)"

From $x^g \wedge y^g \leq \alpha$, we know that $A^g(x \wedge y) \vee \alpha \geq A^g(x) \wedge \beta$ and from $x^g \wedge y^g \leq y$.

We conclude that $A^g(x \wedge y) \vee \alpha \geq A^g(y) \wedge \beta$. Thus $A^g(x \wedge y) \vee \alpha \geq (A^g(x) \wedge \beta) \vee (A^g(y) \wedge \beta) = (A^g(x) \vee A^g(y)) \wedge \beta$.

Definition 3.2: A fuzzy subset A of a lattice L is said to be fuzzy ideal with thresh hold of L if, for all $x, y \in L$ (FIL₁) $A(x \wedge y) \vee \alpha \geq (A(x) \wedge A(y)) \wedge \beta$ and (FIL₂) $A(x \vee y) \vee \alpha \geq (A(x) \vee A(y)) \wedge \beta$.

Theorem 3.3: Let A be a fuzzy sub lattice of L and G a finite group which acts on L. Then the following are equivalent;

- (i) A^α is a fuzzy ideal with threshold α of L;
- (ii) A^α is fuzzy ideal of L for any $p \in [\alpha, \beta]$ where $A_p \neq \Phi$.

Proof: “(i) implies (ii)”
Let A be a fuzzy ideal with threshold α of L and G a finite group which acts on L.

For any $p \in [\alpha, \beta]$, such that $A_p \neq \Phi$.
We need to show that $x^\alpha y^\alpha \in A_p$ for all $x^\alpha, y^\alpha \in A_p$.
From $A^\alpha(x) = A(x) \geq p$. we obtain that $A^\alpha(x \wedge y) \vee \alpha = A(x \wedge y) \vee \alpha = A(x^\alpha \wedge y^\alpha) \vee \alpha \geq A((x^\alpha) \wedge (y^\alpha)) \wedge \beta \geq (A^\alpha(x) \wedge A^\alpha(y)) \wedge \beta$. Then we conclude that $A^\alpha(x \wedge y) \geq p$ since $\alpha < p$. so $x^\alpha y^\alpha \in A_p$.

“(ii) implies (i)” Conversely, Let A_p be an ideal of L for all $p \in [\alpha, \beta]$, where $A_p \neq \Phi$. If there exists $x^\alpha, y^\alpha \in L$ such that $A^\alpha(x \wedge y) \vee \alpha < p = (A^\alpha(x) \wedge A^\alpha(y)) \wedge \beta \geq p$ then $p \in [\alpha, \beta]$. $A^\alpha(x) \vee A^\alpha(y) \geq p$, so $x^\alpha \in A_p$ or $y^\alpha \in A_p$. But $A^\alpha(x \wedge y) < p$, that is $x^\alpha y^\alpha \notin A_p$. This is a contradiction with that A_p is an ideal of L. Thus $A^\alpha(x \wedge y) \vee \alpha \geq (A^\alpha(x) \wedge A^\alpha(y)) \wedge \beta$ holds for $x^\alpha, y^\alpha \in L$. The proof is ended.

Theorem 3.4: Let $f: L_1 \rightarrow L_2$ be a lattice homomorphism and let A be fuzzy sub lattice with threshold α of L_1 and G a finite group which acts on L. Then $f(A^\alpha)$ is a fuzzy sub lattice with threshold α of L_2 , where

$$f(A^\alpha)(y) = \sup \{ A^\alpha(x) / f(x) = y \}, \text{ for all } y \in L_2, x \in L_1$$

Proof:
If $f^{-1}(y) = \emptyset$ or $f^{-1}(y) \neq \emptyset$ for any $y_1, y_2 \in L_2$, then $f(A^\alpha)(y_1 \vee y_2) \vee \alpha \geq (f(A^\alpha)(y_1) \wedge f(A^\alpha)(y_2)) \wedge \beta$.

Suppose that $f^{-1}(y) \neq \emptyset$ or $f^{-1}(y) = \emptyset$ for any $y_1^\alpha, y_2^\alpha \in L_1$,
Then $(f(A^\alpha)(y_1 \vee y_2) \vee \alpha) = \sup \{ A^\alpha(t) / f(t) = y_1^\alpha \vee y_2^\alpha \} \vee \alpha$
 $t \in L_1$
 $= \sup \{ A^\alpha(t) \vee \alpha / f(t) = y_1^\alpha \vee y_2^\alpha \} \vee \alpha$
 $\geq \sup \{ A^\alpha(x_1 \vee x_2) / f(x_1 \vee x_2) = y_1^\alpha \vee y_2^\alpha \} \vee \alpha$
 $x_1^\alpha, x_2^\alpha \in L_1$
 $= \sup \{ A^\alpha(x_1) \wedge A^\alpha(x_2) \wedge \beta / f(x_1) = y_1^\alpha, f(x_2) = y_2^\alpha \} \vee \alpha$
 $x_1^\alpha, x_2^\alpha \in L_1$
 $= \sup \{ A^\alpha(x_1) / f(x_1) = y_1^\alpha \} \wedge \sup \{ A^\alpha(x_2) / f(x_2) = y_2^\alpha \} \wedge \beta$
 $x^\alpha \in L_1$

$= (f(A^\alpha)(y_1) \wedge f(A^\alpha)(y_2)) \wedge \beta$. Similarly, we have $(f(A^\alpha)(y_1 \wedge y_2) \vee \alpha) \geq (f(A^\alpha)(y_1) \wedge f(A^\alpha)(y_2)) \wedge \beta$. So $f(A^\alpha)$ is fuzzy sub lattice with threshold α of L_2 .

Theorem 3.5: Let $f: L_1 \rightarrow L_2$ be a surjective homomorphism and let A be fuzzy ideal with threshold α of L_1 and G a finite group which acts on L. Then $f(A^\alpha)$ is a fuzzy ideal with threshold α of L_2 .

Proof: For any $y_1^\alpha, y_2^\alpha \in L_2$, $f^{-1}(y_1)$ and $f^{-1}(y_2)$ are non empty. We have

$$\begin{aligned} \text{Then } (f(A^\alpha)(y_1 \wedge y_2) \vee \alpha) &= \sup \{ A^\alpha(t) / f(t) = y_1^\alpha \wedge y_2^\alpha \} \vee \alpha. \\ &= \sup \{ A^\alpha(t) \vee \alpha / f(t) = y_1^\alpha \wedge y_2^\alpha \} \vee \alpha. \\ &= \sup \{ A^\alpha(x_1 \vee x_2) / f(x_1 \vee x_2) = y_1^\alpha \wedge y_2^\alpha \} \vee \alpha \\ &= \sup \{ (A^\alpha(x_1) \wedge A^\alpha(x_2)) \wedge \beta / f(x_1) = y_1^\alpha, f(x_2) = y_2^\alpha \} \vee \alpha \\ &= \sup \{ A^\alpha(x_1) / f(x_1) = y_1^\alpha \} \wedge \sup \{ A^\alpha(x_2) / f(x_2) = y_2^\alpha \} \wedge \beta \\ &= (f(A^\alpha)(y_1) \wedge f(A^\alpha)(y_2)) \wedge \beta. \end{aligned}$$

Theorem 3.6: Let $f: L_1 \rightarrow L_2$ be lattice homomorphism and let B be a fuzzy sub lattice with threshold α of L_2 and G a finite group which acts on L. Then $f^{-1}(B^\alpha)$ is a fuzzy sub lattice with threshold α of L_1 , where $f^{-1}(B^\alpha)(x) = B(f(x)) = B(f(x^\alpha))$, for all $x \in L_1$.

Proof: For any $x_1^\alpha, x_2^\alpha \in L_1$.
 $f^{-1}(B^\alpha)(x_1 \vee x_2) \vee \alpha = B(f(x_1 \wedge x_2)) \vee \alpha$
 $= B(f(x_1) \wedge f(x_2)) \vee \alpha$ (since f is lattice homomorphism)
 $\geq (B(f(x_1)) \vee B(f(x_2))) \wedge \beta$
 $= (f^{-1}(B^\alpha)(x_1) \wedge f^{-1}(B^\alpha)(x_2)) \wedge \beta$

Similarly, we have
 $f^{-1}(B^\alpha)(x_1 \wedge x_2) \vee \alpha \geq (f^{-1}(B^\alpha)(x_1) \wedge f^{-1}(B^\alpha)(x_2)) \wedge \beta$, so $f^{-1}(B)$ is a fuzzy sub lattice with threshold α of L_1 .

Theorem 3.7: Let $f: L_1 \rightarrow L_2$ be a lattice homomorphism and let B be fuzzy ideal with threshold α of L_2 and G a finite group which acts on L. Then $f^{-1}(B)$ is a fuzzy ideal with threshold α of L_1 .

Proof: For any $x_1^\alpha, x_2^\alpha \in L_1$.
 $f^{-1}(B^\alpha)(x_1 \wedge x_2) \vee \alpha = B(f(x_1 \wedge x_2)) \vee \alpha$
 $= B(f(x_1) \wedge f(x_2)) \vee \alpha$
 $\geq (B(f(x_1)) \vee B(f(x_2))) \wedge \beta$ (since f is lattice homomorphism)
 $= (f^{-1}(B^\alpha)(x_1) \wedge f^{-1}(B^\alpha)(x_2)) \wedge \beta$. so $f^{-1}(B)$ is a fuzzy ideal of L_1 .

4. Fuzzy sub lattice with threshold α of Complemented Lattices

Let L be a lattice with greatest element 1 and the least element 0. Let $x \in L$. By a complement of x in L is meant an element y in L such that $x \wedge y = 0$ and $x \vee y = 1$.

Definition 4.1 [4]: A lattice L with the greatest element 1 and the least element 0 is called complemented if all its elements have unique complements.

Definition 4.2: A fuzzy subset A of a complemented lattice L is said to be fuzzy sub lattice with threshold α of L if, for all $x, y \in L$ (FSC1) $A(x \wedge y) \vee \alpha \geq (A(x) \wedge A(y)) \wedge \beta$ and (FSC2) $A(x \vee y) \vee \alpha \geq (A(x) \vee A(y)) \wedge \beta$ and $A(c) \vee \alpha \geq A(c) \wedge \beta$ where c^1 is the complement of c.

Theorem 4.1: Let A be a fuzzy sub lattice of a complemented lattice L and g a finite group which acts on L. Then the following are equivalent;

- (i) A^α is a fuzzy sub lattice with threshold α of L;
- (ii) A^α is a sub lattice of L for any $p \in [\alpha, \beta]$ where $A_p \neq \Phi$.

Proposition 4.1: If A be a fuzzy sub lattice of a complemented lattice L and G a finite group which acts on L, then $A^\alpha(0) \vee \alpha \geq A^\alpha(x) \wedge \beta$ and $A^\alpha(1) \vee \alpha \geq A^\alpha(x) \wedge \beta$ for $x \in L$.

Proof: For $x \in L$ and let x^1 be the complement of x. Then $A^\alpha(1) \vee \alpha = A^\alpha(x \vee x^1) \vee \alpha = (A^\alpha(x) \vee A^\alpha(x^1)) \wedge \beta \vee \alpha \geq ((A^\alpha(x) \wedge A^\alpha(x^1)) \wedge \beta) \vee \alpha = (A^\alpha(x) \wedge \beta) \vee \alpha \geq A^\alpha(x) \wedge \beta$. Again, $A^\alpha(0) \vee \alpha = (A^\alpha(x \wedge x^1) \vee \alpha) \vee \alpha \geq ((A^\alpha(x) \wedge A^\alpha(x^1)) \wedge \beta) \vee \alpha = (A^\alpha(x) \wedge \beta) \vee \alpha \geq A^\alpha(x) \wedge \beta$.

Proposition 4.2: If A be a fuzzy sub lattice of a complemented lattice L and G a finite group which acts on L. Suppose that $A^\alpha(0) \neq A^\alpha(1)$, then either $A^\alpha(0) \vee \alpha \geq \beta$ holds or $A^\alpha(0) \wedge A^\alpha(1) \geq \beta$ holds.

Proof: Suppose $A^\alpha(0) < A^\alpha(1)$, If $A^\alpha(0) \vee \alpha \geq \beta$ and $A^\alpha(0) \wedge A^\alpha(1) < \beta$.

Four cases are possible.
Case (i) : If $A^\alpha(0) > \alpha$ and $A^\alpha(0) < \beta$, then $A^\alpha(0) \vee \alpha = A^\alpha(0) < A^\alpha(1)$. Note that $A^\alpha(0) < \beta$, we obtain that $A^\alpha(0) <$

$A^\alpha(1) \wedge \beta$. that is $Ag(0) \vee \alpha < Ag(1) \wedge \beta$. This is a contradiction with the previous proposition.

Case(ii): : If $A^\alpha(0) > \alpha$ and $A^\alpha(1) < \beta$, then $A^\alpha(0) \vee \alpha = A^\alpha(0) < A^\alpha(1) = A^\alpha(1) \wedge \beta$. This is a contradiction with the previous proposition.

Case(iii): : If $A^\alpha(1) > \alpha$ and $A^\alpha(0) < \beta$, then from $A^\alpha(0) < \beta$ and $A^\alpha(0) < A^\alpha(1)$. we obtain that $A^\alpha(0) < A^\alpha(1) \wedge \beta$. From $\alpha < A^\alpha(1)$ and $\alpha < \beta$.we conclude that $\alpha < A^\alpha(1) \wedge \beta$. So $A^\alpha(0) \vee \alpha < A^\alpha(1) \wedge \beta$. This is a contradiction with the previous proposition.

Caes(iv): : If $A^\alpha(1) > \alpha$ and $A^\alpha(1) < \beta$, then from $A^\alpha(0) < A^\alpha(1)$ and $\alpha < A^\alpha(1)$.we obtain that $A^\alpha(0) \vee \alpha < A^\alpha(1) = A^\alpha(1) \wedge \beta$. This is a contradiction with the proposition 4.1.If $A^\alpha(1) < A^\alpha(0)$, we can prove the results dually.

Definition 4.3: A fuzzy subset A of a complemented lattice L is said to be fuzzy ideal with thresh hold of L if, for all $x, y \in L$ $(FSCI_1) A(x \wedge y) \vee \alpha \geq (A(x) \wedge A(y)) \wedge \beta$ and $(FSCI_2) A(x \vee y) \vee \alpha \geq (A(x) \vee A(y)) \wedge \beta$ and $(FSCI_3) A(c^1) \vee \alpha \geq A(c) \wedge \beta$ where c^1 is the complement of c.

Theorem 4.2: Let A be a fuzzy subset of L and G a finite group which acts on a complemented lattice L. Then the following are equivalent;

- (i) A^α is a fuzzy ideal with thresh hold of L;
- (ii) A^α is a sub lattice of L for any $p \in [\alpha, \beta]$ where $A_p \neq \Phi$.

Theorem 4.3: Let $f: L_1 \rightarrow L_2$ be a surjective homomorphism where L_1 and L_2 are complemented lattices and let A be fuzzy sub lattice with thresh hold of L_1 and G a finite group which acts on L_1 . Then $f(A^\alpha)$ is a fuzzy ideal with thresh hold of L_2 .

Theorem 4.4: :Let $f: L_1 \rightarrow L_2$ be lattice homomorphism where L_1 and L_2 are complemented lattices and let B be a fuzzy sub lattice with thresh hold of L_2 and G a finite group which acts on L_2 . Then $f^{-1}(B^\alpha)$ is a fuzzy sub lattice with thresh hold of L_1 , where $f^{-1}(B^\alpha)(x) = B(f(x))$, for all $x \in G$.

Theorem 4.5: Let L be a complemented lattice on which G acts on L and let f be a G- lattice homomorphism from L into L' . If B be a G-invariant fuzzy sub lattice with thresh hold of L' , then $f^{-1}(B)$ is a G-invariant fuzzy sub lattice with thresh hold of L.

Proof: Since B is G-invariant fuzzy sub lattice with thresh hold of L' . Therefore, $B^g = B$, for all $g \in G$. Now, $(f^{-1}(B))^g \vee \alpha = f(B^g) \vee \alpha \geq f(B) \wedge \beta$, for all $g \in G$. Therefore, $f^{-1}(B)$ is G-invariant fuzzy sub lattice with thresh hold of L.

Theorem 4.6: Let L be a complemented lattice on which G acts on L and let f be a bijective G-lattice homomorphism from L into L' . If A is a G-invariant fuzzy sub lattice of L, then $f(A)$ is a G-invariant fuzzy sub lattice of L' .

Proof: Since A is G-invariant fuzzy sub lattice with thresh hold of L. Therefore, $A^g = A$, for all $g \in G$. Now, $(f(A))^g \vee \alpha = f(A^g) \vee \alpha \geq f(A) \wedge \beta$, for all $g \in G$. Therefore, $f(A)$ is G-invariant fuzzy sub lattice with thresh hold of L' .

Conclusion: In this paper, we define the group action on fuzzy sub lattice lattices and introduce the notion fuzzy sub lattice and fuzzy ideals with thresh hold of complemented lattices. We also study the concept of G-invariant sub lattice of L. The homomorphic image and pre-image of fuzzy sub lattice with thresh hold of L also established. A number of associated results will be obtained. One can obtain the results in the field of bipolar fuzzy structures and soft substructures.

References

1. Ali T, Ray AK. On product of fuzzy sub lattices, The Journal of Fuzzy mathematic. 2007; 15(2):375-381.
2. Ajmal N, Thomas KV. Fuzzy Lattice-I, the Journal of Fuzzy Mathematics. 2012; 10(2):255-274.
3. Ajmal N, Thomas KV. Fuzzy Lattice-II, the Journal of Fuzzy Mathematics. 2012; 10(2):275-296.
4. Ajmal N, Thomas KV. Fuzzy Lattices, Infor Sciences 1994; 79:271-291.
5. Bhakat SK, Das P. Fuzzy subrings and ideals redefined, Fuzzy Sets Syst 1996; 81:383-393.
6. Birkhoff G. Lattice theory, American Mathematical Society, Providence, RI, 1984.
7. Bo Y, Wu Wang Ming. Fuzzy ideals on a distributive lattice, Fuzzy Sets Syst 1990; 35:231-240.
8. Goguen JA. L Fuzzy Sets, J Math Anal Appl. 1967; 18:145-174.
9. Han JC. Group Actions in a Regular Ring. Bulletin of the Korean Mathematical Society. 2005; 42:807-815.
10. Koguel BBN, Nkuimi C, Lele C. On fuzzy prime ideals of lattices, SAMSA Journal of Pure and Applied Mathematics. 2008; 3:1-11.
11. Liu WJ. Fuzzy invariant subgroups and fuzzy ideals, Fuzzy Sets Syst 1982; 8:133-139.
12. Rosenfeld: Fuzzy groups, J Math Anal Appl. 1971; 35:512-517.
13. Sharma RP, Sharma S. Group Action on Fuzzy Ideals. Communications in A, 1998.
14. Satya Saibaba GSV. Fuzzy lattice ordered groups, South East Asian Bulletin of Mathematics 32, 749-766 2008 | algebra, 26:4207-4220.
15. Tepavacevic A, Trajkovski G.L-fuzzy lattices: an introduction, Fuzzy Sets Syst 2001; 123:209-216.
16. Yao B. (λ, μ) -fuzzy normal subgroup and (λ, μ) -fuzzy quotient subgroups, Journal of fuzzy mathematics. 2005, 695-705.
17. Yao B. (λ, μ) - fuzzy subrings and (λ, μ) - fuzzy ideals, The Journal of fuzzy mathematics. 2007; 15(4):981-987.
18. Yao B. Fuzzy theory on group and ring, Science and Technolgy Press, Beijing (In Chinese), 2008.
19. Yuan X, Zhang CC, Ren Y. Generlized fuzzy groups and many-valued implications, Fuzzy sets and systems 2003; 138:205-211.
20. Zadeh LA. Fuzzy sets, Inform and Control 1965; 8:338-353



Dr. R. Nagarajan is Associate Professor and Head of Mathematics at J.J. College of Engineering and Technology, Trichy. He received the Ph.D degree from Bharathidasan University, Trichy. His main research interests are Group theory, Neutrosophic soft group, Near-ring, soft set and its applications and fuzzy algebraic structures.



ISSN Print: 2394-7500
 ISSN Online: 2394-5869
 Impact Factor: 5.2
 IJAR 2016; 2(6): 957-964
 www.allresearchjournal.com
 Received: 16-04-2016
 Accepted: 17-05-2016

Nagarajan R
 Associate Professor,
 Department of Mathematics,
 J.J. College of Engg& Tech,
 Trichirappalli-09, Tamil Nadu,
 India.

Saleem Abdullah S
 Associate Professor,
 Department of Mathematics,
 Abdul Wali khan University,
 Mardan, KP, Pakistan.

Balamurugan K
 Assistant Professor, M.A.M
 School of Engineering,
 Trichirappalli-105, Tamil
 Nadu, India.

Correspondence
Nagarajan R
 Associate Professor,
 Department of Mathematics,
 J.J. College of Engg& Tech,
 Trichirappalli-09, Tamil Nadu,
 India.

Brief discussions on T-level complex fuzzy subgroup

Nagarajan R, Saleem Abdullah S and Balamurugan K

Abstract

In this article, we combine complex fuzzy set and fuzzy subgroups. We introduce the notion of T-level complex fuzzy subgroups, step complex fuzzy subgroups and study fundamental properties. Also the basic operations like union, intersection, product, Cartesian product of two complex fuzzy subgroups are studied. Furthermore, we define a T-level subset and T-level subgroups and then some of their properties are studied.

Keywords: Complex fuzzy group, T-level subgroup, T-norm. Step complex fuzzy group, Cartesian product, phase term

1. Introduction

The concept of the fuzzy set was first introduced by Zadeh in a seminal paper in 1965 [13]. This is the generalization of crisp Set in terms of membership function. The notion of the fuzzy set A on the universe of discourse U is the set of order pair $\{(x, \mu_A(x)), x \in U\}$ with a membership function $\mu_A(x)$, taking the value on the interval $[0, 1]$. In [10] Rosenfeld used this concept to develop the theory of fuzzy groups. In fact, many basic properties in group theory are found to be carried over to fuzzy groups. Anthony and Sherwood [1] redefined fuzzy subgroups in terms of a t-norm which replaced the minimum operation and they characterized basic properties of t-fuzzy subgroups in [1, 2]. Sherwood [11] defined products of fuzzy subgroups using t-norms and gave some properties of these products. Ramot. [9], extended the fuzzy set to complex fuzzy set with membership function $z = r_s e^{-iws(x)}$ where $i = \sqrt{-1}$, which ranges in the interval $[0, 1]$ to a unit circle. Ramot *et al.* [8] also introduced different fuzzy complex operations and relations, like union, intersection, complement etc., still it is necessary to determine the membership functions correctly, which will give the appropriate or approximate result for real life applications. The membership function defined for the complex fuzzy set $z = r_s e^{iws(x)}$, which compromise an amplitude term $r_s(x)$ and phase term w_s . The amplitude term retains the idea of “fuzziness” and phase term signifies declaration of complex fuzzy set, for which the second dimension of membership is required. The complex fuzzy set allows extension of fuzzy logic that is i to continue with one dimension gradeness of membership. XinFu *et al.* [12] defined the fuzzy complex membership function of the form $z=a+ib$, where x, y are two fuzzy numbers with membership function $\mu_A(x), \mu_B(x)$ respectively. If b does not exist, z degenerates to a fuzzy number.

Xin Fu *et al.* [12], also discussed a complex number in cartesian form where $a=r_s \cos(x)$ and $b=r_s \sin(x)$, which are in polar forms defined in [8]. The fuzzy number is created by interpolating complex number in the support of fuzzy set [3-5, 8]. The membership function are usually difficult to determine accurately and one may argue of accurate or precise membership function are necessary in reality.

Following the above recent development the fuzzy set theory Zhang *et al.* [14] studies d-equality of complex fuzzy set. This is the logical development since a complex membership function should more difficult that a real membership function to be determine in practice. Complex fuzzy set is a unique framework over the advantage of traditional fuzzy set. The support of complex fuzzy set is unrestricted, may include any kind of object such as number, name etc, which is off course a complex number. The notion of T-norm and T-co norm are used throughout this paper [6].

This paper is organized in the following order. The review of complex fuzzy set and operations on it are discussed in section 2 and section 3 discussed t-level subgroups and its properties. The idea of step fuzzy complex subgroups are studied in section 4 followed by summary and suggestion for future work are given in section 5.

2. Complex fuzzy sets and operators

Definition -2.1: A complex fuzzy subset A, defined on a universe of discourse X, is characterized by a membership function $\tau_A(x)$ that assigns any element $x \in X$ a complex valued grade of membership in A. The values of $\tau_A(x)$ all lie within the unit circle in the complex plane and thus all of the form $P_A(x) e^{j\mu_A(x)}$ where $P_A(x)$ and $e^{j\mu_A(x)}$ are both real valued and $P_A(x) \in [0, 1]$. Here $P_A(x)$ is termed as amplitude term and $e^{j\mu_A(x)}$ is termed as phase term.

The complex fuzzy set may be represented in the set form as $A = \{(x, \tau_A(x)) / x \in X\}$. It is denoted by CFS.

The phase term of complex membership function belongs to $(0, 2\pi)$. Now we take those forms which Ramot. *et al.* presented in [8] to define the game of winner, neutral and lose.

$$\mu_{A \cup B}(x) = \begin{cases} \mu_A(x) & \text{if } p_A > p_B \\ \mu_B(x) & \text{if } p_A < p_B \end{cases}$$

This is a novel concept and it is the generalization of the concept “winner take all” introduced by Ramot. *et al.* [8] for the union of phase terms.

Example 2.1: Let $X = \{x_1, x_2, x_3\}$ be a universe of discourse. Let A and B be complex fuzzy sets in X as shown below.

$$\begin{aligned} A &= \{0.6 e^{i(0.8)}, 0.3 e^{i\frac{3\pi}{4}}, 0.5 e^{i(0.3)}\} \\ B &= \{0.8 e^{i(0.9)}, 0.1 e^{i\frac{\pi}{4}}, 0.4 e^{i(0.5)}\} \\ A \cup B &= \{0.8 e^{i(0.9)}, 0.3 e^{i\frac{3\pi}{4}}, 0.5 e^{i(0.3)}\} \end{aligned}$$

We can easily calculate the phase terms $e^{i\mu_{A \cap B}(x)}$ on the same line by winner, neutral and loser game.

Definition-2.2: Here a complex fuzzy subset A of a group G is said to be a complex fuzzy subgroup of G if for all $x, y \in G$ (CFSG1) $A(xy) \geq \min \{A(x), A(y)\}$, (CFSG2) $A(x^{-1}) \geq A(x)$ where the product x and y is denoted by xy and the inverse of x by x^{-1} . It is well known and easy to see that a complex fuzzy subgroup G satisfies $A(x) \leq A(e)$ and $A(x^{-1}) = A(x)$ for all $x \in G$, where ‘e’ is the identity of G.

Definition-2.3 [11]: A triangular norm (briefly a t-norm) is a function $T: [0,1] \times [0,1] \rightarrow [0,1]$ satisfying, for each p, q, r, s $\in [0,1]$

- (1) $T(p, 1) = p$
- (2) $T(p, q) \leq T(r, s)$ if $p \leq r$ and $q \leq s$,
- (3) $T(p, q) = T(q, p)$,
- (4) $T(p, T(q, r)) = T(T(p, q), r)$.

The following are the basic properties of operations on complex fuzzy sets.

Proposition 2.1: Let A, B, C be those complex fuzzy sets on X. Then

- (i) $(A \cup B) \cap C = (A \cap C) \cup (B \cap C)$
- (ii) $(A \cap B) \cup C = (A \cup C) \cap (B \cup C)$

Proof: Let A, B, C be those complex fuzzy sets on X and $\mu_A(x), \mu_B(x), \mu_C(x)$ are membership functions. Then we have

$$\begin{aligned} \tau_{(A \cup B) \cap C}(x) &= P_{(A \cup B) \cap C}(x) e^{i\mu_{(A \cup B) \cap C}(x)} \\ &= \min \{P_{A \cup B}(x), P_C(x)\} e^{i \min \{\mu_{A \cup B}(x), \mu_C(x)\}} \\ &= \min \{\max\{P_A(x), P_B(x)\}, P_C(x)\} e^{i \min \{\max\{\mu_A(x), \mu_B(x)\}, \mu_C(x)\}} \\ &= \max \{\min\{P_A(x), P_C(x)\}, \min\{P_B(x), P_C(x)\}\} e^{i \max \{\min\{\mu_A(x), \mu_C(x)\}, \min\{\mu_B(x), \mu_C(x)\}\}} \\ &= \max \{P_{A \cap C}(x), P_{B \cap C}(x)\} e^{i \max \{\mu_{A \cap C}(x), \mu_{B \cap C}(x)\}} \\ &= P_{(A \cap C) \cup (B \cap C)}(x) e^{i\mu_{(A \cap C) \cup (B \cap C)}(x)} \\ &= \tau_{(A \cap C) \cup (B \cap C)}(x) \end{aligned}$$

Similarly, we can show (ii).

Proposition 2.2: Let A and B be two complex fuzzy sets in X. Then

- (i) $(A \cup B) \cap A = A$
- (ii) $(A \cap B) \cup A = A$.

Proof: Let A and B be two complex fuzzy sets in X and $\mu_A(x), \mu_B(x)$ are membership functions. Then we have

$$\begin{aligned} \tau_{(A \cup B) \cap A}(x) &= P_{(A \cup B) \cap A}(x) e^{i\mu_{(A \cup B) \cap A}(x)} \\ &= \min \{P_{A \cup B}(x), P_A(x)\} e^{i \min \{\mu_{A \cup B}(x), \mu_A(x)\}} \\ &= \min \{\max\{P_A(x), P_B(x)\}, P_A(x)\} e^{i \min \{\max\{\mu_A(x), \mu_B(x)\}, \mu_A(x)\}} \end{aligned}$$

$$\begin{aligned}
 &= P_A(x) e^{i\mu_A(x)} \\
 &= \tau_A(x)
 \end{aligned}$$

Similarly, we can show (ii).

Proposition 2.3: Let A and B be two complex fuzzy sets in X. Then

- (i) $A \vee (A \wedge B) = A$
- (ii) $A \wedge (A \vee B) = A$ (Absorption laws)

Proof

$$\begin{aligned}
 \tau_{A \cup (A \cap B)}(x) &= P_{A \cup (A \cap B)}(x) e^{i\mu_{A \cup (A \cap B)}(x)} \\
 &= \max \{P_A(x), P_{A \cap B}(x)\} e^{i\max\{\mu_A(x), \mu_{A \cap B}(x)\}} \\
 &= \max \{P_A(x), \min\{P_A(x), P_B(x)\}\} e^{i\max\{\mu_A(x), \min\{\mu_A(x), \mu_B(x)\}\}} \\
 &= \min\{\max\{P_A(x), P_A(x)\}, \max\{P_A(x), P_B(x)\}\} e^{i\min\{\max\{\mu_A(x), \mu_A(x)\}, \max\{\mu_A(x), \mu_B(x)\}\}} \\
 &= P_A(x) e^{i\mu_A(x)} \\
 &= \tau_A(x)
 \end{aligned}$$

Similarly, we can show (ii).

Proposition 2.4: Let A and B be two complex fuzzy sets in X. Then

- (i) $A \vee B = B \vee A$
- (ii) $A \wedge B = B \wedge A$ commutative Law

Proof: Let A and B be two complex fuzzy sets in X and $\mu_A(x), \mu_B(x)$ are membership functions. Then we have

$$\begin{aligned}
 \tau_{A \cup B}(x) &= P_{A \cup B}(x) e^{i\mu_{A \cup B}(x)} \\
 &= \max \{P_A(x), P_B(x)\} e^{i\max\{\mu_A(x), \mu_B(x)\}} \\
 &= \max \{P_B(x), P_A(x)\} e^{i\max\{\mu_B(x), \mu_A(x)\}} \\
 &= P_{B \cup A}(x) e^{i\mu_{B \cup A}(x)} \\
 &= \tau_{B \cup A}(x)
 \end{aligned}$$

Similarly, we can show (ii).

Definition-2.4: Let S be a groupoid and T is a t-norm. A function $B: S \rightarrow [0,1]$ is a subgroupoid of S iff for every x, y in S, $B(xy) \geq T\{B(x), B(y)\}$. If S is group, a t-complex fuzzy subgroupoid B is a t-complex fuzzy subgroup of S iff for each $x \in S$, $B(x^{-1}) \geq B(x)$.

Definition-2.5: For each $i = 1, 2, \dots, n$, let A_i be a t-complex fuzzy subgroup in a group X_i . Let T be a T-norm. The T-product of A_i ($i = 1, 2, \dots, n$) is the function,

$$\begin{aligned}
 &A_1 \times A_2 \times \dots \times A_n : X_1 \times X_2 \times \dots \times X_n \rightarrow [0,1] \text{ defined by} \\
 &(A_1 \times A_2 \times \dots \times A_n)(x_1, x_2, \dots, x_n) = T(A_1(x_1), A_2(x_2), \dots, A_n(x_n)).
 \end{aligned}$$

Definition-2.6: For each $i = 1, 2, \dots, n$, let A_i be a complex fuzzy subgroup under a minimum operation in a group X_i , the membership function of the product

$$\begin{aligned}
 &A = A_1 \times A_2 \times \dots \times A_n \text{ in } X = X_1 \times X_2 \times \dots \times X_n \text{ is defined by} \\
 &(A_1 \times A_2 \times \dots \times A_n)(x_1, x_2, \dots, x_n) = \min\{A_1(x_1), A_2(x_2), \dots, A_n(x_n)\}.
 \end{aligned}$$

Definition-2.7: Let A be a complex fuzzy subset of a set X and let $t \in [0,1]$. The set $A_t = \{x \in X : A(x) \geq t\}$ is called a level subset of A.

Definition-2.8: A complex fuzzy subgroup A of a group X is called complex fuzzy normal if for all x, y in G it fulfills the following condition: $A(xy) = A(yx)$.

Definition-2.9: A complex fuzzy subgroup A of a group X is said to be conjugate to a complex fuzzy subgroup B of G if there exists x in G such that for all g in G $A(g) = B(x^{-1}gx)$.

The following are the properties of Complex fuzzy sets

Theorem-2.1: Every complex fuzzy subset A of the universe of discourse X is a complex fuzzy subgroup of X.

Proof: Let A be a complex fuzzy subset of X. Then for all $x, y \in X$.

$$\begin{aligned}
 \text{CFG-1 } A(xy) &= p(xy) e^{j\mu(xy)} \\
 &\geq \min \{p(x), p(y)\} \cdot e^{j \min\{\mu(x), \mu(y)\}} \\
 &\geq \min \{p(x), p(y)\} \cdot e^{j\mu(x)} \cdot e^{j\mu(y)} \\
 &\geq \min \{p(x) e^{j\mu(x)}, p(y) e^{j\mu(y)}\} \\
 &\geq \min \{A(x), A(y)\}
 \end{aligned}$$

$$\text{CFG-2 } A(x^{-1}) = p(x^{-1}) e^{j\mu(x^{-1})} \geq p(x) e^{j\mu(x^{-1})} \geq p(x) e^{j\mu(x)} \geq A(x)$$

Complex fuzzy subgroup conditions satisfied.

Therefore A forms a Complex fuzzy subgroup of X.

Theorem 2.2: Intersection of non-empty collection of complex fuzzy subgroup is a complex fuzzy subgroup.

Proof:

$$\begin{aligned} \text{CFG-1 } (\bigcap_{i \in I} A_i)(xy) &= \text{Inf}_{i \in I} A_i(xy) \\ &\geq \text{Inf}_{i \in I} \{\min\{A_i(x), A_i(y)\}\} \\ &\geq \min\{\text{Inf}_{i \in I} A_i(x), \text{Inf}_{i \in I} A_i(y)\} \\ &\geq \min\{\bigcap_{i \in I} A_i(x), \bigcap_{i \in I} A_i(y)\} \end{aligned}$$

$$\text{CFG-2 } (\bigcap_{i \in I} A_i)(x^{-1}) = \text{Inf}_{i \in I} A_i(x^{-1}) \geq \text{Inf}_{i \in I} A_i(x^{-1}) \geq \bigcap_{i \in I} A_i(x)$$

Definition-2.10: Let A and B be two complex fuzzy sets on X, and $\tau_A(x) = r_A(x) e^{j\mu_A(x)}$ and $\tau_B(x) = r_B(x) e^{j\mu_B(x)}$ be their membership functions, respectively. The union and intersection of A and B if denoted as $A \cup B$ and $A \cap B$, which is specified by a function

$$\tau_{A \cup B}(x) = r_{A \cup B}(x) e^{j\mu_{A \cup B}(x)} = (r_A(x) \vee r_B(x)) e^{j(\mu_A(x) \vee \mu_B(x))}, \text{ where } \vee \text{ denote the max operator.}$$

$$\tau_{A \cap B}(x) = r_{A \cap B}(x) e^{j\mu_{A \cap B}(x)} = (r_A(x) \wedge r_B(x)) e^{j(\mu_A(x) \wedge \mu_B(x))}, \text{ where } \wedge \text{ denote the min operator.}$$

Theorem-2.3: Union of two complex fuzzy subgroups is also a complex fuzzy subgroup.

Proof: Let A and B be two complex fuzzy subgroups.

Now let $x, y \in X$,

$$\begin{aligned} \text{(CFG-1) } \tau_{A \cup B}(xy) &= r_{A \cup B}(xy) e^{j\mu_{A \cup B}(xy)} \\ &= (r_A(xy) \vee r_B(xy)) e^{j(\mu_A(xy) \vee \mu_B(xy))} \\ &\geq ((r_A(x) \wedge r_A(y)) \vee ((r_B(x) \wedge r_B(y)) e^{j((\mu_A(x) \wedge \mu_A(y)) \vee (\mu_B(x) \wedge \mu_B(y)))}) \\ &\geq ((r_A(x) \vee r_A(y)) \wedge ((r_B(x) \vee r_B(y)) e^{j((\mu_A(x) \vee \mu_A(y)) \wedge (\mu_B(x) \vee \mu_B(y)))}) \\ &\geq (r_A(x) \vee r_B(x)) e^{j\mu_{A \cup B}(x)} \wedge (r_A(y) \vee r_B(y)) e^{j\mu_{A \cup B}(y)} \\ &\geq \min\{\tau_{A \cup B}(x), \tau_{A \cup B}(y)\} \end{aligned}$$

$$\begin{aligned} \text{(CFG-2) } \tau_{A \cup B}(x^{-1}) &= r_{A \cup B}(x^{-1}) e^{j\mu_{A \cup B}(x^{-1})} \\ &= (r_A(x^{-1}) \vee r_B(x^{-1})) e^{j(\mu_A(x^{-1}) \vee \mu_B(x^{-1}))} \\ &\geq (r_A(x) \vee r_B(x)) e^{j(\mu_A(x) \vee \mu_B(x))} = r_{A \cup B}(x) e^{j\mu_{A \cup B}(x)} \geq \tau_{A \cup B}(x) \end{aligned}$$

Theorem 2.4: Intersection of two complex fuzzy subgroups is also a complex fuzzy subgroup.

Proof: The result is obvious.

Theorem 2.5: The product of complex fuzzy subgroup is also a complex fuzzy subgroup.

Proof: Let A and B be two complex fuzzy subgroups of X.

Now let $x, y \in X$,

$$\begin{aligned} \text{(CFG-1) } \tau_{A \cup B}(xy) &= r_{A \cup B}(xy) e^{j\mu_{A \cup B}(xy)} \\ &= (r_A(xy) \cdot r_B(xy)) e^{j2\pi \left(\frac{\mu_A(xy)}{2\pi} \cdot \frac{\mu_B(xy)}{2\pi} \right)} \\ &\geq (\min\{r_A(x), r_A(y)\} \cdot \min\{r_B(x), r_B(y)\}) e^{j2\pi \left(\frac{\min\{\mu_A(x), \mu_A(y)\}}{2\pi} \cdot \frac{\min\{\mu_B(x), \mu_B(y)\}}{2\pi} \right)} \\ &\geq \min\{r_A(x) \cdot r_B(x), r_A(y) \cdot r_B(y)\} e^{j2\pi \left(\frac{\mu_{A \cup B}(x)}{2\pi} \cdot \frac{\mu_{A \cup B}(y)}{2\pi} \right)} \\ &\geq \min\{r_{A \cup B}(x), r_{A \cup B}(y)\} e^{j\mu_{A \cup B}(x)} \cdot e^{j\mu_{A \cup B}(y)} \\ &\geq \min\{r_{A \cup B}(x) e^{j\mu_{A \cup B}(x)}, r_{A \cup B}(y) e^{j\mu_{A \cup B}(y)}\} \\ &\geq \min\{\tau_{A \cup B}(x), \tau_{A \cup B}(y)\} \end{aligned}$$

CFG-1 is satisfied.

$$\text{(CFG-2) } \tau_{A \cup B}(x^{-1}) = r_{A \cup B}(x^{-1}) e^{j\mu_{A \cup B}(x^{-1})} \geq r_{A \cup B}(x) e^{j\mu_{A \cup B}(x)} \geq \tau_{A \cup B}(x) \text{CFG-2 is satisfied.}$$

Definition-2.11: Let A and B be two complex fuzzy sets on X, and $\tau_A(x) = r_A(x) e^{j\mu_A(x)}$ and $\tau_B(x) = r_B(x) e^{j\mu_B(x)}$ be their membership functions, respectively. The complex product of A and B, denoted as $A \circ B$ and is specified by a function

$$\tau_{A \circ B}(x) = r_{A \circ B}(x) e^{j\mu_{A \circ B}(x)} = (r_A(x) \cdot r_B(x)) e^{j2\pi \left(\frac{\mu_A(x)}{2\pi} \cdot \frac{\mu_B(x)}{2\pi} \right)}$$

Definition 2.12: Let A and B be two complex fuzzy sets on X. Then the cartesian product of A and B is defined as

$$\begin{aligned} (A \times B)(x, y) &= r_{A \times B}(x, y) e^{j\mu_{A \times B}(x, y)} \\ &= \min\{r_A(x), r_B(y)\} \cdot e^{j(\mu_A(x) \vee \mu_B(y))} \\ &= \min\{r_A(x), r_B(y)\} \cdot e^{j\mu_A(x)} \cdot e^{j\mu_B(y)} \\ &= \min\{r_A(x) e^{j\mu_A(x)}, r_B(y) e^{j\mu_B(y)}\} \\ &= \min\{A(x), B(y)\} \text{ where } A(x) = r_A(x) e^{j\mu_A(x)} \end{aligned}$$

Note 2.6: Complement of complex fuzzy subgroup is not a complex fuzzy subgroup.

Proof: By definition,

$$\begin{aligned} \tau_{C(S)}(x) &= P_{C(S)}(x) e^{j\mu_{C(S)}(x)} \\ &= (1 - P_S(x)) e^{j(2\pi - \mu_S(x))} \end{aligned}$$

$$\begin{aligned} \text{Now, } \tau_{C(S)}(xy) &= (1 - P_S(xy)) e^{j(2\pi - \mu_S(xy))} = 1 - \tau_S(xy) \\ &\leq 1 - \min \{ \tau_S(x), \tau_S(y) \} \\ &\leq \max \{ 1 - \tau_S(x), 1 - \tau_S(y) \} \\ &\leq \max \{ \tau_{C(S)}(x), \tau_{C(S)}(y) \} \end{aligned}$$

Complement of complex fuzzy subgroup is not a complex fuzzy subgroup.

Proposition 2.5: For all $a, b \in [0, 1]$ and 'm' is any positive integer, verify that

- (i) If $a < b$, then $a^m < b^m$ and
- (ii) $\text{Min}\{a, b\} = \min\{a^m, b^m\}$.

Proof: It is obvious.

Proposition 2.6: If X is a group, then $X^m = \{x, (A_X(x))^m / x \in X\}$ is a complex fuzzy subgroup.

Proof: Let X is a complex fuzzy subgroup, where (X, \cdot) is a group. Thus (X^m, \cdot) is a group for all positive integer m . Let 'm' is a positive integer and $x, y \in X^m$.

$$\begin{aligned} \text{(CFG-1) } (A^m(xy)) &= (A(xy))^m \\ &\geq \min\{A(x), A(y)\}^m \\ &= \min \{ (A(x))^m, (A(y))^m \} \\ &= \min \{ mA(x), mA(y) \} \\ \text{(CFG-1) } (A^m(x^{-1})) &= (A(x^{-1}))^m \geq (A(x))^m \geq (A^m(x)) \\ \therefore (X^m, \cdot) &\text{ is a complex fuzzy subgroup.} \end{aligned}$$

Corollary-2.7: The complex fuzzy subgroup X^n is a complex fuzzy subgroup of X^m , if $m \leq n$.

Proof: Clearly X^n and X^m are complex fuzzy subgroups by above theorem, for all $x \in [0, 1]$, $X^m \geq X^n$ implies then $X^n \subset X^m$. (Since $A_n(x) \leq A_m(x)$ for all $x \in X$).

3. T-level subgroup

In this section, we introduce a definition of a t-level subset of a complex fuzzy subset and then we give some of the important algebraic results.

Definition-3.1: Let 'A' be a complex fuzzy subset of a set X , T a t-norm and $r \in [0, 1]$. Then we define a T-level subset of a complex fuzzy subset A as

$$A_r^T = \{x \in G / T(A(x), r) \geq r\}.$$

The following are the main results based on the above definition 3.1

Theorem-3.1: Let X be a group and A be T-complex fuzzy subgroup of X , then the t-level subset $A_r^T, r \in [0, 1]$, is a subgroup of X .

Proof: $A_r^T = \{x \in G / T(A(x), r) \geq r\}$ is clearly non-empty.

Let $x, y \in A_r^T$, then $T(A(x), r) \geq r$ and $T(A(y), r) \geq r$.

Since 'A' is T-complex fuzzy subgroup of X , $A(xy) = p(xy) e^{j\mu(xy)} \geq T(A(x), A(y))$ is satisfied.

This means $T(A(xy), r) \geq T(T(A(x), A(y)), r) = T(A(x), T(A(y), r)) \geq T(A(x), r) \geq r$.

Hence $xy \in A_r^T$.

Since 'A' is T-complex fuzzy subgroup, $A(x^{-1}) = A(x)$ and hence $T(A(x^{-1}), r) = T(A(x), r) \geq r$.

This means that $x^{-1} \in A_r^T$. Therefore A_r^T is a subgroup of X .

Theorem-3.2: Let X be a group and A be a complex fuzzy subgroup of X , then the T-level subset $A_r^T, r \in [0, 1]$, $T(A(e), r) \geq r$, is a subgroup of X , where 'e' is the identity of X .

Proof: $A_r^T = \{x \in G / T(A(x), r) \geq r\}$ is clearly non-empty.

Let $x, y \in A_r^T$, then $T(A(x), r) \geq r$ and $T(A(y), r) \geq r$.

Since 'A' is a subgroup of X , $A(xy) = p(xy) e^{j\mu(xy)} \geq \min \{A(x), A(y)\}$ is satisfied.

This means that $T(A(xy), r) \geq T(\min \{A(x), A(y)\}, r)$, where there are two cases:

$\min \{A(x), A(y)\} = A(x)$ or $\min \{A(x), A(y)\} = A(y)$.

Since $x, y \in A_r^T$, also in two cases $T(\min \{A(x), A(y)\}, r) \geq r$.

Therefore $T(A(xy), r) \geq r$. Thus we get $xy \in A_r^T$. It is easily seen that, as above $x^{-1} \in A_r^T$. Hence

A_r^T is a subgroup of X .

Theorem-3.3: Let X be a group and A be a complex fuzzy subset of X such that A_r^T is a subgroup of X for all $r \in [0, 1]$, $T(A(x), r) \geq r$, then A is a T-fuzzy complex subgroup of X .

Proof: Let $x, y \in X$ and let $T(A(x), r_1) = r_1$ and $T(A(y), r_2) = r_2$.

Then $x \in A_{r_1}^T, y \in A_{r_2}^T$. Let us assume that $r_1 < r_2$. Then these follows $T(A(x), r_1) < T(A(y), r_2)$

And $A_{r_2}^T \subseteq A_{r_1}^T$. So $y \in A_{r_1}^T$. Thus $x, y \in A_{r_1}^T$ and since $A_{r_1}^T$ is a subgroup of X , by hypothesis,

$xy \in A_{r_1}^T$. Therefore $T(A(xy), r_1) \geq r_1 = T(A(x), r_1)$, $T(A(y), r_1) = T(T(A(x), A(y)), r_1)$.

Thus we get $T(A(xy), r_1) \geq T(T(A(x), A(y)), r_1)$. As a T-norm is monotone with respect to each variable and symmetric, we have $A(xy) = p(xy) e^{i\mu(xy)} \geq T(A(x), A(y))$.

Next, let $x \in X$ and $T(A(x), r) = r$. Then $x \in A_r^T$. Since A_r^T is a subgroup, $x^{-1} \in A_r^T$.

Therefore $T(A(x^{-1}), r) \geq r$ and hence $T(A(x^{-1}), r) \geq T(A(x), r)$. So we have $A(x^{-1}) \geq A(x)$.

Thus A is a T-complex fuzzy subgroup of X .

Theorem-3.4: Let A and B be t-level subsets of the sets X_1 and X_2 , respectively, and let $r \in [0, 1]$. Then $A \times B$ is also a T-level subset of $X_1 \times X_2$.

Proof: Since any T-norm T is associative, using definition-2.5 and definition-3.1, we can write the following statements,

$$T((A \times B)(a, b), r) = T(T(A(a), B(b)), r) = T(A(a), T(B(b), r)) \geq T(A(a), r) \geq r.$$

This completes the proof.

Definition-3.2: Let X be a group and A be a T-complex fuzzy subgroup of X . The subgroups A_r^T , $r \in [0, 1]$ and $T(A(x), r) \geq r$ are called T-level subgroup of A .

The following theorems are proved based on the definition 3.2

Theorem-3.5: Let X_1 and X_2 be two groups. A and B a T-complex fuzzy subgroup of X_1 and X_2 respectively. Then the T-level subset $(A \times B)_r^T$; for $r \in [0, 1]$ is a subgroup of $X_1 \times X_2$, where e_{x_1} and e_{x_2} are identities of X_1 and X_2 respectively.

Proof: $(A \times B)_r^T = \{(x, y) \in X_1 \times X_2; T((A \times B)(x, y), r) \geq r\}$.

Since $T((A \times B)(e_{x_1}, e_{x_2}), r) = T(T(A(e_{x_1}), B(e_{x_2})), r) \geq T(A(e_{x_1}), r) \geq r$

$\therefore (A \times B)_r^T$ is non empty. Let $(x_1, y_1), (x_2, y_2) \in (A \times B)_r^T$, then $T((A \times B)(x_1, y_1), r) \geq r$ and

$T((A \times B)(x_2, y_2), r) \geq r$. Since $A \times B$ is a t-complex fuzzy subgroup of $X_1 \times X_2$,

we get $(A \times B)((x_1, y_1)(x_2, y_2)) = T(A(x_1x_2), B(y_1y_2))$.

Using A and B are t-complex fuzzy subgroup, we get

$$T((A \times B)(x_1x_2, y_1y_2)) \geq T(T(A(x_1x_2), B(y_1y_2)), r)$$

$$= T(A(x_1x_2), T(B(y_1y_2), r)) \geq T(A(x_1x_2), r) \geq r$$

Hence $(x_1, y_1), (x_2, y_2) \in (A \times B)_r^T$. Again $(x, y) \in (A \times B)_r^T$ implies

$$T((A \times B)(x, y)^{-1}, r) = T((A \times B)(x^{-1}, y^{-1}), r)$$

$$= T(T(A(x^{-1}), B(y^{-1})), r) = T(A(x^{-1}), T(B(y^{-1}), r)) \geq T(A(x^{-1}), r) \geq r$$

This means that $(x, y)^{-1} \in (A \times B)_r^T$. Therefore $(A \times B)_r^T$ is a subgroup of $X_1 \times X_2$.

Theorem-3.6: Let X be a group and A_r^T a T-level subgroup of X . If A is a normal t-complex fuzzy subgroup, then A_r^T is a normal subgroup of X .

Proof: By theorem-3.1 A_r^T is a T-level subgroup of X . Now let us show that A_r^T is normal. For all

$a \in X$ and $x \in A_r^T$, $T(A(axa^{-1}), r) = T(A(aa^{-1}x), r) = T(A(x), r) \geq r$.

Thus $axa^{-1} \in A_r^T$. Hence A_r^T is a normal subgroup of X .

Theorem-3.7: Let A, B be complex fuzzy subsets of the sets X_1 and X_2 , respectively, T be a t-norm and $r \in [0, 1]$. Then $A_r^T \times B_r^T = (A \times B)_r^T$.

Proof: Let (a, b) be an element of $A_r^T \times B_r^T$. Then $a \in A_r^T$ and $b \in B_r^T$. By definition-3.1, we can write $T(A(a), r) \geq r$ and $T(B(b), r) \geq r$.

Using definition-2.3 and definition-2.5 we get

$$T((A \times B)(a, b), r) = T(T(A(a), B(b)), r) = T(A(a), T(B(b), r)) \geq T(A(a), r) \geq r.$$

Thus we have $(a, b) \in (A \times B)_r^T$. Now let $(a, b) \in (A \times B)_r^T$, this is required following statements

$$T((A \times B)(a, b), r) = T(T(A(a), B(b)), r) = T(A(a), T(B(b), r)) \geq r = T(1, r). \text{ Thus the inequality}$$

$$T(A(a), r) \geq r \text{ and } T(B(b), r) \geq r \text{ is satisfied. Hence } (a, b) \text{ is in } A_r^T \times B_r^T.$$

This completes the proof.

Theorem-3.8: Let A_1, A_2, \dots, A_n be complex fuzzy subgroups under a minimum operation in groups X_1, X_2, \dots, X_n respectively, $r \in [0, 1]$. Then

$$(A_1 \times A_2 \times \dots \times A_n)_r^T = A_{1r}^T \times A_{2r}^T \times \dots \times A_{nr}^T.$$

Proof: Let (a_1, a_2, \dots, a_n) be an element of $(A_1 \times A_2 \times \dots \times A_n)_r^T$.

Using definition-2.3 and definition-2.5 we can write

$$T(\min((A_1 \times A_2 \times \dots \times A_n)(a_1, a_2, \dots, a_n)), r) = T(\min(A_1(a_1), A_2(a_2), \dots, A_n(a_n)), r).$$

For all $i=1, 2, \dots, n$, $\min(A_1(a_1), A_2(a_2), \dots, A_n(a_n)) = A_i(a_i)$.

This gives us $T(\min(A_1(a_1), A_2(a_2), \dots, A_i(a_i), \dots, A_n(a_n)), r) = T(A_i(a_i), r) \geq r$.

Thus we have $a_i \in A_{ir}^T$. That is $(a_1, a_2, \dots, a_n) \in A_{1r}^T \times A_{2r}^T \times \dots \times A_{nr}^T$.

Similarly, let (a_1, a_2, \dots, a_n) be an element of $A_{1r}^T \times A_{2r}^T \times \dots \times A_{nr}^T$. Then for all $i=1, 2, \dots, n$,

$a_i \in A_{ir}^T$. That is, $T(A_i(a_i), r) \geq r$.

Since $\min(A_1(a_1), A_2(a_2), \dots, A_i(a_i), \dots, A_n(a_n)) = A_i(a_i)$ and $T(A_i(a_i), r) \geq r$, we get $T((A_1 \times A_2 \times \dots \times A_n)(a_1, a_2, \dots, a_n), r) = T(\min(A_1(a_1), A_2(a_2), \dots, A_i(a_i), \dots, A_n(a_n)), r) = T(A_i(a_i), r) \geq r$.

Thus $(a_1, a_2, \dots, a_n) \in (A_1 \times A_2 \times \dots \times A_n)_r^T$.

Finally, this completes the proof.

4. Step complex fuzzy subgroup

Let X be a group and T be a t-norm. We have the following.

Definition-4.1: Let 'A' be a complex fuzzy subgroup of X with respect to T . Then 'A' is called step complex fuzzy subgroup of X with respect to T if for every $\lambda \in [0,1]$ A_λ is a subgroup of X when $A_\lambda \neq \emptyset$.

Theorem-4.1: Let 'A' be a complex fuzzy subgroup of X with respect to T . Then λ is a step complex fuzzy subgroup of X with respect to T if and only if $A(xy) \geq \min\{A(x), A(y)\}$ for all $x, y \in X$.

Proof: Suppose $A(xy) \geq \min\{A(x), A(y)\}$ for all $x, y \in X$.

When $A_\lambda \neq \emptyset$, $\lambda \in [0,1]$. Let $x, y \in A_\lambda$. Then

$A(xy^{-1}) \geq \min\{A(x), A(y^{-1})\} = \min\{A(x), A(y)\} \geq \lambda$.

Hence $xy^{-1} \in A_\lambda$ is a subgroup of X .

Conversely, suppose there are $x, y \in X$ such that $A(xy) < \min\{A(x), A(y)\}$.

Put $\lambda = \min\{A(x), A(y)\}$, then $x, y \in A_\lambda$. Because $A(xy) < \min\{A(x), A(y)\} = \lambda$.

$\therefore xy \notin A_\lambda$. A_λ is not a subgroup of X .

Consider the t-norm T , $T_0(a, b) = \min\{a, b\}$, for all $(a, b) \in [0,1] \times [0,1]$. We get the following corollary.

Corollary-4.2: Suppose A is a complex fuzzy subgroup of X with respect to T . Then

(i) A is a step complex fuzzy subgroup of X with respect to T_0 .

(ii) Furthermore, A is a step complex fuzzy subgroup of X with respect to T , where T is an arbitrary t-norm.

Proof: (i) Because $A(xy) \geq T_0(A(x), A(y)) = \min\{A(x), A(y)\}$ for all $x, y \in X$, it follows from the above theorem that A is a step complex fuzzy subgroup of X with respect to T_0 .

(ii) This conclusion follows from (i) and that fact $T_0 \geq T$.

Definition-4.2: Let 'A' be a step complex fuzzy subgroup of X with respect to T . Suppose $A(X)$ is the range of A . $A(X) = \{A(x) / x \in X\}$.

If the $A(X)$ is finite; $A(X) = \{a_0, a_1, \dots, a_m\}$, with $1 \geq a_0 \geq a_1 \geq \dots \geq a_m \geq 0$, the integer m is called the length of A .

If the $A(X)$ is countable; $A(X) = \{a_0, a_1, \dots, a_m, \dots\}$, with

$1 \geq a_0 \geq a_1 \geq \dots \geq a_m \geq \dots \geq 0$, the length of A is defined by $+\infty$.

Theorem-4.3: Let 'A' be a step complex fuzzy subgroup of X with respect to T , the length of A is ℓ . $A(X) = \{a_0, a_1, \dots, \frac{a}{2}\}$, with $1 \geq a_0 \geq a_1 \geq \dots \geq \frac{a}{2} \geq 0$. Suppose

$A = \{A_\lambda / \lambda \in [0,1], A_\lambda \neq \emptyset\}$. Then $B = \{A_{c_1}, A_{c_2}, \dots, A_{c_\ell}\}$ and we can get a subgroup series without repetition in X : $\{e\} \leq A_{a_0} \leq A_{a_1} \leq \dots \leq A_{a_\ell} = X$.

Proof: Let i be an integer.

Case-(i) : If $0 \leq i \leq \ell$, then there exists a $x_i \in X$; $A(x_i) = a_i$, hence $A_{a_i} \neq \emptyset$. By definition 3.1,

A_{a_i} ($i=0,1,2,\dots,\ell$) is a subgroup of X .

Case-(ii) : If $1 \leq i < i+1 \leq \ell$, then clearly $A_{a_i} \subseteq A_{a_{i+1}}$. Because there is a $x_{i+1} \in X$ such that

$A(x_{i+1}) = a_{i+1}$. And $a_{i+1} < a_i$, then $x_{i+1} \in A_{a_{i+1}}$, $x_{i+1} \notin A_{a_i}$. Hence $A_{a_i} \neq A_{a_{i+1}}$,

$A_{a_i} < A_{a_{i+1}}$.

Because $e = \min A(X)$, then for all $x \in X$, $A(x) \geq a_\ell$, thus $A_{a_\ell} \supseteq X$. Hence $A_{a_\ell} = X$.

Therefore, we get sequence $\{e\} \leq A_{a_0} \leq A_{a_1} \leq \dots \leq A_{a_\ell} = X$.

For all $A_\lambda \in B$, if $a_{i+1} \leq \lambda \leq a_i$, $1 \leq i+1 \leq \ell$, then

$A_\lambda = \{x / x \in X, A(x) \geq \lambda\} = \{x / x \in X, A(x) \geq a_i\} \cup \{x / x \in X, \lambda \leq A(x) \leq a_i\} = A_{a_i} \cup \emptyset = A_{a_i}$.

If $\lambda > a_0$, then $A_\lambda = \emptyset$, $A_\lambda \notin B$.

If $\lambda < a_\ell$, then $A_\lambda \supseteq A_{a_\ell} = X$, hence $A_\lambda = A_{a_\ell}$.

$\therefore B \subseteq \{A_{a_0}, A_{a_1}, A_{a_2}, \dots, A_{a_\ell}\}$.

5. Summary and future work: The work presented in this paper is the novel frame work of step complex fuzzy subgroups. In this paper the various properties and operation of complex fuzzy set are investigated. We also presented the properties of t-level complex fuzzy subgroups. A further study is required to implement these notions in real life applications such as soft set, Bipolar fuzzy complex set, vague set and rough set etc.

6. References

1. Anthony JM, Sherwood H. Fuzzy groups redefined, J. Math. Anal. Appl. 1979; 69:124-130.
2. Anthony JM, Sherwood H. A characterization of fuzzy subgroups, Fuzzy Sets and Systems. 1982; 7:297-305.
3. Buckley JJ. Fuzzy Complex Number in Proceedings of ISFK, Gaungzhou, China, 1987, 597-700.
4. Buckley JJ. Fuzzy Complex Number”, Fuzzy Sets & Systems. 1989; 33:333-345.
5. Buckley JJ. Fuzzy Complex Analysis I: Differentiation, Fuzzy Sets & Systems. 1991; 4:269-284.
6. Jang JSR, Sun CT, Mizutani E. Neuro-Fuzzy and Soft Computing, PHI, New Delhi, 2005.
7. Pedrycz, Gomide F. Introduction to Fuzzy Set Analysis and Design, PHI, New Delhi, 2004.
8. Ramot Daniel, Menahem Friedman, Gideon Langholz, Abraham Kandel. Complex Fuzzy Logic, IEEE Transactions on Fuzzy Systems, 2003, 11-4.
9. Ramot Daniel, Menahem Friedman, Gideon Langholz, Abraham Kandel, Complex Fuzzy Set, IEEE Transactions on Fuzzy Systems, 2002, 10-2.
10. Rosenfeld A, Fuzzy groups J. Math Anal Appl. 1971; 35:51-517.
11. Sherwood H. Products of fuzzy subgroups, Fuzzy Sets and Systems. 1983; 11:79-89.
12. Xin Fu, Qiang Shen. A Novel Framework of Complex Fuzzy Number and Its Application to Computational Modeling, FUZZ –IEEE 2009, Korea, 2009, 20-24.
13. Zadeh LA. Fuzzy Sets, Information & Control. 1965; 8:338-353.
14. Zhang Guangquan, Tharam Singh Dillon, Kai-yung Cai Jun Ma, Jie Lu. δ -Equality of Complex Fuzzy Relations, 24th IEEE International Conference on Advance Information Networking and Application, 2010.
15. Zhang GQ. Fuzzy distance and limit of fuzzy number, fuzzy system and mathematics. 1992; 6(1):21-28.
16. Zhang GQ Fuzzy limit theory of fuzzy complex number, fuzzy Set system. 1992; 46:227-235.



Dr. R. Nagarajan is Associate Professor and Head of Mathematics at J.J. College of Engineering and Technology, Trichy. He received the Ph.D degree from Bharathidasan University, Trichy. His main research interests are Group theory, Neutrosophic soft group, Near-ring, soft set and its applications and fuzzy algebraic structures.